BAW-1621

July 1980

— B&W 177-FA Owners Group —

EFFECTS OF ASYMMETRIC LOCA LOADINGS

— Phase II Analysis —

BABCOCK & WILCOX
Power Generation Group
Nuclear Power Generation Division
P. O. Box 1260
Lynchburg, Virginia 24505

AUTHORS

Contributing authors from Babcock & Wilcox:

R. B. Allen
R. L. Antoun
M. K. Au-Yang
D. J. Ayres
R. C. Ballou
J. R. Biller
J. C. Brown
J. J. Canning
D. A. Chipley
D. C. Compton
W. J. deCooman
T. W. Elvin
J. E. Galford
C. E. Harris
R. L. Howard
D. L. Howell
R. C. Jones
C. C. Lin
E. A. Malone
W. D. Maxham
W. C. Nester
R. P. Potekhen
J. E. Ramsey
F. M. Rundle
N. K. Savani
S. J. Shah
K. C. Shieh
E. B. Tuttle

Contributing authors from EDS Nuclear:

J. M. Eidin[illegible]
S. Esfandiari
B. M. Hinton
A. T. Jackson
C. T. Liu
M. Manrique
W. G. Morimoto
J. P. Morray, Jr.
T. O. Muraki
P. R. Shah
P. C. Strange

ACKNOWLEDGMENT

The Babcock & Wilcox Company wishes to express its gratitude to EDS Nuclear, Inc., of San Francisco, California, for their professional advice and input to the evaluations documented herein.

CONTENTS

CONTENTS (Cont'd)

CONTENTS (Cont'd)

CONTENTS (Cont'd)

CONTENTS (Cont'd)

List of Tables

Tables (Cont'd)

Tables (Cont'd)

Tables (Cont'd)

Tables (Cont'd)

List of Figures

Figures (Cont'd)

Figures (Cont'd)

Figures (Cont'd)

Figures (Cont'd)

Figures (Cont'd)

Figures (Cont'd)

Figures (Cont'd)

Figures (Cont'd)

Figures (Cont'd)

Figures (Cont'd)

Figures (Cont'd)

1. INTRODUCTION AND SCOPE

On January 25, 1978, the U. S. Nuclear Regulatory Commission's Division of Operating Reactors requested all PWR licensees to proceed with an evaluation of asymmetric LOCA (loss of coolant accident) loadings. In response to that request, The Babcock & Wilcox Company (B&W) has performed a detailed Phase II evaluation to determine the effects of these loadings on components and equipment within the reactor vessel subcompartment for the B&W 177-Fuel Assembly Owners Group plants. In addition, a preliminary assessment of the effects of asymmetric loadings within the steam generator compartment was also performed.

This report summarizes the results and describes the methods and techniques used in performing these evaluations for the following member utilities of the B&W 177-FA Owners Group:

Arkansas Power & Light	Arkansas Nuclear One, Unit 1 (ANO-1)
*Consumers Power Company	Midland Units 1 and 2
Duke Power Company	Oconee Units 1, 2, and 3
Florida Power Corporation	Crystal River 3 (CR-3)
Metropolitan Edison Company	Three Mile Island 1 and 2 (TMI-1,-2)
Sacramento Municipal Utility District	Rancho Seco
Toledo Edison Company	Davis-Besse 1 (DB-1)

- - - - -

*Consumers Power Company has participated in this program for the evaluation of the Midland 1 and 2 fuel assemblies and reactor internals only.

2. SUMMARY OF RESULTS

Using the methods described in section 5, linear elastic loadings were developed for the components and structures affected by the postulated primary piping guillotine ruptures within the reactor vessel subcompartment; these loadings are tabulated in section 9. Estimated loadings were also developed for the steam generator supports and for the unbroken primary coolant piping for the postulated guillotine pipe breaks within the steam generator subcompartment; methods for estimating these loadings are discussed in section 11. Each component or structure was then evaluated for the applied loadings and the resultant stresses were compared to the acceptance limits; the methods used in evaluating these components are discussed in sections 6 and 11 of this report. A plant-specific summary of this Phase II evaluation is shown in Table 2-1. Detailed plant-specific results are presented in section 10. Additional analyses were performed to verify the assumptions used in the analysis and to evaluate vessel support stability and function. These results are discussed in section 12.

For postulated pipe ruptures within the reactor vessel subcompartment (Table 2-1):

- The Oconee 1, 2, and 3 reactor vessel support exceeded acceptance limits by 10%, and the control rod drive mechanisms exceeded the acceptance limits by 5% for the applied loadings developed by linear elastic techniques. In no instance was a loss of function or a structural instability predicted for these components. The vessel support embedment exceeded acceptance limits, but gross structural integrity and stability were maintained. Core flood line integrity and a core coolable geometry were demonstrated.
- For TMI-1, the stresses in the reactor vessel supports, embedments, and control rod drive attachments exceeded acceptance limits for the postulated hot leg rupture. However, as discussed in section 12, the existing hot leg restraint can be modified to reduce the hot leg break opening area so that

the postulated cold leg rupture would become the governing design case. For the postulated cold leg rupture, the results for all components would be within acceptance limits except for the reactor vessel support, which would exceed limits by only 1.5%, which is considered acceptable. Core flood line supports near the nozzle are overloaded, but these supports are not necessary for LOCA and the effects on piping stresses were included in the core flood piping analysis. The reactor cavity walls exceeded limits but gross structural integrity was demonstrated.

- For TMI-2, the detailed Phase II evaluations have not been completed; the applied loadings and available stress results are tabulated throughout this report to provide information until the detailed evaluations can be concluded.
- For Crystal River 3, the stresses in the reactor vessel supports, embedments, and control rod drive attachments exceeded acceptance limits for the postulated hot leg rupture. However, as discussed in section 12, the existing hot leg restraints can be modified to reduce the hot leg break opening area so that the postulated cold leg rupture would become the governing design case. For the postulated cold leg rupture, the stresses for all components would be within acceptance limits except for the reactor vessel support, which would exceed limits by only 1.5%, which is considered acceptable. In the present configuration, without hot leg restraint modifications, core flood line stresses are within acceptance limits. Line supports near the nozzle are overloaded, but these supports are not necessary for LOCA and the effects on piping stresses were included in the core flood piping analysis. A core coolable geometry was also demonstrated for Crystal River with the present hot leg restraint configuration and reactor vessel stability was demonstrated.
- For ANO-1, the results were within the acceptance limits except for the reactor cavity walls, which exceeded limits by 10%. The walls experienced localized yielding only, and this is considered acceptable for structural integrity for reinforced concrete. Core flood line supports near the nozzle are overloaded, but these supports are not necessary for LOCA and the effects on piping stresses were included in the core flood piping analysis.
- For Rancho Seco, the results were within the acceptance limits except for the reactor vessel support embedment. For the embedment, local stresses were exceeded only at the hatchway for only one of the postulated cold leg

ruptures and gross structural integrity and stability were maintained. A capacity reduction factor of 0.85 was included in the embedment evaluation, which if set to unity would provide ratios within acceptance limits.

- The Davis-Besse 1 results were within limits for the postulated pipe ruptures.
- The Midland 1 and 2 reactor internals and fuel assemblies were also within the acceptance limits. Midland participated in this program for an evaluation of reactor internals and fuel assemblies only.
- As discussed in section 12, additional evaluations were performed to validate certain assumptions used in the phase II analysis to confirm the final results. It was determined that lateral clearances were required in the cable trays and walkways between the service support structure and the refueling walls to prevent high stresses from occurring in the service support structure shell during the postulated pipe ruptures. As previously discussed, it was also determined that the existing hot leg restraints on TMI-1 and Crystal River 3 could be modified to limit the hot leg break opening area so that the acceptance criteria would be within limits for all components for these plants. It was also determined that vessel support stability was maintained for all plants with the exception of TMI-1 and TMI-2; for TMI-1, the hot leg restraint modification would ensure vessel stability. The evaluation of vessel stability for TMI-2 has not been completed.

For postulated ruptures within the steam generator subcompartment (Table 2-1):

- For the postulated breaks within the steam generator subcompartment, the steam generator supports and the remaining attached unbroken piping were demonstrated to be acceptable for all plants except for the piping on Davis-Besse 1. In developing these estimated loadings for Davis-Besse, the gapped piping restraints in the reactor vessel wall penetrations were modeled as linear elements with the subsequent effect that highly conservative loadings were developed for this evaluation. Additional evaluations would be expected to demonstrate acceptability for the Davis-Besse piping.

Table 2-1. Summary of Results – Ratio of Limiting Stress or Strain to Acceptance Limits

Component	Oconee 1, 2, 3	TMI-1	TMI-2	Crystal River-3	ANO-1	Rancho Seco	Davis Besse-1	Midland 1, 2
Reactor vessel support	1.10[d][o]	1.32[a] 1.015[b][o]	See Note[c]	1.32[a][o] 1.015[b][o]	Acceptable	Acceptable	Acceptable	See Note[i]
RV support embedment	1.29[e]	1.02[a][m] Acceptable[b]		1.04[a][m'] Acceptable[b]	Acceptable	1.08[f]	Acceptable	
Reactor internals and fuel assemblies	Acceptable	Acceptable		Acceptable	Acceptable	Acceptable	Acceptable	Acceptable
Core flood lines	Acceptable	Acceptable		Acceptable	Acceptable	Acceptable	Acceptable	See Note (i)
Core flood line supports	Acceptable	See Notes(g) & (g')		See Notes(g) &(g')	See Note(g)	Acceptable (g')	Acceptable (g')	
Unbroken piping (for pipe ruptures within RV compartment)	Acceptable	Acceptable		Acceptable	Acceptable	Acceptable	Acceptable	
Reactor cavity walls	Acceptable	1.09[n]		Acceptable	1.10[i]	Acceptable	Acceptable	
Service support structures — Structures	Acceptable	Acceptable		Acceptable	Acceptable	Acceptable	Acceptable	
Service support structures — RV Att'mt	Acceptable	Acceptable		Acceptable	Acceptable	Acceptable	Acceptable	
Control rod drives — Mechanism	1.05[n]	Acceptable		Acceptable	Acceptable	Acceptable	Acceptable	
Control rod drives — RV Att'mt	Acceptable	1.42[a] Acceptable[b]		1.42[a] Acceptable[b]	Acceptable	Acceptable	Acceptable	
Hot leg rupture restraints	Acceptable	Acceptable[b]		Acceptable	Acceptable	Acceptable	Acceptable[k]	
Steam generator supports	Acceptable	Acceptable	Acceptable	Acceptable	Acceptable	Acceptable	Acceptable	
Unbroken primary piping (for pipe ruptures within steam generator compartment)	Acceptable	Acceptable	Acceptable	Acceptable	Acceptable	Acceptable	See Note[j]	

Table 2-1. (Cont'd)

(a) Results given for hot leg pipe rupture.

(b) Results given for modified hot leg rupture restraint to reduce hot leg break opening area. (See Section 12)

(c) Portions of the TMI-2 detailed evaluations have not yet been completed, therefore, a component specific summary is not possible at this time. The completed results are recorded throughout this report for information only.

(d) Loadings developed using linear elastic techniques.

(e) Ratio based on strain limits as predicted by non-linear analysis. Ratio based on load is 1.07 with only localized yielding. A capacity reduction factor of 0.75 is included which if set to unity will result in an acceptable ratio. Gross structural integrity and stability is maintained. (Section 6.2).

(f) Local stress exceeded at notchway only. Capacity reduction factor of 0.85 is included; if capacity reduction factor were set to unity, acceptable ratios would result. Gross structural integrity and stability is maintained. (Section 6.2).

(g) One or more active supports in direction of load fails and is considered in the piping analysis. Failed supports are not req. red for LOCA loading. (Section 6.9).

(g') Credit taken for 100% increase in rated load of snubbers for LOCA loading. (Section 6.9).

(h) Results based on stress criteria and inelastic analysis. Maximum strain ratio is 0.34 (See discussion of functionality.(Section 6.10).

(i) Localized yielding only - considered acceptable for structural integrity.

(j) Limits exceeded at one location only (Section 11). Loadings determined by conservative linear methods

(k) As documented in Toledo Edison Verification Report Docket No. 50-346, Rev. 1, dated March 7, 1980.

(l) Evaluations of these components were not performed in this analysis. Consumers Power Co. participated in this program for the evaluation of the Midland 1 and 2 Fuel Assemblies and Reactor Internals only.

(m) Ratio based on strain limits as predicted by non linear analysis. Ratio based on load would be less than 1% over allowable. Capacity reduction factor is included. If capacity reduction factor were set to unity acceptable ratios would result. Gross structural integrity and stability is maintained. (Section 6.1).

(m') Ratio based on elastic analysis. Insignificant as redundant load paths were not considered. Capacity reduction factor is included; if set to unity acceptable ratios would result.

(n) Results for Control Rod Drives which have been mechanically hone. Results are within acceptance limits for all remaining drives (Section 10.4).

(o) Reactor Vessel Stability is maintained (Section 12).

3. CONCLUSIONS

For Postulated pipe ruptures within the reactor vessel subcompartment:

- The results of this analysis using the methods, techniques, and assumptions described in this report have demonstrated that core coolable geometry, core flood line integrity, and reactor vessel stability are maintained for Oconee 1, 2, 3, Crystal River 3, ANO-1, Rancho Seco, and Davis-Besse 1 for the postulated pipe ruptures within the reactor vessel subcompartment. For TMI-1, coolable geometry, core flood line integrity, and reactor vessel stability will be provided by modifying the existing hot leg restraint to limit the pipe break opening area.
- For Midland Units 1 and 2, the reactor internals and fuel assemblies are acceptable for LOCA loadings, and no further evaluation is required for these components.
- The detailed Phase II evaluations have not been completed for TMI-2; thus, specific conclusions cannot be made at this time.

For postulated pipe ruptures within the steam generator subcompartment:

- For Oconee 1, 2, 3, TMI-1 and 2, Crystal River 3, ANO-1, and Rancho Seco, the steam generator supports and unbroken piping stresses are within acceptance limits for these postulated pipe ruptures.
- For Davis-Besse 1, the steam generator support stresses are within acceptance limits, and additional evaluations (if required) would be expected to demonstrate the acceptability of the remaining attached primary piping.

4. METHODOLOGY FOR DEVELOPMENT OF PRESSURE LOADINGS

The following sections describe the methods used to select pipe break locations, to determine the effective pipe break opening areas and times, and to determine the asymmetric fluid pressures acting within the reactor internals and subcompartment for the selected breaks.

4.1. Pipe Break Locations

In evaluating the effects of asymmetric loadings on components in the reactor vessel subcompartment, hot and cold leg guillotine pipe breaks were considered at the terminal ends of the reactor vessel nozzles, at the entrance to the lower hot leg elbow, and at the cold leg elbow exit, as illustrated in Figure 4.1-1. These break locations were selected on the basis of actual pipe stress calculations performed in accordance with references 7 and 8. Locations for breaks near the reactor vessel are identical for both nozzle-supported and skirt-supported reactor vessels.

Figure 4.1-1. Pipe Break Locations for Reactor Vessel Cavity Evaluation

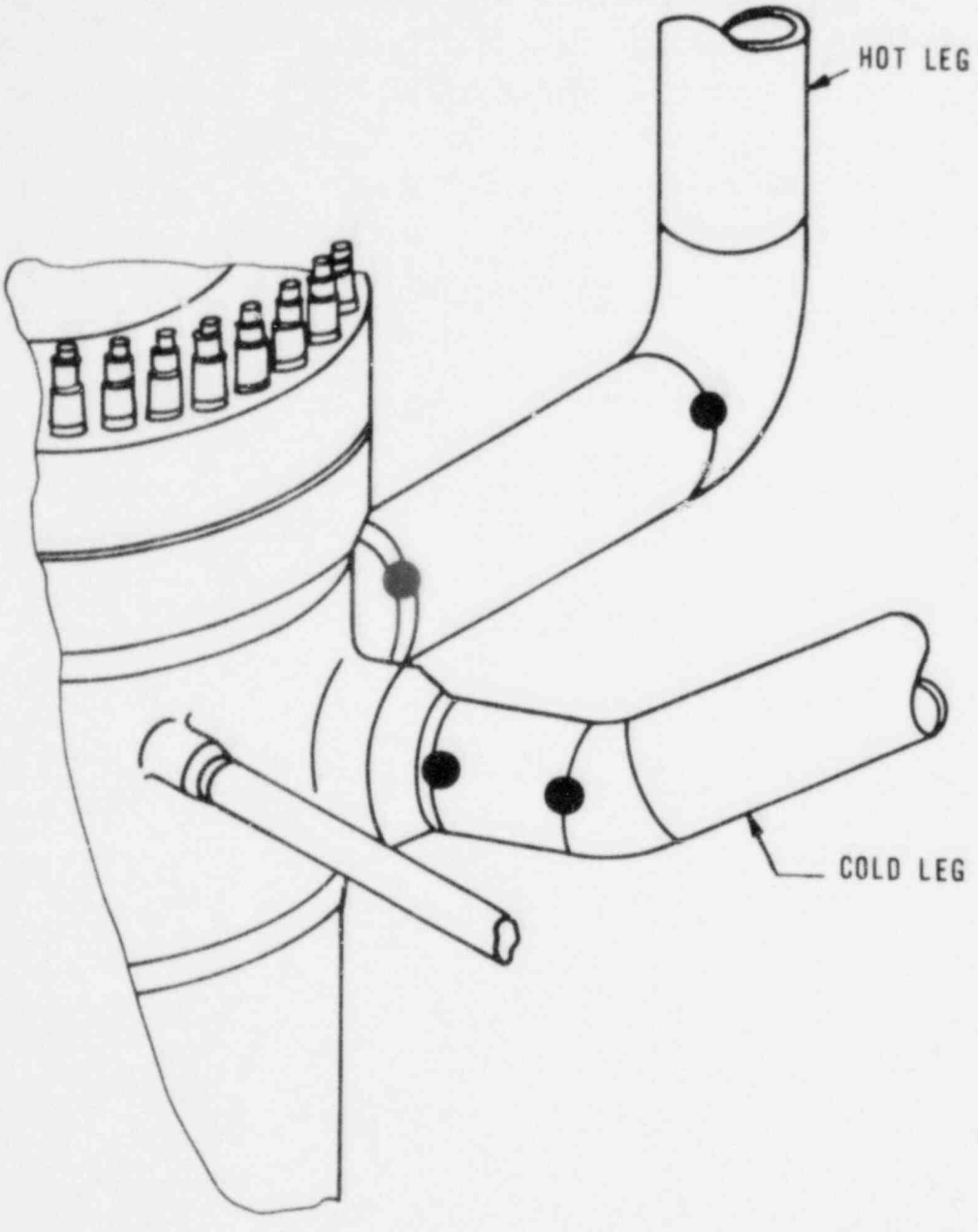

4.2. Determination of Break Opening Areas and Times

The break opening area (BOA) is the size of the opening through which primary cooling water can escape through a broken-end pipe section. The largest possible BOA is referred to as a 2A break, which implies that the coolant water escapes freely from the full area (A) of each end of the broken pipe without interference from the other end. Break opening area is a function of pipe backout, dt, and offset, dn (see Figure 4.2-2). Break opening time is the time at which a break occurs. Together BOA and break opening times determine the break opening schedule. Break opening schedules, i.e. BOA versus time, may be determined by any of the following three methods. The most conservative method is to assume that a break develops within 10 ms (linearly) to a 2A final BOA. This is the fastest postulated break opening time for a 2A guillotine break.

A less conservative method involves what is called the "generic" break opening schedule. The generic break opening time is determined by applying a constant PA forcing function to the broken-end piping in an isolated model of each piping section. Boundary conditions are modeled appropriately. No piping restraint effects are included for the generic analysis, so that the broken-end pipe moves freely without interferences. The generic analysis yields two sets of data; one for skirt-supported plants and one for the nozzle-supported plant. The time required for a 2A break to open would be longer than the 10 ms mentioned in the first method. The time before a 2A break would represent the fastest possible break opening time for a particular type of plant if there were no piping restraints.

The most realistic method is to determine actual BOA time histories based on plant-specific data, i.e., including all effects due to piping restraints. Comparing the generic method to the plant-specific method would show that for a specific BOA the generic method would always yield the faster opening time.

This section discusses the techniques used in evaluating the break opening areas and summarizes the plant-specific results.

4.2.1. Break Opening Area Equation

For a double-ended rupture that is not restrained, the two ends separate and move apart in space. This results in fluid releases from both pipe ends and is called a 2A break opening area.

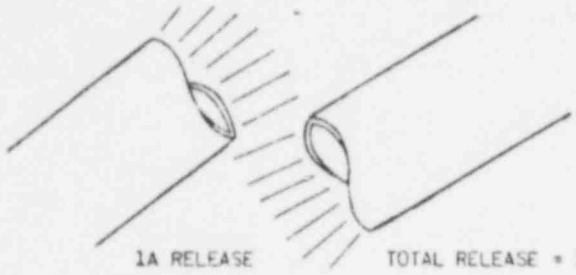

The displacements of the reactor coolant piping may be limited by pipe whip restraints and adjacent concrete walls or structures. This limitation of pipe displacement may result in a break opening "flow" area of less than 2A, which is referred to as a limited displacement rupture. The displacement of the broken pipe ends, and hence the BOA, is monitored as a function of time in a nonlinear pipe whip analysis (section 5.2).

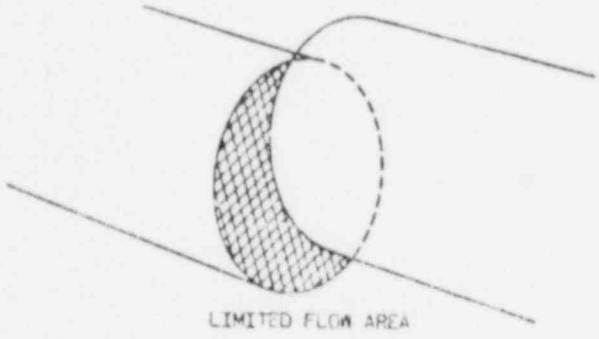

The basic theory used to calculate the break area from pipe end separation and lateral movement is as follows:

The broken ends of the pipe segment under consideration are designated a and b. The relative displacement of ends a and b determines the opening area associated with a double-ended rupture. These relative displacements are calculated by

$$\Delta x = Ux_{b-a}(t) = Ux_b(t) - Ux_a(t),$$

$$\Delta y = Uy_{b-a}(t) = Uy_b(t) - Uy_a(t),$$

$$\Delta z = Uz_{b-a}(t) = Uz_a(t) - Uz_z(t)$$

where Ux, Uy, and Uz are displacements in the global X, Y, and Z directions; and Δx, Δy, and Δz are relative displacements between two ends of the broken pipes in the global direction.

The opening area is calculated by

$$A = 2\left\{\pi r_i^2 - (r_i^2\theta_i + r_o^2\theta_o) + \frac{1}{2}(r_i^2 \sin 2\theta_i + r_o^2 \sin 2\theta_o) + [ABS(d_t)](r_i\theta_i + r_o\theta_o)\right\}$$

if $dn > t$ or $A = 2\pi r_i d_t$ if $dn < t$

where

r_i = inner radius of pipe,

r_o = outer radius of pipe,

$t = r_o - r_i$,

$\theta_i = \cos^{-1}[(r_i^2 + dn^2 - r_o^2)/2dn\ r_i]$,

$\theta_o = \sin^{-1}[(r_i \sin \theta_i)/r_o]$,

$d_t = \Delta x \sin \alpha_y \cos \alpha_x + \Delta y \cos \alpha_y - \Delta z \sin \alpha_y \sin \alpha_x$,

$dn^2 = d^2 - d_t^2$,

$d^2 = \Delta x^2 + \Delta y^2 + \Delta z^2$.

α_y and α_x are the orientation angles of the undeformed pipe where guillotines are postulated (see Figure 4.2-1). The geometric parameters are detailed in Figure 4.2-2.

4.2.2. Use of BOA Time Histories

The BOA time history, as discussed in 4.2.1, is used in calculating the mass-energy release, which is used to calculate asymmetric cavity pressures (section 4.3). The BOA time history is also the basis for calculation of blowdown pressure differentials across the reactor vessel internals (section 4.4).

4.2.3. Break Opening Area Data

Tables 4.2-1 and 4.2.2 and Figures 4.2-3 through 4.2-17 summarize the BOAs and opening times for each plant. These data were produced from analyses of the pipe whip models described in Appendix B.

Table 4.2-1. Summary of Owners Group Plant Hot Leg Breaks — Break Opening Area and Time

Plant	Break location	Peak BOA			Peak flow area ratio including RV motion	Figure No.
		Flow area ratio(a)	Time to peak, s	Time to peak unrestrained, s		
Oconee	RV nozzle	0.46A	0.027	0.0157	0.52A	4.2-3
	Elbow	0.45A	0.020	0.0157	(b)	4.2-4
TMI-1	RV nozzle	1.29A	0.045	0.0259	1.39A	4.2-5
	Elbow	1.04A	0.033	0.0235	(b)	4.2-6
CR-3	RV nozzle	1.09A	0.046	0.0241	1.17A	4.2-7
	Elbow	.85A	0.033	0.0211	(b)	4.2-8
ANO-1	RV nozzle	0.31A	0.030	0.0127	0.38A	4.2-9
	Elbow	0.27A	0.018	0.0121	(b)	4.2-10
Rancho Seco	RV nozzle	0.68A	0.041	0.0193	0.74A	4.2-11
	Elbow	0.55A	0.026	0.0175	(b)	4.2-12
DB-1	RV nozzle	1.02A	0.063	0.0265	(c)	4.2-13
	Elbow	1.03A	0.056	0.0265	(c)	4.2-14

(a) 1A hot leg = 1017.87 in.^{2}

(b) Reactor vessel displacement due to hot leg elbow breaks is negligible since most of the deflection results from horizontal cavity loads, and the elbow break is located outside the cavity. Therefore, the BOA is not effected by elbow breaks.

(c) The Davis-Besse 1 plant displacements and loads were calculated using plant-specific results, i.e., cavity forces were calculated from the reported BOA time histories, whereas the skirt supported plants were based on a spectrum of generic BOAs and times. The contribution of reactor vessel displacement to BOA for the skirt-supported plants was calculated to ensure that the BOA was within the analyzed curve. The Davis-Besse 1 BOA due to RV displacement is negligible.

Table 4.2-2. Summary of Owners Group Plant Cold Leg Breaks — Break Opening Area and Time

Plant	Break location	Peak BOA			Peak flow area ratio including RV motion	Figure No.
		Flow area ratio[a]	Time to peak, s	Time to peak unrestrained, s		
Oconee	RV nozzle	2.0	0.027	Same	(b)	4.2-15
	Elbow	2.0	0.027	Same	(b)	4.2-15
TMI-1	RV nozzle	2.0	0.027	Same	(b)	4.2-15
	Elbow	2.0	0.027	Same	(b)	4.2-15
CR-3	RV nozzle	2.0	0.027	Same	(b)	4.2-15
	Elbow	2.0	0.027	Same	(b)	4.2-15
ANO-1	RV nozzle	2.0	0.027	Same	(b)	4.2-15
	Elbow	2.0	0.027	Same	(b)	4.2-15
Rancho Seco	RV nozzle	2.0	0.027	Same	(b)	4.2-15
	Elbow	2.0	0.027	Same	(b)	4.2-15
DB-1	RV nozzle	0.25	0.100	0.0163	(c)	4.2-16
	Elbow	1.17	0.049	0.036	(c)	4.2-17

(a) 1A cold leg = 615.75 in.^{2}

(b) Not applicable to 2A breaks.

(c) See note (c) on Table 4.2-1.

Figure 4.2-1. Undeformed Pipe

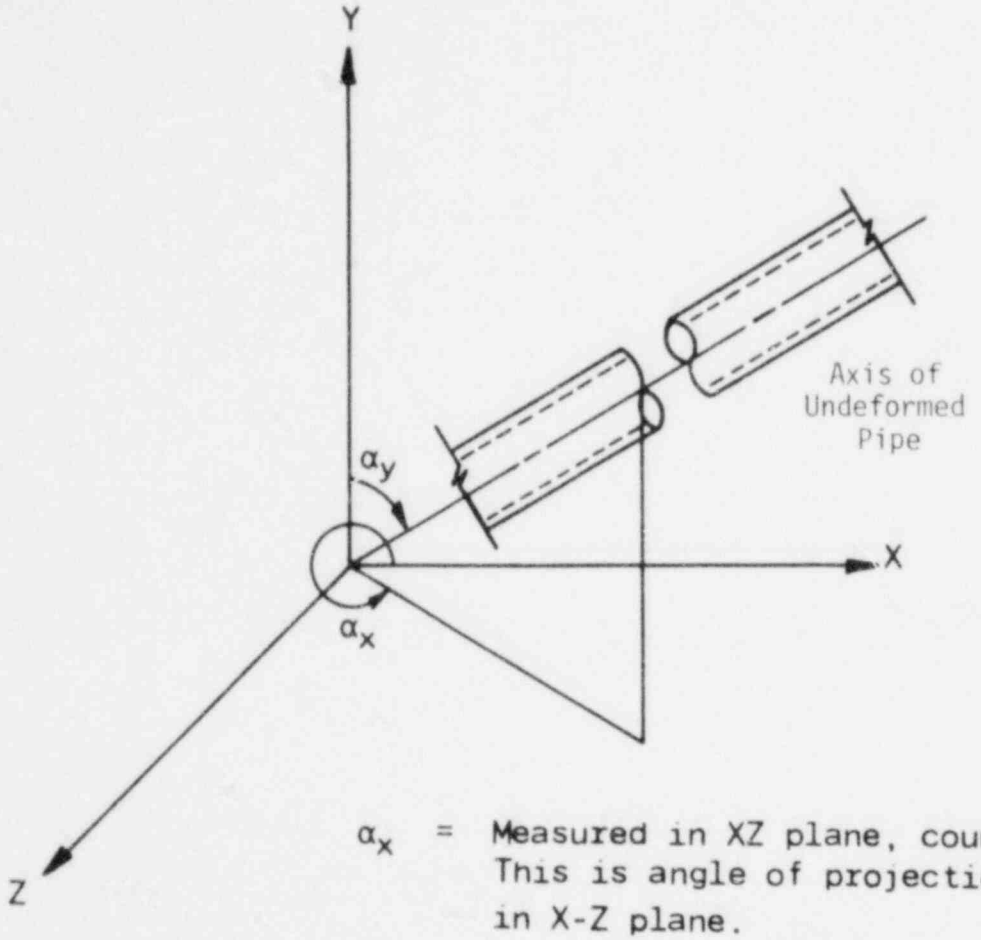

α_x = Measured in XZ plane, counter clockwise. This is angle of projection of the pipe in X-Z plane.

α_y = Angle with respect to vertical axis

X,Y,Z = Global axes

Figure 4.2-2. Pipe Break Area Due to Axial Plus Radial Displacements

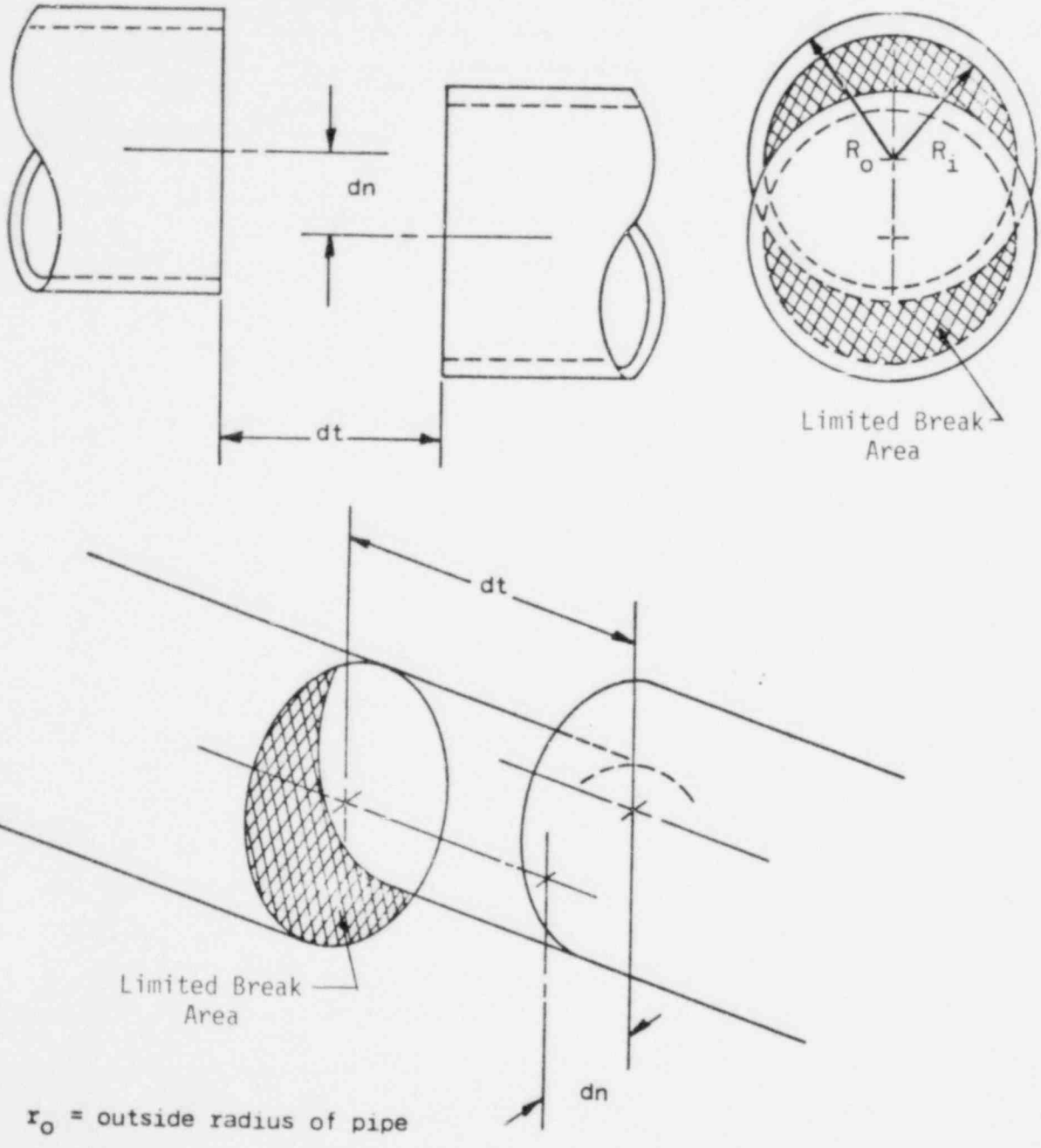

r_o = outside radius of pipe

r_i = inside radius of pipe

dn = radial displacement

dt = axial displacement

Figure 4.2-3. Hot Leg Guillotine Break at Reactor Vessel – Oconee

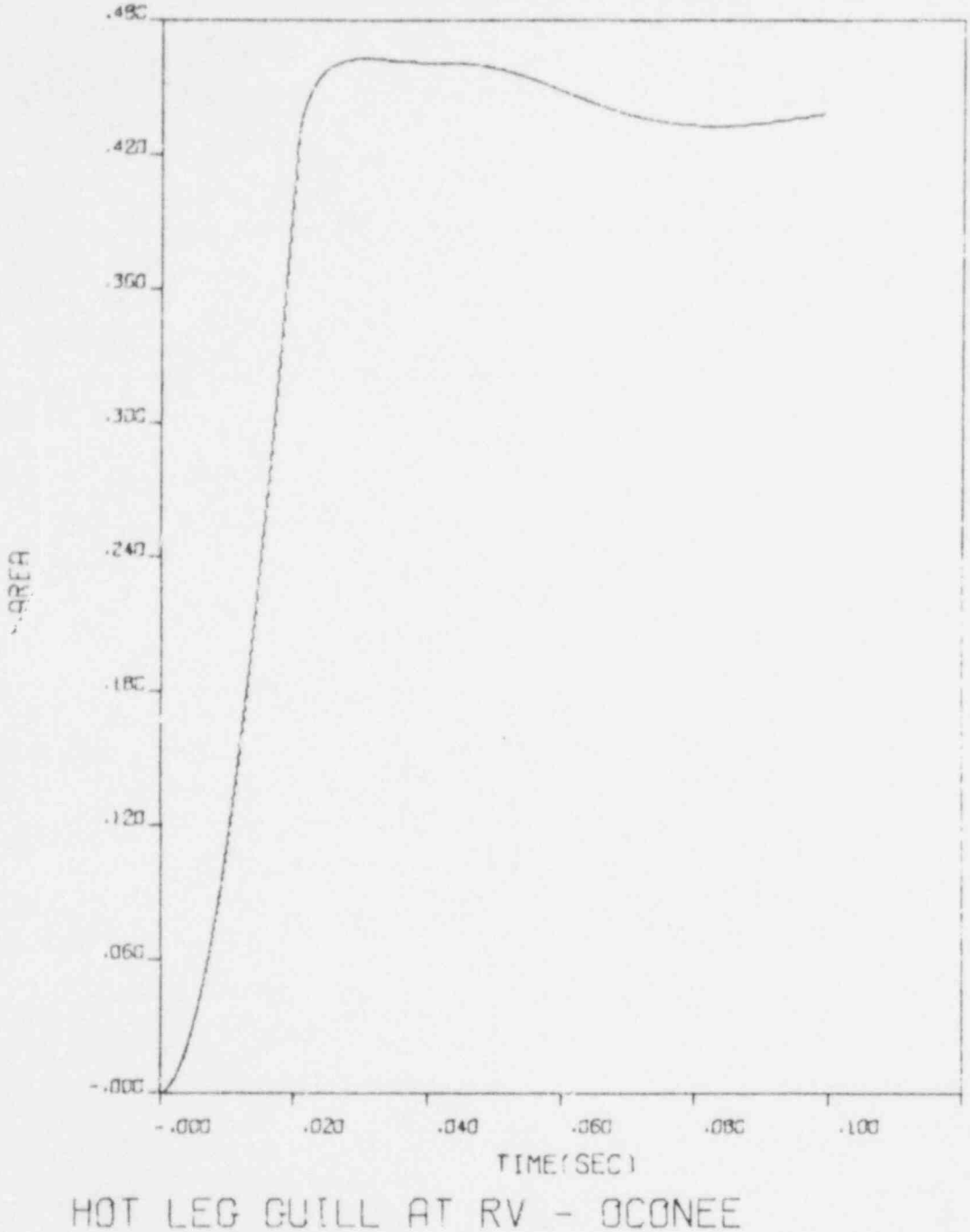

Figure 4.2-4. Hot Leg Guillotine Break at Elbow – Oconee

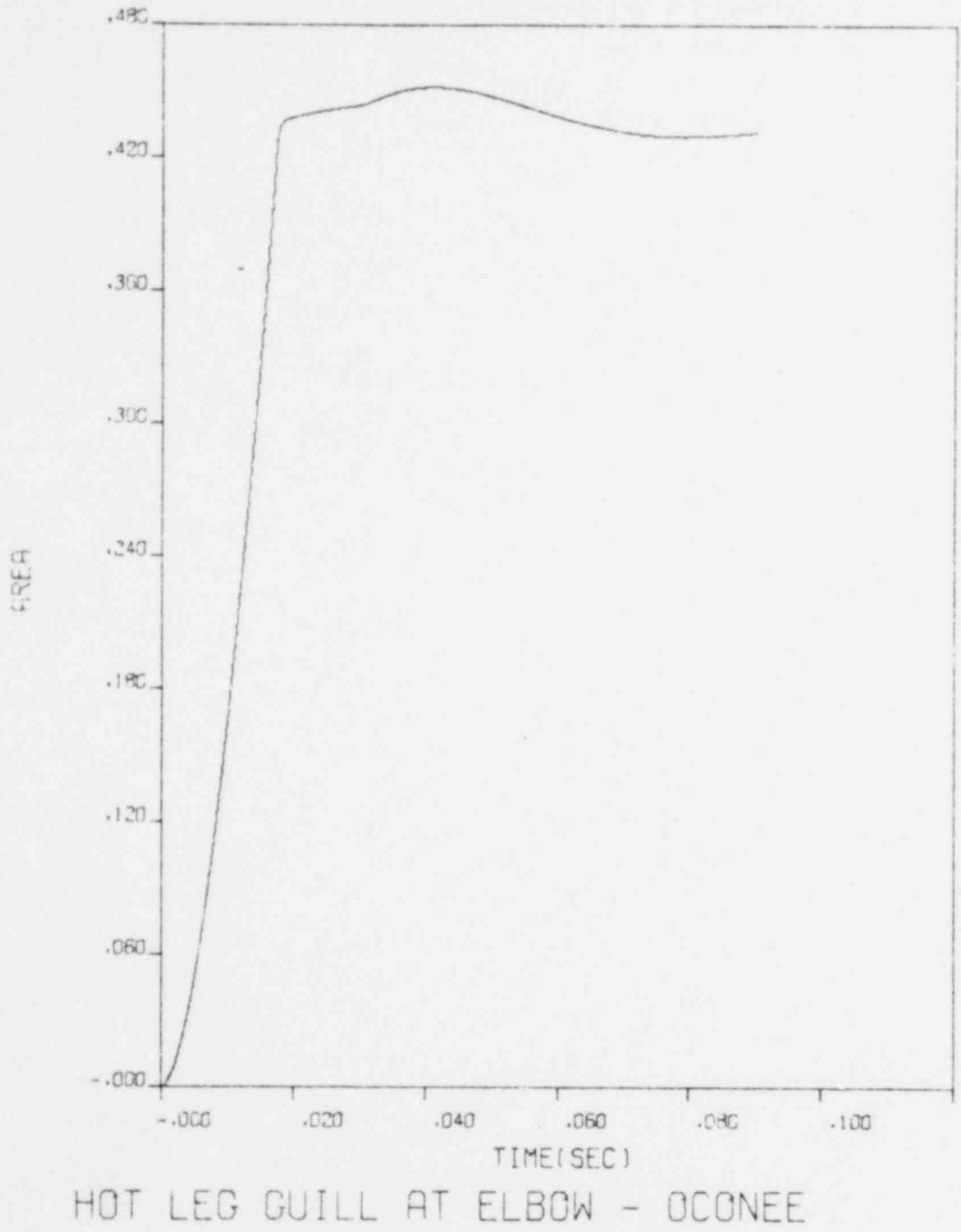

Figure 4.2-5. Hot Leg Break at Reactor Vessel — TMI-1

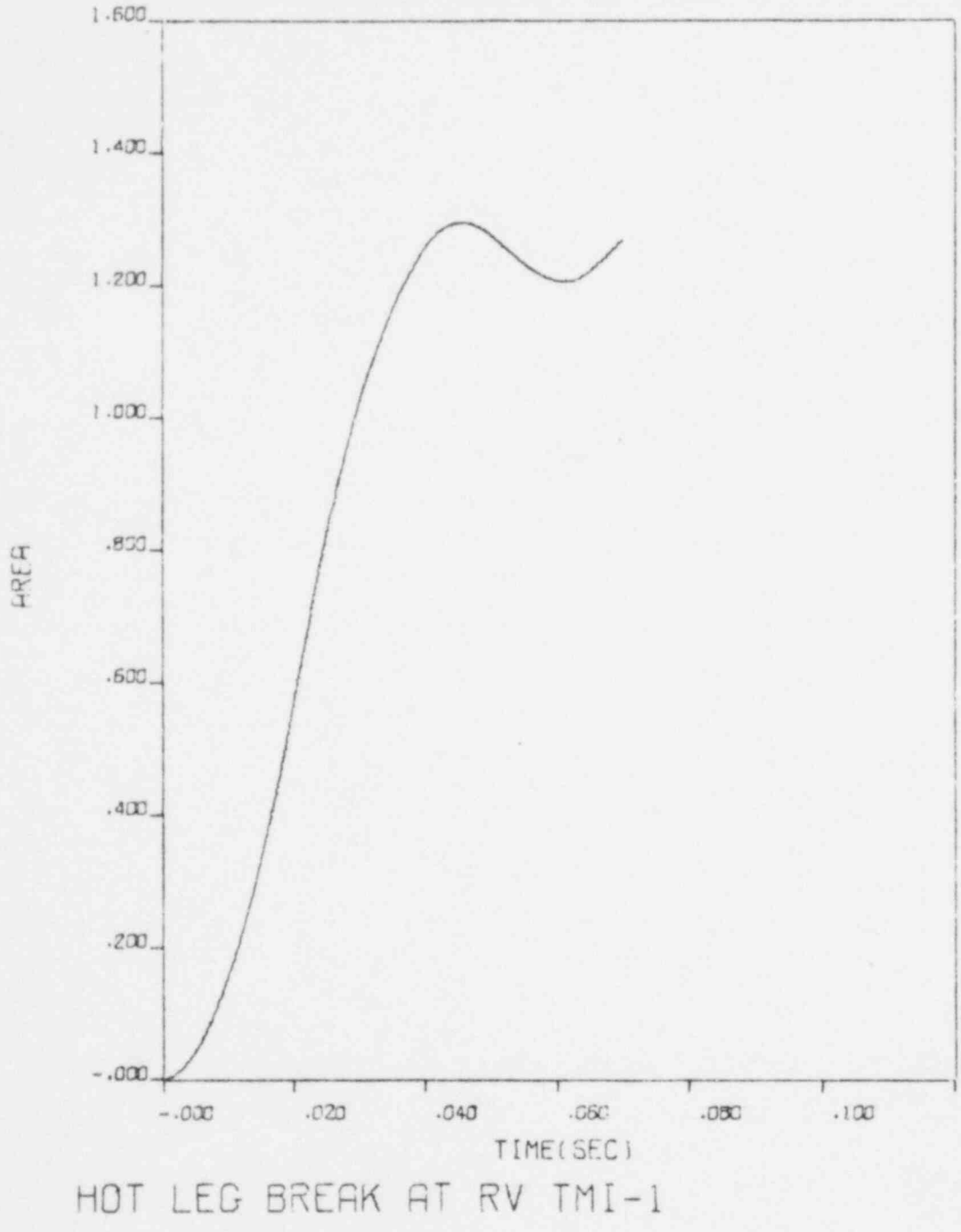

Figure 4.2-6. Hot Leg Break at Elbow, TMI-1

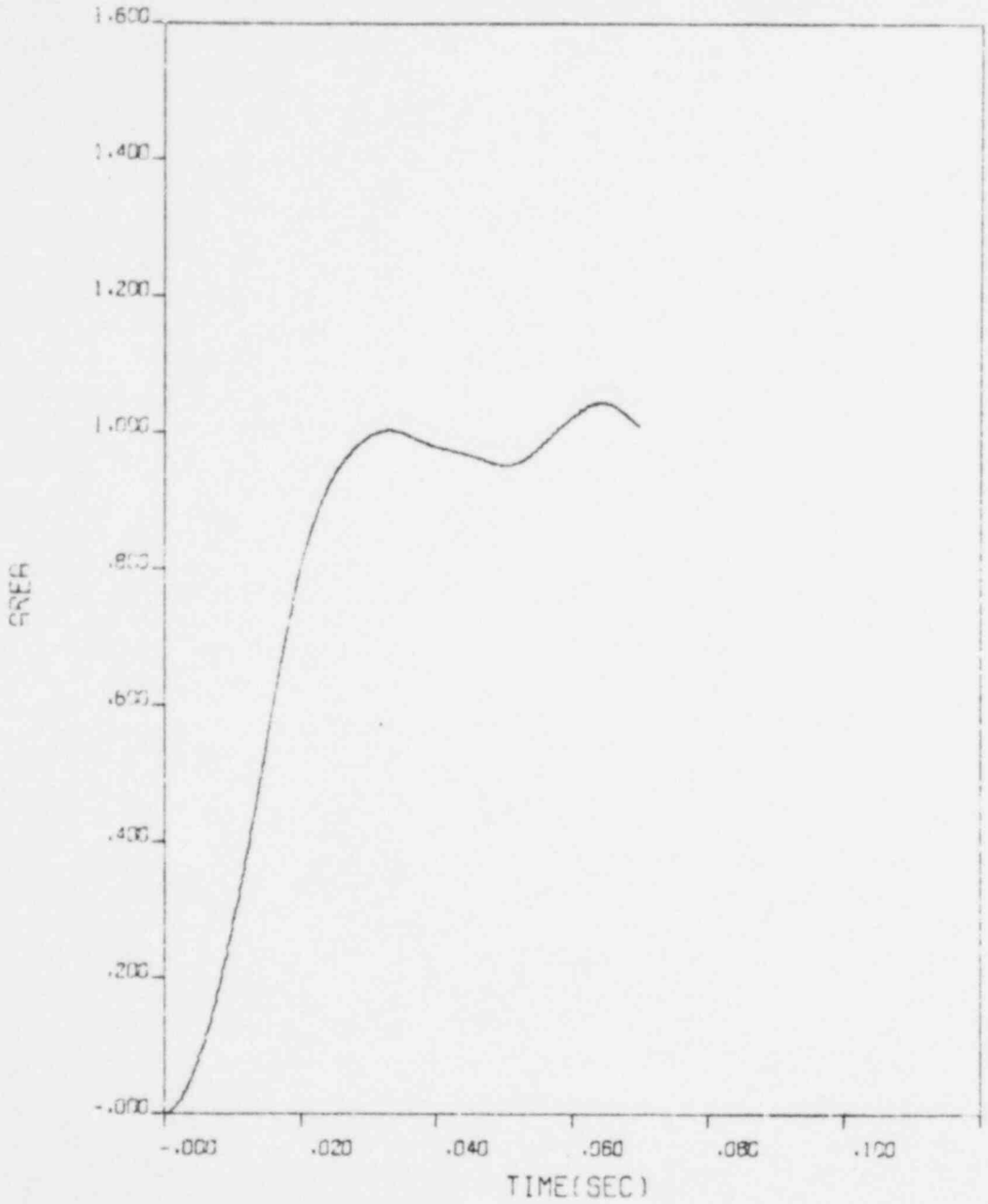

Figure 4.2-7. Hot Leg Guillotine Break at Reactor Vessel, Crystal River

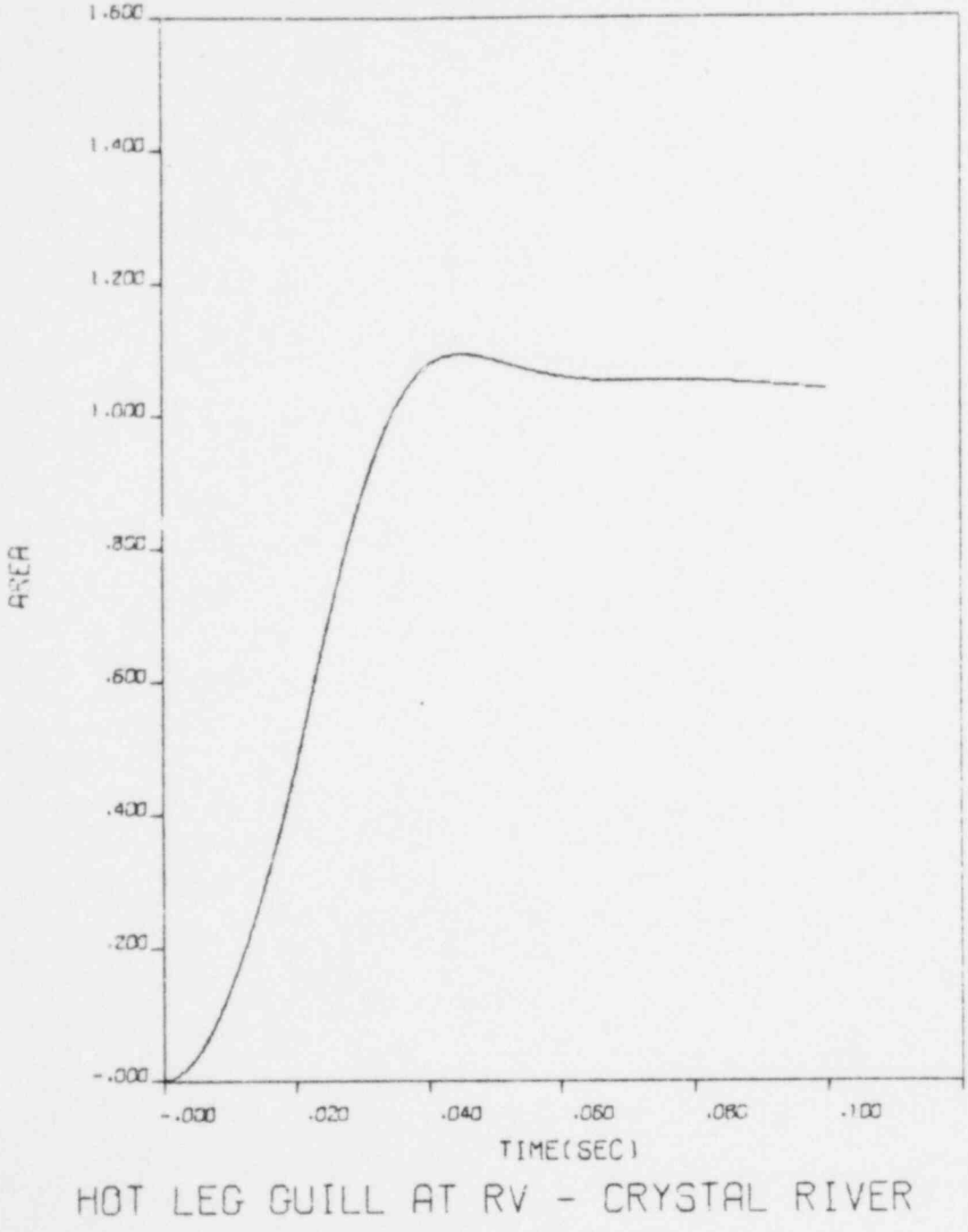

Figure 4.2-8. Hot Leg Break at Elbow, Crystal River

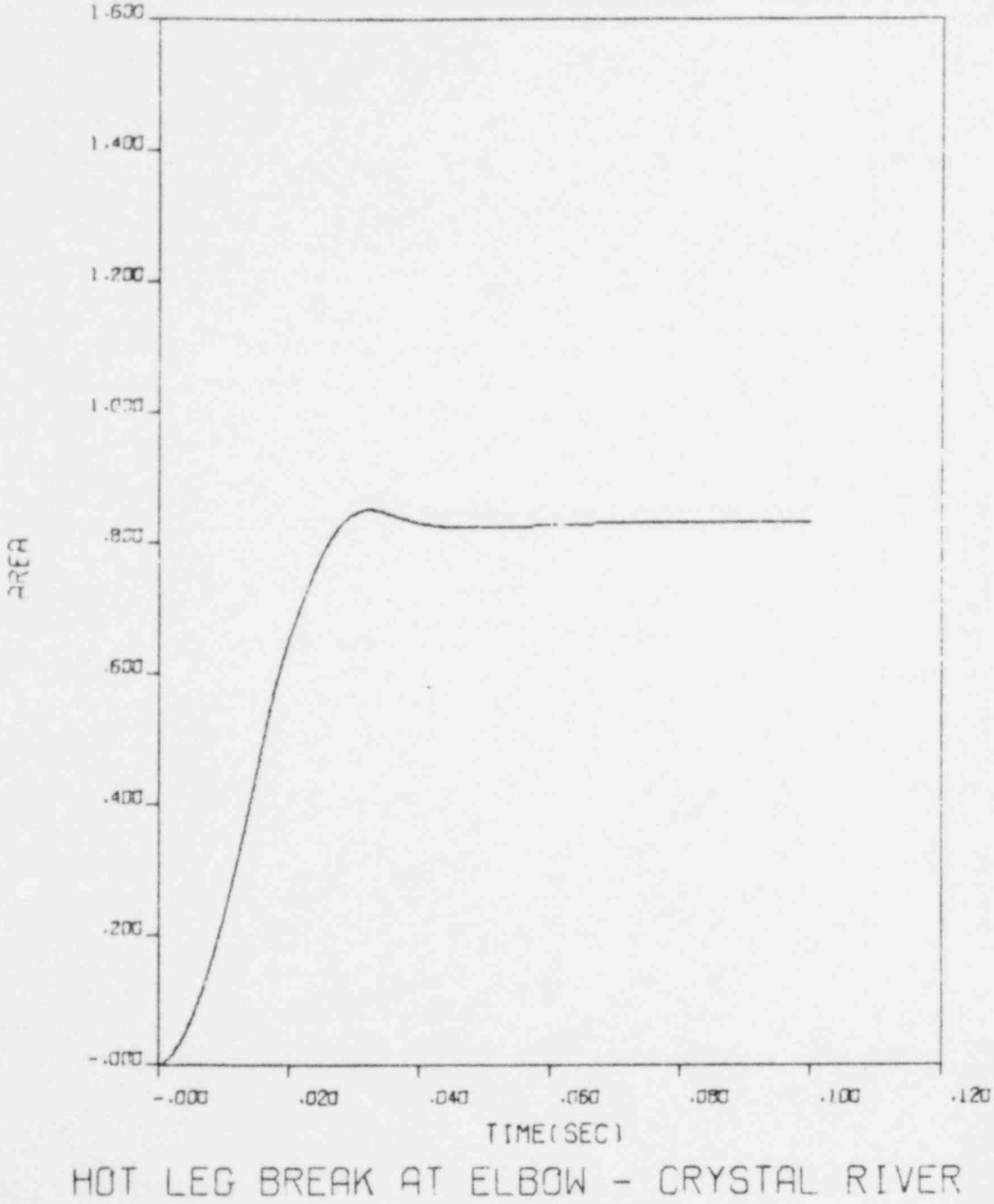

Figure 4.2-9. Hot Leg Break at Reactor Vessel, ANO-1

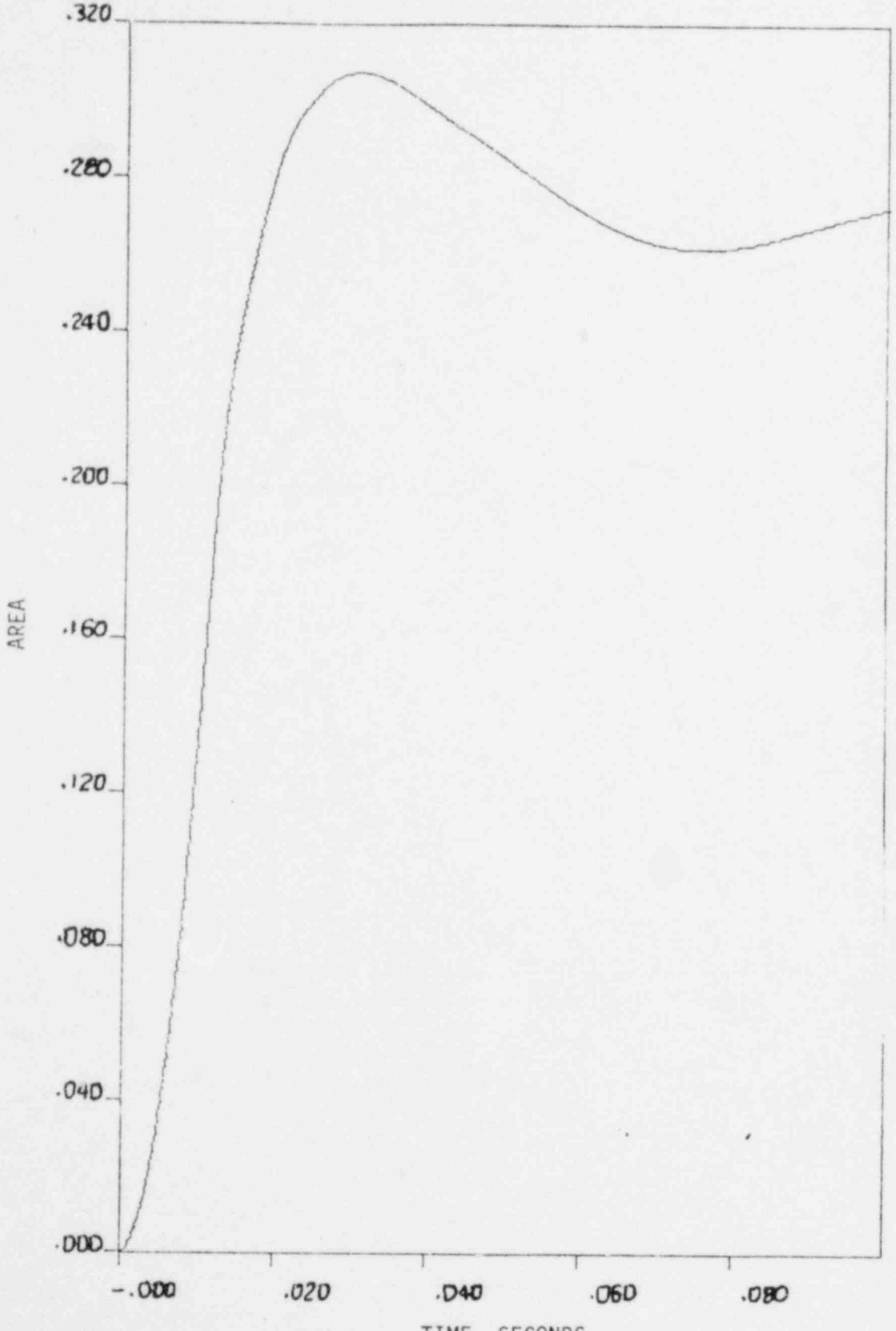

Figure 4.2-10. Hot Leg Break at Elbow, ANO-1

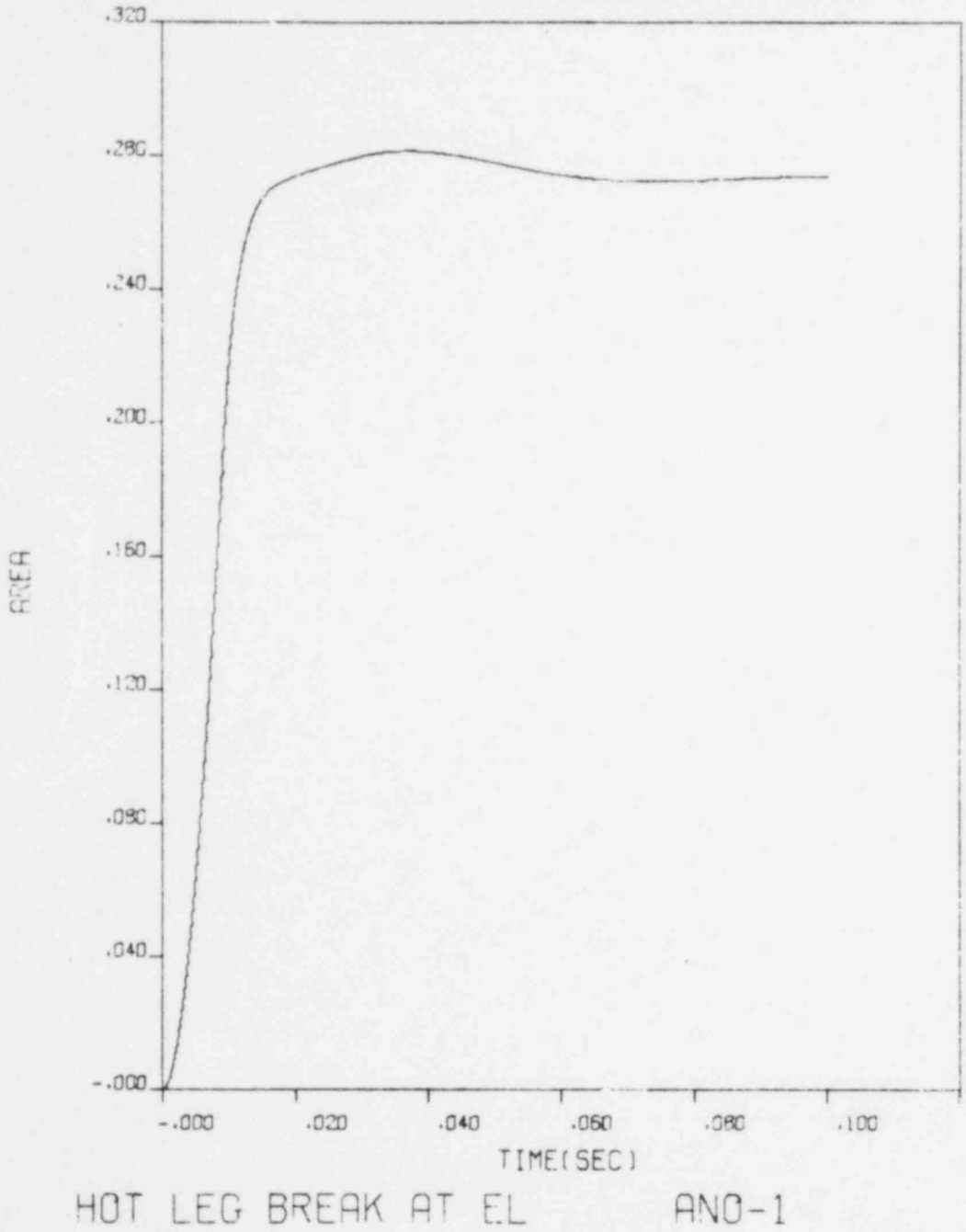

Figure 4.2-11. Hot Leg Break at Reactor Vessel, Rancho Seco

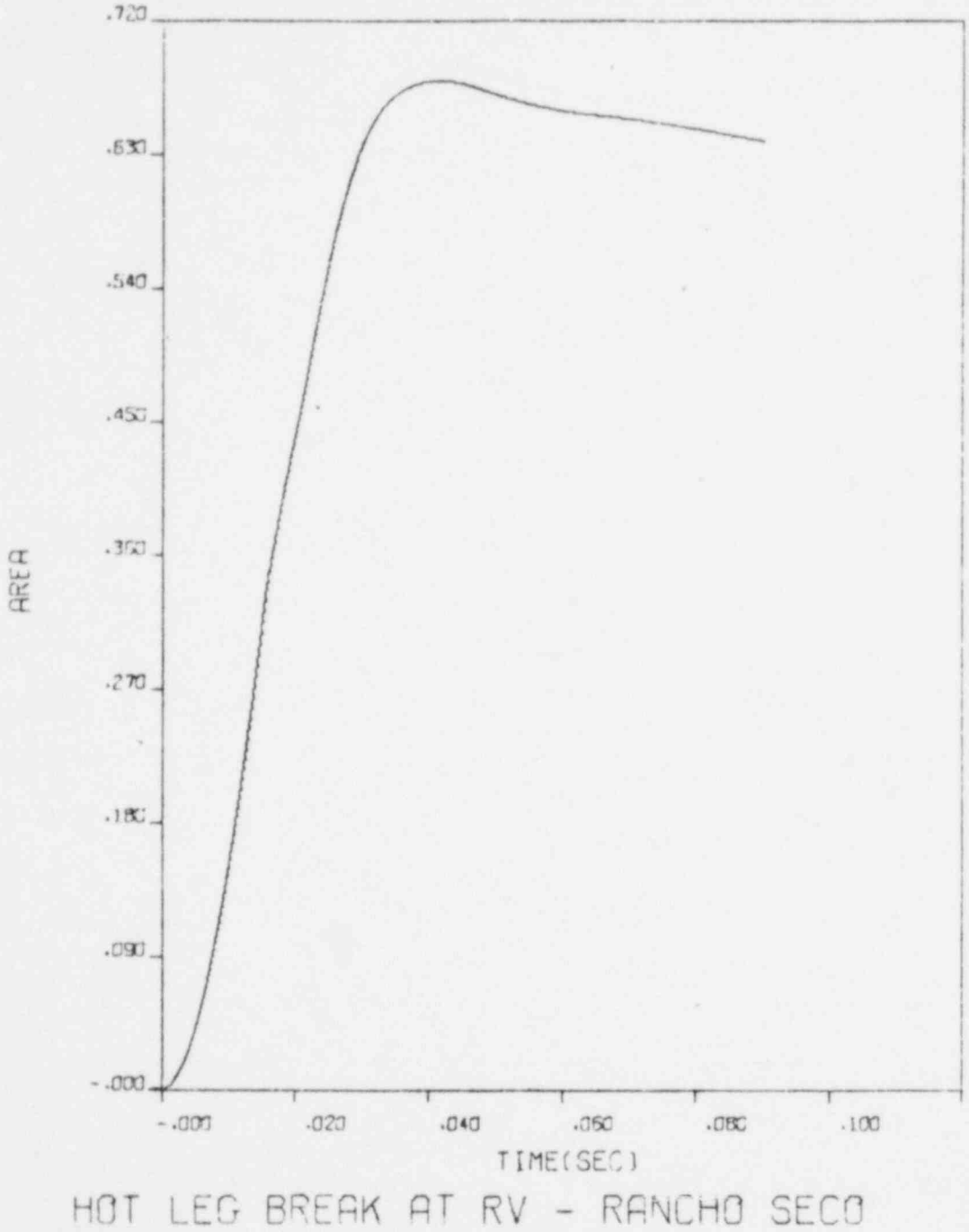

Figure 4.2-12. Hot Leg Break at Elbow, Rancho Seco

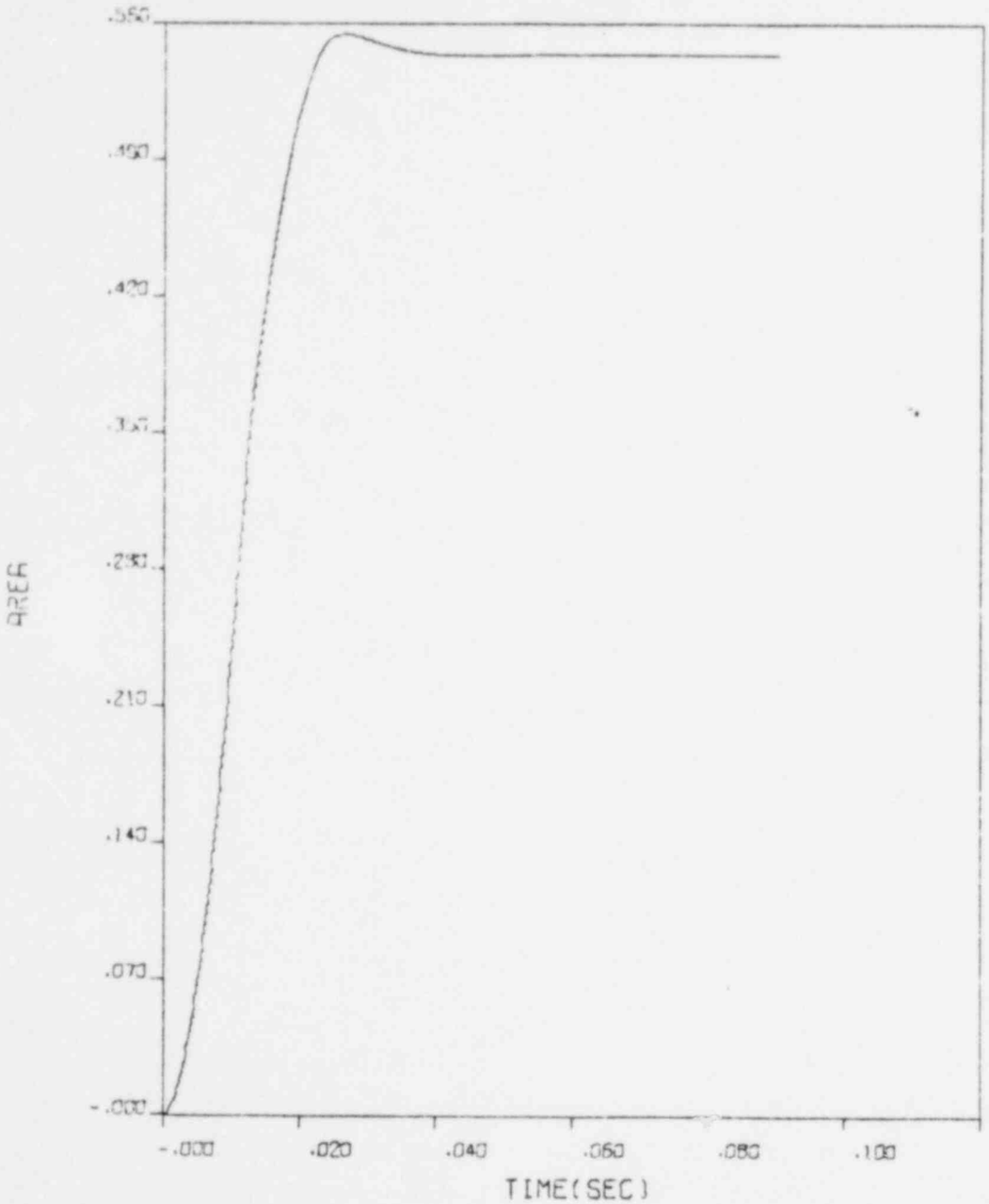

Figure 4.2-13. Hot Leg Break at Reactor Vessel Outlet, Davis-Besse 1

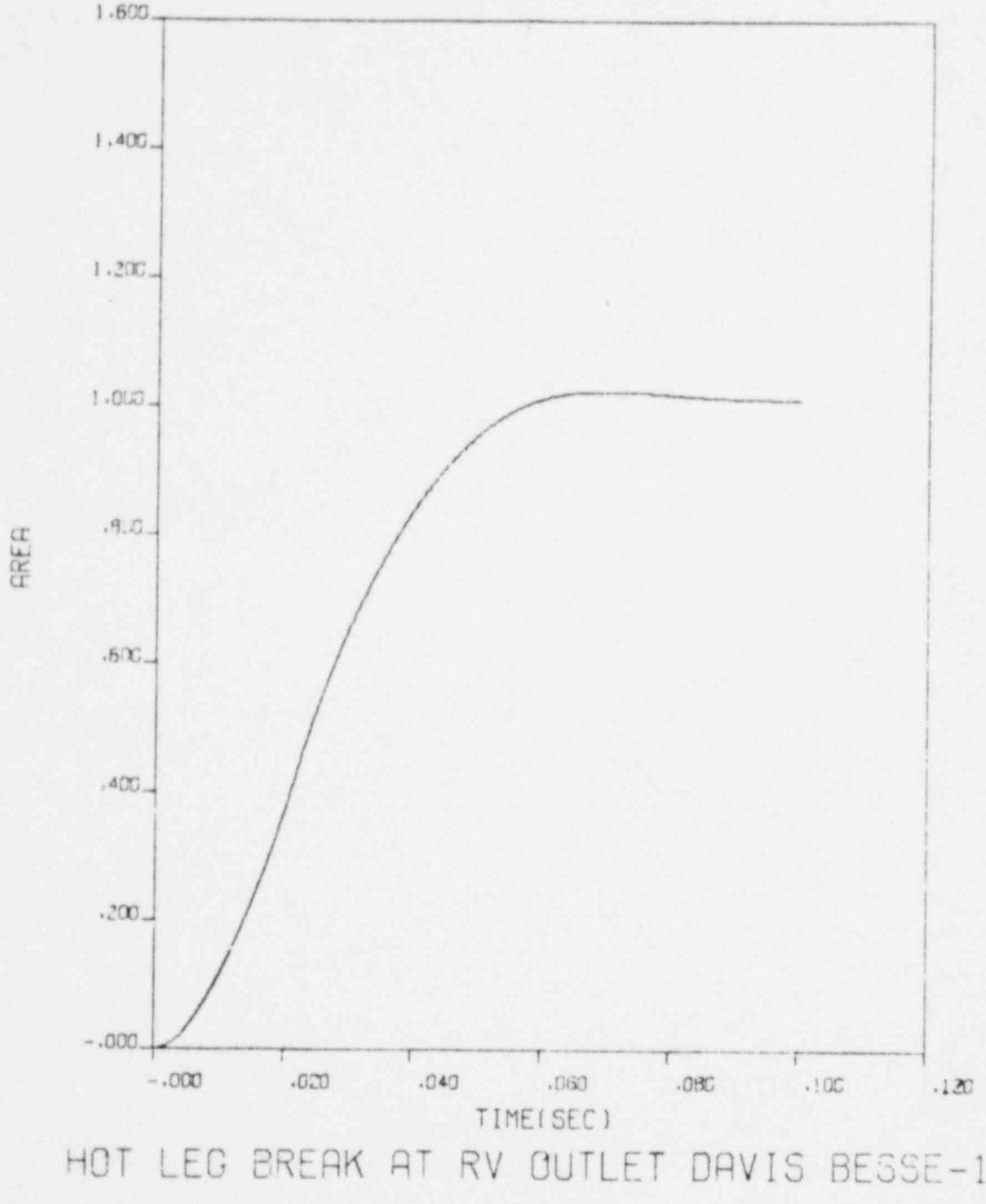

Figure 4.2-14. Hot Leg Break at Lower Elbow, Davis-Besse 1

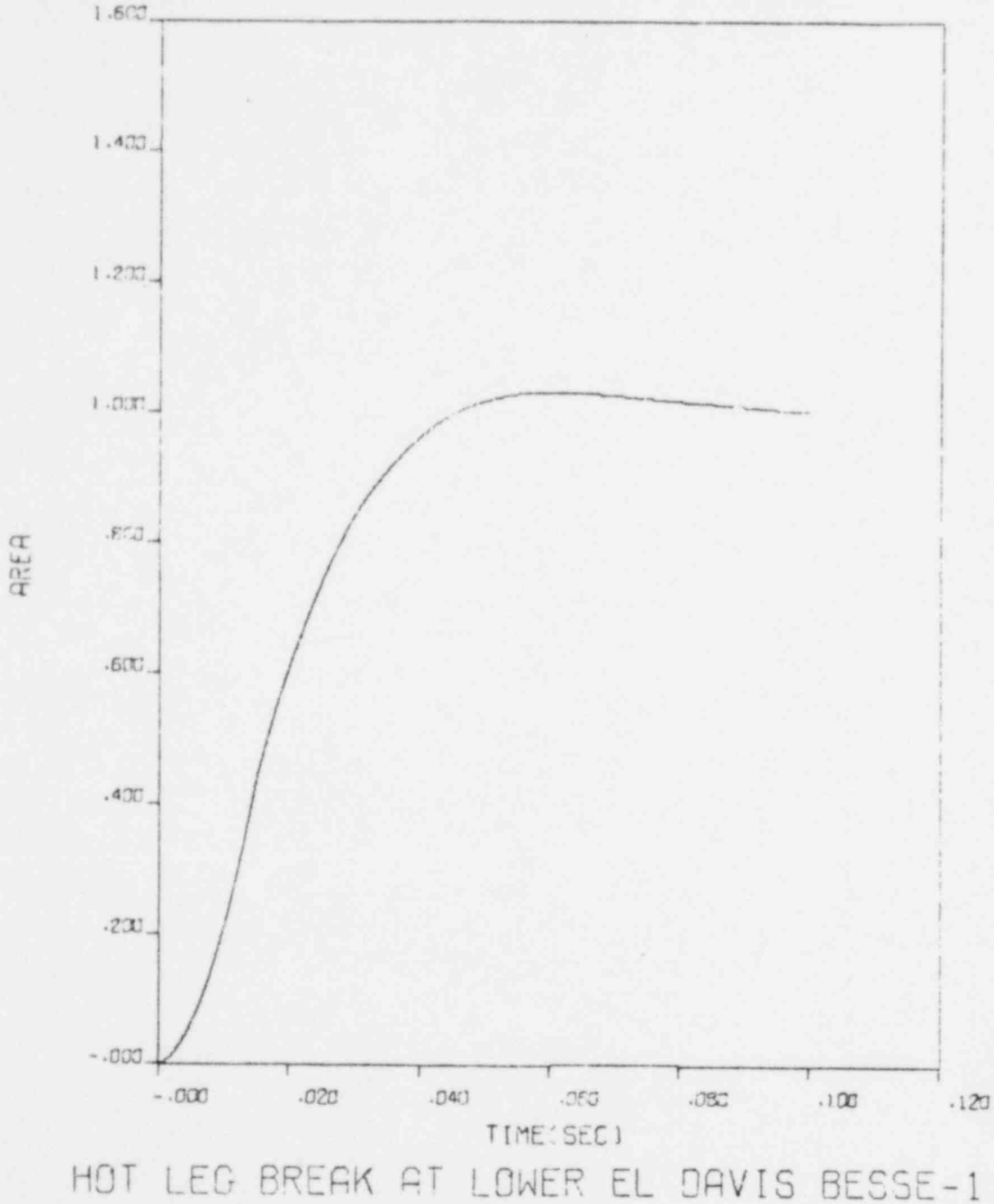

Figur 4.2-15. Cold Leg Guillotine Break at Reactor Vessel, Skirt-Supported Reactor

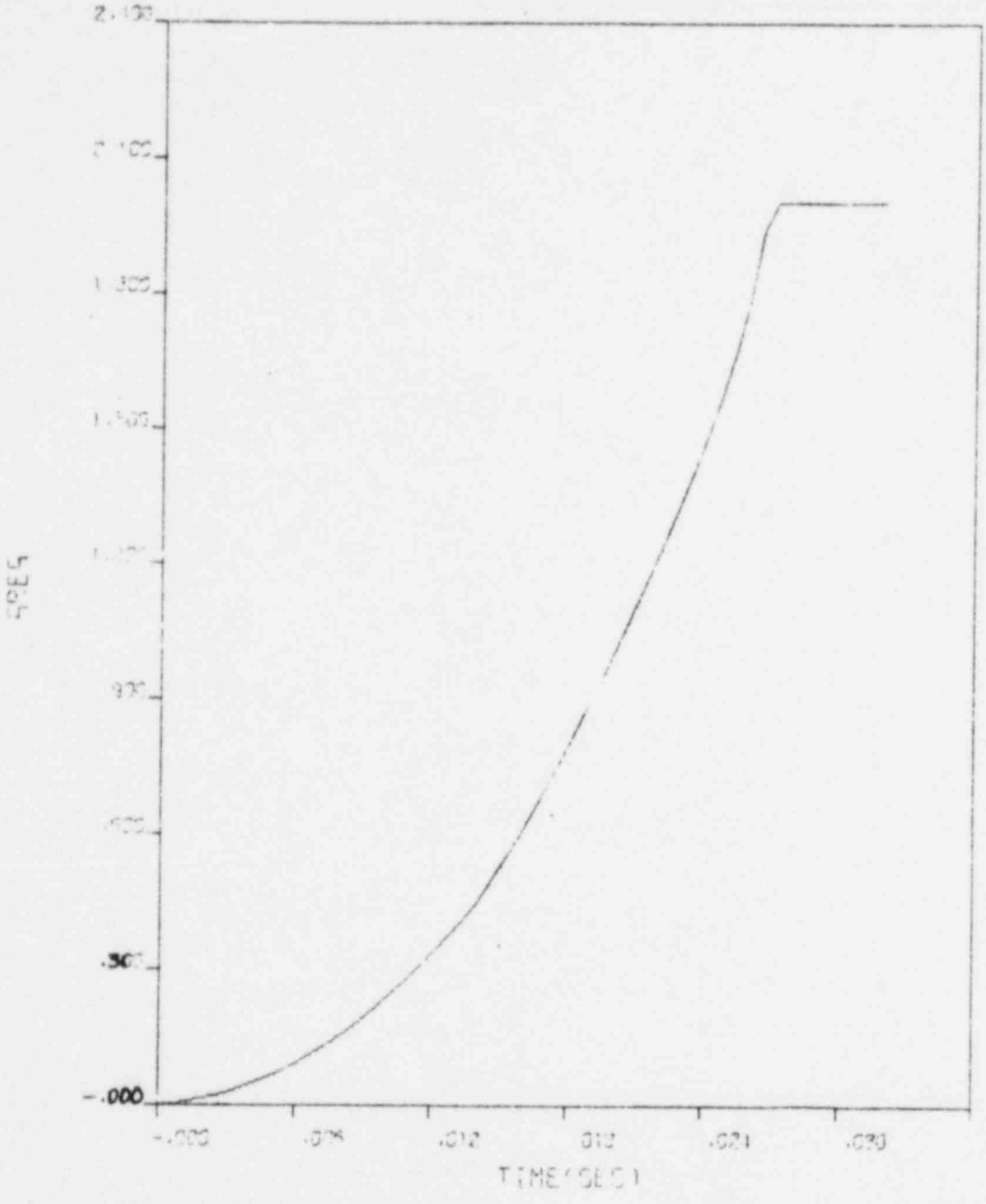

Figure 4.2-16. Cold Leg Break at Reactor Vessel Inlet, Davis-Besse 1

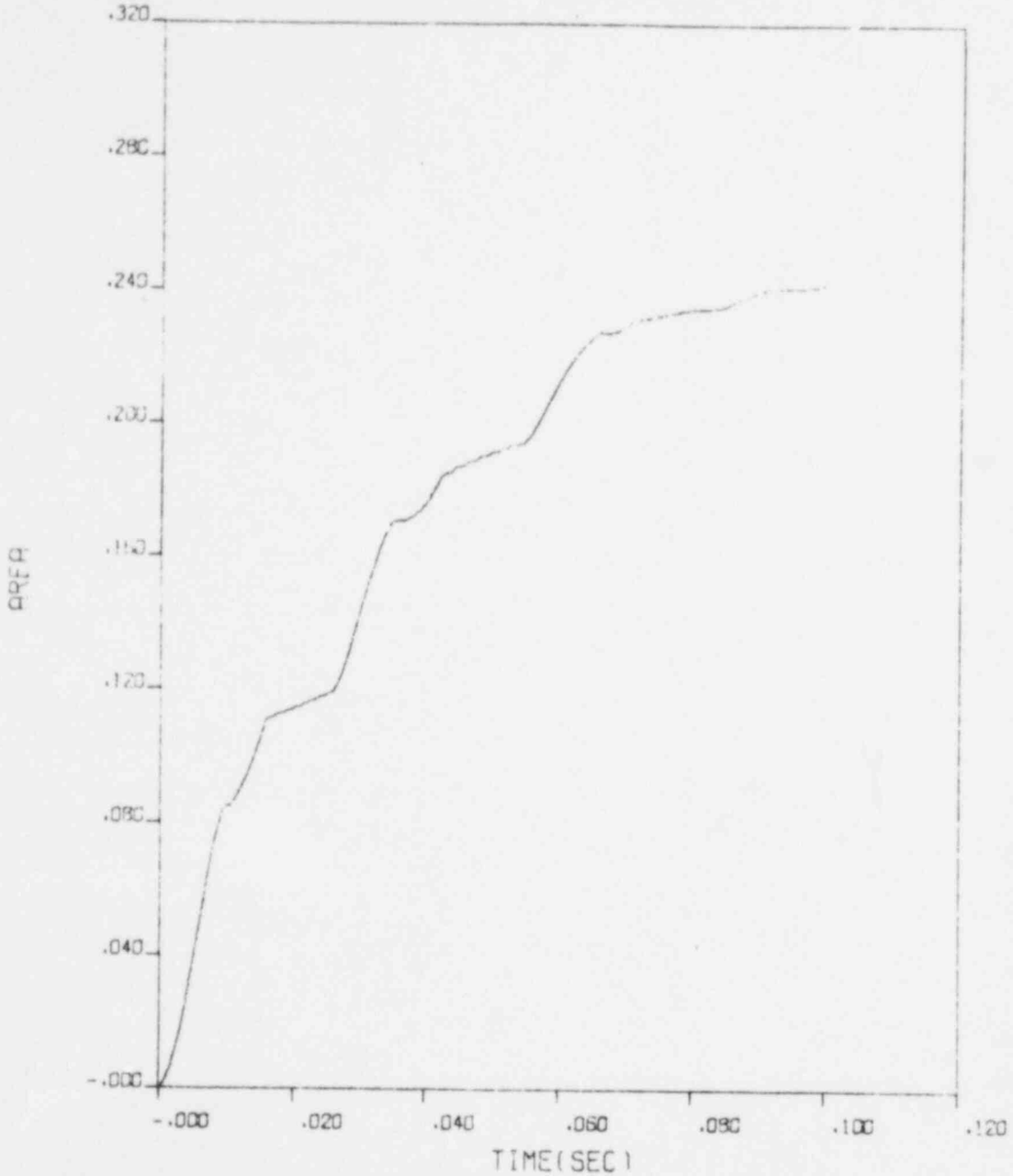

Figure 4.2-17. Cold Leg Break at Lower Elbow, Davis-Besse 1

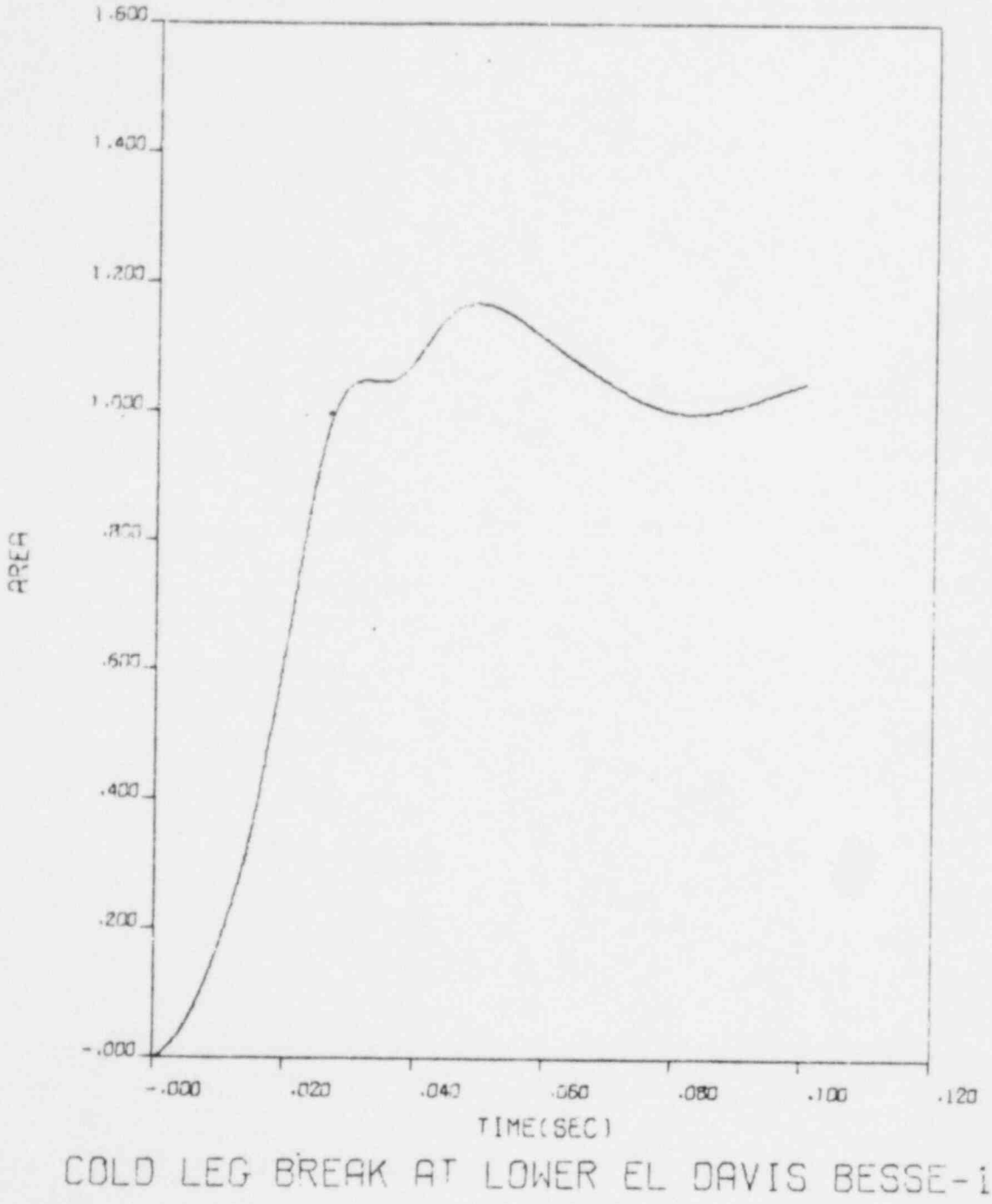

4.3. Determination of Reactor Vessel Cavity Pressures

4.3.1. Reactor Cavity Groupings

The conceptual design of the reactor vessel primary shield walls and foundations for all 177-FA lowered-loop plants is basically the same (see Appendix A). However, seemingly minor differences in design can potentially translate into significant differences in the results of a reactor cavity pressurization study. Rather than resolving these differences through a myriad of sensitivity studies, only those plants that were, for all practical purposes, identical in design were grouped generically. The following key design parameters are capable of influencing the transient response of the reactor cavity:

1. Piping penetration vent areas.
2. Neutron shield plug/tank design.
3. Inside diameter of reactor cavity.
4. Volume of lower reactor cavity.
5. Height of reactor cavity below nozzle belt C_L.
6. Height of reactor cavity above nozzle belt C_L.
7. Out-of-core neutron detector thimble design.

A summary of these parameters for each plant is presented in Table 4.3-1. Other design considerations influencing reactor cavity pressurization transient responses are the presence of stairwells and inspection equipment tracks.

As can be seen from the table, the ANO-1 and Rancho Seco plants are very similar in design. The major differences are the reactor cavity inner diameter and the piping penetration sizes. Despite their similarity, the differences in the piping penetration vent areas were deemed important enough that separate models were created. However, the lower three levels of the ANO-1 model (see Figures 4.3-15 through 4.3-18) were used directly in the Rancho Seco model (see Figures 4.3-21 through 4.3-24). The smaller inner cavity diameter of the ANO-1 plant and the similarities between the out-of-core detector thimble designs permit the use of ANO-1's lower three levels in the Rancho Seco model without introducing severe conservatism. This is also verified by the fact that most of the lateral force on the reactor vessel is concentrated in the nozzle belt region, i.e., the top two levels in the models.

From Table 4.3-1, it is seen that the CR-3 and TMI-1 plants are virtually identical in every aspect. Hence, these two plants were modeled generically.

The only differences between these plants are found in the sizes of the neutron shield plugs and the lower reactor cavities. Even the neutron shield plugs are identical except for the amount of arc subtended by an individual plug. Therefore, these translational venting devices were modeled in a fashion that is conservative for both plants (minimum vent area). The lower reactor cavity was chosen to be the smaller of the two designs for conservatism.

Below the nozzle belt centerline, the TMI-2 plant exhibits only two deviations from the CR-3 and TMI-1 designs. First, TMI-2's lower reactor cavity is larger than that of either CR-3 or TMI-1. Second, and more important, there is an inspection equipment track directly beneath the TMI-2 nozzle belt. Thus, the Crystal River 3/TMI-1 model below the nozzle belt was incorporated into the TMI-2 model with modifications to account for the inspection equipment track. The remainder of the TMI-2 cavity model — from the nozzle belt region upward to the bottom of the shield tanks — was generated separately because this portion of the cavity is unique. The TMI-2 cavity contains an additional level above the nozzle belt because of the placement of its rotational venting devices.

The Oconee 1, 2, and 3 plants are identical in every aspect except for piping penetration vent areas. All Oconee vent areas are relatively small, so using the smallest vent areas to represent all three plants does not introduce unwarranted conservatism. Therefore, the three Oconee plants are encompassed by a single model.

Finally, Davis-Besse 1 (DB-1) is sufficiently different from the lowered-loop plants that it requires a separate model. DB-1 differs from the lowered-loop plants in the following areas:

1. Its reactor vessel is nozzle supported.
2. Neutron shield plugs at the top of the cavity are not used.
3. Its lower reactor cavity is not separated from the main body of the reactor cavity.

Additional differences in vent areas and heights above and below the nozzle belt are shown in Table 4.3-1.

4.3.2. Reactor Cavity Modeling Philosophy

The CRAFT2 computer code (Version 13.0) was used to determine the pressures in the reactor vessel cavities. Application of the CRAFT2 code to the present cavity pressurization studies has been demonstrated to the NRC.

In the model, elevation pressure drops were accounted for, and all flow paths were checked for choke flow at each CRAFT2 calculational time using the Moody choked flow correlation with a discharge coefficient of 0.6. Length/area ratio (L/A) calculations were based on geometric considerations. All area changes were considered as step functions with the total L/A being equal to the sum of the individual L/A components for a given flow path. All flow path areas were chosen as the minimum flow areas along the paths. All form loss factors were calculated based on formulas for abrupt contractions and expansions. As a minimum, the form loss factor for a sudden contraction is

$$K = 0.4(1 - \sigma),$$

while for a sudden expansion it is

$$K = (1 - \sigma)^2$$

where σ is the ratio of the small flow area to the large flow area. All form loss factors for a given flow path were normalized to the path flow area by multiplying by the square of the ratio of the path flow area to the smaller area used to compute the form loss factor. The CRAFT2 generalized loss coefficients, $K_f (= fL/D_h)$ were based on a maximized value of L/D_h. L/D_h was maximized by computing the hydraulic diameter D_h at the point along any given flow path that minimized its value. For flow paths containing 90° turns, the frictional L/D_h was supplemented with an additional L/D_h of 30.

Except for the ANO-1, Davis-Besse 1, and Rancho Seco plants, there is some type of venting device, governed by translational or rotational dynamics, at the top of the reactor cavity annulus. As the pressure in the annulus builds up, these devices either blow out or rotate out of the way, providing pressure relief to the containment. The equations of motion governing the translational and rotational devices (respectively) are

$$m \frac{d^2x}{dt^2} = \Delta P A_s - f_g mg - D \frac{dx}{dt}$$

and

$$mR_{cg}^2 \frac{d^2\theta}{dt^2} = \Delta P A_s R_{\Delta P} - f_g mg R_{cg} \cos\theta - D R_{cg} \frac{d\theta}{dt},$$

where

m = mass of venting device,

ΔP = pressure drop across device,

A_s = surface area over which ΔP is applied,

f_g = gravity term multiplier,

g = gravitational acceleration,

D = coefficient of friction or drag,

R_{cg} = moment arm from hinge axis to center of gravity of device,

$R_{\Delta P}$ = moment arm from hinge axis to center of action of pressure force (see Figure 4.3-1),

θ = angular position,

x = position,

t = time.

These equations are solved numerically in CRAFT2 (Version 13.0) for each blowout device. Associated with each blowout device is a table of vent area versus position. As the vent area opens, CRAFT2 iterates between the momentum equation for fluid flow and the equation governing the motion of the blowout device in order to obtain a converged pressure distribution within the cavity at each time point. At some position, the vent area achieves its full value, and the solution of the equation of motion of the blowout device is terminated thereafter. Owing to the absence of experimental data, the drag coefficient is assumed to be zero. Therefore, to account for this and other unknown effects, the gravity term multiplier is set equal to 2.0, thus doubling the resistance to motion due to the device's own weight. The formulation of the equation of motion in CRAFT2 for rotational venting devices conservatively assumes that θ_1, as defined in Figure 4.3-1, is zero.

Insulation is the final item for consideration in this section. The initial volume of the insulation was conserved and as such was unavailable for occupation by any fluid within the reactor vessel cavity. Geometric flow path quantities used in modeling the hydraulics of the cavity were determined based on the assumption that the insulation was collapsed around the reactor vessel. Since the volume of the insulation was conserved, its effective thickness was increased because of its collapse about a smaller diameter. The effective increase in the insulation thickness results directly in a conservative determination of flow path lengths, areas, and hydraulic diameters. In locations where obstructions on the concrete side of the cavity, such as detector thimbles, were encountered, geometric quantities were modified further to reflect

a wrapping of the obstruction with a uniform layer of insulation. This approach combines the conservatisms associated with placing the insulation next to the concrete and those associated with placing the insulation next to the reactor vessel. No insulation was assumed to blow out in such a manner as to plug the piping penetrations. It was assumed, however, that the close-fitting piping insulation remains intact. Therefore, penetration vent areas were based on the outer diameter of the piping insulation, not the piping itself. It was also assumed that the insulation between the reactor vessel flange and the neutron shield plug lifts and blocks the small flow path between the vessel and the plugs which results in slightly higher pressures in the cavity volumes below.

4.3.3. Reactor Cavity Sensitivity Study

Sensitivity studies were performed to determine a convergent reactor cavity noding scheme for both lowered- and raised-loop plants. The studies include time step, nodalization, impact of mass and energy release rates and break location, and the effect of shield block blowout. The ANO-1 reactor cavity with no venting through the area between the shield wall and the reactor vessel at the top of the cavity and the mass and energy releases from the 2A hot leg break were used in the majority of the lowered-loop studies. They are discussed in the following sections.

4.3.3.1. Time Step Sensitivity

A time step study was made using the 70-node ANO-1 model as shown in Figures 4.3-6 and 4.3-15. The development of this model is presented in section 4.3.3.2. The time steps were successively reduced until a convergent solution was obtained. The peak lateral load, moment, and pressures in the break nodes from time steps of 0.0001 and 0.00005 second are shown in Table 4.3-2.

The study shows that the results differ by less than 0.2%. Therefore, a time step of 0.0001 second was selected for use in all production calculations.

4.3.3.2. Nodalization Sensitivity

The noding sensitivity study was performed for the annular volume between the reactor vessel and the shield wall and for the break nodes surrounding the ruptured pipe. Four ANO-1 models containing axial and circumferential variations within the annulus gap were studied. One node for each pipe penetration volume inside the shield wall and one node for the lower cavity below the reactor vessel support skirt were used in all four models.

In the 42-node model, the annulus was axially divided into four levels, one level in the nozzle belt region and three levels below, as shown in Figure 4.3-2. The lower boundary of the nozzle belt region was located at the discontinuity in the reactor vessel outside diameter. Each level contained eight circumferential nodes as shown in Figure 4.3-3. The blowdown mass and energy were deposited in node 27. The 50-node model was constructed from the 42-node model by dividing the nozzle belt region into two levels as shown in Figures 4.3-4 and 4.3-5. The circumferential noding and the three levels below the nozzle belt remain unchanged from the 42-node model. The blowdown mass and energy were equally divided between the two break nodes, 27 and 35.

The 70-node model retained the same axial spacings as the 50-node model, as shown in Figure 4.3-6, while each level was increased from eight to twelve circumferential nodes. This arrangement increased the number of break nodes from two to four. The blowdown mass and energy were deposited in nodes 39, 40, 51, and 52. In the 82-node model, the three levels below the nozzle belt in the 70-node model were rearranged into four levels as shown in Figures 4.3-7 and 4.3-8. The two levels in the nozzle belt region remain unchanged from the 70-node model.

These four models provided enough variation in the number of nodes within the cavity annulus to determine a convergent model for use in the production reactor cavity pressurization analysis. The peak lateral load, moment, and uplift were used as convergence criteria. As shown in Figure 4.3-9, the results from the 70- and 82-node models converged to within 1%. The 42-node model predicted the highest moment as a result of lateral force concentration in the nozzle belt region. This was caused primarily by the axial noding scheme in the nozzle belt region. The 42-node model contained only one level in this region, while the 50-node model comprised two levels. The downflow path from the node containing the nozzle in the one-level model (42-node model) t the level below the nozzle belt is modeled to include the losses due to area change across the nozzle. This results in a downflow reduction and a pressure buildup in the nozzle belt region. The downflow path in the two-level nozzle belt model (50-node model) is modeled to originate from the bottom of the nozzle and does not contain the losses across the nozzle. Thus, in the 50-node model more break effluent was diverted toward the lower levels and less force was concentrated in the nozzle belt region. Using the 50- and 70-node models, the nodalization of

the reactor vessel cavity was also investigated for a 0.6A hot leg break and a 2A cold leg break. The results showed trends similar to those presented in Figure 4.3-9 for the 2A hot leg break. Based on the results of this nodalization study, it was concluded that the noding scheme for the 70-node model was detailed enough to provide a convergent solution. Thus, the 70-node model was chosen as the base model for the reactor cavity pressurization analysis for the skirt-support plants.

The DB-1 reactor cavity design was similar to that of the skirt-supported plants except for the following:

1. There were no removable shield blocks between the wall and the reactor vessel at the top of the cavity.
2. No support skirt was present to act as a physical barrier between the annulus and the lower cavity.

A mini-nodalization sensitivity study using the mass and energy releases from the 2A hot leg break was performed to assess the impact of these unique DB-1 features. Three models were used in the study. The first contained five levels and 72 nodes, much like the base model used for the skirt-supported plants. Figures 4.3-10 and 4.3-11 show the axial and circumferential noding schemes for the 72-node model. The second model was constructed from the first by dividing the top level above the centerline of the nozzles into two levels to permit even axial spacing in the nozzle belt region. The levels below the centerline of the nozzles remained unchanged; this model contained 84 nodes, as shown in Figures 4.3-12 and 4.3-46. The 84-node model was constructed to determine the effect of the noding scheme on the direct venting out of the top of the reactor cavity. The third model was similar to the 72-node model except that a single volume was used to represent the bottom level in the annulus containing the reactor vessel lower head. This model contained five levels and 61 nodes, as shown in Figures 4.3-13 and 4.3-14. In the absence of a support skirt, this model was built to determine the effect of the noding scheme on the reactor vessel uplift force. Table 4.3-3 shows the peak lateral force, moment, and uplift (which again were used as convergence criteria) resulting from the DB-1 nodalization study. Based on the results presented in this table and the trends observed in the skirt-supported plant nodalization study, the 84-node model was chosen as the base model for the Davis Besse-1 reactor cavity pressurization analysis.

It was noted in Table 4.3-1 that the heights above the nozzle belt centerline for Davis Besse-1 and TMI-2 were approximately equal as well as significantly different from the heights of the other plants. Therefore, based on the result of the DB-1 nodalization study, an additional level — level 6 in Figures 4.3-33 and 4.3-39 — above the nozzle belt was incorporated into the 70-node skirt supported base model to represent TMI-2. The 70-node model was retained as the base model for all other skirt-supported plants.

4.3.3.3. Mass and Energy Release Rates and Break Location

In general, the external loads on the reactor vessel and the cavity pressure were proportional to the break area, as can be seen from the results of the spectrum analysis shown in section 8.1. The impact of break opening time on the external load on the reactor vessel was investigated using the 70-node skirt-supported model and mass and energy releases from the 2A hot leg break. The results showed that the peak lateral load for an opening time of 0.033 second was approximately 17% higher than that for a 0-second opening time. The gradual increase in discharge rate due to the 0.033-second opening time pressurized the cavity at a slower rate and delayed the time to reach the maximum pressure gradient across the reactor vessel. As a result of the delayed peak ΔP, approximately 37% more mass and energy were discharged into the cavity. The time required to reach a peak lateral load increased from 0.023 second for a 0-second opening time to 0.044 second for a 0.033-second opening time. It was concluded that the use of physically realistic opening times, particularly for large break areas, must be considered in a reactor cavity pressurization analysis. Note that the reactor cavity pressurization studies contained herein were based on realistic break opening times.

The effect of break location relative to the out-of-core detector thimbles, the access well at the bottom of the cavities, and the decay heat line penetration into the hot leg vent was investigated. While the impact of these items on the peak load was determined to be negligible, the study indicated that the mass and energy should be deposited in the receiver, which offers the minimum potential for pressure relief. Therefore, mass and energy were deposited into those receivers furthest removed from the access wells or in the hot leg receiver, whose penetration contained the decay heat line.

4.3.3.4. Blowout Devices

A study on the effect of shield block blowout on the peak lateral load was conducted for the TMI-1/CR-3 and the Oconee group cavities. The results for the 2A hot leg break showed that the peak lateral load occurred before the first block was completely blown out of the cavity to permit venting. Thus, the additional vent area provided by the blowout model does not relieve the peak lateral load. However, the translational blowout devices reduced the final cavity pressure and the uplift force by about 50% at 0.5 second (the run end-time). The impact of the shield tank device placed on the top of the TMI-2 cavity was also investigated. The shield tank design provides venting earlier than that of the translational shield block since it is a rotational device that is capable of relieving pressure immediately upon its initial movement. The results for the 2A hot leg break showed a 5% reduction in the peak lateral load and a reduction of more than 50% in the cavity pressure.

4.3.4. Reactor Cavity Model Inputs

4.3.4.1. Geometric Inputs

Examples of control volume and flow path inputs to the CRAFT2 code for the ANO-1 and DB-1 cavity groups are tabulated below.

Reactor cavity group	Control volumes	Flow paths
ANO-1	Table 4.3-4	Table 4.3-5
DB-1	Table 4.3-6	Table 4.3-7

All flow paths were checked for choking using the Moody correlation with a multiplier of 0.6. Reverse form losses set to zero are considered identical to their corresponding forward form losses. The friction and turning losses were combined and input in the form of the ratio of path length to hydraulic diameter, (L/D_h). This value multiplied by the friction factor (f) calculated internally by CRAFT2 represents the K-factor for friction and turning losses.

The corresponding models for the six reactor cavity groups mentioned above are presented in Figures 4.3-15 through 4.3-53. As evidenced from these Figures and discussed in section 4.3.1, all six cavities were based on a similar

noding scheme, which was individually customized to incorporate the unique features of the reactor vessel cavity for each plant group.

Mass and energy inputs to the six models were taken from the data presented in section 4.3.4.2. A single consistent spectrum of hot and cold leg mass and energy data were used to perform the reactor cavity pressurization analysis for the skirt-supported plants. The Davis-Besse 1 cavity pressurization analysis was performed for the actual hot and cold leg break areas. As such, the mass and energy used in DB-1 model were reflective of the plants actual break areas.

All mass and energy data were deposited into receiver nodes furthest removed from pressure-relieving portions of the cavities. All receiver volumes were considered at either the reactor vessel inlet or outlet nozzles.

4.3.4.2. Mass and Energy Inputs

Individual subcompartment mass and energy spectra were generated for the skirt- and nozzle-supported plants using the CRAFT2 computer code (version 13.0). These analyses were not directly coupled to the subcompartment pressurization work (i.e., no cavity backpressure effect was fed back into the mass and energy work).

The analyses were performed in accordance with "Standard Review Plan 6.2.1.2," BAW-10132P-A, and BSAR-205. The basic large-break CRAFT2 models were taken from BAW-10103 and BAW-10105 for the skirt- and nozzle-supported plants, respectively. According to the methodologies in these reports, the large-break models were modified in the following manner:

1. A single node core.
2. No core crossflow paths.
3. Delayed departure from nucleate boiling (DNB) in the core.
4. High liquid level in the pressurizer.
5. No ECC bypass model.
6. The heat transfer coefficients in the steam generators are the same for primary-to-secondary heat transfer as for secondary-to-primary.
7. No momentum losses in any flow path.
8. Instantaneous opening of the vent valves.
9. 102% power.

The generic skirt-supported plants mass and energy release rates were based on the Moody discharge model with C_D=1.21. The nozzle-supported plant was based on the modified Zaloudek and Moody correlations with C_D=1.0. The NRC has approved both of these methods for use in subcompartment mass and energy calculations.

The break opening times were based on a single set (one hot leg and one cold leg history) of generic break opening time histories (see section 4.2). The histories were valid for both the nozzle- and skirt-supported plants and for break areas from zero to a full 2A guillotine opening at the reactor vessel inlet and outlet.

The initial conditions for the mass and energy models are presented in Table 4.3-8. Figures 4.3-54 through 4.3-61 illustrate the results of the mass and energy spectrum analyses. Figures 4.3-62 through 4.3-66 show the node/flow path diagrams for the two mass and energy models.

Table 4.3-1. Key Reactor Cavity Design Parameters

Plant	Vent area, ft^2			Type of neutron shield, plug/tank	Reactor cavity ID, ft-in.	Lower reactor cavity vol., ft^3	Height below nozzle belt C_L, ft-in.	Height above nozzle belt C_L, ft-in.	Detector thimble design
	Hot leg	Cold leg	CF line						
ANO-1	8.410	36.100	1.325	Concrete plugs anchored w/bolts	22-8	1193.0	23-4.5	3-9.5	Standoff
Rancho Seco	4.300	29.091	0.928	Concrete plugs anchored w/bolts	23-0	1274.5	23-4.5	3-6	Standoff
CR-3	2.143	1.668	0.185	Blow-out 45° sand plugs	23-0	1334.4	23-4.5	4-0	Recessed
TMI-1	2.143	1.668	0.185	Blow-out 30° sand plugs	23-0	1226.8	23-4.5	4-0	Recessed
TMI-2	6.436	5.345	0.873	Hinged, water-filled tanks	23-0	1226.8[a]	23-4.5	6-11.188	Recessed
Ocoree[b] 1,2,3	0.573	1.374	1.025	Blow-out concrete plugs	23-0	1257.1	23-4.5	3-11	Standoff
DB-1	6.54	11.296	0.502	No blow-out devices, cavity open at top	23-0	N/A[c]	34-0[d]	7-0	Standoff

[a] First three levels of model taken from Crystal River-3/TMI-1 model.

[b] Penetration vent areas are values of smallest vent areas of the three plants.

[c] No physical barrier between main cavity and cavity under vessel.

[d] Measured to concrete below vessel since no barrier between main cavity and cavity under vessel.

N/A — Not applicable.

Table 4.3-2. Time Step Sensitivity Study, Skirt-Supported Plants

Time step, s	Force at 0.022 s, 10^6 lbf	Moment, 10^6 in-lbf	Break node pressure at 0.022 s, psia			
			39	40	51	52
0.0001	6.63	1399.51	396.48	396.48	425.07	425.07
0.00005	6.64	1401.19	396.61	396.61	425.20	425.20

Table 4.3-3. Noding Sensitivity Study, Nozzle-Supported Plants

Model, nodes	Lateral force, 10^6 lbf	Moment, 10^6 in.-lbf	Uplift force, 10^6 lbf
61	10.90	321.0	5.17
72	11.09	302.4	6.73
84	11.28	288.1	7.16

Table 4.3-4. ANO-1 Control Volume Data

Node No.	Area, ft^2	Height, ft	Initial pressure, psia
1	15.759	7.583	14.700
2	14.032	7.583	14.700
3	14.032	7.583	14.700
4	14.032	7.583	14.700
5	14.032	7.583	14.700
6	15.759	7.583	14.700
7	15.759	7.583	14.700
8	14.032	7.583	14.700
9	14.032	7.583	14.700
10	14.032	7.583	14.700
11	14.032	7.583	14.700
12	15.759	7.583	14.700
13	15.750	6.000	14.700
14	13.052	6.000	14.700
15	13.052	6.000	14.700
16	13.052	6.000	14.700
17	13.052	6.000	14.700
18	15.759	6.000	14.700
19	15.759	6.000	14.700
20	13.052	6.000	14.700
21	13.052	6.000	14.700
22	13.052	6.000	14.700
23	13.052	6.000	14.700
24	15.759	6.000	14.700
25	15.759	6.000	14.700
26	13.658	6.000	14.700
27	13.658	6.000	14.700
28	13.658	6.000	14.700
29	13.658	6.000	14.700
30	15.759	6.000	14.700
31	15.759	6.000	14.700
32	13.658	6.000	14.700
33	13.658	6.000	14.700
34	13.658	6.000	14.700
35	13.658	6.000	14.700
36	15.759	6.000	14.700
37	11.283	3.792	14.700
38	9.556	3.792	14.700
39	7.789	3.792	14.700
40	7.789	3.792	14.700
41	9.556	3.792	14.700
42	11.283	3.792	14.700
43	11.283	3.792	14.700
44	9.556	3.792	14.700
45	7.789	3.792	14.700
46	7.789	3.792	14.700
47	9.556	3.792	14.700
48	11.283	3.792	14.700
49	9.627	3.792	14.700
50	9.192	3.792	14.700
51	7.425	3.792	14.700
52	7.425	3.792	14.700
53	9.192	3.792	14.700
54	9.627	3.792	14.700
55	9.627	3.792	14.700
56	9.192	3.792	14.700
57	7.425	3.792	14.700
58	7.425	3.792	14.700
59	9.192	3.792	14.700
60	9.627	3.792	14.700
61	17.996	5.344	14.700
62	17.996	5.344	14.700
63	29.891	6.938	14.700
64	29.891	6.938	14.700
65	29.891	6.938	14.700
66	29.891	6.938	14.700
67	6.803	1.938	14.700
68	6.803	1.938	14.700
69	114.988	10.375	14.700
70	20787.500	80.000	14.700

Table 4.3-5. ANO-1 Flow Path Data

PATH	TYPE*	FROM NODE	TO NODE	INITIAL FLOW RATE (LBM/SECONDS)	LENGTH OVER AREA (1/FT)	CROSS SEC. AREA (FT**2)	REV. FORM LOSS** K-FACTOR	FORWARD FORM LOSS	L/D$_h$
1	5	1	2	0.	2.20000E-01	2.330E+01	0.	0.	1.633E+00
2	5	2	3	0.	2.92000E-01	1.540E+01	0.	2.500E-01	2.320E+00
3	5	3	4	0.	2.20000E-01	2.330E+01	0.	0.	1.633E+00
4	5	4	5	0.	2.92000E-01	1.540E+01	0.	2.500E-01	2.320E+00
5	5	5	6	0.	2.20000E-01	2.330E+01	0.	0.	1.633E+00
6	5	6	7	0.	2.20000E-01	2.330E+01	0.	0.	1.633E+00
7	5	7	8	0.	2.20000E-01	2.330E+01	0.	0.	1.633E+00
8	5	8	9	0.	2.92000E-01	1.540E+01	0.	2.500E-01	2.320E+00
9	5	9	10	0.	2.20000E-01	2.330E+01	0.	0.	1.633E+00
10	5	10	11	0.	2.92000E-01	1.540E+01	0.	2.500E-01	2.320E+00
11	5	11	12	0.	2.20000E-01	2.330E+01	0.	0.	1.633E+00
12	5	12	1	0.	2.20000E-01	2.330E+01	0.	0.	1.633E+00
13	5	13	14	0.	2.78000E-01	1.843E+01	0.	0.	1.379E+00
14	5	14	15	0.	4.51000E-01	1.018E+01	0.	3.790E-01	2.267E+00
15	5	15	16	0.	2.78000E-01	1.843E+01	0.	0.	1.379E+00
16	5	16	17	0.	4.51000E-01	1.018E+01	0.	3.790E-01	2.267E+00
17	5	17	18	0.	2.78000E-01	1.843E+01	0.	0.	1.379E+00
18	5	18	19	0.	2.78000E-01	1.843E+01	0.	0.	1.379E+00
19	5	19	20	0.	2.78000E-01	1.843E+01	0.	0.	1.379E+00
20	5	20	21	0.	4.51000E-01	1.018E+01	0.	3.790E-01	2.267E+00
21	5	21	22	0.	2.78000E-01	1.843E+01	0.	0.	1.379E+00
22	5	22	23	0.	4.51000E-01	1.018E+01	0.	3.790E-01	2.267E+00
23	5	23	24	0.	2.78000E-01	1.843E+01	0.	0.	1.379E+00
24	5	24	13	0.	2.78000E-01	1.843E+01	0.	0.	1.379E+00
25	5	25	26	0.	2.78000E-01	1.843E+01	0.	0.	1.379E+00
26	5	26	27	0.	4.09000E-01	1.142E+01	0.	2.970E-01	2.077E+00
27	5	27	28	0.	2.78000E-01	1.843E+01	0.	0.	1.379E+00
28	5	28	29	0.	4.09000E-01	1.142E+01	0.	2.970E-01	2.077E+00
29	5	29	30	0.	2.78000E-01	1.843E+01	0.	0.	1.379E+00
30	5	30	31	0.	2.78000E-01	1.843E+01	0.	0.	1.379E+00
31	5	31	32	0.	2.78000E-01	1.843E+01	0.	0.	1.379E+00
32	5	32	33	0.	4.09000E-01	1.142E+01	0.	2.970E-01	2.077E+00
33	5	33	34	0.	2.78000E-01	1.843E+01	0.	0.	1.379E+00
34	5	34	35	0.	4.09000E-01	1.142E+01	0.	2.970E-01	2.077E+00
35	5	35	36	0.	2.78000E-01	1.843E+01	0.	0.	1.379E+00
36	5	36	25	0.	2.78000E-01	1.843E+01	0.	0.	1.379E+00

Table 4.3-5. (Cont'd)

PATH	TYPE	FROM NODE	TO NODE	INITIAL FLOW RATE (LBM/SECONDS)	LENGTH OVER AREA (1/FT)	CROSS SEC. AREA (FT**2)	REV. FORM LOSS K-FACTOR	FORWARD FORM LOSS	L/Dh
37	5	37	38	0.	1.22000E+00	4.24CE+00	0.	6.240E-01	3.024E+00
38	5	38	39	0.	6.34000E-01	7.077E+00	0.	2.720E-01	2.079E+00
39	5	39	40	0.	1.85700E+00	2.78[illegible]E+00	0.	8.580E-01	3.775E+00
40	5	40	41	0.	[illegible]	[illegible]	0.	2.720E-01	[illegible]
41	5	41	42	0.	1.22000E+00	4.24CE+00	0.	6.240E-01	3.024E+00
42	5	42	43	0.	4.69000E-01	1.1C3E+01	0.	0.	1.469E+00
43	5	43	44	0.	1.[illegible]	4.24[illegible]	0.	6.240E-01	3.024E+00
44	5	44	45	0.	6.34000E-01	7.077E+00	0.	2.720E-01	2.079E+00
45	5	45	46	0.	1.857[illegible]	2.78[illegible]	0.	8.580E-01	3.775E+00
46	5	46	47	0.	6.34000E-01	7.077E+00	0.	2.720E-01	2.079E+00
47	5	47	48	0.	1.22000E+00	4.24CE+00	0.	6.240E-01	3.024E+00
48	5	48	37	0.	4.69000E-01	1.1C3E+01	0.	0.	1.469E+00
49	5	49	50	0.	1.17300E+00	4.141E+00	0.	6.340E-01	4.799E+00
50	5	50	51	0.	6.67000E-01	7.013E+00	0.	4.000E-01	2.399E+00
51	5	51	52	0.	1.92500E+00	2.687E+00	0.	8.710E-01	6.550E+00
52	5	52	53	0.	6.67000E-01	7.013E+00	0.	4.000E-01	2.399E+00
53	5	53	54	0.	1.17300E+00	4.141E+00	0.	6.340E-01	4.799E+00
54	5	54	55	0.	6.66000E-01	5.534E+00	0.	5.200E-01	4.598E+00
55	5	55	56	0.	1.17300E+00	4.141E+00	0.	6.340E-01	4.799E+00
56	5	56	57	0.	6.67000E-01	7.013E+00	0.	4.000E-01	2.399E+00
57	5	57	58	0.	1.92500E+00	2.687E+00	0.	8.710E-01	6.550E+00
58	5	58	59	0.	6.67000E-01	7.013E+00	0.	4.000E-01	2.399E+00
59	5	59	60	0.	1.17300E+00	4.141E+00	0.	6.340E-01	4.799E+00
60	5	60	49	0.	6.66000E-01	5.534E+00	0.	5.200E-01	4.598E+00
61	5	1	13	0.	4.74000E-01	1.576E+01	0.	0.	1.825E+00
62	5	2	14	0.	5.49000E-01	1.305E+01	5.0000000E-03	2.800E-02	2.498E+00
63	5	3	15	0.	5.49000E-01	1.305E+01	5.0000000E-03	2.800E-02	2.498E+00
64	5	4	16	0.	5.49000E-01	1.305E+01	5.0000000E-03	2.800E-02	2.498E+00
65	5	5	17	0.	5.49000E-01	1.305E+01	5.0000000E-03	2.800E-02	2.498E+00
66	5	6	18	0.	4.74000E-01	1.576E+01	0.	0.	1.825E+00
67	5	7	19	0.	4.74000E-01	1.576E+01	0.	0.	1.825E+00
68	5	8	20	0.	5.49000E-01	1.305E+01	5.0000000E-03	2.800E-02	2.498E+00
69	5	9	21	0.	5.49000E-01	1.305E+01	5.0000000E-03	2.800E-02	2.498E+00
70	5	10	22	0.	5.49000E-01	1.305E+01	5.0000000E-03	2.800E-02	2.498E+00
71	5	11	23	0.	5.49000E-01	1.305E+01	5.0000000E-03	2.800E-02	2.498E+00
72	5	12	24	0.	4.74000E-01	1.576E+01	0.	0.	1.825E+00
73	5	13	25	0.	4.19000E-01	1.576E+01	0.	0.	1.613E+00
74	5	14	26	0.	5.01000E-01	1.305E+01	2.8000000E-02	5.000E-03	2.207E+00
75	5	15	27	0.	5.01000E-01	1.305E+01	2.8000000E-02	5.000E-03	2.207E+00
76	5	16	28	0.	5.01000E-01	1.305E+01	2.8000000E-02	5.000E-03	2.207E+00
77	5	17	29	0.	5.01000E-01	1.305E+01	2.8000000E-02	5.000E-03	2.207E+00
78	5	18	30	0.	4.19000E-01	1.576E+01	0.	0.	1.613E+00

Table 4.3-5. (Cont'd)

PATH	TYPE	FROM NODE	TO NODE	INITIAL FLOWRATE (LBM/SECOND)	LENGTH OVER AREA (1/FT)	CROSS SEC. AREA(FT**2)	REV. FORM LOSS K-FACTOR	FORWARD FORM LOSS	L/D_h
79	5	19	31	0.	4.190000E-01	1.576E+01	0.	0.	1.613E+00
80	5	20	32	0.	3.010000E-01	1.305E+01	2.800000000E-02	5.000E-03	2.207E+00
81	5	21	33	0.	5.010000E-01	1.305E+01	2.800000000E-02	5.000E-03	2.207E+00
82	5	22	34	0.	5.010000E-01	1.305E+01	2.800000000E-02	5.000E-03	2.207E+00
83	5	23	35	0.	3.010000E-01	1.305E+01	2.800000000E-02	5.000E-03	2.207E+00
84	5	24	36	0.	4.190000E-01	1.576E+01	0.	0.	1.613E+00
85	5	25	37	0.	3.420000E-01	1.576E+01	0.	0.	1.316E+00
86	5	26	38	0.	3.840000E-01	1.403E+01	0.	0.	1.628E+00
87	5	27	39	0.	3.840000E-01	1.403E+01	0.	0.	1.628E+00
88	5	28	40	0.	3.840000E-01	1.403E+01	0.	0.	1.628E+00
89	5	29	41	0.	3.840000E-01	1.403E+01	0.	0.	1.628E+00
90	5	30	42	0.	3.420000E-01	1.576E+01	0.	0.	1.316E+00
91	5	31	43	0.	3.420000E-01	1.576E+01	0.	0.	1.316E+00
92	5	32	44	0.	3.840000E-01	1.403E+01	0.	0.	1.628E+00
93	5	33	45	0.	3.840000E-01	1.403E+01	0.	0.	1.628E+00
94	5	34	46	0.	3.840000E-01	1.403E+01	0.	0.	1.628E+00
95	5	35	47	0.	3.840000E-01	1.403E+01	0.	0.	1.628E+00
96	5	36	48	0.	3.420000E-01	1.576E+01	0.	0.	1.316E+00
97	5	37	49	0.	7.510000E-01	5.559E+00	0.	6.490E-01	3.132E+00
98	5	38	50	0.	6.396000E-01	6.528E+00	0.	4.640E-01	2.452E+00
99	5	39	51	0.	8.330000E-01	5.073E+00	0.	6.310E-01	2.790E+00
100	5	40	52	0.	8.230000E-01	5.073E+00	0.	6.310E-01	2.790E+00
101	5	41	53	0.	6.396000E-01	6.528E+00	0.	4.640E-01	2.452E+00
102	5	42	54	0.	7.510000E-01	5.559E+00	0.	6.490E-01	3.100E+02
103	5	43	55	0.	7.510000E-01	5.559E+00	0.	6.490E-01	3.132E+00
104	5	44	56	0.	6.396000E-01	6.528E+00	0.	4.640E-01	2.452E+00
105	5	45	57	0.	8.330000E-01	5.073E+00	0.	6.310E-01	2.790E+00
106	5	46	58	0.	8.230000E-01	5.073E+00	0.	6.310E-01	2.790E+00
107	5	47	59	0.	6.396000E-01	6.528E+00	0.	4.640E-01	2.452E+00
108	5	48	60	0.	7.510000E-01	5.559E+00	0.	6.490E-01	3.132E+00
109	5	38	61	0.	2.010000E+00	1.206E+00	0.	3.230E-01	8.728E+01
110	5	40	61	0.	2.010000E+00	1.206E+00	0.	3.230E-01	8.728E+01
111	5	45	62	0.	2.010000E+00	1.206E+00	0.	3.230E-01	8.728E+01
112	5	46	62	0.	2.010000E+00	1.206E+00	0.	3.230E-01	8.728E+01
113	5	37	63	0.	4.770000E-01	1.121E+01	0.	3.000E-04	4.681E+01
114	5	38	63	0.	4.770000E-01	1.121E+01	0.	3.000E-04	4.681E+01
115	5	41	64	0.	4.770000E-01	1.121E+01	0.	3.000E-04	4.681E+01
116	5	42	64	0.	4.770000E-01	1.121E+01	0.	3.000E-04	4.681E+01
117	5	43	65	0.	4.770000E-01	1.121E+01	0.	3.000E-04	4.681E+01
118	5	44	65	0.	4.770000E-01	1.121E+01	0.	3.000E-04	4.681E+01
119	5	47	66	0.	4.770000E-01	1.121E+01	0.	3.000E-04	4.681E+01
120	5	48	66	0.	4.770000E-01	1.121E+01	0.	3.000E-04	4.681E+01
121	5	31	61	0.	1.075000E+00	5.517E+00	0.	2.150E-01	5.956E+01
122	5	32	61	0.	1.075000E+00	5.517E+00	0.	2.150E-01	5.956E+01
123	5	37	62	0.	1.075000E+00	5.517E+00	0.	2.150E-01	5.956E+01
124	5	38	62	0.	1.075000E+00	5.517E+00	0.	2.150E-01	5.956E+01
125	5	41	63	0.	4.770000E-01	1.121E+01	0.	3.000E-04	4.681E+01
126	5	50	63	0.	6.250000E-01	7.223E+00	0.	1.360E-01	5.127E+01

Table 4.3-5. (Cont'd)

PATH	TYPE	FROM NODE	TO NODE	INITIAL FLOW RATE (LBM/SECOND)	LENGTH OVER AREA (1/FT)	CROSS SEC. AREA (FT**2)	REV. FORM LOSS K-FACTOR	FORWARD FORM LOSS	L/D_h
127	5	53	64	0.	6.25000E-01	7.223E+00	0.	1.360E-01	5.127E+01
128	5	54	64	0.	6.25000E-01	7.223E+00	0.	1.360E-01	5.127E+01
129	5	55	64	0.	6.25000E-01	7.223E+00	0.	1.360E-01	5.127E+01
130	5	56	64	0.	6.25000E-01	7.223E+00	0.	1.360E-01	5.127E+01
131	5	57	64	0.	6.25000E-01	7.223E+00	0.	1.360E-01	5.127E+01
132	5	60	66	0.	6.25000E-01	7.223E+00	0.	1.360E-01	5.127E+01
133	5	61	66	0.	6.25000E-01	7.223E+00	0.	1.360E-01	5.127E+01
134	5	62	66	0.	6.25000E-01	7.223E+00	0.	1.360E-01	5.127E+01
135	5	63	66	0.	6.25000E-01	7.223E+00	0.	1.360E-01	5.127E+01
136	5	64	66	0.	6.25000E-01	7.223E+00	0.	1.360E-01	5.127E+01
137	5	61	70	0.	4.06000E-01	8.410E+00	0.	1.000E+00	5.776E+00
138	5	62	70	0.	4.06000E-01	8.410E+00	0.	1.000E+00	5.776E+00
139	5	63	70	0.	8.19000E-02	1.681E+01	0.	1.000E+00	1.191E+00
140	5	64	70	0.	8.19000E-02	1.681E+01	0.	1.000E+00	1.191E+00
141	5	65	70	0.	8.19000E-02	1.681E+01	0.	1.000E+00	1.191E+00
142	5	66	70	0.	8.19000E-02	3.610E+01	0.	1.000E+00	1.191E+00
143	5	67	70	0.	2.04800E+00	1.345E+00	0.	1.000E+00	1.612E+01
144	5	68	70	0.	2.04800E+00	1.345E+00	0.	1.000E+00	1.612E+01
145	5	1	69	0.	6.39000E-01	4.670E-01	0.	1.400E+00	4.178E+02
146	5	2	69	0.	6.39000E-01	4.670E-01	0.	1.400E+00	4.178E+02
147	5	3	69	0.	6.39000E-01	4.670E-01	0.	1.400E+00	4.178E+02
148	5	4	69	0.	6.39000E-01	4.670E-01	0.	1.400E+00	4.178E+02
149	5	5	69	0.	6.39000E-01	4.670E-01	0.	1.400E+00	4.178E+02
150	5	6	69	0.	6.39000E-01	4.670E-01	0.	1.400E+00	4.178E+02
151	5	7	69	0.	6.39000E-01	4.670E-01	0.	1.400E+00	4.178E+02
152	5	8	69	0.	6.39000E-01	4.670E-01	0.	1.400E+00	4.178E+02
153	5	9	69	0.	6.39000E-01	4.670E-01	0.	1.400E+00	4.178E+02
154	5	10	69	0.	6.39000E-01	4.670E-01	0.	1.400E+00	4.178E+02
155	5	11	69	0.	6.39000E-01	4.670E-01	0.	1.400E+00	4.178E+02
156	5	12	69	0.	6.39000E-01	4.670E-01	0.	1.400E+00	4.178E+02
157	5	49	70	0.	5.92100E+00	4.190E-01	0.	1.386E+00	2.235E+02
158	5	50	70	0.	5.92100E+00	4.190E-01	0.	1.386E+00	2.235E+02
159	5	51	70	0.	5.90500E+00	4.190E-01	0.	1.386E+00	2.235E+02
160	5	52	70	0.	5.90500E+00	4.190E-01	0.	1.386E+00	2.235E+02
161	5	53	70	0.	5.90500E+00	4.190E-01	0.	1.386E+00	2.235E+02
162	5	54	70	0.	5.92100E+00	4.190E-01	0.	1.386E+00	2.235E+02
163	5	55	70	0.	5.92100E+00	4.190E-01	0.	1.386E+00	2.235E+02
164	5	56	70	0.	5.90500E+00	4.190E-01	0.	1.386E+00	2.235E+02
165	5	57	70	0.	5.90500E+00	4.190E-01	0.	1.386E+00	2.235E+02
166	5	58	70	0.	5.90500E+00	4.190E-01	0.	1.386E+00	2.235E+02
167	5	59	70	0.	5.92100E+00	4.190E-01	0.	1.386E+00	2.235E+02
168	5	60	70	0.	5.92100E+00	4.190E-01	0.	1.386E+00	2.235E+02

*Type 5 flow paths are designated as those paths which are checked for choking using Moody choked flow correlation with $C_D = 0.6$.

**The reverse form loss factor in CRAFT2 may be set to zero if it is identical to the forward form loss factor.

Table 4.3-6. Davis-Besse 1 Control Volume Data

NODE NUMBER	AREA (FEET SQ)	HEIGHT (FEET)	INITIAL PRESSURE (PSIA)
1	7.460	4.750	14.700
2	11.560	4.750	14.700
3	10.420	4.750	14.700
4	0.930	4.750	14.700
5	11.790	4.750	14.700
6	10.130	4.750	14.700
7	7.460	4.750	14.700
8	11.560	4.750	14.700
9	10.420	4.750	14.700
10	0.930	4.750	14.700
11	11.790	4.750	14.700
12	10.130	4.750	14.700
13	8.650	4.260	14.700
14	11.790	4.260	14.700
15	10.680	4.260	14.700
16	15.440	4.260	14.700
17	12.050	4.260	14.700
18	10.410	4.260	14.700
19	8.650	4.260	14.700
20	11.790	4.260	14.700
21	10.680	4.260	14.700
22	15.440	4.260	14.700
23	12.050	4.260	14.700
24	10.410	4.260	14.700
25	17.020	5.167	14.700
26	15.640	5.167	14.700
27	13.850	5.167	14.700
28	15.900	5.167	14.700
29	15.640	5.167	14.700
30	13.890	5.167	14.700
31	17.020	5.167	14.700
32	15.640	5.167	14.700
33	13.850	5.167	14.700
34	15.900	5.167	14.700
35	15.640	5.167	14.700
36	13.890	5.167	14.700
37	17.020	7.950	14.700
38	17.880	7.950	14.700
39	15.750	7.950	14.700
40	13.750	7.950	14.700
41	17.280	7.950	14.700
42	13.810	7.950	14.700
43	17.020	7.950	14.700
44	17.280	7.950	14.700
45	15.750	7.950	14.700
46	15.750	7.950	14.700
47	17.280	7.950	14.700
48	15.810	7.950	14.700
49	21.820	7.950	14.700
50	21.820	7.950	14.700
51	21.680	7.950	14.700
52	21.680	7.950	14.700
53	21.820	7.950	14.700
54	21.680	7.950	14.700
55	21.820	7.950	14.700
56	21.820	7.950	14.700
57	21.680	7.950	14.700
58	21.680	7.950	14.700
59	21.820	7.950	14.700
60	21.680	7.950	14.700
61	38.820	8.333	14.700
62	155.270	9.000	14.700
63	41.679	7.000	14.700
64	6.687	6.500	14.700
65	8.687	6.500	14.700
66	12.810	6.000	14.700
67	12.810	6.000	14.700
68	17.810	6.000	14.700
69	17.810	6.000	14.700
70	1.254	2.000	14.700
71	1.254	2.000	14.700
72	34109.321	80.000	14.700
73	5.836	2.250	14.700
74	5.836	2.250	14.700
75	5.836	2.250	14.700
76	5.836	2.250	14.700
77	5.836	2.250	14.700
80	5.836	2.250	14.700
81	5.836	2.250	14.700
82	5.836	2.250	14.700
83	5.836	2.250	14.700
84	5.836	2.250	14.700

Table 4.3-7. Davis-Besse 1 Flow Path Data

PATH	* TYPE	FROM NODE	TO NODE	INITIAL FLOW RATE (LBM/SECONDS)	LENGTH OVER AREA (1/FT)	CROSS SEC. AREA (FT**2)	REV. FORM LOSS K-FACTOR**	FORWARD FORM LOSS	L/D_h
1	5	1	13	0.	1.49700E+00	1.169E+00	1.21000000E+00	1.280E+00	1.291E+01
2	5	2	14	0.	4.68000E-01	8.324E+00	3.60000000E-01	2.900E-01	2.242E+00
3	5	3	15	0.	4.93400E-01	7.991E+00	3.20000000E-01	2.400E-01	2.278E+00
4	5	4	16	0.	3.63400E-01	8.008E+00	2.23000000E-01	2.610E-01	3.243E+00
5	5	5	17	0.	4.28100E-01	9.369E+00	2.49700000E-01	2.300E-01	1.593E+00
6	5	6	18	0.	5.48000E-01	7.990E+00	3.10000000E-01	2.400E-01	2.081E+00
7	5	7	19	0.	1.49700E+00	1.169E+00	1.21000000E+00	1.280E+00	1.291E+01
8	5	8	20	0.	4.68000E-01	8.324E+00	3.60000000E-01	2.900E-01	2.242E+00
9	5	9	21	0.	4.93400E-01	7.991E+00	3.20000000E-01	2.400E-01	2.278E+00
10	5	10	22	0.	3.63400E-01	8.008E+00	2.23000000E-01	2.610E-01	3.243E+00
11	5	11	23	0.	4.28100E-01	9.369E+00	2.49700000E-01	2.300E-01	1.593E+00
12	5	12	24	0.	5.48000E-01	7.990E+00	3.10000000E-01	2.400E-01	2.081E+00
13	5	13	25	0.	2.97000E-01	9.209E+00	1.80000000E-01	2.060E-01	3.217E+00
14	5	14	26	0.	4.04000E-01	1.106E+01	4.02000000E-01	3.960E-01	2.934E+00
15	5	15	27	0.	4.62000E-01	8.977E+00	4.26000000E-01	4.200E-01	4.067E+00
16	5	16	28	0.	2.99000E-01	1.529E+01	0.	4.000E-02	1.295E+00
17	5	17	29	0.	4.04000E-01	1.106E+01	4.02000000E-01	3.960E-01	2.934E+00
18	5	18	30	0.	4.59000E-01	9.683E+00	4.53000000E-01	4.460E-01	3.713E+00
19	5	19	31	0.	2.97000E-01	9.209E+00	1.80000000E-01	2.060E-01	3.217E+00
20	5	20	32	0.	4.04000E-01	1.106E+01	4.02000000E-01	3.960E-01	2.934E+00
21	5	21	33	0.	4.62000E-01	8.977E+00	4.26000000E-01	4.200E-01	4.067E+00
22	5	22	34	0.	2.99000E-01	1.529E+01	0.	4.000E-02	1.295E+00
23	5	23	35	0.	4.04000E-01	1.106E+01	4.02000000E-01	3.960E-01	2.934E+00
24	5	24	36	0.	4.52000E-01	9.683E+00	4.53000000E-01	4.460E-01	3.713E+00
25	5	25	37	0.	3.86000E-01	1.701E+01	0.	0.	1.609E+00
26	5	26	38	0.	4.64000E-01	1.106E+01	3.91000000E-01	3.760E-01	4.082E+00
27	5	27	39	0.	5.50000E-01	8.977E+00	4.64000000E-01	4.680E-01	5.659E+00
28	5	28	40	0.	4.13000E-01	1.589E+01	0.	0.	1.722E+00
29	5	29	41	0.	4.64000E-01	1.106E+01	3.91000000E-01	3.760E-01	4.082E+00
30	5	30	42	0.	5.68000E-01	8.612E+00	4.40000000E-01	4.490E-01	5.939E+00
31	5	31	43	0.	3.86000E-01	1.701E+01	0.	0.	1.609E+00
32	5	32	44	0.	4.64000E-01	1.106E+01	3.91000000E-01	3.760E-01	4.082E+00
33	5	33	45	0.	5.50000E-01	8.977E+00	4.64000000E-01	4.680E-01	5.659E+00
34	5	34	46	0.	4.13000E-01	1.589E+01	0.	0.	1.722E+00
35	5	35	47	0.	4.64000E-01	1.106E+01	3.91000000E-01	3.760E-01	4.082E+00
36	5	36	48	0.	5.68000E-01	8.612E+00	4.40000000E-01	4.490E-01	5.939E+00

Table 4.3-7. (Cont'd)

PATH	* TYPE	FROM NODE	TO NODE	INITIAL FLOW RATE (LBM/SECONDS)	LENGTH OVER AREA (1/FT)	CROSS SEC. AREA (FT**2)	REV. FORM LOSS K-FACTOR**	FORWARD FORM LOSS	L/D_h
37	5	37	49	0.	4.570000E-01	1.701E+01	6.500000000E-02	3.900E-02	1.950E+00
38	5	38	50	0.	4.540000E-01	1.727E+01	6.100000000E-02	3.000E-02	1.775E+00
39	5	39	51	0.	4.690000E-01	1.519E+01	9.300000000E-02	3.300E-02	2.237E+00
40	5	40	52	0.	4.750000E-01	1.589E+01	8.200000000E-02	3.500E-02	2.067E+00
41	5	41	53	0.	4.540000E-01	1.727E+01	6.100000000E-02	3.000E-02	1.775E+00
42	5	42	54	0.	4.610000E-01	1.482E+01	1.000000000E-01	4.200E-02	2.716E+00
43	5	43	55	0.	4.570000E-01	1.701E+01	6.500000000E-02	3.900E-02	1.950E+00
44	5	44	56	0.	4.540000E-01	1.727E+01	6.100000000E-02	3.000E-02	1.775E+00
45	5	45	57	0.	4.690000E-01	1.519E+01	9.300000000E-02	3.300E-02	2.237E+00
46	5	46	58	0.	4.750000E-01	1.589E+01	8.200000000E-02	3.500E-02	2.067E+00
47	5	47	59	0.	4.540000E-01	1.727E+01	6.100000000E-02	3.000E-02	1.775E+00
48	5	48	60	0.	4.610000E-01	1.482E+01	1.000000000E-01	4.200E-02	2.716E+00
49	5	49	61	0.	2.990000E-01	2.039E+01	1.210000000E-01	1.000E-01	1.511E+00
50	5	50	61	0.	2.990000E-01	2.039E+01	1.210000000E-01	1.000E-01	1.511E+00
51	5	51	61	0.	2.990000E-01	2.025E+01	1.230000000E-01	1.000E-01	1.624E+00
52	5	52	61	0.	2.990000E-01	2.025E+01	1.230000000E-01	1.000E-01	1.624E+00
53	5	53	61	0.	2.990000E-01	2.039E+01	1.210000000E-01	1.000E-01	1.511E+00
54	5	54	61	0.	2.990000E-01	2.025E+01	1.230000000E-01	1.000E-01	1.624E+00
55	5	55	61	0.	2.990000E-01	2.039E+01	1.210000000E-01	1.000E-01	1.511E+00
56	5	56	61	0.	2.990000E-01	2.039E+01	1.210000000E-01	1.000E-01	1.511E+00
57	5	57	61	0.	2.990000E-01	2.025E+01	1.230000000E-01	1.000E-01	1.624E+00
58	5	58	61	0.	2.990000E-01	2.025E+01	1.230000000E-01	1.000E-01	1.624E+00
59	5	59	61	0.	2.990000E-01	2.039E+01	1.210000000E-01	1.000E-01	1.511E+00
60	5	60	61	0.	2.990000E-01	2.025E+01	1.230000000E-01	1.000E-01	1.624E+00
61	5	61	62	0.	1.260000E-01	1.260E+02	2.700000000E-02	6.500E-02	7.824E+00
62	5	61	63	0.	4.170000E-01	2.100E+01	5.670000000E-01	3.500E-01	8.742E+00
63	5	49	50	0.	1.330000E-01	3.728E+01	0.	0.	1.032E+00
64	5	50	51	0.	1.380000E-01	3.728E+01	0.	0.	1.032E+00
65	5	51	52	0.	1.400000E-01	3.066E+01	0.	2.060E-01	1.256E+00
66	5	52	53	0.	1.380000E-01	3.728E+01	0.	0.	1.032E+00
67	5	53	54	0.	1.380000E-01	3.728E+01	0.	0.	1.032E+00
68	5	54	55	0.	1.400000E-01	3.066E+01	0.	1.030E-01	1.256E+00
69	5	55	56	0.	1.380000E-01	3.728E+01	0.	0.	1.032E+00
70	5	56	57	0.	1.380000E-01	3.728E+01	0.	0.	1.032E+00
71	5	57	58	0.	1.400000E-01	3.066E+01	0.	2.060E-01	1.256E+00
72	5	58	59	0.	1.380000E-01	3.728E+01	0.	0.	1.032E+00
73	5	59	60	0.	1.380000E-01	3.728E+01	0.	0.	1.032E+00
74	5	60	47	0.	1.400000E-01	3.066E+01	0.	1.030E-01	1.256E+00
75	5	37	38	0.	1.920000E-01	2.671E+01	0.	0.	1.148E+00
76	5	38	39	0.	1.920000E-01	2.671E+01	0.	0.	1.148E+00
77	5	39	40	0.	2.480000E-01	1.859E+01	0.	2.130E-01	1.478E+00
78	5	40	41	0.	1.920000E-01	2.671E+01	0.	0.	1.148E+00

Table 4.3-7. (Cont'd)

PATH	TYPE	FROM NODE	TO NODE	INITIAL FLOW RATE (LBM/SECONDS)	LENGTH OVER AREA (1/FT)	CROSS SEC. AREA (FT**2)	REV. FORM LOSS K-FACTOR	FORWARD FORM LOSS	L/D$_h$
79	5	41	42	0.	1.920000E-01	2.671E+01	0.	0.	1.148E+00
80	5	42	43	0.	2.270000E-01	1.838E+01	0.	2.250E-01	1.710E+00
81	5	43	44	0.	1.920000E-01	2.671E+01	0.	0.	1.148E+00
82	5	44	45	0.	1.920000E-01	2.671E+01	0.	0.	1.148E+00
83	5	45	46	0.	2.480000E-01	1.859E+01	0.	2.130E-01	1.678E+00
84	5	46	47	0.	1.920000E-01	2.671E+01	0.	0.	1.148E+00
85	5	47	48	0.	1.920000E-01	2.671E+01	0.	0.	1.148E+00
86	5	48	37	0.	2.270000E-01	1.838E+01	0.	2.250E-01	1.710E+00
87	5	25	26	0.	5.130000E-01	2.852E+00	7.5000000E-01	4.600E-01	7.920E+00
88	5	26	27	0.	7.760000E-01	2.020E+00	0.	1.472E+00	1.391E+01
89	5	27	28	0.	5.690000E-01	2.852E+00	3.1500000E-01	4.300E-01	7.713E+00
90	5	28	29	0.	5.130000E-01	2.852E+00	7.5000000E-01	4.600E-01	7.920E+00
91	5	29	30	0.	7.760000E-01	2.020E+00	0.	1.472E+00	1.391E+01
92	5	30	31	0.	5.430000E-01	2.852E+00	2.9500000E-01	4.420E-01	7.816E+00
93	5	31	32	0.	5.130000E-01	2.852E+00	7.5000000E-01	4.600E-01	7.920E+00
94	5	32	33	0.	7.760000E-01	2.020E+00	0.	1.472E+00	1.391E+01
95	5	33	34	0.	5.690000E-01	2.852E+00	3.1500000E-01	4.300E-01	7.713E+00
96	5	34	35	0.	5.130000E-01	2.852E+00	7.5000000E-01	4.600E-01	7.920E+00
97	5	35	36	0.	7.760000E-01	2.020E+00	0.	1.472E+00	1.391E+01
98	5	36	25	0.	5.430000E-01	2.852E+00	2.9500000E-01	4.420E-01	7.816E+00
99	5	13	14	0.	5.526000E-01	5.763E+00	3.0100000E-01	2.510E-01	2.748E+00
100	5	14	15	0.	7.248000E-01	6.393E+00	0.	3.090E-01	4.333E+00
101	5	15	16	0.	4.352000E-01	1.050E+01	1.8800000E-01	1.500E-01	3.454E+00
102	5	16	17	0.	3.883000E-01	1.050E+01	7.0000000E-02	1.000E-01	3.454E+00
103	5	17	18	0.	7.248000E-01	6.393E+00	0.	3.090E-01	4.333E+00
104	5	18	19	0.	5.908000E-01	5.763E+00	2.9100000E-01	2.510E-01	2.748E+00
105	5	19	20	0.	5.526000E-01	5.763E+00	3.0100000E-01	2.710E-01	2.748E+00
106	5	20	21	0.	7.248000E-01	6.393E+00	0.	3.090E-01	4.333E+00
107	5	21	22	0.	4.352000E-01	1.050E+01	1.8800000E-01	1.500E-01	3.454E+00
108	5	22	23	0.	3.883000E-01	1.050E+01	7.0000000E-02	1.000E-01	3.454E+00
109	5	23	24	0.	7.248000E-01	6.393E+00	0.	3.090E-01	4.333E+00
110	5	24	13	0.	5.908000E-01	5.763E+00	2.9100000E-01	2.510E-01	2.748E+00
111	5	1	2	0.	5.389000E-01	5.667E+00	2.9000000E-01	3.800E-01	3.353E+00
112	5	2	3	0.	6.214000E-01	6.462E+00	5.5000000E-01	5.500E-01	2.875E+00
113	5	3	4	0.	4.882000E-01	6.479E+00	2.0300000E-01	2.000E-01	4.454E+00
114	5	4	5	0.	4.338000E-01	6.479E+00	2.5000000E-01	3.000E-01	4.454E+00
115	5	5	6	0.	6.214000E-01	6.462E+00	5.5000000E-01	5.500E-01	2.875E+00
116	5	6	7	0.	5.788000E-01	5.667E+00	3.8000000E-01	3.700E-01	3.353E+00
117	5	7	8	0.	5.389000E-01	5.667E+00	2.9000000E-01	3.800E-01	3.353E+00
118	5	8	9	0.	6.214000E-01	6.462E+00	5.5000000E-01	5.500E-01	2.875E+00
119	5	9	10	0.	4.882000E-01	6.479E+00	2.0300000E-01	2.000E-01	4.454E+00
120	5	10	11	0.	4.338000E-01	6.479E+00	2.5000000E-01	3.000E-01	4.454E+00
121	5	11	12	0.	6.214000E-01	6.462E+00	5.5000000E-01	5.500E-01	2.875E+00
122	5	12	1	0.	5.788000E-01	5.667E+00	3.8000000E-01	3.700E-01	3.353E+00
123	5	1	64	0.	6.870000E-01	3.270E+00	8.9200000E-01	8.490E-01	7.714E+00
124	5	7	65	0.	6.870000E-01	3.270E+00	8.9200000E-01	8.490E-01	7.714E+00
125	5	13	64	0.	6.560000E-01	3.270E+00	1.0020000E+00	9.250E-01	7.054E+01
126	5	19	65	0.	6.560000E-01	3.270E+00	1.0020000E+00	9.250E-01	7.054E+01

Table 4.3-7. (Cont'd)

PATH	TYPE	FROM NODE	TO NODE	INITIAL FLOW RATE (LBM/SECONDS)	LENGTH OVER AREA (1/FT)	CROSS SEC. AREA (FT**2)	REV. FORM LOSS K-FACTOR	FORWARD FORM LOSS	
131	5	5	69	0.	1.08100E+00	2.824E+00	4.985[illegible]E-01	4.470E-01	7.955E+01
132	5	6	67	0.	1.10600E+00	2.824E+00	4.460000[illegible]E-01	4.080E-01	7.966E+01
133	5	8	68	0.	1.08100E+00	2.824E+00	4.985[illegible]E-01	4.470E-01	7.955E+01
134	5	9	68	0.	1.10600E+00	2.824E+00	4.460[illegible]E-01	4.080E-01	7.966E+01
135	5	11	69	0.	1.08100E+00	2.824E+00	4.985[illegible]E-01	4.470E-01	7.955E+01
136	5	12	69	0.	1.10600E+00	2.824E+00	4.460[illegible]E-01	4.080E-01	7.966E+01
137	5	14	66	0.	1.07800E+00	3.175E+00	5.830000[illegible]E-01	4.520E-01	6.201E+01
138	5	15	66	0.	1.11600E+00	3.175E+00	8.010000[illegible]E-01	7.590E-01	6.201E+01
139	5	17	67	0.	1.07800E+00	3.175E+00	5.830000[illegible]E-01	4.520E-01	6.201E+01
140	5	18	67	0.	1.11600E+00	3.175E+00	8.010000[illegible]E-01	7.590E-01	6.201E+01
141	5	20	68	0.	1.07800E+00	3.175E+00	5.830000[illegible]E-01	4.520E-01	6.201E+01
142	5	21	68	0.	1.11600E+00	3.175E+00	8.010000[illegible]E-01	7.590E-01	6.201E+01
143	5	23	69	0.	1.07800E+00	3.175E+00	5.830000[illegible]E-01	4.520E-01	6.201E+01
144	5	24	69	0.	1.11600E+00	3.175E+00	8.010000[illegible]E-01	7.590E-01	6.201E+01
145	5	66	72	0.	1.60000E-01	1.772E+01	4.810000[illegible]E-01	1.041E+00	1.393E+00
146	5	67	72	0.	1.60000E-01	1.772E+01	4.810000[illegible]E-01	1.041E+00	1.393E+00
147	5	68	72	0.	1.60000E-01	1.772E+01	4.810000[illegible]E-01	1.041E+00	1.393E+00
148	5	69	72	0.	1.60000E-01	1.772E+01	4.810000[illegible]E-01	1.041E+00	1.393E+00
149	5	4	70	0.	5.10300E+00	5.018E-01	9.060000[illegible]E-01	4.810E-01	1.246E+02
150	5	10	71	0.	5.10300E+00	5.018E-01	9.060000[illegible]E-01	4.810E-01	1.246E+02
151	5	70	72	0.	4.98000E+00	5.020E-01	4.000000[illegible]E-01	1.000E+00	1.497E+01
152	5	71	72	0.	4.98000E+00	5.020E-01	4.000000[illegible]E-01	1.000E+00	1.497E+01
153	5	73	72	0.	2.37900E-01	4.843E+00	5.183000[illegible]E-01	1.054E+00	9.900E-01
154	5	74	72	0.	2.37900E-01	4.843E+00	5.183000[illegible]E-01	1.054E+00	9.900E-01
155	5	75	72	0.	2.37900E-01	4.843E+00	5.183000[illegible]E-01	1.054E+00	9.900E-01
156	5	76	72	0.	2.37900E-01	4.843E+00	5.183000[illegible]E-01	1.054E+00	9.900E-01
157	5	77	72	0.	2.37900E-01	4.843E+00	5.183000[illegible]E-01	1.054E+00	9.900E-01
158	5	78	72	0.	2.37900E-01	4.843E+00	5.183000[illegible]E-01	1.054E+00	9.900E-01
159	5	79	72	0.	2.37900E-01	4.843E+00	5.183000[illegible]E-01	1.054E+00	9.900E-01
160	5	80	72	0.	2.37900E-01	4.843E+00	5.183000[illegible]E-01	1.054E+00	9.900E-01
161	5	81	72	0.	2.37900E-01	4.843E+00	5.183000[illegible]E-01	1.054E+00	9.900E-01
162	5	82	72	0.	2.37900E-01	4.843E+00	5.183000[illegible]E-01	1.054E+00	9.900E-01
163	5	83	72	0.	2.37900E-01	4.843E+00	5.183000[illegible]E-01	1.054E+00	9.900E-01
164	5	84	72	0.	2.37900E-01	4.843E+00	5.183000[illegible]E-01	1.054E+00	9.900E-01
165	5	73	1	0.	3.84700E-01	5.615E+00	2.400000[illegible]E-01	2.749E-01	2.498E+00
166	5	74	2	0.	3.75000E-01	5.615E+00	2.370000[illegible]E-01	2.890E-01	2.498E+00
167	5	75	3	0.	3.78400E-01	5.615E+00	2.240000[illegible]E-01	2.360E-01	2.498E+00
168	5	76	4	0.	4.10900E-01	5.615E+00	2.142000[illegible]E-01	1.860E-01	2.498E+00
169	5	77	5	0.	3.75000E-01	5.615E+00	2.370000[illegible]E-01	2.890E-01	2.498E+00
170	5	78	6	0.	3.78400E-01	5.615E+00	2.240000[illegible]E-01	2.360E-01	2.498E+00
171	5	79	7	0.	3.84700E-01	5.615E+00	2.400000[illegible]E-01	2.749E-01	2.498E+00
172	5	80	8	0.	3.75000E-01	5.615E+00	2.370000[illegible]E-01	2.890E-01	2.498E+00
173	5	81	9	0.	3.78400E-01	5.615E+00	2.240000[illegible]E-01	2.360E-01	2.498E+00
174	5	82	10	0.	4.10900E-01	5.615E+00	2.142000[illegible]E-01	1.860E-01	2.498E+00
175	5	83	11	0.	3.75000E-01	5.615E+00	2.370000[illegible]E-01	2.890E-01	2.498E+00

Table 4.3-7. (Cont'd)

PATH	* TYPE	FROM NODE	TO NODE	INITIAL FLOW RATE (LBM/SECONDS)	LENGTH OVER AREA (1/FT)	CROSS SEC. AREA (FT**2)	REV. FORM LOSS K-FACTOR**	FORWARD FORM LOSS	L/D_h
176	5	84	12	0.	3.78400E-01	5.615E+00	2.2400000E-01	2.360E-01	2.498E+00
177	5	73	74	0.	1.74250E+00	2.745E+00	0.	0.	3.810E+00
178	5	74	75	0.	1.74250E+00	2.745E+00	0.	0.	3.810E+00
179	5	75	76	0.	1.74250E+00	2.745E+00	0.	0.	3.810E+00
180	5	76	77	0.	1.74250E+00	2.745E+00	0.	0.	3.810E+00
181	5	77	78	0.	1.74250E+00	2.745E+00	0.	0.	3.810E+00
182	5	78	79	0.	1.74250E+00	2.745E+00	0.	0.	3.810E+00
183	5	79	80	0.	1.74250E+00	2.745E+00	0.	0.	3.810E+00
184	5	80	81	0.	1.74250E+00	2.745E+00	0.	0.	3.810E+00
185	5	81	82	0.	1.74250E+00	2.745E+00	0.	0.	3.810E+00
186	5	82	83	0.	1.74250E+00	2.745E+00	0.	0.	3.810E+00
187	5	83	84	0.	1.74250E+00	2.745E+00	0.	0.	3.810E+00
188	5	84	73	0.	1.74250E+00	2.745E+00	0.	0.	3.810E+00

*Type 5 flow paths are designated as those paths which are checked for choking using Moody choked flow correlation with C_D = 0.6.

**The reverse form loss factor in CRAFT2 is set equal to the K-factor if entered as zero.

Table 4.3-8. Initial Conditions for Mass and Energy Release Rates

	Skirt-supported plant	Nozzle-supported plant
Reference core power (102%), MWt	2827	2827
T_{inlet}, F	560	555
T_{outlet}, F	611	608
System mass flow, 10^6 lbm/h	138	131

Figure 4.3-1. Rotational Venting Device

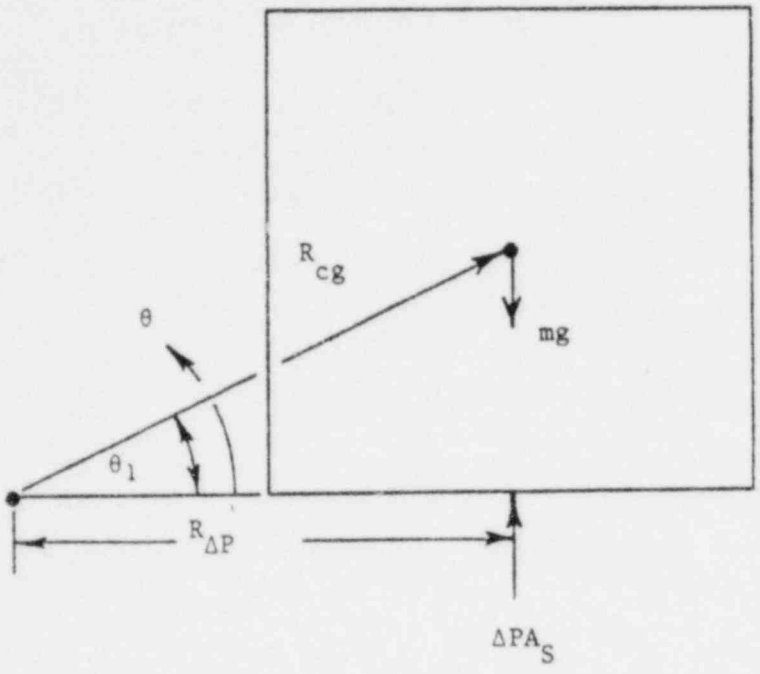

Figure 4.3-2. ANO-1 Reactor Cavity, Elevation View of 42-Node Model

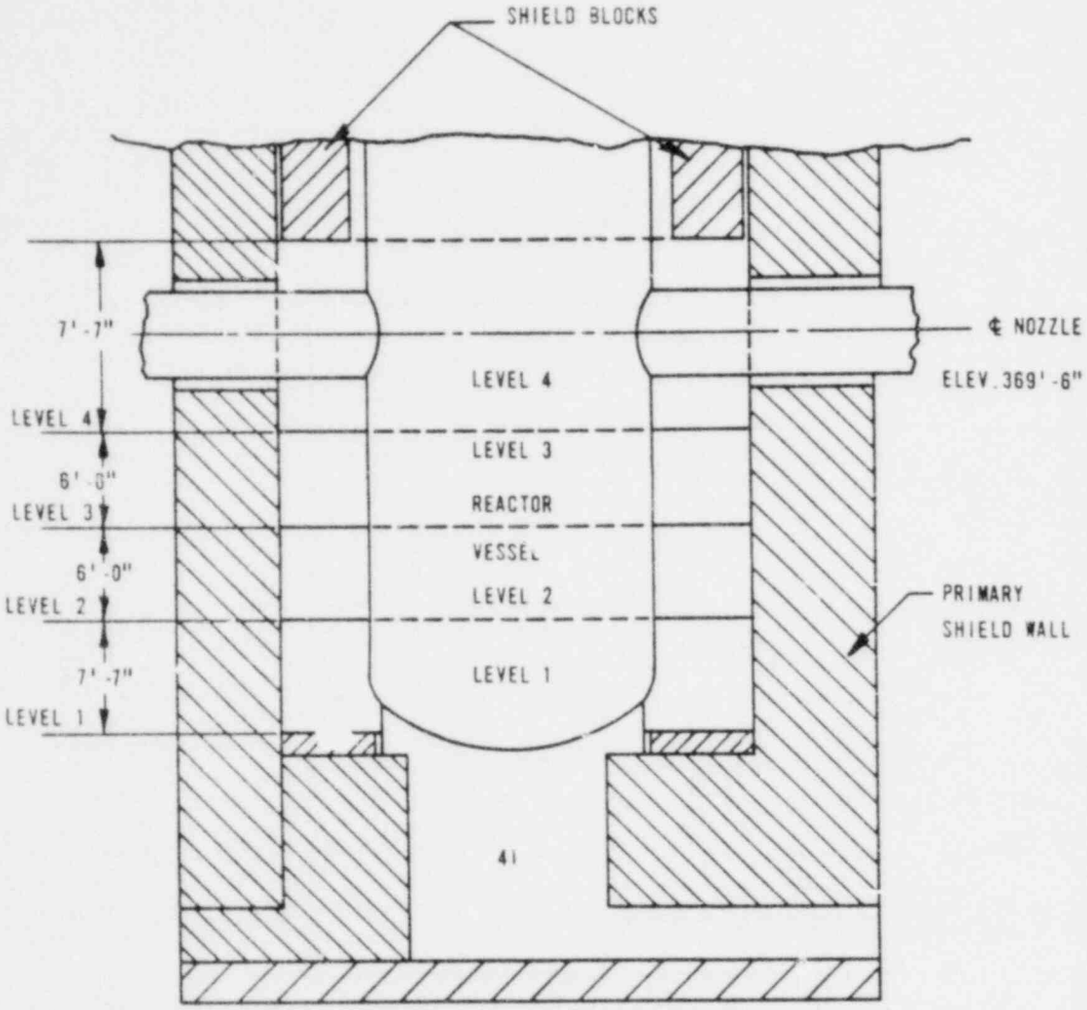

Figure 4.3-3. ANO-1 Reactor Cavity, Developed View of 42-Node Model

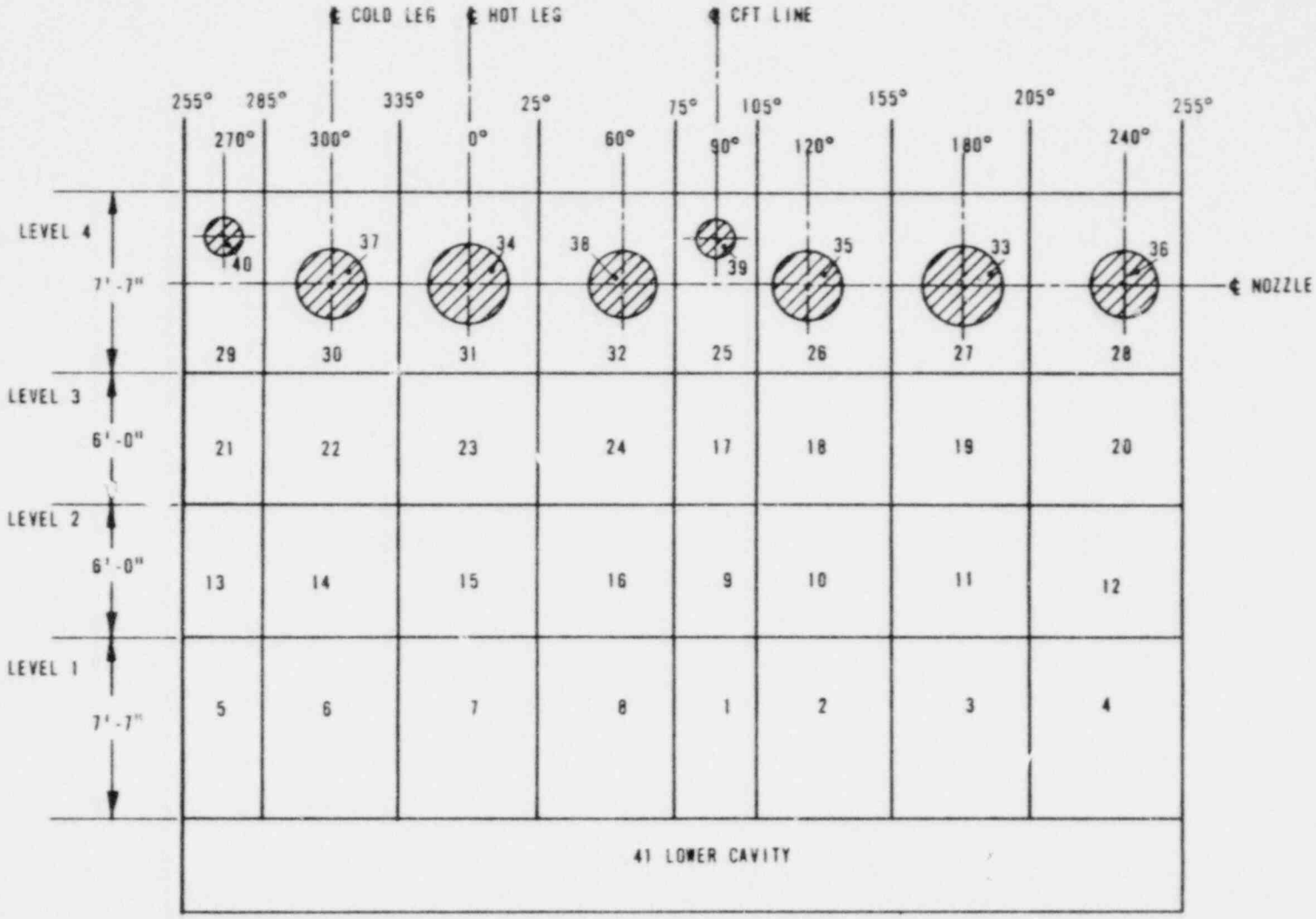

Figure 4.3-4. ANO-1 Reactor Cavity, Elevation View of 50-Node Model

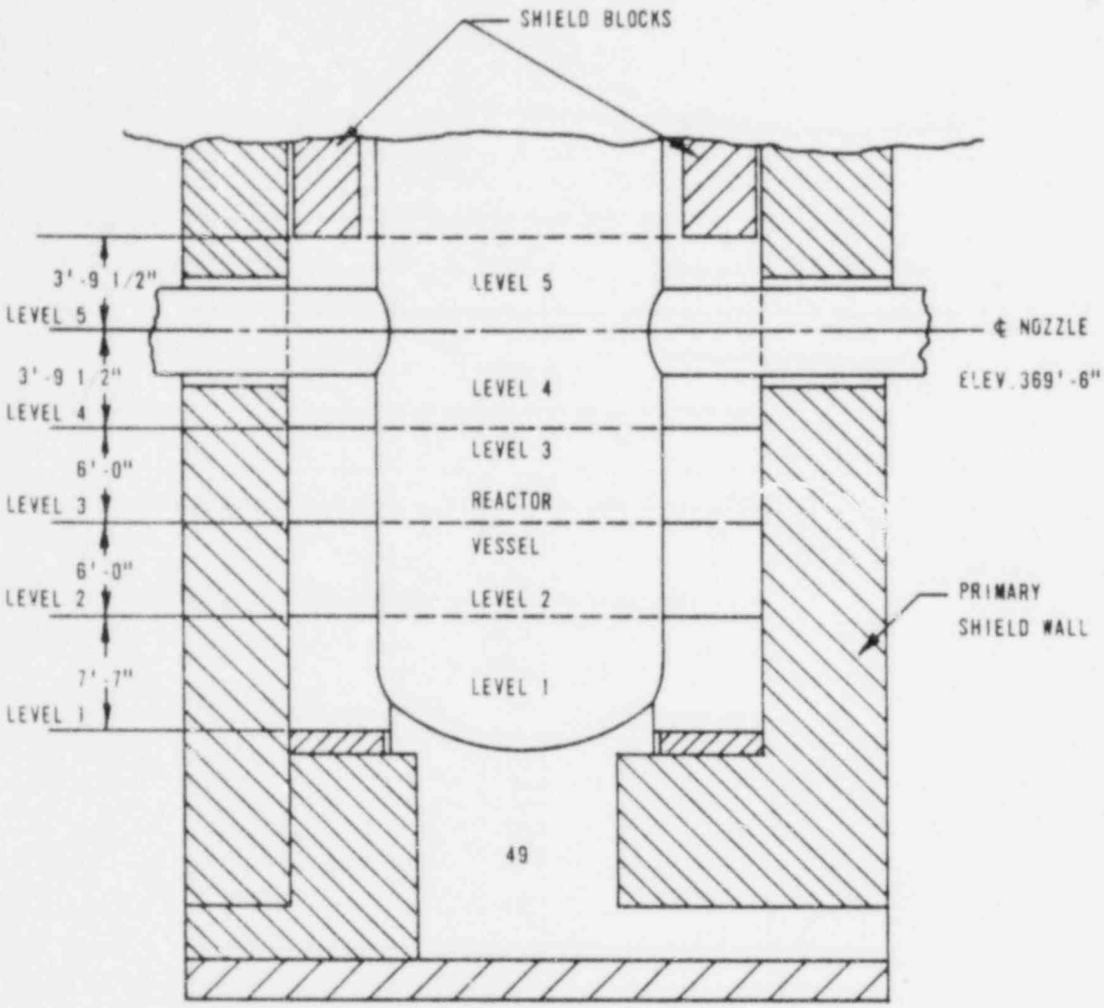

Figure 4.3-5. ANO-1 Reactor Cavity, Developed View of 50-Node Model

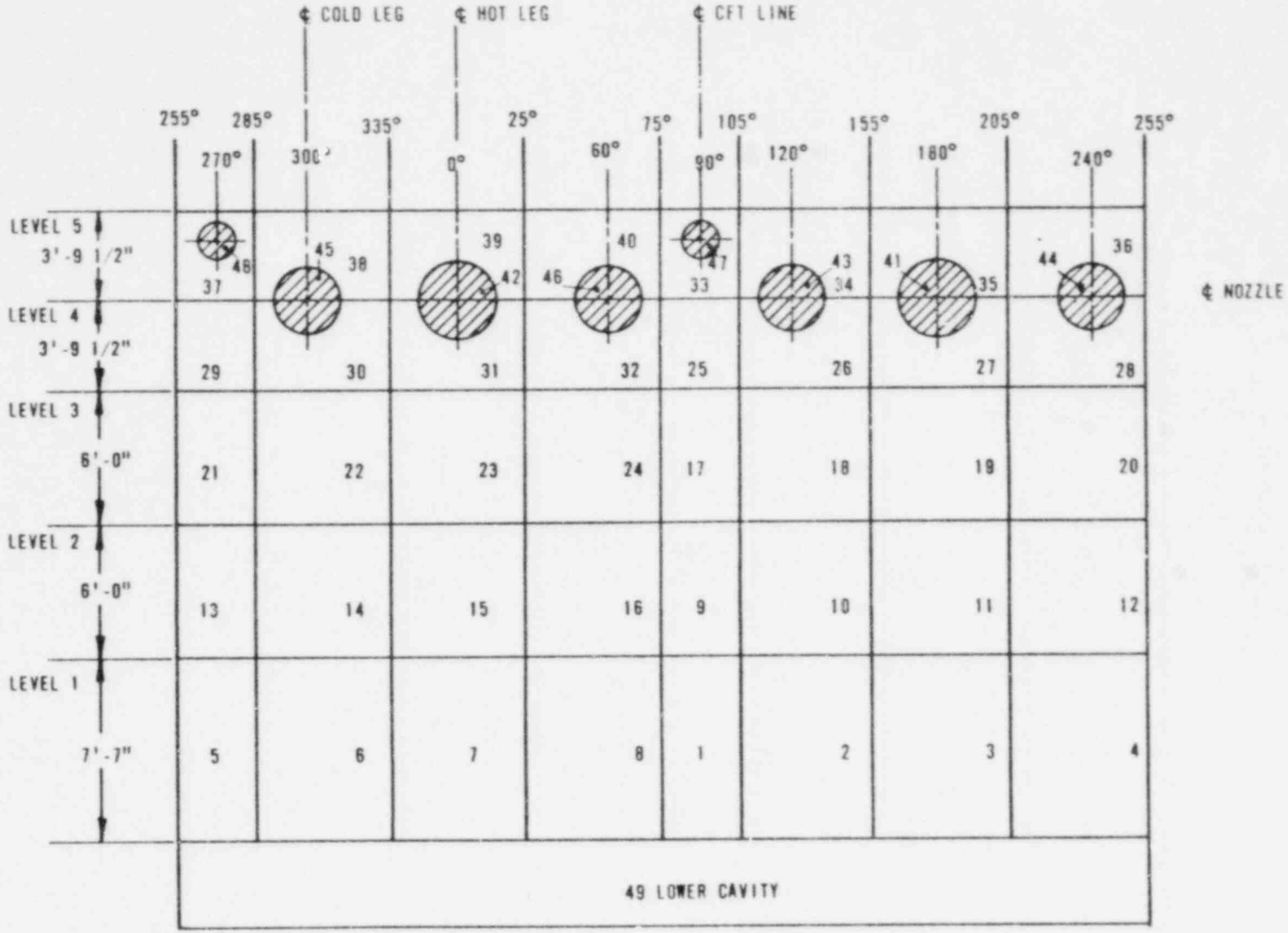

Figure 4.3-6. ANO-1 Reactor Cavity – Elevation View, 70-Node Model

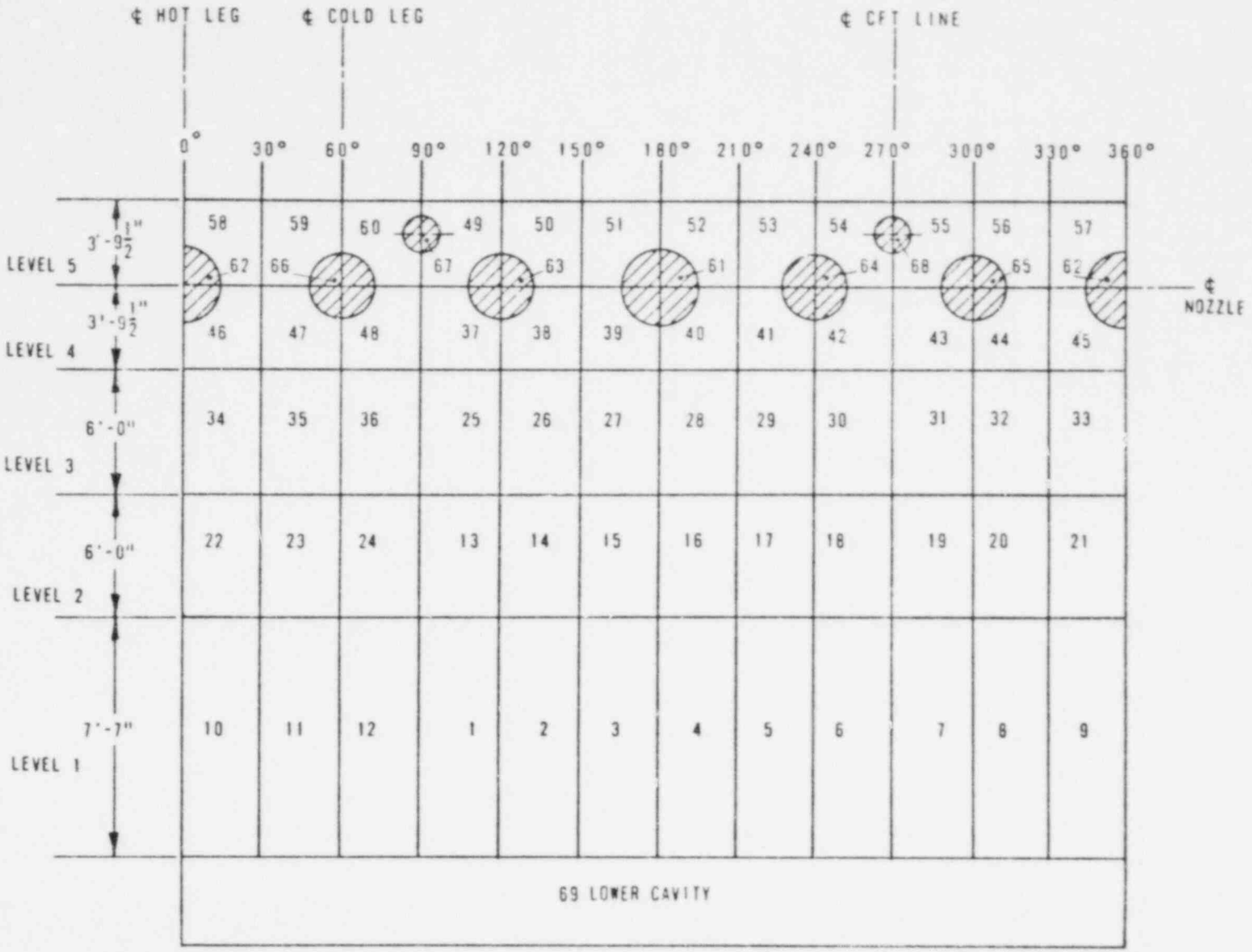

Figure 4.3-7. ANO-1 Reactor Cavity, Elevation View of 82-Node Model

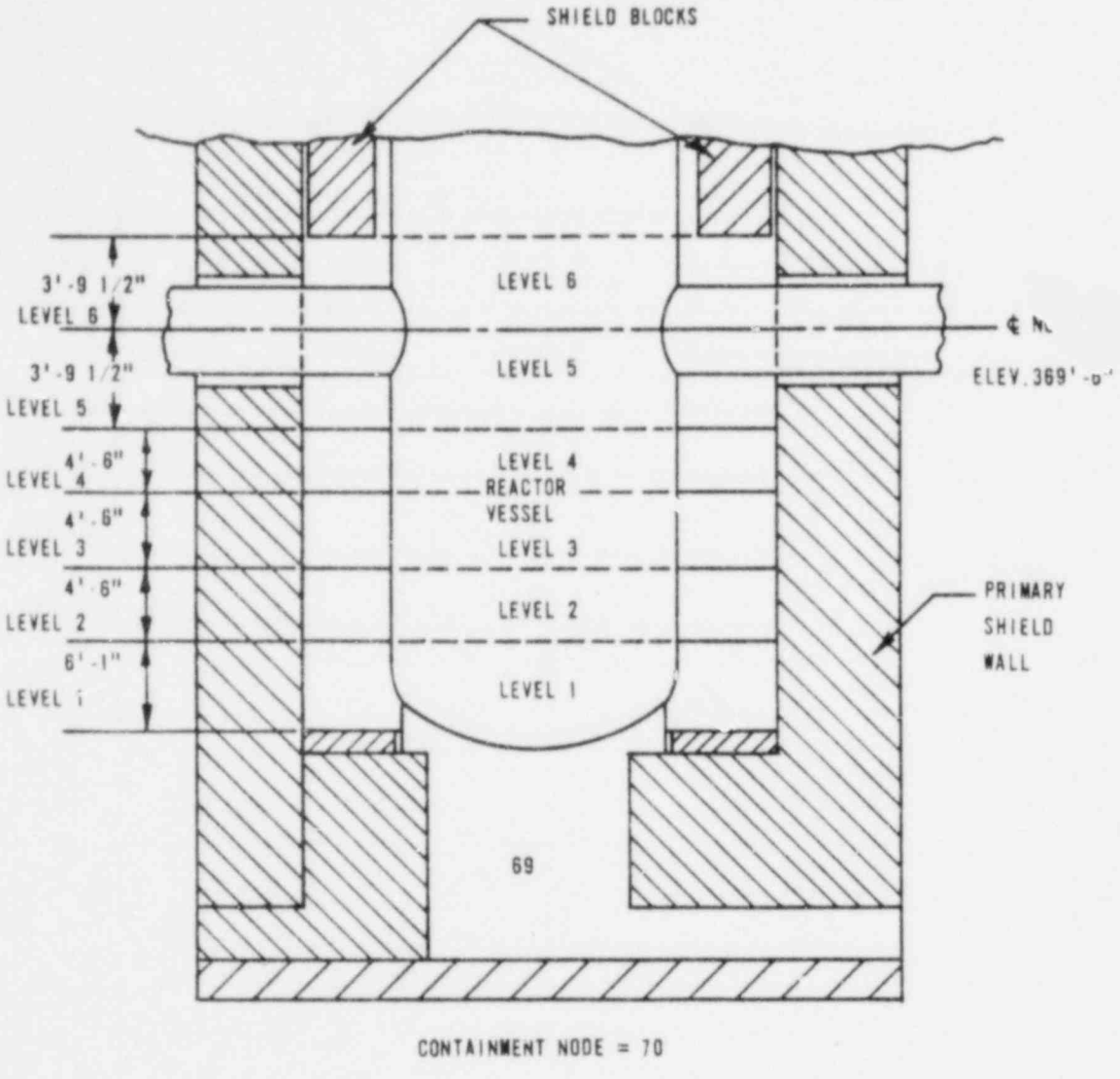

Figure 4.3-8. ANO-1 Reactor Cavity, Developed View of 82-Node Model

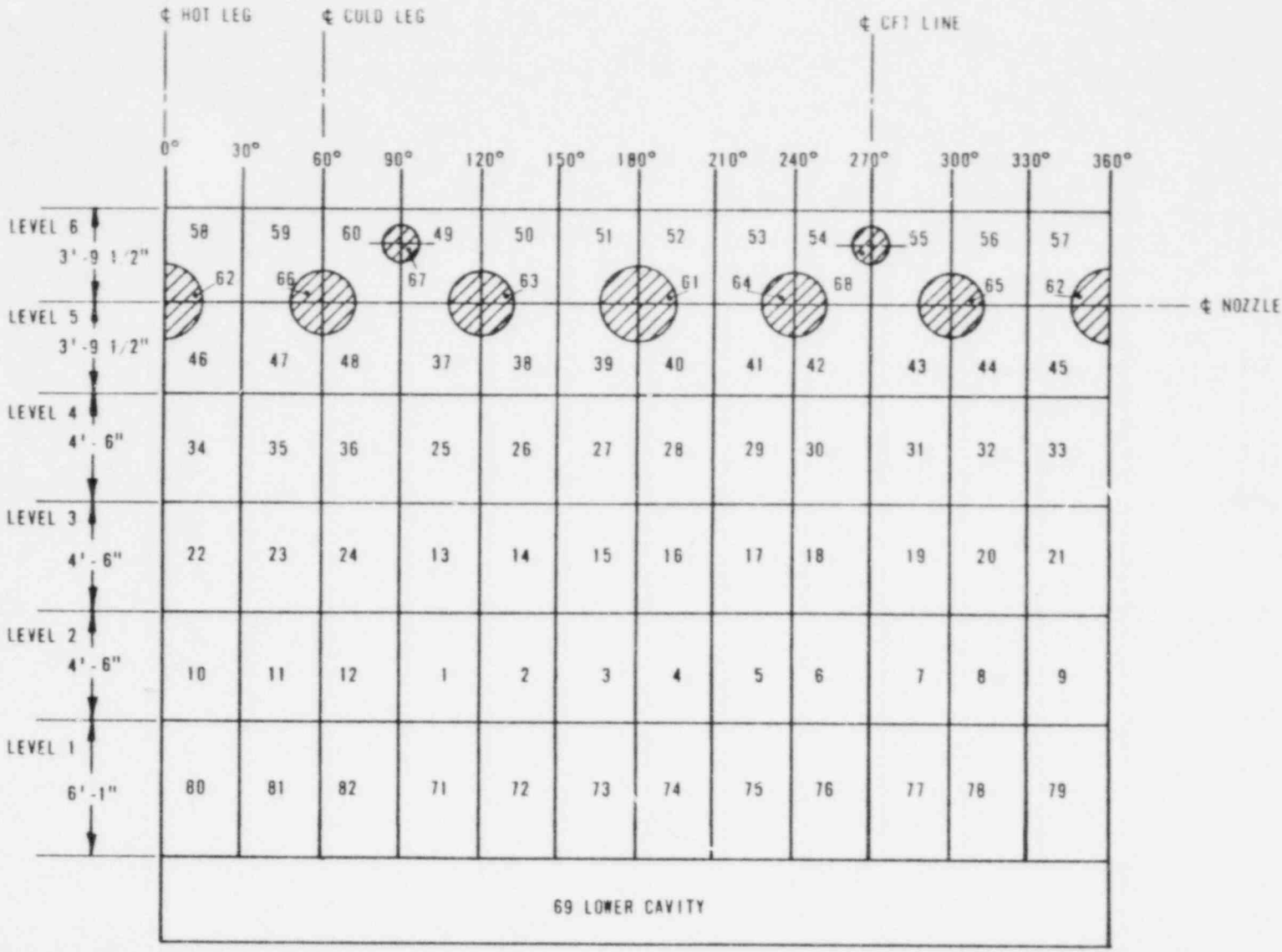

Figure 4.3-9. Peak Lateral Force, Moment, and Uplift Vs Number of Nodes

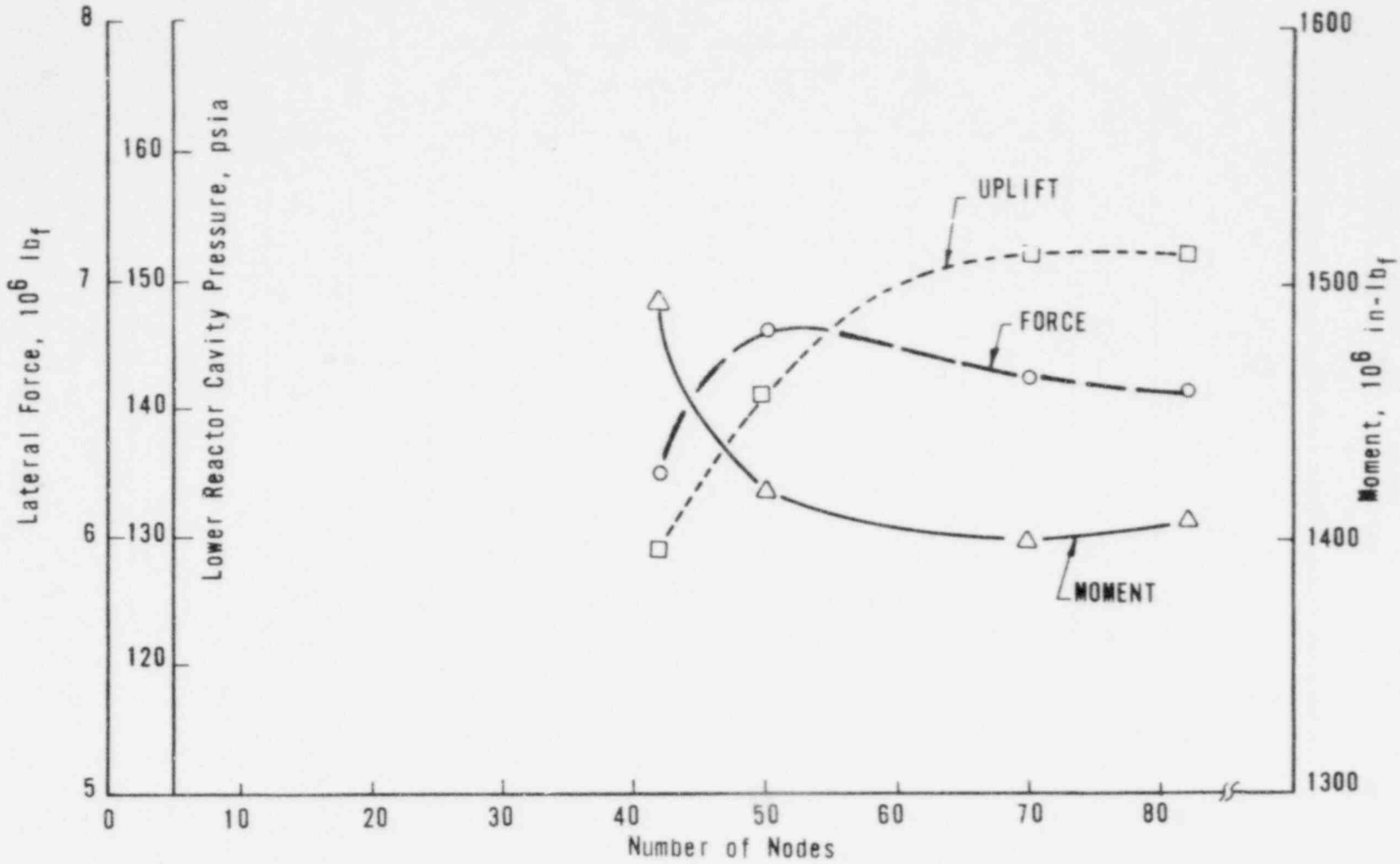

Figure 4.3-10. Davis-Besse 1 Reactor Cavity, Elevation View of 72-Node Model

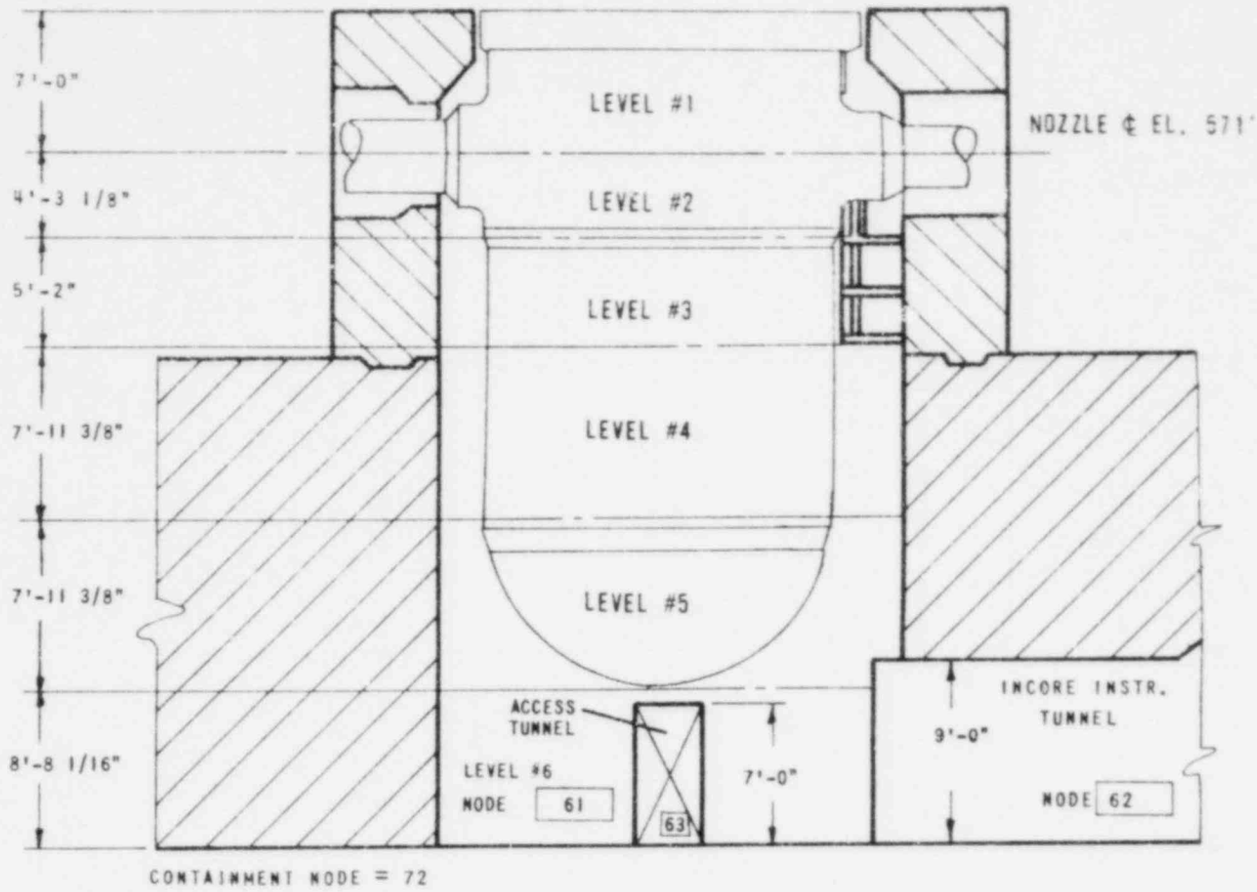

Figure 4.3-11. Davis-Besse 1 Reactor Cavity, Developed View of 72-Node Model

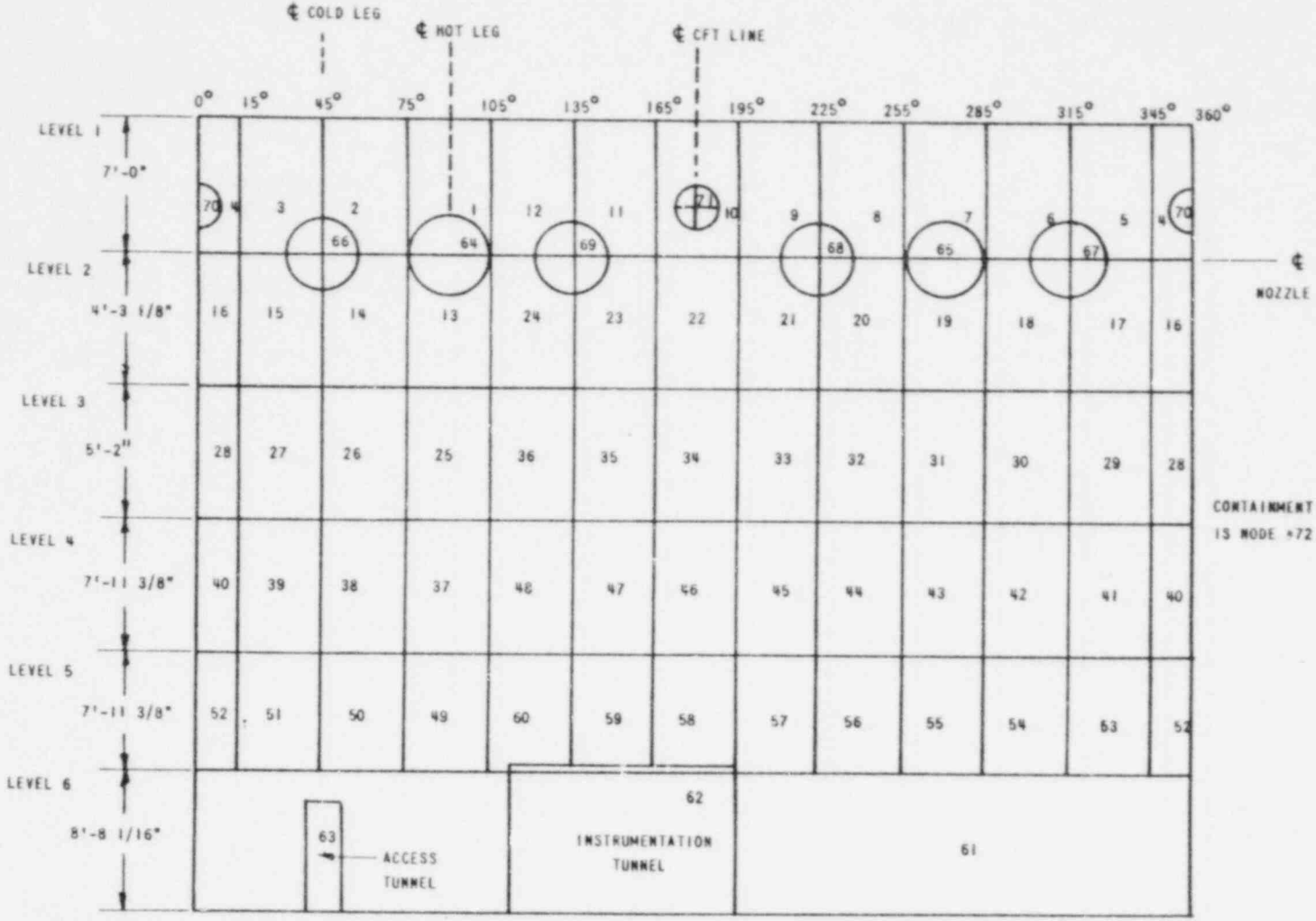

Figure 4.3-12. Davis-Besse 1 Reactor Cavity, Developed View of 84-Node Model

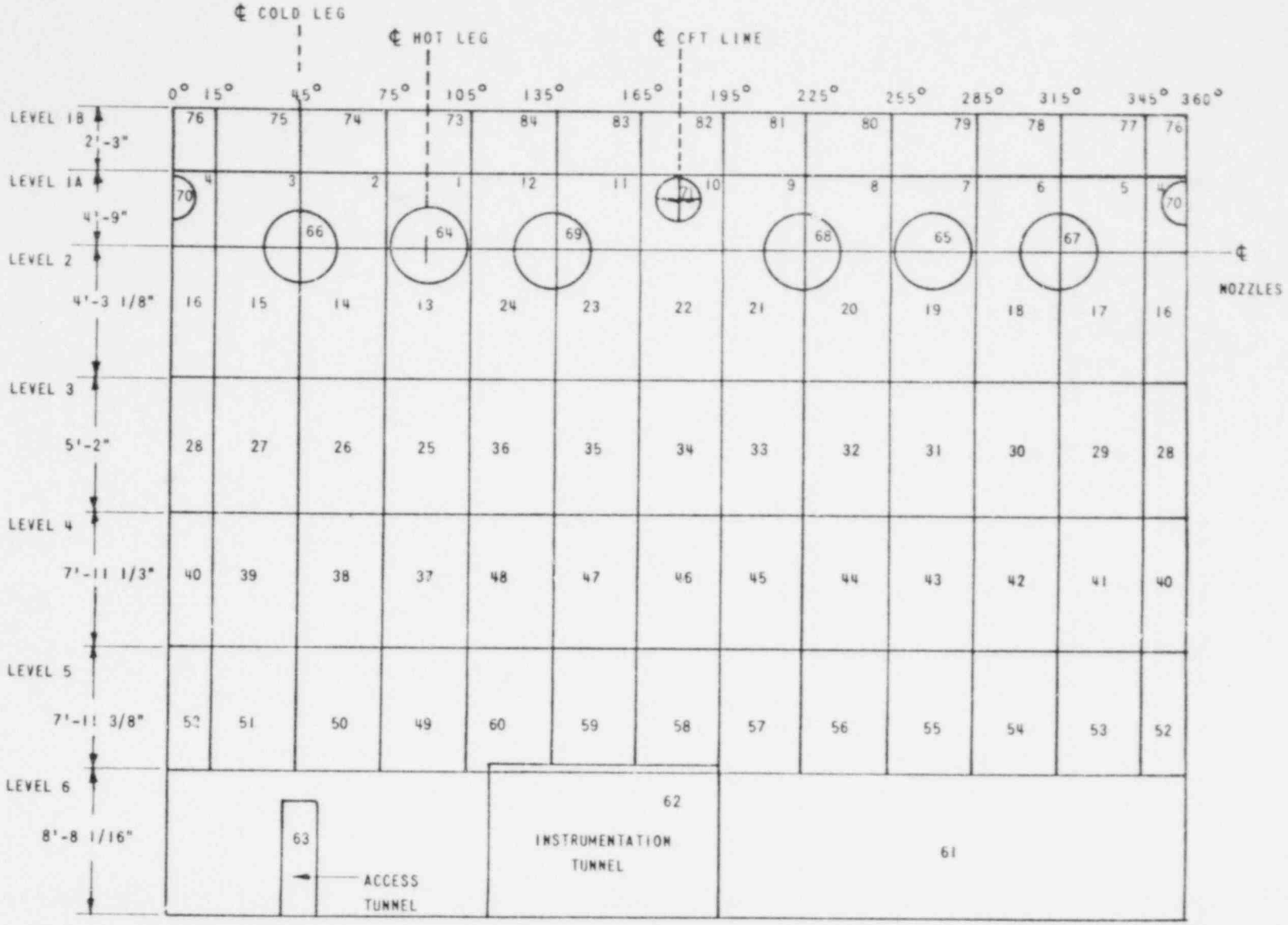

Figure 4.3-13. Davis-Besse 1 Reactor Cavity, Elevation View of 61-Node Model

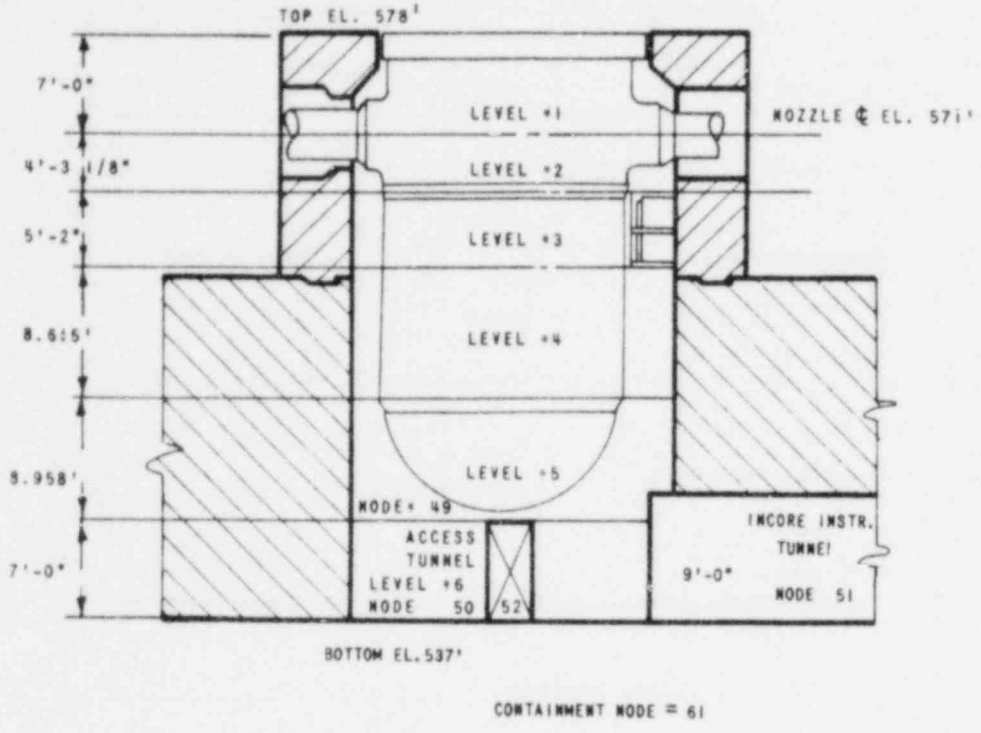

Figure 4.3-14. Davis-Besse 1 Reactor Cavity, Developed View of 61-Node Model

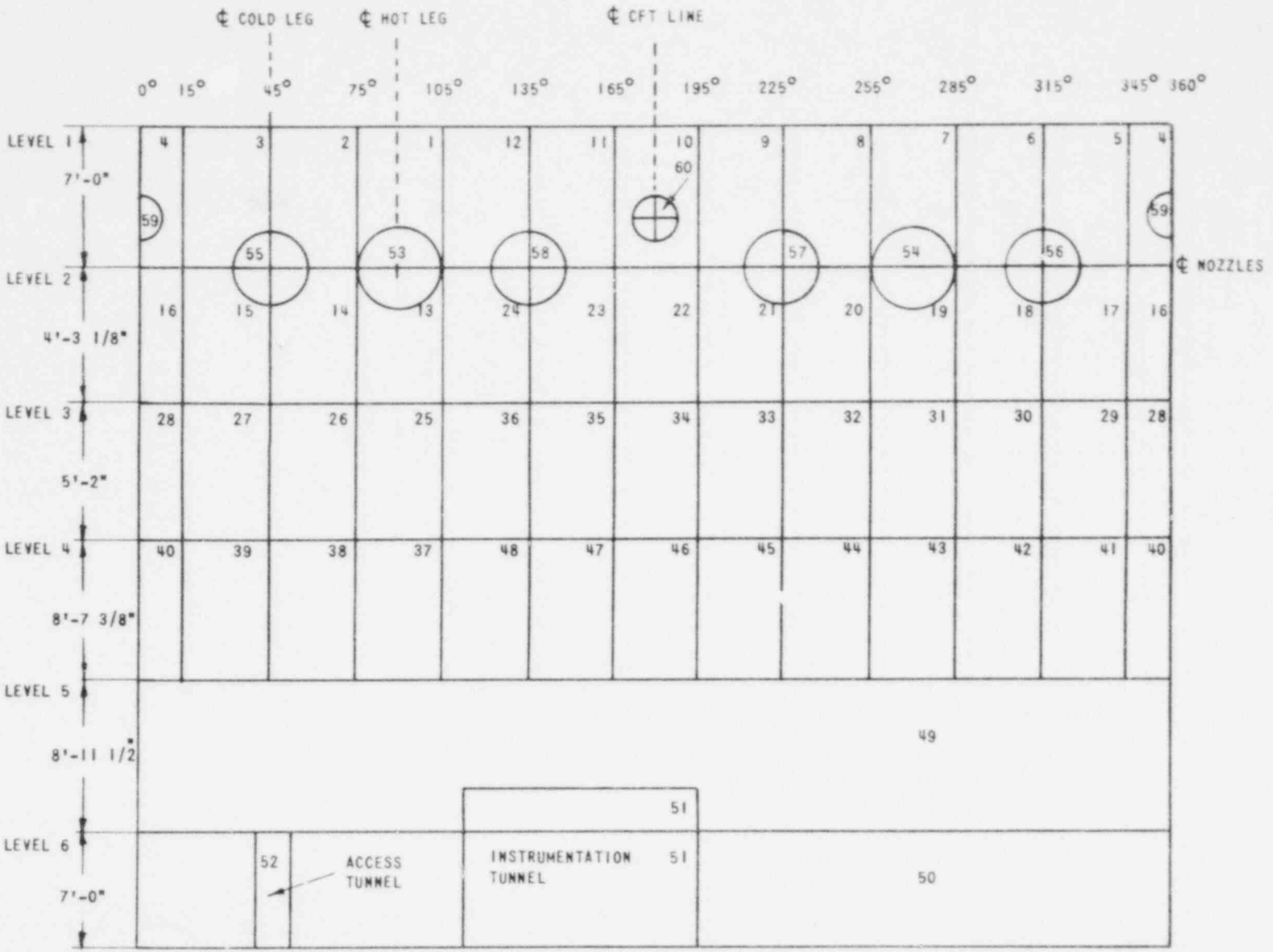

Figure 4.3-15. ANO-1 Reactor Cavity, Elevation View of 70-Node Model

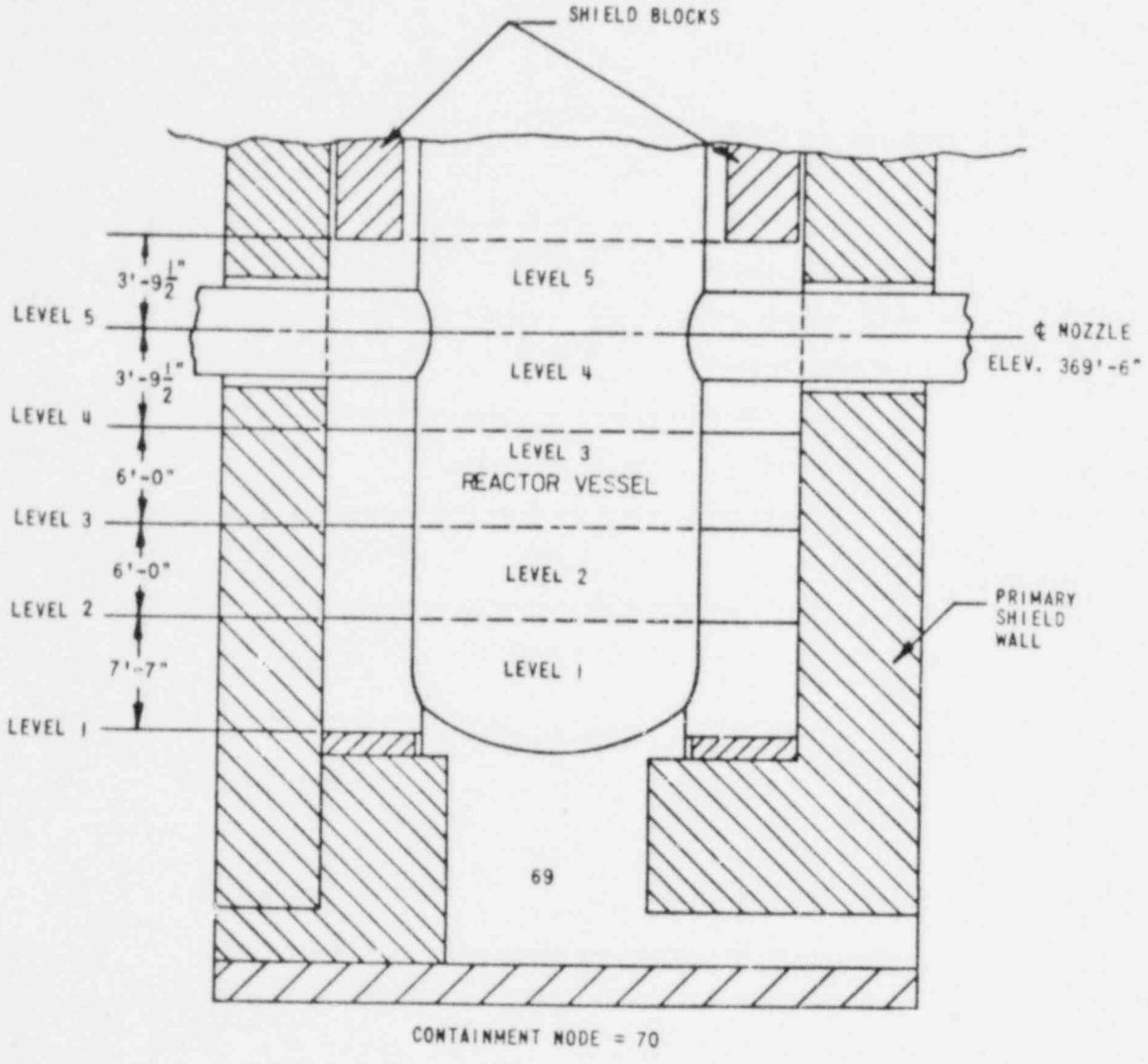

Figure 4.3-16. ANO-1 Reactor Cavity, Plan View of Level 1

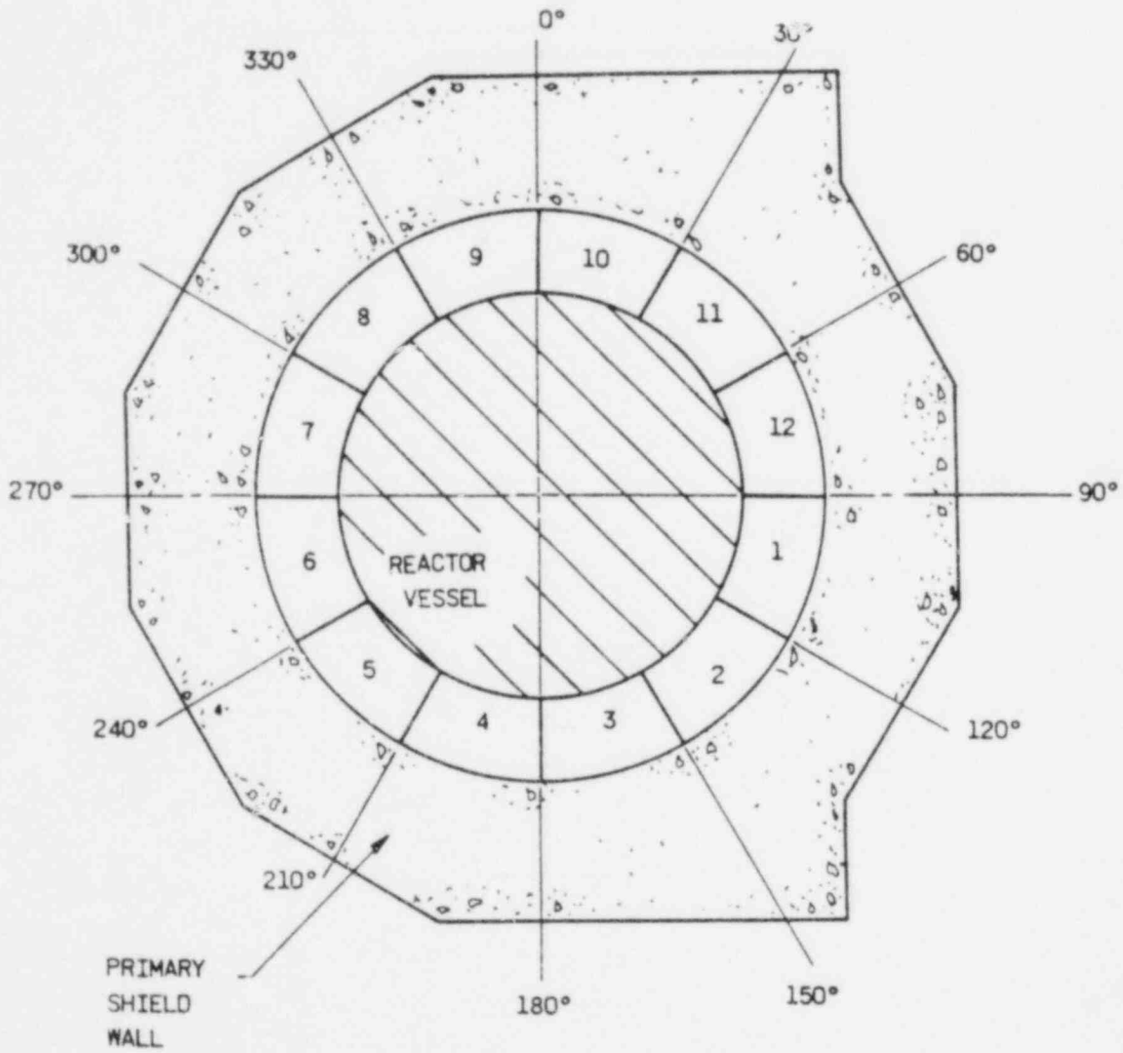

Figure 4.3-17. ANO-1 Reactor Cavity, Plan View of Level 2

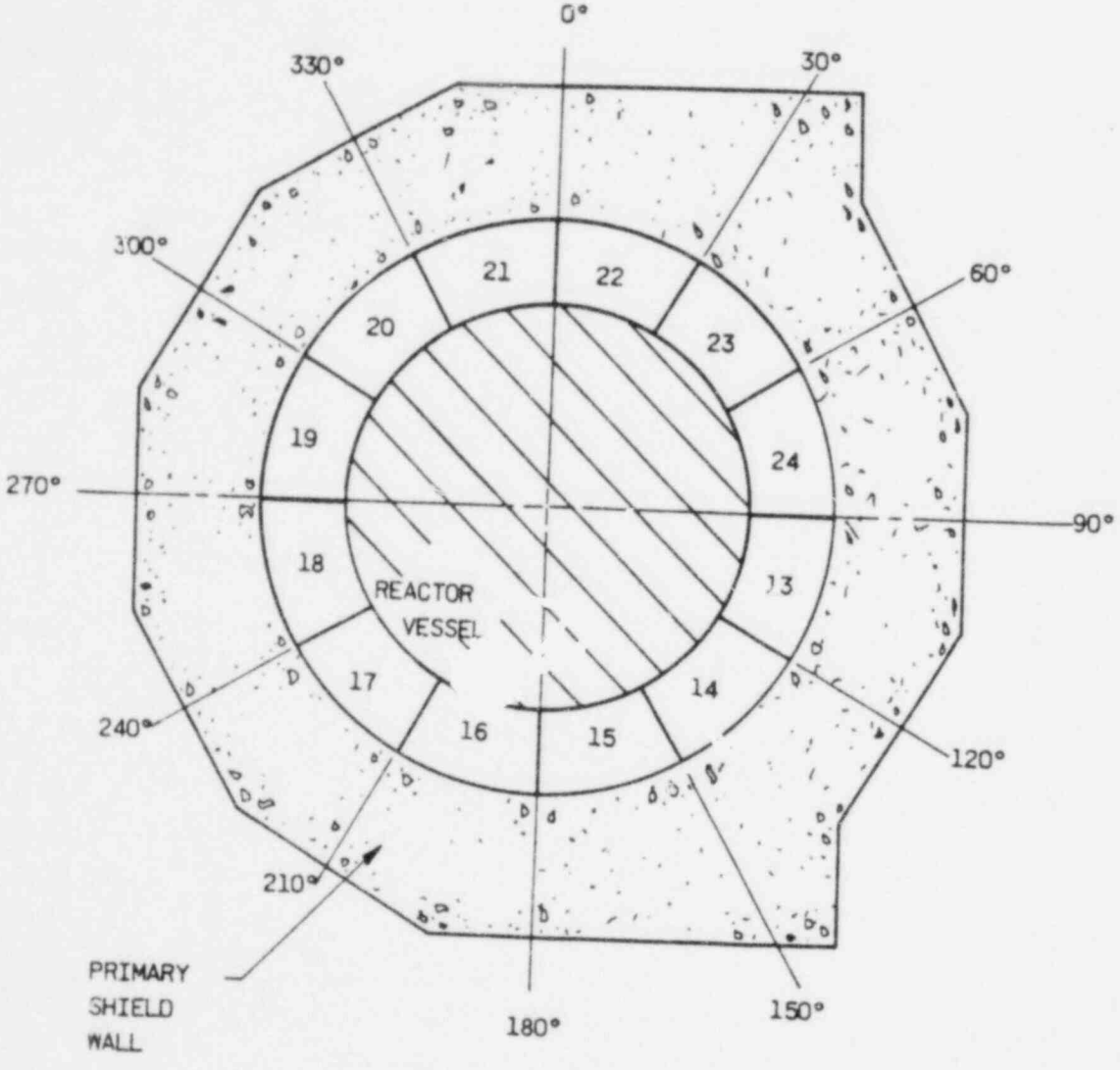

Figure 4.3-18. ANO-1 Reactor Cavity, Plan View of Level 3

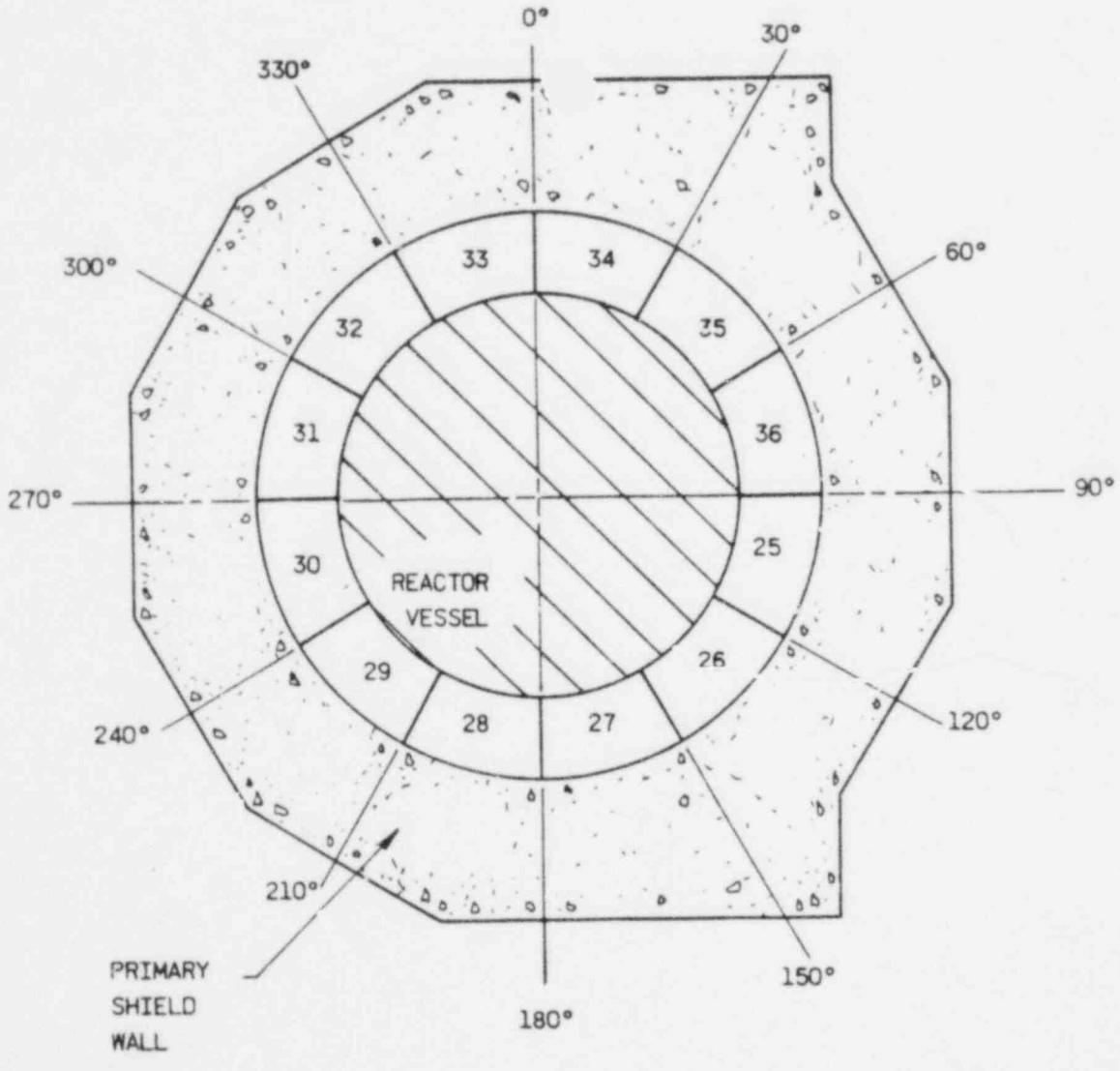

Figure 4.3-19. ANO-1 Reactor Cavity, Plan View of Level 4

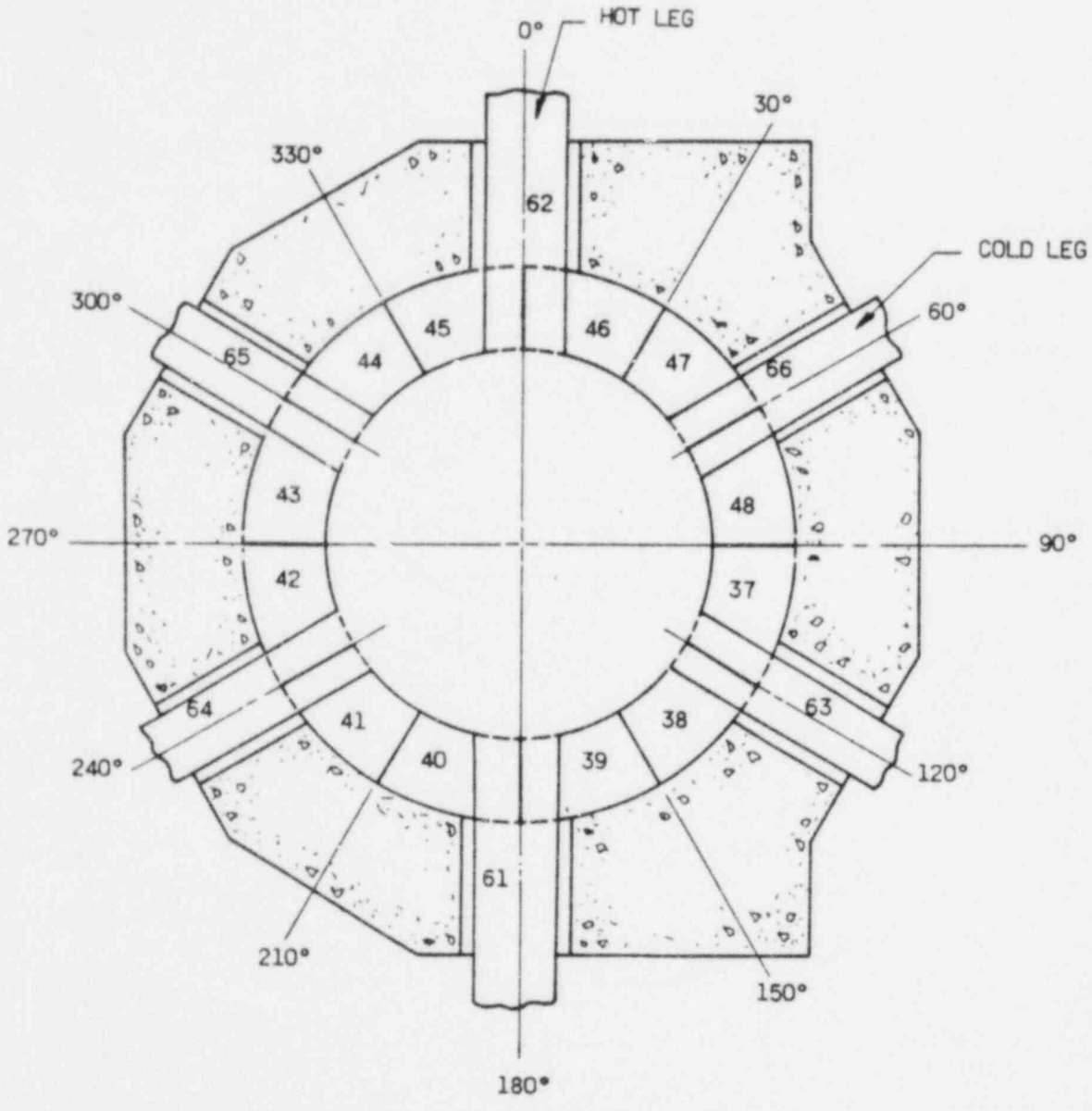

Figure 4.3-20. ANO-1 Reactor Cavity, Plan View of Level 5

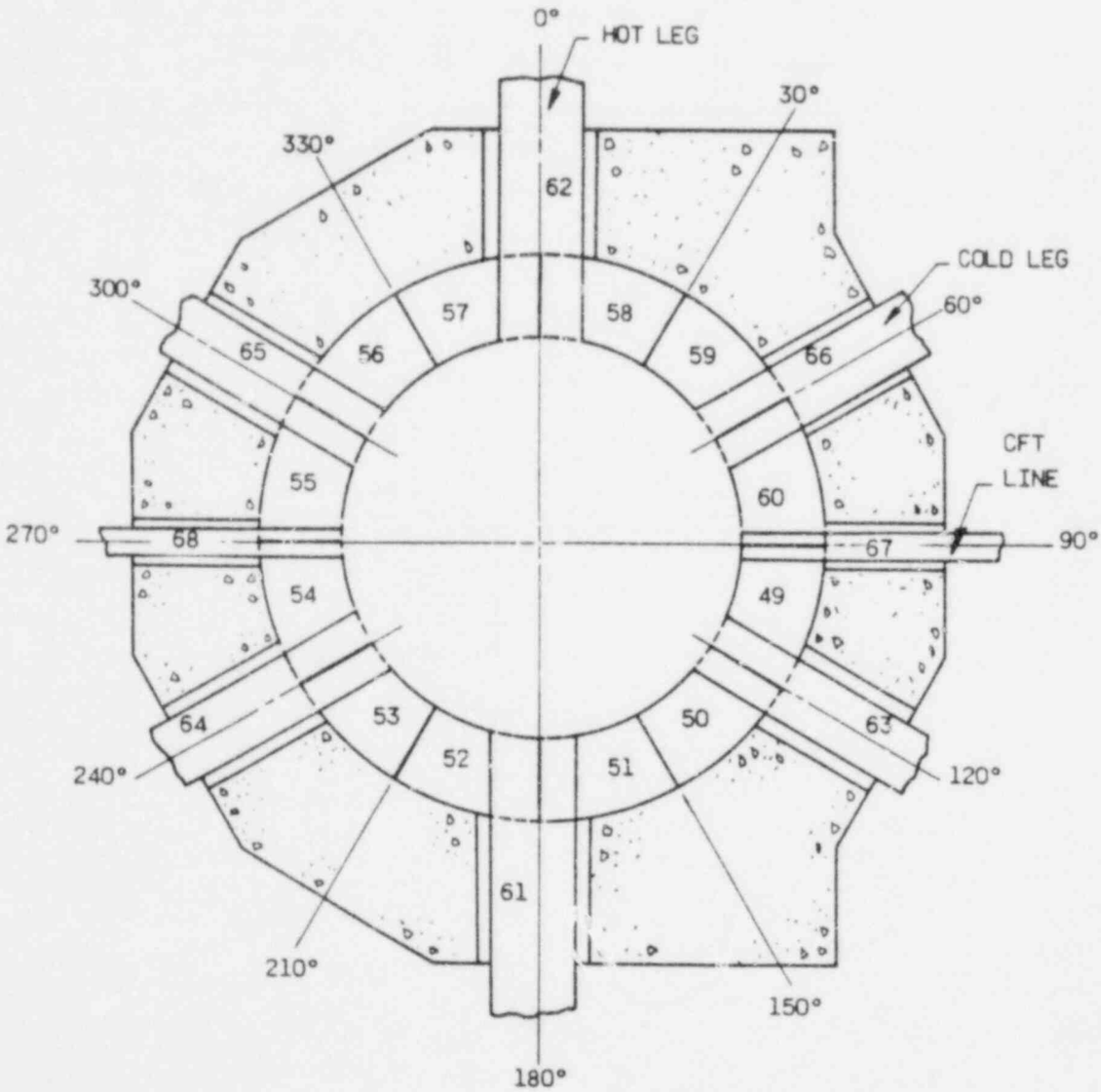

Figure 4.3-21. Rancho Seco Reactor Cavity, Elevation View

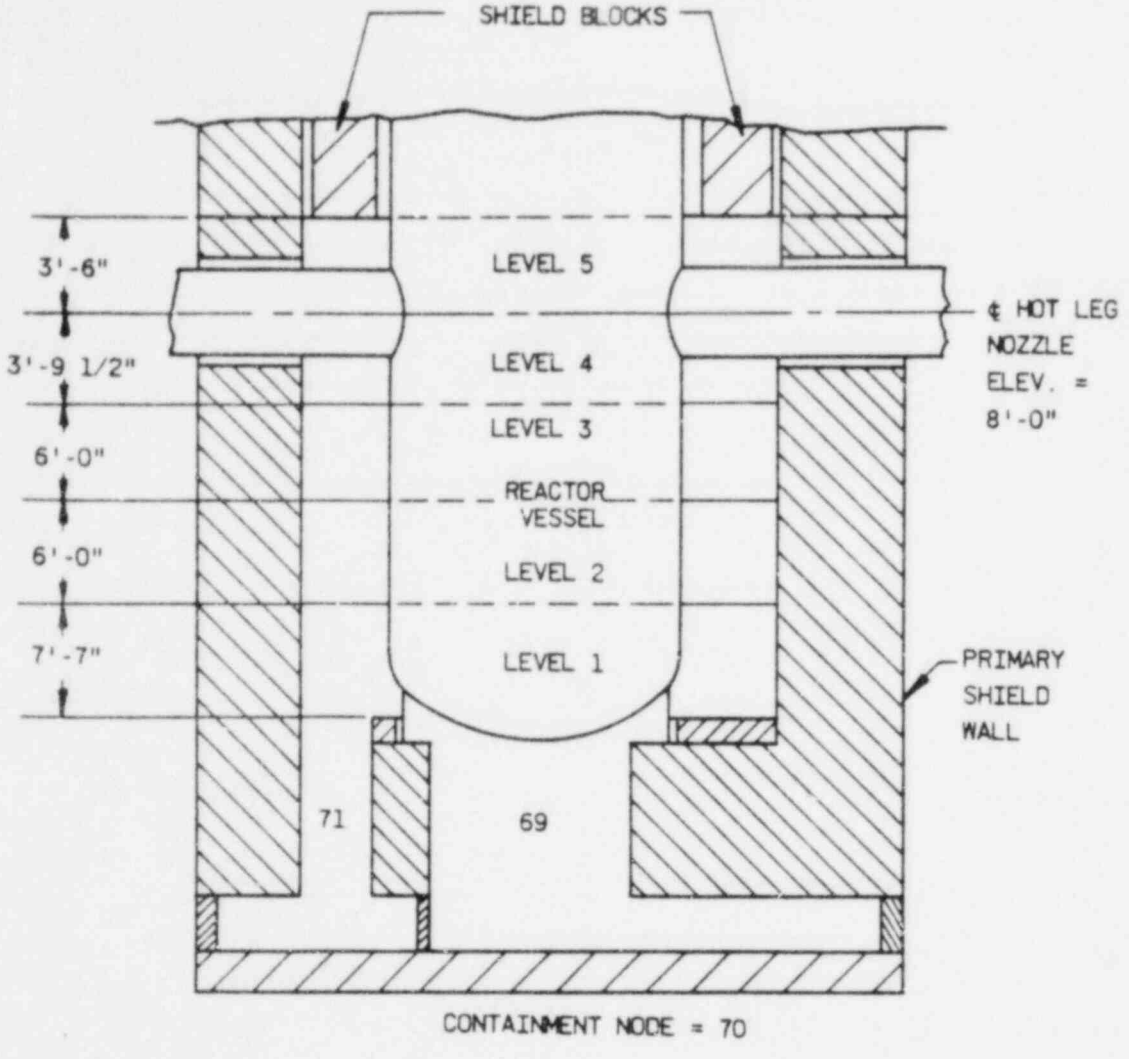

Figure 4.3-22. Rancho Seco Reactor Cavity, Plan View of Level 1

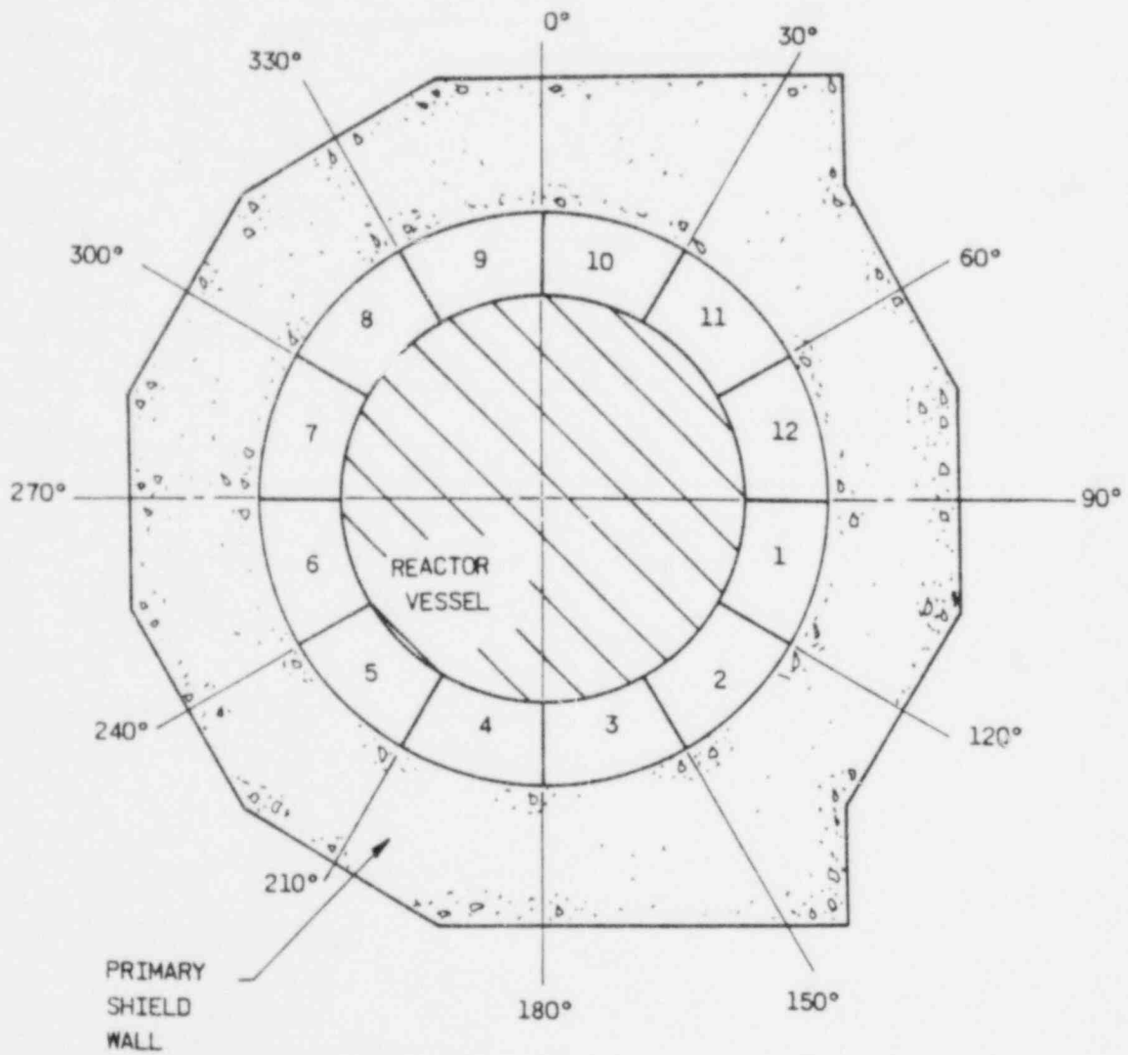

Figure 4.3-23. Rancho Seco Reactor Cavity, Plan View of Level 2

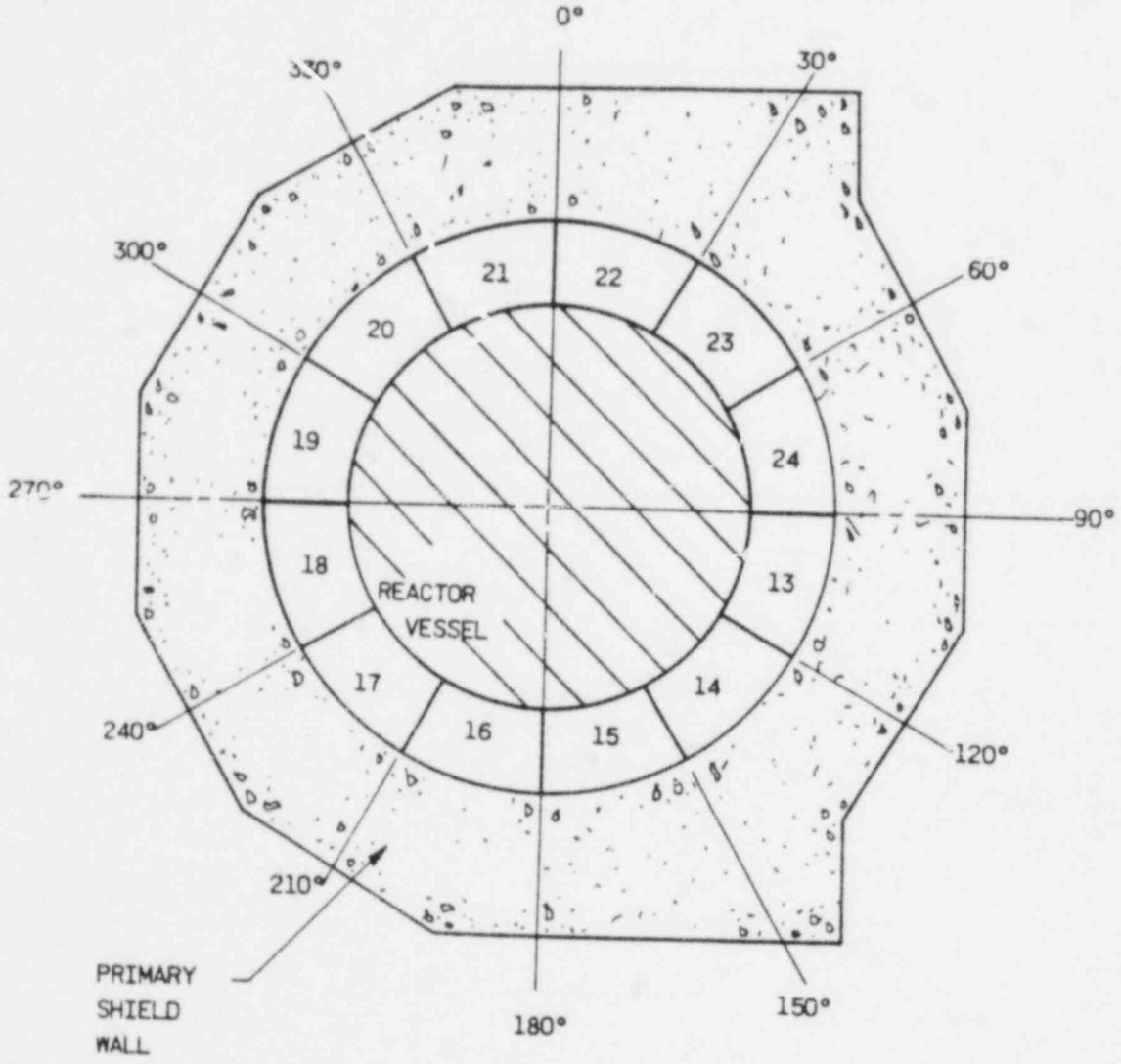

Figure 4.3-24. Rancho Seco Reactor Cavity, Plan View of Level 3

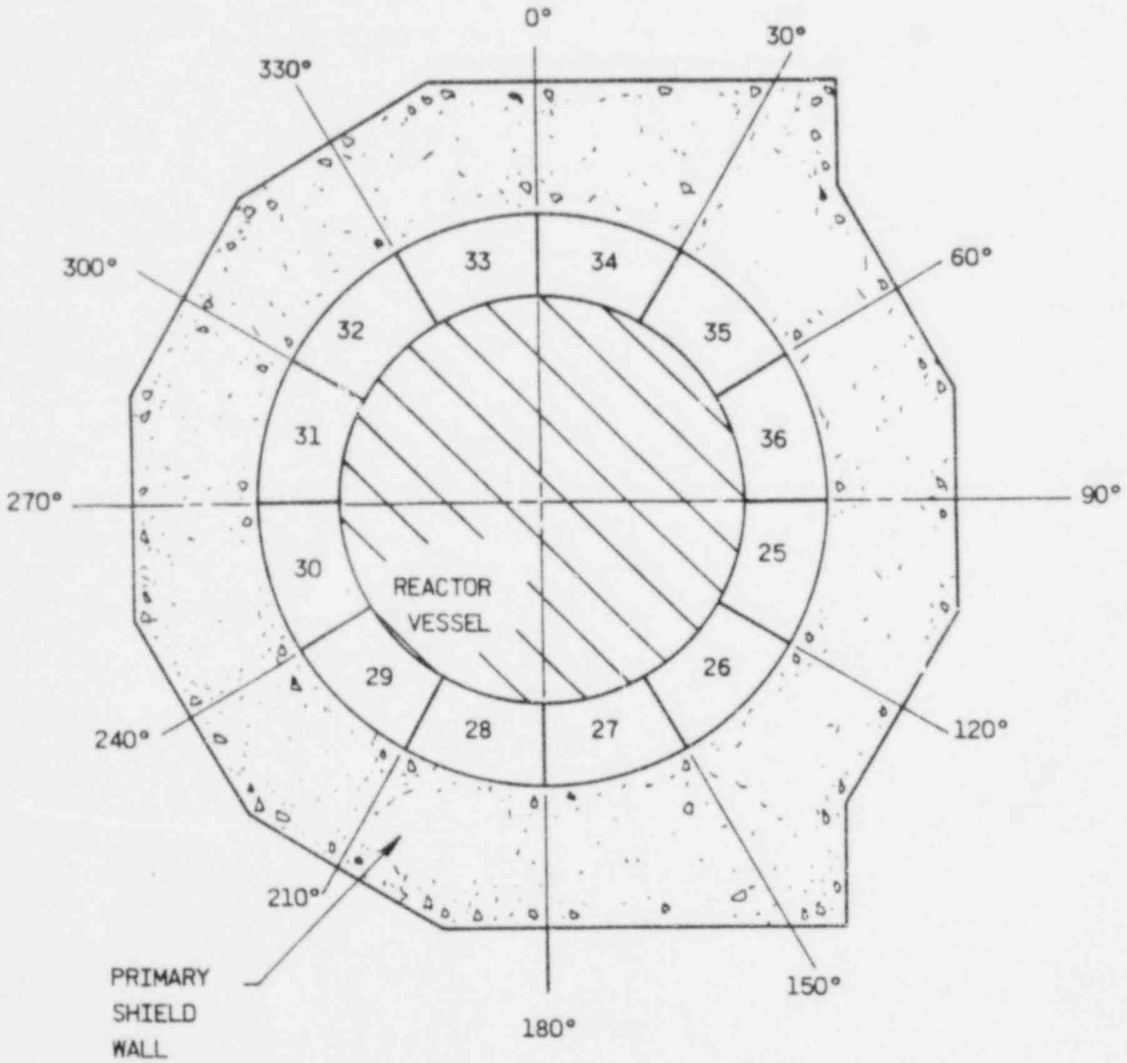

Figure 4.3-25. Rancho Seco Reactor Cavity, Plan View of Level 4

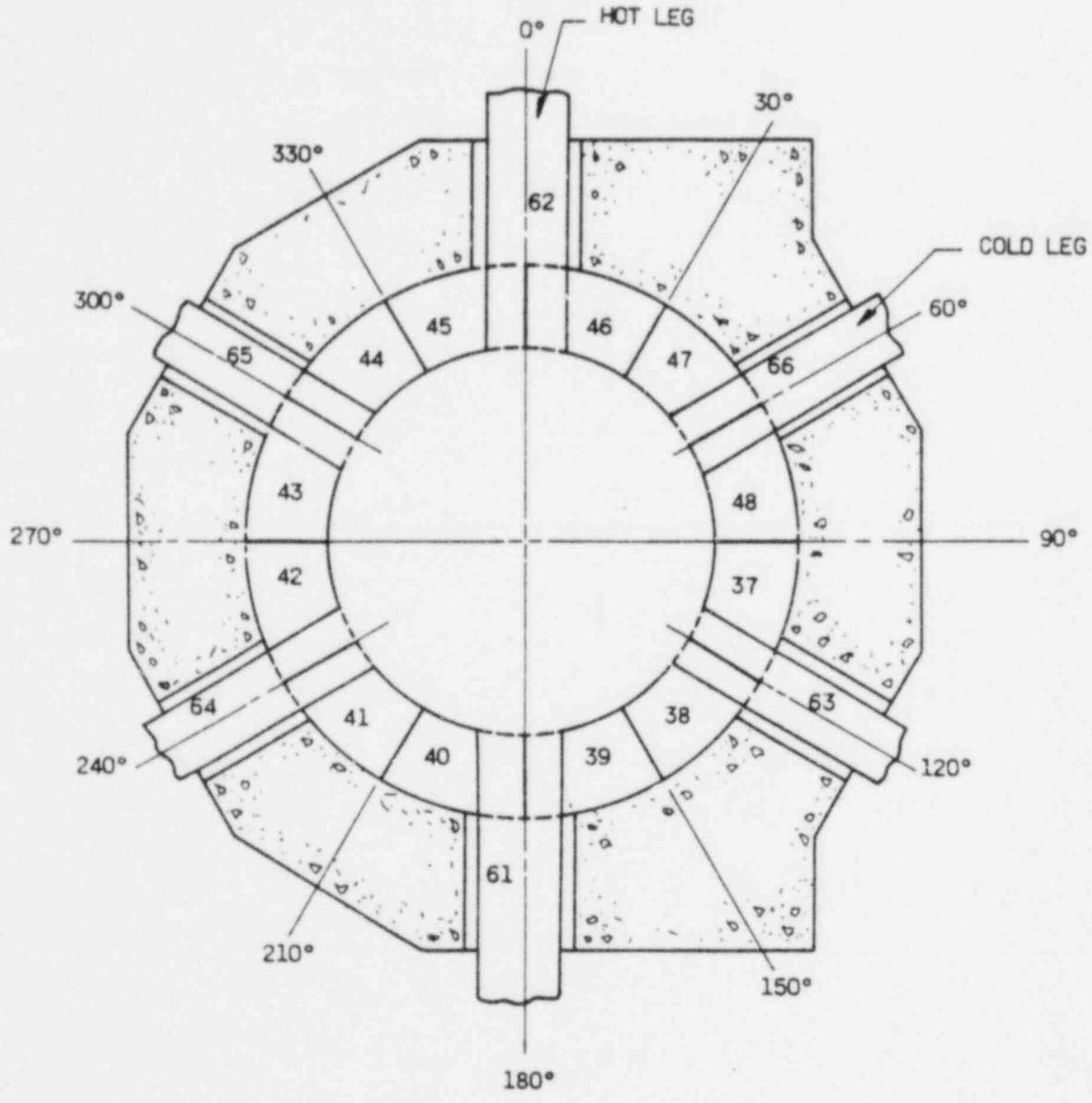

Figure 4.3-26. Rancho Seco Reactor Cavity, Plan View of Level 5

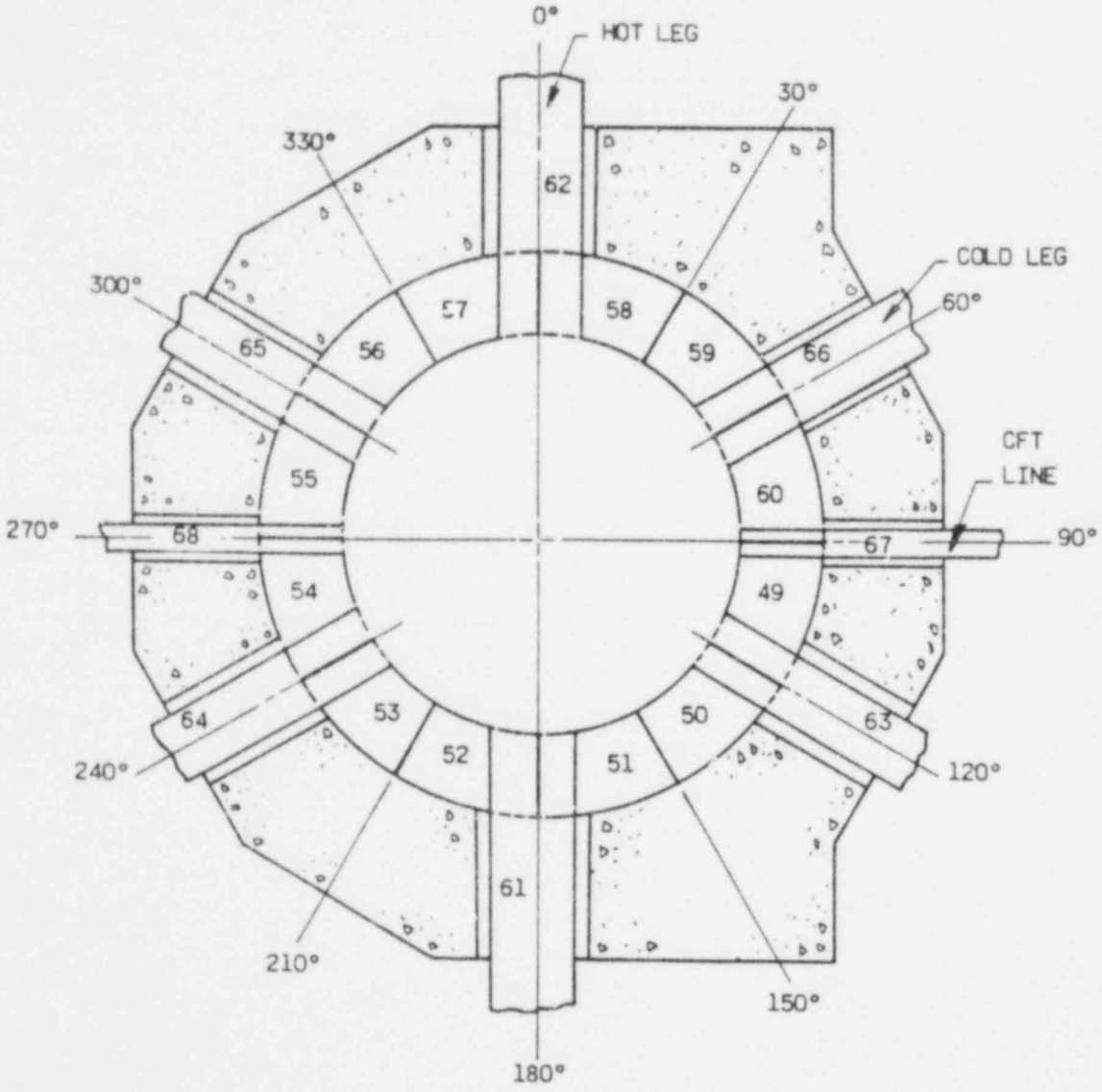

Figure 4.3-27. CR-3/TMI-1 Reactor Cavity, Elevation View

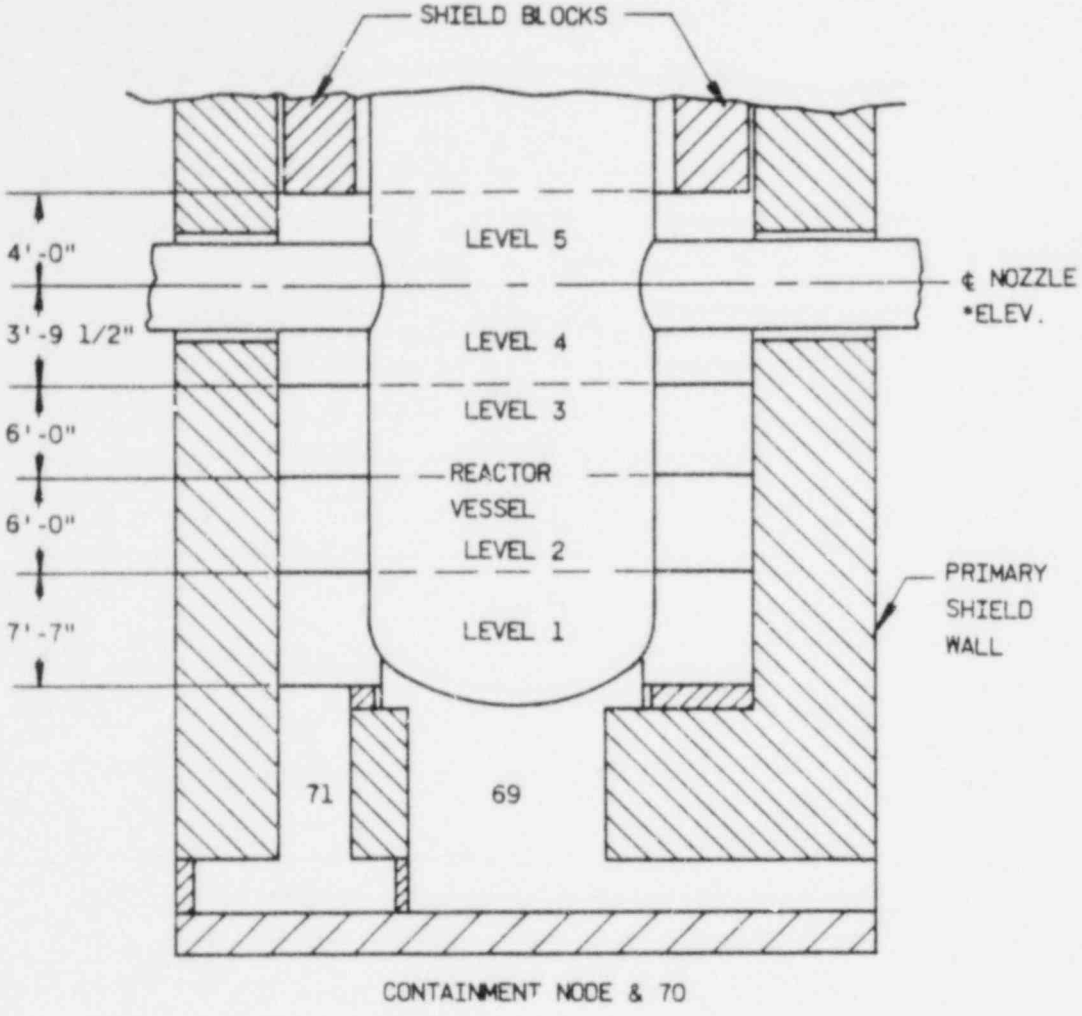

*ELEV = 128'-0" FOR FLORIDA
= 314'-0" FOR TMI-1

Figure 4.3-28. CR-3/TMI-1 Reactor Cavity, Plan View of Level 1

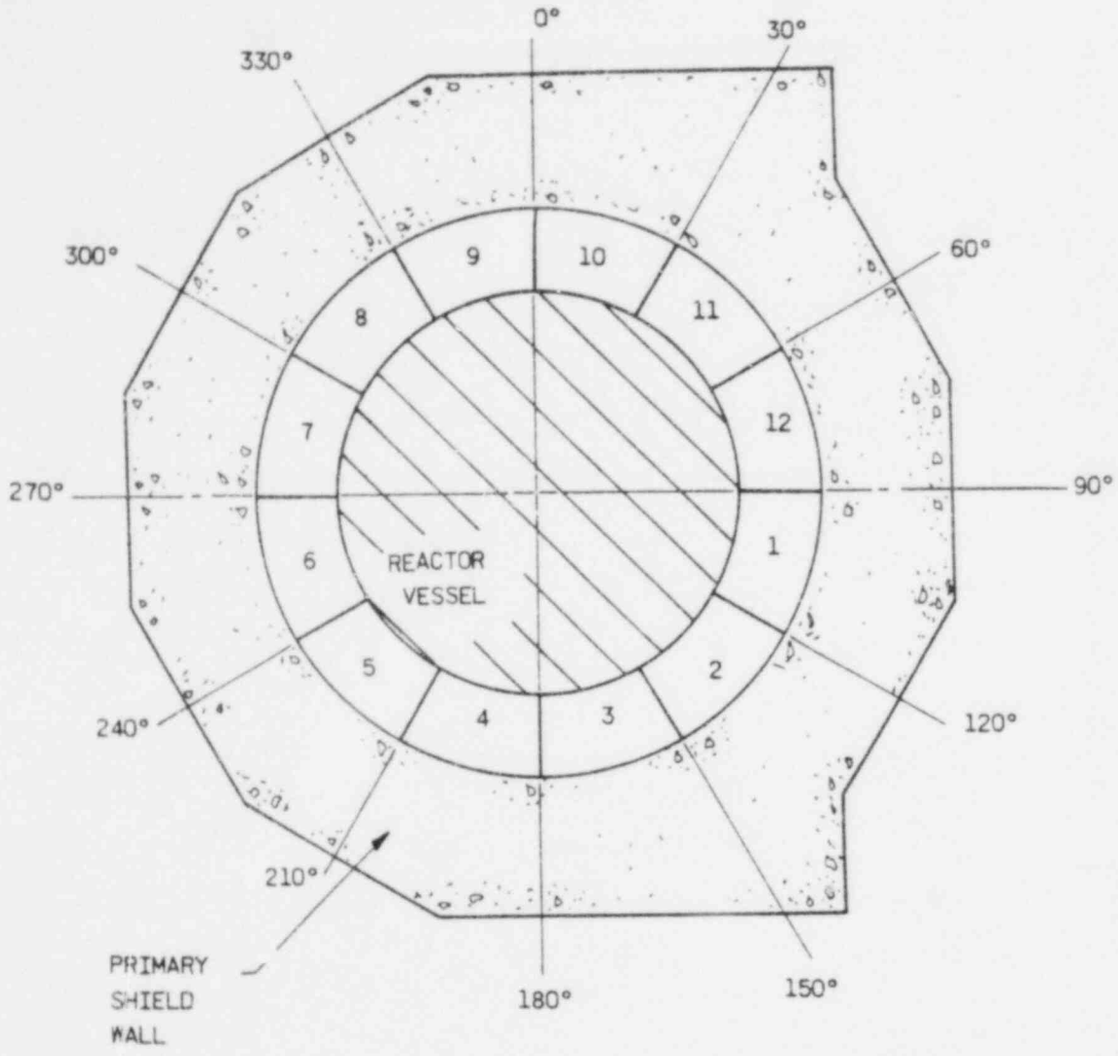

Figure 4.3-29. CR-3/TMI-1 Reactor Cavity, Plan View of Level 2

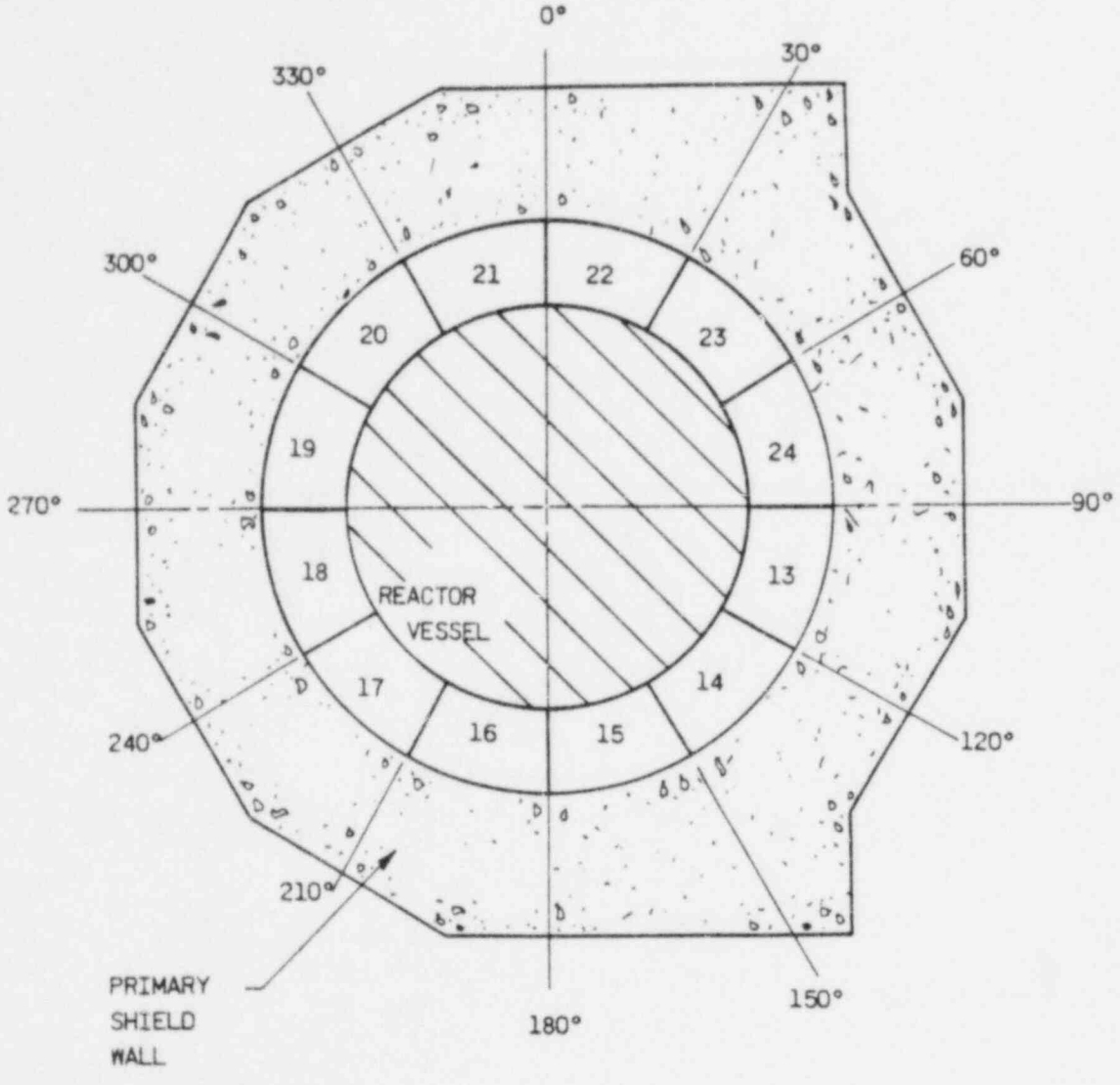

Figure 4.3-30. CR-3/TMI-1 Reactor Cavity, Plan View of Level 3

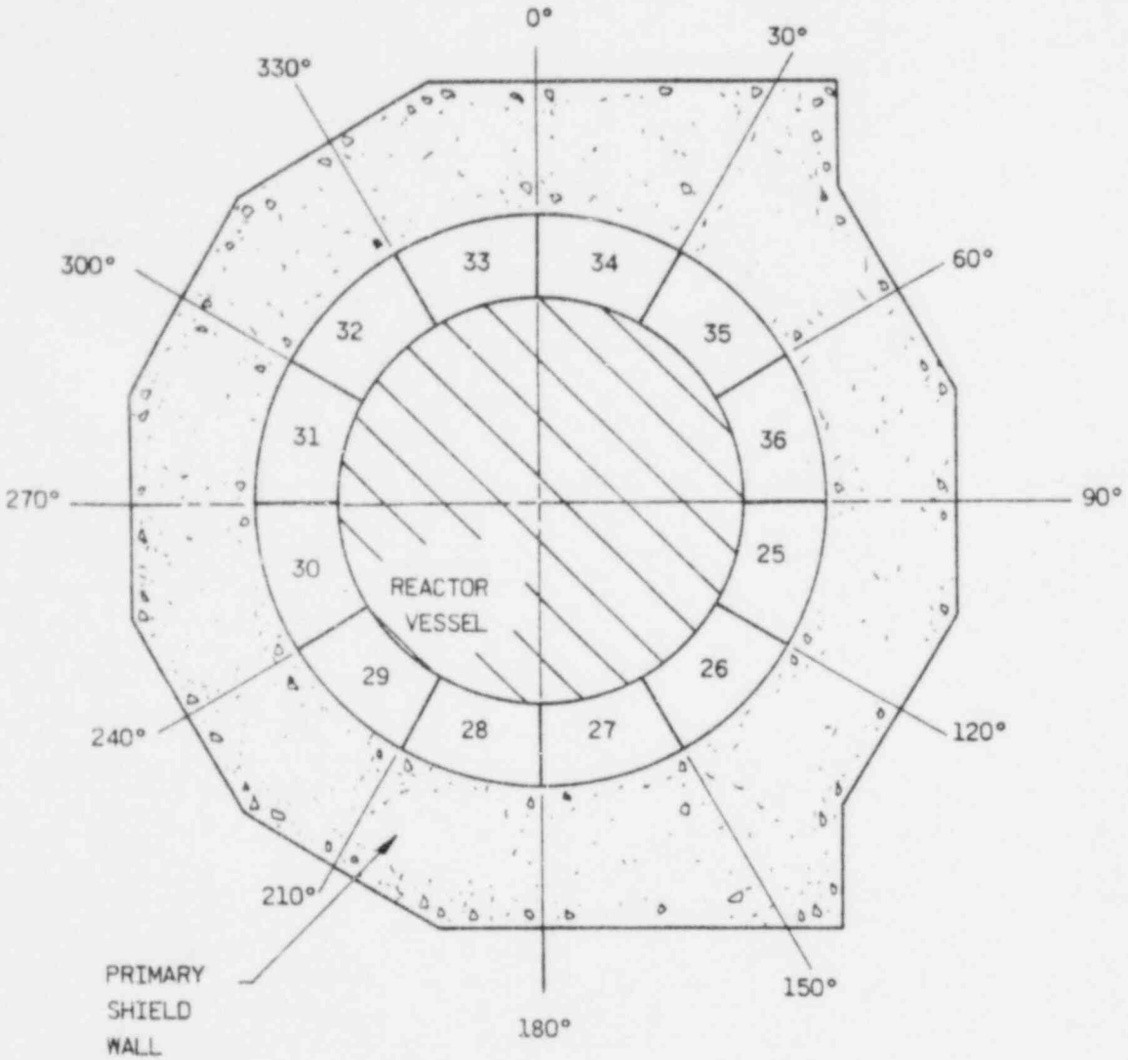

Figure 4.3-31. CR-3/TMI-1 Reactor Cavity, Plan View of Level 4

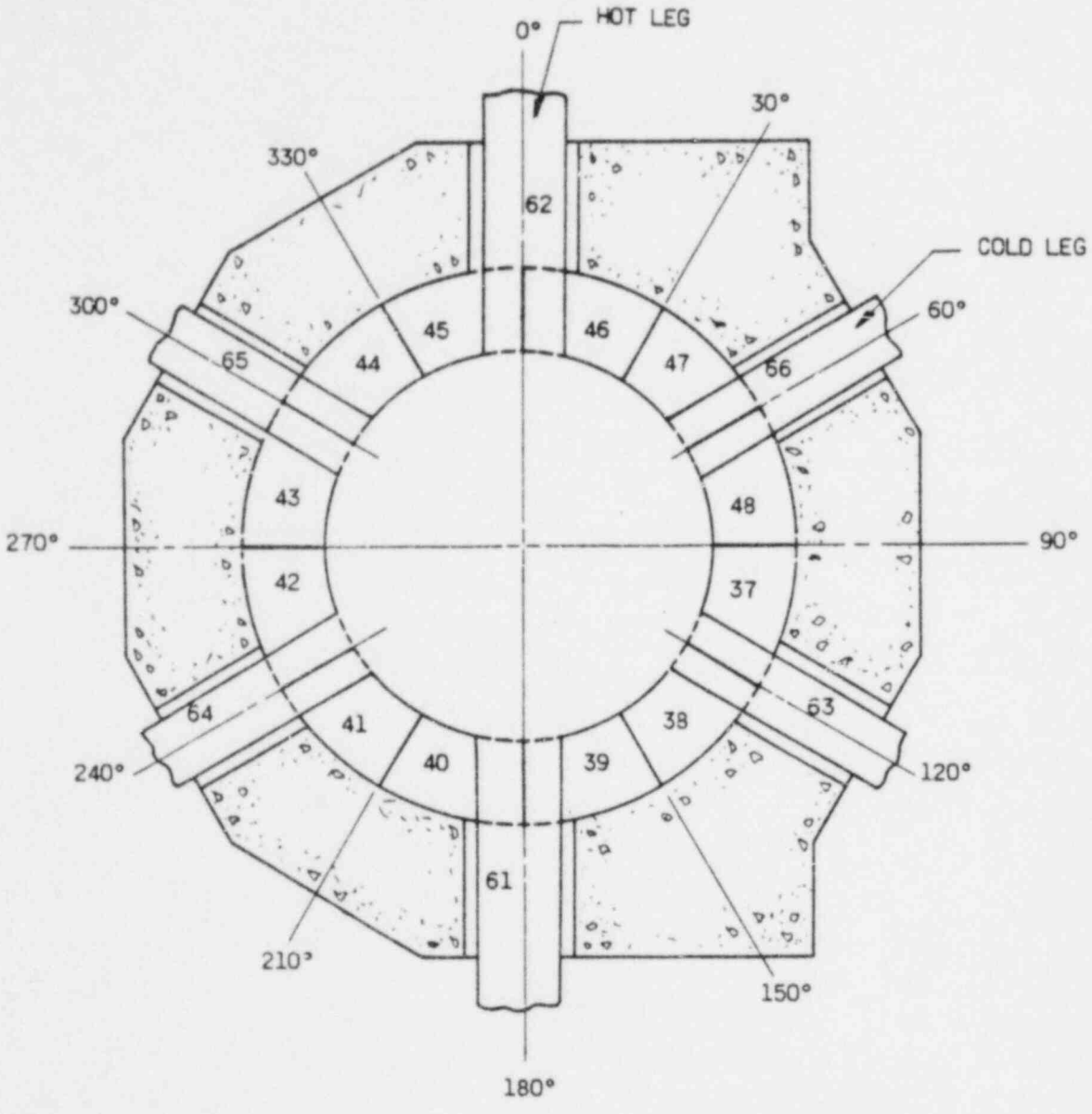

Figure 4.3-32. CR-3/TMI-1 Reactor Cavity, Plan View of Level 5

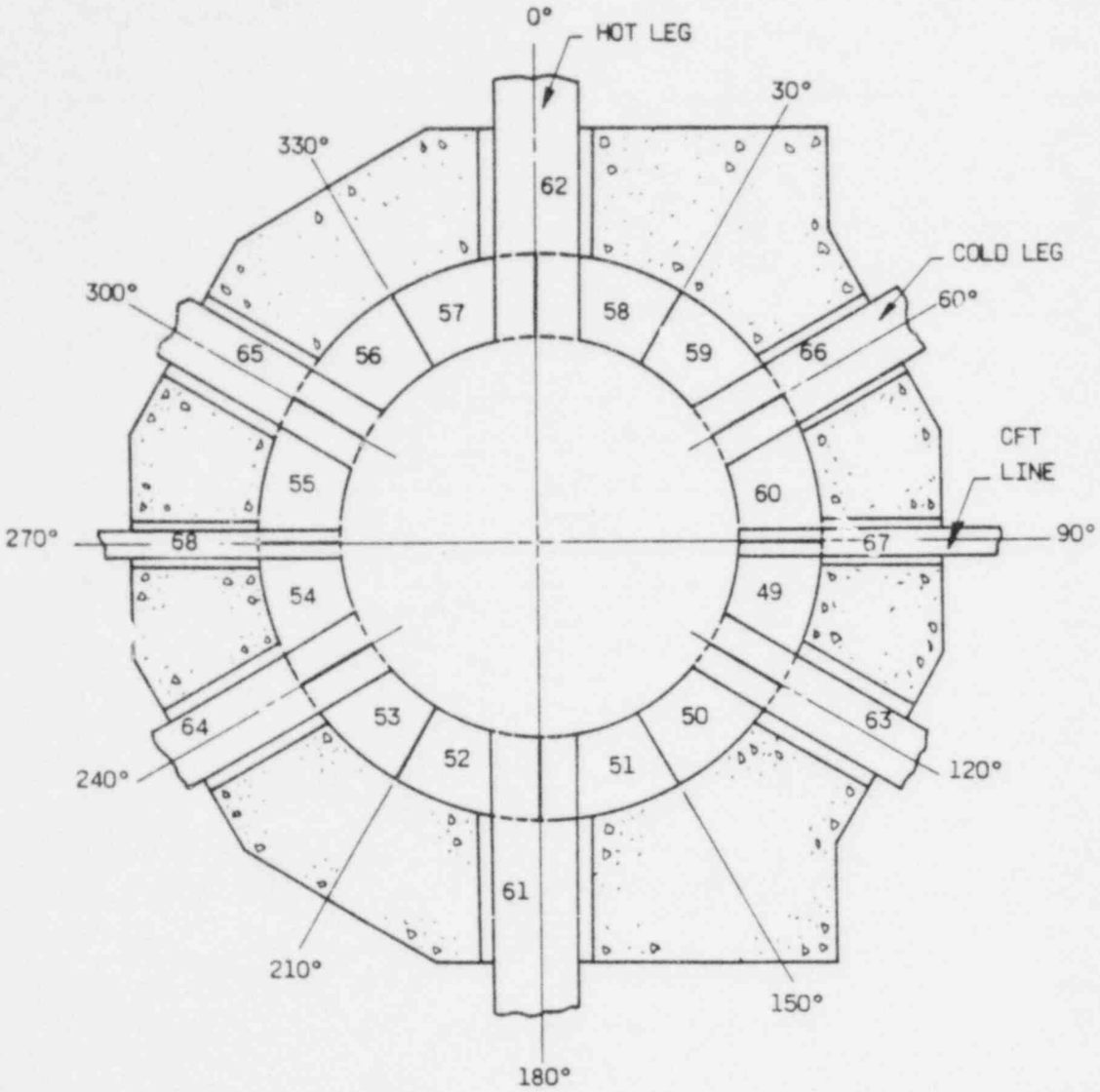

Figure 4.3-33. T' 1-2 Reactor Cavity, Elevation View

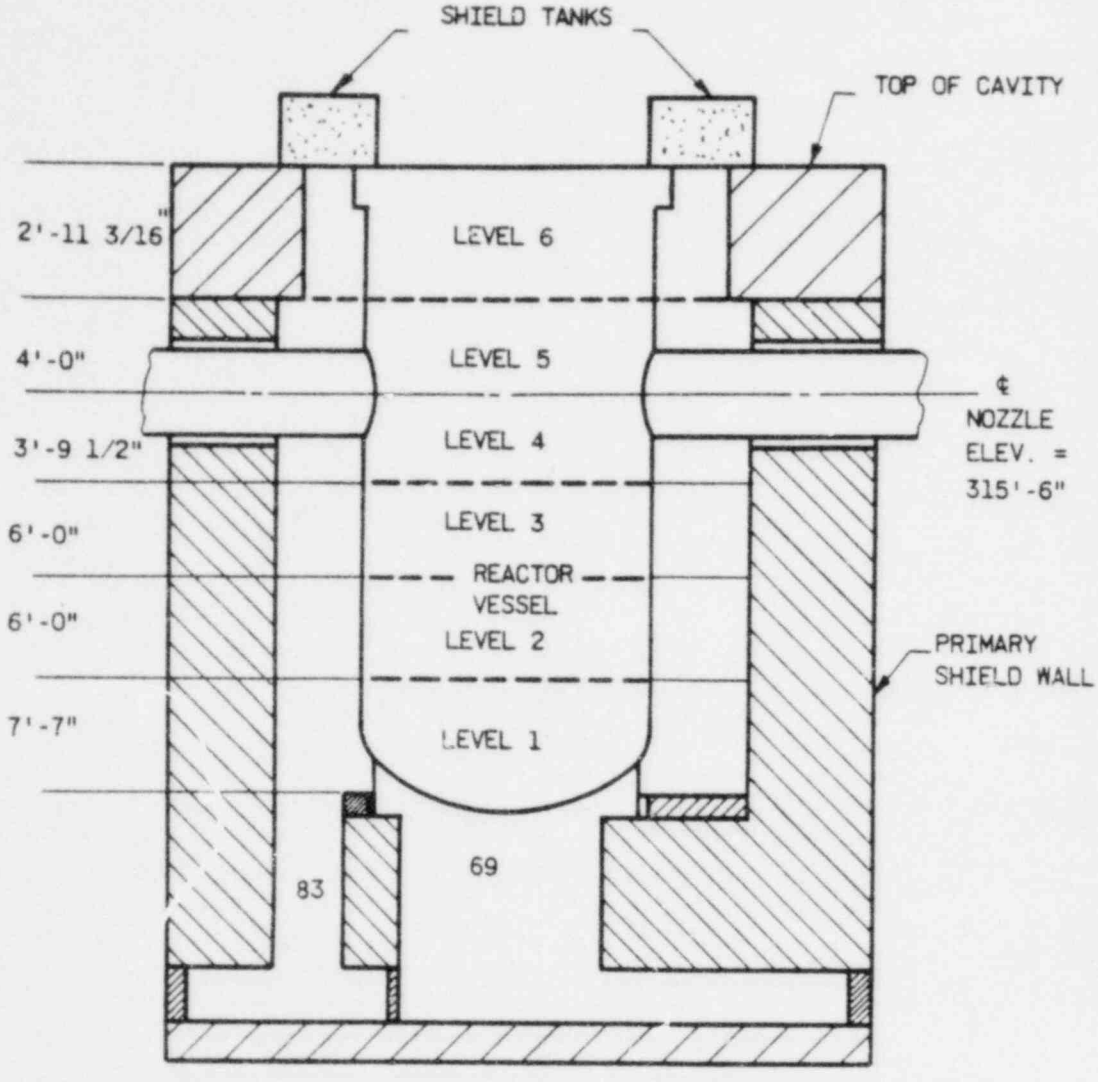

CONTAINMENT NODE = 70

Figure 4.3-34. TMI-2 Reactor Cavity, Plan View of Level 1

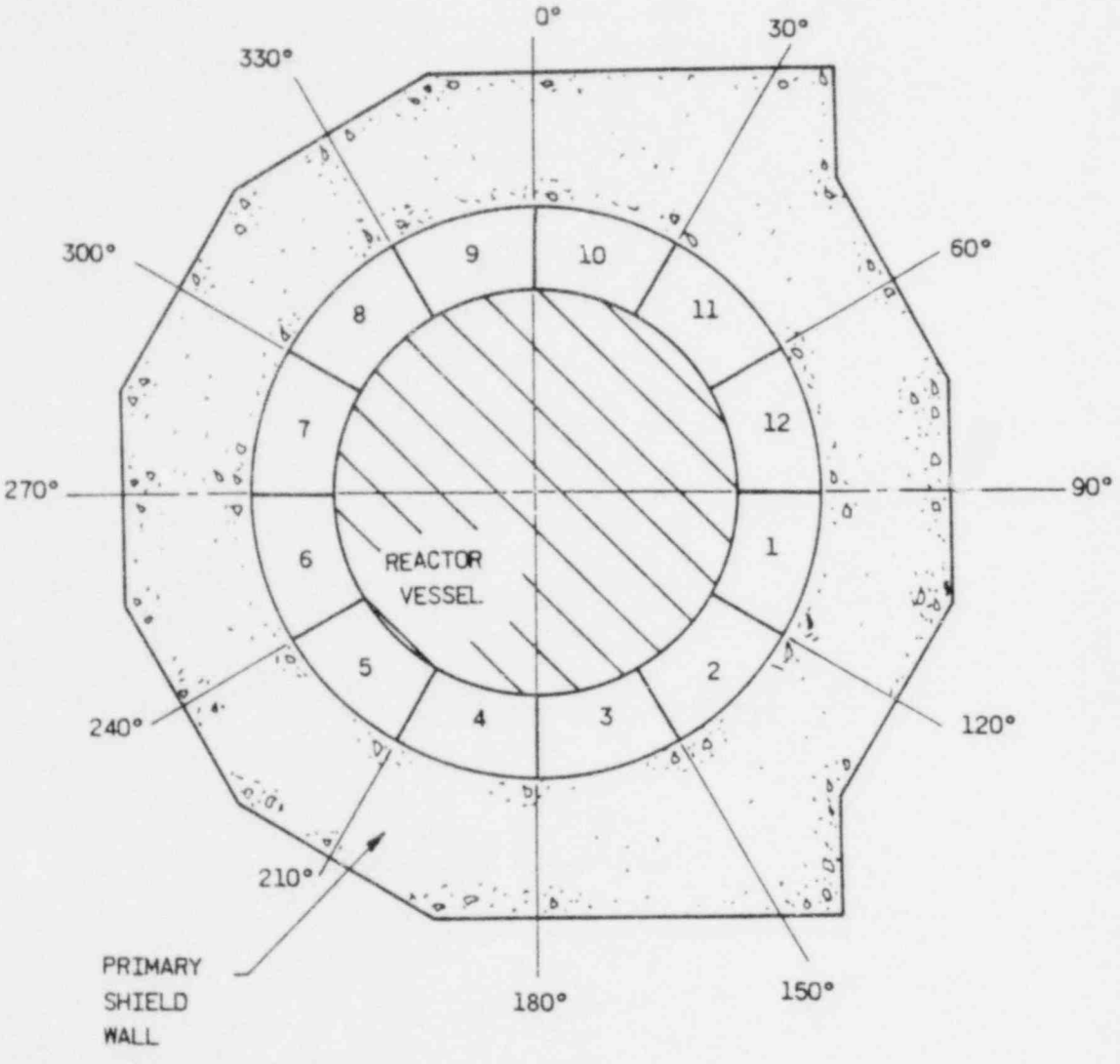

Figure 4.3-35. TMI-2 Reactor Cavity, Plan View of Level 2

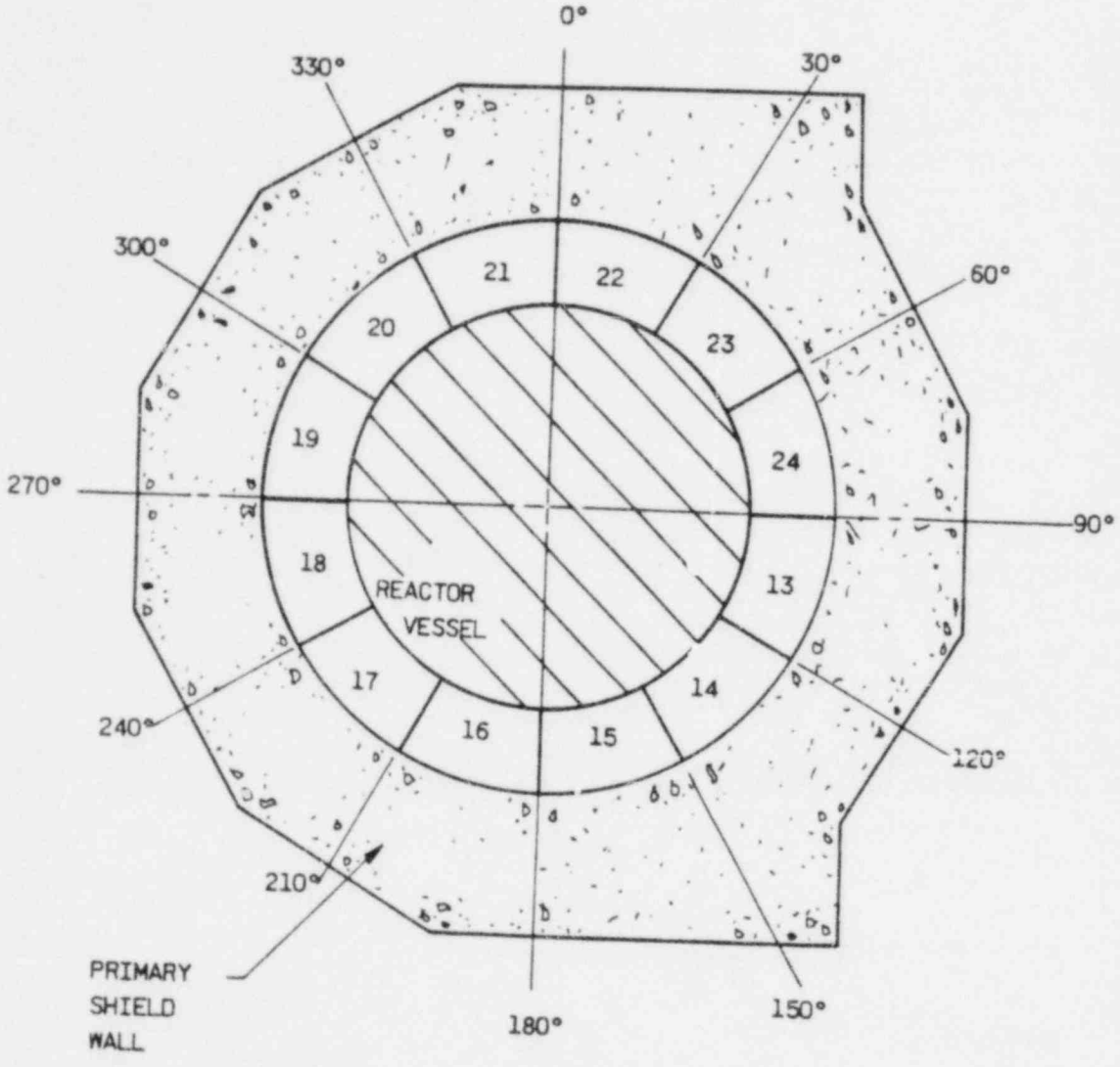

Figure 4.3-36. TMI-2 Reactor Cavity, Plan View of Level 3

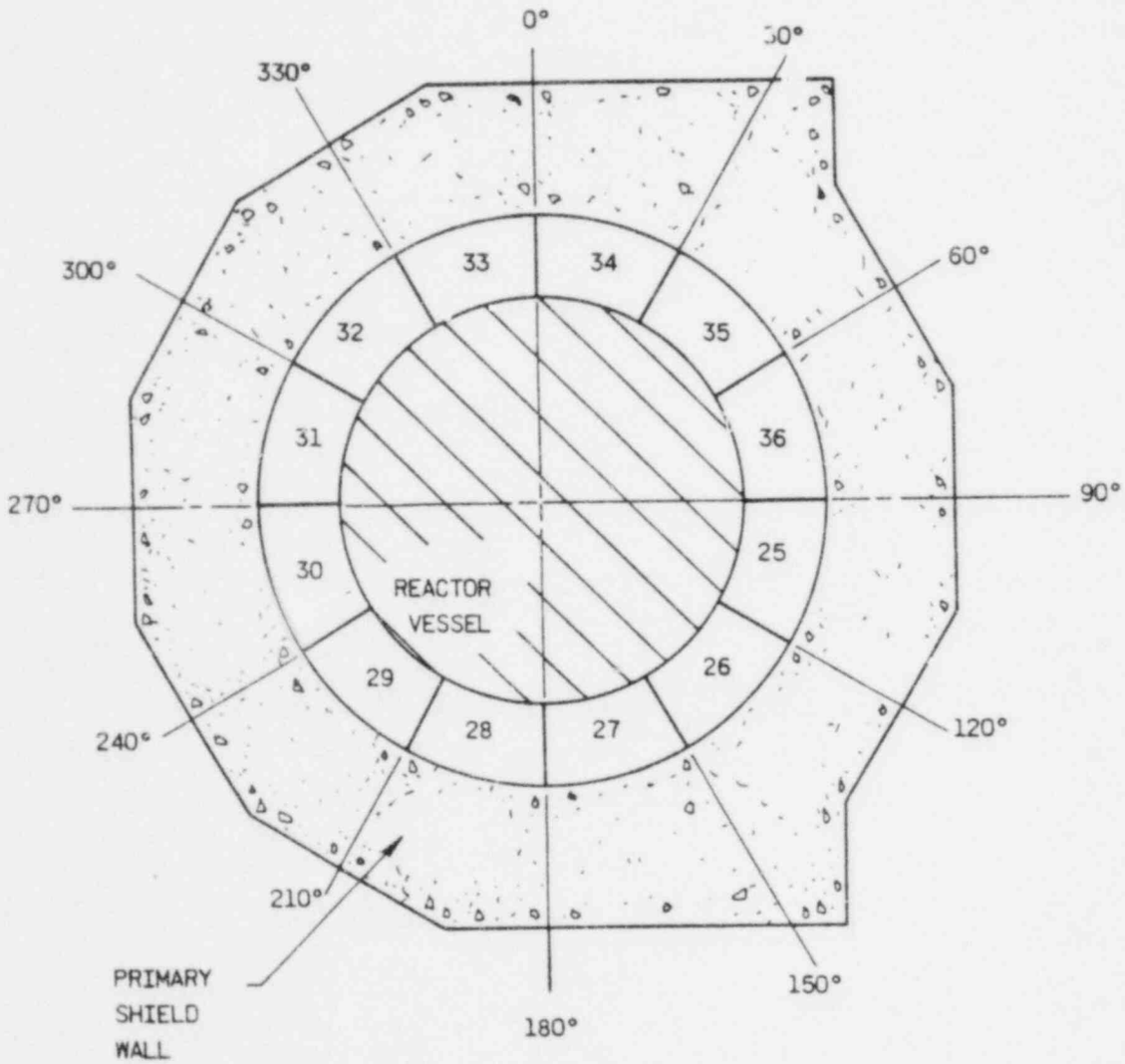

Figure 4.3-37. TMI-2 Reactor Cavity, Plan View of Level 4

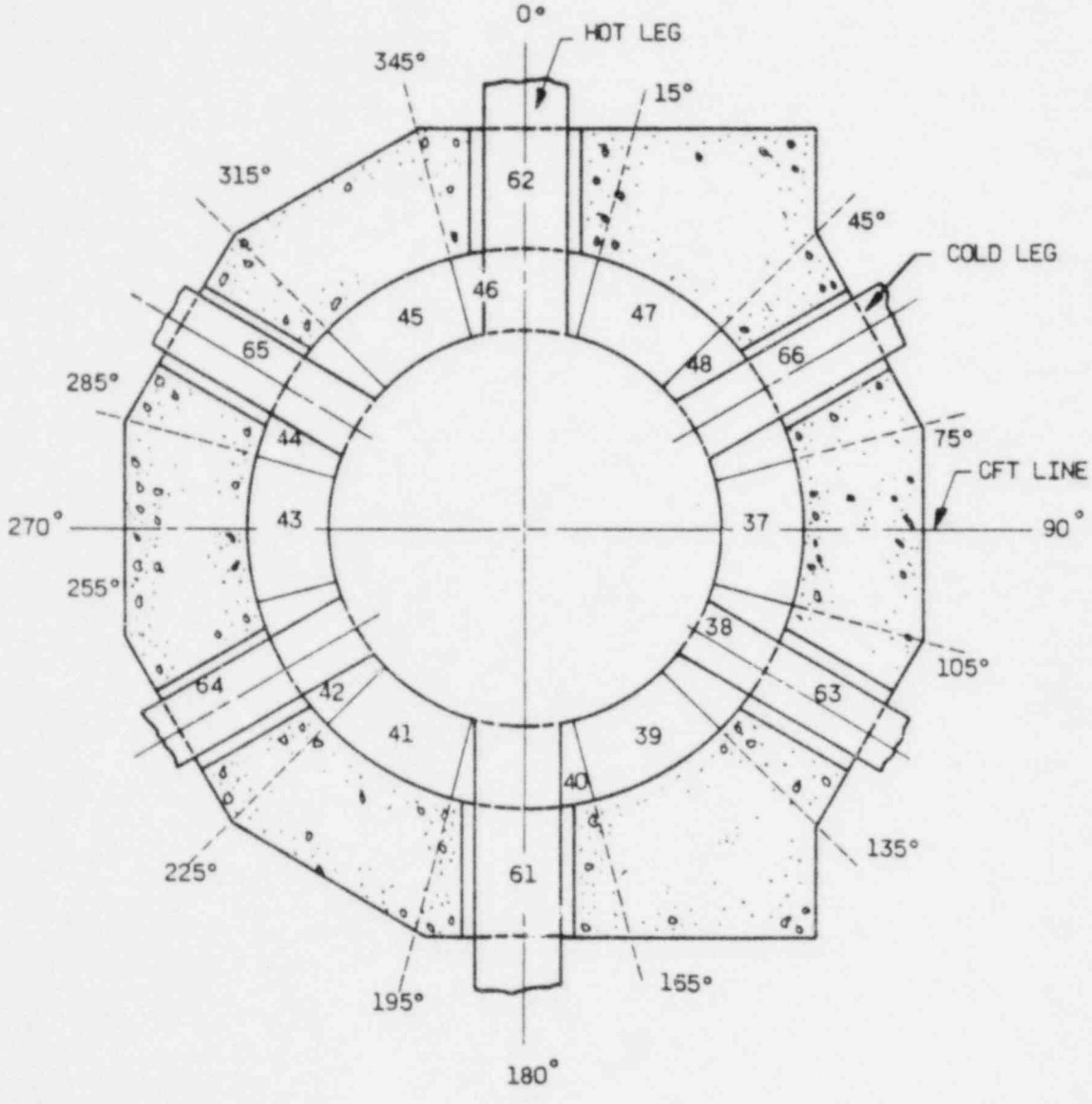

Figure 4.3-38. TMI-2 Reactor Cavity, Plan View of Level 5

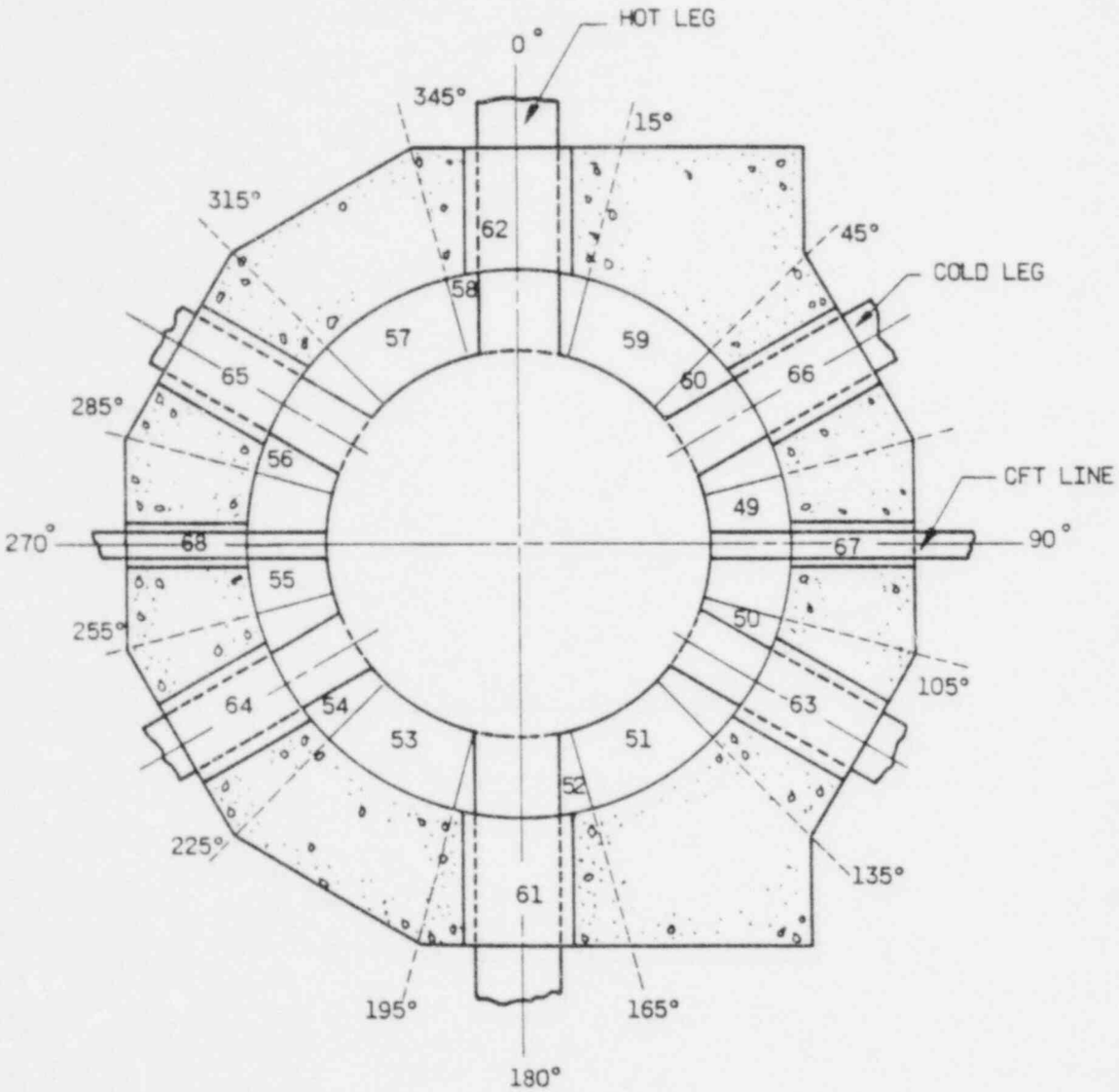

Figure 4.3-39. TMI-2 Reactor Cavity, Plan View of Level 6

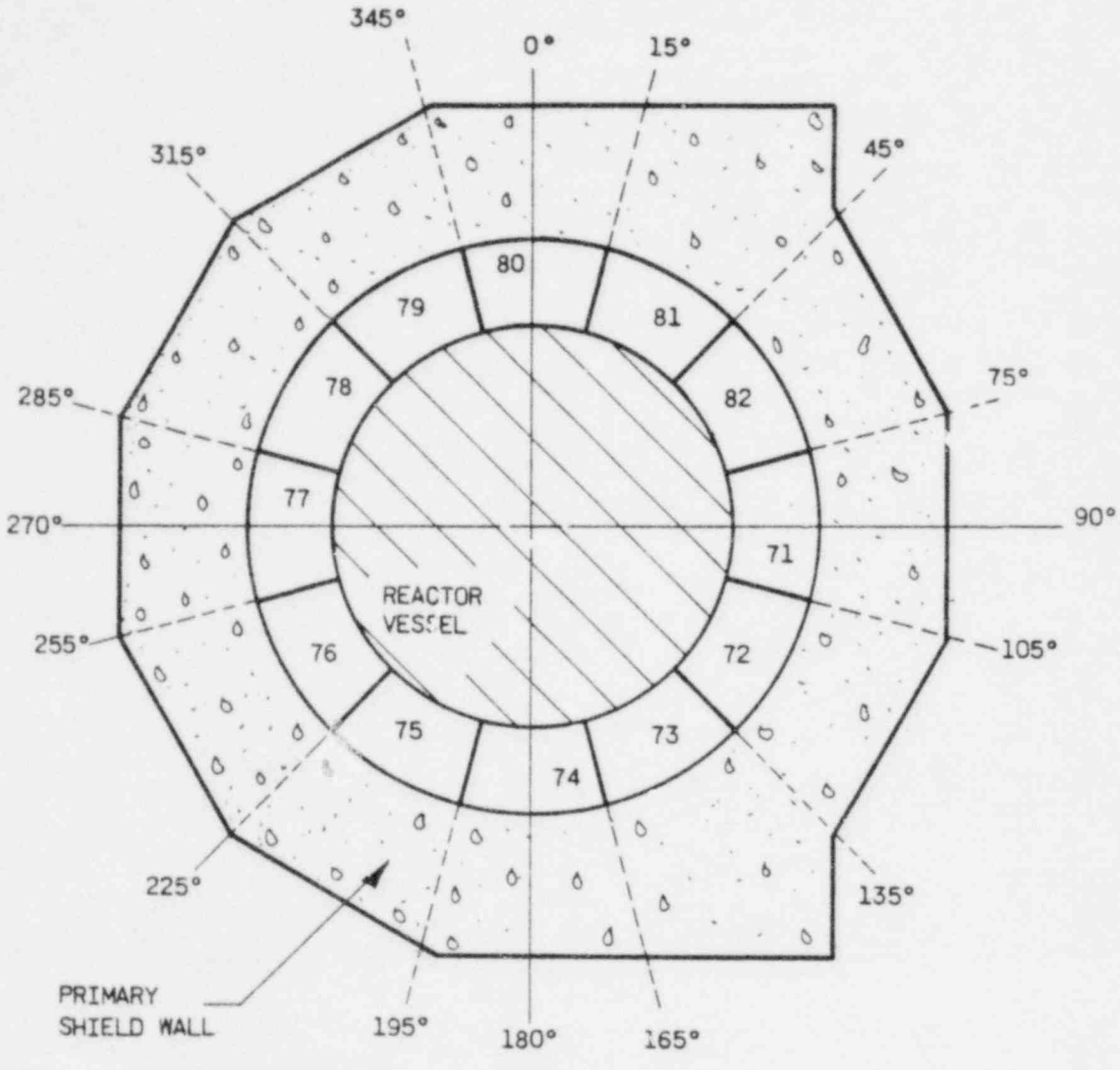

Figure 4.3-40. Oconee Reactor Cavity, Elevation View

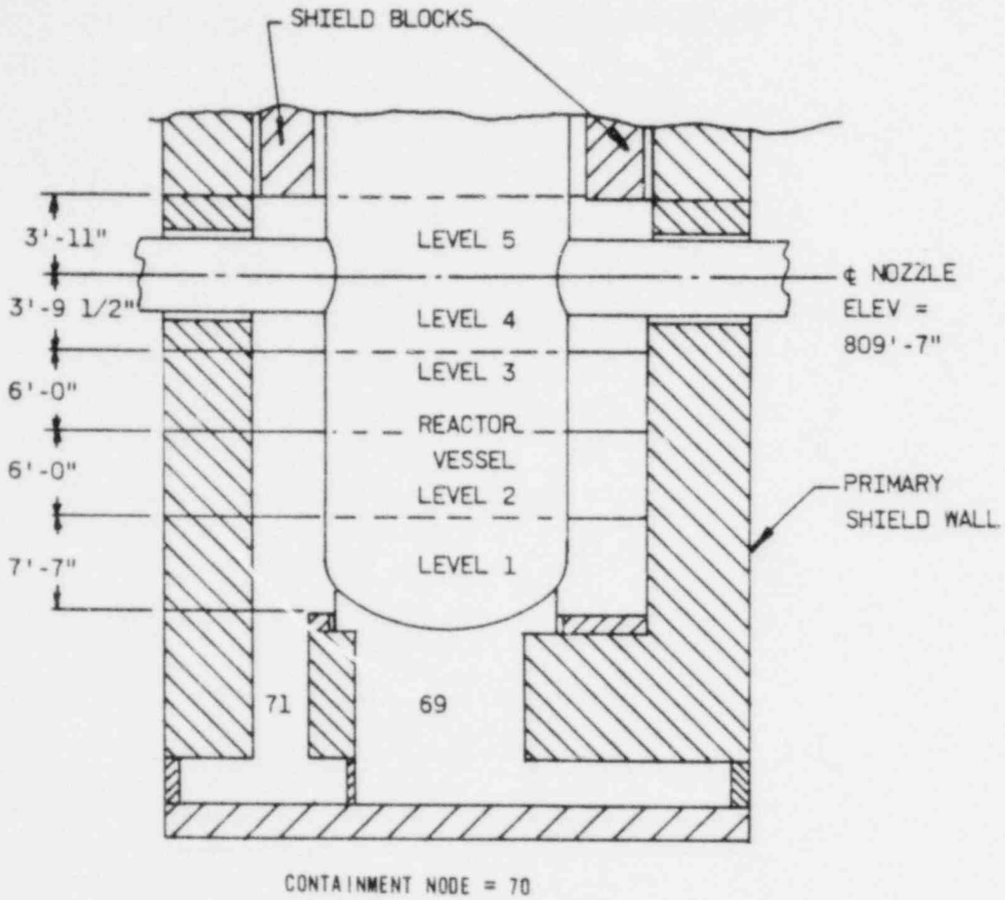

Figure 4.3-41. Oconee Reactor Cavity, Plan View of Level 1

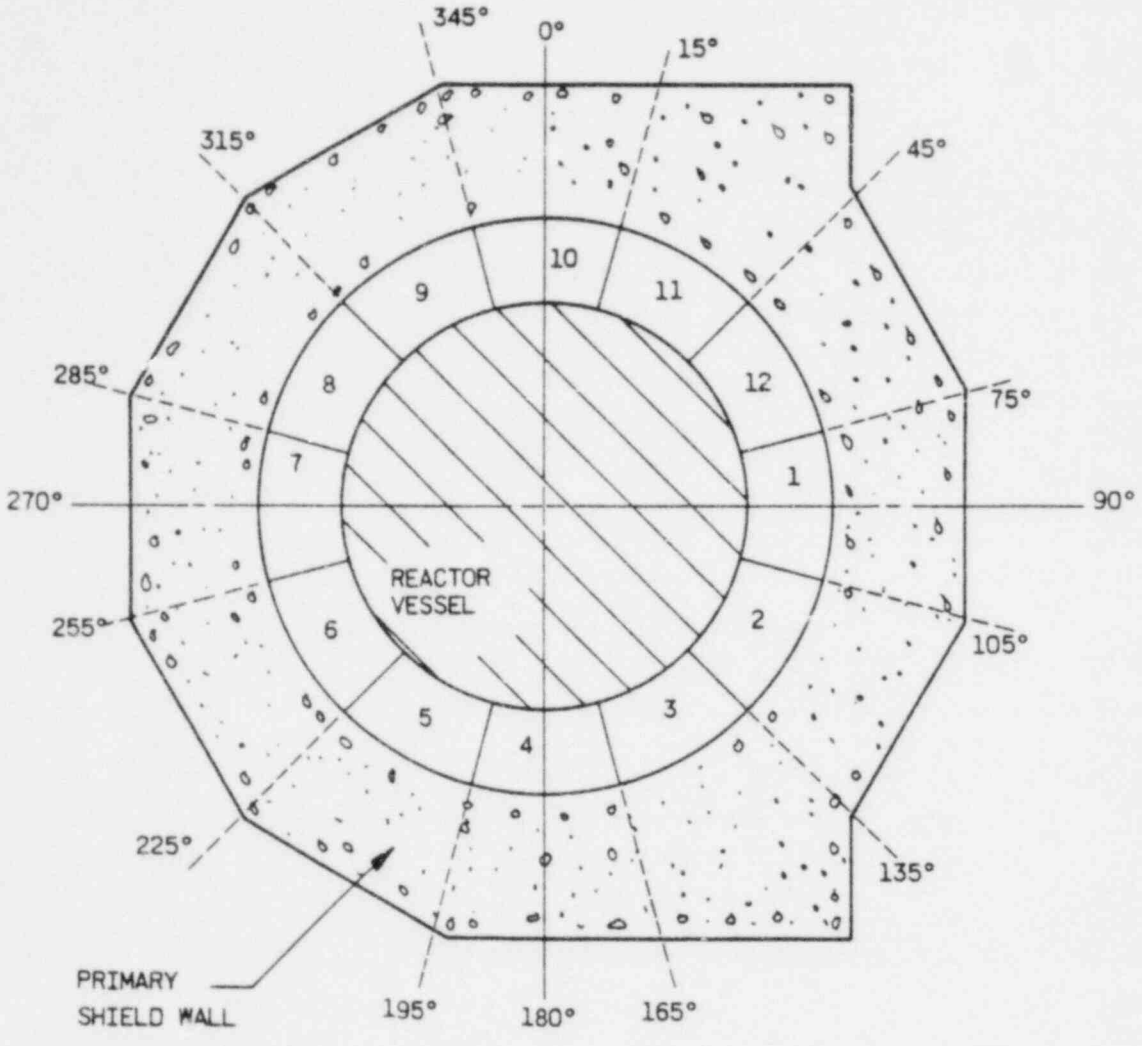

Figure 4.3-42. Oconee Reactor Cavity, Plan View of Level 2

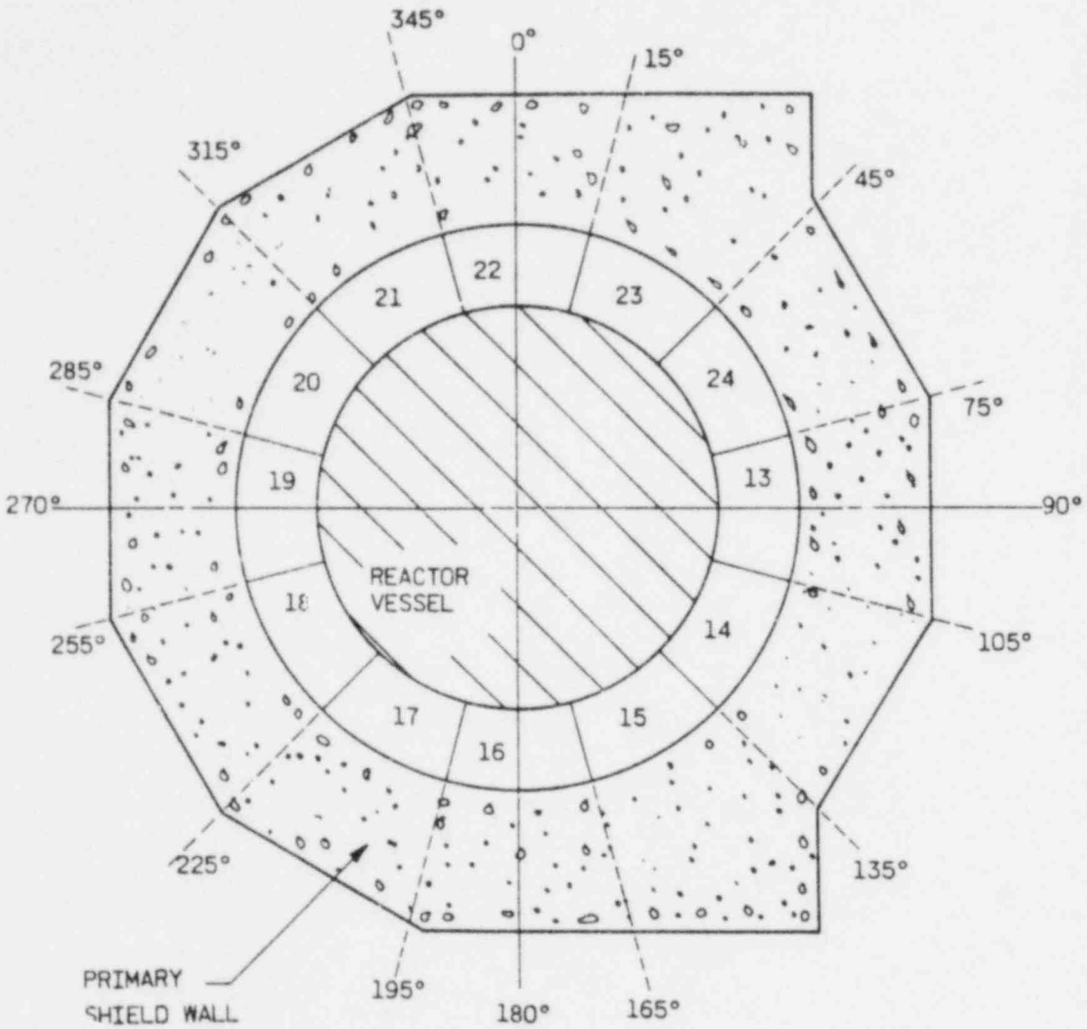

Figure 4.3-43. Oconee Reactor Cavity, Plan View of Level 3

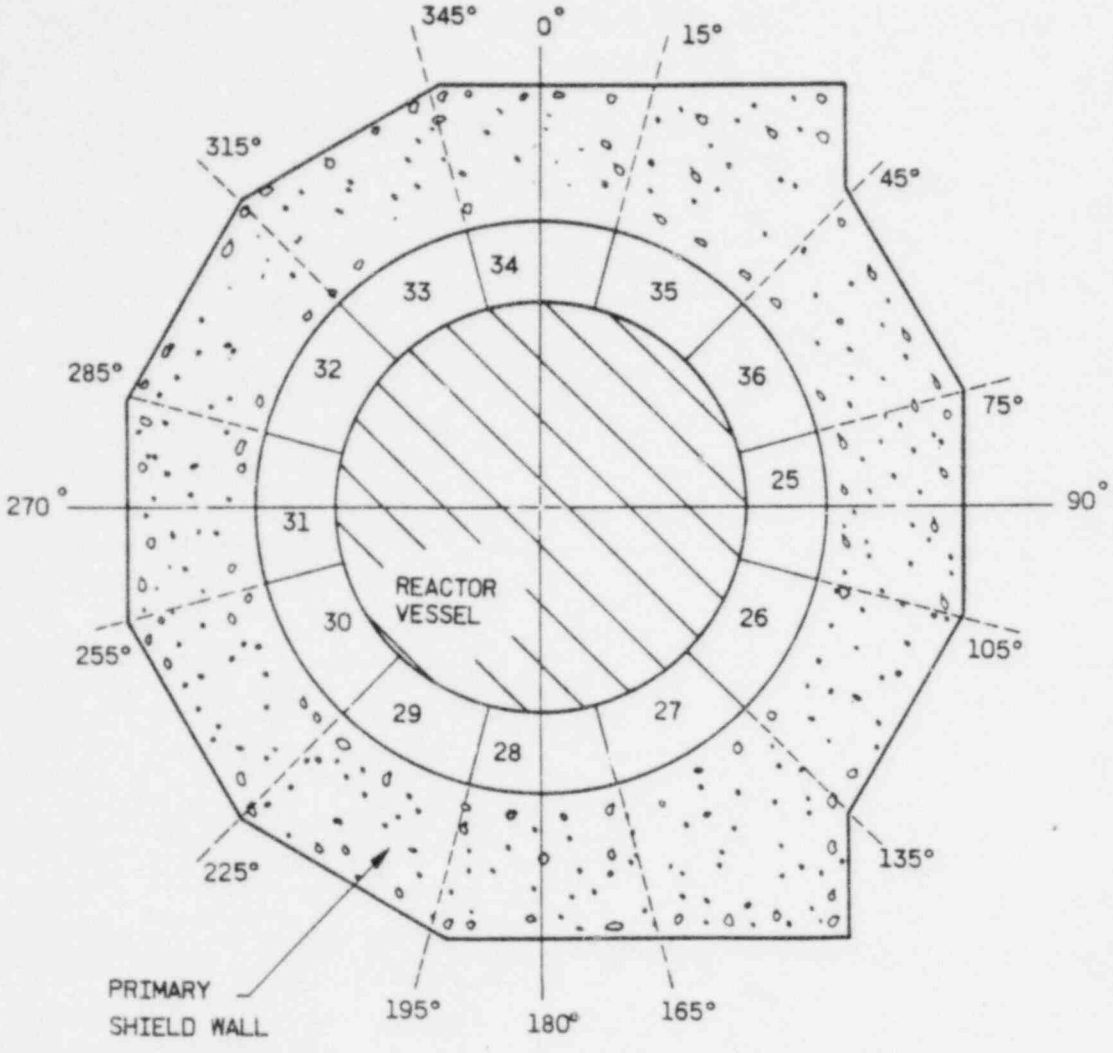

Figure 4.3-44. Oconee Reactor Cavity, Plan View of Level 4

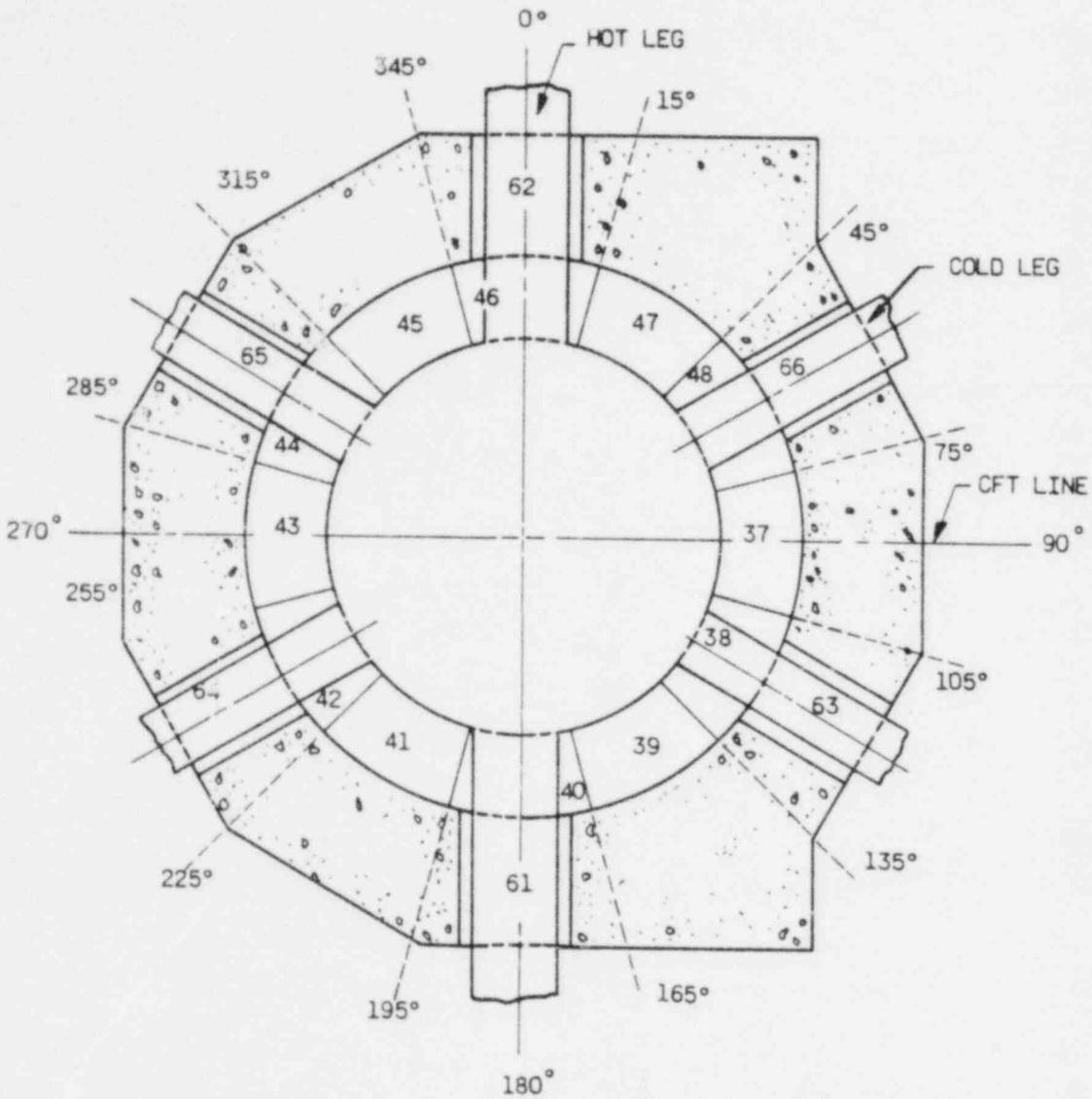

Figure 4.3-45. Oconee Reactor Cavity, Plan View of Level 5

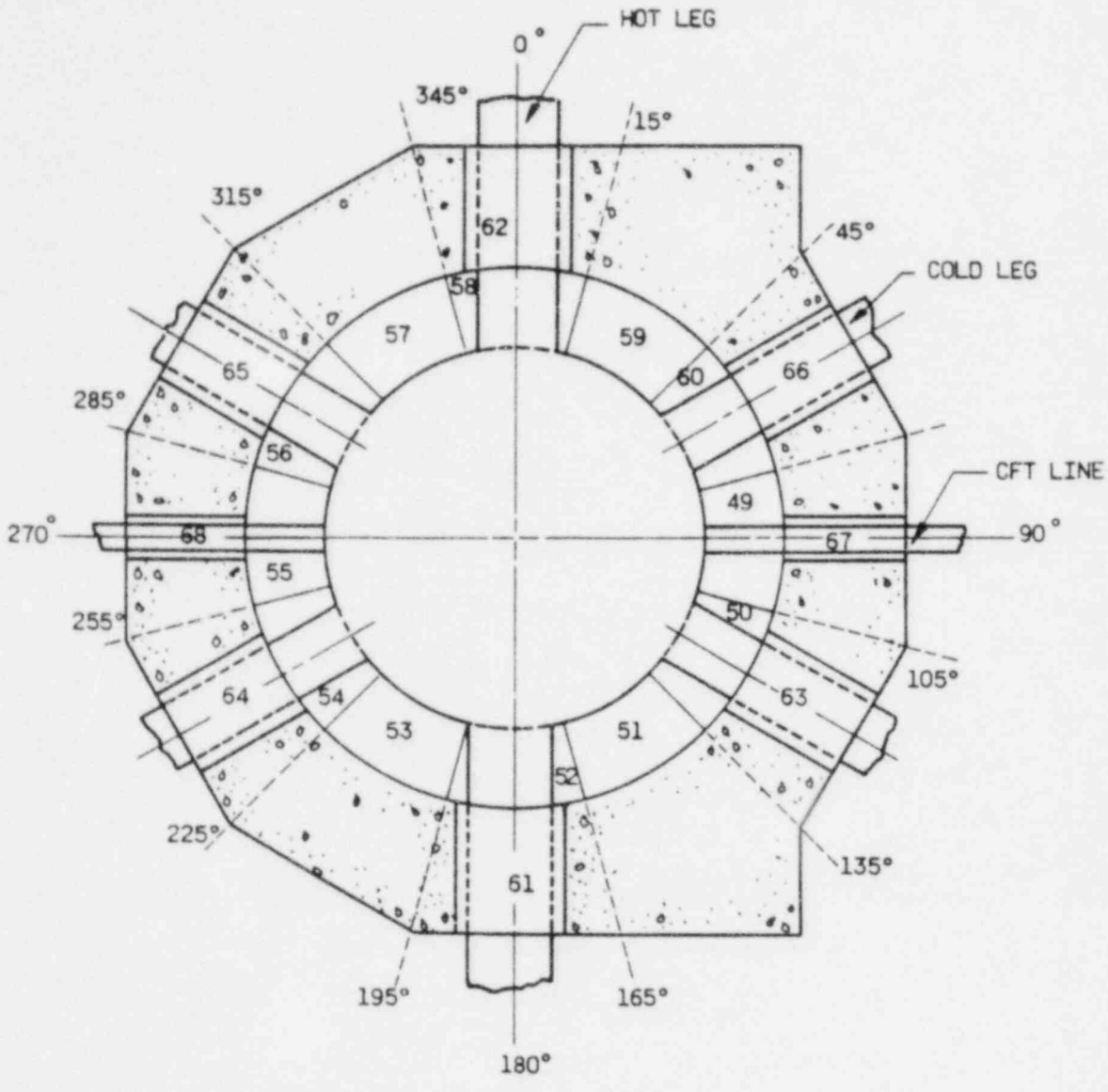

Figure 4.3-46. Davis-Besse 1 Reactor Cavity, Elevation View

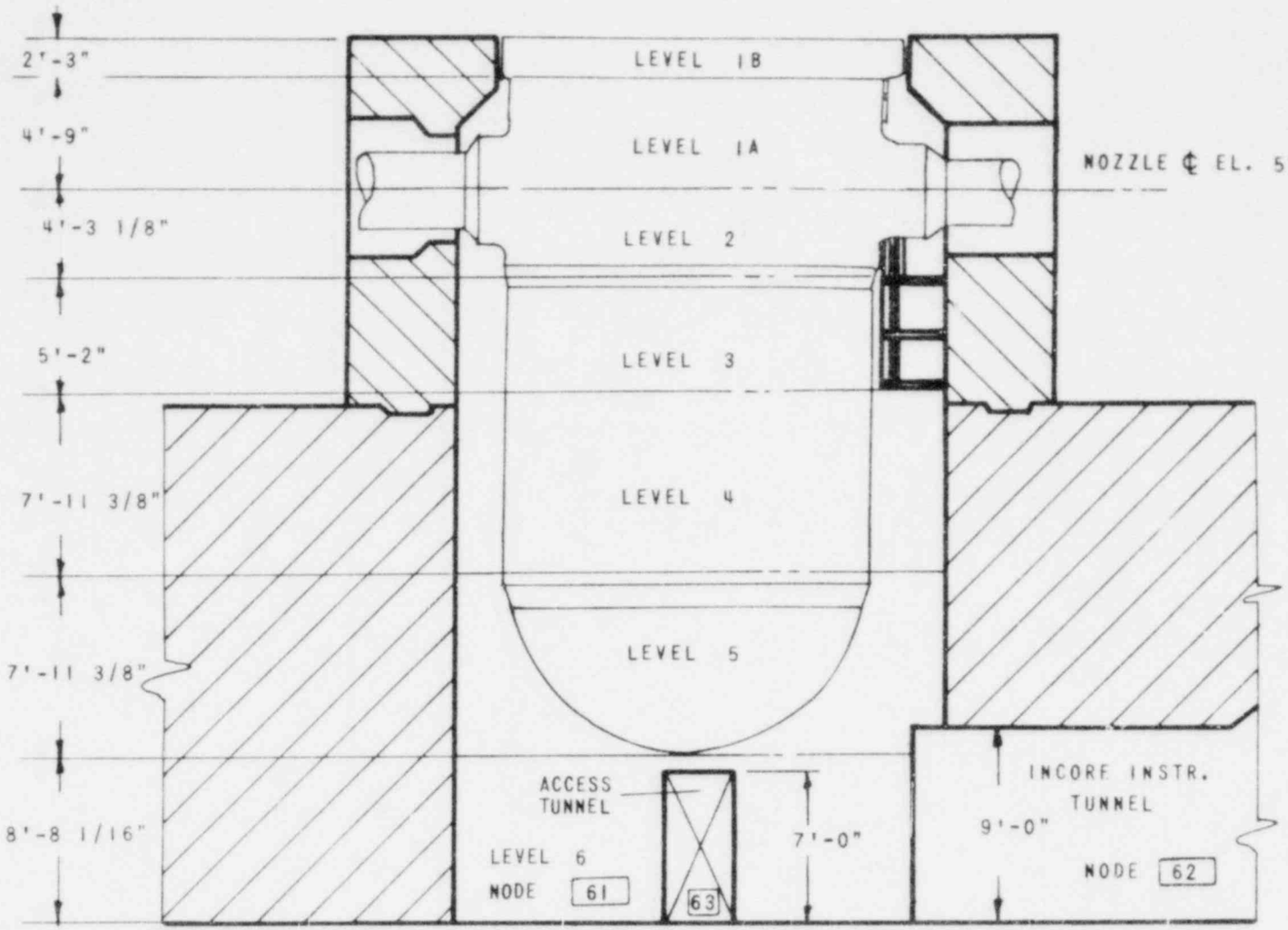

CONTAINMENT NODE = 72

Figure 4.3-47. Davis-Besse 1 Reactor Cavity Noding Plan, Level 1B

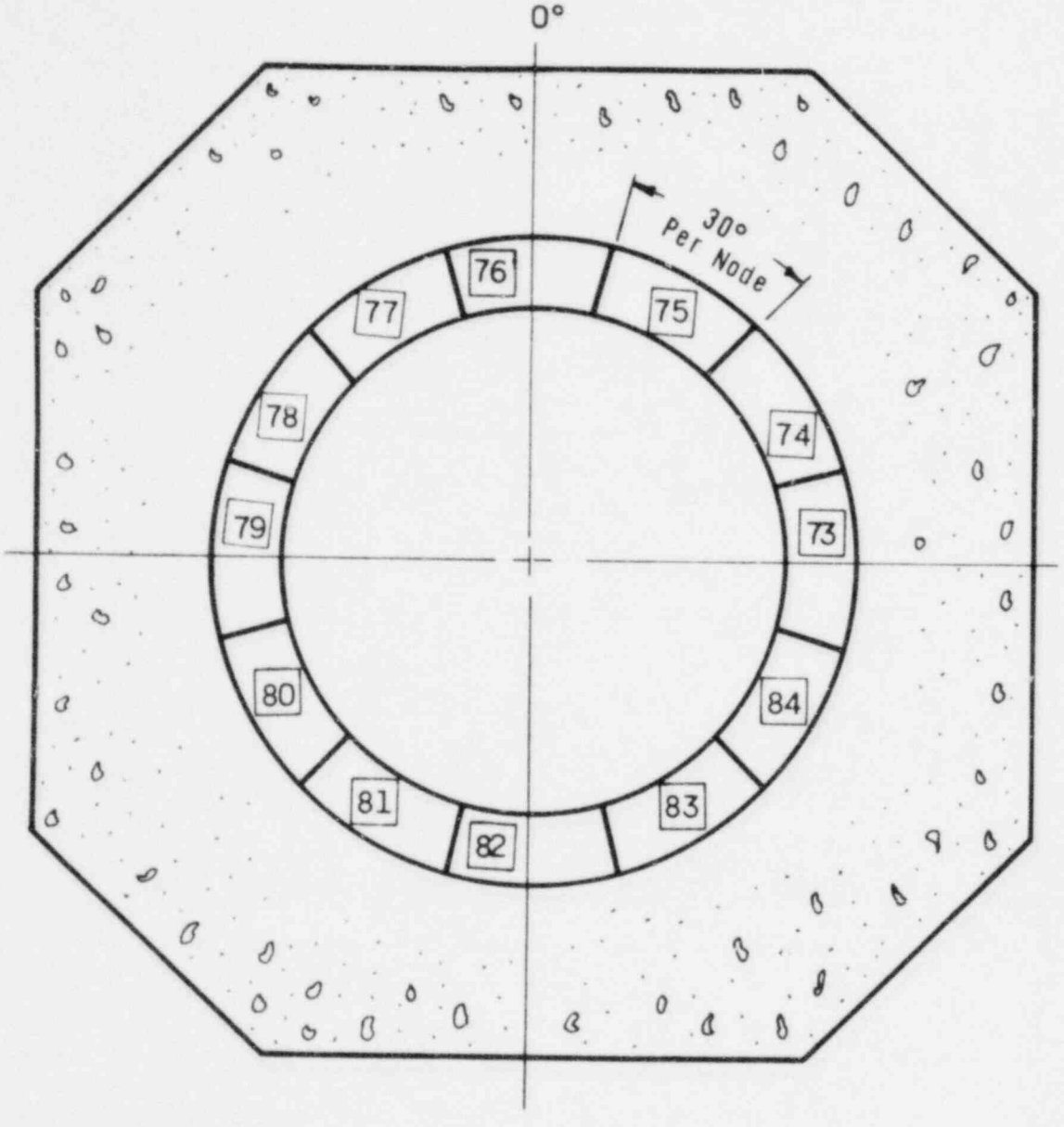

Figure 4.3-48. Davis-Besse 1 Reactor Cavity Noding Plan, Level 1A

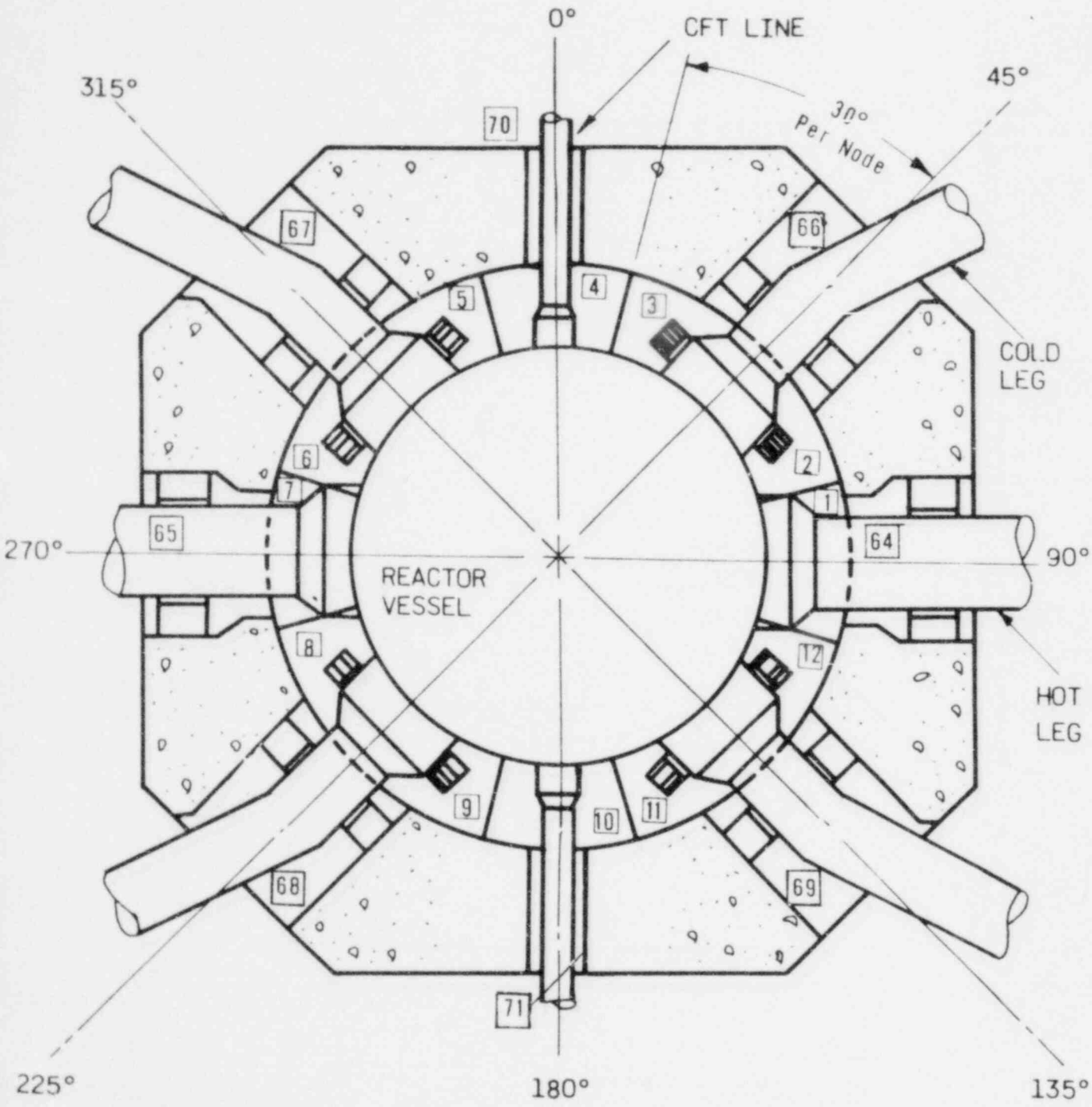

LEVEL #1A

Figure 4.3-49. Davis-Besse 1 Reactor Cavity Noding Plan, Level 2

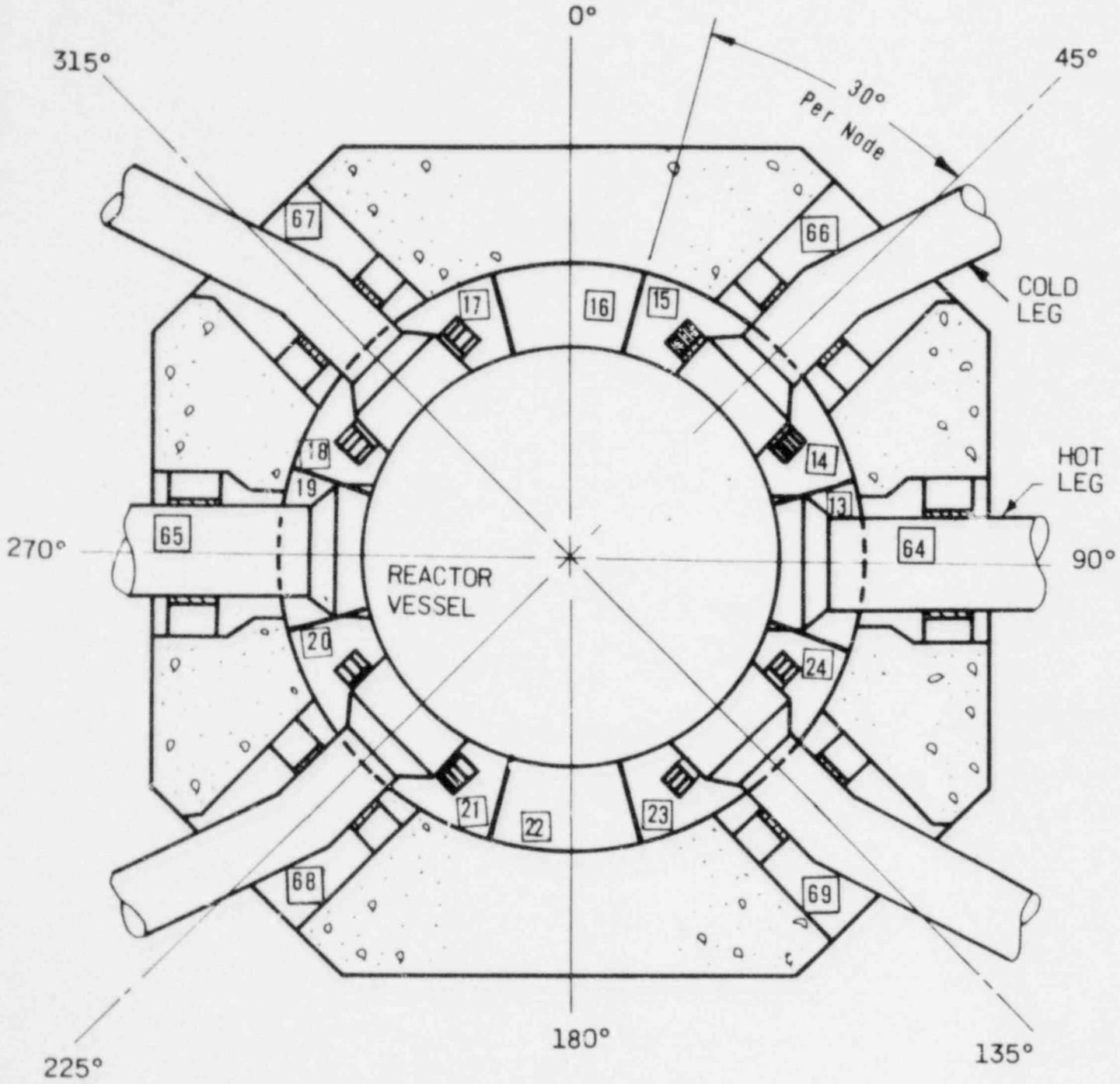

Figure 4.3-50. Davis-Besse 1 Reactor Cavity Noding Plan, Level 3

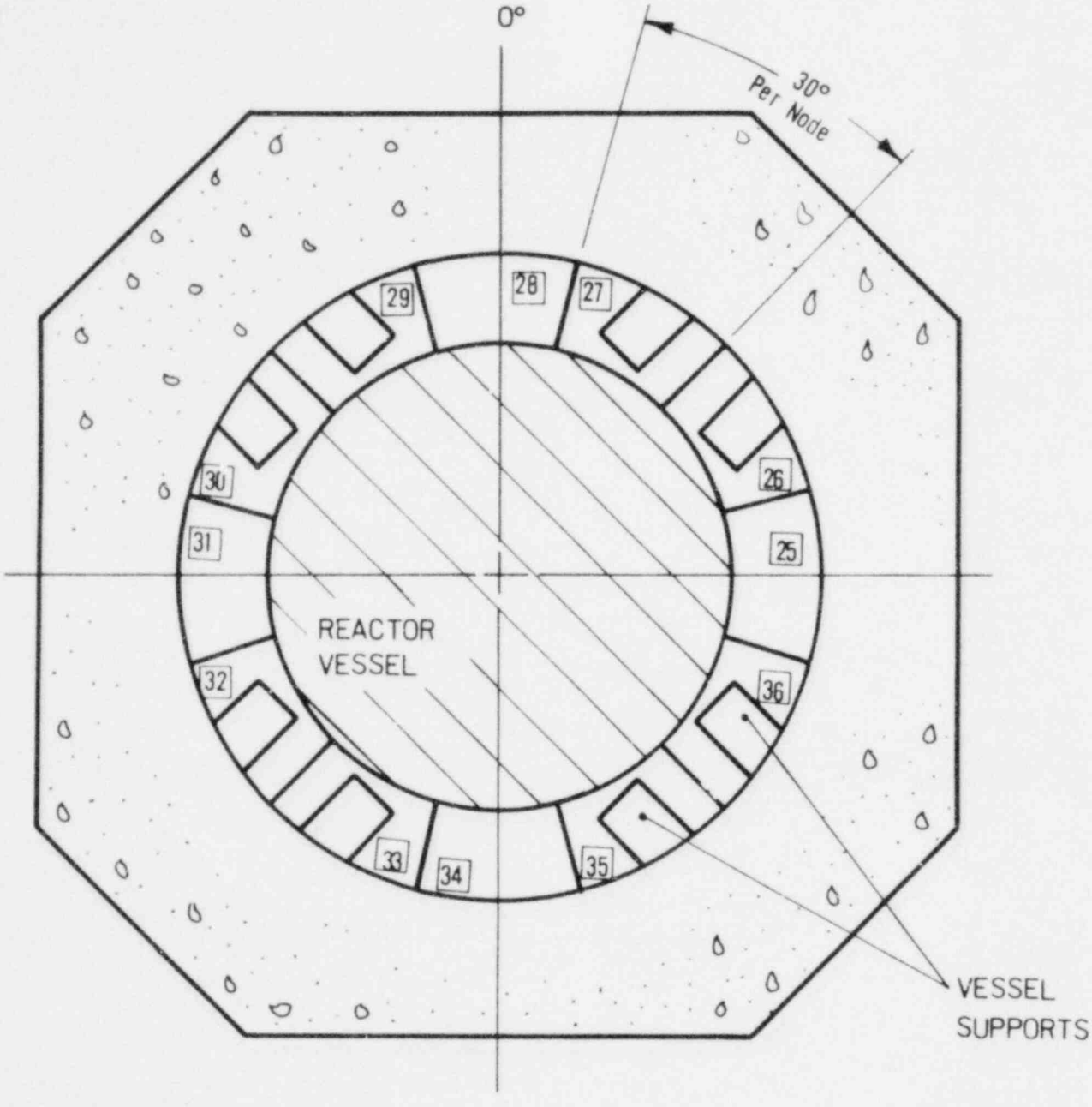

Figure 4.3-51. Davis-Besse 1 Reactor Cavity Noding Plan, Level 4

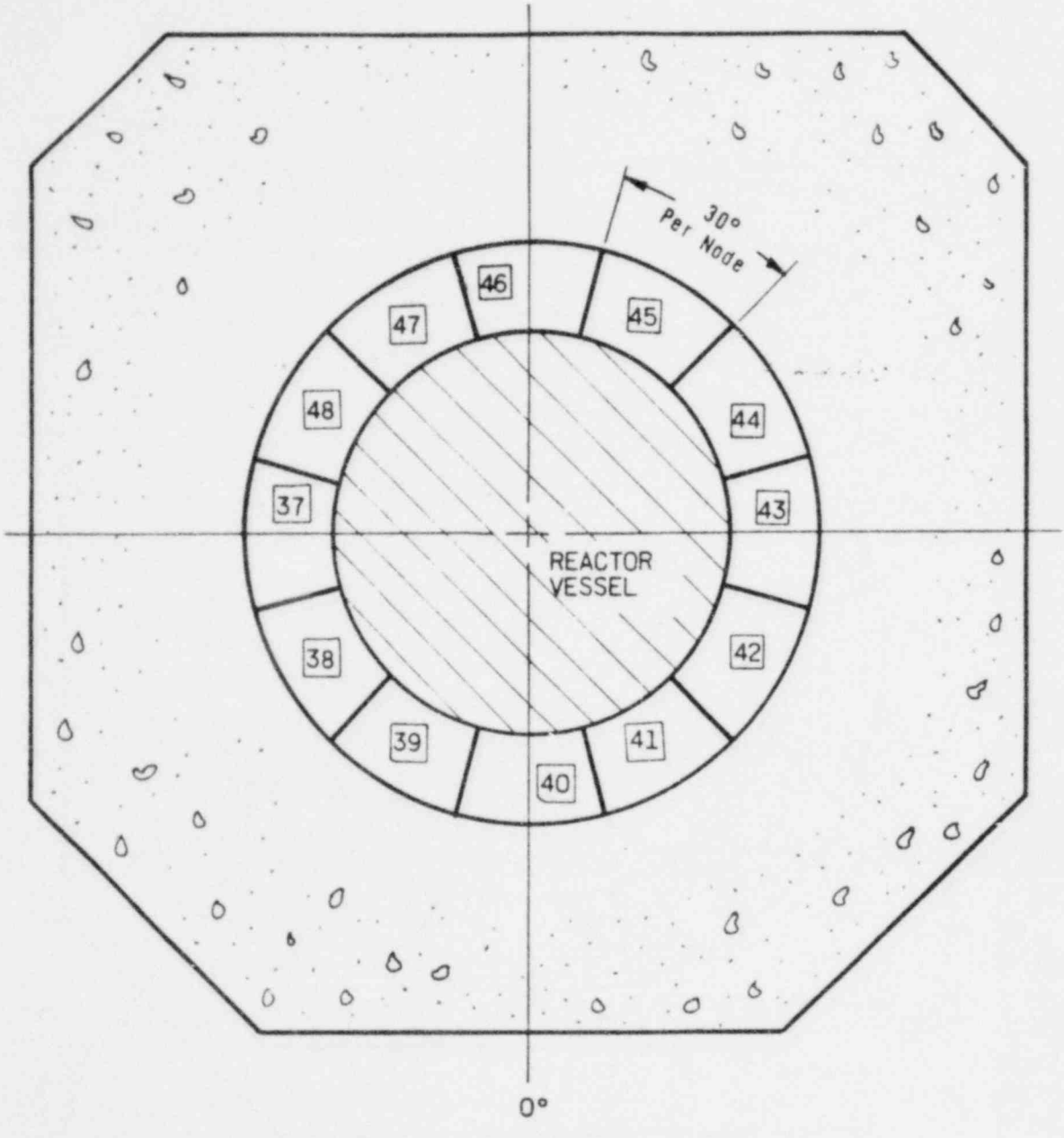

Figure 4.3-52. Davis-Besse 1 Reactor Cavity Noding Plan, Level 5

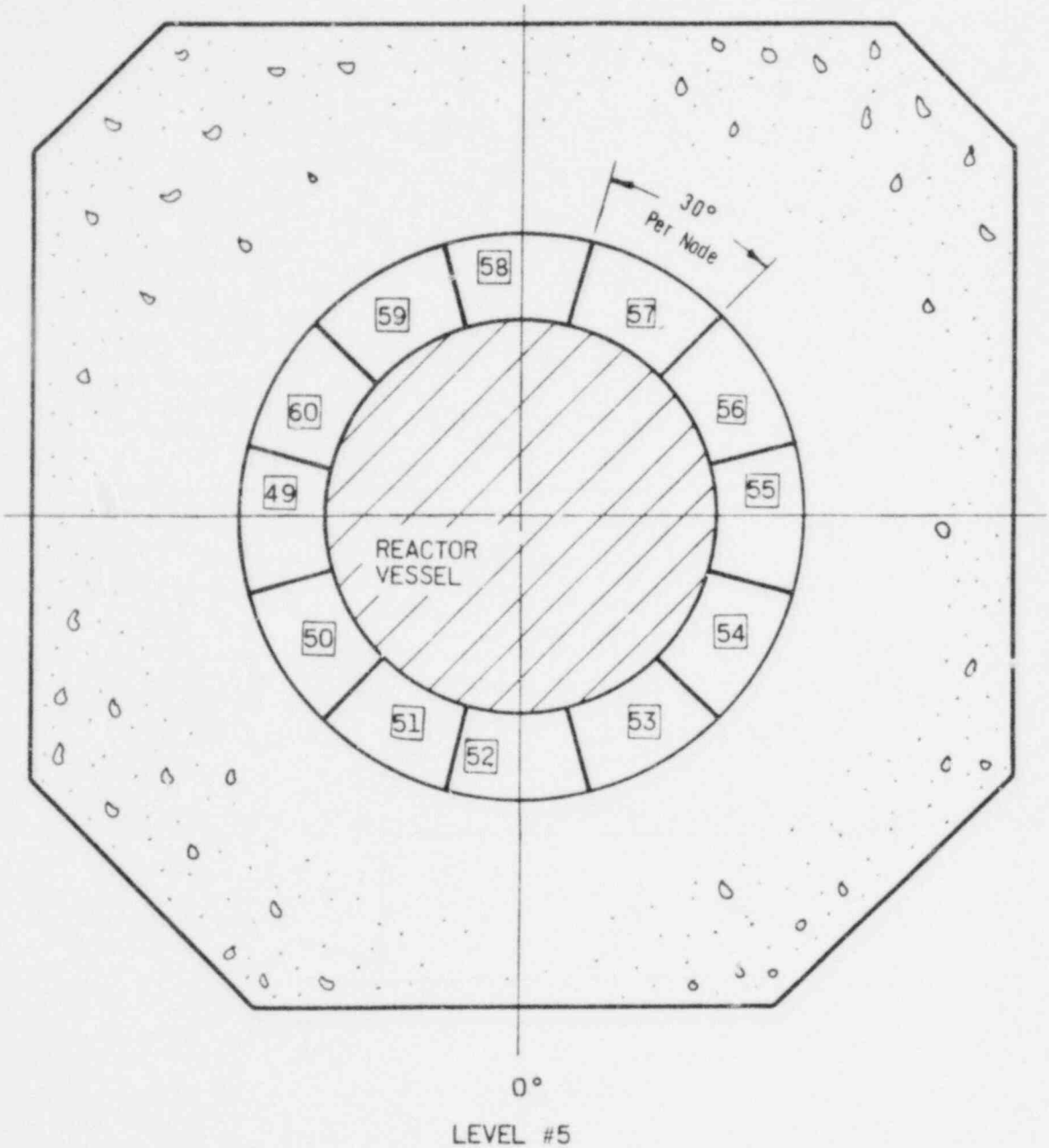

Figure 4.3-53. Davis-Besse 1 Reactor Cavity Noding Plan, Level 6

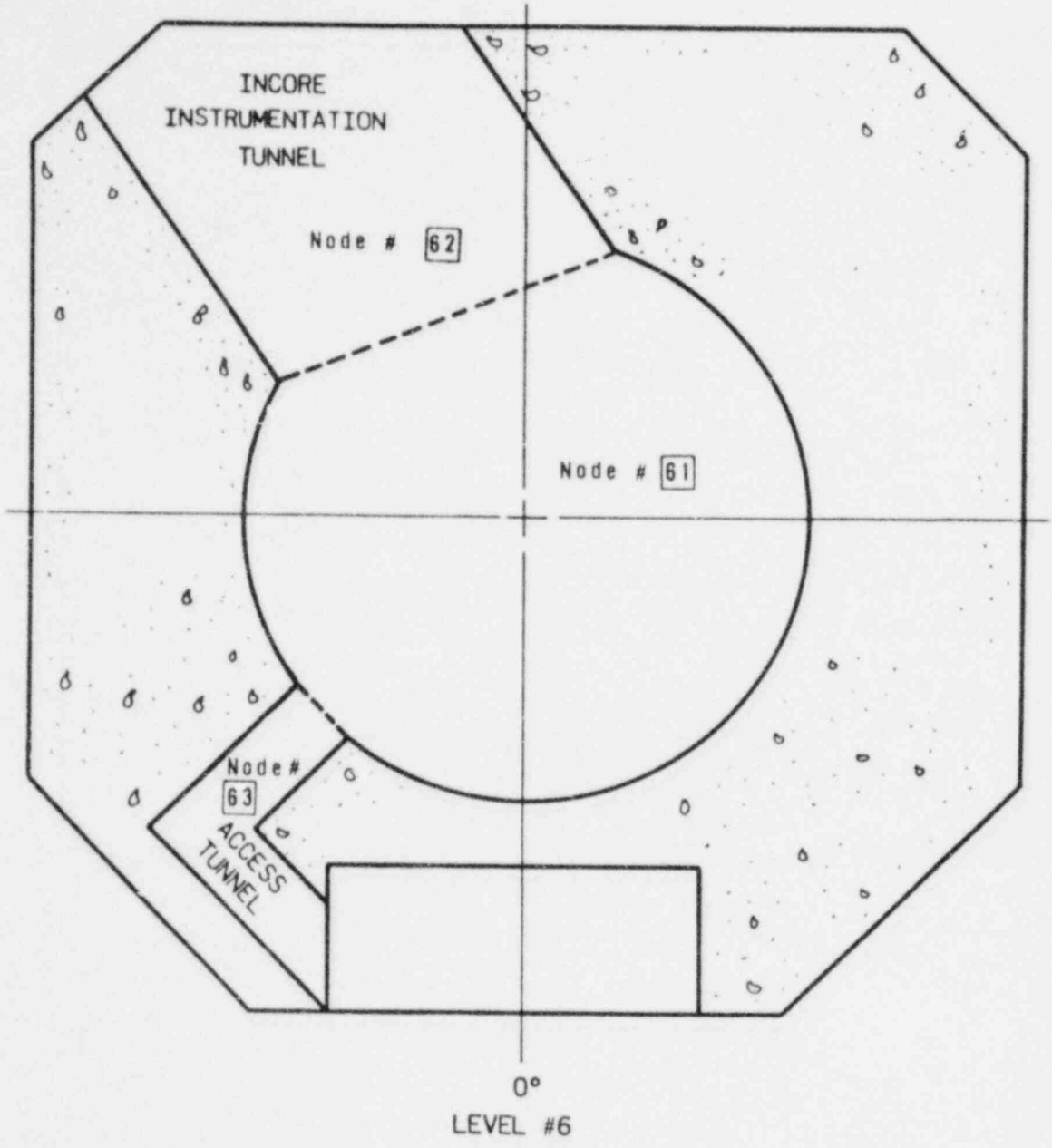

Figure 4.3-54. Integrated Leak Mass Flow for Guillotine Break at Reactor Vessel Inlet – Skirt-Supported Plants

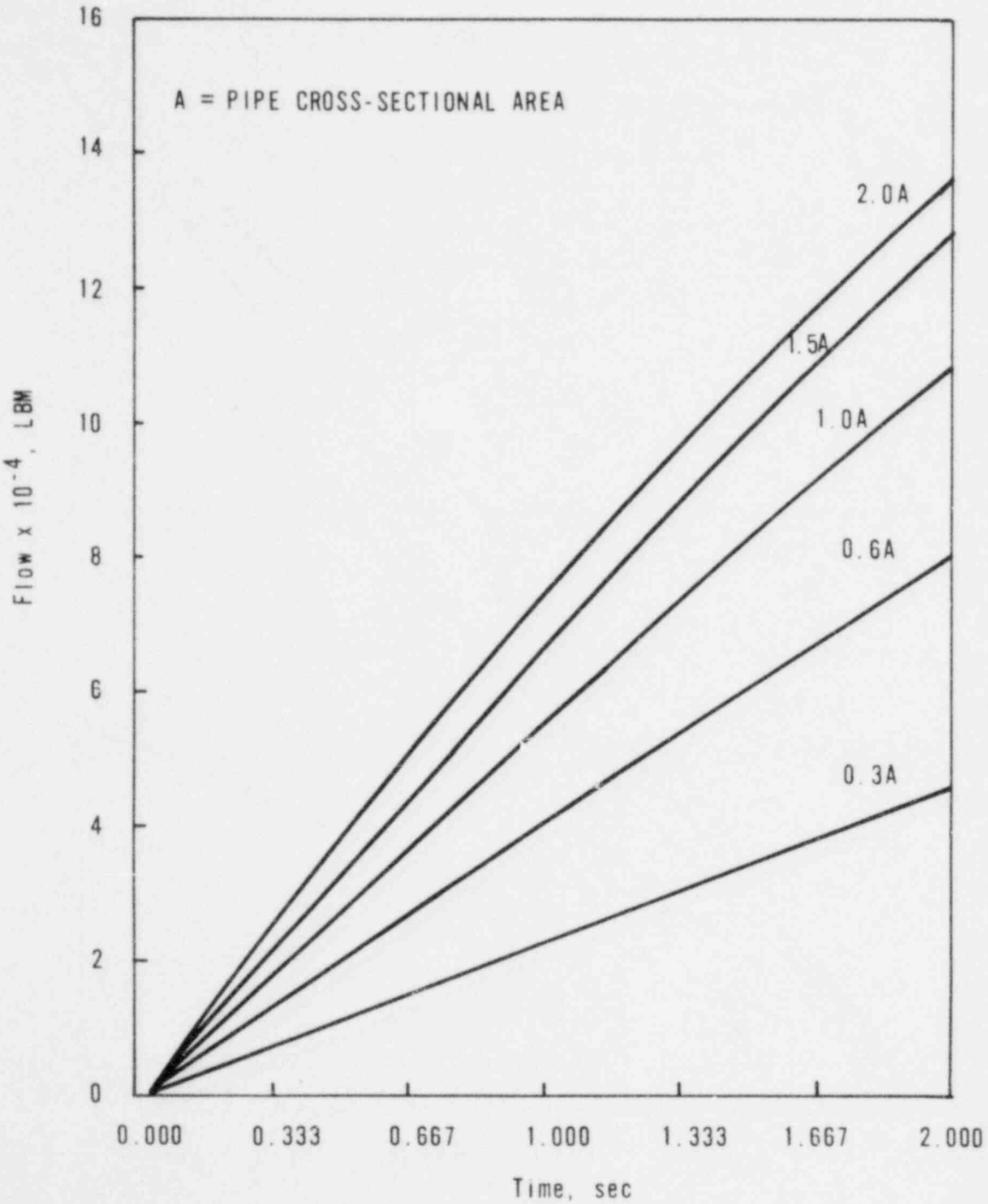

Figure 4.3-55. Integrated Leak Energy Flow for Guillotine Break at Reactor Vessel Inlet – Skirt-Supported Plants

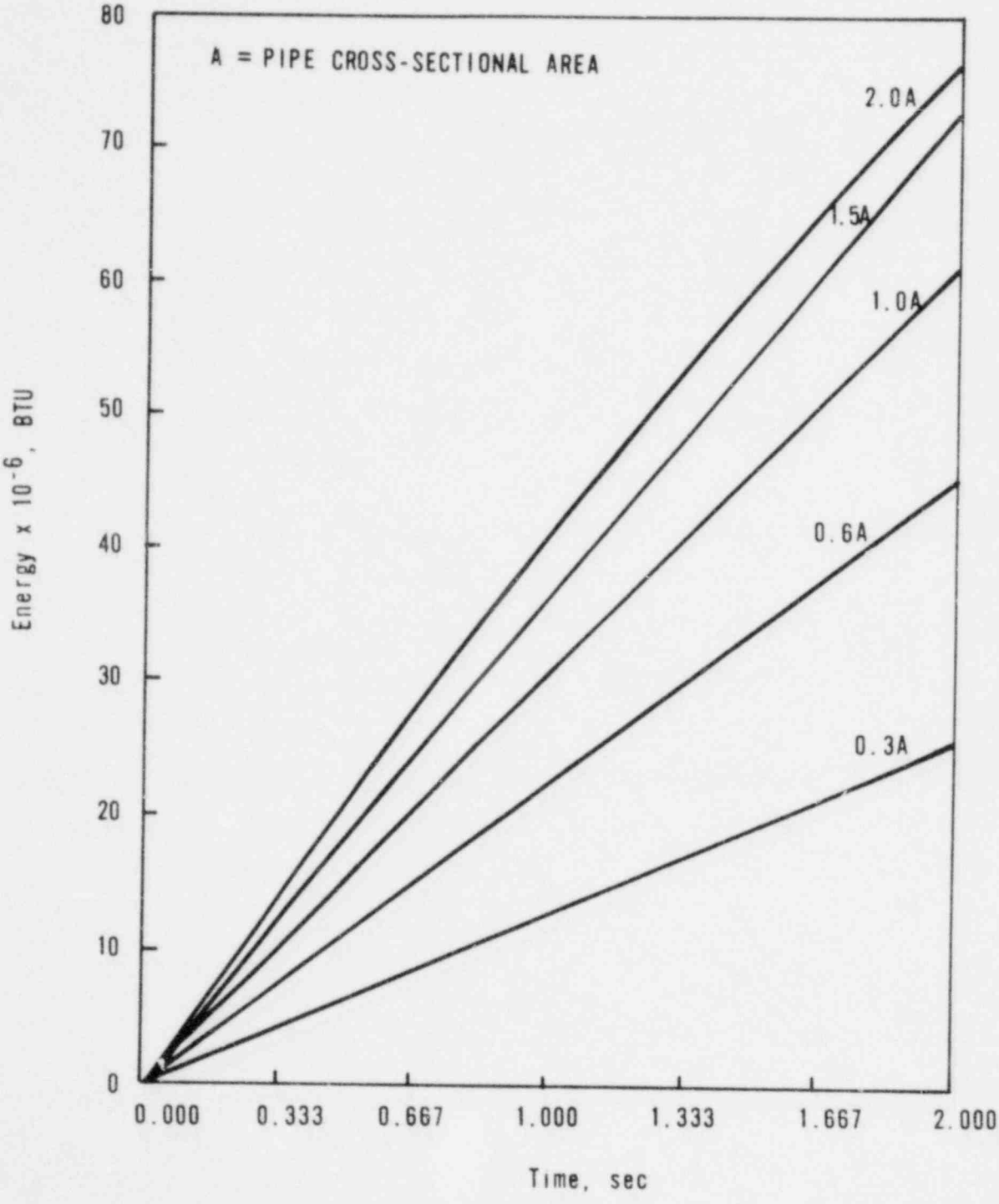

Figure 4.3-56. Integrated Leak Mass Flow for Guillotine Break at Reactor Vessel Outlet -- Skirt-Supported Plants

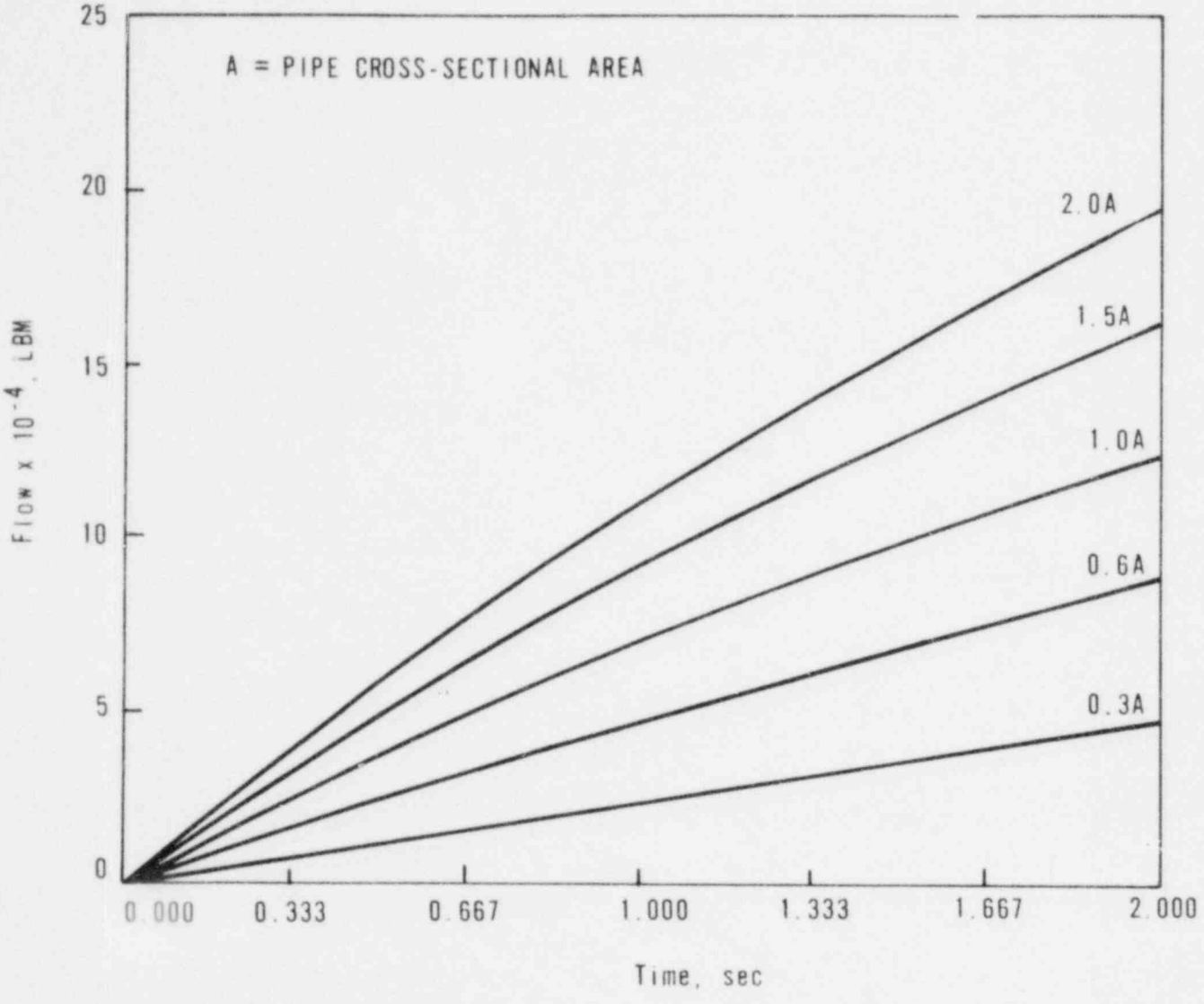

Figure 4.3-57. Integrated Leak Energy Flow for Guillotine Break at Reactor Vessel Outlet — Skirt-Supported Plants

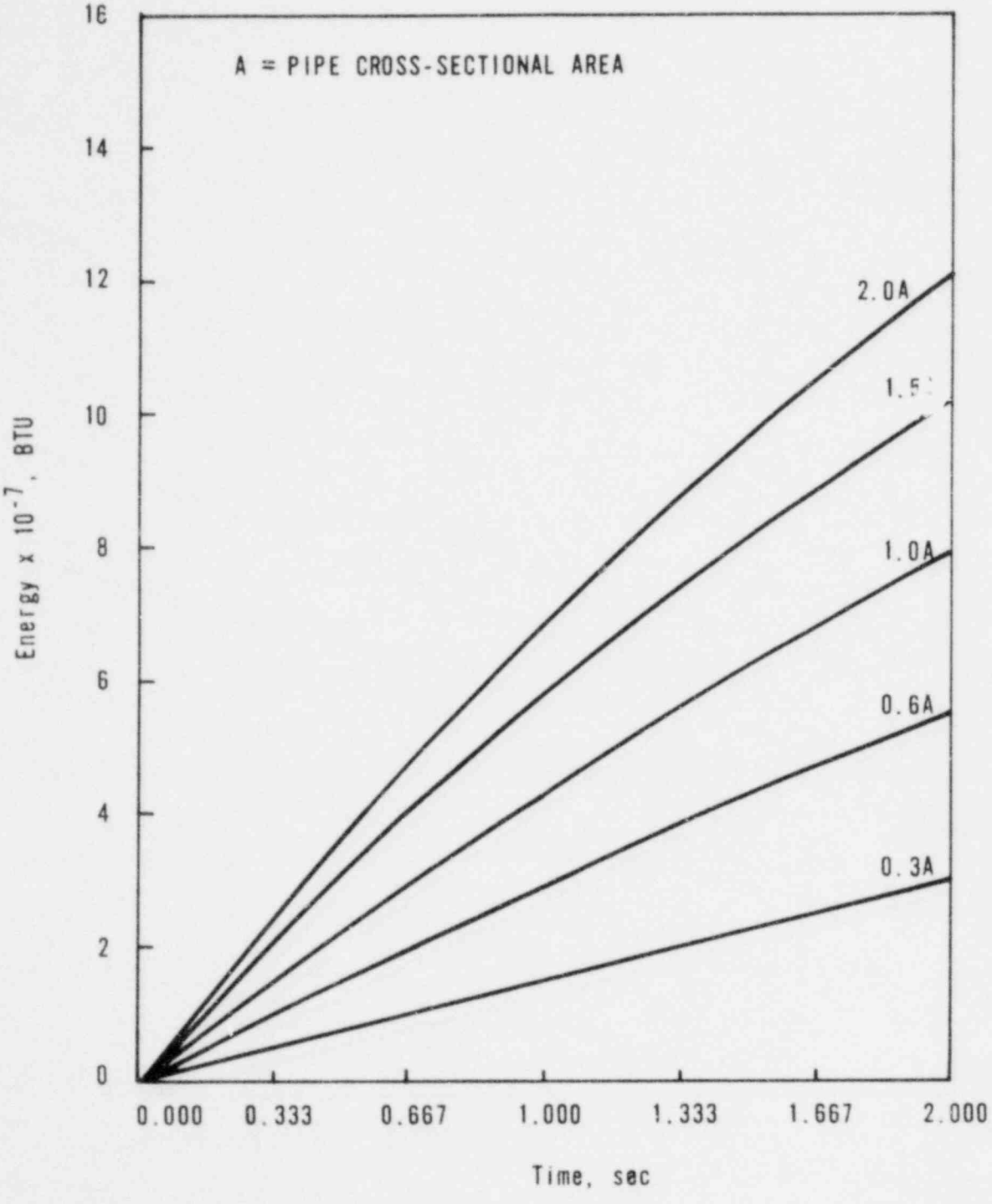

Figure 4.3-58. Integrated Leak Mass Flow for Guillotine Break at Reactor Vessel Inlet – Nozzle-Supported Plant

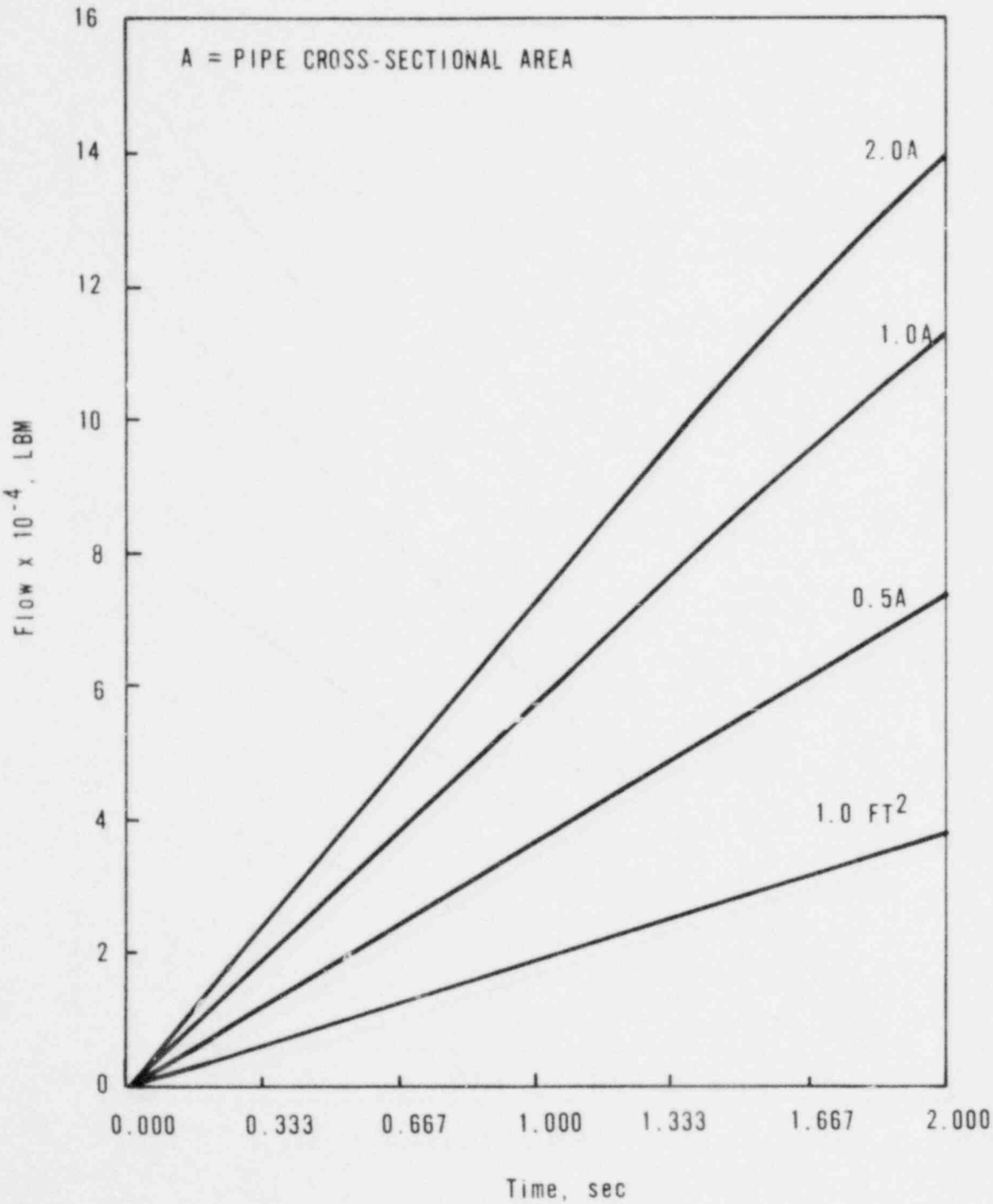

Figure 4.3-59. Integrated Leak Energy Flow for Guillotine Break at Reactor Vessel Inlet — Nozzle-Supported Plant

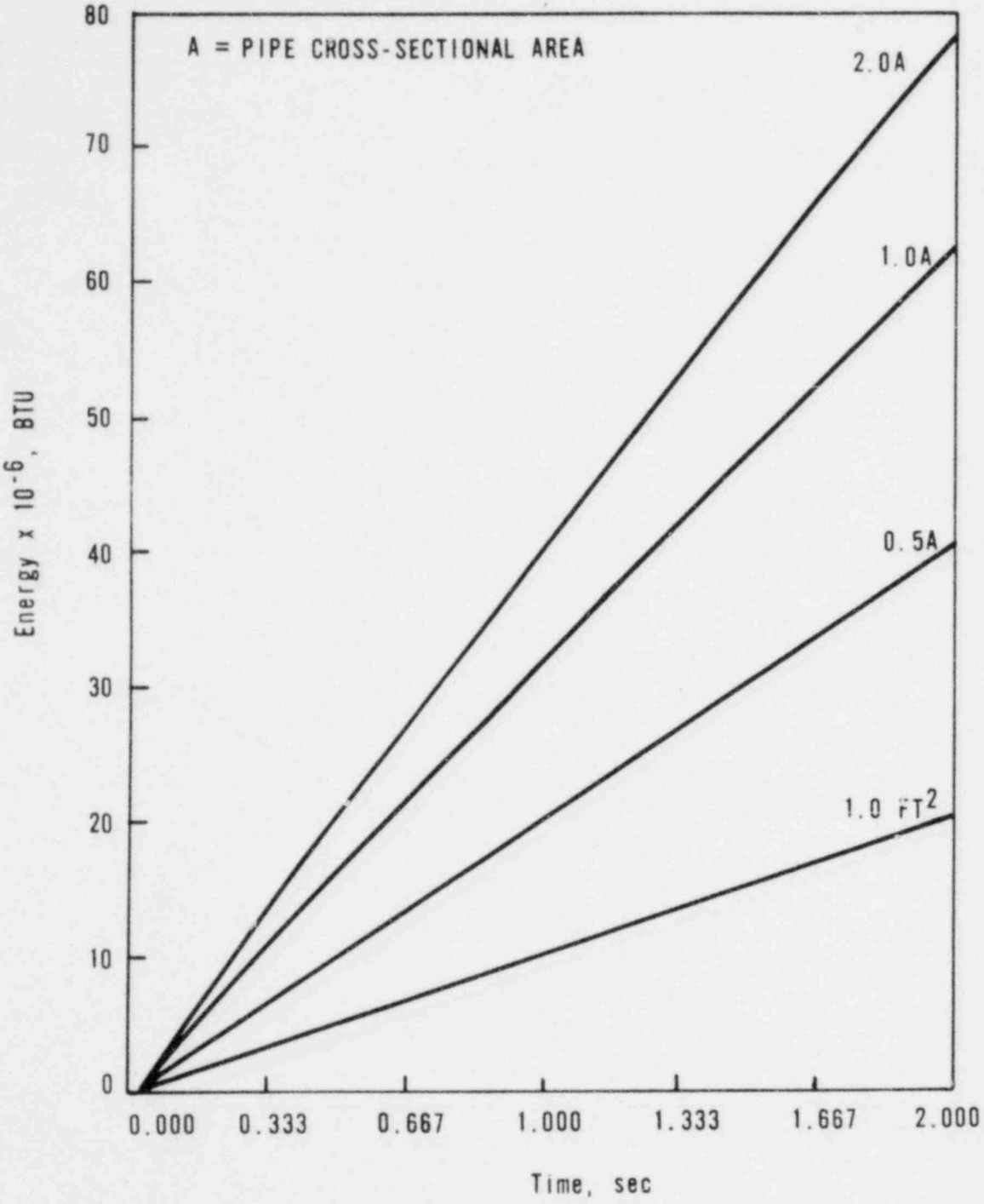

Figure 4.3-60. Integrated Leak Mass Flow for Guillotine Break at Reactor Vessel Outlet — Nozzle-Supported Plant

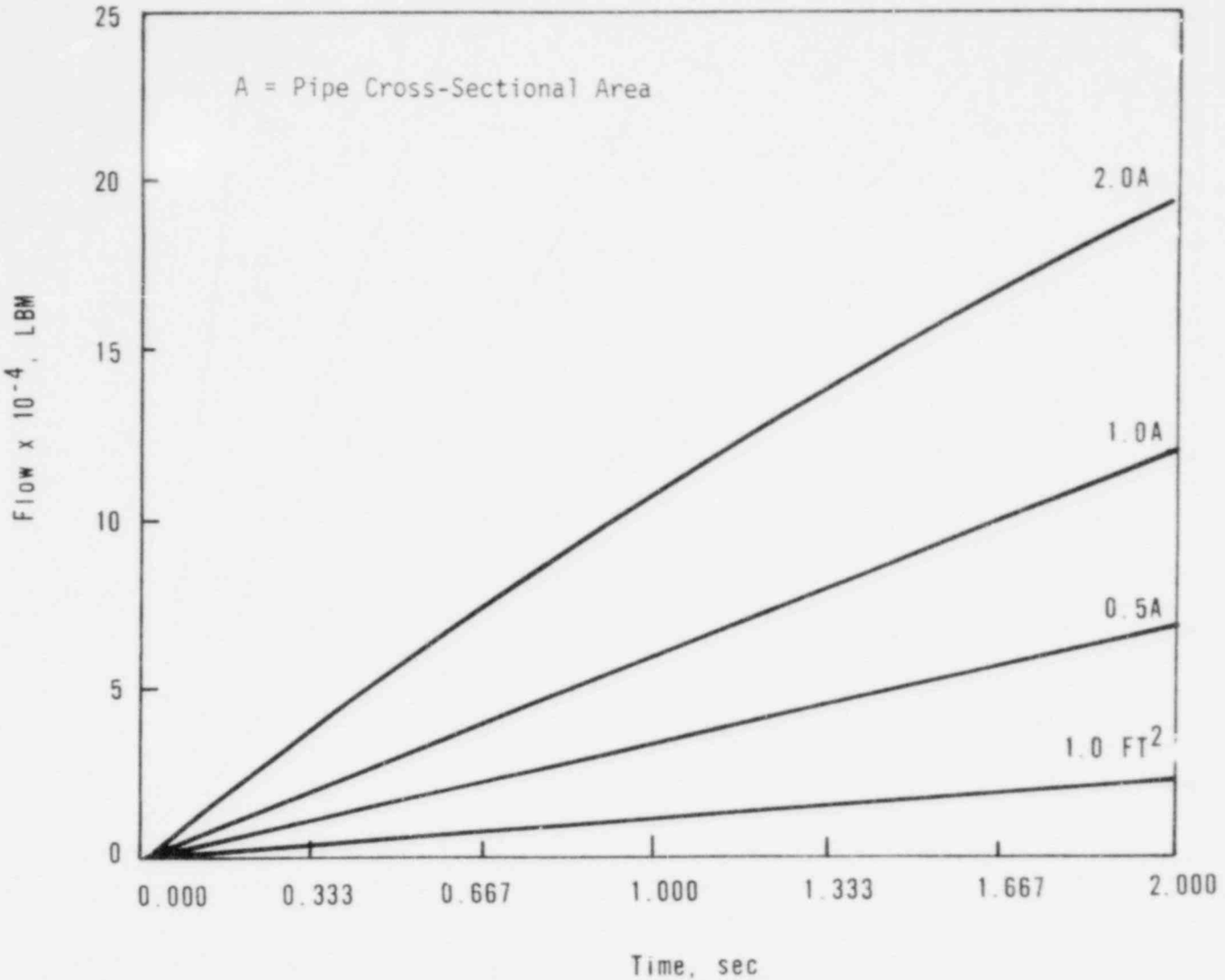

Figure 4.3-61. Integrated Leak Energy Flow for Guillotine Break at Reactor Vessel Outlet – Nozzle-Supported Plant

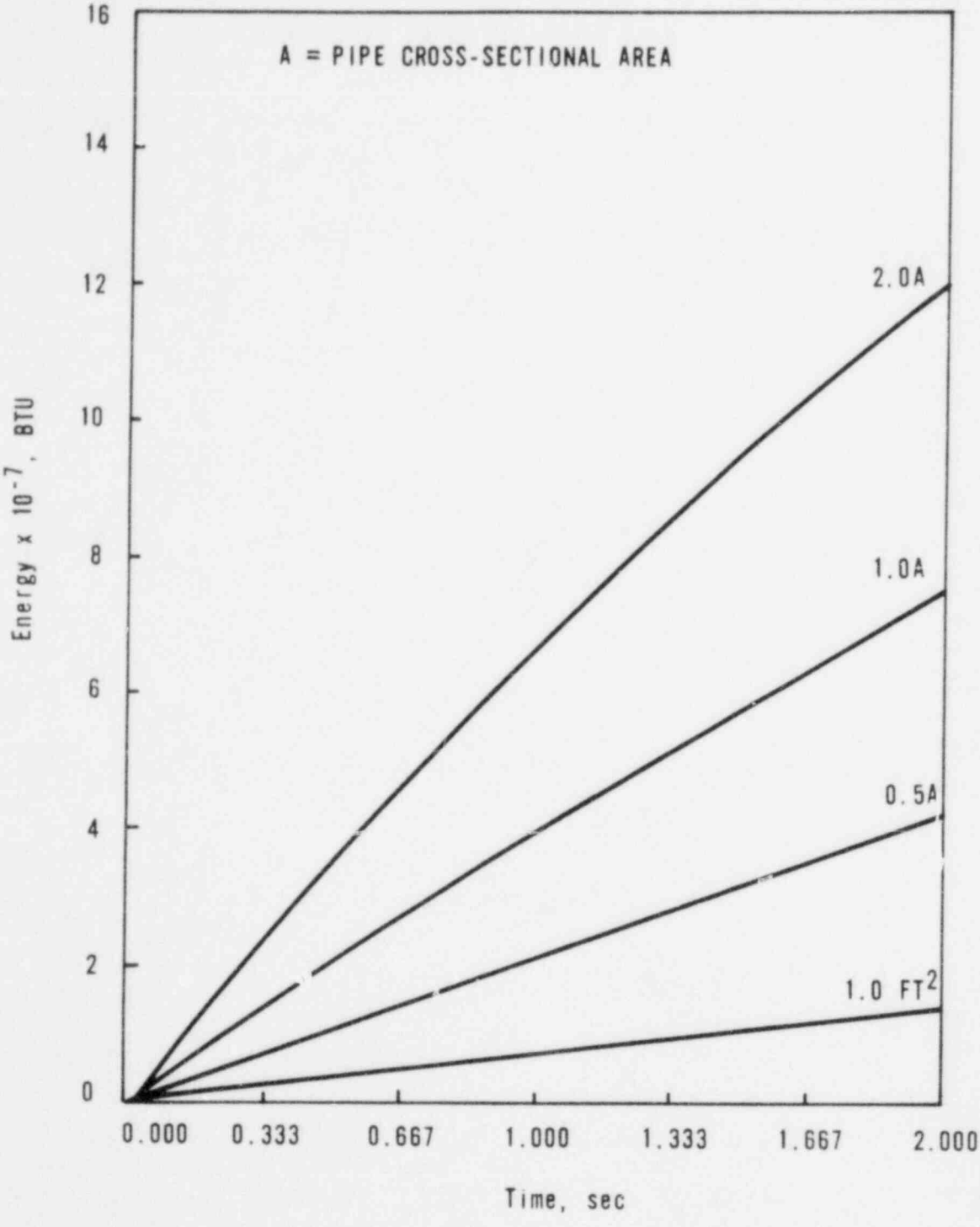

Figure 4.3-62. M&E Node/Flow Path Diagram — Skirt-Supported Plants

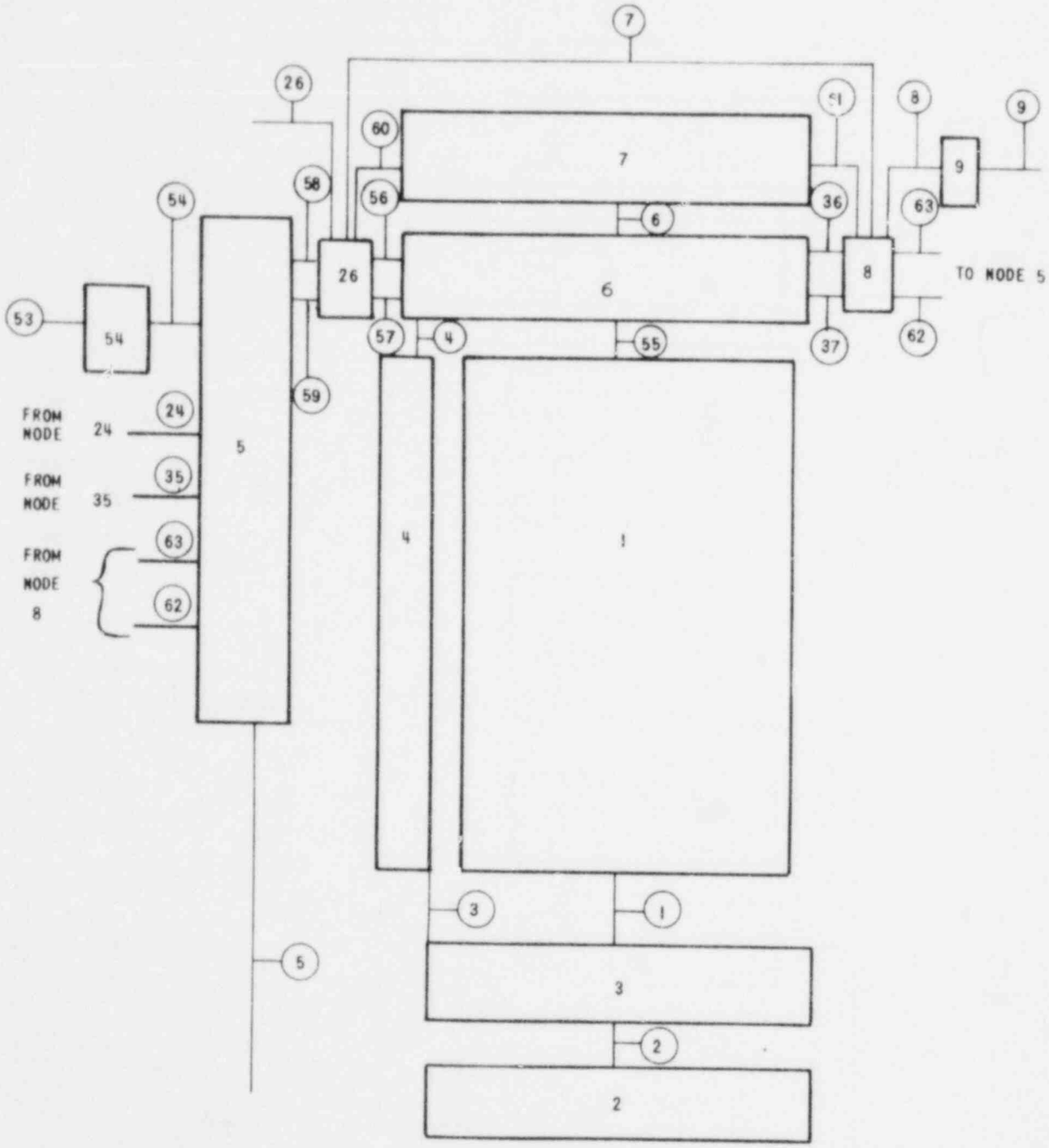

Figure 4.3-63. M&E Node/Flow Path Diagram — Skirt-Supported Plants

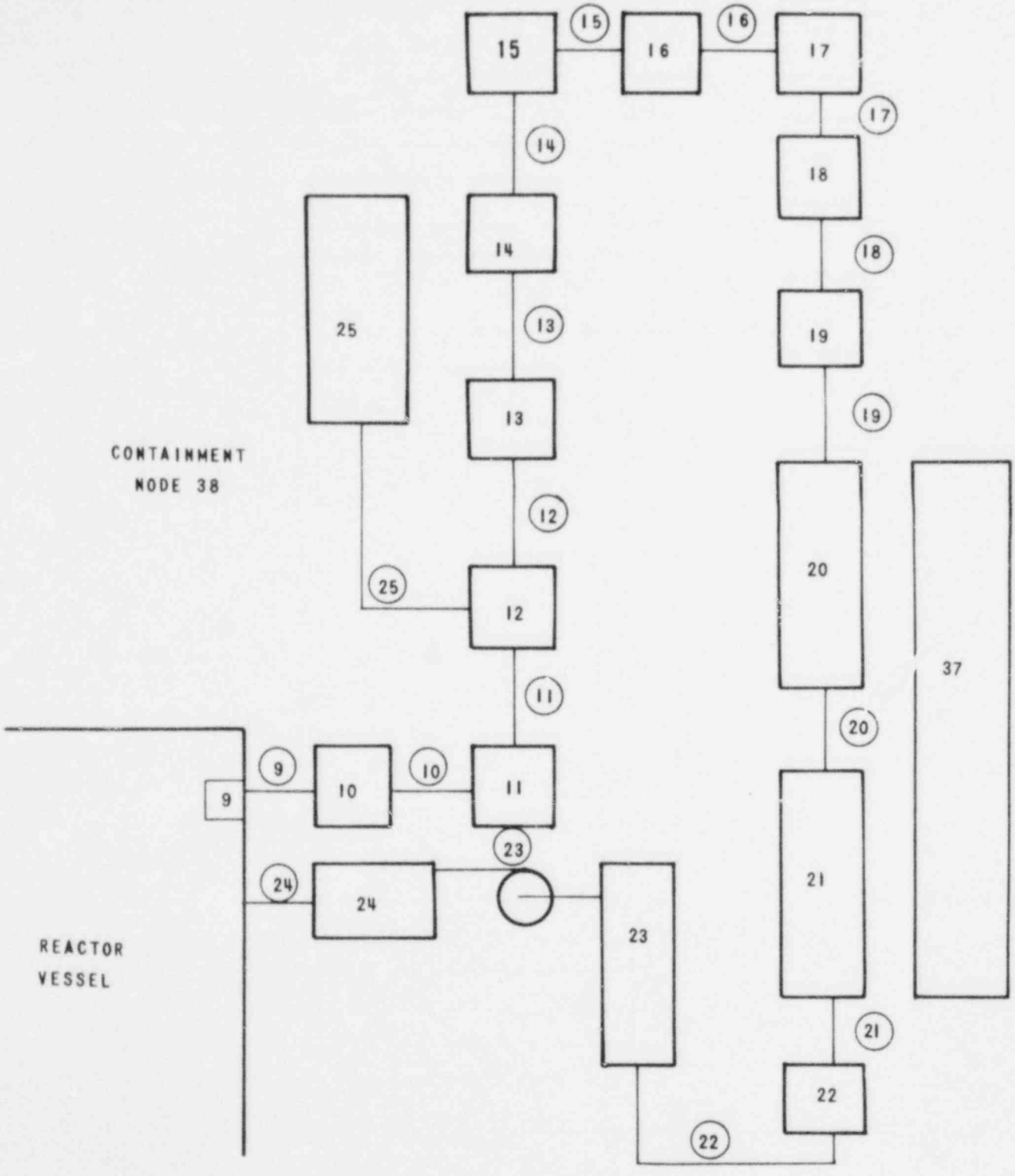

Figure 4.3-64. M&E Node/Flow Path Diagram — Skirt-Supported Plants

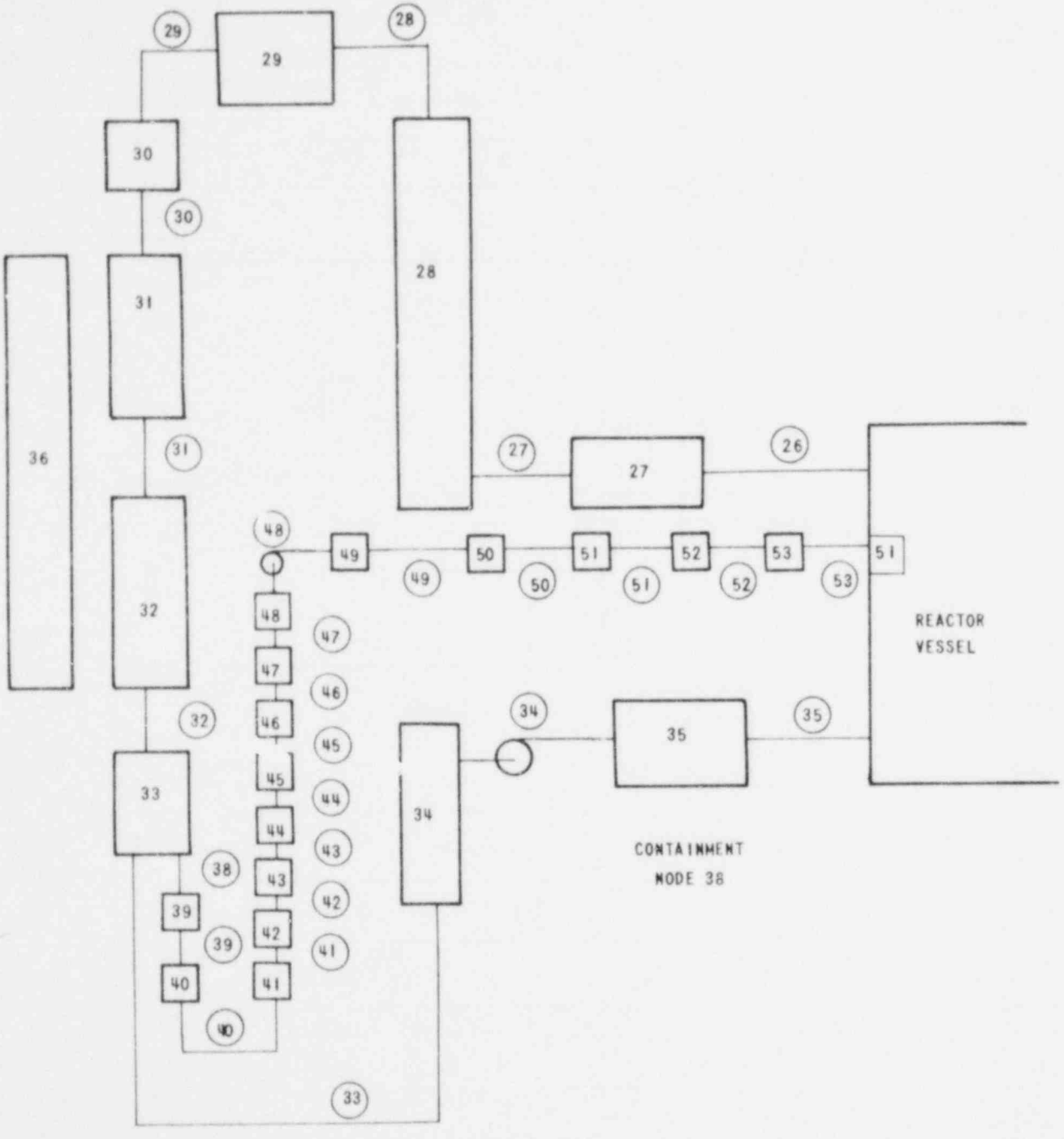

Figure 4.3-65. M&E Node/Flow Path Diagram — Nozzle-Supported Plants

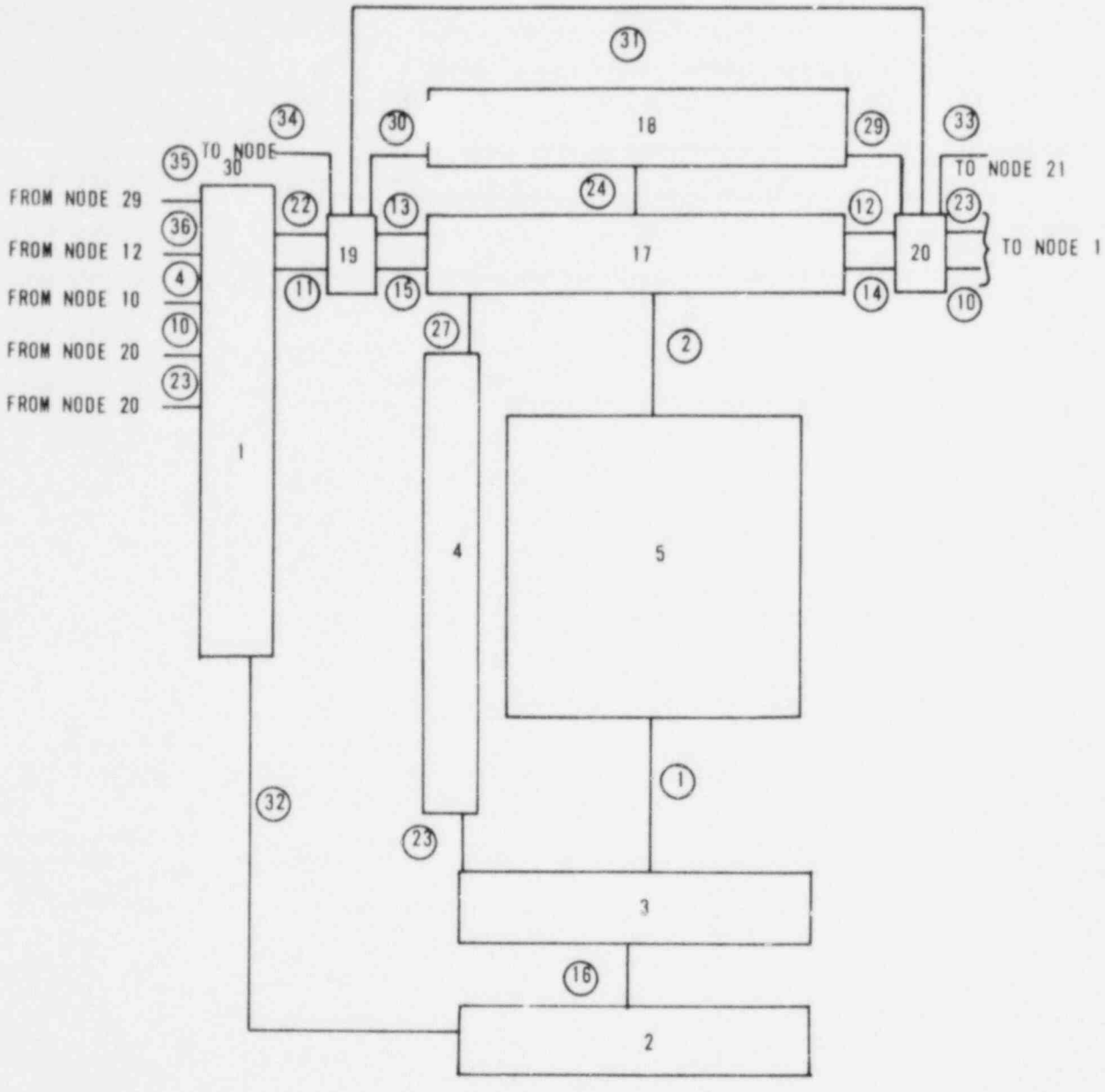

Figure 4.3-66. M&E Node/Flow Path Diagram — Nozzle-Supported Plant

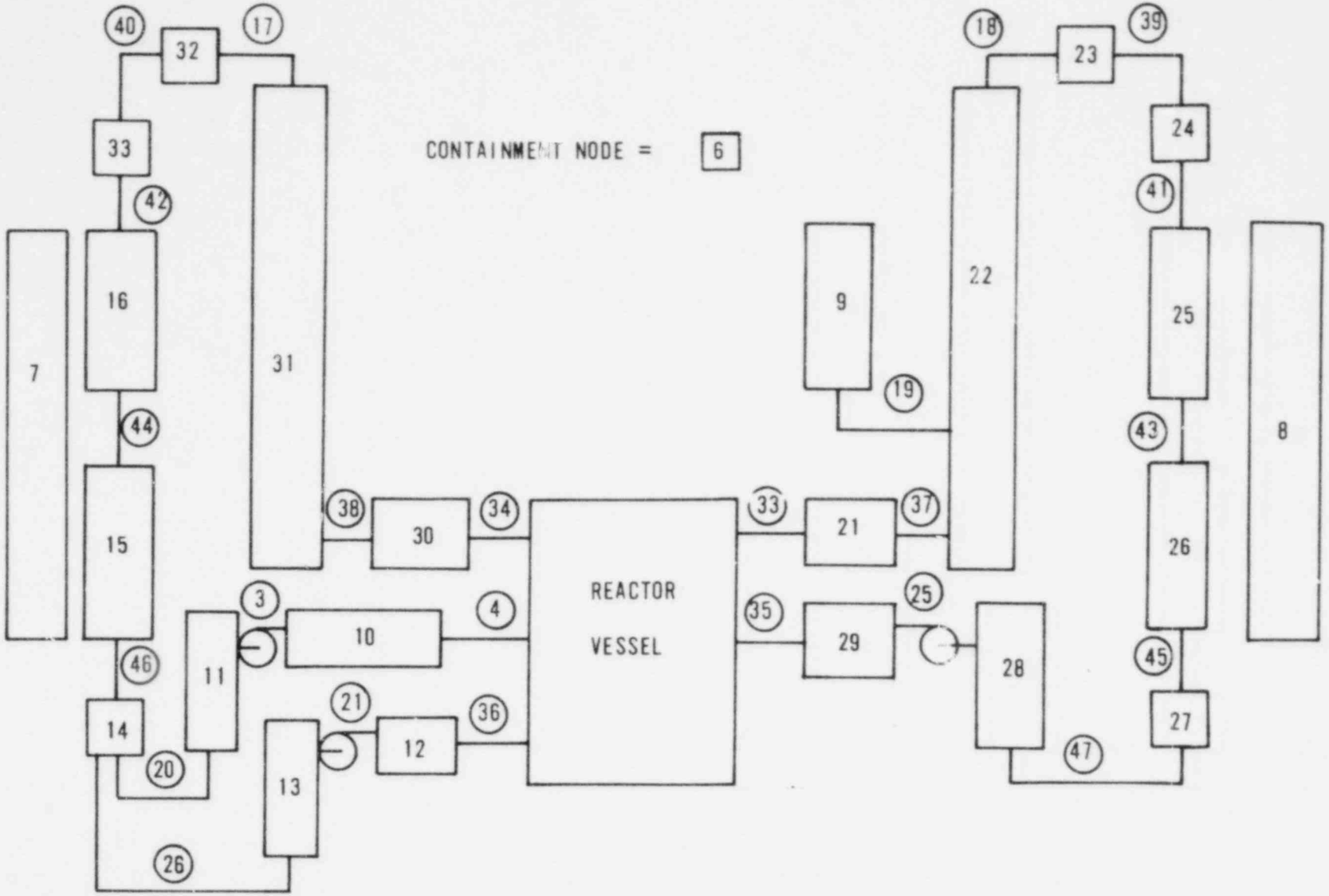

4.4. Reactor Internals Pressure Differentials

Transient differential pressure loadings on the reactor vessel internals were calculated for B&W's operating plants with the CRAFT2 computer code (version 13.0). Calculations were performed for a spectrum of guillotine break sizes — 2.0A, 1.5A, 1.0A, 0.6A, and 0.3A for the skirt-supported plants, while the nozzle-supported plant was analyzed for its actual break areas. Break locations were considered at the reactor vessel inlet and outlet as well as the next closest (to the reactor vessel) hot leg and cold leg break locations.

The CRAFT2 models were developed as per B&W topical report BAW-10132P-A, which includes a description of modeling methodology and a discussion of the applicability of the CRAFT2 computer code to LOCA differential pressure calculations.[5] As described in this report the Moody discharge model, with a C_D multiplier of 1.21, was used to simulate the break. For each of the postulated breaks, the generic BOA versus time data in section 4.2 were used.

The CRAFT2 computer models are presented in Appendix C, and the results of the analyses are given in section 8.2.

5. METHODOLOGY FOR DEVELOPMENT OF STRUCTURAL LOADINGS

This analysis focused on the components in and near the reactor vessel subcompartment with special emphasis on asymmetric LOCA loadings. The LOCA results reported in section 9 were obtained from four different types of structural dynamic analysis. The first consisted of a reactor vessel isolated model — described in Appendix D — which used linear elastic finite element methods. This model was used for the majority of the loading analyses required in the Phase II effort. The nonlinearity associated with vertical core motion (termed core bounce) is presented in a nonlinear substructured model, also discussed in Appendix D. The third source of loadings was the nonlinear pipe whip restraint models presented in Appendix G. The remaining source was the half-loop type of model described in Appendix F. The half-loop model was used to estimate effects of the asymmetric loadings in the steam generator compartment using linear elastic techniques.

This section discusses the approach taken in developing plant-specific loading data with the reactor vessel isolated model, the response of individual components, and the pipe whip restraint loading calculations. A discussion of the development of loads on the half-loop model with the steam generator subcompartment is presented in section 11.

The analytical data obtained from analyses in the form of break opening areas (BOAs), cavity pressures, and reactor internals pressures are presented in sections 4.2 and 8. This data base represents the loadings that were applied to the structural models described in this section. The calculational methods used in determining asymmetric cavity pressure were evaluated by the NRC. As a result of this review, the vertical cavity forces were modified for the input to the system dynamic response as requir d by reference 12. The vertically applied forces were obtained as describe n section 1 of Appendix B and multiplied by 1.10, thus defining a vertical uplift load representing an additional 10% as a function of time.

5.1. Reactor Vessel Isolated Model Linear Analysis

Initially, it is assumed that the loads to which the reactor vessel (RV) is subjected will not produce component yielding. Therefore, model construction and subsequent analyses are geared to linear analytical techniques. No consideration is given to nonlinear material properties or such geometric nonlinearities as gaps. The validity of this assumption is verified by comparing the linearly derived dynamic stresses to yield stresses when the analysis is complete.

Because of the complexity of the RV loading conditions and the number of attachments to the vessel, a detailed isolated model of this component is constructed. This model is a complete representation of the reactor vessel and its appurtenances (e.g., CRDMs and SSS). It also includes the hot legs extending to the steam generators and the cold legs extending to the pumps for loops A and B. Boundary conditions are imposed at the ends of the pipes where they connect to the components. These boundary conditions consist of stiffness matrices that represent the characteristics of the structures to which the pipes are attached. They are obtained from the system model by disconnecting the pipes at the component nozzles and computing a stiffness matrix of the remaining component with its supporting structures and other attached piping. A typical isolated model is shown in Figures D-5 through D-10. The model is so constructed that a few minor changes in element connections, joint coordinates, section properties, and external boundary conditions enable the model to accurately represent either a nozzle- or skirt-supported vessel.

The various components that make up the total RV and its internals are identified in Figure D-1, which depicts a skirt-supported vessel; a nozzle-supported vessel is shown in Figure D-4.

By comparing Figure D-6 with the lumped-mass model shown in Figure D-7, a correlation can be seen between the components and the model elements representing them. The model-component correlation is addressed in more detail in Appendix D.

The Phase II analysis has focused on the components in and near the RV subcompartment with special emphasis on asymmetric LOCA loadings. These loadings comprise integrated differential pressures existing inside the RV and integrated differential pressures in the primary reactor cavity and acting on the exterior

RV surface. The internal pressures act both horizontally and vertically over the RV internal components. The latter vertical pressure differential is the only nonlinear requisite other than the pipe whip analyses discussed in section 5.2. Since the fuel assemblies are spring-mounted between the upper and lower grids, the vertical response of the FAs results in a time-varying force due to the structural representation and differential pressure. Therefore, a nonlinear situation exists — it is referred to as core bounce. The nonlinear core bounce analysis is presented in more detail in Appendix D.

5.1.1. Reactor Vessel Supports

As mentioned previously, there are two different designs for supporting the 177-fuel assembly reactor vessels. One is a nozzle-supported scheme, and the other employs a cylindrical shell called a skirt that fits underneath the vessel. The skirt is modeled with beam elements as shown in Figure D-5. The section properties of the representative beam elements are derived from the ANSYS model of the skirt presented in Appendix E. Actually, force/deflection and moment/rotation relationships are derived from the ANSYS model. From these, stiffness equivalent beam cross sections are computed (e.g., area and moments of inertia).

The reactor vessel supports for the DB-1 plant comprise concrete and steel structures beneath the four cold leg inlet nozzle pads and steel (LOCA) rings surrounding each of six primary coolant pipes and embedded in the reactor vessel shield wall. The pads are rectangular reinforcements on the underside of the nozzles. There is a gap of approximately 0.125 inch between the pipe OD and the ID of the LOCA rings. For seismic events, the reactor vessel pads provide support for the RV. For a LOCA, the reactor vessel pads are considered to be broken, and the RV is supported by the LOCA rings. The LOCA rings are modeled as a linear support system using spring rates from finite element models of the rings and concrete (see Appendix K).

Loads are determined on the support for each of the break locations defined in section 4.1. Refer to Appendix D for modeling details.

5.1.2. Reactor Vessel Support Embedments

The skirt support is equipped with flanges, as shown in Figure K-2, which are bolted to anchors embedded in the underlying concrete basemat. Anchor bolts extending through the flange on both sides of the skirt are fixed to anchor

plates deep within the concrete but are otherwise debonded from the surrounding concrete medium. This embedment system is illustrated in Figures K-1 and K-2 (Appendix K).

Three finite element models were developed to determine the reaction of the embedments to LOCA loading. These models, described in Appendix K, include the following:

1. A generic embedment model – a detailed, three-dimensional model of the skirt/pedestal interface and the pedestal concrete.
2. An axisymmetric model – includes the cavity wall and basemat and is used for sensitivity studies.
3. A nonlinear embedment model – developed from the generic embedment model, accounts for inelastic behavior of the pedestal concrete.

Using the first two models, the stiffness of each plant's skirt embedment system was determined and incorporated into the RV isolated structural model. The calculation of these stiffnesses was based on the assumption that the concrete remained elastic (described in detail in Appendix K).

The loads on the RV support embedments are the same as those on the RV supports with one exception. On Davis-Besse 1, although no credit is taken for the RV pad support during LOCA, LOCA loads are given on the concrete beneath the pads, which are equivalent to the maximum load that could be transmitted before the pad supports break. This is in addition to the load on the LOCA ring embedments, which carry the entire RV LOCA load produced analytically. In this manner, the LOCA load on the shield wall and concrete embedments is maximized without using nonlinear analysis.

5.1.3. Control Rod Drive Service Structure

The control rod drive service structure, often called the service support structure or SSS, is located atop the reactor vessel as illustrated in Figure 9.3-1. The primary function of this structure, as its name implies, is to provide lateral support for the control rod drive mechanisms (CRDMs). The SSS is modeled with elastic beam elements, and its mass is distributed at various joints along its length as shown in Figure D-5. Another function of the SSS is to support the service platform located at its top. This platform provides access to the CRDMs and vertical support for the electrical cables attached to them.

Consequently, the mass of the service platform and the apportionate mass of the cables supported by it are lumped into the mass joint located on top of the SSS model (see Figure D-5).

5.1.4. Control Rode Drive Mechanisms

In modeling the CRDMs, each drive is considered a long tube whose lower end is joined to a flange on the RV closure head. The upper ends are supported laterally by a framework of beams and plates which resembles a template. This framework is in turn attached to the SSS described above.

Not all CRDMs are modeled individually. Composite elements are included in the mathematical model, as shown in Figure D-5, which will produce the gross dynamic behavior of all units. The masses and stiffnesses of all CRDMs are appropriately lumped together to produce the representative elements, and like the SSS, the CRDMs masses are appropriately distributed to the mass joints along the length of the composite elements.

5.1.5. Core Support Assembly

The core support cylinder is suspended from the RV flange as shown in Figure D-1; attached to it are other structures that make up the core support assembly. The main assembly includes the flow distributor, upper and lower grids, and a thermal shield. In addition to supporting the fuel elements, the assembly also directs the flow of water downward as it enters the reactor vessel and up past the fuel elements.

The cylindrical elements found in the core support assembly (e.g., plenum and core support cylinder) are incorporated into the linear elastic isolated model as beam elements. However, their stiffness properties are developed from more sophisticated shell models. From the shell model's force-deflection and moment-rotation relationships, equivalent cross-sectional areas and moments of inertia can be determined. It is important to note that the independent shell models reflect the presence of the various cutouts or holes found in the actual cylindrical structures. The equivalent beam elements of the plenum cylinder, thermal shield, and core support cylinder (or core barrel) can be seen in Figure D-5.

5.1.6. Fuel Assemblies

The fuel assembly response to the LOCA loading on the reactor vessel was analyzed using time history techniques. Horizontal response was determined with a

core model consisting of fuel assemblies in a planar array with gaps between inner and outer FAs and the core baffle plates. The upper and lower grid plate motions obtained from the reactor vessel isolated model linear analysis described in Appendix D were applied to the core model simultaneously, and the FA responses (displacements, moments, and impact forces) were obtained. The core model used to analyze the fuel assembly horizontal response is described in Appendix J, and the FA vertical response was obtained from the core bounce model described in Appendix D. Force-time histories resulting from the LOCA pressure wave were applied to the core bounde model. The resultant output of the analysis provided the maximum force generated in the various fuel assembly components.

5.1.7. Reactor Coolant Piping

Reactor coolant piping is included in the models of both the nozzle- and skirt-supported plants. However, the entire primary piping system is not required. It has been determined through various model development studies that the segments of cold leg piping from the reactor vessel to the pumps and the segments of hot leg piping from the vessel to the steam generators (with the appropriate boundary conditions) are sufficient to accurately predict the static and dynamic behavior of the reactor vessel and its appurtenances, including the modeled piping. The boundary conditions consist of a 6 by 6 stiffness matrix applied at the end of each pipe where it attaches to a pump or steam generator. All four cold legs and both hot legs are included. Further modeling details are presented in Appendix D, and examples of the piping discussed here are illustrated in Figures D-6 through D-8.

5.1.8. Core Flood Line Piping

Since the mass and stiffness of the core flood lines are small compared to the mass and stiffness of the reactor vessel itself, the core flood lines are not included in the reactor vessel model. Instead, time history motions are calculated in the analysis of the reactor vessel, which are subsequently utilized in a separate analysis of the core flood lines. A description of core flood line model is given in Appendix H. The time history motions are calculated at the centerline of the vessel at the elevation of the core flood nozzles, and must be modified in two ways prior to application in the core flood line analysis.

First, since the motions are calculated at the centerline of the vessel, a geometric transformation based on the radius of the vessel must be performed to determine corresponding motions at the core flood nozzle locations at the periphery of the vessel. Second, while vessel motions are calculated only for a sufficient time interval to ensure maximum response of the vessel (0.3-0.5 seconds), and maximum core flood piping response could occur at a later time, the calculated time histories must be extended in time prior to application in the core flood piping analysis. The time histories have been projected to a total duration of 0.9 seconds, based on the dominant frequency of the reactor vessel response and an assumed 7% damping for skirt support plants and 4% damping for the nozzle supported plant. Finally, core flood nozzle response spectra have been developed based on the resultant time histories. The resultant core flood nozzle time histories and response spectra are given in section 9.9.

5.1.9. Reactor Vessel Components

Because of the very large stiffness of the reactor vessel, the cylindrical section readily lends itself to representation by a stiff beam. Since the cylindrical portion is not uniform along its length, several elements are required to represent it. Each element simply requires the outside radius and the material thickness to describe its cross section. From this information total areas, shear areas, and moments of inertia can be determined.

More consideration, however, is given to the hemispherical sections of the vessel from which the upper and lower heads are constructed. They are in fact domes, which are treated in a special way in order to obtain the stiffness values for an equivalent beam. The technique is discussed in Appendix D.

All interface points between the reactor vessel and its appendages are considered a part of the RV component. As such, loadings from the attached piping, the CRDMs, and the service support structure are considered in determining the total load acting on the reactor vessel. The RV appendages are included in the linear isolated model with the exception of the core flood line, which is modeled as an isolated component on a plant-unique basis.

5.2. Nonlinear Pipe Whip Analysis

The nonlinear pipe whip analyses determines both plant-specific and generic BOA time history curves and plant-specific restraint time history loadings. Restraint loading time history was used to qualify the restraints for LOCA. BOA was used in determining internal and external pressures acting on the RV and its appendages.

The analytical method and the modeling techniques are described on the following pages. For a more detailed description of the individual pipe whip restraint models, see Appendix B.

5.2.1. Pipe Whip Model Analysis

The ANSYS computer code[9] has been used for the detailed nonlinear time history analysis using the plant-unique pipe whip analytical models described in Appendix B. ANSYS was selected because of its nonlinear capabilities, which allow for the introduction of nonlinear stress-strain relationships and gapped elements that are applicable to the BOA calculation. The governing equations are numerically integrated at each time point, which allows the governing parameters (mass, damping, and stiffness) to vary with time in any desired fashion.

At time zero, initial conditions are imposed on the piping model. These conditions reflect the level of stress maintained in the piping system due to the operating conditions of deadweight and thermal and steady-state fluid hydraulics. At time 0^+ the pipe being studied is instantaneously broken, and the ANSYS code then tracks the governing parameters in a time-incrementing fashion to determine when nonlinear conditions exist. When such conditions are detected, the mass, damping, and stiffness matrices are recalculated. These conditions will exist when gapped elements close, yield forces are exceeded, or material behaviors change.

The analytical calculations are governed by the small deflection theory. Because of the incremental nature of the computations, the displacements and member forces or moments calculated for a given time increment may exceed allowable values. If an overshoot condition occurs, an iterative process based on reducing calculation increments maintains the amount of overshoot within specified bounds.

The analysis tracks stresses in the piping starting with the initial operating stress level. The existence of plastic conditions is checked in each member at

each increment of time. When a plastic condition is reached, the plastic behavior that follows is accounted for by reducing the value of the modulus of elasticity. The transition from a plastic to an elastic condition is accomplished by reassigning to the member the original modulus of elasticity.

5.2.2. Details of Special Elements

ANSYS provides several elements with nonlinear input capabilities. The pipe whip restraint analysis incorporates three-dimensional plastic straight and curved pipe elements for the reactor coolant system piping. These plastic pipe elements are used in the piping loops where the LOCAs are postulated; three-dimensional elastic elements were used in the components and piping away from the breaks. The plastic pipe element requires that nonlinear stress-strain properties be input. The pipe whip restraints and snubbers use a combination element (a spring and damper) in series with a gapped element. The element requires that a spring rate, damping value, and gap size be input in addition to a force value that specifies when the spring element becomes a slider element. This force is analogous to the yield force of a particular structure. Other supports and restraints use three-dimensional beam elements with plastic capabilities. The steam generator is represented by a three-dimensional elastic pipe element, while the pump is represented by a three-dimensional elastic beam element. The elements described above are explained in more detail in the ANSYS User's Manual.[9]

5.2.2.1. Boundary Conditions

For the pipe break cases analyzed by the isolated model technique, the steady-state displacements of the reactor vessel centerline and the OTSG base are input as boundary conditions at those points. This is done because the RV centerline and the OTSG base act as fixed points in the analysis. This fact allows the isolated model technique to produce accurate results when modeling only a portion of the total primary piping system.

5.2.2.2. Equivalent Spring Rates of Gapped Restraints

Finite element models of each restraint and its embedments were used to generate equivalent spring rates to the restraints. The equivalent spring rate is a combination of the individual spring rates of each portion of the restraining structure. The restraint spring rate considers the restraint design, anchor

bolts, and all base plates and embedments. Restraint models used to determine spring rates are described in detail in Appendix G.

5.2.2.3. Gap Requirements

The sizes of the gaps input to the mathematical model are based on the specific cold gap of the restraint and the displacement of the pipe at the support elevation under steady-state operating conditions. The specified cold gap of the restraint refers to the space between the pipe OD and the restraint with the system at ambient conditions.

5.2.2.4. Elastic Material Properties

For each material used in the model, the values of Young's modulus (E), the coefficient of thermal expansion (α), Poisson's ratio (μ), and the density (ρ) are input. The input density for a particular element includes the density of the metal, water, and insulation. These properties are evaluated at the operating temperature of the component.

5.2.2.5. Nonlinear Material Properties

Data points on the stress-strain curves of the appropriate materials are input so that the ANSYS program can compute Young's modulus at the time the dynamics begin.

5.2.2.6. Structural Definition of Break

To represent the guillotine break point analytically, two model joints are located at the break point. This is necessary in order to represent the resultant separation of the two pipe sections adjoining the break point. To analytically represent the actual guillotine break, the "capped" pipe section or bar representation capabilities of ANSYS are utilized. An initial mechanical loading of P*A is applied to each capped pipe section at the break point to reflect the pressure release. Also at the break point, displacements are imposed at time zero to account for the internal structural reaction due to pressure expansion, thermal expansion, and deadweight effects. The imposed displacements bring the two joints that represent the break together at t=0; this brings the state of stress to the operational level. At time 0 the displacements are released, simulating a double-ended rupture. The release of this displacement models the mechanical release forces in the pipe.

Thus, the guillotine break action is represented analytically by imposed displacements and forces at the break point. This method permits each of the pipe sections at the break to respond to the mechanical release force and internal pressures.

5.2.2.7. Operating Condition Loads

A steady-state operating condition analysis is performed using a full-loop model. This analysis produces the system behavior due to deadweight, thermal loading, and pressure distribution. The system has a characteristic set of displacement and level of piping stress due to these operating conditions. The initial state of stress in the system piping is incorporated into the isolated model by incorporating the full-loop analysis displacements at time 0.

5.2.2.8. Thermal and Dead Weight Load Distribution

The temperatures and masses of the piping and components are accounted for in the ANSYS nonlinear analysis. These temperatures and masses correspond to those used in the linear analysis of the RC loop. By this method, the thermal expansion and deadweight motions of the system are incorporated in the analytical results.

5.2.2.9. Applied Forcing Function After Break

Forcing functions were applied in either of two ways: the more conservative method assumes a zero BOA, yielding a constant PA forcing function through time. The second method, which was used in some cases to reduce the conservative loads applied by the constant-BOA assumption, employs pipe reaction forces generated for a reduced-area break. The final BOA and the BOA used in generating reduced-area pipe reaction forces are monitored to ensure continuity. This process is described by a flow chart in Figure 5.2-1.

Figure 5.2-1. Pipe Reaction Force

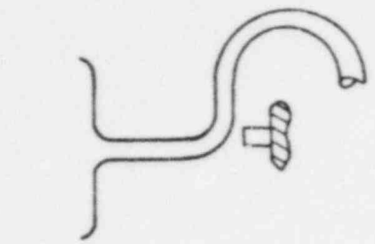

INITIAL CONDITIONS

- PIPE INTACT
- PLANT AT STEADY-STATE FLOW, TEMPERATURE, AND PRESSURE

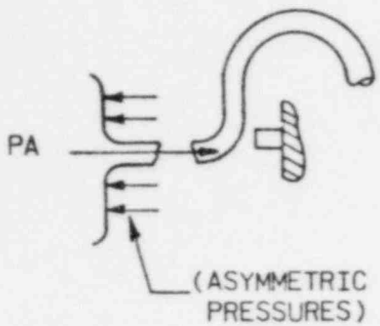

INITIAL BREAK

- TRANSIENT EVENT STARTS FROM STEADY-STATE INITIAL CONDITIONS ABOVE
- INSTANTANEOUS PIPE SEVERANCE
- ZERO OPENING AREA ASSUMED, WHICH GIVES CONSTANT PA PIPE REACTION FORCES, I.E.,

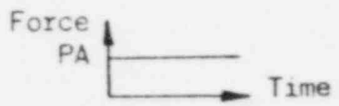

- PIPE TIME-HISTORY DISPLACEMENTS AND AREA DETERMINED
- PIPE REACTION FORCES CALCULATED USING DETERMINED AREA CRAFT CODE

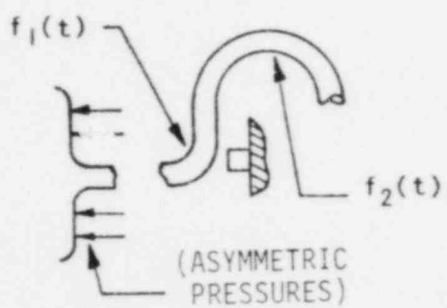

ITERATION PHASE

- INSTANTANEOUS PIPE SEVERANCE FROM STEADY STATE CONDITION
- CALCULATED PIPE REACTION FORCES APPLIED
- NEW PIPE TIME HISTORY DISPLACEMENTS AND AREAS DETERMINED
- NEW PIPE REACTION FORCES DETERMINED
- PROCESS REPEATED UNTIL AREA CONVERGENCE IS REACHED

5.3. Reactor Vessel Cavity Wall Analysis

5.3.1. Introduction

For all plants, the primary structural loading on the cavity wall is that due to the internal pressurization. For the Davis-Besse plant, the reactor vessel supports also impose significant loads on the cavity wall.

This section describes the selection of the critical pipe break cases, the development of the pressure loading, the application of this pressure loading to the cavity wall models and the application of other load conditions on the cavity wall. Additional loads due to the reactor vessel support beams and LOCA rings for the Davis-Besse plant are discussed in Section 5.3.6.

5.3.2. Pipe Break Opening Area

The actual pipe break opening area for each plant was determined by a pipe whip analysis, as discussed in Section 5.2.1. The break opening areas were computed for a break at the reactor vessel nozzle, as this is the break location which causes internal pressurization of the cavity wall. These are summarized in Table 3.10-2.

5.3.3. Development of the Pressure Loading on Cavity Wall Models

Pressure-time histories for each plant were generated using CRAFT2 models (Section 4.3). For plants other than Davis-Besse, pressure time histories for break opening areas of 0.3A, 0.6A, 1.0A, 1.5A and 2.0A were developed for both hot and cold leg breaks. For Davis-Besse, pressure time histories were developed for the exact breaks of 1.0243A (hot leg) and 0.243A (cold leg).

As discussed in Section 6.10.2, a minimum of two pressure load sets were needed to evaluate cavity wall response by means of static analyses, for either a hot or cold leg break. Each pressure load set is comprised of as many individual pressure values as there are individual finite elements in the cavity wall models. The first load set corresponded to pressure at the time of peak asymmetric load on the cavity wall. The second corresponded to

pressure at the time of peak steady-state load on the cavity wall. A dynamic load factor of 1.15 was applied to the asymmetric load set. This dynamic load factor was determined from explicit dynamic analyses, as discussed in Section 6.10.4.5 and 6.10.4.6.

The asymmetric pressure load set corresponded to the time of the peak asymmetric load on the cavity wall. This was determined as follows: for each time step of the CRAFT2 pressure-time history, the pressure from each nodal "volume" was integrated over its respective cavity wall surface area. The resulting load vectors' components parallel to the line of thrust of the blowdown force were then summed to yield the net asymmetric load on the cavity wall. The variation of this asymmetric load with time for each cavity wall is shown in Figures 9.10-1 to 9.10-6.

The time of the peak steady-state pressure load set was determined by inspection of the time history values for all individual CRAFT2 pressure time histories. These times are given in Tables 9.10-1 and 9.10-2.

Except for the Davis-Besse plant, actual hot leg break sizes did not exactly match those for which CRAFT2 pressure sets were developed. Hence, it was necessary to interpolate between the CRAFT2 spectrum of break opening areas for which pressure time histories had been developed. To do so, the peak steady-state uniform internal pressure was determined for each of the break opening areas for which pressure time histories were developed. By linearly interpolating between break opening areas, the critical steady state uniform internal pressure was determined for each plant's true break opening area. The final steady-state pressures are given in Table 9.10-2. A similar interpolation procedure was used to determine the asymmetric pressure load set, with that interpolation being based upon the ratio of peak asymmetric blowdown loads.

To perform explicit dynamic analyses for the ANO-1 and Rancho Seco cavity walls, each individual finite element in the cavity wall models had the full pressure time history applied to it. To maintain accuracy between the CRAFT2 and EDS-SNAP time histories, a time step size of 0.001 seconds was utilized.

5.3.4. Application of the Pressure Loading

The differential pressure developed in the cavity due to the LOCA event was applied to the inner surfaces of the cavity wall and penetrations.

Since the nodalization schemes for the CRAFT2 subcompartment models and the EDS-SNAP finite element models were not identical, a mapping procedure was employed to apply the pressure loading from the CRAFT2 "volumes" onto the EDS-SNAP "surfaces". For those areas where the CRAFT2 and EDS-SNAP model surfaces did not correlate exactly, CRAFT2 volume pressure data were extended to match EDS-SNAP surfaces. Hence, equal or slightly greater loads were always applied to the EDS-SNAP models from the previously generated CRAFT2 data.

Where portions of several CRAFT2 volumes overlaid a single EDS-SNAP surface, weighted averages based on subareas of individual CRAFT2 volumes were used to determine the net average pressure over the entire EDS-SNAP surface. In applying the net average pressures onto the EDS-SNAP finite element surfaces, curved surfaces were accounted for by exactly considering the curved surface area and the normal directions of the surface.

For the Oconee linear and the TMI-1 nonlinear analyses, it was conservatively assumed that all the reactor shield plugs or other devices are blown out before the time of the peak asymmetric load. Therefore, the pressure on the cavity wall at the elevation below the reactor shield plugs was applied up to the top of the cavity wall exposed by the absence of the reactor shield plugs. No pressure loading was applied to fuel canal walls.

5.3.5. General Loading for all Plants

The postulated loss-of-coolant accident (LOCA) results in a number of loading conditions on the cavity wall:

1. A differential pressure load, P_a;
2. Thermal loads, $(T_o + T_a)$;
3. Pipe whip restraint reactions, $(R_o + R_a)$;
4. Dead Load, D.

The differential pressure load, P_a, results from the build-up of pressure within the cavity as a result of a pipe rupture. Two phases of this pressure loading can be identified: an asymmetric phase, during which high local pressures near the break location induce an asymmetrical load component on the cavity wall; and a steady-state phase, during which the cavity pressure is essentially uniform around the full vessel perimeter. The asymmetric load peaks at approximately 40 milliseconds, while the steady-state load develops after approximately 200 milliseconds. The individual volume pressure time history data is given in Section 8.1.

The thermal loading consists of two parts: T_o, the thermal load due to normal operating temperature gradients, and T_a, the thermal load due to the postulated loss-of-coolant accident. These are self-limiting loads which do not significantly affect the capacity of the cavity walls to resist the relatively high pressure loading. This has been further verified in experimental findings.[19] Thus, they were not explicitly considered for cavity wall qualification.

The pipe whip restraint reactions consist of two parts: R_o, the normal operating loads, and R_a, the pipe whip reactions. The former are zero, as gaps exist between the primary loop piping and the restraints. The latter, pipe whip reactions, do not cause significant global loading on the cavity wall, but can create local zones of high punching shear in the fuel canal floor slab. Evaluation of the pipe whip restraint embedments against failure due to punching shear, which is described in Secton 6.8, considered the influence of global cavity wall stresses on local shear strengths.

Dead-weight of the primary shield walls was included in the analyses. A concrete density of 150 pcf was assumed. Live loads are not significant, and were disregarded. This is conservative, as live loads exert compressive load on the cavity wall which, in general, increase the concrete's strength in bending and shear. In addition, dead weight exerted on the cavity wall by the fuel canal floor, walls, and related equipment and components was conservatively neglected.

5.3.6. Development of Davis-Besse Reactor Vessel Support Reactions on Cavity Wall

Two systems exist for resisting lateral and vertical reactions of the Davis-Besse reactor vessel subjected to LOCA loading. These are the support beams and the LOCA rings.

5.3.6.1. Davis-Besse Support Beam Loading

Under normal operating conditions, the support beams resist the vertical dead load of the reactor vessel. No horizontal loads are exerted on the support beams.

The reactor vessel reaction loads on the support beams due to the LOCA event were determined from the reactor vessel isolated linear model, as described in Section 5.1. These loads were used for analysis and qualification of the cavity wall, with the following load components being considered:

1. Peak asymmetric pressurization;
2. Reactor Vessel reactions due to LOCA and seismic;
3. Dead weight of reactor vessel.

5.3.6.2. Davis-Besse LOCA Ring Loading

Under normal operating conditions, the six LOCA rings (two on hot legs, four on cold legs) take no horizontal or vertical loads, due to the one-eighth inch gap between them and the primary piping.

The cavity wall was checked for the following simultaneous combination of LOCA ring loads, at time of peak asymmetric loading:

1. Peak horizontal loads on LOCA rings;
2. Vertical loads on LOCA rings acting with peak horizontal LOCA ring loads;
3. Peak loads on cavity wall due to asymmetric pressurization.

The cavity wall was also checked for the following simultaneous combination of LOCA ring loads, at the time of peak steady-state cavity pressurization:

1. Peak vertical loads on LOCA rings;
2. Horizontal loads on LOCA rings acting simultaneously with peak vertical LOCA ring loads;
3. Loads on cavity wall due to steady-state pressurization.

5.3.6.3. Davis-Besse Individual LOCA Ring Reactions

In evaluation of the cavity walls due to individual LOCA ring loading, the horizontal reaction R applied to the cavity wall by one LOCA ring was determined as follows:

$$R = (H^2 + F^2)^{1/2}$$

H = horizontal load applied to cavity wall by one LOCA ring

V = vertical load applied to cavity wall by one LOCA ring

$$F = (0.42)\ (H^2 + V^2)^{1/2} = \text{friction load}$$

Values for R and V are given in Section 9.10.2.2.

5.3.6.4. Davis-Besse Combined LOCA Ring Reactions

Due to either a hot or a cold leg break, all six LOCA rings are loaded. As a result of the geometry of the plant, each ring will typically have a different reaction. The total thrust of the six rings must be taken by the cavity wall system. For nozzle breaks, the total thrust is conservatively calculated by neglecting the LOCA ring on the broken pipe, as its reaction is opposite in direction to the remaining five.

The total thrust is calculated for each break at two time intervals: at asymmetric and at steady-state loading. The thrust is calculated by summing the peak individual reactions for each LOCA ring at the appropriate time step, multiplied by the appropriate direction angle. A summary of the net thrust loads is given in Table 9.10-3.

6. METHODOLOGY FOR STRUCTURAL EVALUATION OF COMPONENTS AND REACTOR BUILDING STRUCTURES

This section describes the methodology used to evaluate the structural integrity of the NSS components and supports and the reactor building structures for the Phase II LOCA loads described in sections 5 and 9. The methodology for the structural evaluations varies with the components, because of different structural characteristics and applied loads. In addition, many components possessed a high enough margin of safety that demonstrating their acceptability for the Phase II LOCA loads did not warrant a detailed stress analysis. For these cases only a brief description of the methodology is presented herein.

6.1. Reactor Vessel Supports

The reactor vessel supports were analyzed using the loads presented in section 9.1. Faulted condition seismic loads were combined with both the hot and cold leg guillotine LOCA loads by the square root of the sum of the squares technique defined in NUREG 0484. The evaluation was performed for both the nozzle- and skirt-supported vessels.

The evaluation of the nozzle-supported vessel (Davis-Besse 1) utilized the results of an existing stress analysis. A detailed plastic analysis considering design basis earthquake loads, thermal loads, dead weight, and LOCA loads had previously been performed for the DB-1 reactor vessel supports. It was concluded from this analysis that the supports were acceptable for ASME Code Section III criteria. The loads that were used in the existing analysis were compared with Phase II asymmetric loads, and it was determined that the Phase II loads were lower. It can therefore be concluded without further analysis that the supports are acceptable for the Phase II asymmetric loads.

The bending stress in the RV skirt was determined to be the critical stress in the skirt-supported vessels. The bending strength of a material in the plastic range can be established by using a ficticious bending stress called the bending modulus. This method assumes that the extreme fibers of a cross section in bending are stressed to the ultimate tensile strength of the material, resulting in a trapezoidal stress distribution. The bending modulus is determined from the stress distribution and combined with the section modulus to calculate the allowable moment. This procedure is outlined in Appendix A-9400 of reference 1.

Two locations on the supported skirt were analyzed, as shown in Figure 6.1-1. Location 1 was the support skirt location with twelve 9.5-inch-diameter holes and was the location having the least cross-sectional skirt area. Location 2 was the support flange, which was subjected to the bending stress caused by the bolts resisting the overturning moment.

The maximum allowable bending stress at location 1 was calculated using equation A-9413 in reference 1. As discussed in section 7.1.2.4 the ASME Code minimum values for ultimate and yield strengths were increased by 5 and 10%, respectively, for the bending stress calculation. The overturning moment that would

produce this stress was then calculated. This maximum allowable moment was compared to the applied loads to determine the acceptability of the skirt at location 1.

The maximum allowable bending stress at the flange location was calculated as above, again using the increased ultimate and yield strengths discussed in section 7.1.2.4. The bending stress distribution was determined by assuming that the bolt stress on the tensile side was the value necessary to place the flange bending stress at the maximum allowable value. The compressive stress was assumed to be 0.7 S_u, the maximum allowed by Table F-1322.2-1 of reference 1. The overturning moment that would produce this stress distribution was computed and compared with the applied loads.

Figure 6.1-1. Analysis Locations for Reactor Vessel Support Skirt

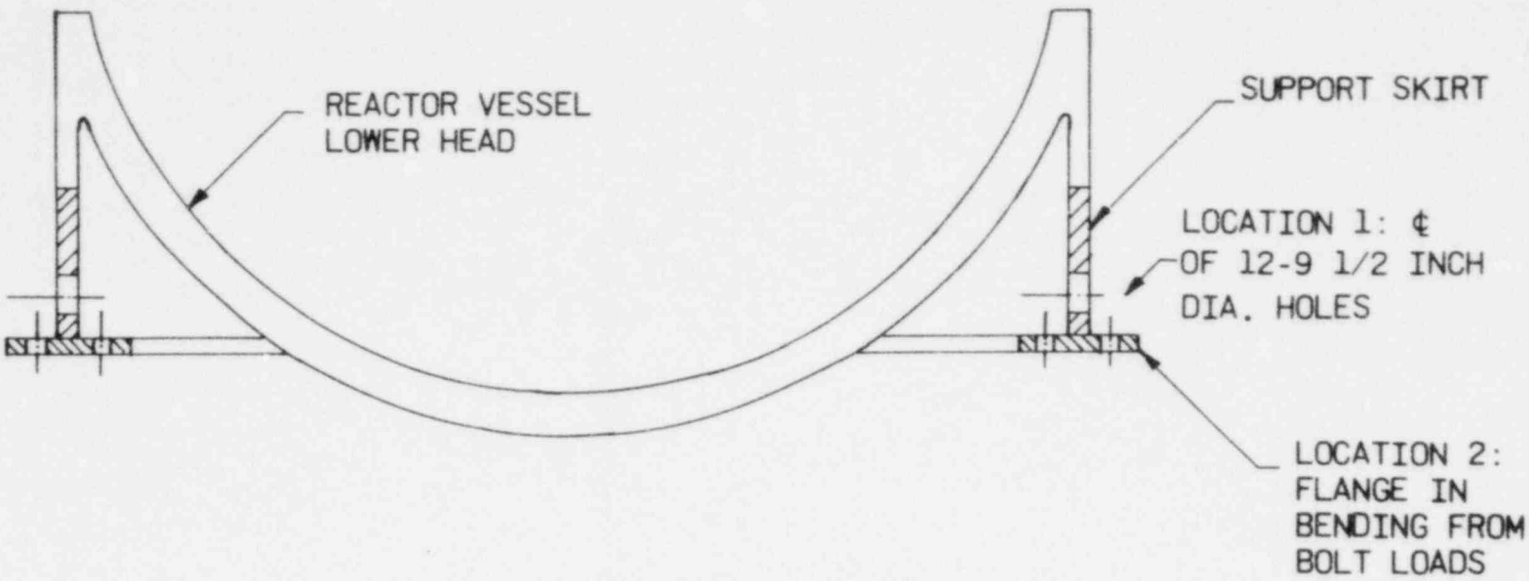

6.2. Reactor Vessel Support Embedments

6.2.1. Skirt-Supported Plants

6.2.1.1. Introduction

The skirt-supported plants - ANO-1, Oconee, Crystal River 3, Three Mile Island 1 and 2, and Rancho Seco - have very similar embedment configurations. In each plant, the reactor vessel is supported on a steel skirt, which is fixed to a concrete pedestal. The pedestal is a heavily reinforced, thick-walled, hollow cylinder, and forms an extension to the concrete basemat. The skirt is fixed to the embedment through a steel flange, which is bolted to the pedestal by 48 pairs of prestressed anchor bolts. These anchor bolts are fixed to anchor plates deep within the pedestal, but are otherwise debonded from the surrounding concrete medium. This embedment system is illustrated in Figures K-1 and K-2 (Appendix K).

Four finite element models were developed to determine the reaction of the embedments to LOCA loading. These models are described in Appendix K. They are:

1. A generic embedment model, which is a detailed three-dimensional model of the skirt/pedestal interface and the pedestal concrete;
2. An axisymmetric model, which includes the cavity wall and the basemat, and was used for sensitivity studies;
3. A nonlinear embedment model, which was developed from the generic embedment model and determines the nonlinear response of the pedestal to an overturning moment; and
4. An embedment substructure model, which is a detailed two-dimensional model used to determine the inelastic response of the pedestal concrete under the applied loading.

The axisymmetric model was analyzed using the finite element computer program ANSYS. The remaining three models were developed and analyzed using the EDS Nuclear computer program EDS-SNAP[9].

Using the first two models, the stiffness of each plant's embedment system was determined, and this stiffness was incorporated into the reactor vessel isolated structural models (Appendix D).

6.2.1.2. Embedment Loading

The postulated loss-of-coolant accident results in a number of loading conditions on the embedment. The loadings which are applied to the embedment through the skirt were determined by the reactor vessel isolated structural model analyses (Section 5.1). They are defined at the skirt/pedestal interface, and consist of:

1. A lateral force;
2. An overturning moment, which acts about a horizontal axis;
3. A torsional moment, which acts about the vertical axis;
4. A vertical force due to pressure loading and core bounce; and
5. A downward force due to the weight of the reactor vessel.

Of these, the first two arise from the asymmetry of the LOCA event. Their peaks occur approximately 60 to 70 milliseconds into the event. The torsional moment is small. The vertical force resulting from the unbalanced pressures acting on the top and bottom of the reactor vessel does not become significant until after the asymmetric LOCA loads have diminished substantially, while that due to core bounce is of relatively high frequency and lesser magnitude.

There are three other principal sources of loading on the embedment due to a LOCA:

1. Mechanical loading applied through the cavity wall (for which the pedestal forms the base);
2. Pressure loading on the inner face of the pedestal; and
3. Thermal loading due to a temperature differential across the pedestal.

Of these, only the cavity wall reactions will coincide with the asymmetric loadings applied through the reactor vessel support skirt. Both the pressure and thermal loading induced by the LOCA are insignificant at the time of peak asymmetric loading.

6.2.1.3. Embedment Response

The skirt-supported plant embedment is a relatively massive and durable structure. Its size and strength indicate a high resistance to uniformly applied loadings, such as pressure. For mechanical loadings, such as those that are applied through the reactor vessel support skirt, the strength of the embedment is largely governed by the strength of the mechanism by which the loading is transferred into the concrete. Thus, if failure occurred, it would take place in local regions, rather than globally.

For this reason, the most severe loading on the embedment is that imposed during the asymmetric phase of the LOCA event, when large loadings are applied through the reactor vessel support skirt. As discussed in Section 6.2.1.2, these include a lateral force, a vertical force, an overturning moment, and a torsional moment. The torsional moment is relatively small and will not have a significant effect on the stresses in the embedment. The lateral force, vertical force, and overturning moment, however, induce significant local stresses.

The overturning moment applied at the interface between the skirt and the pedestal is resisted by a couple formed by compression reactions in the concrete and tension forces in the anchor bolts. As the skirt is initially pre-stressed to the pedestal, a lift-off phenomenon occurs when the tensile forces produced by the moment exceed the preload compression forces. Lift-off induces a significant change in the stiffness of the embedment, as the anchor bolts are considerably more flexible than the concrete. When lift-off occurs (at approximately 30 percent of the peak LOCA moment), the neutral axis about which the pedestal rotates moves towards the compression zone. The area of the compression zone thus decreases, with a corresponding increase in concrete stress.

Elastic analyses, using the generic embedment model, indicated that the uniaxial compressive strength of the concrete is reached before yield of the anchor bolts occurs. In reality, this is a conservative assumption on which to base calculation of the ultimate capacity of the embedment. The concrete under the compression flange of the skirt is well confined and well reinforced, and is capable of undergoing significant nonlinear deformation at higher stresses.

Nonlinear response of the concrete has two effects. First, it allows a wider arc of concrete in the compression zone to approach maximum stress, and thus increases the embedment's moment resisting capacity (a direct analogy can be drawn to the plastic behavior of a beam in bending). Secondly. the softening of the concrete slows the migration of the neutral axis toward the compression sector, resulting in a more balanced response of the system and the development of more of the anchor bolt capacity.

The lateral load applied through the skirt can be transmitted across the skirt/pedestal interface in three ways: by friction between the sole plate and the underlying concrete, by direct thrust of the vertical bearing plates against the concrete, and through shear anchors beneath the sole plate. Only in the case of the shear anchors, which occur on three of the plants, will the lateral load be transmitted around the full 360-degree perimeter of the interface. The friction load will be proportional to the contact stress between the sole plate and the concrete, and will thus be highest in the compression zone. The bearing stress will be transferred exclusively in the compression zone. Local nonlinear deformation of the concrete will have little effect upon the distribution of these stresses around the interface, as the flexibility of the skirt in this plane is considerably greater than that of the concrete, and therefore governs.

6.2.1.4. Embedment Material Properties

The strength of the embedded steel was calculated in accordance with the criteria outlined in Section 7.2. The 5 percent increase in minimum specified stress properties due to overstrength, and the 10 percent increase in yield stress due to strain rate effects were included for all steel components.

For the embedment concrete, three factors which directly influence both its strength and its stiffness were considered: strain rate effects, overstrength, and aging.

The supplier of concrete for nuclear power plants is required to meet strict performance criteria regulating the concrete's strength. Regular strength tests are made as construction proceeds, and the results of these tests must meet predetermined, statistically based standards. These standards guard

against the placing of any significant quantity of understrength concrete. As the strength of concrete varies under even the strictest control conditions, the supplier must establish a mean strength significantly greater than the minimum specified design strength.[5] Thus a finite overstrength is assured.

The minimum specified design strength must be achieved at twenty-eight days. However, the hydration of concrete continues beyond this time.[6] The strength increase with further aging depends principally on curing, use of admixtures, and cement type. Overseas codes[7] allow a significant strength increase to be assumed for structures which will not be loaded within ninety days.

To allow for overstrength and aging, the analysis and qualification of the reactor vessel support embedments was based on concrete strengths determined from tests at ninety days. The embedment concrete strength was taken as neither greater than the average of any three consecutive strength tests, nor more than 500 lb/in^2 greater than any individual test. This is consistent with the interpretation of tests for concrete quality control. The resulting uniaxial compressive strengths are listed in Table 6.2-1.

The elastic stiffness of the concrete was determined from the following formula (Reference 1, Section 8.3):

$$E_c = 33\ w^{1.5}\ (f'_c)^{\frac{1}{2}}$$

where E_c = modulus of elasticity, lb/in^2
w = weight of concrete, lb/ft^3
f'_c = compressive strength, lb/in^2

Where nonlinear concrete stiffness relationships were used, they were correlated to this elastic stiffness, which approximates to the secant stiffness at a stress equal to one half the uni-axial strength. Poisson's ratio for concrete was set equal to 0.2 for all analyses.

Increases in concrete strength and stiffnesses due to the relatively high strain rates induced by the LOCA were adopted. The guidelines of ACI 349-76, Appendix C were used to determine the dynamic strength. An increase of 25 percent in compression and 10 percent in shear and tension strengths resulted.

In accordance with published test data[43], a 10 percent increase in concrete stiffness was also assumed.

6.2.1.5. Analysis Procedure

Two alternative analysis procedures were used to determine the response of the skirt-supported plant embedments to the LOCA loads. For ANO-1 and Crystal River 3, analyses were performed using the generic embedment model. The nonlinear response of the concrete was not considered, and these analyses are referred to as elastic analyses. For Oconee, Three Mile Island 1, and Rancho Seco, analyses were performed using the nonlinear embedment and embedment substructure models. These inelastic analyses explicity considered the nonlinear response of the concrete in the compression zone.

A generic summary of these two analysis methods is included in this section. Plant-specific features of the individual analyses are discussed in Section 6.2.1.6.

In each analysis, the most severe loading condition (that occuring during the asymmetric phase of the LOCA) was considered. The peak overturning moment and lateral force applied through the vessel skirt were considered to act simultaneously. In reality, they are slightly out-of-phase. Also included were the vertical load applied through the skirt and the reactions induced by the LOCA at the interface of the cavity wall with the pedestal. These were calculated for a time approximating the occurrence of the peak overturning moment. A load factor of unity was used in all analyses.

The elastic and inelastic analyses used for qualification were static analyses to the peak loadings identified in the dynamic reactor vessel structural model analyses (Section 5.1). A sensitivity study on the dynamic response of the embedment is described in Section 6.2.1.8.

Seismic loadings were not considered in the plant specific analyses described in Section 6.2.1.6. The combination of seismic and LOCA loading, and its effect on embedment analyses and qualification, is addressed in Section 6.2.1.9.

Elastic Analyses

The elastic analyses of ANO-1 and Crystal River 3 were three-dimensional analyses using the generic embedment model. The concrete stiffness was the dynamic elastic stiffness defined in Section 6.2.1.4. Reactor vessel loadings were applied at the top of the vessel skirt, while cavity wall reactions were modeled by concentrated forces distributed around the pedestal circumference at the appropriate nodal points.

Inelastic Analyses

The inelastic analyses of Oconee, Three Mile Island 1, and Rancho Seco considered the effect of nonlinear concrete behavior on the embedments' response to the applied LOCA moment. These analyses were performed on the nonlinear embedment model described in Appendix K. The properties of the nonlinear compression truss elements in this model were derived by explicit nonlinear analyses of the embedment substructure model.

The embedment substructure model is described in Appendix K. Use of this model allowed an accurate estimate to be made of the concrete response in the highly stressed region beneath the compression flange of the reactor vessel skirt. The model considers both stress enhancement under multi-axial stress states and the nonlinearity introduced by tension cracking.

The multi-axial failure envelope adopted for the concrete in compression is shown in Figure 6.2-1. This envelope closely resembles that defined by Khan and Saugy[32], and is generally a lower bound to published research data.[33,34,35,36] For concrete in multi-axial tension, the failure envelope was that defined by the maximum normal stress theory. The envelope for the combined tension-compression regions was then derived by straight-line interpolation. The tensile strength of concrete was assumed to be

$$t = 5.625\ (f'_c)^{\frac{1}{2}}$$

where f'_c is the lesser of the uniaxial compressive strengths and 7,000 lb/in^2.

The anchor bolts, embedded steel, and effective reinforcement were modeled explicitly. Development lengths of the reinforcement were not considered to be effective for resisting load.

The load versus deflection relationships defined by analyses of the embedment substructure model were correlated to generic embedment model analysis results at elastic stress levels, and were included in the nonlinear embedment model.

An inelastic analysis of the embedments' response to lateral loading was not performed. The distribution of stress in the pedestals due to the applied lateral load will be independent of nonlinear concrete response, due to the relative flexibility of the skirt with respect to this loading. Thus, the lateral load distributions determined in the elastic analyses of ANO-1 and Crystal River 3 were generically applied to the three remaining plants. However, the effect of the lateral loading on the nonlinear concrete response was considered.

6.2.1.6. Plant Specific Analyses

ANO-1

An elastic analysis was performed for the most severe asymmetric loading induced by a cold leg break. The cold leg break loading is marginally more severe than that for a hot leg break. The peak lateral load and overturning moment were applied simultaneously. For the vertical load induced by the LOCA, which is of relatively high frequency due to the predominant influence of core bounce at this stage of the event, a mean value was adopted. The effect of the oscillatory loading was, however, considered for qualification.

ANO-1 has no shear anchors beneath its sole plate. All lateral load was assumed to be transferred by radial compressive thrust through the vertical bearing plate.

The analysis indicated that, for the applied loading, lift-off occurs around approximately one half of the pedestal circumference and none of the anchor bolts yield.

Oconee

Oconee was analyzed for a cold leg break, which, for the asymmetric embedment loading, is approximately 8 percent more severe than a hot leg break. The

inelastic analysis method was used. No vertical LOCA force was included in the analysis; however, its effect was considered for qualification.

The distribution of lateral load around the interface was derived from the ANO-1 analysis, neither plant having shear anchors. A coefficient of friction of 10 percent was assumed to act between the sole plate and the concrete. The remaining lateral force was applied as a radial thrust to the vertical bearing plate.

Lift-off was predicted around 220 degrees of the skirt perimeter. Slight tensile yielding of the anchor bolts most remote from the neutral axis was predicted.

Crystal River 3

For Crystal River 3, an elastic analysis was performed for the peak loading imposed by a hot leg break. The cold leg break loading is approximately 20 percent less. As for ANO-1, the vertical load varies rapidly. The most severe vertical force occurring within one wavelength of the peak overturning moment was applied in the generic embedment model analysis.

Crystal River 3 has substantial shear anchors welded to the underside of the sole plate. Their effect was modeled by specifying displacement continuity between this plate and the underlying concrete. Subsequent analysis indicated that local crushing of the concrete would occur against the shear anchors. The load carried in radial thrust through the vertical bearing plates was increased to allow for the resulting redistribution of lateral load across the interface.

Lift-off was shown to occur around slightly more than one half the circumference. Tensile yielding of the anchor bolts most remote from the neutral axis was predicted.

Three Mile Island 1

The loading applied to the Three Mile Island 1 reactor vessel support embedment closely approximated that used in the Crystal River 3 analysis.

Only the cavity wall reactions and the prestress level differed. An inelastic analysis was performed.

The distribution of lateral load around the interface was derived from the Crystal River 3 analysis. A coefficient of friction of 10 percent was assumed to act between sole plate and concrete. The lateral force not transferred by friction or anchor plate action was applied to the vertical bearing plate.

Lift-off was shown to occur around approximately 200 degrees of the skirt perimeter. The anchor bolt stresses indicated that a clear margin exists against yield.

Rancho Seco

An inelastic analysis was performed for the peak asymmetric loading induced by a hot leg break. This loading is approximately 8 percent greater than that induced by a cold leg break. Unlike Oconee and Three Mile Island 1, a specific embedment substructure model analysis was not performed for Rancho Seco. Due to the similarity of the Rancho Seco and Oconee embedments, the nonlinear response of the Rancho Seco pedestal concrete was derived from the Oconee substructure analysis.

The distribution of lateral load around the interface was derived from the ANO-1 analysis.

6.2.1.7. Qualification Procedure

Specific qualification was performed for the ANO-1, Oconee, Crystal River 3, Three Mile Island 1, and Rancho Seco embedments.

Consistent qualification criteria were used. These criteria, which are outlined in Section 7.2, reflected a conservative estimate of the ultimate strength of the embedments. Where possible, the ultimate strength provisions specified in ACI 349-76[1] were followed. Interpretations of this code for the unique geometry and behaviour exhibited by the embedments are discussed in this section. Due to the specific nature of the inelastic analyses, and of certain postulated failure planes, ACI 349-76 did not always apply. In these

instances, recourse was made to published research data and material behavior theories.

ACI 349-76 is a design and construction code. Capacity reduction factors are applied to calculated strengths to account for material strength variability and inaccurancies in design equations, to avoid nonductile failure, and to

reflect the generic structural importance of certain elements. These factors have been adopted in the acceptance criteria, and are considered in all qualifications. The resulting stress (or strain) ratios may exceed unity, but the absolute strength of the embedment still be greater than that required to resist the applied LOCA load. Thus, ratios are also reported for capacity reduction factors of unity.

In calculation of the ratios, the most unfavorable neighboring peak of vertical load was superimposed on the asymmetric LOCA loading. This is conservative. Not only will the embedment be relatively insensitive to the high frequency loading component due to core bounce, but also, coincidence of the loading peaks is improbable.

The failure modes considered during qualification of each plant included:

1. Tensile overstress (or overstrain) of the anchor bolts;
2. Pull-out of the anchor bolts due to shear failure of the reinforced concrete;
3. Bearing failure of the concrete above the anchor plates, against the vertical bearing plate, and beneath the sole plate;
4. Sliding shear failure beneath the sole plate in the compression zone; and
5. Separation at the liner plate level.

A description of the qualification methodology used to evaluate the resistance of the embedments against each of these failure modes follows.

Anchor Bolt Stress

The peak anchor bolt load was determined directly from the analyses. The stress was calculated using the effective stress area defined for each

particular anchor bolt size and thread type. The allowable stresses and strains are defined in Section 7.2.

Anchor Bolt Pull-Out

Pull-out of one, two, or more anchor plates was considered, and the most critical combination checked. Reference was made to Section 15.5.5 of ACI 349-76 to determine the contribution of anchor bolts adjacent to postulated shear planes.

Allowable shear stresses were computed from Section 11 of ACI 349-76. A capacity reduction factor, ϕ, of 0.85 was used. Due to the geometry of the embedments, cold leg breaks generally controlled pull-out failure adjacent to openings. Where a postulated shear failure surface intersected an opening, no credit was taken for the strength of any steel lining.

Bearing Failure

Maximum nominal, or average bearing stresses were calculated above the anchor plate, against the vertical bearing plate, and, for ANO-1 and Crystal River 3, beneath the sole plate. No redistribution of load due to the nonlinear response of the concrete was considered in these cases. The nominal bearing stresses were checked against allowable values calculated using Section 10.14 of ACI 349-76. A capacity reduction factor of 0.70 was applied.

For the three plants for which nonlinear analyses were performed, the maximum compressive strain, rather than the compressive stress, was checked beneath the pedestal. This strain was the peak local value calculated over a gauge length of less than three inches. This was compared to the allowable strain defined in Section 7.2, which has a capacity reduction factor of 0.75 included.

Sliding Shear Failure

Although Codes[1,44] do not require an explicit check of this failure mode in reinforced concrete, it was considered. The shear failure plane was assumed to extend from the vertical bearing plate to the inner face of the pedestal. Any slippage along such a plane results in wedge-like interaction between the moving block and the intact pedestal concrete. The allowable shear stress was

taken as 0.3 f'_c, which allows for the resulting large compressive force acting across the plane.[3]

Separation at the Liner Plate

Two plants, Crystal River 3 and Three Mile Island 1, were checked for separation at the liner plate level. ANO-1 and Oconee have vertical reinforcing extending through the liner plate and into the basemat, and separation is precluded. Rancho Seco has core flood line walls extending almost to the pedestal. These ensure stability.

For Crystal River 3 and Three Mile Island 1, the loading imposed by the cavity wall reactions, skirt loading, and dead weight at the liner plate level was summed. The resulting overturning moment is resisted by a couple formed by the concrete in compression and by the shear in the 24-inch-thick slab which is cast above the liner plate. Qualification of the system was performed by treating the pedestal as an eccentrically loaded short column. A capacity reduction factor of 0.90 was used.

Should this resistance be exceeded, instability would not be imminent. Rather, the cavity wall would resist the tendency of the pedestal to lift. As the cavity wall is loaded by an effectively equal and opposite pressure force, global stability is assured. Thus the check for lift-off at the liner plate serves as a verification of the assumed response, rather than as a means of establishing a safety factor against instability.

6.2.1.8. Dynamic Analysis

The analyses described in Section 6.2.1.6 were static analyses. The LOCA loads applied were the peak loads determined by dynamic analyses of the reactor vessel isolated structural models (Appendix D). These latter analyses include any dynamic amplification of the reactor vessel response and hence of the embedment loading.

The embedment mass was not included in the reactor vessel isolated structural models. Its contribution to the overall response, relative to that of the reactor vessel mass, is clearly insignificant. However, to confirm this, a dynamic analysis of the Three Mile Island 1 embedment for the hot leg break

loading was performed, using the nonlinear embedment model described in Appendix K. The response was compared to that for a 'massless', or static, analysis. The correlation was excellent.

Thus, the adequacy of the analysis techniques used for the embedment was confirmed.

6.2.1.9. Seismic Loading

The reactor vessel support embedments may be subject to seismic loading during the LOCA event. The effect of the coincidence of the LOCA and seismic loadings on the embedment response was considered.

For skirt-supported plants, seismic loadings induce a horizontal force, a vertical force, and an overturning moment on an embedment. These loads arise from the inertia of the reactor vessel, and are applied through its support skirt. The stress pattern they produce in the embedmert will closely follow that induced by asymmetric LOCA loading.

The design seismic loads are known. The magnitude of the design seismic overturning moment relative to that of the peak LOCA overturning moment is summarized in Table 10.2-6. The seismic loads were determined using pre-lift-off embedment stiffnesses. As the LOCA loading induces lift-off, the stiffness of the embedment, and hence its response to seismic loading, changes. To allow for this, the following conservative technique was used to estimate the effect of seismic loading.

First, the design seismic loads were increased to reflect the decreased embedment stiffness after lift-off. The corresponding lengthening of the fundamental period of the reactor vessel and its support system was calculated, and the maximum increase possible in the seismic load determined by reference to NRC Regulatory Guide 1.60.[40] This approach is conservative: lift-off under the LOCA loading occurs for a relatively short time, considerably shorter than the time required to build up full seismic response.

The energy associated with this increased seismic loading, known as the energy demand, was determined, and the response of the embedment increased to provide the corresponding additional energy capacity. This method, of equating energy demand and capacity, is consistent with the reserve energy technique proposed by Blume[41] and the inelastic response spectrum technique of Newmark.[42]

The conservatism of this approach is clear. As noted, the lift-off due to a LOCA is of short duration. The assumed coincidence of the peak seismic loading with the inital, asymmetric phase of the LOCA is not probable. Also, the energy absorption capacity of other elements of the support system was disregarded.

The resulting increases in the embedment loading are summarized and their effect on qualification is addressed in Section 10.2.

6.2.2. Nozzle-Supported Plant

6.2.2.1. Introduction

The Davis-Besse reactor vessel is supported on four pairs of support beams, one pair to each cold leg. These support beams have considerable strength against vertical loading, and thus resist the dead-weight of the vessel and the vertical force induced by the LOCA. The lateral, or horizontal resistance offered by the support beams is limited by the strength of the connection at the cold leg nozzle. In cases where this strength is exceeded, the lateral load induced by the asymmetry of the LOCA event is resisted by the LOCA rings, which enclose each hot and cold leg in its cavity wall penetration.

Finite element models have been developed to represent the support beams and LOCA rings. These models are described in Appendix K. Each model represents both the component and its surrounding concrete.

Spring rates were developed for each support and included in the reactor vessel isolated structural model (Appendix D). The development of these spring rates is described in Appendix K. The loading defined by the reactor vessel isolated structural analyses is summarized in Section 9.2.

Analyses and qualifications were performed for the support beams and for the hot and cold leg LOCA rings. The methodology used is described in Section 6.2.2.4. Qualification results are summarized in Section 10.2.

6.2.2.2. Loading

Support Beams

Each cold leg nozzle is supported by one pair of support beams. The support beams are subjected to both vertical and horizontal LOCA loading. The maximum vertical LOCA load is of similar magnitude to the dead-weight loading. The horizontal load, for which the strength of the nozzle connection defines an upper bound, acts tangentially to the wall only; no horizontal load is applied in the direction of cold leg pipe axis.

LOCA Rings

The loadings on the hot and cold leg LOCA rings are given in Section 9.2. During the asymmetric phase of the LOCA event, the horizontal load dominates. Significant vertical load develops only after the asymmetric phase of the LOCA has diminished, and results from the pressure differential acting between the top and the bottom of the reactor vessel. The loads defined in Section 9.2 act normal to the LOCA ring axis only. Frictional restraint, acting along the LOCA ring (and pipe) axis, was not considered in the reactor vessel isolated structural model analysis. For qualification, however, frictional loads equal in magnitude to 42 percent of the normal load were applied. Clearly, this is conservative. Had this frictional restraint been considered in the load definition analysis, both the applied normal loads and the reactor vessel displacements would have been significantly reduced.

6.2.2.3. Response of Supports

Support Beams

The loads on the short, deep support beam are resisted by bearing stresses between its web and flanges and the concrete. The cantilever moment induced by the horizontal load is resisted by a couple formed by the bearing stresses on the embedded support beam web. The moment produced by the vertical load,

on the other hand, is resisted by a couple formed by the bearing stresses on the support beam flange and the tension forces in the anchor bolts.

Both local and global stresses are induced in the cavity wall. The local stresses are the bearing, or compressive stresses at the beam/concrete interface, while the global stresses result from the global moment and force induced by the eccentric applied load. These latter stresses are considered in the cavity wall analysis (Section 6.10).

LOCA Rings

The loading applied to the LOCA rings is transmitted through the shims upon which the pipe impacts. There is very little clearance between this pipe and the shims: thus, the pipe wall and the inside plate of the LOCA ring are forced to adopt a common displaced shape. As a result, the radial compression struts, which are the prime load resisting mechanism of the LOCA ring, displace relatively uniformly. Yielding of one strut causes neighboring struts to assume a compensatory portion of the load. The struts on the "tension" side of the LOCA ring carry little or no load.

Again, both local and global stresses are induced in the concrete cavity wall, the latter being considered in Section 6.10.

6.2.2.4. Analysis and Qualification Procedure

Support Beams

An analysis of a support beam for the applied LOCA loading was performed, and the stresses in the beam and its anchor bolts checked against allowables.

The analysis was performed using the support beam model described in Appendix K. Debonding of the steel/concrete interface under tension, and local crushing of the concrete at the inner face of the cavity wall were considered. As expected, the bearing stresses on the concrete were highest near the inner face of the cavity wall, beneath the support beam. They diminished toward the outer end of the beam, which "lifted off," putting the outermost group of anchor bolts into tension.

The stresses in the support beam and in its anchor bolts were compared to allowable stresses evaluated in accordance with the ASME Code, Section III, Appendix F.

LOCA Rings

Analyses of both the hot and cold leg LOCA rings were performed, using the models described in Appendix K. The peak loads defined in Section 9.2 were applied, together with the corresponding friction force.

The hot leg LOCA ring was analyzed elastically and qualified against allowable stresses evaluated in accordance with the ASME Code, Section III, Appendix F.

The more highly loaded cold leg LOCA ring was analyzed inelastically. The load distribution into the individual struts is shown in Figure 6.2-2. Slight yielding occurred in the struts. Allowable stresses and strains were computed in accordance with Section 7.2. Bolt stress allowables were taken to be 60 percent of ultimate in tension, and 45 percent in shear.

Nominal bearing stresses on the concrete were calculated for both the support beam and the LOCA rings, and compared wih allowables defined in ACI 349-76.

6.2.2.5. Seismic Loading

As for the skirt-supported plants, the Davis-Besse reactor vessel supports may be subject to seismic loading during the LOCA event. The effect of the coincidence of the LOCA and seismic loadings on the supports' response and qualification was considered.

The design seismic loads are known. They are summarized in Section 9.1. All seismic loading is resisted by the support beams.[45]

The combined effective load on the support beams was determined by taking the square root of the sum of the squares (SRSS) of the peak values of the seismic and LOCA loads. This method of combination was possible because the response of the support beam remains elastic under the combined loading.

The support beams were reanalyzed for this combined load, using the method outlined for the LOCA load analysis in the preceding section. The results are summarized in Section 10.2.

Table 6.2-1. Uni-axial Compressive Strength Of Embedment Concrete

Plant	Minimum Specified Design Strength at 28 days, lb/in^2	Tested Strength at 90 days, lb/in^2
ANO-1	5,500	5,500
Oconee	5,000	6,355
Crystal River 3	5,000	7,035
Three Mile Island 1	5,000	6,650
Three Mile Island 2	5,000	7,455
Rancho Seco	5,000	7,275

Figure 6.2-1. Multi-Axial Compressive Failure Envelope for Concrete

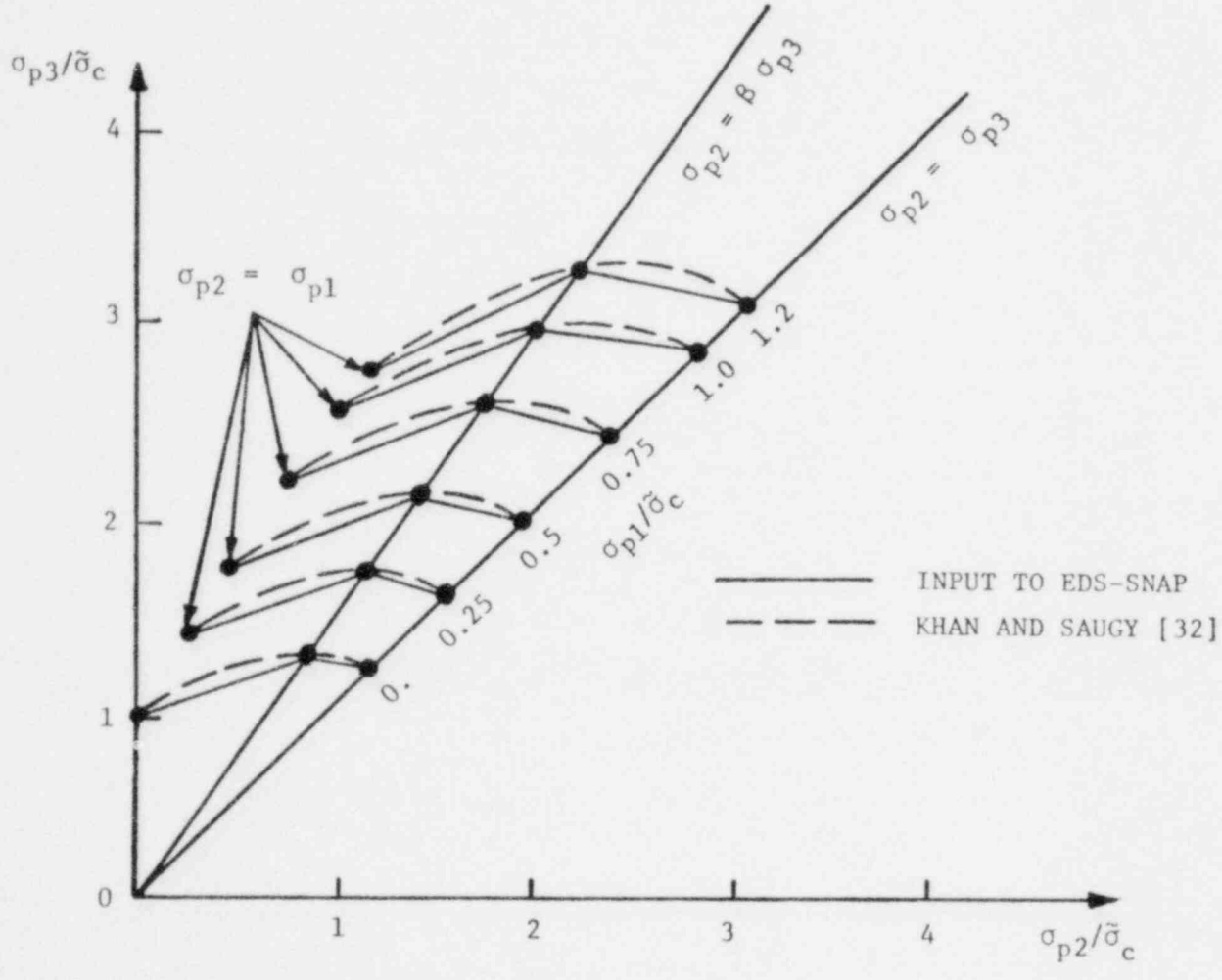

$\tilde{\sigma}_c$ = uniaxial maximum compressive stress.

σ_{p1}, σ_{p2}, σ_{p3} are principal stress values.

$\beta = 0.75$

Figure 6.2-2. Cold Leg LOCA Ring
Force Distribution

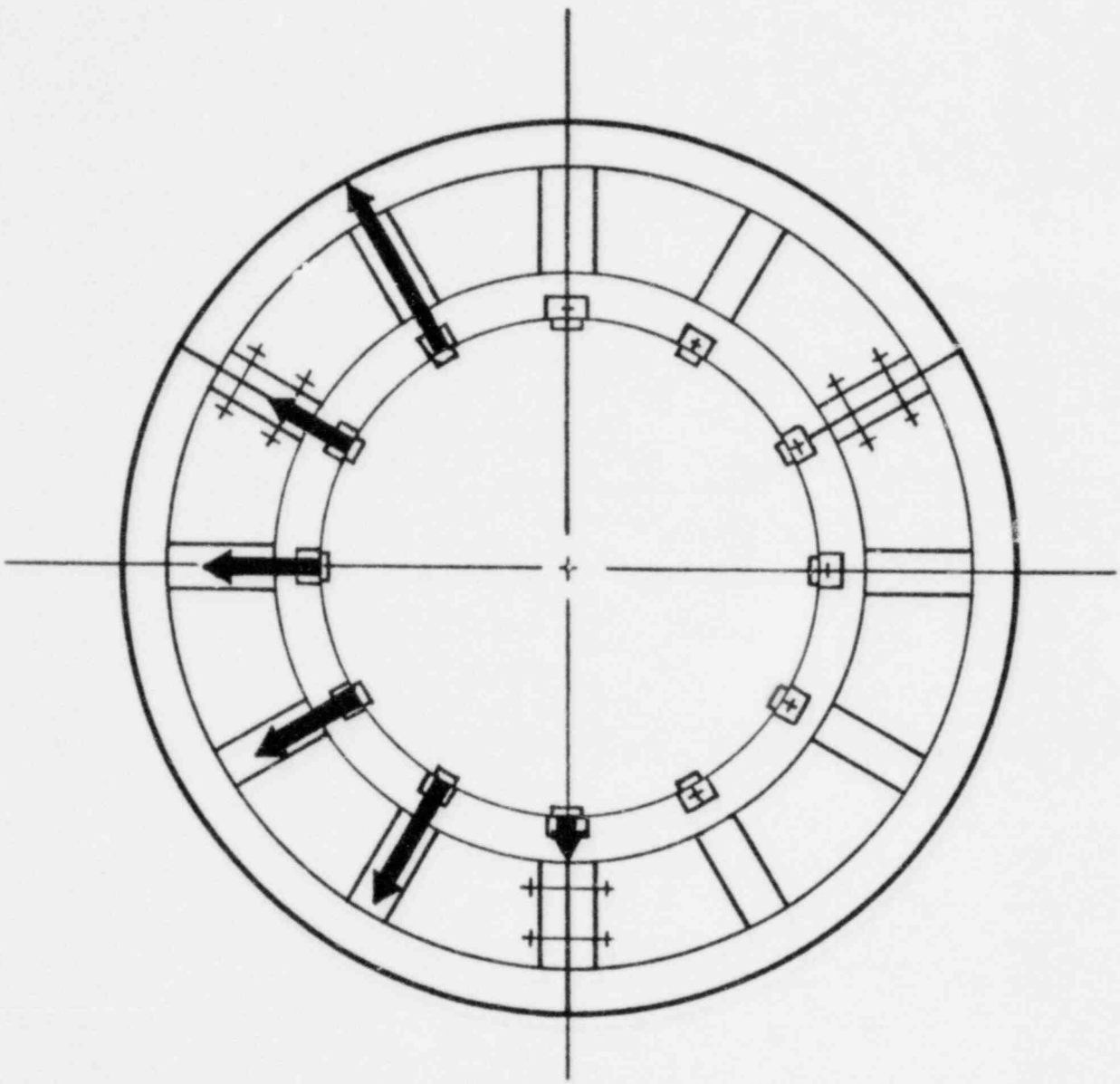

6.3. Control Rod Drive Service Structure

6.3.1. Service Structure

The control rod drive service support structures, shown in Figures 6.3-1 and 6.3-2, were evaluated and analyzed for the applied asymmetric loadings. In order to determine the stress conditions, an evaluation making use of an existing stress analysis and load ratios was used. Results of the load ratio evaluation indicated that the gussets and their attachments to both the channels and the flange were overstressed. The gussets transfer load from the seismic tie plates to the shell, see Figure 6.3-2. However, a review of the previously completed analysis indicated that very conservative simplifying assumptions were used to determine the loading distribution in this highly redundant structure. In order to obtain a realistic load distribution through the service structure, a finite element computer model was constructed; the model is described in Appendix L. The computer analysis, which is applicable to all plants, provided the loads at each gusset location, but not the actual gusset stresses. The maximum stress in the gusset was found by classical stress analysis methods, assuming that the gusset acts as an eccentrically loaded column.

6.3.2. SSS Mounting Flange

It had been determined from detailed stress analyses that the critical area of the CRD service support structure shell was the flange connecting the service structure shell to the RV head, as shown in Figure 6.3-3. The loading of the structure must be such that the bolted flange does not develop a plastic hinge condition.

The critical stress for a plastic hinge at the flange was determined to be the bending stress induced by the bolt load resisting the overturning moment on the SSS. The bending strength of a material in the plastic range can be established by using a ficticious bending stress called a bending modulus. This method assumes that the extreme fibers of the cross section are stressed in bending to the ultimate tensile strength of the material, resulting in a trapezoidal stress distribution. The bending modulus is determined from the stress distribution and combined with the section modulus to calculate the allowable moment. This procedure is outlined in Appendix A-9400 of reference 1.

The ASME Code minimum values for ultimate and yield strengths were increased by 5 and 10%, respectively as discussed in section 7.1.2.4. The bending stress was represented as an evenly distributed load on the tension side of the neutral axis. The compressive stress was assumed to be 0.7 S_u, the maximum allowed by Table F-1322.2-1 of reference 1. The overturning moment that would produce this stress distribution was then determined and compared with the applied loads.

Figure 6.3-1. Side View of Service Structure

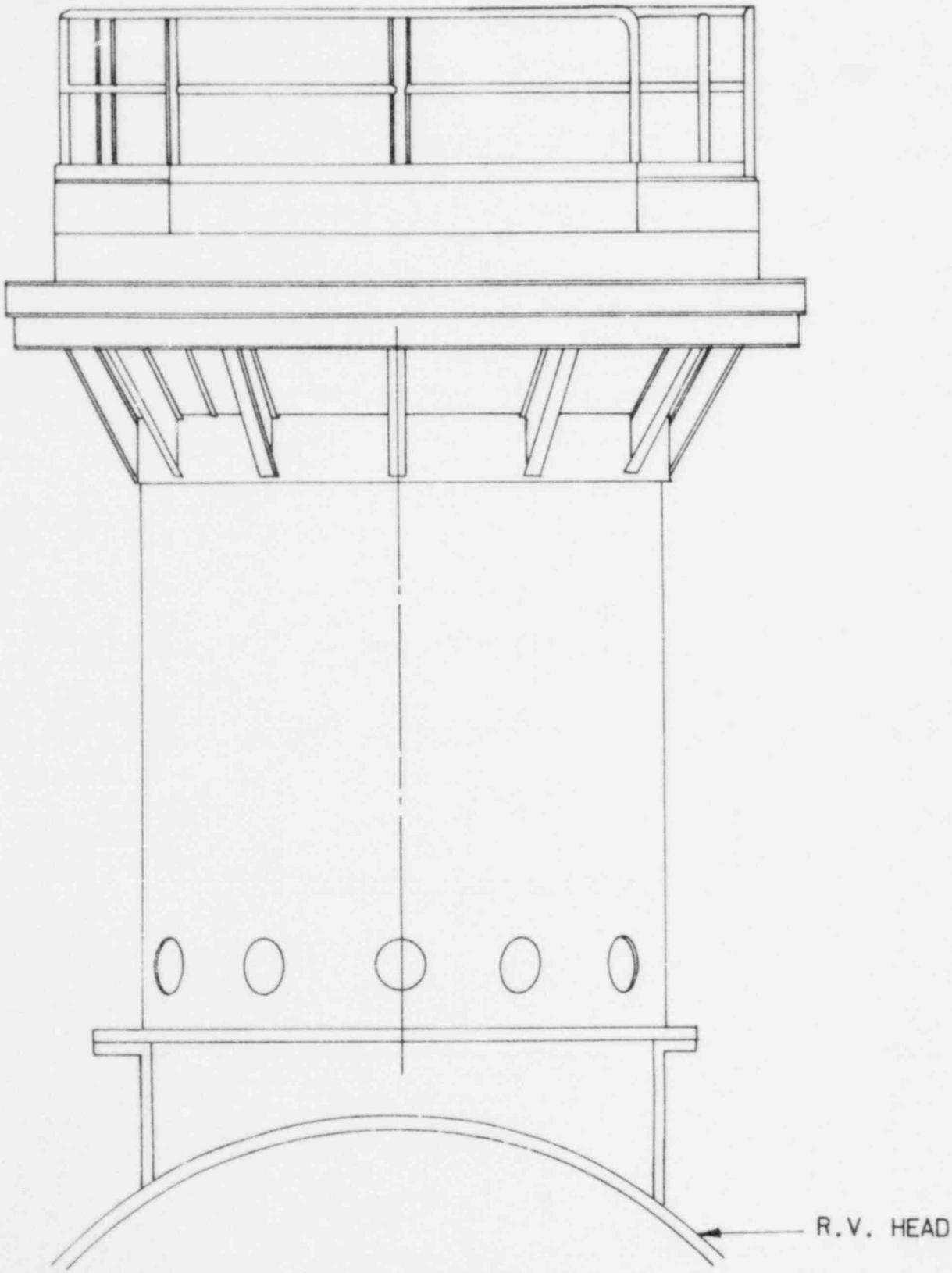

Figure 6.3-2. Plan View of Service Structure

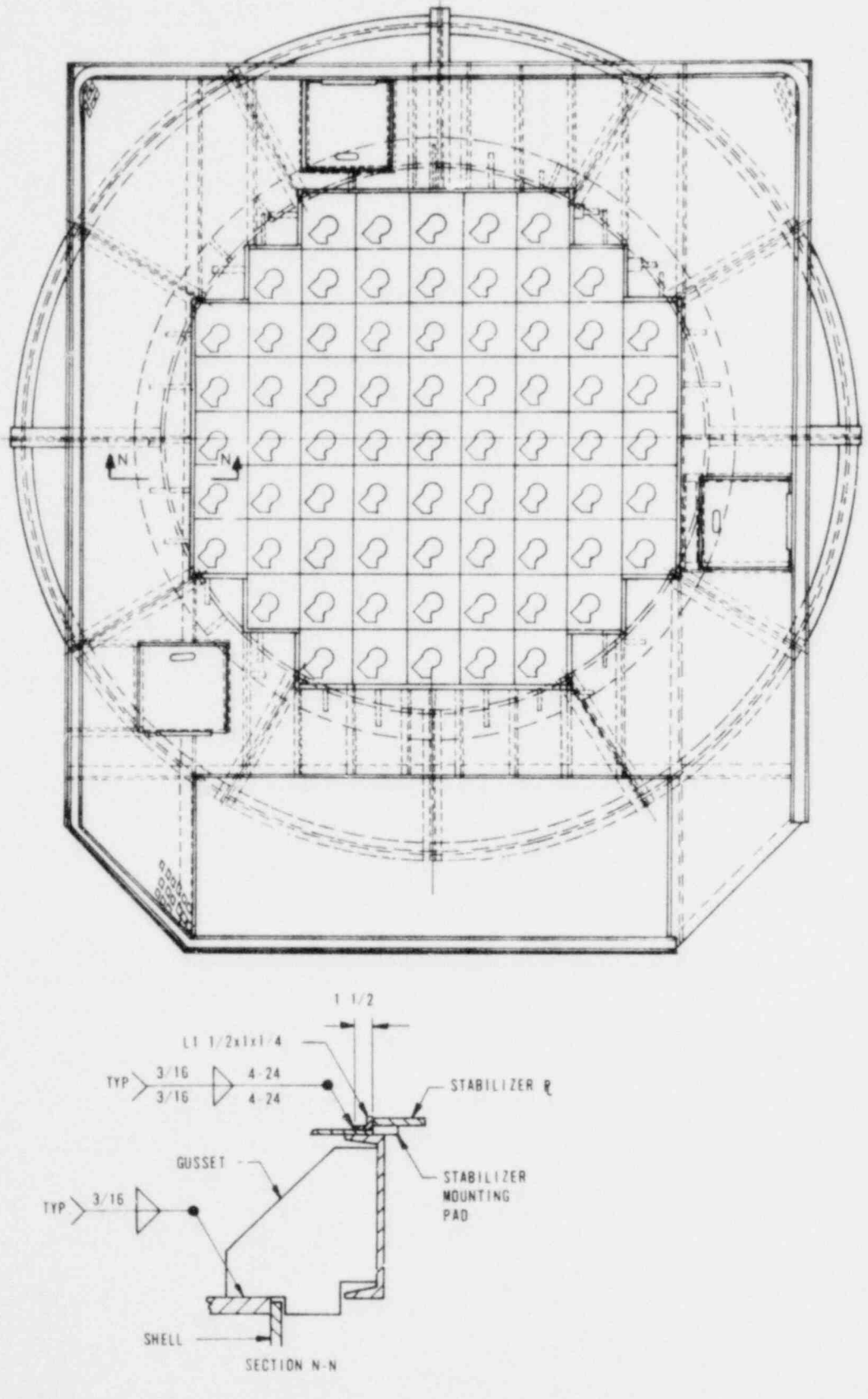

Figure 6.3-3. Service Support Structure Shell

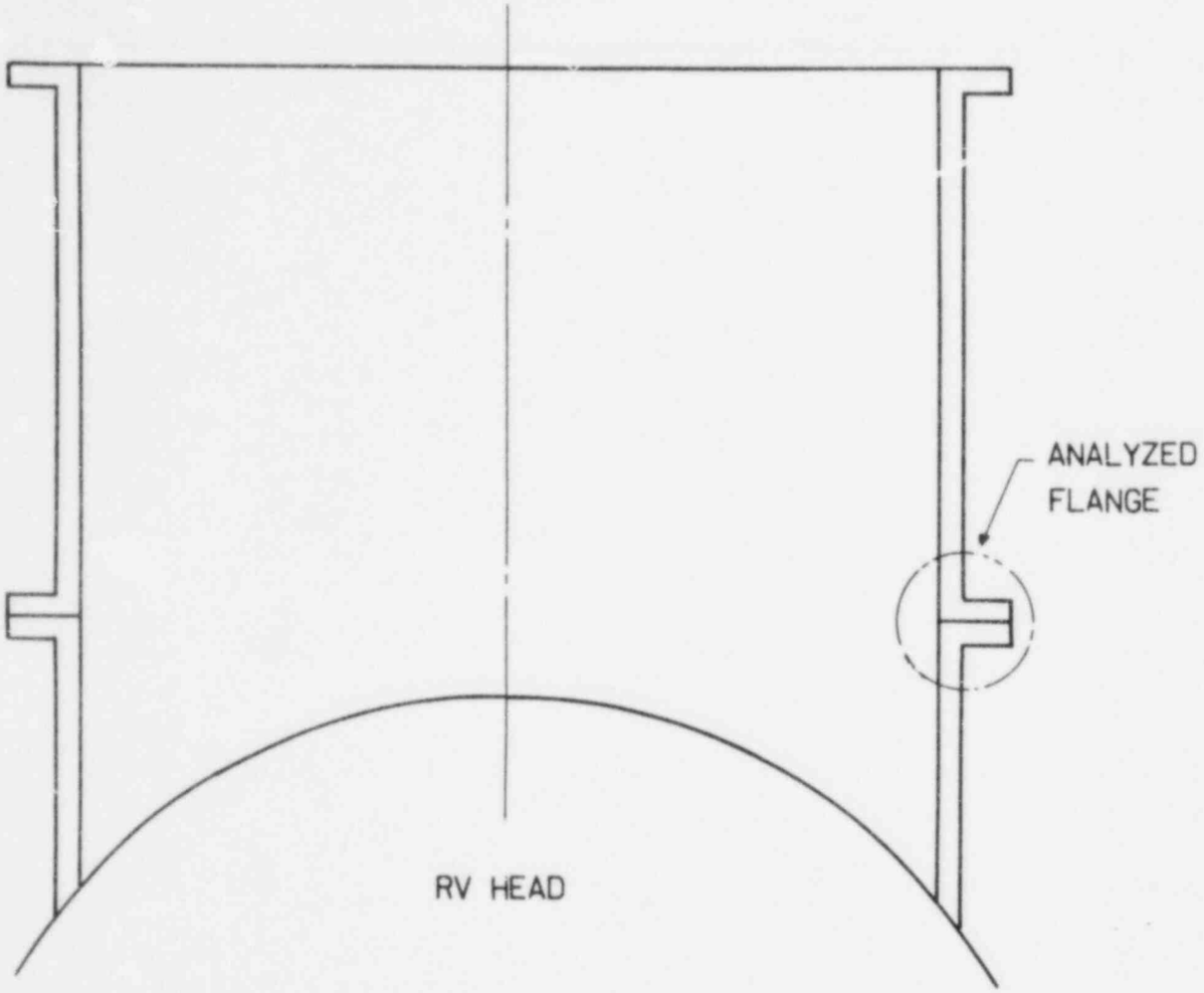

6.4. Control Rod Drives

6.4.1. Control Rod Drive Mechanism

6.4.1.1. Structural Evaluation of CRDMs

The control rod drive mechanism (CRDM) stresses were rigorously evaluated using a dynamic, nonlinear (gapped-element), finite element model, which is described in Appendix M. The principal dynamic effects experienced by the CRDM were those brought about by the LOCA event. To impose these effects on the CRDMs, time-dependent displacements were defined at three points: the center of gravity of the RV head, the RV head-nozzle junction, and the upper CRDM support (Figure 6.4-1). The dynamic analysis was performed with the CRDM mounted on both the longest and shortest nozzles of the reactor vessel head. Drive types A and C were evaluated in the analysis. (Drive type B was not evaluated since it is very similar to type A.)

Three LOCA cases were selected for the detailed CRDM LOCA stress analysis on the basis of a CRDM peak LOCA loads comparison. The LOCAs — designated LOCA 1, LOCA 2, and LOCA 3 — correspond to the TMI-1/CR-3 hot leg break without restraint modifications, TMI-1/CR-3 hot leg break with restraint modifications and the Oconee cold leg break, respectively. The results of these three LOCA cases were used to evaluate the acceptability of the other LOCA cases.

6.4.1.2. Evaluation of Pressure Boundary

The dynamic stresses due to the LOCA displacements produced a normal stress across the cross section of the CRDM. ANSYS (Appendix N) uses piping theory to calculate the stress occurring in the section. The normal stress was divided into two components: membrane stress, which is equal to the stress at the midplane of the CRDM wall; and bending stress, which is equal to the difference between the outside surface bending stress and the membrane stress. Membrane stresses were also calculated due to the internal pressure present in the drive at the time of the LOCA event. The LOCA and pressure stresses were combined, and ASME Code stress intensities were computed from the resultant principal stresses.

6.4.1.3. Evaluation of Lower Flanged Joint

An analysis of the bolts attaching the lower flange of the drives to the CRDM housing was performed. The stresses in the bolt were computed due to the

initial bolt preload, thermal effects, pressure, LOCA bending moments on the joint, and LOCA axial forces on the joint. The average stress across the bolt and the maximum stress at the bolt periphery were computed using standard analytical techniques for bolted joints with gaskets.

Calculations were also performed to ensure that a tight, sealed joint is maintained during and after the LOCA event. Standard ASME Code gasket sealing calculations were performed that accounted for the load required to react the external applied loads on the joint and to seat the gaskets.

6.4.2. CRDM Housing

The control rod drive housings (CRDHs) are made of two materials – stainless steel and Inconel – as shown in Figure 6.4-2. Sixty-nine CRDHs of various lengths are attached to the reactor vessel head. The CRDMs are attached to the CRDHs. The stress evaluation of these structures consisted of calculating the maximum allowable overturning moment on the CRDH and comparing it to the calculated loads.

The CRDH was treated as a cantilever beam experiencing bending from a concentrated moment. The bending strength of the material in the plastic range was established using a procedure outlined in Appendix A-9400 of reference 1. This method assumed that the extreme fibers of the cross section in bending were stressed to the ultimate tensile strength of the material, resulting in a trapezoidal stress distribution. A ficticious bending stress called the bending modulus was determined from the stress distribution, then combined with the section modulus to calculate the allowable moment. The utlimate and yield strengths were increased by 5 and 10%, respectively, for this evaluation as discussed in section 7.1.2.4.

Figure 6.4-1. LOCA Loading Nodes

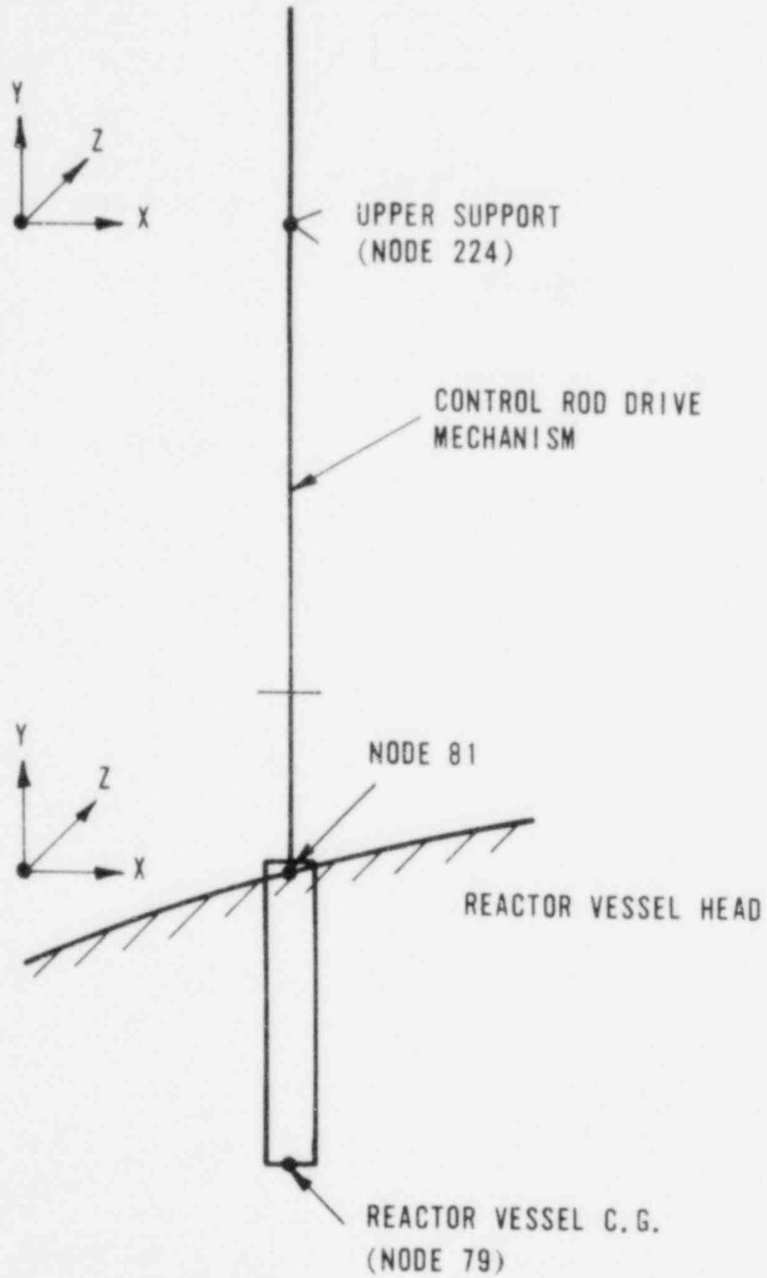

Figure 6.4-2. Control Rod Drive Housing

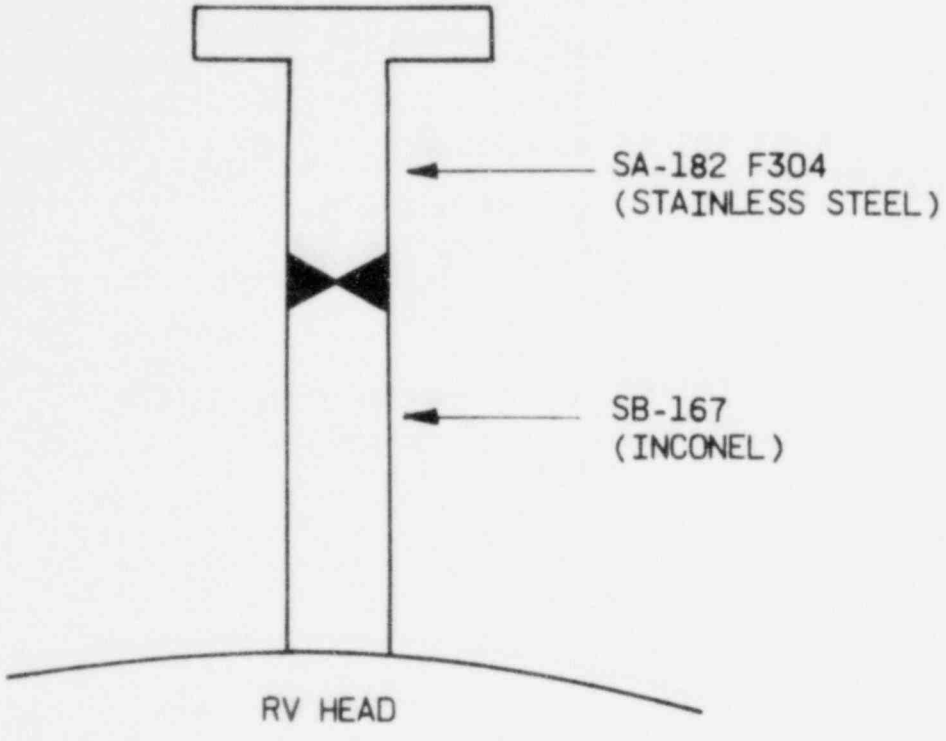

6.5. Reactor Internals/Core Support Assembly

The basis of the evaluation of the Owner's Group reactor internals for asymmetric loads was a pre-existing detailed stress analysis for LOCA loads. This base analysis is applicable to the Owner's Group Phase II evaluation because the loading components of the LOCA loads, i.e., F_x, F_y, F_z, etc., are the same but of different magnitude. Only the plenum assembly of the Owner's Group differs from those of the base analysis. However, the stress results were applicable to the Owner's Group plants when modified to reflect the structural differences described below.

The major difference in the plenum cover geometry is that the plenum cover of the base analysis is a 12.5-inch-thick perforated plate, while the Owner's Group cover is a ribbed weldment with a 2.0-inch-thick perforated plate welded on top of it. The weldment is 18.0 inches thick in the center region and reduced to 8.375 inches at the edge. The plenum cylinder of the base analysis is a cylindrical shell 130.0 inches in OD and 2.0 inches thick with ten 24-inch-diameter holes in the upper region. The Owners Group plenum cylinder is a 1.5-inch thick cylindrical shell 130.0 inches in diameter with six 34-inch and four 22-inch-diameter holes in the upper region. The column weldments of the base analysis are 9.1-inch-OD tubes 121.25 inches long with a wall thickness of 0.35 inch. The Owners Group column weldments are 8" schedule 40 pipes 124.0 inches long, 8.625 inches in OD, and 0.322 inch thick.

Ratios between the LOCA loads of the base analysis and the Owner's Group Phase II asymmetric loads were determined. For the plenum assembly these load ratios were further modified to account for the structural differences. The structural integrity of the reactor internal components was evaluated by applying the load ratios to the base analysis stresses or factors of safety and computing new factors of safety due to the Phase II loads.

6.6. Fuel Assemblies

The fuel assembly structural component stress analysis was performed using the loads generated by the LOCA analysis. The acceptance criteria for LOCA are described in section 7. Vertical and horizontal dynamic analyses were performed as described in section 5. The LOCA load cases that were analyzed for the horizontal analysis and vertical analyses are identified in section 9.6. The result of each of these was a load versus time history. Each time history was examined for a maximum load. The force in the other direction was taken from the corresponding force versus time history at the coincident time. This resulted in two load cases of horizontal and vertical forces for each event. These load cases were examined for the worst case, which was chosen for the stress analysis.

The ASME Code, Subsection NG-3000, and Appendix F were used as guides for the fuel assembly general stress criteria.[1] The analysis for most components used classic techniques. In some cases, failure loads established by testing were incorporated according to the ASME code. The upper and lower end fittings were analyzed using the finite element code FESAP.[2] A guide tube buckling analysis was performed using the Euler equations. The fuel assembly stresses resulting from the maximum probable fuel assembly deflection and from the maximum moment applied on the end fitting were evaluated. It was determined that the maximum moment applied on the end fitting provides higher stresses than those resulting from the fuel assembly maximum probable deflection. The fuel assembly maximum probable deflection was calculated using the accumulated fuel assembly gaps of the row having the maximum number of fuel assemblies across diameter. This is the maximum deflection allowed by the reactor internals constraint system (core baffle plates).

The spacer grid maximum impact forces occur at the center grids of a fuel assembly (FA) adjacent to the baffle wall. The grid impact forces were significantly lower for other grid positions above and below the center grid positions. The inner FA positions also experience considerably lower impact loads. The grid permanent deformation was obtained (as a function of impact loading) during the dynamic impact tests. An upper bound limit curve of the grid permanent deformation was obtained from the test data. This curve was used to obtain the spacer grid permanent deformation from the impact forces obtained from the analysis. Consequently, the theoretical reduction in grid cell flow area due to the

grid permanent deformation was calculated based on spacer grid geometry. This calculated reduction in the flow area was compared with the maximum reduction in grid cell flow area corresponding to a fully collapsed grid. A fully collapsed grid is defined as one in which grid straps (hardstops) are in hard contact with the fuel rods and all grid softstops are fully compressed so that the fuel rod is in contact with the spacer grid strips. This definition of a fully collapsed grid is consistent with the definition provided in draft Branch Technical Position 4.2.1. ECCS calculations were performed to show the acceptability of the deformation associated with a fully collapsed grid. Further discussion of coolability criteria that involve thermal-hydraulic considerations is provided in section 7.4.

6.7. Reactor Coolant Piping

Piping stresses are evaluated using the simplified pipe stress equation (from section 7.3.1):

$$B_1\left(\frac{PDo}{2t}\right) + B_2\left(\frac{Do}{2I}\right)M_i \leq 3S_m.$$

To reduce the number of repetitive stress computations, the pipe geometries of both the nozzle-supported and skirt-supported plants were reviewed for similarity. Five different pipe sections were identified for evaluation:

1. Hot leg straight, carbon steel.
2. Hot leg elbows, carbon steel.
3. Cold leg straight, carbon steel.
4. Cold leg elbow, carbon steel.
5. Cold leg safe-ends, stainless steel.

Again, to reduce the number of computations, the LOCA forces and moments were reviewed for the six skirt-supported plants. The highest LOCA loading for each of the five sections listed above was selected. No specific skirt-supported plant was evaluated – rather, a combination of the highest loaded joints. The LOCA forces and moments are combined by the square root sum of squares method for M_i. The equation combines axial stress (PDo/2t) due to internal pressure and axial bending stresses (Mc/I). A pressure of 2250 psia was used; this pressure adds some conservatism since the system operating pressure is 2200 psi, and at the time of the LOCA some immediate reduction in system pressure can be expected.

Stress indices are included in the stress computation to account for the specific pipe configurations being evaluated. All the parameters used in the equation are in accordance with Subsection NB-3650 of the ASME Code.[1] The geometry and loads of the skirt-supported plants were evaluated using this simplified stress analysis and met the criteria.

For the nozzle-supported plant, hot leg straights, hot leg elbows, cold leg straights, and cold leg safe-ends also met the simplified stress analysis criteria. However, the nozzle-supported cold leg elbow pipe stresses exceeded the simplified criteria. Therefore, a more rigorous stress analysis of the cold leg elbows was performed in accordance with Nuclear Power Piping Code USAS

B31.7-1969 using the criteria of B31.7, Appendix F. These calculations were performed with a computer code in which the LOCA forces and moments are oriented along the pipe axis and the principal stresses are computed. From these stresses the largest absolute value becomes the stress intensity, which is compared with the allowable $3S_m$.

6.8. Pipe Whip Restraints

6.8.1. Introduction

Pipe whip restraints are designed to stop a whipping pipe after a postulated guillotine break. Unless a pipe whip restraint doubles as a pipe support, a gap must be provided between it and the pipe to ensure that no contact occurs in normal operating modes. Because of this gap, a ruptured pipe develops large amounts of kinetic energy before it strikes the restraint. To absorb this energy, most restraints are designed to deform inelastically.

The load and deformation experienced by a restraint depends on its stiffness and mass characteristics. Thus, pipe whip analysis and restraint qualification is a three-stage process. First, the effective stiffness and mass of the restraint must be determined. These are then incorporated into the second stage, the dynamic analysis of the interaction between the whipping pipe and the restraint. The third stage is the qualification of the restraint.

The second stage, the pipe whip analysis, is described in Section 5.2. For the first and third stages, linear and nonlinear analyses were performed for restraints impacted after a LOCA. In general, these analyses were performed using conservative, simplified models. Where the response of restraints was not clearly within the range required for qualification, more detailed finite element models were developed using EDS-SNAP[9] and PWHIP[13], and qualification was based on analyses of these models. A complete description of the models developed for each plant is included in Appendix G, together with a description of each restraint and a review of the effective stiffness and mass formulation.

In this section, the evaluation of the response of the pipe whip restraints to the applied LOCA loading is discussed. Conclusions as to the adequacy of the pipe whip restraints are presented in Section 10.8.

6.8.2. Loading

The loading on an individual restraint is dependent on the properties of the restraint, the piping geometry, and the blowdown force. Generally, the load increases with the stiffness of the restraint, with the size of the gap between the pipe and the restraint, and with the blowdown force. The loading is rapid, and induces very high material strain rates.

The loading on each restraint was determined by pipe whip analyses taking into account all of the above effects. The peak loads from the resulting time histories are summarized in Section 9.8. For qualification, these peak loads were applied statically.

6.8.3. Plant-Specific Evaluation

6.8.3.1. Oconee

Two restraints are active in stopping the hot leg. The first and principal restraint is a large, multi-plate, steel bumper which is clamped around the lower hot leg elbow. Pipe motion causes this restraint to move against the steam generator. Loads are carried by direct compression in the steel plates. The second active hot leg restraint is a collar-type restraint located above the bumper restraint. Loads are transferred into the fuel canal walls by tension in this restraint.

There is also a restraint on the first cold leg elbow outside the cavity wall. This restraint was considered to be failed, and unable to stop the cold leg. As this was directly accounted for in the determination of the break opening area, detailed evaluation was not required.

Hot Leg Bumper Restraint - this restraint was analyzed for the peak loads resulting from the nozzle and elbow breaks. The highest YZ shear loads for elements 7, 8 (see Figure G-2) occur for a break at the hot leg elbow, while the remaining peak element loads are due to a hot leg nozzle break. Thus, the loading assumed for qualification is an envelope, and is conservative.

Hot Leg Collar Restraint - the peak load on this restraint arises from a break at the hot leg elbow, which causes the restraint to go into tension.

Cold Leg Restraint - this restraint was modeled in the ANSYS pipe whip analysis (Section 5.2), but was found to take loads exceeding its ultimate strength of 2400 kips. It was considered failed, and the cold leg break therefore assumed to be 2.0A.

6.8.3.2. Three Mile Island 1

One seven-element U-bar restraint is active in stopping the hot leg. The peak load, both on the restraint and on an individual U-bar element, is caused by a break at the hot leg nozzle. Both the total load on the restraint and the loads on individual components such as bars, clevises, pins, and brackets were considered for qualification.

The bearing stresses exerted by the four-inch diameter A490 pin against the A36 bracket plate caused the bracket plate to be the critical component of the restraint. Calculations based on a nominal bearing area indicated a stress over $0.90S_y$. As yielding and distortion of the hole in the bracket plate will thus occur, a detailed finite element model of the plate was developed, using the computer program EDS-SNAP. The model is described in Appendix G.

Analysis using this model showed onset of significant yield at a load of approximately 1000 kips per bracket plate. Hole distortion of 0.1 inches occurs when tensile elongation reaches the allowable strain limit. Based on the ultimate bearing capacity formulae specified in Section 7.1, failure of this bracket would be by large-hole distortions, not by shear-out failure. The finite element analysis confirmed this. The three-inch thick bracket is not susceptible to buckling failure.

At the tensile strain limit for the A36 steel bracket, the allowable load per bracket was determined to be 1125.9 kips (or 2251.8 kips for each of the seven U-bar elements in the restraint). The maximum load applied to the restraint is given in Section 9.8.

All components other than the bracket plate were evaluated to individual U-bar and combined loads higher than those given in Section 9.8. Under these higher loads, their response meets the acceptance criteria. Thus, detailed evaluation of the restraint for the actual loads was not necessary.

6.8.3.3. Three Mile Island 2

The Three Mile Island 2 pipe whip restraint is a seven-element U-bar restraint of similar configuration to that for Three Mile Island 1. The peak load on this restraint was for a break at the hot leg nozzle, while the peak load on an individual U-bar element was for an elbow break.

As for Three Mile Island 1, both the total load on the restraint and the individual loads on its constituent elements were considered for qualification. All elements qualified to the loads derived from the pipe whip analysis, with the exception of two individual U-bar elements.

Using the peak load derived for the lowest bar in the assembly, the peak strain was shown to reach 9 percent, exceeding the allowable of 5.75 percent. However, further analysis showed that, in order for this outermost U-bar to be strained to this extent, compatibility required that considerable load redistribution to other U-bars in the restraint occur. Thus, a check was made to ensure that the restraint as a whole had enough energy-absorption capacity to stop the pipe, with a factor of safety of 2.0 against failure. Assuming each bar could be strained to its qualification limit (5.75 percent), the ratio of the required energy absorption capacity to the allowable energy absorption capacity was found to be 0.59 for the most severe break case.

6.8.3.4 Crystal River

One U-bar restraint, similar to that described for Three Mile Island 1, stops the hot leg. The restraint is an eight-element U-bar restraint. The peak loads both on the restraint and on an individual U-bar element are those induced by a break at the reactor vessel nozzle.

The highest loaded U-bar in the restraint reaches a final strain of 3.90 percent, well within the allowable for A36 Steel. All other elements in the restraint remain elastic.

The bearing stress exerted on the 2-3/4 inch thick A-36 bracket plate by the 2-3/4 inch diameter A588 pin exceeds $0.90S_y$. Applying the criteria in Section 7.1 for ultimate bearing capacity, (for L/d ratio less than 3), showed that the allowable bearing stress is 50 percent greater than that actually applied. Evaluation of the bracket plate by this method indicates that it is adequate to carry the one time pipe whip loading.

6.8.3.5. ANO-1

One restraint acts to stop the hot leg after the postulated rupture. This is a single, U-shaped tension strap located above the elbow and fixed to the fuel canal floor. The peak loads on this restraint were induced by a break at the hot leg nozzle.

Due to the applied loading, only a slight excursion into the inelastic region occurs, resulting in stresses in the steel only marginally (approximatly 1 percent) over yield. All welds are full penetration welds, and are therfore stressed to the same values as the steel strap.

6.8.3.6. Rancho Seco

Two restraints act to stop the whipping pipe after a postulated hot leg rupture. Both are built-up, thick-plate box sections which wrap around the hot leg and are fixed to embedments in the fuel canal wall or floor. Both are tension restraints.

The restraints are loaded by both hot leg nozzle and elbow breaks. A hot leg nozzle break induces the peak loads on both the restraints.

6.8.3.7. Davis Besse-1

The Davis Besse-1 lower hot leg restraints are described in the Toledo Edison Verification Report, Docket No. 50-346, Rev. 1, dated March 7, 1980.[50]

6.9. Core Flood Line Piping

6.9.1. Introduction

An evaluation of the structural and functional adequacy of the core flood line piping was made for the asymmetric LOCA loads. Both hot leg and cold leg breaks at the reactor vessel nozzles were considered for all plants. For Davis-Besse, additional breaks at the elbows were considered. Each of the two core flood lines was evaluated for each postulated break.

Detailed models were generated and dynamic analyses performed based on the nozzle motions calculated in the reactor vessel isolated model analysis. The resulting pipe stresses and support loads were compared with the specified acceptance criteria to determine the structural and functional adequacy of the system.

The results of the analyses and evaluations presented in Section 10.9 demonstrate that the core flood line piping is structurally adequate and will remain functional after a LOCA. Core flood line piping supports for TMI-1, Crystal River and ANO-1 experienced overloads as a result of the LOCA response but this did not adversely affect the adequacy of the piping.

6.9.2. Overview

The LOCA results in a movement of the core flood line nozzles on the reactor vessel. These nozzles impose time-varying displacements on the core flood line piping system. The other piping supports, which are attached to the building structure, remain stationary during the event. The development of the displacement time histories for the core flood line nozzles is discussed in Section 5.1.8. Typical forcing functions are presented in Section 9.9.

Stresses are induced in the piping system during the LOCA event due to two efects:

1. inertial, and
2. anchor movement.

The first is a time-dependent response resulting from the inertial resistance of the system to the input motion. The stress developed in the piping components and the supports due to this inertial response is a primary stress.

The anchor movement response is a pseudo-static effect and is equivalent to the response assuming that the reactor vessel displacement is slowly applied, or that the piping has zero mass. The stress developed due to this response is secondary for the piping components and primary for the supports.

In addition to the LOCA loading, sustained loads due to internal pressure, deadweight, and thermal expansion were considered for analysis. The pressure and deadweight stress is primary for both piping and supports. The expansion stress is secondary for the piping and primary for the supports.

6.9.3. Analysis

A finite element model for at least one of the two core flood line systems for each plant was developed. Both core flood line systems for TMI-1, Crystal River and Oconee were modeled. Each model included the main core flood line from the reactor pressure vessel nozzle to the core flood tank and the decay heat removal branch line, which is connected to a containment penetration. A description of the finite element models is contained in Appendix H.

A linear elastic dynamic analysis was performed with the SUPERPIPE program for each core flood line model using the response spectrum method. In this method, the inertial response was computed by a multiple response spectra input analysis. The acceleration response spectra at the core flood nozzle were used as the forcing functions; all other supports remained stationary. The responses of the system were combined by absolute summation for the directional components. The modal combination was performed by SRSS, with closely spaced modes (within 10 percent) grouped and combined by absolute summation. The anchor movement response was computed by a static analysis using the maximum displacement and rotation at the core flood nozzle. The response to the individual components of anchor movement were combined by absolute summation. The effects of anchor movement were combined with the inertia effects by absolute summation for calculation of support loads.

The results of these analyses, which are summarized in Table 10.9-1, indicated similar basic response characteristics for all lines. The maximum piping stresses typically occurred in the first span from the reactor vessel, and in some cases slightly exceeded the allowable values. The stress at locations remote from the reactor vessel were typically low. The supports near the reactor vessel were highly loaded and in some cases, depending on support orientation relative to the input motion, exceeded the capacity of the supports.

Primary stresses were evaluated using Equation 9 of NB-3650 (Reference 11) according to Level C limits. The secondary stress due to anchor movement effects were evaluated relative to 3Sm. The allowable support capacity for each support was set at the yield load. For rigid supports loaded axially, the yield load was defined as that load for which the membrane stress equaled the yield stress; for rigid supports loaded in bending, the yield load was defined as the plastic moment capcity of the section. For snubber supports, the yield load could not be explicitly determined; therefore, the capacity was set at a factor of 2.05 times the rated design load. The factor on the design load capacity was established based on data in Reference 49, which provides "one-time" load ratings applicable to Level C conditions.

Review of the results indicated that high secondary stresses were being predicted due to the artificially high restraint stiffness of the supports near the reactor vessel which were loaded above their capacity. In actual service, the overloaded supports would yield, their stiffness would decrease and the secondary piping stress would be lower than predicted. However, at the same time, the primary piping stress and loads on adjacent supports would possibly increase above the predicted levels. Therefore, analysis was performed in order to account for this effect and to conservatively envelope the piping response considering the overloaded supports. The analysis was performed using the response spectrum method previously described, with the overloaded supports removed from the model.

The results of these analyses, which are summarized in Table 10.9-2, demonstrated the primary and secondary piping stresses to be within acceptable levels for all plants. For some plants, however, support load continued to be unacceptably high. The principal reason for the high loads was the

conservatism of the response spectrum method. Therefore, in order to obtain the most realistic evaluation of the core flood line response, a linear elastic time history analysis was performed to preserve the correct phase relationship of the individual load components with the modal response of the piping.

The time history analysis was performed for Oconee, TMI-1 and Crystal River. For these analyses, the modal superposition method was used. All modes up to 33 Hz were considered with a missing mass correction applied to account for the higher frequency modes. The time history analyses from TMI-1 and Crystal River were performed with the overloaded supports conservatively removed from the model, as they undergo significant yielding during the event. Oconee had no overloaded supports.

The results of these analyses, which are summarized in Table 10.9-3, verify that significant load reductions are achieved when time history analysis is used instead of response spectrum analysis. The piping stresses and support loads are acceptable.

6.9.4. Qualification

Qualification of the core flood line piping systems for the asymmetric LOCA load effects is established by comparison of calculated loads and stresses to allowable values prescribed in Section 7. Not all systems are explicitly analyzed; therefore qualification of unanalyzed lines is established by comparison with similar lines which were analyzed for similar loadings. The following discussion presents, for each plant, the evaluation and basis for qualification of the core flood line piping. Tables 10.9-1, 10.9-2 and 10.9-3 summarize the maximum stress/load ratios for all plants.

6.9.4.1. Oconee

Loop A was analyzed for both hot and cold leg breaks using the response spectrum method. The results of this analysis showed that the maximum primary piping stress and support load exceeded the allowables. In order to verify the acceptability of the loop, time history analysis was performed to eliminate excessive conservatism. The maximum pipe stress and supp t load ratios were thereby demonstrated to be accpetable.

Loop B was analyzed for the cold leg break using the response spectrum method of anlysis. The hot leg loads were enveloped by the cold leg case. The results showed the maximum pipe stress ratio to be acceptable. There are no intermediate supports on this line.

6.9.4.2. Three Mile Island 1

Loop A was initially analyzed using the response spectrum method for both hot and cold leg breaks. The pipe stresses were acceptable, with the maximum ratio occuring for the cold leg break. However, the first support was loaded significantly above its capacity for both breaks with the cold leg break governing. Therefore, both breaks were reanalyzed using the response spectrum method with the overloaded support conservatively removed. Piping stresses and support loads were shown to be acceptable. Additionally, the cold leg break case was analyzed without the overloaded support by the time history method. This analysis showed significant reduction in both the piping stresses and support loads.

Loop B was also analyzed using the response spectrum method. Piping stresses were acceptable with the maximum ratio occuring at the second elbow for the cold leg break. The supports were acceptable for the cold leg break but were significantly overloaded for the hot leg break. Therefore, the hot leg break was reanalyzed, conservatively deleting the overloaded supports. A time history analysis was performed for hot leg break without the overload supports. This analysis showed significant reduction in both the piping stresses and support loads.

6.9.4.3. Crystal River

Loop A was initially analyzed using the response spectrum method for both hot and cold leg breaks. The pipe stresses were acceptable with the maximum ratio occurring for the hot leg break. However, the fourth snubber support was loaded above its capacity for both breaks. Therefore, both breaks were reanalyzed using the time history method.

Loop B was also initially analyzed using the response spectrum method for both hot and cold leg breaks. The pipe stresses were acceptable, however the second and fourth snubber supports were loaded significantly above the allowable. Therefore, the line was reanalyzed for both breaks by the time history method conservatively removing the overloaded supports. Piping stresses and support loads were shown to be acceptable.

6.9.4.4. ANO-1

Loop A was analyzed for both break cases by the response spectrum method. The first support, a cantilevered wide flange beam was loaded above its plastic moment capacity. Reanalysis for both break cases by the response spectrum method without the failed support showed the piping stress and remaining support loads to be acceptable. Time history analysis would further reduce the loads and stresses.

Loop B was not specifically analyzed. This loop is similar to the ANO-1 Loop A and the Oconee Loop A which has significantly higher input loads. Therefore, the Loop B loads and stresses were enveloped by these lines and are acceptable.

6.9.4.5. Rancho Seco

Loop A was not specifically analyzed. This loop is similar to Rancho Seco Loop B and Oconee Loop A, which has similar input loads. Therefore, the Loop A loads and stresses are enveloped by these lines and are acceptable.

Loop B was analyzed by the response spectrum method for both hot and cold leg breaks. The piping stresses and support loads are acceptable except for one snubber support on the decay heat line for the hot leg break. This is considered acceptable since time history analysis would be expected to reduce the loads based on the load reductions experienced for Oconee, TMI-1 and Crystal River with time history analysis.

6.9.4.6. Davis-Besse

Loop A was analyzed by the response spectrum method for both hot and cold-leg breaks, for both nozzle and elbow break locations. Piping stresses and support loads were acceptable.

Loop B was not specifically analyzed. This loop is similar to Loop A and therefore is acceptable based on the margins determined for Loop A using the conservative response spectrum method.

6.10. Reactor Cavity Walls Evaluation

6.10.1. Introduction

The reactor cavity walls (also called primary shield walls or reactor subcompartment walls) are 5-foot-thick reinforced concrete cylinders which surround the reactor vessel. A gap of three and one-half feet separates the reactor vessel from the inner face of the cavity wall. The principal function of the cavity wall is to provide radiation shielding during plant operation. On one plant (Davis-Besse), the wall also serves as support for the reactor vessel under both dead weight and LOCA reaction load conditions.

Under LOCA loading conditions, the cavity wall acts as a partial pressure retaining boundary. After the LOCA event pressure loading subsides, the wall must remain integral and be able to withstand all subsequent loads.

The analysis of the reactor cavity walls is a two-stage process. First, pressures inside the cavity wall are generated using the CRAFT2 code, as discussed in Section 4.3. Secondly, the pressures corresponding to actual break sizes are applied to the EDS-SNAP cavity wall models, as discussed in Section 5.3.

Conclusions as to the adequacy of the cavity walls are presented in Section 10.10.

6.10.2. Cavity Wall Response

The cavity wall responds as a thick-walled cylinder during the two main loading phases of the LOCA event. First, the cavity wall must withstand the peak blowdown (asymmetric) load, which is localized around the break penetration, and occurs approximately 40 milliseconds into the LOCA event. Secondly, the cavity wall must withstand the peak steady-state internal pressure, which occurs between 0.20 and 1.20 seconds into the LOCA event, depending on the plant configuration.

The cavity wall responds to the latter, generally more severe, uniform loading as a cylindrical shell. It expands in the radial direction, with the principal load resistance being provided by hoop tension. At discontinuities in the cavity wall, the load resistance mechanism is a combination of hoop tension, shear, and out-of-plane bending.

For one plant, Three Mile Island 1, hoop tension loads were large enough to cause general yielding of hoop reinforcing steel over much of the wall. A plant-specific nonlinear analysis showed that radial deflections are controlled as the vertical steel reinforcing effectively stiffens the wall after the hoop steel has yielded. Overall, all cavity walls can be considered as ductile structures and retain their functionality even after some steel yields. The post-yield behavior of the Three Mile Island 1 wall is further discussed in Section 6.10.4.2.

The main boundary discontinuities in the cavity walls are the attachments of the cavity wall to the pedestal below, and to the fuel canal slab above. The pedestal to cavity wall interface was assumed to be fixed for all cavity walls. Highest out-of-plane shears and bending moments occur at this location. At the interface with the fuel canal slab, only partial fixity is offered by the slab, and the shears and bending moments are typically not as high as those at the pedestal interface.

Three plants have core flood line shield walls (see Table I-1). No major out-of-plane shears or bending moments occur in the cavity walls near the interface with these walls.

The other major discontinuity in the cavity walls is the set of eight large penetrations at the nozzle belt elevation. For every plant, the hot leg and cold leg penetrations were explicitly modeled. For three plants, the smaller core flood line penetrations were also modeled.

In general, it was found that the penetration areas were not critical locations in the wall. During the LOCA event, the concrete between the penetrations resists load primarily by transferring applied pressure loads into hoop "rings" directly above or below the penetration level. Due to the low aspect ratio of the concrete between the penetrations (thickness = 5 feet,

height = 5 feet, approximately), the concrete transfers the load through "strut" action into the hoop rings above and below. Very large "diagonal tension" (or principal tension) stresses do not occur.

The compressive strut analogy is well documented.[15] As this action takes place, vertical compressive stresses occur on the inside face of the cavity wall at the penetration level, and vertical tension stresses occur on the outside face. This is equivalent to a bending moment across the section, and the concrete was qualified to take this loading.

In addition, vertical axial load, radial-vertical shear, and some minimal hoop tension occur at the penetration level. The shear capacity of the wall was determined from concrete and stirrup strengths. The capacity of the wall to resist the combined axial force and moment was determined using moment-axial force interaction curves.

During the peak blowdown load, the cavity walls behave as a combination beam and cylinder. The large thrust load in one direction pushes the entire cavity wall in the direction of the break, with peak deformations occuring at the break. Sample deformations are shown in Figure 6.10-1. In this respect, the wall is behaving as a beam, fixed at one end, partially fixed at the other end, and loaded with a point load near its center.

It was found that in the nozzle belt regions, stresses at the peak blowdown condition were of similar magnitude to the stresses at the steady-state load condition. The high bending moments at peak blowdown were replaced by high hoop tensions at steady-state. However, actual stresses in individual reinforcing bars did not change significantly between load phases.

In addition, near the break, the cavity wall distributes the peak blowdown thrust by acting as a cylinderical shell. Load is carried into hoop rings directly above and below the penetration level. Some load was also transferred into the fuel canal slab. In areas of the cavity wall more than a few feet away from the break, stress intensities were low. Thus, when evaluating the cavity wall for stresses due to the peak blowdown thrust, it was only necessary to check the stresses in the nozzle belt region near the actual break location.

For the Davis-Besse plant, the cavity wall and related structures undergo additional loading due to reactor vessel support reactions. Details as to the wall response due to these reactions are given in Section 6.10.4.7.

6.10.3. Generic Evaluation Procedure

For each plant, evaluation of the cavity walls considered all significant types of loads that the walls undergo. These loads are divided into three groups: hoop stresses, combined moment-axial forces, and shear stresses.

Materials - The concrete for the cavity walls is a high-strength material especially suited for a high-temperature environment. The concrete has a minimum specified 28-day compressive strength of 5000 psi in all plants except ANO-1, which has a strength of 5500 psi. Main reinforcing steel is specified as ASTM A615 Grade 60 on all plants except Three Mile Island 1 and Crystal River, for which steel is specified as ASTM A615 Grade 40, and Oconee Unit 1, for which the reinforcing steel is either A15 intermediate grade (f_y = 40 ksi) or A432 (f_y = 60 ksi).

For the Three Mile Island 1 plant, actual "as-built" material properties were employed. These values were 6650 psi for concrete compressive strength and 45 ksi for main reinforcing steel. The values are based upon material test results.

Hoop Stresses - The cavity walls behave as thick-wall cylinders, resisting internal pressures by hoop tension. It was assumed that the concrete cracks in the radial direction and therefore the steel must resist all hoop tension forces. Cracking of the concrete in no way impairs the strength or functionality of the cavity wall given that the reinforcing steel is sufficiently strong to resist the applied loading.

In evaluating results from elastic cavity wall analyses, yielding of hoop steel over short lengths was not considered to constitute failure or to induce excessive distortion of the wall. This is reasonable provided that the local sections over which this yielding occurs do not extend completely around a hoop or significantly up or down the wall. Further, in any local section where yielding did take place, it was verified that vertical reinforcing was

sufficiently strong to redistribute excess load to other portions of the cavity wall.

For the Three Mile Island 1 plant, extensive yielding of the hoop steel was predicted. Hence, an explicit nonlinear analysis was performed to verify that functionality of the cavity wall was maintained.

Combined Moment-Axial Forces - When the cavity wall is pressurized, moments and axial forces are induced in the wall. For walls evaluted based upon elastic analyses, vertical stresses were converted to equivalent axial forces and bending moments. To evaluate the capacity of the cavity wall for this type of loading, moment-axial force interaction curves were developed. For these curves,

$$P_o = (A_s + A'_s) \times (f_y)$$

$$M_o = f'_c \; bd^2W \; (1-0.59W)$$

$$W = p \, f_y/f'_c$$

$$\emptyset = 0.9$$

p = tension steel ratio

Implicitly it was assumed that the interaction curve is linear up to the balanced condition.

Following the above procedure for determining the interaction curve, and after calculating actual P_a and actual M_a at a section, the section was considered to be qualified if

$$\frac{P_a}{P_o} + \frac{M_a}{\emptyset M_o} = 1.0$$

P_a and M_a were calculated from the vertical stress distribution through the wall.

As discussed in Section 6.10.2, the highest moments occur at the cavity wall/pedestal interface. For sections where moment capacity was exceeded, the excess moment was redistributed as hoop forces in the cavity wall. The cavity wall was then qualified for the maximum hoop stress.

Evaluation of bending moment and axial forces in the Three Mile Island 1 nonlinear analyses followed a more direct approach. As the analysis stress results incorporate all redistribution effects due to concrete cracking and steel yielding, tensile and compressive stresses were directly compared against allowable values.

Shear Stress - Unless more detailed analyses were made, the maximum shear stress carried by the concrete, v_c, was taken to be $2(f'_c)^{1/2}$. Where reinforcing steel was found to share part of the shear load, the additional stress carried by the steel was calculated in accordance with ACI 349-76 Section 11.6, with a limit that the value $v_u - v_c$ not exceed $8(f'_c)^{\frac{1}{2}}$.

Two kinds of shear stress were checked: The first was the circumferential-vertical shear, caused by the net asymmetric thrust on the cavity wall. The wall is well reinforced for this type of shear, as main vertical and horizontal steel acts as reinforcing for this case, causing the entire cavity wall to work as a shear wall.

The second was the out-of-plane shear stress, in the vertical-radial direction. Where stirrups were placed through the wall in the radial direction, allowable stresses could exceed v_c as calculated above. This radial-vertical stress was usually found to be highest at the cavity wall/pedestal interface. If the shear stress at this interface was over the allowable, it was assumed that the excess shear was redistributed, causing higher hoop forces in the cavity wall. The cavity wall was then qualified for these higher hoop forces.

For the Davis-Besse cavity wall evaluation, additional and more detailed considerations were made in regards to the cavity wall resistance to the applied vessel support beam and LOCA ring reaction loads. These are further discussed in Section 6.10.4.7.

6.10.4. Plant-Specific Analysis

6.10.4.1. Analysis of Oconee Cavity Wall

The peak break areas for Oconee are 0.46A for a hot leg and 2.0A for a cold leg. Detailed analyses were performed for a 0.6A hot leg break and a 2.0A cold leg break. The stresses for the 0.46A hot leg break were linearly interpolated by comparing peak pressures due to 0.6A and 0.3A breaks (as cavity pressures for a 0.46A break were not generated from the CRAFT2 analyses). Analyses were performed using linear elastic models.

Figures 6.10-1 and 6.10-2 show sectional and plan views of the Oconee cavity wall deflected shapes for blowdown and steady-state loads. Largest deflections occur near the actual break, at the time of peak blowdown. This is apparent from the plan view, where it is seen that, at 33 milliseconds, the entire wall is moving in the blowdown direction.

Evaluation of stresses in the Oconee cavity wall indicated that the wall could sustain a 0.82A hot leg break without any of the qualification criteria being exceeded.

6.10.4.2. Three Mile Island 1 Cavity Wall Analysis

The actual break sizes for the Three Mile Island 1 plant are 1.295A (hot leg) and 2.0A (cold leg). Both these breaks were analyzed using a linear elastic model, as described in Appendix I, Section 3.4. Significant yielding of the steel reinforcement was predicted for the hot leg break. To accurately account for the stress redistribution resulting from inelastic behavior, a nonlinear analysis of the Three Mile Island 1 plant was performed. Results of both these analyses are detailed as follows.

Linear Analysis - For the cold leg break, a stress ratio of 1.30 over yield for a very local region was predicted by the linear analysis. This overloaded region extended approximately 60 degrees around the wall circumference, and was concentrated beneath the core flood line and cold leg penetrations. Ratios were less than 1.0 at other locations at this level, and at all

locations further than 5 feet beneath the penetration level. Ratios above the penetration level were significantly less than 1.0.

The reasons for this localized overload are twofold. First, there is slightly less steel around the four recesses in the wall. Hence, hoop tension forces cause higher stresses in these areas. Second, the wall subjected to the pressure load has a slight tendency to oval. This was partially due to the load concentrating at the cold leg penetration, and also due to the wall being stiffer near the core flood line penetrations. This stiffening was induced by the four-foot-thick fuel canal slab. The ovalling elongates the wall at the core flood line penetration area. Hence, high hoop forces are predicted at these locations.

It was concluded that the cold leg analysis results using the linear analysis were reasonably accurate, as only small amounts of load redistribution are expected from the localized yielding.

For the hot leg break, stress ratios showed overloads of 32 percent under the hot leg penetration, 40 percent under the core flood line penetration, and 20 percent under the hot leg penetration opposite to the broken pipe. The model predicted the region of overload to extend from just below the penetration level to just above the cavity wall/pedestal interface, and around the full wall circumference. Hence it is expected that significant yielding in hoop steel will occur over much of the cavity wall.

These stress ratios do not predict loss of functionality of the wall. A stress ratio of 1.40 over yield (from the conservative linear analysis) is equal to a stress of approximately 80 percent of ultimate. However, due to the yielding of the cavity wall under these high stresses, accurate assessment of the true ultimate behavior could not be adequately predicted by the linear analysis. Hence, a nonlinear analysis was performed.

Nonlinear Analysis

The nonlinear model used for analysis of the Three Mile Island 1 cavity wall is described in Appendix I, Section 3.2. This model was analyzed for pressure

loads resulting from a 1.295A hot leg break. These pressures correspond to maximum steady-state pressure at 0.1596 seconds, and were applied over the full height of the cavity wall, including the fuel canal floor and the pedestal.

The nonlinear cavity wall analysis included an evaluation of first cracking of the concrete, radial crack propagation, yielding of both hoop and vertical steel, and the cavity wall's behavior at maximum load. In addition, an assessment of the extent of expected concrete cover spalling was made. Finally, ductility characteristics and the functionality of the cavity wall were assessed.

First yield load is defined as the load at which first yielding of the hoop reinforcement occurred. Yielding of the hoop reinforcement is important because it is the primary load carrying mechanism after the concrete cracks. The yield load is also significant because it provides information for evaluating the ductility of the cavity wall.

The analysis indicated that as the pressure on the wall increases, the cavity wall exhibits the following behavior:

1. Cracking of the concrete begins due to applied moments at the cavity wall/pedestal interface, followed by radial cracking due to high hoop stresses in the cavity wall;
2. Yielding of the hoop reinforcement begins below the nozzle belt region, and then extend up and down the cavity wall height;
3. The vertical reinforcement carries load induced by "two way action" in the cavity wall, particularly after hoop reinforcement has yielded.

At maximum load, cracking of the concrete spreads to the pedestal region. The total load applied to the cavity wall is resisted as follows:

1. Hoop Reinforcement (57 percent);
2. Fuel Canal Slab and Fuel Canal Wall System (18 percent);
3. Pedestal (25 percent).

Although yielding of the hoop reinforcement extended over the full height of the cavity wall, the maximum stress reached was 49 ksi (with a strain of 1.27 percent or a strain ratio of 0.34). It is noted that this is 17 percent lower than peak hoop stress (58 ksi) predicted by linear analysis, and verifies that load redistribution is significant at maximum pressurization. Based upon a yield stress of 45 ksi (as described in Appendix I), the peak stress ratio is 1.09. Thus, both stress and strain criteria indicate the wall is well below ultimate strength. Further, the strain ratio drops to 0.06 just above the pedestal/cavity wall interface, and the hoop reinforcement in the pedestal region remains elastic. Figure 6.10-3 shows the pressure versus strain variation for the maximum strained hoop reinforcement.

Maximum radial displacement of the cavity wall is 1.91 inches, and occurs below the nozzle belt region. Deflected shapes of the cavity wall are shown in Figure 6.10-4. Crushing of the confined concrete is not expected to occur. The concrete cover at the inside face of the wall is predicted to have the highest compressive stress. Conservatively, the concrete cover's strength was assumed to be 85 percent of the uniaxial strength, or 5650 psi. Maximum stress in the concrete cover is predicted to be 4140 psi, giving a stress ratio of 0.73. Therefore spalling of the concrete cover is not expected to occur.

As expected, the most significant cracking of the wall occurred in the radial direction. It is considered that these cracks would close at least partially as the pressure inside the wall is dissipated. This has been confirmed in experimental tests[19] performed on reinforced concrete containment models. However, complete closure of the cracks is not expected due to the residual strain of the hoop reinforcement.

Ductility Considerations - The ductility of the cavity wall has been experimentally verified by tests performed on small scale models of reinforced concrete containment vessels under internal pressure.[19,47,48] These tests have shown that failure of the vessels does occur in a ductile manner. This is due to the presence of both hoop reinforcement and vertical reinforcement, providing two redundant load carrying systems, each capable of substantial deformation before failure.

Based on the ratio of radial displacement at first yield of the hoop reinforcement to the radial displacement at maximum load, the nonlinear analysis predicted a ductility ratio of about 7.8.

Functionality - In assessing the cavity wall functionality after a 1.295A hot leg break, consideration is given to the extent of concrete damage and yielding of the reinforcing steel.

1. Extent of concrete damage: The major cracks in the cavity wall are expected to be in the radial direction. These cracks will likely follow the vertical reinforcement pattern. Crushing of the concrete is not expected to occur. Some minor and localized spalling of the concrete cover may occur in regions of weakened concrete.
2. Extent of yielding of the reinforcing steel: The reinforcing steel in the hoop direction is expected to yield over the full height of the cavity wall. In the pedestal region, with the exception of one layer of steel, all hoop reinforcement remains elastic. Yielding of the vertical reinforcement occurs at midheight on the outside face of the cavity wall and at the pedestal/cavity wall interface. However, no pulling through of the bars due to bond failure is expected. Maximum strains in the hoop and vertical reinforcement are 1.27 and 1.42 per cent, respectively.

Based on the above assessment, the wall is considered adequate to withstand the prescribed hot leg LOCA loading. Maximum radial displacements are less than 2 inches, and the wall remains integral through the event.

6.10.4.3. Analysis of Three Mile Island 2 Cavity Wall

The Three Mile Island 2 cavity wall model was analyzed for the following hot leg break sizes: 2.0A, 1.5A, 1.0A, and 0.6A. The model was also analyzed for the cold leg 2.0A break. Two pressure load sets were chosen for each break size, as follows:

1. Pressures corresponding to t = 0.0456 seconds (both hot and cold leg breaks). This corresponds to the peak asymmetric thrust acting on the wall in the direction of the break, as discussed in Section

5.3.3. Stresses resulting from these loads were increased by a dynamic load factor of 1.15.

2. Pressures corresponding to t = 0.5396 and 0.4896 seconds, for the hot and cold leg breaks, respectively. This corresponds to the maximum steady-state pressure over the cavity wall. In general, it was found that stresses due to this load condition control the qualification of the wall.

Analyses were performed using the computer program EDS-SNAP. Due to the size of the actual breaks, and the results of analyses performed for other plants, an orthotropic material law was used. Further discussion of orthotropic behavior is found in Section 6.10.4.5. For the hot leg break, the maximum outward radial displacement of the cavity wall was 0.3 inches, and occurred at the break region after 0.5396 seconds. The corresponding maximum displacement for the cold leg break was 0.11 inches. Figures 6.10-5 and 6.10-6 show the deflected shape of the wall under both load cases (1) and (2) for the hot leg break.

Stresses at various locations in the cavity wall due to the hot and cold leg breaks are tabulated in Tables 10.10-7 and 10.10-8.

For both hot and cold leg breaks, excess shear loads were redistributed at the bottom layer of the cavity wall, resulting in increased loads on the hoop steel. The stress values in Table 10.10-7 reflects this. In addition, due to the hot leg 1.71A break, some yielding of vertical steel is expected at the cavity wall/pedestal interface. The excess moment was resolved by appropriately increasing hoop tensions in the lower part of the cavity wall. These local overstresses in the secondary load carrying systems do not impair the functionality of the wall.

In conclusion, the Three Mile Island 2 cavity wall has sufficient strength to safely withstand the effects of the hot leg or cold leg LOCA pressure loadings.

6.10.4.4. Analysis of Crystal River Cavity Wall

The cavity wall model developed for the Crystal River plant is discussed in Appendix I. Detailed analyses were performed for the hot leg 1.0A and 2.0A

breaks, and for the cold leg 2.0A break. Six load steps were analyzed for each break size. Three steps were for pressure loadings near 40 milliseconds and three steps were for loadings near 160 milliseconds. The first three steps correspond to the peak blowdown thrust, and the latter three steps correspond to the peak steady-state load. The loading is shown in Figure 9.10-2 and Table 9.10-1. A dynamic load factor of 1.15 was applied to the pressure loadings at peak asymmetric load.

Peak stresses in the cavity wall occurred at the steady-state pressurization and are tabulated in Tables 10.10-9 and 10.10-10. Hoop stresses are slightly below yield level both for the 1.092A hot leg and 2.0A cold leg breaks. Deflected shapes for the cavity wall are shown in Figures 6.10-7 to 6.10-9. At the pedestal/cavity wall interface, the moment capacity of the vertical reinforcing steel is exceeded. Hence, a hinge was assumed to form, with all excess moment redistributed into the cavity wall. This excess moment caused higher hoop tensions at the base of the cavity wall, but within allowables.

Checks were made for shear and moment at other locations within the cavity wall, and were found to be within allowables.

6.10.4.5. Analysis of ANO-1 Cavity Wall

The peak break sizes for ANO-1 are a hot leg 0.31A and a cold leg 2.0A. Detailed analyses have been performed for hot leg 2.0A and cold leg 2.0A break pressure loads, using the EDS-SNAP cavity wall finite element model described in Appendix I. The loads applied to the wall were comprised of a net asymmetric thrust acting on the wall in the direction of the break and a uniform pressure over the entire wall. The net asymmetric thrust reaches its peak after 44 milliseconds as shown in Figure 9.10-4. Static and dynamic analyses were performed for a 2.0A hot leg break using the orthotropic material law available in EDS-SNAP. The concrete was assumed to be fully cracked in the hoop direction, but uncracked in the vertical and radial directions. Results from these analyses indicated that little dynamic amplification takes place. This is because the lowest natural frequencies of this wall are well above the exciting frequencies of the blowdown thrust. Figure 6.10-10 shows typical time history responses of the cavity wall for nodes located immediately below

the hot leg break opening for both the ANO-1 and Rancho Seco plants. Figure 6.10-11 shows the time history base shear reactions for these plants.

Some vibration does occur in the ANO-1 wall, and from this response the frequency was determined to be over 30 Hz. For the analysis, damping was taken to be 7 percent of critical, in conformance with the NRC Regulatory Guide 1.61 value for reinforced concrete structures under SSE or design basis accident conditions. As the ANO-1 plant is isolated from surrounding structures, it has the most flexible cavity wall configuration. Thus, less vibration is expected for other stiffer cavity wall configurations.

The maximum displacement of the ANO-1 cavity wall coincides with the peak asymmetric thrust, and is approximately 0.61 inches. It occurs below the break region and is in the direction of the thrust. The maximum displacement of the wall under steady-state loading is 0.57 inches, and occurs at the same location. Figure 6.10-12 shows the deflected shapes of the cavity wall.

For the ANO-1 cavity wall, stresses used for qualification were taken from the explicit dynamic analysis. Hence, no additional dynamic load factor was applied.

The calculated stresses, as tabulated in Tables 10.10-11 and 10.10-12, indicate that the cavity wall is acceptable for the hot leg break. For the cold leg break, the wall is adequate globally, but the hoop stress ratio slightly exceeds 1.0 in one local area. This overstress occurs in the hoop steel immediately below the cold leg penetration. Further analysis showed the overstress to be localized, and the ratio drops below 1.0 within a few feet of the overstressed area. This slight local overload is not considered capable of inducing large cracks in the cavity wall.

6.10.4.6. Analysis of Rancho Seco Cavity Wall

The peak break areas for Rancho Seco are a hot leg 0.679A and a cold leg 2.0A. Detailed analyses have been performed for hot leg 2.0A and cold leg 2.0A pressure loads. Loads applied to the Rancho Seco wall are shown in Figure 9.10-5. The cavity wall model is described in Appendix I.

Static and dynamic analyses were performed for a 2.0A hot leg break. Figure 6.10-10 gives the time history of the radial displacement of the wall directly below the hot leg break. Little or no vibration takes place, and the dynamic response closely match that from static analyses at equivalent time steps.

It was concluded that the lowest natural frequency of the Rancho Seco cavity wall is well above the exciting frequencies of the blowdown thrust load depicted in Figure 9.10-5. Of all cavity walls, Rancho Seco has the stiffest configuration, as the four foot thick fuel canal walls extend almost to the pedestal, significantly stiffening the cavity wall. As is discussed in Section 6.10.4.5, the ANO-1 plant has the most flexible cavity wall configuration, and yet exhibits only minor resonance effects. Hence, since all other cavity walls have frequencies between those of Rancho Seco and ANO-1, the dynamic analysis results presented herein are bounding for all plants.

From Figures 6.10-10 and 6.10-11, ANO-1 is shown to have a frequency of approximately 30 Hz, and Rancho Seco a frequency near 50 Hz. As the blowdown pulse approximates a sine-wave pulse of half period t_d = 0.06 to 0.08 seconds, then

$$1.82 = \frac{.06}{.033} \leq \frac{t_d}{T} \leq \frac{.08}{.02} = 4.0$$

From Biggs,[12] the maximum possible dynamic load factor for this load case is 1.15. This holds for all cavity walls, for both lower bound and upper bound assumptions regarding the hoop stiffness of cracked concrete. Hence the approach used to account for dynamic resonance effects in the cavity wall analyses was to perform static analysis at time of peak blowdown load, and then to apply a dynamic load factor of 1.15 to the resulting stresses.

6.10.4.7. Analysis of Davis-Besse Cavity Wall

Response due to Pressurization

For the analysis of the Davis-Besse cavity wall under pressurization, the finite element model described in Appendix I was used. The model was analyzed for one hot leg and one cold leg break case. For each break case, two

different pressure loadings were considered. All analyses utilized isotropic material laws.

Pressure loadings applied to the cavity wall were for the hot leg 1.0243A and cold leg 0.243A nozzle breaks. Unlike other cavity wall analyses, no interpolation of loadings was necessary, as the CRAFT2 analyses were for exact break sizes. Pressure loading corresponding to time of peak asymmetric blowdown loads were applied as a static pressure load to the finite element model multiplied by a dynamic load factor of 1.15 (see Section 6.10.4.6).

The hoop stresses due to tne pressure loads were integrated over the cross-sectional area of the finite element, to produce a hoop force. This hoop force was then applied to the reinforcing steel in the concrete. All hoop reinforcing steel is A615 Grade 60.

Figures 6.10-13 and 6.10-14 show the deflected shapes of the cavity wall for the pressure loads at the two time points. Time point 0.041 seconds corresponds to the peak asymmetric load, and time point 0.7396 seconds corresponds to the peak steady-state load.

Stresses and stress ratios due to these two pressure loadings are given in Tables 10.10-15 and 10.10-16.

Response due to Reactor Vessel Reactions

The cavity wall must withstand additional loadings due to support beam and LOCA ring reactions. These reaction were combined with cavity wall pressurization results. Stress ratios are given in Tables 10.10-17 and 10.10-18.

Support Beams - The support beams apply three types of loading onto the cavity wall. First, the beams transmit a vertical load into the wall, due to the reactor vessel motion. Bearing stresses are highest immediately beneath the support beams at the first set of stiffner plates, about 20 inches into the wall. Due to additional bearing plates detailed in the beam design at this location, there is a 24 by 31½ inch bearing surface between steel and

concrete. This bearing area is large enough to maintain concrete bearing stresses below allowables.

Second, due to the location of the applied vertical and horizontal loads on the support beams, moments are induced in the cavity wall. These moments are essentially resisted by tension and compression vertical reactions in the wall. These reactions are added to those in the wall due to pressurization, with resultant values still below allowables.

Third, the support beams apply horizontal thrusts on the cavity wall. In resisting these thrusts, the cavity wall was evaluated for bearing stresses and for in-plane shear failure. Bearing stresses were low and do not cause significant response in the wall. A potential shear failure surface immediately beneath and adjacent to the support beams was checked against allowable shear in concrete, based upon deep beam behavior. Additional strength due to reinforcing steel was conservatively neglected. Based on these assumptions, the stress ratios were at low levels.

LOCA Rings - In general, the LOCA ring loading on the cavity wall is a more severe load case than support beam loading. As determined in the load combinations discussed in Section 9.10, the extreme LOCA ring loads are due to the hot leg nozzle break. The following checks were made for cavity wall integrity:

1. Total thrust on the cavity wall and fuel canal floor due to combined LOCA ring horizontal reactions;
2. Local shear failures at the penetration level of the cavity wall due to individual LOCA ring horizontal reactions;
3. Cavity wall capacity to resist LOCA ring vertical loads;
4. Bearing stress failures of concrete immediately adjacent to LOCA rings.

The LOCA ring reactions caused cavity wall loading opposite in direction to that caused by pressurization. In addition, peak cavity wall stresses due to LOCA ring reactions occurred before 50 milliseconds into the LOCA event, when cavity wall stresses near the non-broken piping LOCA rings were minimal.

Thus, in evaluating wall response, stresses due to pressurization and LOCA ring reactions were conservatively uncoupled when of opposite direction.

In resisting the total thrust of the combined LOCA ring reactions, loads may be transmitted upwards into the cavity wall or downwards into the fuel canal floor. The capacity of the cavity wall and fuel canal floor to resist this load was calculated both at the asymmetric and steady-state portion of the loading. Both systems act as shear walls. Both are well reinforced, and are capable of withstanding high shear stresses. These shear stresses were qualified in accordance with ACI 349-76, Section 11.15.2. At the time of steady-state pressurization, much of the steel in the cavity wall is working in resisting hoop tensions. Hence no steel in the cavity wall is assumed effective in resisting lateral thrusts at time of steady-state pressurization. Evaluation of the cavity wall and fuel canal floor capacities indicated that peak applied thrusts (Table 9.10-3) for any break do not impose overloads.

The second load check made was for prevention of local shear failure of the concrete immediately resisting the LOCA ring reactions. The smallest concrete section occurs at midheight in the penetration level of the cavity wall. The concrete in this area acts as a corbel in carrying reaction loads upwards or downwards to the fuel canal floor and main cavity wall sections. The concrete was evaluated for corbel action, in accordance with ACI 349-76 Section 11.13. It was found that when evaluated as a corbel with a double failure surface (one failure surface just beneath the fuel canal floor, and one failure surface just at the bottom of the penetration level), substantial safety margins exist. In ensuring that the penetration level concrete does act as a corbel, qualification for induced bending moments was made. Evaluation of effects of concrete cracking at steady-state pressurization showed that while some capacity of the concrete is lost, the applied LOCA ring reactions are very much reduced. Thus, the stress ratios were most critical at the time of peak asymmetric load.

The third load check was made for LOCA ring vertical reactions on the cavity wall. The critical vertical load on the LOCA rings occurs at steady-state pressurization. Hence, induced cavity wall stresses are directly added to those due to wall pressurization. The load path in resisting these steady-state vertical upward loads causes tension in the cavity wall vertical

reinforcing. When all stresses are combined, the wall is shown to still have reserve capacity, as vertical steel is not highly stressed under pressurization loads alone.

The fourth, and most critical load check was for bearing stresses directly adjacent to the LOCA ring. While the detailed LOCA ring model evaluation predicted that about 150 degrees of the circumference of a LOCA ring would be loaded in compression (as discussed in Section 6.2), it was assumed that only 120 degrees of the ring's circumference would be totally effective in carrying bearing stresses into the concrete. In accordance with ACI 349-76 Section 10.14, a minimum of 6 inches of additional concrete on either side of the LOCA ring was assumed effective in resisting the local bearing stresses. Due to the highly confined nature of the concrete behind the LOCA rings, the 6 inch minimum was considered a lower bound. These bearing stress calculations gave the highest stress ratios of any of the load combinations for the reactor vessel reactions on the Davis-Besse cavity wall, but were still within allowables.

Figure 6.10-1. Oconee Cavity Wall Deflected Shape, Hot Leg Break 0.6A at Peak Asymmetric Load

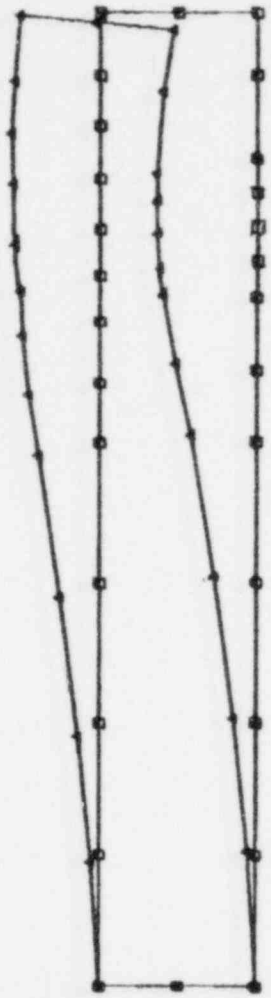

Section A-A

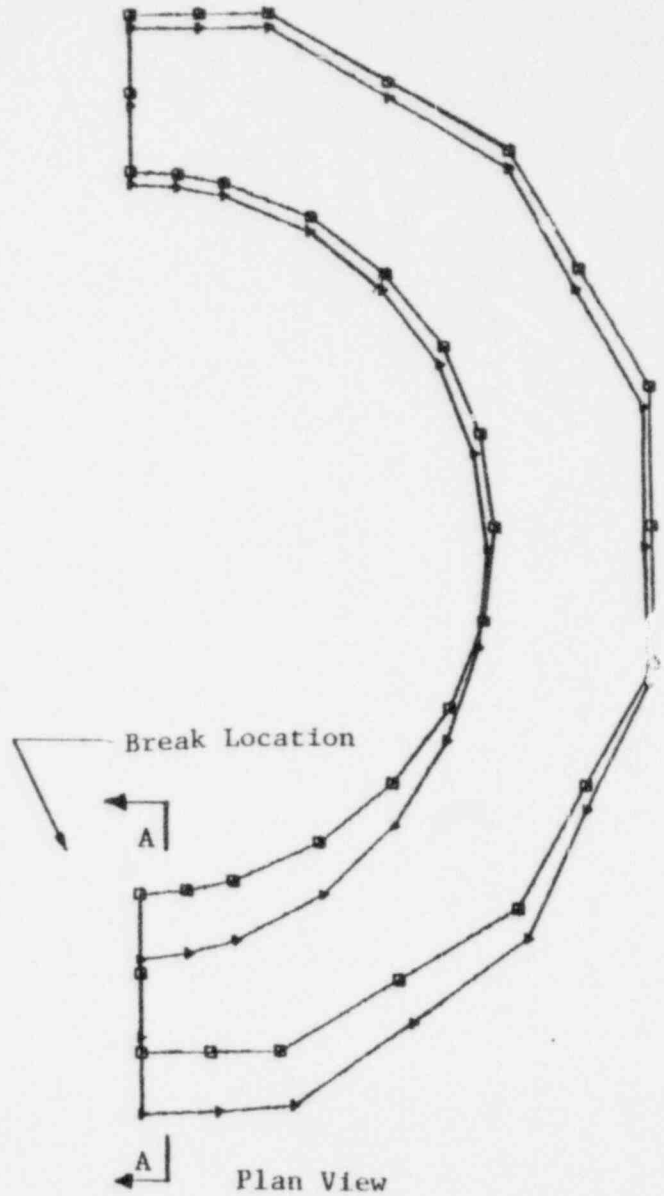

Plan View

Figure 6.10-2. Oconee Cavity Wall Deflected Shape, Hot Leg Break 0.6A at Steady State

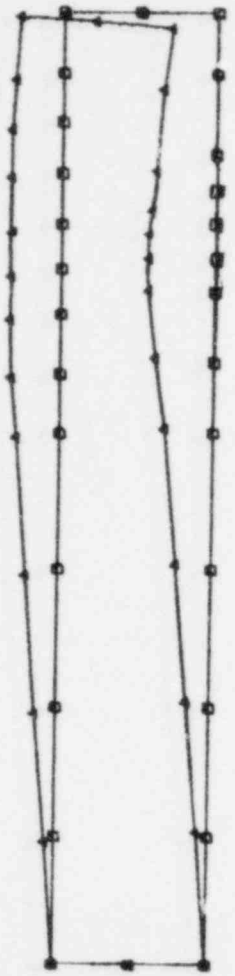

Section A-A

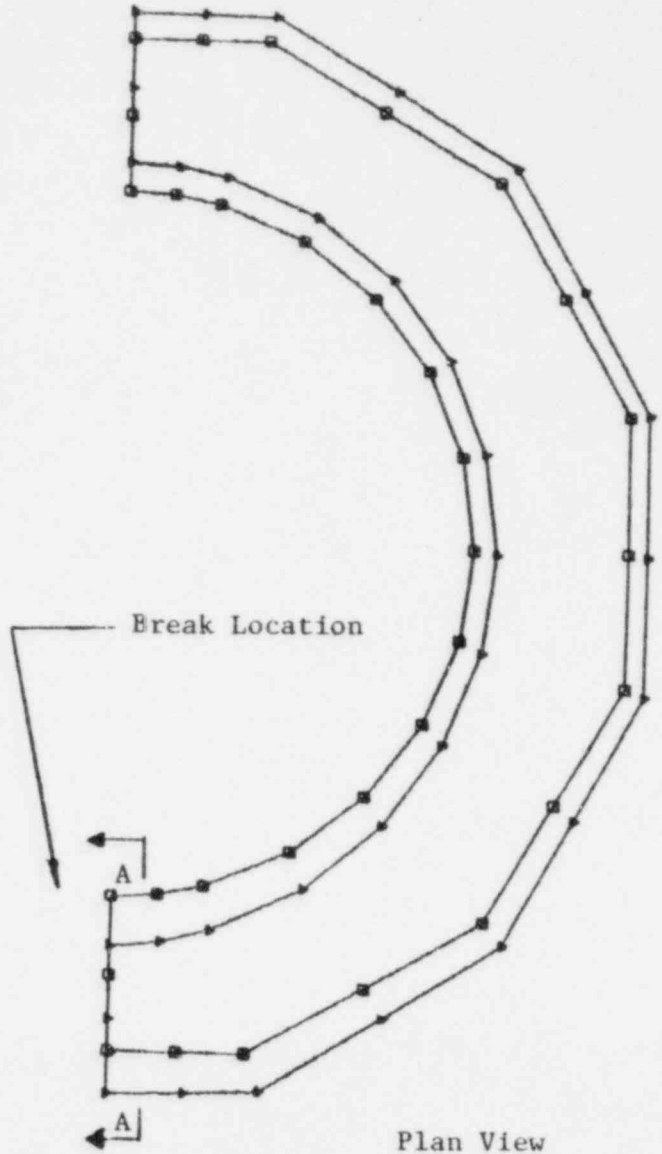

Plan View

Figure 6.10-3. Three Mile Island-1 Cavity Wall
Peak Strain in Hoop Steel

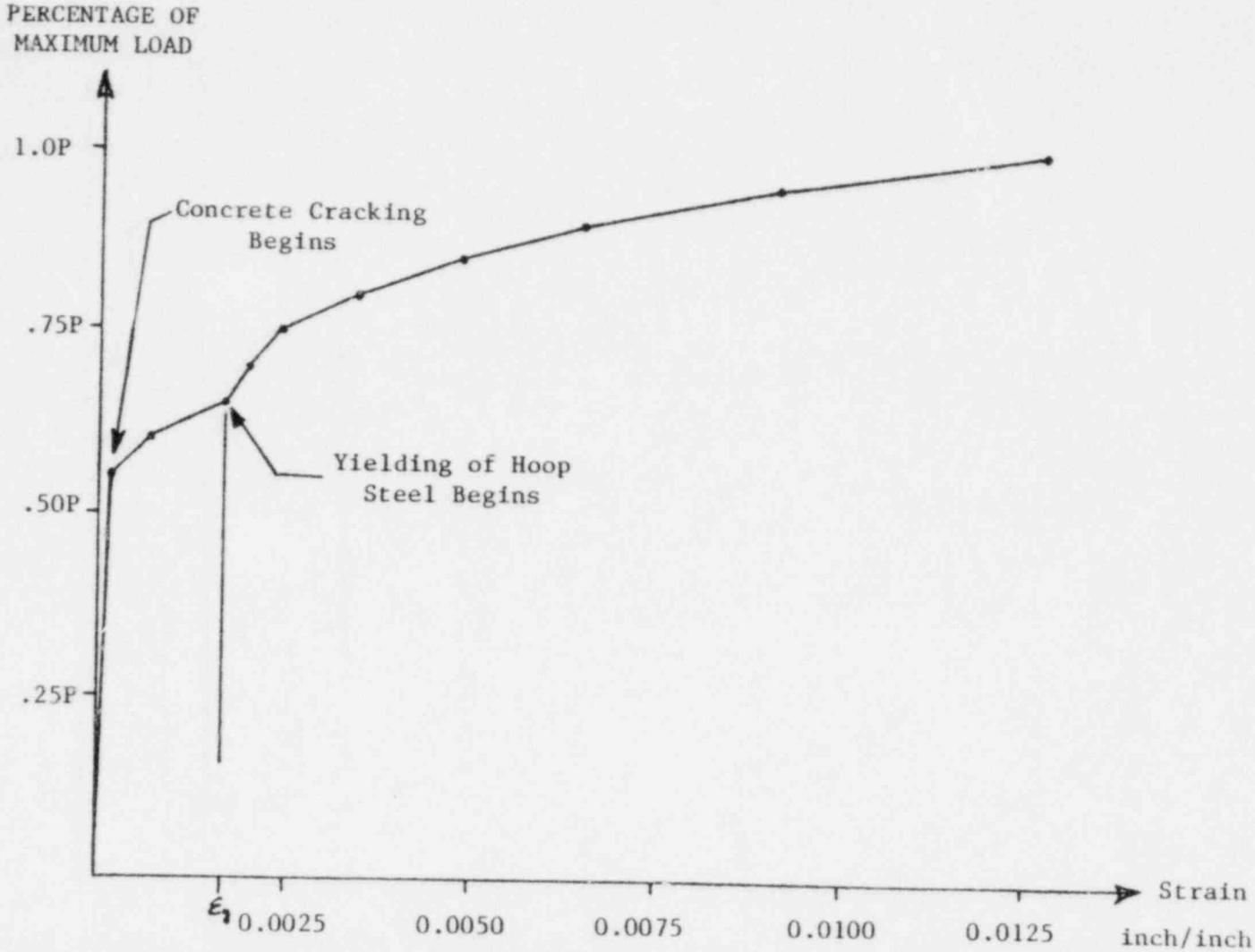

Figure 6.10-4. Three Mile Island-1 Cavity Wall Deflected Shapes

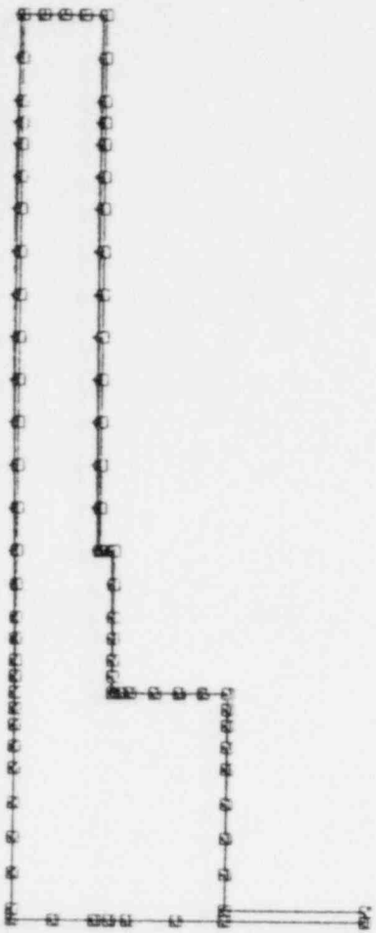

a. 0.65 Maximum Load

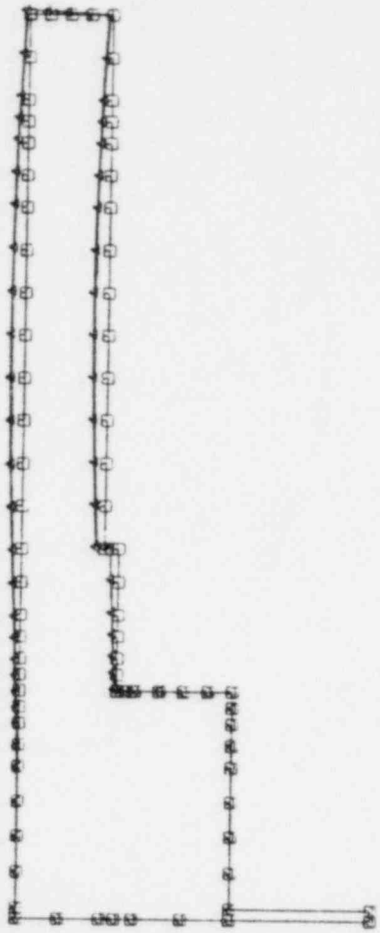

b. 0.865 Maximum Load

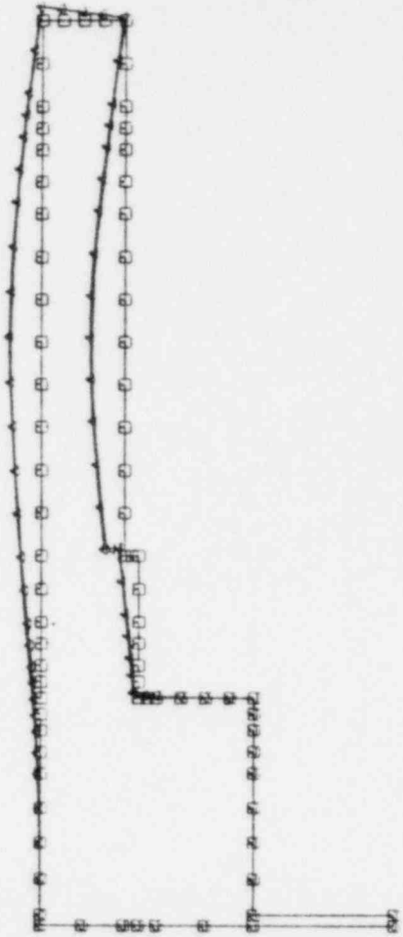

c. 1.0 Maximum Load

Figure 6.10-5. Three Mile Island-2 Cavity Wall Deflected Shape
Hot Leg Break 2.0A at Peak Asymmetric Load

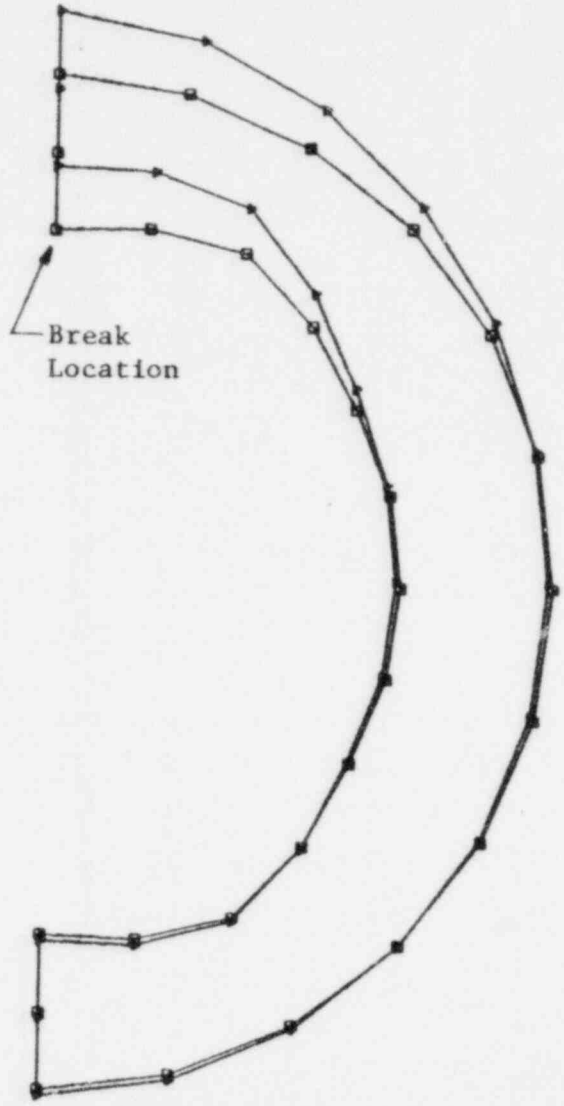

Plan View

Figure 6.10-6. Three Mile Island 2 Cavity Wall Deflected Shape, Hot Leg Break 2.0A at Steady State

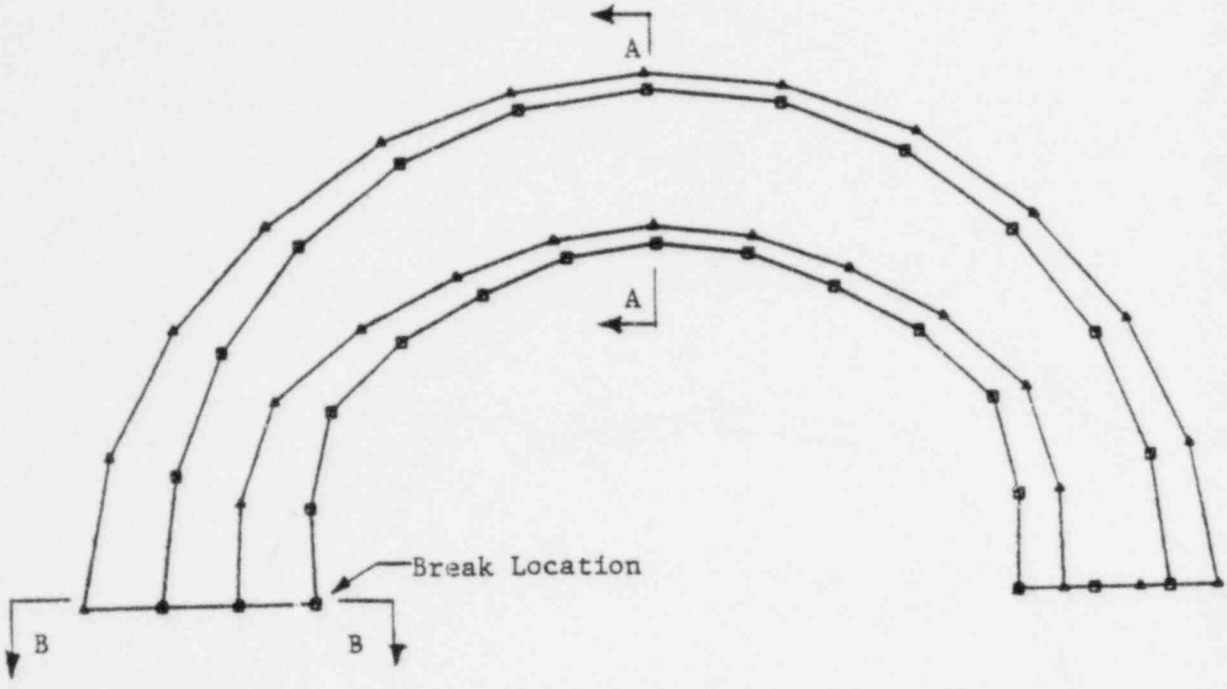

Plan View

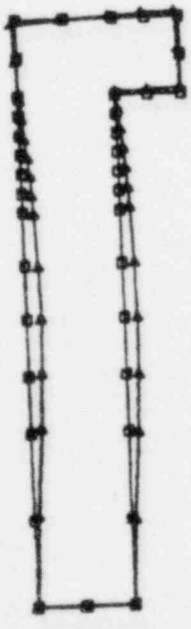

Section A-A

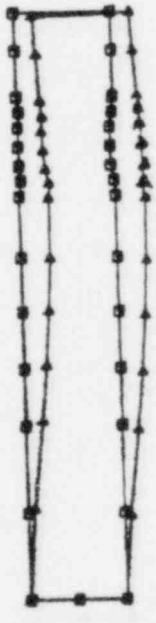

Section B-B

6.10-7. Crystal River Cavity Wall Deflected Shape,
Hot Leg 1.0A Break at Peak Asymmetric Load

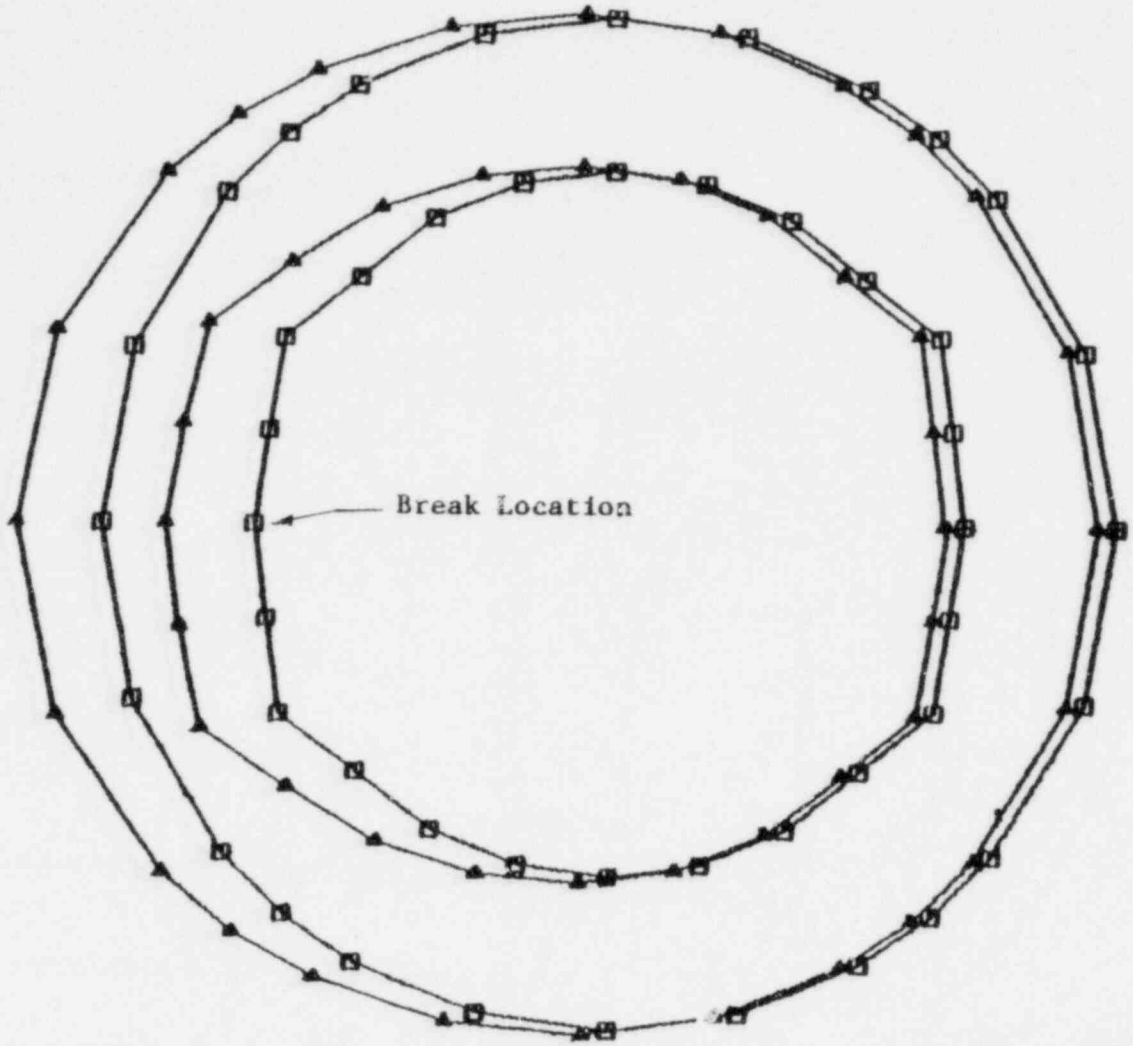

Plan View

Figure 6.10-8. Crystal River Cavity Wall Deflected Shape, Hot Leg 1.0A Break at Steady State

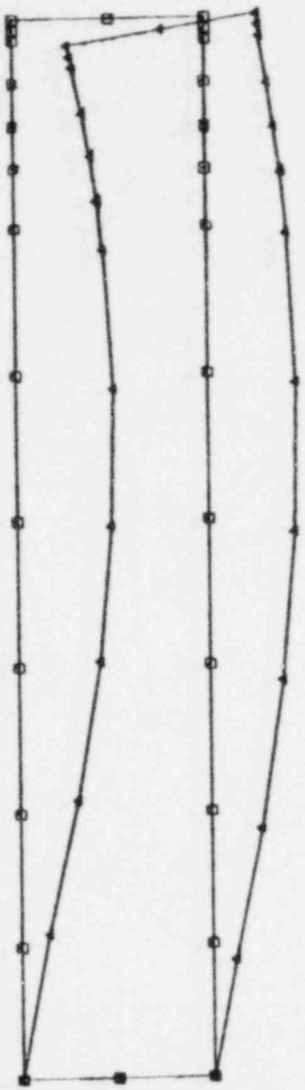

Section A-A

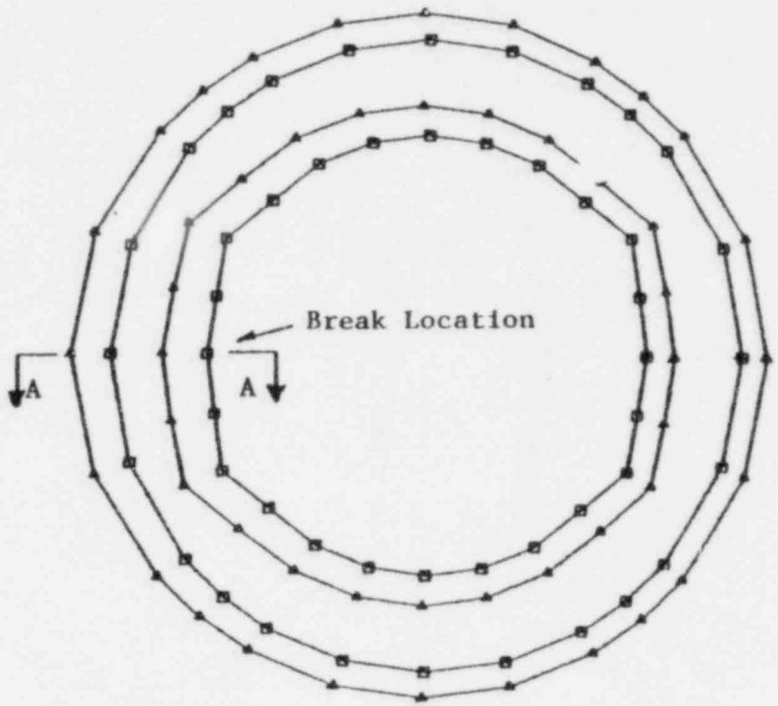

Plan View

Figure 6.10-9. Crystal River Cavity Wall Deflected Shape, Cold Leg 2.0A Break at Peak Asymmetric Load

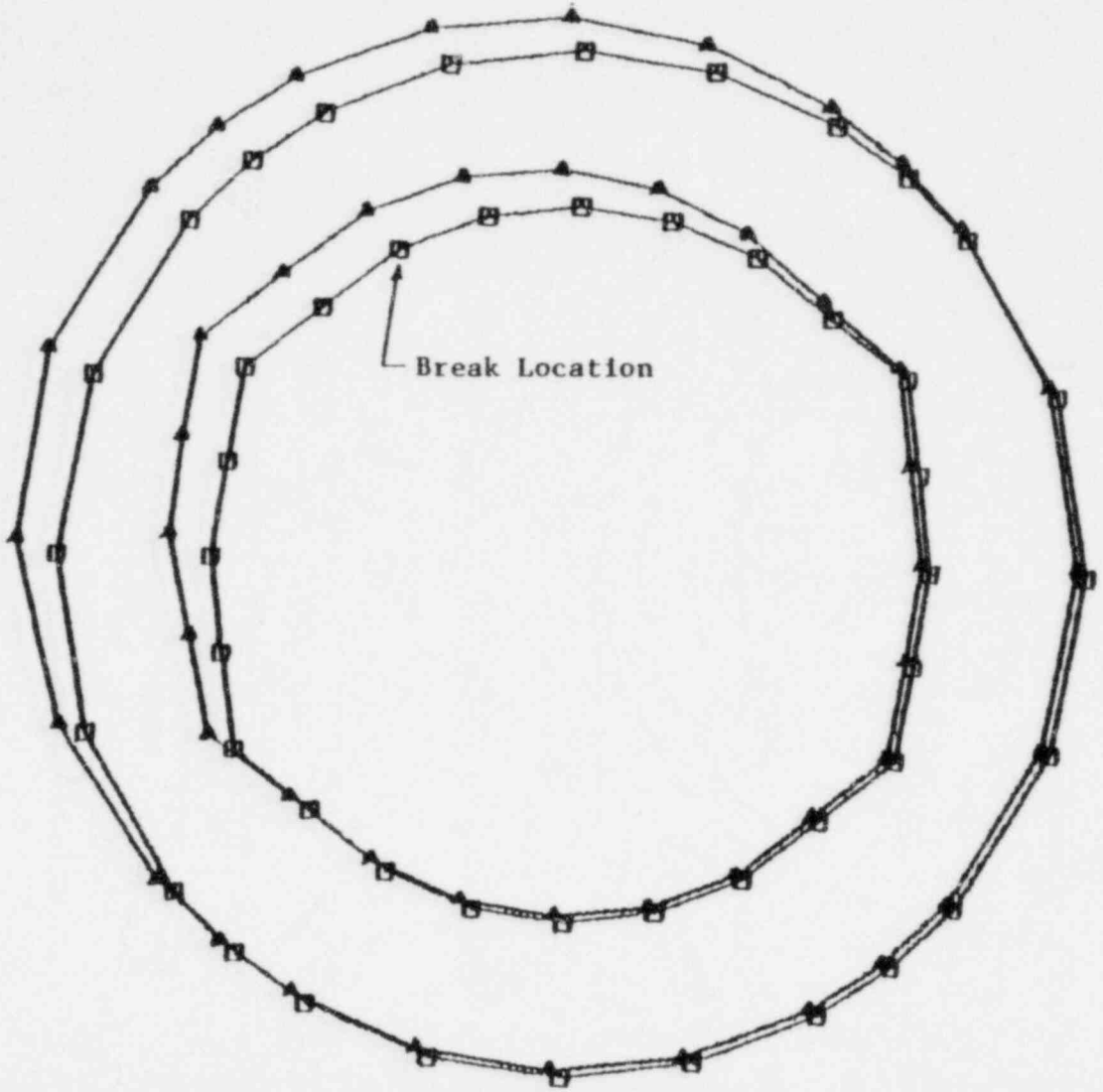

Plan View

Figure 6.10-10. ANO-1 and Rancho Seco Cavity Walls – Radial Displacements Below Penetration Level Due to Hot Leg 2.0A Break

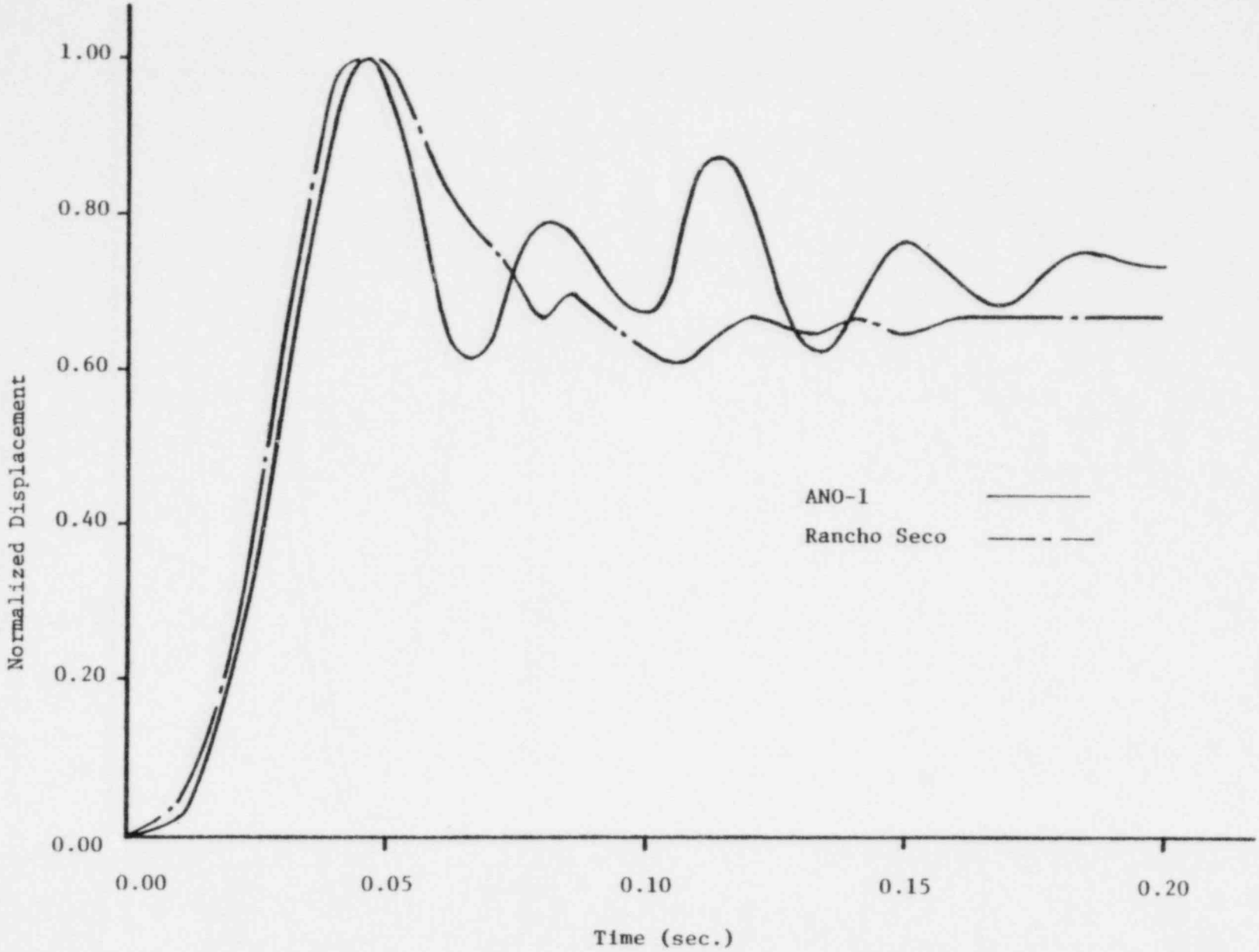

Figure 6.10-11. ANO-1 and Rancho Seco Cavity Walls — Base Shear Reactions Due to Hot Leg 2.0A Breaks

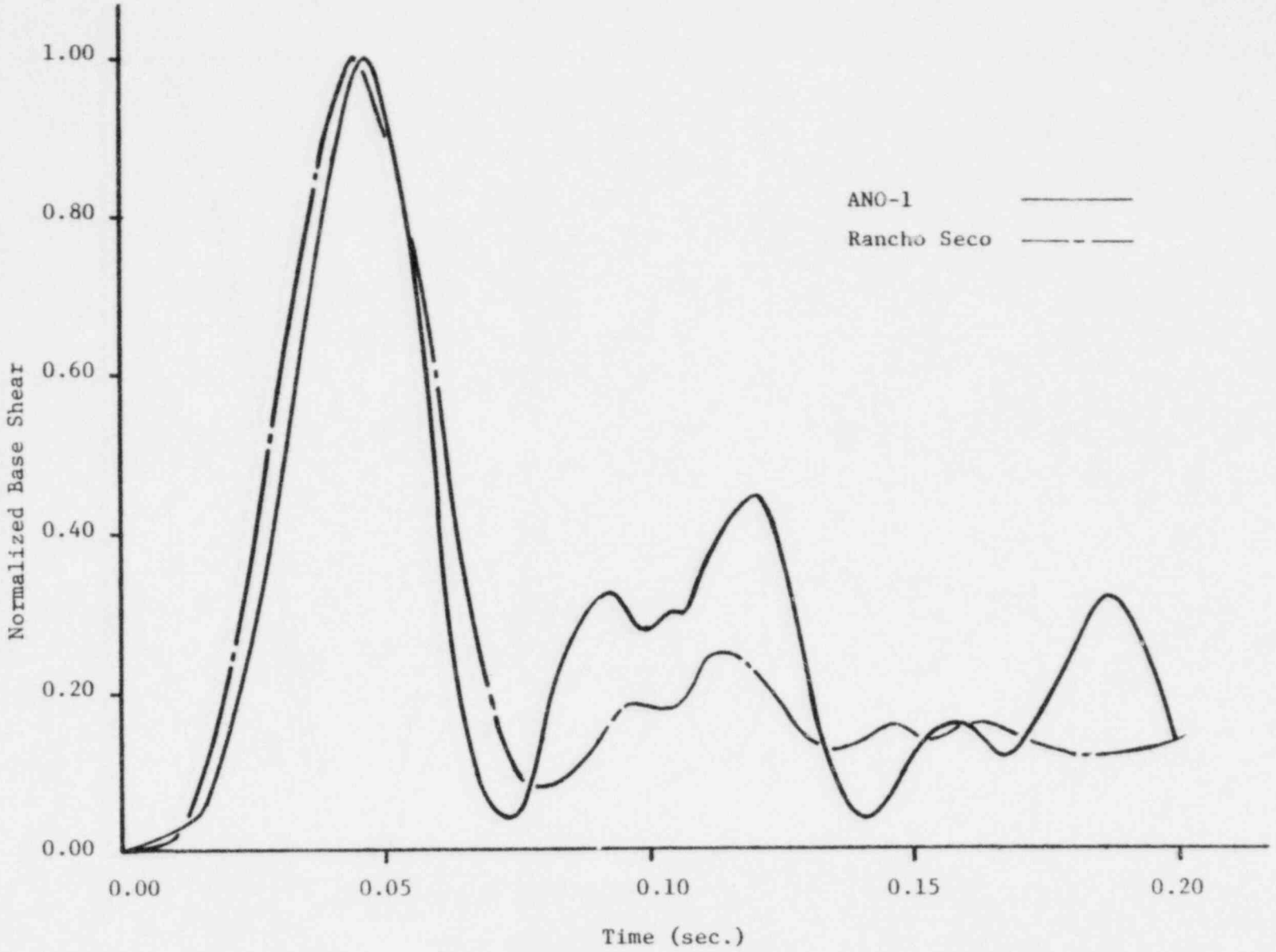

Figure 6.10-12. ANO-1 Cavity Wall Deflected Shape — Hot Leg 2.0A Break

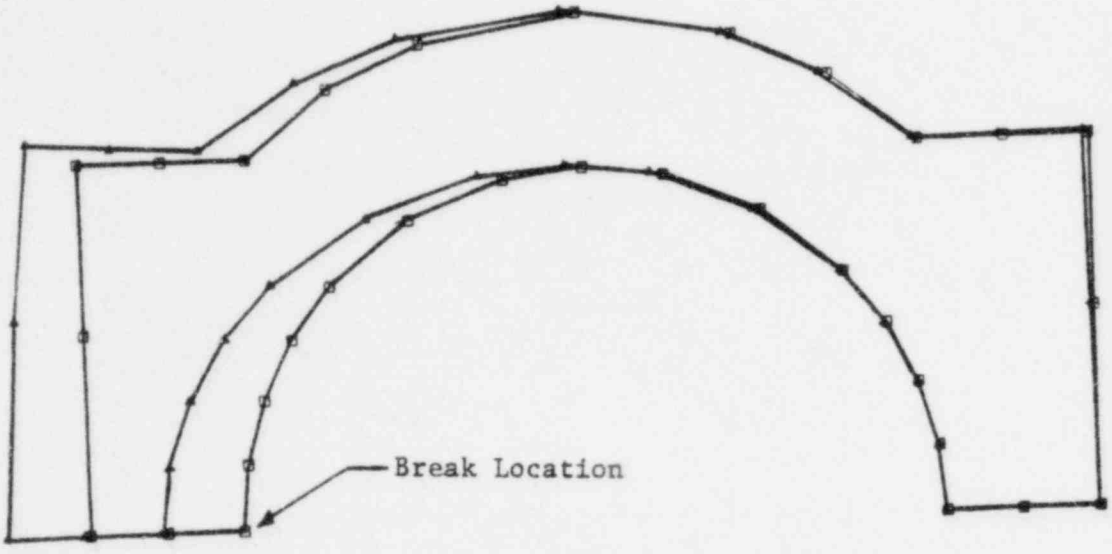

Plan View at Peak Asymmetric Load

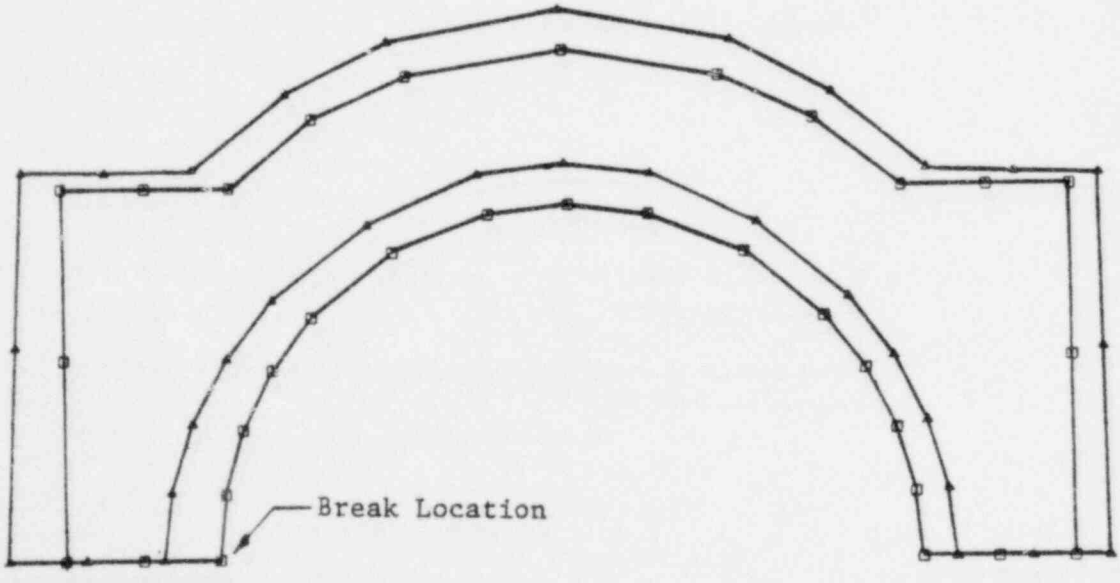

Plan View at Steady State

Figure 6.10-13. Davis-Besse Cavity Wall Deflected Shape — Hot Leg
1.0243A Break at Peak Asymmetric Load

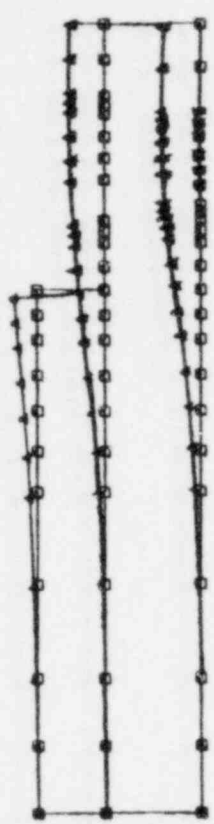

Section A-A

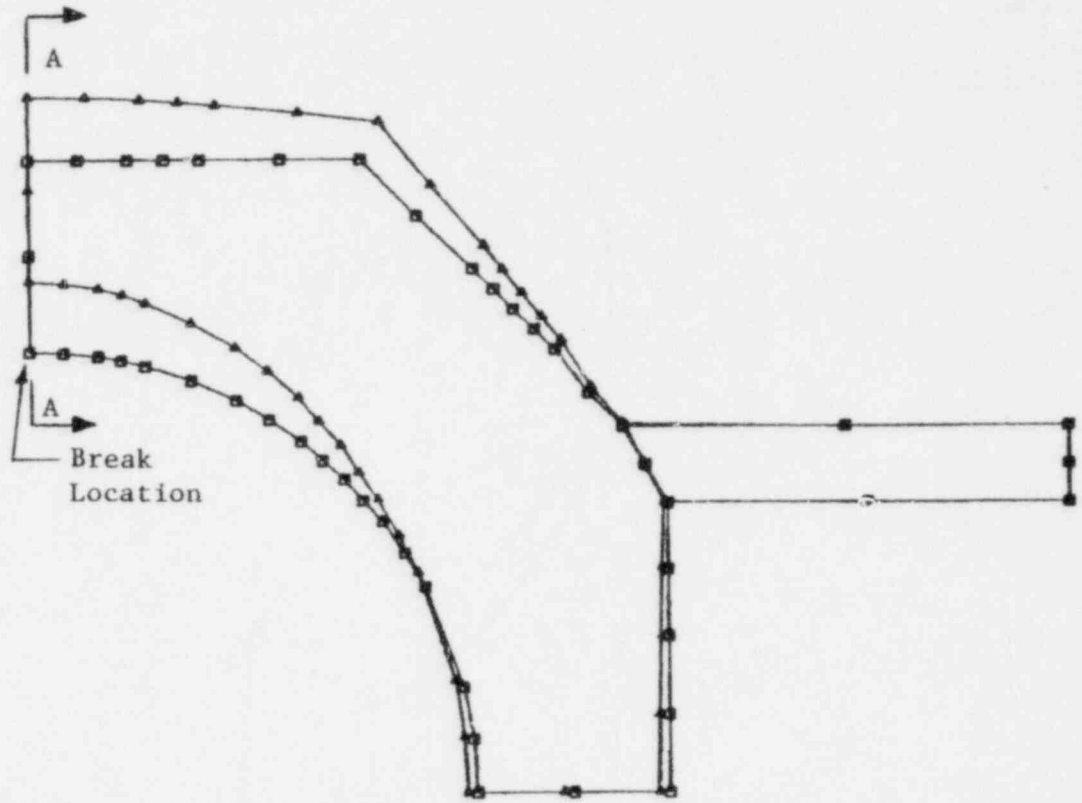

Plan View

Figure 6.10-14. Davis-Besse Cavity Wall Deflected Shape — Hot Leg Break 1.0243A at Steady State

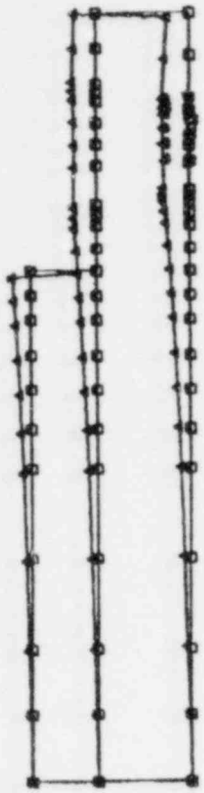

Section A-A

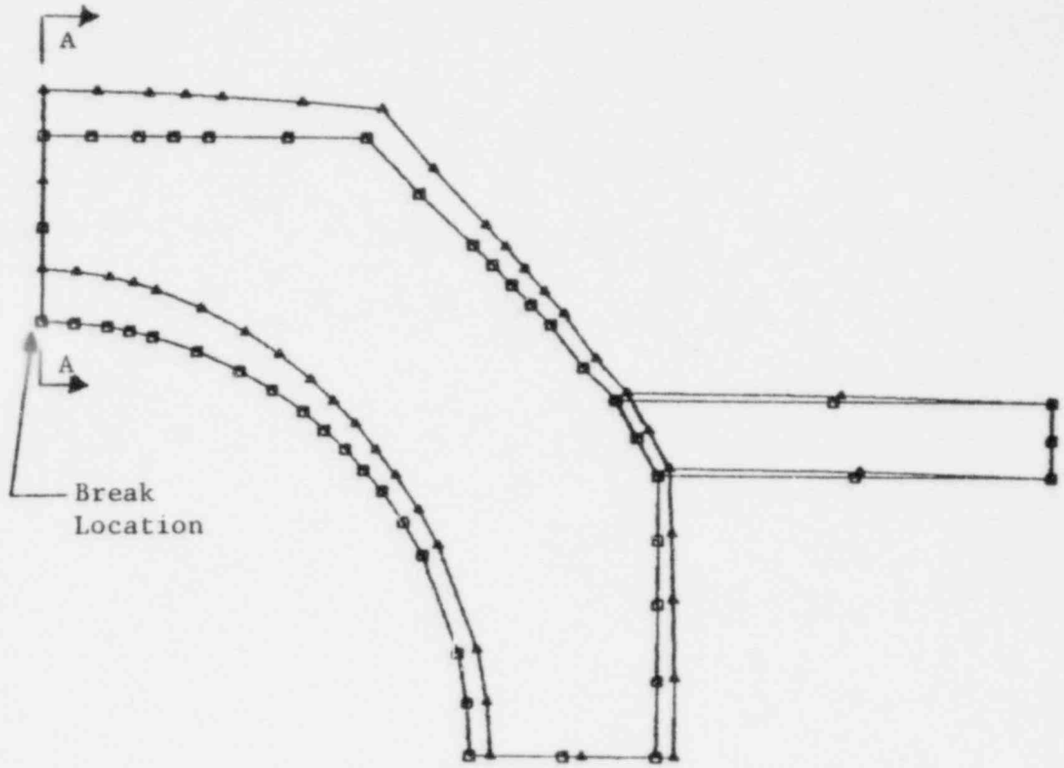

Plan View

7. ACCEPTANCE CRITERIA FOR STRUCTURAL EVALUATIONS

The following criteria were used to determine the structural acceptability of the components when subjected to the effects of asymmetric LOCA loadings.

7.1. Steel Components

7.1.1. Pipe Rupture Restraints and Davis-Besse Support Components

7.1.1.1. Material Properties

The following procedures were used to define the steel properties for use in the evaluation analyses.

Temperature – material properties appropriate to normal operating conditions were used.

Stress – the minimum specified yield and ultimate stresses (S_y, S_u) were increased by 5% to account for overstrength due to normal production variations.[2,37-39] As the asymmetric portion of the LOCA loading occurs in less than 50 milliseconds the yield stress was increased a further 10% to accont for strain rate effects. This is in accordance with the provisions of the Standard Review Plan 3.6.2.[14] Thus, the following properties were adopted:

S_y = 1.15 × minimum ASTM value,
S_u = 1.05 × minimum ASTM value.

Strain – the ultimate uniform strain (e_{uu}) for steel was taken equal to one-half the ultimate strain (e_u), the latter being that specified by the appropriate ASTM Standard.

7.1.1.2. Acceptance Limits

The following acceptance limits were used for the evaluation of steel components.

7.1.1.3. Elastic Analyses

For components evaluated by elastic analyses, the acceptance criteria are those specified by the ASME Code, Section III, Appendix F. For welds, however, the acceptance criteria given in section 7.1.1.4 apply.

7.1.1.4. Inelastic Analyses

For components evaluated by inelastic analyses, the following acceptance criteria apply.

Strain – the allowable strain is one-half of the ultimate uniform strain, e_{uu}.

Tensile stresses – the allowable tensile stress is S_y, as defined in section 7.1.1.

Compressive stresses – the allowable compressive stress is the lesser of the buckling and yield stresses. For columns, the buckling stress is that defined by ASME XVII-2213, equation 4, increased by a factor of 1.7 (per ASME XVII-4211, equation 4).

Shear stresses – the von Mises yield criterion is assumed to apply. Thus, the allowable shear stress is 0.577 S_y. This value is slightly greater than that specified by ASME XVII-4000[11] (section 4211), which allows 0.55 S_y. The adopted value is based on section 2.5 of the AISC Code[4], the commentary of which states that the allowable shear stress shold be reduced by 5% as most applications pertain to beam webs. Thus, it is assumed in the AISC Code that:

$$d_{web} = 0.95\ d_{total}.$$

This is not applicable to non-beam applications. Therefore, the 5% reduction factor is not applied.

Combined shear and tension stresses – the value of the following interaction formula must be less than or equal to unity.

$$\frac{f_v^2}{F_v^2} + \frac{f_t^2}{S_y^2}$$

where f_v = actual shear stress,
F_v = allowable shear stress,
f_t = actual tensile stress,
S_y = allowable tensile stress.

Bearing stresses – for pins bearing against reamed, drilled, or bored holes, the bearing stress is acceptable if it is less than 0.90 S_y.

If the bearing stress exceeds 0.90 S_y, the following acceptance criteria apply:

For L/d less than 3.0:

$$f_b = 1.4\ S_a(L/d - 0.5)$$

where

L = distance from hole centerline to edge of plate,

d = pin diameter,

f_b = allowable nominal bearing stress.

This criterion is based upon experimental test data,[30] and defines a lower bound bearing stress at which shear-out failure will occur. The allowable stress, S_a, is the average of S_y and S_u, and corresponds to a strain of one-half the uniform ultimate strain.

For L/d greater than 3.0, the material strain limit specified elsewhere in this section applies (in this range, shear-out failure does not dominate: rather, failure is characterized by large distortions of the pin hole).

Full penetration welds – the allowable stress on a full penetration weld is that for the base metal.

Fillet welds – the allowable stress is 0.68 S_u where S_u is the tensile strength of the fillet weld material.

Pins – the requirements for shear or combined shear and tension stresses are applicable. If yielding occurs, the allowable stress is 0.68 S_u.

7.1.2. Pressure Boundary Components and Component Supports

The steel components comprising the reactor coolant pressure boundary (RCPB), reactor internals, core support assembly, and RCPB component supports were evaluated using the following acceptance criteria.

7.1.2.1. Components, Other Than Supports

The stress analysis was performed and evaluations were made in accordance with the rules of the ASME Code, Section III, Appendix F, paragraph F-1323.

7.1.2.2. Component Supports

Component supports were analyzed and evaluations were made in accordance with the rules of the ASME Code, Section III, Appendix F, paragraphs F-1323 and F-1370.

7.1.2.3. Stress Criteria for Special Elements

1. Columns and Other Compression Elements – the limits of the ASME Code, Section III, Appendix F, are applicable.

2. Bolts – the limits of the ASME Code, Section III, Appendix F, are applicable.

3. Pins – the limits of the ASME Code, Section III, Appendix F, are applicable.

4. Welds – butt welds: The ultimate capacity of the weld will be equal to the tensile yield stress of the base metal as defined by the above component acceptance criteria. Fillet Welds: The maximum shear stress in fillet welds was evaluated using the following relationship:

$$\tau_{max} = 0.68\ F_{ultimate}$$

where $F_{ultimate}$ is equal to the ultimate tensile strength of the weld metal.

7.1.2.4. Material Properties

The following guidelines were used to define the material properties for use in the above described acceptance criteria:

1. The minimum specified stress properties were increased by 5%. This results in a conservative band, which adequately accounts for the average overstrength due to normal production variations.

2. Since the asymmetric portion of the LOCA loading occurs in less than 50 milliseconds, credit was taken for higher elastic strengths as a result of strain rate effects during this period. A 10% increase in yield properties was used in the acceptance criteria.

3. Material properties appropriate for normal operating temperatures were used.

7.2. Concrete and Reinforcing Steel

7.2.1. Material Properties

Concrete – the mirimum specified compressive strength (f'_c) was taken either as the design basis, 28-day strength, or as the in situ strength. For components where the in situ strength was used, a description of the method by which it was evaluated is included in the appropriate section.

Since the asymmetric portion of the LOCA loading occurs in less than 50 milliseconds, the effect of strain rate was considered in accordance with ACI 349-76, Appendix C. This allows an increase in allowable shear and compressive strengths of 10 and 25%, respectively. The modulus of elasticity was also increased by 10% to account for strain rate effects. No strength or stiffness increases were assumed for the steady-state portion of the LOCA event.

Reinforcing steel – for all grades of reinforcing steel, yield (S_y) and ultimate (S_u) stress properties were increased by 5% over those specified for the material by the appropriate ASTM specification. This accounts for production overstrength. Strain rate effects during the asymmetric phase of the LOCA loading were considered by further increasing the yield stress by 10%.

7.2.2. Acceptance Limits

7.2.2.1. Elastic Analyses

Where applicable, the ultimate strength requirements defined in ACI 349-76[1] apply.

Particular interpretations of the requirements of ACI 349-76 for the unique geometry and loading of the cavity wall and embedment structures are described in the relevant sections.

7.2.2.2. Inelastic Analyses

Where inelastic analyses are performed, the criteria specified in section 7.2.2.1 apply, with the following modifications.

Concrete compressive strain – the allowable compressive strain in the concrete is 75% of the strain corresponding to maximum stress in the given stress state. For uniaxial loading, this reduces to an allowable strain of 0.0015.

Reinforcing steel strain – the allowable strain in the reinforcing steel is that specified for steel in section 7.1.2.2.

7.3. Piping

7.3.1. Reactor Coolant Piping

Reactor Coolant Piping was evaluated in accordance with the rules of the ASME Code, Section III, Appendix F. The simplified stress equation 9 of section NB-3650 was modified by the rules of Appendix F and utilized in the primary piping evaluation. When the acceptance criteria using the simplified stress equation were not satisfied, a more rigorous pipe stress analysis was performed. This analysis was performed in accordance with the rules of the Nuclear Power Piping Code, USAS B31.7-1969 using the criteria of B31.7, Appendix F. The allowable stress using this approach was three times the design stress intensity factor ($3\ S_m$).

7.3.2. Core Flood Lines

7.3.2.1. Piping Components

The acceptance criteria for the core flood piping include limits for primary and secondary stresses. Satisfaction of these stress limits demonstrates structural and functional acceptability.

Limits on primary stresses are satisfied for the combined effects of pressure, deadweight, and the inertial portion of the response associated with the LOCA event. The evaluation is in accordance with paragraph NB-3650, equation 9, in the ASME Code. Level C stress limits apply for all piping except tees and branch connections:

$1.5\ S_y$ for austenitic piping components,

$2.25\ S_m$ for ferritic piping components.

For tees and branch connections, level D stress limits apply:

$2.0\ S_y$ for austenitic piping components,

$3.0\ S_m$ for ferritic piping components.

The $3\ S_m$ limit, specified by the Code for range of secondary stresses, is satisfied for the combined effects of thermal expansion and anchor movements associated with the LOCA event.

7.3.2.2. Piping Supports

The acceptance criteria for the core flood piping supports are specified as maximum allowable load limits. The allowable load limits are satisfied for the combined effects of deadweight, thermal expansion, and the LOCA event, including both the inertial and anchor movement contributions. The allowable load limit for each support is set at the yield load. In rigid supports, this load is defined as

> The axial load for which the membrane stress equals the yield stress, or the plastic moment capacity of the section.

For snubber supports this load is defined as

> The rated design capacity times a load factor of 2.05.

This allowable load limit for snubbers is derived from the "one-time" load rating data applicable to level C conditions given in reference 49.

If the initial piping analysis shows supports exceeding the allowable load limits, then the overloaded supports must be removed and the analysis rerun to show the acceptability of the piping (in accordance with section 7.3.2.1) and of the remaining supports.

7.4. Fuel Assembly

Loads and permanent deflection for the LOCA were limited as follows:

Requirement – the fuel assembly shall maintain structural integrity and a coolable geometry.

Service Level – In order to meet the fuel assembly general criteria for the LOCA condition, level D service limits of the ASME Section III Code are used for all of the fuel assembly components except for spacer grids.

Criteria – the stress intensity limits for all of the fuel assembly components except for spacer grids were determined using ASME Code Appendix F, Table F-1332.2-1.

Exception – the spacer grid shall not exceed a permanent deformation limit which has shown to maintain a coolable core geometry. The acceptance criteria for the coolable geometry will be based on maintaining the peak cladding temperature and the cladding metal-water reaction within the requirement of 10 CFR 50.46 as follows:

Disfiguration of the core can occur if mechanical loads on the reactor vessel internals caused by the rapid system depressurization are severe enough to cause permanent distortion. The loading calculations which have been performed show that only the peripheral fuel assemblies would incur minor deformation to the outside fuel pin lattice structure. Since only the exterior portions of the core is affected, no gross core blockage, i.e., blockage that would reduce the core flow area by 90 to 100%, will occur as a result of these mechanical loadings and the core geometry will remain amenable to cooling.

Additionally, NRC Standard Review Plan 4.2, Rev. 1, requires that, for the LOCA event, structural deformation should not cause the 2200F cladding temperature and 17% cladding oxidation limits of 10 CFR 50.46 to be exceeded. An analysis was performed to examine the coolability of the Mark-B fuel assuming that structural deformation does occur in the peripheral fuel assemblies. In performing this evaluation, it was assumed that the grid was fully collapsed as defined by draft Branch Technical Position 4.2.1. The assumption of a fully collapsed grid results in a 0.380 inch displacement of the grid and a resultant 41% decrease in the subchannel flow area.

To investigate the effect of the structural deformation on peak cladding temperature, and Appendix K evaluation was carried out in accordnace with B&W's approved evaluation model for the 177 FA lowered-loop plants.[13,14] The following changes were made to the model in order to evaluate the effect of collapsed grids:

1. The radial and axial peaking factors were lowered to reflect the power in the peripheral fuel assemblies.
2. The net core flow area for the entire bundle was reduced by 41% in order to account for the effect of a fully collapsed grid.
3. The CRAFT2 computer model was altered slightly such that the fluid boundry conditions reflect those for an assembly at the periphery.

Peak cladding temperature evaluations were performed for a peripheral fuel bundle with and without fully collapsed grids. In both cases. the peak cladding temperature and the local metal-water reactions were less than 2200F and 17%, respectively. The effect of the grid deformation was to increase the peak cladding temperature by only 12F. Since the deformation had only a minor impact on peak cladding temperature, it is expected that a fully collapsed grid would not result in peak cladding temperatures above 2200F even at the LOCA limit values.

While the above calculations were performed for the 177 FA lowered-loop plants, the conclusions are equally applicable to the 177 FA raised-loop design. Since both plant types utilize the same fuel design (Mk-B), the relative influence of the collapsed grid would be similar for both plants.

As shown, grid collapse, caused by the initial mechanical loadings of the reactor vessel during a LOCA, up to and including a fully collapsed grid does not significantly impact the fuel coolability. Thus, grid displacements up to 0.380 inches on the peripheral fuel assemblies are acceptable for evaluation of the effect of mechanical loadings of the fuel assembly.

8. PRESSURE LOADING DATA

This section provides reactor vessel cavity pressure and reactor internals differential pressure data.

8.1. Reactor Vessel Cavity Pressure

Reactor vessel asymmetric cavity pressurization studies were performed for all B&W 177-fuel assembly plants. The three Oconee units were considered as one model, as were the CR-3 and TMI-1 plants. The remaining plants — ANO-1, Rancho Seco, TMI-2, and DB-1 — were considered individually.

A spectrum of break sizes — 2.0A, 1.5A, 1.0A, 0.6A, and 0.3A — for guillotine breaks at the reactor vessel inlet and outlet was analyzed for the skirt-supported plants, while Davis Besse-1 was studied only for its actual inlet and outlet break areas.

The results of the cavity pressurization production calculations, in the form of peak lateral loads, moments, and uplifts, are shown in Tables 8.1-1 through 8.1-13. Examples of non-integrated results in the form of node pressure-time histories are shown in Figures 8.1-1a through 8.1-4h. The node and cavity level numbers are defined in Figures 4.3-15 through 4.3-20 for ANO-1 and in Figures 4.3-46 through 4.3-53 for Davis Besse-1.

The results of the sensitivity study and the analyses for a spectrum of breaks verify that the six-group categorization used by B&W to represent the Owner's Group cavities is appropriate and conservative. The results from the spectrum analysis show that the cavity pressure and external loads on the reactor vessel are generally proportional to the break area.

The peak lateral load on the reactor vessel is primarily dependent on the flow area and resistance in the annulus and on the broken pipe penetration vent area. Flow restrictions around the reactor vessel, such as hot leg, cold leg, and core flood line nozzles; stand-off out-of-core detector thimbles (assuming that they remain intact during the transient); and permanently placed in-service inspection equipment are the major resistances controlling the lateral load.

The peak volume average cavity pressure is proportional to the total vent area. Additional vents created by the blowout devices during the transient significantly reduce the cavity pressure as well as the reactor vessel uplift force.

Figure 8.1-1. RV Asymmetric Cavity Pressure — ANO-1

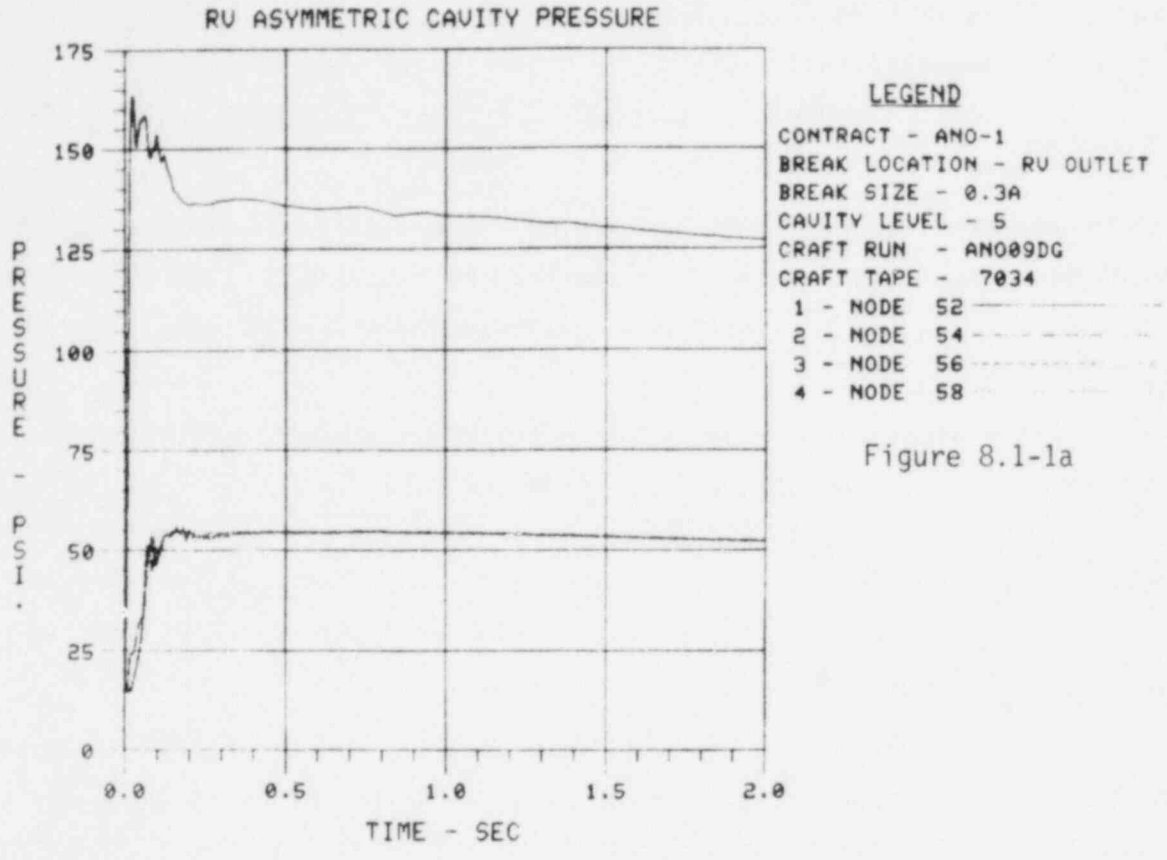

Figure 8.1-1a

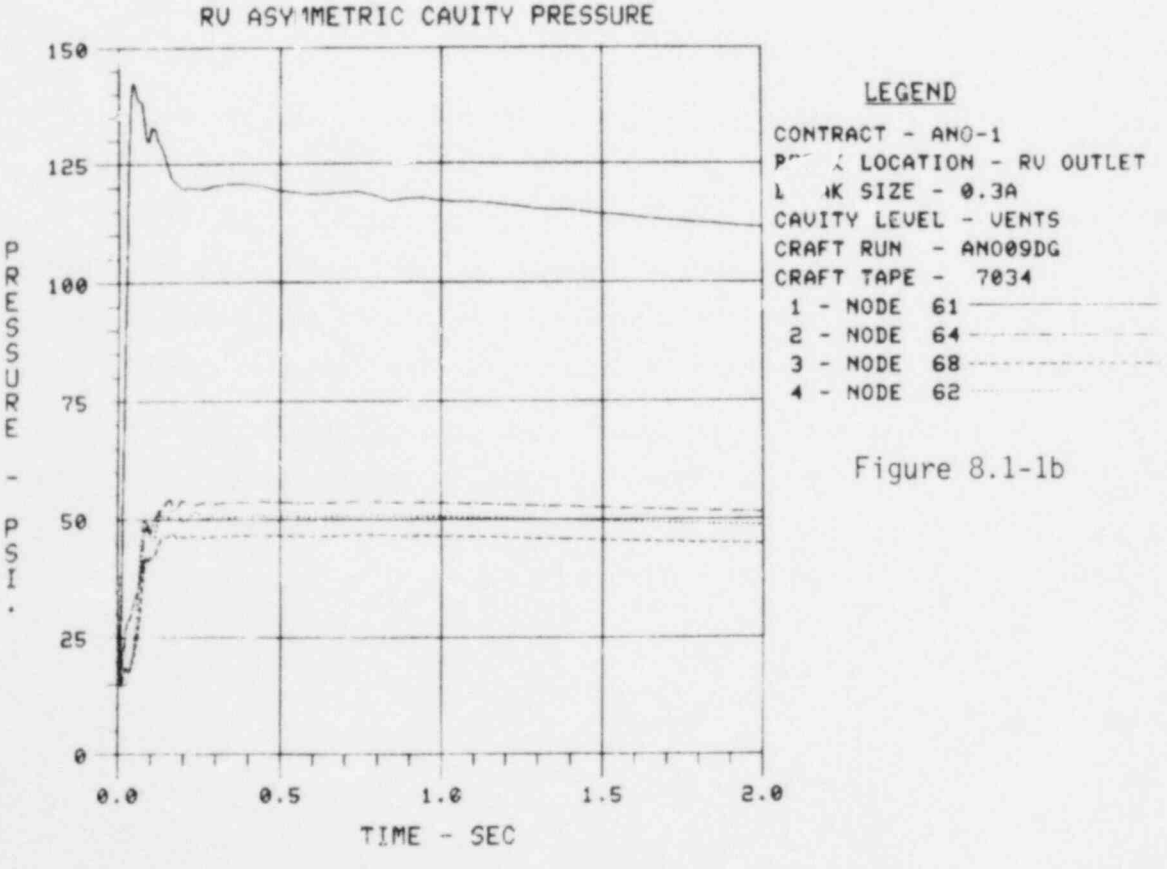

Figure 8.1-1b

Figure 8.1-1. (Cont'd)

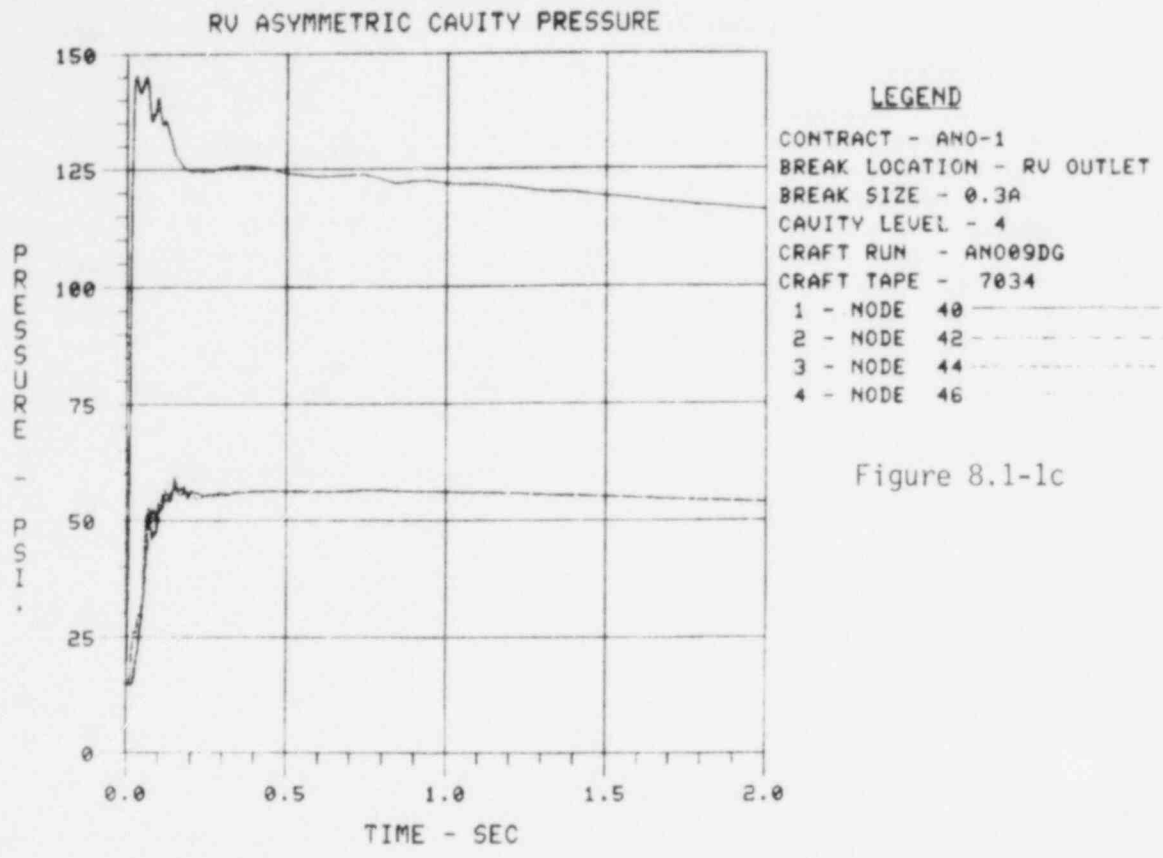

Figure 8.1-1c

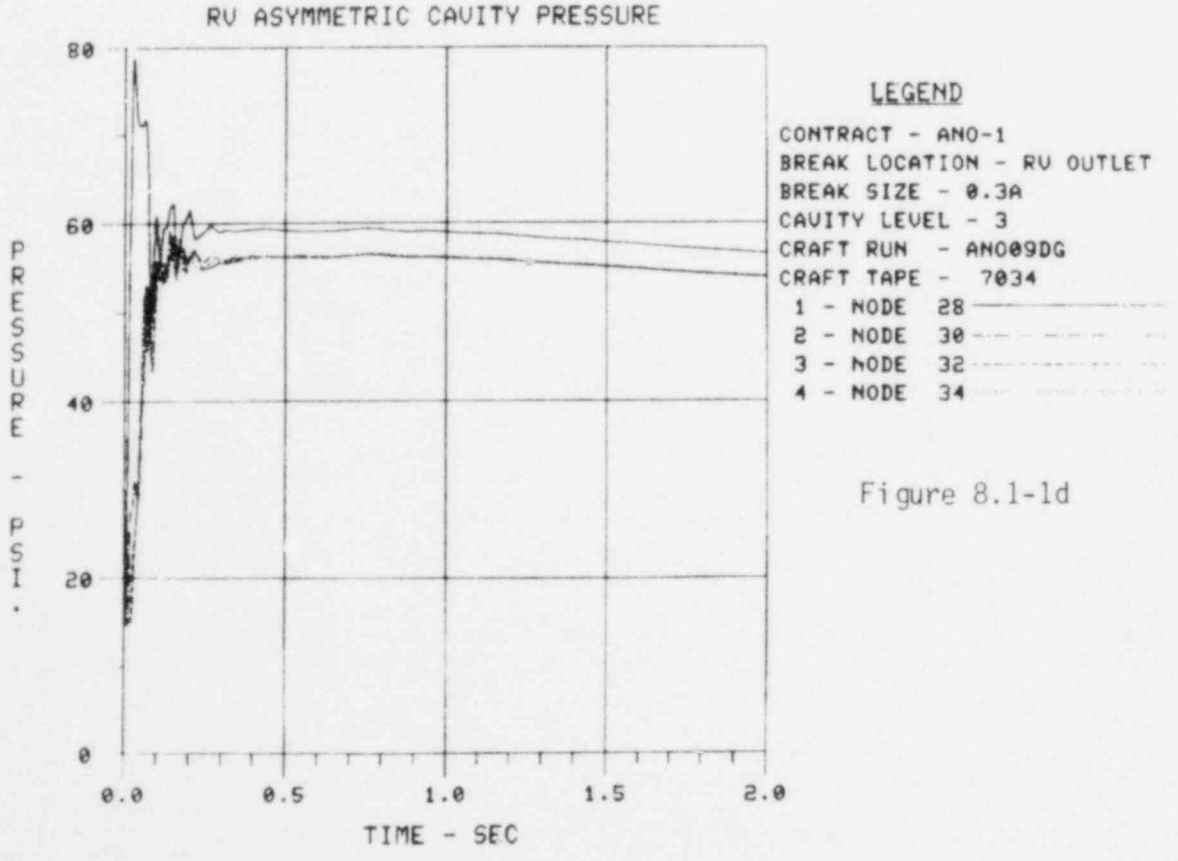

Figure 8.1-1d

Figure 8.1-1. (Cont'd)

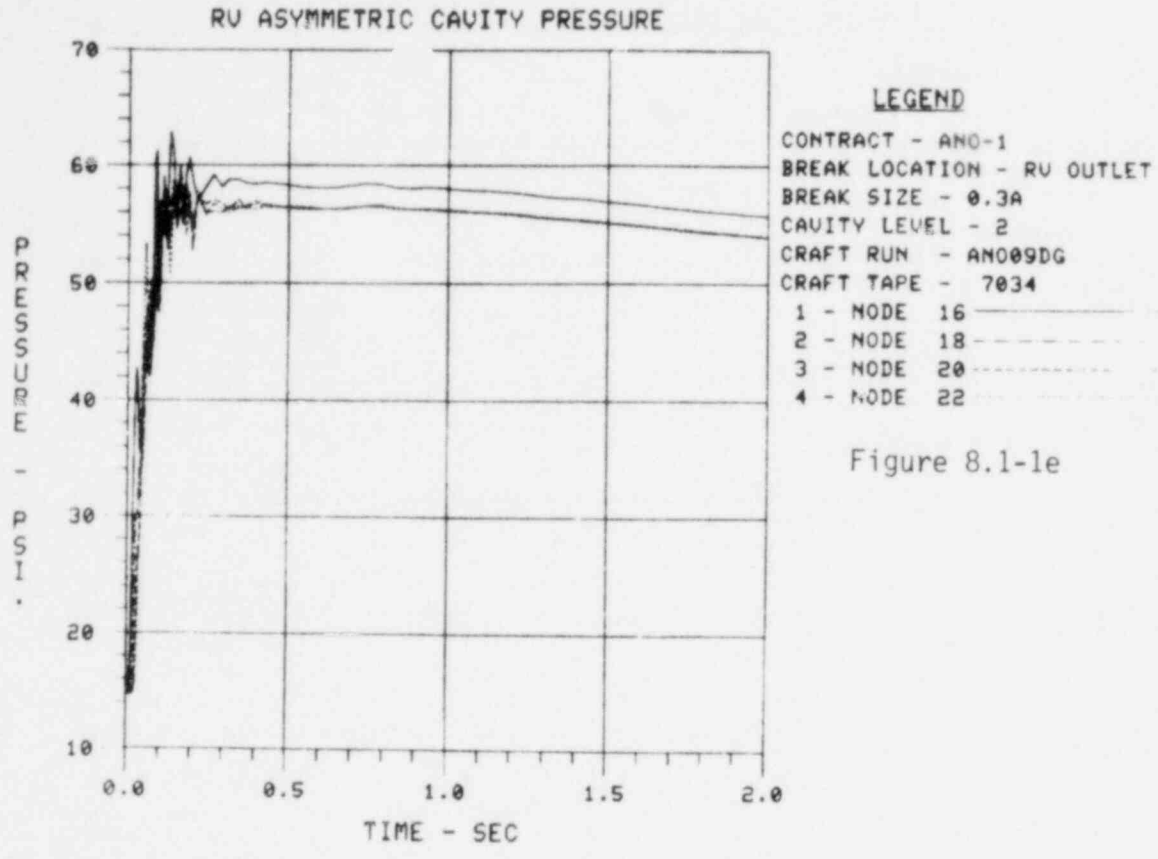

Figure 8.1-1e

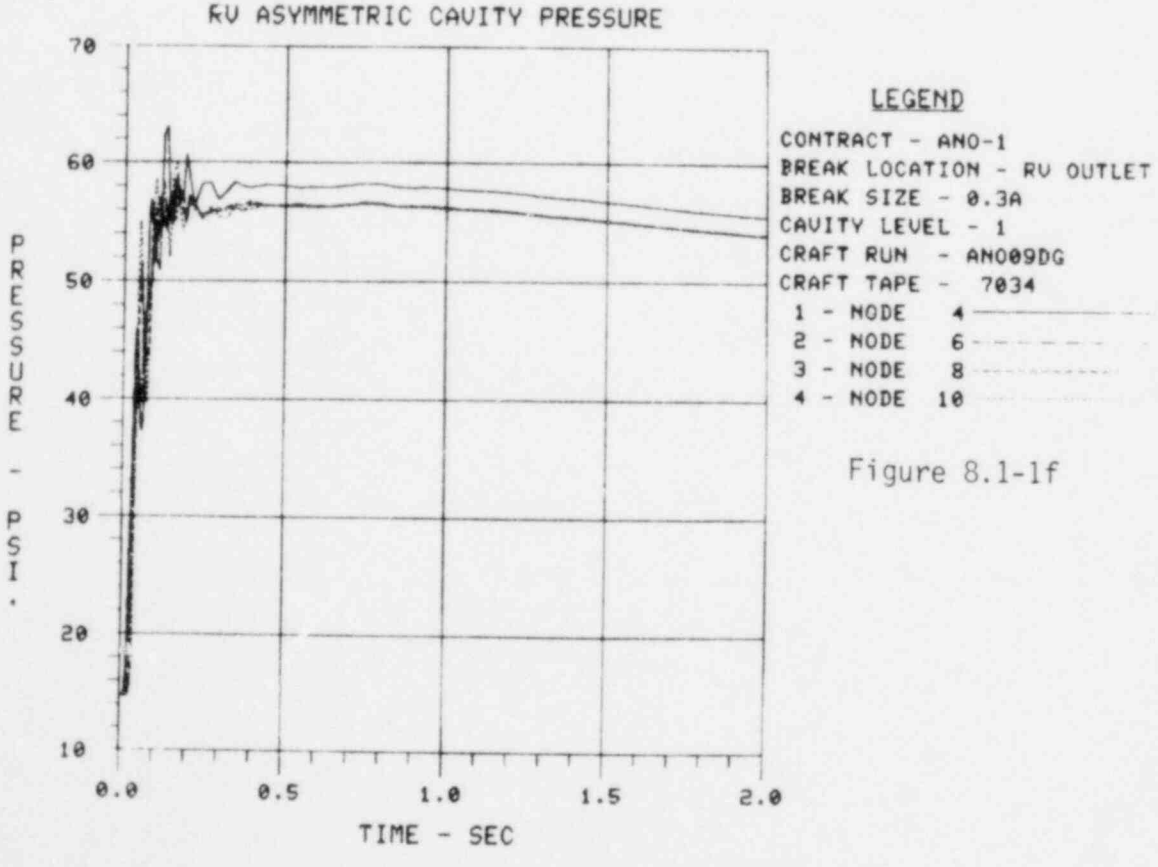

Figure 8.1-1f

Figure 8.1-1. (Cont'd)

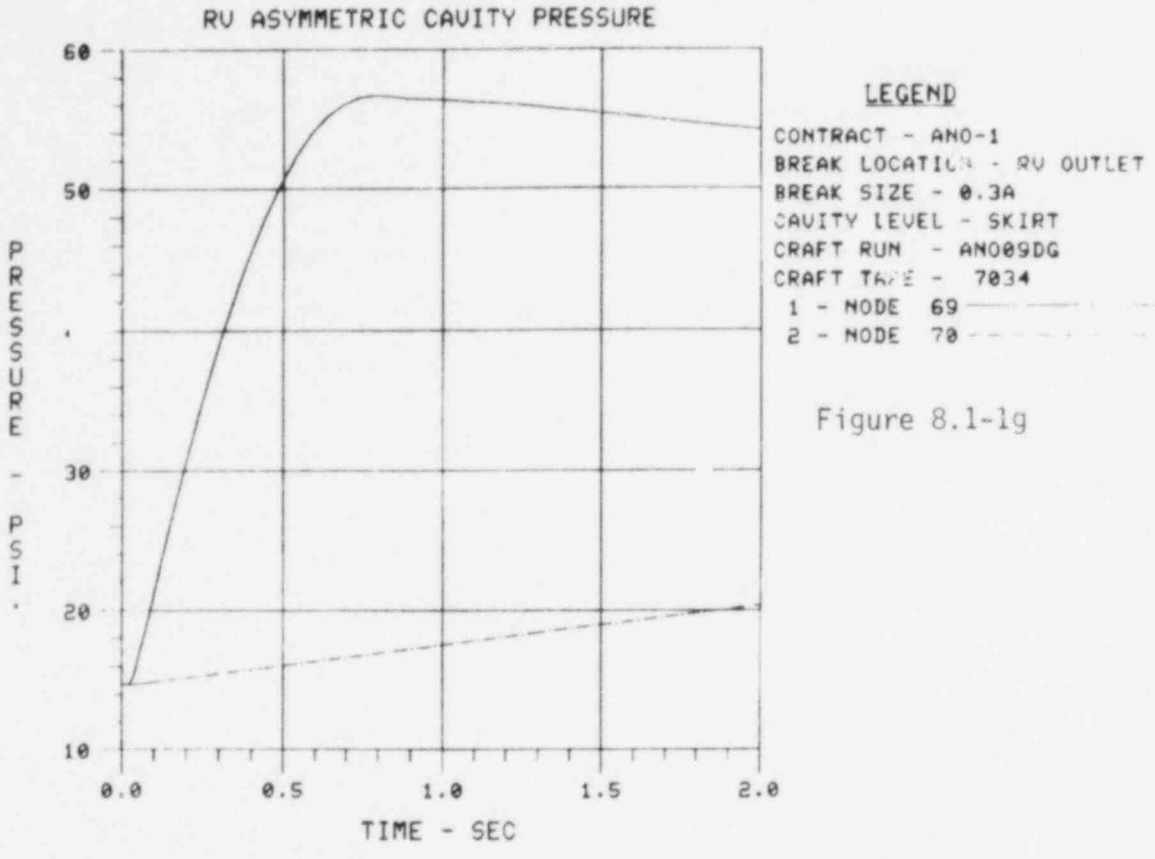

Figure 8.1-1g

Figure 8.1-2. RV Asymmetric Cavity Pressure — ANO-1

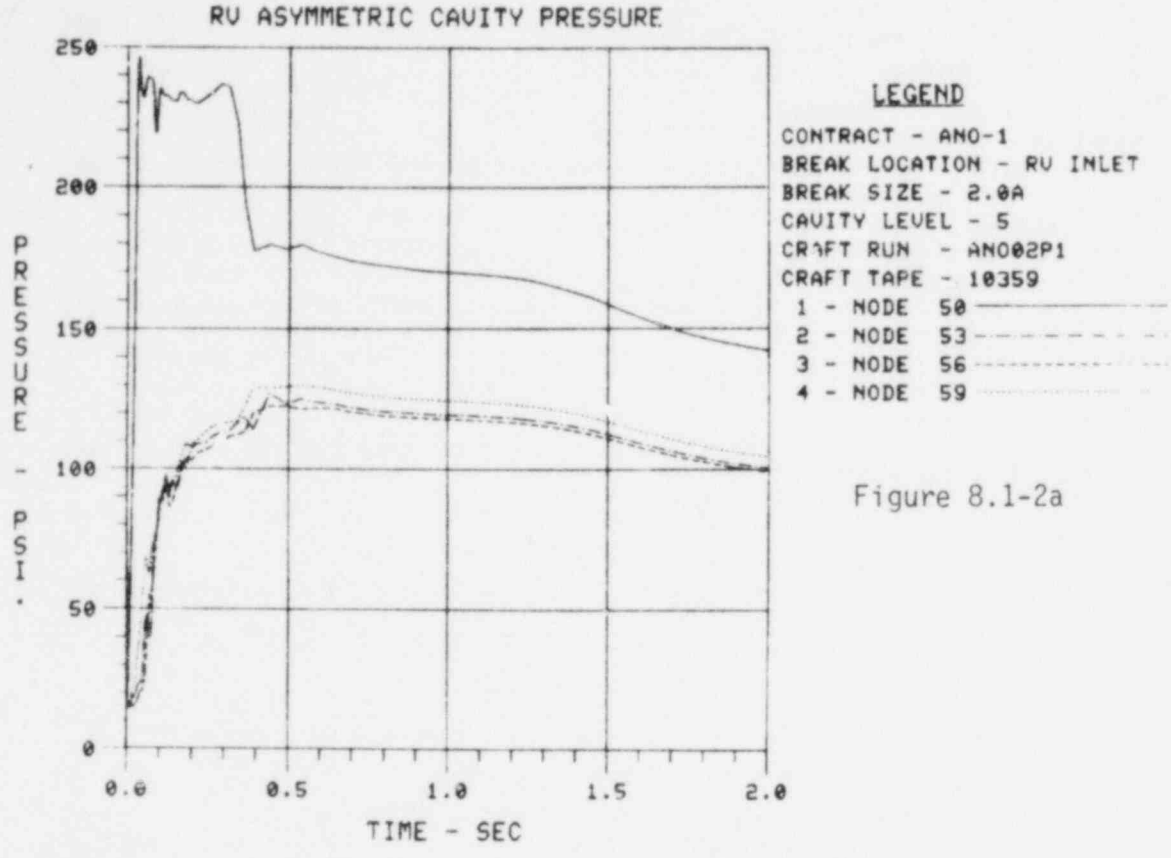

Figure 8.1-2a

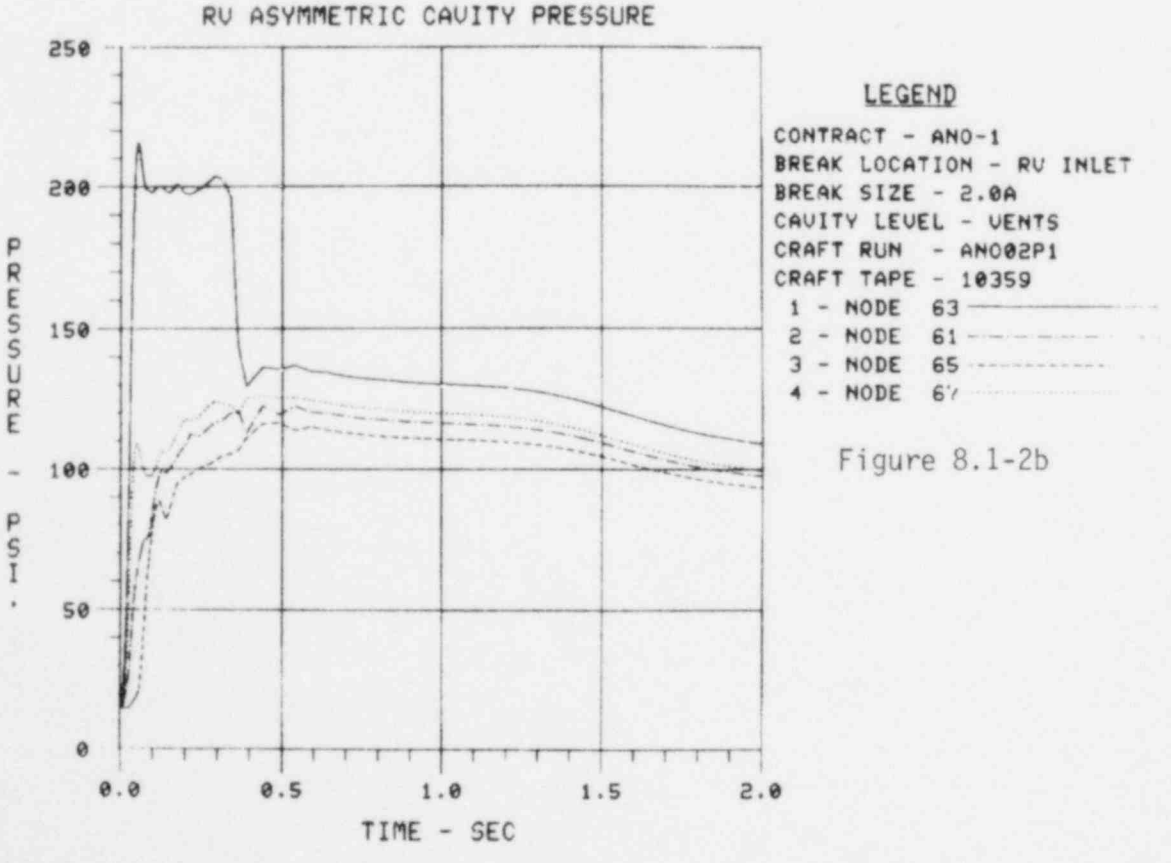

Figure 8.1-2b

Figure 8.1-2. (Cont'd)

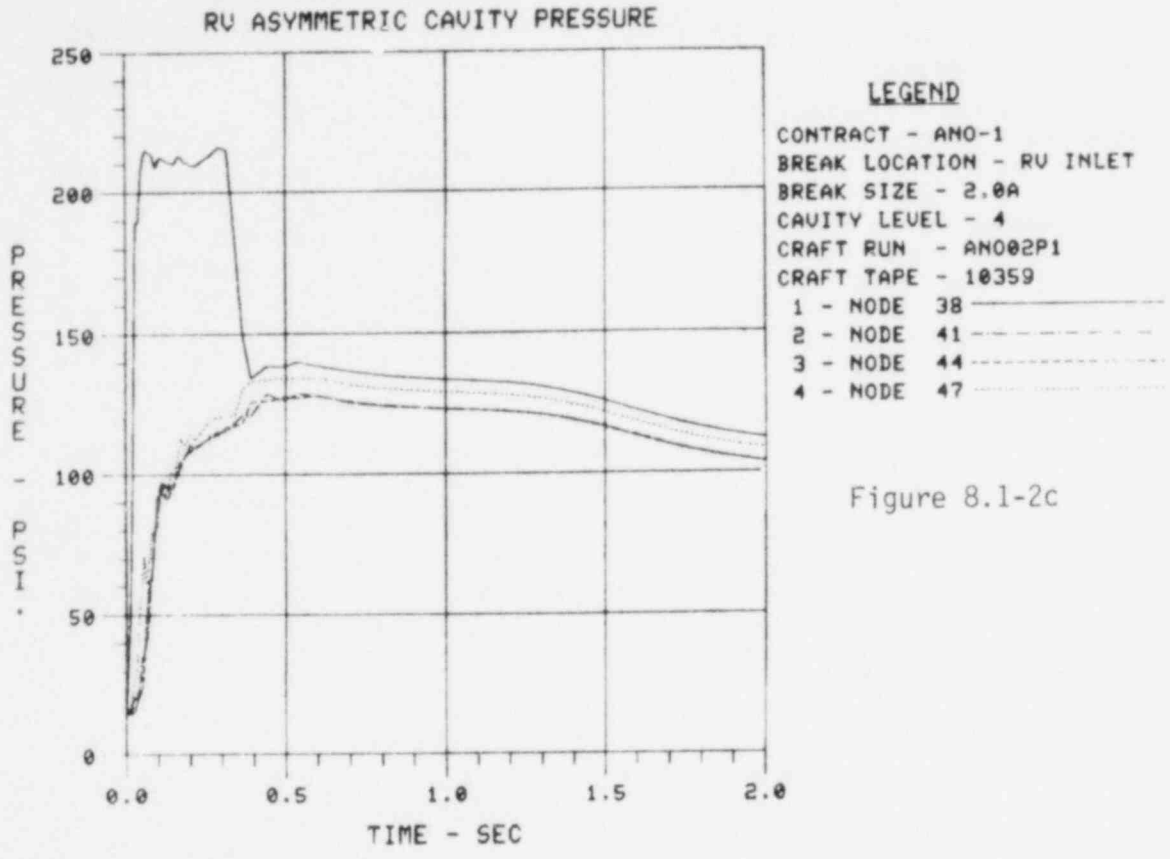

Figure 8.1-2c

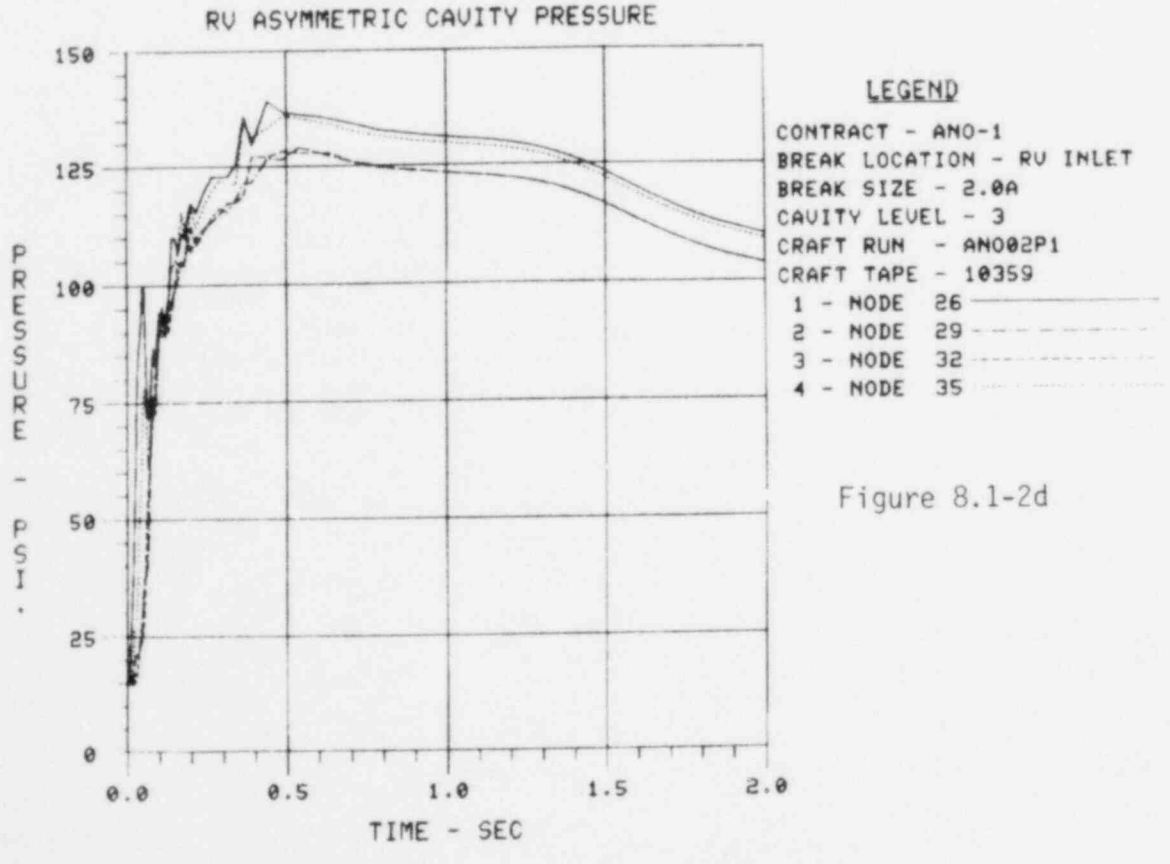

Figure 8.1-2d

Figure 8.1-2. (Cont'd)

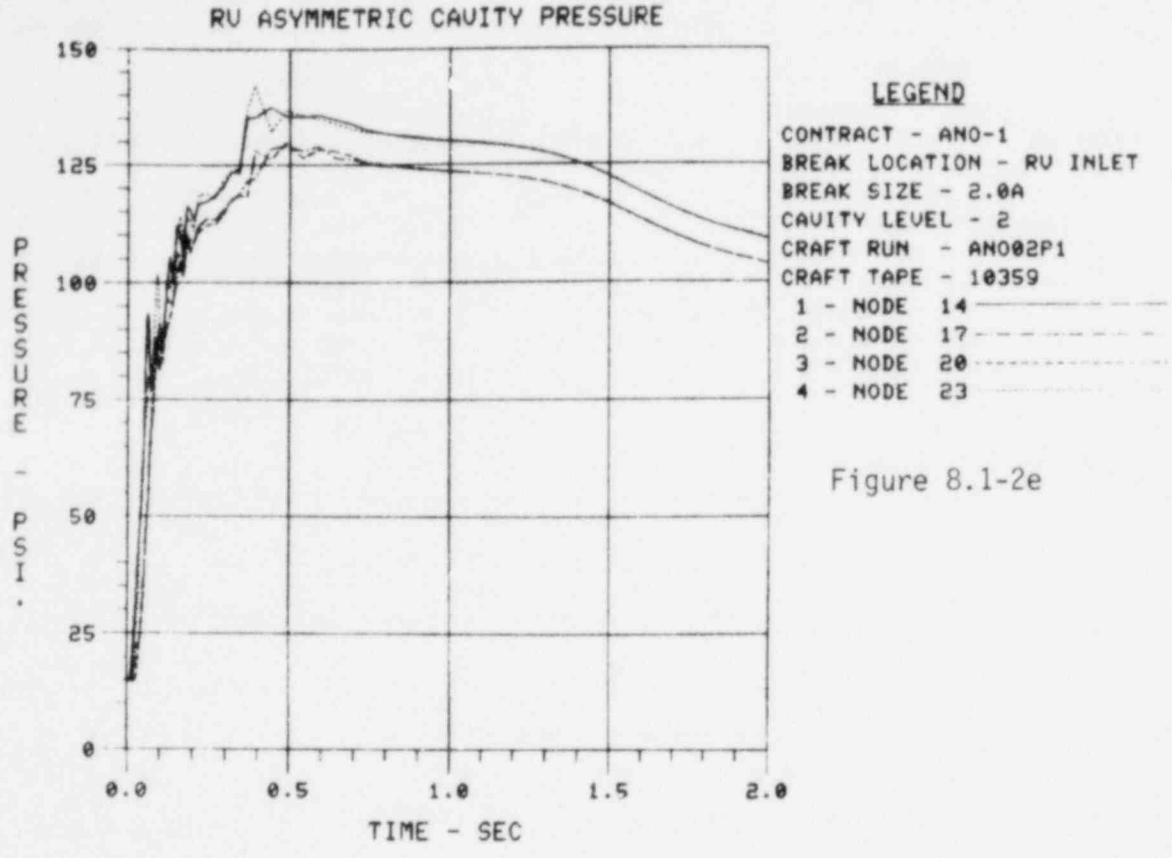

Figure 8.1-2e

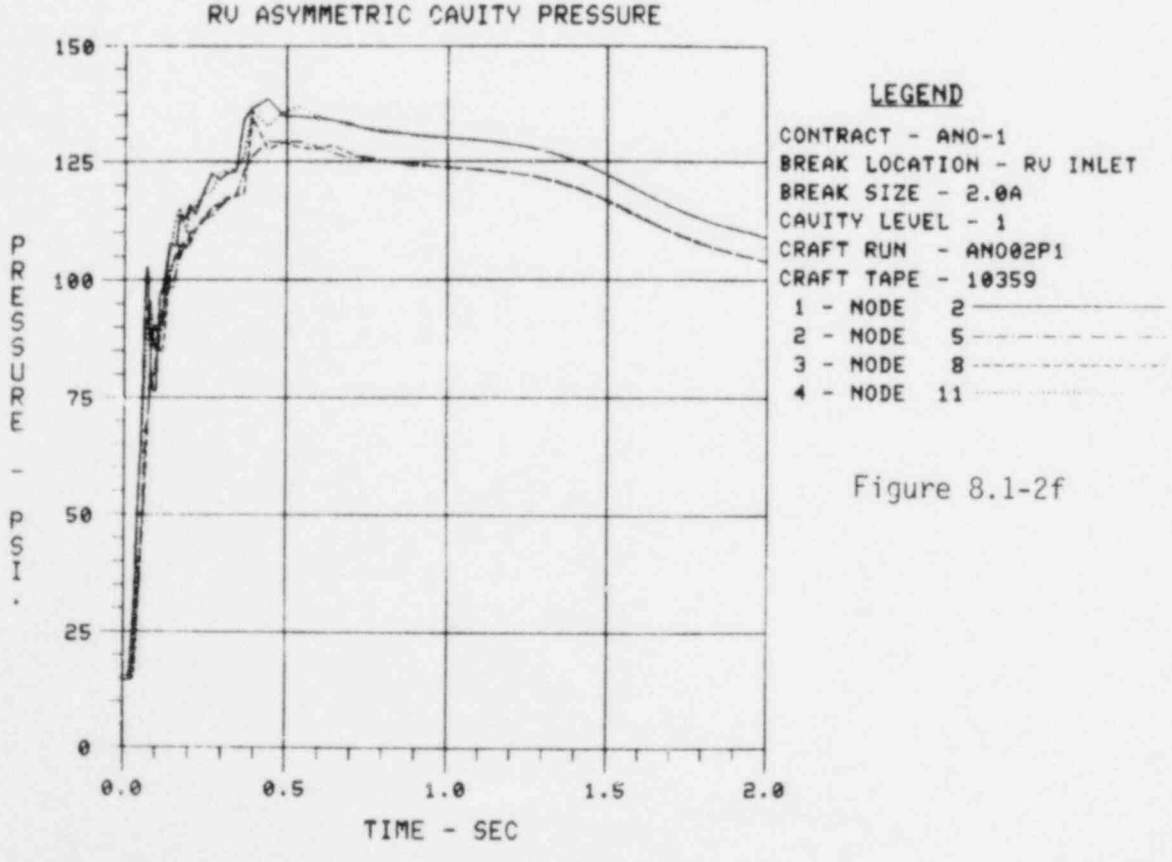

Figure 8.1-2f

Figure 8.1-2. (Cont'd)

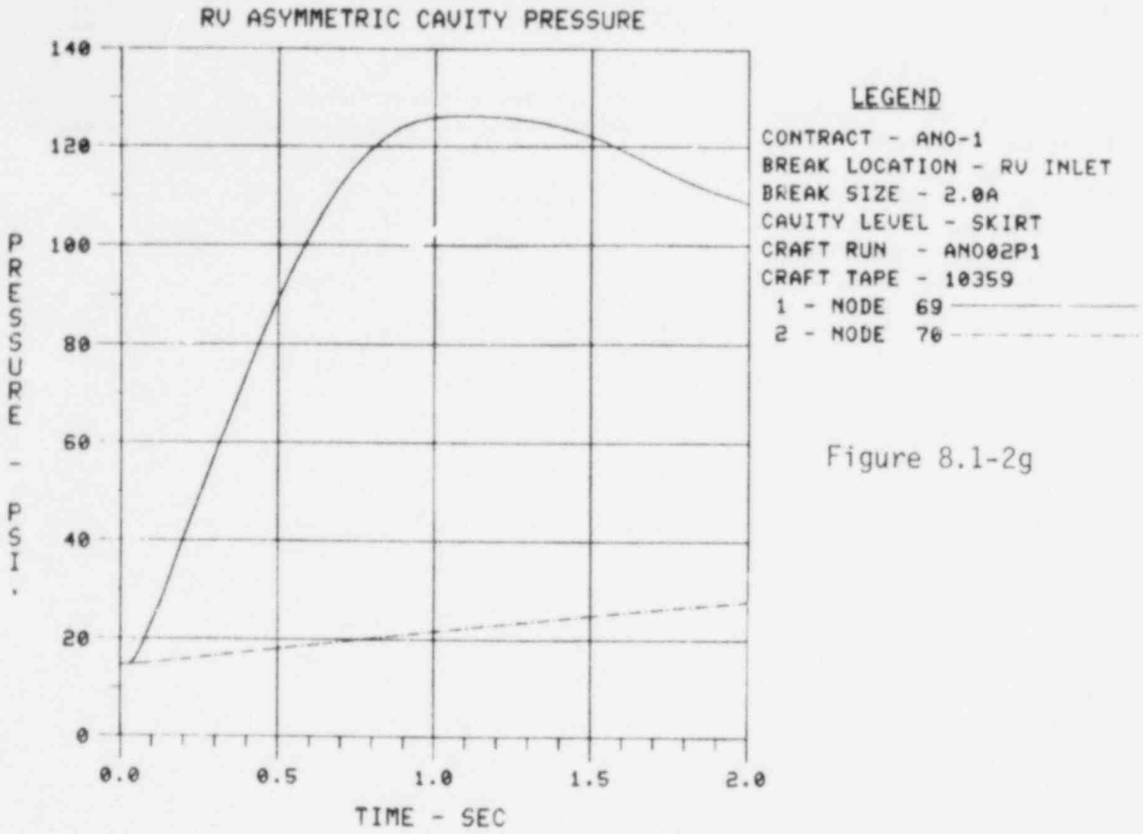

Figure 8.1-2g

Figure 8-1-3. RV Asymmetric Cavity Pressure — Davis-Besse 1

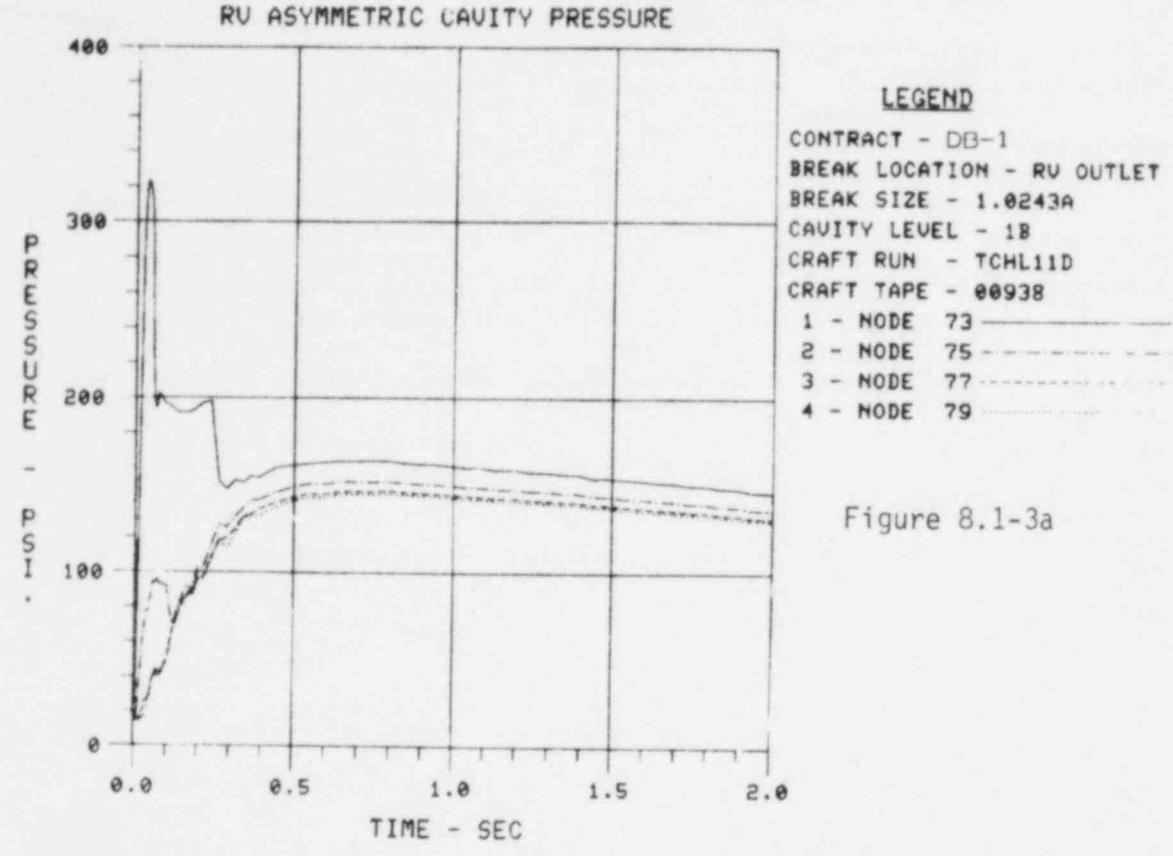

Figure 8.1-3a

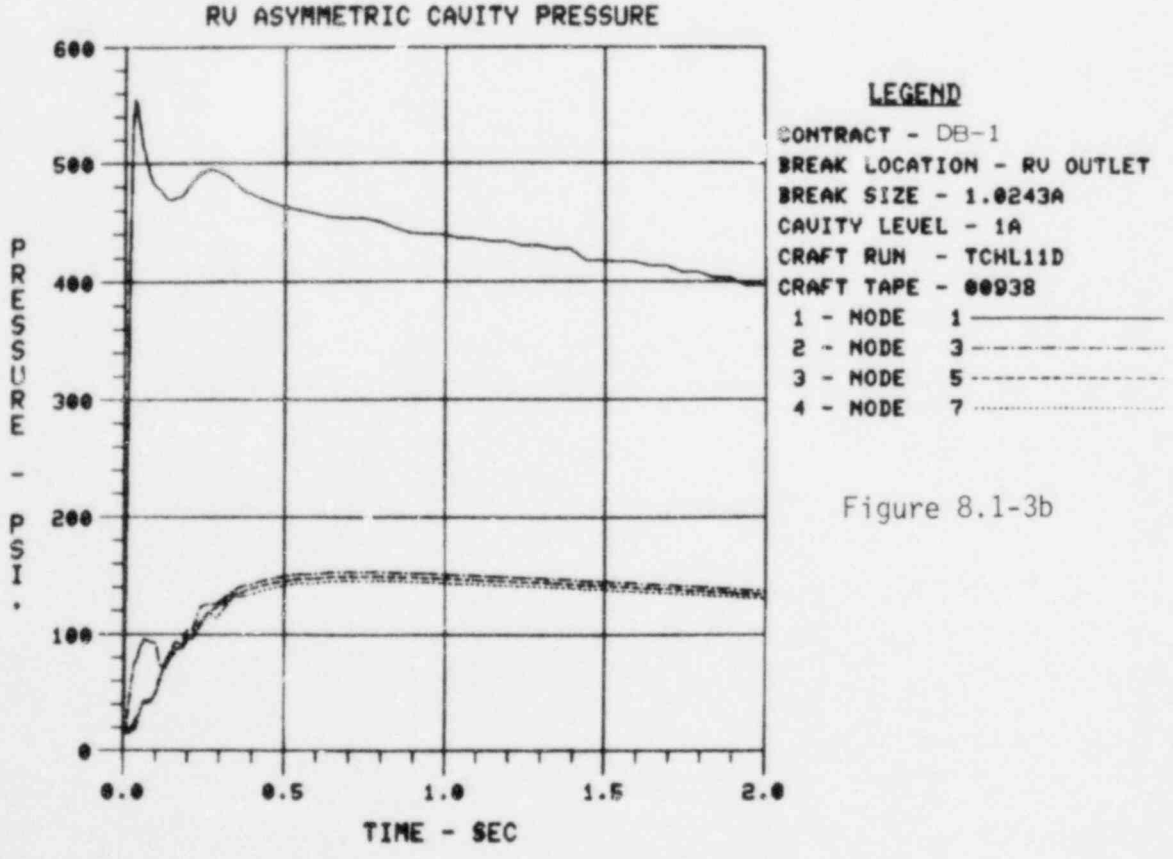

Figure 8.1-3b

Figure 8.1-3. (Cont'd)

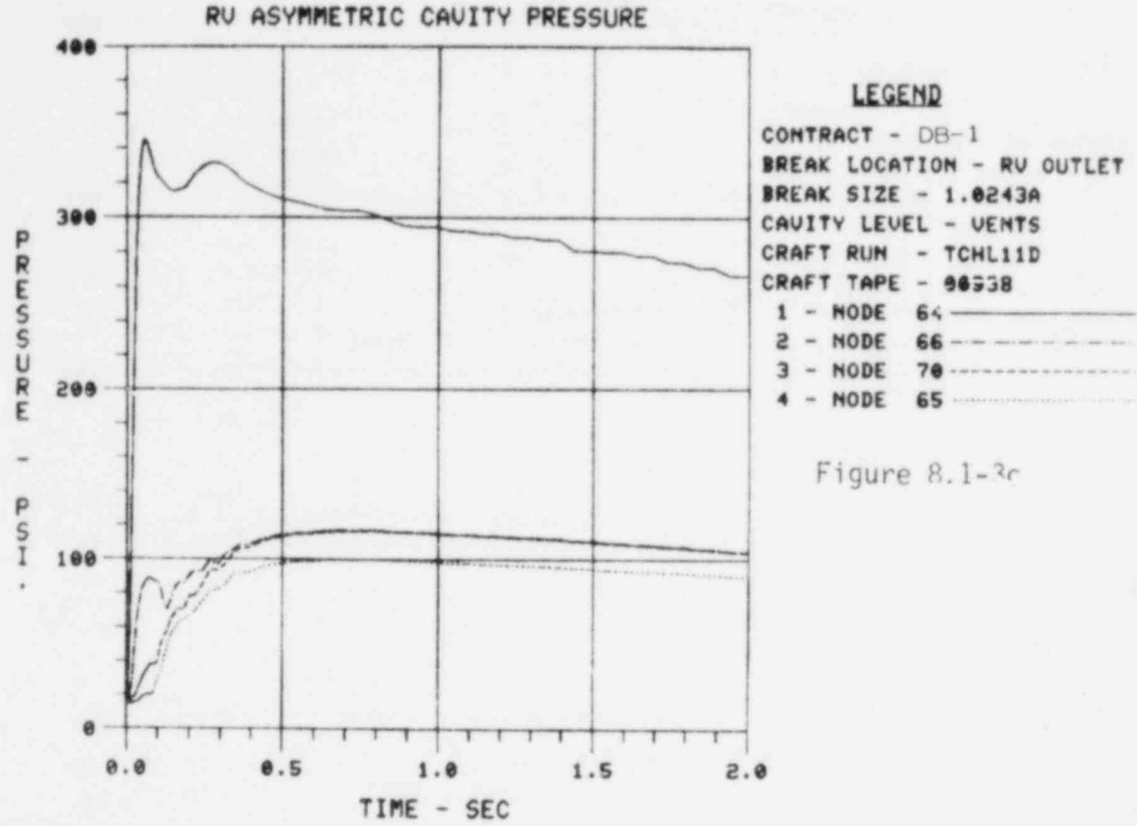

Figure 8.1-3c

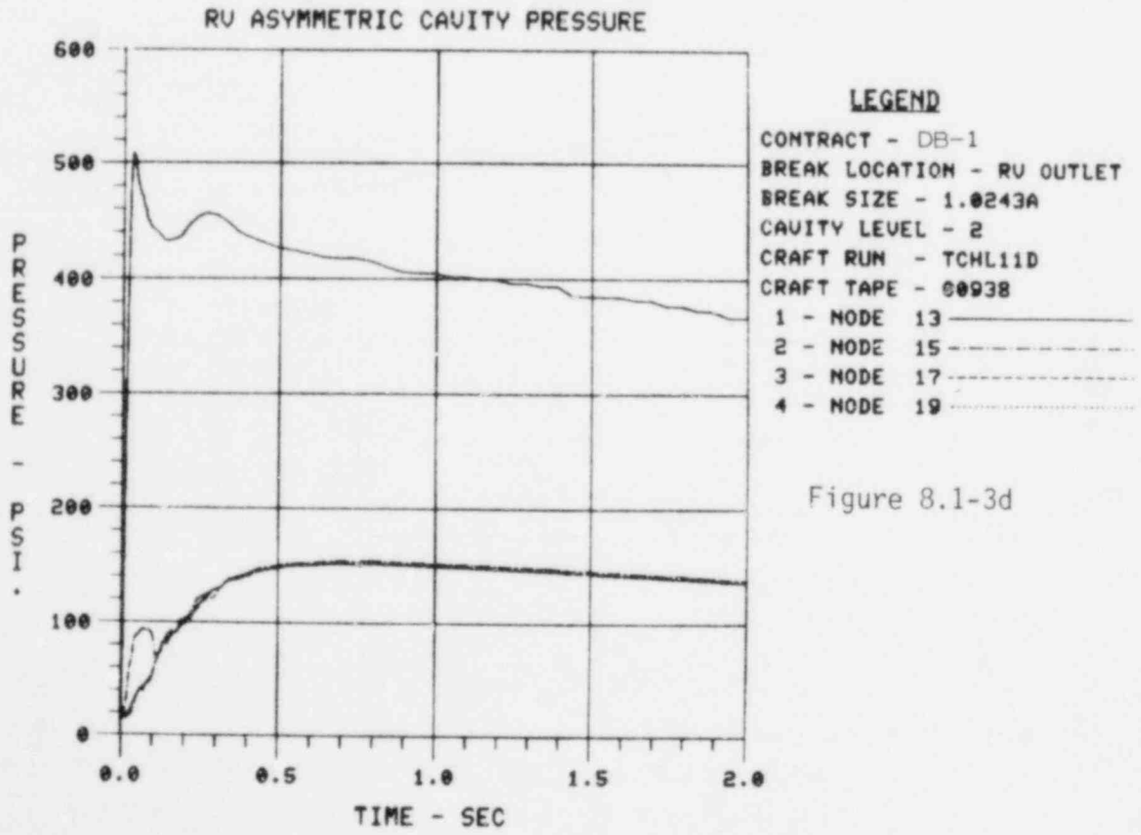

Figure 8.1-3d

Figure 8.1-3. (Cont'd)

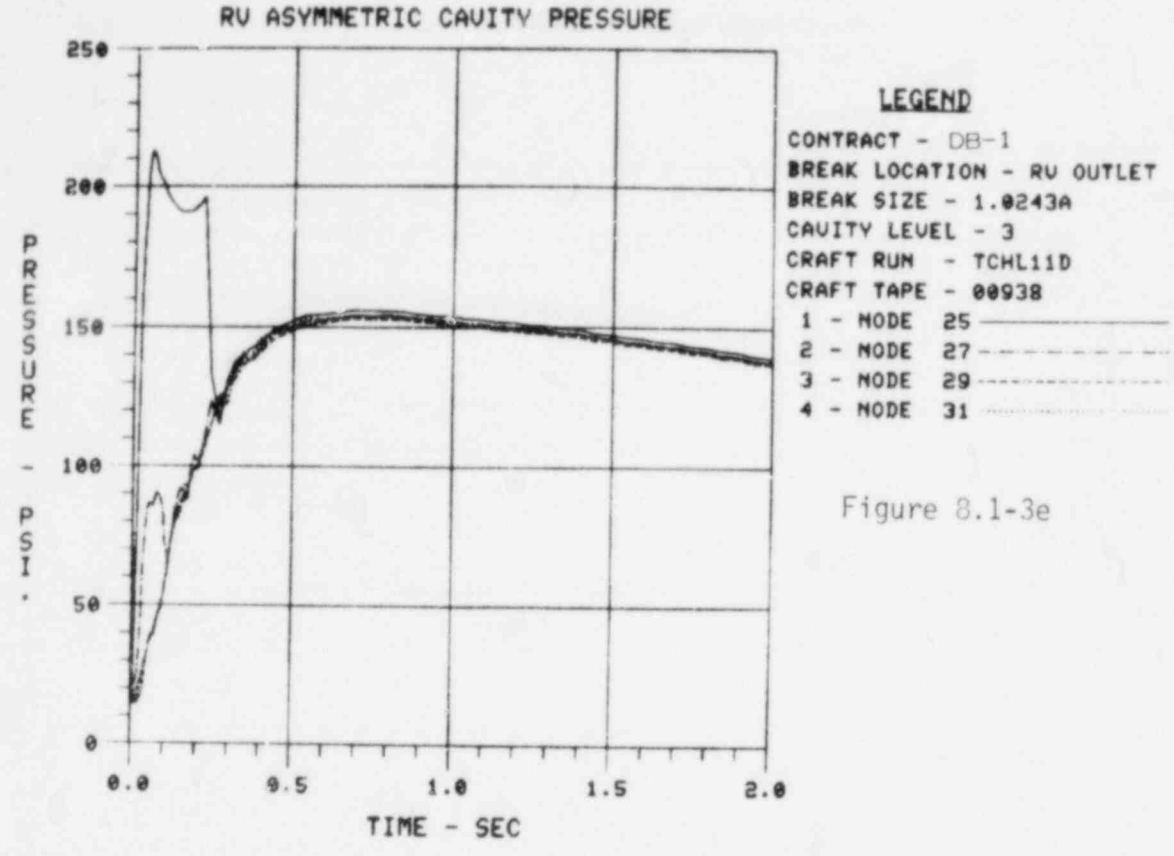

Figure 8.1-3e

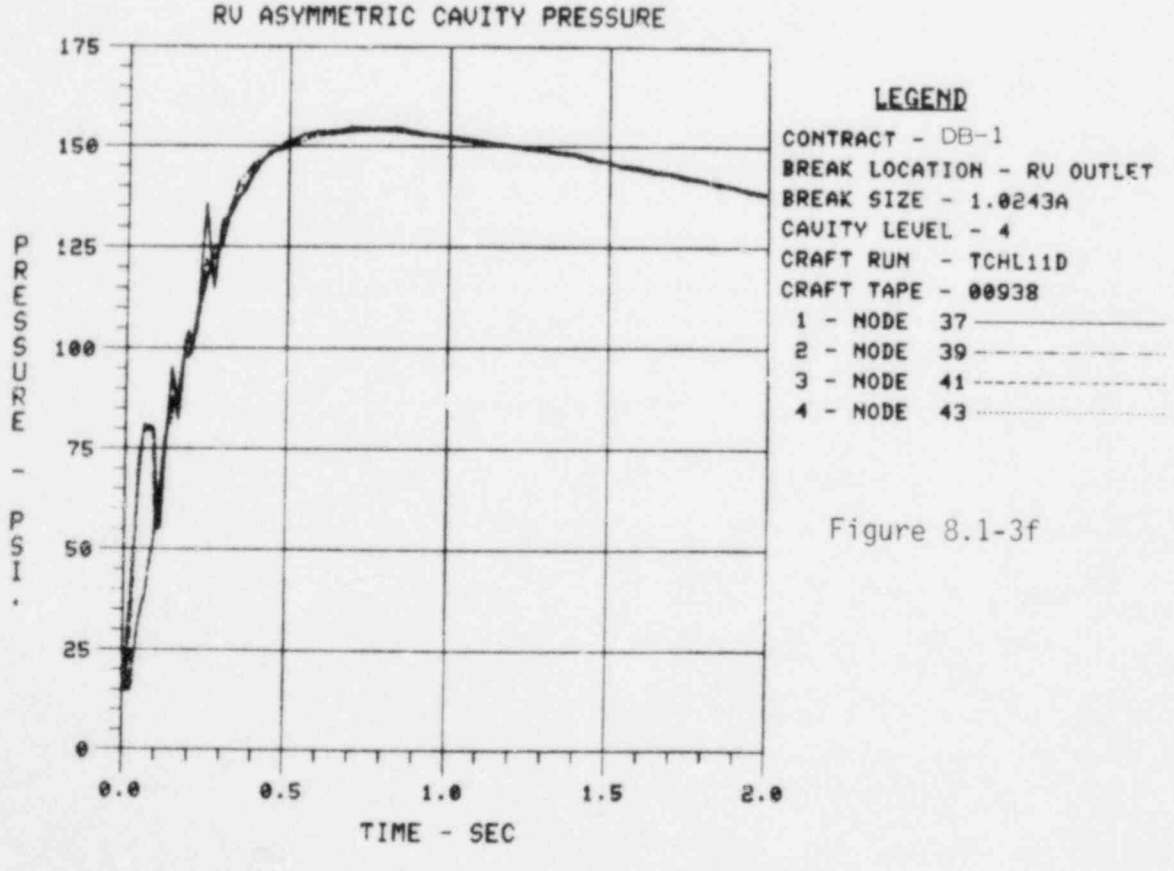

Figure 8.1-3f

Figure 8.1-3. (Cont'd)

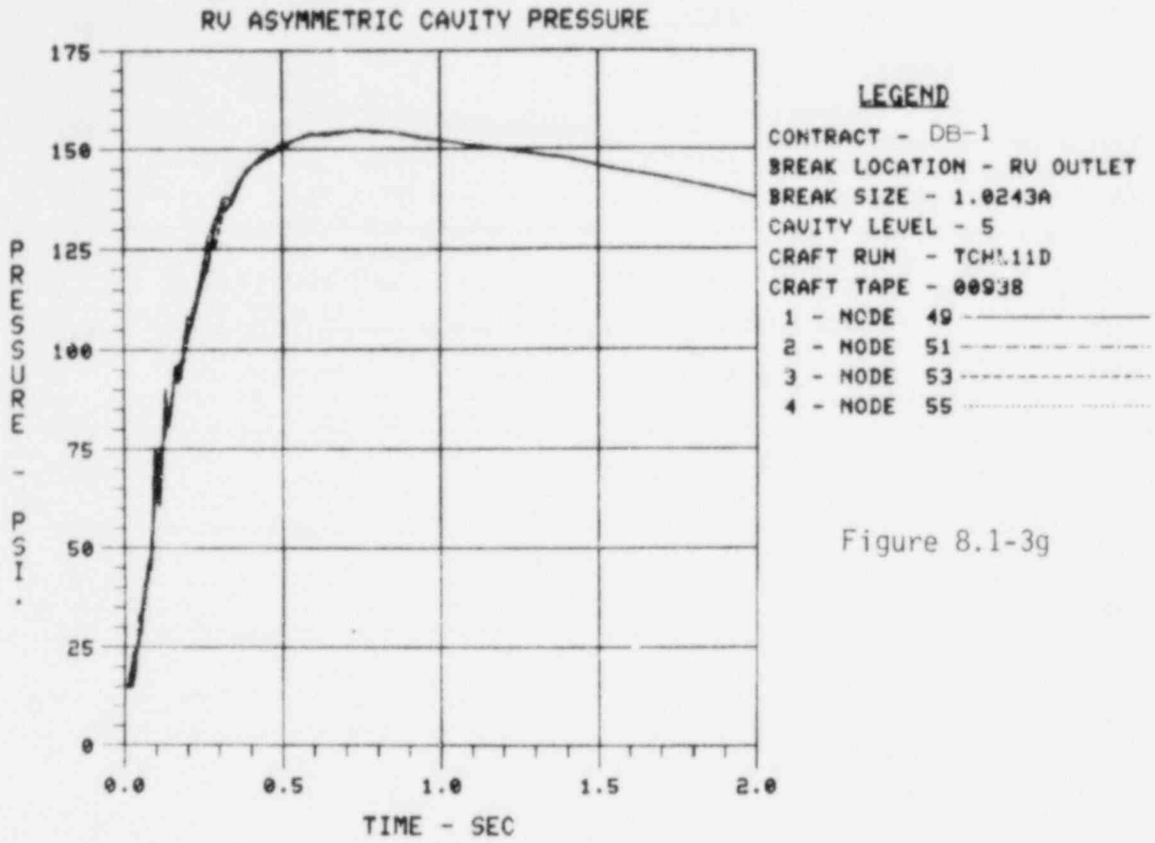

Figure 8.1-3g

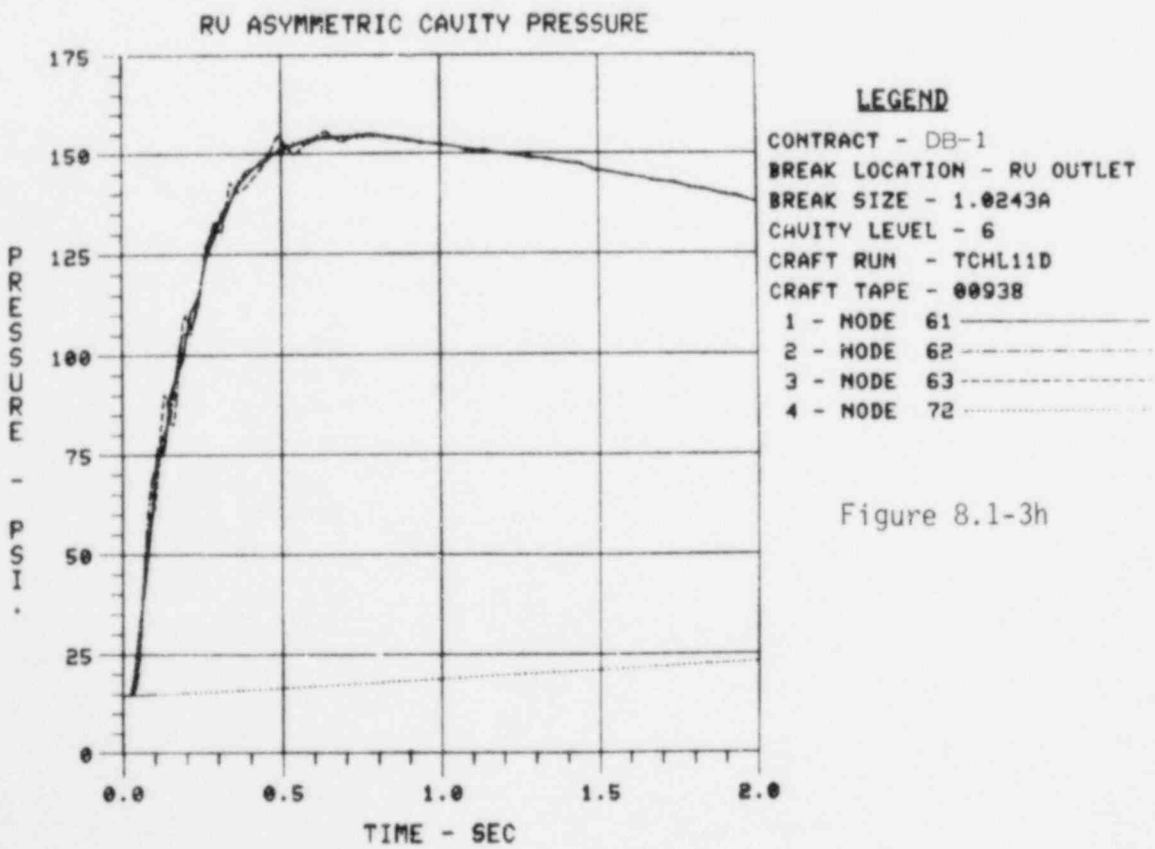

Figure 8.1-3h

Figure 8.1-4. RV Asymmetric Cavity Pressure — Davis Besse-1

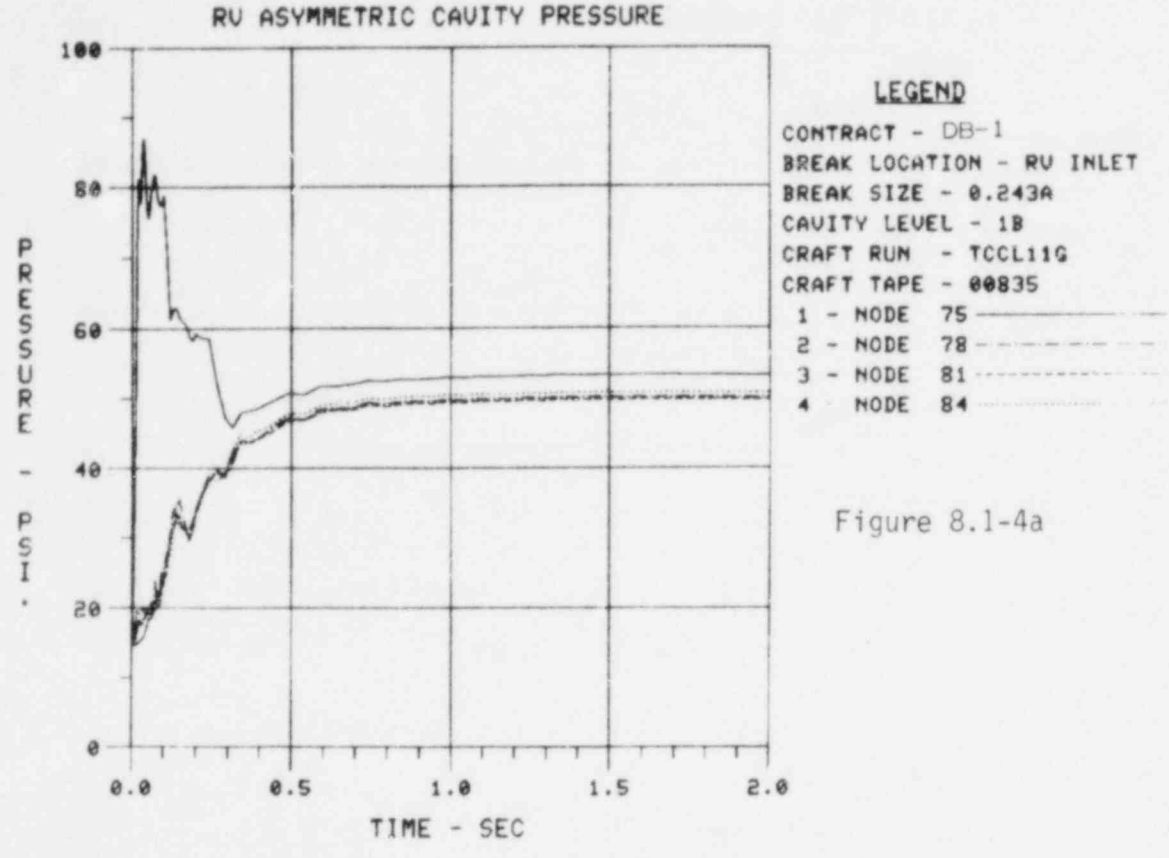

Figure 8.1-4a

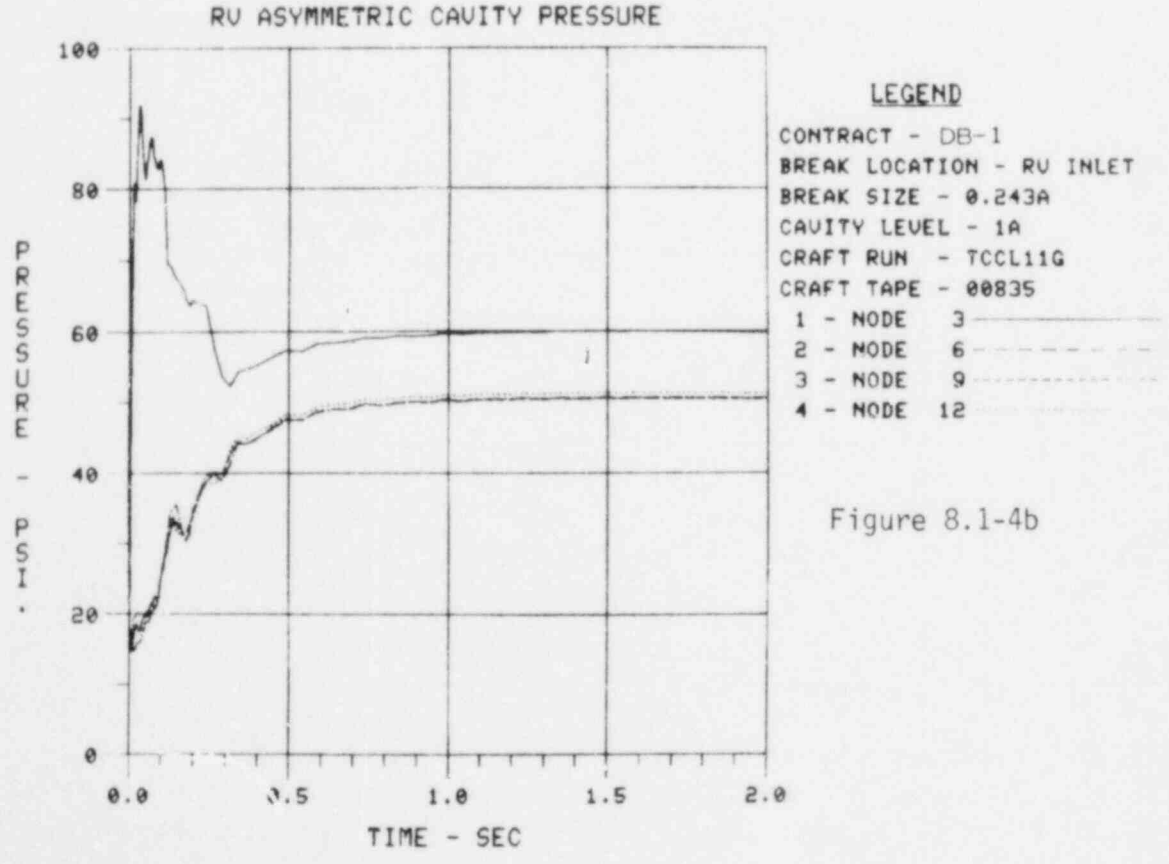

Figure 8.1-4b

Figure 8.1-4. (Cont'd)

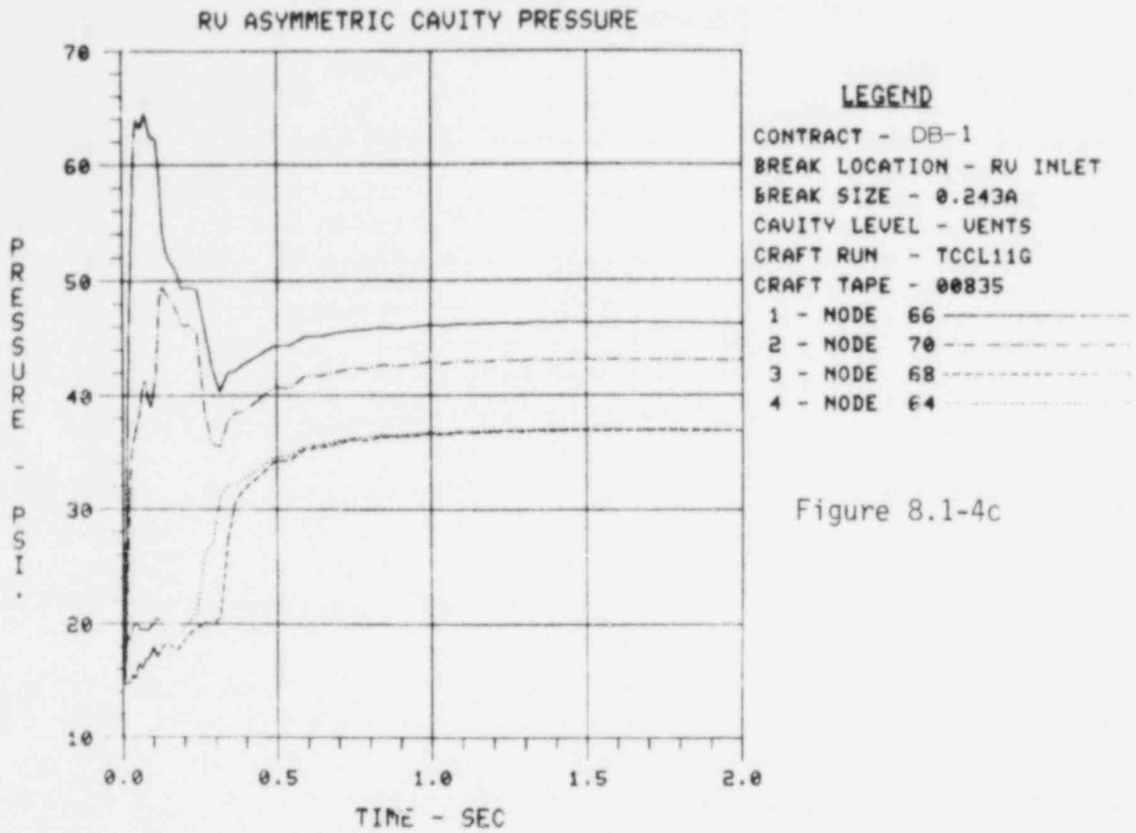

Figure 8.1-4c

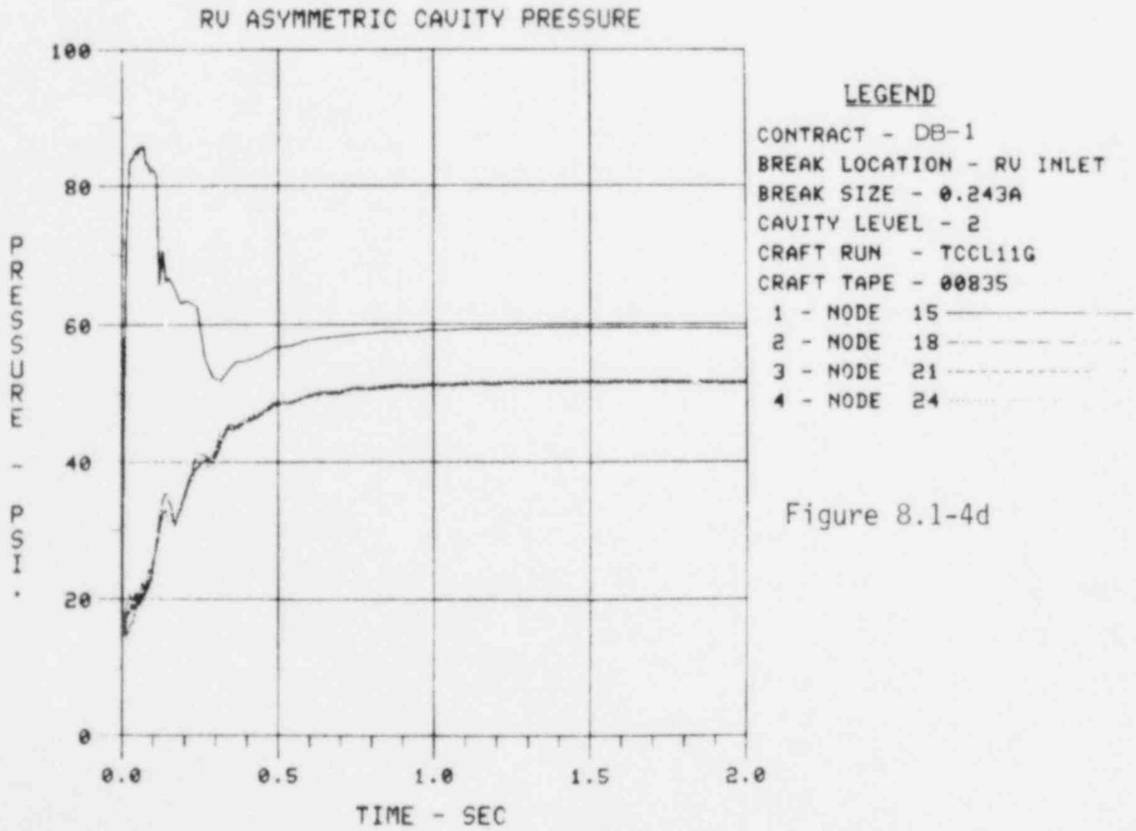

Figure 8.1-4d

Figure 8.1-4. (Cont'd)

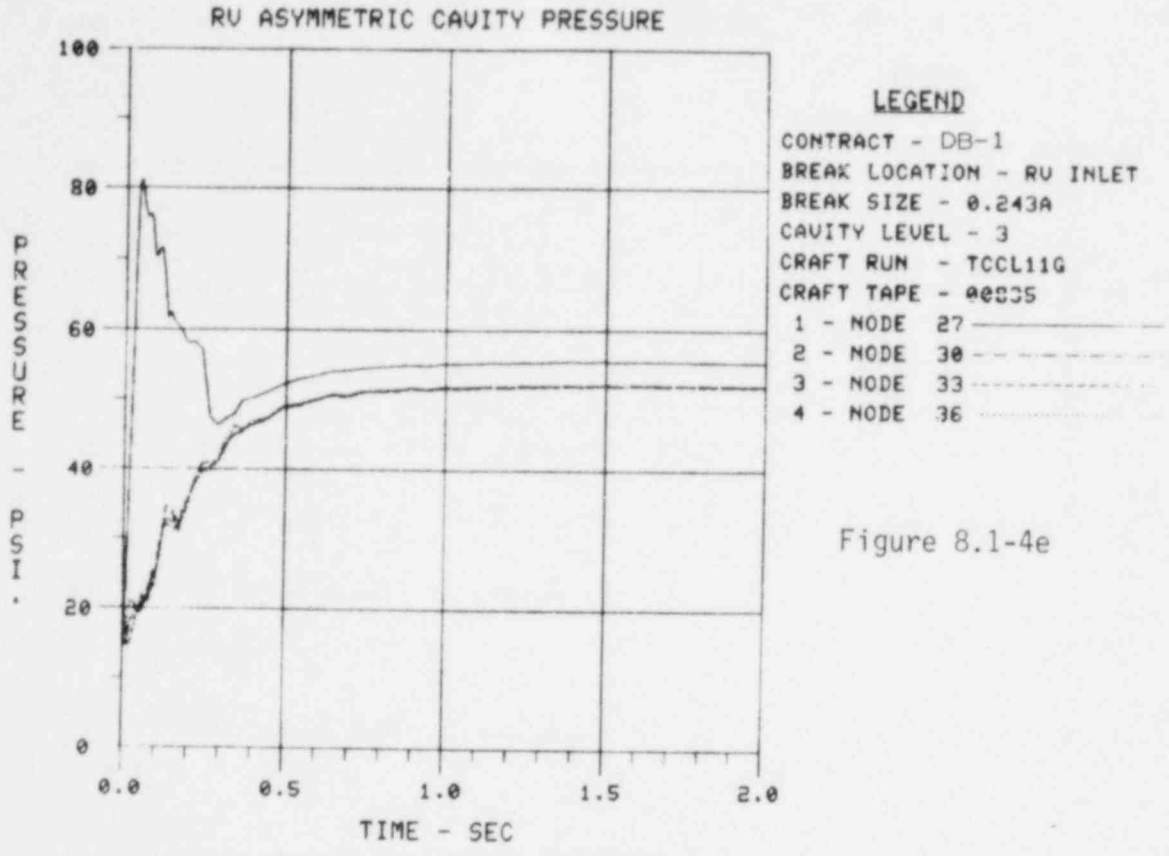

Figure 8.1-4e

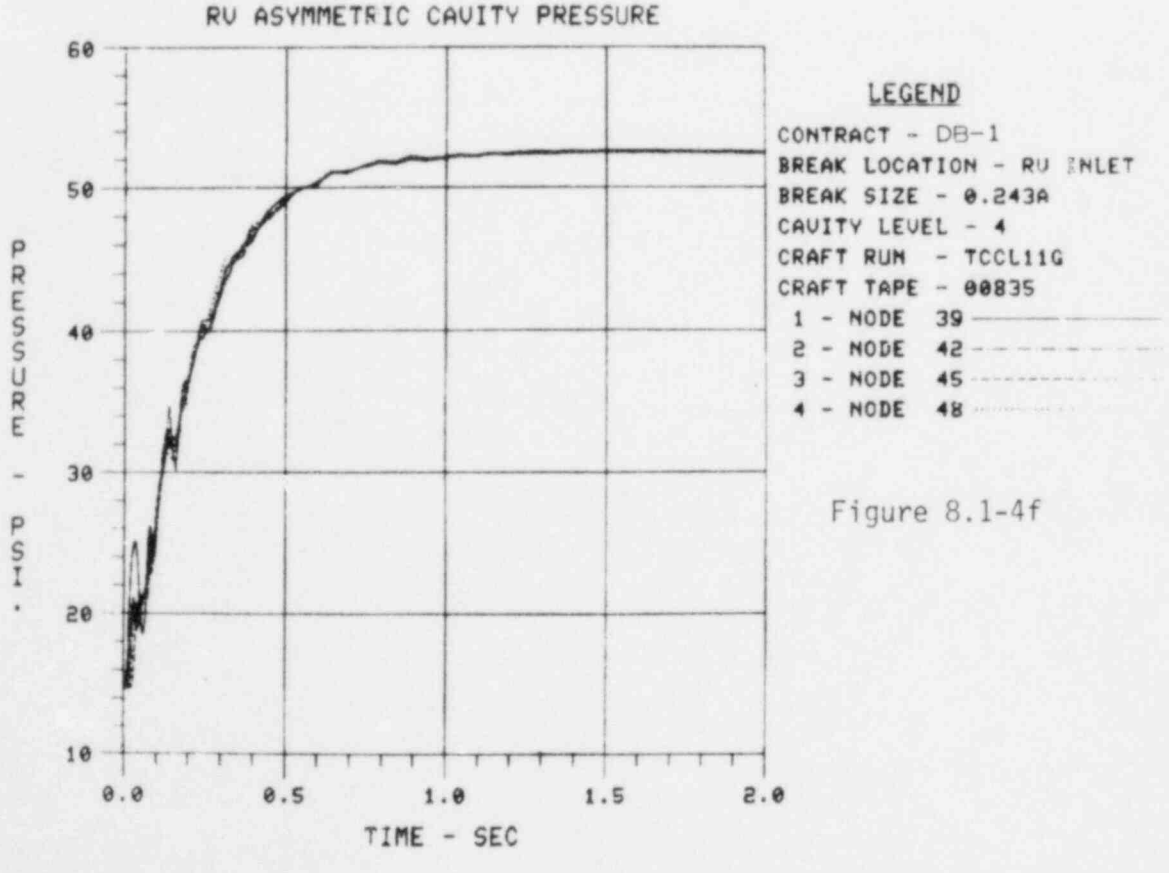

Figure 8.1-4f

Figure 8.1-4. (Cont'd)

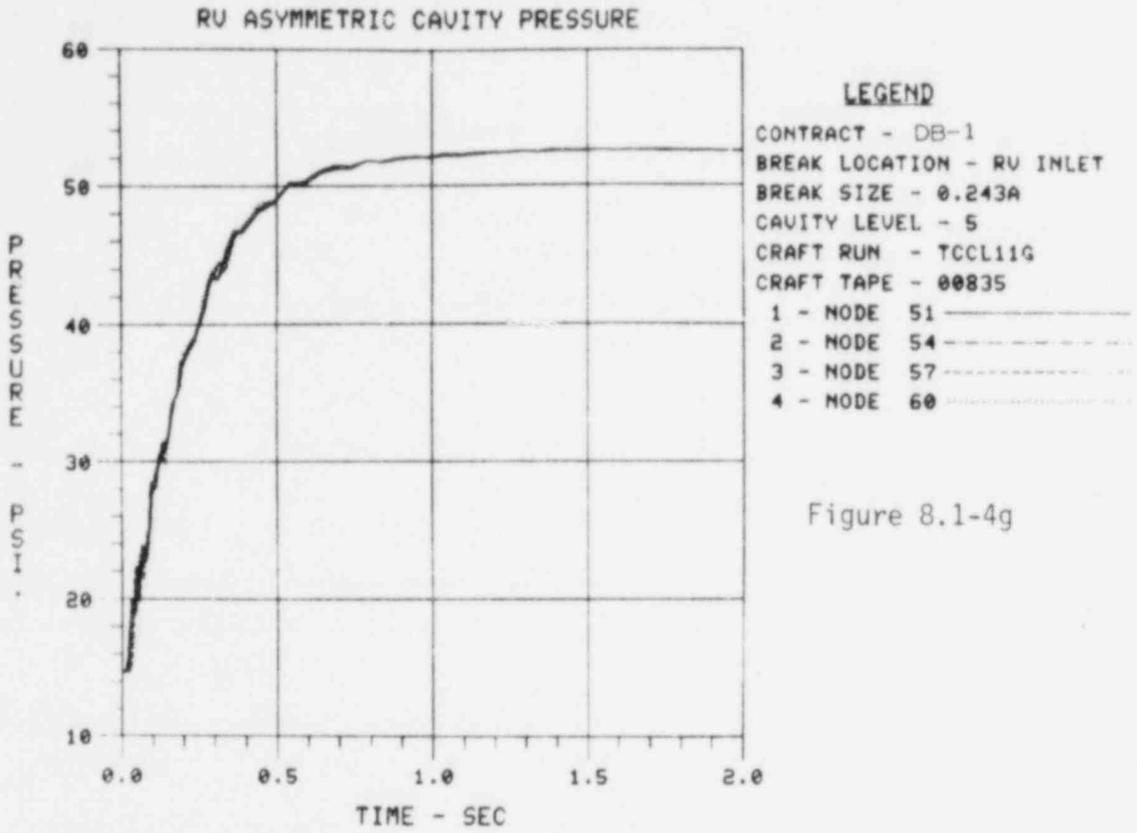

Figure 8.1-4g

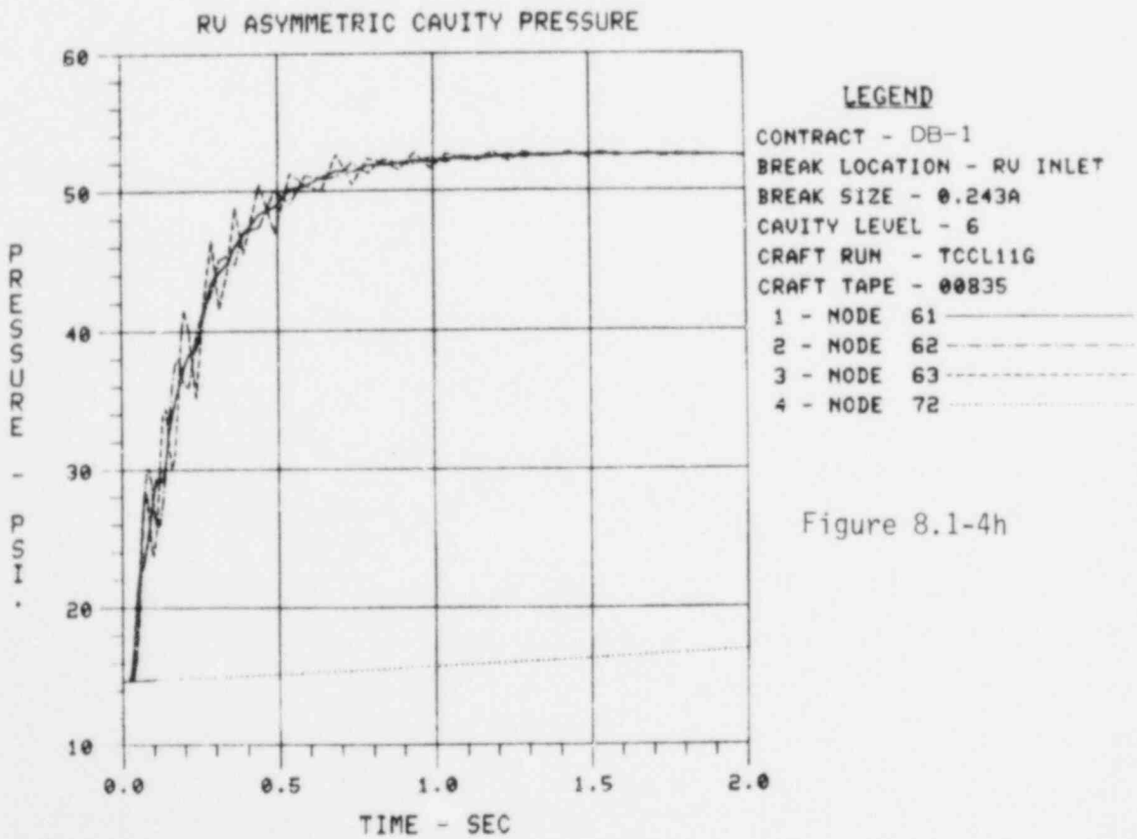

Figure 8.1-4h

Figure 8.1-5. Global Coordinate System, B&W Nuclear Steam System

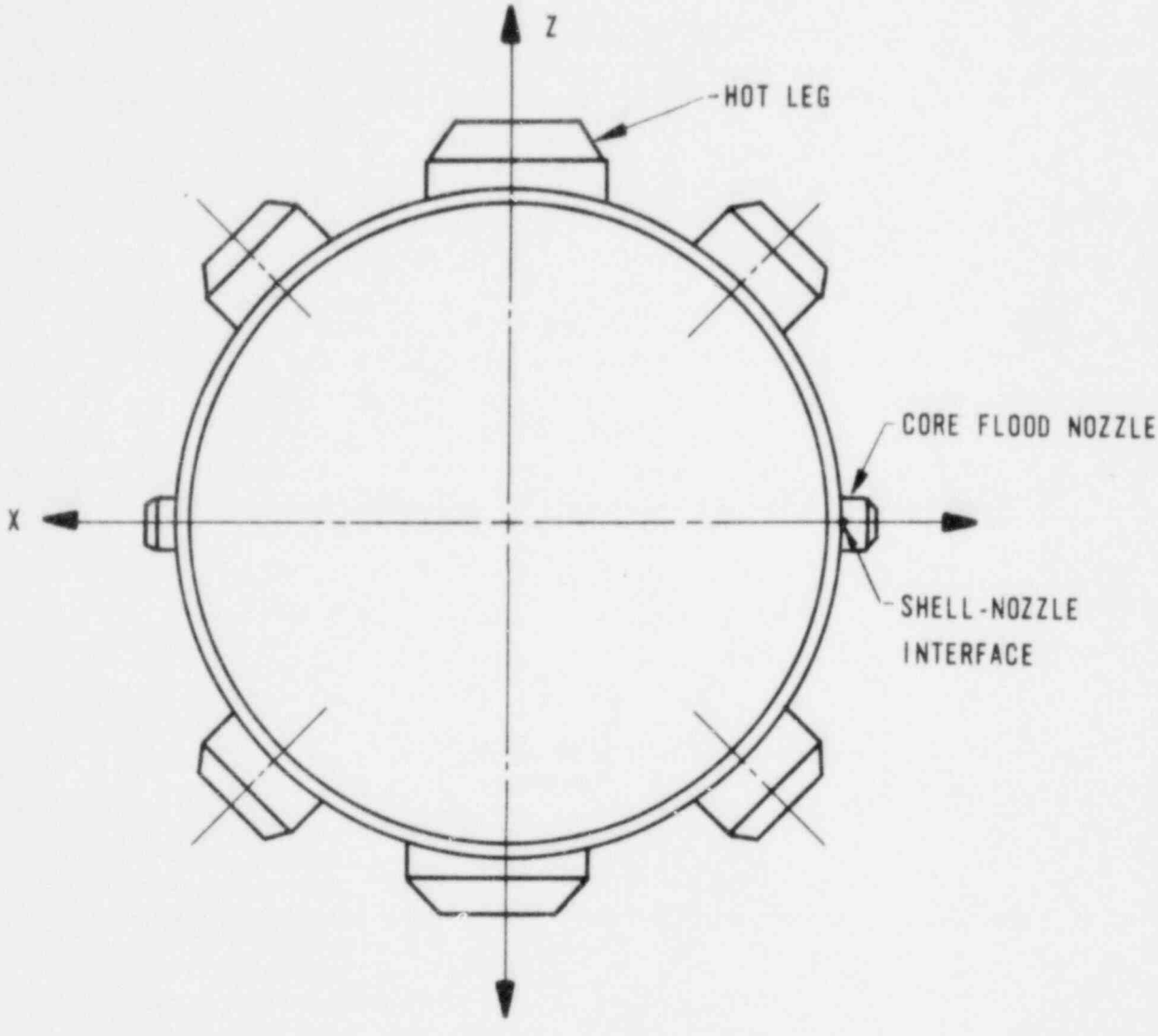

REACTOR VESSEL (PLAN VIEW)

Figure 8.1-6. Reactor Vessel Elevation View

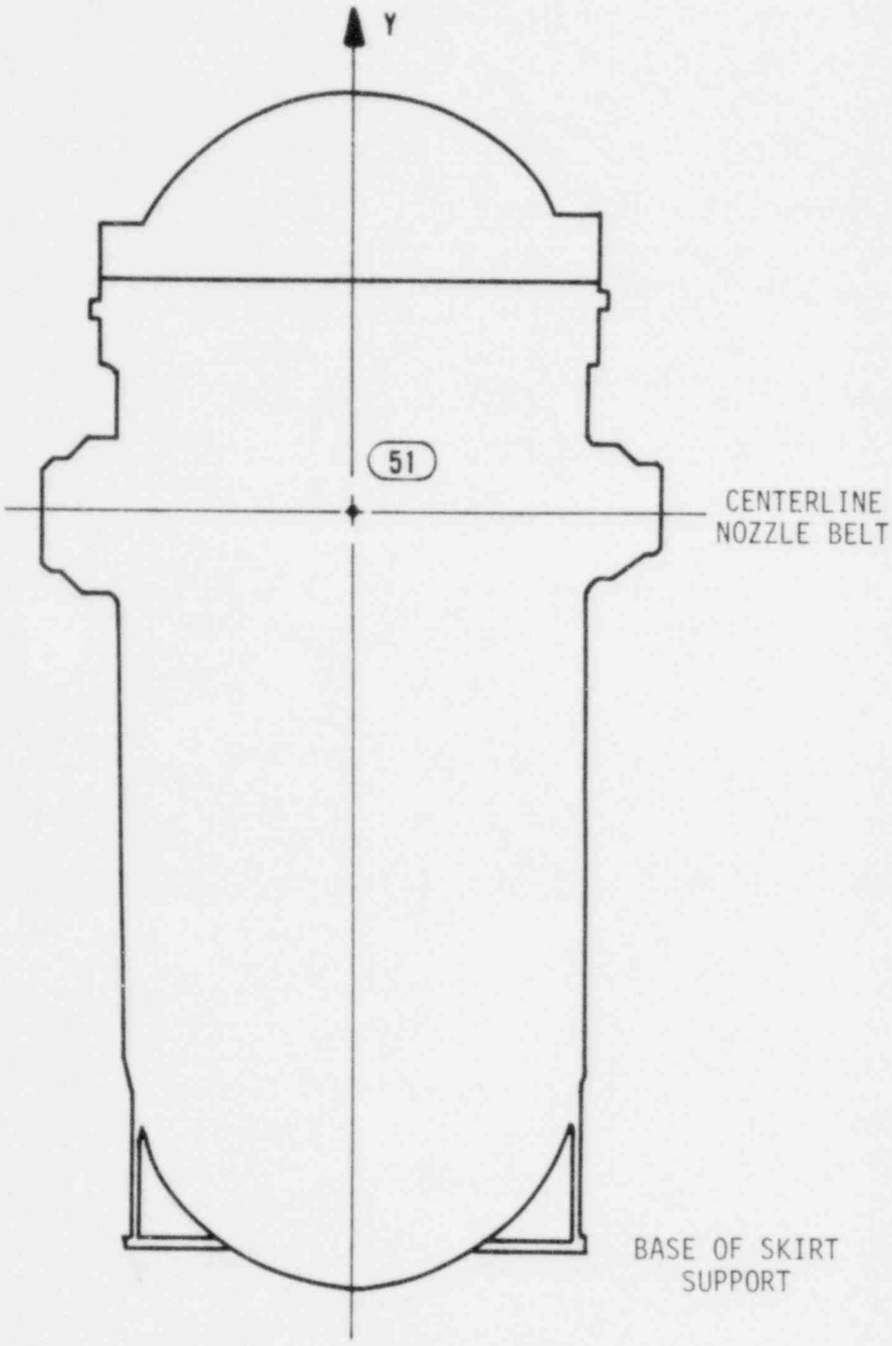

Table 8.1-1. Asymmetric Cavity Loadings

Plant	Cold leg		Hot leg	
	Peak values (tables)	Time history plots (figures)	Peak values (tables)	Time history plots (figures)
Oconee 1, 2, 3	8.1-2	8.1-7	8.1-8	8.1-13
Crystal River 3	8.1-3	8.1-8	8.1-9	8.1-14
TMI-1	8.1-3	8.1-8	8.1-9	8.1-14
TMI-2	8.1-4	8.1-9	8.1-10	8.1-15
ANO-1	8.1-5	8.1-10	8.1-11	8.1-16
Rancho Seco	8.1-6	8.1-11	8.1-12	8.1-17
Davis-Besse 1	8.1-7	8.1-12	8.1-13	8.1-18

Note: All moments are taken about the RV nozzle centerline. For multi-linear plots, the following break opening area (BOA) legend applies:

———— 2A

· · · · · · · · · · 1.5A

—·—·—·—·— 1.0A

- - - - - - - - - - 0.6A

— — — — — — 0.3A

Table 8.1-2. Oconee 1, 2, 3 Cold Leg Peak Force Summary

Break area	Resultant horizontal force, lb	Vertical at peak horiz force pt, lb	Resultant moment, in.-lb
2.0A	5.8 E6	5.0 E5	3.2 E8
1.5A	4.8 E6	4.0 E5	2.8 E8
1.0A	4.1 E6	3.5 E5	2.2 E8
0.6A	3.3 E6	3.0 E5	1.7 E8
0.3A	2.1 E6	1.9 E5	1.1 E8

Figure 8.1-7. Oconee 1, 2, and 3 Cold Leg Break Time History

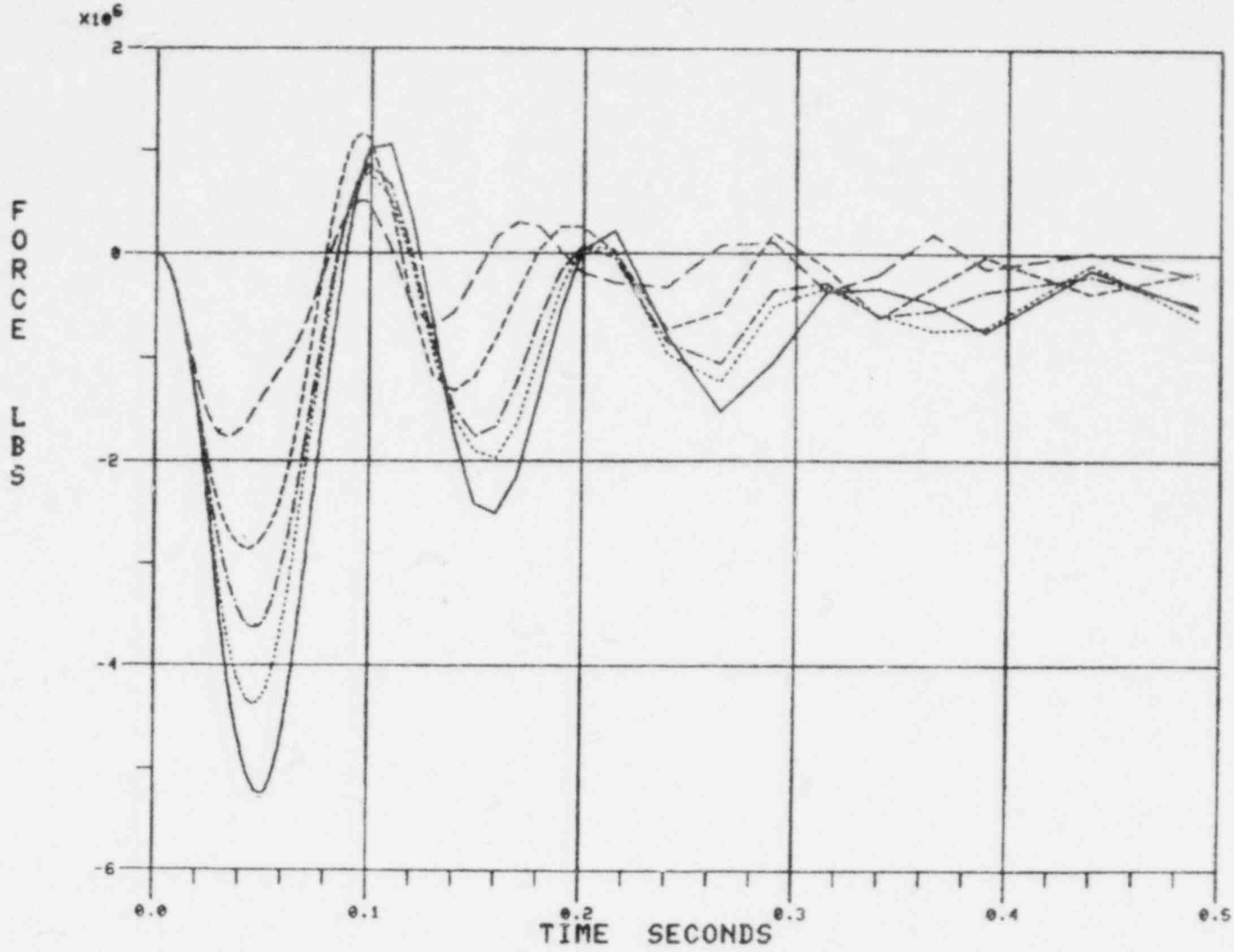

Figure 8.1-7. (Cont'd)

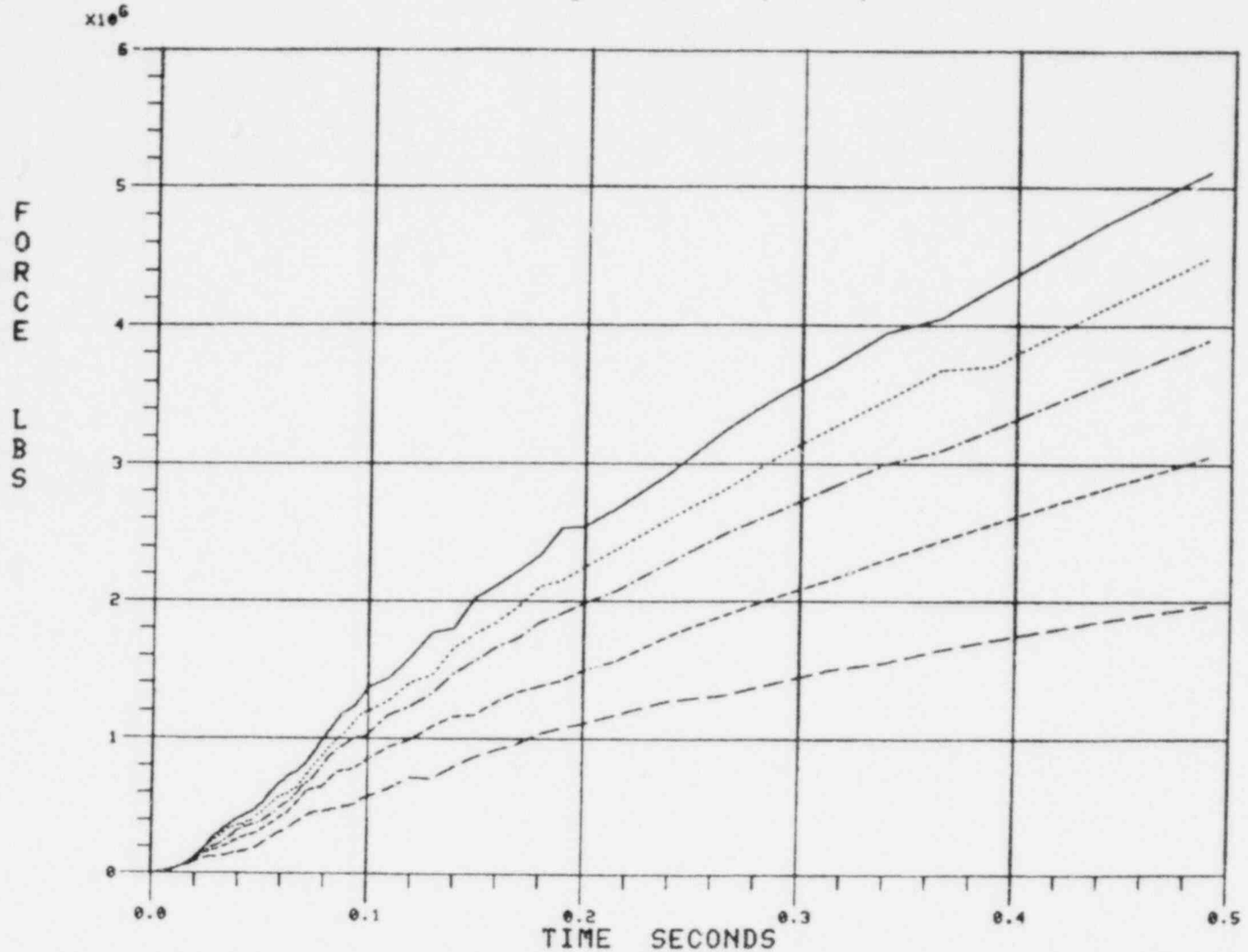

JOINT 51 Y DIR RV

Figure 8.1-7. (Cont'd)

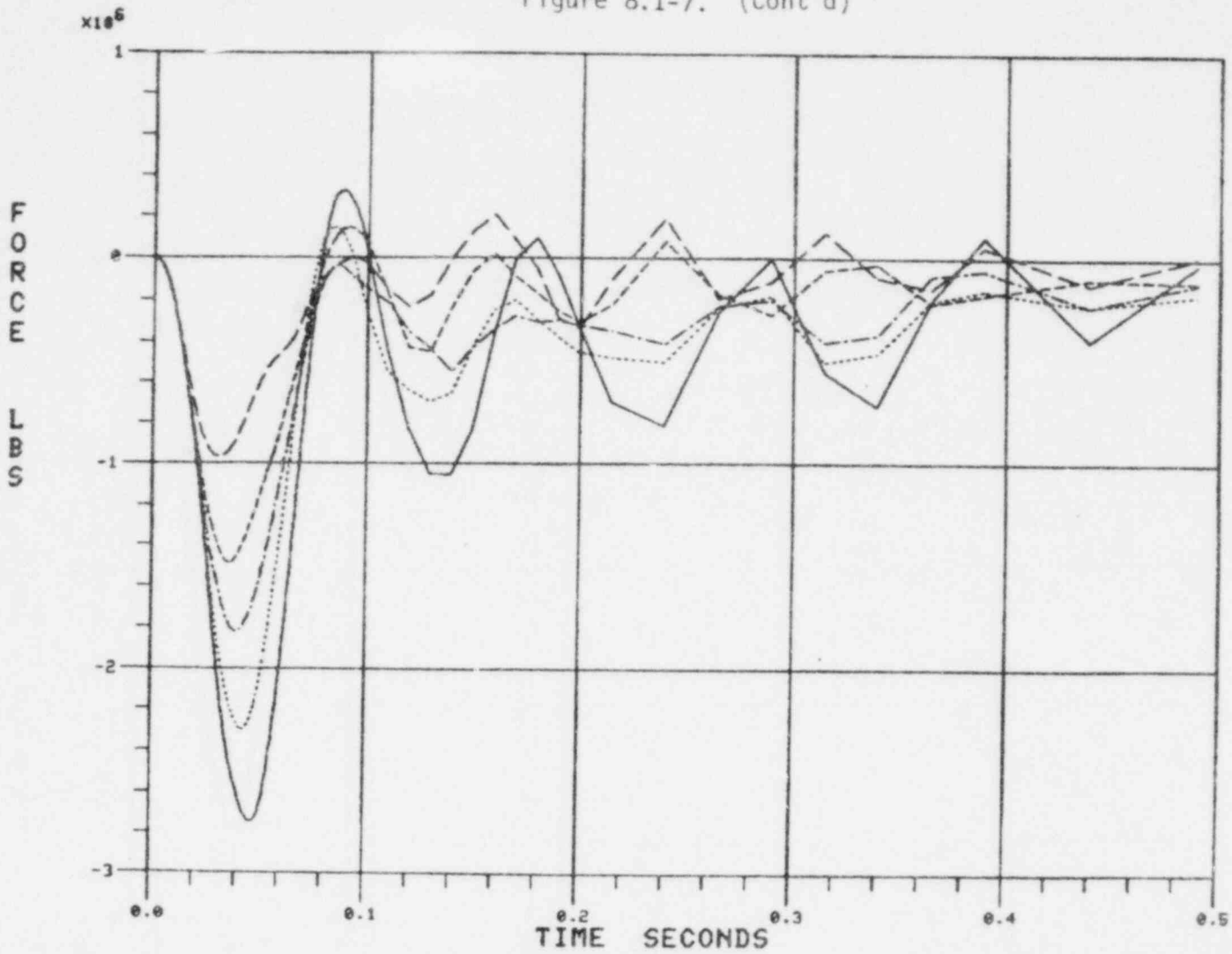

JOINT 51 Z DIR RV

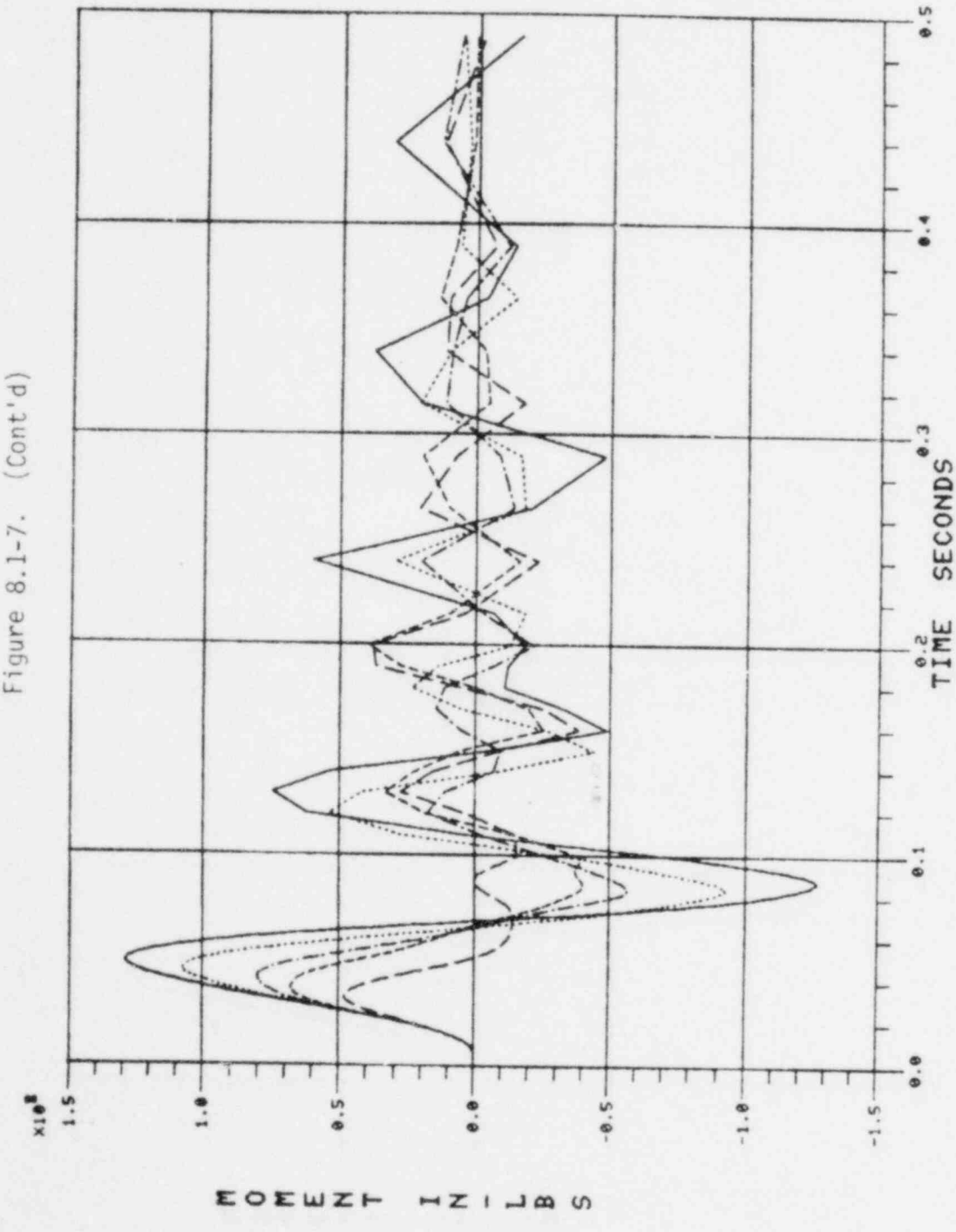

Figure 8.1-7. (Cont'd)

Figure 8.1-7. (Cont'd)

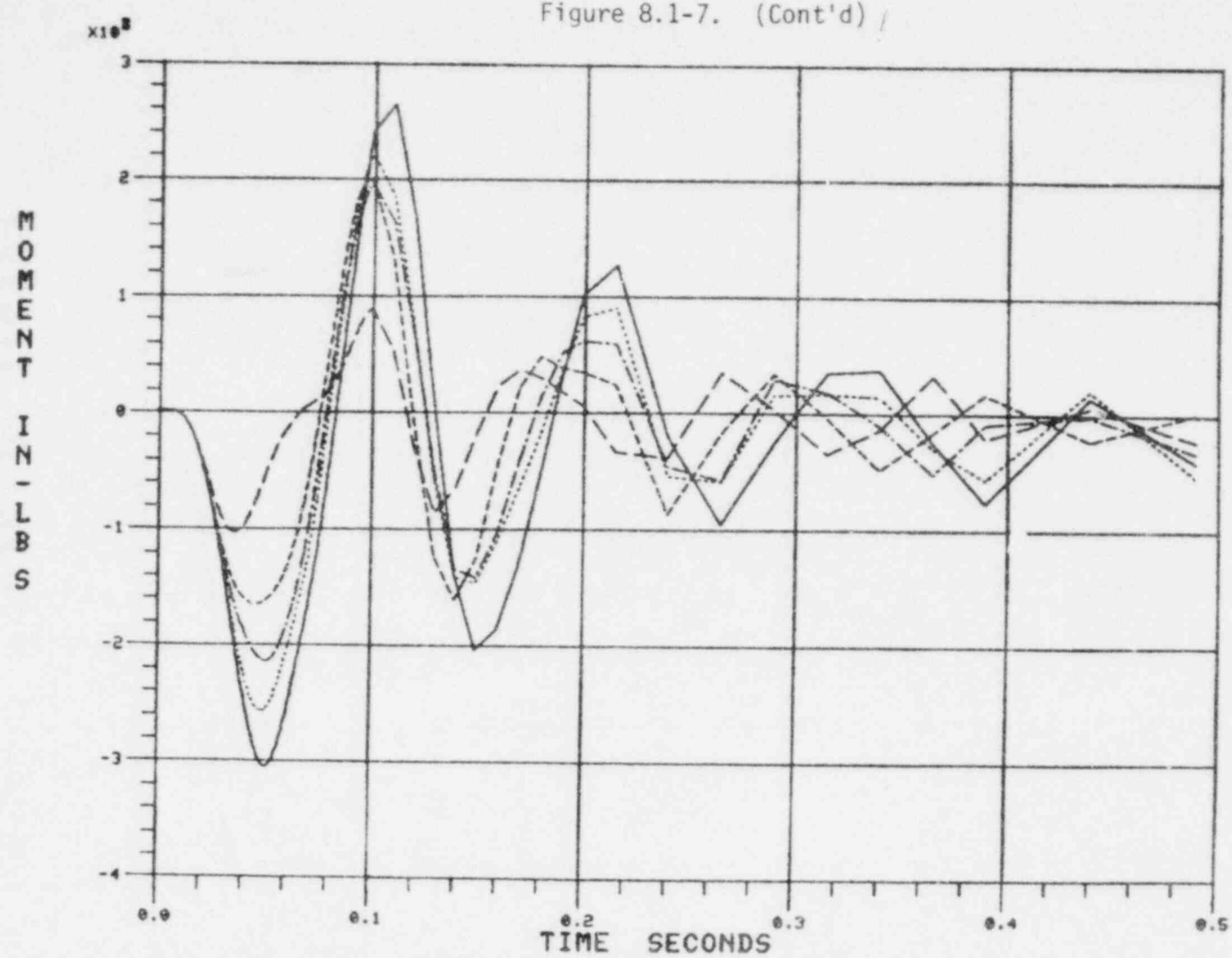

JOINT 51 Z ROT RV

Table 8.1-3. Crystal River 3 and TMI-1 Cold Leg Peak Force Summary

Break area	Resultant horizontal force, lb	Vertical at peak horiz force pt, lb	Resultant moment, in.-lb
2.0A	4.9 E6	6.0 E5	2.0 E8
1.5A	4.1 E6	5.7 E5	1.6 E8
1.0A	3.2 E6	4.5 E5	1.3 E8
0.6A	2.6 E6	3.7 E5	1.1 E8
0.3A	1.6 E6	2.5 E5	0.8 E8

Figure 8.1-8. Crystal River 3 and TMI-1 Cold Leg Break Time History

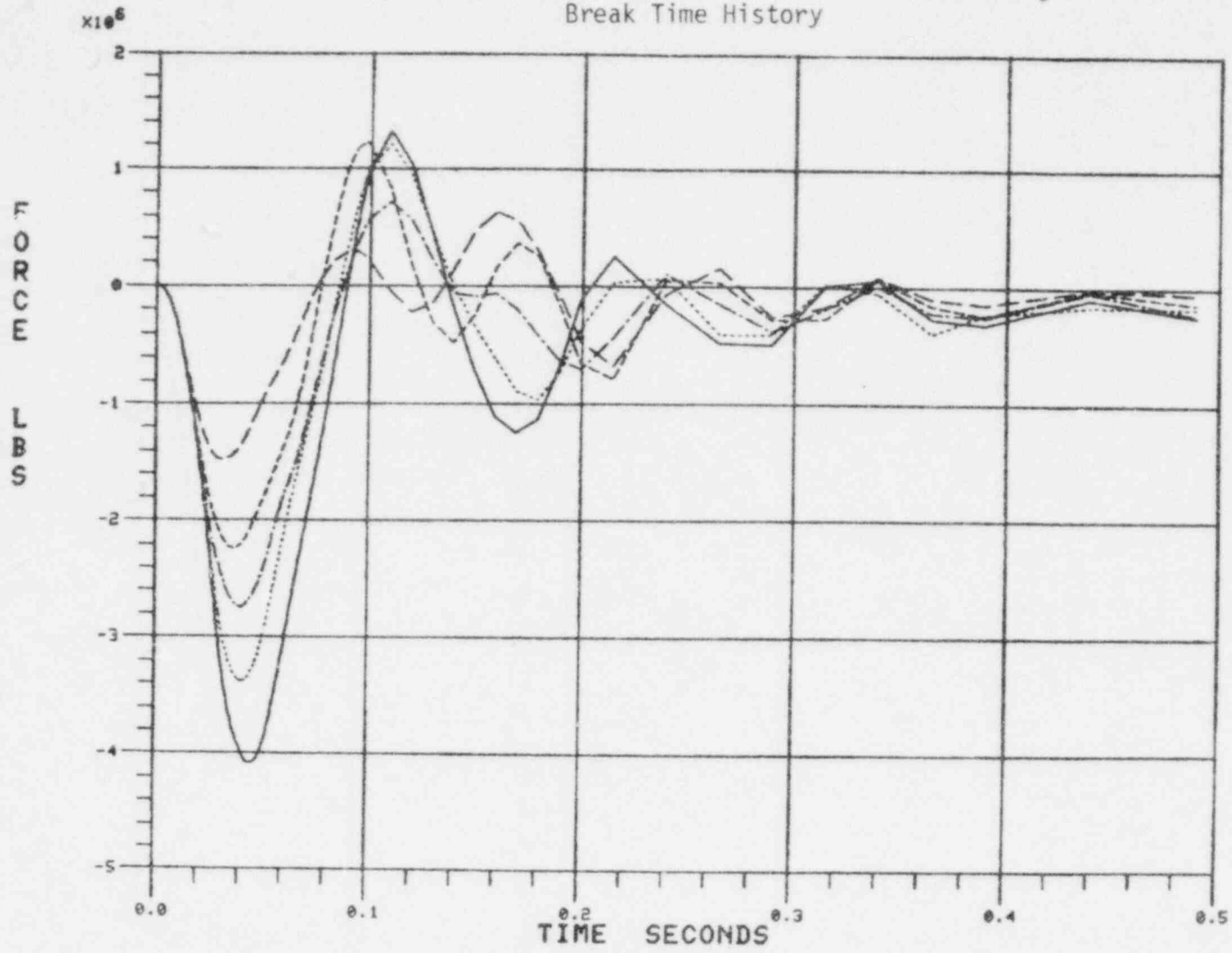

JOINT 51 X DIR RV TMFPC

Figure 8.1-8. (Cont'd)

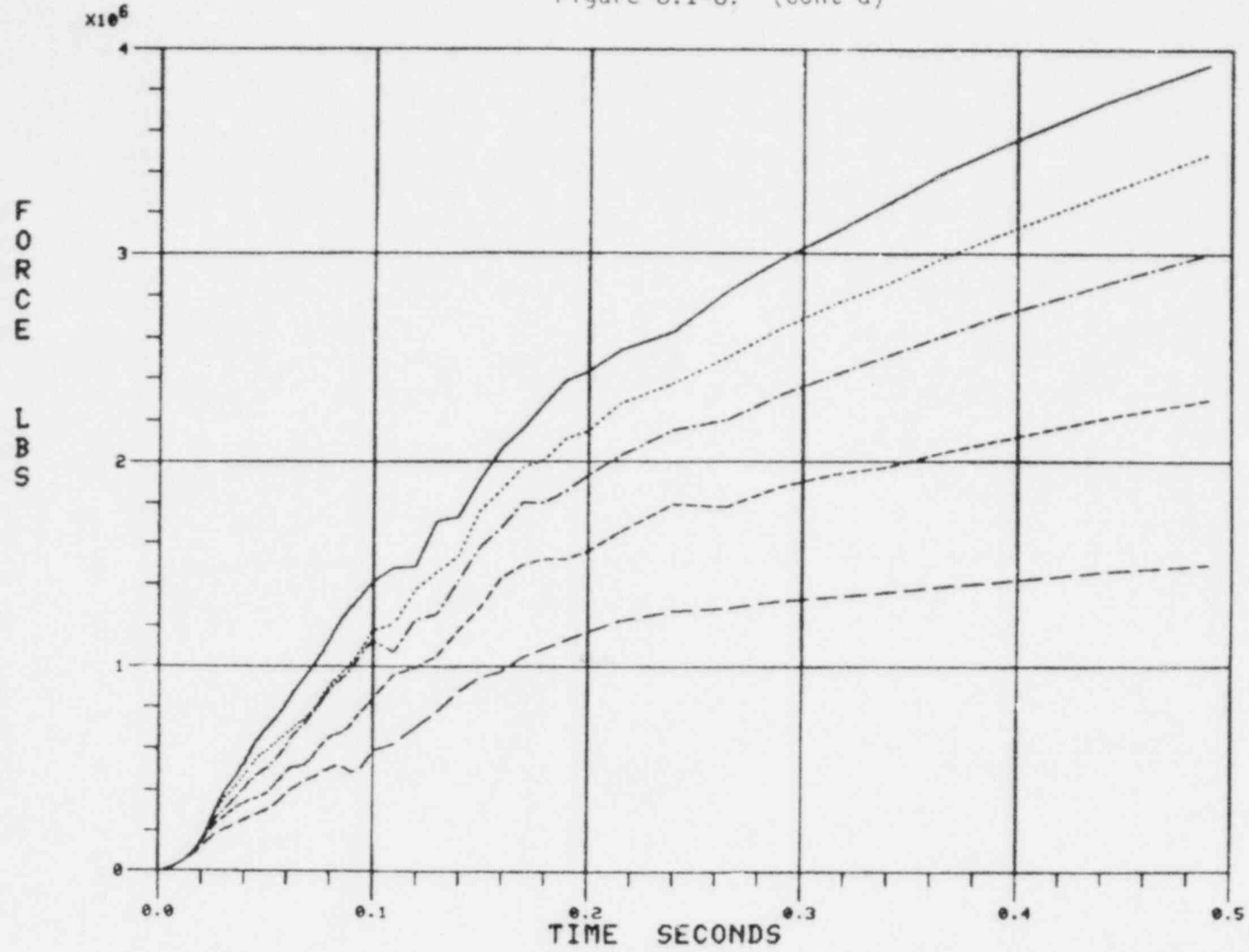

JOINT 51 Y DIR RV TMFPC

Figure 8.1-8. (Cont'd)

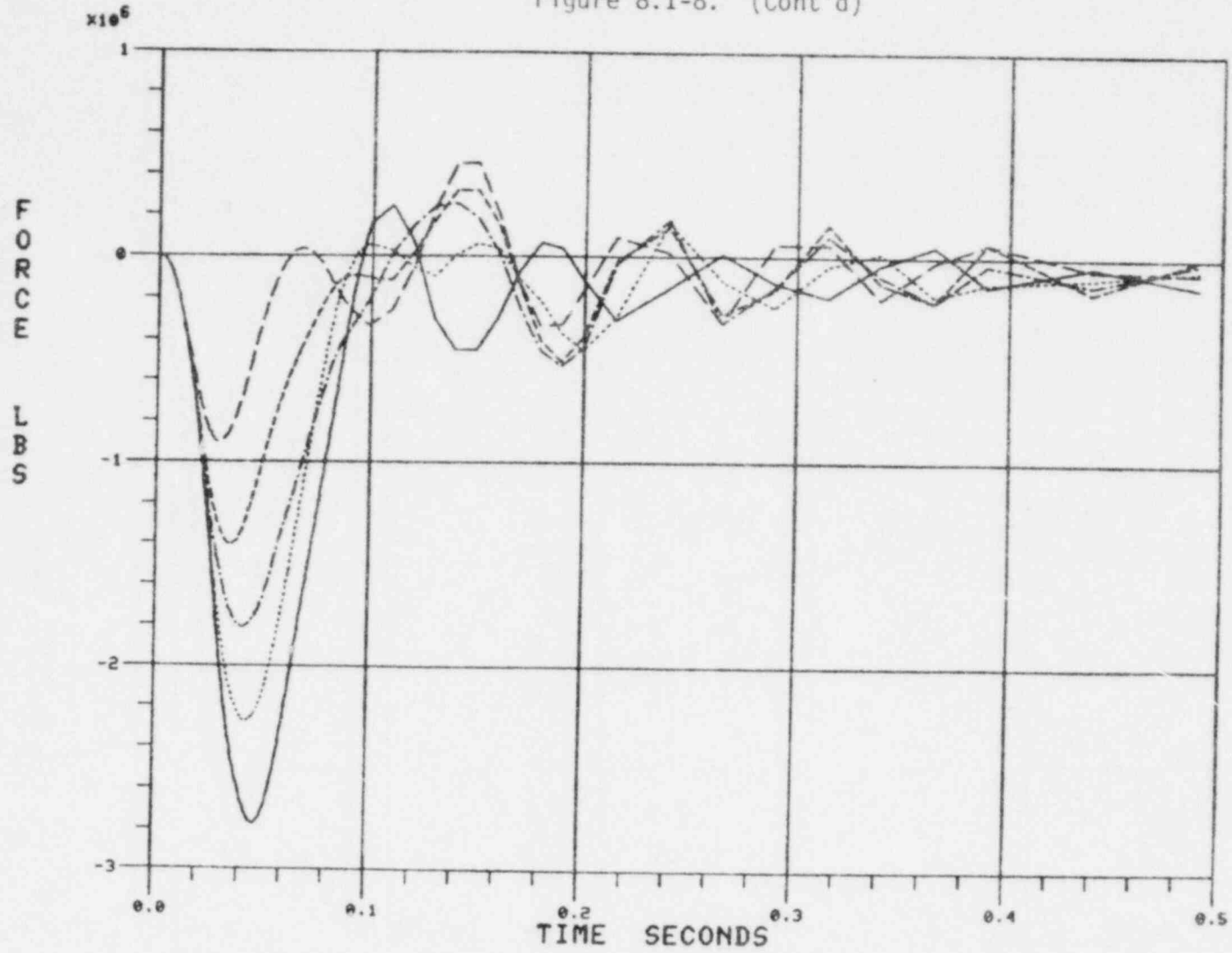

JOINT 51 Z DIR RV TMFPC

(Figure 8.1-8. (Cont'd)

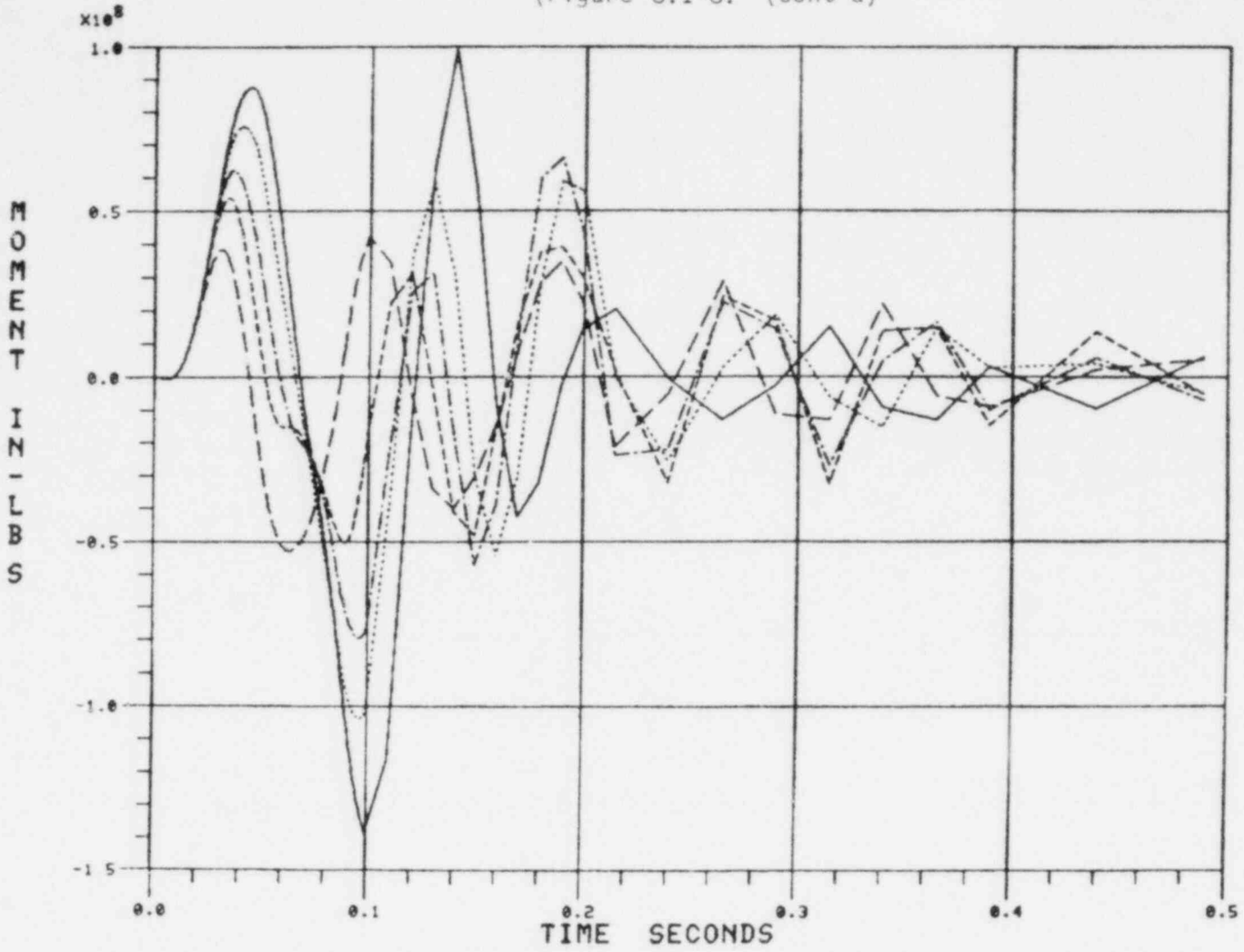

JOINT 51 X ROT RU TMFPC

Figure 8.1-8. (Cont'd)

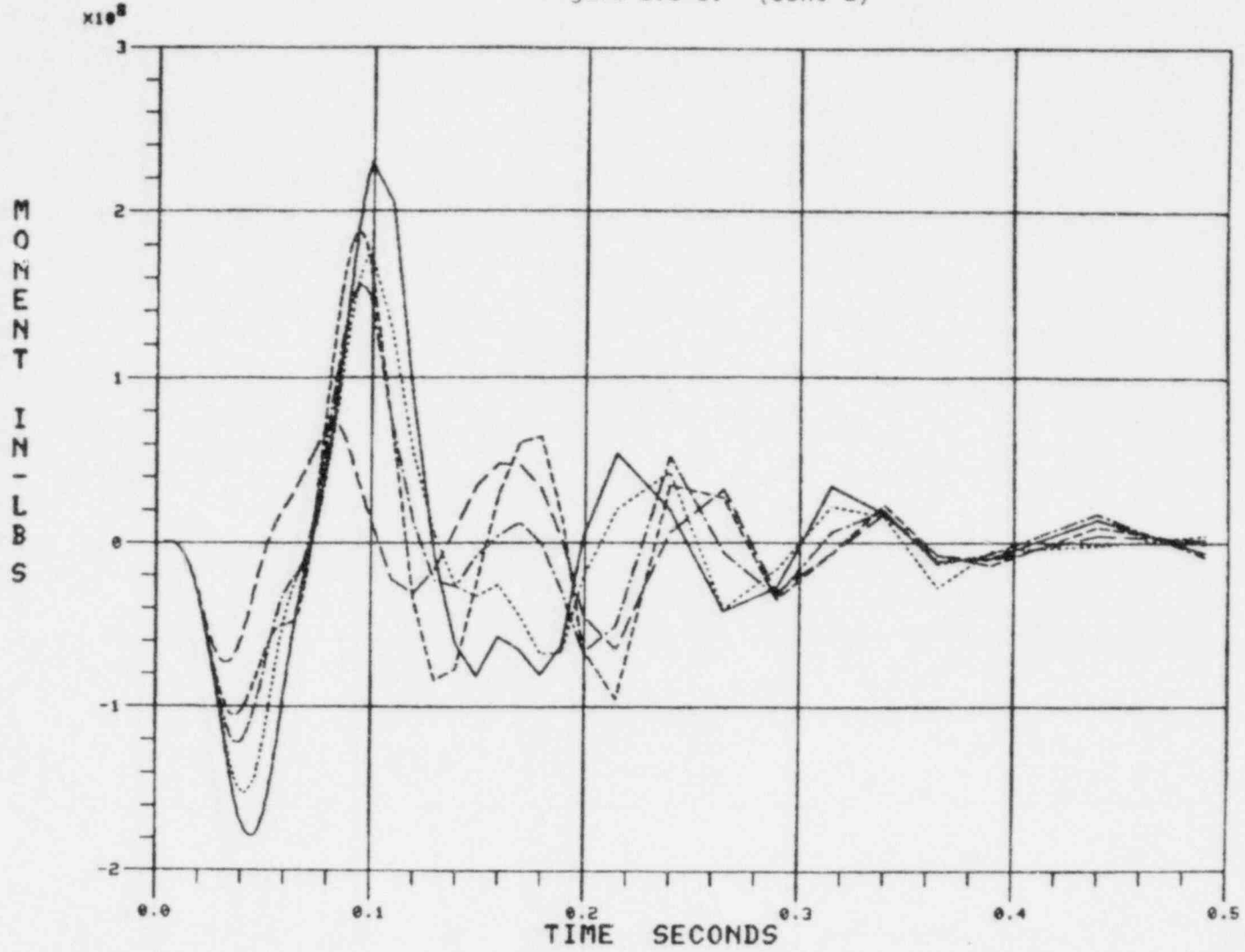

JOINT 51 Z ROT RU TMFPC

Table 8.1-4. TMI-2 Cold Leg Peak Force Summary

Break area	Resultant horizontal force, lb	Vertical at peak horiz force pt, lb	Resultant moment, in.-lb
2.0A	5.3 E6	5.0 E5	2.1 E8
1.5A	4.4 E6	4.0 E5	1.8 E8
1.0A	3.6 E6	3.8 E5	1.5 E8
0.6A	2.9 E6	3.0 E5	1.1 E8
0.3A	2.0 E6	2.0 E5	0.75 E8

Figure 8.1-9. TMI-2 Cold Leg Break Time History

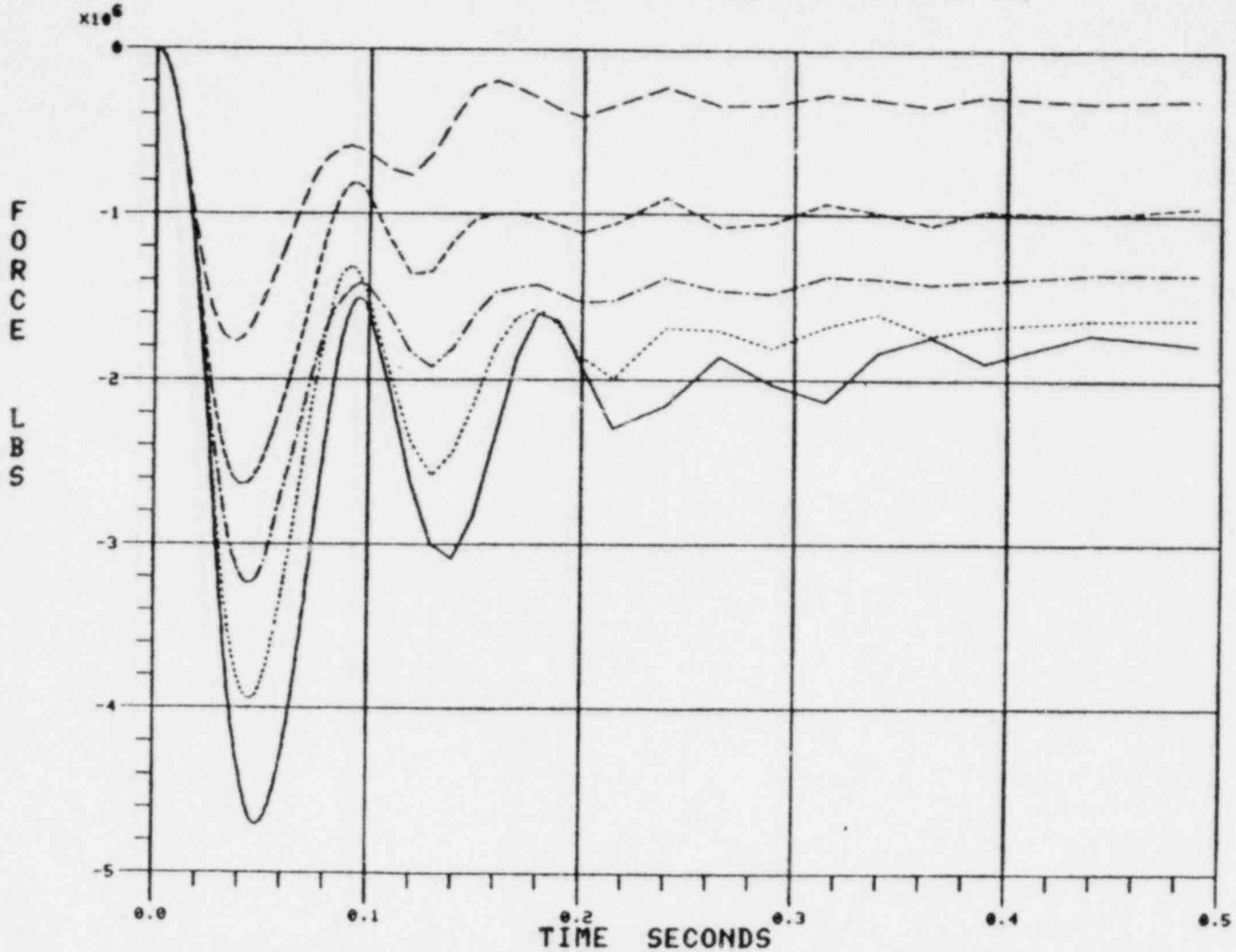

Figure 8.1-9. (Cont'd)

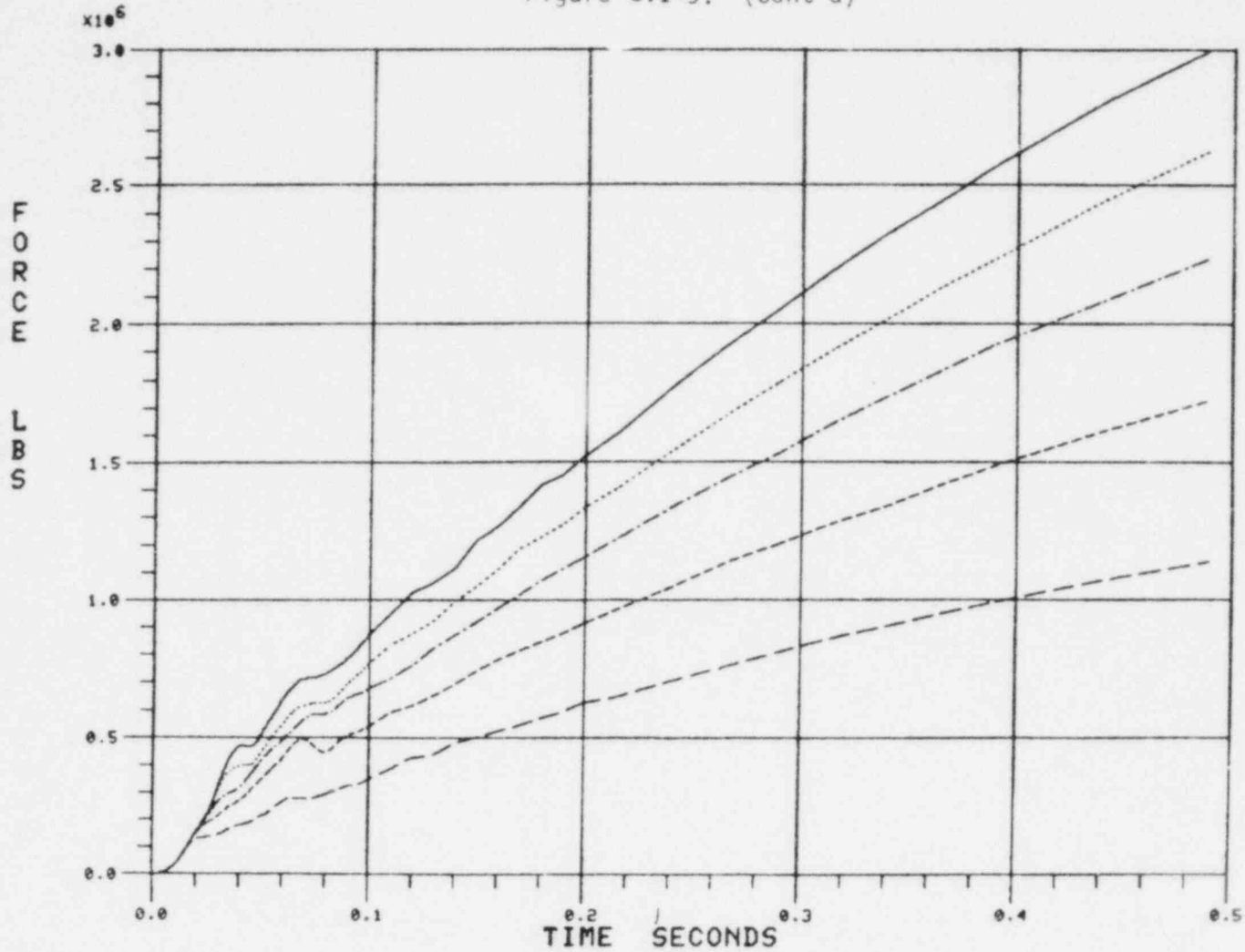

JOINT 51 Y DIR RV

Figure 8.1-9. (Cont'd)

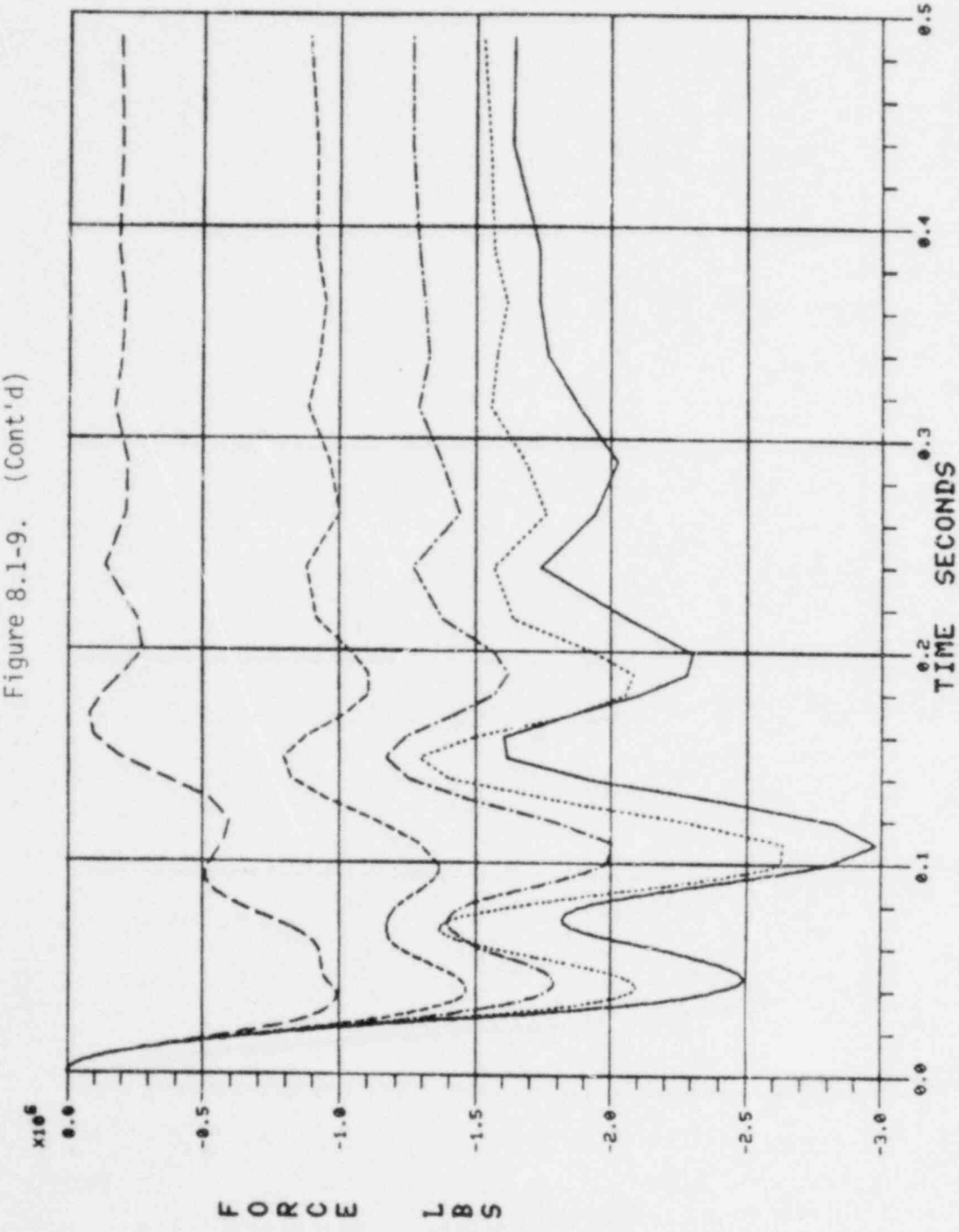

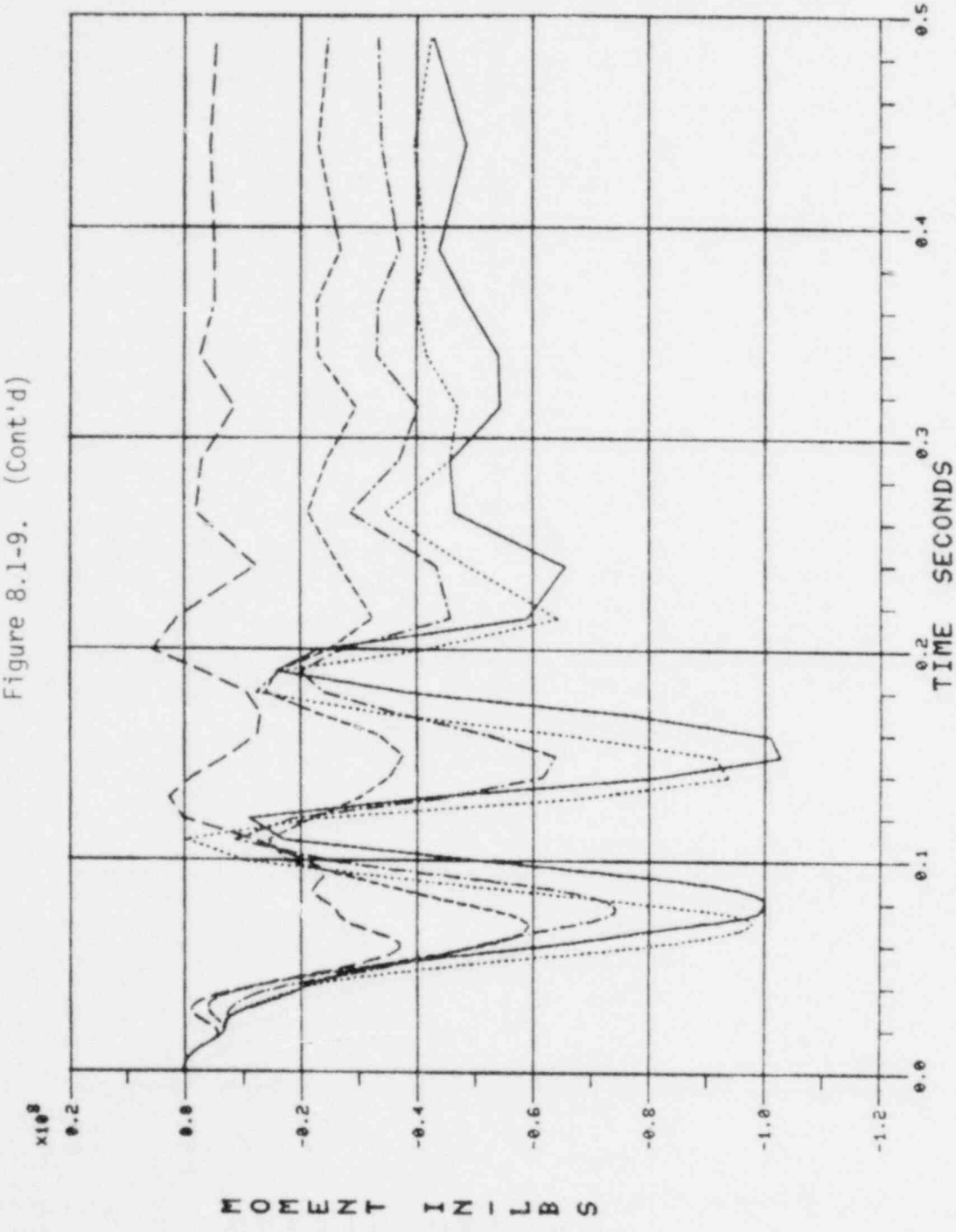

Figure 8.1-9. (Cont'd)

Figure 8.1-9. (Cont'd)

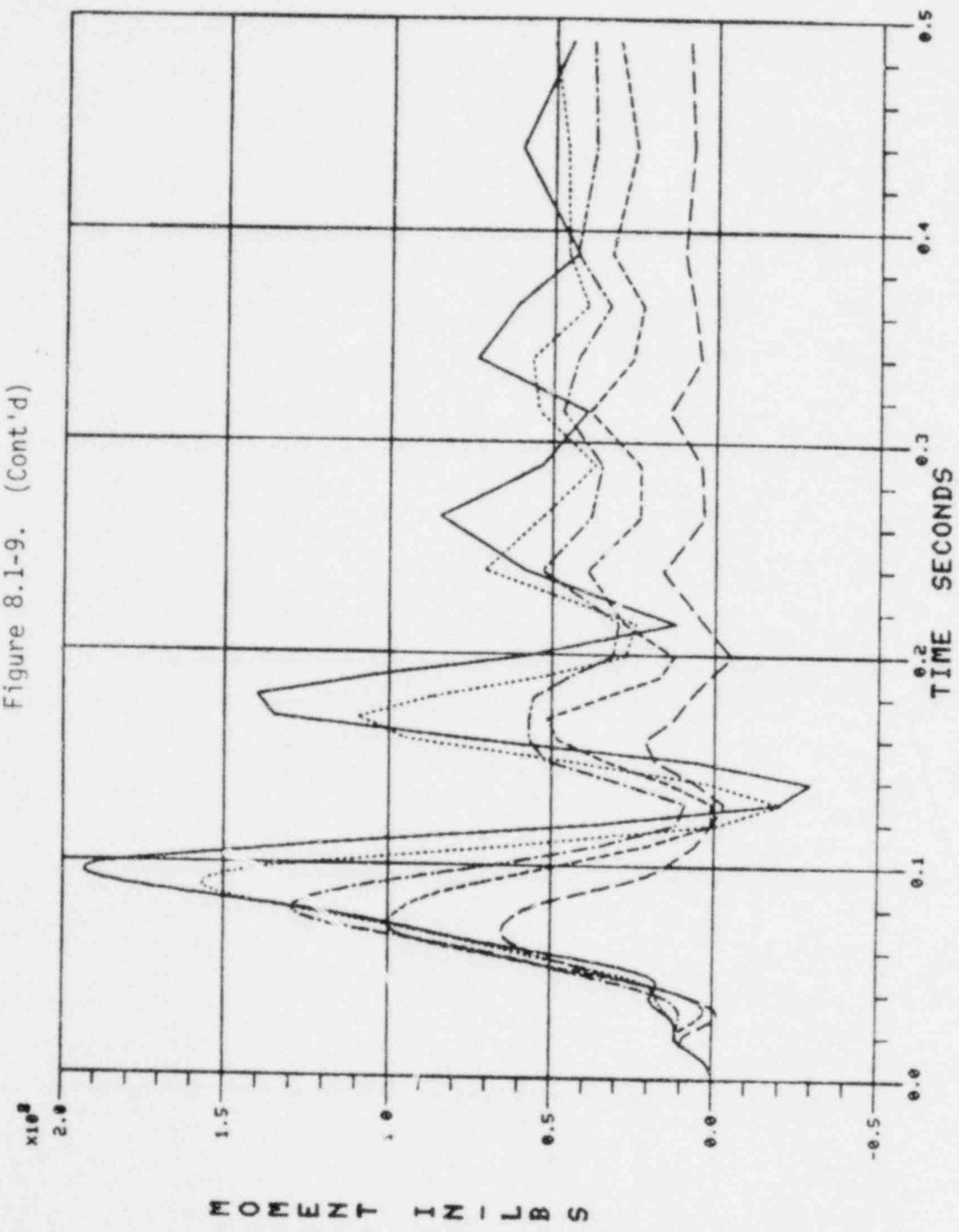

Table 8.1-5. ANO-1 Cold Leg Peak Force Summary

Break area	Resultant horizontal force, lb	Vertical at peak horiz force pt, lb	Resultant moment, in.-lb
2.0A	3.56 E6	4.5 E5	2.0 E8
1.5A	2.6 E6	3.5 E5	1.4 E8
1.0A	2.4 E6	3.0 E5	1.0 E8
0.6A	1.6 E6	2.5 E5	[illegible] E8
0.3A	1.1 E6	1.1 E5	0.6 E8

Figure 8.1-10. ANO-1 Cold Leg Break Time History

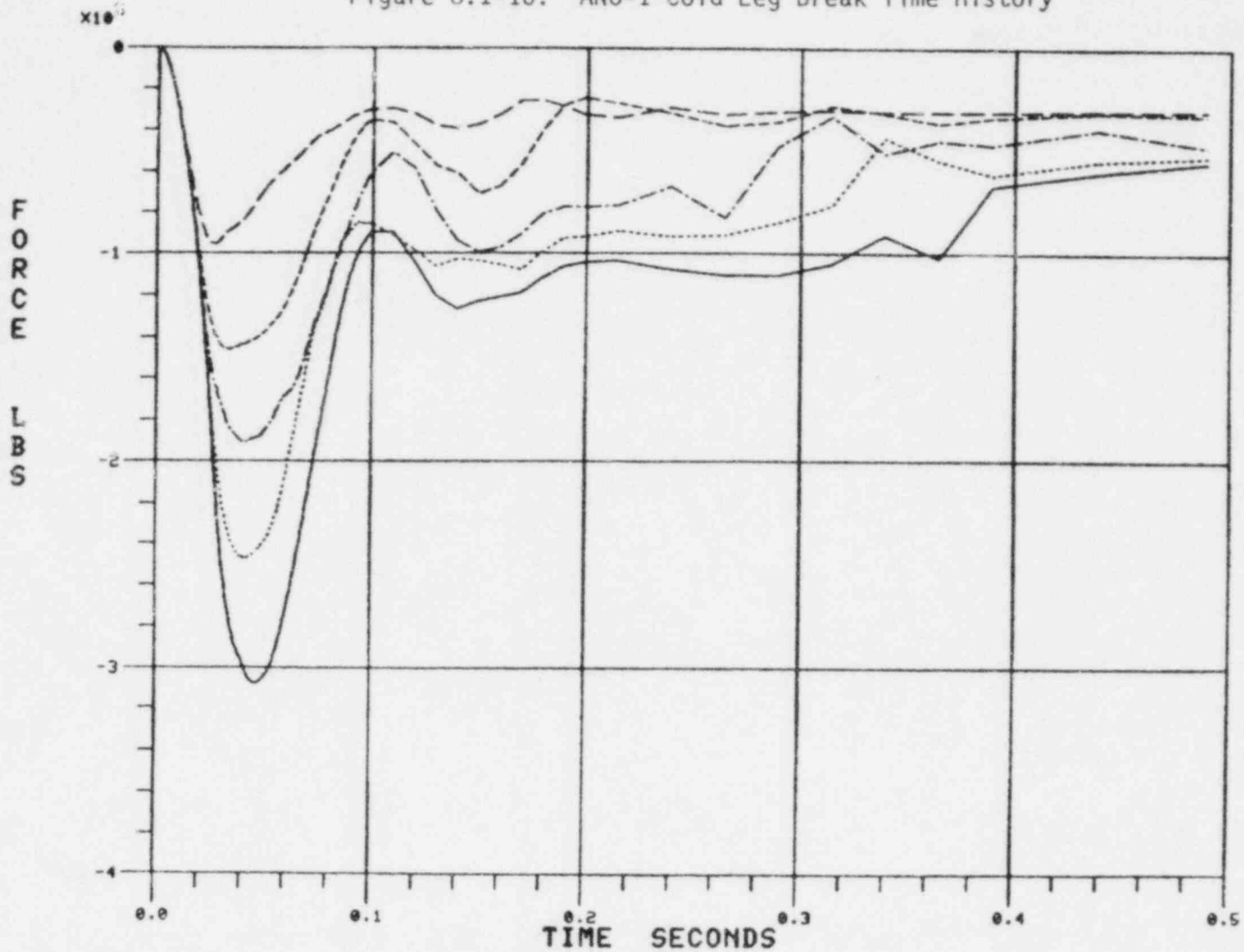

Figure 8.1-10. (Cont'd)

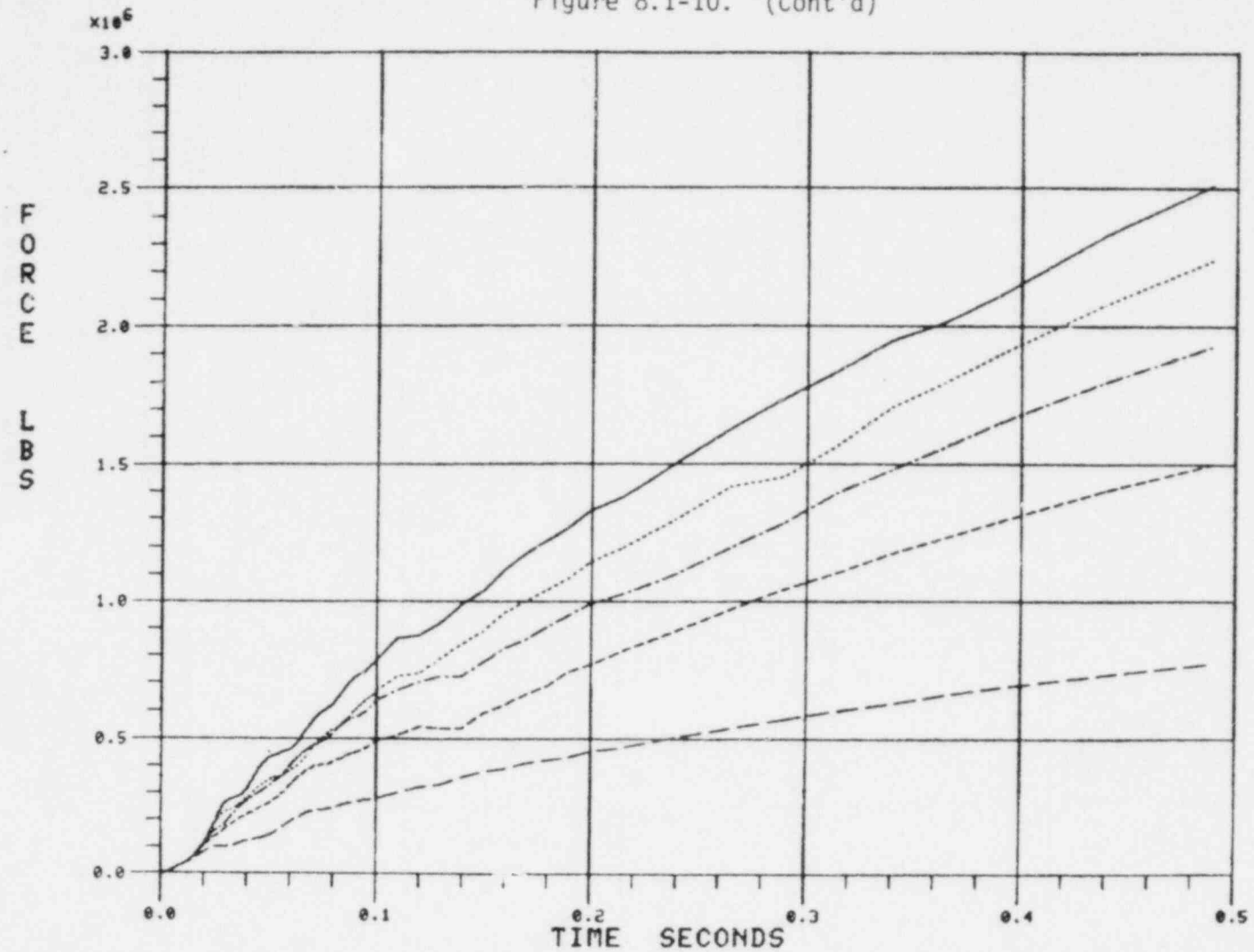

JOINT 51 Y DIR RU

Figure 8.1-10. (Cont'd)

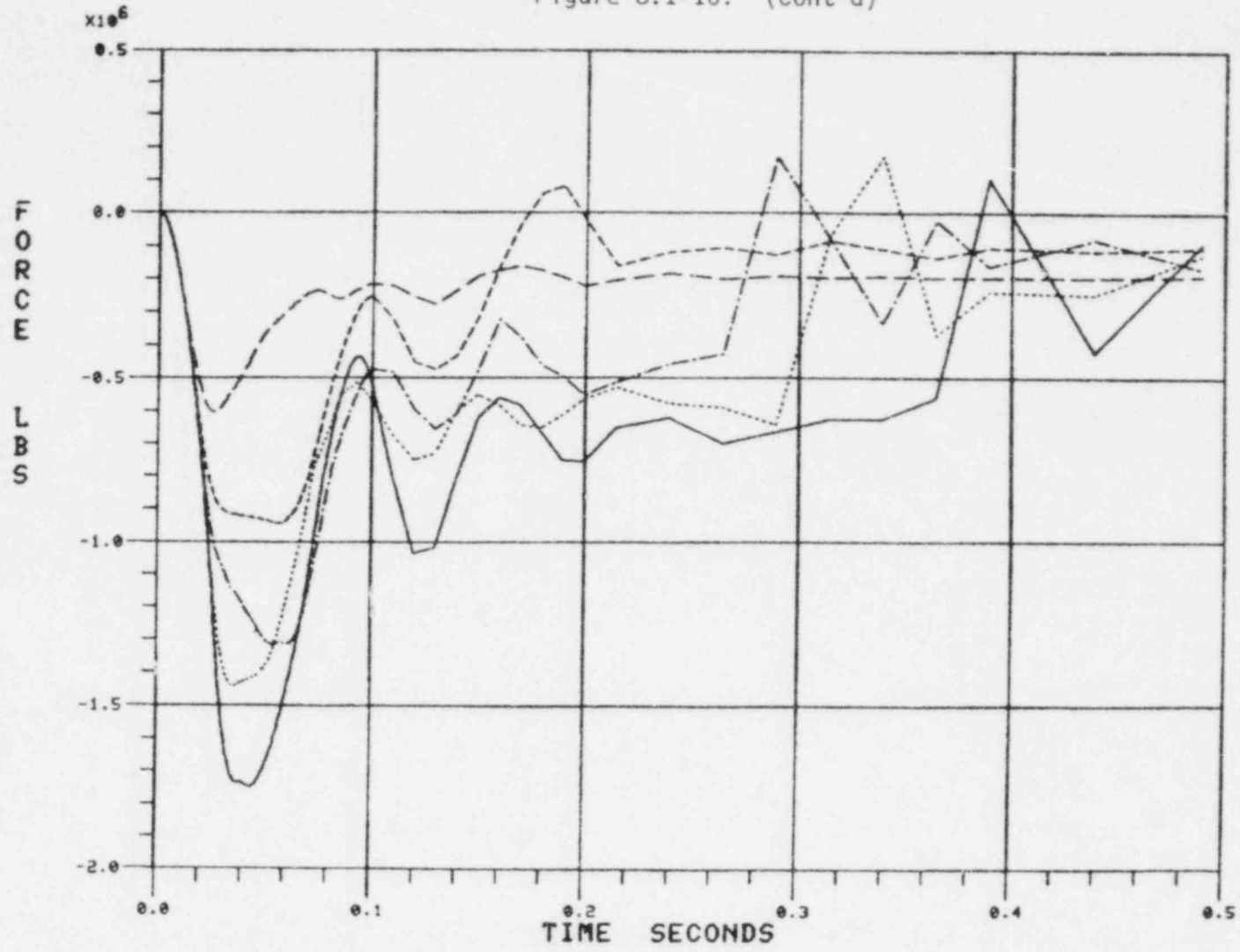

JOINT 51 Z DIR RV

Figure 8.1-10. (Cont'd)

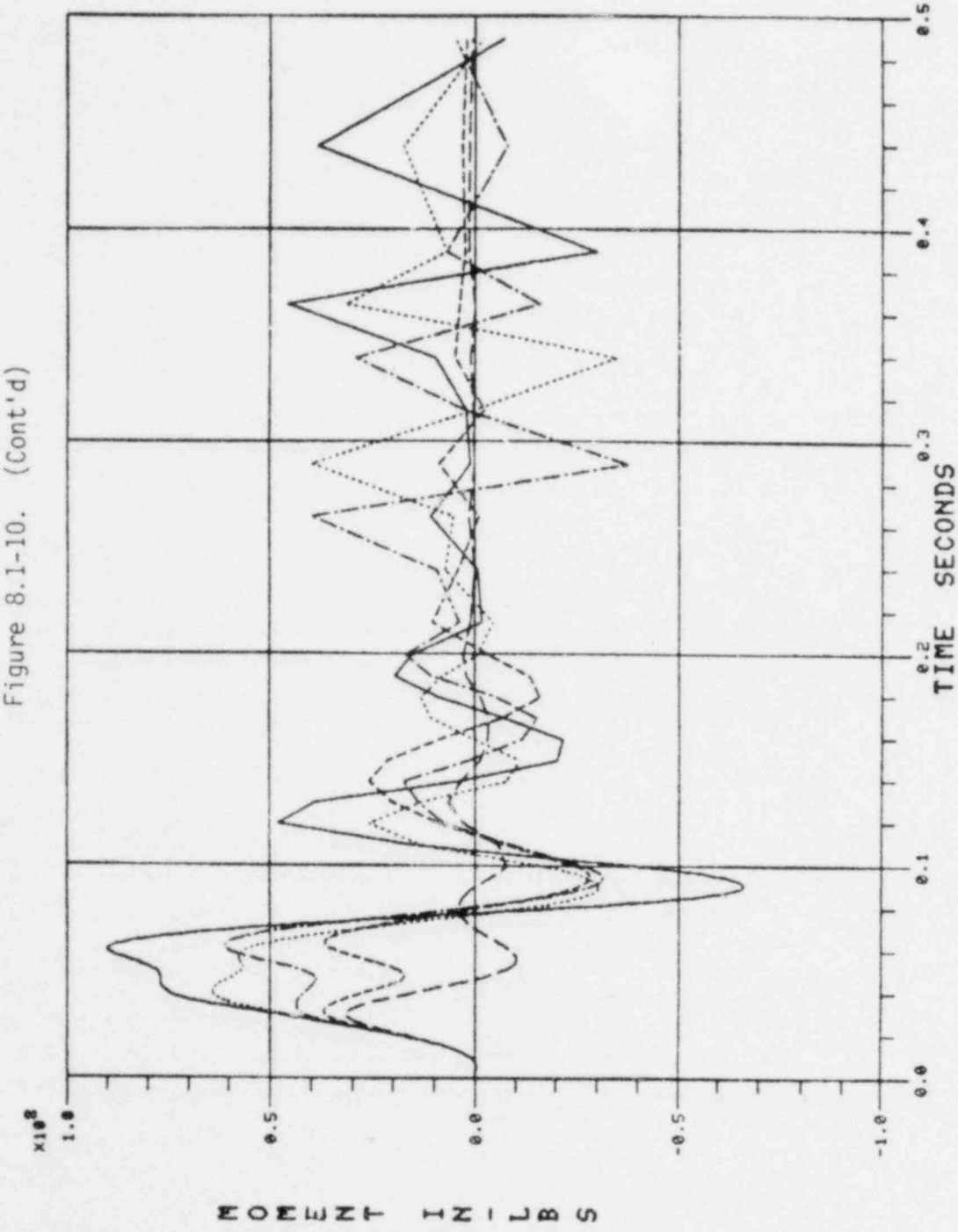

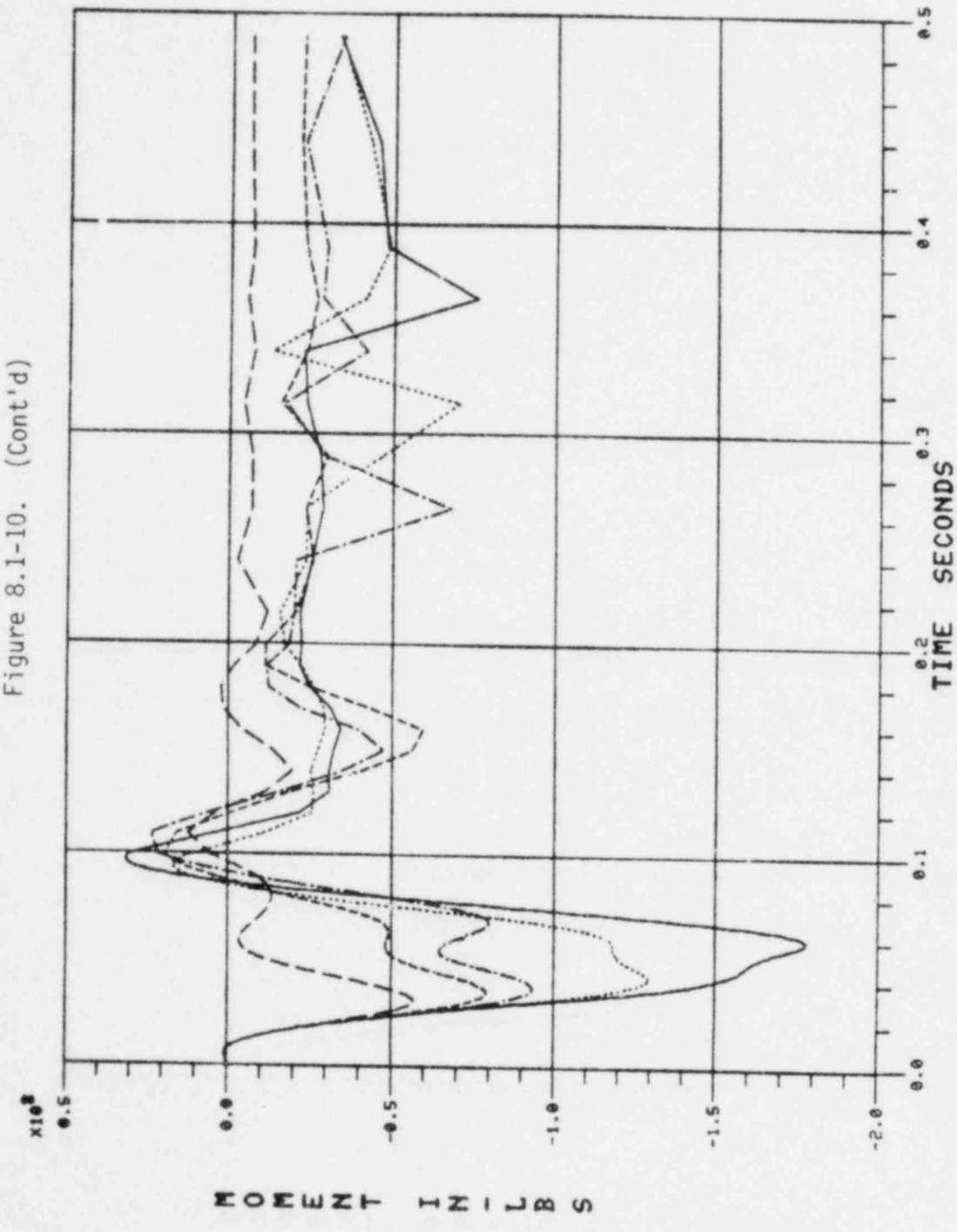

Figure 8.1-10. (Cont'd)

Table 8.1-6. Rancho Seco Cold Leg Peak Force Summary

Break area	Resultant horizontal force, lb	Vertical at peak horiz force pt, lb	Resultant moment, in.-lb
2.0A	3.91 E6	5.0 E5	2.2 E8
1.5A	3.2 E6	4.0 E5	1.9 E8
1.0A	2.6 E6	3.5 E5	1.3 E8
0.6A	1.9 E6	3.0 E5	1.0 E8
0.3A	1.2 E6	1.5 E5	0.7 E8

Figure 8.1-11. Rancho Seco Cold Leg Break Time History

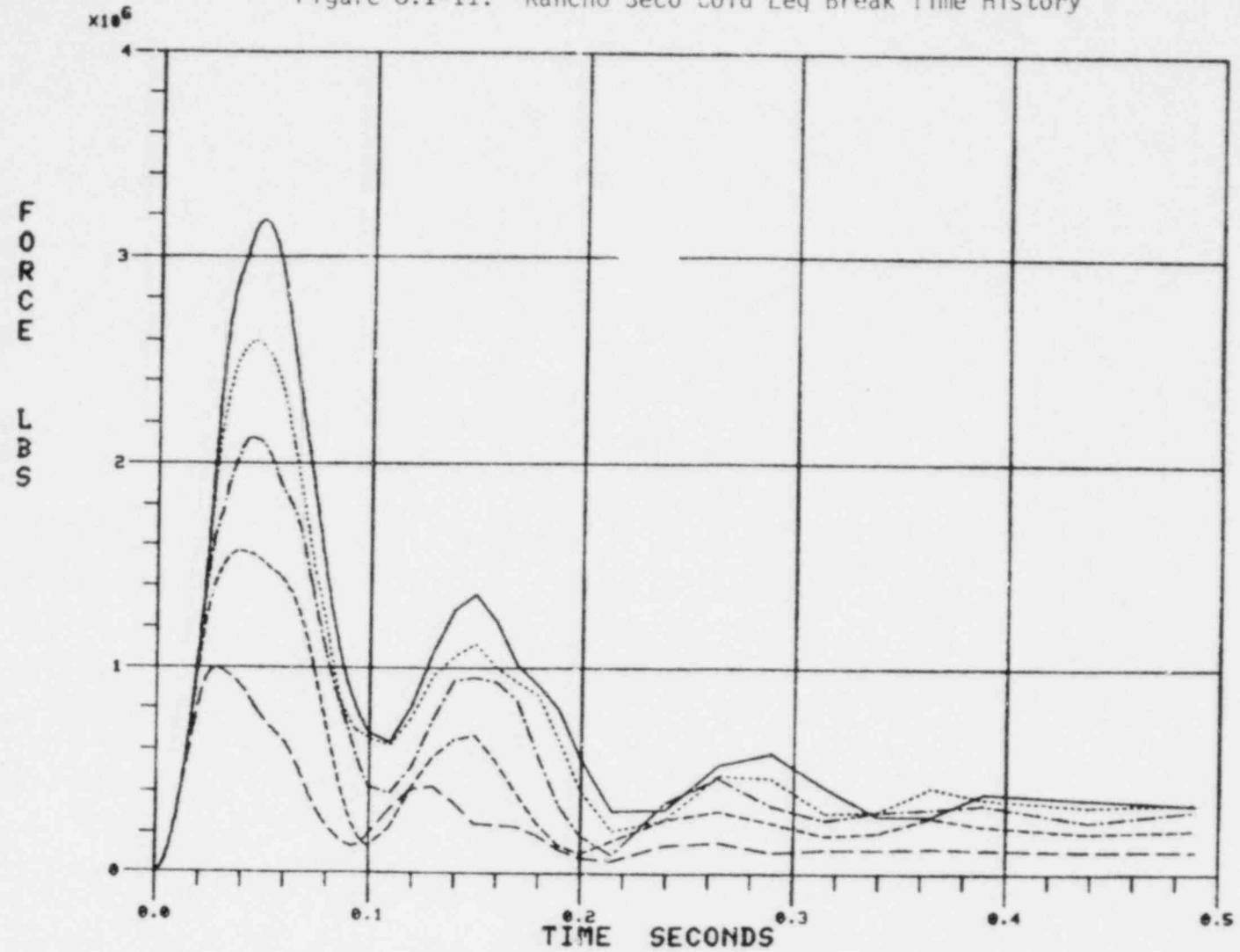

Figure 8.1-11. (Cont'd)

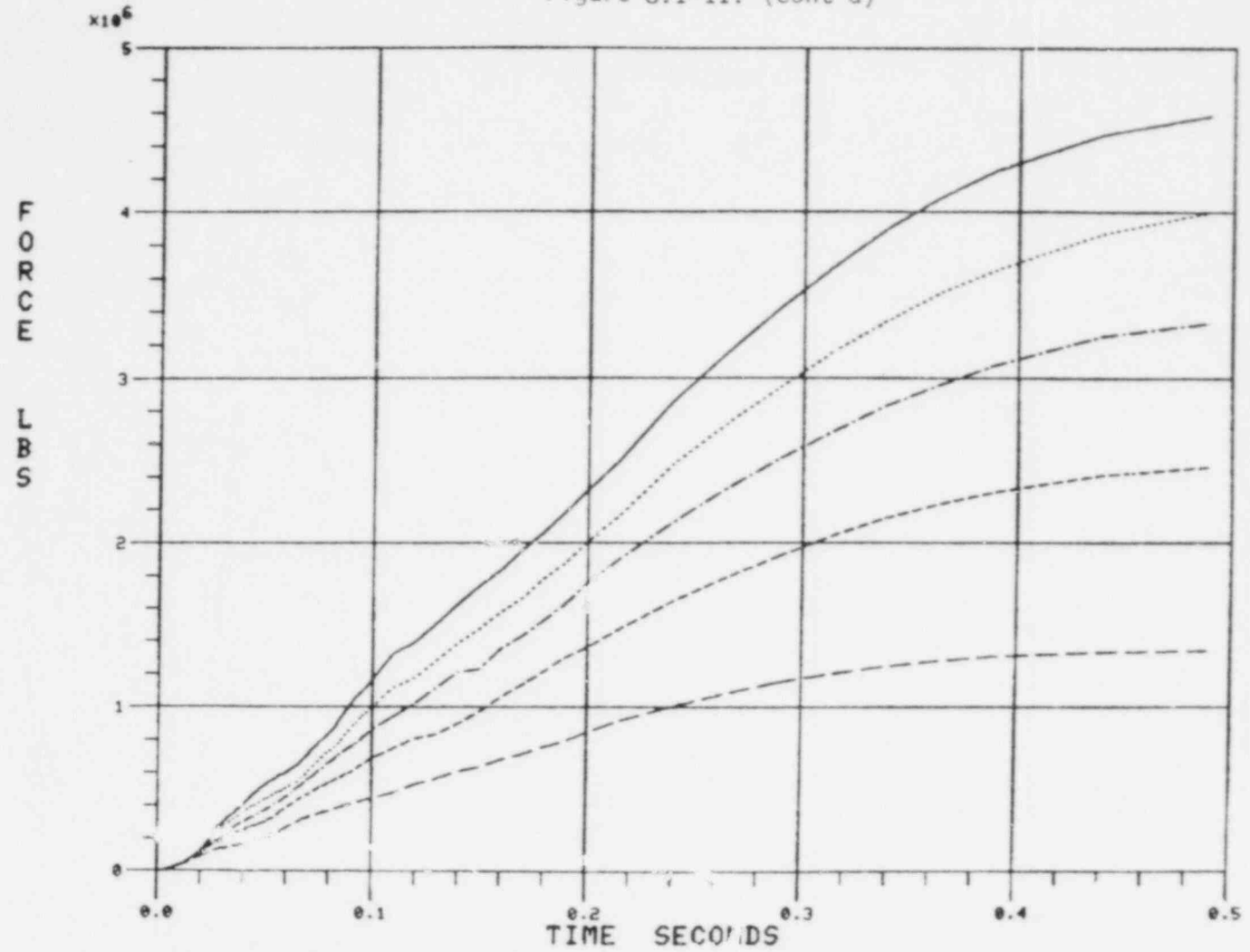

JOINT 51 Y DIR RU

Figure 8.1-11. (Cont'd)

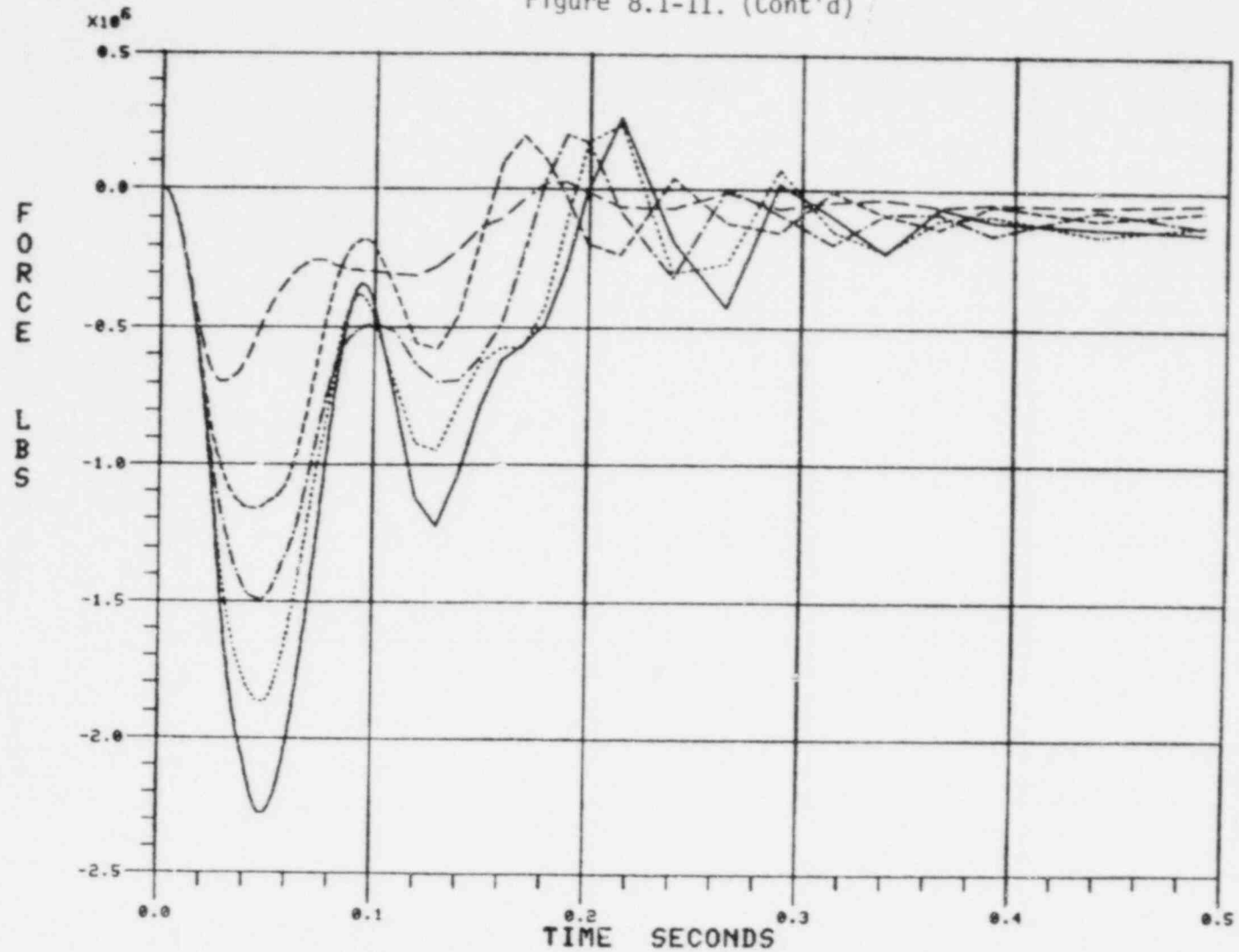

JOINT 51 Z DIR RV

Figure 8.1-11. (Cont'd)

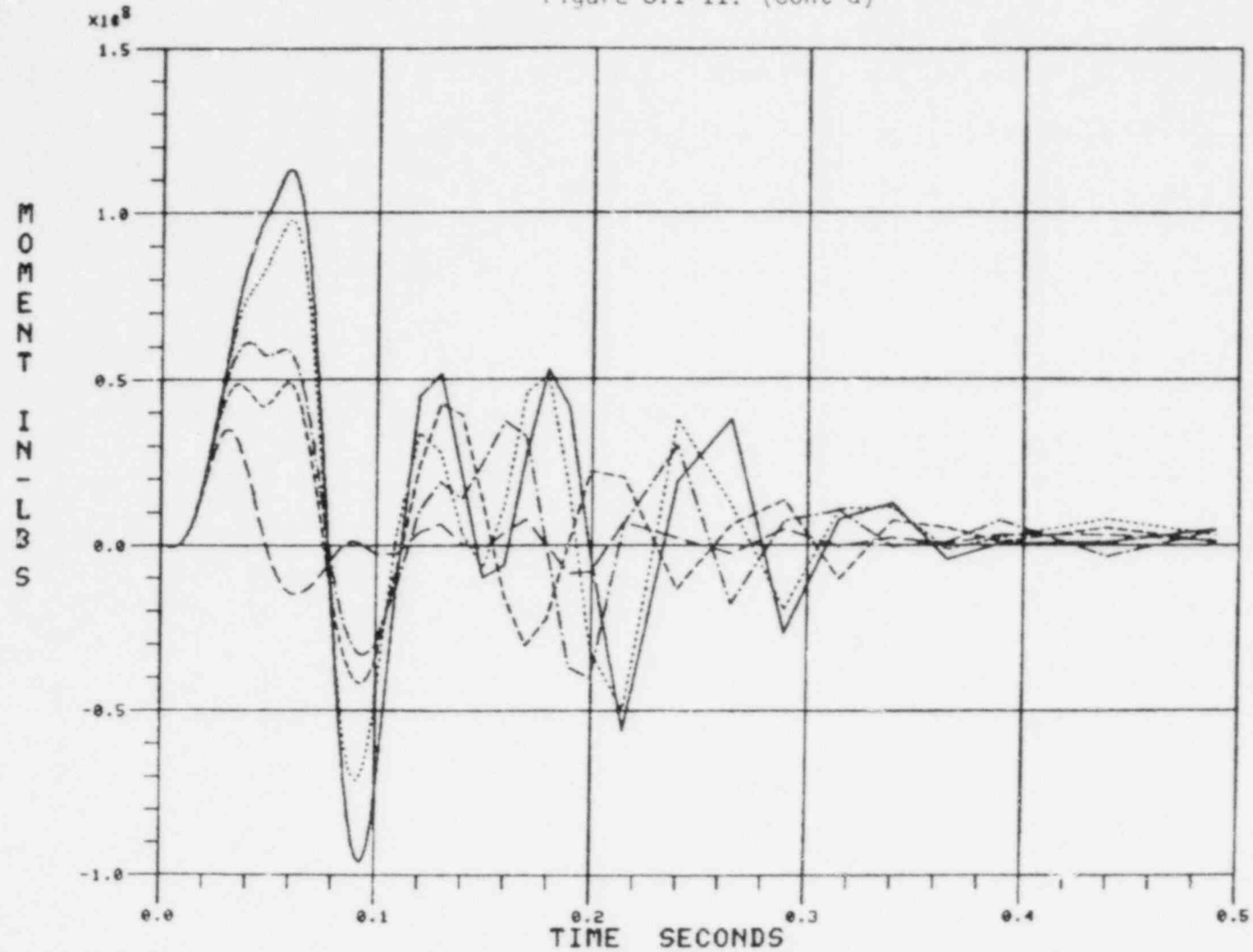

JOINT 51 X ROT RU

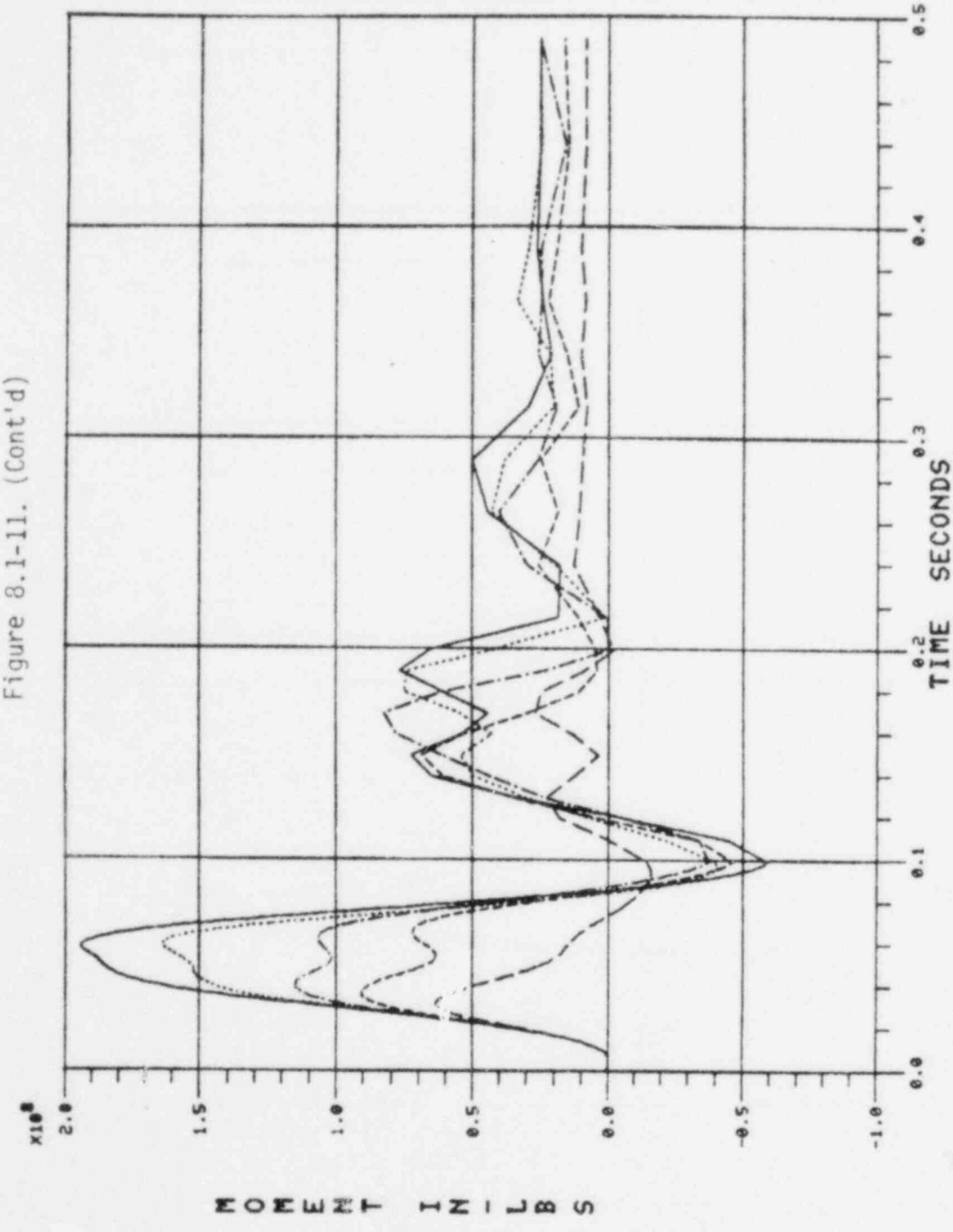

Figure 8.1-11. (Cont'd)

Table 8.1-7. Davis-Besse 1 Cold Leg Peak Force Summary

Break area	Resultant horizontal force, lb	Vertical at peak horiz force pt, lb	Resultant moment, in.-lb
0.24A	1.6 E6	0.16 E6	3.5 E7

Figure 8.1-12. Davis-Besse 1 Cold Leg Break Time History

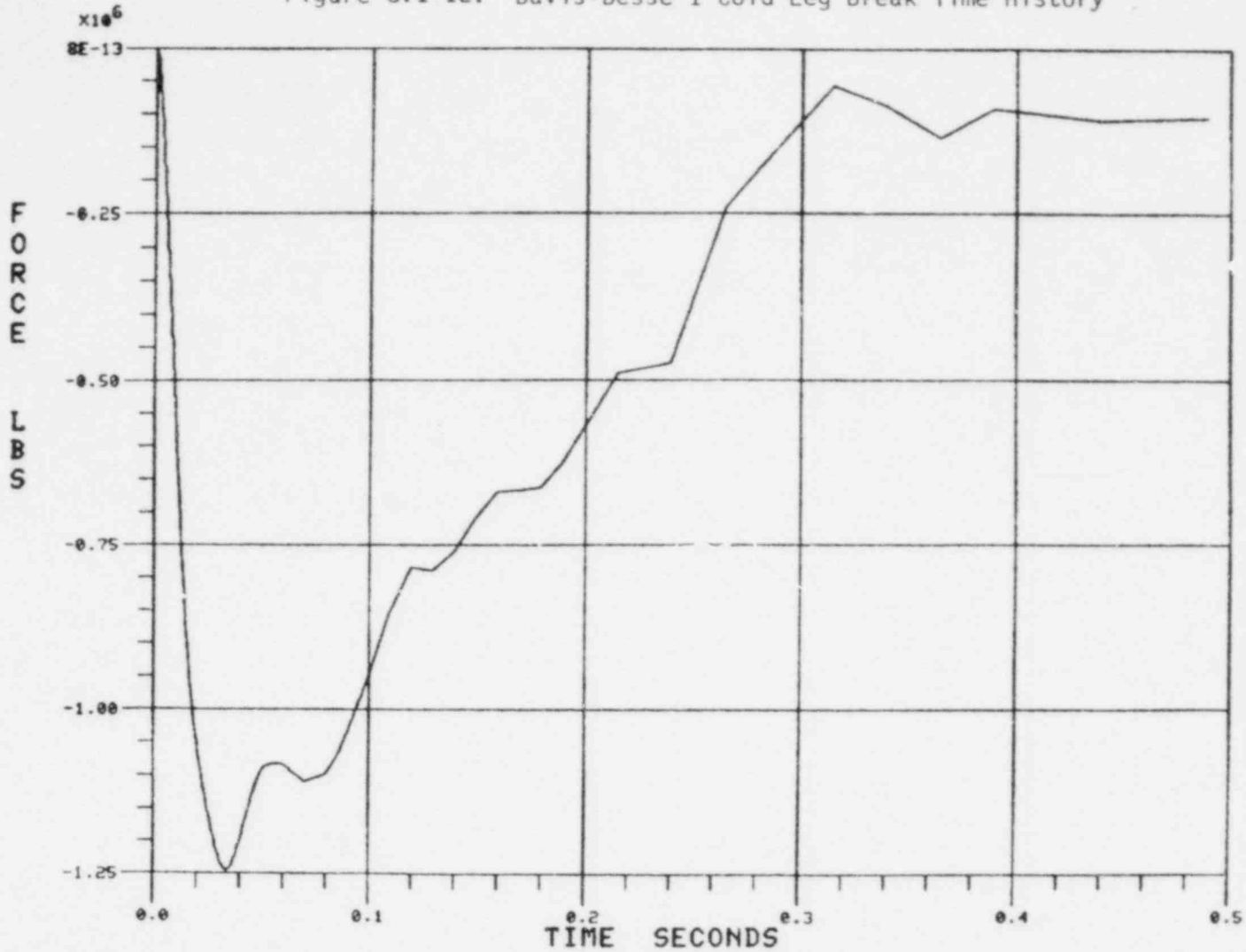

Figure 8.1-12. (Cont'd)

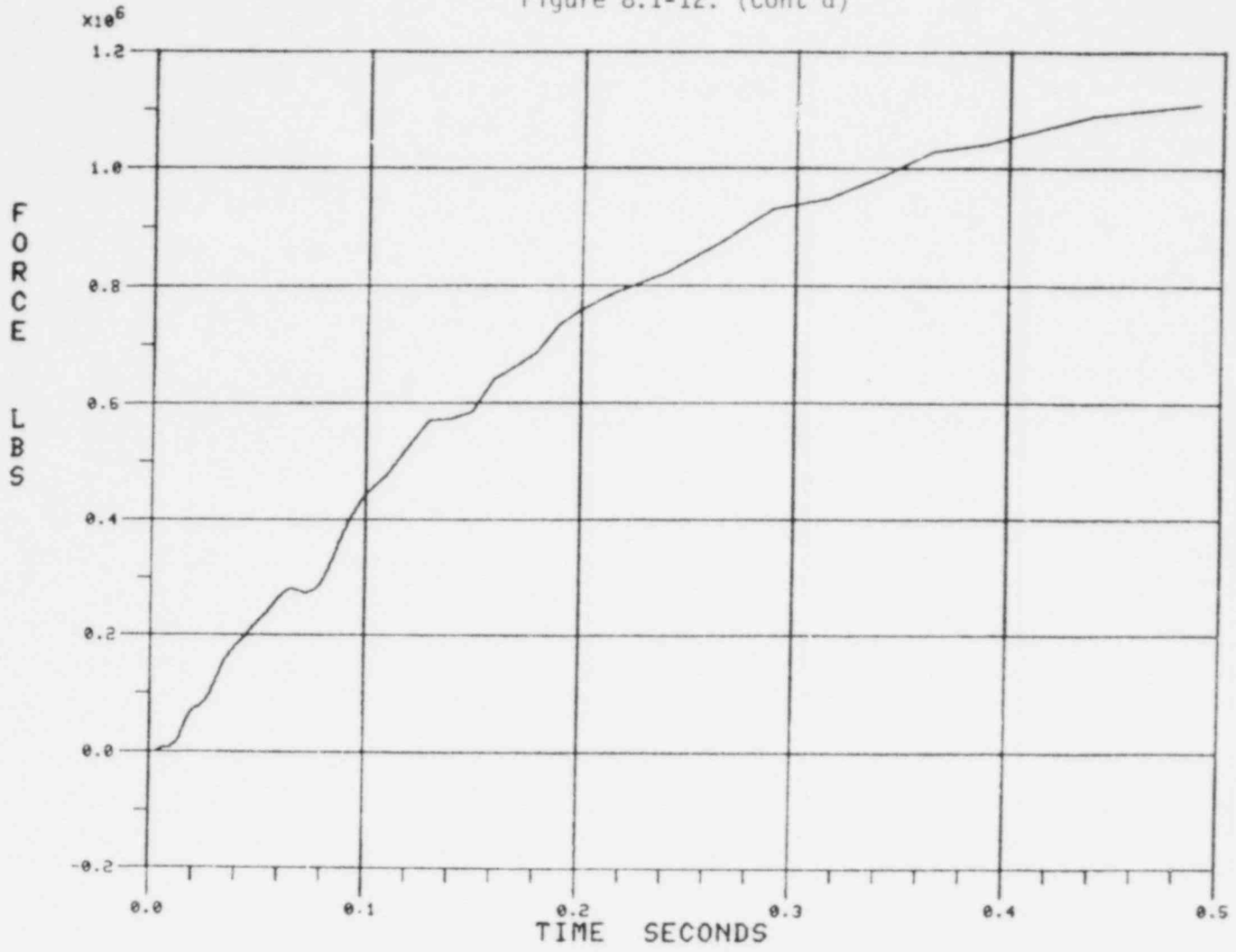

TECO-14 .24A CL BK AT RV FY

Figure 8.1-12. (Cont'd)

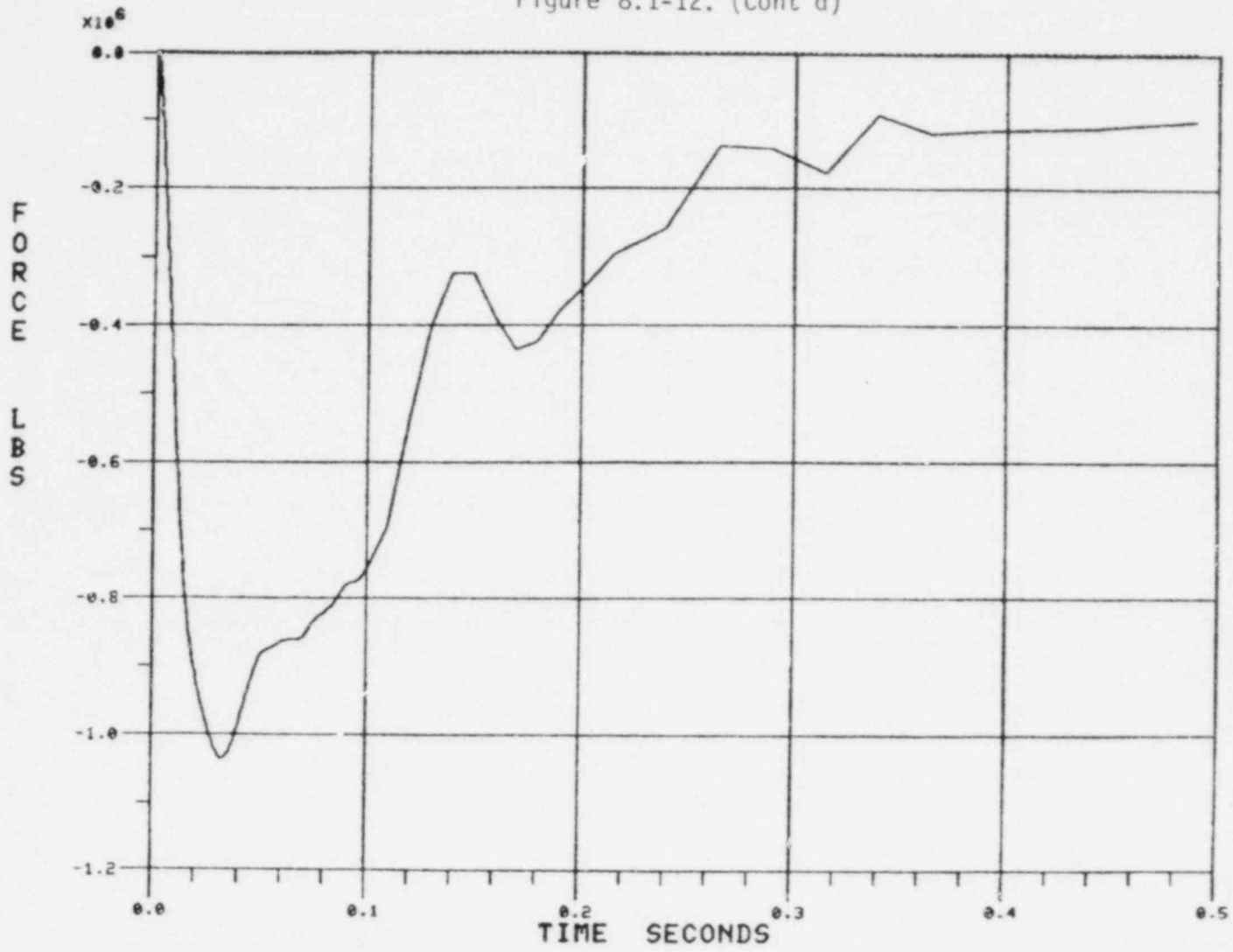

TECO-14 .24A CL BK AT RV FZ

Figure 8.1-12. (Cont'd)

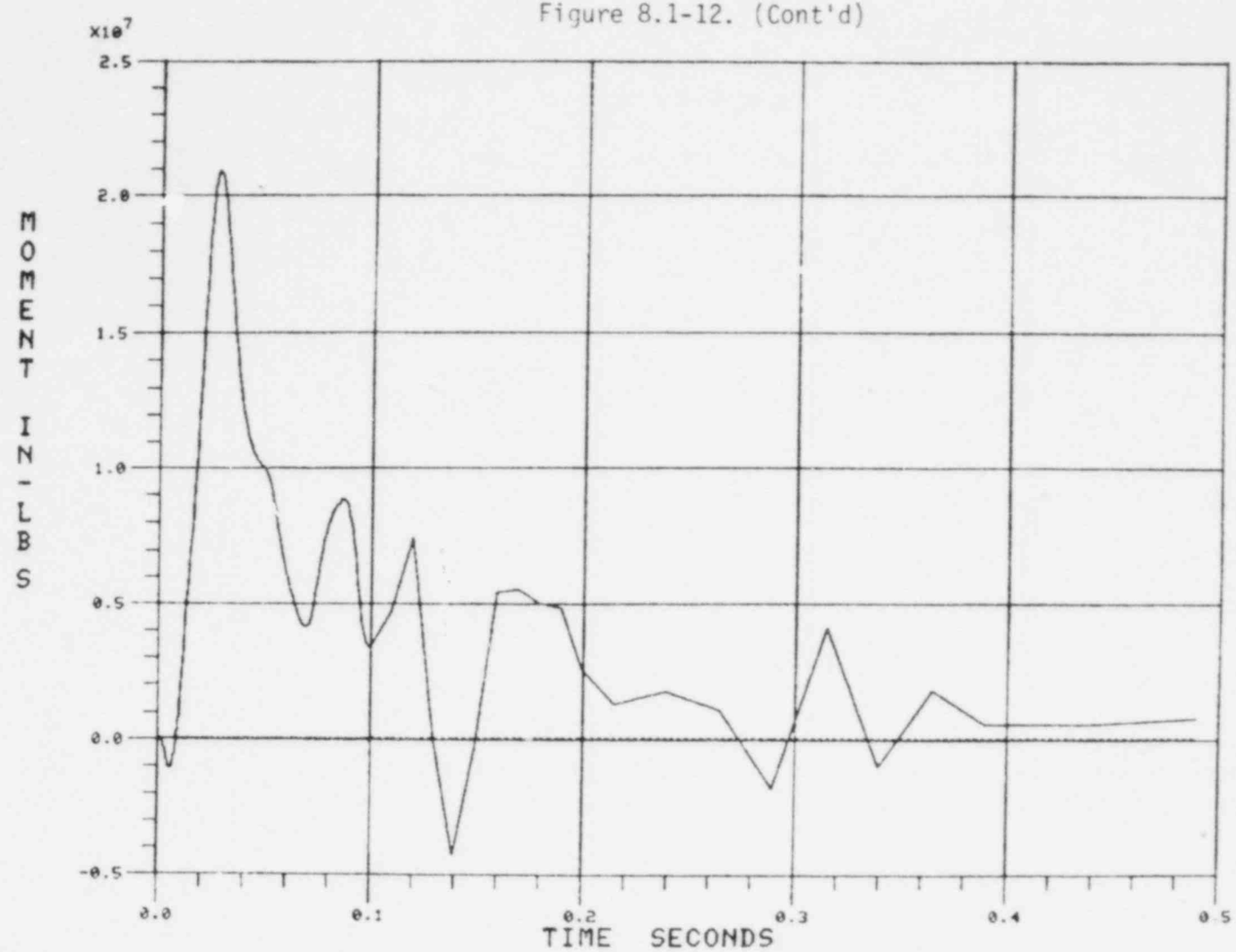

TECO-14 .24A CL BK AT RV MX

Figure 8.1-12. (Cont'd)

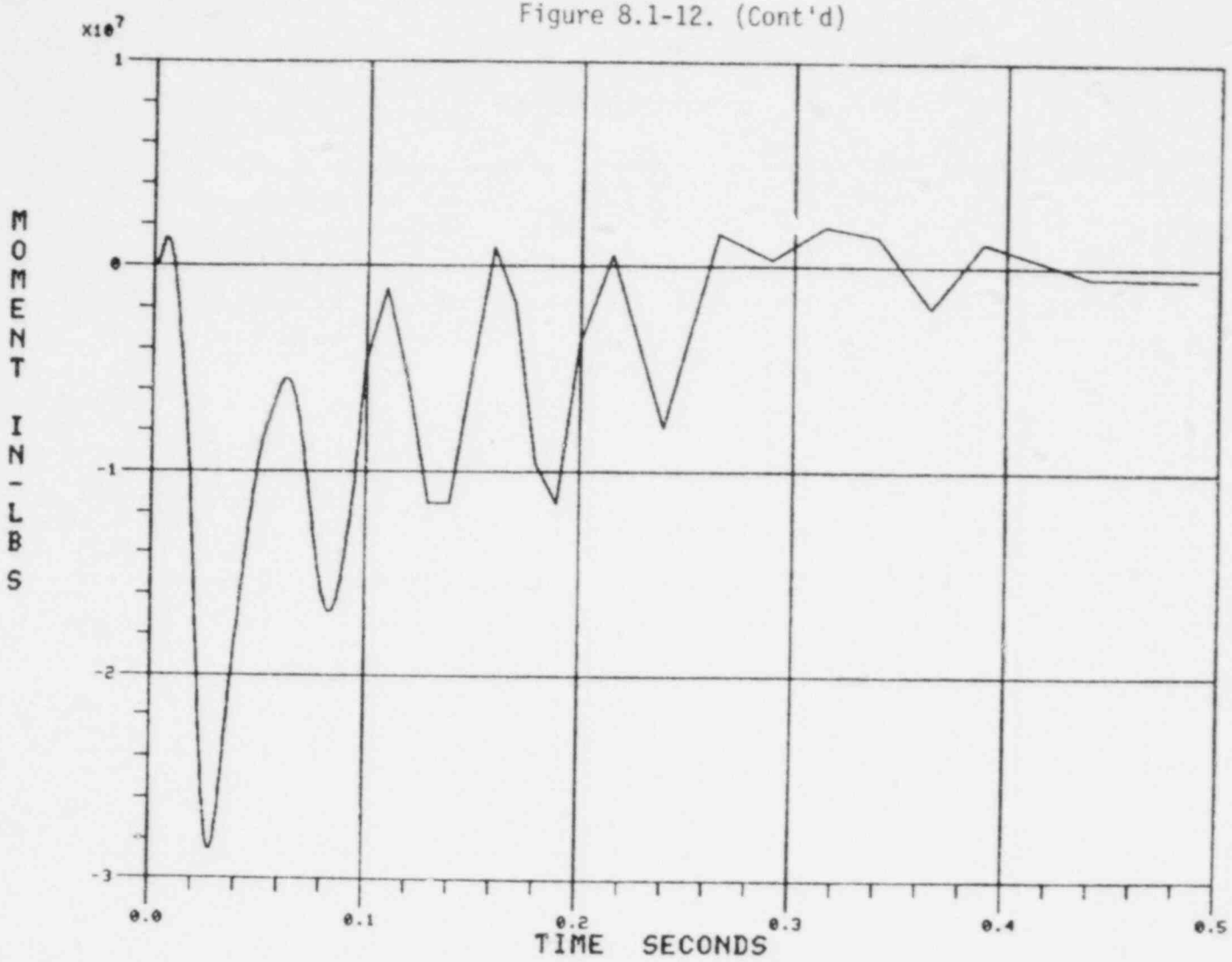

TECO-14 .24A CL BK AT RV MZ

Table 8.1-8. Oconee 1, 2, 3 Hot Leg Peak Force Summary

Break area	Resultant horizontal force, lb	Vertical at peak horiz force pt, lb	Resultant moment, in.-lb
2.0A	1.12 E7	0.5 E6	5.5 E8
1.5A	0.98 E7	0.4 E6	5.0 E8
1.0A	0.75 E7	0.3 E6	4.0 E8
0.6A	0.5 E7	0.2 E6	2.9 E8
0.3A	0.3 E7	0.1 E6	1.9 E8

Figure 8.1-13. Oconee 1, 2, and 3 Hot Leg Break Time History

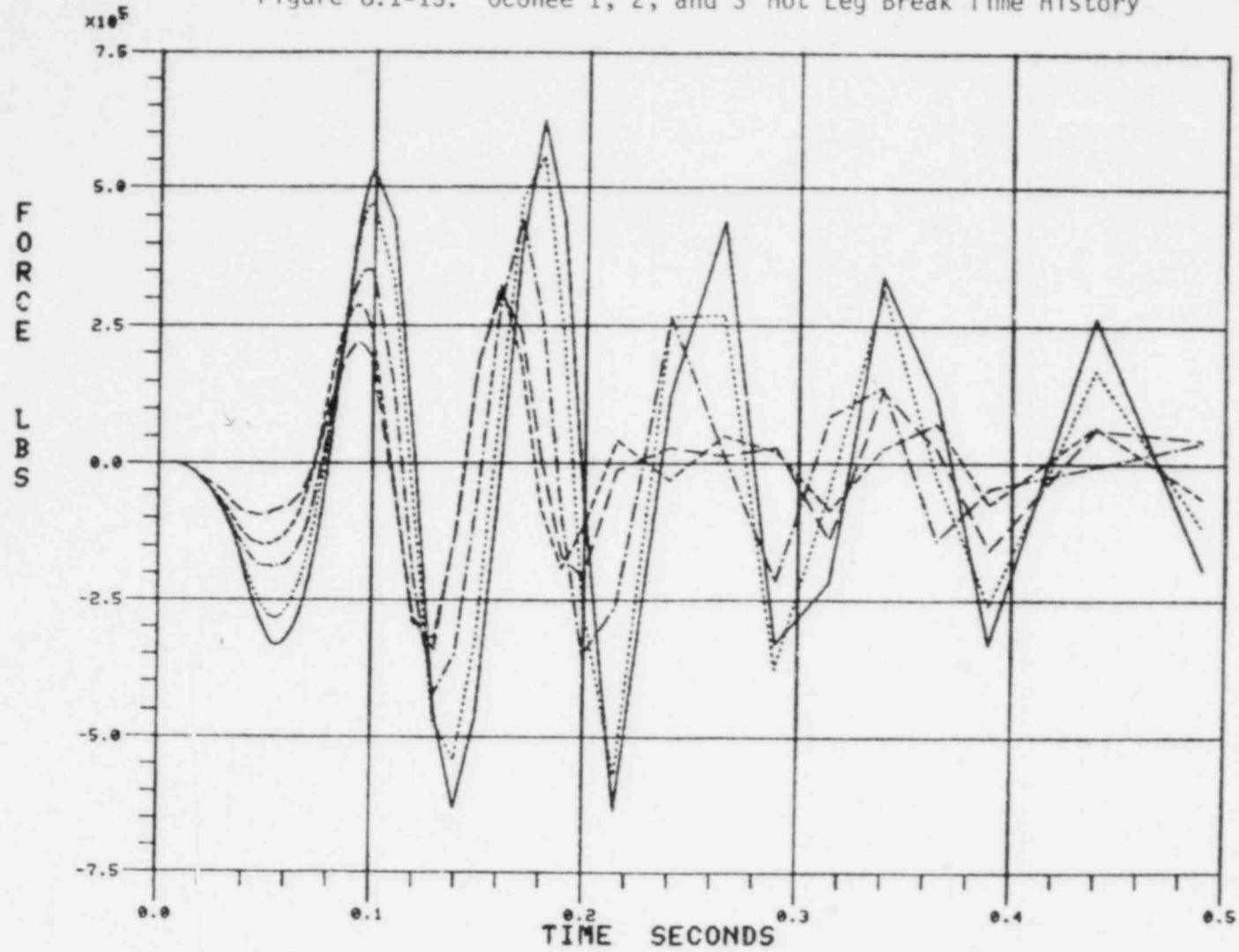

Figure 8.1-13. (Cont'd)

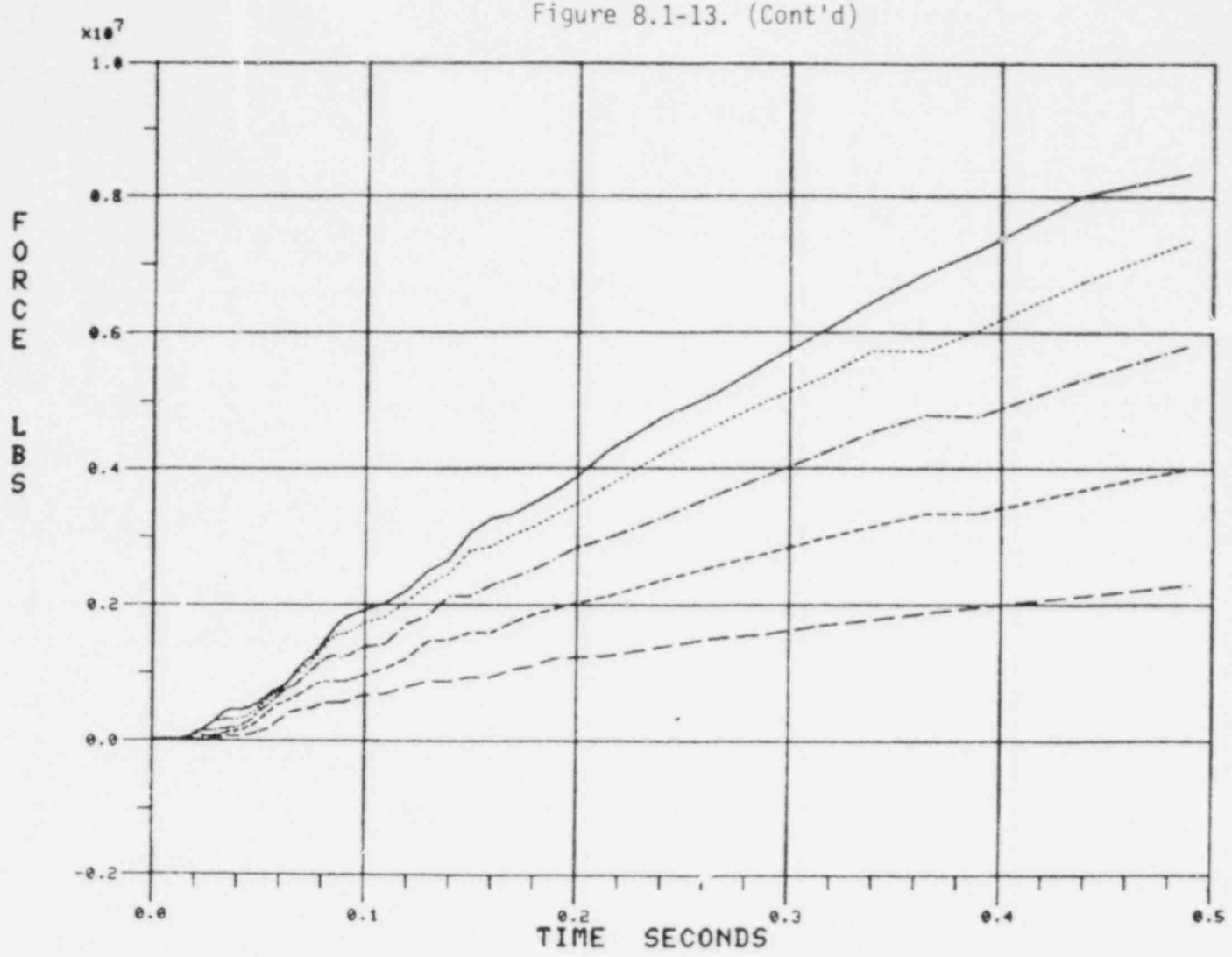

'OINT 51 Y DIR RU DUKEH

Figure 8.1-13. (Cont'd)

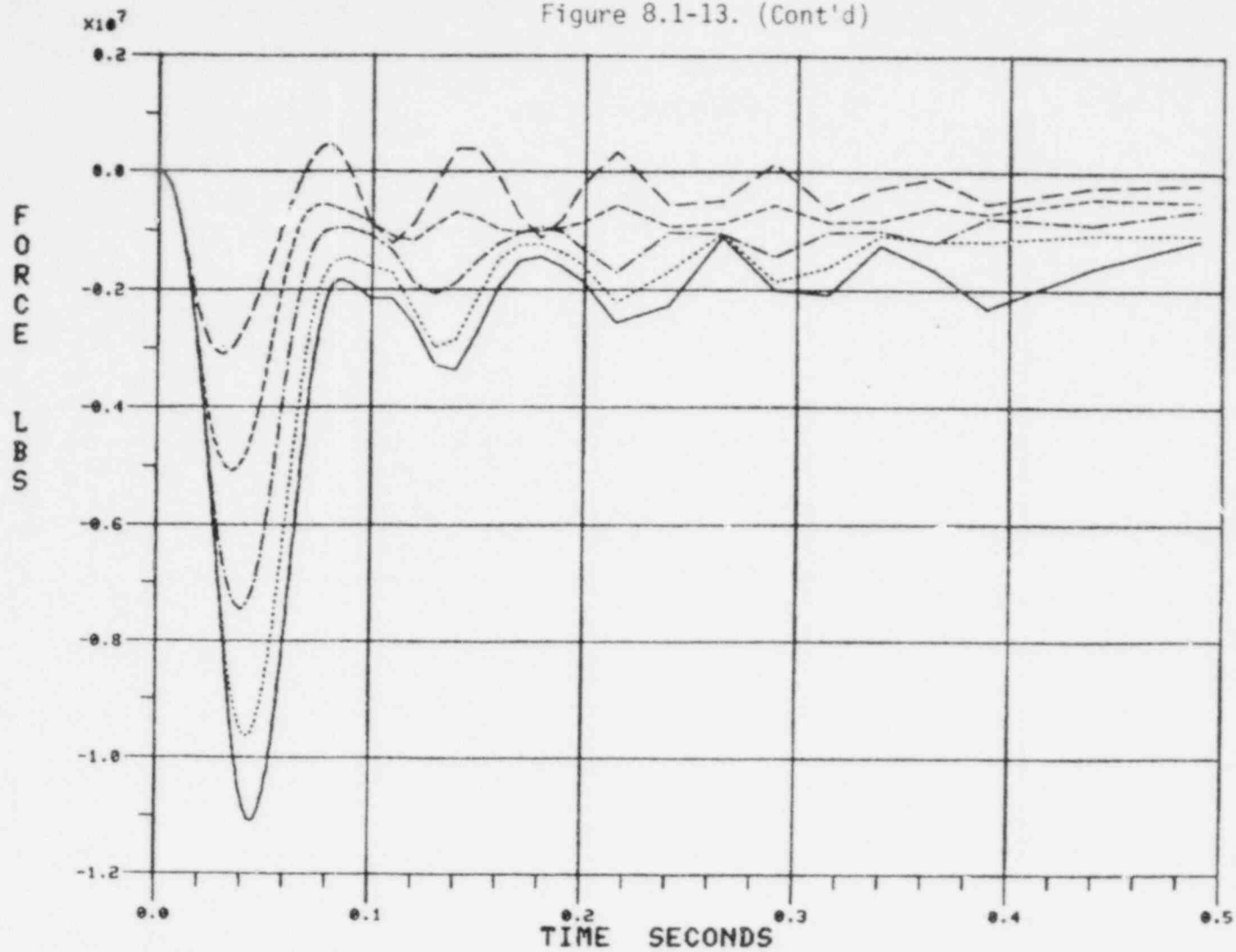

JOINT 51 Z DIR RV DUKEH

Figure 8.1-13. (Cont'd)

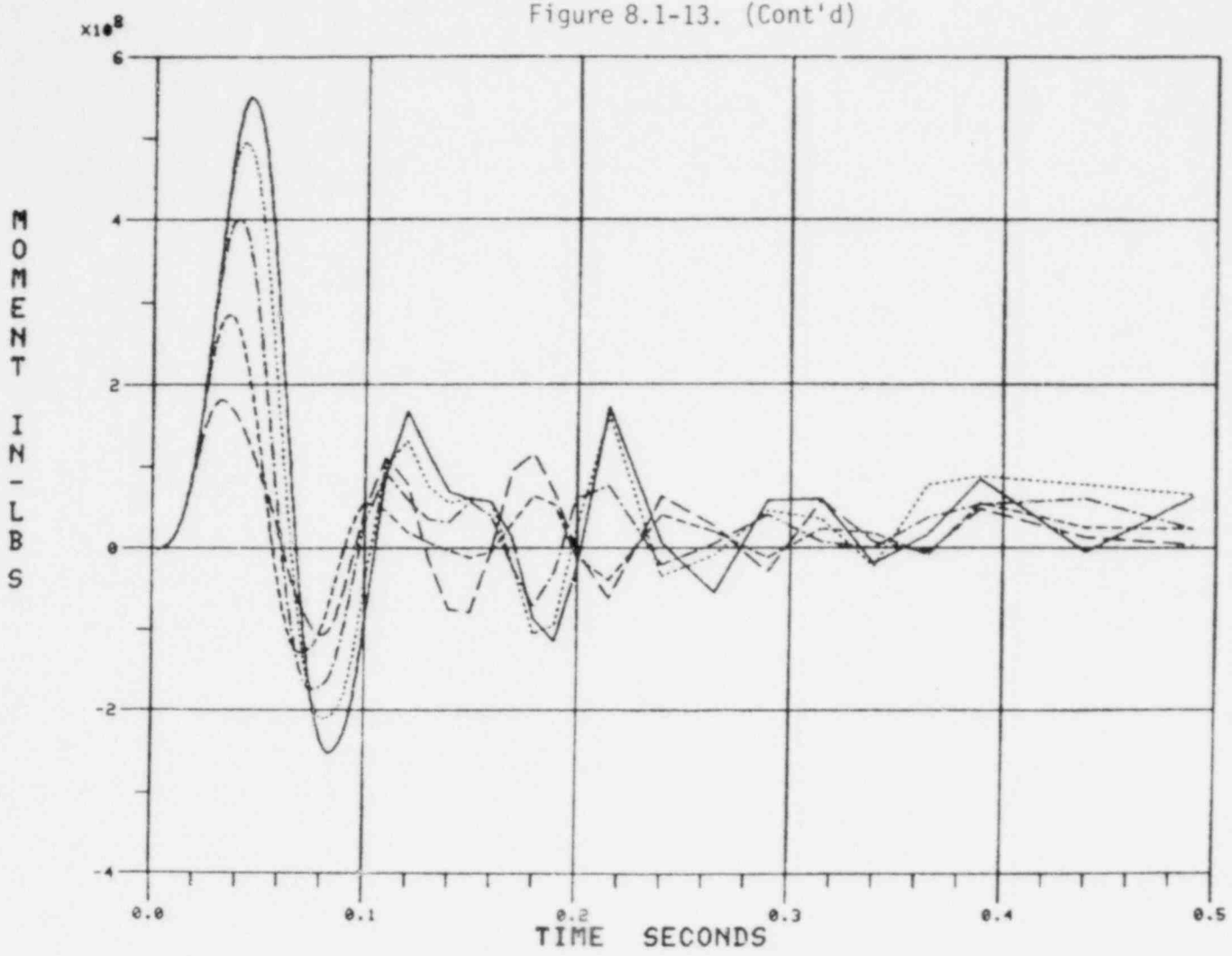

JOINT 51 X ROT DUKEH

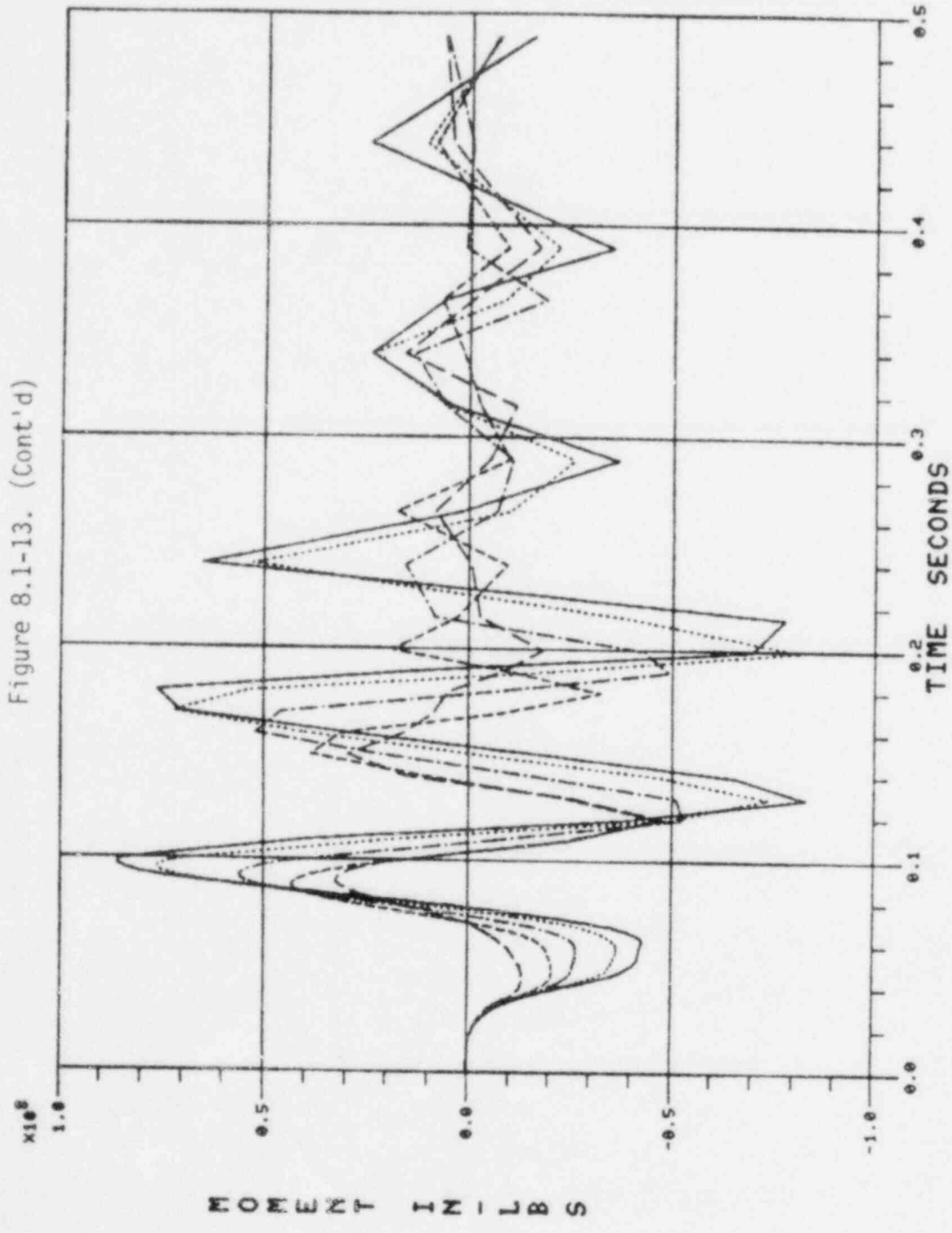

Figure 8.1-13. (Cont'd)

Table 8.1-9. Crystal River 3 and TMI-1 Hot Leg Peak Force Summary

Break area	Resultant horizontal force, lb	Vertical at peak horiz force pt, lb	Resultant moment, in.-lb
2.0A	9.0 E6	1.1 E6	3.2 E8
1.5A	7.5 E6	1.0 E6	2.6 E8
1.0A	5.6 E6	0.8 E6	2.1 E8
0.6A	3.8 E6	0.5 E6	1.6 E8
0.3A	2.1 E6	0.1 E6	1.2 E8

Figure 8.1-14. Crystal River 3 and TMI-1 Hot Leg Break Time History

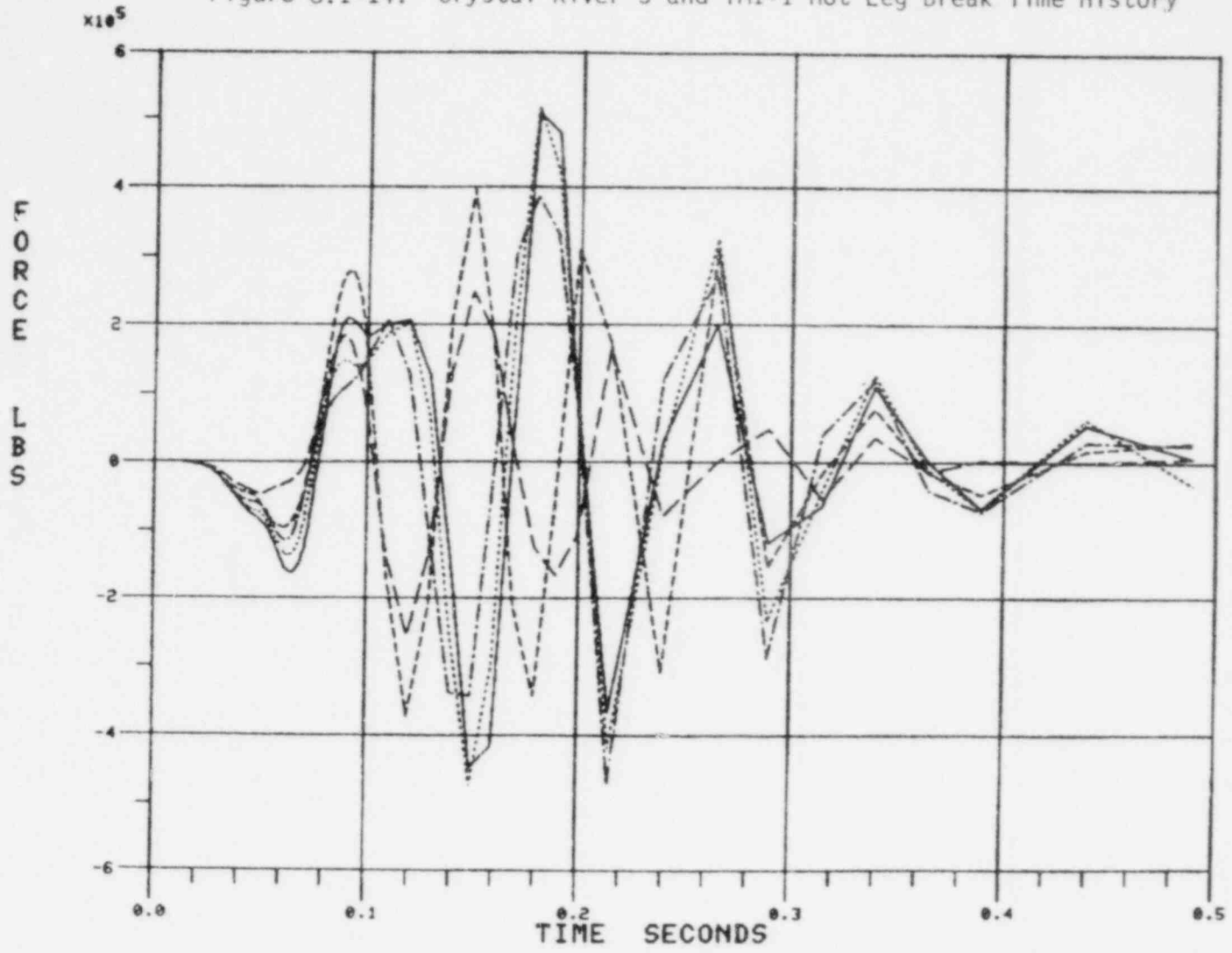

JOINT 51 X DIR RV

Figure 8.1-14. (Cont'd)

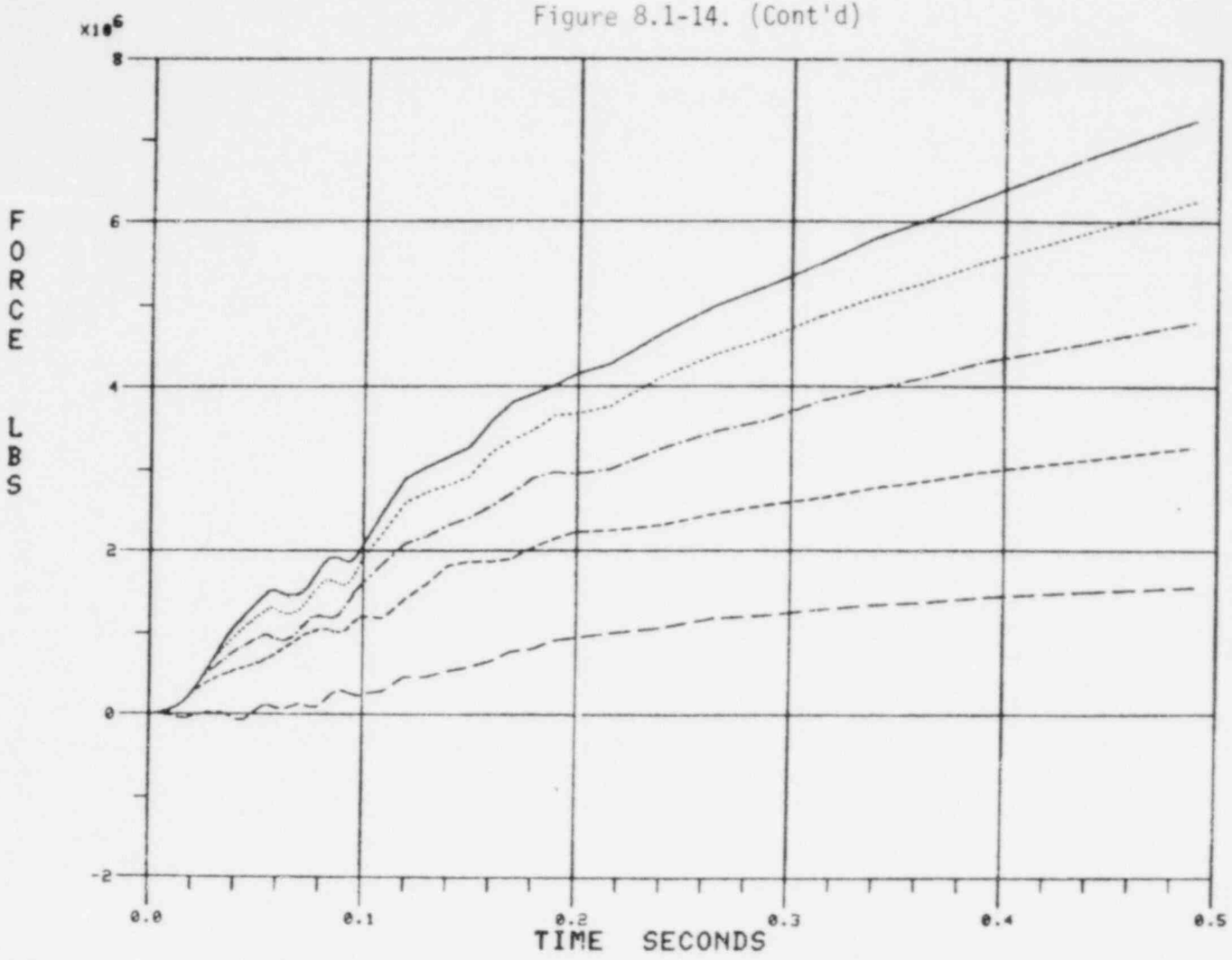

JOINT 51 Y DIR RV

Figure 8.1-14. (Cont'd)

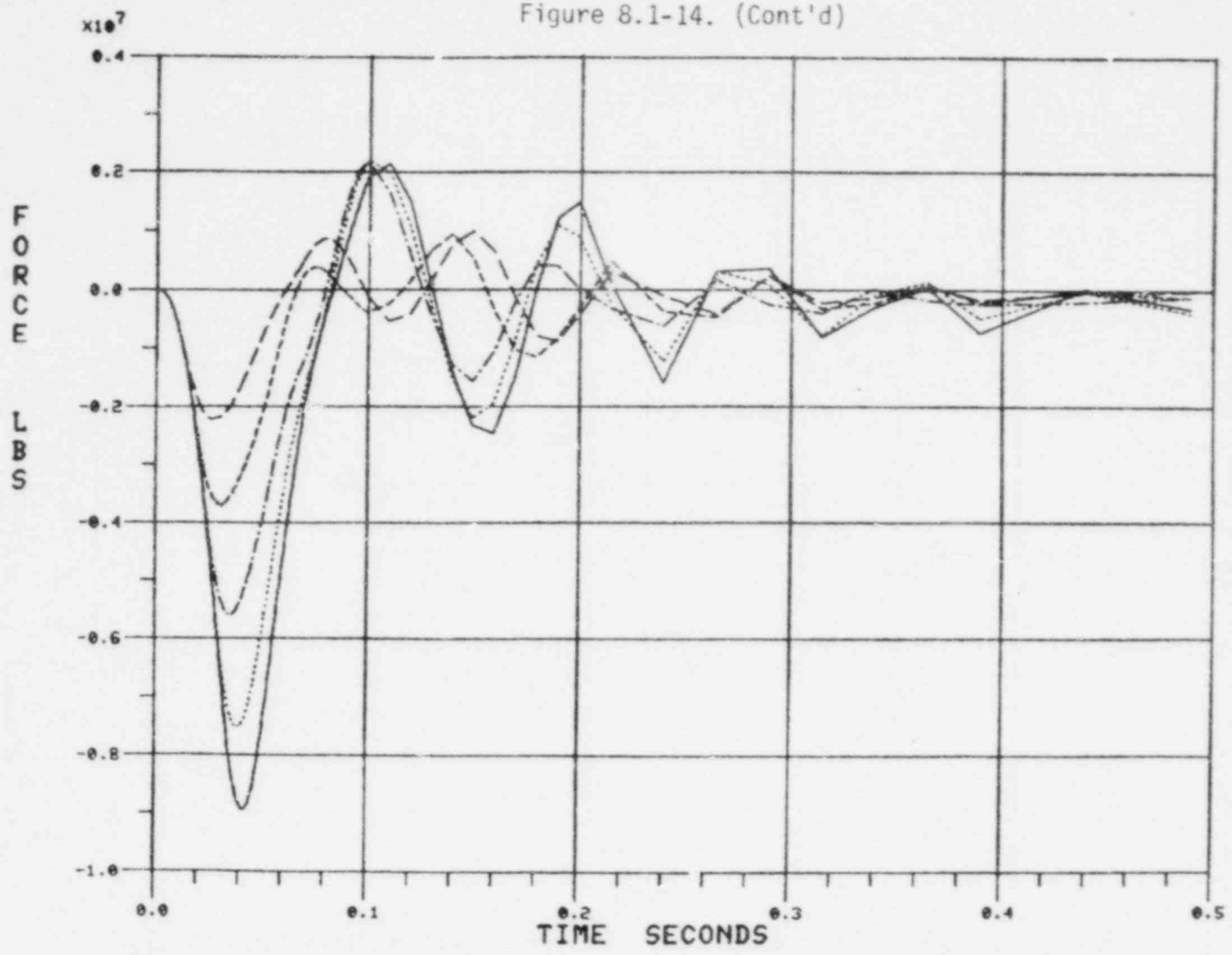

JOINT 51 Z DIR RV

Figure 8.1-14. (Cont'd)

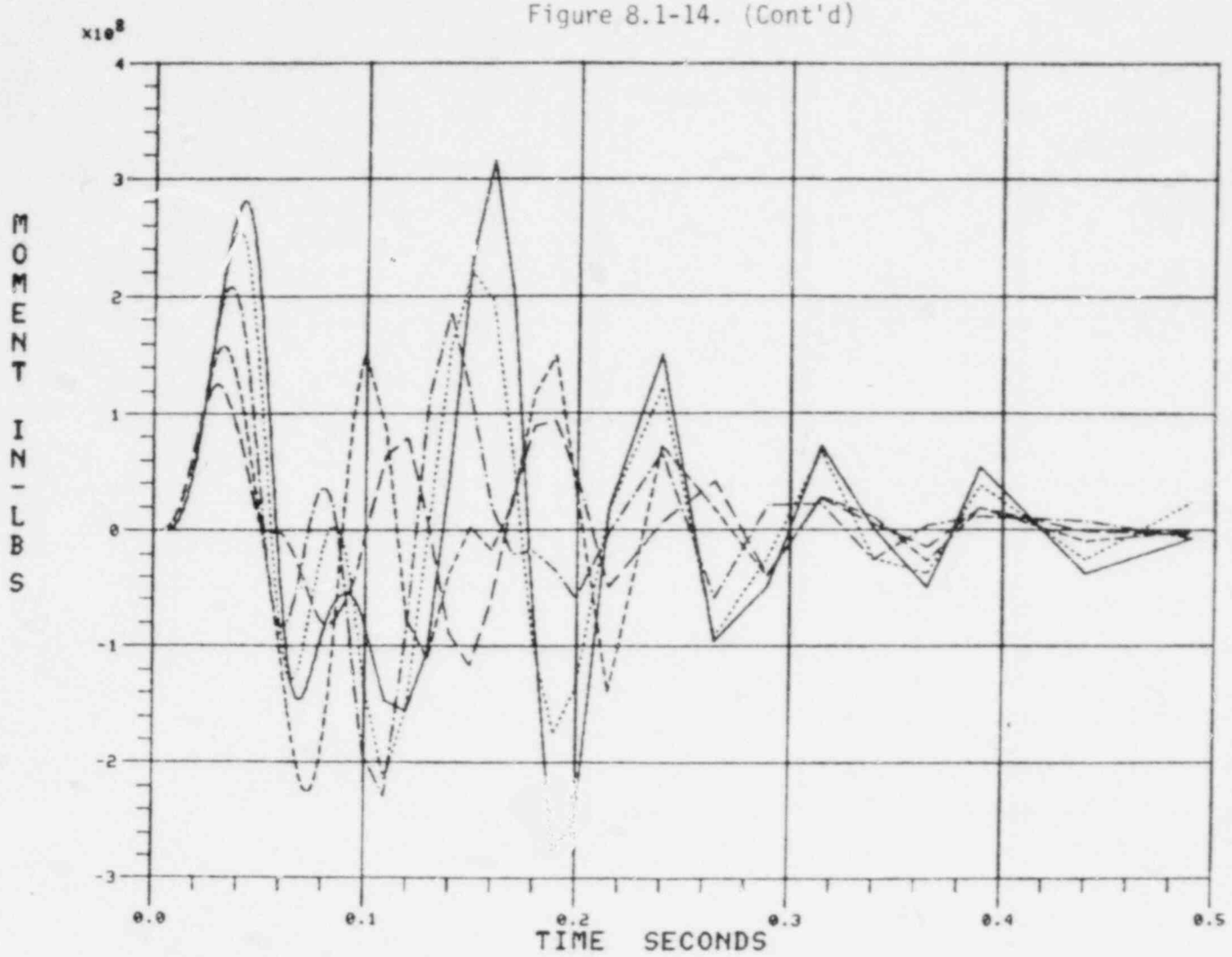

JOINT 51 X ROT RU

Figure 8.1-14. (Cont'd)

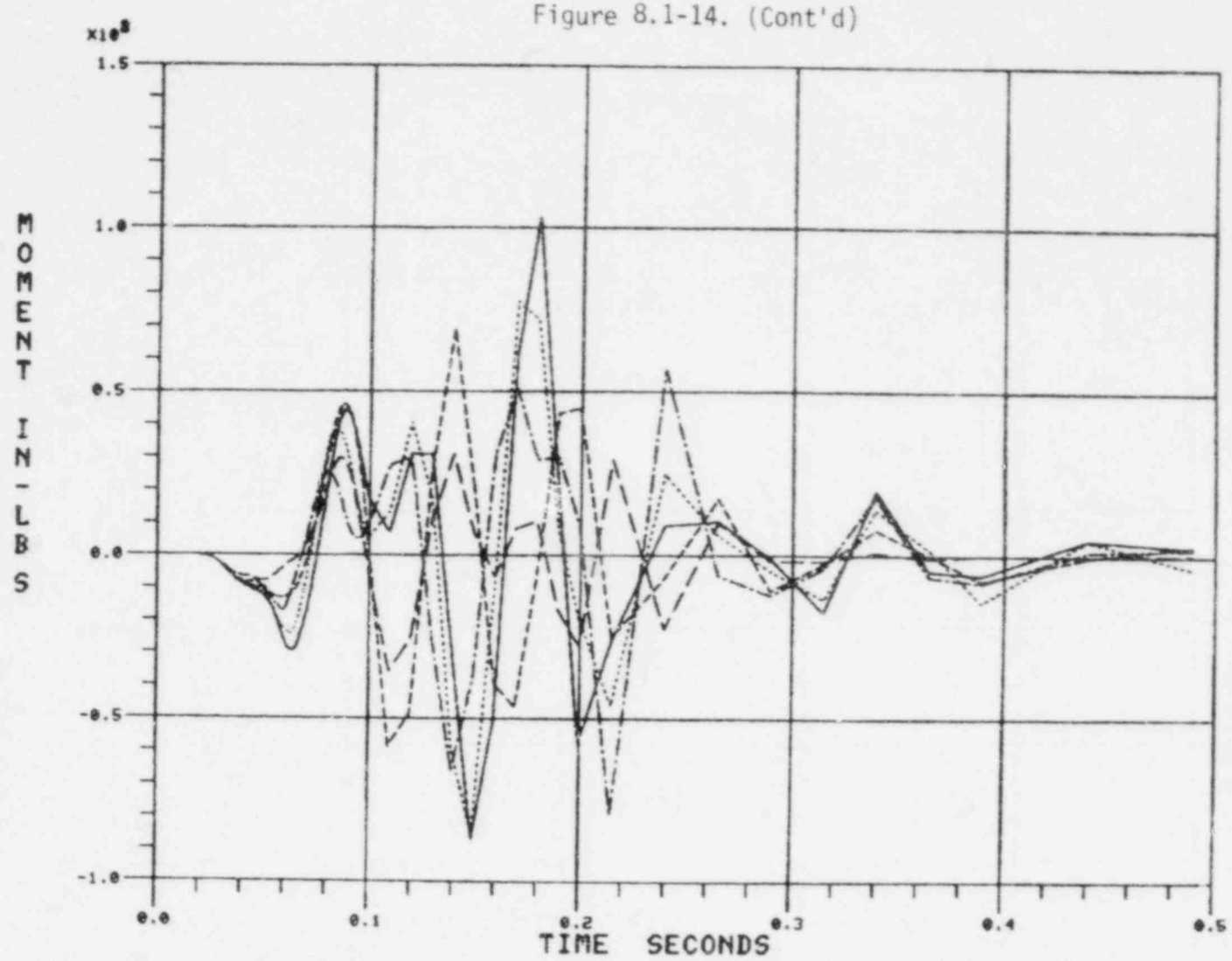

JOINT 51 Z ROT RV

Table 8.1-10. TMI-2 Hot Leg Peak Force Summary

Break area	Resultant horizontal force, lb	Vertical at peak horiz force pt, lb	Resultant moment, in.-lb
2.0A	9.8 E6	1.1 E6	3.2 E8
1.5A	8.3 E6	0.9 E6	2.8 E8
1.0A	6.3 E6	0.6 E6	2.2 E8
0.6A	4.2 E6	0.4 E6	1.6 E8
0.3A	2.5 E6	0.2 E6	1.1 E8

Figure 8.1-15. TMI-2 Hot Leg Break Time History

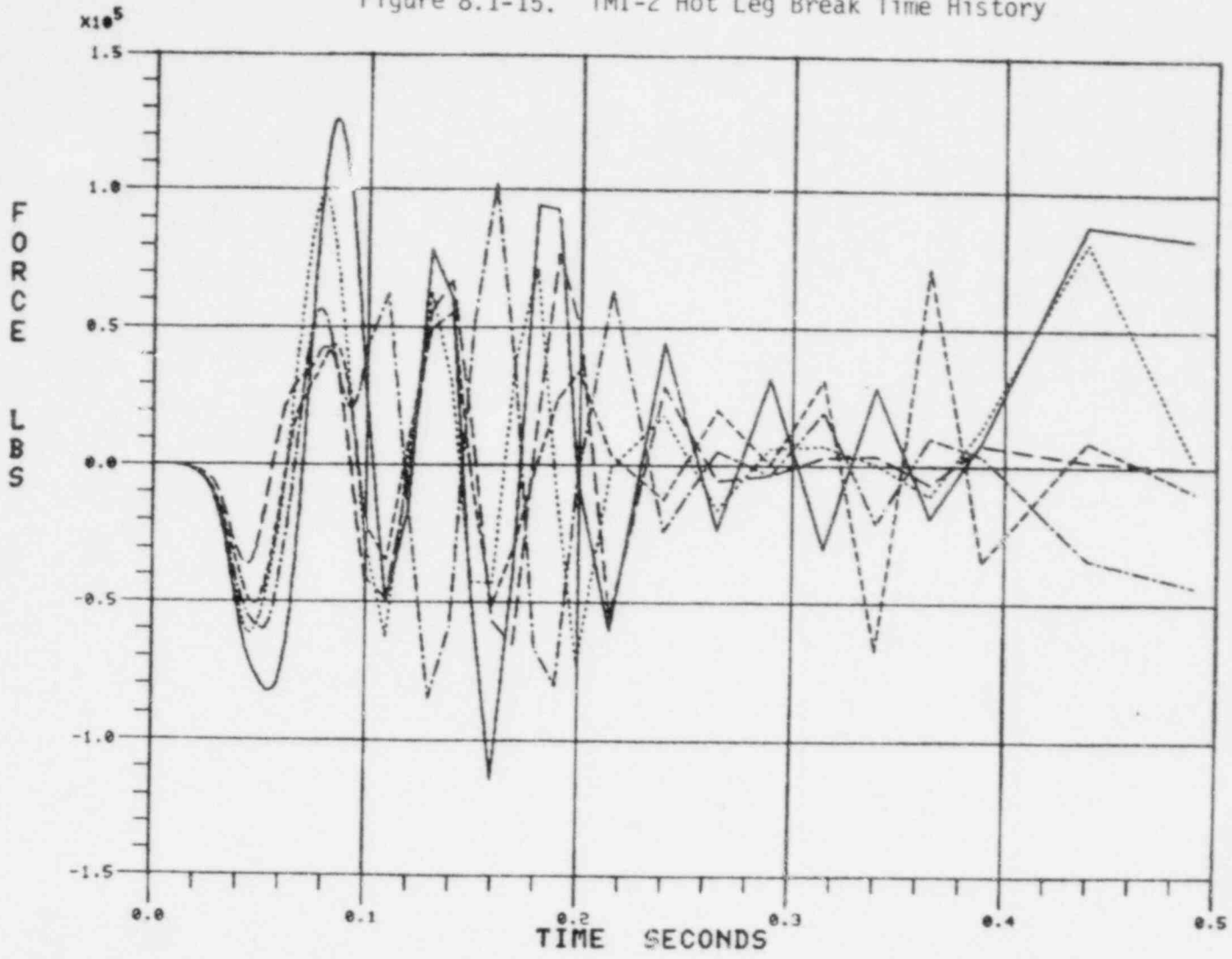

Figure 8.1-15. (Cont'd)

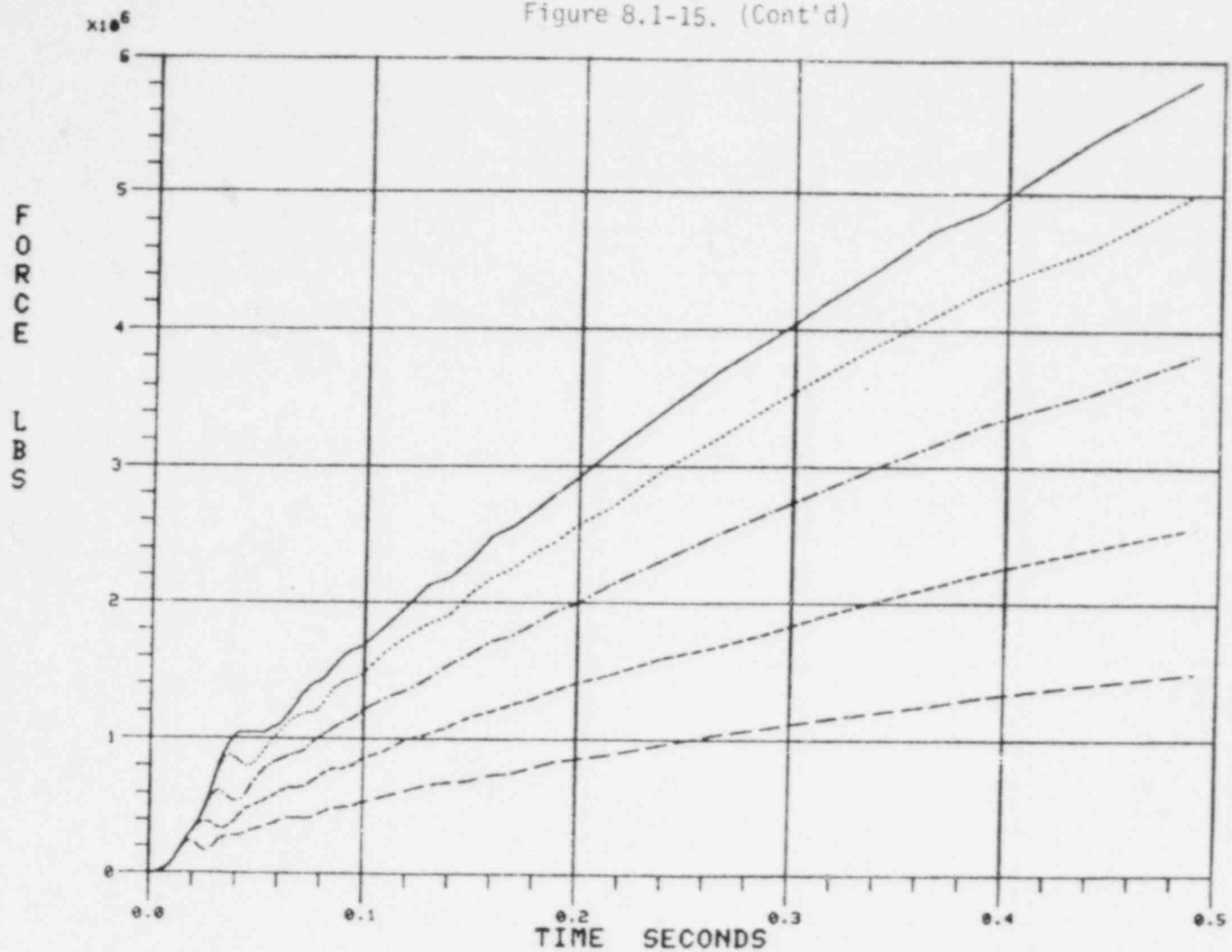

JOINT 51 Y DIR RV TMI2H

Figure 8.1-15. (Cont'd)

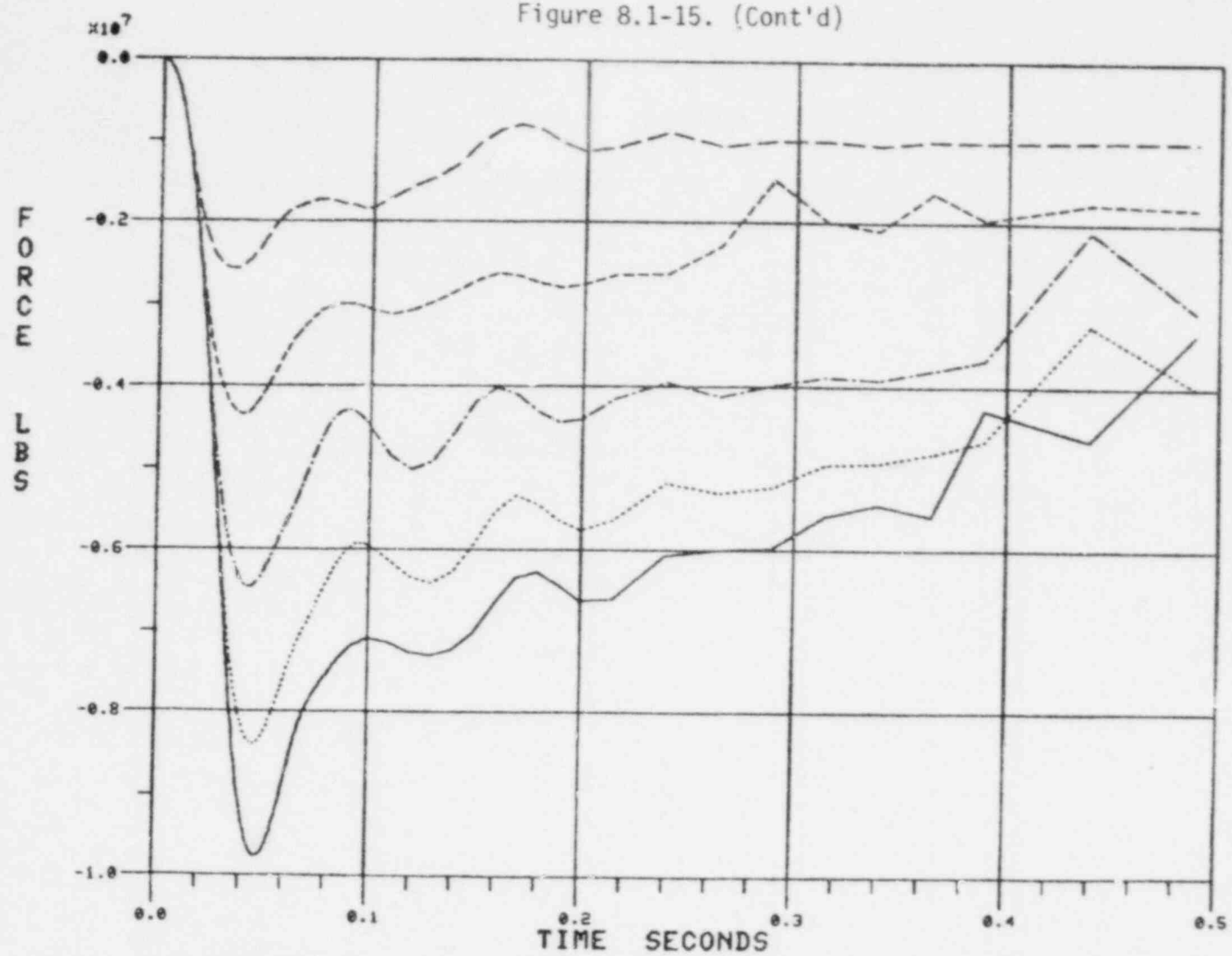

JOINT 51 Z DIR RV :MI2H

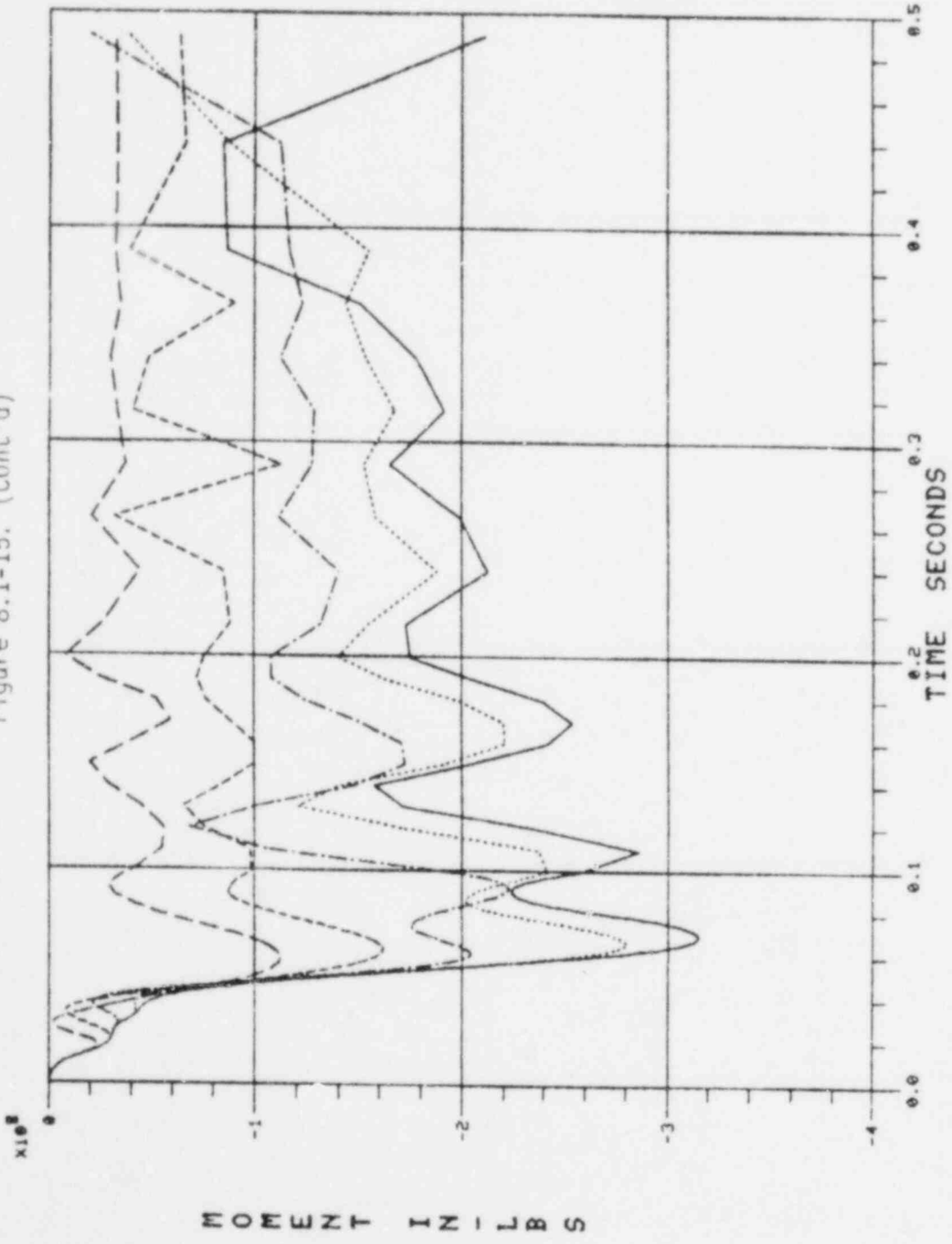

Figure 8.1-15. (Cont'd)

Figure 8.1-15. (Cont'd)

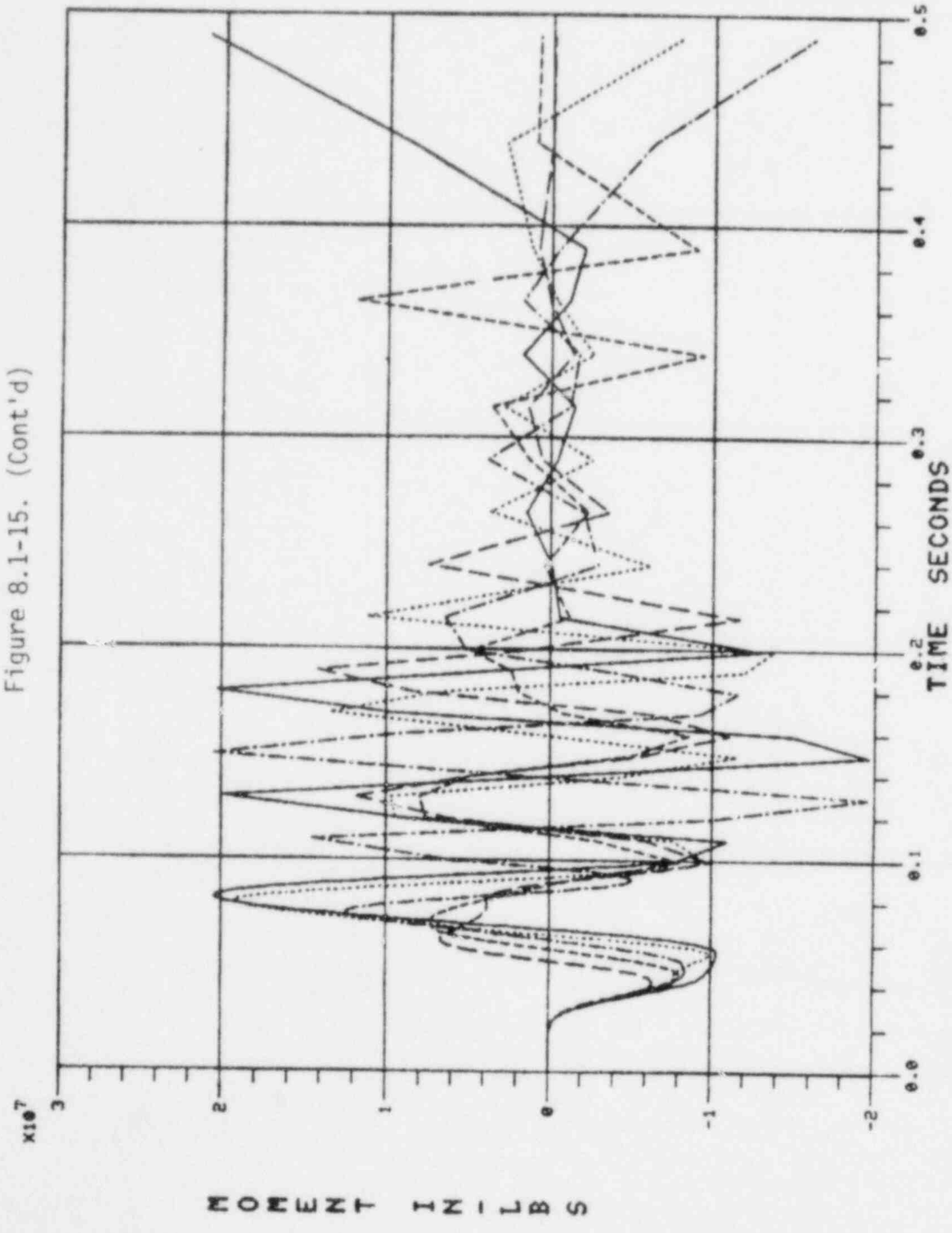

Table 8.1-11. ANO-1 Hot Leg Peak Force Summary

Break area	Resultant horizontal force, lb	Vertucal at peak horiz force pt, lb	Resultant moment, in.-lb
2.0A	9.8 E6	1.0 E6	4.5 E8
1.5A	8.0 E6	0.9 E6	3.8 E8
1.0A	6.0 E6	0.6 E6	2.8 E8
0.6A	3.8 E6	0.4 E6	1.9 E8
0.3A	2.2 E6	0.3 E6	1.3 E8

Figure 8.1-16. ANO-1 Hot Leg Break Time History

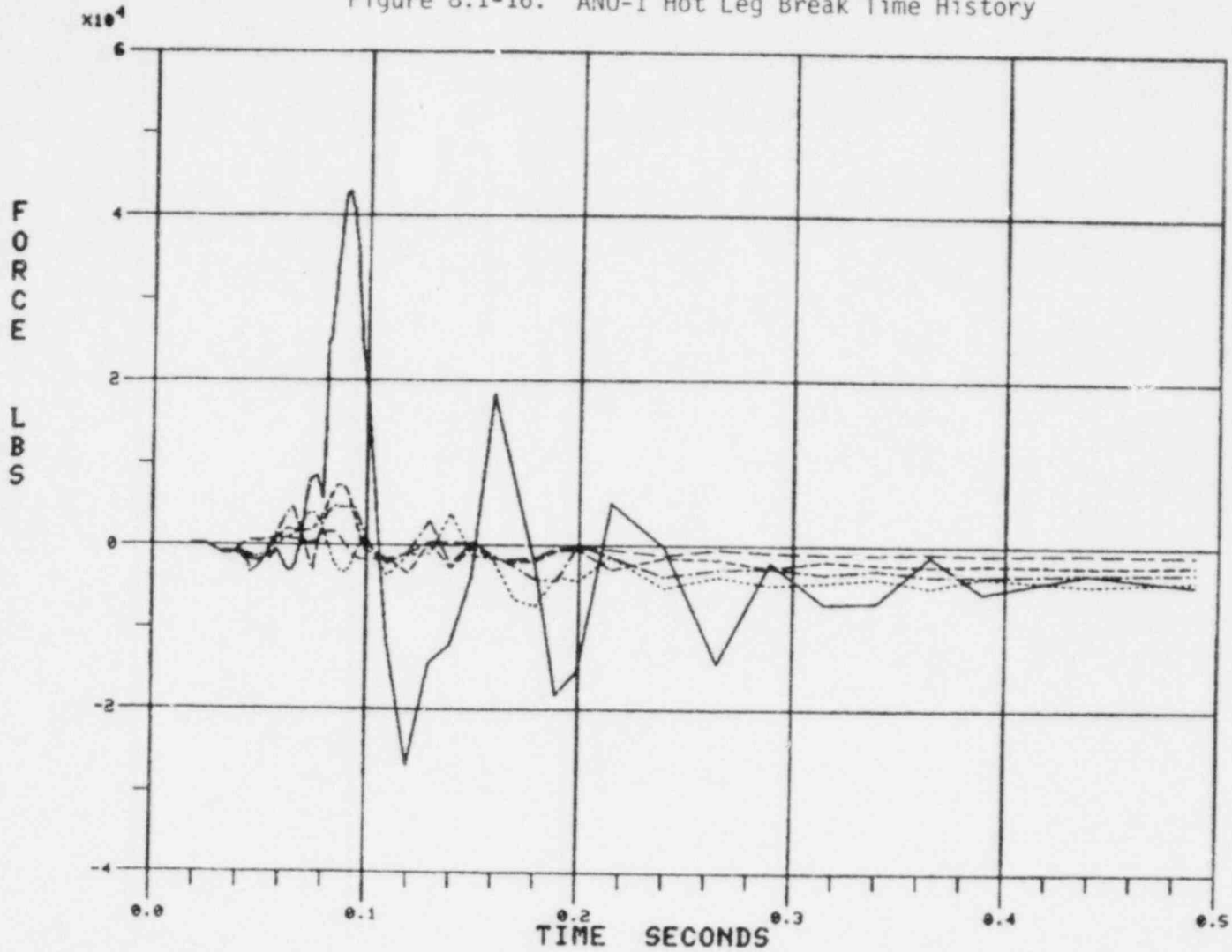

Figure 8.1-16. (Cont'd)

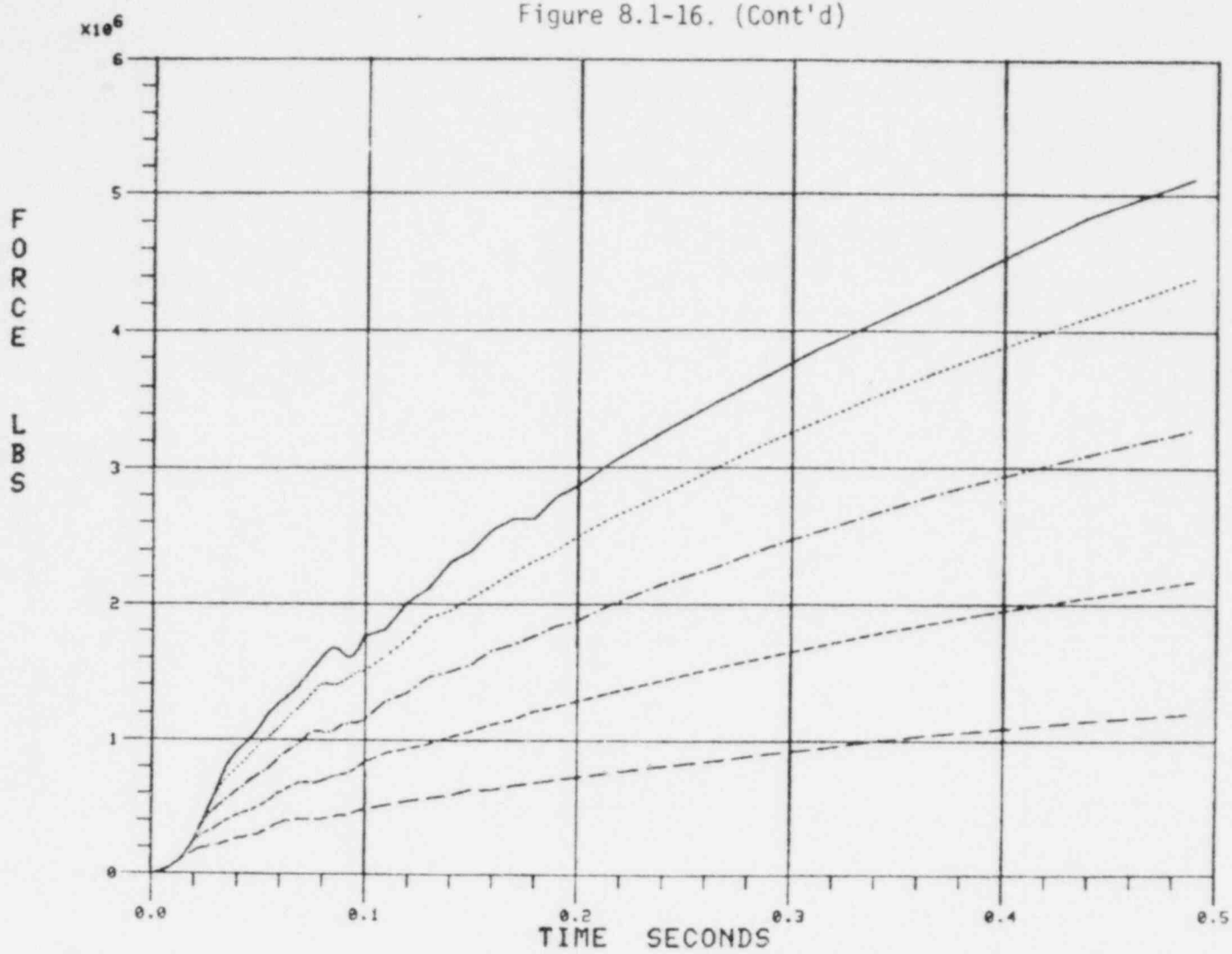

JOINT 51 Y DIR RV ANO1H

Figure 8.1-16. (Cont'd)

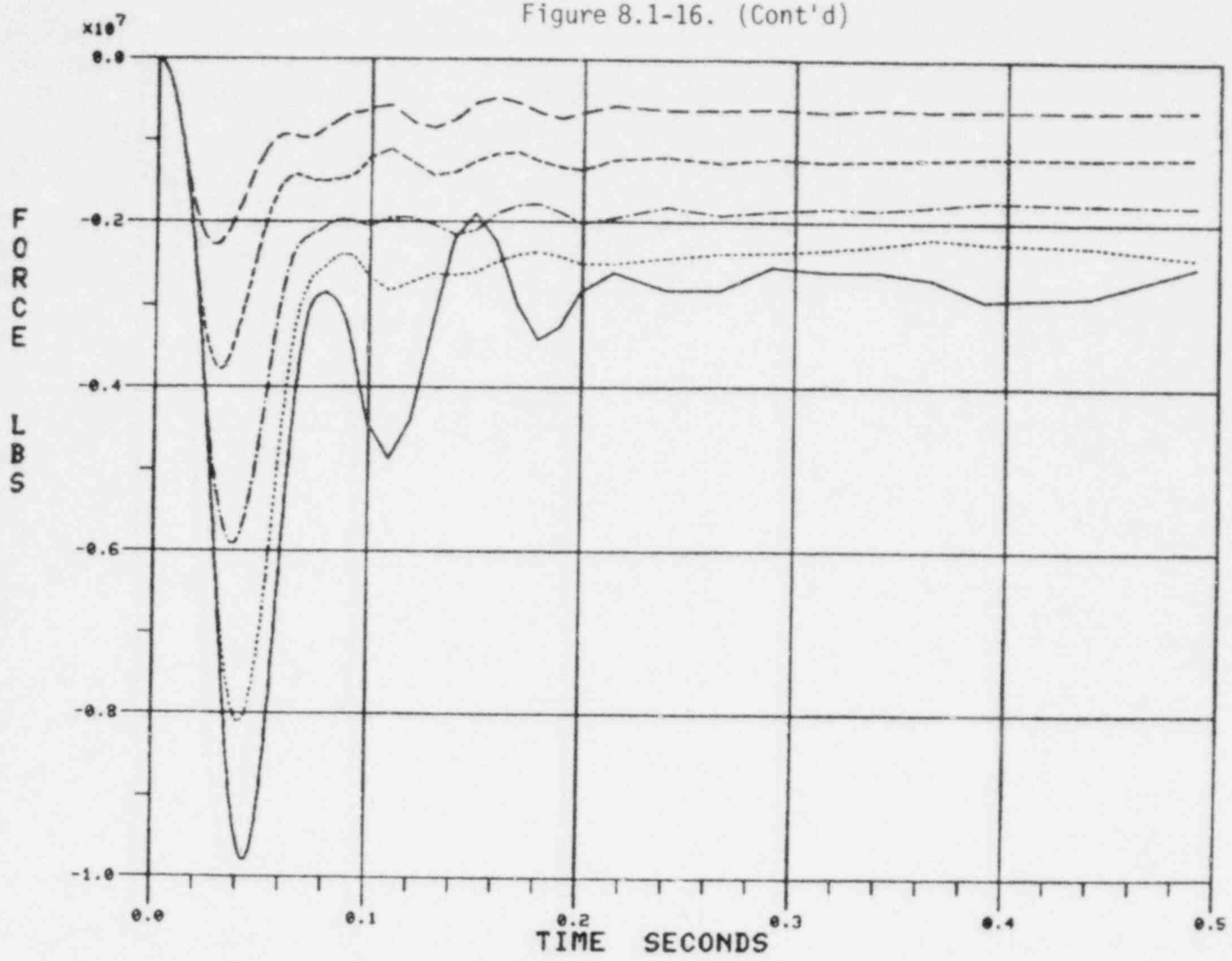

JOINT 51 Z DIR RU AN01H

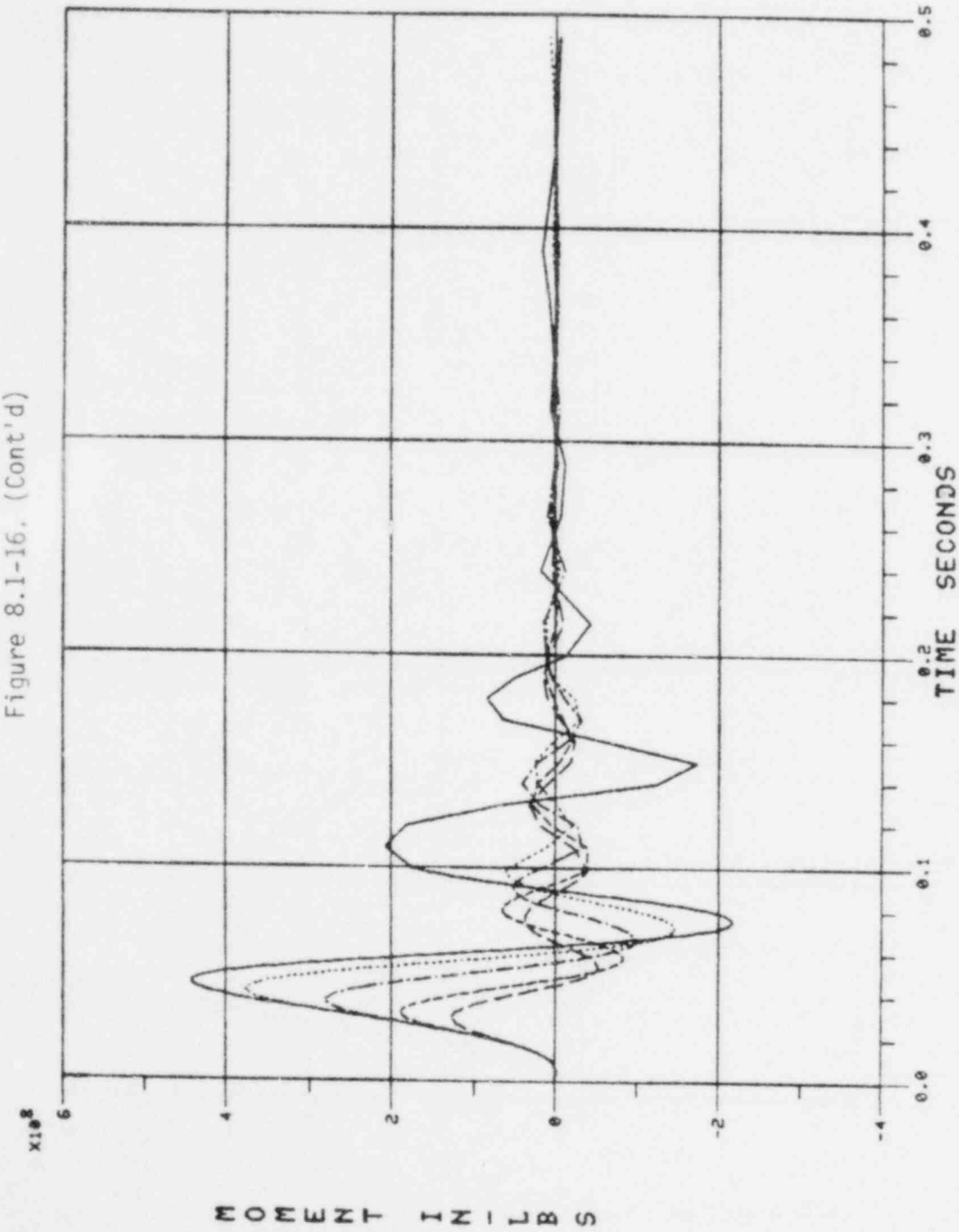

Figure 8.1-16. (Cont'd)

Figure 8.1-16. (Cont'd)

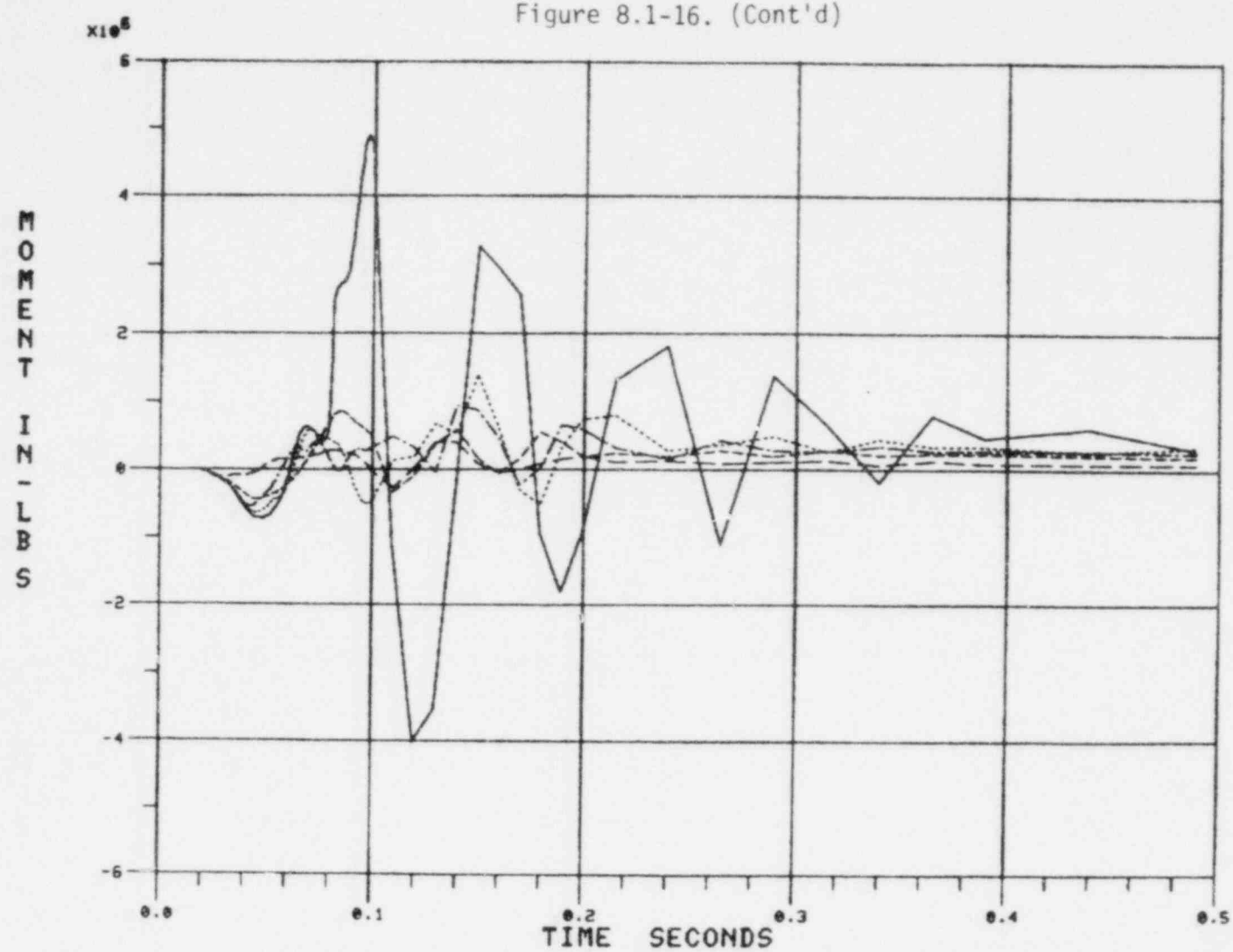

JOINT 51 Z [illegible] AN01H

Table 8.1-12. Rancho Seco Hot Leg Peak Force Summary

Break area	Resultant horizontal force, lb	Vertical at peak horiz force pt, lb	Resultant moment, in.-lb
2.0A	9.3 E6	1.1 E6	4.2 E8
1.5A	7.8 E6	0.9 E6	3.6 E8
1.0A	5.8 E6	0.8 E6	2.8 E8
0.6A	3.8 E6	0.5 E6	2.0 E8
0.3A	2.2 E6	0.2 E6	1.3 E8

Figure 8.1-17. Rancho Seco Hot Leg Break Time History

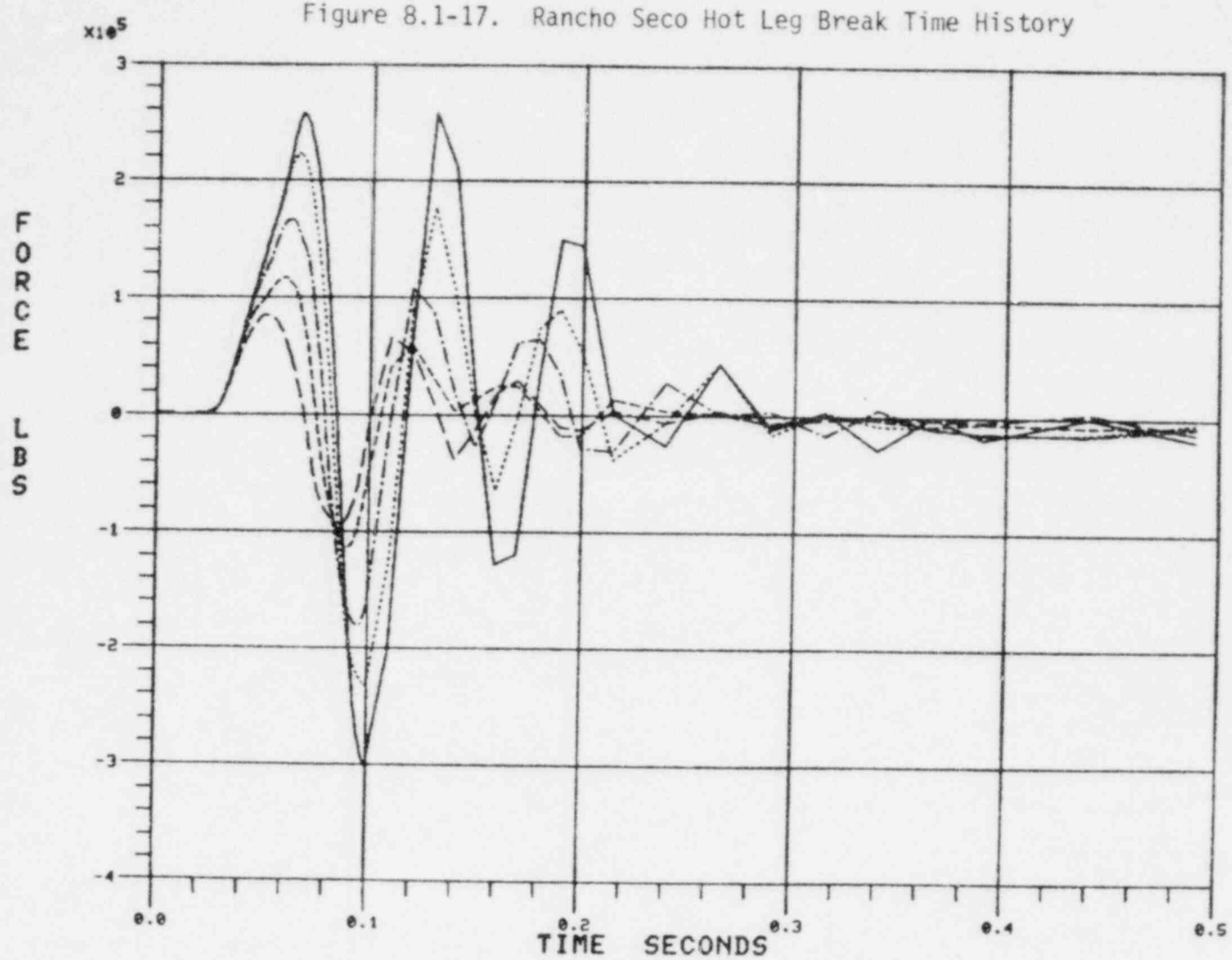

JOINT 51 X DIR RV SMUDH

Figure 8.1-17. (Cont'd)

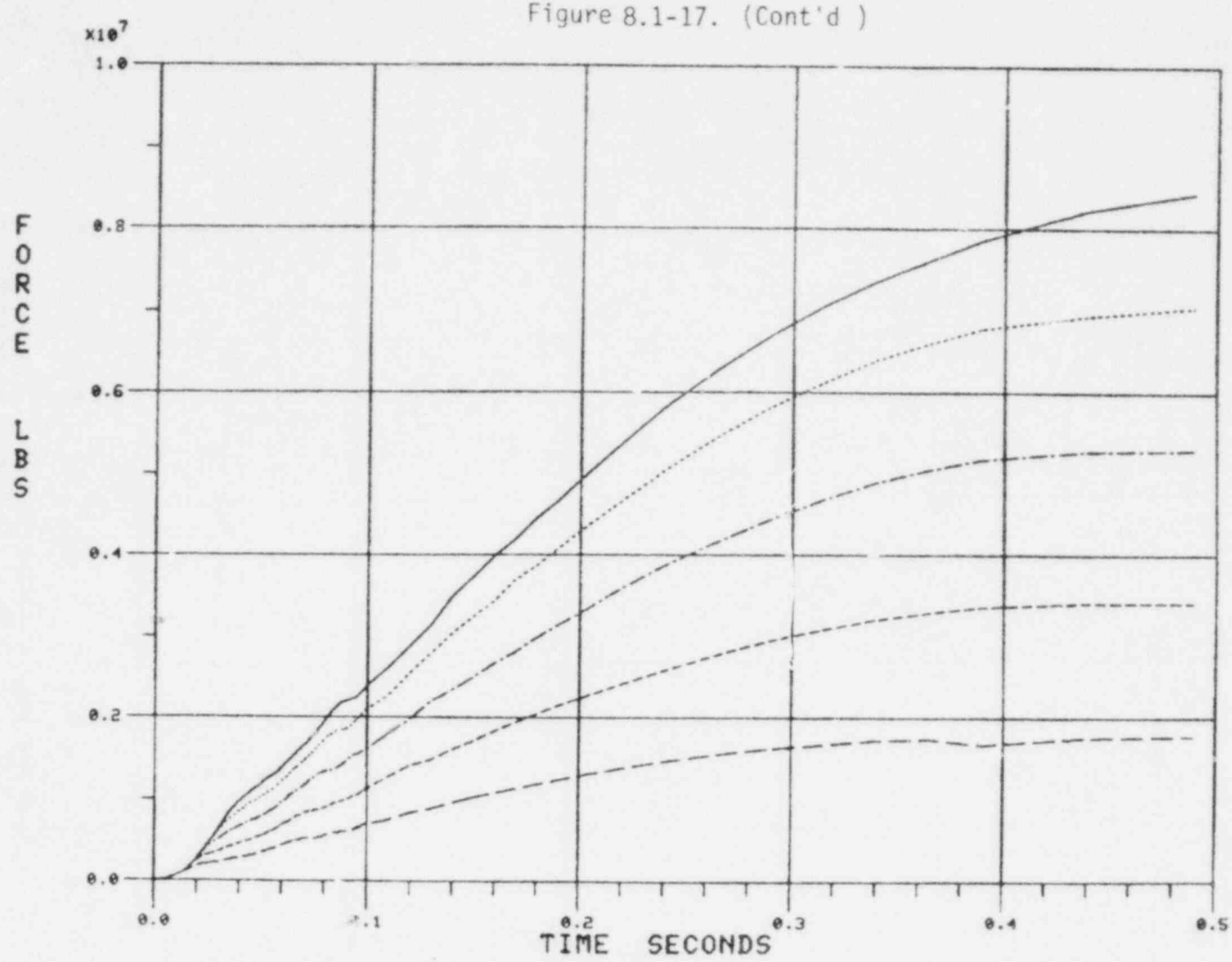

JOINT 51 Y DIR RV SMUDH

Figure 8.1-17. (Cont'd)

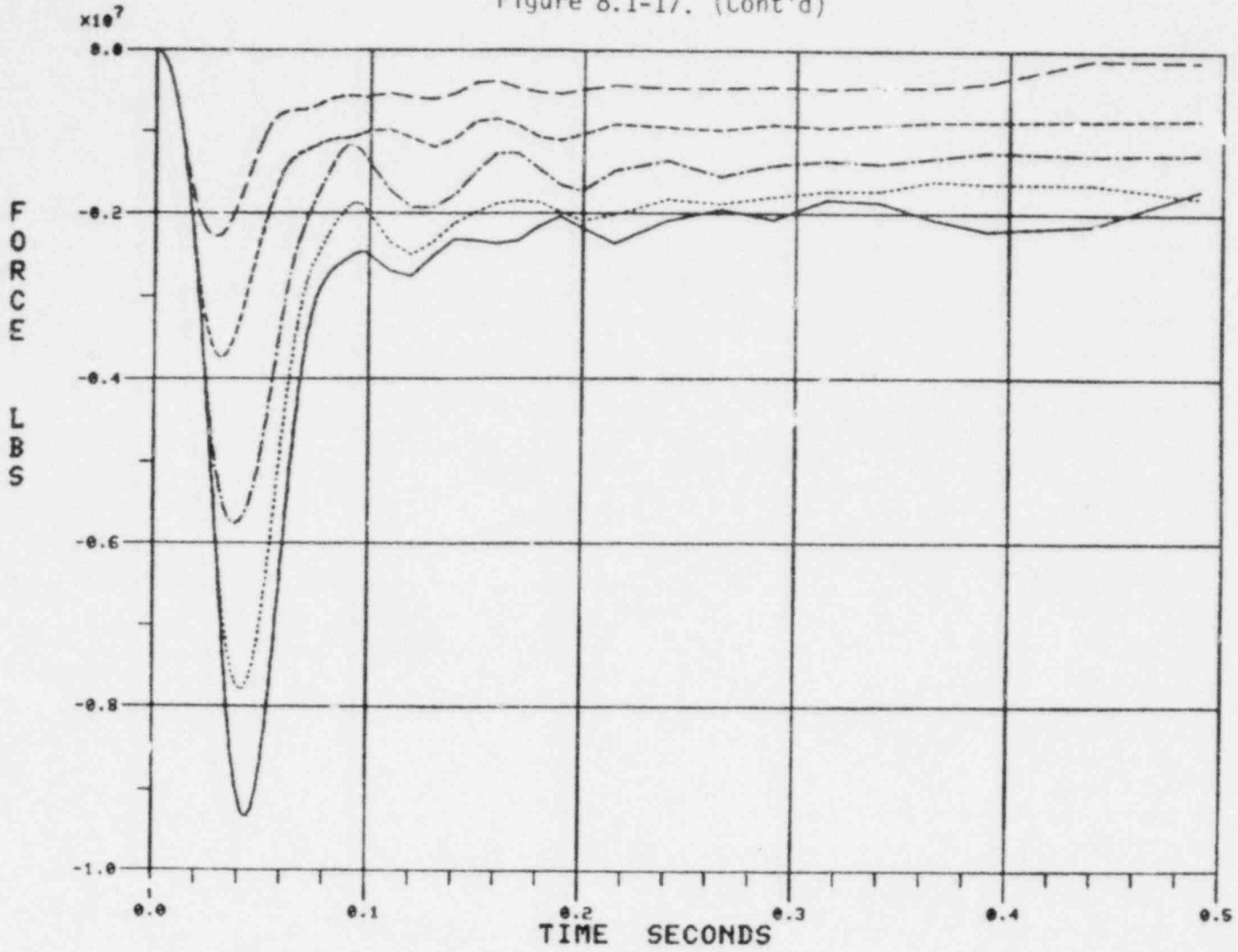

JOINT 51 Z DIR RV SMUDH

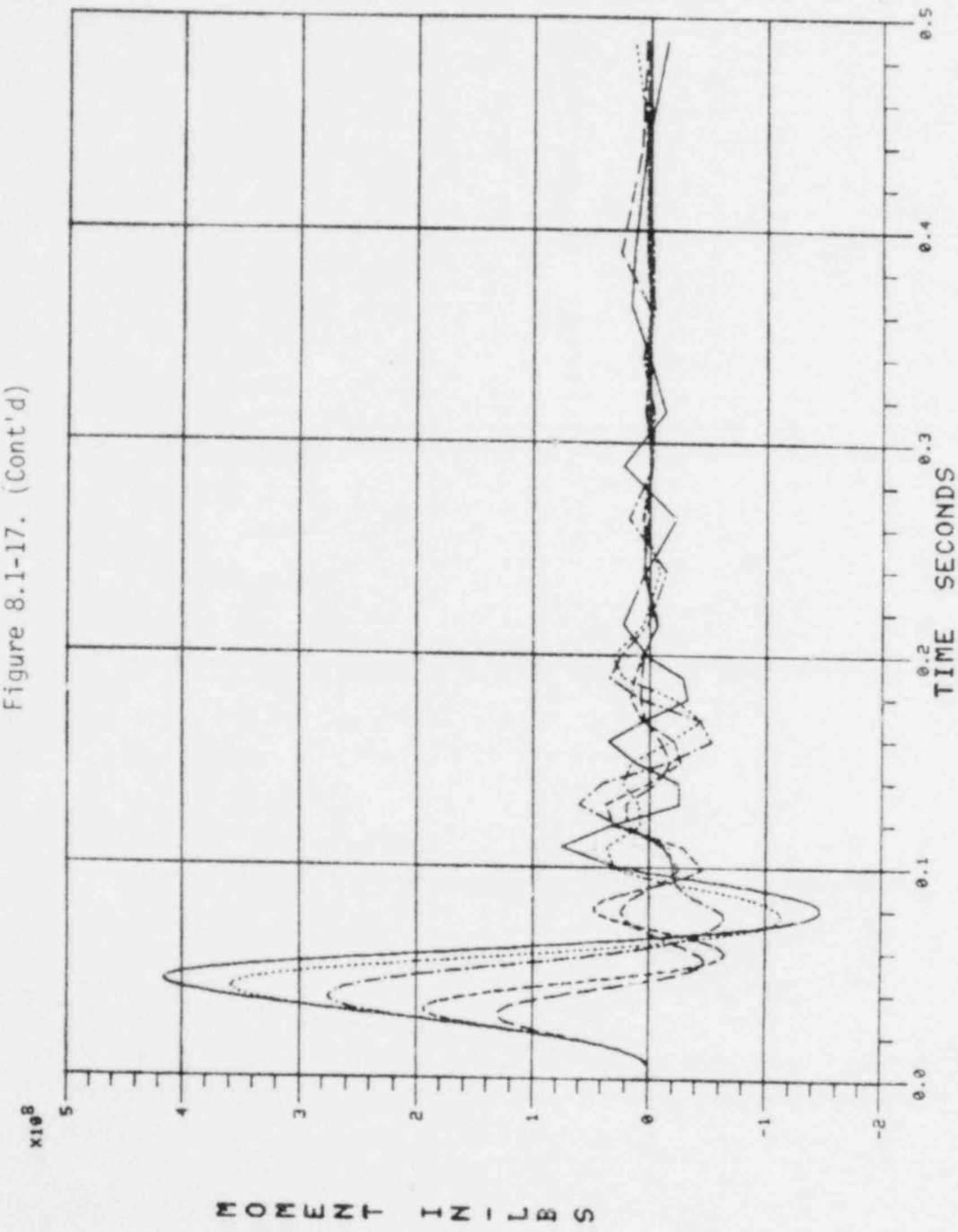

Figure 8.1-17. (Cont'd)

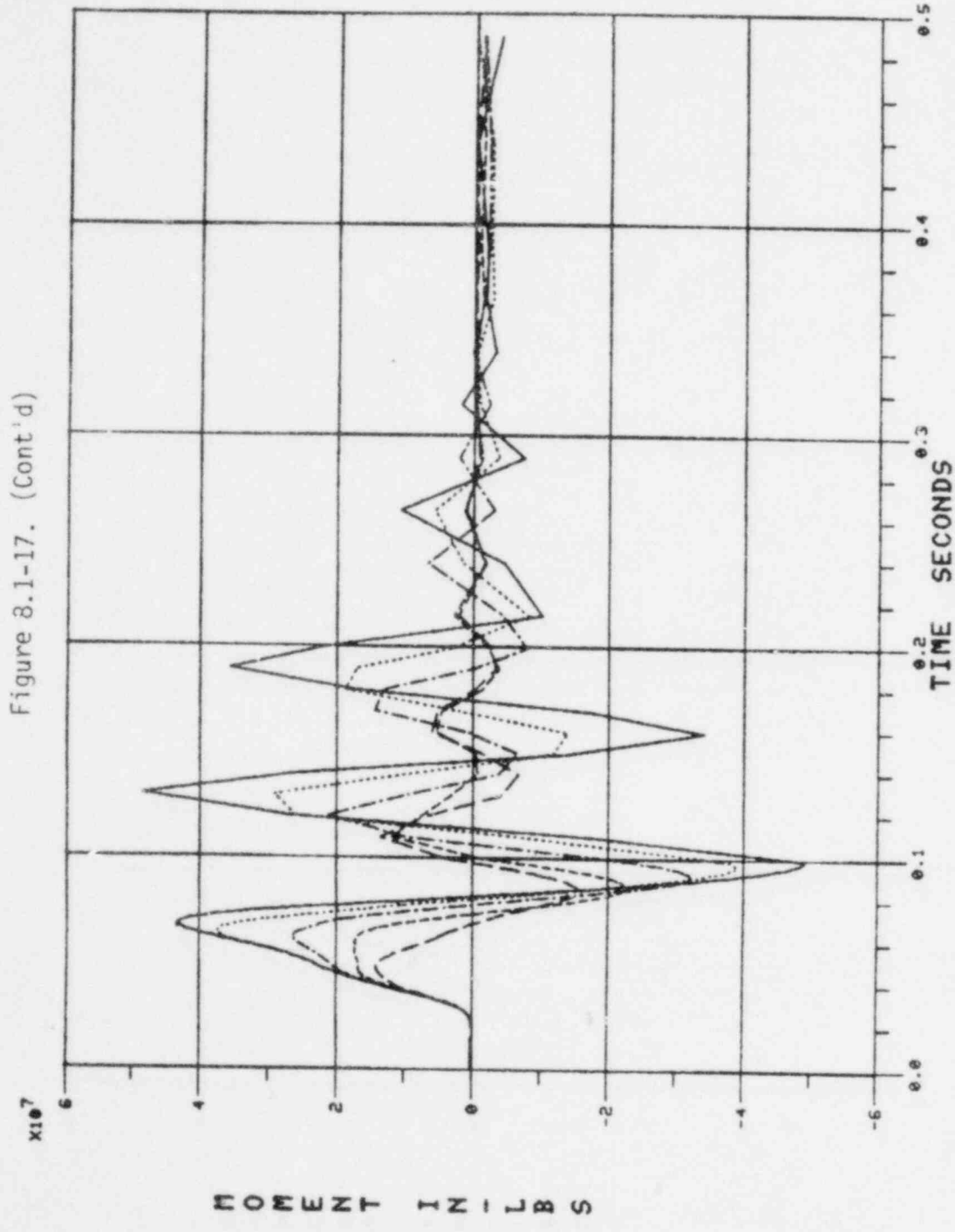

Figure 8.1-17. (Cont'd)

Table 8.1-13. Davis-Besse 1 Hot Leg Peak Force Summary

Break area	Resultant horizontal force, lb	Vertical at peak horiz force pt, lb	Resultant moment, in.-lb
1.02A	6.7 E6	0.7 E6	1.7 E8

Figure 8.1-18. Davis-Besse 1 Hot Leg Break Time History

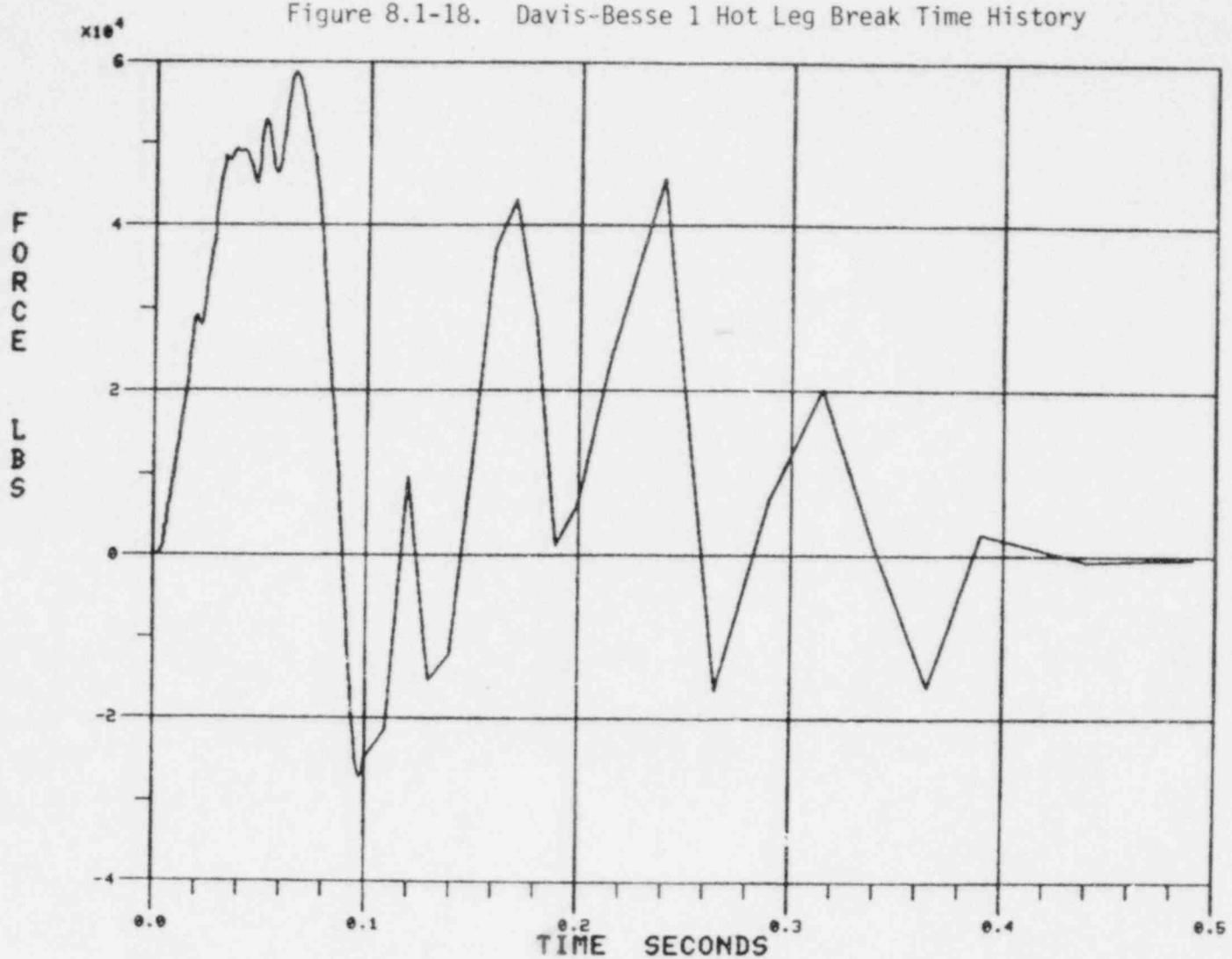

TECO-14 1.02A HL BK AT RU FX

Figure 8.1-18. (Cont'd)

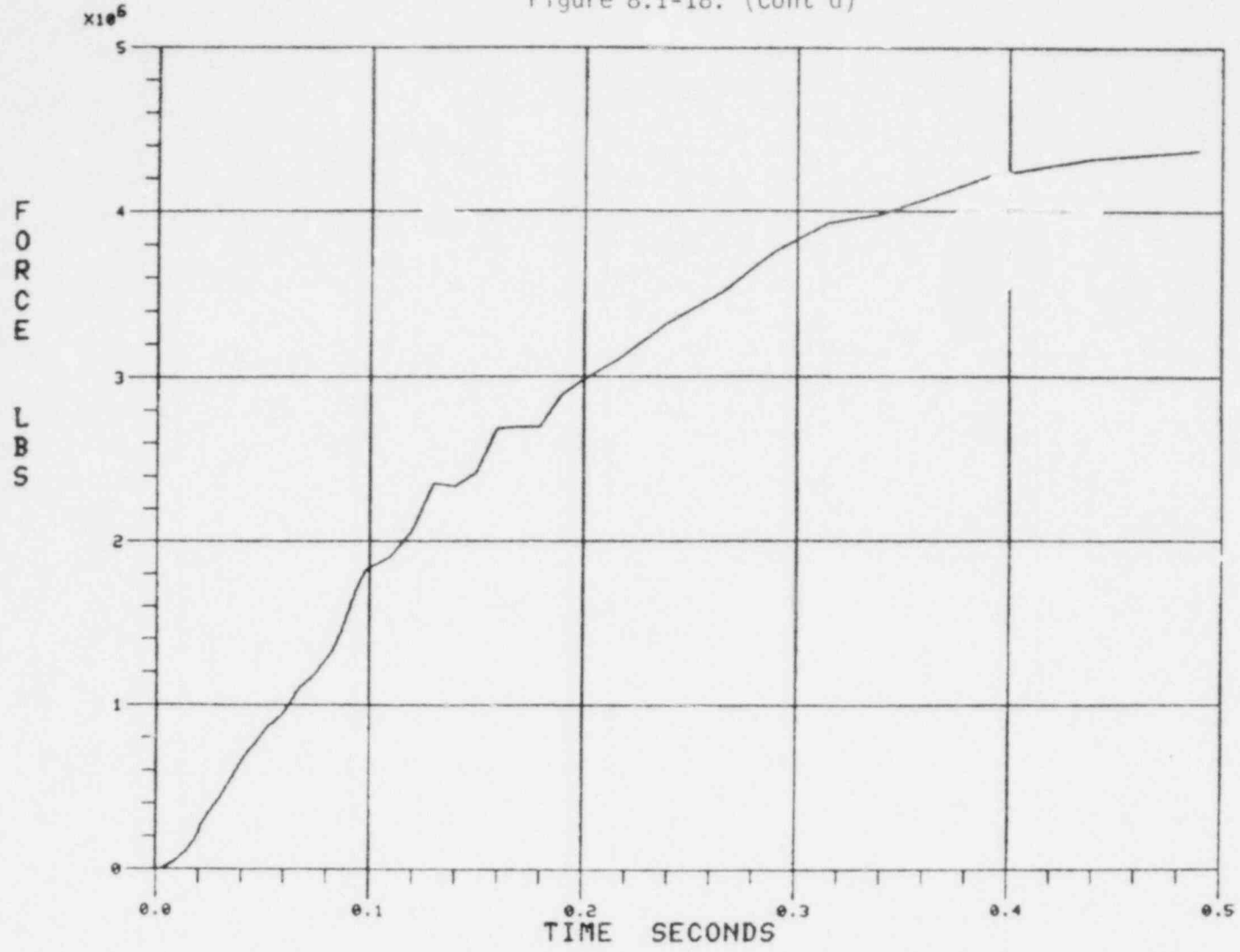

TECO-14 1.02A HL BK AT RU FY

Figure 8.1-18. (Cont'd)

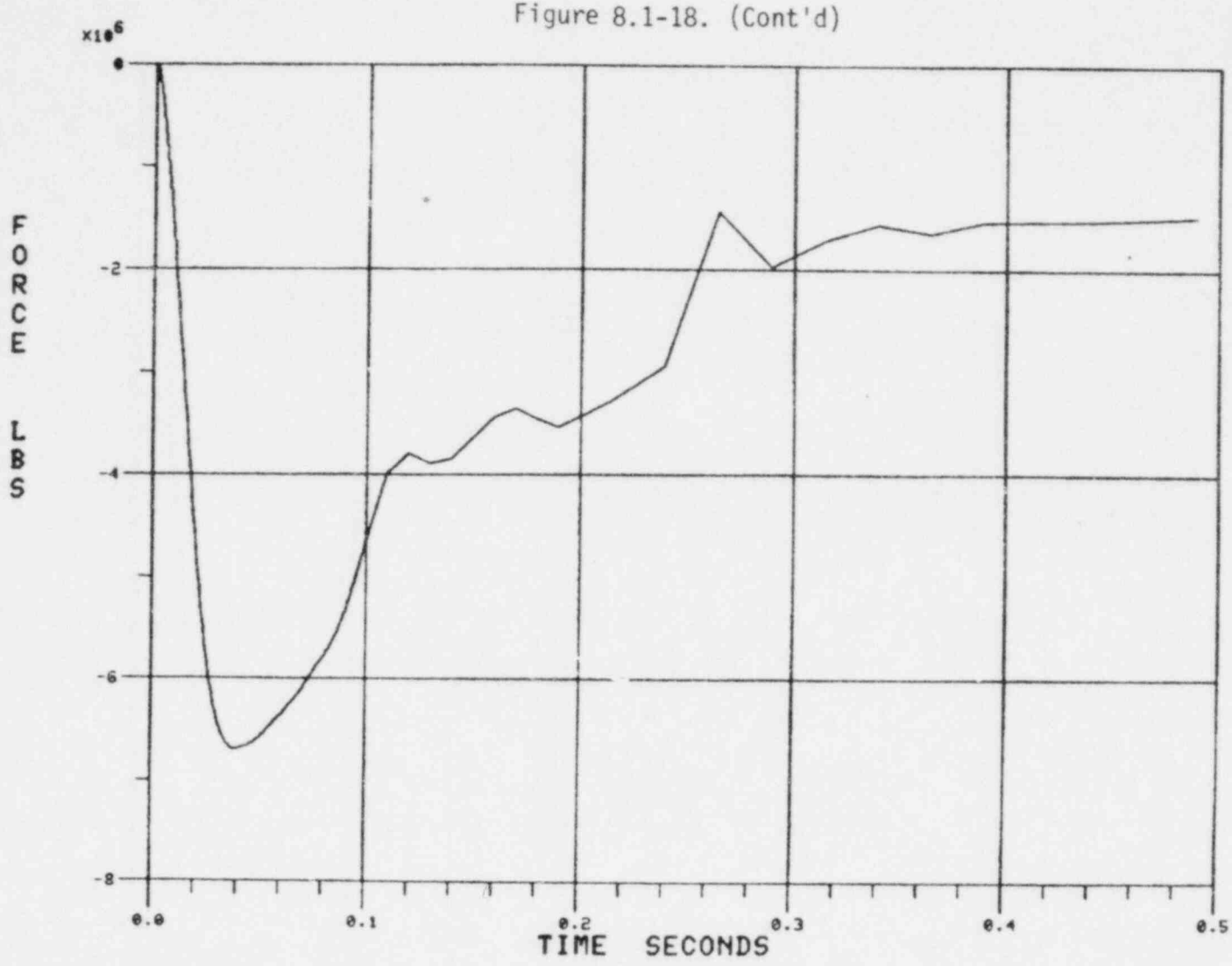

TECO-14 1.02A HL BK AT RV FZ

Figure 8.1-18. (Cont'd)

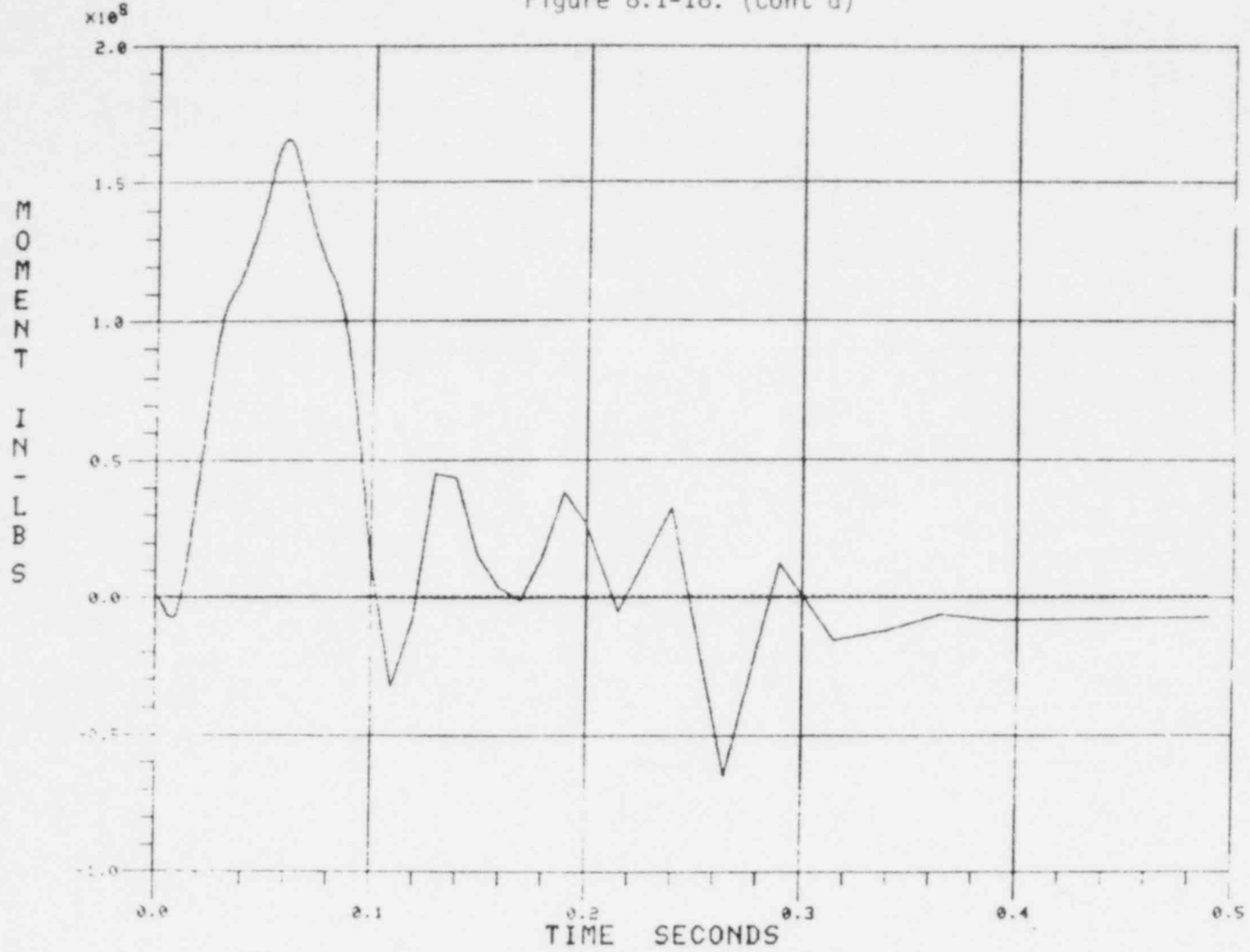

TECO-14 1.02A HL BK AT RU MX

Figure 8.1-18. (Cont'd)

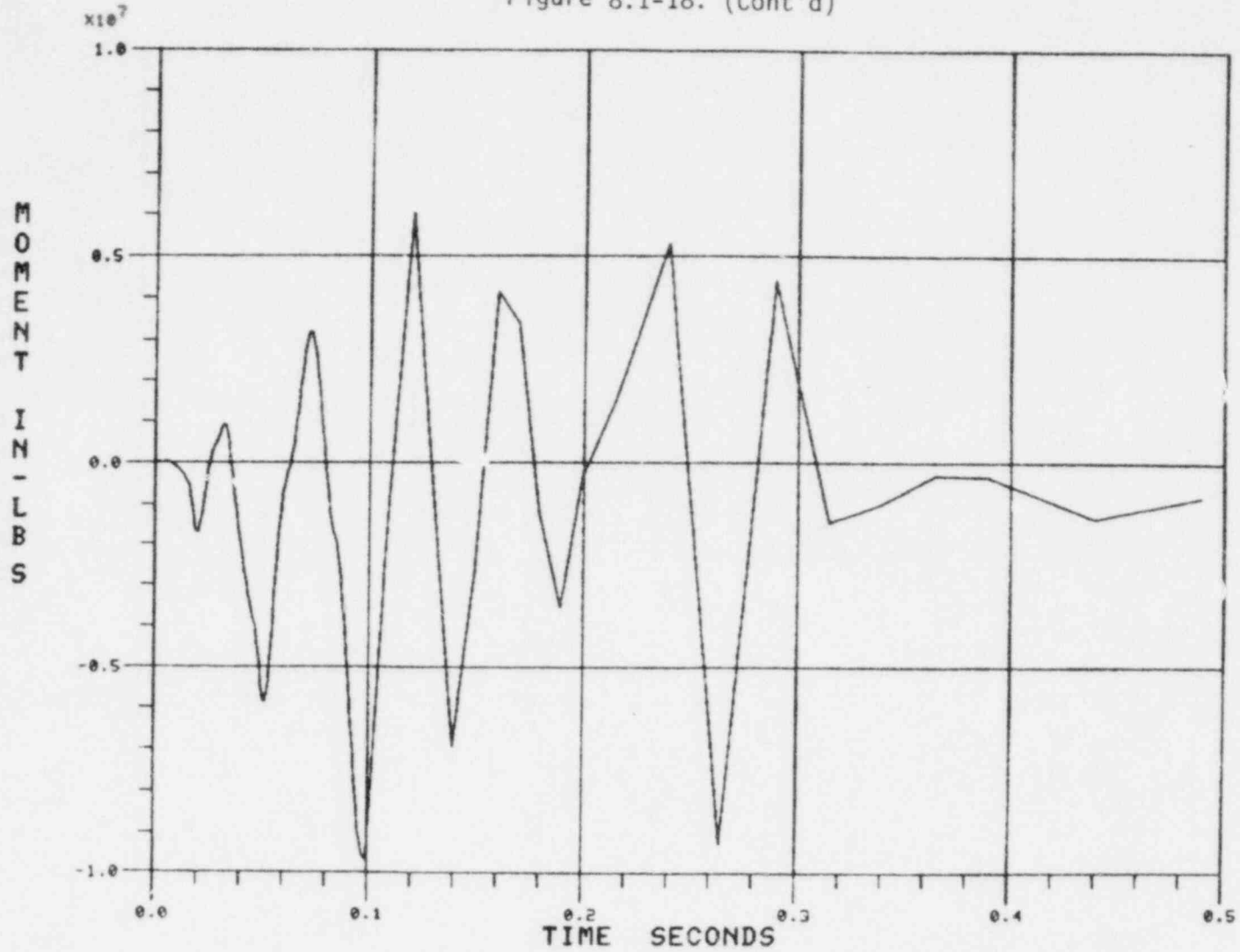

TECO-14 1.02A HL BK AT RV MZ

8.2. Reactor Internals Differential Pressures

Nodal pressure-time histories within the reactor vessel were calculated for a series of assumed break locations and break areas to account for the hydraulically induced LOCA loadings on the reactor internals.

Figures 8.2-1 through 8.2-6 show generic examples of the loadings on the vessel head, the core, and the plenum cylinder for full-area guillotine breaks at the reactor inlet and outlet. These examples are for the skirt-supported plants. Similar information based on actual break areas (except for the nozzle-supported plant) is presented in Figures 8.2-7 through 8.2-12.

Peak component loadings are also shown in Tables 8.2-1 through 8.2-3.

Table 8.2-1. LOCA Load Component Comparison for Hot Leg Breaks in Reactor and Steam Generator Cavities

LOCA load component and break description	Break location	
	RV nozzle	Inside SG cavity
Lateral forces on planum cylinder, 10^6 lbf		
2.0A hot leg break	1.65	1.30
1.5A hot leg break	1.65	
1.0A hot leg break	1.65	1.28
0.6A hot leg break	1.63	
0.3A hot leg break	1.45	
Upward forces on core, 10^6 lbf		
2.0A hot leg break	0.444	0.360
1.5A hot leg break	0.444	
1.0A hot leg break	0.444	0.360
0.6A hot leg break	0.425	
0.3A hot leg break	0.300	
Reactor head pressure differential, psi		
2.0A hot leg break	168	129
1.5A hot leg break	168	
1.0A hot leg break	168	129
0.6A hot leg break	168	
0.3A hot leg break	149	

Table 8.2-2. LOCA Load Component Comparison for Cold Leg Breaks in Reactor and Steam Generator Cavities

LOCA load component and break description	Break location: RV nozzle	Break location: Inside SG cavity
Lateral force on core support cylinder, 10^6 lbf		
2.0A cold leg break	4.0	2.67
1.5A cold leg break	4.0	
1.0A cold leg break	3.36	2.44
0.6A cold leg break	2.46	
0.3A cold leg break	2.38	
Downward force on core, 10^6 lbf		
2.0A cold leg break	0.63	0.63
1.5A cold leg break	(a)	
1.0A cold leg break	0.525	0.29
0.6A cold leg break	0.30	
0.3A cold leg break	0.30	
Reactor head pressure differential, psi		
2.0A cold leg break	92.0	95.5
1.5A cold leg break	107.0	
1.0A cold leg break	68.0	72.5
0.6A cold leg break	45.0	
0.3A cold leg break	63.0	

(a) Not available.

Table 8.2-3. LOCA Load Component Comparison for Hot and Cold Leg Breaks

LOCA load component	0.242A CL @ RV	1.167A CL @ first elbow
Cold leg breaks		
Lateral force on core support cyl, 10^6 lbf	1.54	3.07
Downward force on core, 10^6 lbf	0.23	0.55
Reactor head Δ^D, psi	46.2	57.0
	1.024A HL @ RV	1.033A HL @ first elbow
Hot leg breaks		
Lateral force on upper plenum cyl, 10^6 lbf	1.04	1.51
Upward force on core, 10^6 lbf	0.31	0.28
Reactor head ΔP, psi	114.0	115.0

Figure 8.2-1. RV Head Differential Pressure Vs Time — 177-FA Skirt-Supported Plant, 2.0A Hot Leg Break at RV

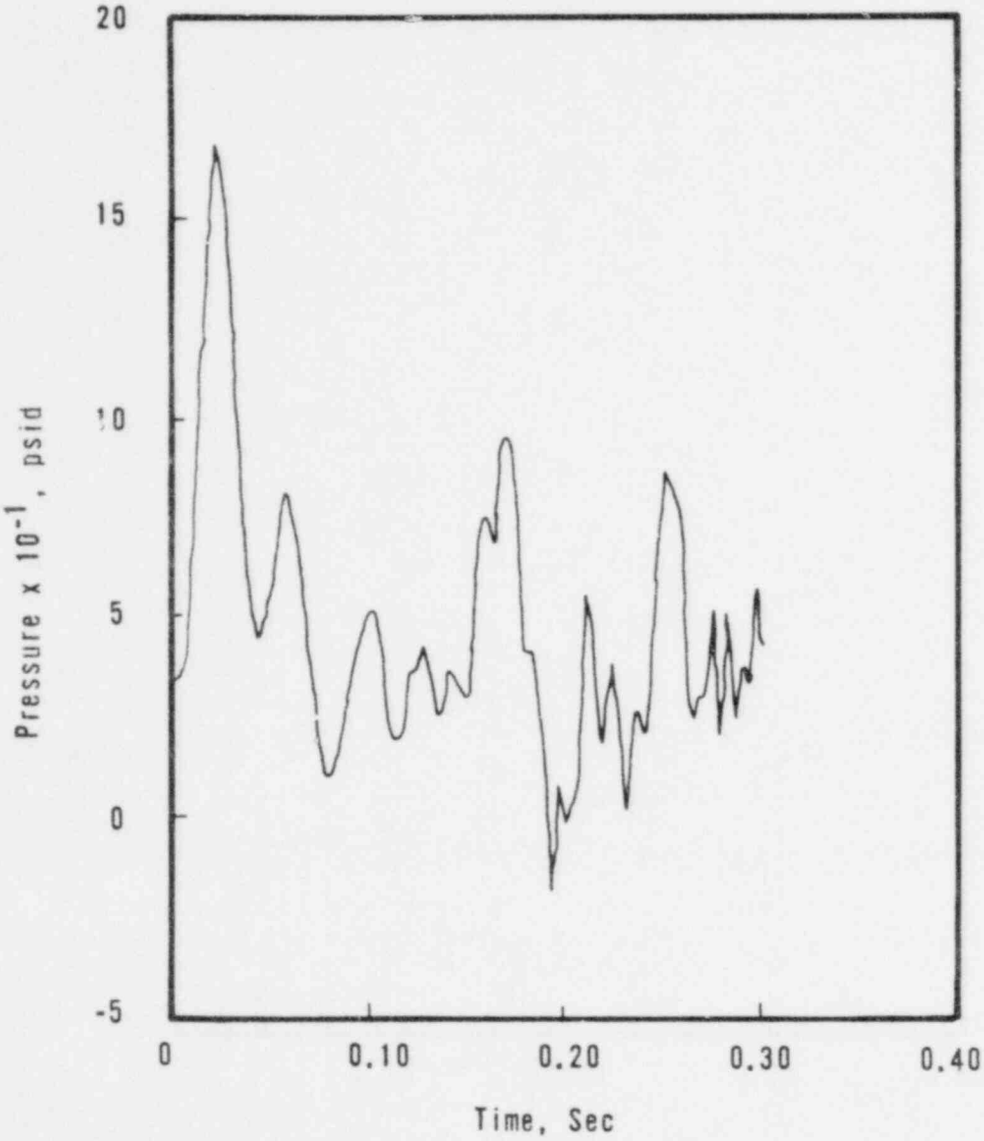

Figure 8.2-2. Total Force on Core Vs Time — 177-FA Skirt-Supported Plant, 2.0A Hot Leg Break at RV

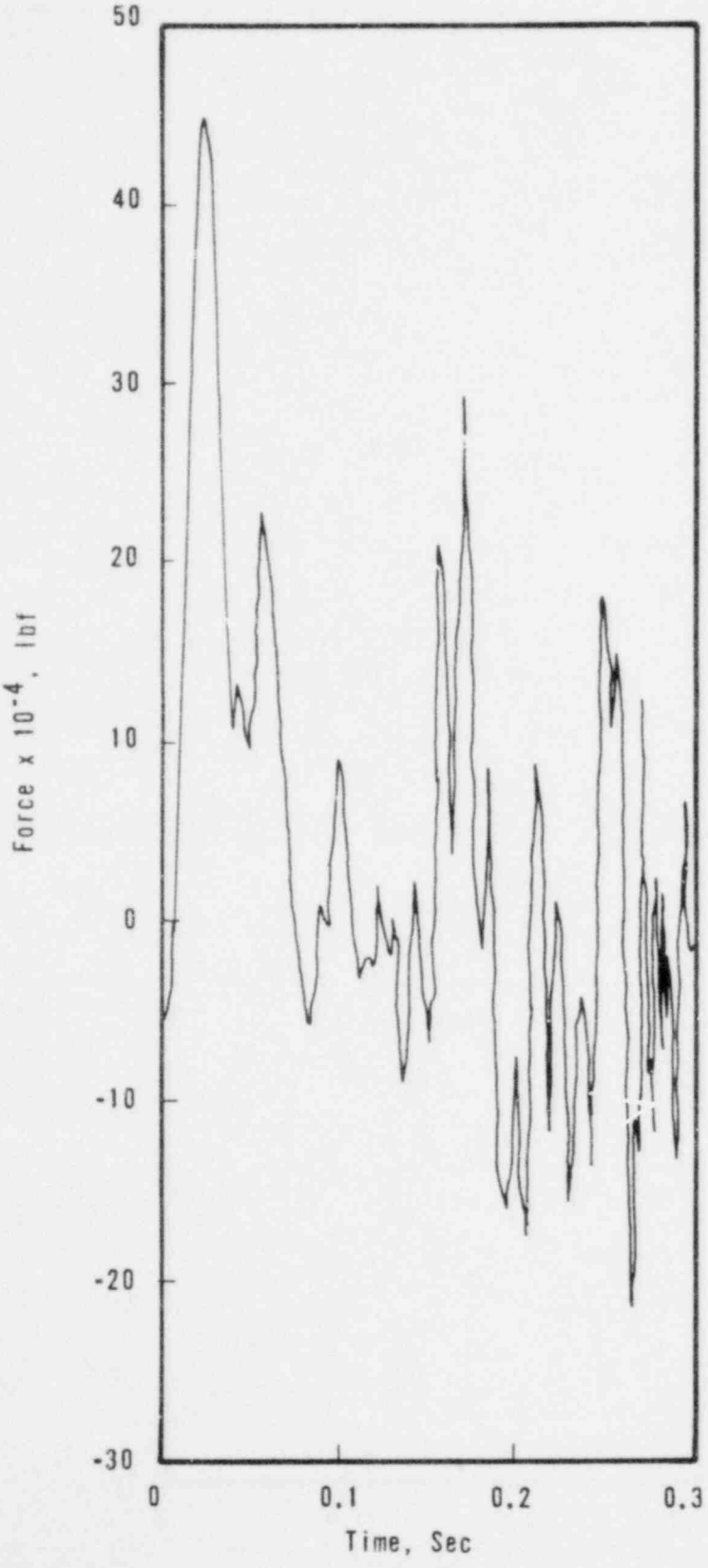

Figure 8.2-3. Total Lateral Force in Plenum Cylinder Vs Time — 177-FA Skirt-Supported Plant, 2.0A Hot Leg Break at RV

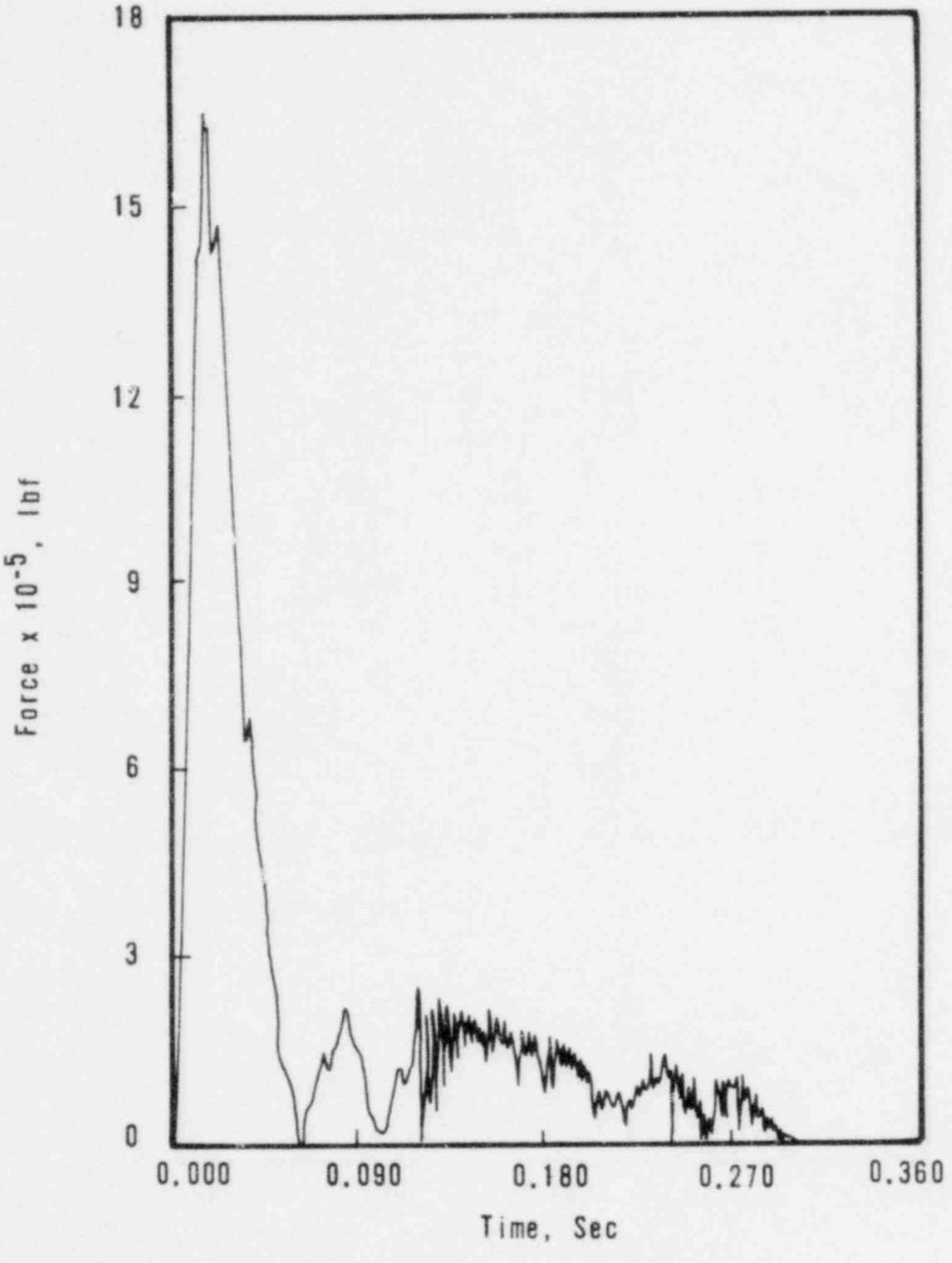

Figure 8.2-4. RV Head Differential Pressure Vs Time — 177-FA Skirt-Supported Plant, 2.0A Cold Leg Break at RV

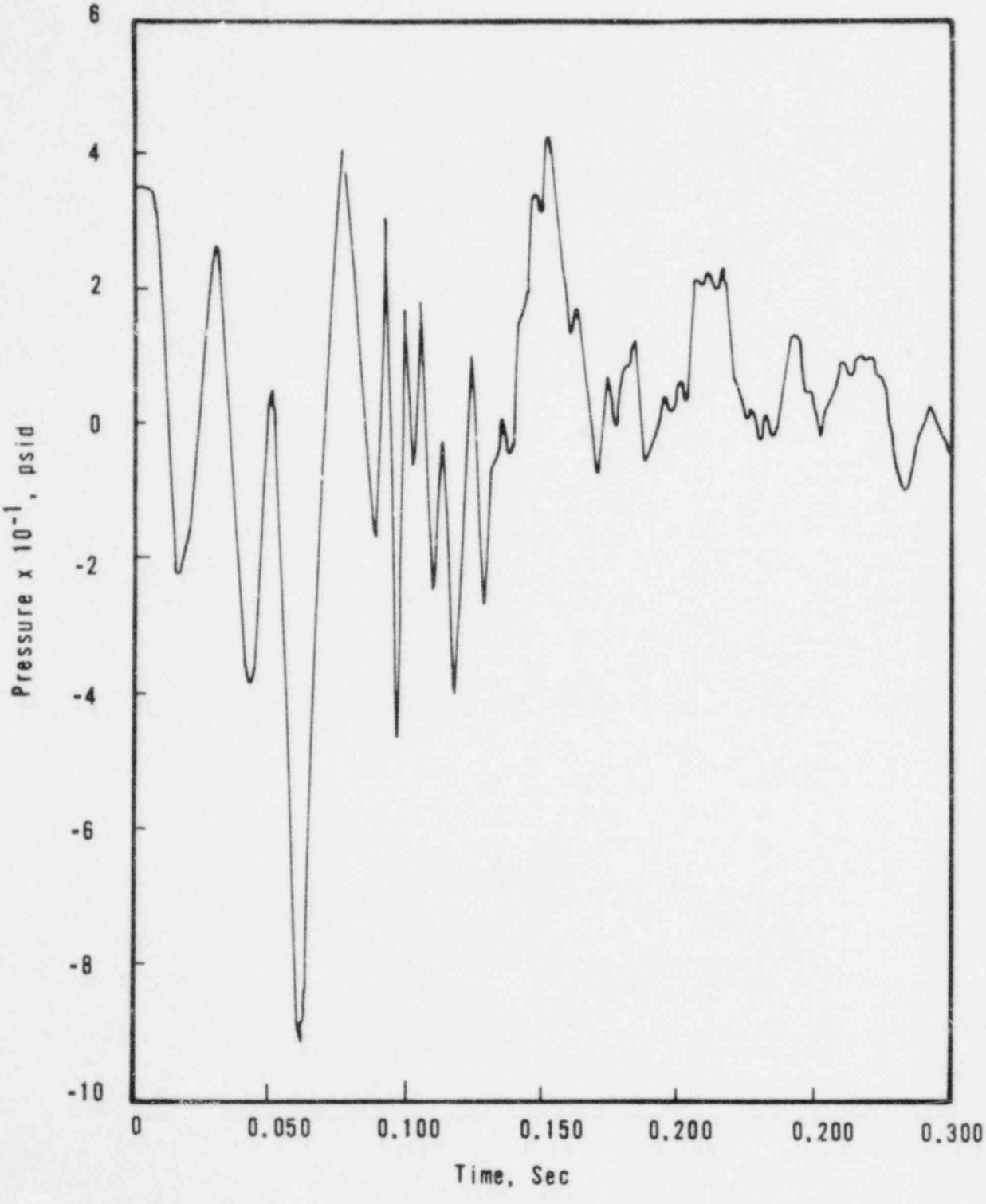

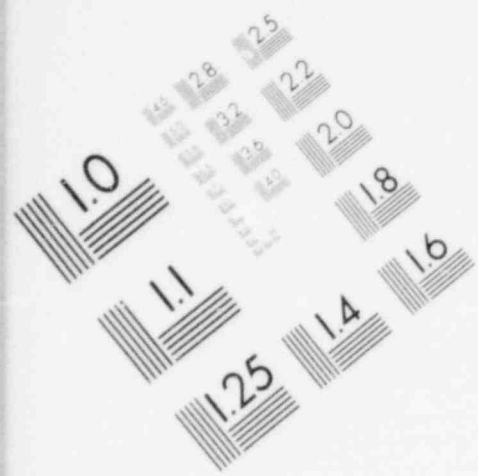

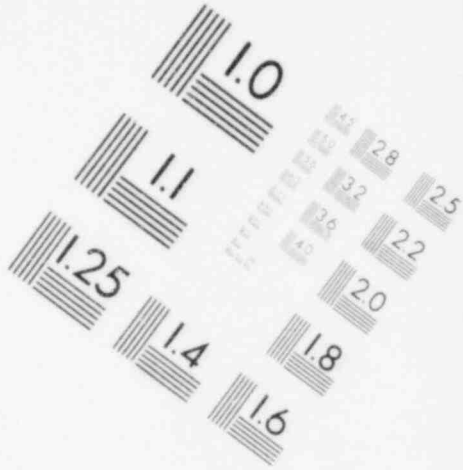

IMAGE EVALUATION
TEST TARGET (MT-3)

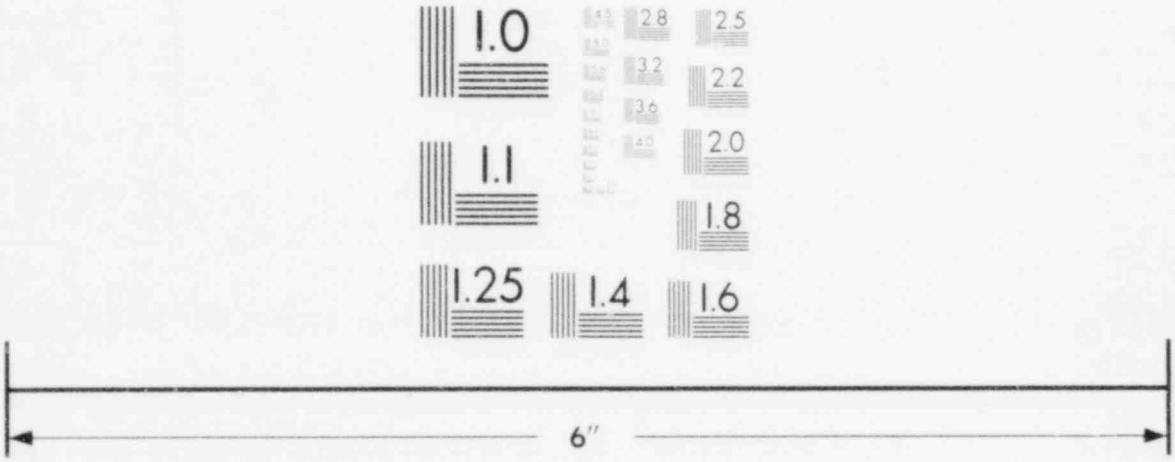

MICROCOPY RESOLUTION TEST CHART

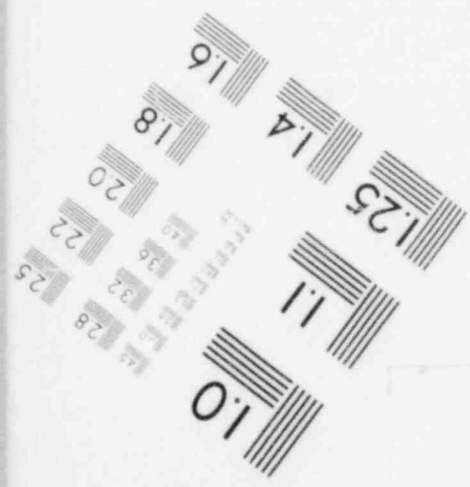

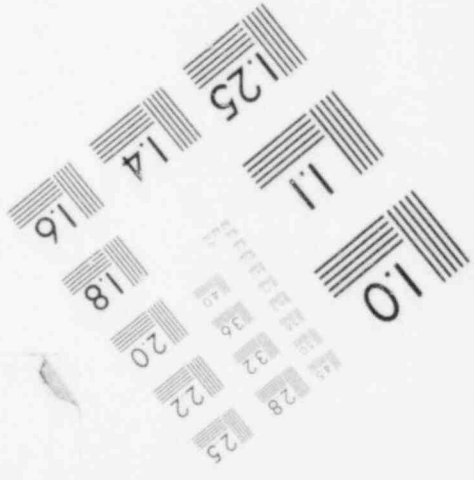

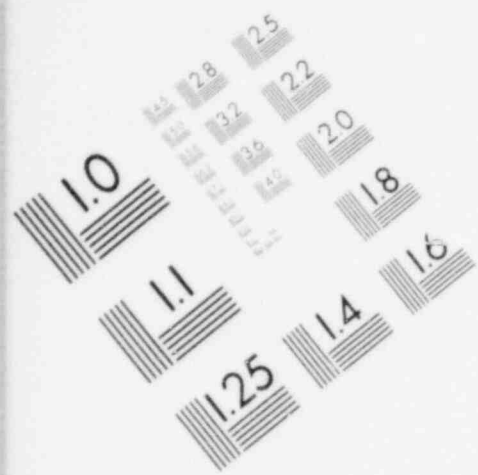

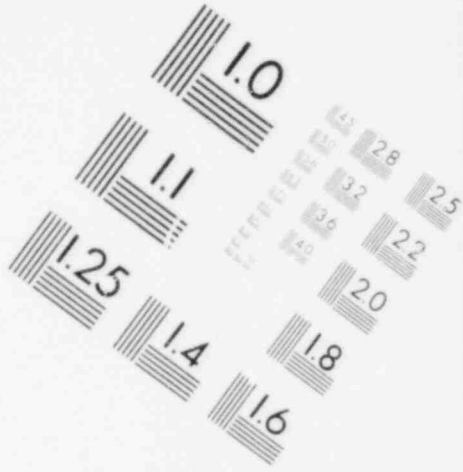

IMAGE EVALUATION
TEST TARGET (MT-3)

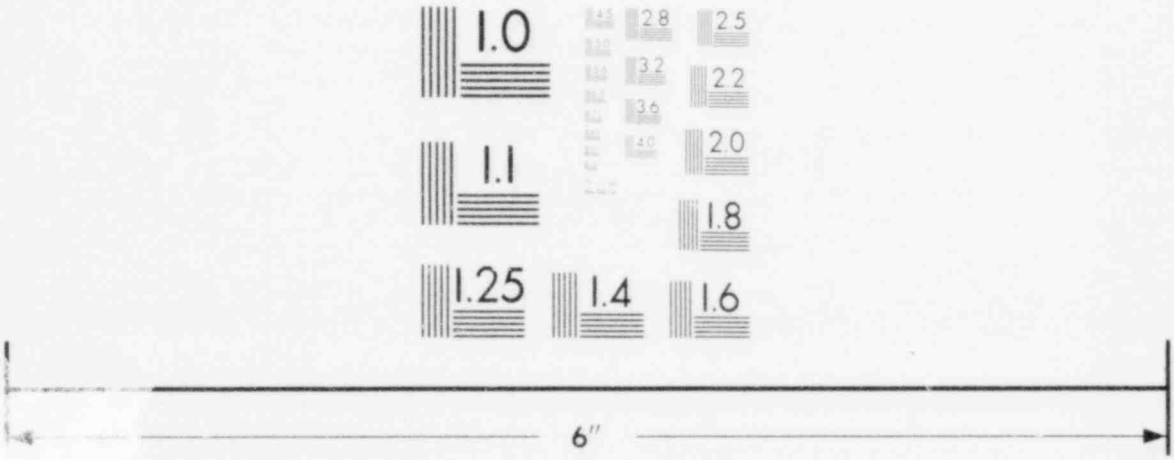

MICROCOPY RESOLUTION TEST CHART

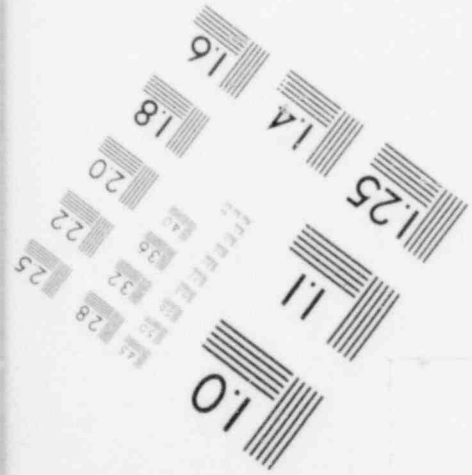

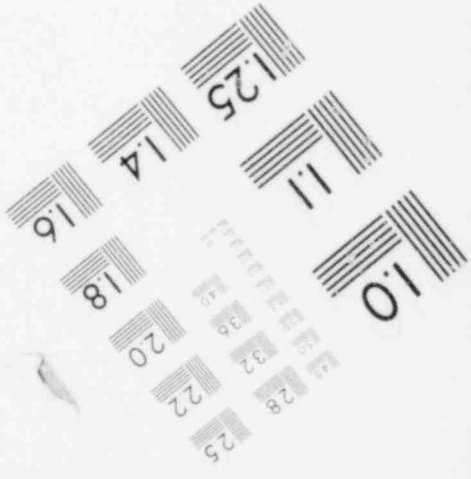

Figure 8.2-5. Total Force on Core Vs Time — 177-FA Skirt-Supported Plant, 2.0A Cold Leg Break at RV

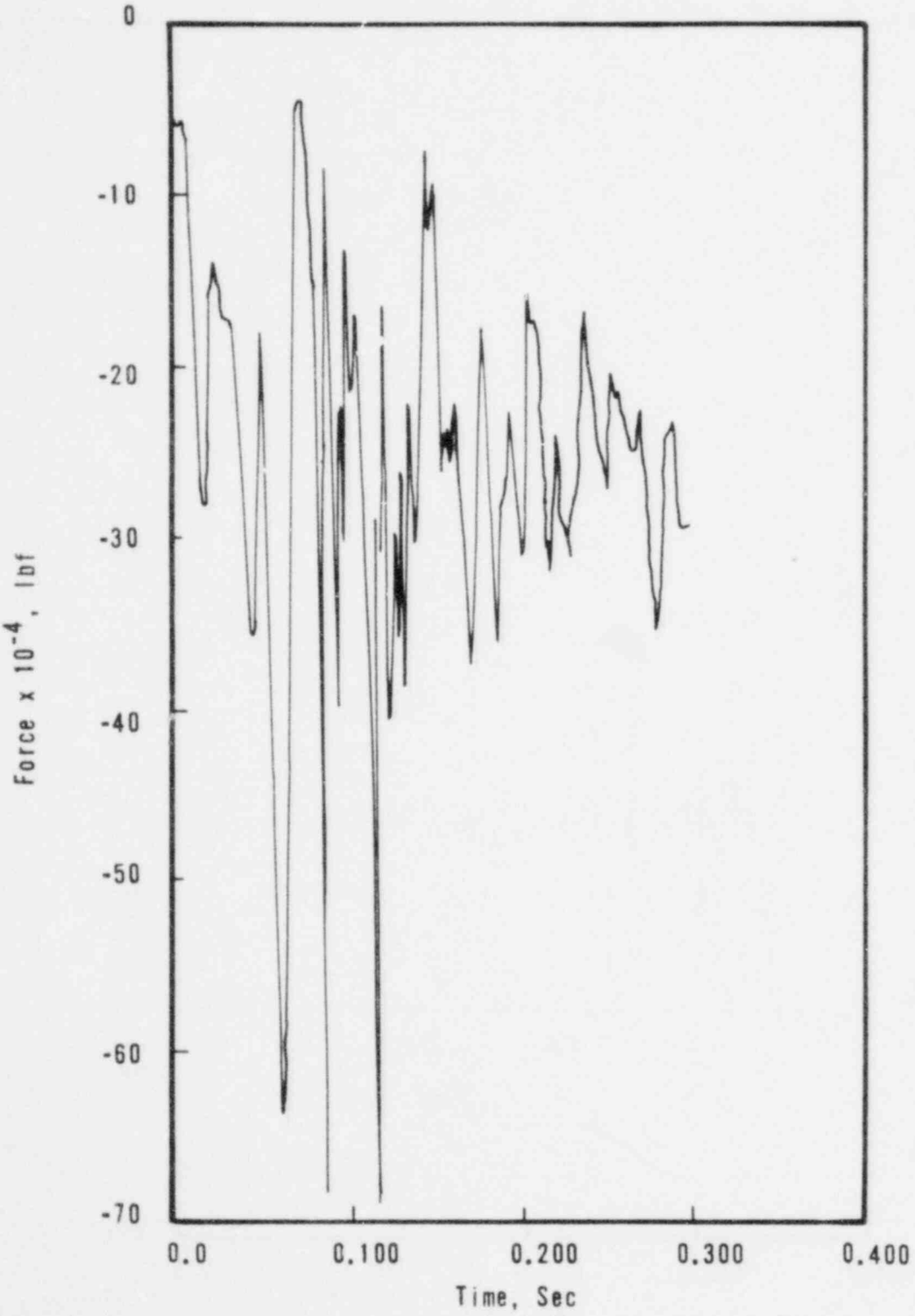

Figure 8.2-6. Total Lateral Force on Plenum Cylinder Vs Time — 177-FA Skirt-Supported Plant, 2.0A Cold Leg Break at RV

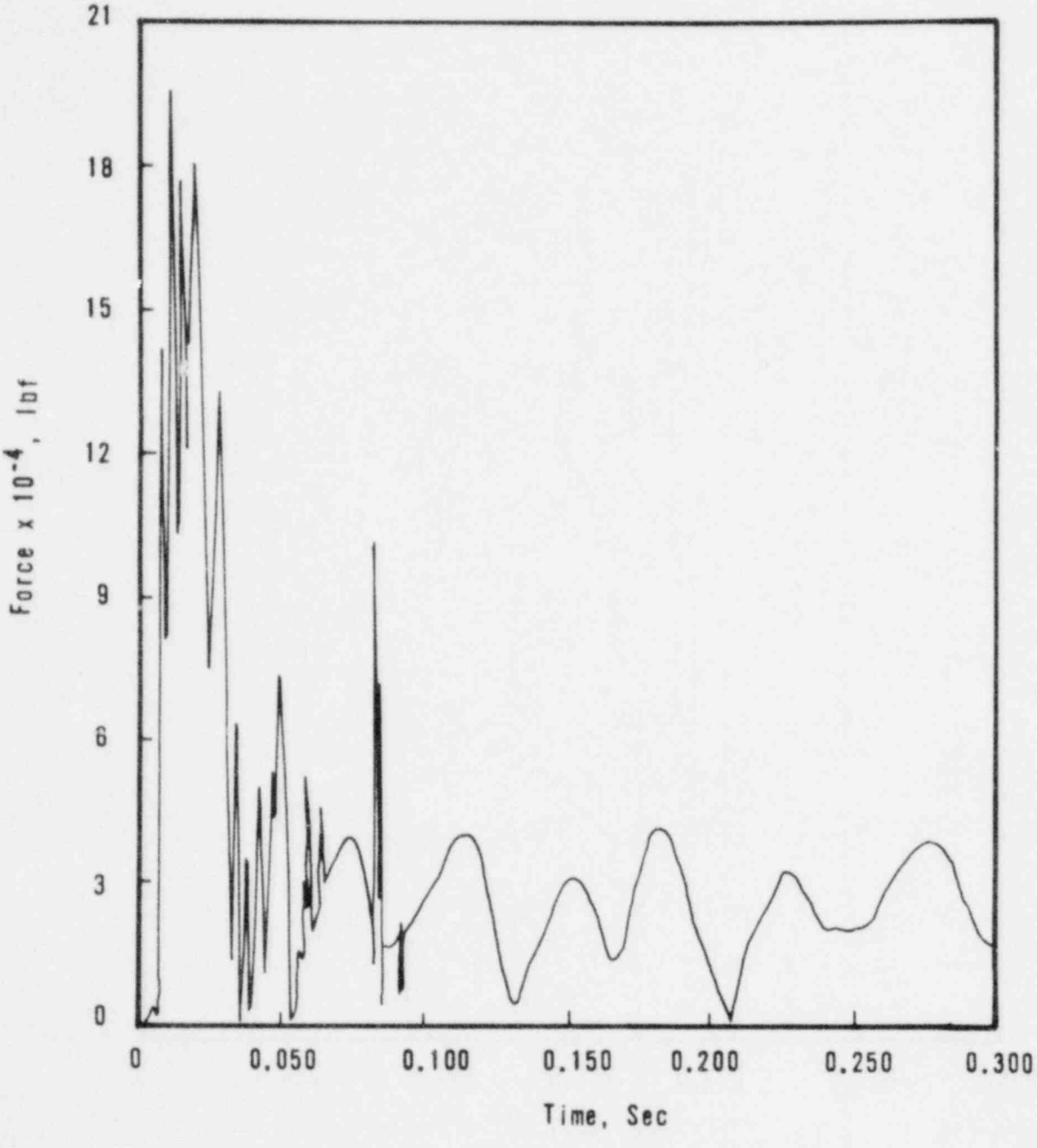

Figure 8.2-7. RV Head Differential Pressure Vs Time — 177-1/ Nozzle-Supported Plant, 1.024A Hot Leg Guillotine Break at RV

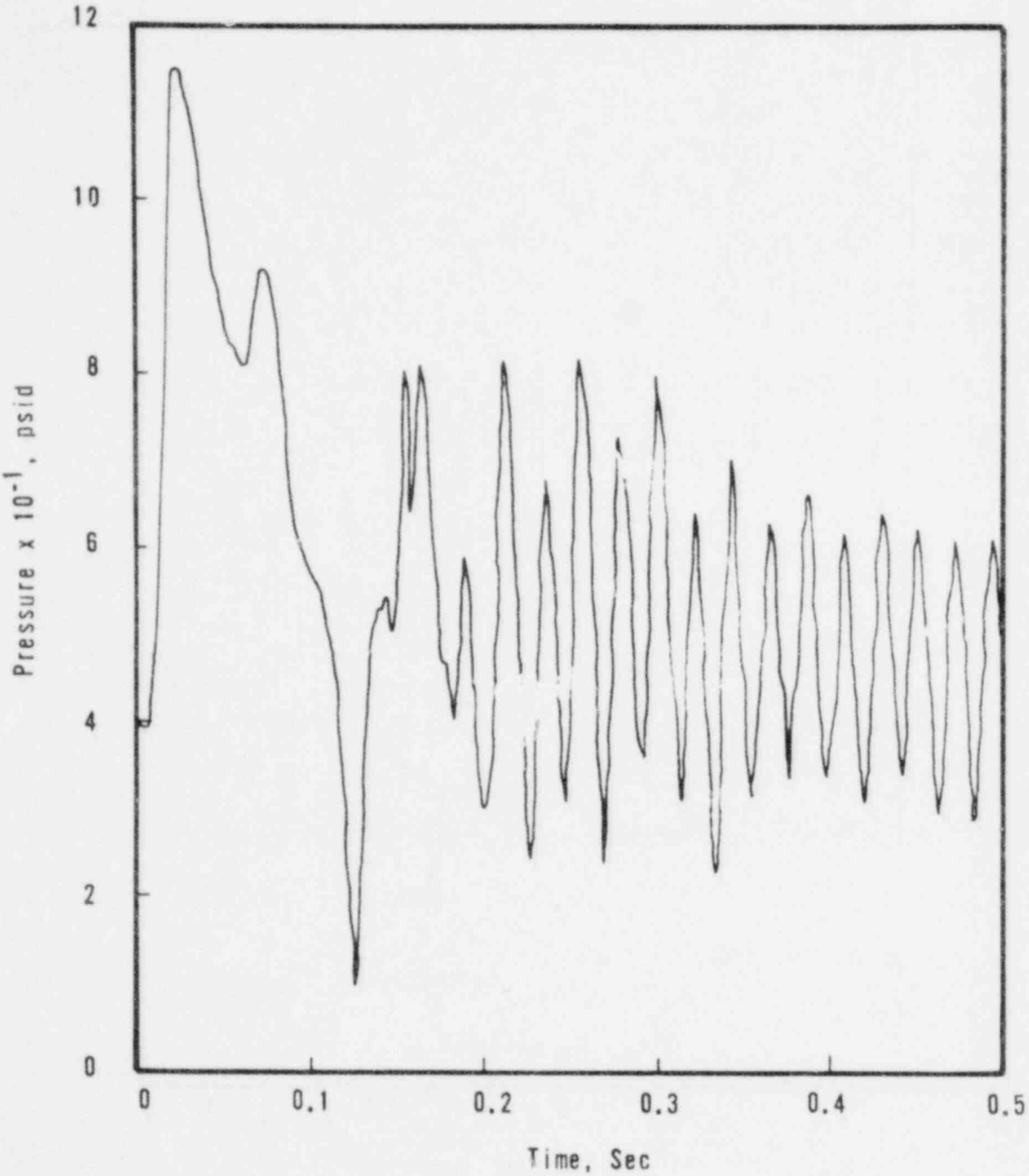

Figure 8.2-8. Total Force on Core Vs Time — 177-FA Nozzle-Supported Plant, 1.024A Hot Leg Guillotine Break at RV

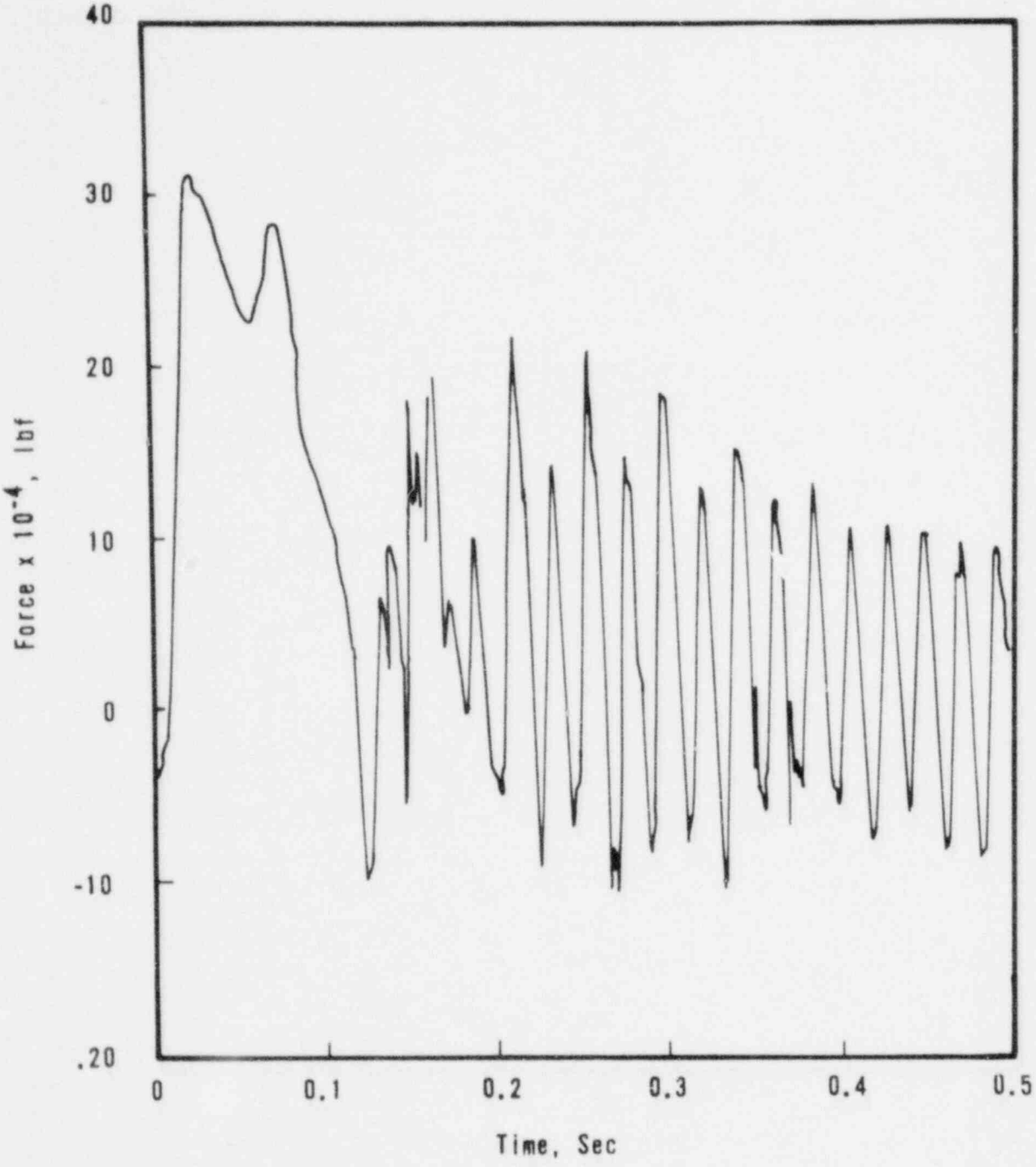

Figure 8.2-9. Total Lateral Force on Plenum Cylinder Vs Time — 177-FA Nozzle-Supported Plant, 1.024A Hot Leg Guillotine Break at RV

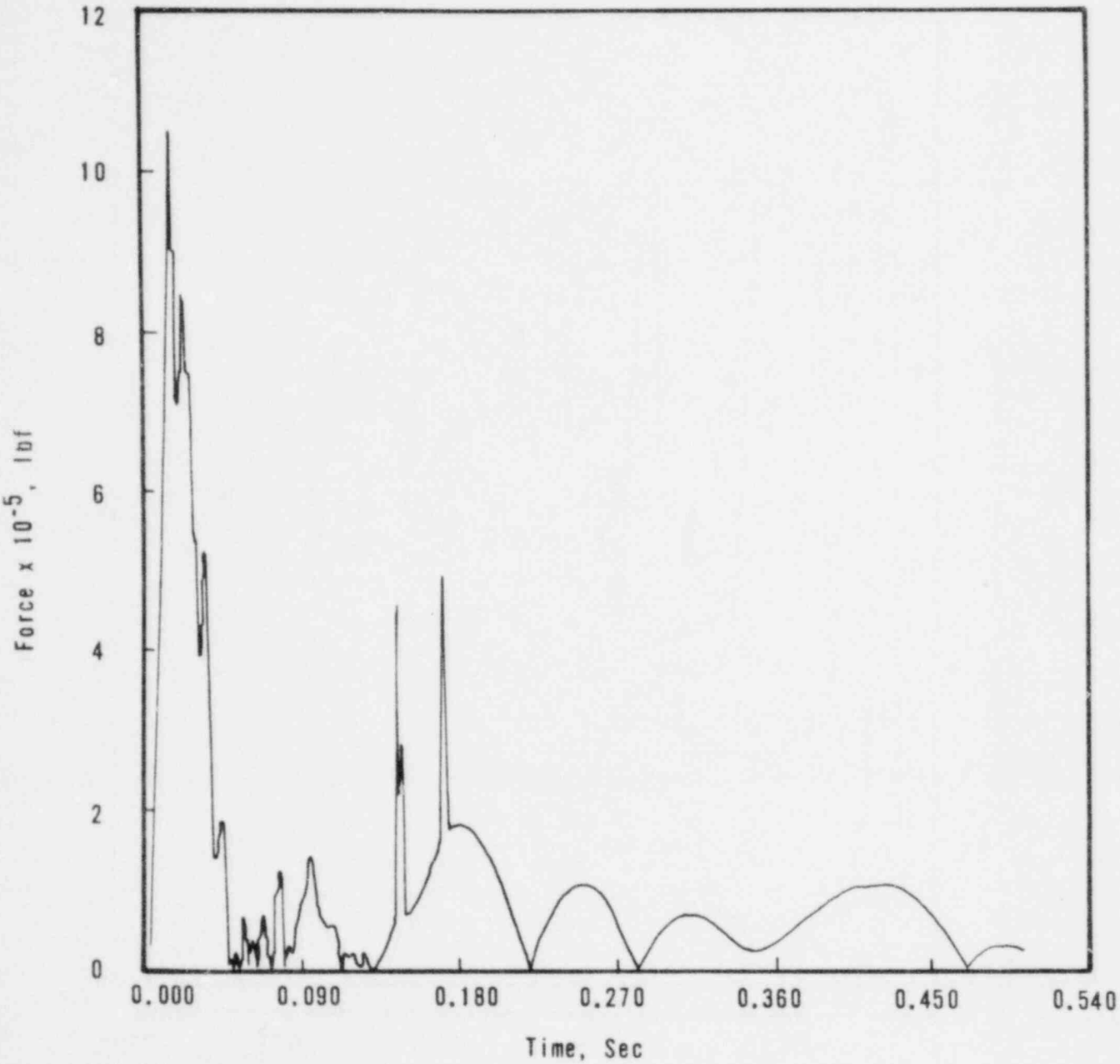

Figure 8.2-10. RV Head Differential Pressure Vs Time — 177-FA Nozzle-Supported Plant, 0.242A Cold Leg Guillotine Break at RV

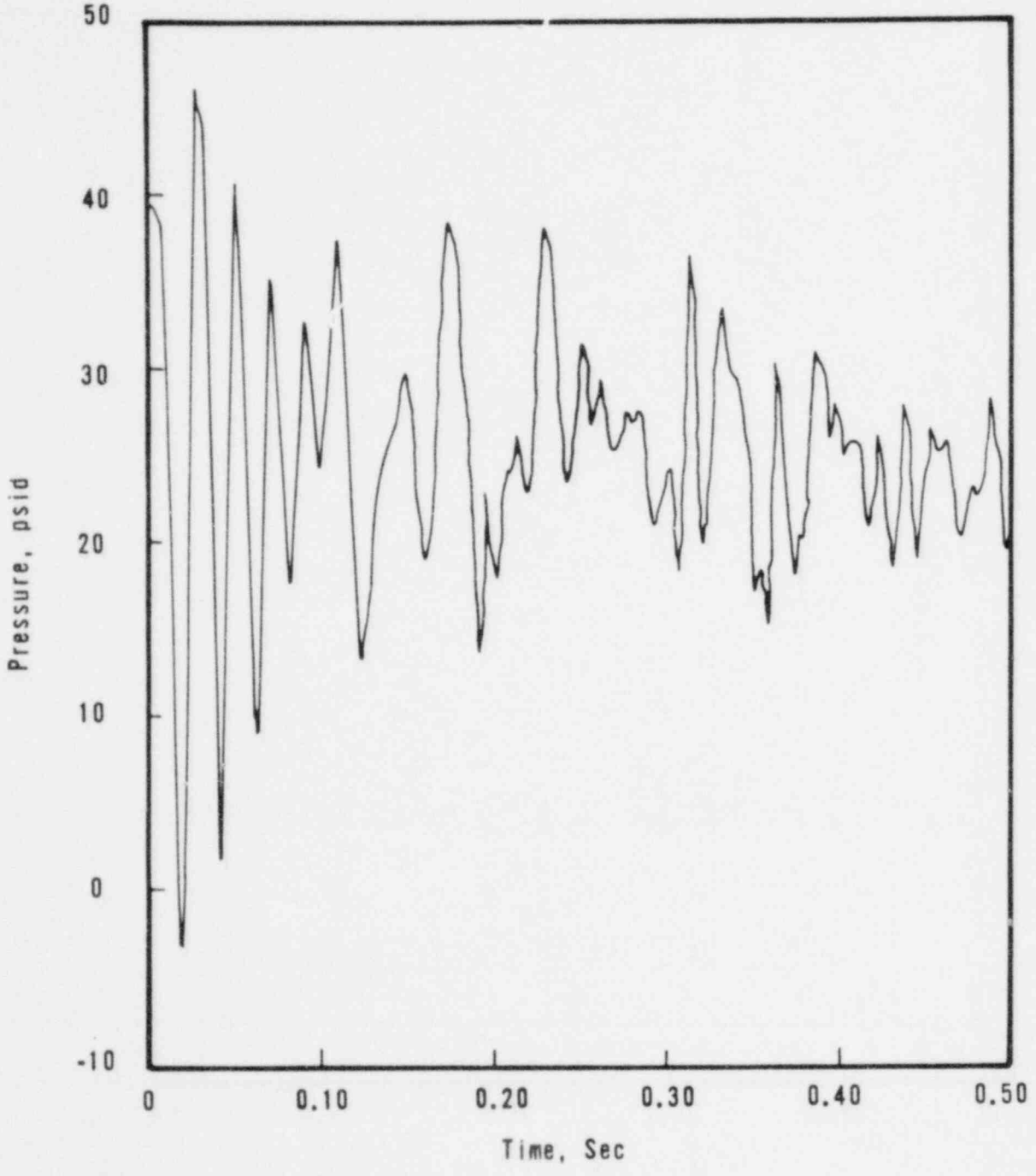

Figure 8.2-11. Total Force on Core Vs Time — 177-FA Nozzle-Supported Plant, 0.24A Cold Leg Guillotine Break at RV

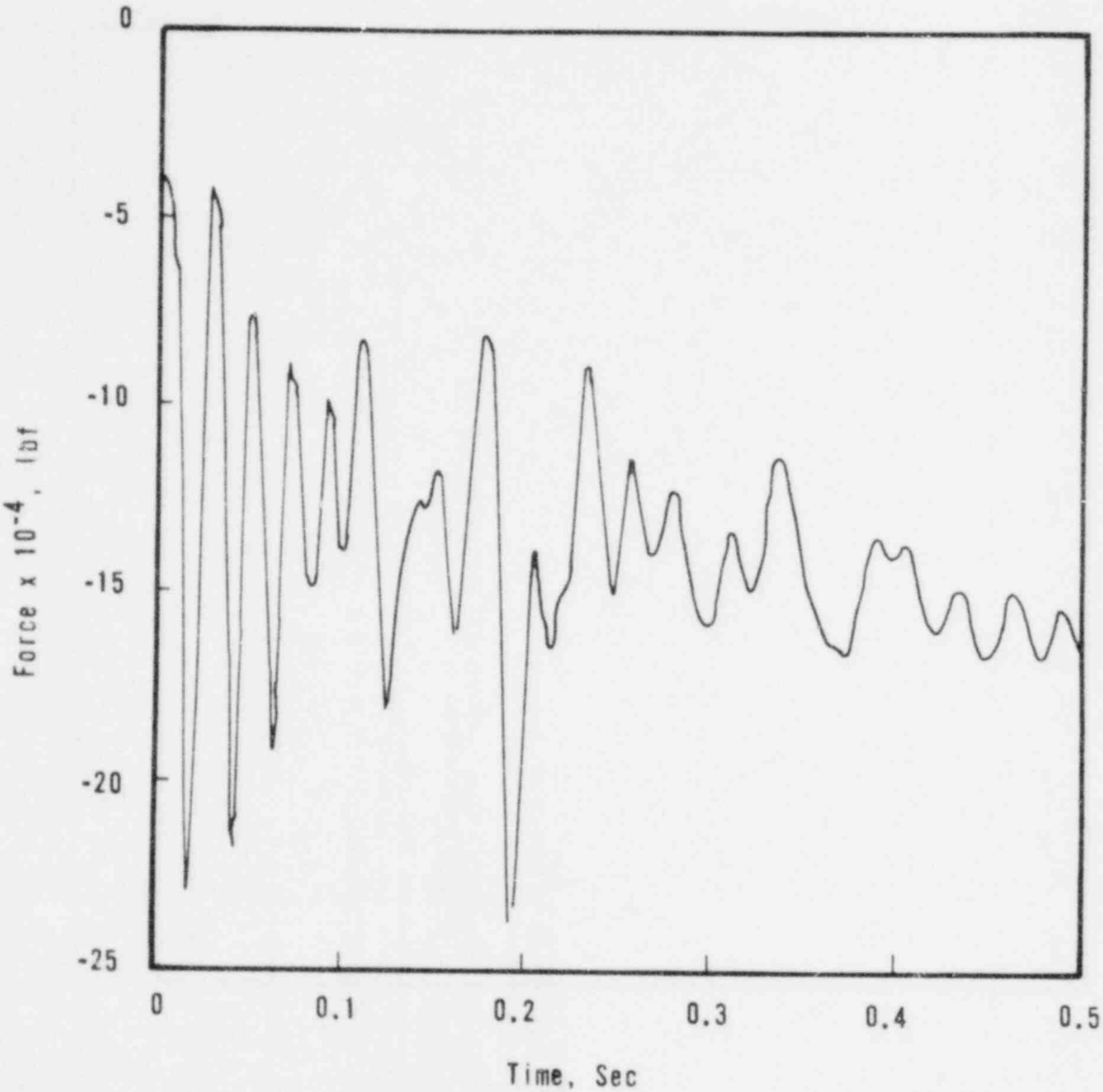

Figure 8.2-12. Total Lateral Force on Plenum Cylinder Vs Time — 177-FA Nozzle-Supported Plant, 0.242A Cold Leg Guillotine Break at RV

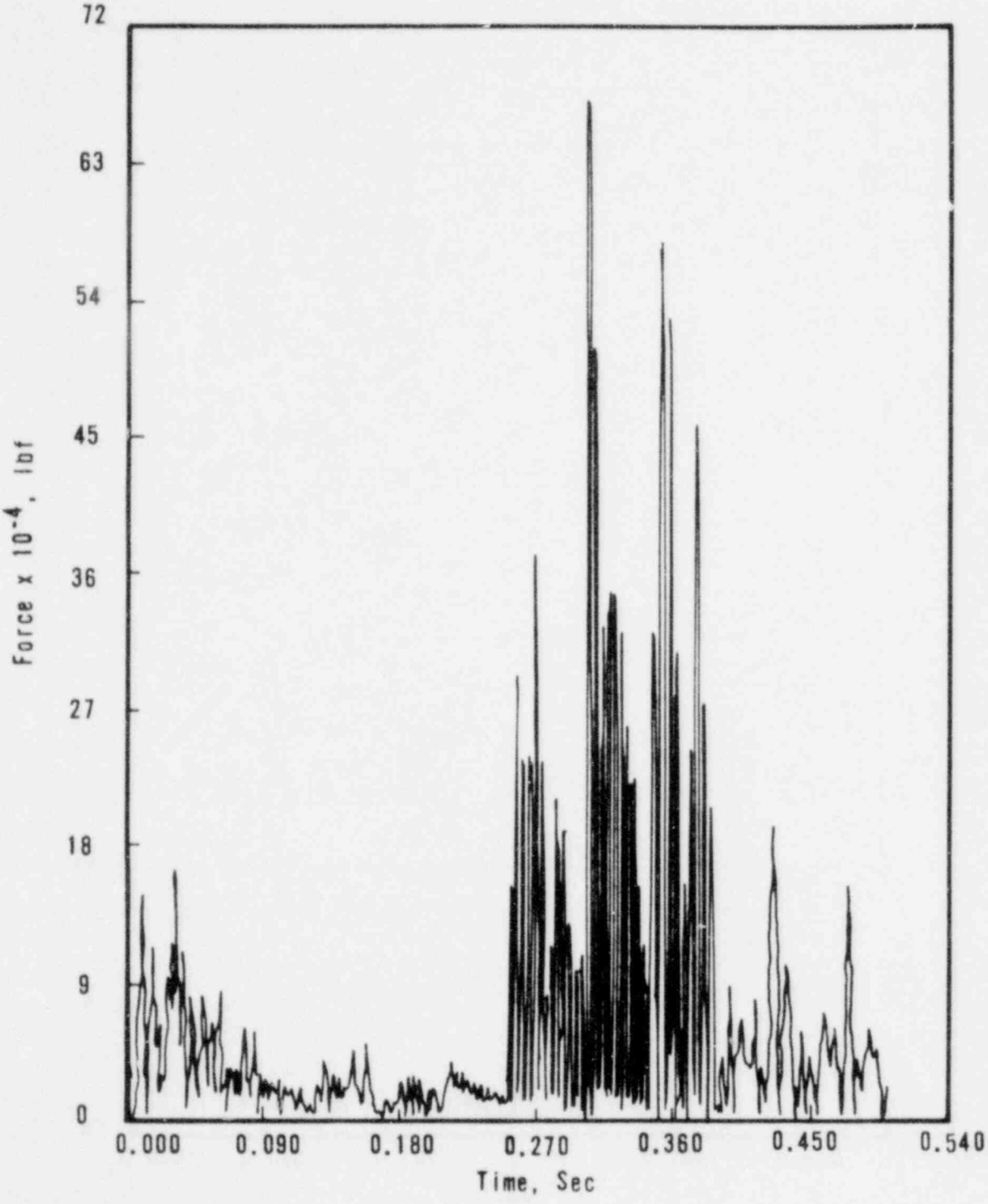

9. STRUCTURAL LOADING DATA

This section presents loading data derived from the Phase II analysis efforts. Included are maximum forces, moments, displacements, and accelerations for each component as deemed applicable by the stress analyst. All data have been calculated in accordance with the methods and procedures presented in section 5 and Appendix D of this report.

The primary objective of this section is to present loading data in a concise, useful form. Since copious amounts of information have been generated as a part of the Phase II effort, this involves considerable screening and data reduction. Consequently, each of the following subsections contains enough data to exhibit trends between the various plants and loading conditions. However, no attempt is made to supply all the data used in the stress analysis. Unless otherwise noted, all data are absolute values and should be considered to act in either a plus or minus direction.

In addition to the tabulations presented in this section, bar charts of the most important data are included. These graphs provide comparisons of the operating plants using five types of data. Resultant forces represent the square-root-sum-of-squares (SRSS) of F_X and F_Z, resultant displacements are the SRSS of D_X and D_Z, bending moment is the SRSS of M_X and M_Z, total moment is the SRSS of M_X, M_Y and M_Z, and total acceleration is the SRSS of the X, Y, and Z accelerations.

9.1. Reactor Vessel Supports

Force and moment tabulations are presented in Tables 9.1-1 through 9.1-5 for deadweight, faulted seismic, and LOCA conditions for both skirt- and nozzle-supported plants. In addition, key LOCA data for skirt-supported reactor vessels are presented graphically in Figures 9.1-1 and 9.1-2 to provide a comparison of the various plants.

The deadweight and seismic loads for all plants were taken from the loading specifications prepared during the operating license process. These loadings are not presented for other components.

Table 9.1-1. Deadweight Forces and Moments

Type of plant	10^6 lb		ft-lb	
	F_H	F_V	M_H	M_T
Skirt support at anchor[(a)]	0	2.595	0	0
Nozzle support at each pad[(b)]	0	0.535	0	0
Nozzle support at each wagonwheel[(b)]	0	0.0	0	0

where F_H = resultant horizontal force,
F_V = vertical force (downward),
M_H = resultant horizontal moment,
M_T = torsional moment about vertical axis.

(a) All plants except Davis-Besse 1.
(b) Davis-Besse 1.

Table 9.1-2. Maximum Seismic Forces and Moments, Faulted Condition

Plant	F_H, 10^6 lb	F_V 10^6 lb	M_H, 10^6 ft-lb	M_T, ft-lb
Oconee 1,2,3 (joint 50)	0.35	0.28	8.3	0
TMI-1, -2 (joint 50)	1.1	0.28	27.6	0
CR-III (joint 50)	0.44	0.18	10.2	0
ANO-1 (joint 50)	0.45	0.362	11.7	0
Rancho Seco (joint 50)	1.6	0.312	36.5	0
DB-1 (each pad)	0.41	0.63	0	0

where

F_H = resultant horizontal force,

F_V = vertical force,

M_H = resultant horizontal moment,

M_T = torsional moment about vertical axis.

Table 9.1-3. Skirt Load at Anchor, Joint 50 (Figure D-5)

LOAD CASE		FORCES (KIPS) FX	FY	FZ	MOMENTS (FT-KIPS) MX	MY	MZ
HLG AT RV	OCONEE 1,2 3	182.9	5493.2	8015.2	192102.2	1168.3	4786.4
HLG AT RV	TMI-1	514.0	6358.2	9617.5	249062.8	1469.7	11724.3
HLG AT RV	TMI-2	449.0	6532.0	15415.3	396616.6	1468.1	9651.4
HLG AT RV	CRYSTAL RIVER 3	514.0	6358.2	9617.5	249062.8	1469.7	11724.3
HLG AT RV	ANO-1	388.8	4435.9	6029.1	153273.2	1051.7	8807.0
HLG AT RV	RANCHO SECO	359.8	5119.3	6984.2	171767.3	1087.2	9013.2
CLG AT RV	OCONEE 1,2,3	8176.8	+774.3	4127.7	92307.5	1584.5	186373.7
CLG AT RV	TMI-1	6760.3	4297.1	4117.9	98017.5	1840.8	165383.0
CLG AT RV	TMI-2	7844.9	3328.6	4068.4	103406.8	1885.6	204916.0
CLG AT RV	CRYSTAL RIVER 3	6760.3	4297.1	4117.9	98017.5	1840.8	165383.0
CLG AT RV	ANO-1	6024.5	2982.2	3271.1	70566.7	1277.7	138103.8
CLG AT RV	RANCHO SECO	6063.0	+640.7	3811.0	81195.5	1339.6	137530.8

Table 9.1-4. Load Tabulation for Support on Davis-Besse 1

Bar No.	Joint No.	Loop dsn/ figure No.	Peak horiz load, kips	Vertical load @ time of peak horiz load, kips	Peak vertical load, kips	Horiz load @ time of peak vertical load, kips	Friction factor applied to total load to get shear on LOCA rings
Hot Leg Guillotine at RV, LOCA Rings							
166	101	A1/D-7	4545.4	+120.1	+1861.1	1051.8	0.42
167	97	A2/D-7	4602.7	+104.9	+1853.1	1033.1	0.42
169	96	B1/D-7	4624.5	+463.4	+1101.2	1410.0	0.42
168	99	B2/D-7	4577.7	+448.0	+1105.7	1413.1	0.42
170	95	A/D-8	0.0	0.0	0.0	0.0	0.42
171	94	B/D-8	14.3	+651.6	+752.8	8.2	0.42
Cold Leg Guillotine at RV, LOCA Rings							
166	101	A1/D-7	0.0	0.0	0.0	0.0	0.42
167	97	A2/D-7	1969.0	+61.3	+375.5	662.5	0.42
169	96	B1/D-7	2114.1	-18.2	+529.4	558.4	0.42
168	99	B2/D-7	549.9	+218.5	+225.8	263.4	0.42
170	95	A/D-8	485.1	-73.0	+354.6	91.8	0.42
171	94	B/D-8	547.6	+76.9	+197.8	173.7	0.42

Table 9.1-5. Load Tabulation for Supports on Davis-Besse 1

Bar No.	Joint No.	Loop dsn/ figure No.	Peak horiz load, kips	Vertical load @ time of peak horiz load, kips	Peak vertical load, kips	Horiz load @ time of peak vertical load, kips	Friction factor applied to total load to get shear on LOCA rings
Cold Leg Guillotine at Elbow, LOCA Rings							
166	101	A1/D-7	295.0	+113.0	300.8	209.1	0.42
167	97	A2/D-7	1243.9	-61.0	-116.3	628.3	0.42
169	96	B1/D-7	1267.1	-230.7	-335.0	526.5	0.42
168	99	B2/D-7	381.4	-156.4	-267.4	12.7	
170	95	A/D-8	329.5	-167.0	227.9	66.6	0.42
171	94	B/D-8	329.4	+15.8	-202.3	94.6	0.42
Hot Leg Guillotine at Elbow, LOCA Rings							
166	101	A1/D-7	1290.8	-21.6	+348.1	542.0	0.42
167	97	A2/D-7	1290.9	-22.0	+352.0	540.7	0.42
169	96	B1/D-7	1310.4	-75.9	-394.5	587.5	0.42
168	99	B2/D-7	1310.3	-76.3	-396.2	587.1	0.42
170	95	A/D-8	2.0	+35.6	+183.3	0.5	0.42
171	94	B/D-8	2.0	-30.9	+304.5	0.1	0.42

Figure 9.1-1. Skirt Load at Anchor Jt 50

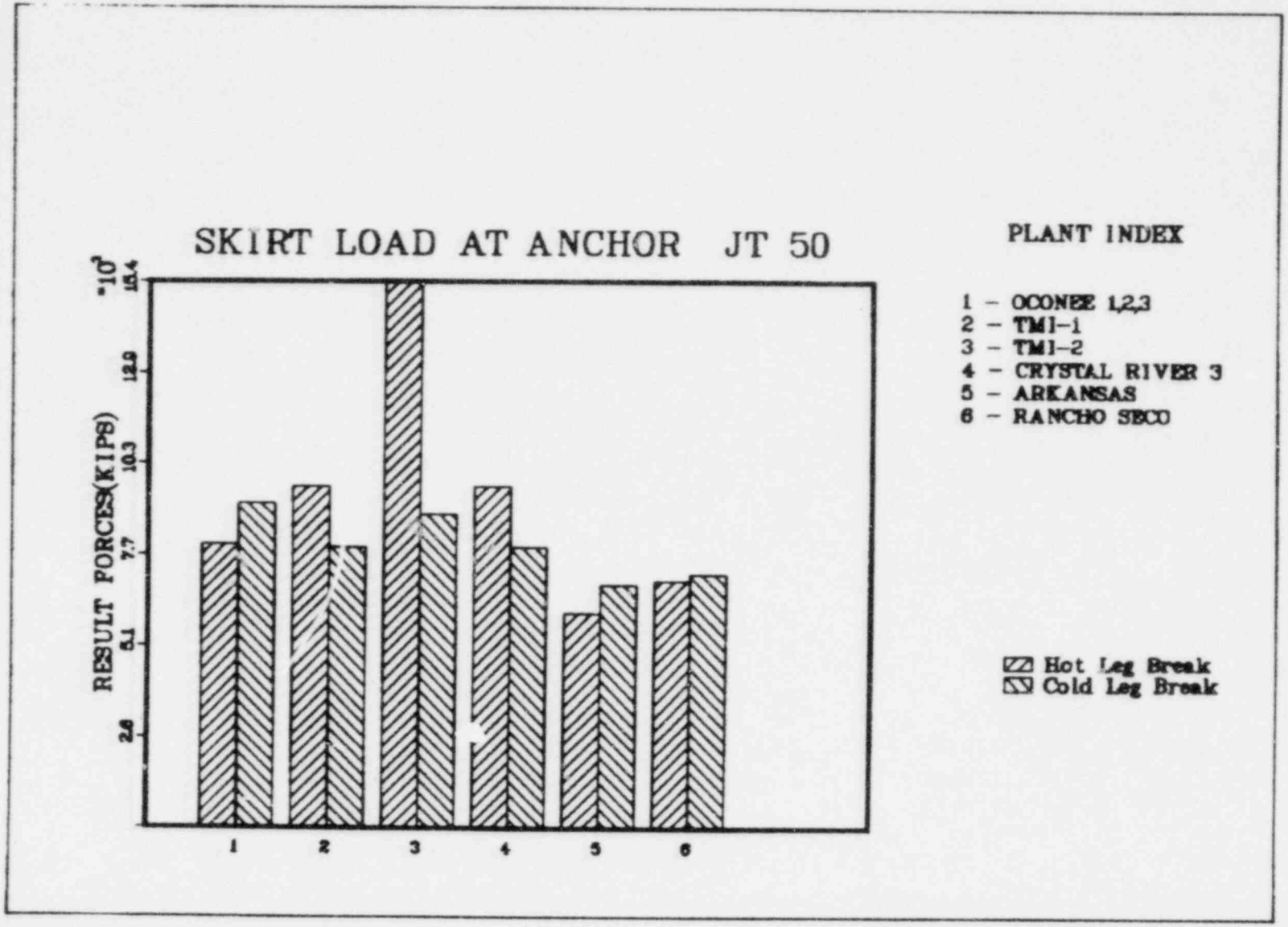

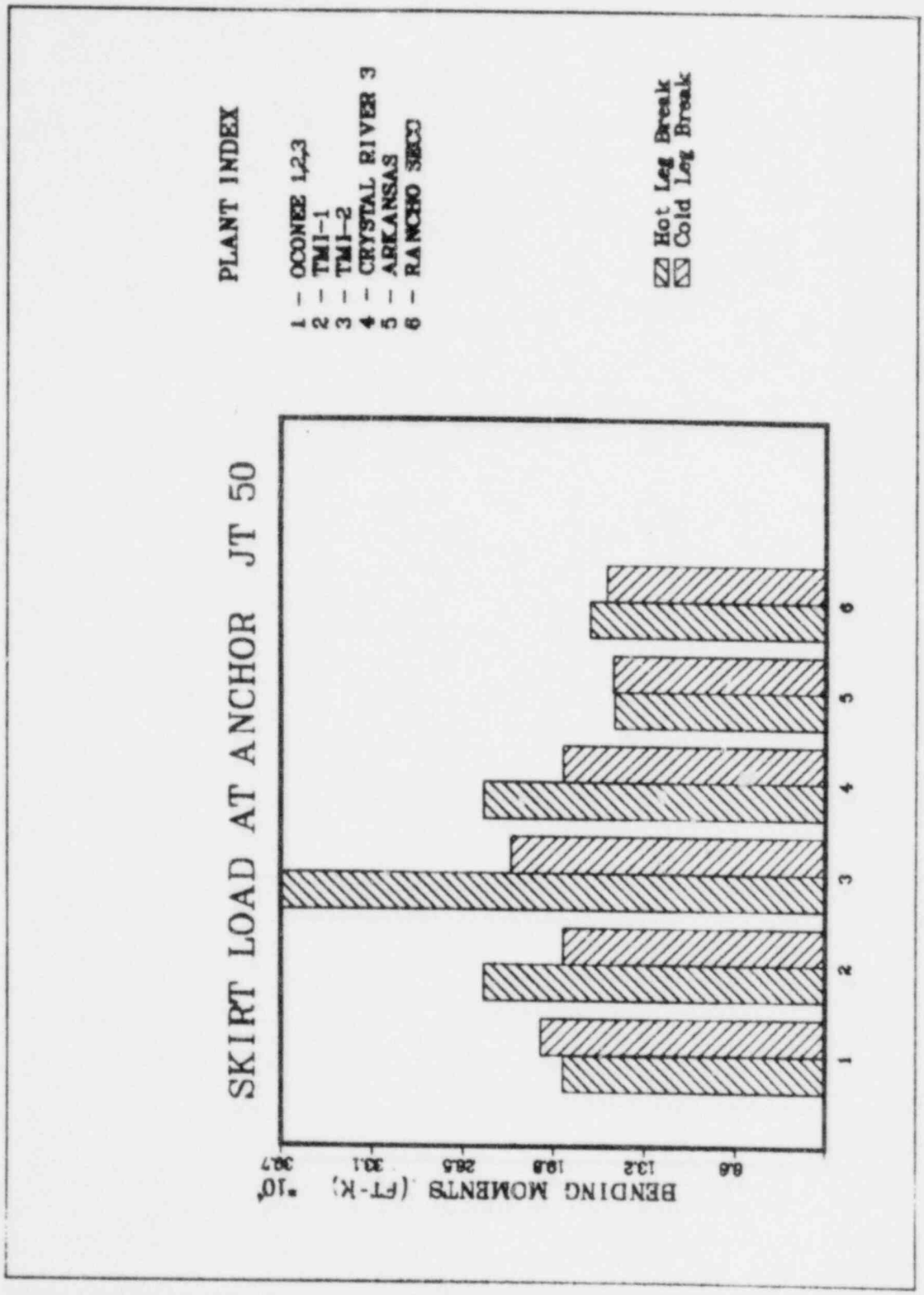

Figure 9.1-2. Skirt Load at Anchor Jt 50

9.2. Reactor Vessel Support Embedments

The reactor vessel support embedments experience the same loading as the supports described in section 9.1, with the exception of those at the Davis-Besse 1 plant. Tables 9.2-1 and 9.2-2 detail the loadings on the embedments beneath the reactor vessel pads. These loadings are in addition to those on the LOCA wagonwheel restraints as reported in section 9.1. Appendix D discusses the modeling concepts of the DB-1 restraint system.

Table 9.2-1. Load Tabulation for Embedments on Davis-Besse 1

Bar No.	Joint No.	Loop dsn/ Figure No.	Peak horizontal load, kips	Peak vertical load, kips
Hot Leg Break at RV, RV Pad Supports[a]				
162	82	A1/D-10	933.0	-175.4
163	78	A2/D-9	933.0	-179.8
164	72	B1/D-9	933.0	-160.0
165	80	B2/D-10	933.0	-162.5
Hot Leg Break at Elbow, RV Pad Supports				
162	82	A1/D-10	933.0	-307.9
163	78	A2/D-9	933.0	-310.2
164	72	B1/D-9	933.0	-394.5
165	80	B2/D-10	933.0	-396.2

[a] See section 9.1 for LOCA ring loads.

Table 9.2-2. Load Tabulation for Embedments on Davis-Besse 1

Bar No.	Joint No.	Loop dsn/ Figure No.	Peak horizontal load, kips	Peak vertical load, kips
Cold Leg Break @ RV, RV Pad Supports				
162	82	A1/D-10	550.1	-225.8
163	78	A2/D-9	933.0	-19.2
164	72	B1/D-9	933.0	-62.0
165	80	B2/D-10	550.1	-72.3
Cold Leg Break @ Elbow, RV Pad Supports				
162	82	A1/D-10	295.0	-273.3
163	78	A2/D-9	933.0	-116.3
164	72	B1/D-9	933.0	-335.0
165	80	B2/D-10	381.4	-267.4

9.3. Control Rod Drive Service Structure

Force and moment tabulations for the CRD service support structure are presented in Tables 9.3-1 through 9.3-3 for each node illustrated in Figure 9.3-1. The number of nodes and their locations are based on previous stress analyses. Bar charts for the resultant shear force (F_R) and moment about the horizontal axis (M_B) are also provided for nodes 113, 137, and 161 in Figures 9.3-2 through 9.3-7.

Figure 9.3-1. Service Support Structure Load Points

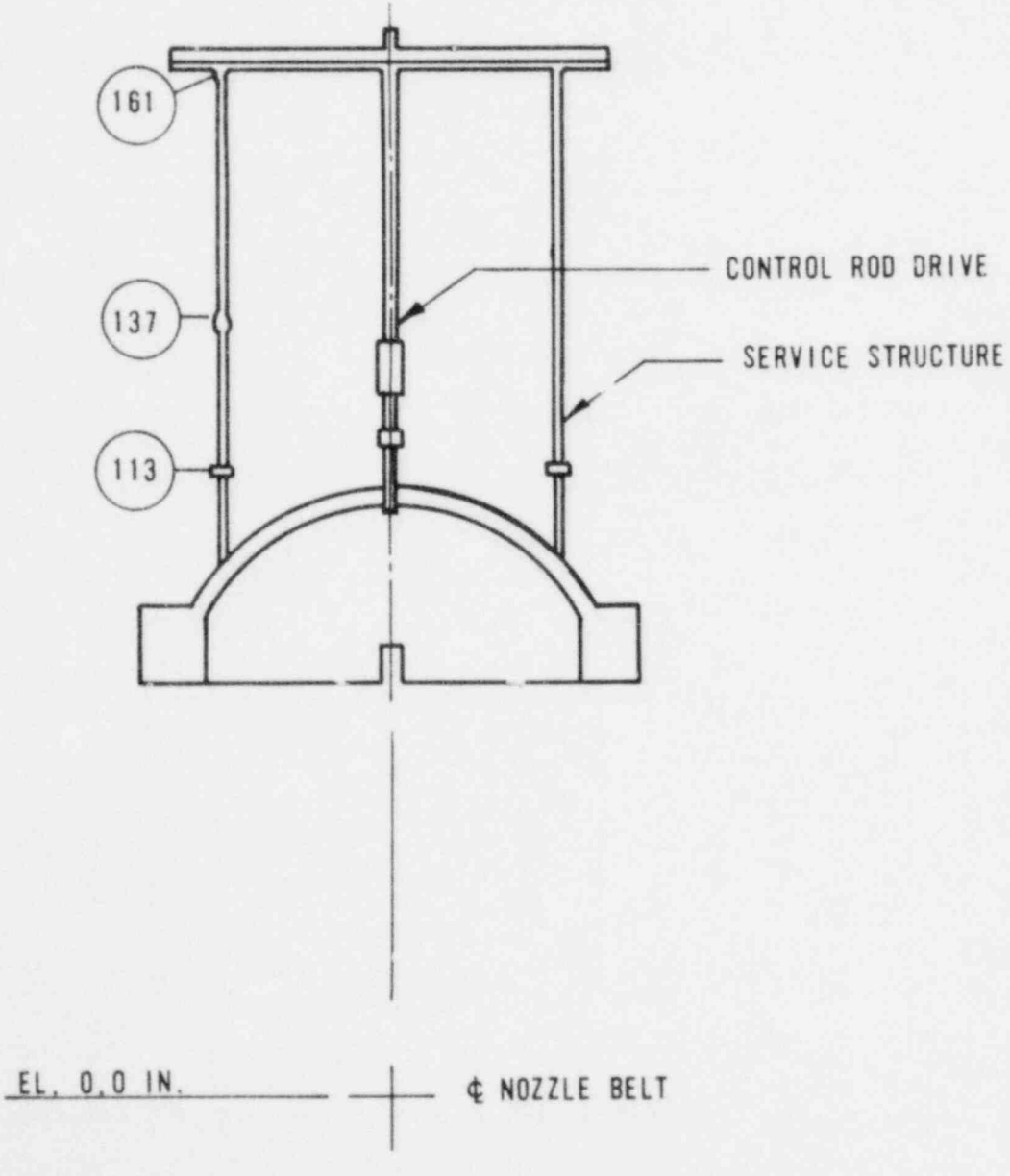

Table 9.3-1. SSS Skirt/SSS Interface, Joint 113

LOAD CASE		FORCES (KIPS) FX	FY	FZ	MOMENTS (FT-KIPS) MX	MY	MZ
HLG AT RV	OCONEE 1,2 3	49.9	235.1	470.3	6798.9	24.2	728.4
HLG AT RV	TMI-1	99.3	196.3	725.4	11009.0	22.8	1481.0
HLG AT RV	TMI-2	48.4	218.1	656.3	9299.8	20.1	773.8
HLG AT RV	CRYSTAL RIVER 3	99.3	196.3	725.4	11009.0	22.8	1481.0
HLG AT RV	ANO-1	31.4	229.2	319.9	4755.3	25.2	476.8
HLG AT RV	RANCHO SECO	39.6	191.3	471.6	7014.0	20.4	554.1
CLG AT RV	OCONEE 1,2,3	518.9	246.5	231.6	3347.1	27.1	7992.8
CLG AT RV	TMI-1	451.4	250.6	227.9	3568.6	26.3	6998.7
CLG AT RV	TMI-2	351.6	236.4	152.4	2107.0	25.1	5742.8
CLG AT RV	CRYSTAL RIVER 3	451.4	250.6	227.9	3568.6	26.3	6998.7
CLG AT RV	ANO-1	280.4	235.1	118.7	1816.9	24.3	4444.6
CLG AT RV	RANCHO SECO	300.8	244.0	138.9	2139.0	24.8	4718.4
HLG AT RV	DAVIS BESSE 1	8.3	148.5	257.8	3989.8	1.4	132.5
HLG AT EL	DAVIS BESSE 1	6.0	98.6	184.0	2493.3	.2	64.7
CLG AT EL	DAVIS BESSE 1	78.1	76.3	107.2	1667.3	2.6	1122.8
CLG AT RV	DAVIS BESSE 1	94.6	49.3	82.8	1083.8	14.8	1198.4

Table 9.3-2. Middle Shell Loads, Bar 95, Joint 137

LOAD CASE	FORCES (KIPS) FX	FY	FZ	MOMENTS (FT-KIPS) MX	MY	MZ
HLG AT RV OCONEE 1,2 3	42.5	106.8	398.3	4088.7	.0	428.6
HLG AT RV TMI-1	86.5	94.4	643.4	6788.0	.0	892.8
HLG AT RV TMI-2	45.4	92.7	546.8	5541.3	.0	490.1
HLG AT RV CRYSTAL RIVER 3	86.5	94.4	643.4	6788.0	.0	892.8
HLG AT RV ANO-1	27.7	108.1	279.5	2881.6	.0	293.5
HLG AT RV RANCHO SECO	32.5	84.5	411.9	4256.7	.0	335.4
CLG AT RV OCONEE 1,2,3	466.1	128.2	195.6	2008.3	.0	4934.8
CLG AT RV TMI-1	409.0	130.6	208.5	2228.1	.0	4340.1
CLG AT RV TMI-2	335.2	126.5	123.8	1252.0	.0	3634.5
CLG AT RV CRYSTAL RIVER 3	409.0	130.6	208.5	2228.1	.0	4340.1
CLG AT RV ANO-1	259.5	126.6	106.0	1094.8	.0	2772.3
CLG AT RV RANCHO SECO	275.3	128.1	124.7	1320.1	.0	2928.3
HLG AT RV DAVIS BESSE 1	7.7	73.2	249.8	2637.2	.0	82.7
HLG AT EL DAVIS BESSE 1	4.7	50.6	142.5	1524.3	.0	52.4
CLG AT EL DAVIS BESSE 1	67.6	38.2	98.0	1047.4	.0	710.5
CLG AT RV DAVIS BESSE 1	70.5	24.7	67.5	681.4	.0	769.2

Table 9.3-3. Upper Shell Loads, Joint 161

LOAD CASE		FORCES (KIPS) FX	FY	FZ	MOMENTS (FT-KIPS) MX	MY	MZ
HLG AT RV	OCONEE 1,2 3	32.9	106.8	321.4	18.0	.0	.8
HLG AT RV	TMI-1	70.5	94.4	550.9	34.4	.0	2.5
HLG AT RV	TMI-2	40.7	92.7	450.0	25.5	.0	1.8
HLG AT RV	CRYSTAL RIVER 3	70.5	94.4	550.9	34.4	.0	2.5
HLG AT RV	ANO-1	25.1	108.1	227.6	12.2	.0	1.2
HLG AT RV	RANCHO SECO	28.5	84.5	336.9	18.3	.0	1.5
CLG AT RV	OCONEE 1,2,3	400.3	128.2	168.8	9.8	.0	21.8
CLG AT RV	TMI-1	353.2	130.6	182.8	9.4	.0	18.2
CLG AT RV	TMI-2	302.8	126.5	96.7	4.6	.0	16.1
CLG AT RV	CRYSTAL RIVER 3	353.2	130.6	182.8	9.4	.0	18.2
CLG AT RV	ANO-1	227.3	126.6	89.4	5.3	.0	10.6
CLG AT RV	RANCHO SECO	239.1	128.1	109.9	6.8	.0	11.1
HLG AT RV	DAVIS BESSE 1	6.8	73.2	214.2	9.5	.0	.2
HLG AT EL	DAVIS BESSE 1	4.8	50.6	136.5	3.3	.0	.1
CLG AT EL	DAVIS BESSE 1	59.8	38.2	86.2	2.4	.0	1.5
CLG AT RV	DAVIS BESSE 1	64.9	24.7	61.3	2.0	.0	2.7

Figure 9.3-2. SSS Skirt/SSS Intrface Jt 113

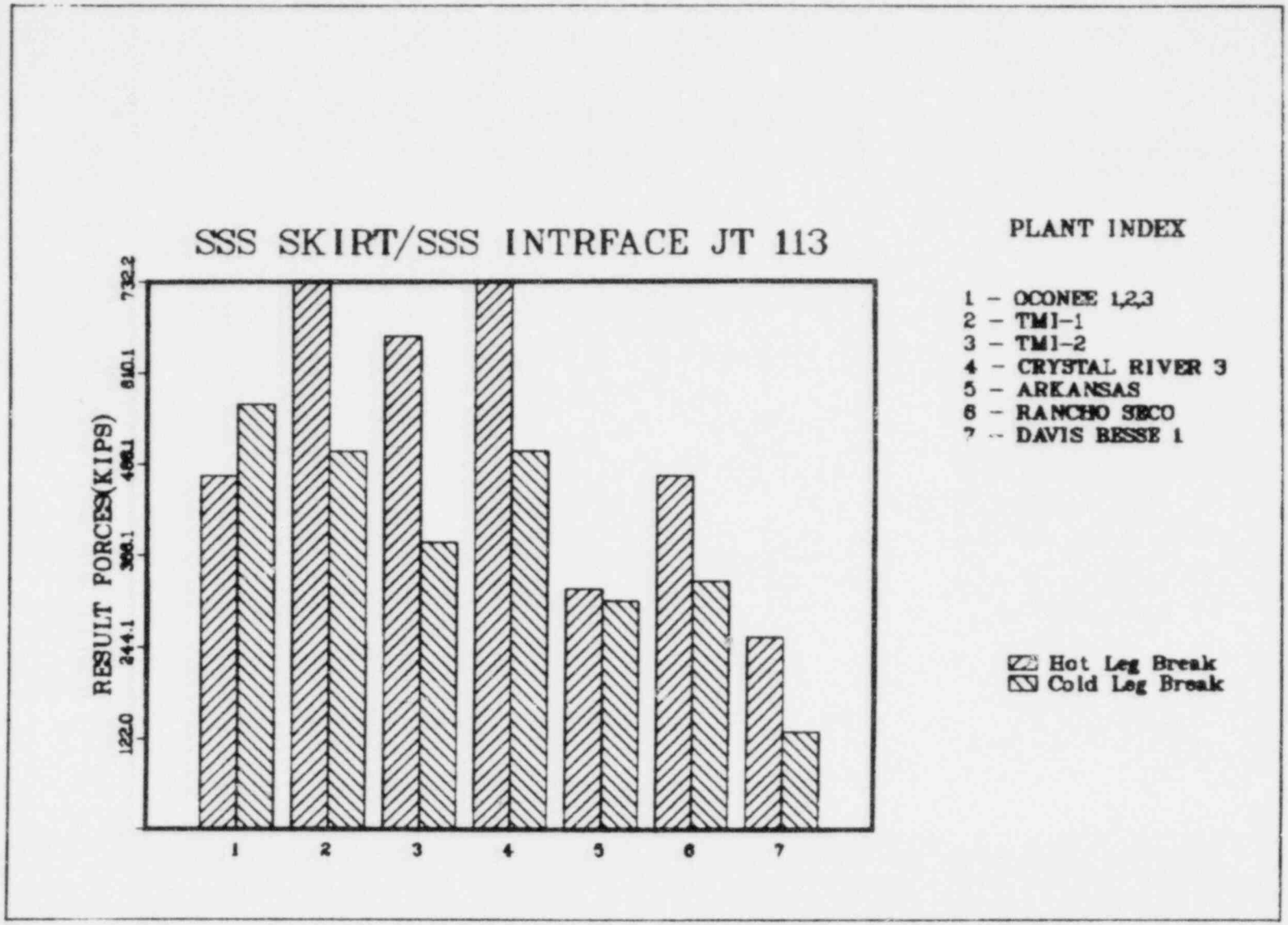

Figure 9.3-3. SSS Skirt/SSS Intrface Jt 113

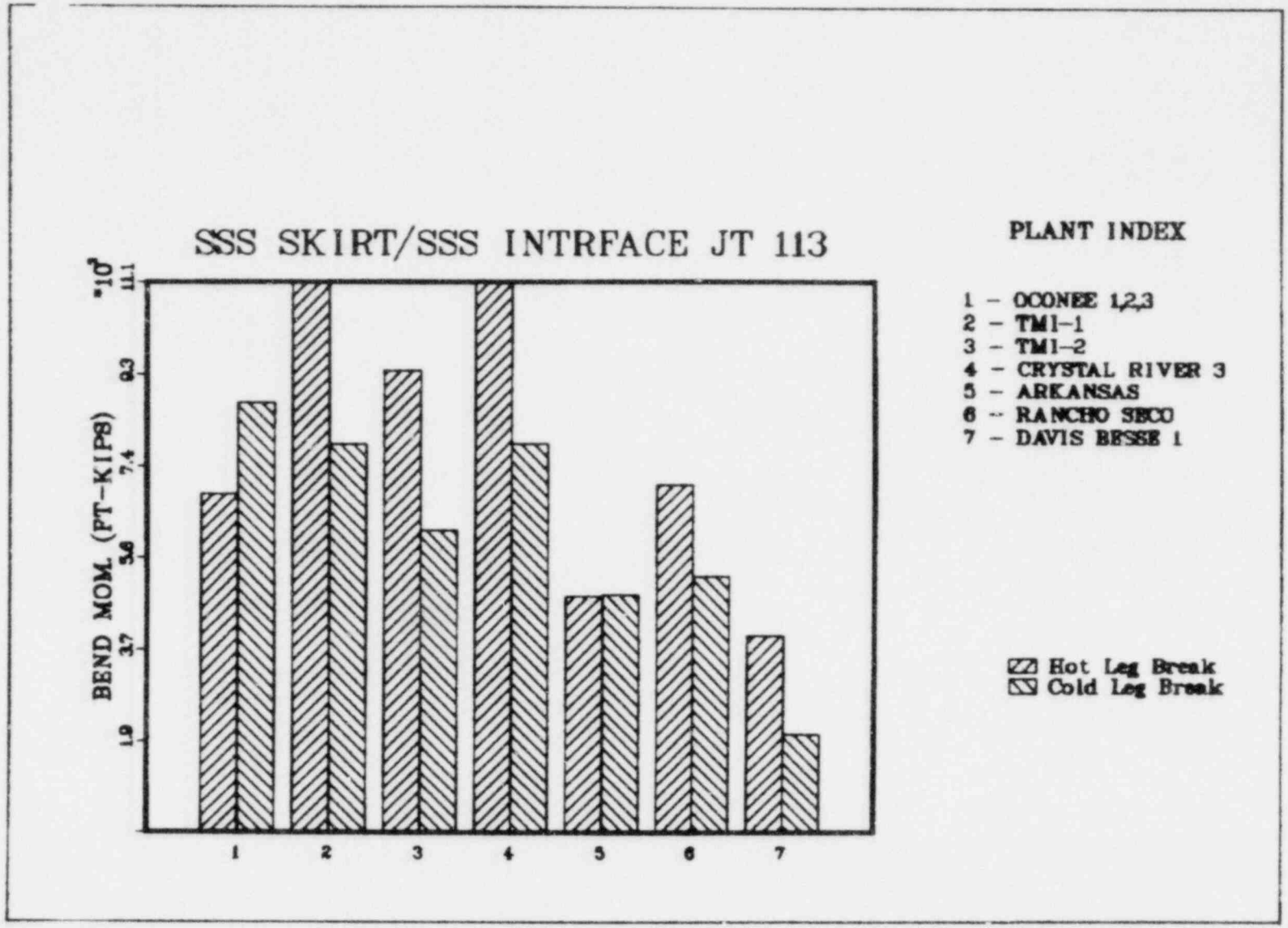

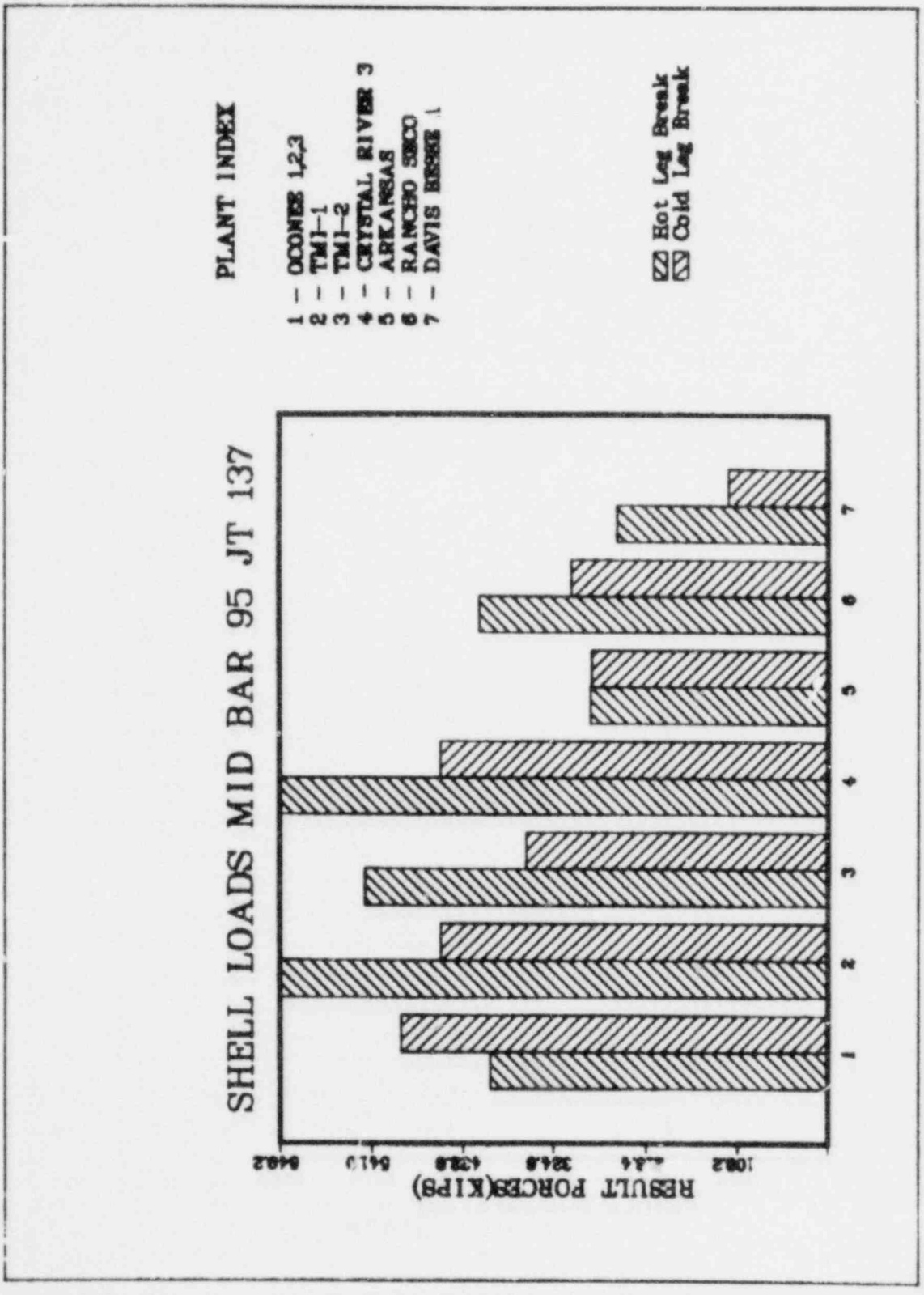

Figure 9.3-4. Shell Loads Mid Bar 95 Jt 137

Figure 9.3-5. Shell Loads Mid Bar 95 Jt 137

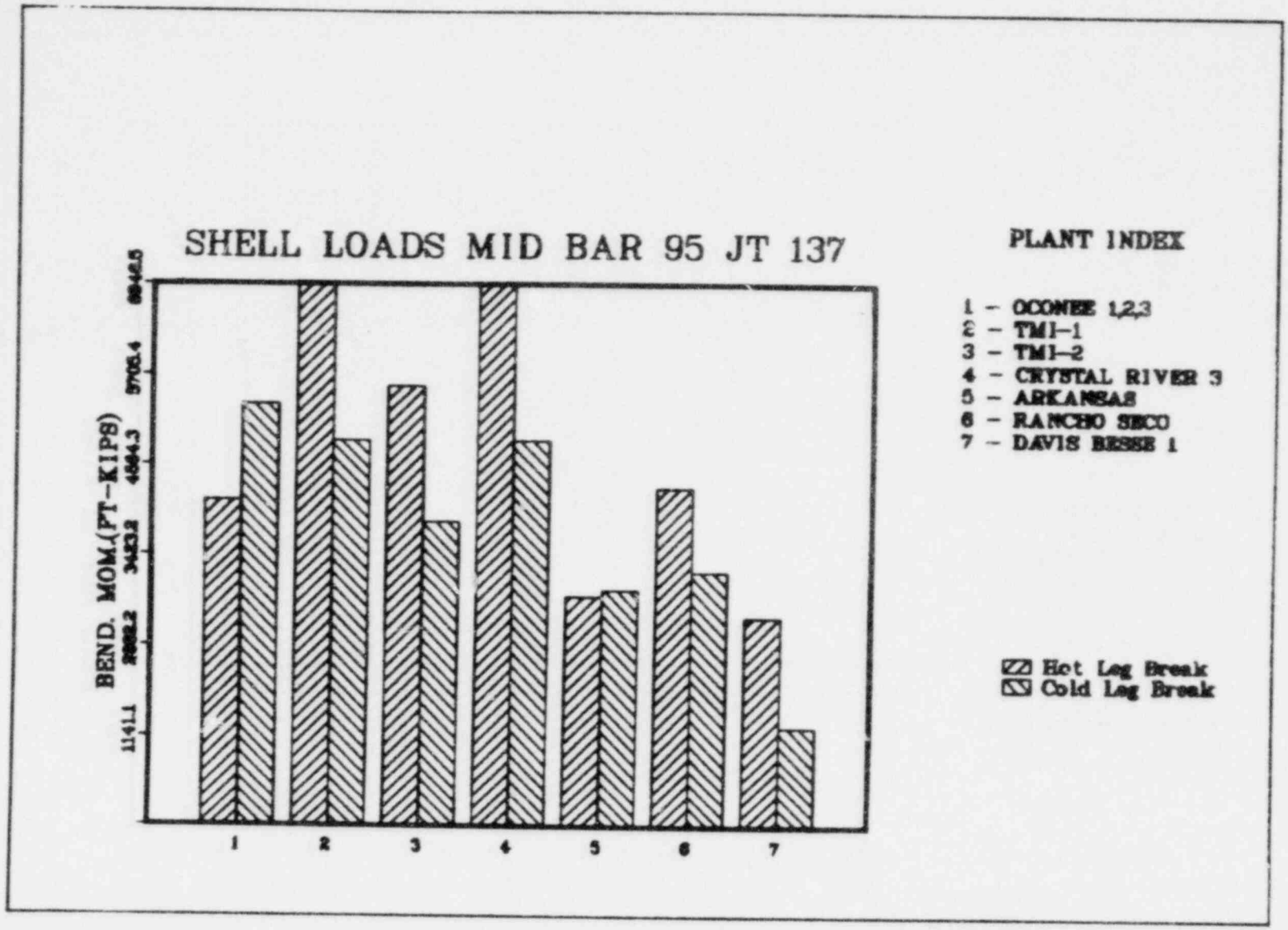

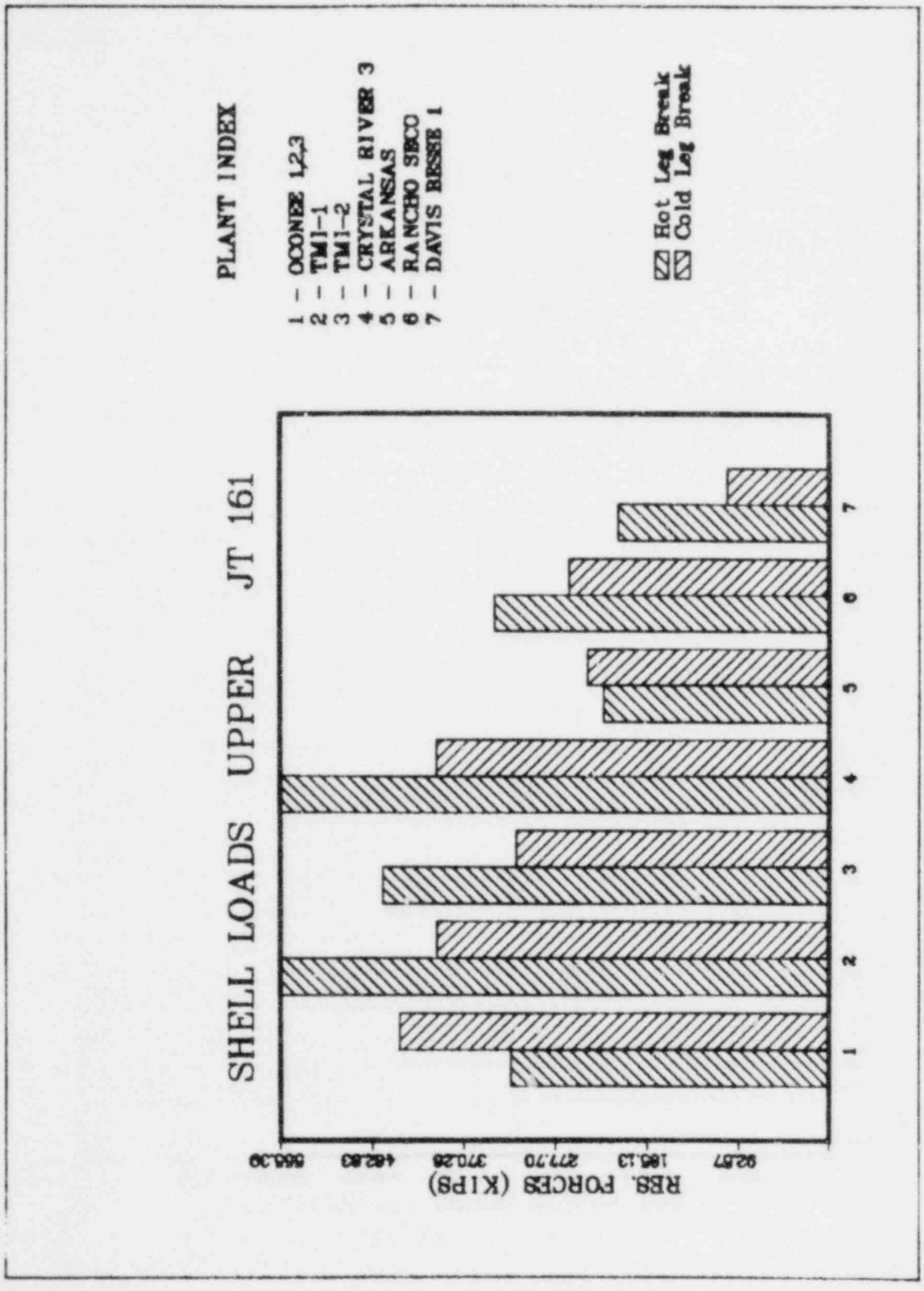

Figure 9.3-6. Shell Loads Upper Jt 161

Figure 9.3-7. Shell Loads Upper Jt 161

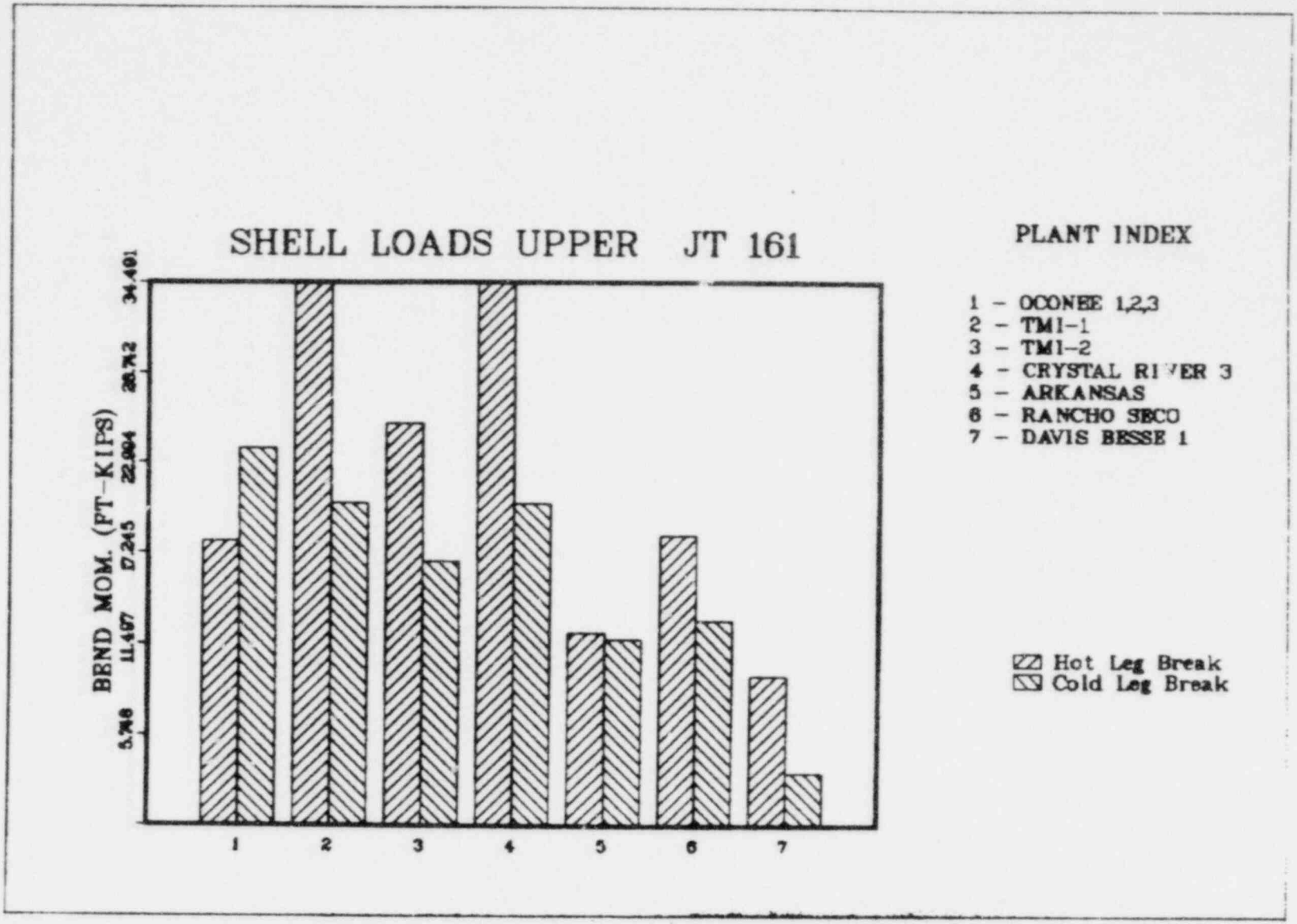

9.4. Control Rod Drive Mechanisms

Peak displacements for the control rod drive mechanisms (CRDMs) are presented in Tables 9.4-1 and 9.4-2 for each node illustrated in Figure 9.4-1. The selection and location of these nodes are based on previous stress analyses. Bar charts are given in Figures 9.4-2 and 9.4-3 to provide a convenient comparison of the horizontal displacements (D_H) and rotations about the horizontal axis (R_H) for nodes 120 and 160.

Figure 9.4-1. Control Rod Drive Nodes

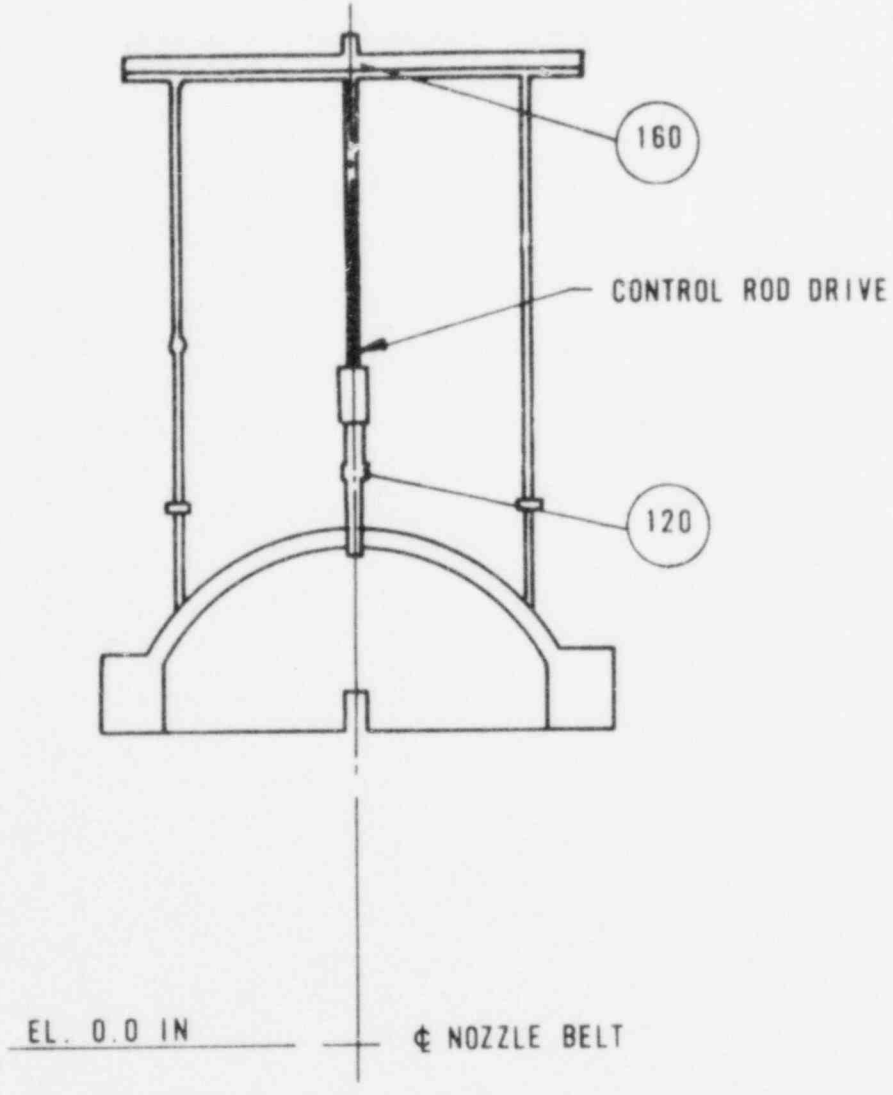

Table 9.4-1. Displacements at Nozzle, Joint 120

LOAD CASE		DISPLACEMENTS (INCHES) X	Y	Z
HLG AT RV	OCONEE 1,2 3	.02364	.02241	1.02350
HLG AT RV	TMI-1	.06917	.02593	1.33007
HLG AT RV	TMI-2	.04928	.02662	2.13152
HLG AT RV	CRYSTAL RIVER 3	.06917	.02593	1.33007
HLG AT RV	ANO-1	.04498	.01813	.82170
HLG AT RV	RANCHO SECO	.04673	.02465	1.11398
CLG AT RV	OCONEE 1,2,3	.99999	.01953	.49412
CLG AT RV	TMI-1	.88492	.01760	.52938
CLG AT RV	TMI-2	1.11125	.01366	.56315
CLG AT RV	CRYSTAL RIVER 3	.88492	.01760	.52938
CLG AT RV	ANO-1	.73788	.01225	.37752
CLG AT RV	RANCHO SECO	.73417	.01899	.43837
HLG AT RV	DAVIS BESSE 1	.00660	.19500	.84600
HLG AT EL	DAVIS BESSE 1	.00030	.04450	.25500
CLG AT EL	DAVIS BESSE 1	.06780	.02410	.13200
CLG AT RV	DAVIS BESSE 1	.15300	.05900	.22900

Table 9.4-2. Displacements at Clamp, Joint 160

LOAD CASE	DISPLACEMENTS (INCHES) X	Y	Z
HLG AT RV OCONEE 1,2,3	.05538	.02391	1.55193
HLG AT RV TMI-1	.12712	.02758	2.07371
HLG AT RV TMI-2	.07874	.02829	3.10271
HLG AT RV CRYSTAL RIVER 3	.12712	.02758	2.07371
HLG AT RV ANO-1	.07313	.01933	1.23200
HLG AT RV RANCHO SECO	.08026	.02626	1.67424
CLG AT RV OCONEE 1,2,3	1.43697	.02072	.72096
CLG AT RV TMI-1	1.29512	.01864	.76270
CLG AT RV TMI-2	1.58746	.01443	.79914
CLG AT RV CRYSTAL RIVER 3	1.29512	.01864	.76270
CLG AT RV ANO-1	1.07545	.01294	.54302
CLG AT RV RANCHO SECO	1.06782	.02014	.61713
HLG AT RV DAVIS BESSE 1	.01060	.19600	.85800
HLG AT EL DAVIS BESSE 1	.00120	.04470	.29200
CLG AT EL DAVIS BESSE 1	.07130	.02420	.16200
CLG AT RV DAVIS BESSE 1	.19500	.05910	.24200

Figure 9.4-2. CRDM Nozzle Jt 120

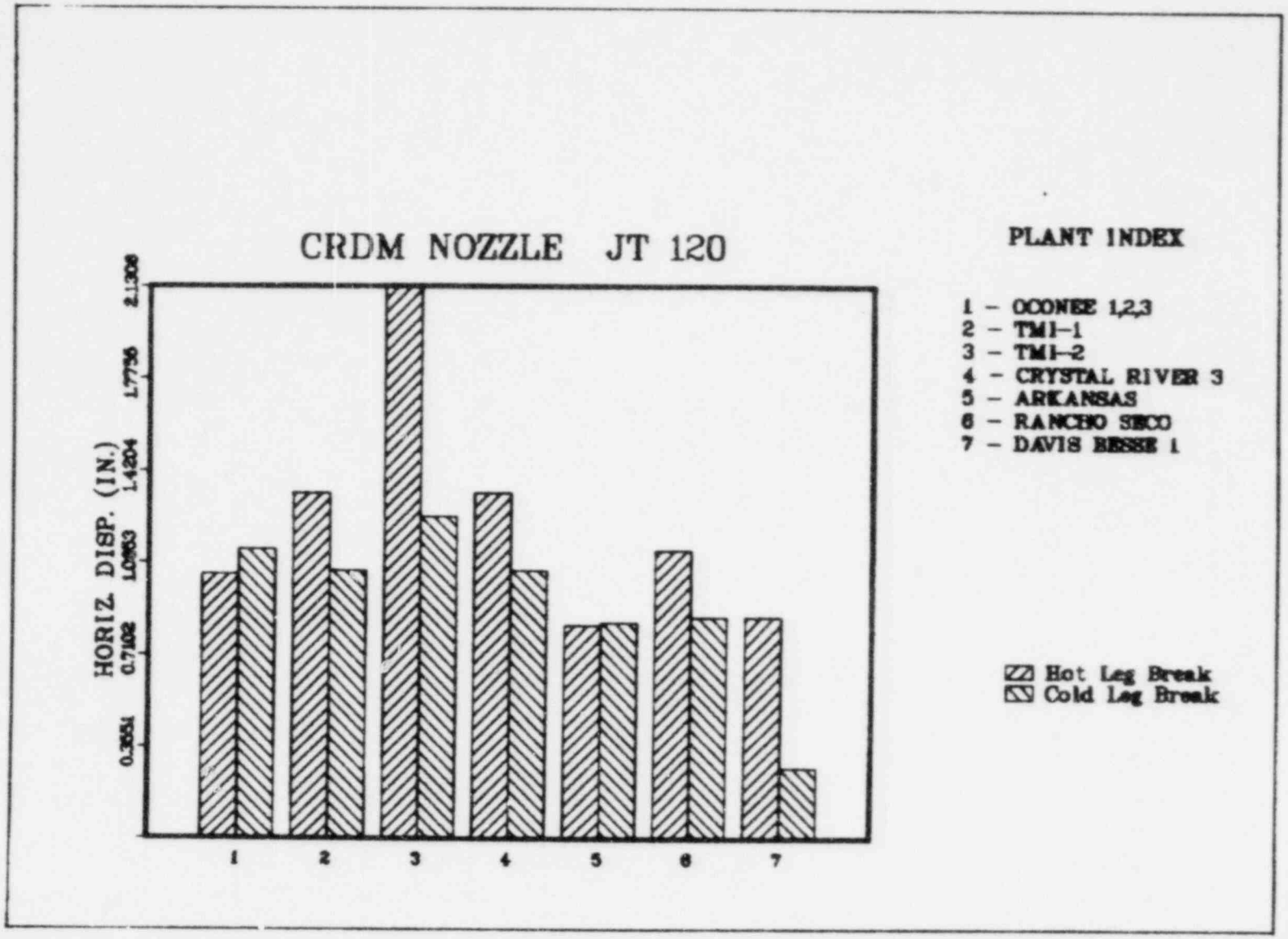

Figure 9.4-3. CRDM Clamp Jt 160

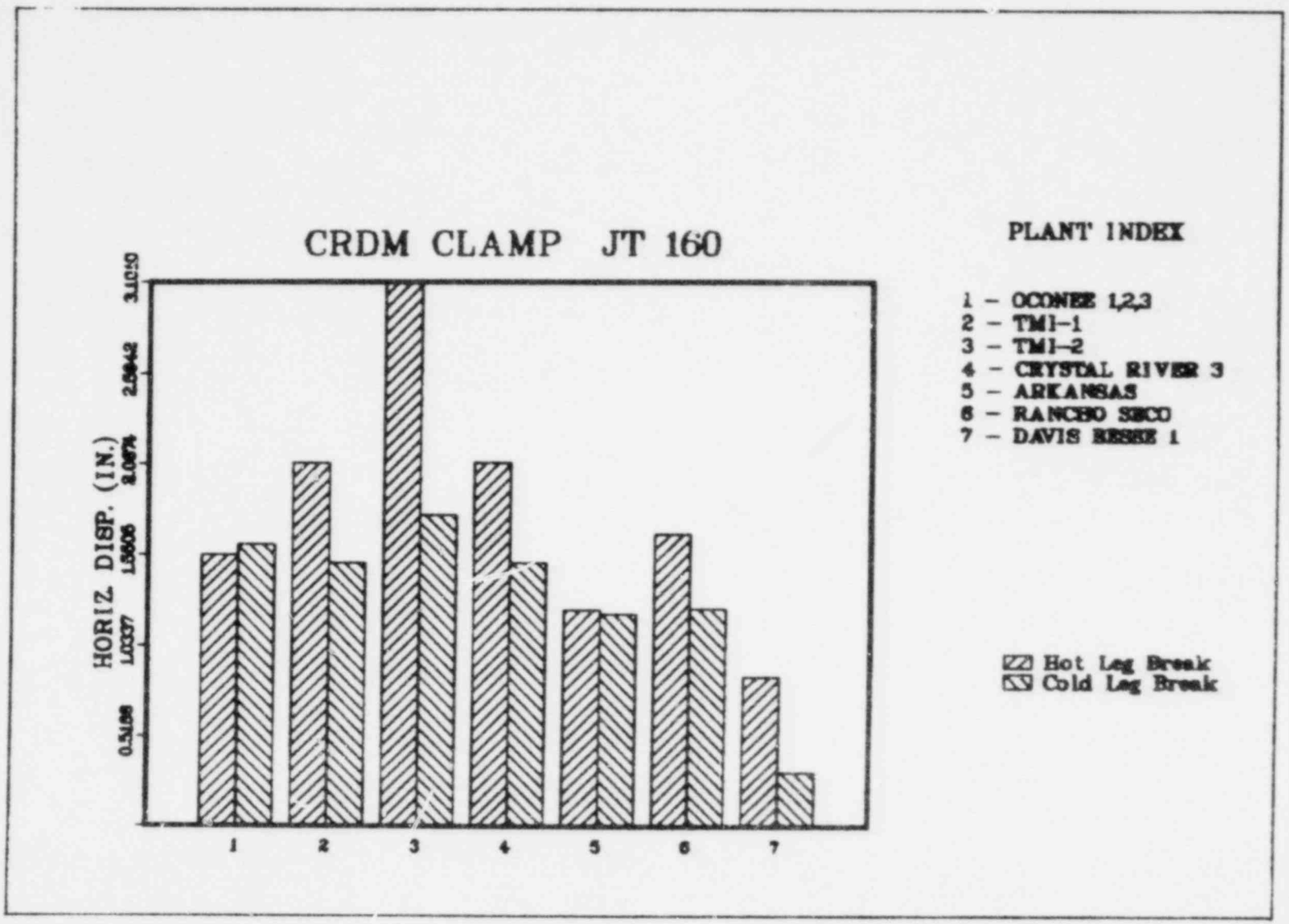

9.5. Reactor Internals

A considerable amount of data have been generated for the reactor internals. These forces and moments can best be presented as ratios to the existing Davis-Besse 2/3 (DB 2/3) loads. (That is, the new load is divided by the DB 2/3 load.) Therefore, ratios for key points are given for each plant in Tables 9.5-1 through 9.5-6 along with a tabulation of the Davis-Besse 2/3 forces and moments in Table 9.5-7. To aid in understanding and comparing the data, a graphic representation of the resultant horizontal forces (F_R) and moments about the horizontal axis (M_B) is also provided in Figures 9.5-1 through 9.5-17. Bar and joint references refer to Figure D-5 of Appendix D.)

Table 9.5-1. Load Ratios – Oconee 1, 2, and 3/Davis-Besse 2 and 3(a)

RATIOS FROM SYSTEM DYNAMIC RESPONSE ANALYSIS

COMPONENT	BAR/JT	HOT LEG			COLD LEG		
		M_i	F_r	F_y	M_i	F_r	F_y
CRGT AT COV	118/53	.42	.29	2.11	.61	.39	.91
CSS/CB AT COV	139/53	.64	.27	1.27	.70	.56	.77
AT BUMPER	134/41	.90	.28	1.19	.69	.51	.70
AT UP GRID	131/11	.50	.27	1.19	.46	.37	.70
AT TH SHLD	146/9	.46	.30	1.19	.44	.36	.70
THERMAL SHLD	127/1	.24	.25	—	.47	.32	—
AT CORE BRRL	130/9	—	.26	—	—	.51	—
AT LOW GRID	121/13	.58	1.18	1.08	.59	.50	1.46
PLENUM CYL AT COV	114/53	.41	.40	1.41	.40	.34	.74
AT UP GRID	110/14	.18	.36	1.68	.17	.45	.83
PLENUM COV AT RV	101/53	.66	.51	1.45	.70	.61	.78
UP GRID AT F.A.	109/14	—	.90	—	—	1.12	—
LOW GRID AT F.A.	104/13	—	3.27	1.06	—	.85	.59
LOW GRID	120/16	.10	.16	1.11	.09	.19	1.48
LOW GRID AT FDH	119/25	—	.12	—	—	.14	—
CR-BRRL at L-GRID	140/13	.28	.27	1.17	.28	.34	.61
CRGT AT U-GRID	115/14	—	.27	1.62	—	.31	.78

F_Y RATIOS FROM CORE BOUNCE ANALYSES

BREAK LOCATION	LOWER GRID	UPPER GRID & PLENUM COVER	PLENUM COVER FROM PLENUM CYLINDER OUT
HOT LEG	0.5661	0.9500	0.7794
COLD LEG	1.2772	3.2700	0.6105

*These load ratios envelope and are applicable to Midland 1 & 2.

Table 9.5-2. Load Ratios – TMI-1 and CR-III/ Davis-Besse 2 and 3[a]

RATIOS FROM SYSTEM DYNAMIC RESPONSE ANALYSIS

COMPONENT	BAR/JT	HOT LEG			COLD LEG		
		M_i	F_r	F_Y	M_i	F_r	F_y
CRGT AT COV	118/53	.41	.29	2.40	.57	.36	.91
CSS/CB AT COV	139/53	1.00	.44	1.03	.70	.55	.76
AT BUMPER	134/41	1.35	.48	1.03	.68	.51	.68
AT UP GRID	131/11	.69	.39	1.03	.43	.37	.68
AT TH SHLD	146/9	.62	.45	1.03	.41	.33	.68
THERMAL SHLD	127/1	.33	.30	----	.47	.30	----
AT CORE BRRL	130/9	----	.35	----	----	.50	----
AT LOW GRID	121/13	.80	1.41	1.07	.55	.48	1.38
PLENUM CYL AT COV	114/53	.41	.40	.86	.40	.33	.73
AT UP GRID	110/14	.14	.36	1.20	.15	.44	.81
PLENUM COV AT RV	101/53	1.13	.76	1.32	.69	.60	.77
UP GRID AT F.A.	109/14	----	.74	----	----	1.02	----
LOW GRID AT F.A.	104/13	----	4.69	.92	----	.79	.58
LOW GRID	120/16	.10	.22	1.07	.09	.18	1.39
LOW GRID AT FDH	119/25	----	.15	----	----	.14	----
CR-BBRL AT L-GRID	140/13	.35	.39	1.03	.26	.33	.60
CRGT AT U-GRID	115/14	----	.21	1.25	----	.30	.76

F_Y RATIOS FROM CORE BOUNCE ANALYSES

BREAK LOCATION	LOWER GRID	UPPER GRID & PLENUM COVER	PLENUM COVER FROM PLENUM CYLINDER OUT
HOT LEG	0.5661	0.9500	0.7794
COLD LEG	1.2772	3.2700	0.6105

[a] These load ratios envelop and are applicable to Midland 1 and 2.

Table 9.5-3. Load Ratios — TMI-2/Davis-Besse 2 and 3

RATIOS FROM SYSTEM DYNAMIC RESPONSE ANALYSIS

COMPONENT	BAR/JT	HOT LEG			COLD LEG		
		M_t	F_r	F_Y	M_t	F_r	F_Y
CRGT AT COV	118/53	.42	.30	2.43	.58	.36	.86
CSS/CB AT COV	139/53	.80	.43	1.47	.71	.56	.68
AT BUMPER	134/41	1.01	.37	1.34	.70	.51	.63
AT UP GRID	131/11	.55	.36	1.34	.43	.37	.63
AT TH SHLD	146/9	.49	.47	1.34	.41	.34	.63
THERMAL SHLD	127/1	.27	.41	----	.45	.32	----
AT CORE BRRL	130/9	----	.32	----	----	.48	----
AT LOW GRID	121/13	.72	1.18	1.30	.56	.43	1.13
PLENUM CYL AT COV	114/53	.41	.40	1.12	.41	.33	.74
AT UP GRID	110/14	.15	.36	1.44	.16	.46	.81
PLENUM COV AT RV	101/53	.86	.68	1.68	.72	.60	.67
UP GRID AT F.A.	109/14	----	.70	----	----	1.01	----
LOW GRID AT F.A.	104/13	----	4.53	1.13	----	.82	.60
LOW GRID	120/16	.12	.23	1.16	.09	.18	1.15
LOW GRID AT FDH	119/25	----	.13	----	----	.13	----
CR-BBRL AT L-GRID	140/13	.28	.28	1.25	.26	.32	.58
CRGT AT U-GRID	115/14	----	.21	1.53	----	.26	.77

F_Y RATIOS FROM CORE BOUNCE ANALYSES

BREAK LOCATION	LOWER GRID	UPPER GRID & PLENUM COVER	PLENUM COVER FROM PLENUM CYLINDER OUT
HOT LEG	0.5661	0.9500	0.7794
COLD LEG	1.2772	3.2700	0.6105

Table 9.5-4. Load Ratios — ANO-1/Davis-Besse 2 and 3

RATIOS FROM SYSTEM DYNAMIC RESPONSE ANALYSIS

COMPONENT	BAR/JT	HOT LEG			COLD LEG		
		M_i	F_r	F_Y	M_i	F_r	F_v
CRGT AT COV	118/53	.41	.28	1.77	.51	.32	.83
CSS/CB AT COV	139/53	.55	.27	1.26	.69	.54	.66
AT BUMPER	134/41	.79	.26	1.22	.68	.50	.62
AT UP GRID	131/11	.43	.23	1.22	.42	.36	.62
AT TH SHLD	146/9	.39	.26	1.22	.39	.33	.62
THERMAL SHLD	127/1	.20	.24	----	.46	.28	----
AT CORE BRRL	130/9	----	.25	----	----	.49	----
AT LOW GRID	121/13	.50	.98	1.06	.54	.45	1.07
PLENUM CYL AT COV	114/53	.41	.40	1.41	.38	.31	.71
AT UP GRID	110/14	.18	.35	1.59	.16	.43	.77
PLENUM COV AT RV	101/53	.58	.59	1.41	.68	.59	.64
UP GRID AT F.A.	109/14	----	.84	----	----	.92	----
LOW GRID AT F.A.	104/13	----	2.72	1.08	----	.79	.56
LOW GRID	120/16	.09	.14	1.11	.09	.18	1.08
LOW GRID AT FDH	119/25	----	.10	----	----	.13	----
CR-BBRL AT L-GRID	140/13	.22	.24	1.19	.26	.32	.57
CRGT AT U-GRID	115/14	----	.27	1.54	----	.28	.74

F_Y RATIOS FROM CORE BOUNCE ANALYSES

BREAK LOCATION	LOWER GRID	UPPER GRID & PLENUM COVER	PLENUM COVER FROM PLENUM CYLINDER OUT
HOT LEG	0.5661	0.9500	0.7794
COLD LEG	1.2772	3.2700	0.6105

Table 9.5-5. Load Ratios — Rancho Seco/Davis-Besse 2 and 3

RATIOS FROM SYSTEM DYNAMIC RESPONSE ANALYSIS

COMPONENT	BAR/JT	HOT LEG			COLD LEG		
		M_1	F_r	F_Y	M_1	F_r	F_y
CRGT AT COV	118/53	.41	.28	2.40	.52	.32	.87
CSS/CB AT COV	139/53	.73	.33	.96	.69	.54	.73
AT BUMPER	134/41	.94	.31	.97	.68	.50	.66
AT UP GRID	131/11	.47	.31	.97	.42	.37	.66
AT TH SHLD	146/9	.42	.35	.97	.40	.33	.66
THERMAL SHLD	127/1	.25	.25	----	.46	.29	----
AT CORE BRRL	130/9	----	.27	----	----	.49	----
AT LOW GRID	121/13	.57	1.25	1.06	.55	.46	1.41
PLENUM CYL AT COV	114/53	.41	.40	.88	.38	.31	.72
AT UP GRID	110/14	.14	.36	1.31	.17	.43	.80
PLENUM COV AT RV	101/53	.82	.59	1.24	.68	.59	.74
UP GRID AT F.A.	109/14	----	.67	----	----	.95	----
LOW GRID AT F.A.	104/13	----	3.28	.83	----	.81	.57
LOW GRID	120/16	.09	.20	.96	.09	.18	1.44
LOW GRID AT FDH	119/25	----	.14	----	----	.14	----
CR-BBRL AT L-GRID	140/13	.26	.28	.95	.26	.32	.58
CRGT AT U-GRID	115/14	----	.21	1.33	----	.29	.76

F_Y RATIOS FROM CORE BOUNCE ANALYSES

BREAK LOCATION	LOWER GRID	UPPER GRID & PLENUM COVER	PLENUM COVER FROM PLENUM CLINDER OUT
HOT LEG	0.5661	0.9500	0.7794
COLD LEG	1.2772	3.2700	0.6105

Table 9.5-6. Load Ratios — Davis-Besse 1/Davis-Besse 2 and 3

RATIOS FROM SYSTEM DYNAMIC RESPONSE ANALYSIS

COMPONENT	BAR/JT	HOT LEG			COLD LEG		
		M_i	F_r	F_Y	M_i	F_r	F_Y
CRGT AT COV	118/53	.53	.57	1.28	.47	.42	.40
CSS/CB AT COV	139/53	1.71	.64	.96	.81	.57	.66
AT BUMPER	134/41	2.38	.62	.94	.84	.52	.64
AT UP GRID	131/11	1.23	.60	.94	.53	.46	.64
AT TH SHLD	146/9	1.11	.69	.94	.50	.37	.64
THERMAL SHLD	127/1	.72	.62	----	.50	.38	----
AT CORE BRRL	130/9	----	.73	----	----	.53	----
AT LOW GRID	121/13	1.27	2.03	1.07	.64	.46	.86
PLENUM CYL AT COV	114/53	.33	.38	1.27	.31	.44	.33
AT UP GRID	110/14	1.32	.57	1.22	1.61	.64	.33
PLENUM COV AT RV	101/53	1.76	.77	.98	.78	.60	.61
UP GRID AT F.A.	109/14	----	1.10	----	----	.73	----
LOW GRID AT F.A.	104/13	----	6.71	.78	----	.61	.57
LOW GRID	120/16	.33	.62	1.13	.10	.17	.87
LOW GRID AT FDH	119/25	----	.50	----	----	.14	----
CR-BBRL AT L-GRID	140/13	.66	.62	.90	.28	.39	.61
CRGT AT U-GRID	115/14	----	.38	1.31	----	.34	.33

F_Y RATIOS FROM CORE BOUNCE ANALYSES

BREAK LOCATION	LOWER GRID	UPPER GRID & PLENUM COVER	PLENUM COVER FROM PLENUM CYLINDER OUT
HOT LEG @ NOZZLE	0.3811	0.8886	0.6915
HOT LEG @ ELBOW	0.3545	0.8950	0.5976
COLD LEG @ NOZZLE	0.3336	0.7000	0.2745
COLD LEG @ ELBOW	0.7527	1.4600	0.5854

Table 9.5-7. Forces and Moments for Davis-Besse 2 and 3 Reactor Internals

LOADS FROM SYSTEM DYNAMIC RESPONSE ANALYSIS, KIPS, FT-KIPS

COMPONENT	BAR/JT	HOT LEG			COLD LEG		
		M_t	F_r	F_Y	M_t	F_r	F_y
CRGT AT COV	118/53	1359	566	89	729	359	186
CSS/CB AT COV	139/53	16582	2441	1028	58666	7511	1415
AT BUMPER	134/41	8889	2438	1026	33511	5724	1430
AT UP GRID	131/11	13078	2378	1026	38622	4840	1430
AT TH SHLD	146/9	13924	1501	1026	39334	3214	1430
THERMAL SHLD	127/1	4394	527	---	8872	846	---
AT CORE BRRL	130/9	---	931	---	---	2388	---
AT LOW GRID	121/13	1492	291	90	3382	1880	89
PLENUM CYL AT COV	114/53	14426	2793	76	10589	1532	184
AT UP GRID	110/14	196	998	54	106	672	124
PLENUM COV AT RV	101/53	17406	2387	1101	63892	7506	1674
UP GRID AT F.A.	109/14	---	162	---	---	169	---
LOW GRID AT F.A.	104/13	---	28	888	---	106	1236
LOW GRID	120/16	3768	1260	130	7160	2636	134
LOW GRID AT FDH	119/25	---	647	---	---	1339	---
CR-BBRL AT L-GRID	140/13	4505	1206	987	10562	2894	1387
CRGT AT U-GRID	115/14	---	328	65	---	217	157

F_Y LOADS FROM CORE BOUNCE ANALYSIS, LB

BREAK LOCATION	LOWER GRID	UPPER GRID & PLENUM COVER	PLENUM COVER FROM PLENUM CYLINDER OUT
HOT LEG	1050000	78772	497000
COLD LEG	546000	58176	590000

Figure 9.5-1. CRGT at Cover Bar/Jt 118/53

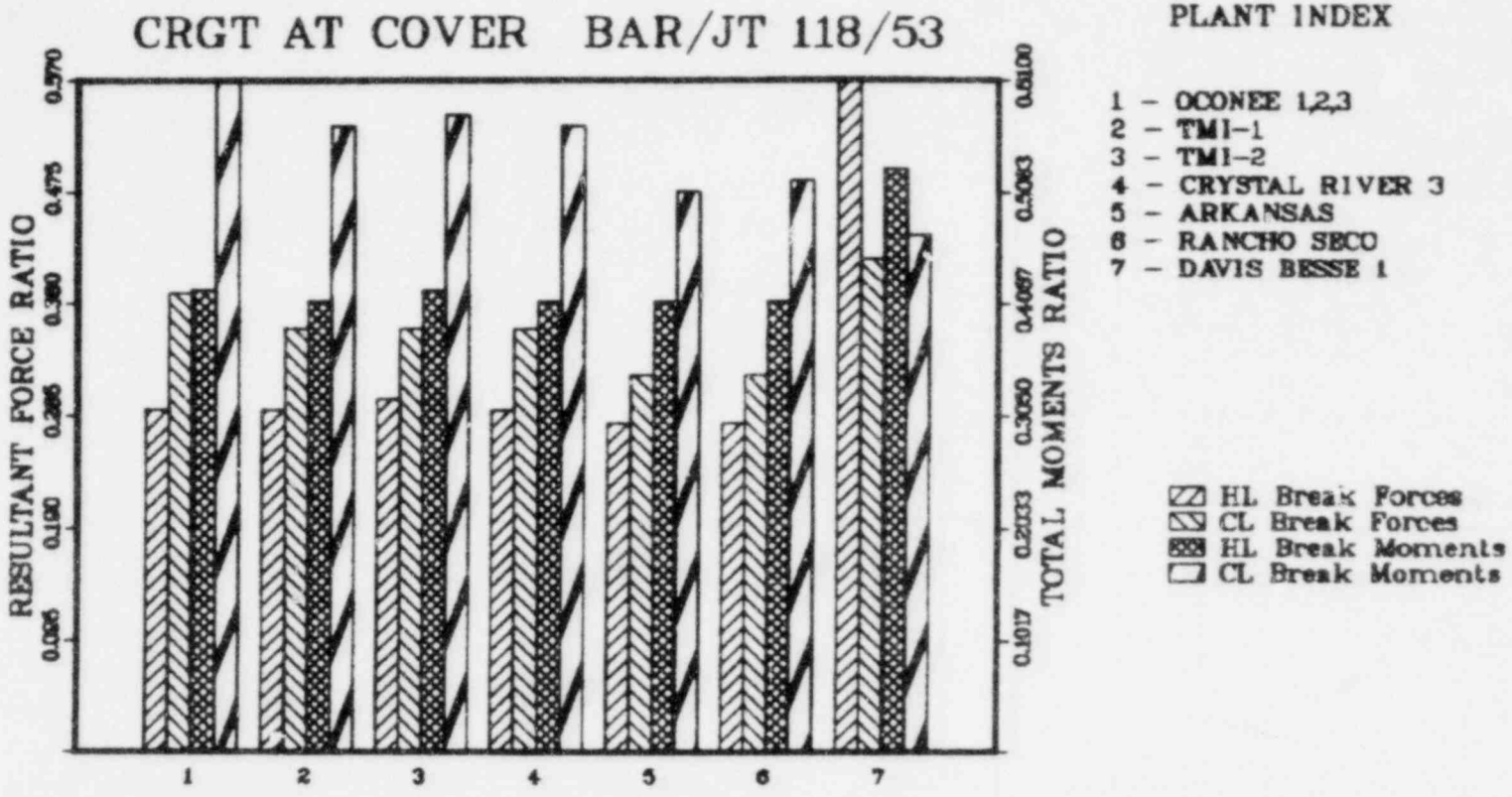

Figure 9.5-2. CSS/CB at COV Bar/Jt 139/53

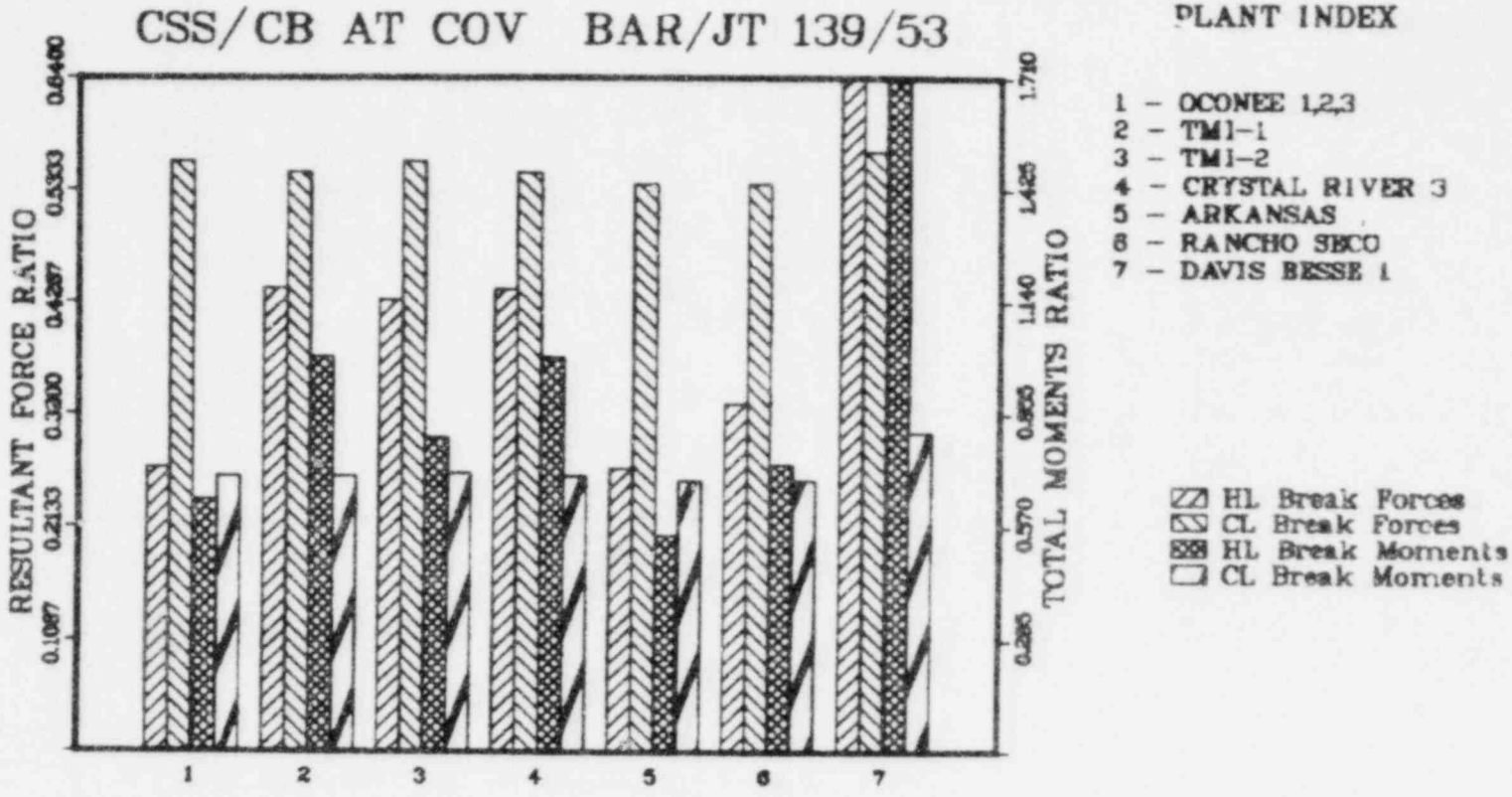

Figure 9.5-3. CSS/CB at Bump Bar/Jt 134/41

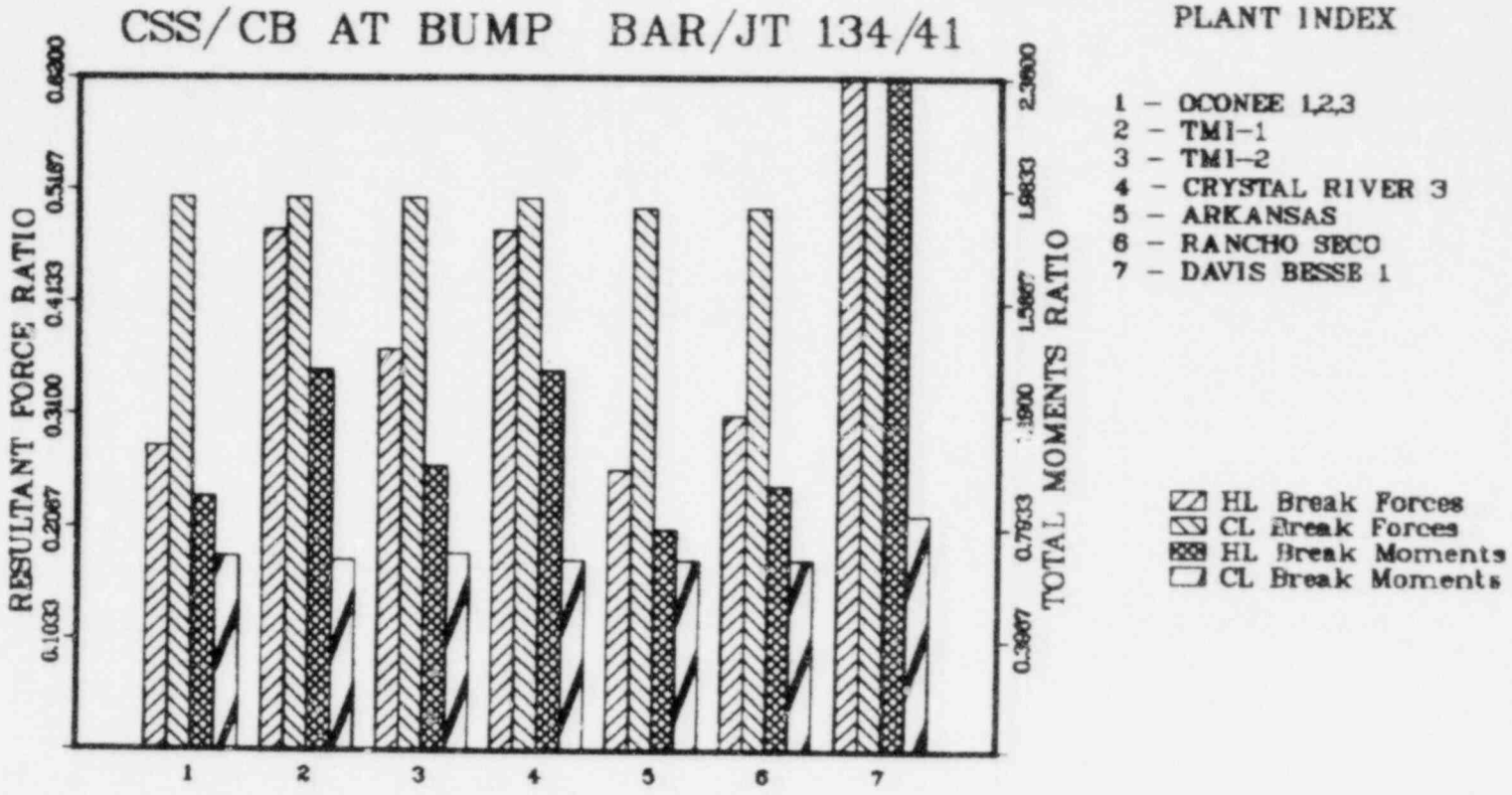

Figure 9.5-4. CSS/CB at Upper Grid 131/11

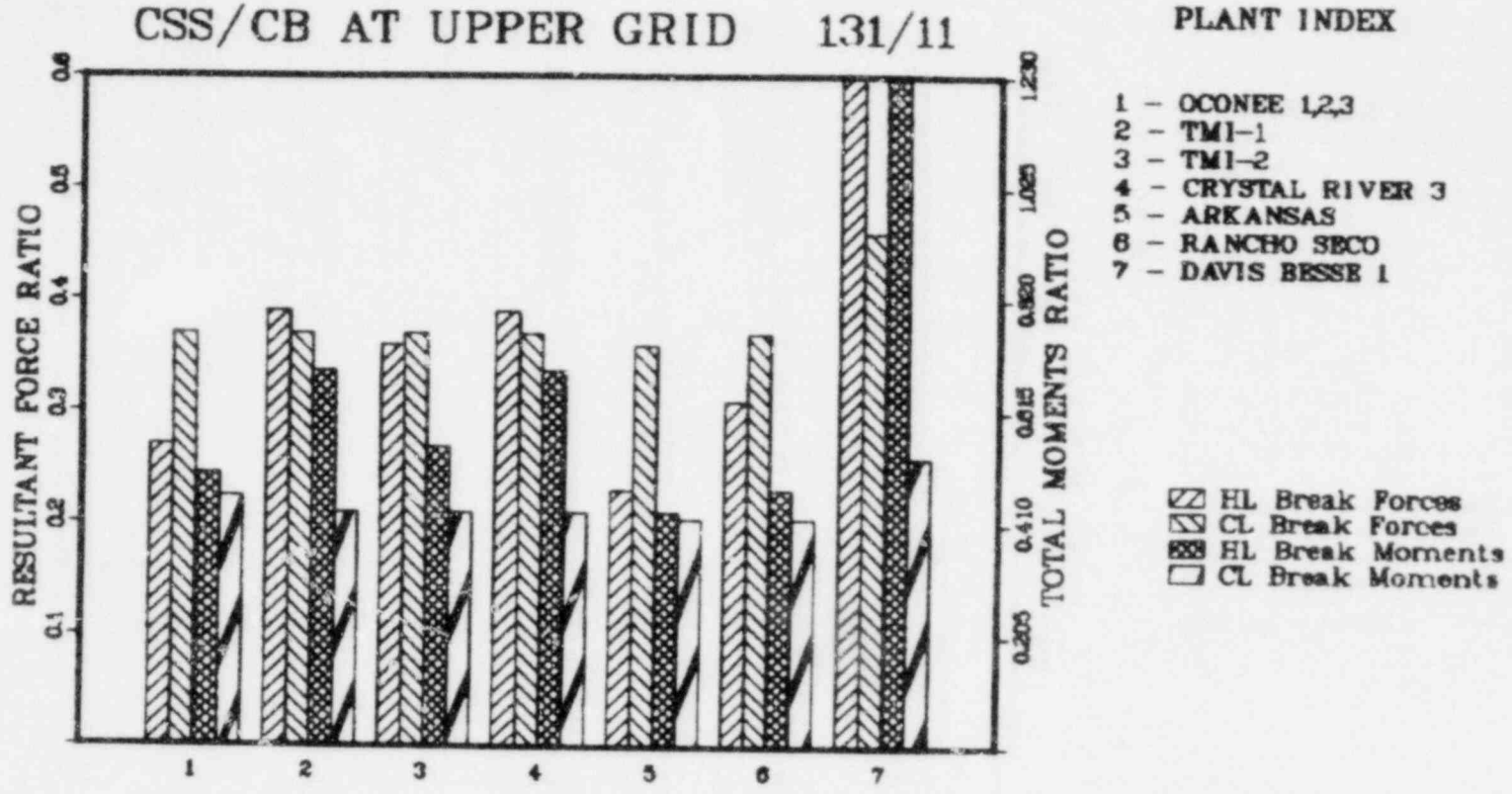

Figure 9.5-5. CSS/CB at Therm Shld 146/9

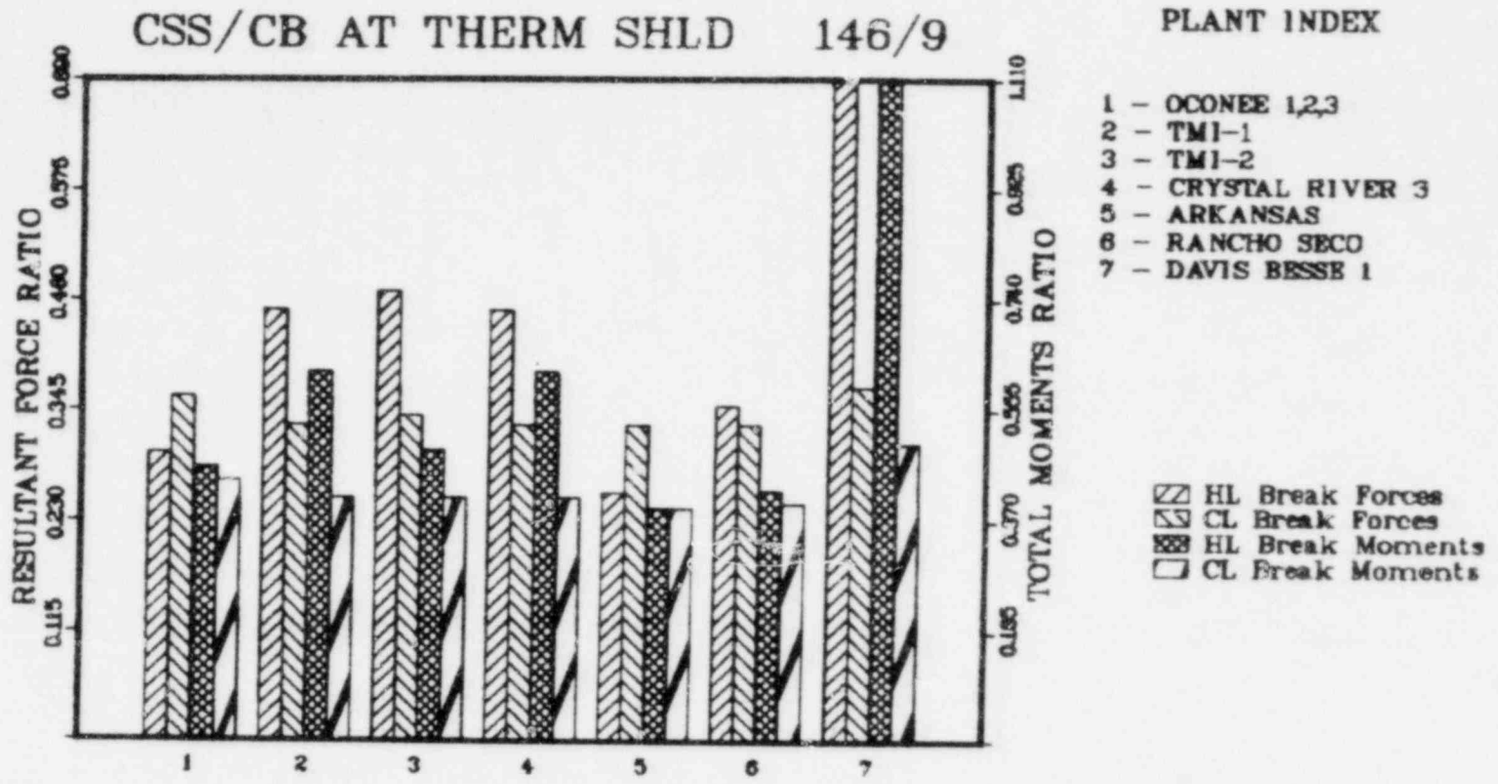

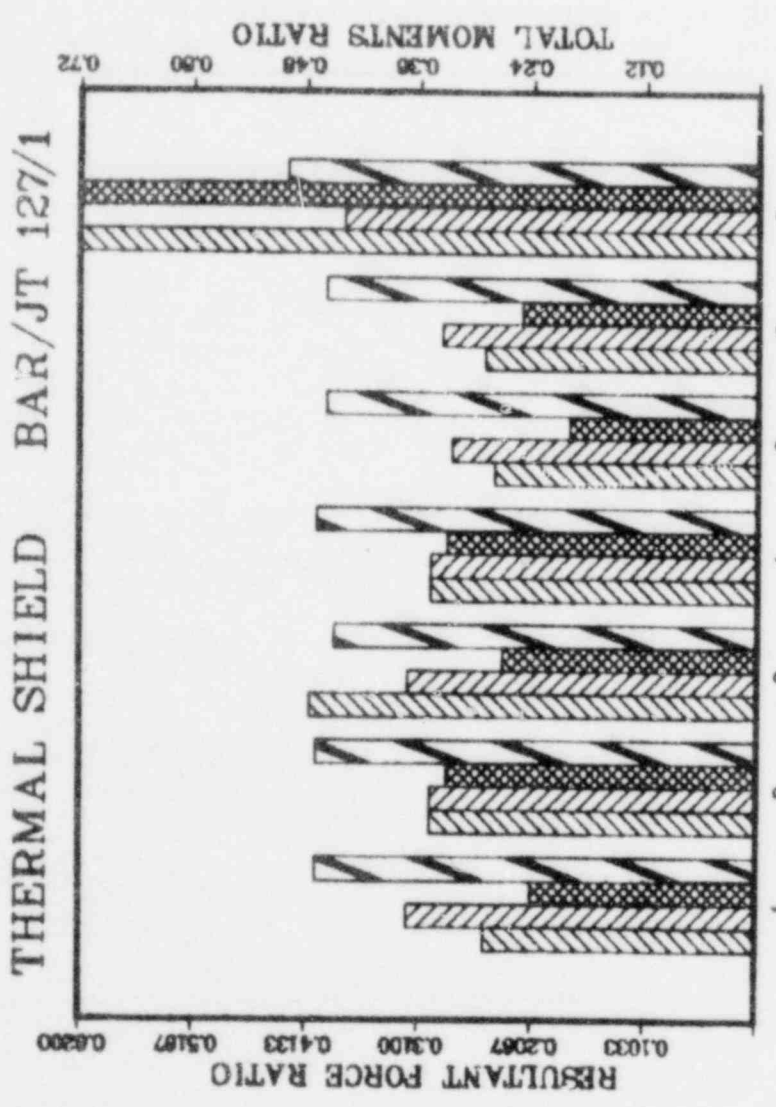

Figure 9.5-6. Thermal Shield Bar/Jt 127/1

Figure 9.5-7. Therm Shld at CB 130/9

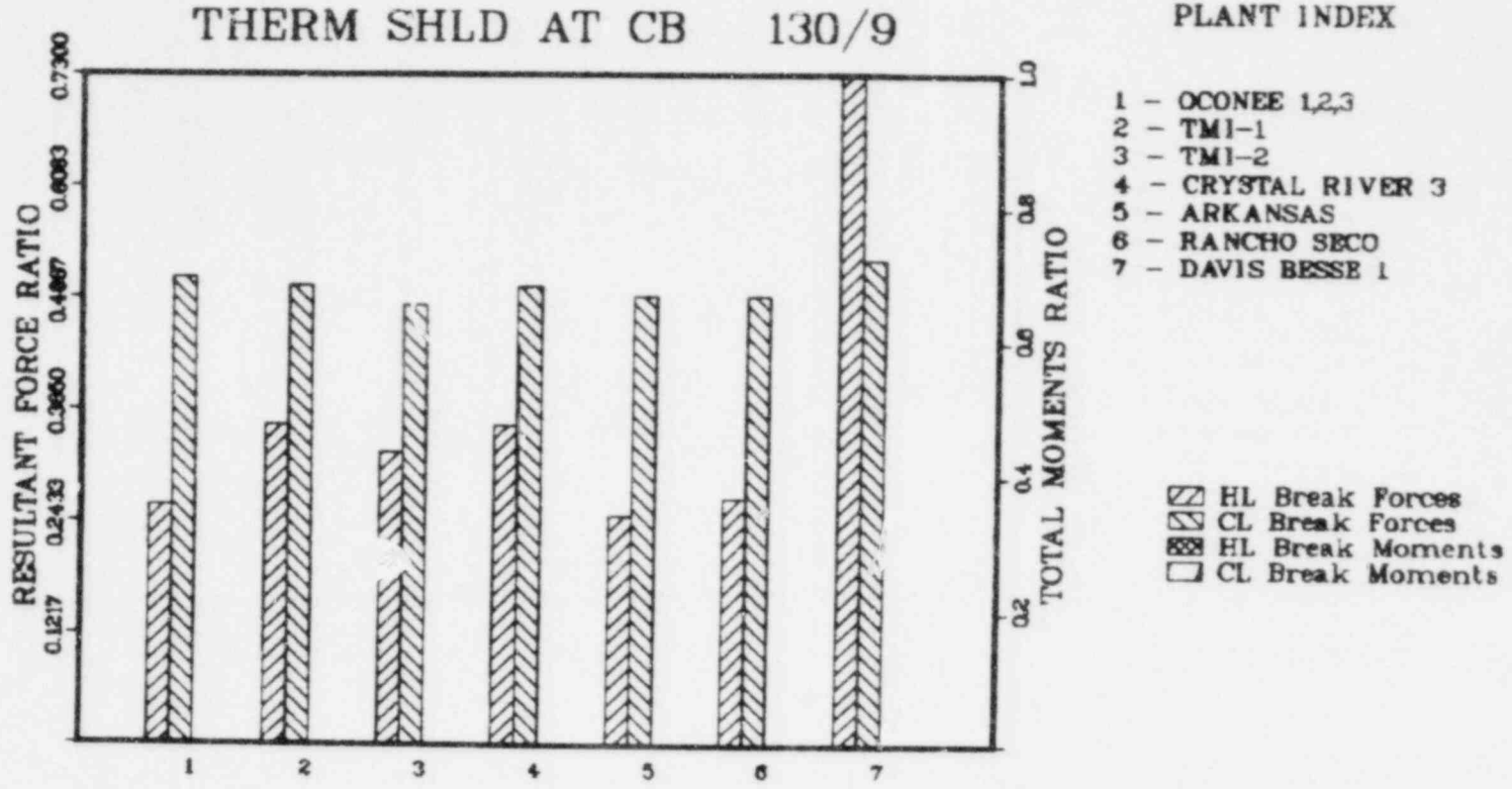

Figure 9.5-8. Therm Shld at Low Grid 121/13

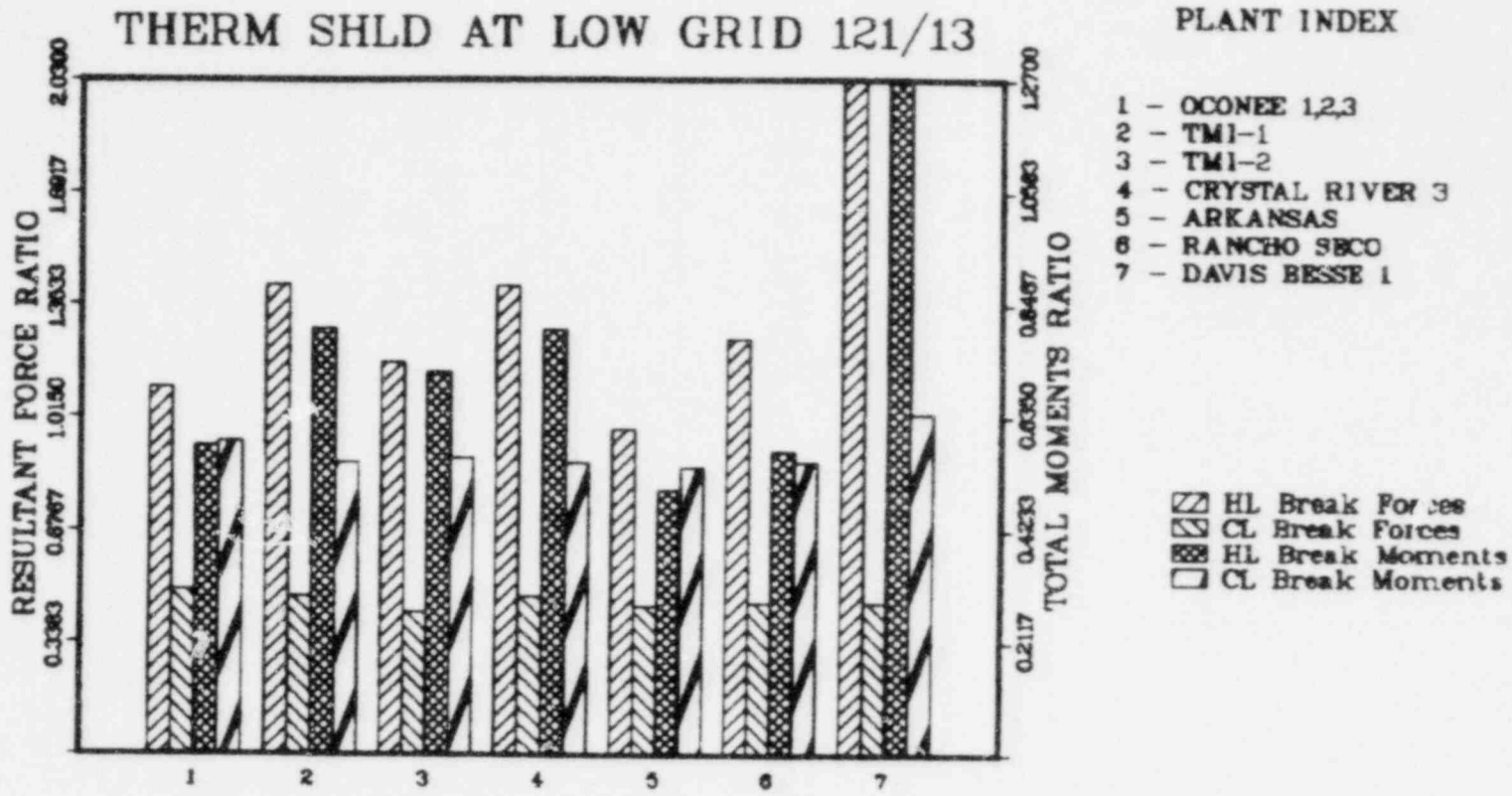

Figure 9.5-9. Plenum Cyl at COV 114/53

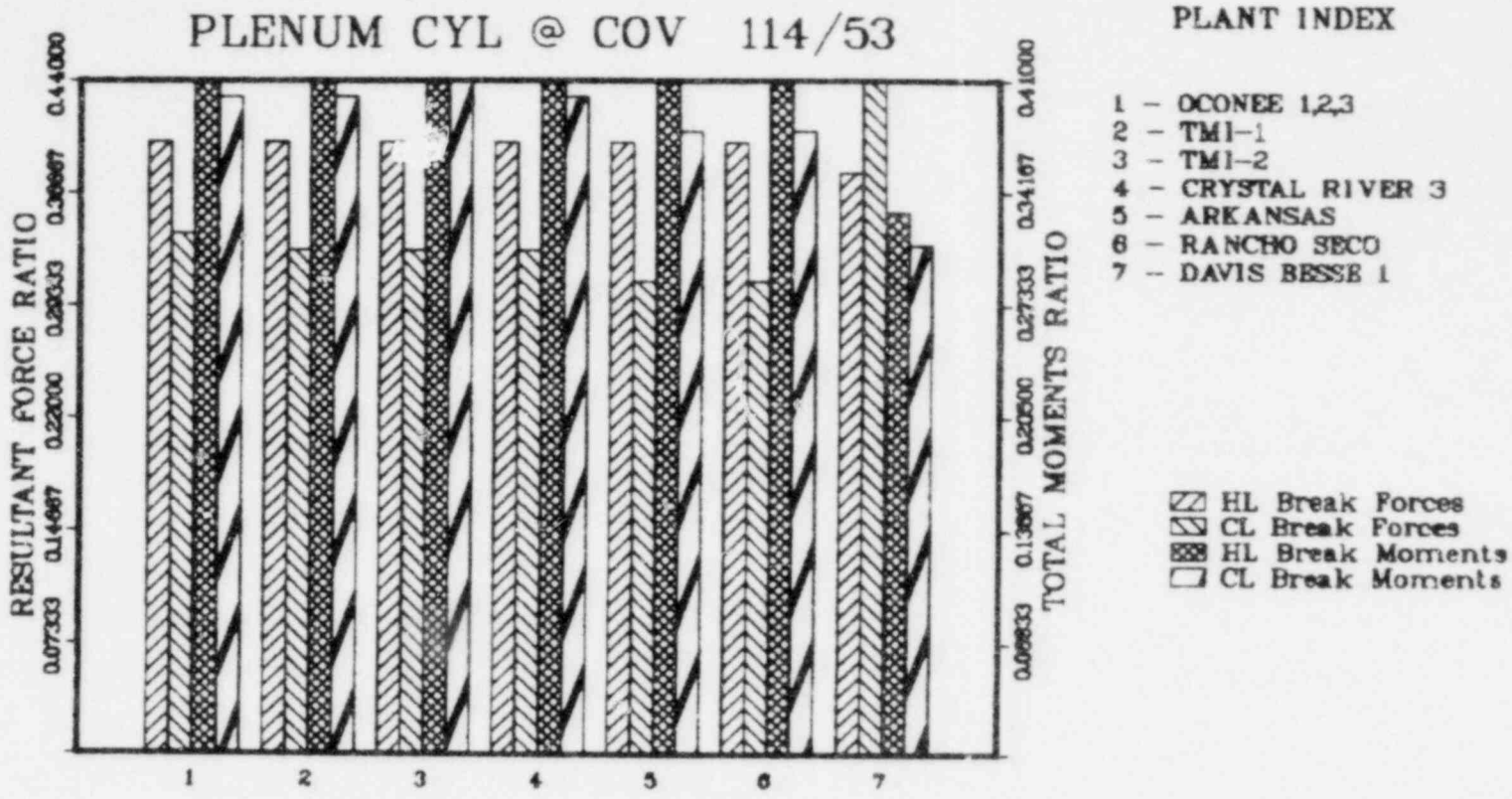

Figure 9.5-10. Plenum Cyl at Up Grid 110/14

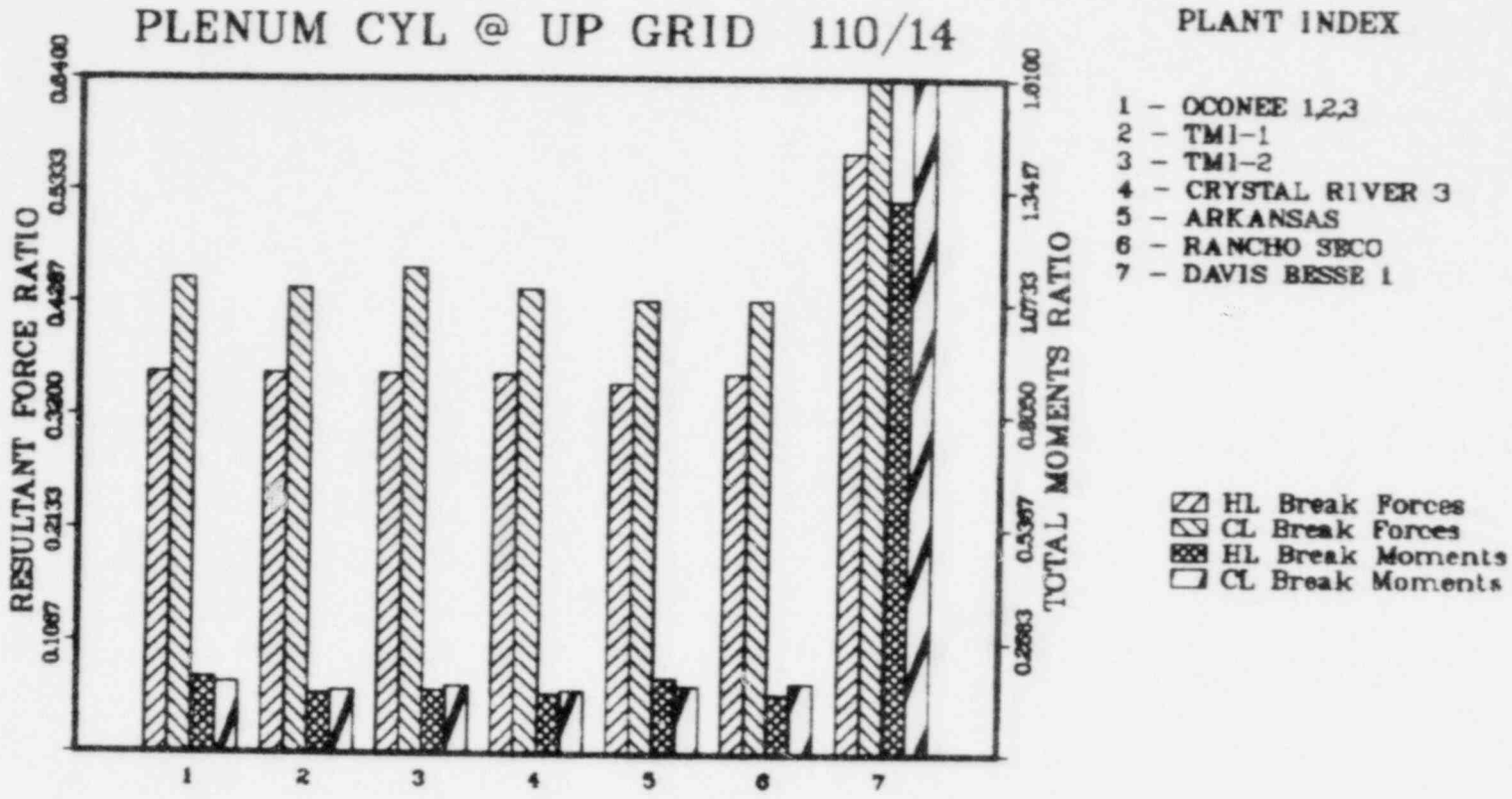

Figure 9.5-11. Plenum COV at RV 101/53

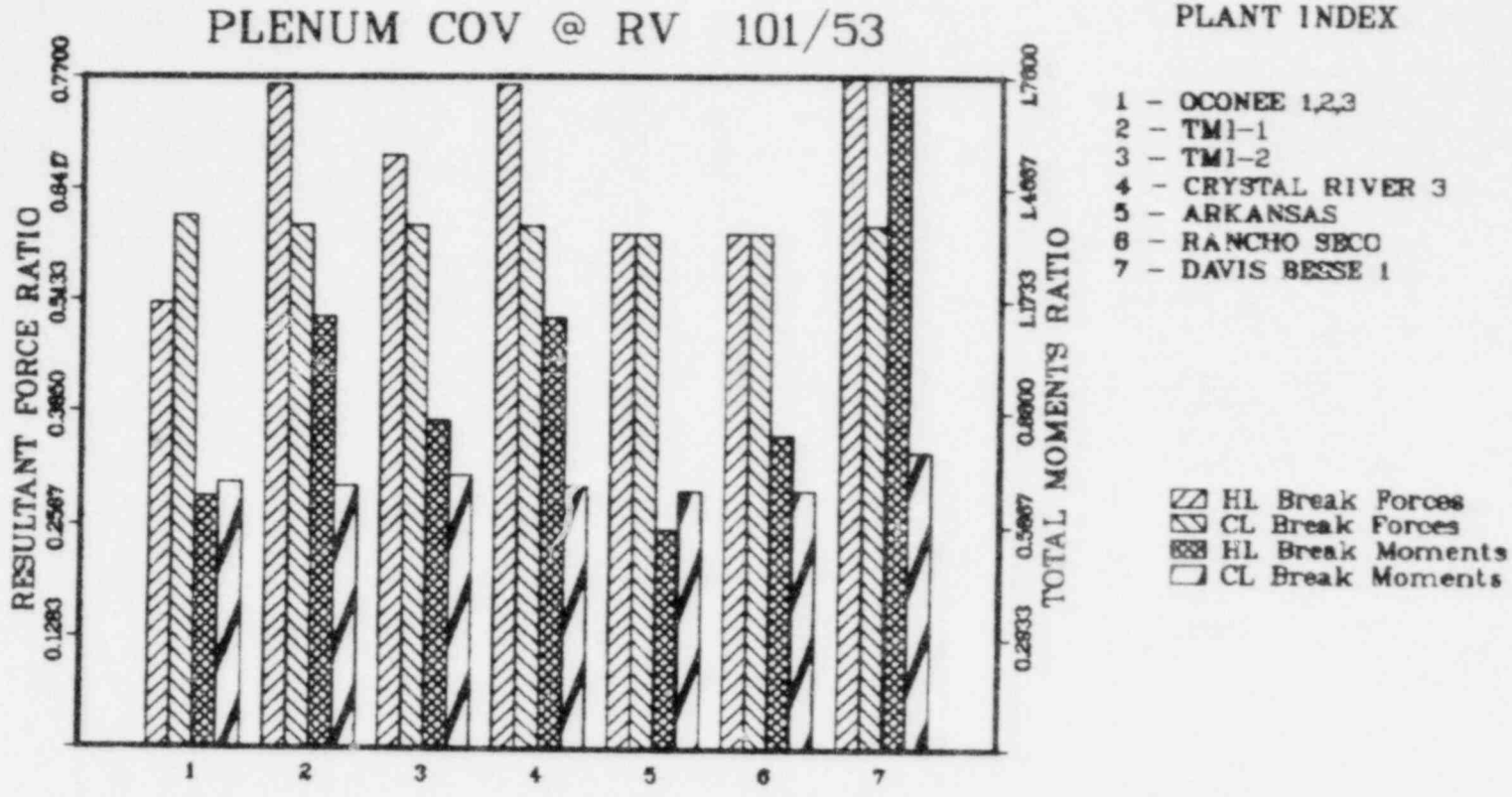

Figure 9.5-12. Upper Grid at F. A. 109/14

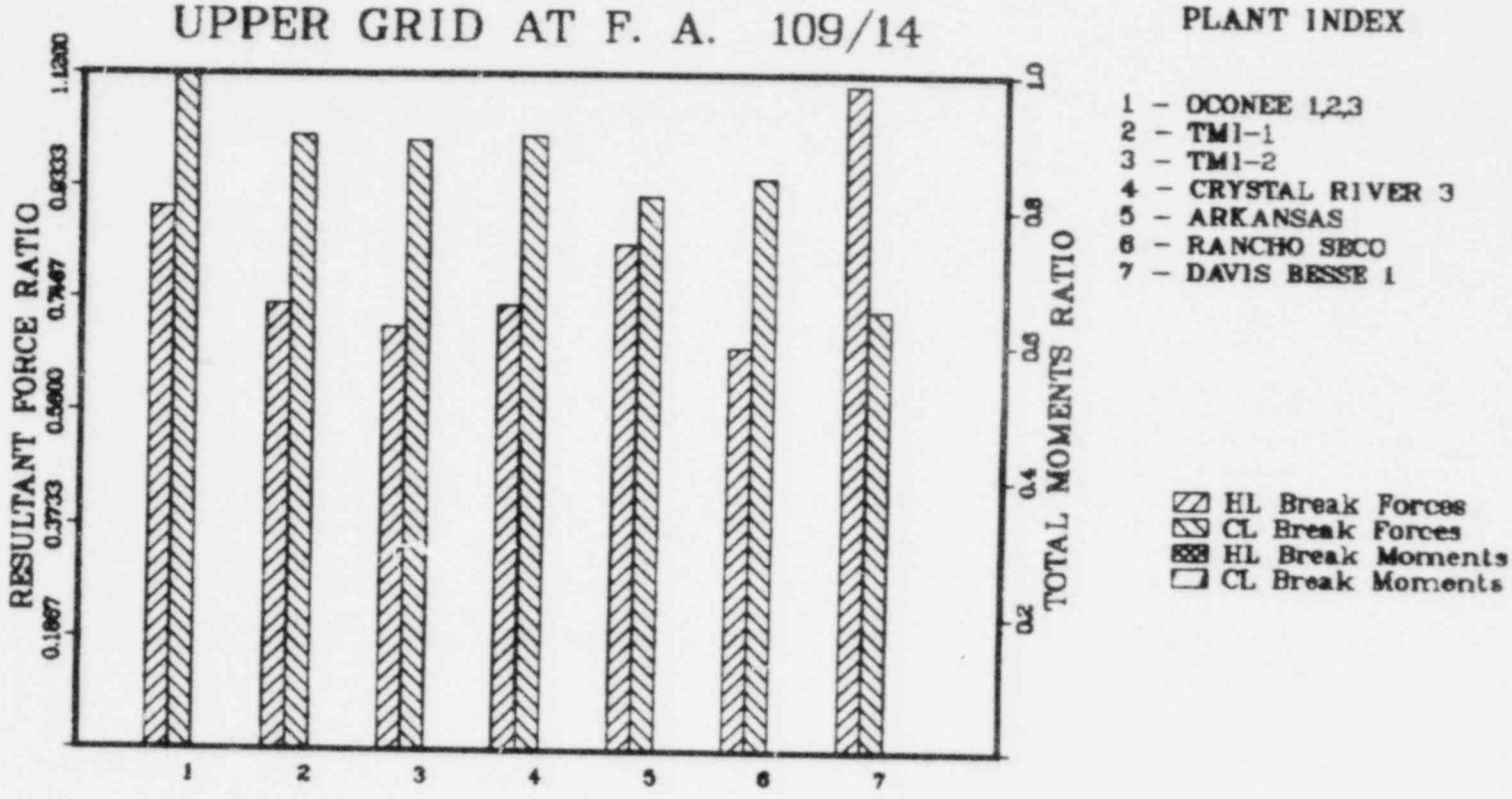

Figure 9.5-13. Low Grid at F. A. 104/13

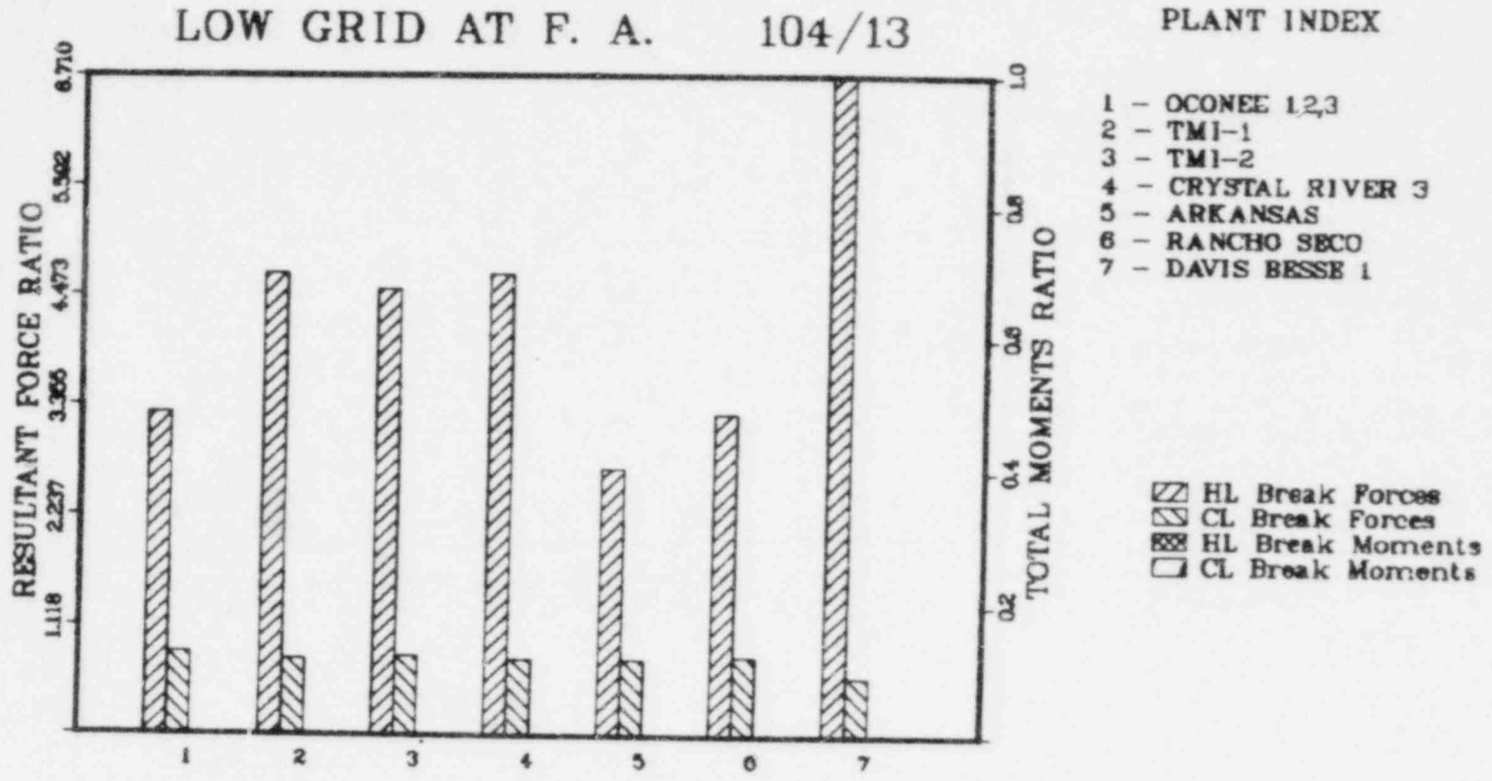

Figure 9.5-14. Low Grid Bar 120 Jt 16

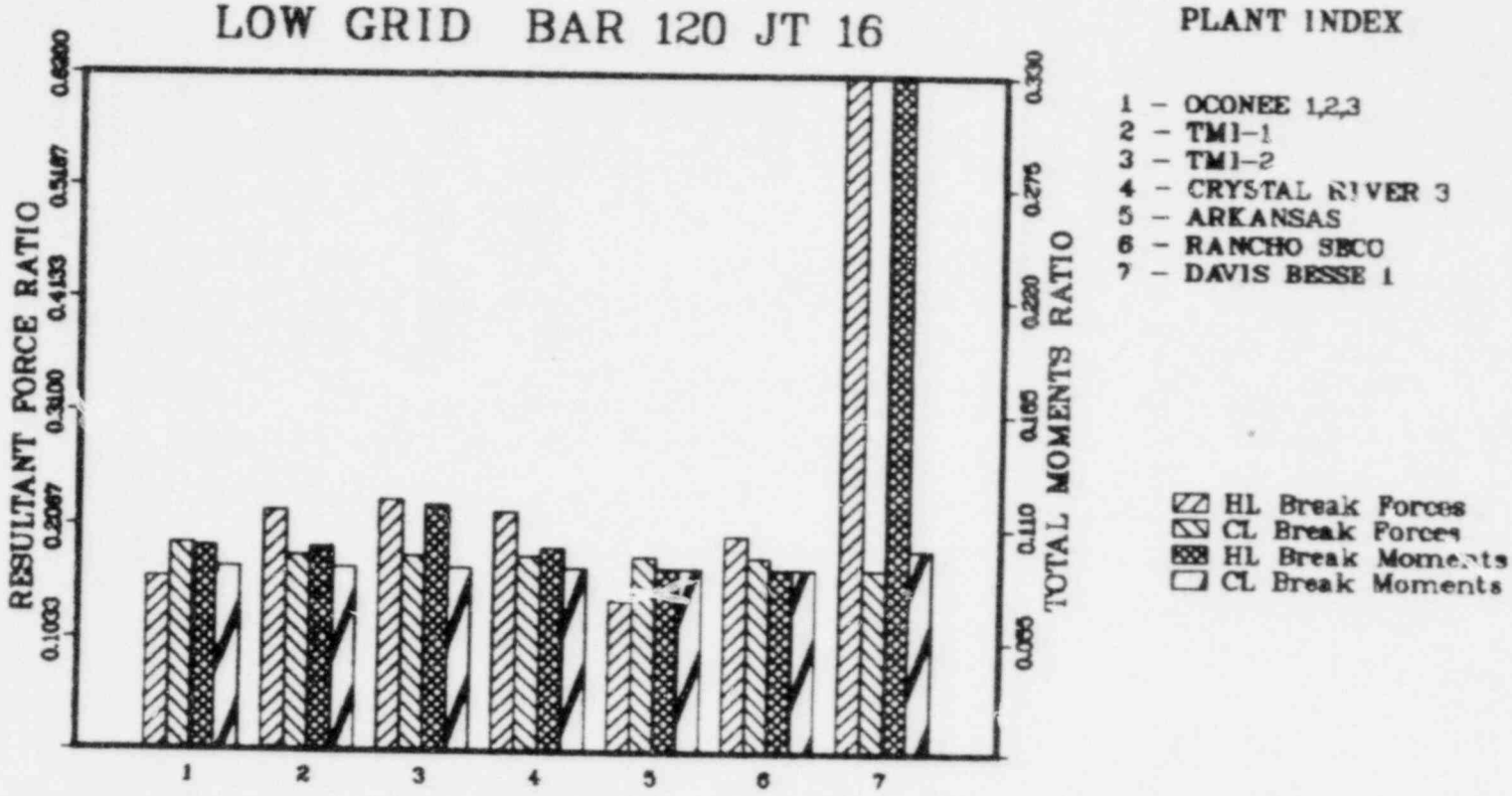

Figure 9.5-15. Low Grid at FDH 119/25

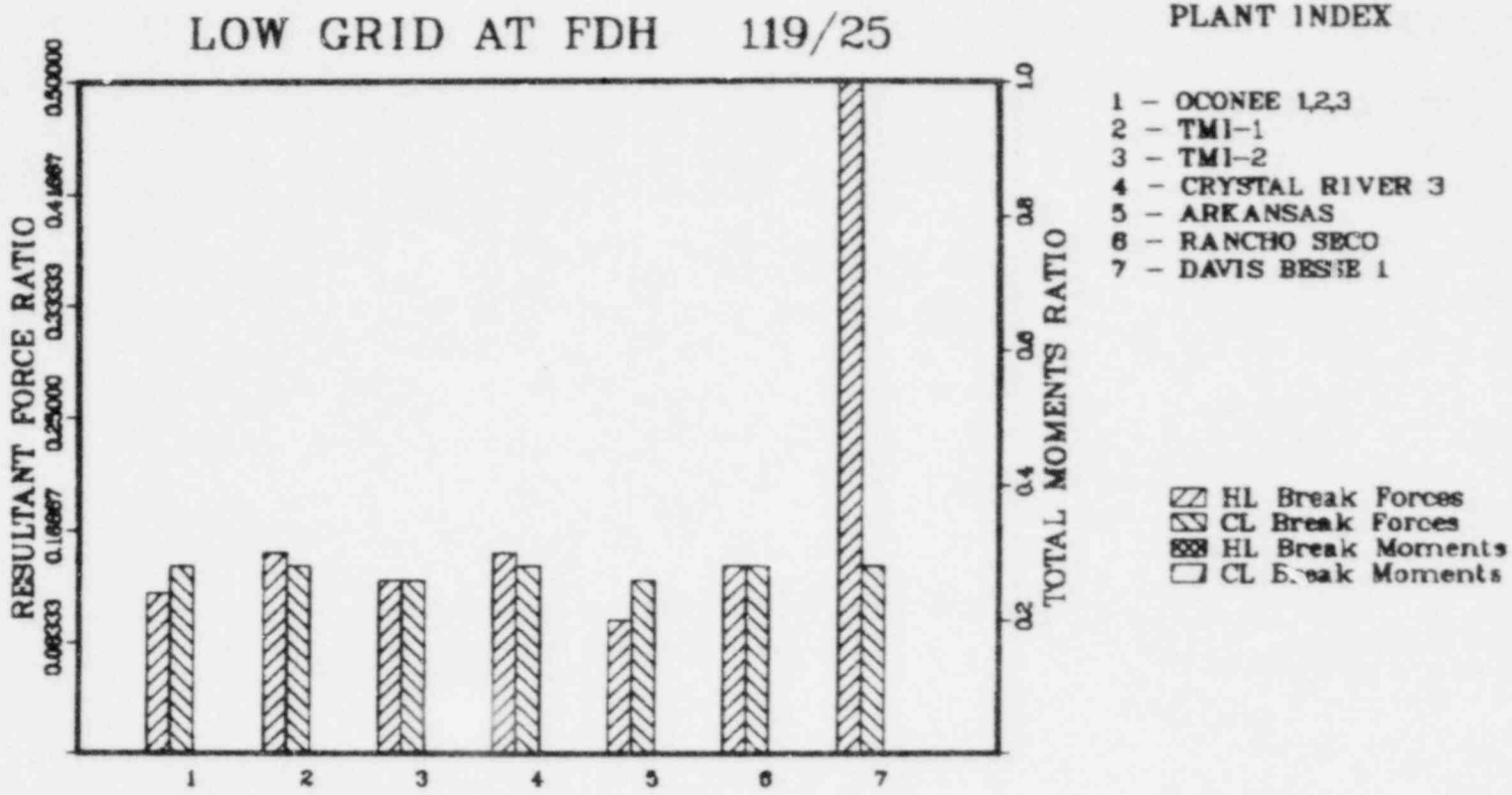

Figure 9.5-16. CR-BBRL at L-Grid 140/13

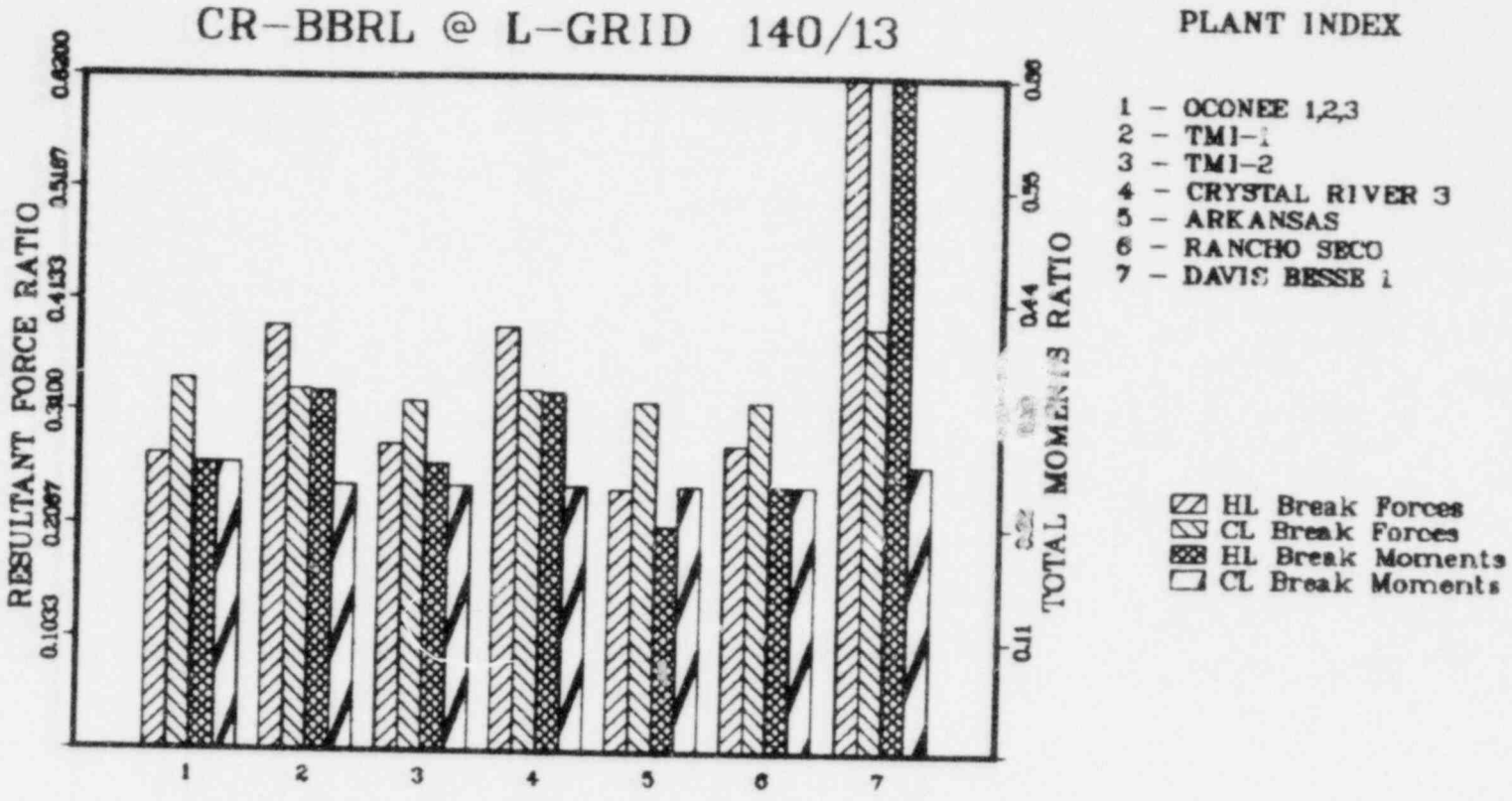

Figure 9.5-17. CRGT at Upper Grid 115/14

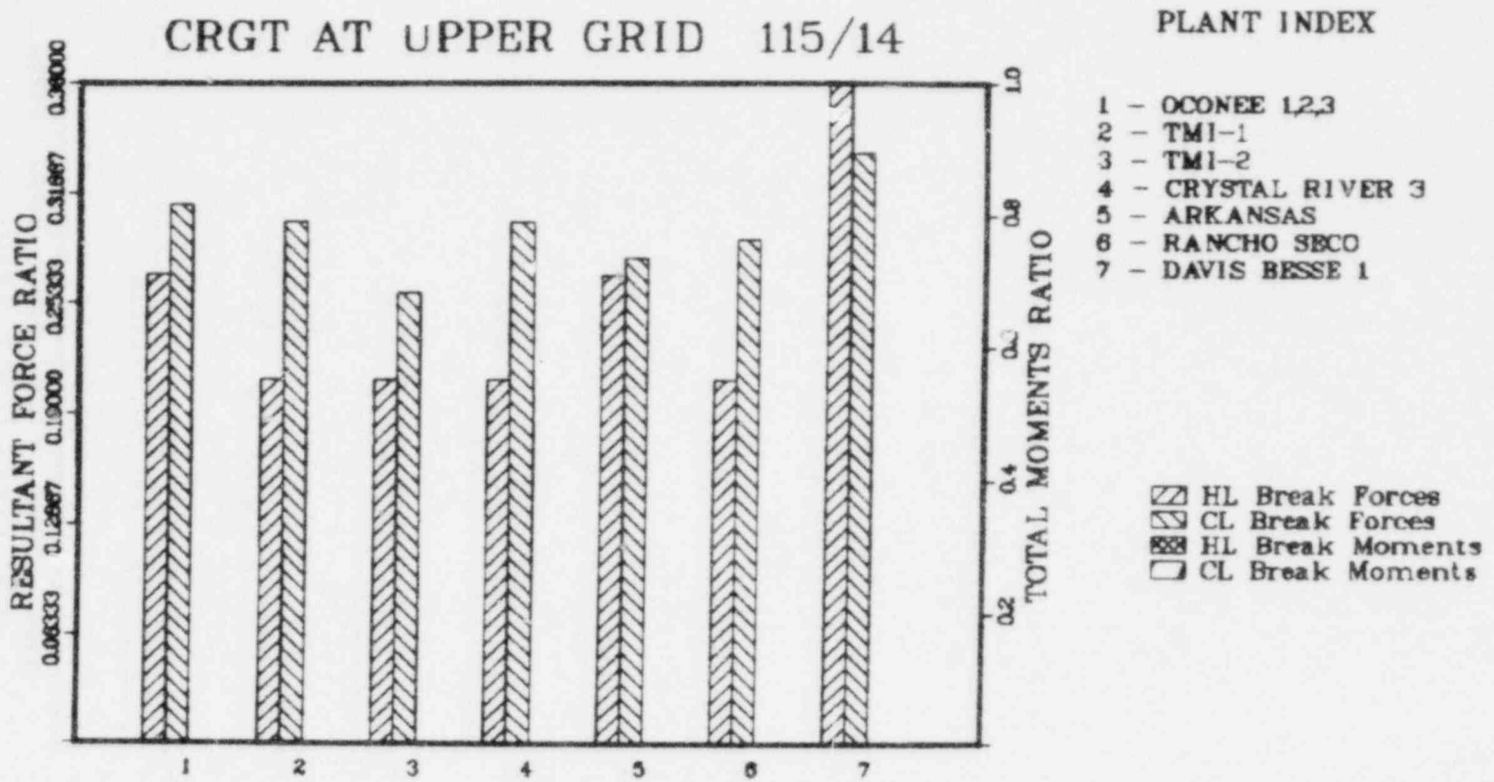

9.6. Fuel Assemblies

Maximum horizontal displacements at the upper and lower grids are presented in Tables 9.6-1 and 9.6-2 along with the vertical forces exerted on each grid by the fuel assemblies. The displacements are also given in bar chart form in Figures 9.6-1 and 9.6-2 to facilitate comparison of break cases and plants.

Table 9.6-1. Upper Grid Peak Forces and Displacements, Joint 14, Figure D-5(a)

LOAD CASE		SYSTEM DYNAMIC RESPONSE ANALYSIS DISPLACEMENTS (INCHES) X	Z	CORE BOUNCE ANALYSIS FORCES (POUNDS) Y
HLG AT RV	OCONEE 1,2 3	.01345	.57927	880.0
HLG AT RV	TMI-1	.03567	.73242	880.0
HLG AT RV	TMI-2	.03496	1.16202	880.0
HLG AT RV	CRYSTAL RIVER 3(a)	.03567	.73242	880.0
HLG AT RV	ANO-1	.03245	.45748	880.0
HLG AT RV	RANCHO SECO	.03332	.61582	880.0
CLG AT RV	OCONEE 1,2,3(a)	.58157	.29147	712.0
CLG AT RV	TMI-1	.50413	.30829	712.0
CLG AT RV	TMI-2	.62359	.31941	712.0
CLG AT RV	CRYSTAL RIVER 3	.50413	.30829	712.0
CLG AT RV	ANO-1	.42307	.22447	712.0
CLG AT RV	RANCHO SECO	.42141	.26064	712.0
HLG AT RV	DAVIS BESSE 1	.00620	.94600	2100.0
HLG AT EL	DAVIS BESSE 1	.00200	.29400	2000.0
CLG AT EL	DAVIS BESSE 1	.05890	.11300	707.0
CLG AT RV	DAVIS BESSE 1	.15900	.24000	704.0

(a)These displacements envelop and are applicable to Midland 1 and 2.

Table 9.6-2. Lower Grid Peak Forces and Displacements, Joint 16, Figure D-5[a]

LOAD CASE	SYSTEM DYNAMIC RESPONSE ANALYSIS DISPLACEMENTS (INCHES) X	Z	CORE BOUNCE ANALYSIS FORCES (POUNDS) Y
HLG AT RV	OCONEE 1,2 3	.00850	.24759	8000.0
HLG AT RV	TMI-1	.03254	.31622	8000.0
HLG AT RV	TMI-2	.03225	.46726	8000.0
HLG AT RV	CRYSTAL RIVER 3[a]	.03254	.31622	8000.0
HLG AT RV	ANO-1	.02891	.19740	8000.0
HLG AT RV	RANCHO SECO	.03129	.27576	8000.0
CLG AT RV	OCONEE 1.2.3[a]	.36431	.16397	6300.0
CLG AT RV	TMI-1	.32219	.17136	6300.0
CLG AT RV	TMI-2	.37343	.16971	6300.0
CLG AT RV	CRYSTAL RIVER 3	.32219	.17136	6300.0
CLG AT RV	ANO-1	.30176	.13996	6300.0
CLG AT RV	RANCHO SECO	.30065	.15690	6300.0
HLG AT RV	DAVIS BESSE 1	.00970	1.14000	2750.0
HLG AT EL	DAVIS BESSE 1	.00150	.29400	6000.0
CLG AT EL	DAVIS BESSE 1	.10400	.15600	3800.0
CLG AT RV	DAVIS BESSE 1	.18300	.28500	2900.0

[a] These displacements envelop and are applicable to Midland 1 and 2.

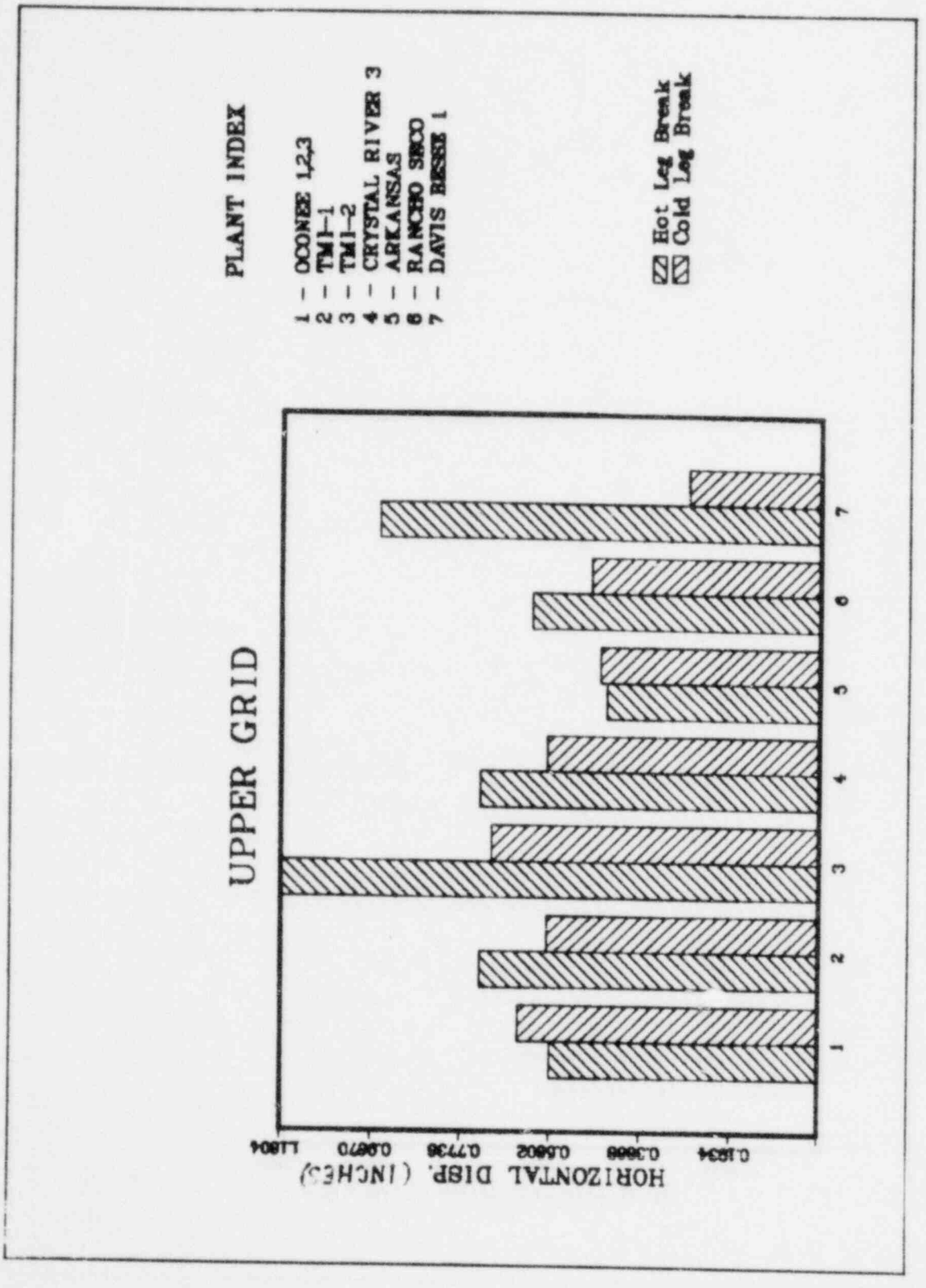

Figure 9.6-1. Upper Grid

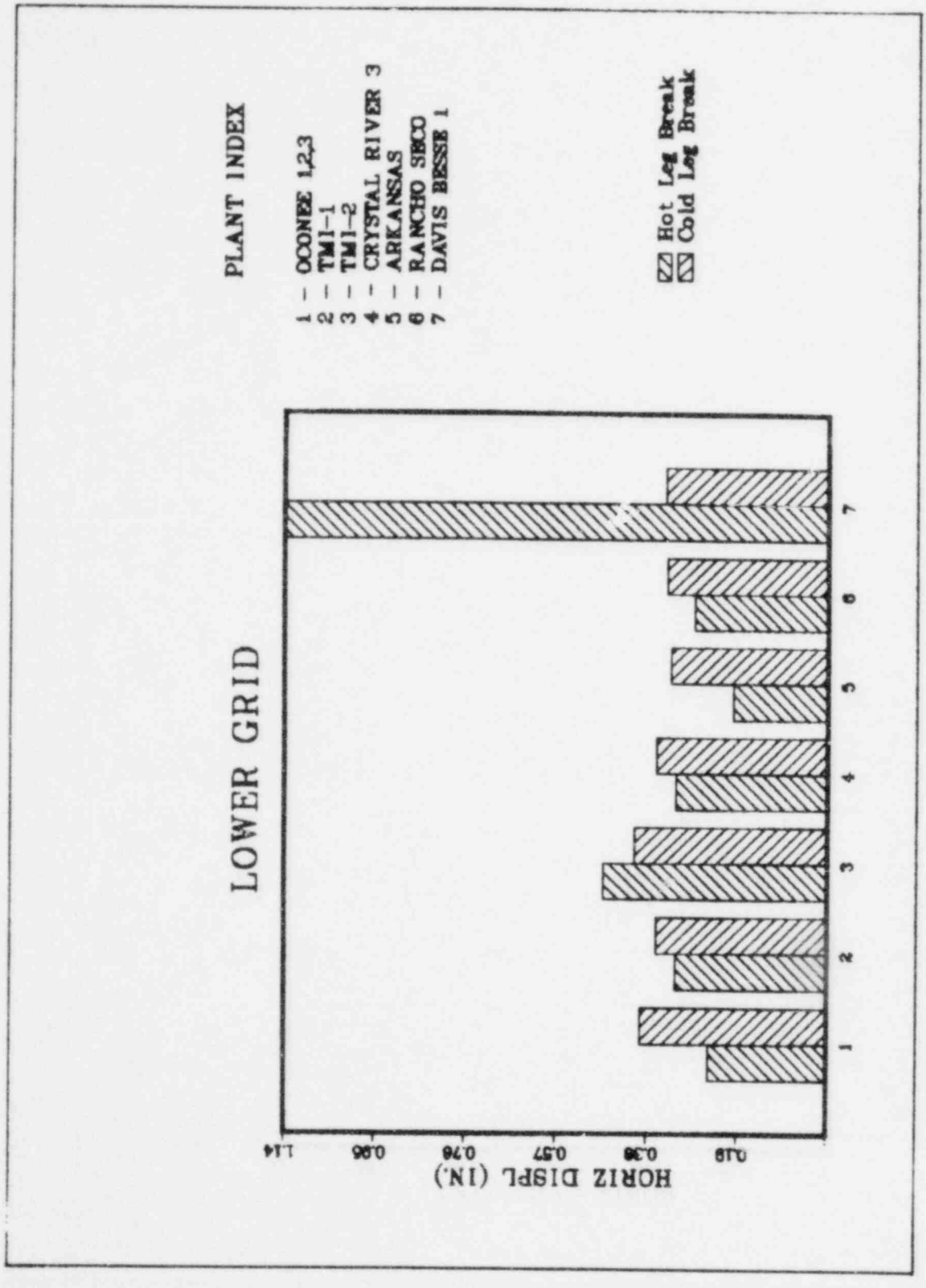

Figure 9.6-2. Lower Grid

9.7. Reactor Coolant Piping

Calculated LOCA moments are presented in Tables 9.7-1 through 9.7-5 for the reactor coolant piping. The maximum data for the hot leg straight and curved sections, cold leg straight and curved sections, and cold leg safe end are presented in tabular form. In addition, the square-root-sum-of-squares of the X, Y, and Z components of moment (designated M_I) are plotted in bar chart form in Figures 9.7-1 through 9.7-5.

Table 9.7-1. Hot Leg Straight Section

Load Case		Moments, ft-kips M_X	M_Y	M_Z	$\sqrt{M_X^2 + M_Y^2 + M_Z^2}$ $M_\perp$, ft-kips
HLG AT RV	OCONEE 1,2 3	2688.0	111.4	279.4	2704.8
HLG AT RV	TMI-1	4702.9	224.1	413.7	4726.4
HLG AT RV	TMI-2	3870.0	419.6	152.8	3895.7
HLG AT RV	CRYSTAL RIVER 3	4702.9	224.1	413.7	4726.4
HLG AT RV	ANO-1	1688.6	99.3	204.2	1703.8
HLG AT RV	RANCHO SECO	2579.9	120.0	349.2	2606.2
CLG AT RV	OCONEE 1,2,3	1488.4	625.0	2587.7	3049.9
CLG AT RV	TMI-1	1252.7	440.0	1945.0	2355.0
CLG AT RV	TMI-2	1178.1	1405.4	1194.2	2188.4
CLG AT RV	CRYSTAL RIVER 3	1252.7	440.0	1945.0	2355.0
CLG AT RV	ANO-1	777.7	299.1	1199.8	1460.8
CLG AT RV	RANCHO SECO	986.5	305.1	1243.8	1616.6
HLG	DAVIS BESSE 1	2673.0	44.4	0.8	2673.4
CLG	DAVIS BESSE 1	56.9	2491.3	114.9	2494.6

Table 9.7-2. Hot Leg Curved Section

Load Case		Moments, ft-kips M_X	M_Y	M_Z	$\sqrt{M_X^2 + M_Y^2 + M_Z^2}$ M_I, ft-kips
HLG AT RV	OCONEE 1,2 3	1539.8	579.6	459.2	1702.9
HLG AT RV	TMI-1	2265.5	1008.9	664.4	2567.4
HLG AT RV	TMI-2	2909.4	734.6	767.4	3097.3
HLG AT RV	CRYSTAL RIVER 3	2265.5	1008.9	664.4	2567.4
HLG AT RV	ANO-1	1249.9	428.8	358.1	1369.1
HLG AT RV	RANCHO SECO	1616.1	580.0	451.0	1775.3
CLG AT RV	OCONEE 1,2,3	445.5	270.3	1526.9	1613.4
CLG AT RV	TMI-1	374.8	199.9	1177.6	1251.9
CLG AT RV	TMI-2	656.2	373.7	1190.2	1409.5
CLG AT RV	CRYSTAL RIVER 3	374.8	199.9	1177.6	1251.9
CLG AT RV	ANO-1	383.2	259.8	831.5	952.5
CLG AT RV	RANCHO SECO	438.2	270.8	823.3	971.2
HLG	DAVIS BESSE 1	1619.0	0.1	4.7	1619.0
CLG	DAVIS BESSE 1	587.7	50.3	78.7	595.1

Table 9.7-3. Cold Leg Straight Section

Load Case		Moments, ft-kips M_X	M_Y	M_Z	$\sqrt{M_X^2 + M_Y^2 + M_Z^2}$ M_T, ft-kips
HLG AT RV	OCONEE 1,2 3	875.2	440.2	469.2	1086.2
HLG AT RV	TMI-1	1110.4	614.7	542.3	1380.2
HLG AT RV	TMI-2	1828.3	709.7	889.4	2153.5
HLG AT RV	CRYSTAL RIVER 3	1110.4	614.7	542.3	1380.2
HLG AT RV	ANO-1	694.7	356.6	422.8	888.0
HLG AT RV	RANCHO SECO	948.4	443.8	501.8	1161.1
CLG AT RV	OCONEE 1,2,3	431.1	961.2	508.1	1169.6
CLG AT RV	TMI-1	488.6	770.3	419.2	1003.9
CLG AT RV	TMI-2	882.0	625.0	419.9	1159.7
CLG AT RV	CRYSTAL RIVER 3	488.6	770.3	419.2	1003.9
CLG AT PV	ANO-1	351.8	677.2	324.7	829.3
CLG AT RV	RANCHO SECO	411.3	703.5	328.5	878.6
HLG	DAVIS BESSE 1	430.3	5703.2	372.7	5731.5
CLG	DAVIS BESSE 1	247.3	2475.2	192.7	2495.0

Table 9.7-4. Cold Leg Curved Section

Load Case		Moments, ft-kip			$\sqrt{M_X^2 + M_Y^2 + M_Z^2}$
		M_X	M_Y	M_Z	M_I, ft-kips
HLG AT RV	OCONEE 1,2 3	686.2	212.7	192.1	743.6
HLG AT RV	TMI-1	910.5	316.9	291.5	1007.2
HLG AT RV	TMI-2	1425.7	375.3	371.2	1520.3
HLG AT RV	CRYSTAL RIVER 3	910.5	316.9	291.5	1007.2
HLG AT RV	ANO-1	546.3	173.0	173.4	598.7
HLG AT RV	RANCHO SECO	757.6	247.7	230.8	829.8
CLG AT RV	OCONEE 1,2,3	633.8	324.3	198.4	739.1
CLG AT RV	TMI-1	628.4	339.0	153.5	730.3
CLG AT RV	TMI-2	746.1	343.5	217.2	849.6
CLG AT RV	CRYSTAL RIVER 3	628.4	339.0	153.5	730.3
CLG AT RV	ANO-1	482.5	300.0	139.6	585.1
CLG AT RV	RANCHO SECO	516.0	313.5	143.7	620.6
HLG	DAVIS BESSE 1	177.5	5461.5	790.8	5521.3
CLG	DAVIS BESSE 1	234.4	2245.1	205.6	2266.6

Table 9.7-5. Cold Leg Safe End

Load Case		Moments, ft-kips M_X	M_Y	M_Z	$\sqrt{M_X^2 + M_Y^2 + M_Z^2}$ M_I, ft-kips
HLG AT RV	OCONEE 1,2 3	628.9	173.7	115.9	662.7
HLG AT RV	TMI-1	812.0	252.0	145.8	862.6
HLG AT RV	TMI-2	1282.1	334.9	188.4	1338.4
HLG AT RV	CRYSTAL RIVER 3	812.0	252.0	145.8	862.6
HLG AT RV	ANO-1	502.9	149.8	98.4	533.9
HLG AT RV	RANCHO SECO	680.0	194.5	126.9	718.6
CLG AT RV	OCONEE 1,2,3	497.7	128.0	120.5	527.8
CLG AT RV	TMI-1	482.4	116.1	121.8	510.9
CLG AT RV	TMI-2	565.8	159.0	103.8	596.8
CLG AT RV	CRYSTAL RIVER 3	482.4	116.1	121.8	510.9
CLG AT RV	ANO-1	385.9	103.5	110.5	414.5
CLG AT RV	RANCHO SECO	407.6	108.9	124.5	439.9
HLG	DAVIS BESSE 1	348.1	2851.5	218.0	2880.9
CLG	DAVIS BESSE 1	10.7	870.2	108.7	877.0

Figure 9.7-1. Hot Leg Straight Section

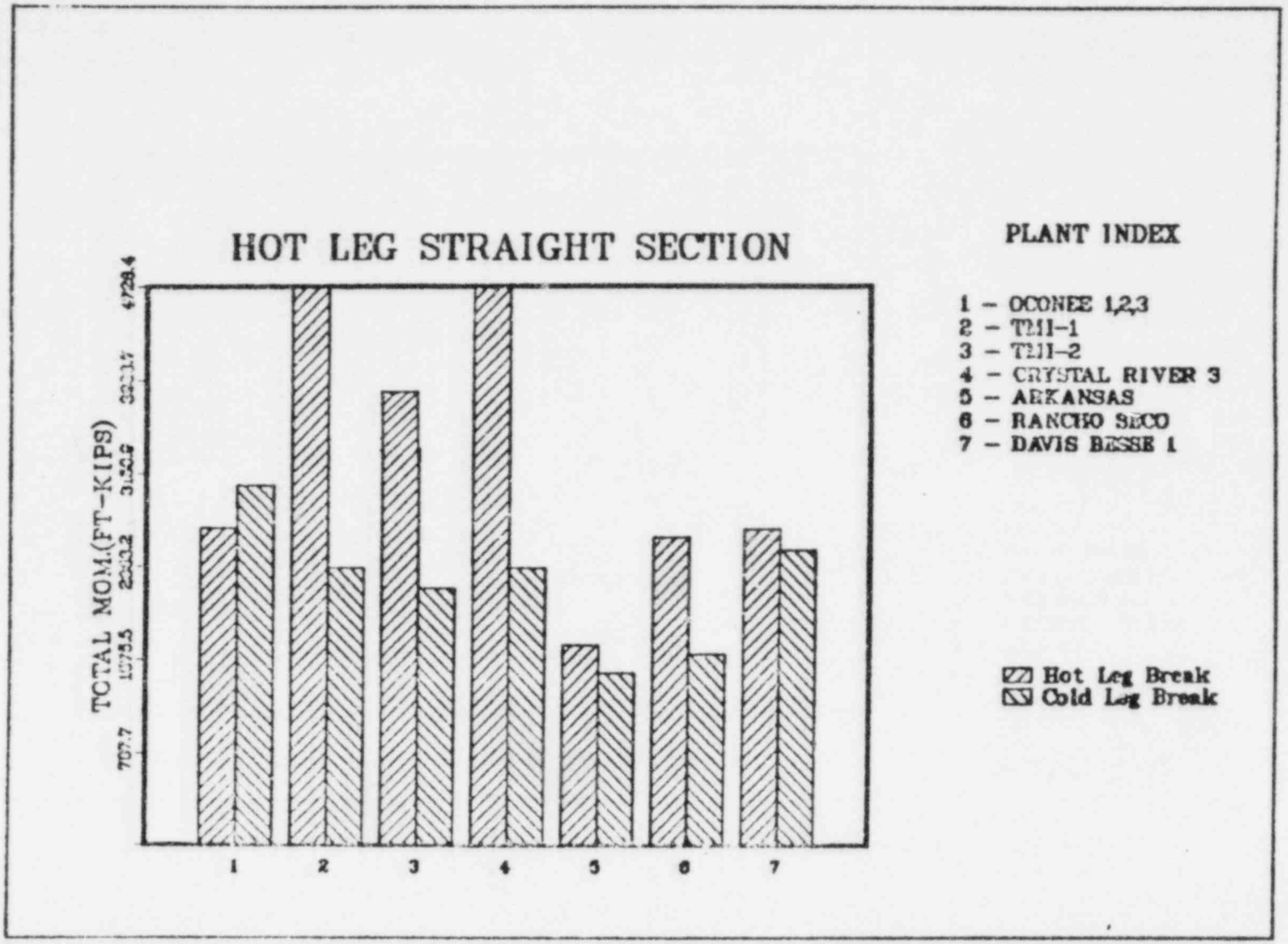

Figure 9.7-2. Hot Leg Curved Section

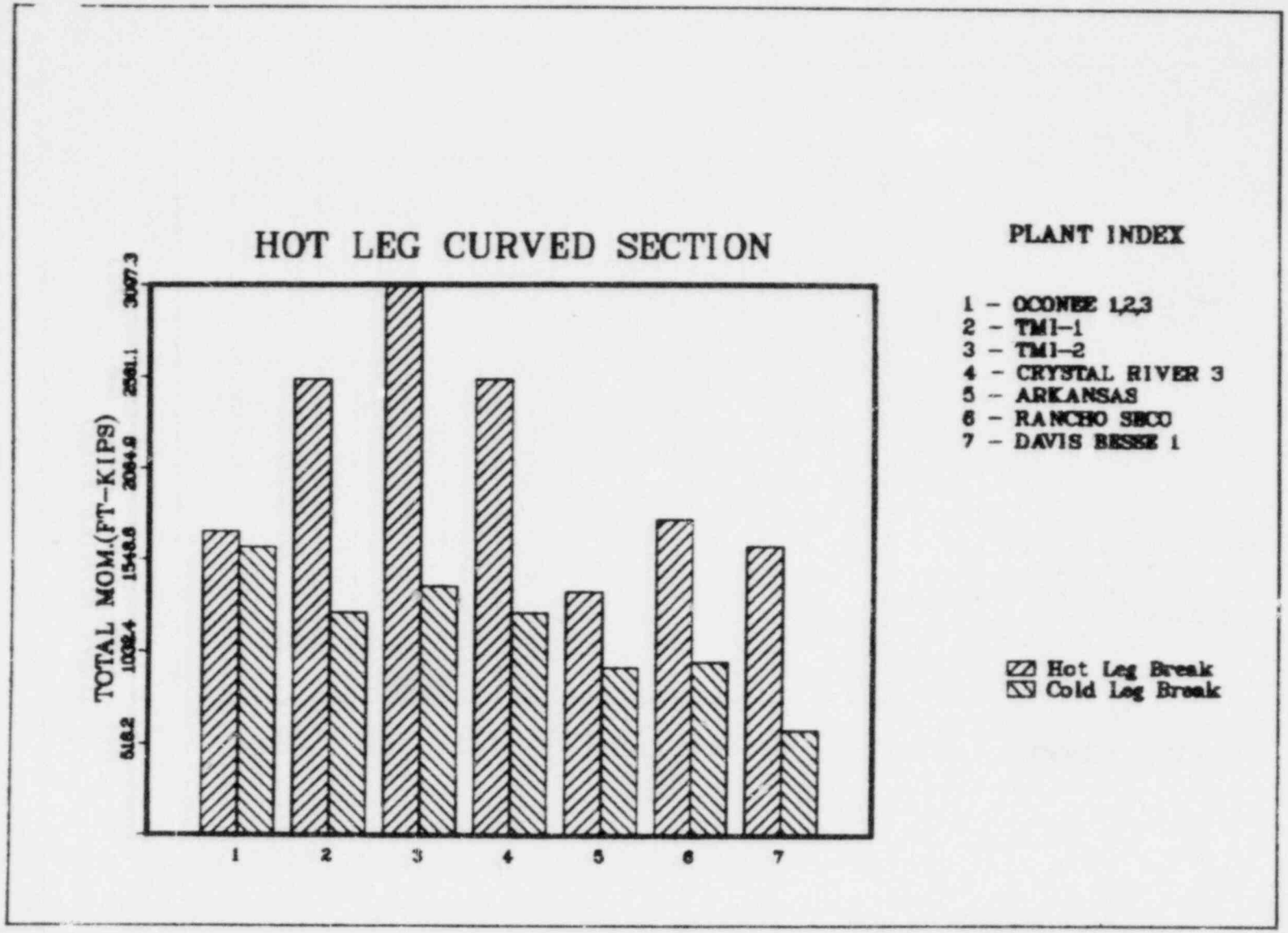

Figure 9.7-3. Cold Leg Straight Section

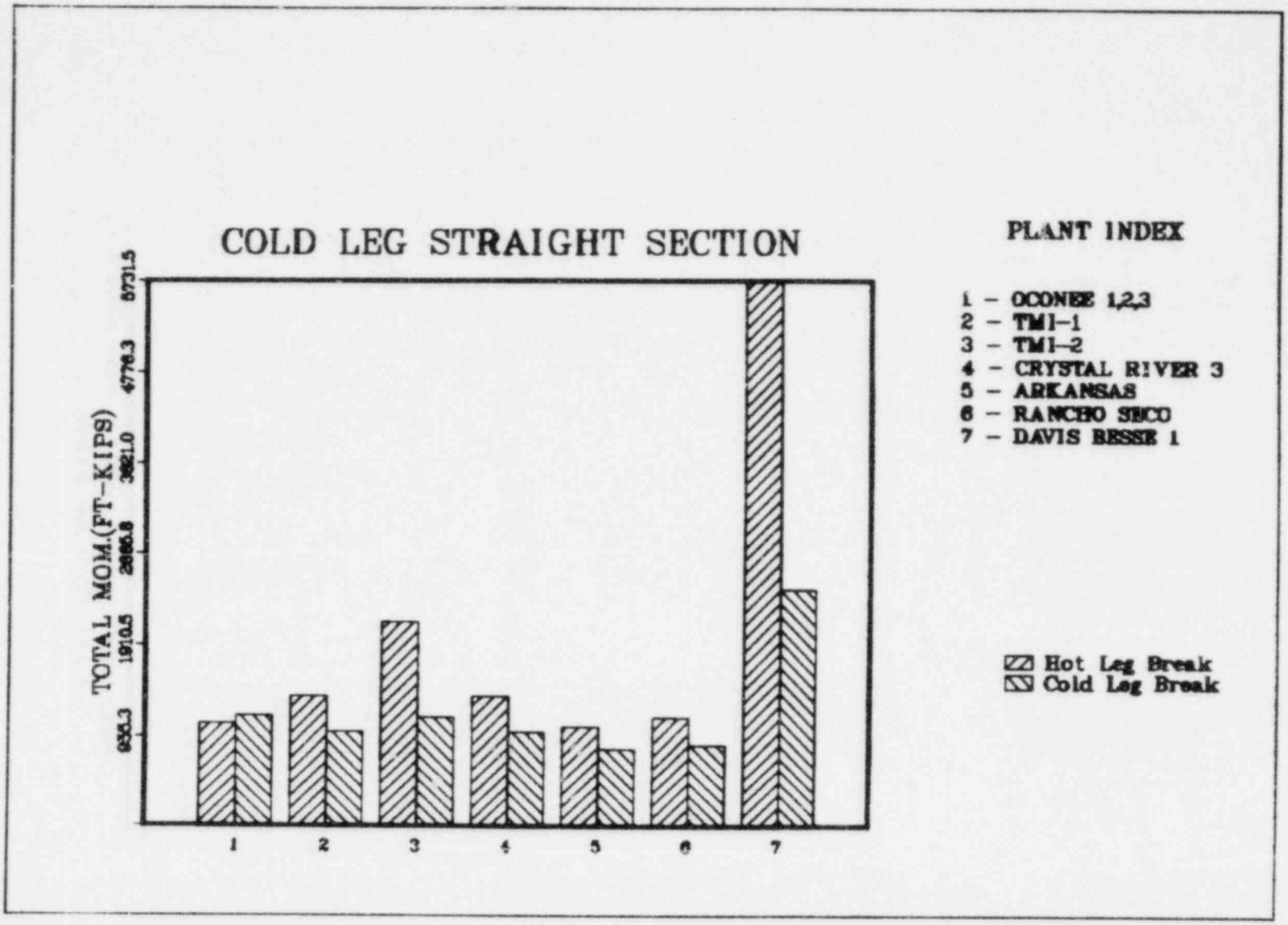

Figure 9.7-4. Cold Leg Curved Section

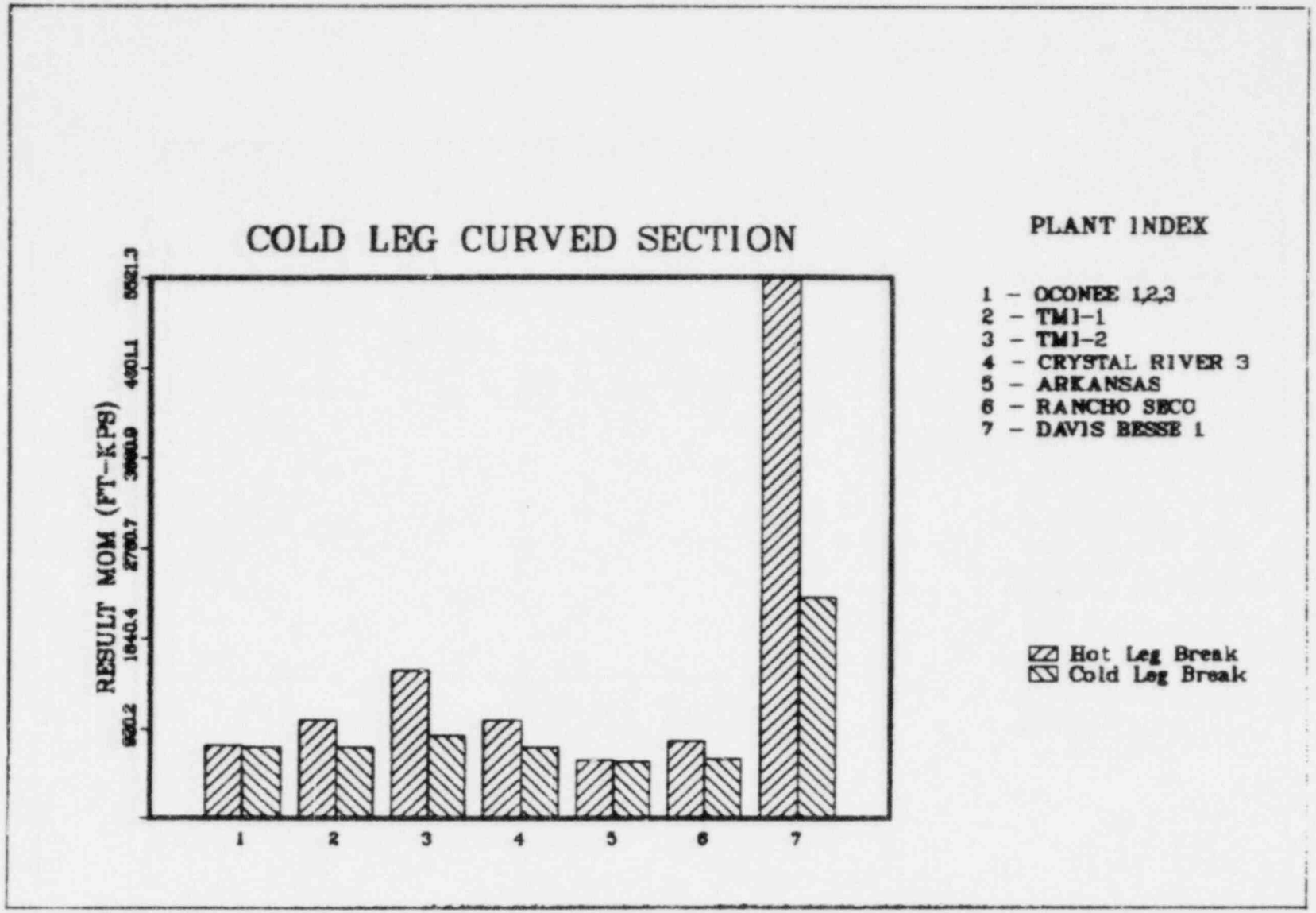

Figure 9.7-5. Cold Leg Safe End

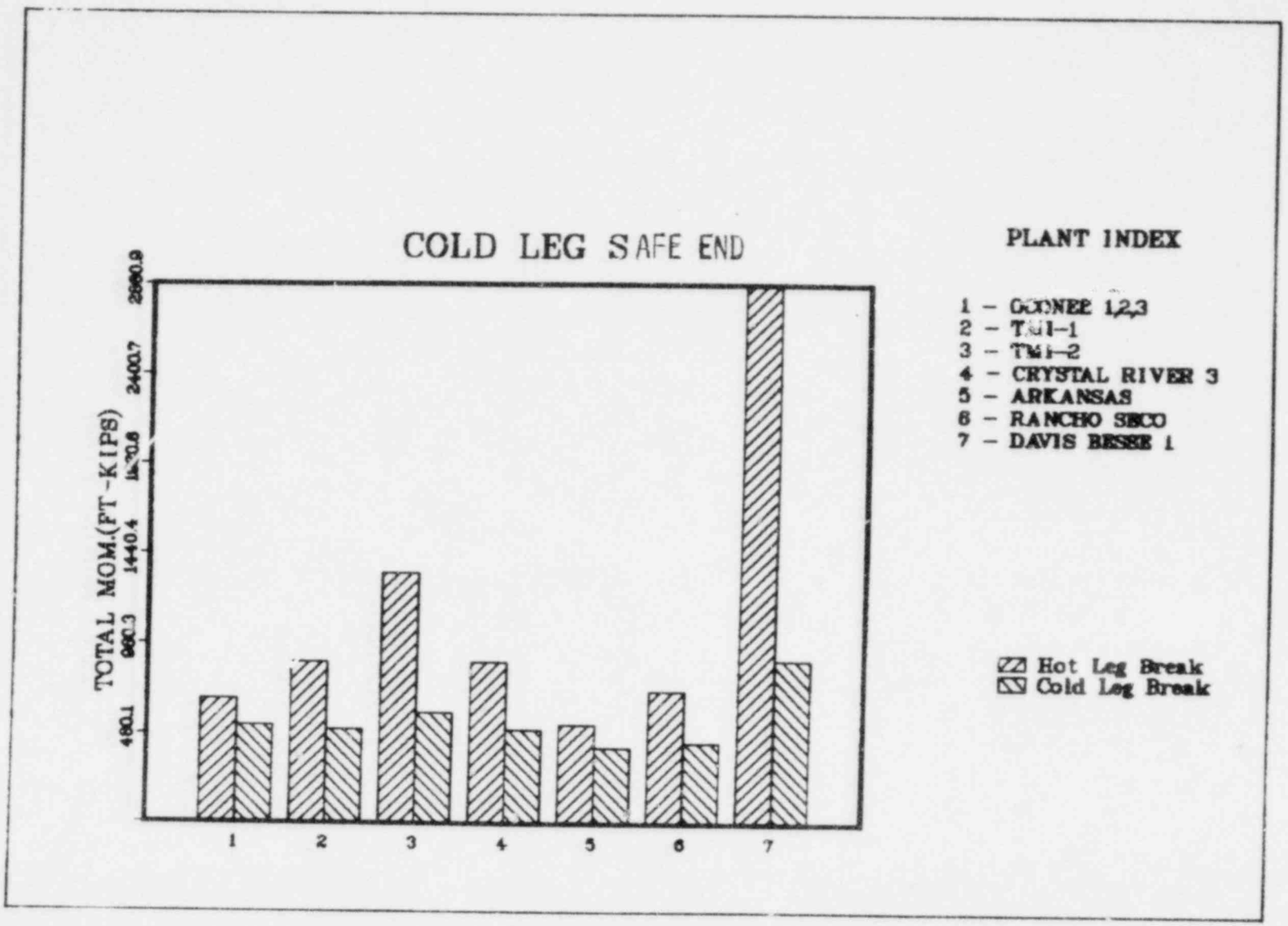

9.8. Pipe Whip Restraints and Embedments

Tables 9.8-1 through 9.8-7 summarize peak as built pipe whip restraint loads for all plants. The figure references are to Appendix B since the loads came from the pipe whip analyses. Figure 9.8-1 summarizes the pipe whip restraint loads excluding friction for every reference.

It should be noted that the term "load description" in the table refers to the load on the physical restraint and not to the mathematical model's representation of the restraint.

The time of initial impact for all restraints except the LOCA rings on Davis-Besse 1 varies from 0.014 to 0.073 second. The LOCA rings were impacted as early as 0.005 second. The detailed time history information has been supplied for stress analysis where necessary.

For TMI-1 and CR-III, the as-built restraints were overstressed. Section 12 addresses the problem by modifying the whip restraints to reduce the gap between the pipe and the restraint. Section 12 also presents whip restraint loads based on the modified restraint system.

Table 9.8-1. Summary of Pipe Whip Restraint Loads for Oconee

Break type	Restraint (see Figure B-1)	Peak load, lb	Load description
Hot leg guill. at RV	No. 1, bar 3	4,555,600	Compression
	bar 4	391,680	Compression
	bars 3, 4	1,828,500	Friction upward
	bars 7, 8	-18,490	X-direction
	bars 7, 8	+3,607	X-direction
	bars 7, 8	1,083,100	Upward
	bars 7, 8	5,098,300	Compression
	No. 2,	452,830	Tensile
Hot leg guill. at elbow	No. 1, bar 3	4,284,770	Compression
	bar 4	368,388	Compression
	bars 3, 4	1,656,570	Upward
	bars 7, 8	-10,800	X-direction
	bars 7, 8	+1,210	X-direction
	bars 7, 8	1,094,240	Upward
	bars 7, 8	4,548,810	Compression
	No. 2	534,268	Tensile
Cold leg guill. at RV	No. 2[a]	2,400,000	Compression

[a] See Figure B-9.

Table 9.8-2. Summary of Pipe Whip Restraint Loads for TMI-1 — As-Built[a]

Break type	Restraint (see Figure B-2)	Peak load, lb	Load description
Hot leg guill. at RV	No. 1, bar 1	2,533,810	Tension
	bar 2	2,513,110	Tension
	bar 3	2,275,870	Tension
	bar 4	868,406	Tension
	bar 5	NI	--
	bar 6	NI	--
	bar 7	NI	--
	Sum	8,161,230	Tension
	Collar	NI	--
	No. 2	NI	--
Hot leg guill. at elbow	No. 1, bar 1	2,543,340	Tension
	bar 2	2,519,150	Tension
	bar 3	2,261,450	Tension
	bar 4	544,007	Tension
	bar 5	NI	--
	bar 6	NI	--
	bar 7	NI	--
	Sum	7,718,890	Tension
	Collar	NI	--
	No. 2	NI	--

Note: NI: not impacted.

(a) See section 12 for restraint loads based on modified restraints.

Table 9.[illegible]-3. Summary of Pipe Whip Restraint Loads for TMI-2

Break type	Restraint (see Figure B-3)	Peak load, lb	Load description
Hot leg guill. at RV	No. 1, bar 1	1,036,410	Tension
	bar 2	982,897	Tension
	bar 3	903,937	Tension
	bar 4	849,209	Tension
	bar 5	820,308	Tension
	bar 6	711,549	Tension
	bar 7	NI	--
	Sum	5,096,010	Tension
	No. 2	NI	--
Hot leg guill. at elbow	No. 1, bar 1	1,063,320	Tension
	bar 2	1,001,490	Tension
	bar 3	915,933	Tension
	bar 4	856,184	Tension
	bar 5	821,609	Tension
	bar 6	130,095	Tension
	bar 7	NI	--
	Sum	4,541,330	Tension
	No. 2	NI	--

Note: NI: not impacted.

Table 9.8-4. Summary of Pipe Whip Restraint Loads for Crystal River – As-Built[a]

Break type	Restraint (see Figure B-5)	Peak load, lb	Load description
Hot leg guill. at RV	No. 1, bar 1	792,878	Tension
	bar 2	776,764	Tension
	bar 3	761,104	Tension
	bar 4	711,676	Tension
	bar 5	697,932	Tension
	bar 6	476,943	Tension
	bar 7	50,679	Tension
	bar 8	34,371	Tension
	Sum	4,212,710	Tension
	No. 2 & 3	NI	--
Hot leg guill. at elbow	No. 1, bar 1	777,953	Tension
	2	764,165	Tension
	3	750,694	Tension
	4	707,655	Tension
	5	695,471	Tension
	bar 6	346,136	Tension
	bar 7	51,329	Tension
	bar 8	37,120	Tension
	Sum	4,029,000	Tension
	No. 2 & 3	NI	--

Note: NI: not impacted.

(a) See section 12 for restraint loads based on shimmed restraints.

Table 9.8-5. Summary of Pipe Whip Restraint Loads for ANO-1

Break type	Restraint (see Figure B-4)	Peak load, lb	Load description
Hot leg guill. at RV	No. 1	3,411,600	Tension
	No. 2, 3, 4	NI	--
Hot leg guill. at elbow	No. 1 sum	3,402,400	Tension
	No. 2, 3, 4	NI	--

Note: NI: not impacted.

Table 9.8-6. Summary of Pipe Whip Restraint Loads for Rancho Seco

Break type	Restraint (see Figure B-6)	Peak load, lb	Load description
Hot leg guill. at RV	No. 2 sum	440,234	Tension
	No. 3 sum	4,419,540	Tension
	No. 1 & 4	NI	--
Hot leg guill. at elbow	No. 3 sum	4,282,560	Tension
	No. 2 sum	399,352	Tension
	No. 1 & 4	NI	--

Note: NI: not impacted.

Table 9.8-7. Summary of Pipe Whip Restraint Loads for Davis-Besse 1

Break type	Restraint (see Figure B-7)	Peak load, lb	Load description
Hot leg guill. at RV	LOCA ring	1,248,120	Downward
	Friction	524,211	Away from RV
	Strap	2,771,530	Tension
	No. 1	630,040	Tension
	No. 1 friction	181,023	Upward
Hot leg guill. at elbow	Strap	2,805,380	Tension
	No. 1	620,803	Tension
	No. 1 friction	251,932	Upward
	(see Figure B-8)		
Cold leg guill. at RV	LOCA ring	801,470	Normal-1[a]
		336,617	Away from RV
	LOCA ring	782,294	Normal-2[a]
		328,563	Away from RV
	Coolant pump	65,828	Normal-3[a]
Cold leg guill. at elbow	Discharge	1,724,610	Normal-4[a]
		689,844	Away from RV
	Coolant pump	638,811	Normal-5[a]
	Coolant pump	133,964	Normal-6[a]

[a]Refer to section view for force orientation.

Figure 9.8-1. Pipe Whip Restraint Loads

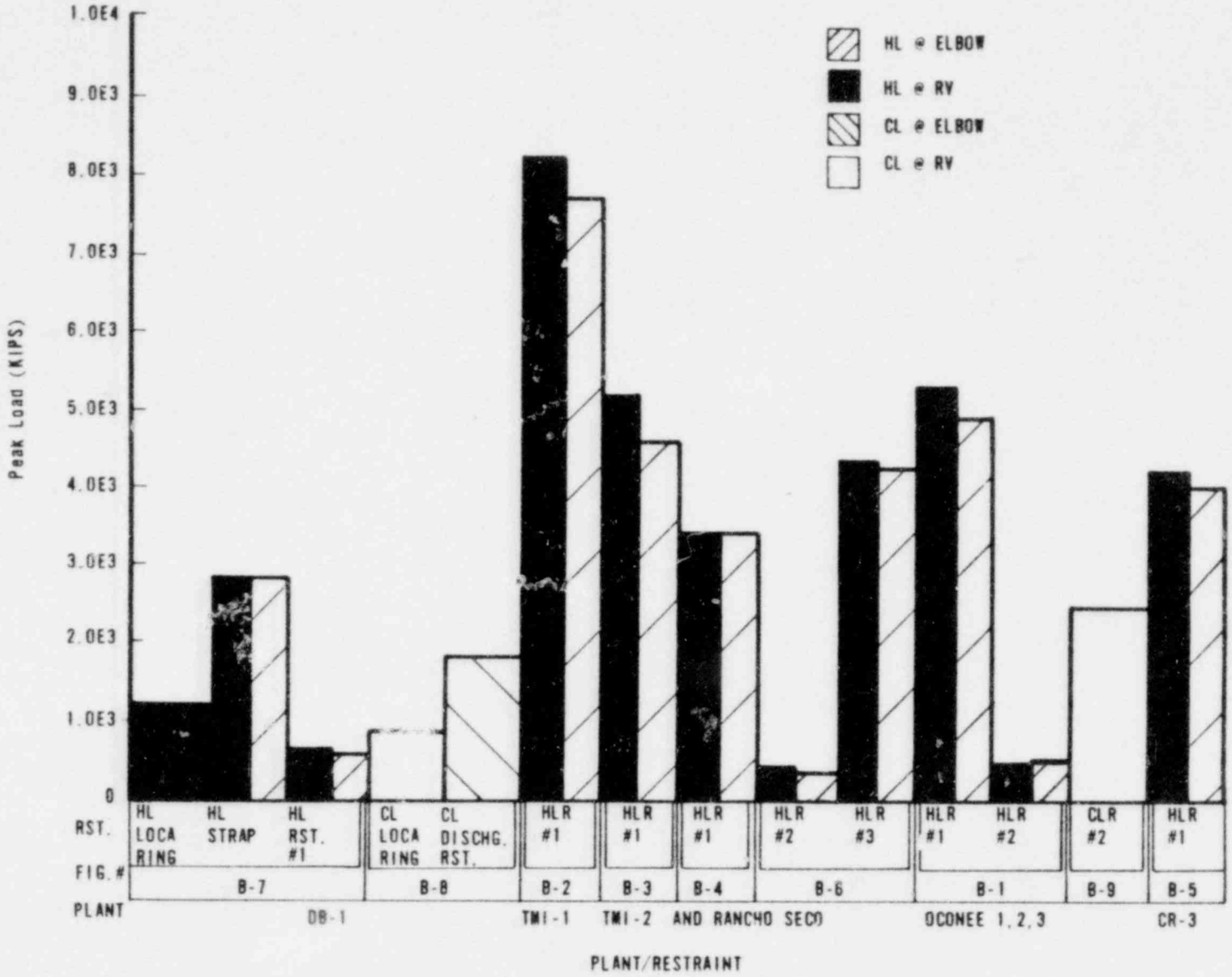

9.9. Core Flood Line Piping

As discussed in Section 5.1.8, the forcing functions used for analysis of the core flood lines were developed from the calculated response of the reactor vessel at the core flood line nozzle elevation. The response of all plants was similar, with only the relative magnitude of the loads varying from plant to plant. Table 9.9-1 provides the peak acceleration and displacement inputs for all plants for comparison. The actual time history and response spectrum input data are provided in Figures 9.9-1 to 9.9-21 for the TMI-1 and Crystal River plants which experience the maximum accelerations.

Figures 9.9-1 to 9.9-5 give the time history response calculated from the reactor vessel model for 0.3 seconds. Figures 9.9-6 to 9.9-11 give time history data for 0.9 seconds developed from the reactor vessel response for use as input in the core flood line analysis. Figures 9.9-12 to 9.9-21 give the response spectra which correspond to the 0.9 seconds time histories.

Table 9.9-1. Maximum Reactor Vessel Response at the Core Flood Nozzle

Plant	Break	Maximum Acceleration, g			Maximum Displacement, inches		
		X	Y	Z	X	Y	Z
Oconee	HL	1.34	9.26	10.88	0.016	0.028	0.676
	CL	11.38	13.05	7.37	0.657	0.235	0.330
TMI-1	HL	2.16	6.90	16.84	0.039	0.041	0.874
	CL	11.58	12.87	6.96	0.578	0.212	0.351
Crystal River	HL	2.16	6.90	16.84	0.039	0.041	0.874
	CL	11.58	12.87	6.96	0.578	0.212	0.351
ANO-1	HL	1.20	9.37	8.09	0.032	0.028	0.540
	CL	7.09	12.20	3.81	0.485	0.172	0.254
Rancho Seco	HL	1.10	6.91	10.81	0.032	0.032	0.732
	CL	7.12	12.46	3.48	0.483	0.151	0.292
Davis-Besse	HL	0.66	8.26	10.91	0.005	0.196	0.874
	CL	3.55	4.02	3.41	0.157	0.084	0.245
	HL elbow	0.72	6.09	10.00	0.000	0.044	0.249
	CL elbow	4.53	5.20	2.74	0.095	0.047	0.132

Figure 9.9-1. Displacement Time-History at the Reactor Vessel Centerline for TMI-1 Hot-Leg Break

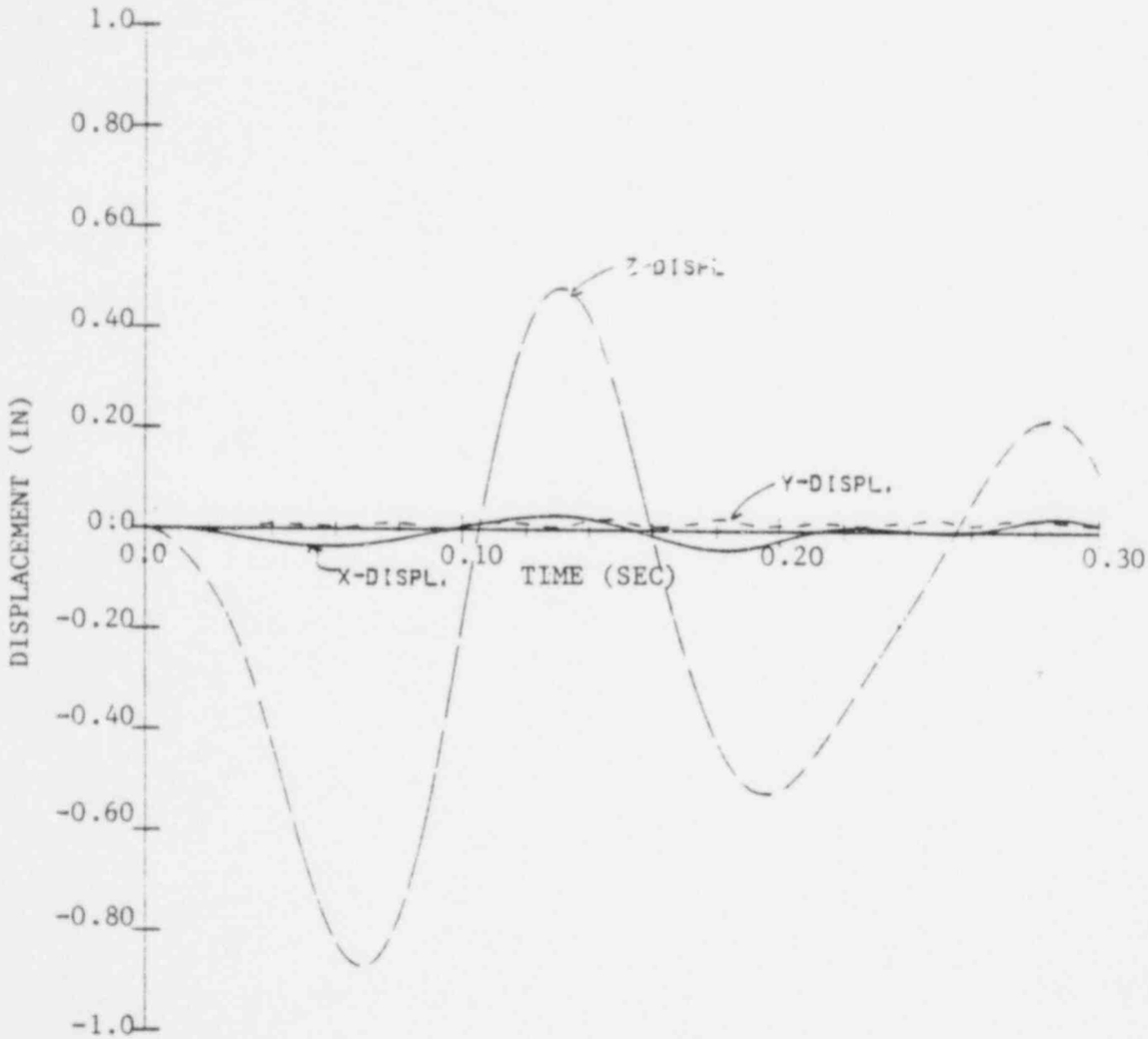

Figure 9.9-2. Acceleration Time-History at the Reactor Vessel Centerline for TMI-1 Hot-Leg Break

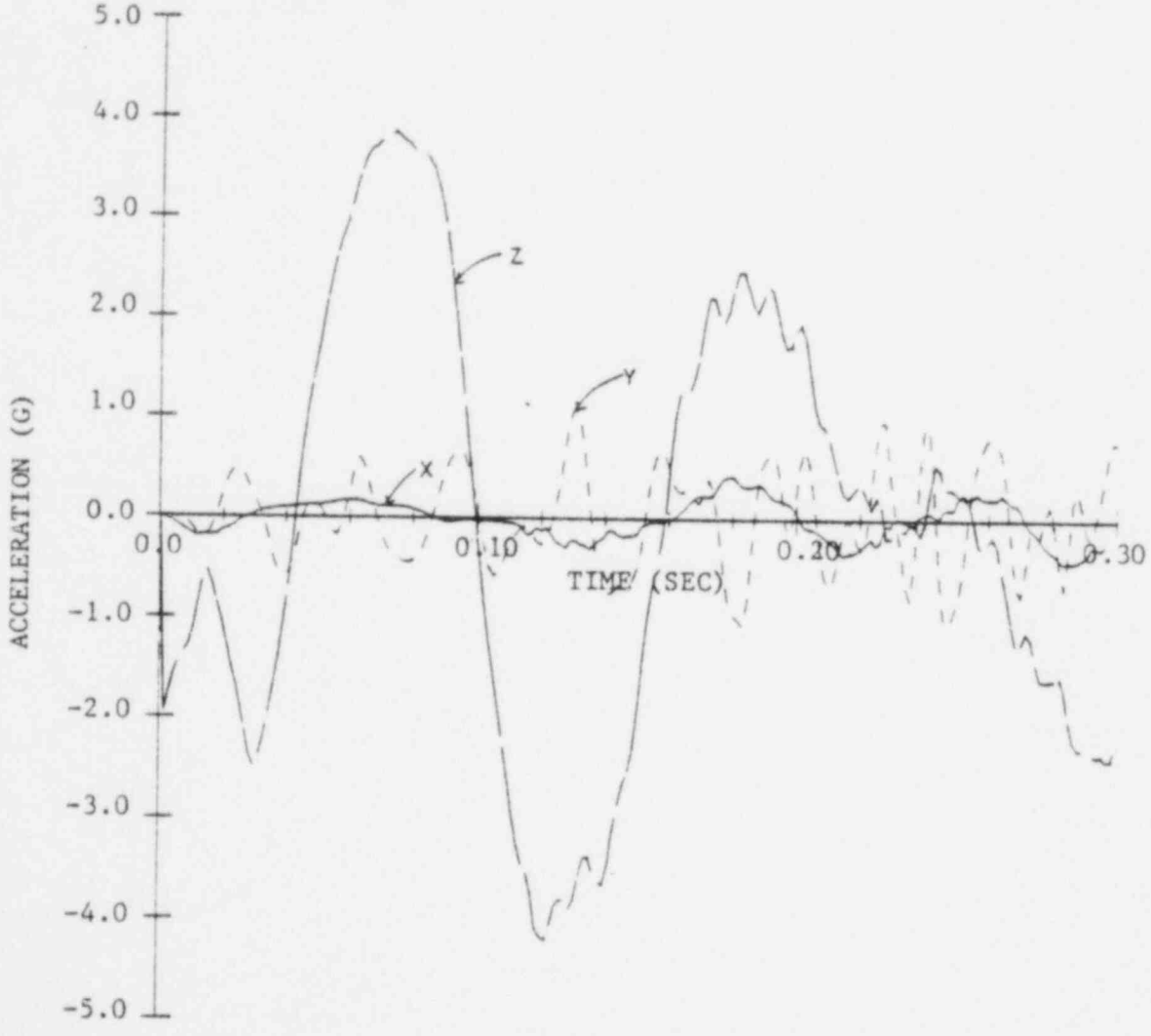

Figure 9.9-3. Displacement Time-History at the Reactor Vessel Centerline for TMI-1 Cold-Leg Break

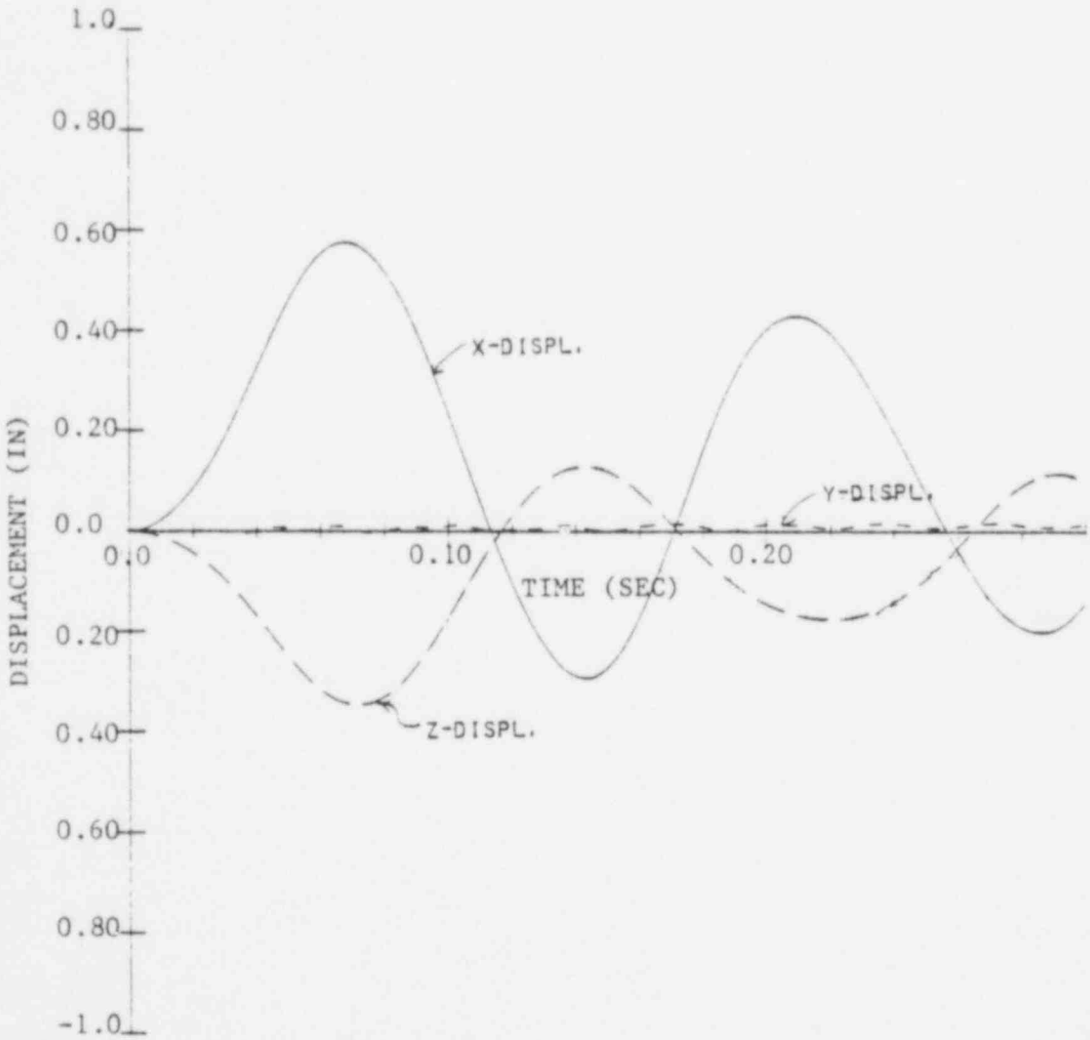

Figure 9.9-4. Rotational Time-History at the Reactor Vessel Centerline for TMI-1 Cold-Leg Break

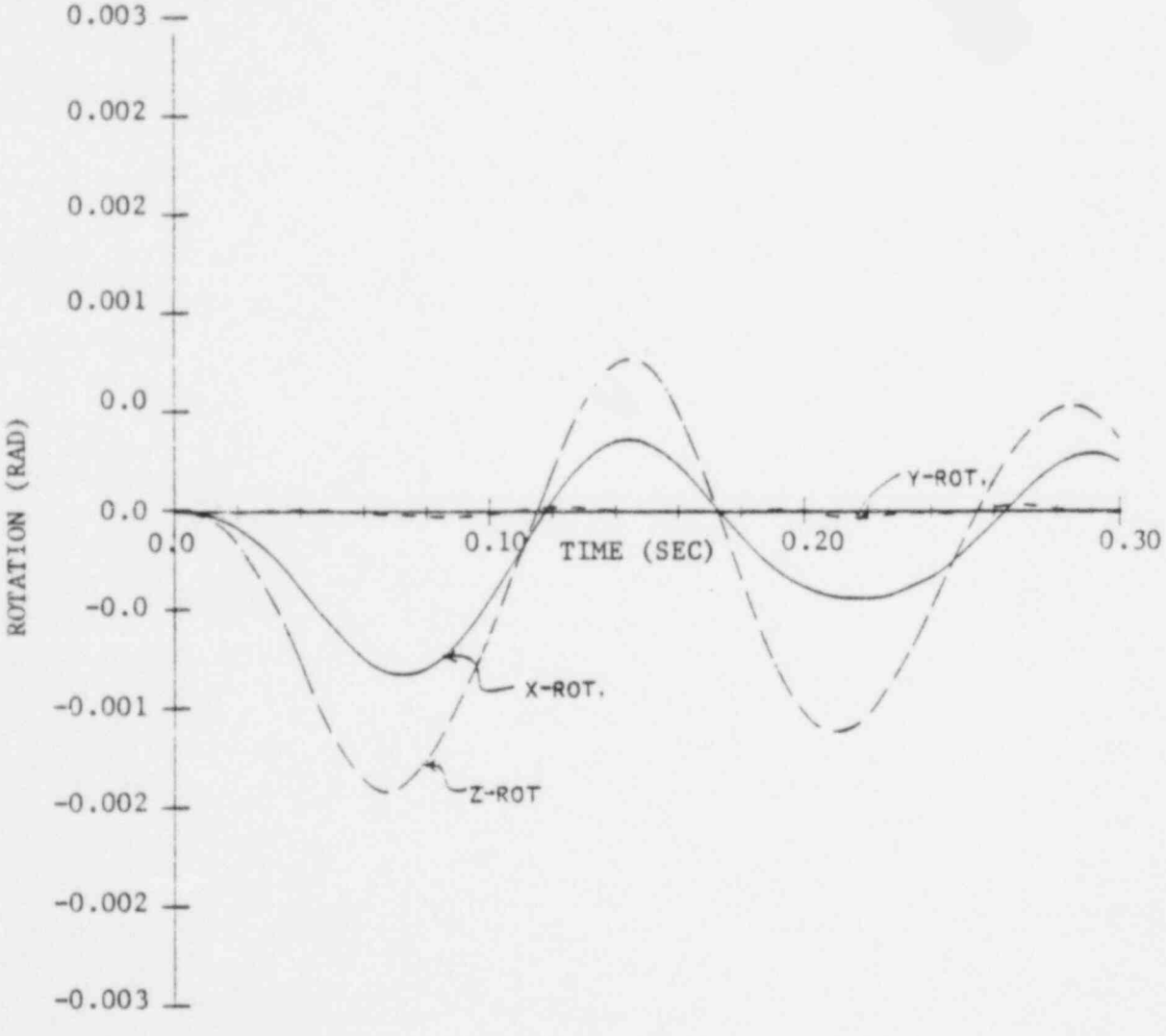

Figure 9.9-5. Acceleration Time-History at the Reactor Vessel Centerline for TMI-1 Cold-Leg Break

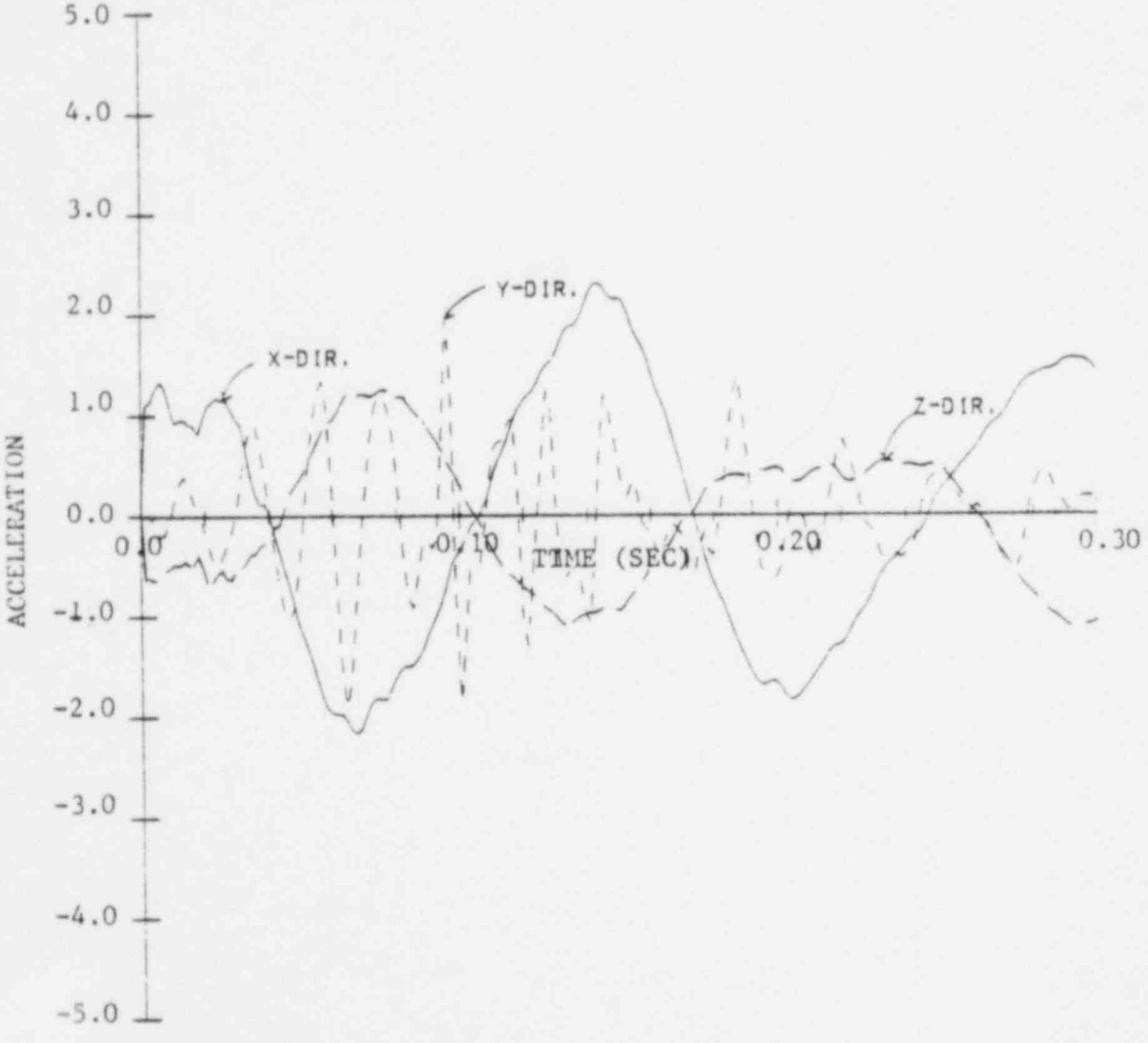

Figure 9.9-6. Extended Displacement Time-History at the CFL Nozzle for TMI-1 Hot-Leg Break

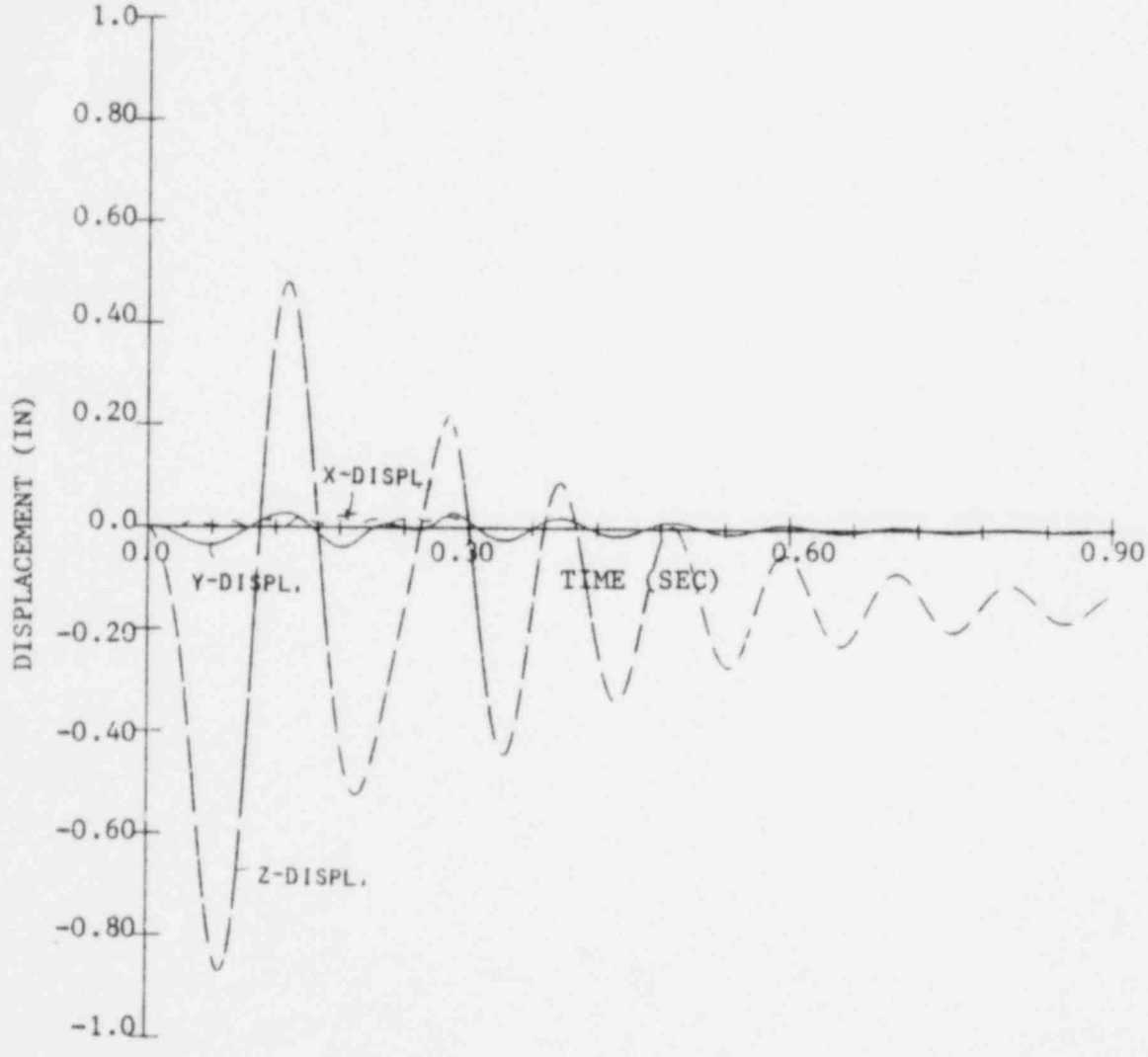

Figure 9.9-7. Extended Acceleration Time-History at the CFL Nozzle for TMI-1 Hot-Leg Break (Positive Rotation)

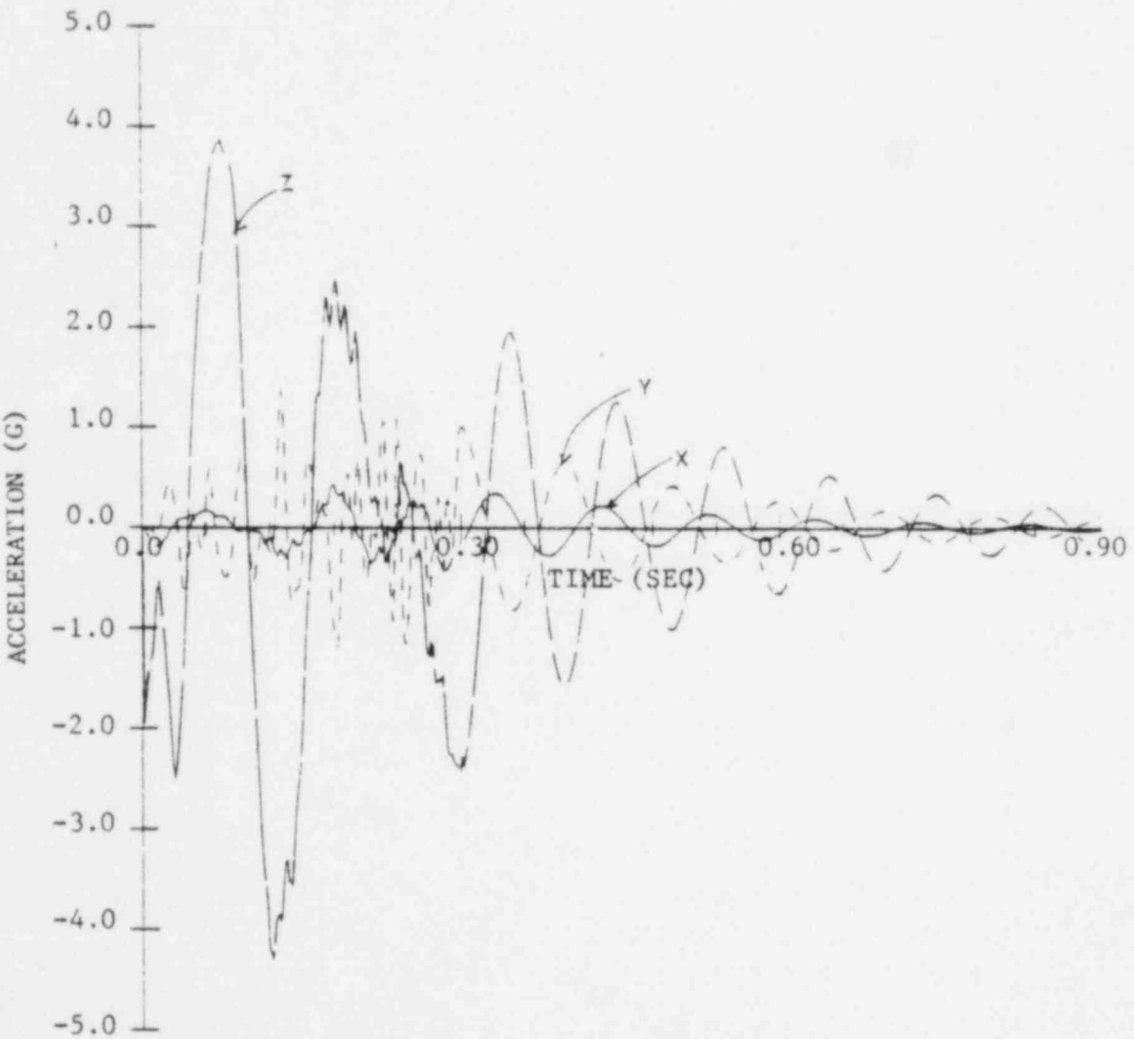

Figure 9.9-8. Extended Acceleration Time-History at the CFL Nozzle for TMI-1 Hot-Leg Break (Negative Rotation)

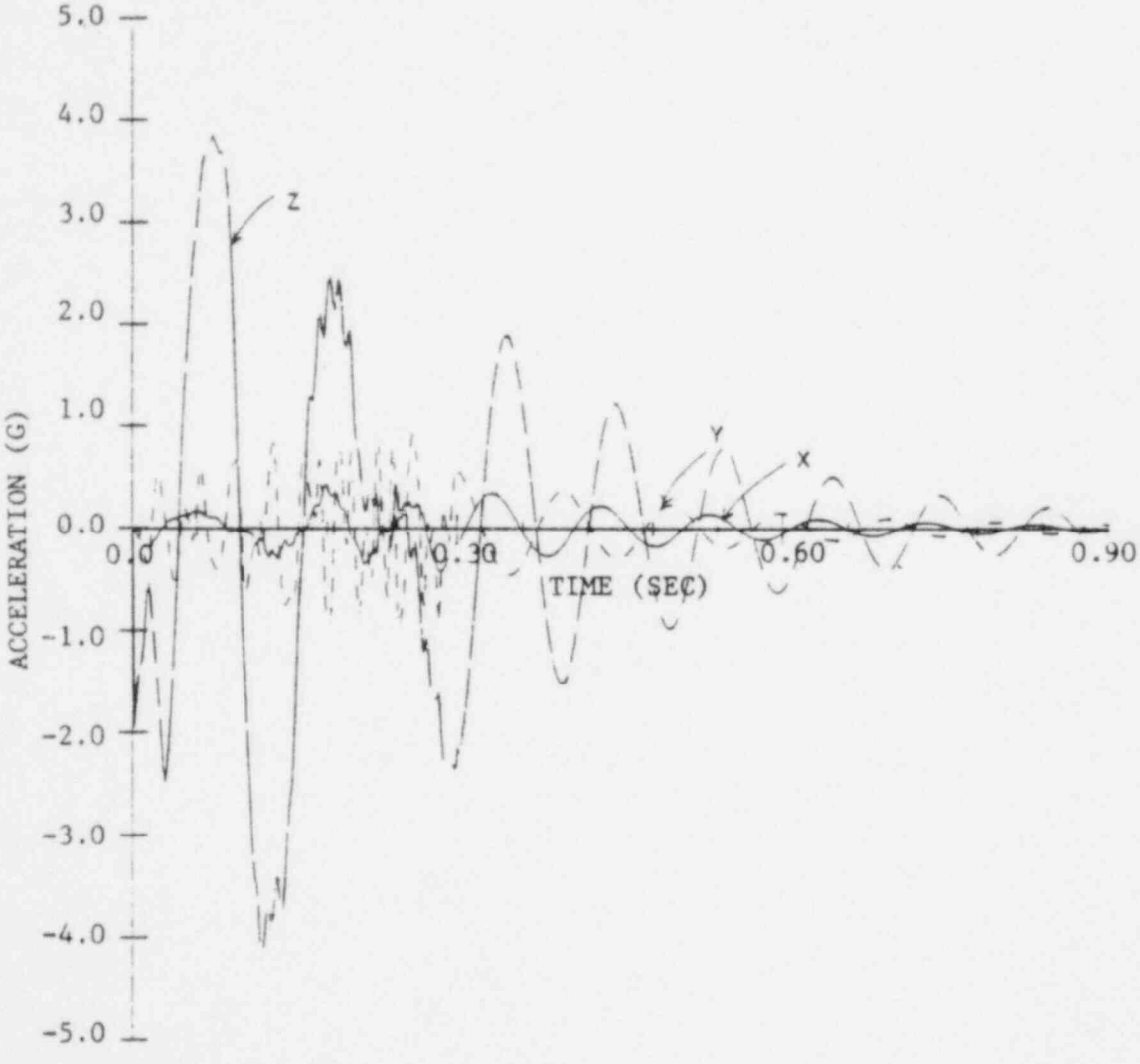

Figure 9.9-9. Extended Displacement Time-History at the CFL Nozzle for TMI-1 Cold-Leg Break

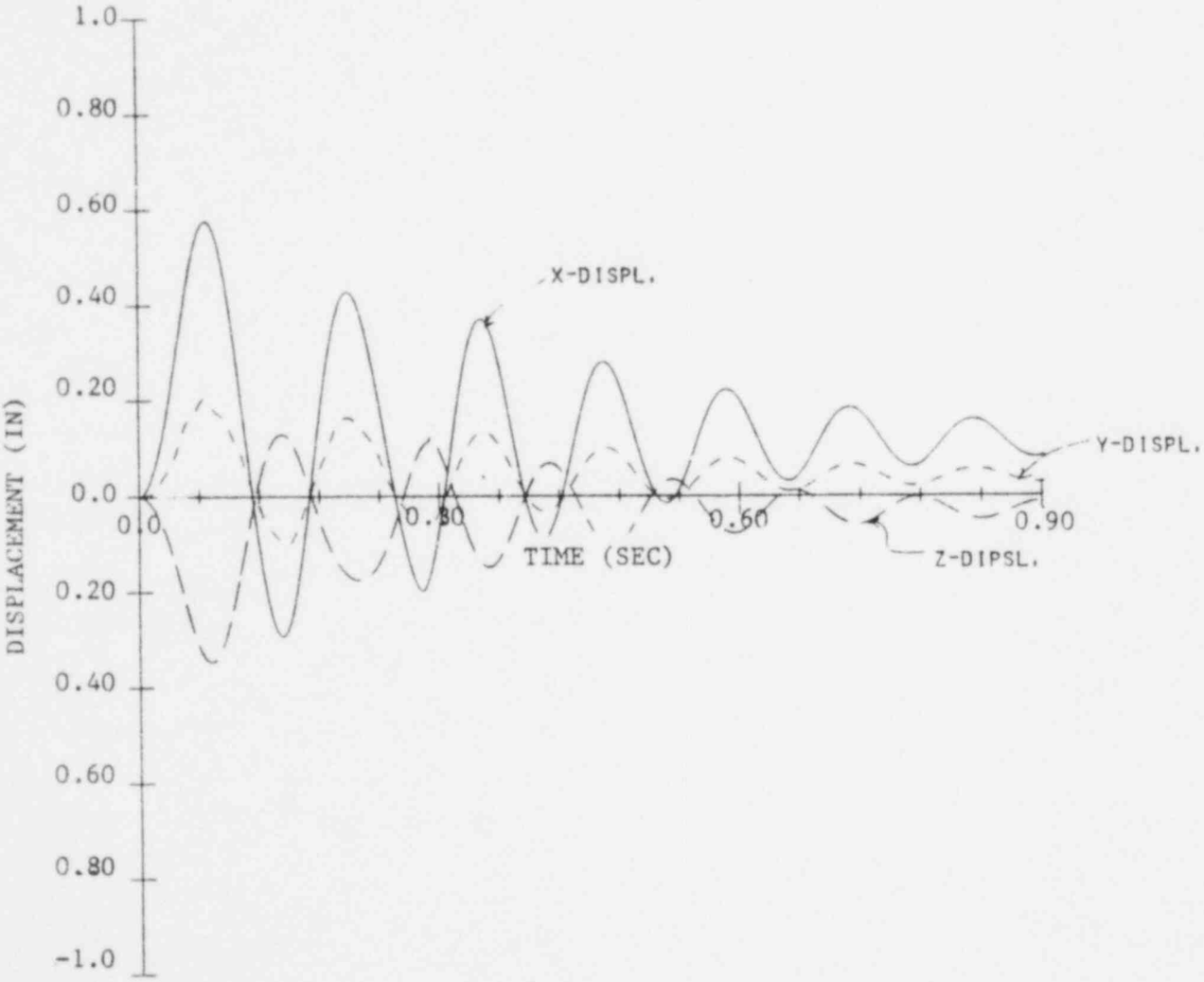

Figure 9.9-10. Extended Acceleration Time-History at the CFL Nozzle for TMI-1 Cold-Leg Break (Positive Rotation)

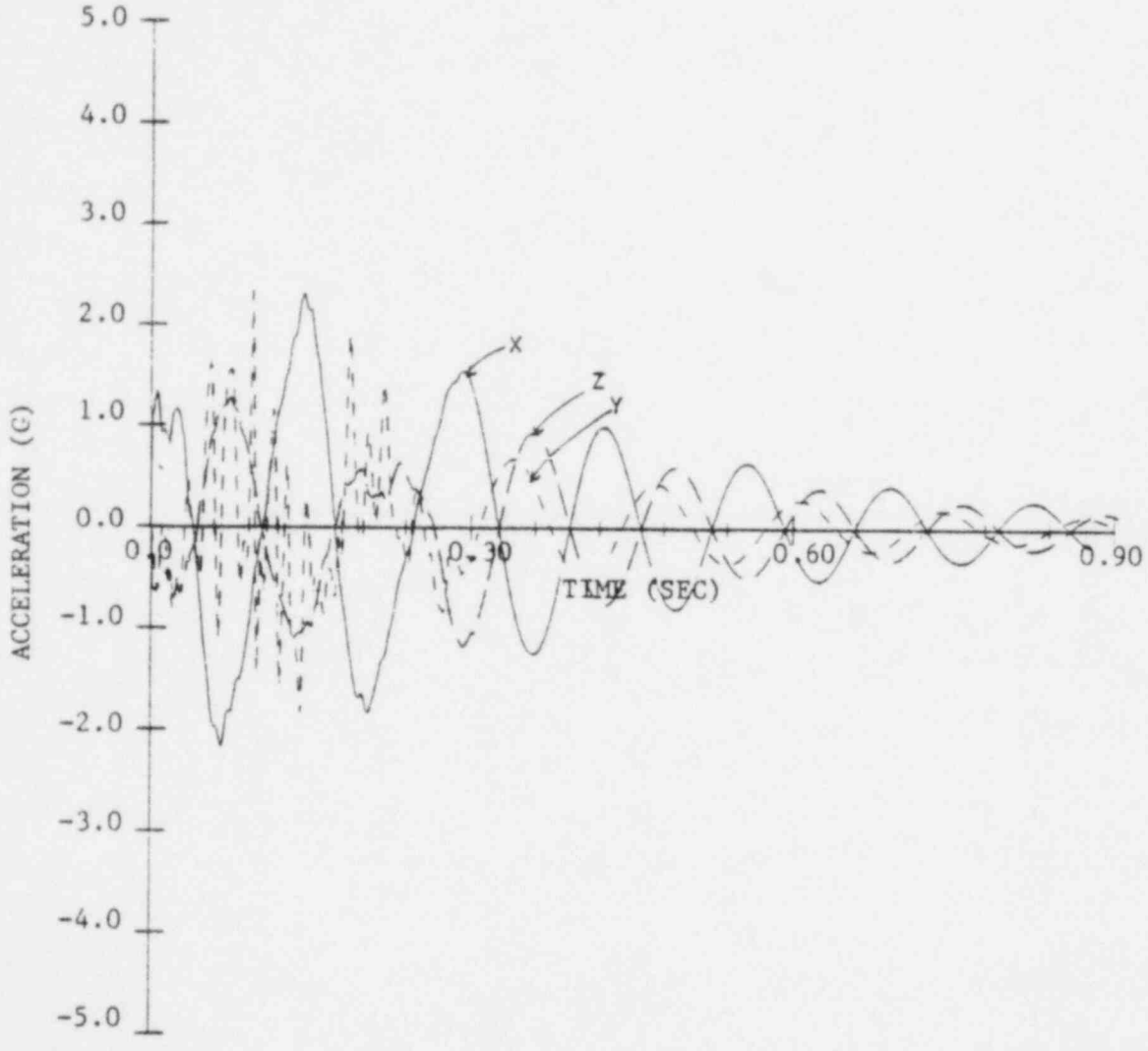

Figure 9.9-11. Extended Acceleration Time-History at the CFL Nozzle for TMI-1 Cold-Leg Break (Negative Rotation)

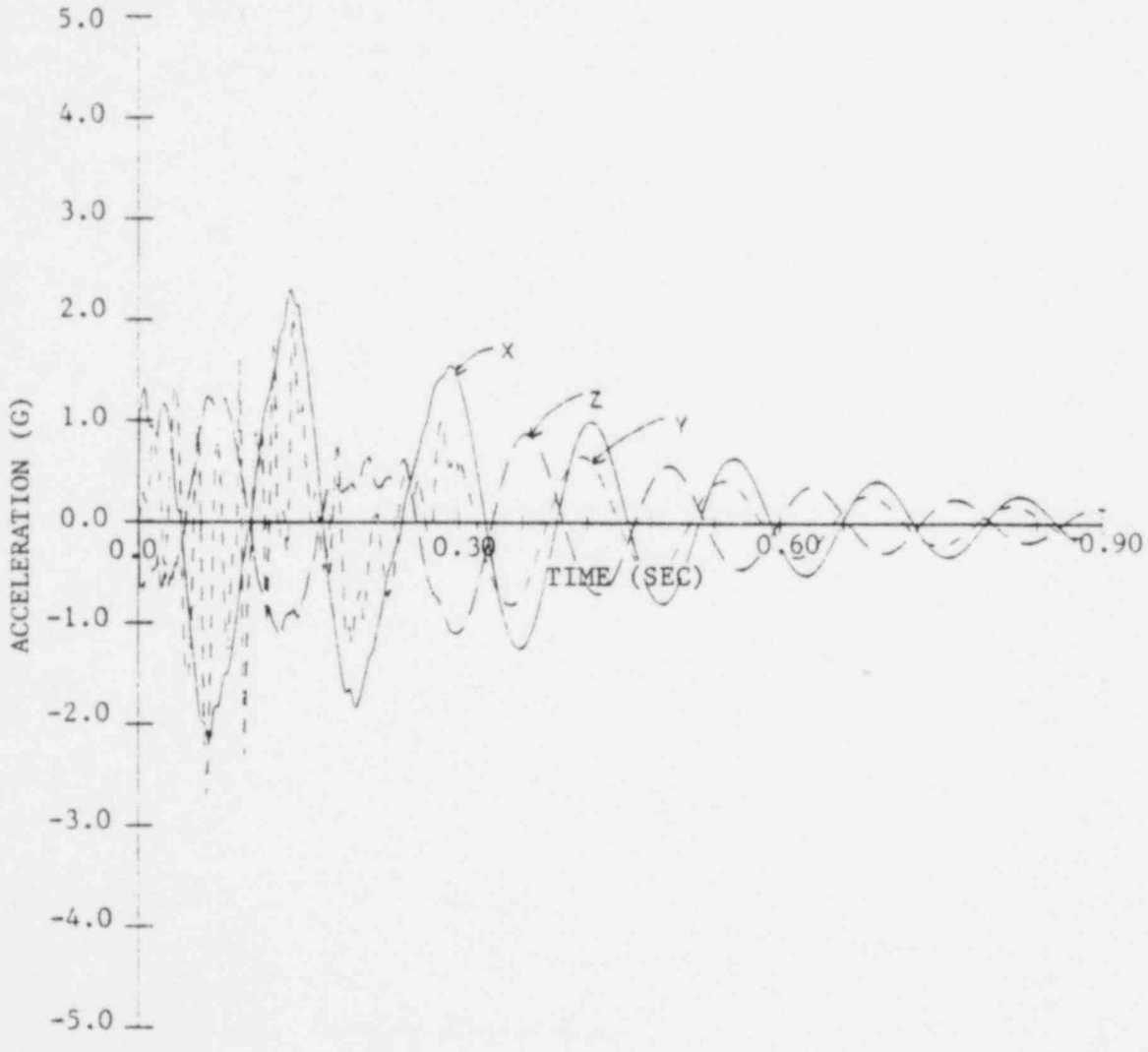

Figure 9.9-12. Acceleration Spectra at CFL Nozzle for TMI-1 Cold-Leg Break

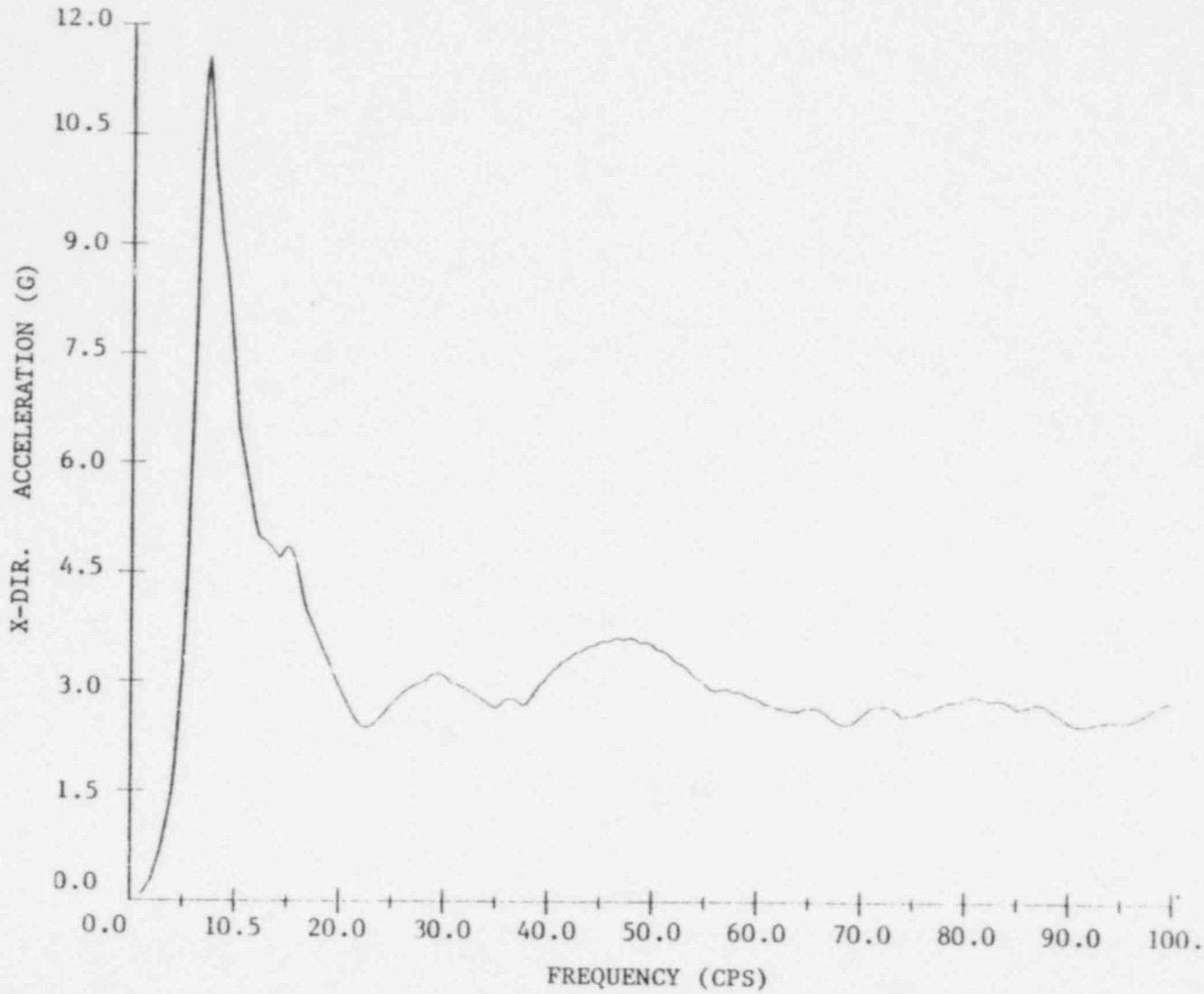

Figure 9.9-13. Acceleration Spectra at CFL Nozzle for TMI-1 Cold-Leg Break (for Positive Rotational Effects)

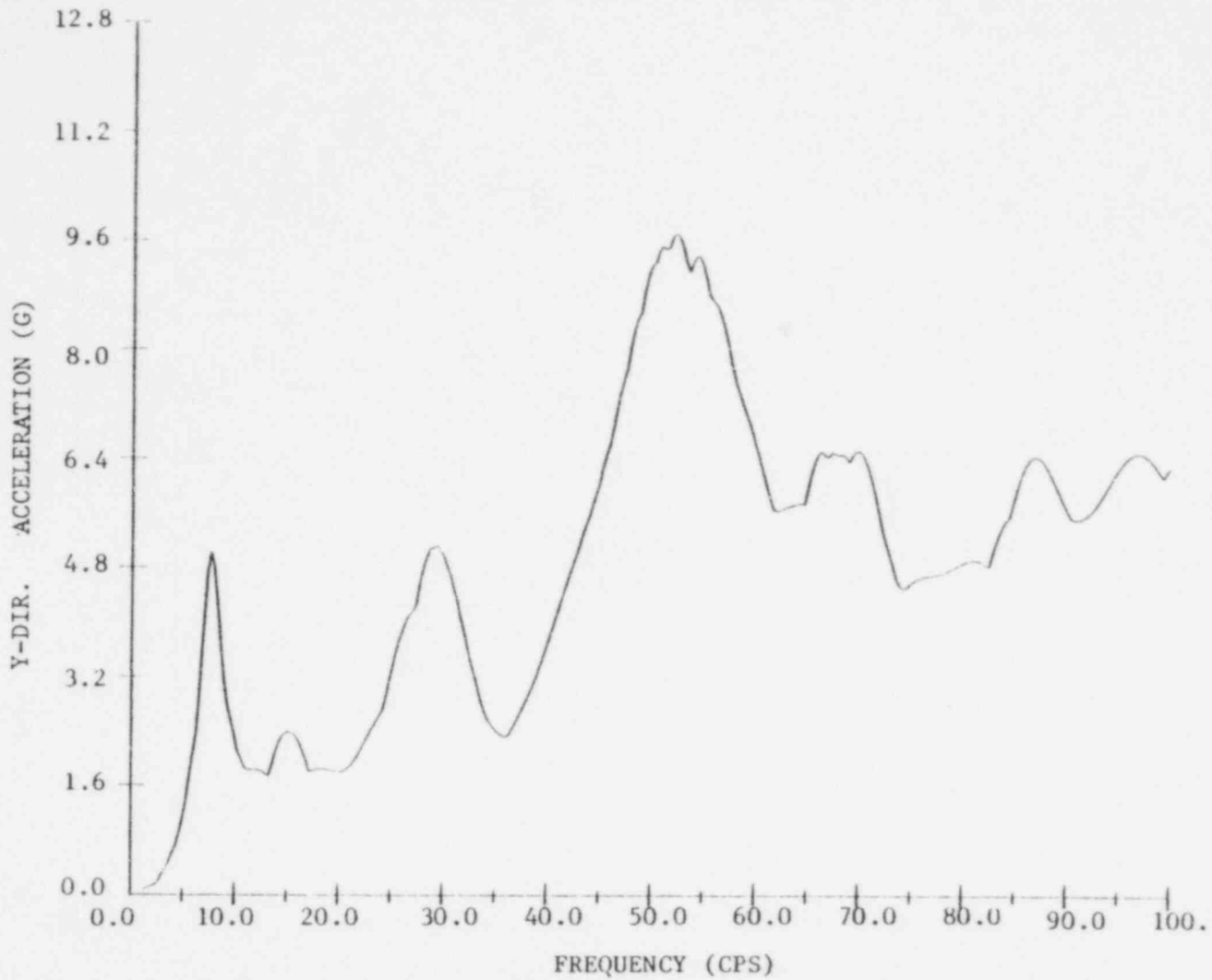

Figure 9.9-14. Acceleration Spectra at CFL Nozzle for TMI-1 Cold-Leg Break (for Negative Rotational Effects)

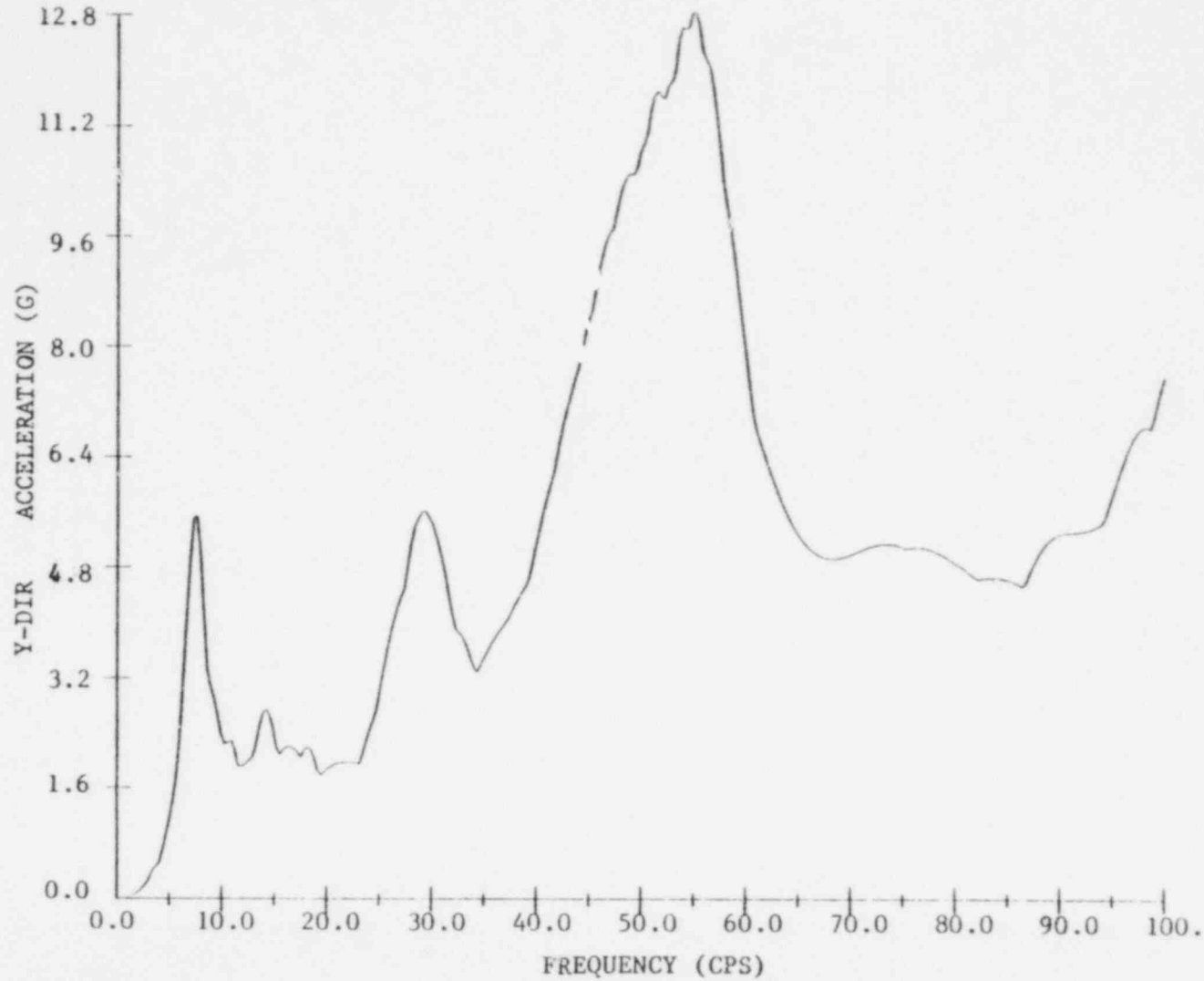

Figure 9.9-15. Acceleration Spectra at CFL Nozzle for TMI-1 Cold-Leg Break (for Positive Rotational Effects)

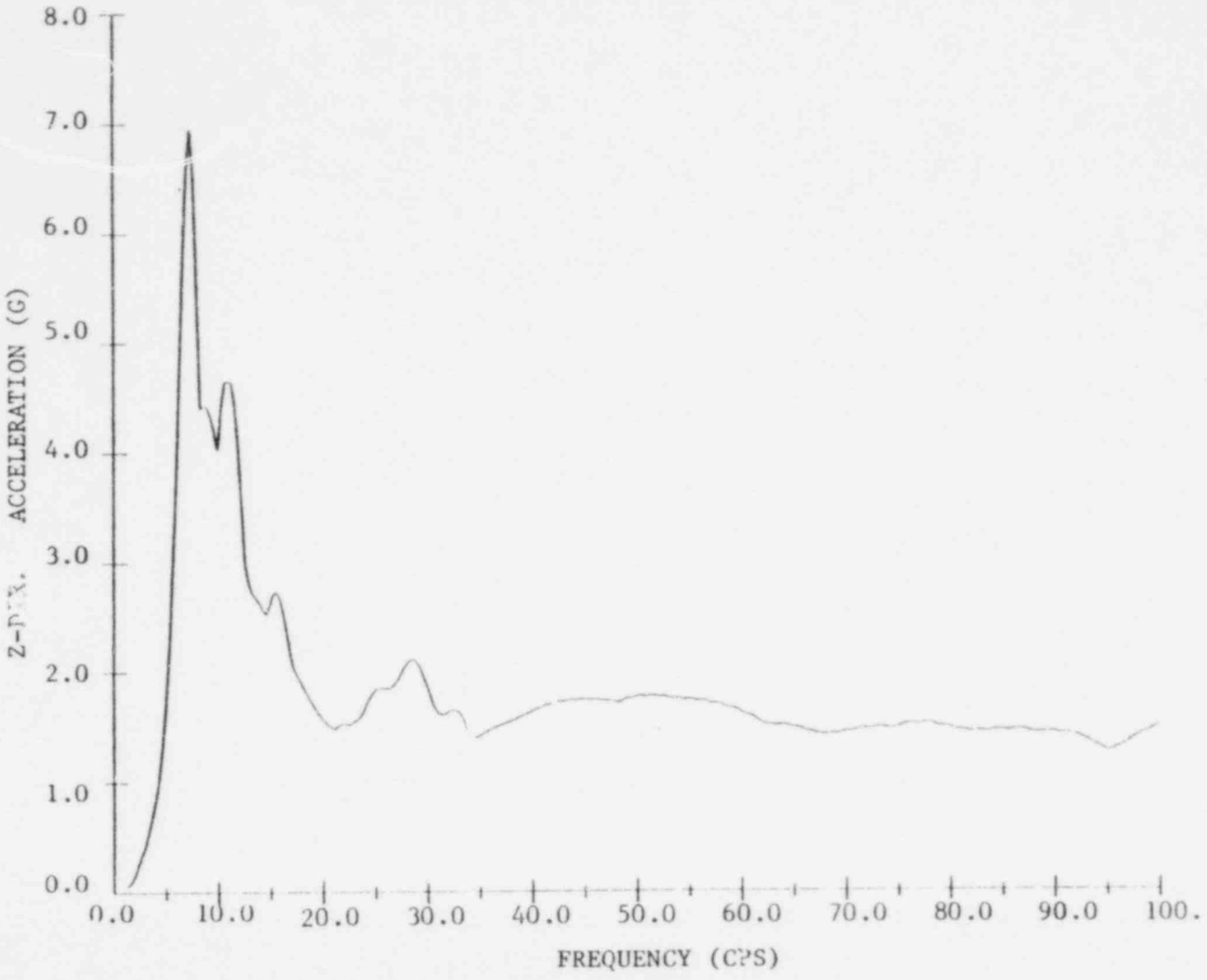

Figure 9.9-16. Acceleration Spectra at CFL Nozzle for TMI-1 Cold-Leg Break (for Negative Rotational Effects)

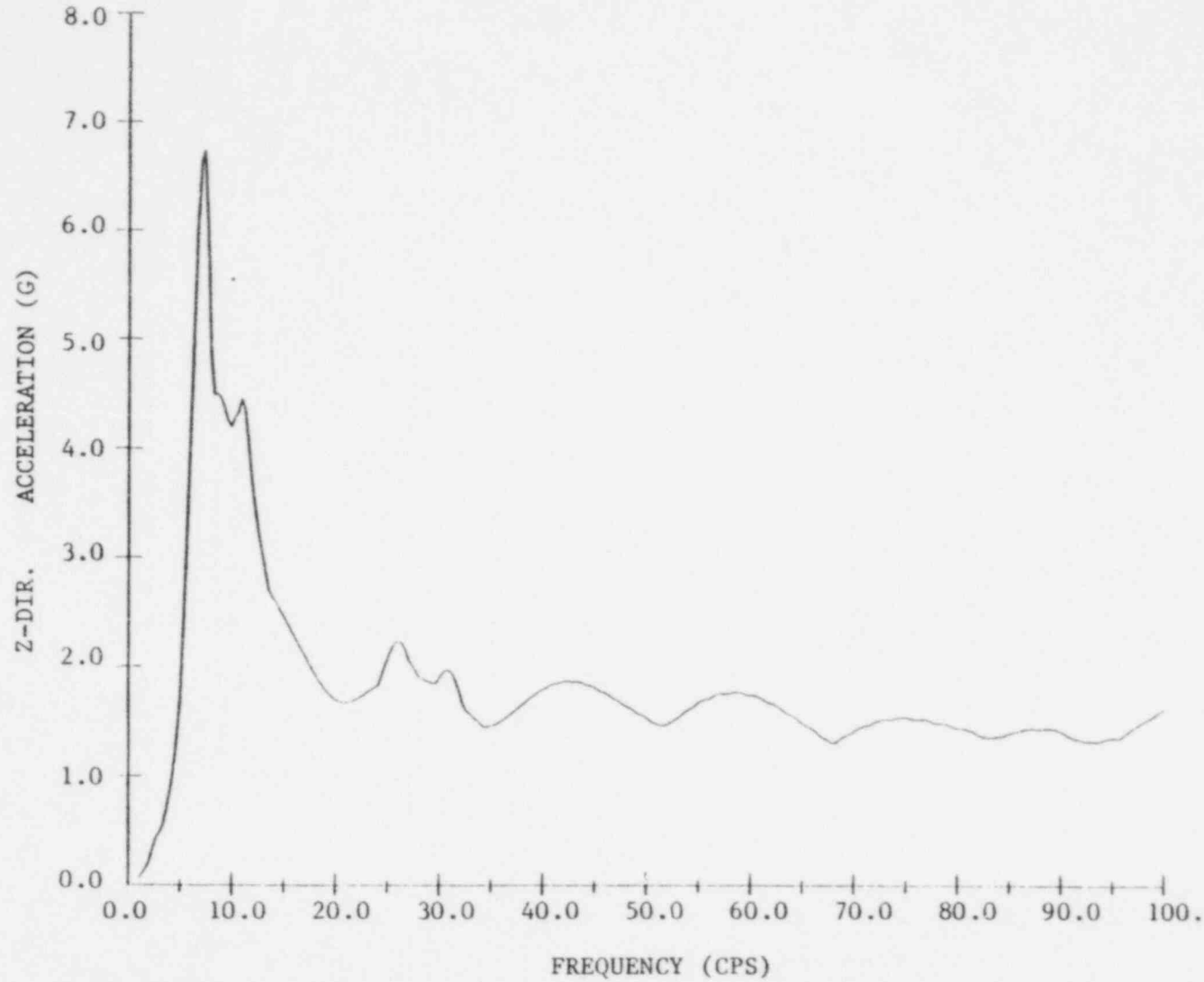

Figure 9.9-17. Acceleration Spectra at CFL Nozzle for TMI-1 Hot-Leg Break

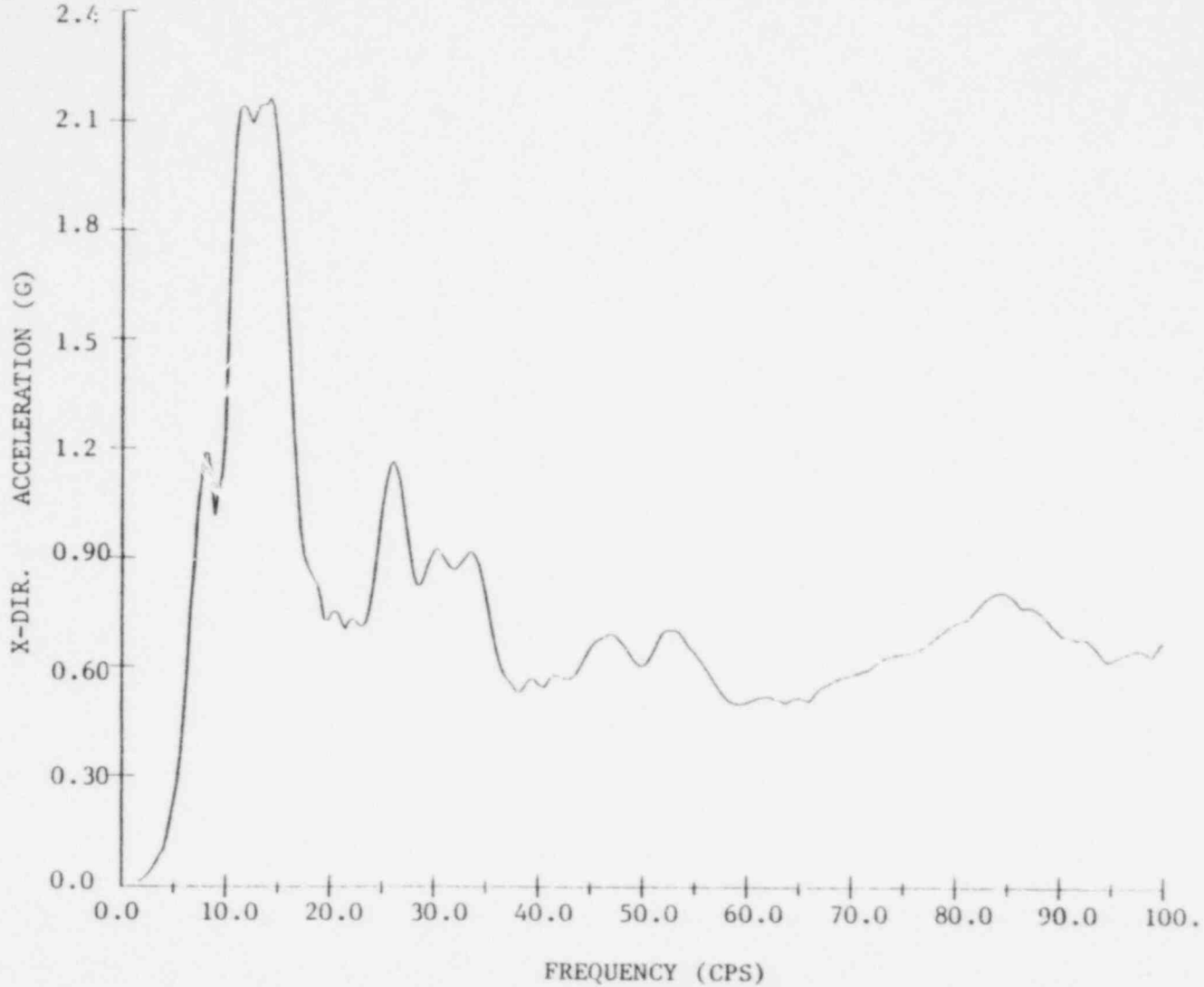

Figure 9.9-18. Acceleration Spectra at CFL Nozzle for TMI-1 Hot-Leg Break (for Positive Rotational Effects)

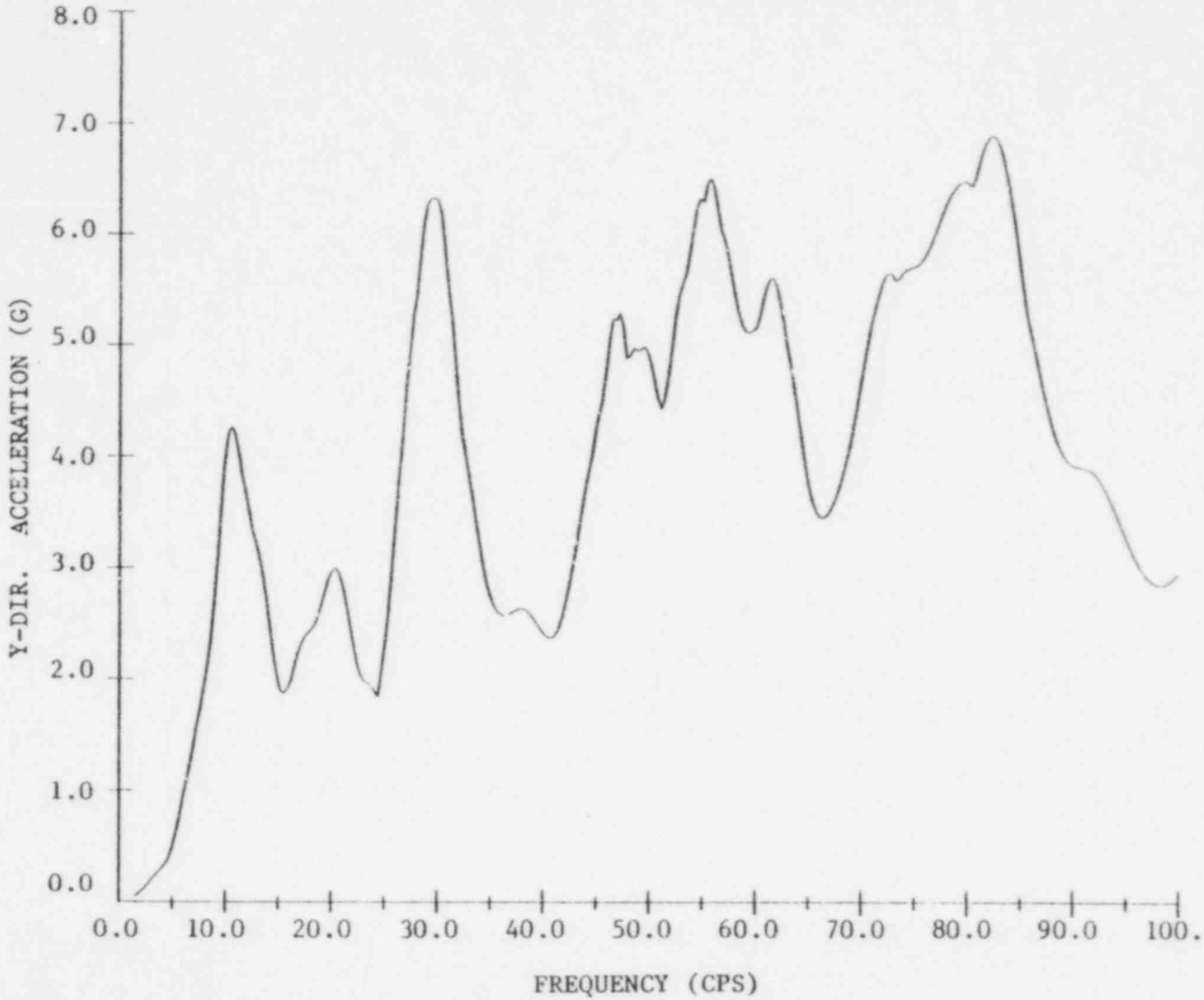

Figure 9.9-19. Acceleration Spectra at CFL Nozzle for TMI-1 Hot-Leg Break (for Negative Rotational Effects)

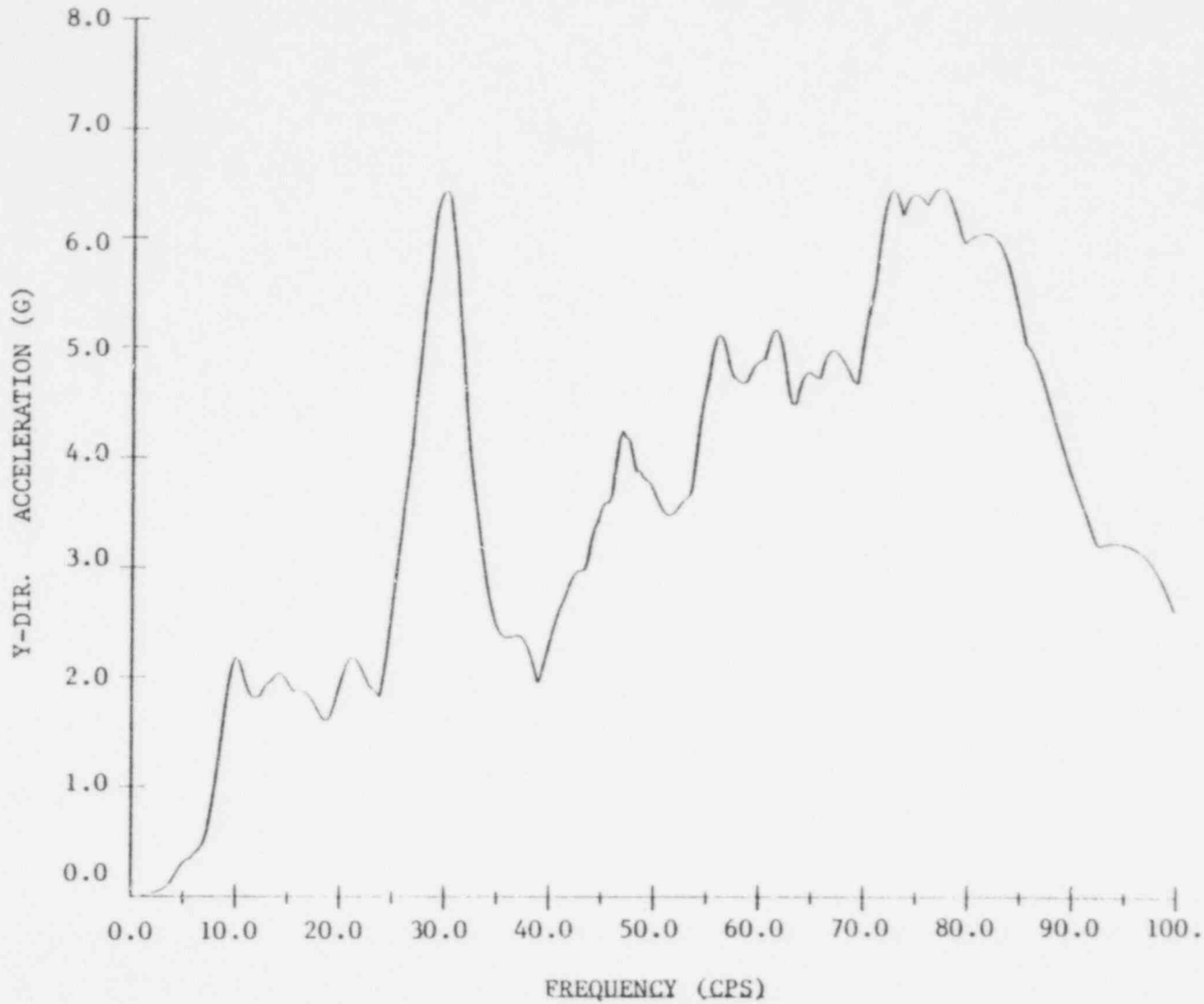

Figure 9.9-20. Acceleration Spectra at CFL Nozzle for TMI-1 Hot-Leg Break (for Positive Rotational Effects)

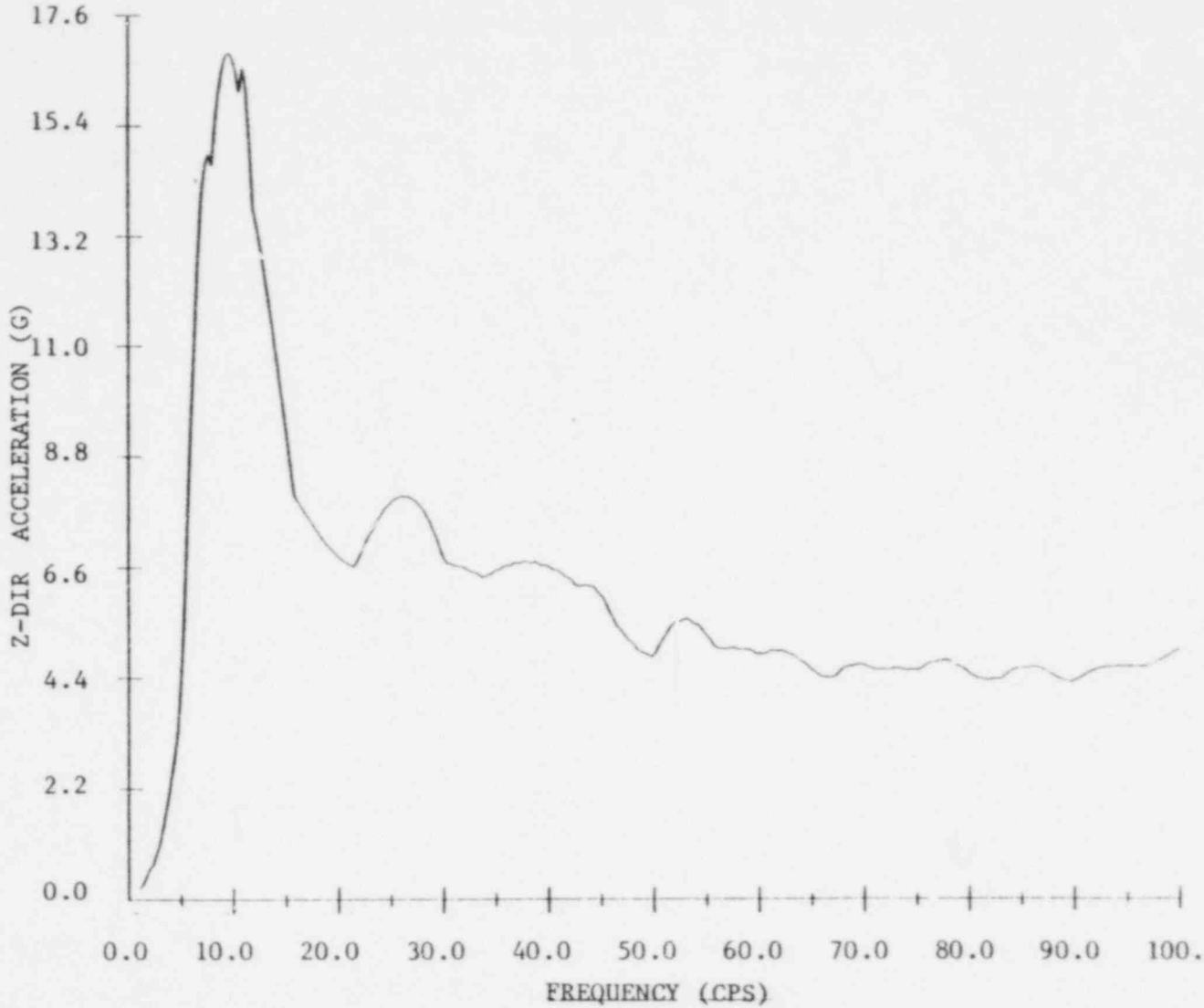

Figure 9.9-21. Acceleration Spectra at CFL Nozzle for TMI-1 Hot-Leg Break (for Negative Rotational Effects)

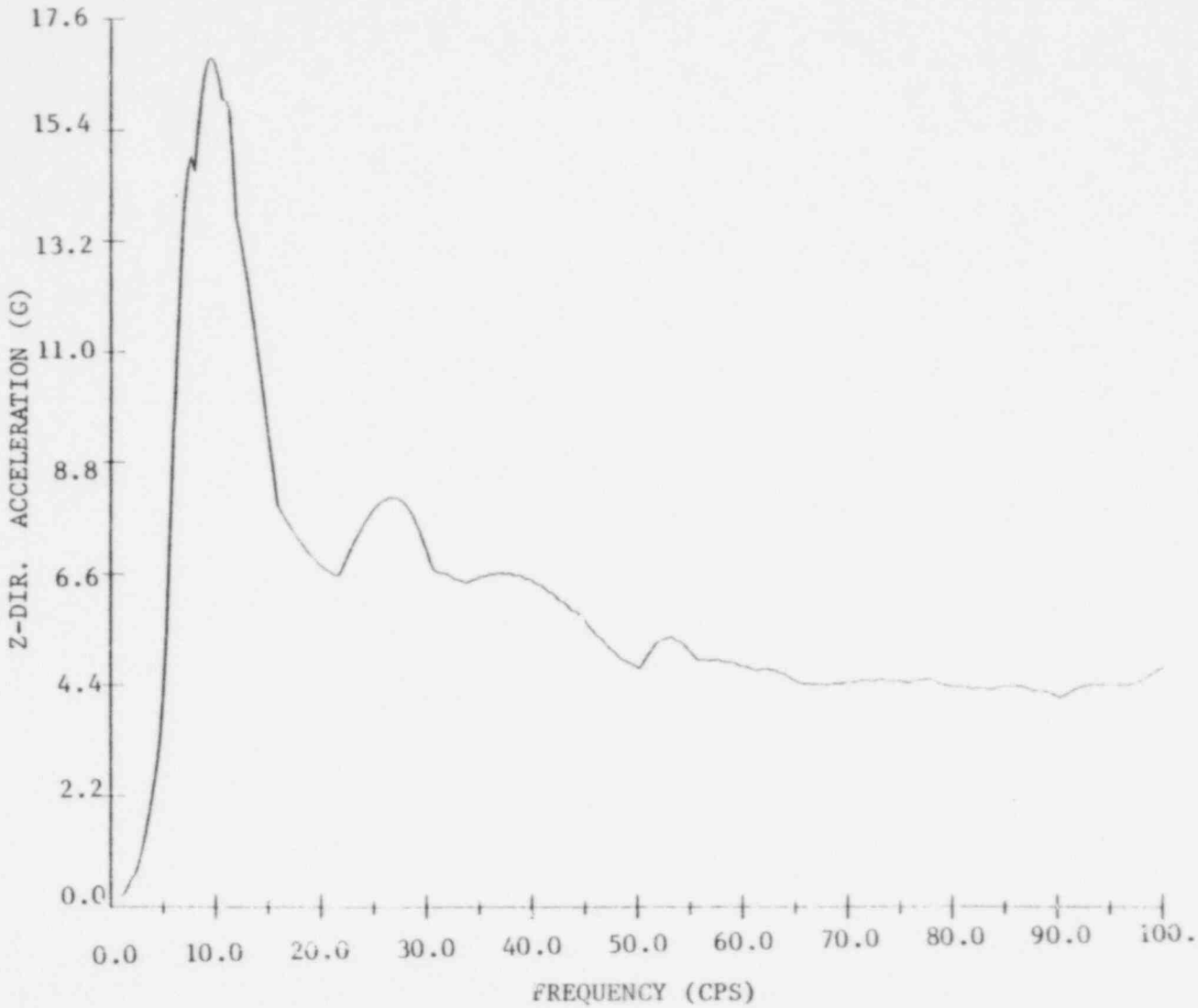

9.10. Reactor Cavity Walls

9.10.1. Pressure Loads for All Plants

Pressure loads for each plant were developed in accordance with the procedures discussed in Section 5.3. Static analyses were performed for two time steps of the pressure time history, and correspond to the peak asymmetric loading and peak steady-state loading.

Table 9.10-1 gives the time values for which analysis of the peak asymmetric loading was performed. The full blowdown load time histories are shown in Figures 9.10-1 to 9.10-6. Table 9.10-2 gives the time values for which analysis of the peak steady-state loading was performed. These time values and corresponding pressures are derived from the highest average pressure corresponding to the individual pressure time histories for the particular break case.

9.10.2. Davis-Besse Reaction Loads

In addition to the pressure loading, the Davis-Besse cavity wall and associated structures must resist vessel support reaction loads. The definition of these loads is discussed in Section 5.3.6.

9.10.2.1. Davis-Besse Support Beams

The loading applied to the cavity wall by the support beams was determined from the reactor vessel isolated linear model analysis and is provided in Section 9.2.

9.10.2.2. Davis-Besse LOCA Rings

When calculated in accordance with the formula in Section 5.3.6.3, the peak horizontal reaction for on a LOCA ring is:

R = 5461 kips	cold leg LOCA ring loaded due to the hot leg nozzle break, at peak asymmetric loading

R = 2200 kips — cold leg LOCA ring loaded due to the hot leg nozzle break, at peak steady-state loading

The peak horizontal reaction loads on any LOCA ring for other break cases are significantly lower than the above values. The peak vertical load, V, on one LOCA ring is 1861 kips, positive upwards, and occurs at the steady-state load condition.

The total thrust applied by all the LOCA rings in the direction opposite to the actual broken pipe is given in Table 9.10-3. The hot leg nozzle break produces the largest thrust.

Table 9.10-1. Peak Asymmetric Loads for all Plants

Plant	Critical Break Size		Peak Asymmetric Blowdown Load, kips	Time of Peak Asymmetric Pressure Load Set, seconds
Oconee	0.460A	Hot Leg	8100	0.033
	2.0A	Cold Leg	11100	0.050
TMI-1	1.295A	Hot Leg	10200	0.037
	2.0A	Cold Leg	7500	0.047
TMI-2	1.710A	Hot Leg	12200	0.046
	2.0A	Cold Leg	6700	0.046
Crystal River	1.092A	Hot Leg	9200	0.036
	2.0A	Cold Leg	7500	0.047
ANO-1	0.307A	Hot Leg	1900	0.034
	2.0A	Cold Leg	3400	0.047
Rancho Seco	0.679A	Hot Leg	5600	0.030
	2.0A	Cold Leg	5000	0.047
Davis-Besse	1.0243A	Hot Leg	7800	0.041
	0.243A	Cold Leg		

Table 9.10-2. Steady-state Pressures for all Plants

Plant	Critical Break Size		Peak Steady-state Pressure, psi	Time of Peak Steady-state Load Set, seconds
Oconee	0.460A	Hot Leg	167	1.1396
	2.0A	Cold Leg	295	1.1896
TMI-1	1.295A	Hot Leg	255	0.1596
	2.0A	Cold Leg	190	0.1596
TMI-2	1.710A	Hot Leg	261	0.5396
	2.0A	Cold Leg	145	0.4896
Crystal River	1.092A	Hot Leg	234	0.1596
	2.0A	Cold Leg	190	0.1596
ANO-1	0.307A	Hot Leg	49	0.4896(a)
	2.0A	Cold Leg	127	0.5396
Rancho Seco	0.679A	Hot Leg	124	0.5396(a)
	2.0A	Cold Leg	157	0.3396
Davis-Besse	1.0243A	Hot Leg	140	0.7396
	0.243A	Cold Leg	38	0.7396

(a) Explicit dynamic time history analyses performed for these plants.

Table 9.10-3. Total Horizontal Thrust by All LOCA Rings on Davis-Besse Cavity Wall

Break Size	Peak at Asymmetric Loading, kips	Peak at Steady-state Loading, kips
Hot Leg 1.0243A Nozzle	19,874	6,840
Hot Leg 1.033A Elbow	6,412	3,765
Cold Leg 0.243A Nozzle	6,845	3,128
Cold Leg 1.167A Elbow	4,935	3,058

Figure 9.10-1. Oconee Cavity Wall Pressure Time Histories

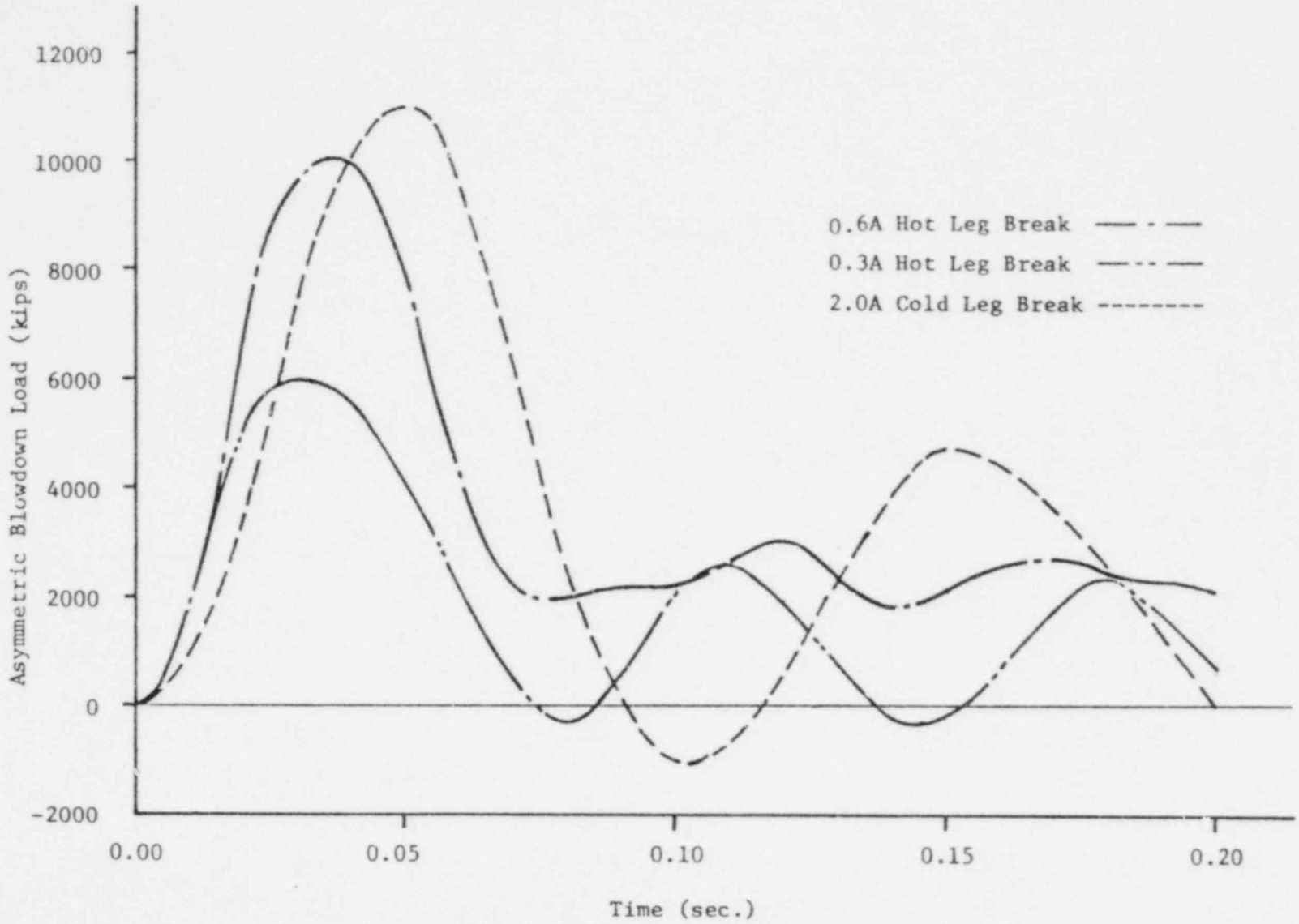

Figure 9.10-2. Three Mile Island 1 and Crystal River Cavity Wall Pressure Time Histories

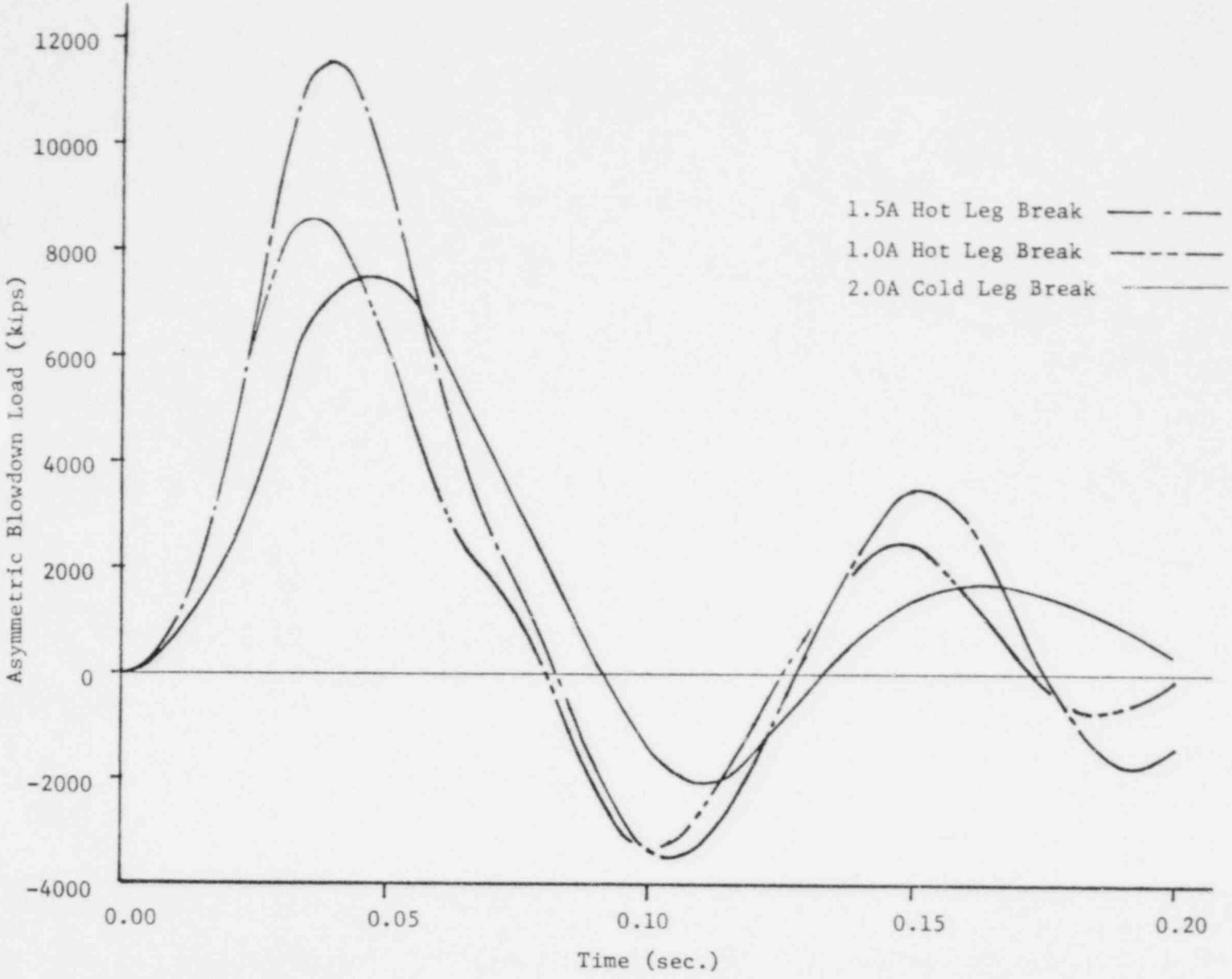

Figure 9.10-3. Three Mile Island 2 Cavity Wall Pressure Time Histories

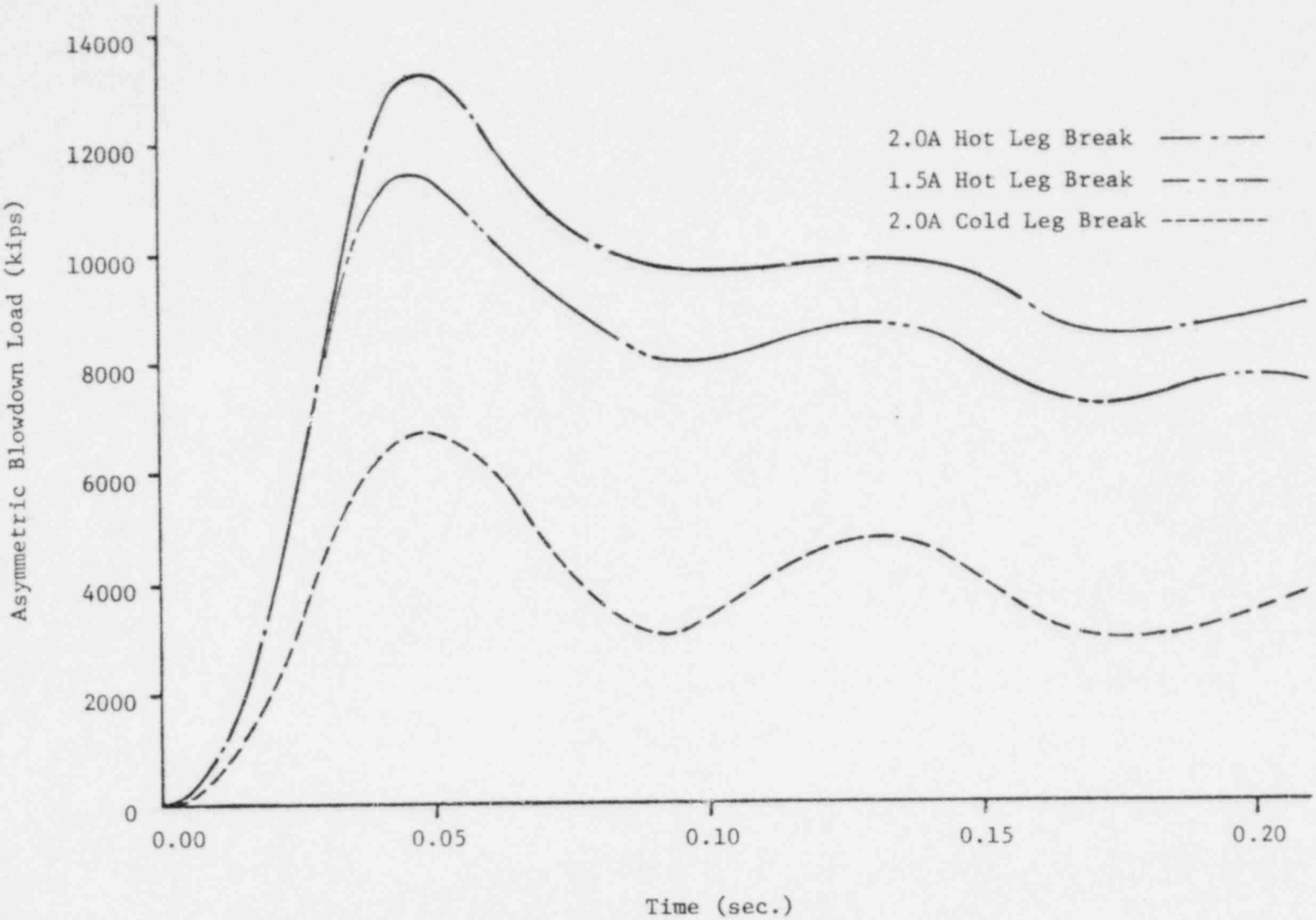

Figure 9.10-4. ANO-1 Cavity Wall Pressure Time Histories

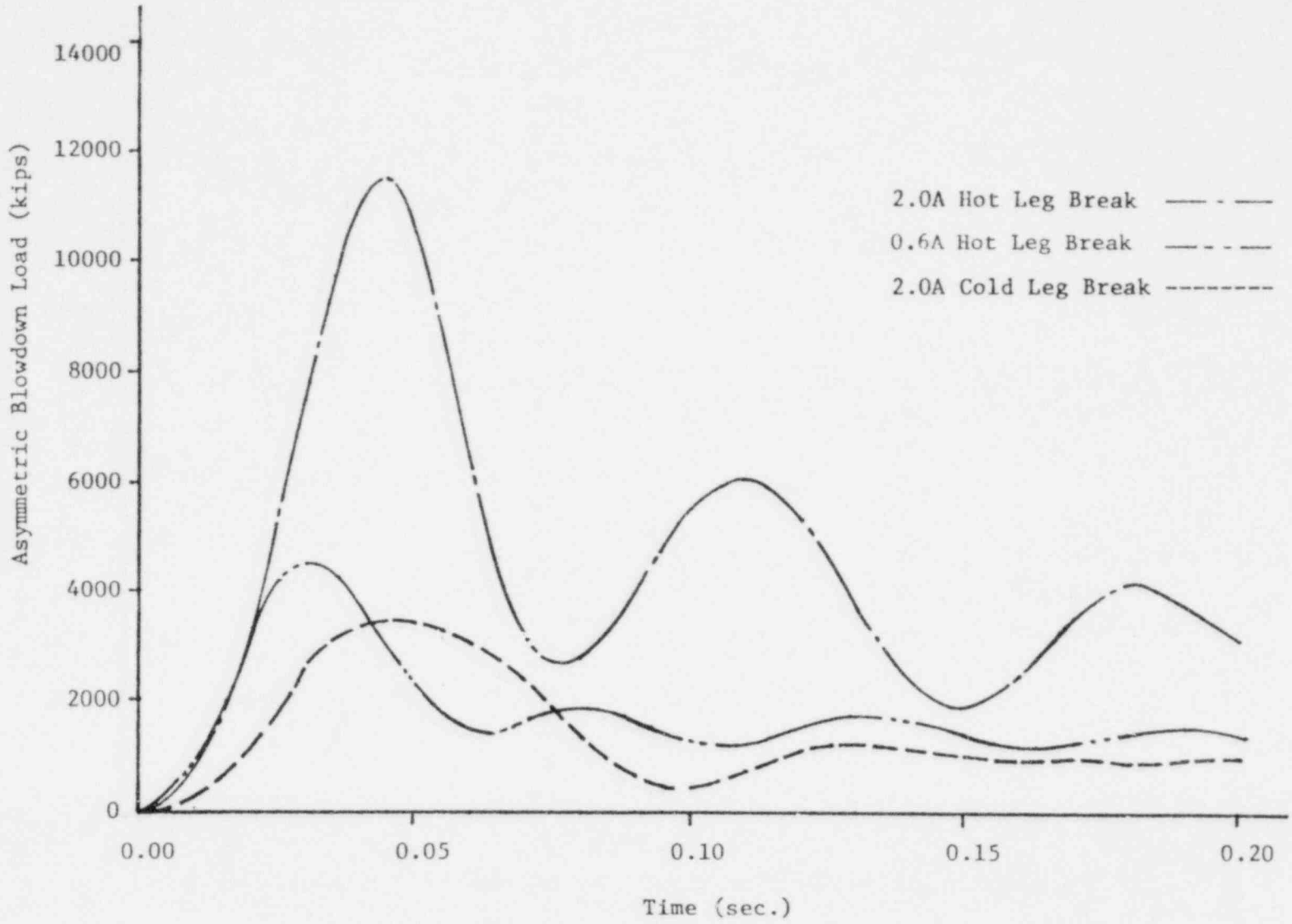

Figure 9.10-5. Rancho Seco Cavity Wall Pressure Time Histories

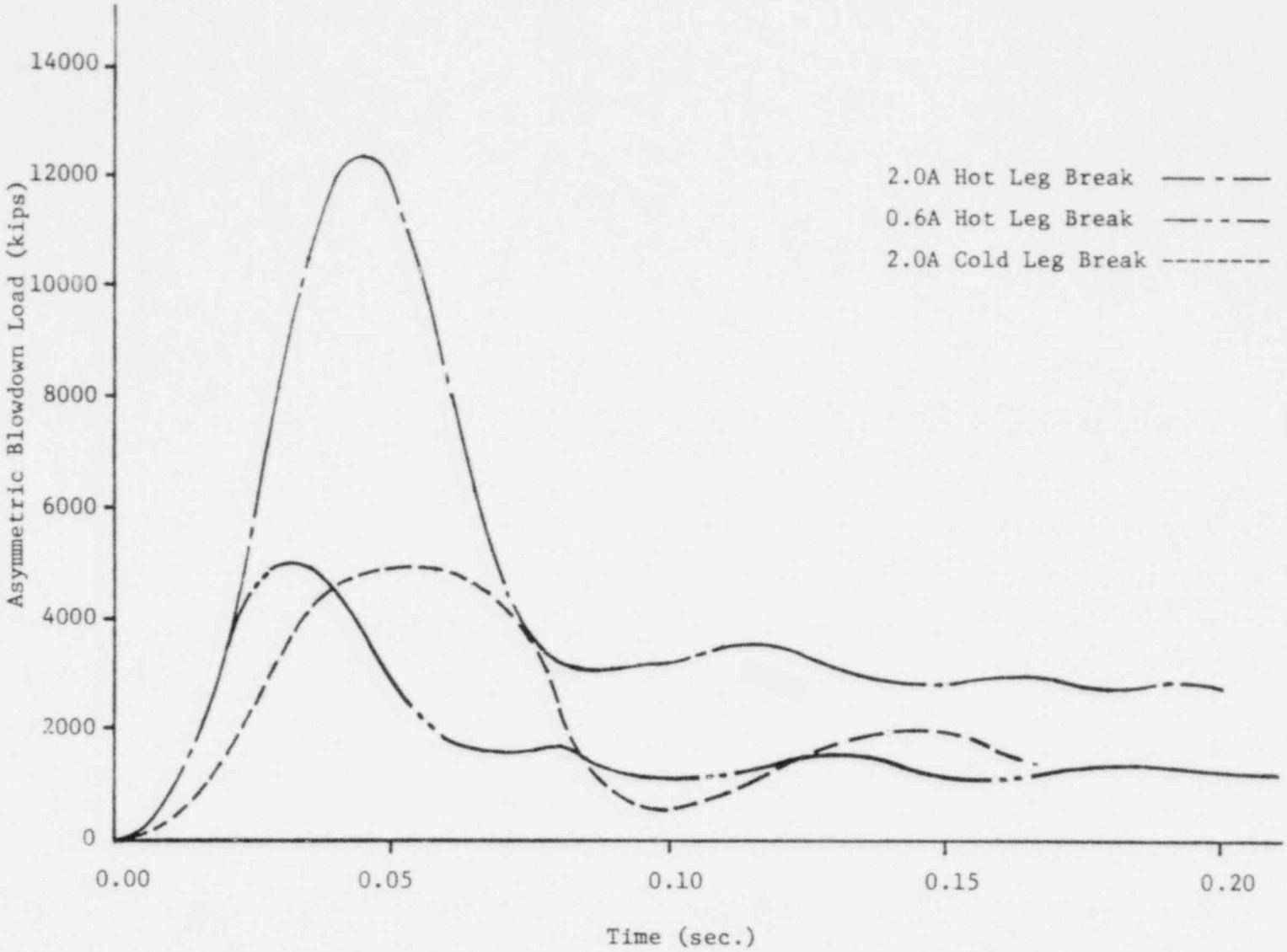

Figure 9.10-6. Davis-Besse Cavity Wall Pressure Time History

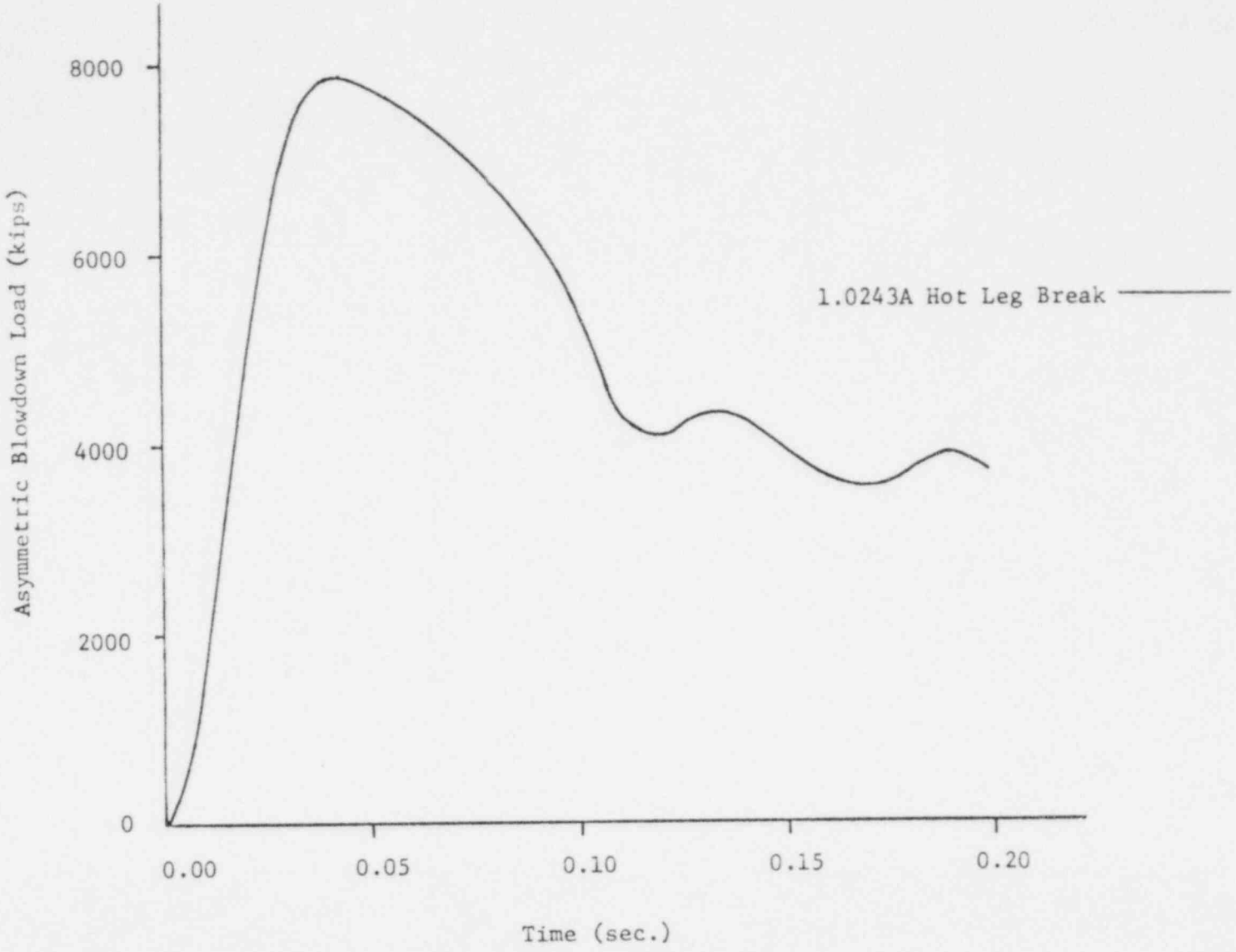

9.11. Reactor Vessel Component

Maximum forces and moments for key points on the CRDM, service support structure skirt, and the reactor vessel skirt and shell are presented in Tables 9.11-1 through 9.11-13 (see Figure D-5). In addition, bar charts of the resultant horizontal forces (F_R) and moments about the horizontal axis (M_B) are given in Figures 9.11-1 through 9.11-24.

Table 9.11-1. Total CRDM Nozzle Load For 69 Drives, Jt 120
(Nozzle Length Equal to Length of Center Nozzle)

LOAD CASE		FORCES (KIPS) FX	FY	FZ	MOMENTS (FT-KIPS) MX	MY	MZ
HLG AT RV	OCONEE 1,2 3	21.7	367.4	448.0	1334.7	.0	75.9
HLG AT RV	TMI-1	61.0	425.0	859.7	2496.0	.0	183.2
HLG AT RV	TMI-2	42.2	412.3	676.5	1924.2	.0	102.2
HLG AT RV	CRYSTAL RIVER 3	61.0	425.0	859.7	2496.0	.0	183.2
HLG AT RV	ANO-1	36.5	292.9	298.8	872.7	.0	94.4
HLG AT RV	RANCHO SECO	40.4	405.1	462.3	1342.2	.0	101.5
CLG AT RV	OCONEE 1,2,3	624.9	291.3	271.3	753.8	.0	1592.9
CLG AT RV	TMI-1	502.7	258.7	243.4	671.0	.0	1273.2
CLG AT RV	TMI-2	428.3	234.0	141.1	371.2	.0	1160.6
CLG AT RV	CRYSTAL RIVER 3	502.7	258.7	243.4	671.0	.0	1273.2
CLG AT RV	ANO-1	287.3	214.2	152.6	418.2	.0	713.2
CLG AT RV	RANCHO SECO	303.0	284.5	193.0	507.6	.0	776.7
HLG AT RV	DAVIS BESSE 1	8.2	150.4	323.3	831.3	.0	13.0
HLG AT EL	DAVIS BESSE 1	4.2	126.8	121.5	303.7	.0	4.3
CLG AT EL	DAVIS BESSE 1	47.3	83.0	90.2	202.5	.0	67.2
CLG AT RV	DAVIS BESSE 1	88.1	53.5	63.0	175.3	.0	261.3

Table 9.11-2. SSS Skirt Load, Joint 113

LOAD CASE		FORCES (KIPS) FX	FY	FZ	MOMENTS (FT-KIPS) MX	MY	MZ
HLG AT RV	OCONEE 1,2 3	57.4	235.1	574.5	6798.9	24.2	728.4
HLG AT RV	TMI-1	112.2	196.3	845.4	11009.0	22.8	1481.0
HLG AT RV	TMI-2	52.7	218.1	838.5	9299.8	20.1	773.8
HLG AT RV	CRYSTAL RIVER 3	112.2	196.3	845.4	11009.0	22.8	1481.0
HLG AT RV	ANO-1	35.7	229.2	386.5	4755.3	25.2	476.8
HLG AT RV	RANCHO SECO	47.4	191.3	562.6	7014.0	20.4	554.1
CLG AT RV	OCONEE 1,2,3	569.3	246.5	279.4	3347.1	27.1	7992.8
CLG AT RV	TMI-1	495.0	250.6	250.7	3568.6	26.3	6998.7
CLG AT RV	TMI-2	385.5	236.4	201.5	2107.0	25.1	5742.8
CLG AT RV	CRYSTAL RIVER 3	495.0	250.6	250.7	3568.6	26.3	6998.7
CLG AT RV	ANO-1	293.6	235.1	122.5	1816.9	24.3	4444.6
CLG AT RV	RANCHO SECO	319.5	244.0	161.8	2139.0	24.8	4718.4
HLG AT RV	DAVIS BESSE 1	9.4	148.5	301.5	3989.8	1.4	132.5
HLG AT EL	DAVIS BESSE 1	8.3	98.6	204.7	2493.3	.2	64.7
CLG AT EL	DAVIS BESSE 1	80.7	76.3	133.0	1667.3	2.6	1122.8
CLG AT RV	DAVIS BESSE 1	121.6	49.3	110.4	1083.8	14.8	1198.4

Table 9.11-3. P1A1 Inlet Nozzle/Shell Interface, Joint 71

LOAD CASE		FORCES (KIPS)			MOMENTS (FT-KIPS)		
		FX	FY	FZ	MX	MY	MZ
HLG AT RV	OCONEE 1,2 3	143.1	82.2	126.9	958.9	567.6	613.0
HLG AT RV	TMI-1	165.7	78.8	177.3	1203.3	789.6	700.7
HLG AT RV	TMI-2	181.6	119.2	215.4	1887.7	758.5	988.5
HLG AT RV	CRYSTAL RIVER 3	165.7	78.8	177.3	1203.3	789.6	700.7
HLG AT RV	ANO-1	116.3	78.2	103.5	767.9	444.7	553.5
HLG AT RV	RANCHO SECO	148.4	74.3	158.9	1034.4	537.7	650.6
CLG AT RV	OCONEE 1,2,3	.0	.0	.0	.0	.0	.0
CLG AT RV	TMI-1	.0	.0	.0	.0	.0	.0
CLG AT RV	TMI-2	.0	.0	.0	.0	.0	.0
CLG AT RV	CRYSTAL RIVER 3	.0	.0	.0	.0	.0	.0
CLG AT RV	ANO-1	.0	.0	.0	.0	.0	.0
CLG AT RV	RANCHO SECO	.0	.0	.0	.0	.0	.0
HLG AT RV	DAVIS BESSE 1	2832.4	1720.8	3371.6	4395.2	15054.9	4878.2
HLG AT EL	DAVIS BESSE 1	816.5	315.9	949.1	784.4	4270.1	927.9
CLG AT EL	DAVIS BESSE 1	207.2	301.5	210.7	1007.7	1396.8	1007.7
CLG AT RV	DAVIS BESSE 1	.0	.0	.0	.0	.0	.0

Table 9.11-4. P1A2 Inlet Nozzle/Shell Interface, Joint 67

LOAD CASE		FORCES (KIPS) FX	FY	FZ	MOMENTS (FT-KIPS) MX	MY	MZ
HLG AT RV	OCONEE 1,2 3	151.8	77.1	133.9	1010.0	463.8	409.7
HLG AT RV	TMI-1	182.5	86.3	179.8	1240.8	531.4	469.7
HLG AT RV	TMI-2	208.2	150.2	199.1	2048.7	622.2	754.0
HLG AT RV	CRYSTAL RIVER 3	182.5	86.3	179.8	1240.8	531.4	469.7
HLG AT RV	ANO-1	122.1	62.6	104.7	799.8	358.0	366.3
HLG AT RV	RANCHO SECO	152.1	72.1	151.5	1061.8	427.8	368.0
CLG AT RV	OCONEE 1,2,3	175.6	62.9	97.1	477.3	1162.2	548.5
CLG AT RV	TMI-1	129.9	65.7	84.1	550.8	920.3	552.7
CLG AT RV	TMI-2	151.7	68.6	91.8	567.5	1075.4	594.0
CLG AT RV	CRYSTAL RIVER 3	129.9	65.7	84.1	550.8	920.3	552.7
CLG AT RV	ANO-1	134.3	47.3	76.2	363.0	746.0	414.4
CLG AT RV	RANCHO SECO	126.1	51.7	76.2	440.8	774.1	436.5
HLG AT RV	DAVIS BESSE 1	2869.9	1712.7	3404.9	4371.8	15230.2	4848.8
HLG AT EL	DAVIS BESSE 1	816.7	316.8	949.1	790.2	4270.4	930.1
CLG AT EL	DAVIS BESSE 1	792.0	111.3	827.5	369.4	3908.0	237.0
CLG AT RV	DAVIS BESSE 1	1250.8	341.8	1300.7	801.6	6105.0	969.5

Table 9.11-5. P1B1 Inlet Nozzle/Shell Interface, Joint 66

LOAD CASE		FORCES (KIPS) FX	FY	FZ	MOMENTS (FT-KIPS) MX	MY	MZ
HLG AT RV	OCONEE 1,2 3	149.3	82.1	132.3	984.0	474.1	431.0
HLG AT RV	TMI-1	186.1	114.0	174.6	1188.5	610.9	613.6
HLG AT RV	TMI-2	210.9	186.0	201.1	2143.1	658.5	971.5
HLG AT RV	CRYSTAL RIVER 3	186.1	114.0	174.6	1188.5	610.9	613.6
HLG AT RV	ANO-1	119.6	71.5	104.7	788.4	339.1	386.5
HLG AT RV	RANCHO SECO	155.0	94.6	146.9	989.1	367.8	509.7
CLG AT RV	OCONEE 1,2,3	175.4	63.6	105.3	472.8	1167.0	610.9
CLG AT RV	TMI-1	130.3	69.4	91.8	541.6	974.2	557.2
CLG AT RV	TMI-2	150.2	75.7	101.2	522.9	1083.9	616.8
CLG AT RV	CRYSTAL RIVER 3	130.3	69.4	91.8	541.6	974.2	557.2
CLG AT RV	ANO-1	133.7	49.1	82.6	382.2	812.3	394.2
CLG AT RV	RANCHO SECO	126.7	53.7	80.8	446.0	850.3	423.6
HLG AT RV	DAVIS BESSE 1	2884.0	1050.5	3426.4	2565.4	15380 1	2745.0
HLG AT EL	DAVIS BESSE 1	823.9	359.8	959.9	1015.7	4313.7	1058.0
CLG AT EL	DAVIS BESSE 1	803.4	315.7	840.8	784.3	3966.3	951.1
CLG AT RV	DAVIS BESSE 1	1353.2	498.0	1404.0	1257.0	6710.9	1368.9

Table 9.11-6. P1B2 Inlet Nozzle/Shell Interface, Joint 69

LOAD CASE		FORCES (KIPS) FX	FY	FZ	MOMENTS (FT-KIPS) MX	MY	MZ
HLG AT RV	OCONEE 1,2 3	141.9	88.3	128.6	303.9	526.4	583.2
HLG AT RV	TMI-1	169.9	107.1	179.2	1100.5	845.4	782.7
HLG AT RV	TMI-2	185.8	162.3	222.1	2019.8	825.6	1221.0
HLG AT RV	CRYSTAL RIVER 3	169.9	107.1	179.2	1100.5	845.4	782.7
HLG AT RV	ANO-1	115.0	86.0	103.5	721.1	409.2	611.6
HLG AT RV	RANCHO SECO	149.1	93.2	160.7	946.5	523.8	671.4
CLG AT RV	OCONEE 1,2,3	258.6	61.2	198.0	832.8	701.3	416.6
CLG AT RV	TMI-1	227.0	59.5	182.6	797.2	706.9	396.0
CLG AT RV	TMI-2	220.6	76.1	174.9	929.0	743.1	573.8
CLG AT RV	CRYSTAL RIVER 3	227.0	59.5	182.6	797.2	706.9	396.0
CLG AT RV	ANO-1	200.3	57.2	173.8	621.3	535.3	425.6
CLG AT RV	RANCHO SECO	213.4	57.7	174.7	673.5	532.1	431.7
HLG AT RV	DAVIS BESSE 1	2857.3	1054.3	3404.3	2540.4	15264.9	2759.6
HLG AT EL	DAVIS BESSE 1	823.8	361.4	959.8	1014.9	4313.4	1063.1
CLG AT EL	DAVIS BESSE 1	235.1	240.4	313.2	690.1	1253.4	685.0
CLG AT RV	DAVIS BESSE 1	324.5	231.8	476.7	603.3	1866.4	640.4

Table 9.11-7. A Outlet Nozzle/Shell Interface, Joint 65

LOAD CASE		FORCES (KIPS) FX	FY	FZ	MOMENTS (FT-KIPS) MX	MY	MZ
HLG AT RV	OCONEE 1,2 3	.0	.0	.0	.0	.0	.0
HLG AT RV	TMI-1	.0	.0	.0	.0	.0	.0
HLG AT RV	TMI-2	.0	.0	.0	.0	.0	.0
HLG AT RV	CRYSTAL RIVER 3	.0	.0	.0	.0	.0	.0
HLG AT RV	ANO-1	.0	.0	.0	.0	.0	.0
HLG AT RV	RANCHO SECO	.0	.0	.0	.0	.0	.0
CLG AT RV	OCONEE 1,2,3	227.1	92.5	113.3	1423.2	2166.9	1089.3
CLG AT RV	TMI-1	174.4	82.5	97.7	1108.9	1727.7	984.9
CLG AT RV	TMI-2	178.1	95.0	115.5	1425.8	1799.4	1190.2
CLG AT RV	CRYSTAL RIVER 3	174.4	82.5	97.7	1108.9	1727.7	984.9
CLG AT RV	ANO-1	117.4	69.9	74.8	930.0	1191.4	831.5
CLG AT RV	RANCHO SECO	120.2	73.0	81.1	973.1	1226.6	824.9
HLG AT RV	DAVIS BESSE 1	.0	.0	.0	.0	.0	.0
HLG AT EL	DAVIS BESSE 1	.8	179.3	62.0	1255.9	4.2	.0
CLG AT EL	DAVIS BESSE 1	327.6	185.6	100.4	898.3	2214.8	184.1
CLG AT RV	DAVIS BESSE 1	488.6	311.1	97.6	1773.8	3282.4	164.5

Table 9.11-8. B Outlet Nozzle/Shell Interface, Joint 64

LOAD CASE		FORCES (KIPS) FX	FY	FZ	MOMENTS (FT-KIPS) MX	MY	MZ
HLG AT RV	OCONEE 1,2 3	22.0	190.2	246.6	2555.9	368.6	79.9
HLG AT RV	TMI-1	33.6	245.9	382.7	3303.1	579.6	212.6
HLG AT RV	TMI-2	36.4	330.8	423.4	4650.4	493.3	152.8
HLG AT RV	CRYSTAL RIVER 3	33.6	245.9	382.7	3303.1	579.6	212.6
HLG AT RV	ANO-1	19.0	150.3	192.5	2034.5	187.3	93.8
HLG AT RV	RANCHO SECO	26.8	200.4	255.8	2666.0	377.9	125.8
CLG AT RV	OCONEE 1,2,3	230.0	109.9	109.1	1508.6	2199.8	1092.6
CLG AT RV	TMI-1	176.6	80.0	100.7	1095.4	1742.9	987.3
CLG AT RV	TMI-2	182.0	101.1	113.6	1414.5	1834.9	1194.2
CLG AT RV	CRYSTAL RIVER 3	176.6	80.0	100.7	1095.4	1742.9	987.3
CLG AT RV	ANO-1	117.7	71.2	73.0	937.7	1196.5	828.7
CLG AT RV	RANCHO SECO	120.8	80.6	80.1	1068.1	1235.0	823.3
HLG AT RV	DAVIS BESSE 1	12.9	682.4	425.8	3955.4	82.8	12.4
HLG AT EL	DAVIS BESSE 1	1.0	304.4	189.9	1587.2	4.3	1.7
CLG AT EL	DAVIS BESSE 1	329.6	189.5	100.1	1044.5	2227.5	183.1
CLG AT RV	DAVIS BESSE 1	544.2	171.1	98.6	993.0	3644.8	157.1

Table 9.11-9. In Shell Upper, Joint 70

LOAD CASE		FORCES (KIPS) FX	FY	FZ	MOMENTS (FT-KIPS) MX	MY	MZ
HLG AT RV	OCONEE 1,2 3	276.3	1827.6	3362.7	23490.5	184.9	1208.7
HLG AT RV	TMI-1	465.8	1846.9	4319.7	40470.0	179.9	4190.3
HLG AT RV	TMI-2	445.5	2096.9	5733.4	32316.9	154.6	4003.9
HLG AT RV	CRYSTAL RIVER 3	465.8	1846.9	4319.7	40470.0	179.9	4190.3
HLG AT RV	ANO-1	510.0	1737.9	2370.6	18504.5	192.9	3231.0
HLG AT RV	RANCHO SECO	536.2	1736.7	3433.2	22623.7	158.0	4203.9
CLG AT RV	OCONEE 1,2,3	4300.6	1585.5	1925.7	15932.4	171.5	39275.5
CLG AT RV	TMI-1	4205.5	1504.5	1782.7	16442.6	188.9	40369.5
CLG AT RV	TMI-2	4040.5	1283.1	1815.4	11135.1	190.8	42124.5
CLG AT RV	CRYSTAL RIVER 3	4205.5	1504.5	1782.7	16442.6	188.9	40369.5
CLG AT RV	ANO-1	4094.1	1218.1	1261.7	11857.5	167.5	40975.1
CLG AT RV	RANCHO SECO	4116.4	1534.1	1521.9	12840.7	155.9	40758.5
HLG AT RV	DAVIS BESSE 1	129.2	1334.0	2434.6	24703.2	11.3	692.7
HLG AT EL	DAVIS BESSE 1	94.9	1135.7	1815.0	11869.2	2.8	300.3
CLG AT EL	DAVIS BESSE 1	3642.9	1095.6	2401.9	27101.9	18.3	40764.3
CLG AT RV	DAVIS BESSE 1	1471.5	462.0	1178.3	10789.0	119.0	13801.5

Table 9.11-10. In Shell Middle, Joint 36

LOAD CASE	FORCES (KIPS) FX	FY	FZ	MOMENTS (FT-KIPS) MX	MY	MZ
HLG AT RV OCONEE 1,2 3	155.0	5493.2	7418.5	108609.3	1168.3	5078.6
HLG AT RV TMI-1	484.1	6358.2	9237.5	143518.8	1469.7	10542.4
HLG AT RV TMI-2	456.3	6532.0	15125.5	218696.1	1468.1	5565.6
HLG AT RV CRYSTAL RIVER 3	484.1	6358.2	9237.5	143518.8	1469.7	10542.4
HLG AT RV ANO-1	411.9	4435.9	5863.6	84766.4	1051.7	4788.5
HLG AT RV RANCHO SECO	364.6	6045.5	8096.2	115327.0	1193.6	5721.2
CLG AT RV OCONEE 1,2,3	7530.7	4774.3	3814.2	49565.1	1584.5	96649.2
CLG AT RV TMI-1	6253.8	4297.1	4027.3	51402.7	1840.8	92110.2
CLG AT RV TMI-2	7878.1	3328.6	4110.9	56143.5	1885.6	115244.4
CLG AT RV CRYSTAL RIVER 3	6253.8	4297.1	4027.3	51402.7	1840.8	92110.2
CLG AT RV ANO-1	5547.2	2982.2	3062.3	34052.2	1277.7	71462.4
CLG AT RV RANCHO SECO	5503.0	4640.7	3573.8	39734.4	1339.6	70985.4
HLG AT RV DAVIS BESSE 1	41.7	.0	993.0	5528.0	.0	188.0
HLG AT EL DAVIS BESSE 1	43.8	.0	603.8	6289.0	.0	285.1
CLG AT EL DAVIS BESSE 1	1067.0	.0	755.4	3188.9	.0	4127.8
CLG AT RV DAVIS BESSE 1	550.5	.0	425.6	2548.6	.0	2138.5

Table 9.11-11. In Shell Lower, Joint 19

LOAD CASE		FORCES (KIPS) FX	FY	FZ	MOMENTS (FT-KIPS) MX	MY	MZ
HLG AT RV	OCONEE 1,2 3	168.0	5493.2	7670.6	153355.9	1168.3	4994.7
HLG AT RV	TMI-1	475.4	6358.2	9414.4	201108.6	1469.7	11112.7
HLG AT RV	TMI-2	433.8	6532.0	15210.2	315532.7	1468.1	7403.7
HLG AT RV	CRYSTAL RIVER 3	475.4	6358.2	9414.4	201108.6	1469.7	11112.7
HLG AT RV	ANO-1	381.3	4435.9	5913.5	121891.3	1051.7	6774.5
HLG AT RV	RANCHO SECO	328.8	6045.5	8333.3	165503.7	1193.6	7592.1
CLG AT RV	OCONEE 1,2,3	7814.0	4774.3	3946.4	72355.2	1584.5	145202.9
CLG AT RV	TMI-1	6503.3	4297.1	4005.3	76776.3	1840.8	131861.6
CLG AT RV	TMI-2	7729.5	3328.6	4025.5	81971.5	1885.6	163895.3
CLG AT RV	CRYSTAL RIVER 3	6503.3	4297.1	4005.3	76776.3	1840.8	131861.6
CLG AT RV	ANO-1	5774.6	2982.2	3120.6	53781.0	1277.7	107280.9
CLG AT RV	RANCHO SECO	5798.3	4640.7	3638.8	61826.8	1339.6	106719.6
HLG AT RV	DAVIS BESSE 1	17.2	.0	525.9	1618.7	.0	52.9
HLG AT EL	DAVIS BESSE 1	23.1	.0	596.5	1836.0	.0	71.1
CLG AT EL	DAVIS BESSE 1	292.6	.0	321.9	990.8	.0	900.7
CLG AT RV	DAVIS BESSE 1	170.7	.0	262.1	806.6	.0	525.4

Table 9.11-12. Skirt Load at RV Attachment Point, Joint 19

LOAD CASE		FORCES (KIPS) FX	FY	FZ	MOMENTS (FT-KIPS) MX	MY	MZ
HLG AT RV	OCONEE 1,2,3	182.9	5493.2	8015.2	153068.5	1168.3	5107.3
HLG AT RV	TMI-1	514.0	6358.2	9617.5	200867.6	1469.7	11314.1
HLG AT RV	TMI-2	449.0	6532.0	15415.3	314883.1	1468.1	7388.4
HLG AT RV	CRYSTAL RIVER 3	514.0	6358.2	9617.5	200867.6	1469.7	11314.1
HLG AT RV	ANO-1	388.8	4435.9	6029.1	121598.1	1051.7	6750.1
HLG AT RV	RANCHO SECO	359.8	5119.3	6984.2	136276.68	1087.2	7562.2
CLG AT RV	OCONEE 1,2,3	8176.8	4774.3	4127.7	72130.8	1584.5	144404.9
CLG AT RV	TMI-1	6760.3	4297.1	4117.9	76520.3	1840.8	131507.2
CLG AT RV	TMI-2	7844.9	3328.6	4068.4	81835.9	1885.6	163608.2
CLG AT RV	CRYSTAL RIVER 3	6760.3	4297.1	4117.9	76520.3	1840.8	131507.2
CLG AT RV	ANO-1	6024.5	2982.2	3271.1	53350.9	1277.7	106651.5
CLG AT RV	RANCHO SECO	6063.0	4640.7	3811.0	61392.0	1339.6	106081.1

Table 9.11-13. Peak Core Flood Line Nozzle Loads

Axial load, kips	Transverse loads, kips	Resultant moment ft-kips
88.2	61.3	354

Figure 9.11-1. CRDM Noz. Load Jt 120

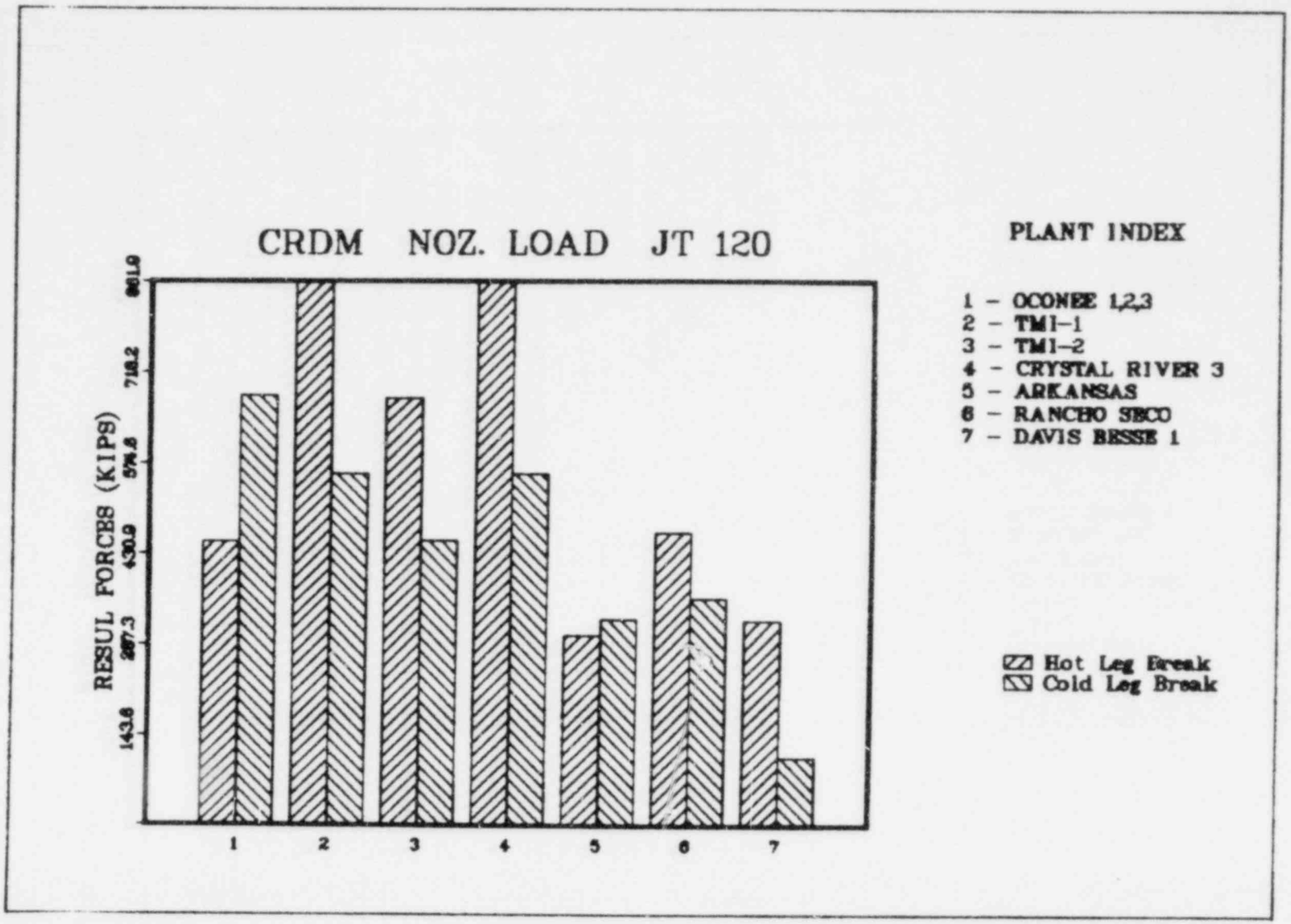

Figure 9.11-2. CRDM Noz. Load Jt 120

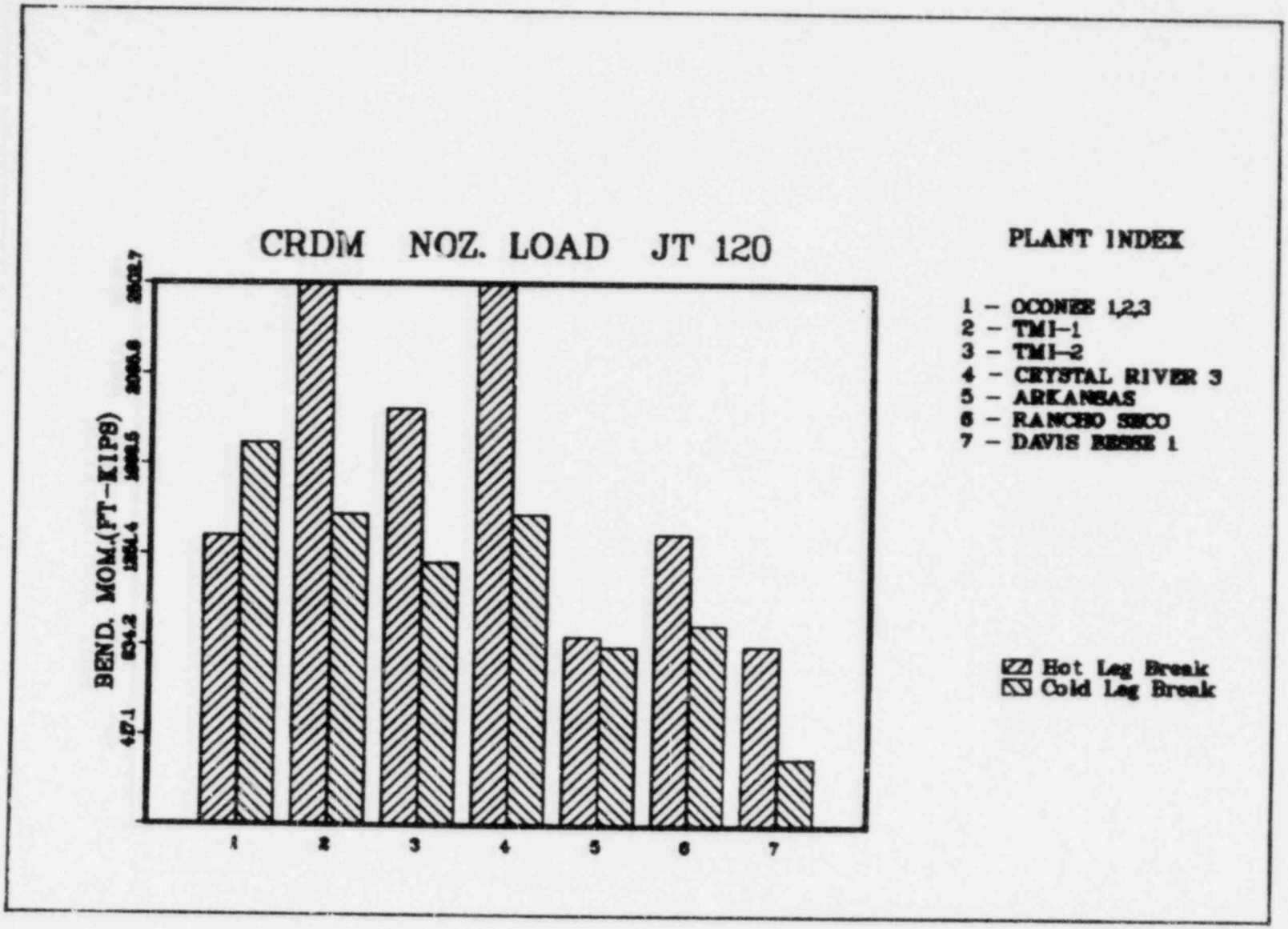

Figure 9.11-3. Cold Leg Straight Section

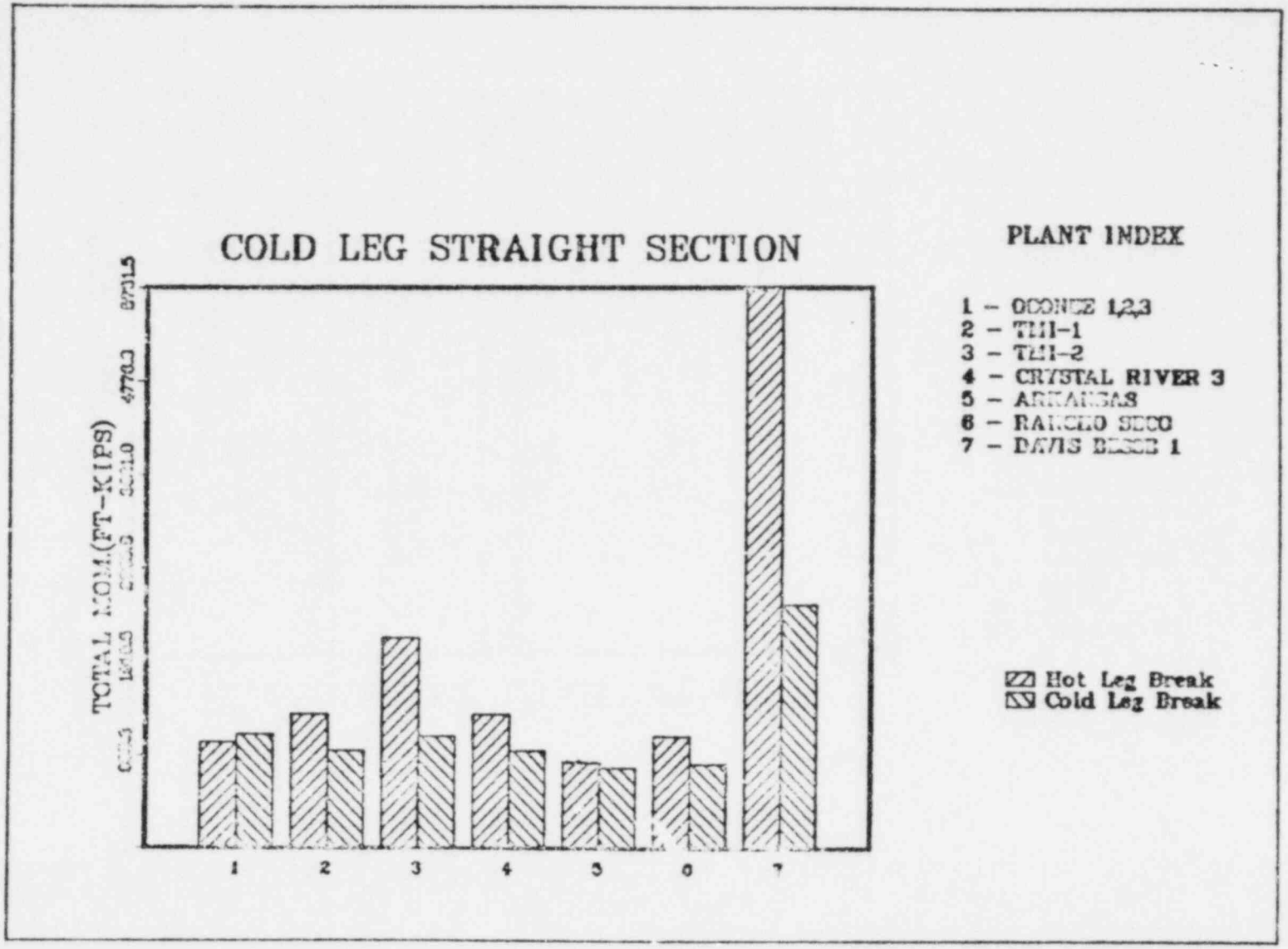

Figure 9.11-4. SSS Skirt Load Jt 113

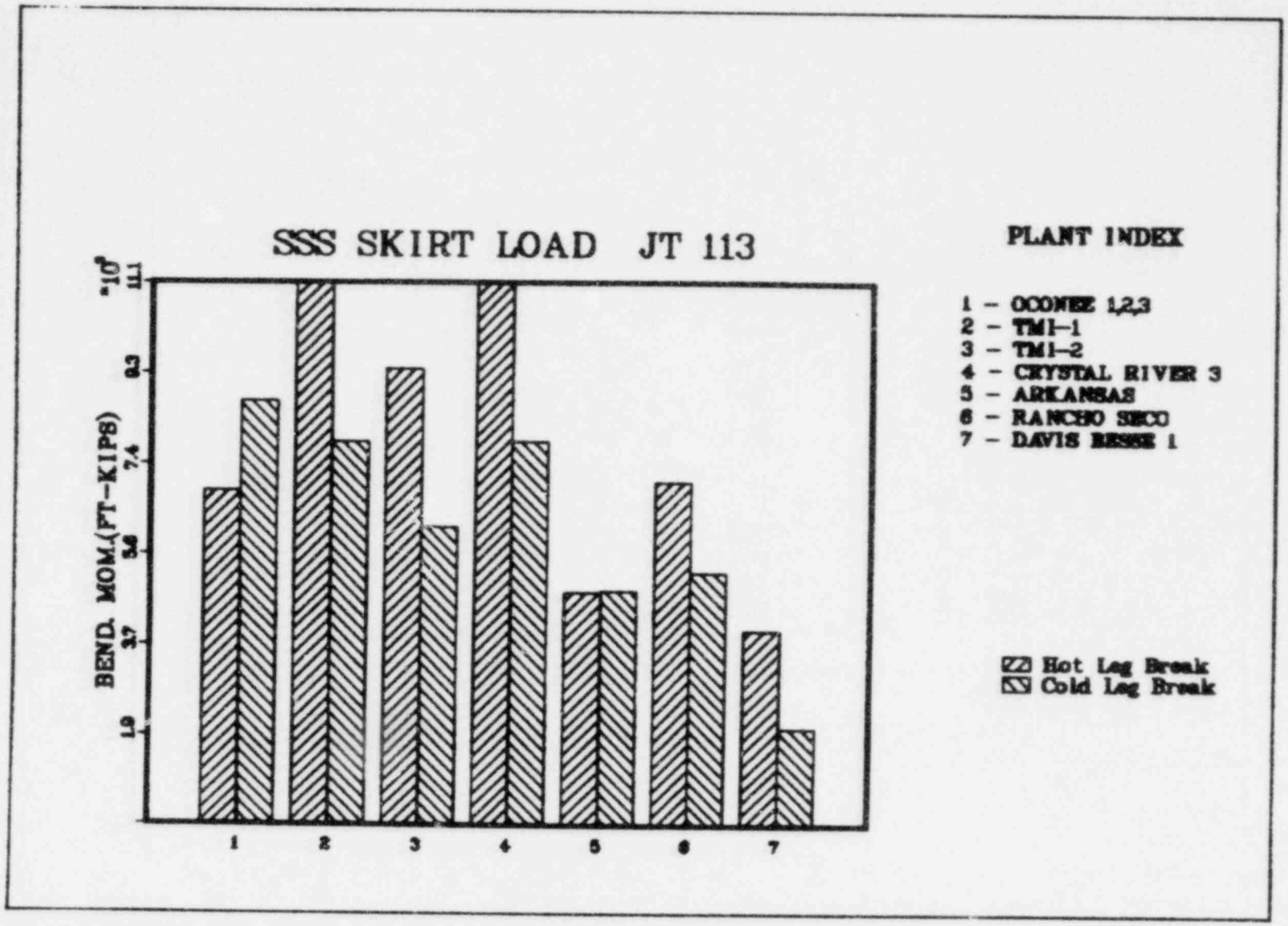

Figure 9.11-5. P1A1 Inlet Noz/Shell Jt 71

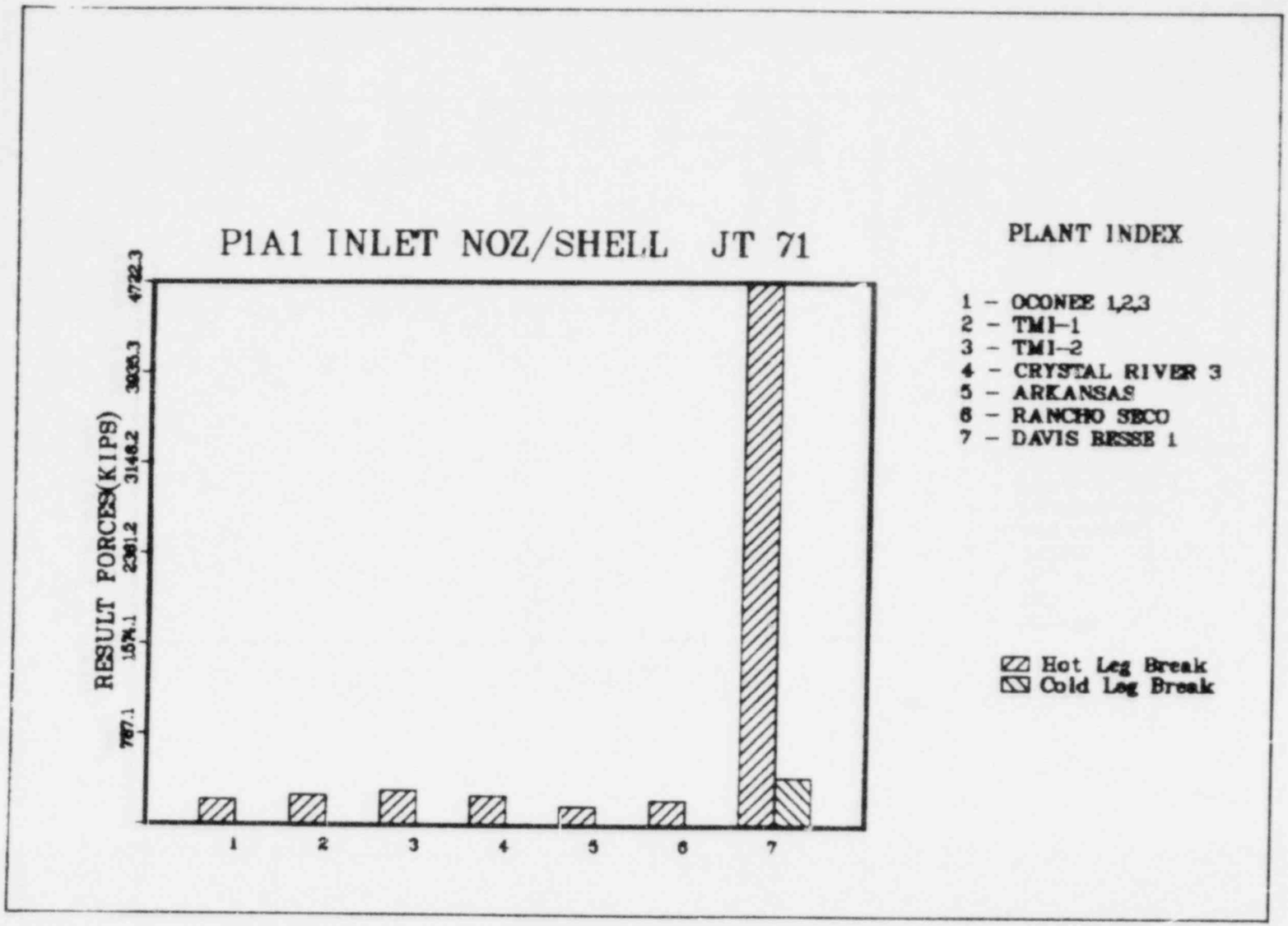

Figure 9.11-6. P1A1 Inlet Noz/Shell Jt 71

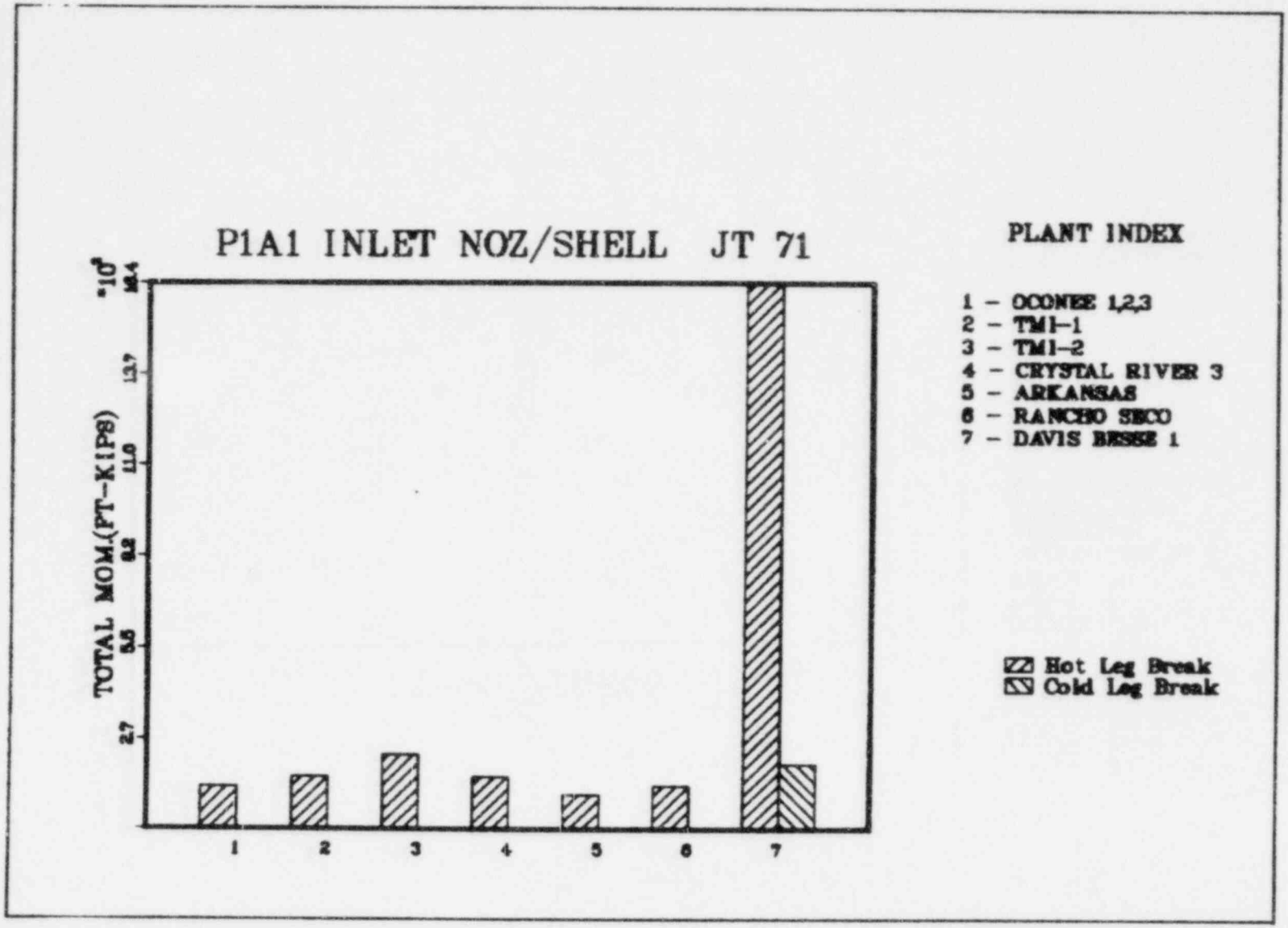

Figure 9.11-7. P1A2 Inlet Noz Jt 67

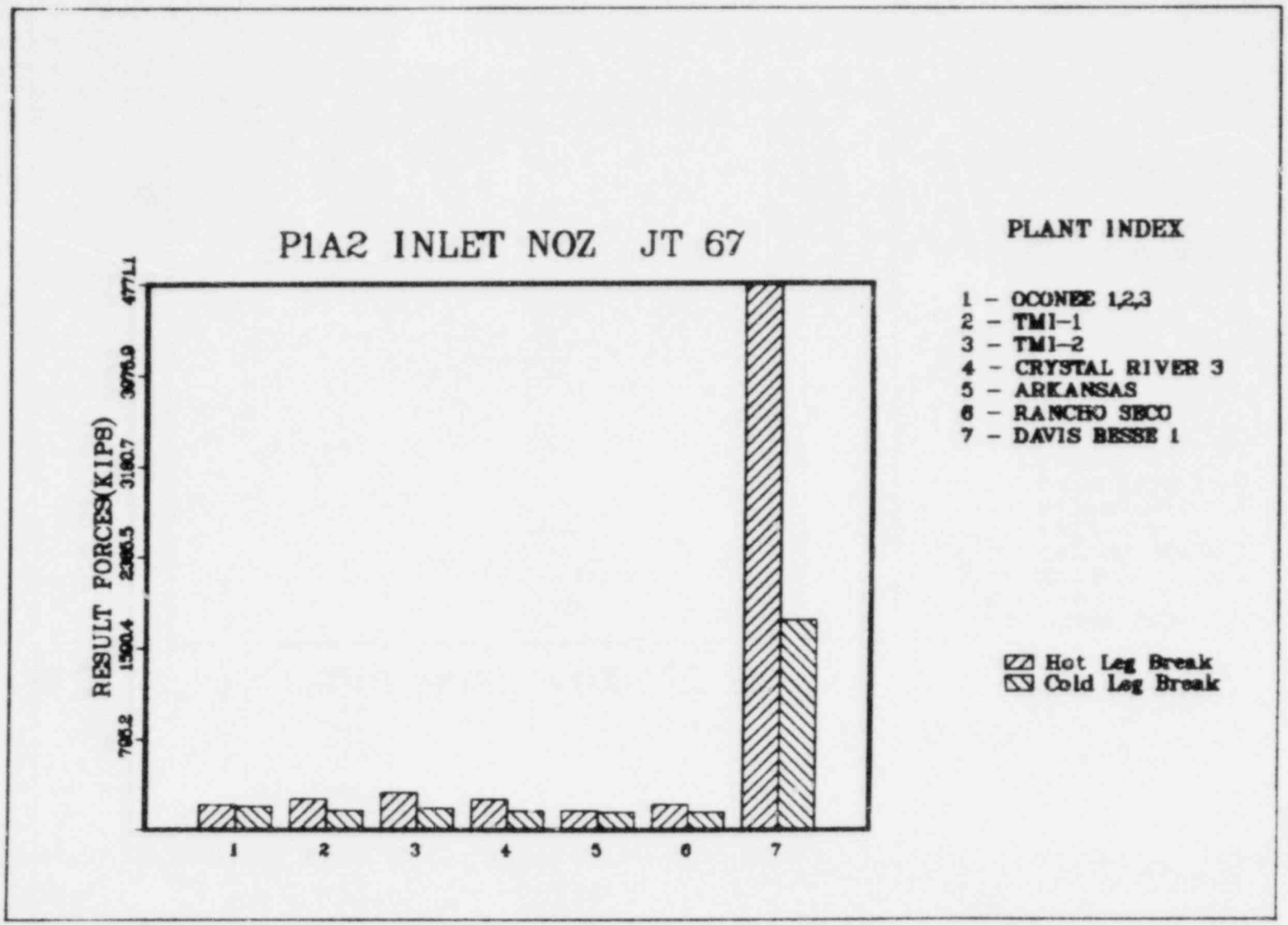

Figure 9.11-8. P1A2 Inlet Noz Jt 67

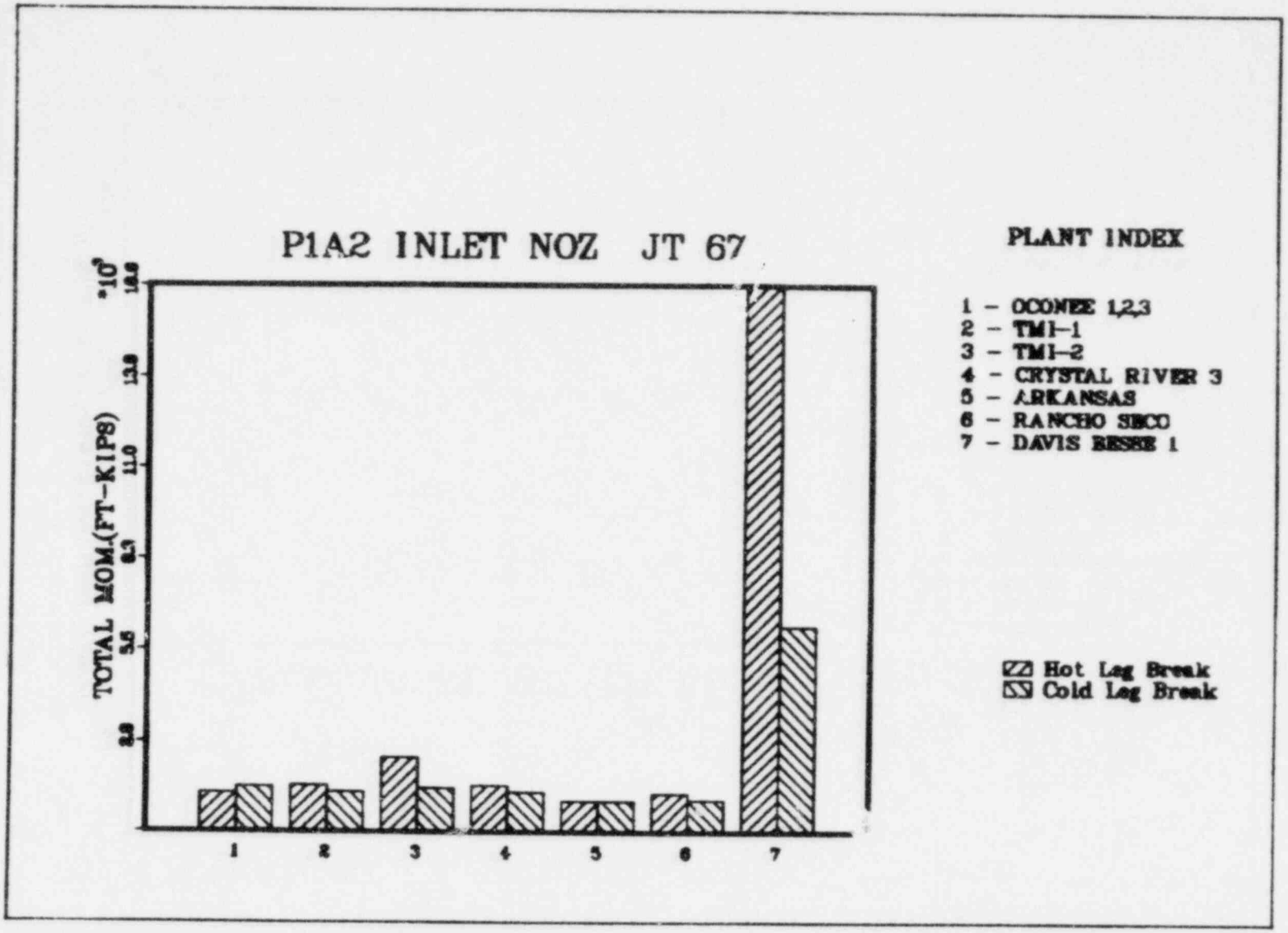

Figure 9.11-9. P1B1 Inlet Noz Intrface Jt 66

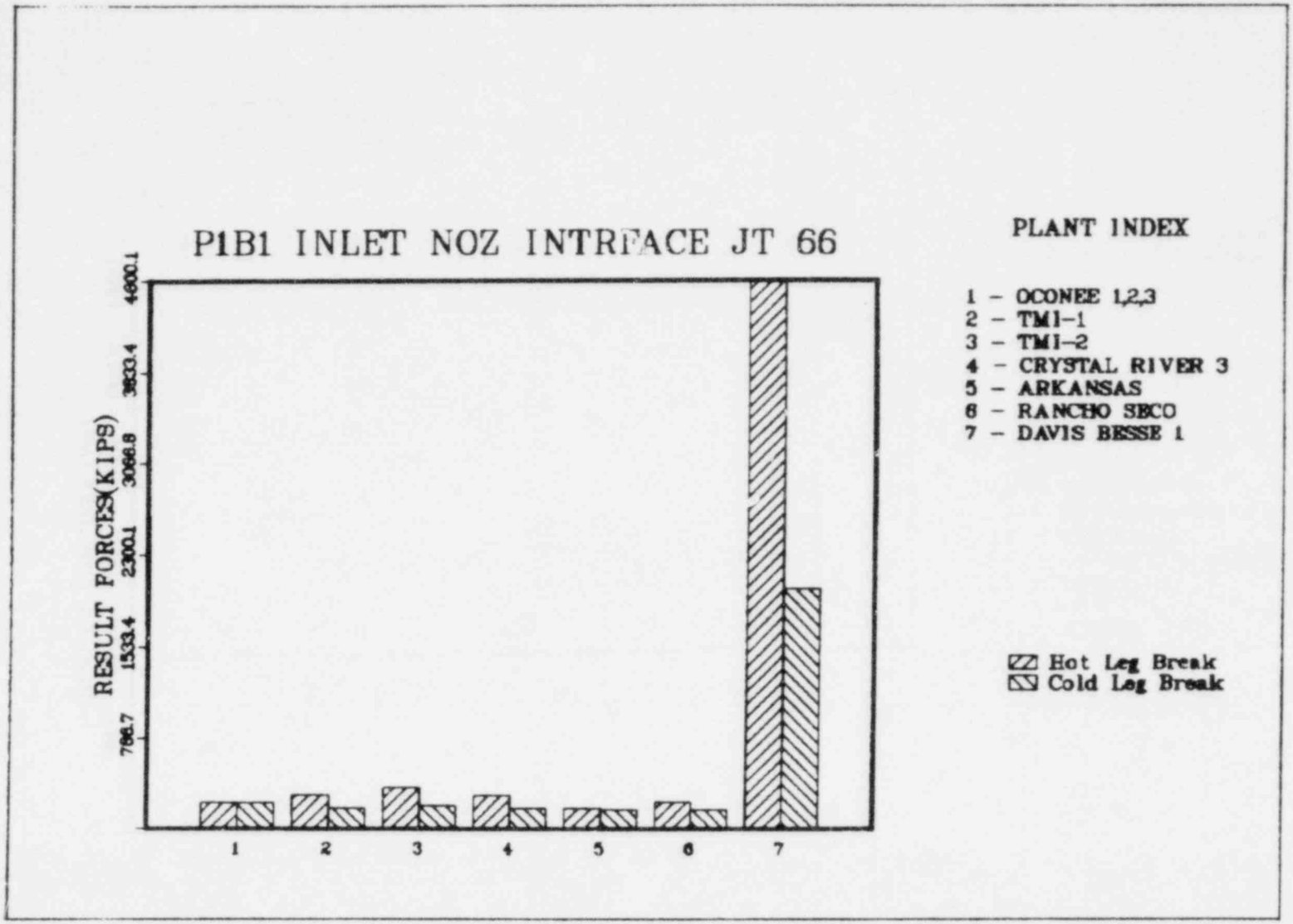

Figure 9.11-10. P1B1 Inlet Noz Jt 66

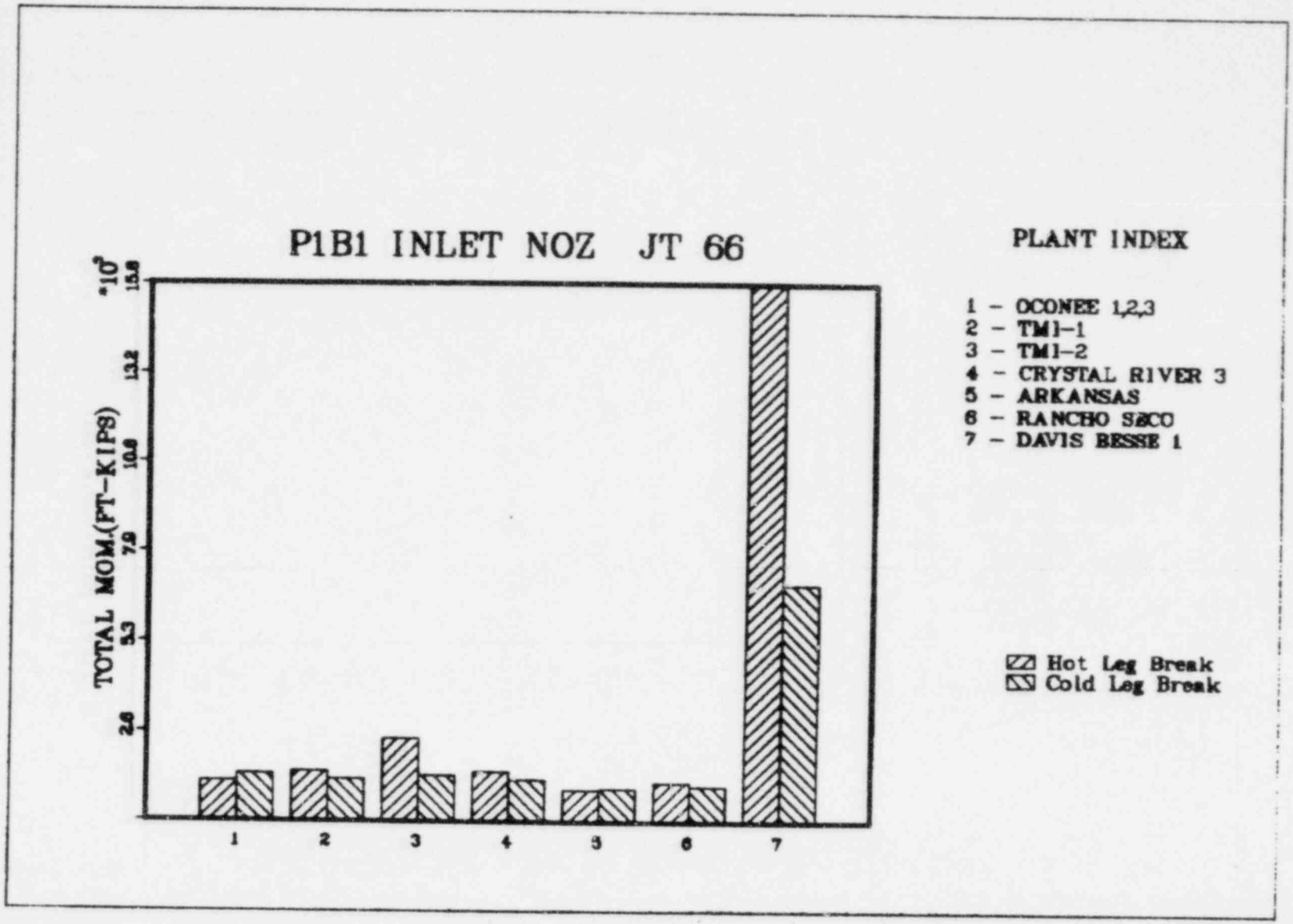

Figure 9.11-11. P1B2 Inlet Noz Jt 69

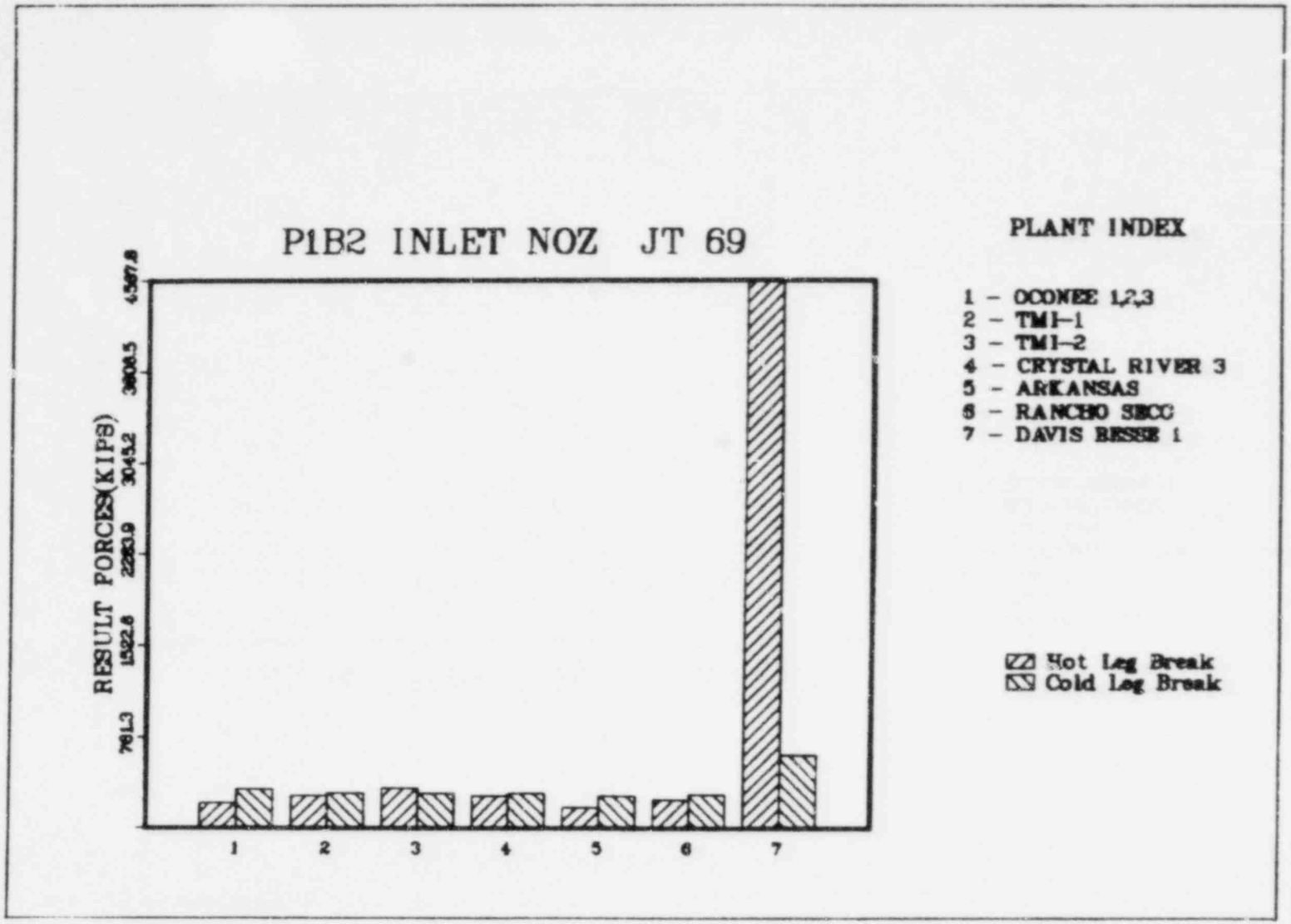

Figure 9.11-12. P1B2 Inlet Noz Jt 69

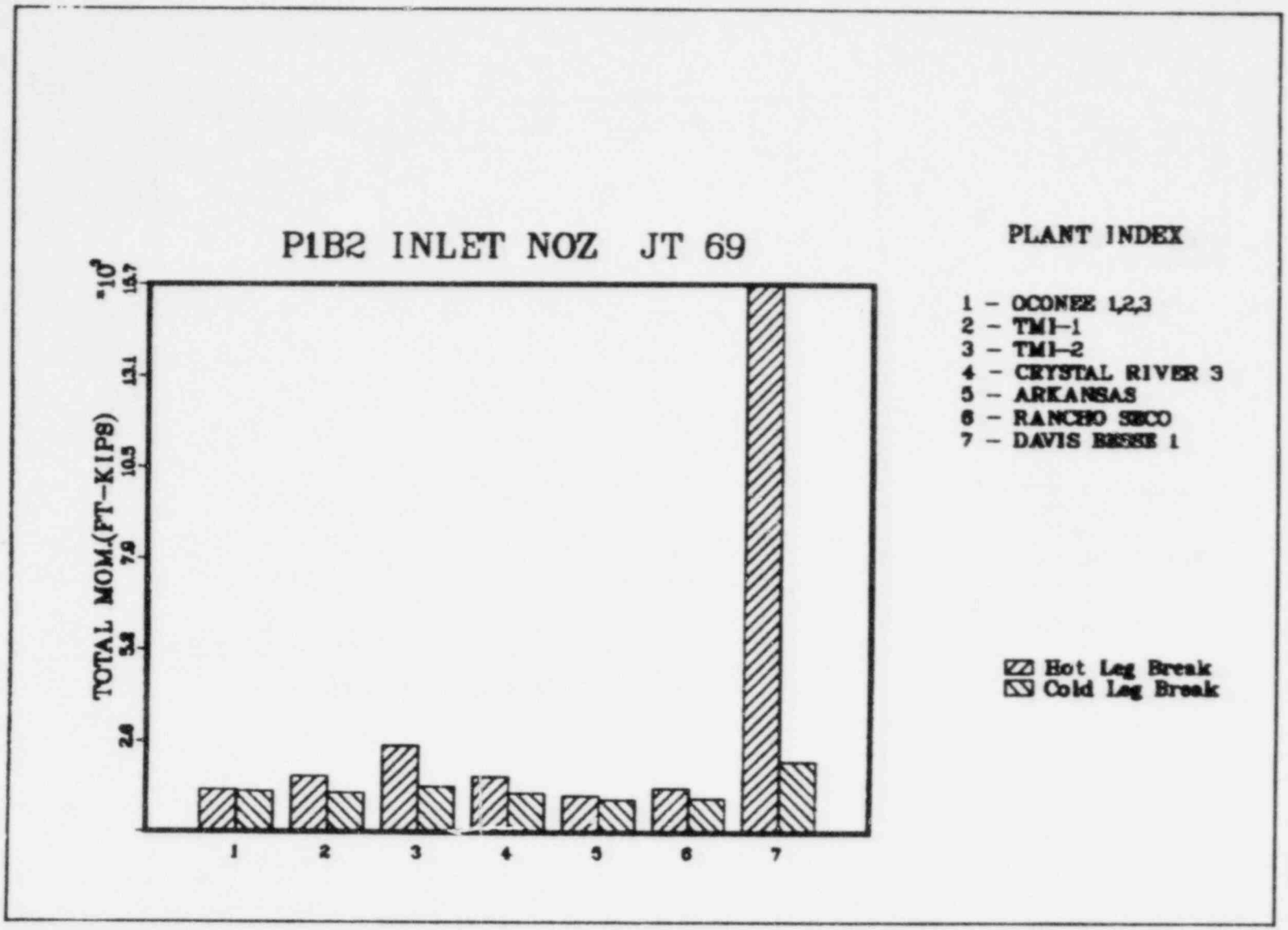

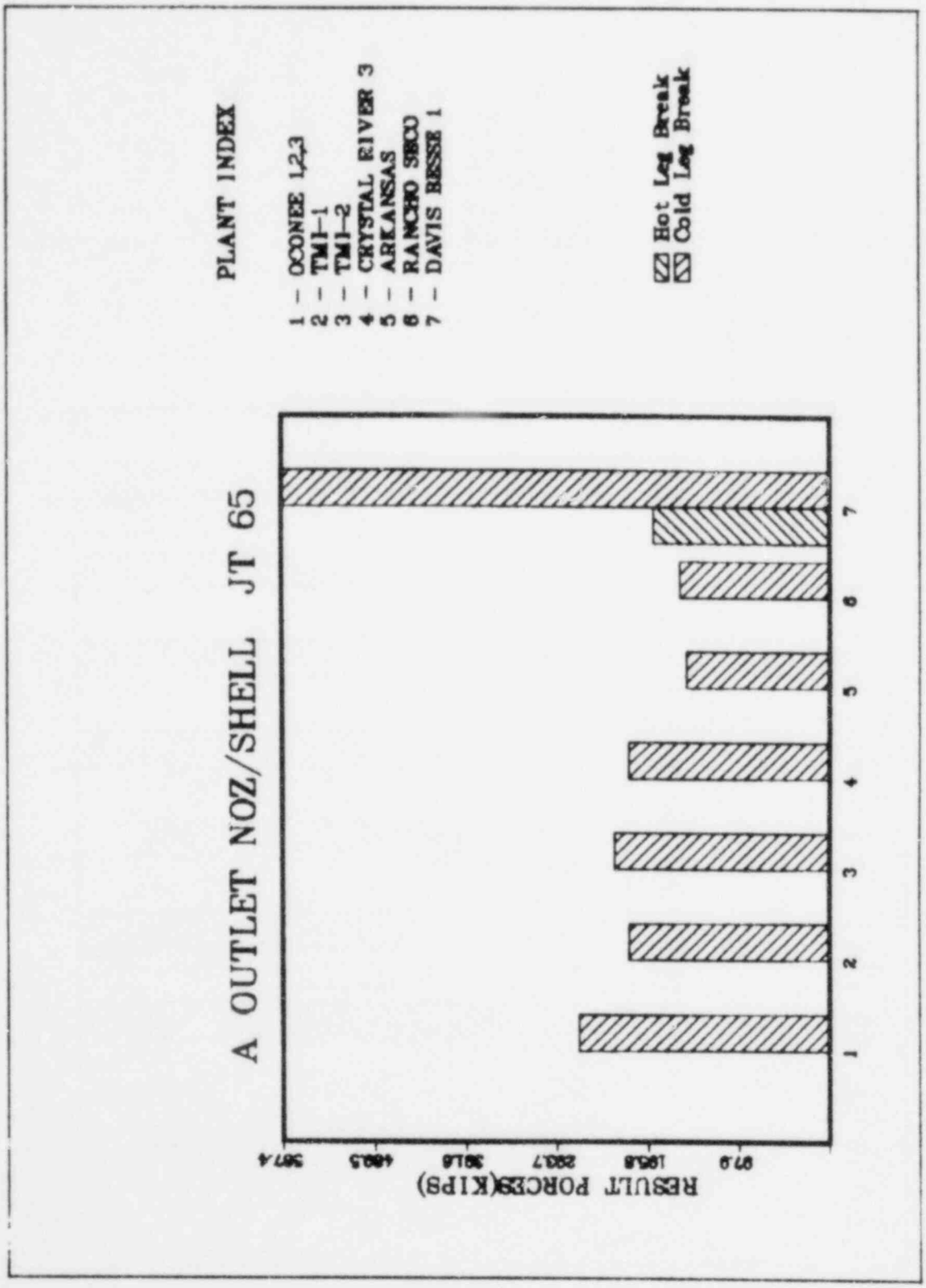

Figure 9.11-13. A Outlet Noz/Shell Jt 65

Figure 9.11-14. A Outlet Noz/Shell Jt 65

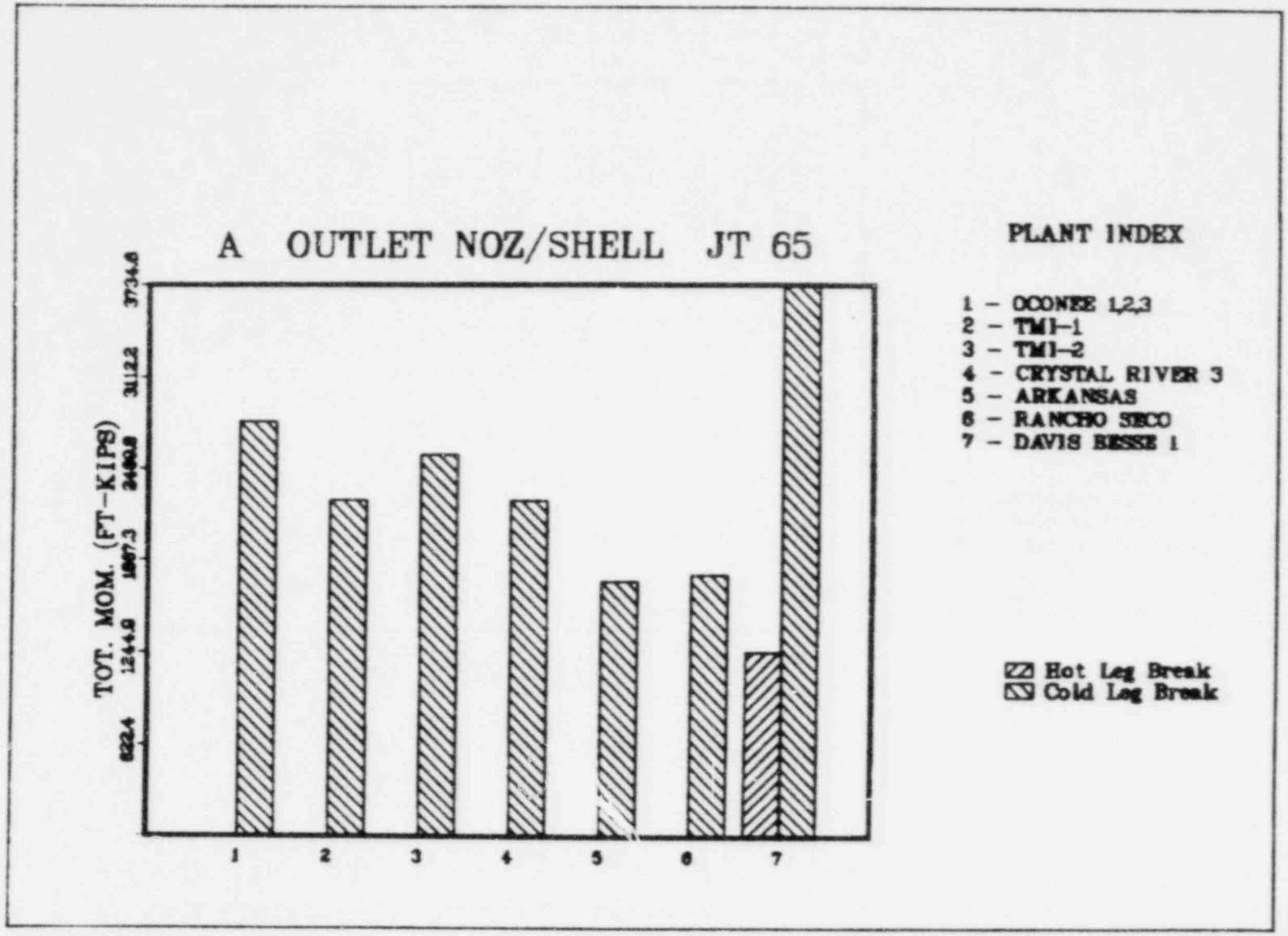

Figure 9.11-15. B Outlet Noz/Shell Jt 64

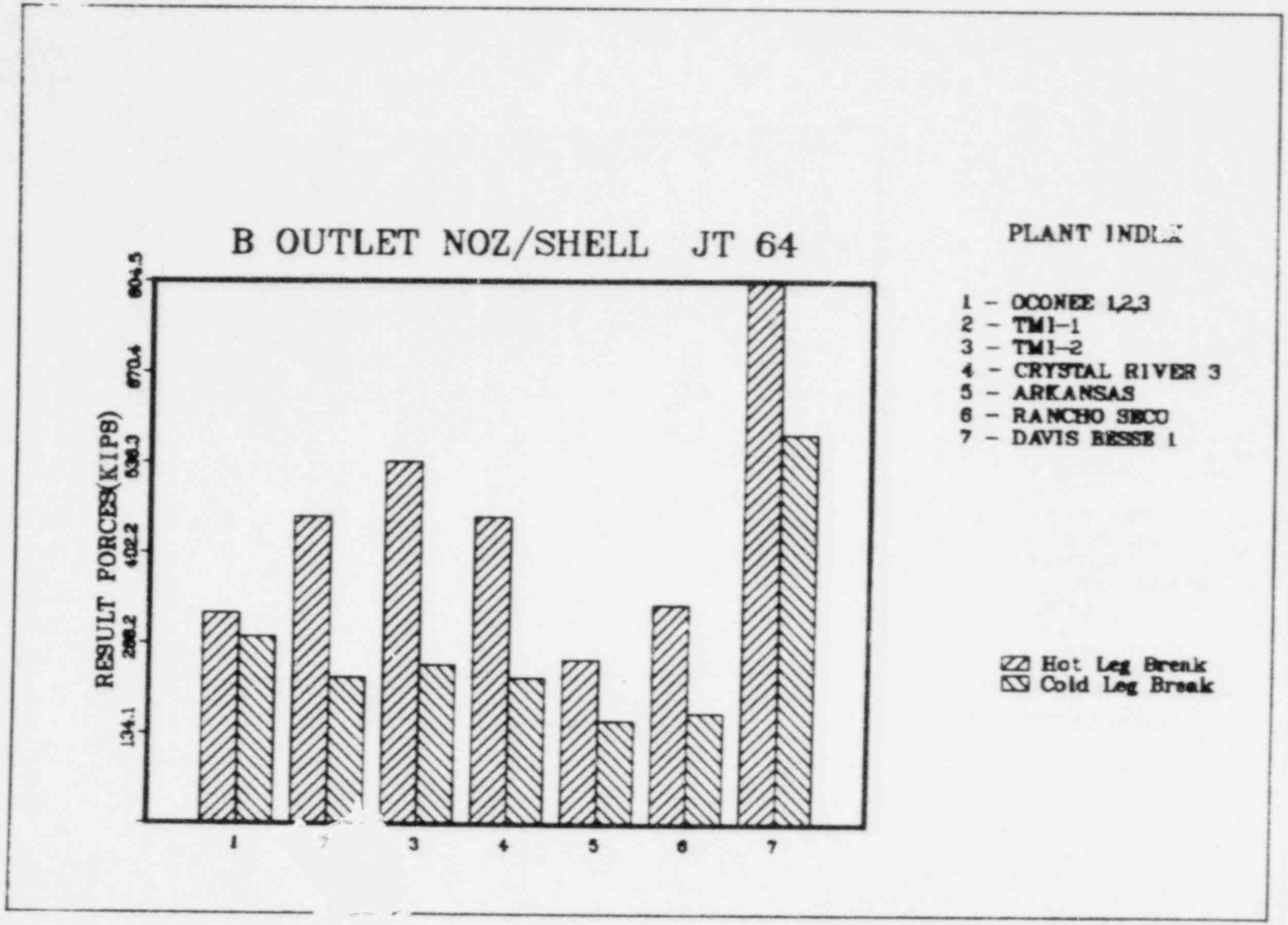

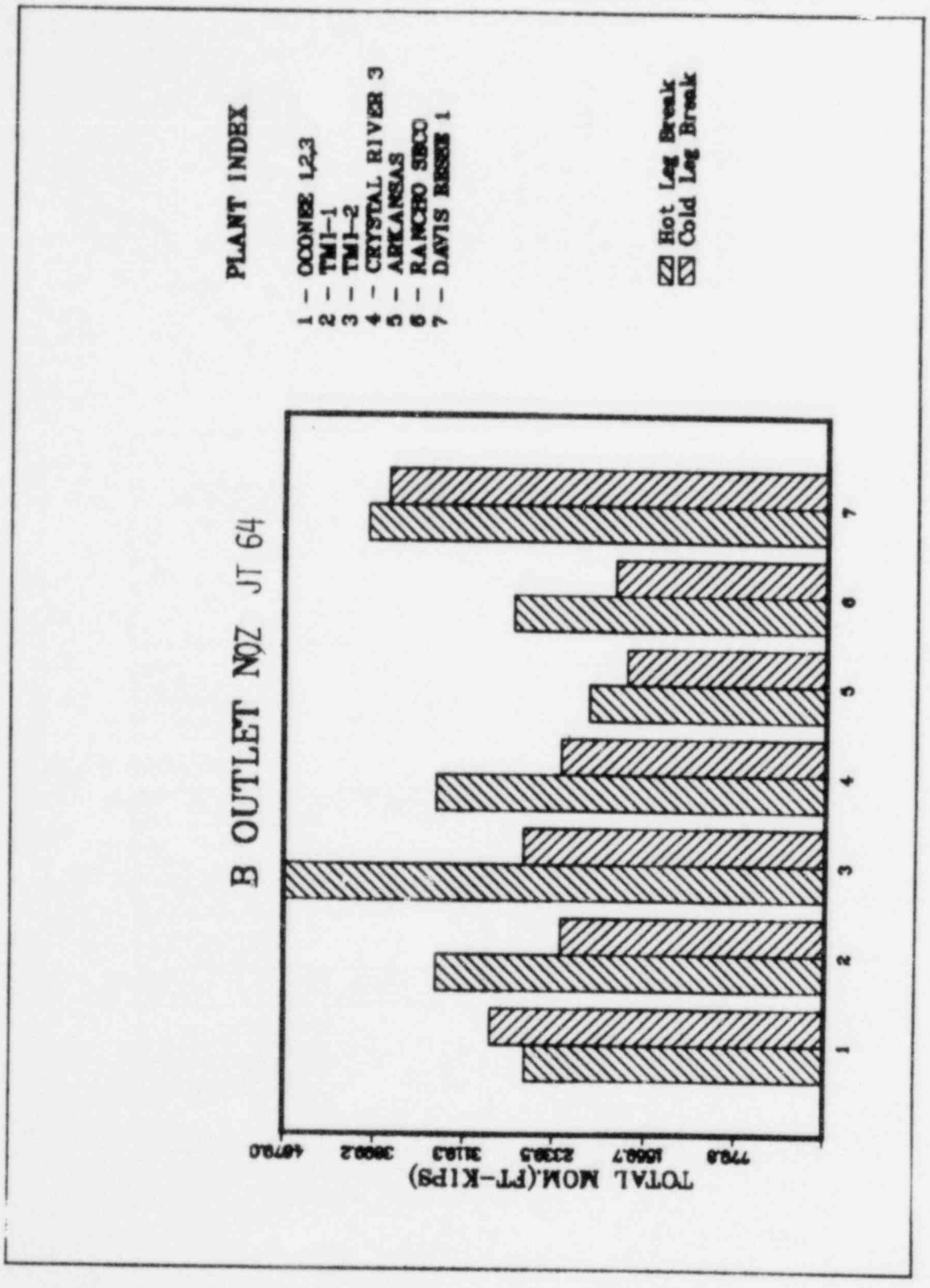

Figure 9.11-16. B Outlet Noz Jt 64

Figure 9.11-17. In Shell Upper Jt 70

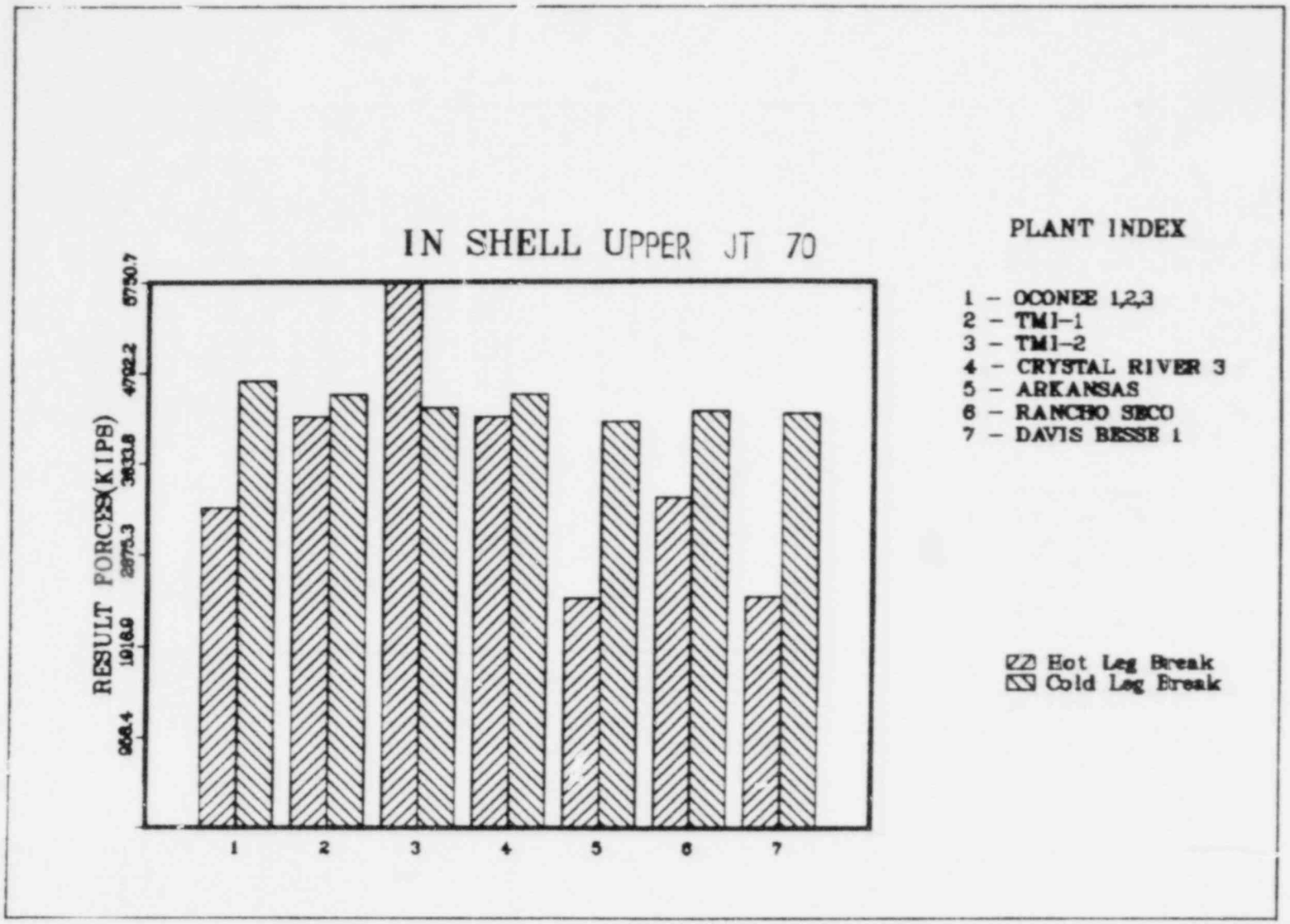

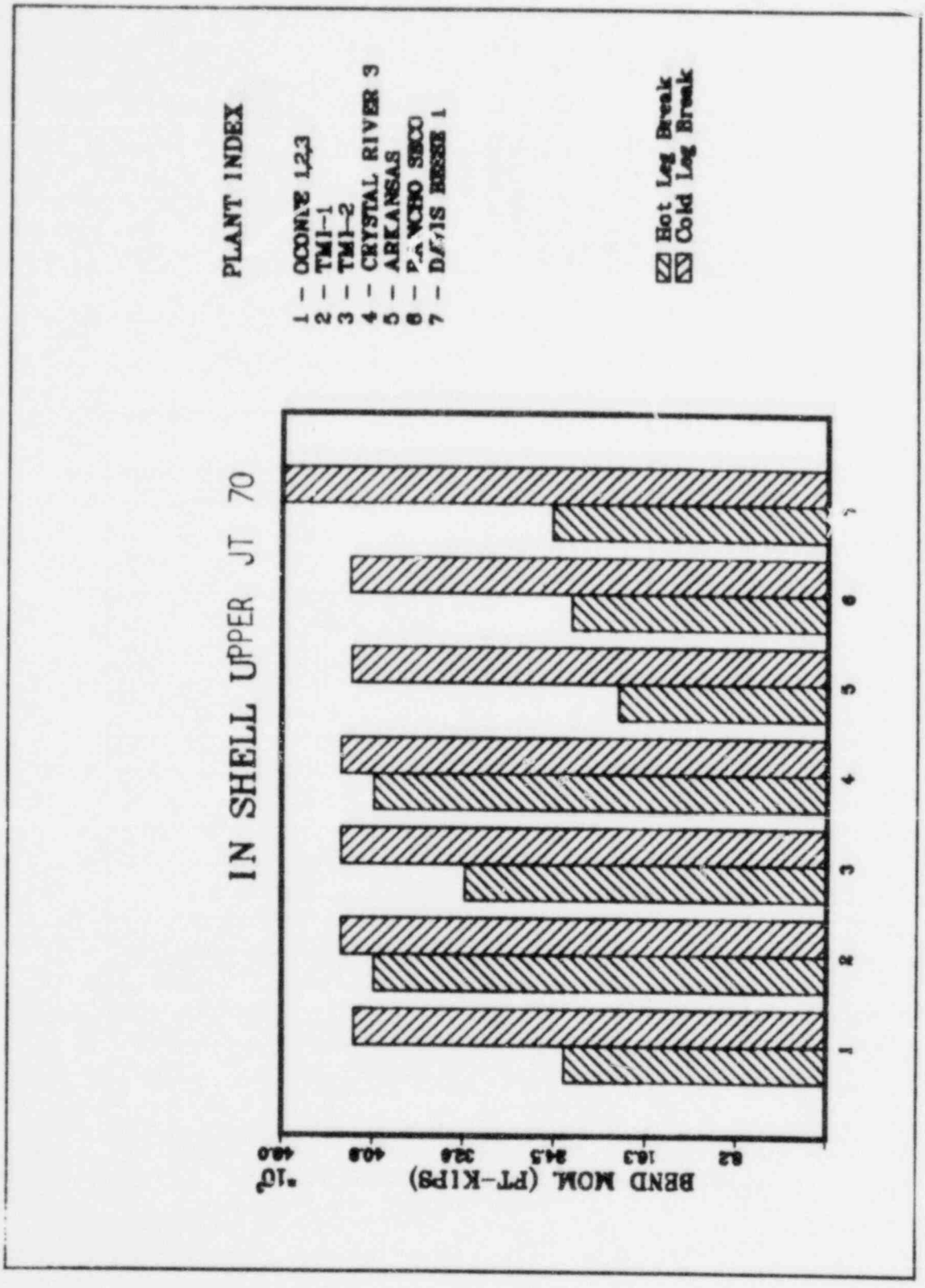

Figure 9.11-18. In Shell Upper Jt 70

Figure 9.11-19. In Shell Middle Jt 36

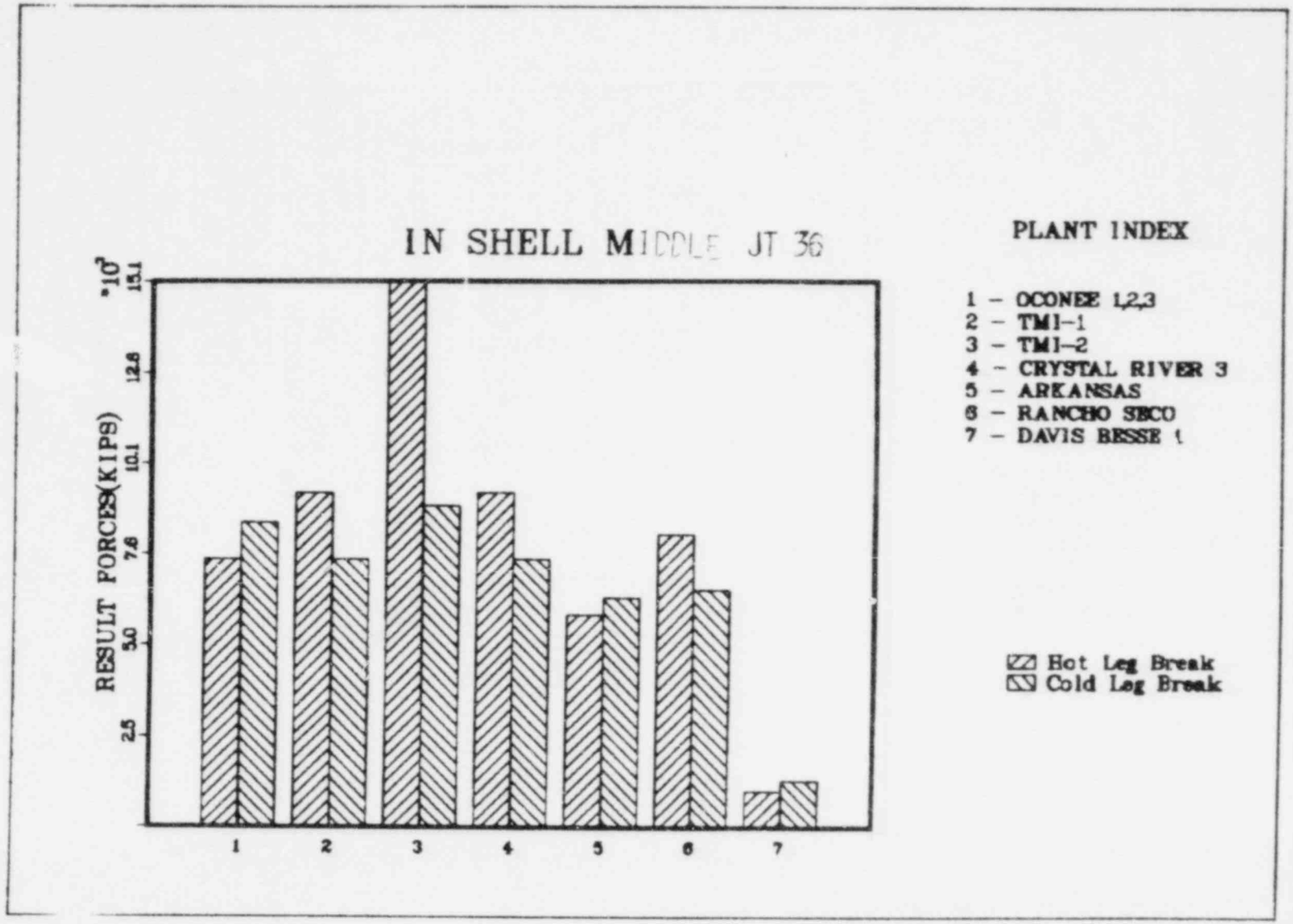

Figure 9.11-20. In Shell Middle Jt 36

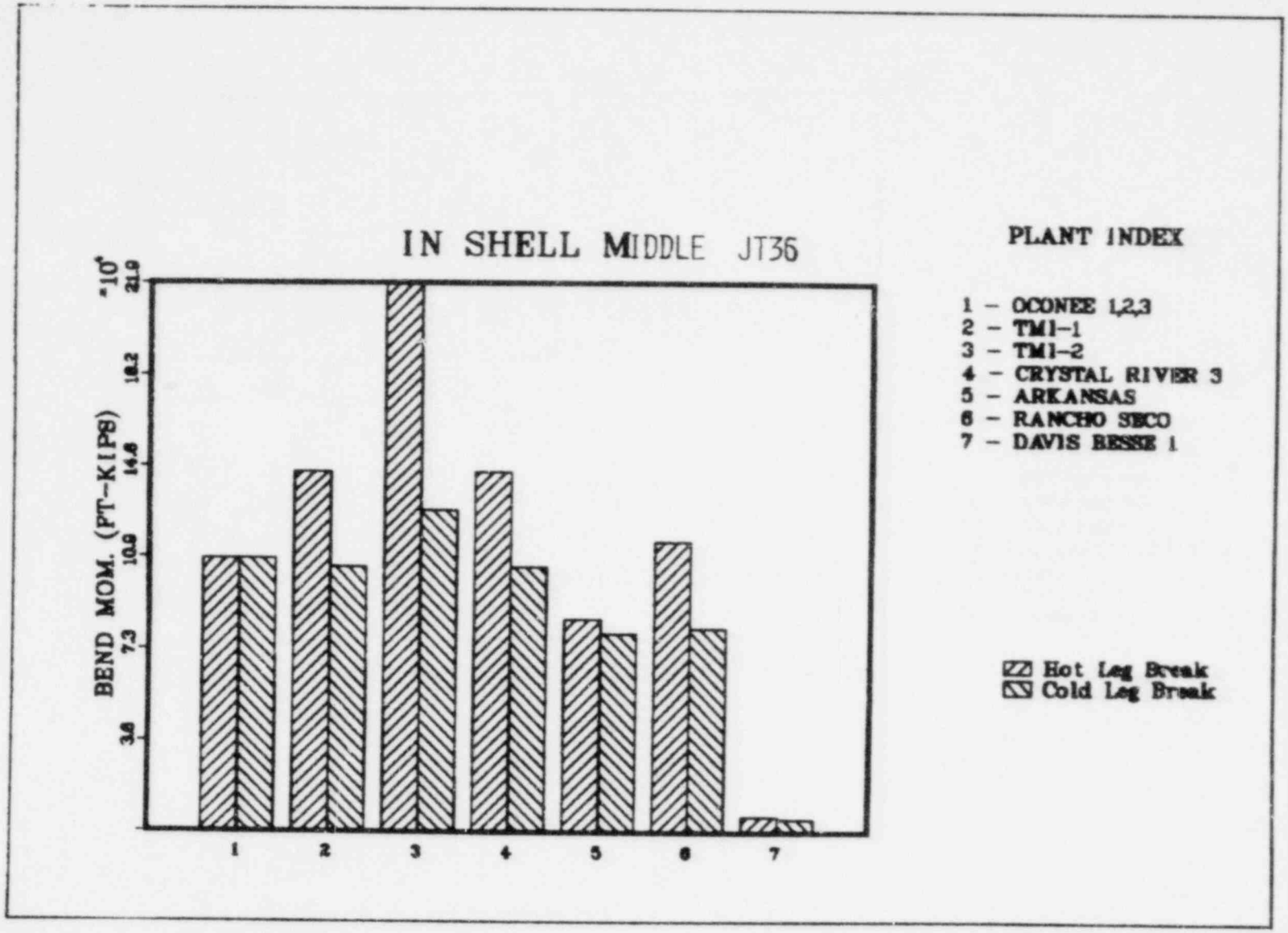

Figure 9.11-21. In Shell Lower Jt 19

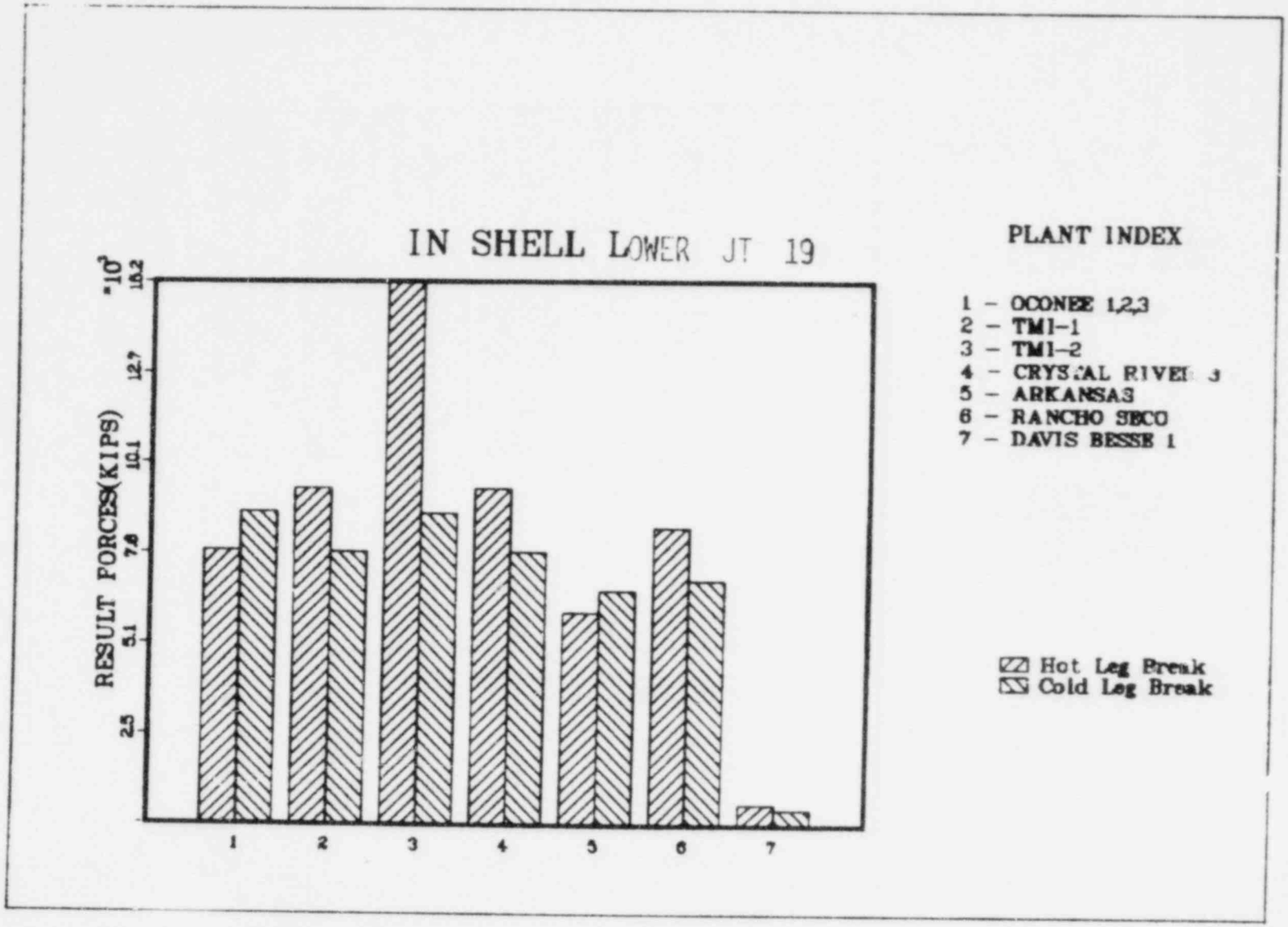

Figure 9.11-22. In Shell Lower Jt 19

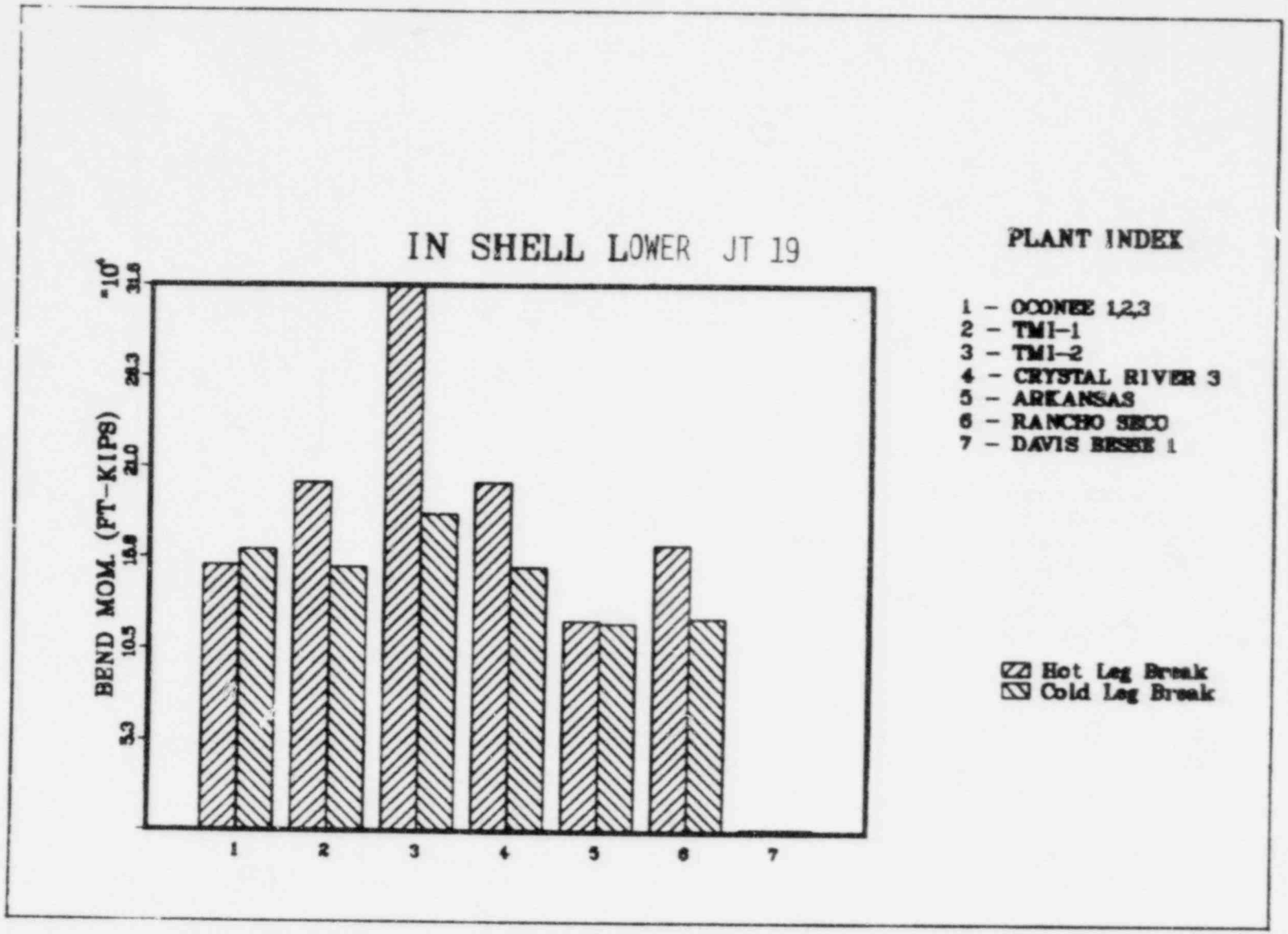

Figure 9.11-23. Skirt Load at RV AT. PT Jt 19

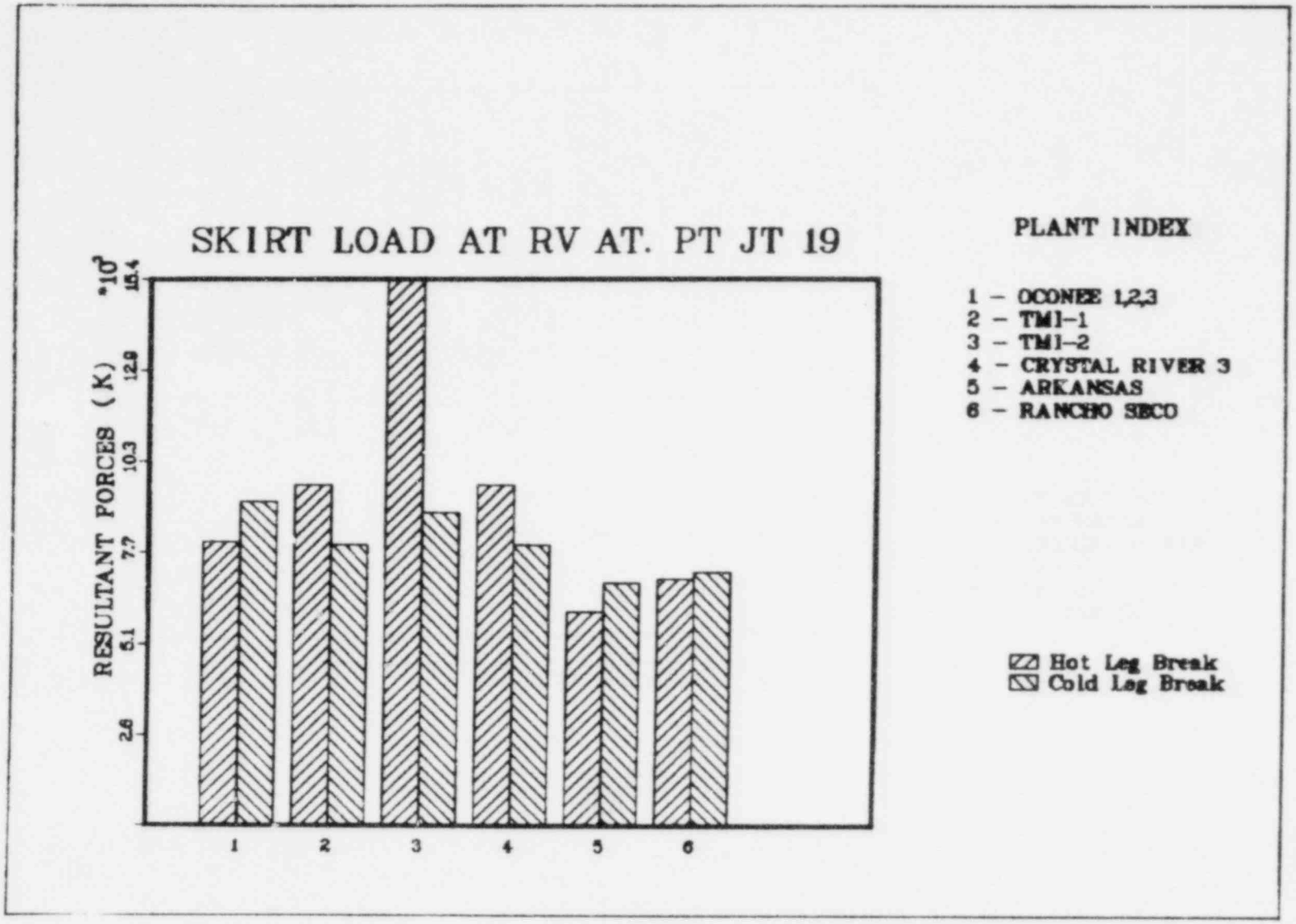

Figure 9.11-24. Skirt Load at RV AT. PT Jt 19

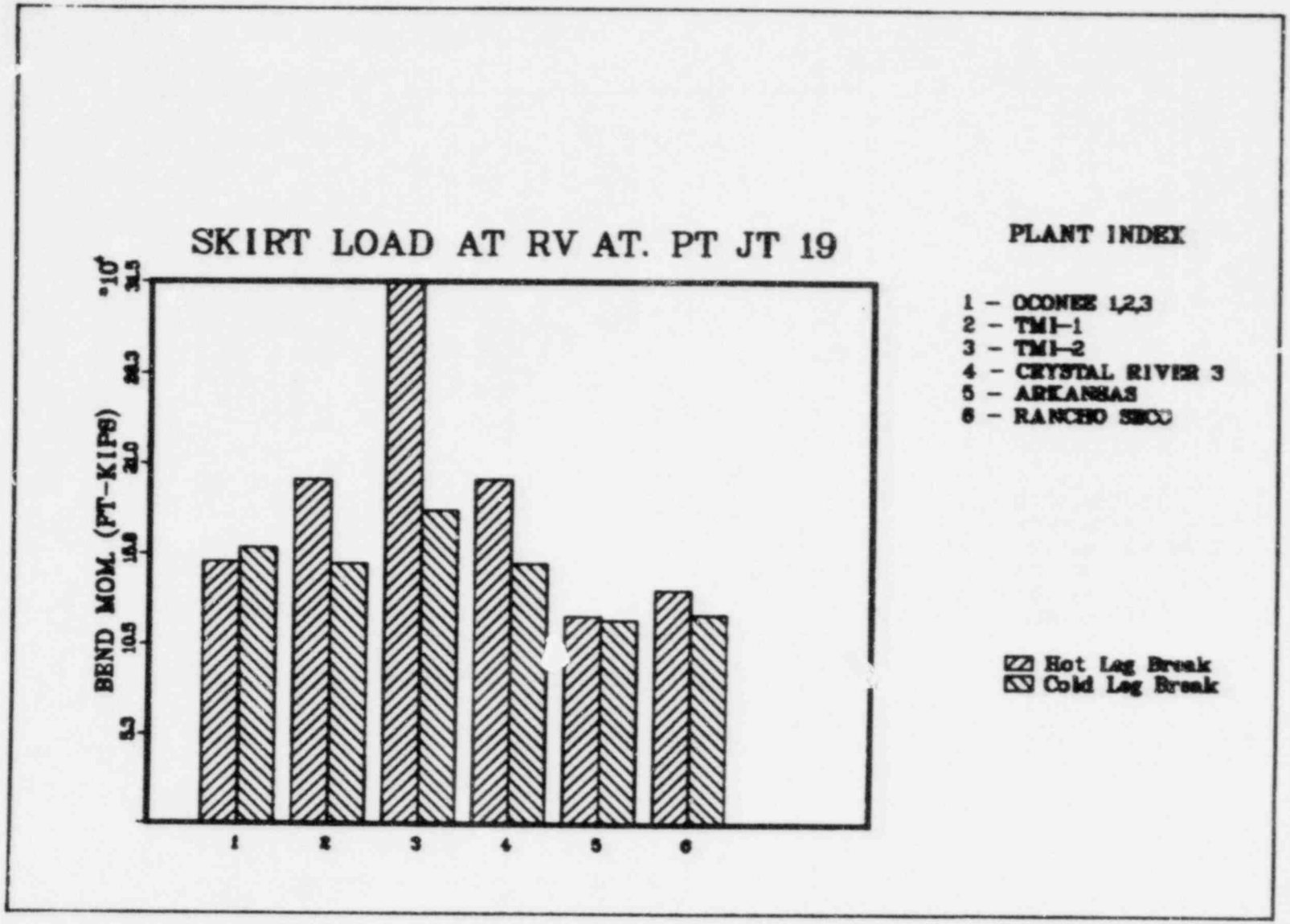

10. STRUCTURAL RESPONSE AND STRESS DATA

This section provides the results of the evaluations performed for each component or structure affected by the asymmetric LOCA loadings resulting from pipe breaks within the reactor vessel subcompartment.

10.1. Reactor Vessel Supports

Table 10.1-1 and 10.1-2 list the ratios of calculated to allowable loads for the RV supports for cold and hot leg guillotine breaks (including seismic loads), respectively. For the skirt-supported plants, ratios are given for both of the analyzed locations discussed in section 6.1. A ratio less than 1.0 indicates an acceptable load. The ratios for each plant are graphically displayed in Figures 10.1-1 and 10.1-2 for cold and hot leg guillotine breaks.

Crystal River-3, Oconee 1, 2, and 3, TMI-1, and TMI-2 are overstressed at one or both locations for the cold leg guillotine. The small amount of overstress indicated CR-3 and TMI-1 are well within the accuracy of the analysis and is not considered significant. Therefore, the Oconee units and TMI-2 are the only plants that should be considered overstressed for the cold guillotine.

Crystal River-3 and TMI-1 and -2 are overstressed for the hot leg guillotine. The hot leg restraint can be modified on the Crystal River-3 and TMI-1 units to limit the break area and thus reduce the loads to about the level of the cold leg cases. This would alleviate the hot leg guillotine overstressed conditions for CR-3 and TMI-1. Additional evaluations will be required for TMI-2 to determine the steps necessary to alleviate the overstressed conditions for the hot leg pipe break.

Table 10.1-1. Reactor Vessel Supports, Cold Leg Guillotine Plus Seismic, for SA-516, Gr. 70

Plant/location	Type load	Load, 10^6 ft-lb		Load ratio, calc/allow.
		Calc	Allow.	
ANO-1				
Support skirt at hole	Moment	149	198	0.753
Support skirt flange		155	189	0.820
CR-3				
Support skirt at hole		186	198	0.939
Support skirt flange		192	189	1.02
Oconee-1, 2, 3				
Support skirt at hole		201	198	1.02
Support skirt flange		208	189	1.10
Rancho Seco				
Support skirt at hole		154	198	0.778
Support skirt flange		160	189	0.847
TMI-1				
Support skirt at hole		186	198	0.939
Support skirt flange		192	189	1.02
TMI-2				
Support skirt at hole		222	198	1.12
Support skirt flange		229	189	1.21
DB-1				
Nozzle support	Vertical force	529,000[(a)]	4,157,000[(a)]	0.127

[(a)] Vertical force measured in lb.

Table 10.1-2. Reactor Vessel Supports, Hot Leg Guillotine Plus Seismic, for SA-516, GR. 70

Plant/location	Type load	Load, 10^6 ft-lb		Load ratio, calc/allow.
		Calc	Allow.	
ANO-1				
Support skirt at hole	Moment	148	198	0.748
Support skirt flange		153	189	0.810
CR-3				
Support skirt at hole		241	198	1.22
Support skirt flange		249	189	1.32
Oconee-1, 2, 3				
Support skirt at hole		186	198	0.939
Support skirt flange		192	189	1.02
Rancho Seco				
Support skirt at hole		166	198	0.838
Support skirt flange		172	189	0.910
TMI-1				
Support skirt at hole		241	198	1.22
Support skirt flange		249	189	1.32
TMI-2				
Support skirt at hole		384	198	1.94
Support skirt flange		397	189	2.10
DB-1				
Nozzle support	Vertical force	1,861,000[a]	4,157,000[a]	0.448

[a] Vertical force measured in lb.

Figure 10.1-1. Load Ratio for Reactor Vessel Supports, Cold Leg Guillotine Plus Seismic

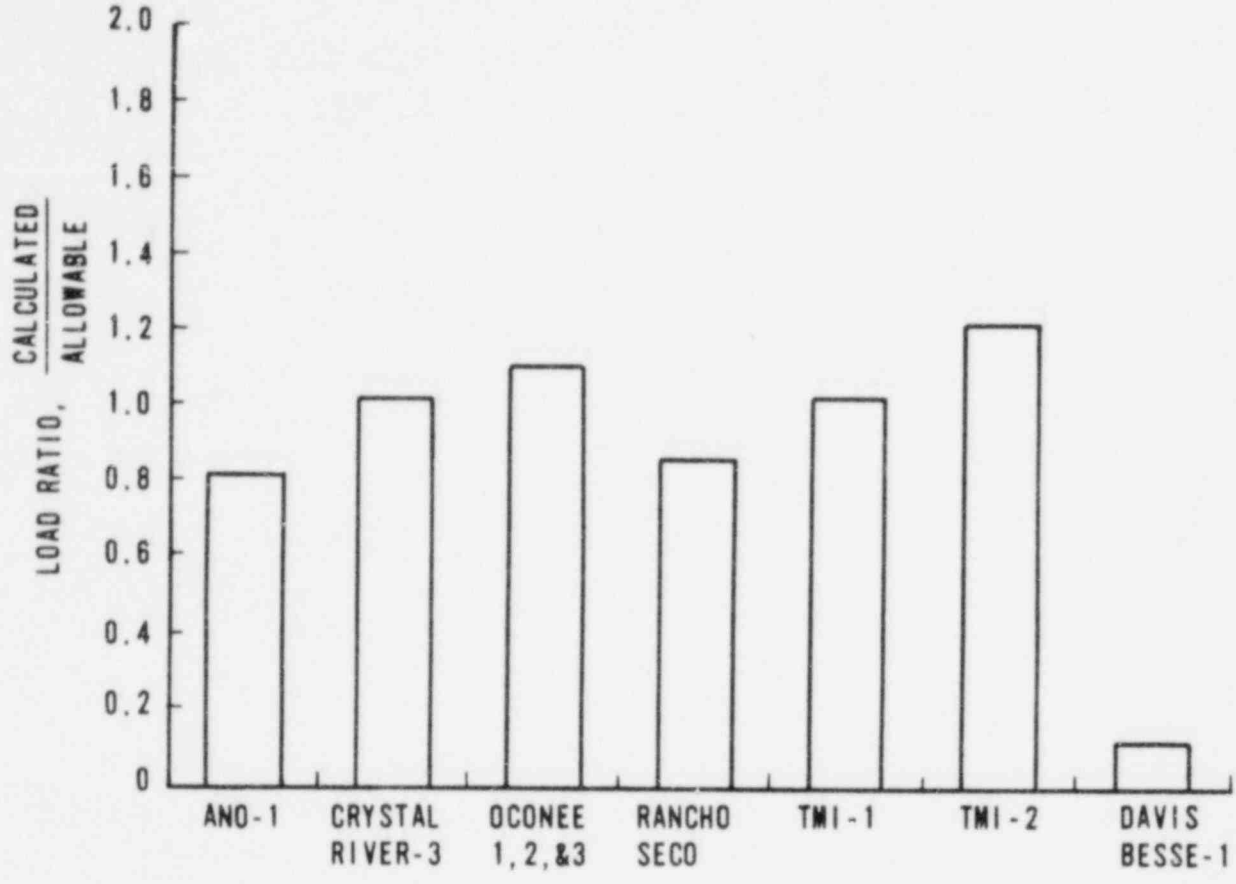

Figure 10.1-2. Load Ratio for Reactor Vessel Supports, Hot Leg Guillotine Plus Seismic

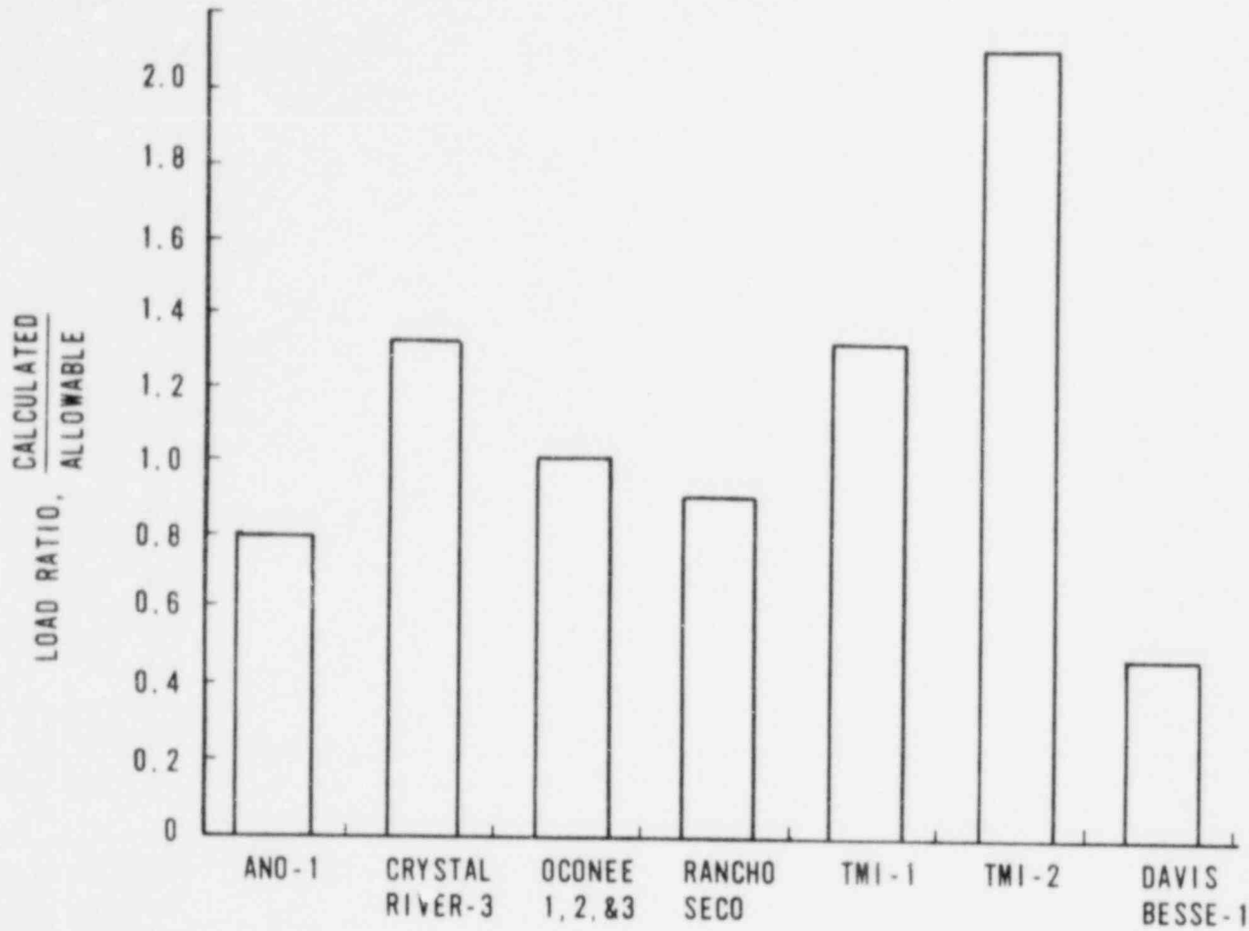

10.2. Reactor Vessel Support Embedments

In this section the qualification results for the reactor vessel support embedments are reviewed. The methodology by which the analysis and qualification of these embedment loadings were performed is described in section 6.2.

10.2.1. Skirt-Supported Plants

10.2.1.1. Overview

The qualification results for specific plants, described in sections 10.2.1.2 and 10.2.1.3, allow the following overall conclusions to be drawn:

The response of the ANO-1 embedment meets the defined acceptance criteria for all postulated breaks.

The acceptance criteria are exceeded slightly for the Crystal River 3 and Three Mile Island 1 embedments for a hot leg break. The response of each embedment to a cold leg break meets the acceptance criteria.

The response of the Oconee embedment exceeds the acceptance criteria by a small amount. For a cold leg break, a reduction in load of approximately 5 percent would lead to acceptable response. For the hot leg break, the reduction required would be considerably less.

The response of the Rancho Seco embedment also exceeds the acceptance criteria by a small margin, which is localized and is based on a relatively conservative analysis.

Due to conservatisms in the analysis and qualification procedures, each embedment has additional load capacity not reflected in the stress ratios. Therefore, slightly exceeding the acceptance criteria is not considered significant.

Exceeding the acceptance criteria for all of these loads only applies for a capacity reduction factor of less than unity. For a capacity reduction factor of unity, the response of each of the embedments is acceptable.

10.2.1.2. Results

Qualification results for skirt-supported plants are summarized in Tables 10.2-1 through 10.2-5. The ratios listed are the ratios of the actual stress or strain to the allowable value. Thus, a ratio of less than unity signifies acceptability.

Two ratios are reported. For the first, capacity reduction factors are applied to the computed strengths. This is in accordance with the acceptance criteria defined in Section 7.2. For the second ratio, the capacity reduction factors are set to one. As discussed in Section 6.2.1.7, this latter ratio indicates whether the calculated stress or strain exceeds the 'mean' strength of the embedment. Should the acceptance criteria be exceeded but this ratio still be less than unity, then the absolute strength of the embedment is greater than that required to resist the applied LOCA load.

The ratios given in Tables 10.2-1 through 10.2-5 do not include the effect of seismic loading. The effect of seismic loading on the response of the embedments was determined using the methodology described in Section 6.2.1.9. Conservative upper bounds to the increase in applied forces due to the coincidence of seismic and LOCA loading are given in Table 10.2-6. Clearly, the effect on the peak loading for Oconee, Three Mile Island 1, and, by interpolation, ANO-1, Three Mile Island 2, and Crystal River 3 is insignificant. A small increase is indicated for Rancho Seco.

10.2.1.3. Conclusions

ANO-1

The maximum ratio reported for ANO-1 is 0.92. The analysis and qualification of ANO-1 was performed using a relatively conservative elastic approach. Furthermore, the most severe combination of LOCA loads was assumed. Thus, the response of the ANO-1 embedment falls significantly within the acceptance criteria for all postulated break cases, and the plant qualifies.

Oconee

The acceptance criteria are exceeded in two areas:

First, a 7 percent discrepancy exists between the calculated and allowable bearing stresses against the vertical bearing plate in the vicinity of the vertical access hatch. The methodology for calculating this bearing stress did not consider the redistribution of the lateral load that will occur subsequent to local yield, and it was assumed that no load was resisted in the region of the hatch. These are significant conservatisms.

Second, the local compressive strain directly beneath the sole plate exceeds the allowable strain by 29 percent. This corresponds to an overload of approxiamtely 5 percent. Furthermore, the effect is localized, and the computed strain does not exceed the strain corresponding to maximum stress.

In conclusion, the Oconee embedment response exceeds that specified by the acceptance criteria by a small margin.

Crystal River 3

For Crystal River 3, the acceptance criteria are exceeded by 4 percent at the liner plate level, for a hot leg break. Acceptability was demonstrated in all other areas for this break. As is discussed in section 6.2.1.7, separation at the liner plate does not induce structural instability. Rather, the resistance imposed by the cavity wall, disregarded in this computation, will counteract the excess load. Also, the 4 percent was calculated assuming an unfavorable coincidence of the high-frequency vertical load with other LOCA loads. Had the mean vertical load been applied, acceptability would have been demonstrated.

In conclusion, the acceptance criteria have been exceeded slightly, using conservative assumptions, for a hot leg break. The response of the embedment to a cold leg break satisfies the acceptance criteria.

Three Mile Island 1

The allowable strain is exceeded by 2 percent in a local region directly beneath the sole plate, for a hot leg break. This corresponds to an overload of much less than 1 percent. Similarly, the liner plate allowable is exceeded by 2 percent. Neither of these conditions is significant. Complete acceptability of embedment response can be inferred for a cold leg break.

Rancho Seco

The acceptance criteria are exceeded by a small amount in three locations:

The allowable anchor bolt pull-out stresses are exceeded above the incore instrumentation trench and around the vertical hatch. This is a localized condition, which occurs for only one of the six postulated LOCA cases. Furthermore, significant conservatism can be identified in the analytical method. First, the peak vertical load (due to core bounce) was superimposed on the peak LOCA moment. Had the average vertical load been used, acceptance would have been achieved. Second, no account was taken for the redistribution of load consequent to local yielding in this zone.

The bearing stress against the vertical bearing plate at the hatch was also exceeded by 7 percent.

For a capacity reduction factor of unity, all ratios are less than one.

10.2.2. Nozzle-Supported Plant

10.2.2.1. Overview

The response of the reactor vessel supports for the Davis-Besse plant to the applied LOCA loading meets the acceptance criteria for all postulated breaks. Similarly, the response is acceptable for combined seismic and LOCA loading.

10.2.2.2. Results

The qualification results for each component are presented in Tables 10.2-7 through 10.2-9. Ratios for LOCA loading and for combined LOCA and seismic loading are given. Dead-weight was considered in all analyses.

10.2.2.3. Conclusions

Support Beam

All ratios are less than one, and the response is acceptable. The highest ratios, those for the welds and for combined stresses in the beam, occur locally around the point of load application, and decrease very quickly away from this region. Even were local yielding to occur, redistribution would allow application of a significantly greater load before collapse was imminent. Thus, a considerable factor of safety was demonstrated.

Hot Leg LOCA Ring

Stresses remain elastic in this LOCA ring. They are relatively small. A large factor of safety is apparent.

Cold Leg LOCA Ring

Yielding of three struts and a section of the inner plate was identified. However, the resulting inelastic strains are within the allowable values defined in the acceptance criteria. Relatively high, but acceptable, stresses were calculated in the bolts. Failure of these bolts would not, however, impair the function of the LOCA ring. Thus, a considerable factor of safety was demonstrated for the cold leg LOCA ring.

Table 10.2-1. Ultimate Stress Evaluation: ANO-1 Embedment

Mode of Failure	Location	Parameter	Allowable Value CRF=ϕ[a]	Allowable Value CRF=1	Ratio CRF=ϕ	Ratio CRF=1
Direct tension	Anchor bolts	Stress, lb/in^2	149,500	149,500	0.60	0.60
Compression in concrete	Below sole plate		5,775	8,250	0.73	0.51
	Above anchor plate		5,775	8,250	0.82	0.57
	Against bearing plate		4,125	5,890	0.92	0.64
Reinforced concrete in shear	Beneath sole plate		1,815	1,815	0.63	0.63
	Anchor bolt pull-out:					
	a) general	Force, lbs x 10^3	14,270	16,790	0.70	0.60
	b) above trench		12,105	14,240	0.83	0.71

(a) CRF = Capacity Reduction Factor

Table 10.2-2. Ultimate Stress Evaluation: Oconee Embedment

Mode of Failure	Location	Parameter	Allowable Value CRF=ϕ[a]	Allowable Value CRF=1	Ratio CRF=ϕ	Ratio CRF=1
Direct tension	Anchor bolts	Strain, in/in	0.0175	0.0175	0.31	0.31
Compression in concrete	Below sole plate		0.0047	0.0063	1.29	0.97
	Above anchor plate	Stress, lb/in^2	6,120	8,740	0.75	0.53
	Against bearing plate:					
	a) general		5,560	7,945	0.84	0.59
	b) at vertical hatch		5,560	7,945	1.07	0.75
Reinforced concrete in shear	Beneath sole plate		2,100	2,100	0.90	0.90
	Anchor bolt pull-out:					
	a) general	Force, lbs x 10^3	10,640	12,520	0.60	0.51
	b) above trench		6,350	7,470	0.94	0.80
	c) around hatch		6,050	7,120	0.72	0.61

(a) CRF = Capacity Reduction Factor

Table 10.2-3. Ultimate Stress Evaluation: Crystal River 3 Embedment

Mode of Failure	Location	Parameter	Allowable Value CRF=ϕ[a]	Allowable Value CRF=1	Ratio CRF=ϕ	Ratio CRF=1
Direct tension	Anchor bolts	Strain, in/in	0.0175	0.0175	0.28	0.28
Compression in concrete	Below sole plate	Stress, lb/in^2	6,750	9,645	0.98	0.69
	Above anchor plate		6,750	9,645	0.96	0.67
	Against bearing plate:					
	a) general		5,230	7,475	0.29	0.20
	b) at vertical hatch		5,230	7,475	0.28	0.20
Reinforced concrete in shear	Beneath sole plate		2,320	2,320	0.99	0.99
	Anchor bolt pull-out:					
	a) general	Force, lbs x 10^3	10,715	12,605	0.76	0.65
	b) around hatch		14,725	17,320	0.71	0.60
Separation at liner plate	Liner plate	Moment, lb-in x 10^6	3,075	3,415	1.04	0.94

(a) CRF = Capacity Reduction Factor

Table 10.2-4. Ultimate Stress Evaluation: TMI-1 Embedment

Mode of Failure	Location	Parameter	Allowable Value CRF=ϕ[a]	Allowable Value CRF=1	Ratio CRF=ϕ	Ratio CRF=1
Direct tension	Anchor bolts	Stress, lb/in^2	149,500	149,500	0.82	0.82
Compression in concrete	Below sole plate	Strain, in/in	0.005	0.0067	1.02	0.77
	Above anchor plate	Stress, lb/in^2	6,400	9,145	0.77	0.54
	Against bearing plate:					
	a) general		5,820	8,315	0.79	0.55
	b) at vertical hatch		5,820	8,315	0.78	0.55
Reinforced concrete in shear	Beneath sole plate		2,195	2,195	0.98	0.93
	Anchor bolt pull-out:					
	a) general	Force, lbs x 10^3	19,335	22,745	0.59	0.50
	b) above trench		14,870	17,495	0.68	0.58
	c) at hatch		9,935	11,685	0.59	0.50
Separation at liner plate	Liner plate	Moment, lb-in x 10^6	3,145	3,490	1.02	0.91

(a) CRF = Capacity Reduction Factor

Table 10.2-5. Ultimate Stress Evaluation: Rancho Seco Embedment

Mode of Failure	Location	Parameter	Allowable Value CRF=ϕ[a]	Allowable Value CRF=1	Ratio CRF=ϕ	Ratio CRF=1
Direct tension	Anchor bolts	Stress, lb/in^2	120,750	120,750	0.67	0.67
Compression in concrete	Below sole plate	Strain, in/in	0.0047	0.0062	0.83	0.63
	Above anchor plate	Stress, lb/in^2	7,000	10,000	0.58	0.40
	Against bearing plate:					
	a) general		5,410	7,730	0.75	0.53
	b) at vertical hatch		5,410	7,730	1.07	0.75
Reinforced concrete in shear	Beneath sole plate		2,400	2,400	0.73	0.73
	Anchor bolt pull-out:					
	a) general	Force, lbs x 10^3	8,385	9,865	0.64	0.54
	b) above trench		4,755	5,595	1.08	0.91
	c) at hatch		4,575	5,370	1.08	0.91

(a) CRF = Capacity Reduction Factor

Table 10.2-6. Combined Seismic and LOCA Loading on Embedments

Plant	Ratio of design seismic moment to peak LOCA moment	Ratio of combined LOCA and seismic moment to peak LOCA moment
ANO-1	0.08	1.002
Oconee	0.04	
Crystal River 3	0.04	
Three Mile Island 1	0.11	1.011
Three Mile Island 2	0.07	
Rancho Seco	0.21	1.065

Table 10.2-7. Stress Evaluation: Davis-Besse Cold Leg Support Beam

Item	Allowable value	LOCA		LOCA + Seismic	
		Maximum value	Ratio	Maximum value	Ratio
Stress intensity in support beam, $lb/in^2 \times 10^3$	43.6	30.1	0.69	34.2	0.78
Tensile stress in anchor bolts, $lb/in^2 \times 10^3$	106.5	2.0	0.02	2.3	0.02
Stress in welds, $lb/in^2 \times 10^3$	50.0	41.0	0.82	47.0	0.94

Table 10.2-8. Stress Evaluation: Davis-Besse Hot Leg LOCA Ring

Item	Allowable value	Maximum value	Ratio
Stress in webs, $lb/in^2 \times 10^3$	40.4	3.7	0.09
Combined stress in bolts, $\frac{f_t^2}{F_{tb}^2} + \frac{f_v^2}{F_{vb}^2}$	1.0	0.05	0.05
Stress in welds, $lb/in^2 \times 10^3$	40.4	3.8	0.09

Table 10.2-9. Stress Evaluation: Davis-Besse Cold Leg LOCA Ring

Item	Allowable value	Maximum value	Ratio
Strain in webs, in/in	0.052	0.042	0.81
Combined stress in bolts, $\frac{f_t^2}{F_{tb}^2} + \frac{f_v^2}{F_{vb}^2}$	1.0	0.82	0.82
Stress in welds, $lb/in^2 \times 10^3$	47.6	21.3	0.45

10.3. Control Rod Drive Service Structure

10.3.1. Service Support Structure

A finite element model of the service structure was used to evaluate loads for both hot and cold leg breaks. This was necessary since the resultant forces of the breaks were of different magnitudes and directions. The hot leg loads for TMI-1 and CR-3 resulted in the highest loads on the gussets. The gusset stresses for TMI-1 and CR-3 are summarized in Table 10.3-1. Load ratios were applied to the stresses in the table to generate the stresses for each plant in Figures 10.3-1 and 10.3-2. The gusset stresses are well within the allowable limits; therefore, the service structures of both the nozzle- and skirt-supported plants are acceptable for Phase II loads.

10.3.2. Service Support Structure Mounting Flange

Tables 10.3-2 and 10.3-3 list the ratios of calculated to allowable load for the service support structure mounting flange for the cold leg guillotine (CLG) and hot leg guillotine (HLG) breaks. The ratios for each plant are graphically displayed in Figures 10.3-3 and 10.3-4 for CLG and HLG breaks. A ratio less than 1.0 indicates an acceptable stress condition. It can be seen from the tables that the service support structure mounting flange is acceptable for all plants for both the CLG and HLG breaks.

Table 10.3-1. Service Support Structure Gusset Stresses

Gusset No.	Load, kips	σ_{act}, ksi	σ_{all}, ksi	Ratio, $\sigma_{act}/\sigma_{all}$
300/349	14.68	13.65	39.10	0.35
301/350	20.31	10.36		0.27
302/351	20.71	9.53		0.24
303/350	21.50	10.97		0.28
304/349	9.49	8.83		0.23
305/348	6.41	8.27		0.21
306/339	0.050	0.103		0.003
307/339	3.52	7.22		0.19
308/339	0.0	0.0		0.0
309/343	5.14	2.83		0.07
310/343	10.96	6.03		0.15
311/341	6.94	4.23		0.11
312/405	14.67	8.95		0.23
313/339	6.42	13.16		0.34
314/338	20.04	13.03		0.33
315/337	28.07	15.33	39.10	0.39

Note: For gusset locations see Figure 10.3-1.

Table 10.3-2. Service Support Structure/RV Head Flange, CLG — Moment Loads, SA-515. Gr. 70

Plant	Load, 10^6 ft-lb		Load ratio, calc/allow.
	Calc.	Allow.	
ANO-1	4.80	16.4	0.292
CR-3	7.86		0.479
Oconee 1, 2, 3	8.67		0.529
Rancho Seco	5.18		0.316
TMI-1	7.86		0.479
TMI-2	6.12		0.373
DB-1	2.01	16.4	0.123

Table 10.3-3. Service Support Structure/RV Head Flange, HLG — Moment Loads, SA-515, Gr. 70

Plant	Load, 10^6 ft-lb		Load ratio, calc/allow.
	Calc.	Allow.	
ANO-1	4.78	16.4	0.291
CR-3	11.1		0.678
Oconee 1, 2, 3	6.84		0.417
Rancho Seco	7.04		0.429
TMI-1	11.1		0.678
TMI-2	9.33		0.569
DB-1	3.99	16.4	0.243

Figure 10.3-1. Service Support Structure Gusset Locations

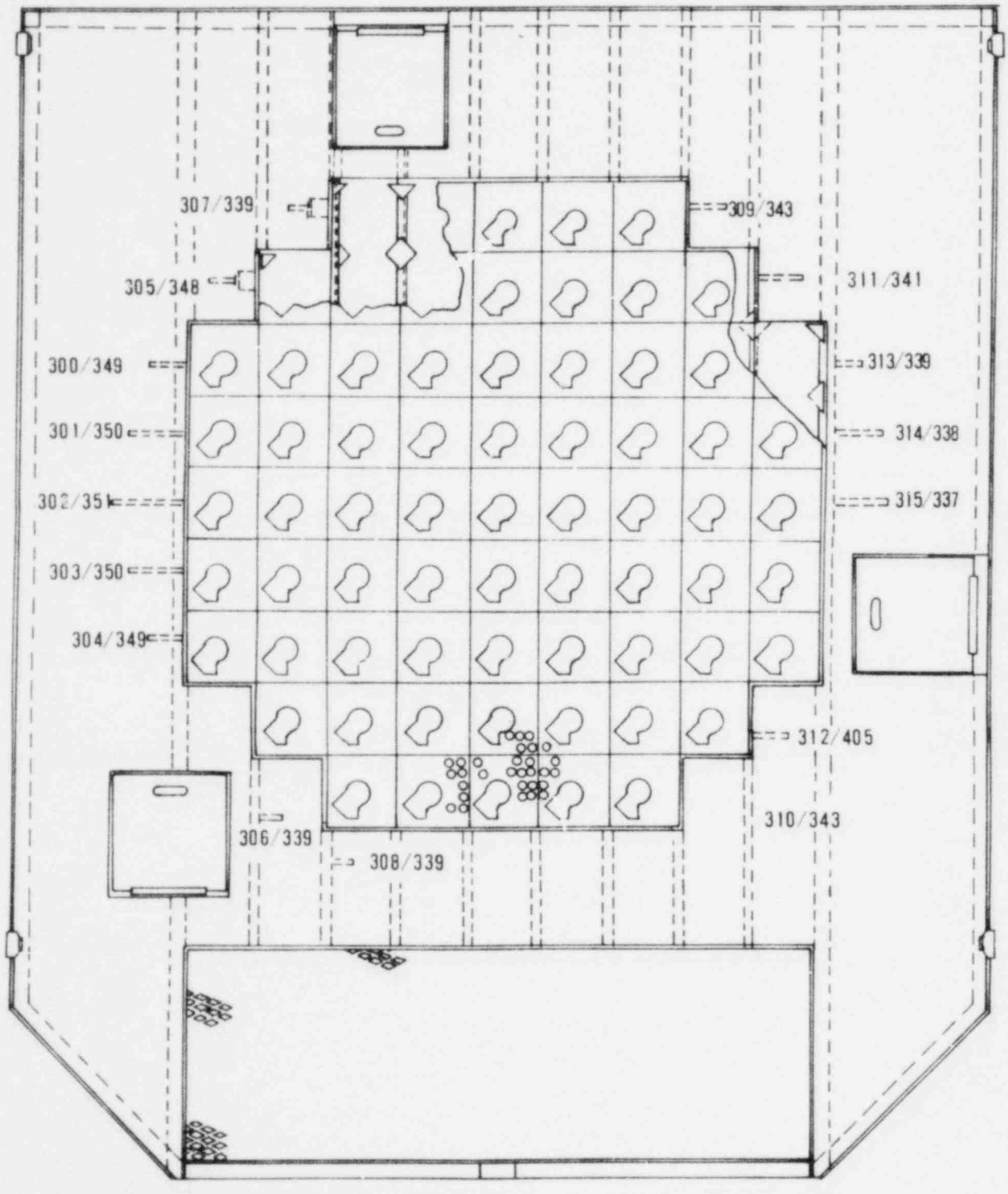

Figure 10.3-2. Service Support Structure Stress Ratio Evaluation for Gusset 315/337

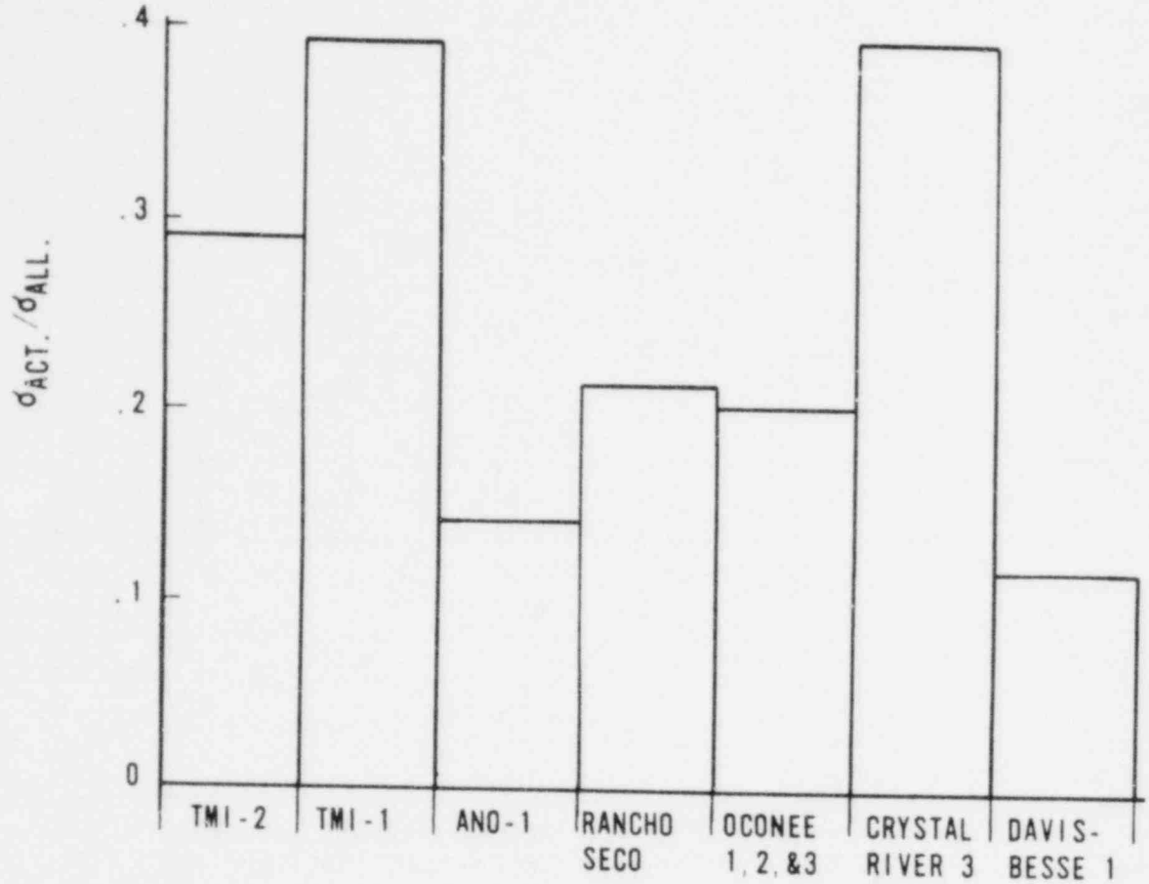

Figure 10.3-3. Load Ratios for Service Support Structure Mounting Flange, Cold Leg Guillotine

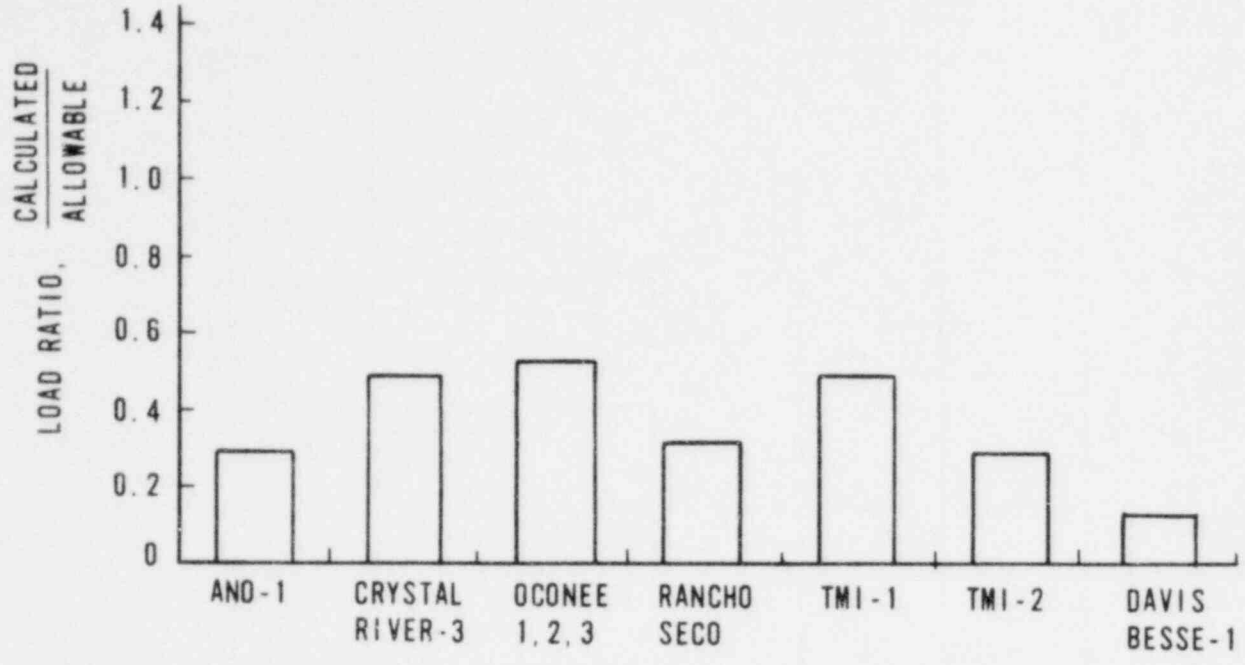

Figure 10.3-4. Load Ratios for Service Support Structure Mounting Flange, Hot Leg Guillotine

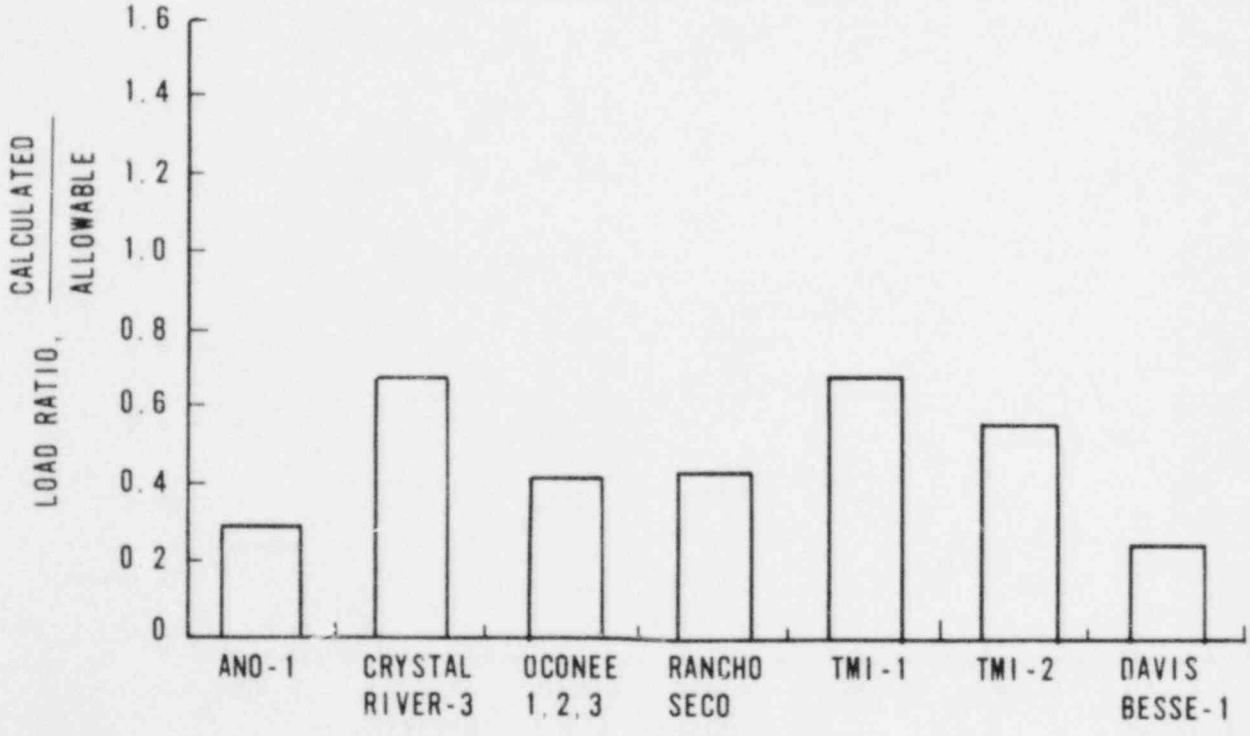

10.4. Control Rod Drive

10.4.1. Control Rod Drive Mechanism

The CRDM analysis was performed in accordance with Appendix F of the ASME Code.[1] Only the primary stresses are considered for this condition. In accordance with Appendix F, a shape factor is determined by dividing the plastic moment (M_p) by the moment at yield (M_y). Because the M_p/M_y ratio is a property of the cross-sectional shape only, the shape factor (k) can be calculated in the following manner:

$$k = \frac{16r_1}{3\pi} \times \frac{r_1^3 - r_2^3}{r_1^4 - r_2^4}$$

where

r_1 = outside radius of motor tube,

r_2 = inside radius of motor tube.

The value of k ranges from 1.334 to 1.379 throughout the motor tube for this analysis. This value is multiplied by the ASME Code allowable stresses for the faulted condition to produce the total Code allowable stresses for that condition.

10.4.1.1. Analysis of Pressure Boundary

Stress analyses were performed for type A and C drives of both long and short nozzles for three representative LOCA cases. These cases correspond to the TMI-1/CR-3 hot leg break without restraint modifications, the same case with modifications, and the Oconee cold leg break. Table 10.4-1 presents stress data for drive type A using a long mounting nozzle with LOCA 3 loads. Table 10.4-2 presents stress data for drive type C using a short mounting nozzle with LOCA 3 loads. These combinations for the respective drives produce the most severe stress intensities. Only those areas of the pressure boundary with safety margins $\leq$15% are listed. These results show that tubes with nominal dimensions meet the faulted conditions acceptance criteria.

10.4.1.2. Evaluation of Modified Pressure Boundaries

Certain CRDMs in the plants have been reworked since their original installation. The motor tubes (pressure boundary) have been honed out on the inside diameter, resulting in a deviation from manufacturing dimensions. This deviation warranted a strength analysis based on the modified dimensions. Table 10.4-3

presents original and modified dimensions for two critical areas in the motor tube.

The maximum bending stress for drive type A occurs at an elevation of 75.0 inches on the motor tube from the lower flange (see Table 10.4-1). A modified stress intensity based on the reduction in material is calculated by adding a delta stress intensity (ΔS) to the stress intensity at that elevation for a normal motor tube.

The delta stress intensity calculation is based on the fact that the bending stresses are proportional to the I/C ratio and the pressure stresses are proportional to the Ri/t ratio.

10.4.1.3. Results for Modified Pressure Boundary

The stress results presented in Tables 10.4-1 and 10.4-2 must be corrected for the dimensions of the modified tubes. The highest stresses occur for the type A drive, long nozzle for LOCA case 3, the Oconee cold leg break. By applying the appropriate ratio factors to account for the differences between the nominal and modified dimensions, the incremental stress is calculated to be 2991 psi. The total stress intensity for the modified tube is equal to the delta stress intensity plus the stress intensity at the same elevation for a normal motor tube.

$\Delta S + S$ = total stress intensity for modified motor tube (at elevation 75.0 inches)

(2,999 + 60,134) psi = 63,133 psi

The shape factor (k) at this elevation is 1.379. The allowable stress is calculated as follows:

$$\text{Allowable} = k(0.7\ S_m)\ (1.05)$$

$$= 1.379\ (0.7 \times 59{,}400)\ (1.05)$$

$$= 60{,}297 \text{ psi}$$

Therefore, the total stress intensity for the modified motor tube at 75.0 inches results in an overstressed region. This is the worst case for modified motor tubes.

$$\text{Margin of safety} = \left(\frac{60{,}297}{63{,}133} - 1\right) \times 100 = -4.5\%$$

While the type A drive, long nozzle, modified tube exceeds the allowable stress limit for LOCA case 3, the Oconee cold leg break, the modified type A drive, short nozzle, and modified type C drive, long and short nozzles are acceptable. The modified tubes are also acceptable for all other LOCA cases. Furthermore, it is felt that the 4.5% overstress condition of the type A drive for LOCA case 3 is well within the accuracy of the LOCA calculations described herein and is considered acceptable.

10.4.1.4. Lower Flange Bolted Joint

The highest average stress intensity in the bolt for the three representative LOCA cases is 50,043 psi. This value is lower than the allowable stress limit of $2S_m$.

The peripheral stress was calculated by combining the tensile stress in the bolt with the torsional stress due to the bolt torque. The maximum tensile stress was due to the LOCA moment applied to the joint and the internal pressure. The highest maximum stress on the bolt for the three representative LOCA cases was 63,542 psi. This value is lower than the allowable stress limit of $3S_m$.

10.4.1.5. Summary of Results for CRDM

The results of the detailed stress analyses of three representative LOCA cases (6.4.1.1) have demonstrated the acceptability of the pressure boundary of the control rod drives and the bolted joint attaching the drives to the reactor vessel head. These results address the type A and C drives; the type B drive is similar to type A and was not quantitatively addressed. Because the LOCA cases of all other plants produce lower loads than the three representative cases quantitatively address, the drives of all cases are considered acceptable.

10.4.2. Control Rod Drive Mechanism Housing

Tables 10.4-4 and 10.4-5 list the ratios of calculated load to allowable load for the Control Rod Drive Housing (CRDH) for the Cold Leg Guillotine (CLG) and the Hot Leg Guillotine (HLG). The ratios for each plant are graphically displayed in Figures 10.4-1 and 10.4-2 for cold leg and hot leg guillotine breaks, respectively. The ratios are based on the stainless steel portion of the CRDH since it had a lower allowable moment than the inconel portion. A ratio less than 1.0 indicates an acceptable stress condition.

All plants were acceptable for the CLG, as shown in Table 10.4-4. For the HLG, Crystal River-3, TMI-1 and TMI-2 showed overstressed conditions. The hot leg restraint on Crystal River-3 and TMI-1 can be shimmed to limit the break opening area, thus reducing the loads to about the level of the cold leg break. This would alleviate the overstresses condition for those plants. For TMI-2, additional evaluations are required, which may eliminate the overstressed condition for the hot leg break.

Table 10.4-1. Type A Stresses for LOCA Case 3, Oconee Cold Leg Break

Elev. from lower flanges, in.	Sa^2	Sh	Sr	LOCA axial stress, psi	Shear stress, psi	Stress intensity, psi	Allowable stress, psi	Margin of safety, %
33.77	11,989	21,282	0	±60,112	5,429	72,914	78,439[a]	7
50.00	3,368	13,033	0	±46,812	291	56,479	60,297	6
75.00	3,368	13,033	0	±50,469	158	60,134	60,297[b]	0

[a]Shape factor (k) = 1.334.

[b]Shape factor (k) = 1.379.

Table 10.4-2. Type C Stresses for LOCA Case 3, Oconee Cold Leg Break

Elev. from lower flange, in.	Sa^2	Sh	Sr	S1	S2	S3	Stress intensity, psi	Allowable stress, psi	Margin of safety, %
137.50	-38,938	11,448	0	0	-38,938	11,448	50,385	58,131[a]	15

[a]Shape factor (K) = 1.334.

Table 10.4-3. Dimensions of Modified Tubes

X elevation, in.	Original dimensions in.		Honed out dimensions, in.		I/C ratio		R_i/t ratio	
	Ri	t	R'i	t'	Original	Honed out	Original	Honed out
33.77 to 37.18	1.765	0.345	1.77	0.335	3.7656	3.6635	5.1159	5.2838
37.18 to 199.68	1.765	0.345	1.808	0.287	3.7656	3.2158	5.1159	6.299

Table 10.4-4. Control Rod Drive Housing, CLG for Moment Loads, Type SA-182F 304

Plant	Load, 10^6 ft-lb		Load ratio calc/allow
	Calc.	Allow.	
ANO-1	0.826	1.77	0.467
CR-3	1.44		0.814
Oconee 1, 2, 3	1.76		0.994
Rancho Seco	0.928		0.524
TMI-1	1.44		0.814
TMI-2	1.22		0.689
DB-1	0.314	↓	0.177

Table 10.4-5. Control Rod Drive Housing, HLG for Moment Loads, Type SA-182F 304

Plant	Load, 10^6 ft-lb		Load ratio, calc/allow.
	Calc.	Allow.	
ANO-1	0.878	1.77	0.496
CR-3	2.51		1.42
Oconee 1, 2, 3	1.33		0.751
Rancho Seco	1.34		0.757
TMI-1	2.51		1.42
TMI-2	1.92		1.08
DB-1	0.831		0.469

Figure 10.4-1. Control Rod Drive Housing, Cold Leg Guillotine

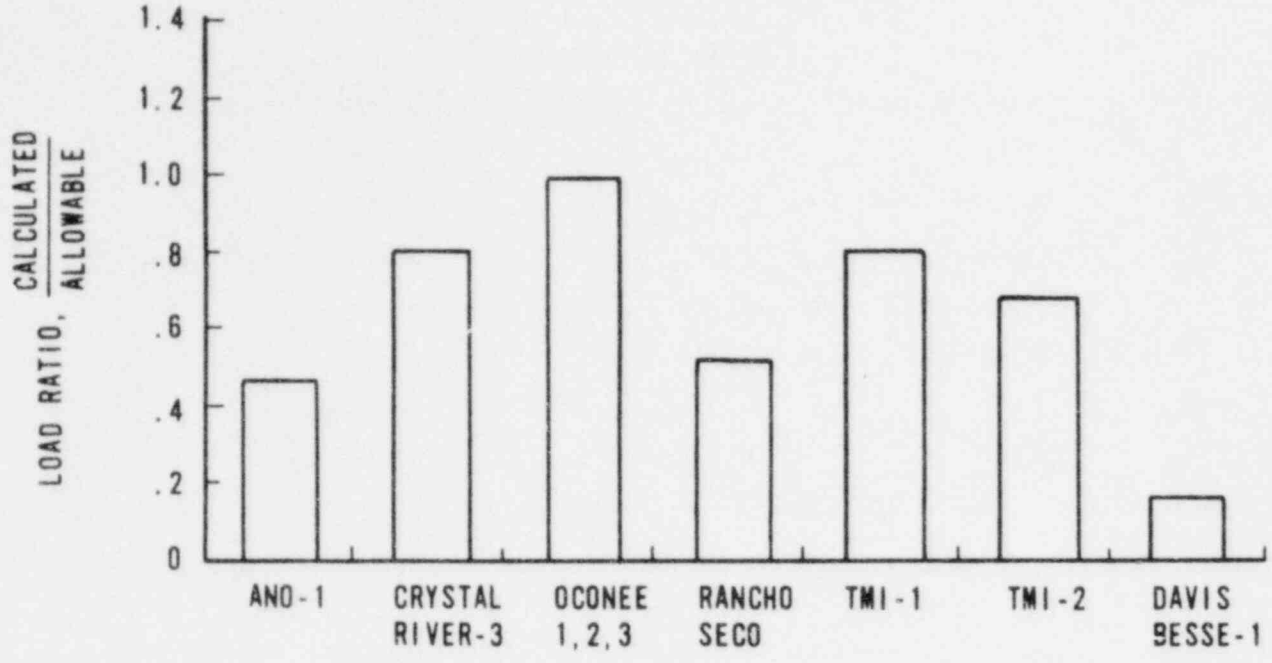

Figure 10.4-2. Control Rod Drive Housing, Hot Leg Guillotine

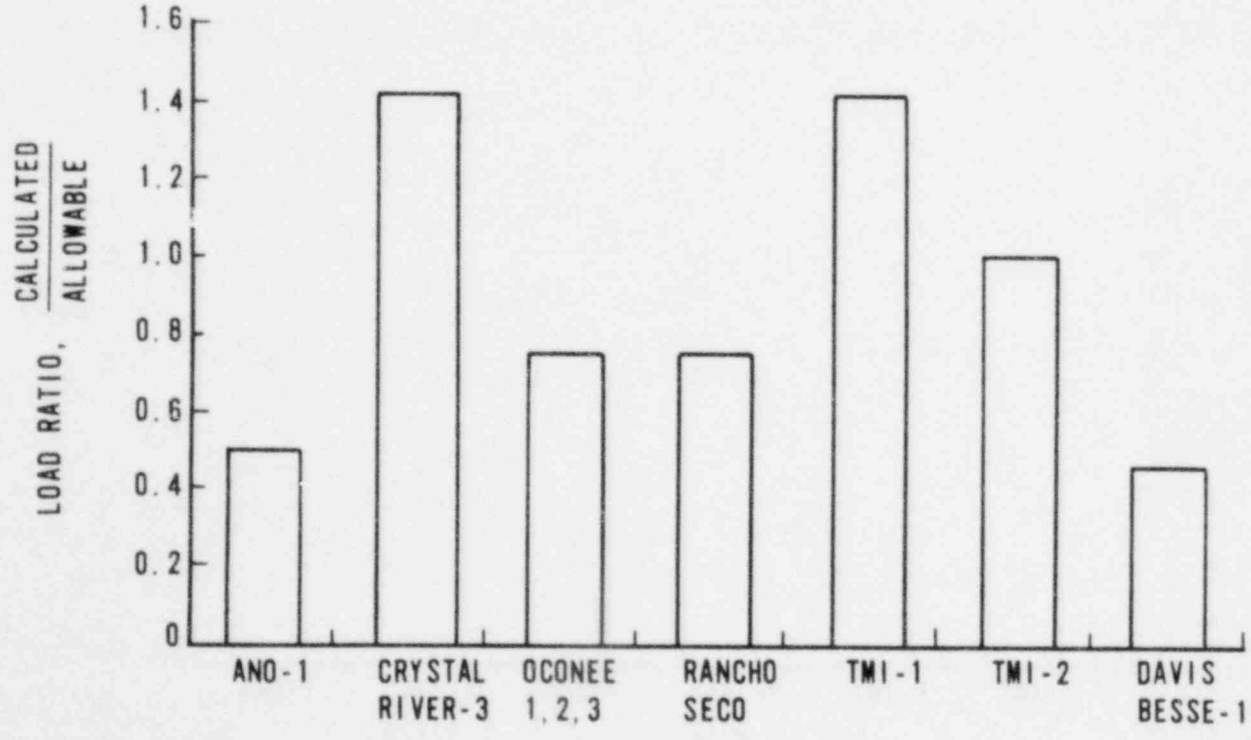

10.5. Reactor Internals/Core Support Assembly

The maximum load ratios for hot and cold leg breaks in the skirt- and nozzle-supported reactor vessels were used to evaluate the structural integrity of the reactor internals/core support assembly. Applying the load ratios to the base analysis stresses or factors of safety showed that the reactor internals/core support assembly components of all Owner's Group plants have stress ratios (actual stress divided by allowable stress) less than 1.0. The maximum stress ratio of 0.91 was obtained for the core support shield upper flange of the skirt-supported reactor vessel for the cold leg guillotine case. Therefore, the reactor internals of all plants are adequate for Phase II loads.

10.6. Fuel Assemblies

The fuel assembly component stress analysis was performed and compared with the acceptance criteria discussed in section 7. The limiting margin for each component for each analysis is reported in Table 10.6-1. The information in the table includes the subcomponent, type of analysis, maximum load, acceptance criteria limit, and margin. Such component properties as yield strength, modulus, etc. have been adjusted for reactor operating temperature.

Table 10.6-1. Fuel Assembly Stress Analysis Results

Component	Dominant[c] applied load	Basis for allowable load	Allowable load	Margin, %
Guide tube[a] assembly, lb	1,800	Buckling	5,152	186
End grid assembly, lb	4,375	Level D	10,573	142
Fuel rod, psi	42,590	Level D	46,900	10.1
Upper end fitting, psi	13,000	Level D	67,050	416
Lower end fitting, psi	33,000	Level D	67,050	103
Spacer grid,[b] in.	0.114	Coolable geometry	0.380	233.3

(a) Loads reported as total load on all components.

(b) The analytical results pertain only to the Inconel grid fuel assembly.

(c) Dominant load is reported, analysis considers effects of loads in all directions.

10.7. Reactor Coolant Piping

10.7.1. Skirt-Supported RV Plants

For the skirt-supported plants the worst-case loading for a particular pipe section (and not for each plant) was selected as the design load. This produced one loading for each of the five different pipe sections and encompassed all plants. The following five pipe sections were evaluated:

1. Hot leg, straight, carbon steel.
2. Hot leg, elbows, carbon steel.
3. Cold leg, straight, carbon steel.
4. Cold leg, elbows, carbon steel.
5. Cold leg, safe-ends, stainless steel.

This approach reduced the number of calculations considerably. The LOCA forces and moments were evaluated using the simplified pipe stress equation. Each pipe section was shown to be acceptable. A summary of the resultant stresses and stress ratios is provided in Table 10.7-1.

10.7.2. Nozzle-Supported RV Plants — DB-1

Again the LOCA forces and moments were evaluated with the simplified stress analysis equation for the hot leg straights and elbows and cold leg straights and safe-ends. The resultant pipe stresses were less than the allowable $3S_m$. These results are summarized in Table 10.7-2. The cold leg elbows required a detailed pipe stress analysis per USAS B31.7-1969, Appendix F, for which B&W's P91308 computer code was used. The results of the detailed pipe stress analysis for the cold leg elbows are shown in Table 10.7-3. The highest loaded joint per pipe section was used in the evaluation. This detailed pipe stress analysis demonstrated the adequacy of the cold leg elbows.

Table 10.7-1. Stresses in Piping of Skirt-Supported RV Plant

Pipe location, section	Moment $m_{i\,global}$, ft-kips	Binding stress, psi		Stress ratio, $f_b/F_B < 1.0$
		Actual f_b	Allow. F_B	
Hot leg, straight	4,726.4	26,040.6	58,920.0	0.442
Cold leg, straight	2,150.1	24,622.8	61,380.0	0.401
Hot leg, elbow	3,097.3	44,967.9	55,920.0	0.804
Cold leg, elbow	1,520.3	30,702.3	58,260.0	0.527
Cold leg, safe-end	1,338,4	15,349.6	52,200.0	0.294

Table 10.7-2. Stresses in Piping of Nozzle-Supported RV Plant — Davis-Besse 1 Only

Pipe location, section	Moment $m_{i\,global}$, ft-kips	Binding stress, psi		Stress ratio, $f_b/F_B < 1.0$
		Actual f_b	Allow. F_B	
Hot leg, straight	2,673.4	18,822.3	58,920.0	0.319
Cold leg, straight	5,731.5	54,724.8	61,380.0	0.892
Hot leg, elbow	1,619.0	25,715.2	55,920.0	0.460
Cold leg, elbow[(a)]	--	--	--	--
Cold leg, safe-end	2,880.9	25,142.8	52,200.0	0.482

[(a)] See Table 10.7-3 for cold leg elbow results.

Table 10.7-3. Nozzle-Supported RV Plant — Results of Detailed Pipe Stress Analysis, Cold Leg Elbows Only

Elbow location and joint No.		Moment $m_{i\,global}$, ft-kips	Bending stress, psi		Stress ratio, f_b/F_B
			Actual f_b	Allow. F_B	
P1A1	110	5,458.95	66,090.0	67,000.0	0.986
	119	5,057.28	60,821.0		0.908
	135	3,239.37	40,469.0		0.604
	143	2,834.41	38,338.0		0.572
P1A2	107	5,511.61	63,066.0		0.941
	117	5,097.78	58,143.0		0.868
	133	3,244.01	38,448.0		0.574
	141	2,831.85	37,140.0		0.554
P1B1	106	5,521.31	65,073.0		0.971
	116	5,127.46	62,919.0		0.939
	132	3,279.88	43,585.0		0.651
	140	2,875.48	39,766.0		0.594
P1B2	108	5,480.16	62,654.0		0.935
	118	5,096.79	59,838.0		0.893
	134	3,279.11	41,144.0		0.614
	142	2,880.93	38,509.0	67,000.0	0.575

10.8. Pipe Whip Restraints

This section summarizes the results of the pipe whip restraint qualification which is discussed in detail in Section 6.8. The cold leg restraints for the Oconee plant are assumed failed. No cold leg restraints exist on other skirt-supported plants. Therefore, this summary only addresses the hot leg pipe restraints.

10.8.1. Oconee

The response of both the hot leg bumper restraint and the hot leg collar restraint are acceptable for the Oconee plant. For the bumper restraint, the highest stress ratio is 0.52, due to shear stresses, while for the collar restraint the highest ratio is 0.36, due to punching shear on the embedment concrete. Full component stress summaries are provided in Tables 10.8-1 and 10.8-2.

10.8.2. Three Mile Island Unit 1

The response of the Three Mile Island Unit 1 hot leg U-bar restraint is acceptable. The maximum capacity of the critically stressed component, the bracket plate, is not exceeded. A full stress summary is provided in Table 10.8.3.

10.8.3. Three Mile Island Unit 2

The response of the Three Mile Island Unit 2 hot leg U-bar restraint is acceptable. The highest stress ratio is 0.87, for the shear stress in the pin joining the clevis to the bracket plate. A full component stress summary is provided in Table 10.8-4.

10.8.4. Crystal River 3

The response of the Crystal River hot leg U-bar restraint is acceptable. The highest ratio is 0.94 for punching shear of the embedment concrete. A full component stress summary is provided in Table 10.8-5.

10.8.5. ANO-1

The response of the ANO-1 hot leg strap restraint is acceptable. The highest stress ratio is 0.78 for the full penetration weld. A full component stress summary is provided in Table 10.8.6.

10.8.6. Rancho Seco

The response of the Rancho Seco hot leg restraints is acceptable. The highest stress ratio for the lower restraint is 0.90 at a bevel weld. The highest stress ratio for the upper restraint, which is very slightly impacted, is 0.35, and is due to the elastic tensile stresses in the restraint. Full component stress summaries are provided in Tables 10.8-7 and 10.8-8.

10.8.7. Davis Besse-1

The Davis Besse-1 lower hot leg restraints are acceptable based upon the conclusions documented in the Toledo Edison Verification Report, Docket No. 50-346, Rev. 1, dated March 7, 1980.[50]

Table 10.8-1. Oconee Hot Leg Bumper Restraint

Part[a]	Material	Governing criteria	Maximum value	Allowable value	Ratio
Steel members 3 and 4	A36	Shear stress, ksi	12.4	23.9	0.52
		Compressive axial stress, ksi	14.8	41.4	0.36
Steel members 7 and 8	A36	Shear stress (XZ), ksi	0.1	23.9	0.
		Shear stress (YZ), ksi	12.2	23.9	0.51
		Compressive axial stress, ksi	13.3	41.4	0.32
Bolts	A325	Shear load, kips	1,094	2,865	0.38

(a) For key to member numbers, see Figure G-2.

Note: This restraint is Restraint 1 in Figure B-1.

Table 10.8-2. Oconee Hot Leg Collar Restraint

Part	Material	Governing criteria	Calculated value	Allowable value	Ratio
Restraint steel box section	A516 Gr. 70	Tension stress, ksi	1.8	43.7	0.04
Restraint steel channel section	A516 Gr. 70	Tension stress, ksi	4.5	43.7	0.10
Embedment steel	A36	Tension stress, ksi	3.8	41.4	0.09
Embedment concrete	f'_c = 4,000 psi	Punching shear, kips	534	1,507	0.36

Note: This restraint is Restraint 2 in Figure B-1.

Table 10.8-3. Three Mile Island 1 U-Bar Rupture Restraint

Part	Material	Break location	Governing criteria	Calculated value	Allowable value	Ratio
Embedment concrete	f'_c = 5,000 psi	Nozzle	Punching shear, kips	8,161	9,110	0.90
Embedment steel	C1046 and A36	Nozzle	Tension force, kips	8,161	15,433	0.53
U-Bar, highest individual	A490	Nozzle	Strain, percent	2.23	3.50	0.63
		Elbow	Strain, percent	2.54	3.50	0.73
Clevis	A490	Elbow	Tension stress, ksi	105.1	149.5	0.70
		Elbow	Bearing stress, ksi	105.1	134.6	0.78
Pin	A490	Elbow	Shear stress, ksi	50.2	86.3	0.58
			Combined shear and bending	0.47	1.0	0.47
Fillet weld	E60XX	Nozzle	Shear stress, ksi	32.5	40.8	0.80
Butt weld	A36 base metal	Elbow	Tension stress, ksi	29.9	41.4	0.72
Bracket(a)	A36		Ultimate capacity per bracket, kips	(c)	1125.9(b)	(c)

(a) See discussion in text for bracket plate.
(b) Two brackets per U-bar, capacity = 2251.8 kips.
(c) See Section 9.8 for applied load.

Note: This restraint is Restraint 1 in Figure B-2.

Table 10.8-4. Three Mile Island 2 U-Bar Rupture Restraint

Part	Material	Break location	Governing criteria	Calculated value	Allowable value	Ratio
Embedment concrete	f'_c = 5,000 psi	Nozzle	Punching shear, kips	5,096	7,602	0.67
Embedment steel	A36	Elbow	Tension stress, ksi	26.8	41.4	0.65
Pins	A36	Elbow	Shear stress, ksi	20.7	23.9	0.87
			Combined shear and bending	0.8	1.0	0.80
Bracket	A36	Elbow	Tension stress, ksi	22.6	41.4	0.55
Fillet weld on U-bar #3	E60XX	Elbow	Shear stress, ksi	26.3	40.8	0.64
Clevis	A36	Elbow	Strain, percent	1.86	5.75	0.32
U-bars	A-441	Nozzle	Strain energy, kip-inch	5,825	11,494	0.51
	A-441	Elbow	Strain energy, kip-inch	6,786	11,494	0.59

Note: This restraint is Restraint 1 in Figure B-3.

Table 10.8-5. Crystal River Hot Leg U-Bar Rupture Restraint

Part	Material	Governing criteria	Calculated value	Allowable value	Ratio
Embedment concrete	f'_c=5000 psi	Punching shear, kips	4213	4457	.94
Embedment steel	A-36 & A-540	Tension load, kips	4213	9576	.44
U-bar, highest individual	A-36	Tension strain, percent	3.90	5.75	.68
Clevis	A-235 Class E	Tension stress, ksi	33.1	43.1	.77
		Compressive bearing stress, kips	47.0	58.2	.81
Bracket plate	A-36	Tension stress, kips	23.3	41.4	.56
		Compressive bearing stress, ksi	52.5	78.7	.67(a)
Pin	A-588	Shear stress, kips	33.4	50.0	.67
		Combined shear and bending	.63	1.0	.63
Butt weld	A-36 Base metal	Tension stress, kips	23.3	41.4	.56

(a) See discussion in text.

Note: This restraint is Restraint 1 in Figure B-5.

Table 10.8-6. ANO-1 Hot Leg Strap Rupture Restraint

Part	Material	Governing criteria	Calculated value	Allowable value	Ratio
Embedment concrete	f'_c = 5,500 psi	Punching shear, kips	3,412	4,422	0.77
Steel restraint strap (includes embedment steel)	A588	Tension strain, percent	0.28	4.50	0.06
Full penetration weld (E70XX)	Base metal A588	Tension stress, ksi	57.7	73.5	0.78

Note: This restraint is Restraint 1 on Figure B-4.

Table 10.8-7. Rancho Seco Hot Leg Upper Rupture Restraint

Part	Material	Governing criteria	Calculated value	Allowable value	Ratio
Embedment concrete	f'_c = 5,000 psi	Punching shear, kips	440	7,244	0.06
Embedment steel anchor bolts	A490	Tension stress, ksi	6.8	149.5	0.05
Anchor bolt sleeves	A36	Tension stress, ksi	2.6	41.4	0.06
Anchor bolt sleeve weld	Base metal A36	Tension stress, ksi	2.1	41.4	0.05
1.75" bevel weld at wall face	Base metal A36	Tension stress, ksi	1.9	41.4	0.05
1.25" bevel weld on restraint	Base metal A36	Tension stress, ksi	2.9	41.4	0.07
Box section restraint	A515 Gr. 70	Tension stress, ksi	15.2	43.7	0.35

Note: This restraint is Restraint 2 on Figure B-6.

Table 10.8-8. Rancho Seco Hot Leg Lower Rupture Restraint

Part	Material	Governing criteria	Calculated value	Allowable value	Ratio
Embedment concrete	f'_c = 5,000 psi	Punching shear, kips	4,420	6,773	0.65
Embedment anchor bolts	4140	Tension stress, ksi	100.2	126.5	0.79
Anchor bolt sleeves	A36	Tension stress, ksi	32.5	41.4	0.79
Anchor bolt sleeve weld	Base metal A36	Tension stress, ksi	27.9	41.4	0.67
1.75" bevel weld at wall face	Base metal A36	Combined shear, tension, and moment	0.9	1.0	0.90
1.25" bevel weld on face	Base metal A36	Tension stress, ksi	14.7	41.4	0.36
Anchor plate bolts	A490	Tension stress, ksi	96.5	149.5	0.65
		Combined shear and tension	0.58	1.0	0.58
Box section restraint	A515 Gr. 70	Tension strain, percent	3.1	5.25	0.59

Note: This restraint is Restraint 3 on Figure B-6.

10.9. Core Flood Line Piping

The results of the analyses performed are tabulated in Tables 10.9-1, 10.9-2 and 10.9-3.

Detailed analysis and comparative evaluation of the core flood lines and comparison of the calculated support loads and piping stresses with the acceptance criteria, indicated that the core flood lines are structurally adequate and will remain functional.

10.9.1. Oconee

Both core flood line systems for Oconee were analyzed. Comparison of the resulting loads and stresses to the acceptance criteria demonstrated that structural integrity and functionality of the piping is maintained for the LOCA loads.

10.9.2. Three Mile Island 1

Both core flood line systems for TMI-1 were analyzed. Comparison of the resulting loads and stresses to the acceptance criteria demonstrated that structural integrity and functionality of the piping is maintained for the LOCA loads. Two snubber supports are overloaded but this does not adversely affect the response of the piping or the other supports.

10.9.3. Crystal River

Both core flood line systems for Crystal River were analyzed. Comparison of the resulting loads and stresses to the acceptance criteria demonstrated that structural integrity and functionality of the piping is maintained for the LOCA loads. Three snubber supports were overloaded for the hot leg break case, but this does not adversely affect the response of the piping or other supports.

10.9.4. ANO-1

Only the Loop A core flood line was analyzed for ANO-1. Comparison of the resulting loads and stresses to the acceptance criteria demonstrated that structural integrity and functionality of the piping was maintained for the LOCA loads. The first support was overloaded but this does not adversely affect the response of the piping or other supports. Loop B response is enveloped by ANO-1 Loop A and Oconee Loop A and is therefore acceptable.

10.9.5. Rancho Seco

Only the Loop B core flood line was analyzed for Rancho Seco. Comparison of the resulting loads and stresses to the acceptance criteria demonstrated that structural integrity and functionality of the piping are maintained for the LOCA loads. Loop A response is enveloped by Rancho Seco Loop B and Oconee Loop A and is therefore acceptable.

10.9.6. Davis-Besse

Only the Loop A core flood line was analyzed for Davis-Besse. Comparison of the resulting loads and stresses to the acceptance criteria demonstrated that structural integrity and functionality of the piping are maintained for the LOCA loads. Loop B is enveloped by Davis-Besse Loop A, and is therefore acceptable.

Table 10.9-1. Response Spectra Analysis Results

Plant	Loop	Break	Maximum Pipe Stress Ratio Primary	Maximum Pipe Stress Ratio Secondary	Maximum Support Load Ratio
Oconee	A	HL	0.75	-	0.81
		CL	1.18	-	1.48(1)
	B	HL	-	-	- (2)
		CL	0.60	0.96	- (3)
TMI-1	A	HL	0.53	1.14	1.22(1)
		CL	0.96	1.10	2.17(1)
	B	HL	0.58	0.73	1.70(1)
		CL	0.57	0.53	0.96
Crystal River	A	HL	0.54	0.75	1.47(1),(7)
		CL	0.48	-	1.60(1)
	B	HL	0.77	0.75	2.60(1),(7)
		CL	0.62	-	1.80(1)
ANO-1	A	HL	0.62	0.85	2.47(1)
		CL	0.46	0.44	1.22(1)
	B	-	-	-	- (4)
Rancho Seco	A	-	-	-	- (5)
	B	HL	0.49	0.27	0.79(6)
		CL	0.39	0.26	0.64(6)
Davis-Besse	A	HL	0.78	0.68	0.87(8)
		CL	0.71	0.53	0.33
		HL	0.63	0.48	0.33(9)
		CL	0.63	0.48	0.37(9)
	B	-	-	-	-(4)

(1) See Tables 10.9-2 and 10.9-3 for further results.
(2) This break case is enveloped by the cold-leg break.
(3) There are no intermediate supports on this line.
(4) The response of this loop is enveloped by Loop A.
(5) The response of this loop is enveloped by Rancho Seco loop B and Oconee loop A.
(6) The support load ratio is based on using an allowable support load equal to the calculated load reported in anchor movement and OBE seismic analysis which is 9.2^{k}. The rated design capacity of the snubber support at this location is only 6^{k} kips for Level C conditions (one-time load rating). This would give a ratio of 1.22. This is considered acceptable since T-H analysis would be expected to lower the loads based on time history analysis performed for Oconee, TMI-1 and Crystal River.
(7) The secondary stress ratio is an enveloping value representing the worst case break.
(8) Maximum stress ratio determined on the basis of Class 2 indices for elbows for Class 2 portions of the line near the core flood tank.
(9) Elbow break case.

Table 10.9-2. Response Spectra Analysis Results
Overload Supports Removed

Plant	Loop	Break	Maximum Pipe Stress Ratio		Maximum Support Load Ratio
			Primary	Secondary	
TMI-1	A	HL	0.86	0.89	0.89(1)
		CL	0.86	0.97	0.99(1),(2)
	B	HL	0.79	0.58	1.19(1),(2)
		CL	0.60	0.58	0.97(1)
ANO-1	A	HL	0.72	0.19	0.67(3)
		CL	0.48	0.27	0.42(3)

(1) The first support from the reactor vessel has been conservatively eliminated from the model to account for the overload identified in Table 10.9-1.
(2) See Table 10.9-3 for further results.
(3) The first support is eliminated from the model to conservatively account for the overload identified in Table 10.9-1.

Table 10.9-3. Time History Analysis Results

Plant	Loop	Break	Maximum Primary Pipe Stress Ratio	Maximum Support Load Ratio
Oconee	A	CL	0.67	0.79(3)
TMI-1	A	CL	0.48	0.39(1)
	B	HL	0.58	0.56(5)
Crystal River	A	HL	0.66	0.40(2)
		CL	0.36	0.71(3)
	B	HL	0.67	0.17(4)
		CL	0.72	0.83(5)

(1) The first support from the reactor vessel has been conservatively eliminated from the model to account for the overload identified in Table 10.9-1.
(2) The first snubber support in the z-direction has been deleted from the model to account for the overload identified in Table 6.9-1.
(3) All support loads meet their acceptance limits.
(4) The snubber supports, two in the z-direction and one in the x-direction, have been eliminated from the model to account for the overload identified in Table 10.9-1.
(5) The two snubber supports in the z-direction have been conservatively eliminated from the model to account for the overload identified in Table 10.9-1.

10.10. Reactor Cavity Walls

This section summarizes the results of cavity wall finite element analysis, which is discussed in detail in Section 6.10.

10.10.1. Oconee

The Oconee cavity wall qualifies for the most severe pressure loading, which is the 2.0A cold leg nozzle break. The highest stress ratio for this break case is 0.91 for hoop stresses below the hot leg penetrations. Full stress summaries are provided in Tables 10.10-1 and 10.10-2.

10.10.2. Three Mile Island 1

10.10.2.1. Cold Leg Break

The Three Mile Island 1 Cavity wall linear elastic analysis predicted local overstress in the hoop steel for the 2.0A cold leg break, as discussed in Section 6.10.4.2. This local overstress is not considered capable of inducing large cracks. Hence the cavity wall is considered adequate to contain pressurizations from a 2.0A cold leg break. Full stress summaries are provided in Tables 10.10-3 and 10.10-4.

10.10.2.2. Hot Leg Break

Evaluation was based on explicit nonlinear analysis, as discussed in Section 6.10.4.2, with detailed results tabulated in Tables 10.10-5 and 10.10-6. Key conclusions are that highest strained steel is at 1.42 percent strain, resulting in a strain ratio of 0.38. Functionality of the wall is preserved, and maximum deflections are under 2 inches.

The wall is thus considered adequate to withstand the hot leg LOCA loading and able to take all operational loads after the LOCA event.

10.10.3. Three Mile Island 2

The Three Mile Island 2 cavity wall is acceptable for both the 1.71A hot leg and 2.0A cold leg breaks. The highest hoop stress ratio is 0.83 for stresses at the penetration level. The shear and moment capacity of the cavity wall/pedestal interface is reached for the hot leg break. Full stress summaries are provided in Tables 10.10-7 and 10.10-8.

10.10.4. Crystal River

The Crystal River cavity wall is acceptable for both the 1.092A hot leg and 2.0A cold leg breaks. The highest stress ratios are 0.96 and 0.88 for hoop stresses below the core flood line penetration for the hot leg and cold leg breaks, respectively. Bending moment capacities at the pedestal/cavity wall interface are fully developed under both breaks. Full stress summaries are provided in Tables 10.10-9 and 10.10-10.

10.10.5. ANO-1

The ANO-1 cavity wall is acceptable for the 0.307A hot leg nozzle break. For the cold leg 2.0A nozzle break, the wall is adequate globally, but is slightly overstressed in one local area. This overstress occurs in the hoop steel immediately below the cold leg penetration where the stress ratio is 1.10. Analysis showed the overstressed area to be localized, and the stress ratio drops to less than 1.0 within a few feet of the overstressed area. This slight local overload is not considered capable of inducing large cracks. Hence the cavity wall is considered adequate to contain pressurization from a 2.0A cold leg break. Full stress summaries are provided in Table 10.10-11 and 10.10-12.

10.10.6. Rancho Seco

The Rancho Seco cavity wall is acceptable for both the 0.679A hot leg and 2.0A cold leg breaks. Under the more severe cold leg break, the largest stress ratio is 0.36 for hoop stresses above the cold leg penetration. Full stress summaries are provided in Tables 10.10-13 and 10.10-14.

10.10.7. Davis-Besse

The Davis-Besse cavity wall is acceptable for the 1.0243A hot leg nozzle break, and the less severe 0.243A cold leg break. The highest stressed area is the hoop steel above the hot leg penetration, which has a stress ratio of 0.93. Full stress summaries are provided in Tables 10.10-15 and 10.10-16.

The Davis-Besse cavity wall and fuel canal floor are qualified to take all reaction loads imposed by the reactor vessel support beams and LOCA rings. Highest stressed areas are the concrete sections immediately adjacent to the support beams and LOCA rings, where bearing stress ratios are 0.64 and 0.84 respectively. Full stress summaries are provided in Table 10.10-17 and Table 10.10-18.

Table 10.10-1. Hoop and Shear Stress Evaluation of Oconee Cavity Wall

Type of Stress	Location	Loading Phase	0.46A Hot Leg Break	2.0A Cold Leg Break	Allowable	Stress Ratio 0.46A Hot Leg Break	Stress Ratio 2.0A Cold Leg Break
Hoop, ksi	Below Core Floodline Penetrations	Steady-state	32.2	51.2	63.0	0.51	0.81
Hoop, ksi	Below Hot Leg Penetrations	Steady-state	29.7	57.3	63.0	0.47	0.91
Hoop, ksi	Fuel Canal Floor Slab	Asymmetric	42.6	-	69.0	0.62	-
		Steady-state	33.9	40.9	63.0	0.54	0.65
Shear, psi	Below Hot Leg Penetration	Asymmetric	219.0	-	383	0.57	-
Shear, psi	Pedestal/ Cavity Wall Interface	Steady-state	214.0	275.0	383	0.56	0.72

Table 10.10-2. Bending Stress Evaluation of Oconee Cavity Wall

Location	Loading Phase	Ratios[a] 0.46A Hot Leg Break	Ratios[a] 2.0A Cold Leg Break
Pedestal/ Cavity Wall Interface	Asymmetric	0.02	0.03
	Steady-state	0.22	0.44
Below Penetrations	Asymmetric	0.34	0.25
	Steady-state	0.36	0.56
Between Penetrations	Asymmetric	-	0.39
	Steady-state	0.29	0.35

(a) Ratios listed are moment-force interaction indices: $\frac{P_a}{P_o} + \frac{M_a}{0.9M_o} \leq 1$

Table 10.10-3. Three Mile Island 1 Linear Analysis Hoop Stress Evaluations

Location	Loading Phase	Stresses, ksi 1.295A Hot Leg Break	Stresses, ksi 2.0A Cold Leg Break	Stresses, ksi Allowable	Stress Ratio 1.295A Hot Leg Break	Stress Ratio 2.0A Cold Leg Break
Above Hot Leg	Steady-state	20.6	14.3	42	0.49	0.34
Below Hot Leg	Steady-state	55.5	41.4	42	1.32	0.99
Below Core Flood Line Penetration	Steady-state	58.9	49.9	42	1.40	1.19
Below Hot Leg, Opposite Break Location	Steady-state	50.6	-	42	1.20	-
Below Cold Leg	Steady-state	-	54.8	42	-	1.30

Table 10.10-4. Three Mile Island 1 Linear Analysis Bending Stress Evaluation

Location	Loading Phase	Ratio[a] 2.0A Cold Leg Break
Pedestal/Cavity Wall Interface	Steady-state	1.0
Below Cold Leg Penetration	Steady-state	0.50
Below Hot Leg Penetration	Steady-state	0.26
Above Penetration Level	Steady-state	0.36
Between Penetrations	Steady-state	0.20

(a) Ratios listed are moment-force interaction indices: $\frac{P_a}{P_o} + \frac{M_a}{0.9M_o} \leq 1$

Table 10.10-5. Hoop and Vertical Reinforcing Steel Strain Evaluation of TMI-1 Cavity Wall - Nonlinear Analysis

Type of Strain	Location	1.295A Hot Leg, percent	Allowable Strain, percent	Ratio
Hoop	Mid-Height of Cavity Wall	1.273	3.75	0.34
Hoop	Below Nozzle Belt	0.9803	3.75	0.26
Hoop	Pedestal/Cavity Wall Interface	0.2149	3.75	0.06
Vertical	Pedestal/Cavity Wall Interface, Inside Face	1.42	3.75	0.38
Vertical	Mid-Height of Cavity Wall, Outside Face	0.7124	3.75	0.19

Table 10.10-6. Concrete Stress Evaluation of TMI-1 Cavity Wall: Nonlinear Analysis

Type of Stress	Location	1.295A Hot Leg, psi	Allowable Stress, psi	Ratio
Compression	Inside Face, Mid-Height of Cavity Wall	4142	5652	0.73
Compression	Outside Face, Cavity Wall/ Pedestal Interface	2169	5652	0.38

Table 10.10-7. Hoop and Shear Stress Evaluation of Three Mile Island 2 Cavity Wall

Type of Stress	Location	Loading Phase	1.71A Hot Leg Break	2.0A Cold Leg Break	Allowable	Stress Ratio 1.71A Hot Leg Break	Stress Ratio 2.0A Cold Leg Break
Hoop, ksi	Below Hot Leg	Steady-state	46.0	23.5	63.0	0.73	0.37
Hoop, ksi	Between Hot and Cold Legs Below Penetration Level	Asymmetric	30.6	-	69.0	0.44	-
		Steady-state	52.3	25.2	63.0	0.83	0.40
Hoop, ksi	Below Core Flood Line Penetrations	Steady-state	39.6	-	63.0	0.63	-
Hoop, ksi	Base of Cavity Wall	Steady-state	31.4	33.5	63.0	0.50	0.53
Shear, psi	Pedestal/Cavity Wall Interface	Steady-state	141	141	141	1.0	1.0
Shear, psi	Between Hot and Cold Leg Penetrations	Steady-state	273	110	392	0.70	0.28
Shear, psi	Between two Cold Leg Penetrations	Steady-state	315	-	392	0.80	-

Table 10.10-8. Bending Stress Evaluation of Three Mile Island 2 Cavity Wall

Location	Loading Phase	Ratio[(a)] 1.71A Hot Leg Break	Ratio[(a)] 2.0A Cold Leg Break
Pedestal/Cavity Wall Interface, Below Break Location	Asymmetric	-	0.04
	Steady-State	1.0	0.68
Pedestal/Cavity Wall Interface, 90° from Break Location	Steady-state	1.0	-
Cavity Wall/Fuel Canal Floor Interface	Steady-state	-	0.20

(a) Ratios listed are moment-force interaction indices: $\frac{P_a}{P_o} + \frac{M_a}{0.9M_o} \leq 1$

Table 10.10-9. Hoop and Shear Stress Evaluation of Crystal River Cavity Wall

Type of Stress	Location	Loading Phase	1.092A Hot Leg Break	2.0A Cold Leg Break	Allowable	Stress Ratio 1.092A Hot Leg Break	Stress Ratio 2.0A Cold Leg Break
Hoop, ksi	Above Hot Leg	Steady-state	16.4	12.2	42	0.39	0.29
Hoop, ksi	Below Hot Leg	Steady-state	33.2	27.4	42	0.79	0.65
Hoop, ksi	Below Core Flood Line Penetration	Steady-state	40.2	37.1	42	0.96	0.88
Hoop, ksi	Below Hot Leg, Opposite Break Location	Steady-state	33.7	-	42	0.80	-
Hoop, ksi	Between Hot and Cold Leg Penetration	Steady-state	38.4	28.4	42	0.91	0.68
Hoop, ksi	Below Cold Leg	Steady-state	-	33.9	42	-	0.81
Hoop, ksi	At Pedestal/ Cavity Wall Interface	Steady-state	36.7	27.3	42	0.87	0.65
Shear, psi	At Pedestal/ Cavity Wall Interface	Steady-state	167.0	139.0	168	0.99	0.83

Table 10.10-10. Bending Stress Evaluation of Crystal River Cavity Wall

Location	Loading Phase	Ratio[(a)] 1.092A Hot Leg Break	Ratio[(a)] 2.0A Cold Leg Break
Pedestal/Cavity Wall Interface	Steady-state	1.0	1.0
Below Penetrations	Steady-state	0.69	0.59
Between Penetrations	Steady-state	0.29	0.28

(a) Ratios listed are moment-force interaction indices: $\frac{P_a}{P_o} + \frac{M_a}{0.9\,M_o} \leq 1$

Table 10.10-11. Hoop and Shear Stress Evaluation of ANO-1 Cavity Wall

Type of Stress	Location	Loading Phase	0.307A Hot Leg Break	2.0A Cold Leg Break	Allowable	Stress Ratio 0.307A Hot Leg Break	Stress Ratio 2.0A Cold Leg Break
Hoop, ksi	Below Hot Leg	Steady-state	20.1	-	63.0	0.32	-
Hoop, ksi	Below Cold Leg	Steady-state	-	68.7	63.0	-	1.09
Hoop, ksi	Below Cold Leg, Adjacent Regions	Steady-state	-	44.1	63.0	-	0.70
Hoop, ksi	Below Core Flood Line Penetration	Steady-state	-	49.1	63.0	-	0.78
Shear, psi	Pedestal/ Cavity Wall Interface	Steady-state	113	148	148	0.76	1.00
Shear, psi	Between Cold Leg Penetra-tions	Steady-state	102	340	673	0.16	0.51

Table 10.10-12. Bending Stress Evaluation of ANO-1 Cavity Wall

Location	Loading Phase	Ratio (a) 0.307A Hot Leg Break	Ratio (a) 2.0A Cold Leg Break
Pedestal/Cavity Wall Interface	Steady-state	0.30	0.99
Between Cold Leg Penetrations	Steady-state	0.21	0.61
Below Hot Leg Penetration	Steady-state	0.44	0.65
Between Hot and Cold Leg Penetrations	Steady-state	0.37	-

(a) Ratios listed are moment-force interaction indices: $\frac{P_a}{P_o} + \frac{M_a}{0.9M_o} \leq 1$

Table 10.10-13. Hoop and Shear Stress Evaluation of Rancho Seco Cavity Wall

Type of Stress	Location	Loading Phase	0.679A Hot Leg Break	2.0A Cold Leg Break	Allowable	Stress Ratio 0.679A Hot Leg Break	Stress Ratio 2.0A Cold Leg Break
Hoop, ksi	Above Hot Leg	Steady-state	9.9	7.8	63.0	0.16	0.12
Hoop, ksi	Below Hot Leg	Steady-state	3.6	3.5	63.0	0.06	0.05
Hoop, ksi	Above Core Flood Line	Steady-state	16.5	-	63.0	0.26	-
Hoop, ksi	Below Core Flood Line	Steady-state	18.0	18.8	63.0	0.29	0.30
Hoop, ksi	Above Cold Leg	Steady-state	-	22.7	63.0	-	0.36
Hoop, ksi	Below Cold Leg	Steady-state	-	21.0	63.0	-	0.33
Hoop, ksi	Below Cold Leg	Asymmetric	-	13.2	69.0	-	0.19
Shear, psi	Pedestal/ Cavity Wall Interface	Steady-state	165	220	630	0.26	0.35
Shear, psi	Between Penetra-tions	Steady-state	117	147	707	0.17	0.21

Table 10.10-14. Bending Stress Evaluation of Rancho Seco Cavity Wall

Location	Loading Phase	Ratio[(a)] 0.679A Hot Leg Break	Ratio[(a)] 2.0A Cold Leg Break
Pedestal/Cavity Wall Interface	Steady-state	0.13	0.16
Below Penetrations	Steady-state	0.12	0.23
Between Penetrations	Steady-state	0.07	0.05
Above Penetrations	Steady-state	-	0.24

(a) Ratios listed are moment-force interaction indices: $\frac{P_a}{P_o} + \frac{M_a}{0.9M_o} \leq 1$

Table 10.10-15. Hoop and Shear Stress Evaluation of Davis-Besse Cavity Wall

Type of Stress	Location	Loading Phase	1.0243A Hot Leg Break	0.243A Cold Leg Break	Allowable	Stress Ratio 1.0243A Hot Leg	Stress Ratio 0.242A Cold
Hoop, ksi	Below Hot Leg Penetration	Asymmetric	45.9		69.0	0.66	
		Steady-state	36.4	6.3	63.0	0.58	0.10
Hoop, ksi	Below Support Beams	Asymmetric	55.3		69.0	0.80	
		Steady-state	57.2	20.1	63.0	0.91	0.32
Hoop, ksi	Above Hot Leg Penetration	Asymmetric	63.8		69.0	0.93	
		Steady-state	50.2	7.9	63.0	0.80	0.13
Hoop, ksi	Above Cold Leg Penetration	Asymmetric	55.4		69.0	0.80	
		Steady-state	44.6	9.6	63.0	0.71	0.15
Shear, psi	Between Hot and Cold Leg Penetrations	Asymmetric	133.0		155.0	0.86	
		Steady-state	102.0	20.0	141.0	0.72	0.14
Shear, psi	Pedestal/Cavity Wall Interface	Asymmetric	25.0		155.0	0.16	
		Steady-state	70.0	18.0	141.0	0.50	0.13

Table 10.10-16. Bending Stress Evaluation of Davis-Besse Cavity Wall

Location	Loading Phase	Ratio(a) 1.0243A Hot Leg Nozzle Break
Between Penetrations	Asymmetric	0.31

(a) Ratios listed are moment-force interaction indices: $\frac{P_a}{P_o} + \frac{M_a}{0.9M_o} \leq 1$

Table 10.10-17. Davis-Besse Cavity Wall Stresses due to Support Beam Loadings

Type of Loading	Location	Loading Phase	Maximum(a) Loading	Allowable	Ratio
Bearing, psi	Below Support Beam	Asymmetric	1913	2975	0.64
Shear, kips	Adjacent to Support Beam	Asymmetric	933.2	2062	0.45
Bending(c)	Below Support Beam	Asymmetric(b)	0.22	1.0	0.22

(a) maximum of horizontal LOCA + vertical LOCA + dead load + seismic.

(b) in combination with cavity wall stresses due to pressurizations.

(c) Ratio listed is moment-force interaction index: $\frac{P_a}{P_o} + \frac{M_a}{0.9M_o} \leq 1$

Table 10.10-18. Davis-Besse Cavity Wall Stresses due to LOCA Ring Loadings

Type of Loading	Location	Loading Phase	1.0243A Hot Leg[a] Nozzle Break	Allowable	Ratio
Shear, psi	Between Cold Leg Penetrations	Asymmetric	480	764	0.63
		Steady-state	220	575	0.38
Shear, psi	Between Hot and Cold Leg Penetrations	Asymmetric	575	764	0.75
		Steady-state	233	482	0.48
Bearing, kips	Adjacent to Cold Leg LOCA Rings	Asymmetric	5,461	6,510	0.84
		Steady-state	2,212	5,277	0.42
Bending[c]	Between Hot and Cold Legs	Steady-state[b]	0.94	1.0	0.94
Shear, kips	Thrust on Fuel Canal and Cavity Wall	Asymmetric	19,874	31,778	0.63
		Steady-state	6,840	20,194	0.34

(a) Hot leg 1.0243A nozzle break is the most severe case.

(b) Due to vertical load on LOCA rings, in combination with cavity wall stresses due to pressurization.

(c) Ratio listed is moment-force interaction index: $\frac{P_a}{P_o} + \frac{M_a}{0.9M_o} \leq 1$

11. PRELIMINARY ASSESSMENT OF ASYMMETRIC LOADING EFFECTS FOR PIPE BREAKS IN STEAM GENERATOR COMPARTMENT

11.1. Steam Generator Support Loadings

A preliminary analysis of pipe breaks in the steam generator subcompartment was performed. This analysis determined the steam generator support loadings and the pipe reactions in the "unbroken" primary piping. A limited number of breaks were considered, and existing data from other plants were used to formulate a data base.

11.1.1. Pipe Break Locations

Terminal end guillotine pipe breaks were considered, including guillotines at the steam generator inlet and outlet nozzles and at the P1A2 pump suction and discharge nozzles. Figures 11.1-1 through 11.1-3 show the break locations applicable for both skirt- and nozzle-supported plants.

11.1.2. RCS Hydraulic Functions

Pipe break opening areas (BOAs) were conservatively assumed to be 2A for all cases considered in this evaluation. No detailed pipe whip analyses were performed in the OTSG cavity to determine the actual BOAs. Available data for estimating the asymmetric cavity pressure (ACP) loadings were taken from Midland 1 and 2 and Davis-Besse 2 and 3. For these plants limited BOAs were defined using pipe whip restraints and detailed nonlinear pipe whip analysis. Therefore, the loadings were recalculated for some portions of the analytical input to reflect the assumed 2A BOAs.

Piping reaction forces were obtained from the CRAFT2 code (subroutine FORCE2).[5] These calculations provide reaction forces at directional flow changes and at changes in flow area due to the momentum and pressure changes occurring during a LOCA. The fluid accelerations produced during a LOCA were also taken into account since they induced reaction loadings on the reactor coolant system piping and pumps and on the steam generator.

The reaction force model for Midland 1 and 2 as shown in Figure 11.1-4 was used to generate piping reaction forces for the skirt-supported plant. This model contains 99 nodes and 110 flow paths for the reactor coolant primary loop. A comparable model from Davis-Besse 2 and 3 was used for the nozzle-supported plant. For these analyses, a break opening time of 0.010 second was assumed. This value has been shown to be highly conservative relative to the actual opening times, which could be determined by a detailed nonlinear pipe whip analysis.

Reaction forces for four 2A guillotine break cases were calculated. Results were applied to the Midland 1 and 2 model for skirt-supported plants, assuming that they were hydraulically similar. Likewise, reaction forces were applied to the Davis-Besse 2 and 3 model for Davis-Besse 1.

Figures 11.1-5 through 11.1-8 show the typical results for reaction forces in the hot leg 90° bend (path 69) for the four example break cases specified above. P is the force on the elbow; its direction is a 45° angle between the straight pipes on both sides of the bend. Each of the force paths has a similar set of reaction forces for the four break cases.

11.1.3. Cavity Pressure and Jet Impingement Loadings

Force time histories for Midland 1 and 2 and for Davis-Besse 2 and 3 were available and used in determining cavity pressure and jet impingement loadings. Table 11-1-1 itemizes the cases for which ACP data were available. Figures 11.1-9 through 11.1-14 are examples of typical ACP force time histories: shown are the worst-case loadings on the pump and OTSG for Midland 1 and 2 and Davis-Besse 2 and 3. Most of the data are for the 1A breaks and were multiplied by a factor of 2.0 in order to make these data applicable for the 2A cases analyzed. In addition, the data were multiplied by a factor of 1.5 to account for the differences in the steam generator compartment configurations for the various plants, as shown in Figures 11.1-15 through 11.1-20. Therefore, the resultant multiplication factor on most of the data was 3.0. This multiplication factor simply factored the force values and retained the shape of the curves. Figures 11.1-21 through 11.1-24 show plots of resultant structural reactions at selected points in the system with respect to cases with a range of factors on the ACP input. This was done in order to establish the sensitivity of the loadings to the various factored ACP inputs.

The jet impingement force time history was obtained from previous impingement analytical data. The jet impingement targets were determined based on the previous analyses and engineering judgment. Table 11.1-2 lists a typical force time history of a jet impingement loading used in the analysis.

11.1.4. RCS Structural Analysis

11.1.4.1. Models and Methods

Topical report BAW-10131[4] outlines the basic or general modeling of the RCS loop; in particular, sections 3, 4, 5, and 6, "Building Wall Modeling," "Support Modeling," "Compartment Modeling," and "Combining the Building and RCS Models," respectively, and 12.2.1, which discusses the special model preparation for a LOCA analysis, are applicable. These referenced methods were modified to include in the model all plant-unique piping arrangements, interior concrete walls, and support configurations. Due to the fact that linear elastic models are being used, any nonlinear restraint such as wire cables or restraints gapped at operating conditions are not included in the model. This adds conservatism to the analysis.

Three separate structural models were used in the analysis. The basic Midland 1 and 2 model was modified to represent (1) a skirt-supported plant with a supported pump and (2) a skirt-supported plant with an unsupported pump. The Davis-Besse 2 and 3 model was modified to represent the nozzle-supported plant. The skirt-supported arrangement basically includes the piping component arrangement of Figures 11.1-25 and 11.1-26, horizontal pump supports at the junction between the casing and motor stand, and an OTSG with an upper bumper support and a lower fixed-base skirt support. This model is applicable to plants with pump supports. The mathematical model is described in Appendix F.

The other skirt-supported arrangement includes the piping and component arrangement of Figures 11.1-27 and 11.1-28, unsupported pumps, and a steam generator with an upper bumper support and a lower fixed-base skirt support. This model is applicable to plants with only nonlinear pump supports or to those in which the pump supports are postulated to be inoperative. This model is very much like that previously described and shown in Appendix F.

The nozzle-supported loop arrangement includes the piping and component arrangement of Figures 11.1-29 and 11.1-30, horizontal pump supports at the

upper portion of the motor, and a steam generator with upper trunnion support and a lower sliding-base skirt support with snubbers and bumpers. The LOCA restraint for the reactor vessel is provided by the wagonwheel restraints in the wall penetrations for the hot leg and upper cold leg piping. This model is applicable to Davis-Besse 1. The mathematical model is described in Appendix F.

To determine the system loadings that result from the postulated ruptures of the primary piping noted in section 11.1.1, a linear dynamic time history analysis was performed as discussed in reference 4, sections 12.2 and 12.3. As noted in that report, the following loading conditions were considered in this analysis: loads due to flowing water through the system (designated as piping reaction forces), compartment pressure loadings, and jet impingement loadings. Detailed descriptions and typical applied force time histories are shown in sections 11.1.2 and 11.1.3. The ACP forces are applied to the degrees of freedom of the appropriate component. As shown in Table 11.1-1, a complete range of ACP cases was not available. A cross application of the data was made in order that each component would be loaded by realistic ACP forces in each case analyzed. The jet impingement forces were applied to a degree of freedom in the target area. Jet impingement forces were not applied to broken piping or to the pump in a broken piping run. Also, jet impingement loadings on pipe whip restraints and non-integral supports were not included as input to the time history dynamic analysis, but were superimposed onto the resultant or output dynamic force on the support. Therefore, only jet impingement time history loadings on the OTSG, the unbroken piping, and the pump in the unbroken piping section were considered in the dynamic analysis.

In this linear analysis, loadings at the connections of broken piping to the components may exceed elastic limits. An iterative process of factoring the forces at the break plane was used to attain loadings at the elastic limit at these connections. Therefore, unrealistic loadings were not transmitted to the unbroken piping and other portions of the reactor coolant system.

11.1.4.2. Structural Response Time Histories

Force time history data for each joint in the model are calculated in the dynamic analysis. As a typical example of these structural response data, Figures 11.1-31 through 11.1-33 are plots of the vertical force at the steam

generator base due to a guillotine break at the steam generator inlet nozzle for the three types of plants analyzed.

11.1.4.3. Steam Generator Support Reactions

Tables 11.1-3 and 11.1-4 list the maximum calculated loads on the steam generator and its supports considering the four LOCA cases analyzed. The loads are peak values taken from force time histories of the type discussed in the previous sections.

Table 11.1-1. Available ACP Cases

	Cases			
Component	Break @ pump dischg.	Break @ pump suct.	Break @ lower hot leg	Break @ upper hot leg
Midland 1				
P1A1 pump	1A	1A	na	2A
P1A2 pump	na	na	na	na
OTSG	1A	1A	na	2A
Davis-Besse 2, 3				
P1A1 pump	1A	1A	1A	na
P1A2 pump	1A	na	1A	na
OTSG	na	na	1A	1A

Notes: 1. A = cross sectional flow area of pipe,
1A = 642.5 $in.^2$ for pump suction or discharge break,
1A = 1018 $in.^2$ for upper or lower hot leg break.
2. na = not available.

Table 11.1-2. Jet Impingement Force Time History on OTSG Due to Break at Pump Suction Nozzle

Time, s	F_X, lbf	F_Y	F_Z, lbf
0.00200	-0.485952E+05	0.	0.280566E+05
0.00400	-0.719271E+05		0.415273E+05
0.00600	-0.759324E+05		0.438398E+05
0.00800	-0.772423E+05		0.445961E+05
0.01000	-0.762621E+05		0.440302E+05
0.01200	-0.764990E+05		0.441670E+05
0.01400	-0.885241E+05		0.511097E+05
0.01600	-0.776267E+05		0.448180E+05
0.01800	-0.763733E+05		0.440943E+05
0.02000	-0.756713E+05		0.436891E+05
0.02200	-0.764835E+05		0.441580E+05
0.02400	-0.100378E+06		0.579535E+05
0.02600	-0.101172E+06		0.584121E+05
0.03000	-0.114558E+06		0.661406E+05
0.03200	-0.119002E+06		0.687061E+05
0.03400	-0.124782E+06		0.720433E+05
0.03600	-0.125796E+06		0.726288E+05
0.03800	-0.131045E+06		0.756590E+05
0.04000	-0.123581E+06		0.713498E+05
0.04200	-0.118781E+06		0.685785E+05
0.04400	-0.114237E+06		0.659550E+05
0.04600	-0.112433E+06		0.649135E+05
0.04800	-0.114003E+06		0.658199E+05
0.05000	-0.113229E+06		0.653730E+05
0.05200	-0.111624E+06		0.644464E+05
0.05400	-0.109848E+06		0.634213E+05
0.05800	-0.112344E+06		0.648623E+05
0.06000	-0.115466E+06		0.666646E+05
0.06200	-0.117877E+06		0.680564E+05
0.06400	-0.118400E+06		0.683584E+05
0.06600	-0.117768E+06		0.679935E+05
0.06800	-0.116401E+06		0.672042E+05
0.07000	-0.115063E+06		0.664320E+05
0.07200	-0.114360E+06		0.660261E+05
0.07400	-0.114187E+06		0.659263E+05
0.07600	-0.114447E+06		0.660762E+05
0.07800	-0.115098E+06		0.664522E+05
0.08000	-0.115860E+06		0.668973E+05
0.08200	-0.116362E+06		0.671817E+05
0.08600	-0.115801E+06		0.668582E+05
0.08800	-0.114780E+06		0.662685E+05
0.09000	-0.113864E+06		0.657342E+05
0.09200	-0.113214E+06		0.653642E+05
0.09400	-0.112608E+06		0.650146E+05
0.09600	-0.111759E+06		0.645246E+05
0.09800	-0.110508E+06	0.	0.638022E+05

Table 11.1-2. (Cont'd)

Time, s	F_X, lbf	F_Y	F_Z, lbf
0.10000	-0.109055E+06	0.	0.629632E+05
0.10200	-0.108044E+06		0.623793E+05
0.10400	-0.107740E+06		0.622040E+05
0.10600	-0.107829E+06		0.622552E+05
0.11000	-0.107598E+06		0.621222E+05
0.11600	-0.105973E+06		0.611839E+05
0.12000	-0.106480E+06		0.614767E+05
0.12400	-0.107564E+06		0.621024E+05
0.12800	-0.107384E+06		0.619985E+05
0.13200	-0.106055E+06		0.612313E+05
0.13600	-0.105660E+06		0.610033E+05
0.14400	-0.106522E+06		0.615006E+05
0.14800	-0.106815E+06		0.616697E+05
0.15200	-0.107350E+06		0.619789E+05
0.15600	-0.107436E+06		0.620282E+05
0.16000	-0.106543E+06		0.615130E+05
0.16400	-0.105582E+06		0.609582E+05
0.17200	-0.103825E+06		0.599436E+05
0.17600	-0.103497E+06		0.597541E+05
0.18000	-0.104632E+06		0.604094E+05
0.18400	-0.106789E+06		0.616549E+05
0.18800	-0.108268E+06		0.625088E+05
0.19200	-0.108028E+06		0.623701E+05
0.20000	-0.104957E+06		0.605973E+05
0.20400	-0.104696E+06		0.604465E+05
0.20800	-0.105267E+06		0.607763E+05
0.21200	-0.106034E+06		0.612190E+05
0.21600	-0.106657E+06		0.615787E+05
0.22000	-0.107210E+06		0.618978E+05
0.23400	-0.104376E+06		0.602620E+05
0.24400	-0.101616E+06		0.586684E+05
0.26200	-0.106478E+06		0.614757E+05
0.27200	-0.104834E+06		0.605265E+05
0.29000	-0.107218E+06		0.619028E+05
0.30000	-0.106498E+06		0.614872E+05
0.31800	-0.101270E+06		0.584686E+05
0.32800	-0.104052E+06		0.600745E+05
0.34600	-0.101957E+06		0.588652E+05
0.35600	-0.103637E+06		0.598350E+05
0.37400	-0.104251E+06		0.601895E+05
0.38400	-0.101374E+06		0.585284E+05
0.40200	-0.105930E+06		0.611689E+05
0.41200	-0.102042E+06		0.589143E+05
0.43000	-0.104645E+06		0.604171E+05
0.44000	-0.106561E+06		0.615232E+05
0.45800	-0.100131E+06		0.578112E+05
0.46800	-0.104332E+06		0.602365E+05
0.48600	-0.100304E+06		0.579108E+05
0.49600	-0.980577E+06	0.	0.566139E+05

Table 11.1-3. OTSG Loadings in Skirt-Supported Plant

	Forces, kips			Moments, ft-kips		
	F_X	F_Y	F_Z	M_X	M_Y	M_Z
Upper horiz. support, X direction, point 51	1,730	0	0	0	0	0
Upper horiz. support, Z direction, point 34	0	0	5,000	0	0	0
Skirt – load on SG, point 25	2,560	6,360	1,970	8,940	2,210	7,750
Skirt – load on floor, point 23	2,560	6,360	5,550	42,750	2,210	190
Inlet nozzle, point 15	160	910	510	3,010	690	1,040
P1A1 discharge nozzle, point 21	1,060	1,070	290	1,480	1,270	4,060
P2A2 discharge nozzle, point 3	1,030	930	410	1,590	700	3,470

Table 11.1-4. OTSG Loadings in Nozzle-Supported Plant

	Forces, kips			Moments, ft-kips		
	F_X	F_Y	F_Z	M_X	M_Y	M_Z
Lower support, snub total, joint 197	0	0	4328	0	0	0
Lower support, outside bump, joint 198	1900	0	0	0	0	0
Lower support, inside bump, joint 192	1880	0	0	0	0	0
Upper support, north trunion, joint 294	0	0	2700	0	0	0
Upper support, east trunion, joint 293	690	0	0	0	0	0
Upper support, south trunion, joint 292	0	0	2700	0	0	0
Upper support, west trunion, joint 295	1190	0	0	0	0	0
Sliding base, joint 217	0	8430	0	0	0	0
P1A1 discharge nozzle, joint 110	870	1290	400	2980	1700	6100
P1A2 discharge nozzle, joint 171	700	940	240	1700	1350	3330

Figure 11.1-1. Postulated LOCA Break Locations for Reactor Coolant System

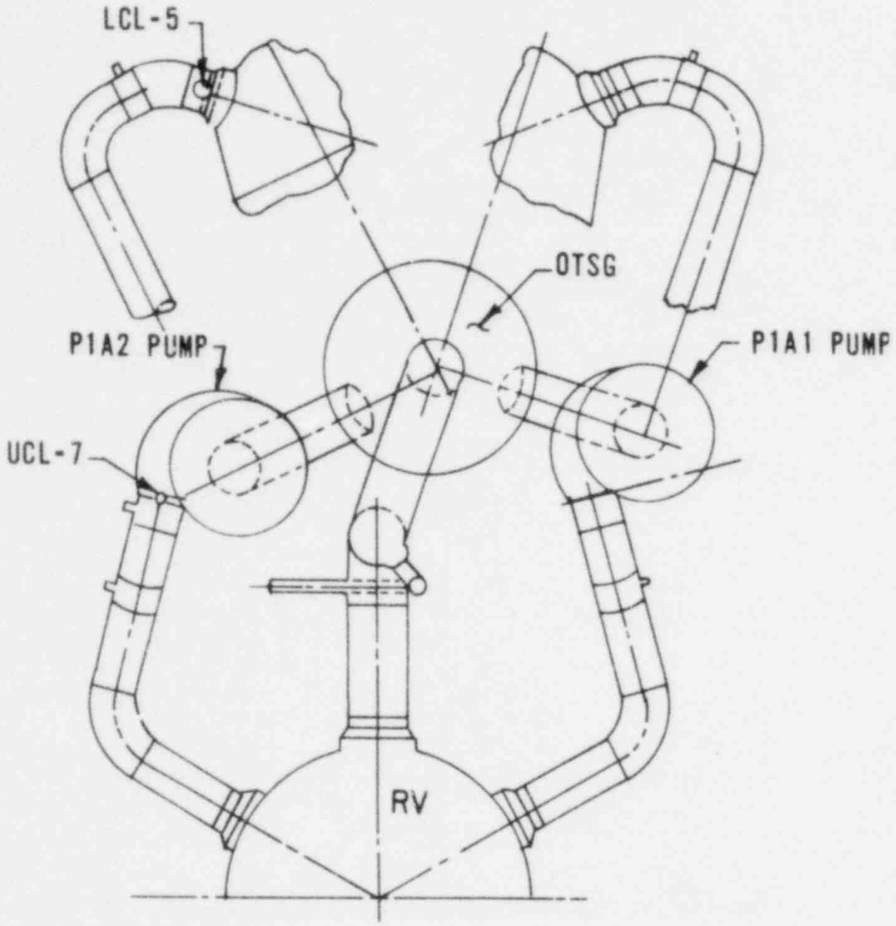

Figure 11.1-2. Hot Leg Postulated LOCA Break Locations, Elevation View

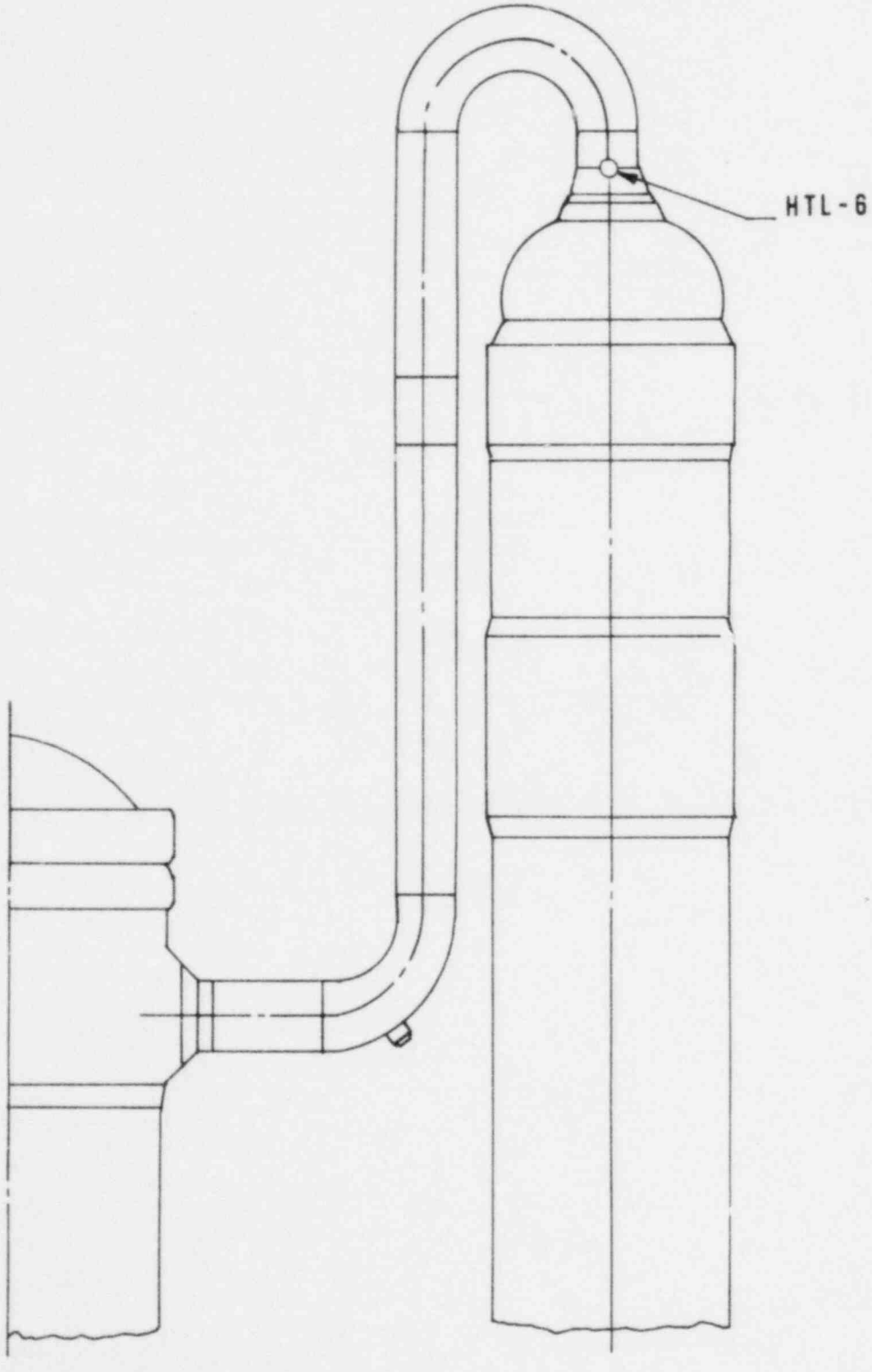

Figure 11.1-4. Nodal Arrangements for Midland Units 1 and 2

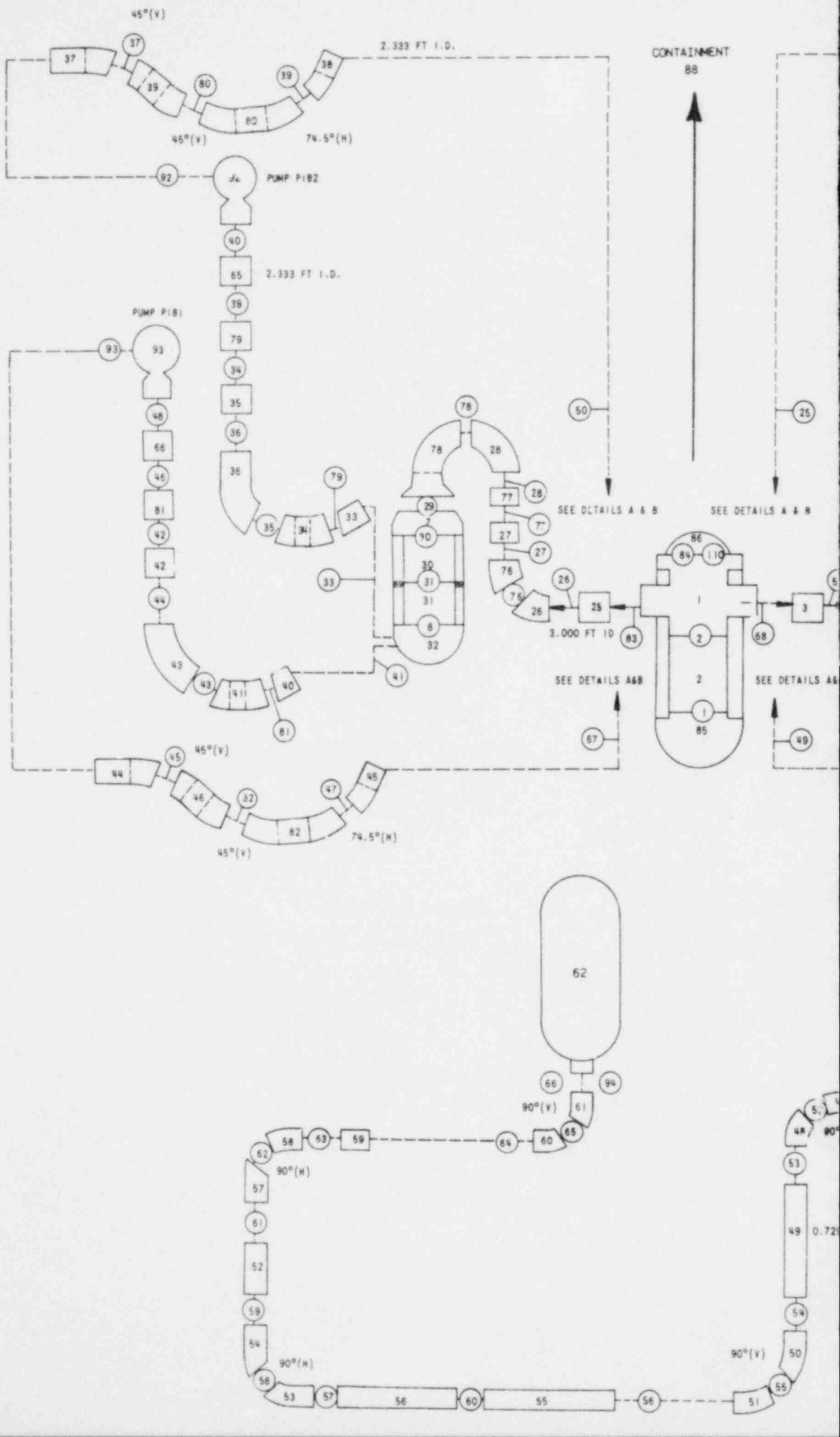

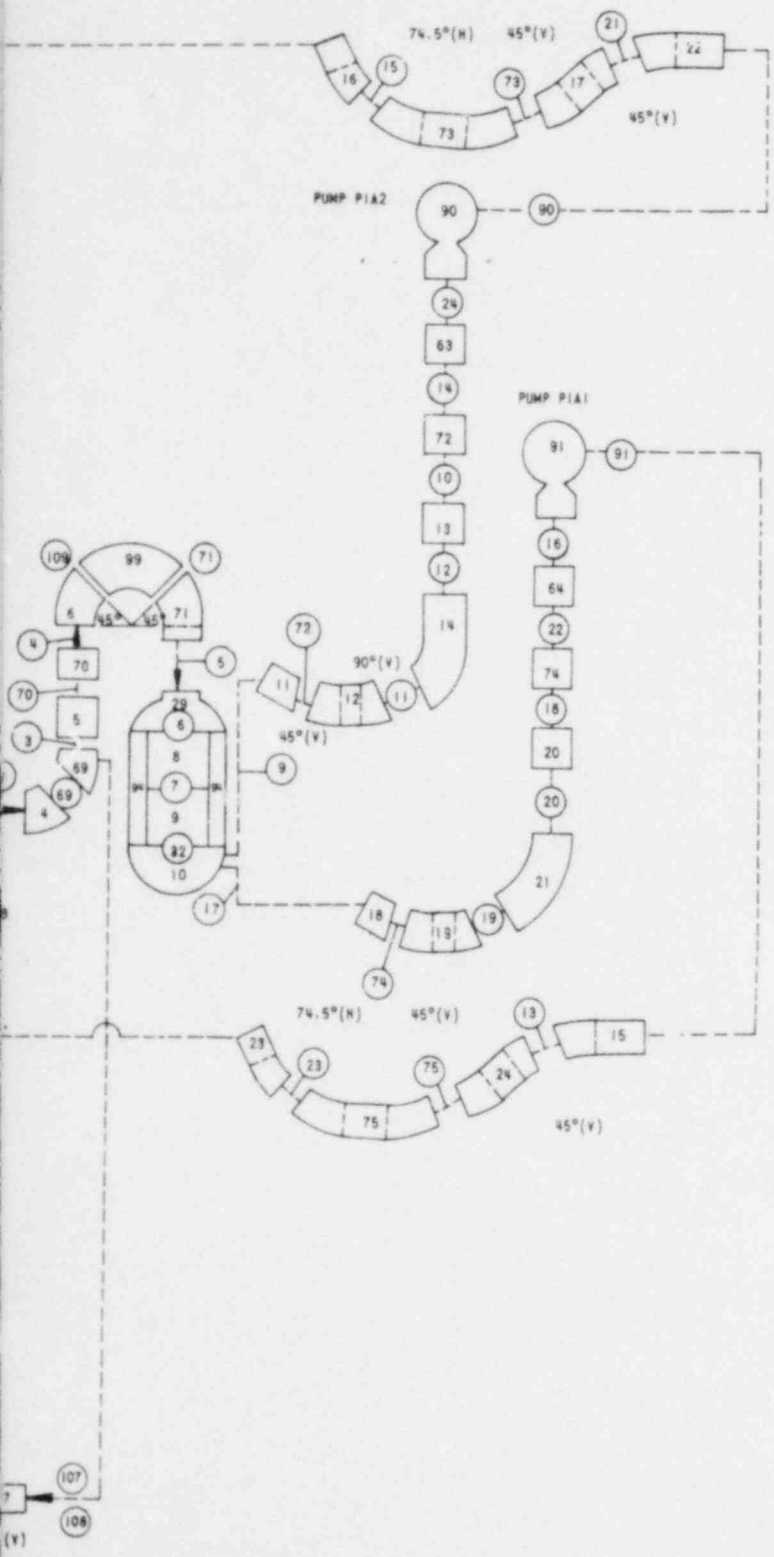

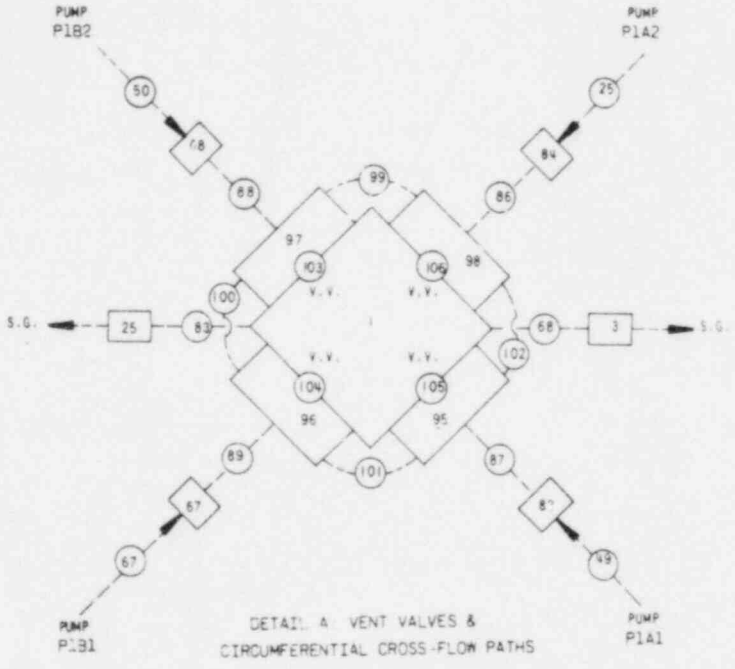

DETAIL A VENT VALVES & CIRCUMFERENTIAL CROSS-FLOW PATHS

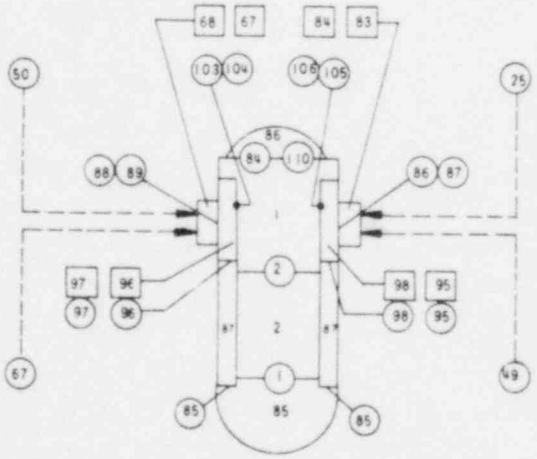

DETAIL B REACTOR VESSEL INLET (CONTROL VOLUMES AND FLOW PATHS)

FT I.D.

Figure 11.1-3. Cold Leg Postulated LOCA Break Locations, Elevation View

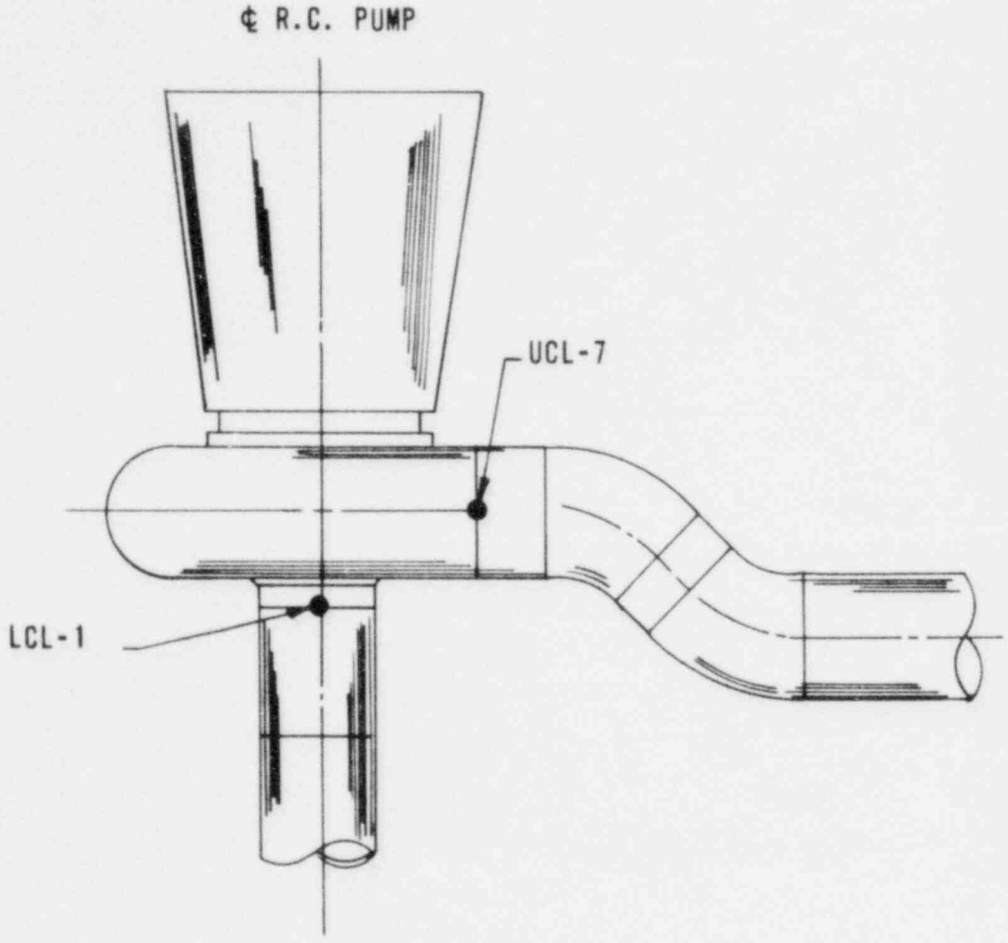

Figure 11.1-5. HTL 6 – OTSG Inlet Nozzle Guillotine, Path 69

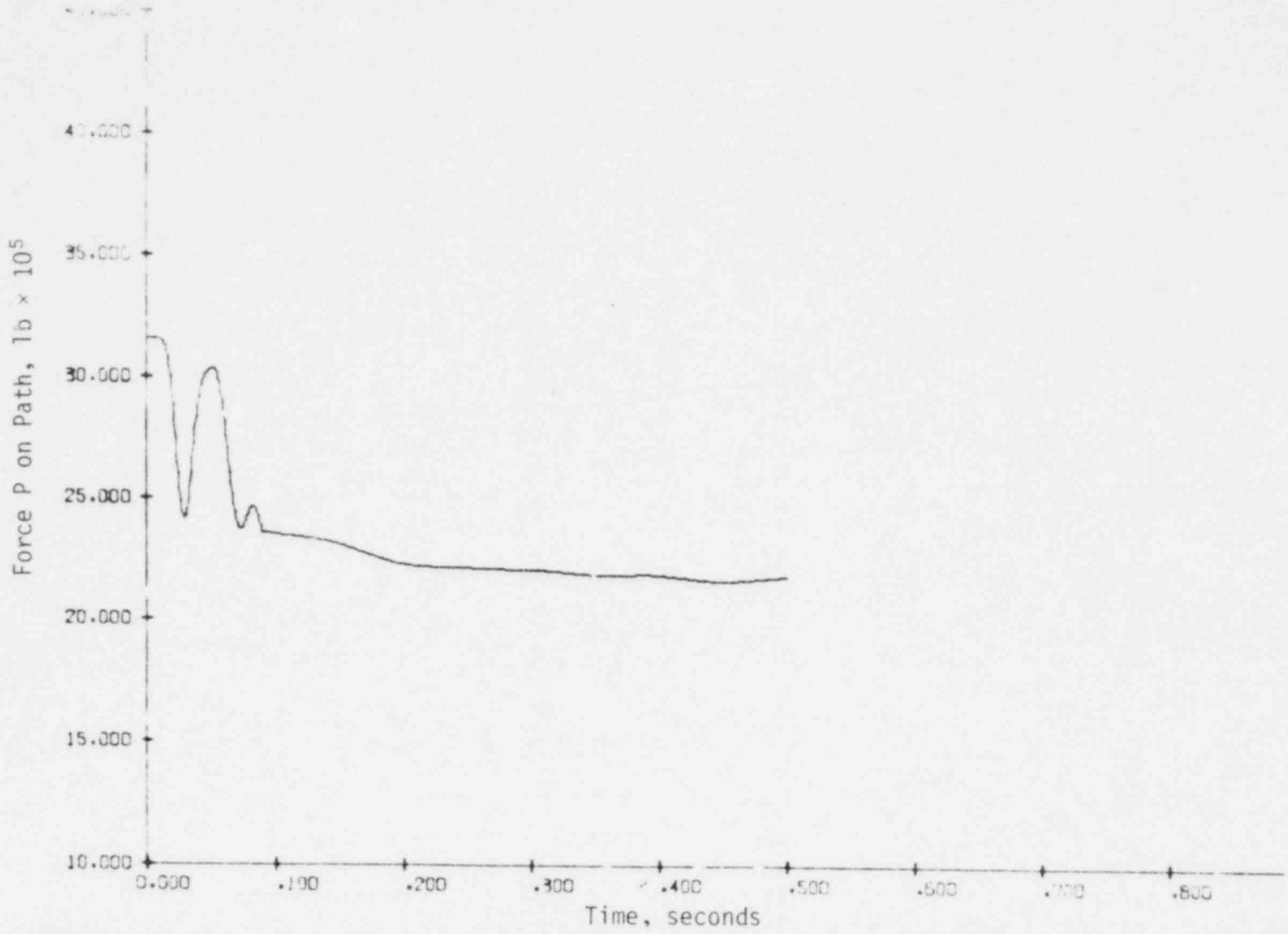

Figure 11.1-6. UCL 7 – Pump Discharge Nozzle Guillotine, Path 69

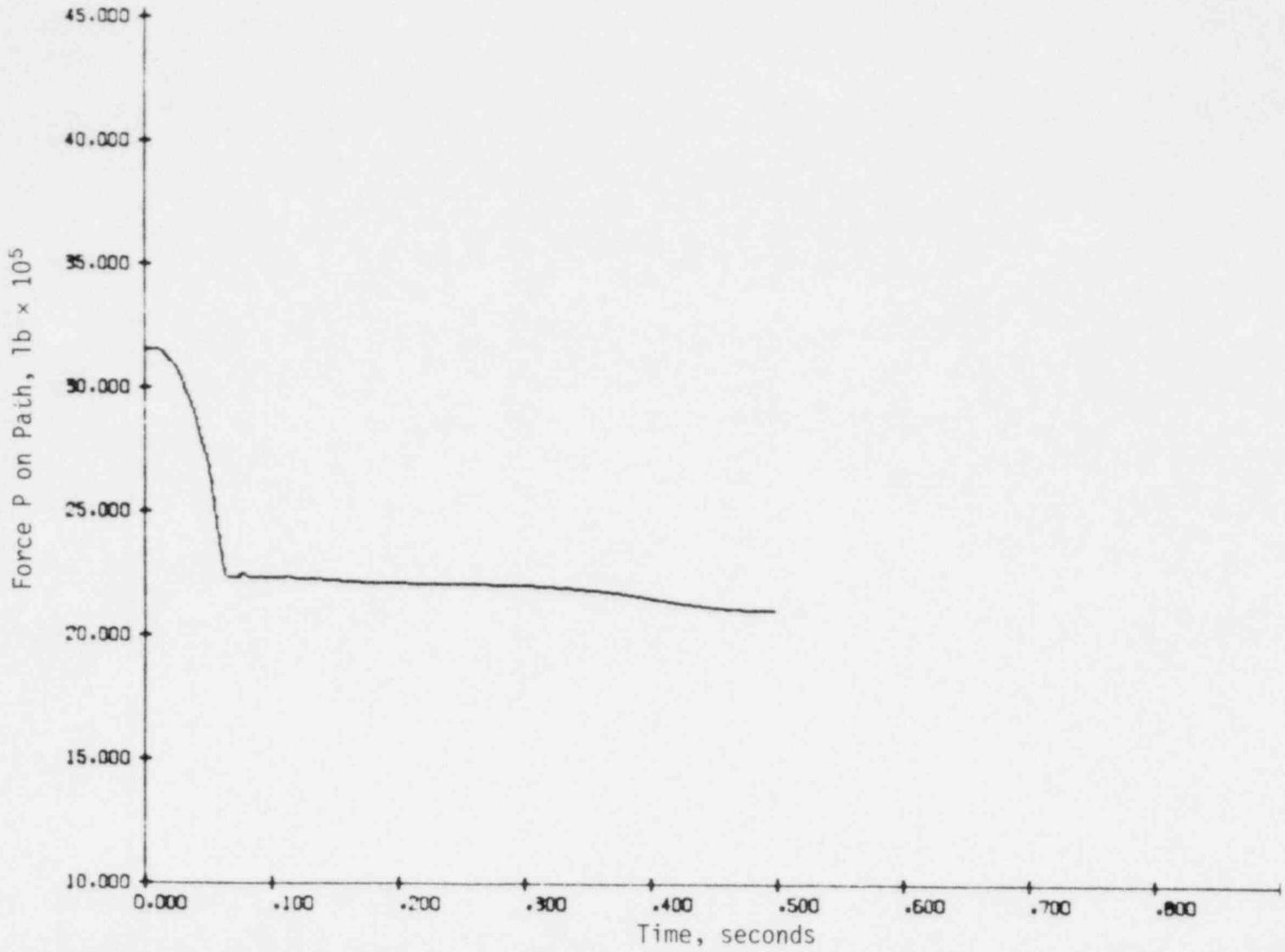

Figure 11.1-7. LCL 1 — Pump Suction Nozzle Guillotine, Path 69

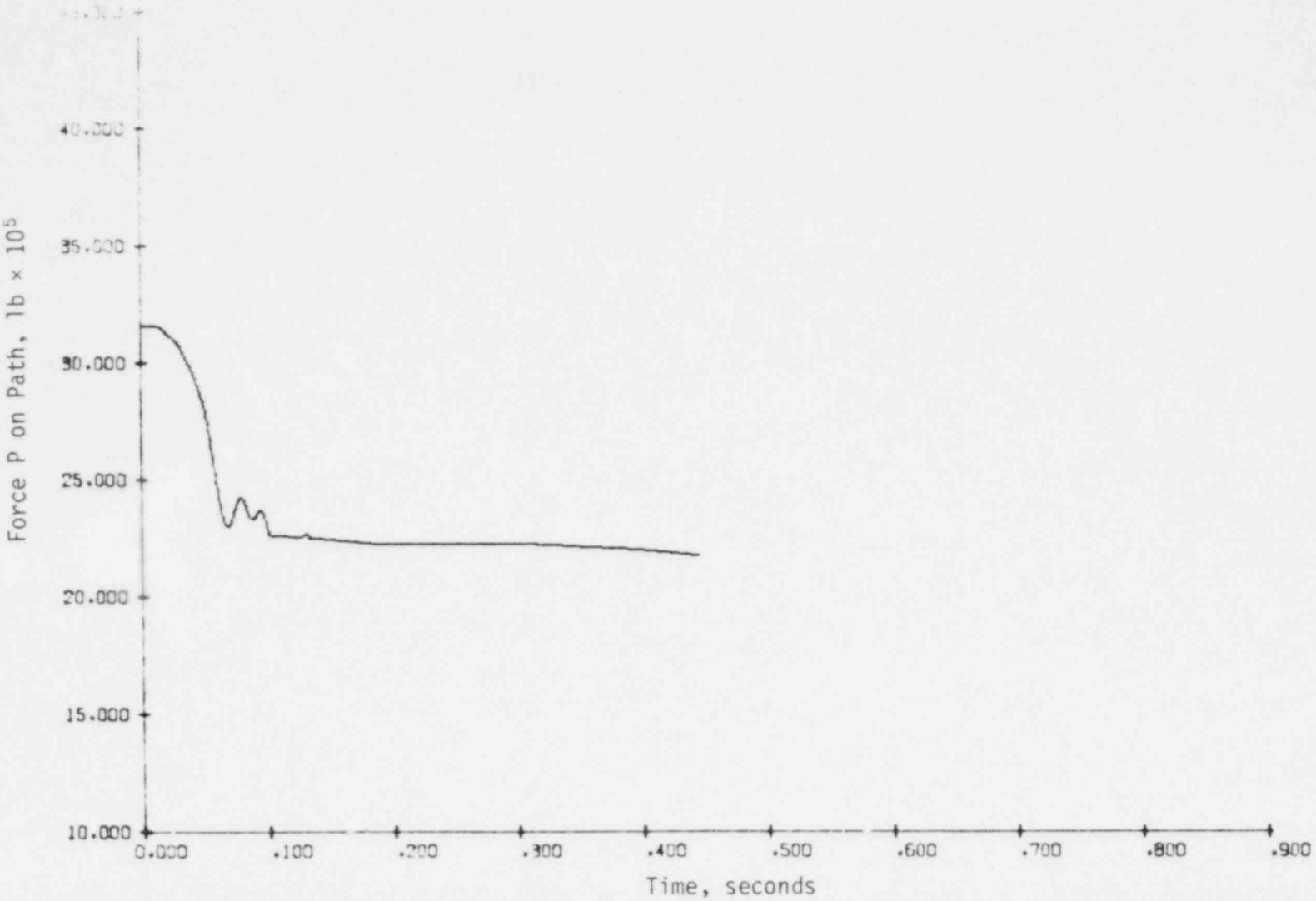

Figure 11.1-8. LCL 5 — OTSG Outlet Nozzle Guillotine, Path 69

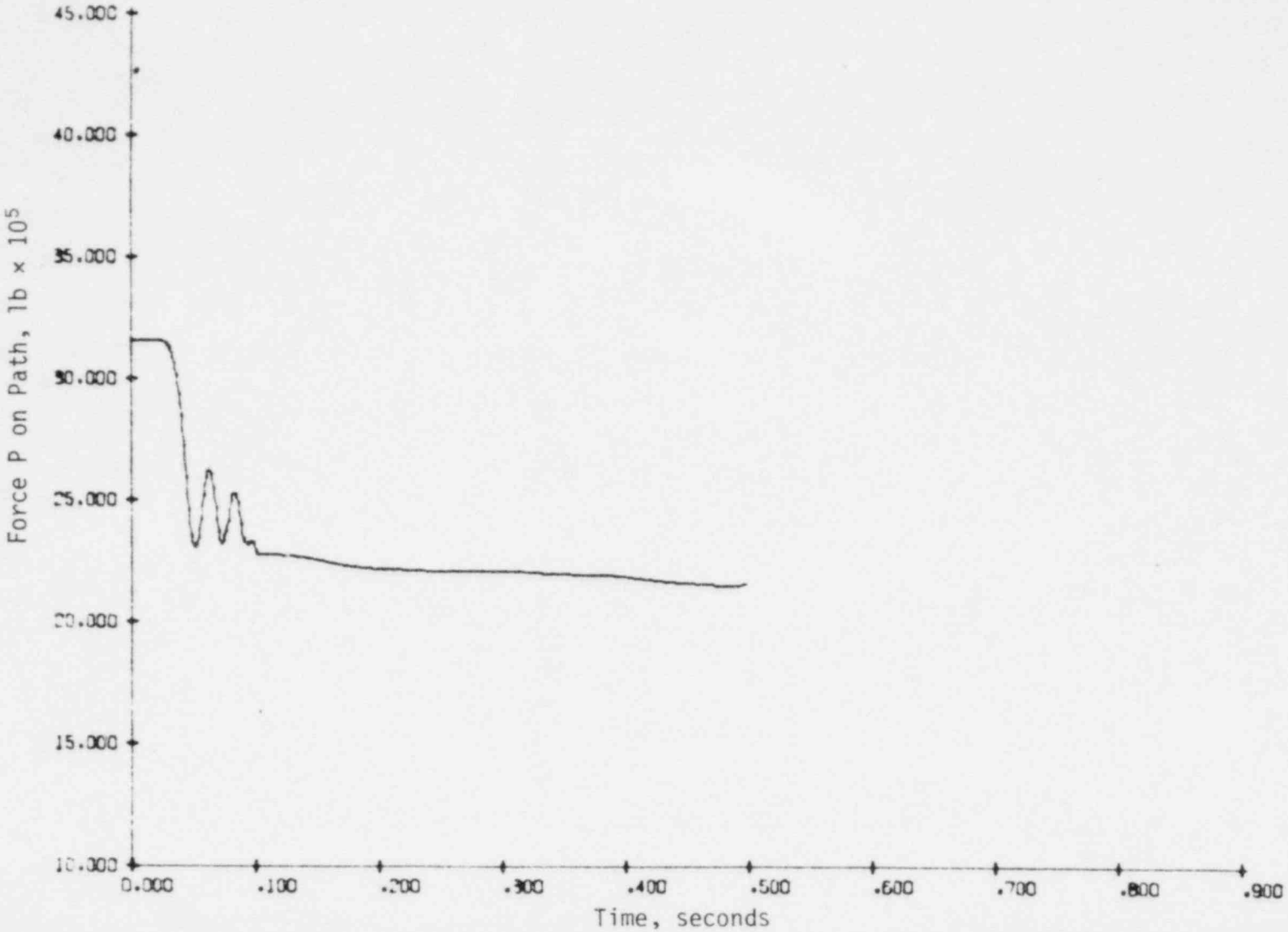

Figure 11.1-9. Component Forces on RC Pump Due to 1A Cold Leg Break at Pump Discharge – Midland 1

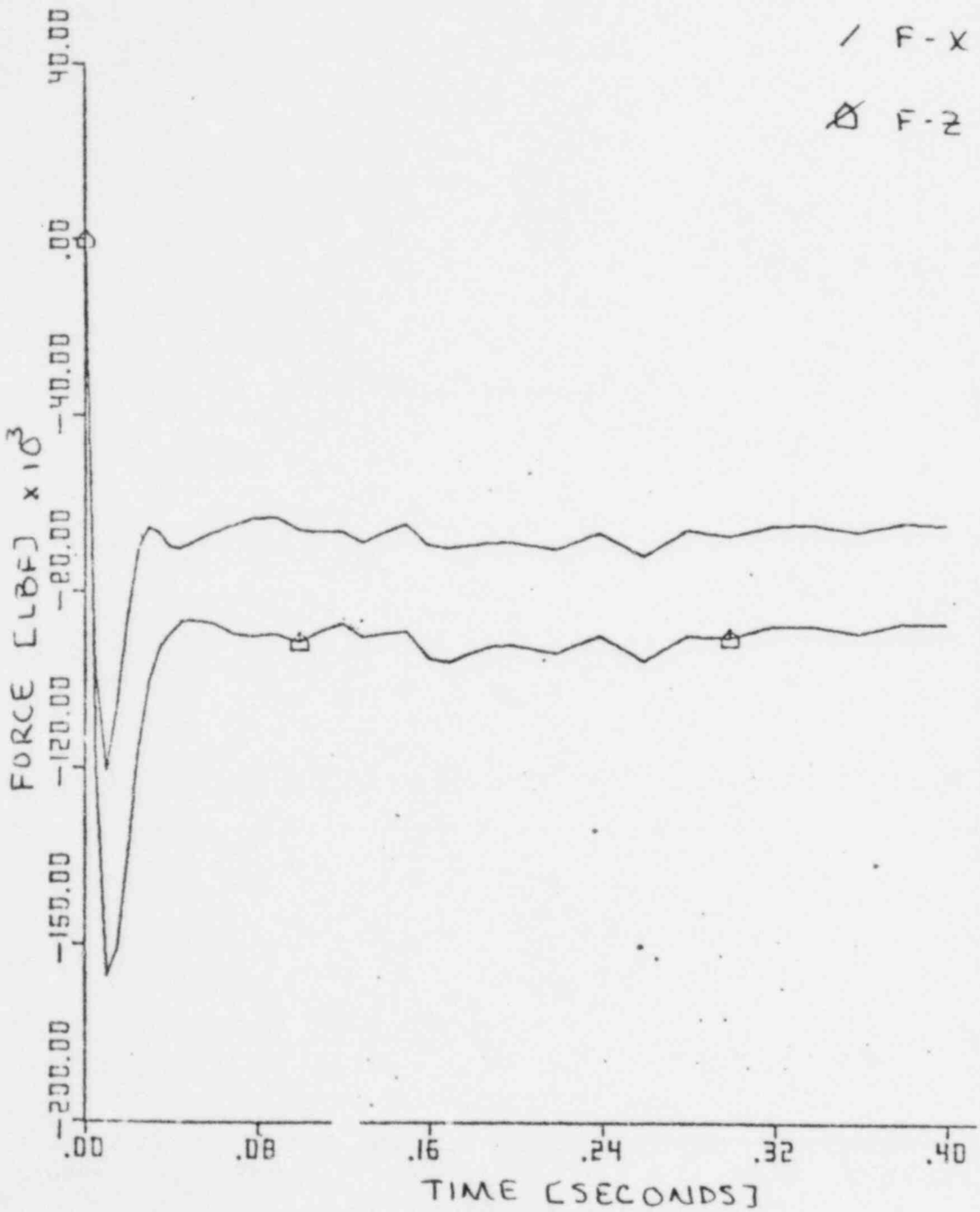

Figure 11.1-10. Vertical Force Acting on RC Pump Due to 1A Cold Leg Break at Pump Discharge – Midland 1

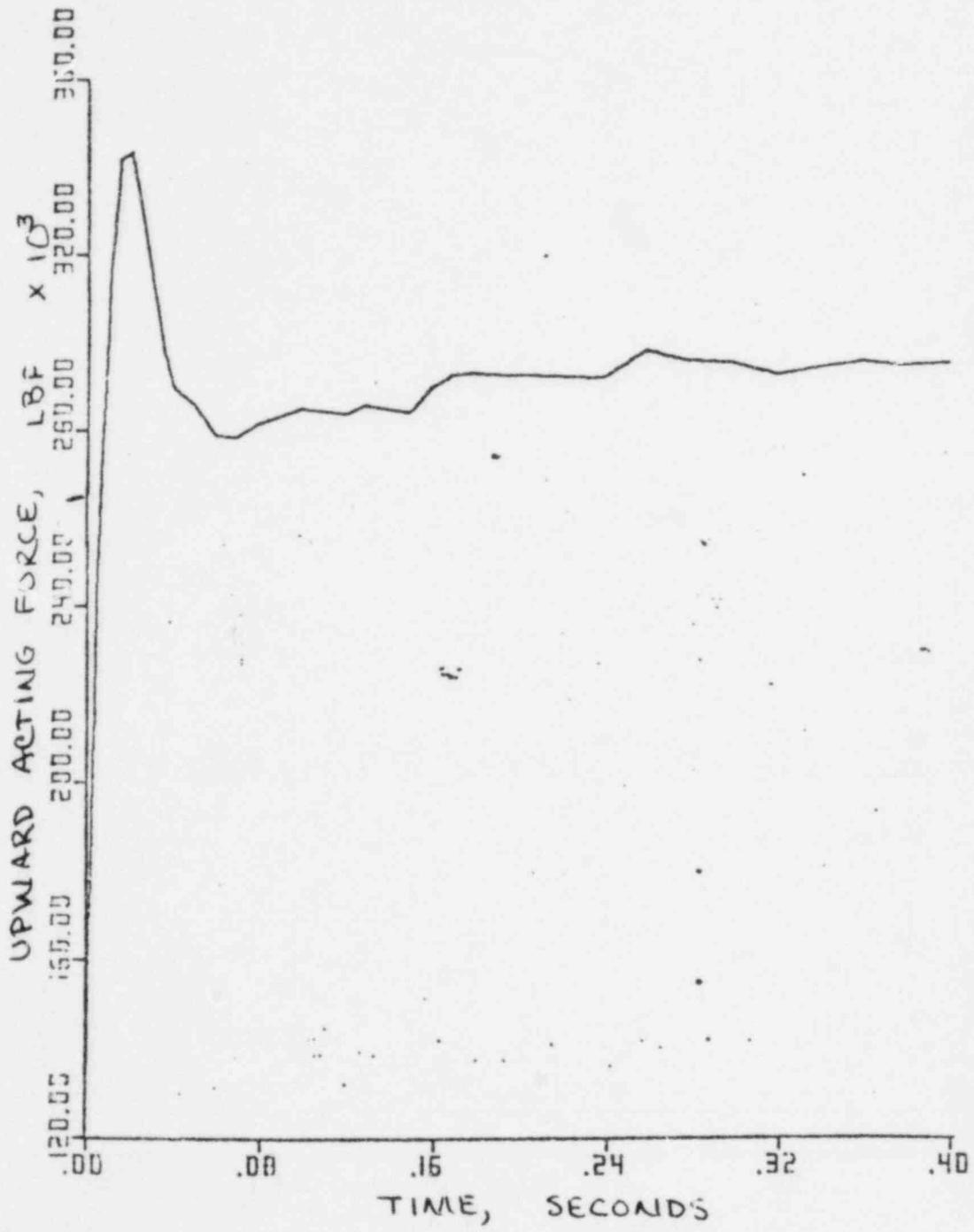

Figure 11.1-11. Component Forces on Steam Generator Due to 1A Cold Leg Break at Pump Discharge — Midland 1

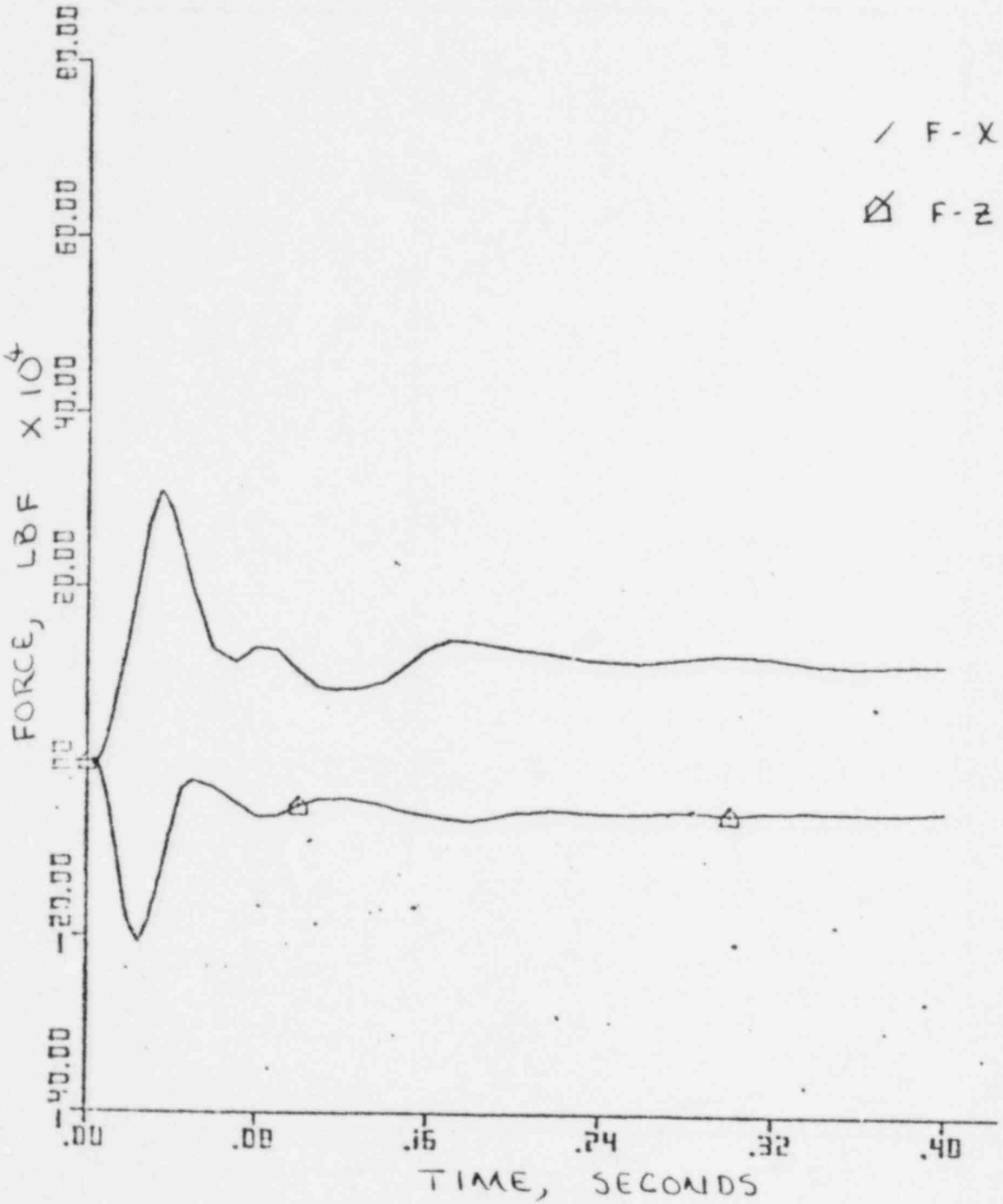

Figure 11.1-12. Forces on Pump Due to 1A Break at Pump Discharge – Davis-Besse 2 and 3

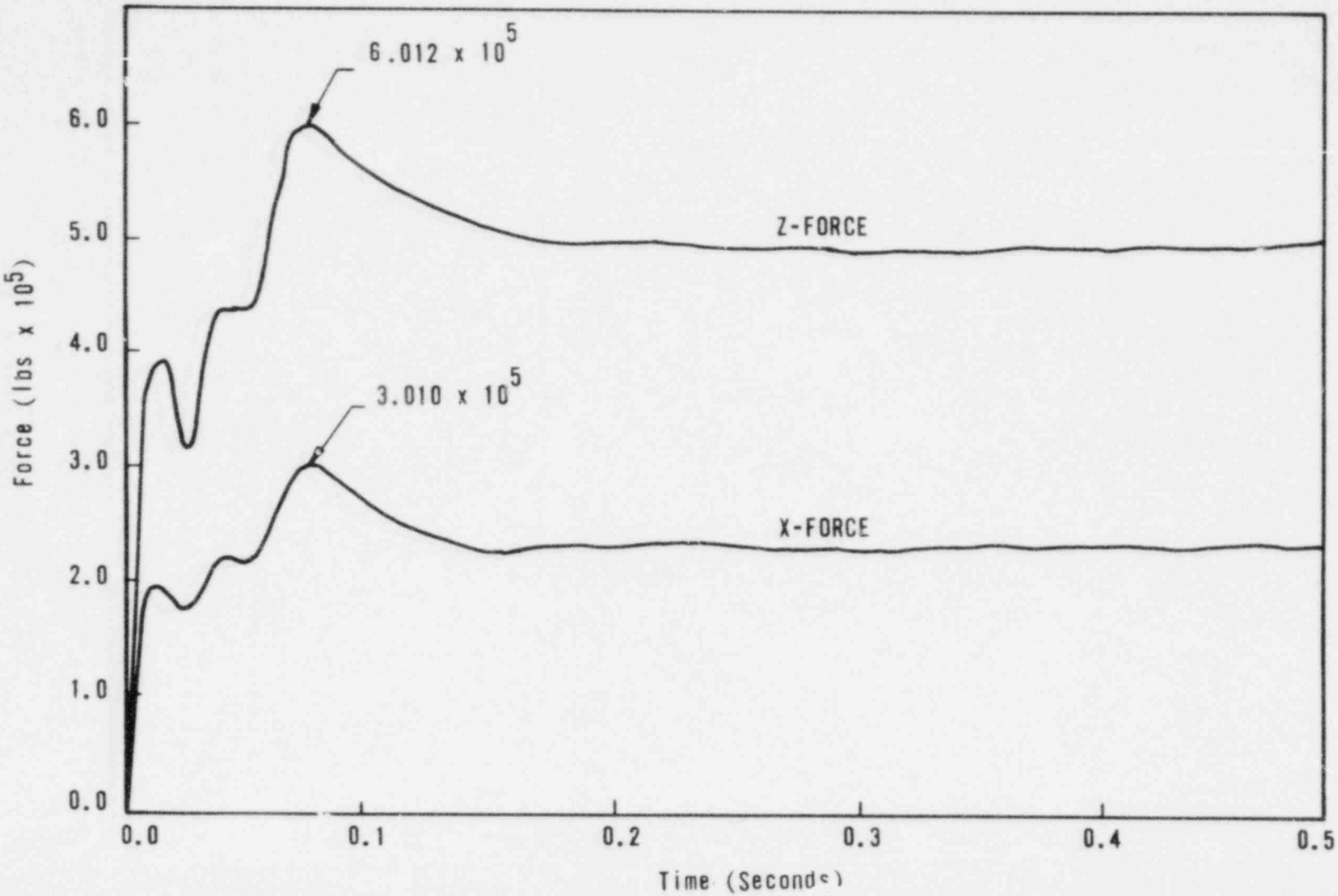

Figure 11.1-13. Uplift Force on Pump Due to 1A Break at Pump Discharge -- Davis-Besse 2 and 3

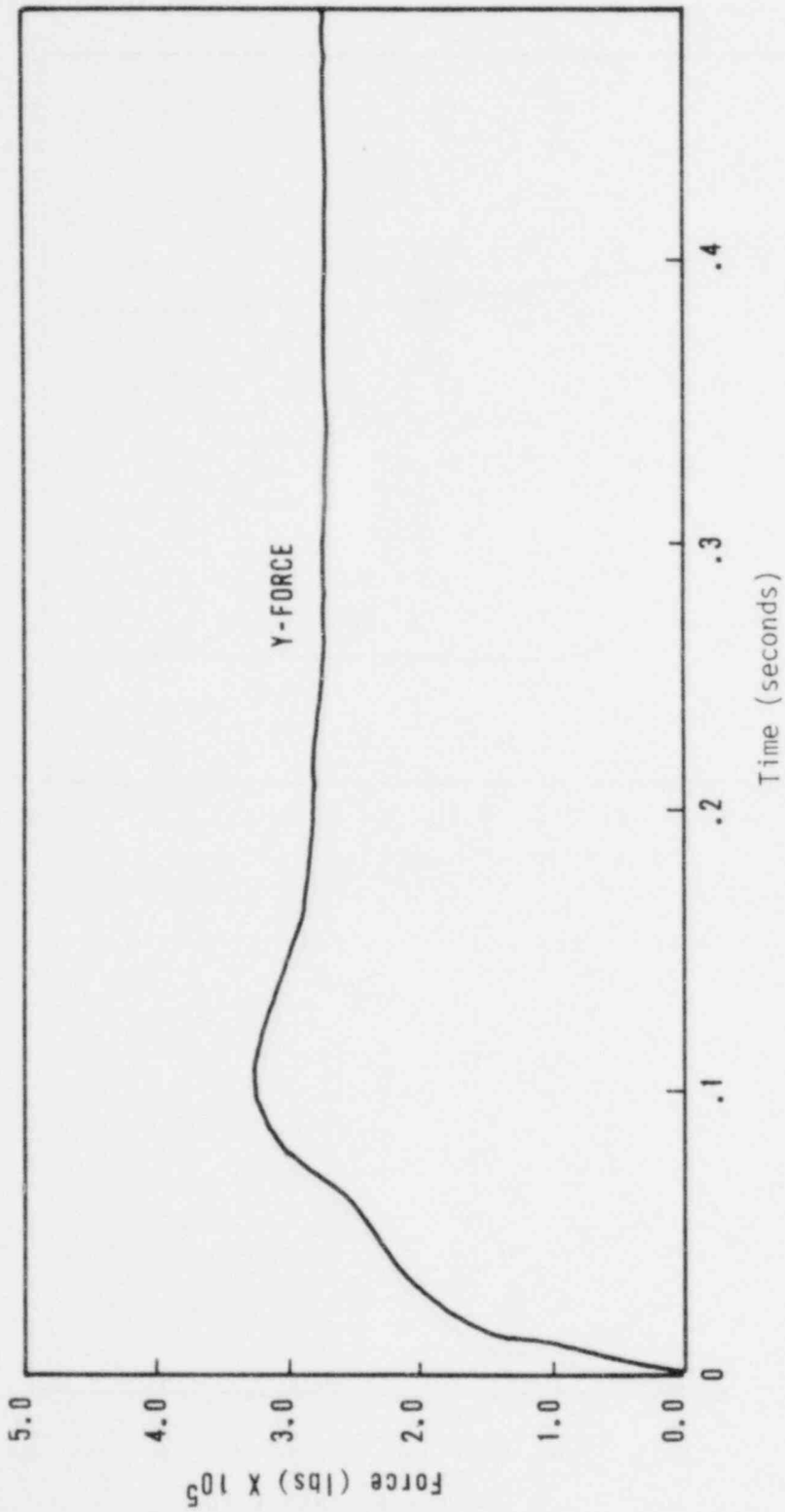

Figure 11.1-14. Forces on Steam Generator Due to 1A Break at Lower End of Hot Leg — Davis Besse 2 and 3

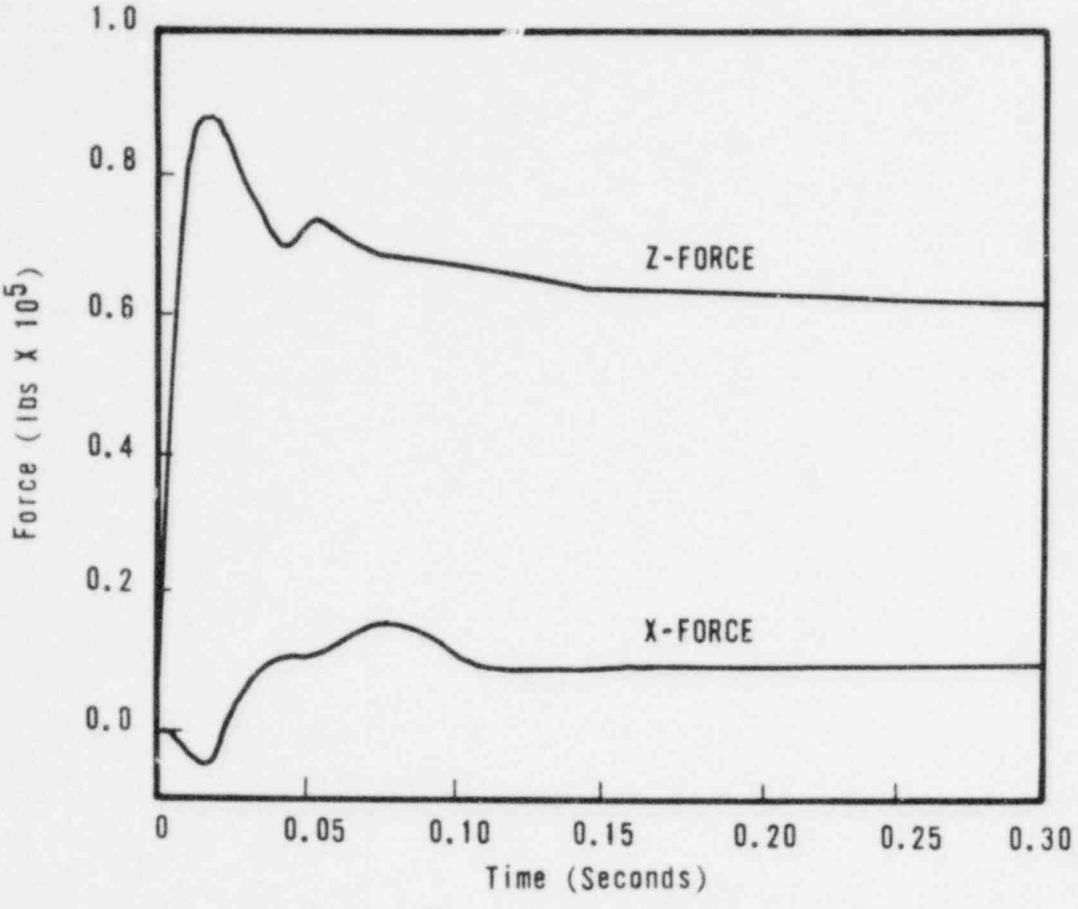

Figure 11.1-15. Duke Power Company, Oconee Plants 1, 2, 3

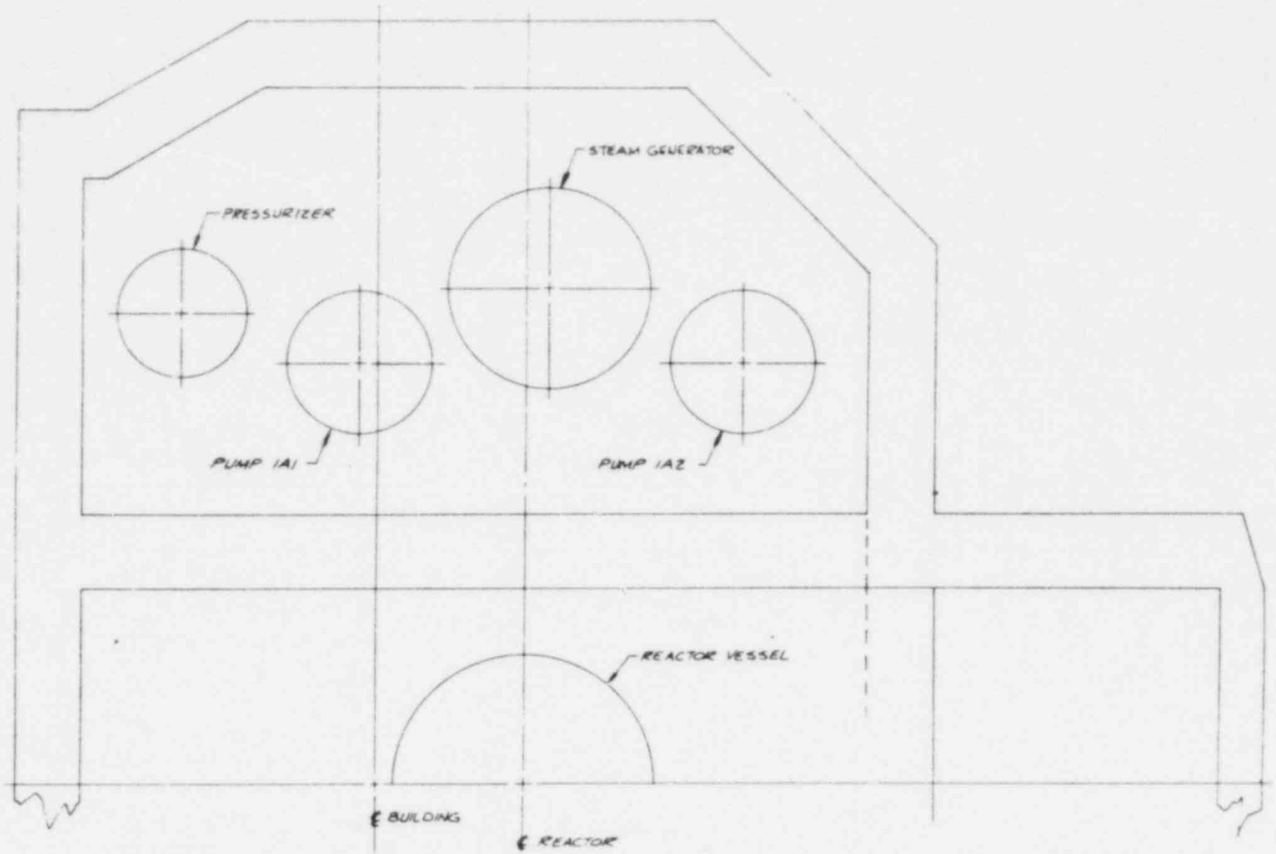

DUKE - OCONEE UNIT 1
PLAN @ EL. 825'-0"
LOOP A
REF DWG NO. O-462

Figure 11.1-16. Davis-Besse 1

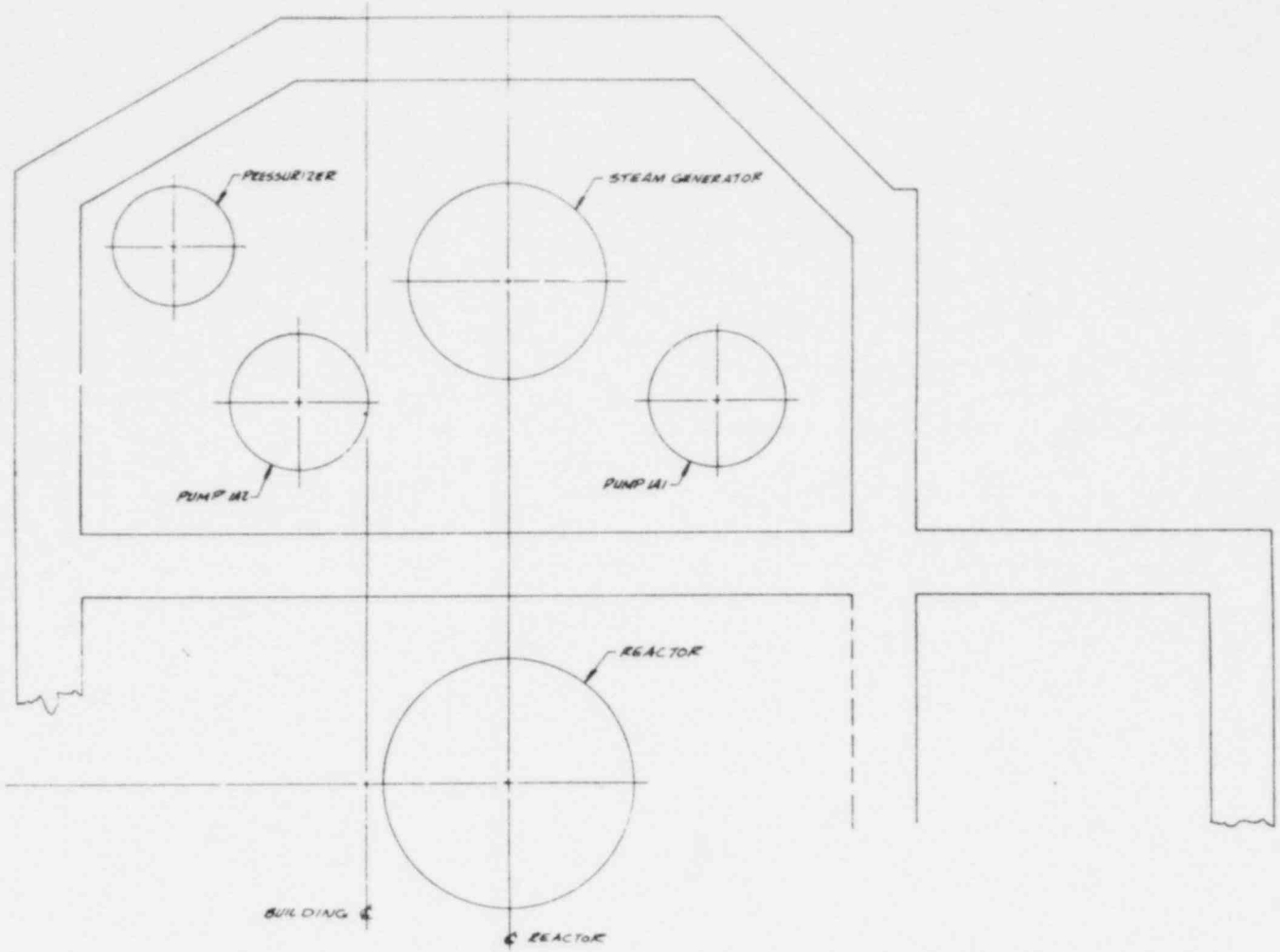

TOLEDO EDISON 1
PLAN @ EL 585'-0"
LOOP A
REF DWG NO M-123

Figure 11.1-17. Arkansas Nuclear One, Unit 1

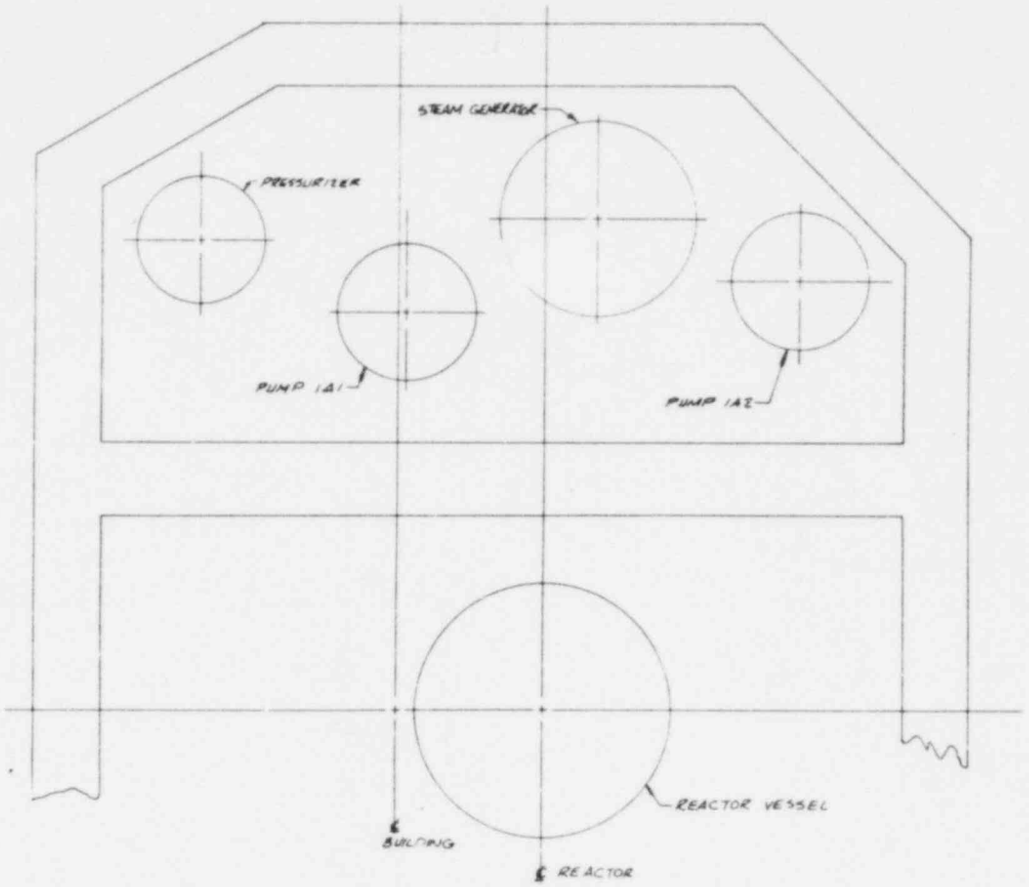

ARKANSAS
PLAN @ EL. 410'-0"
LOOP A
REF DWG NO M-54

Figure 11.1-18. Rancho Seco

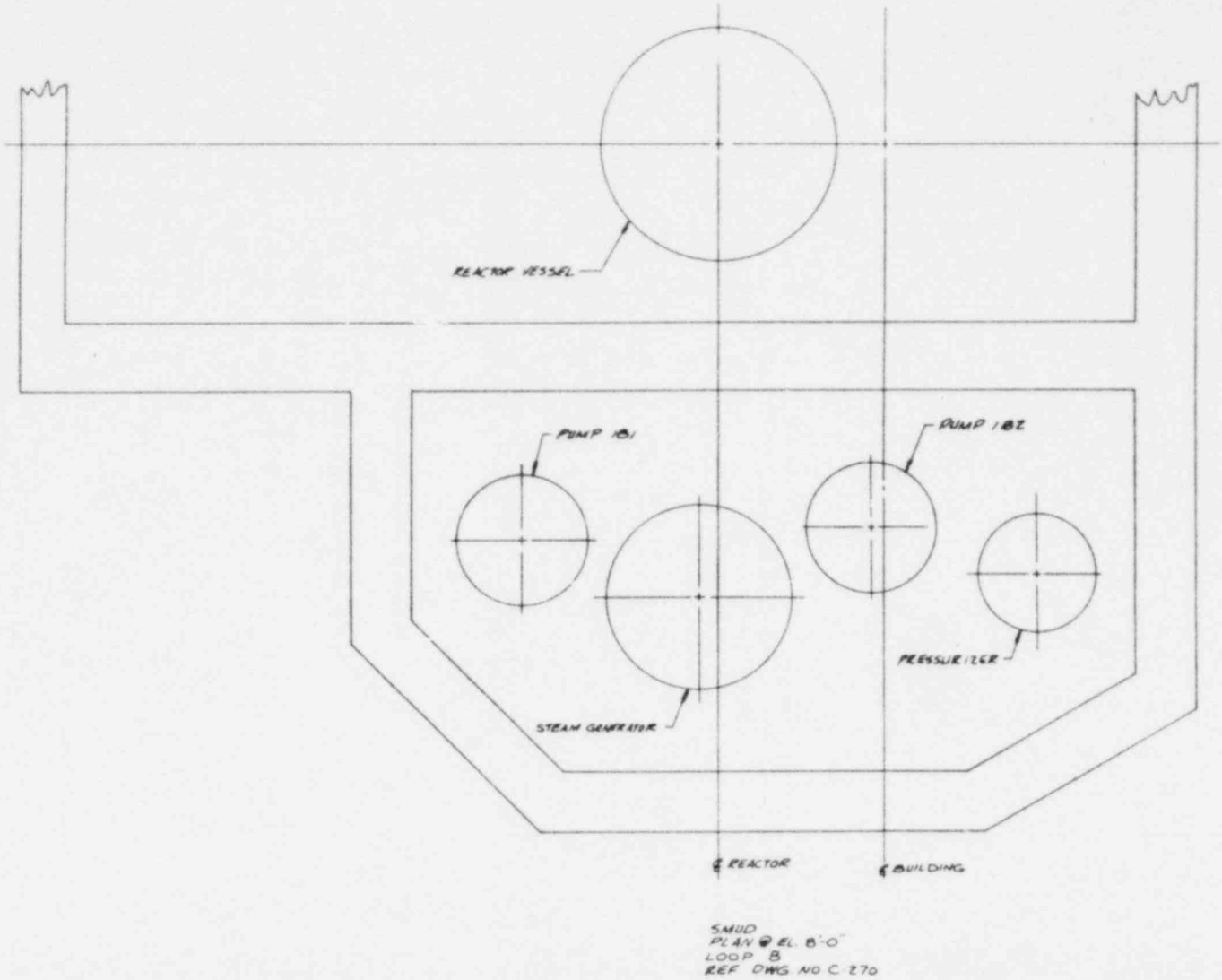

Figure 11.1-19. Crystal River III

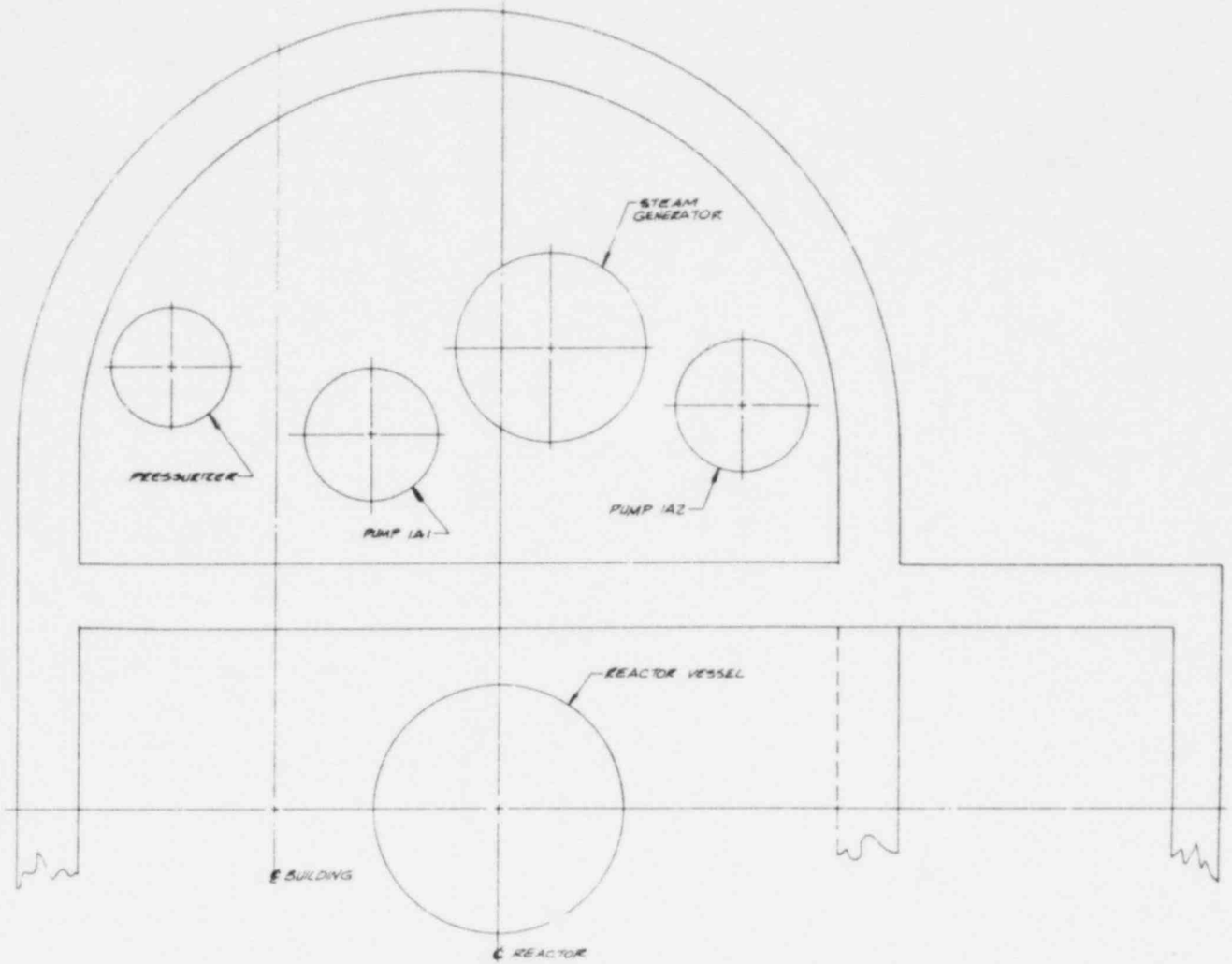

CRYSTAL RIVER
PLAN @ EL 135'-0"
LOOP A
REF DWG NO 5C-42-019

Figure 11.1-20. Three Mile Island Unit 1

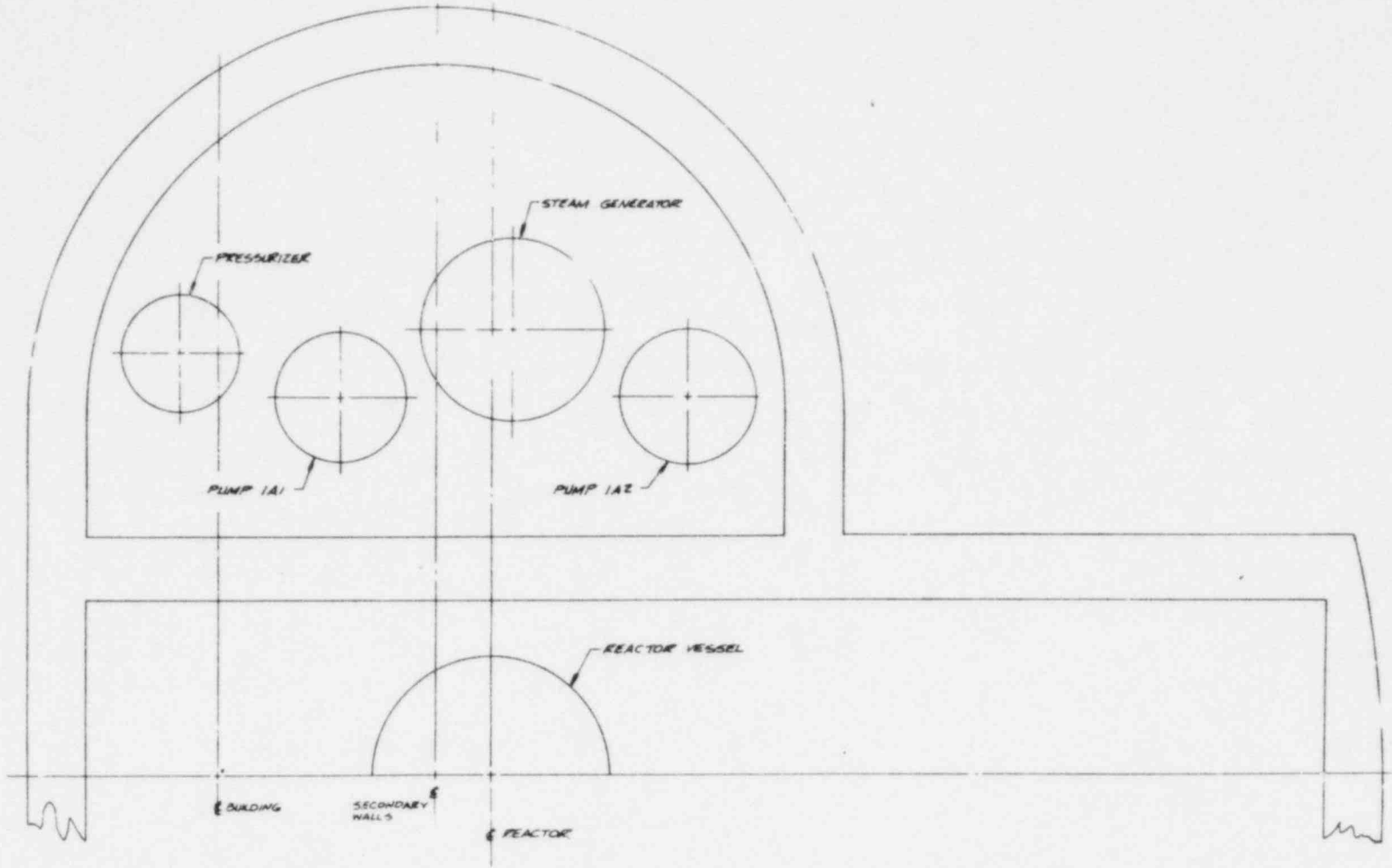

T-M I - I
PLAN @ EL 326'-0"
LOOP A
REF DWG NO E-521-000 & E-421-027

Figure 11.1-21. A1 Suction Nozzle (Unbroken Side), Skirt-Supported Plant

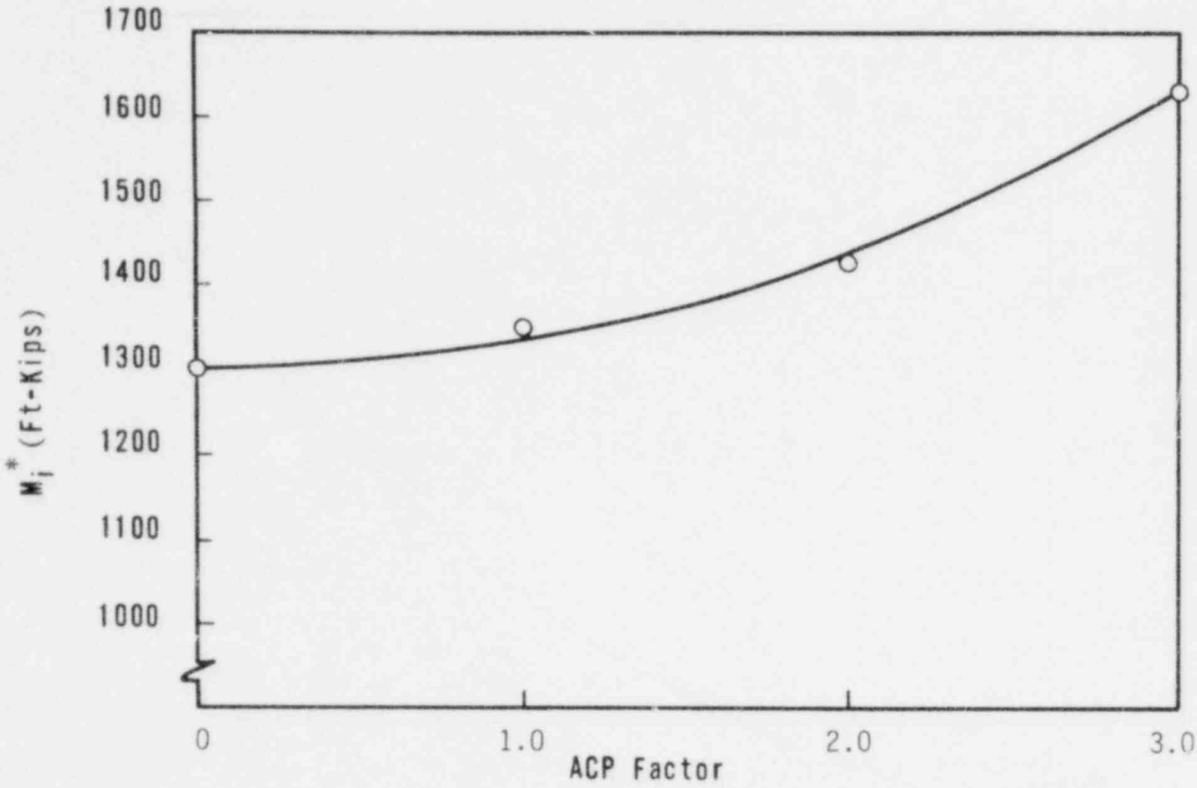

$$*M_i = (M_x^2 + M_y^2 + M_z^2)^{1/2}$$

Figure 11.1-22. A1 Suction Nozzle (Unbroken Side), Nozzle-Supported Plant

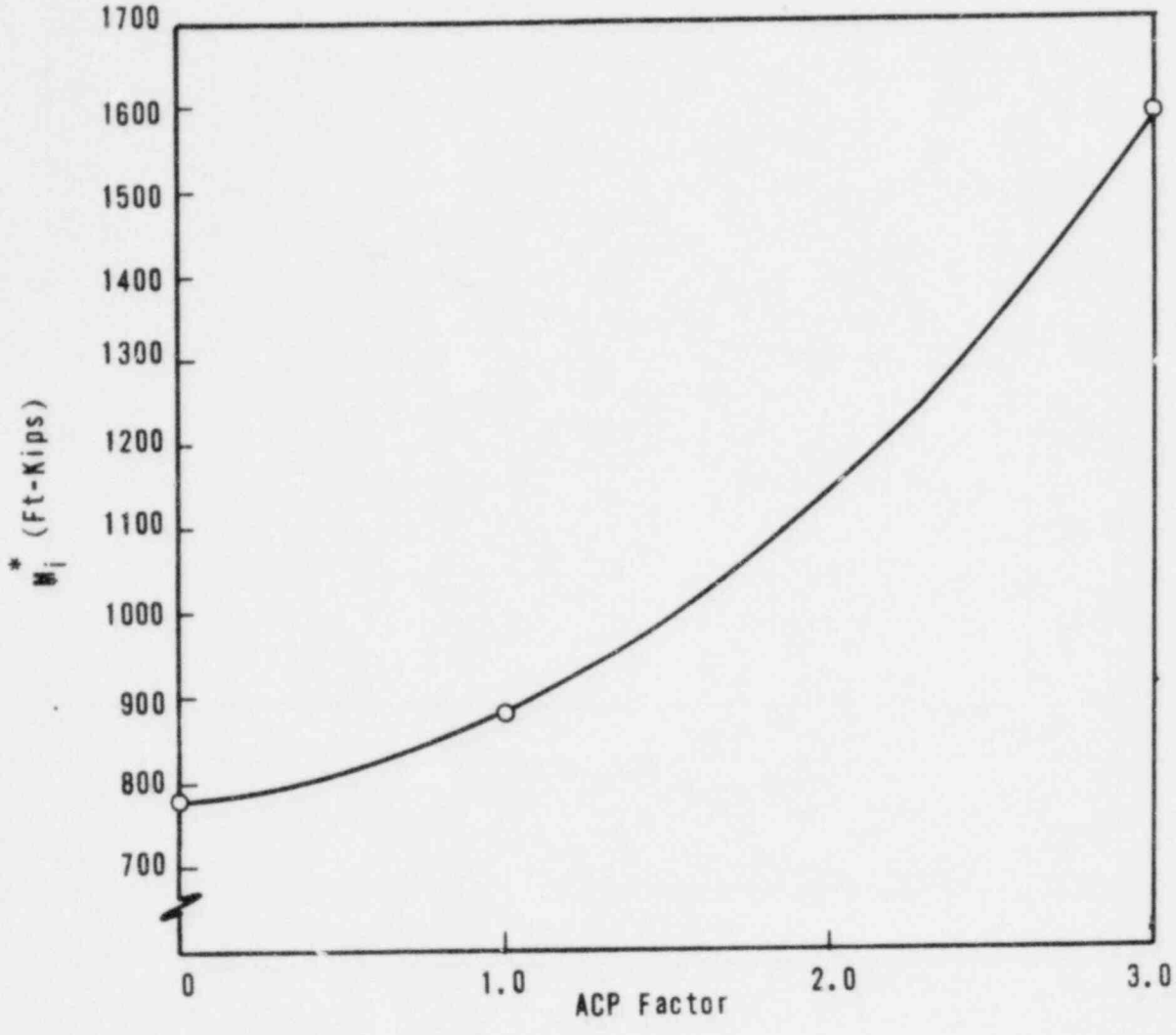

$$*M_i = (M_x^2 + M_y^2 + M_z^2)^{1/2}$$

Figure 11.1-23. OTSG Upper Horizontal Support, Nozzle-Supported Plant

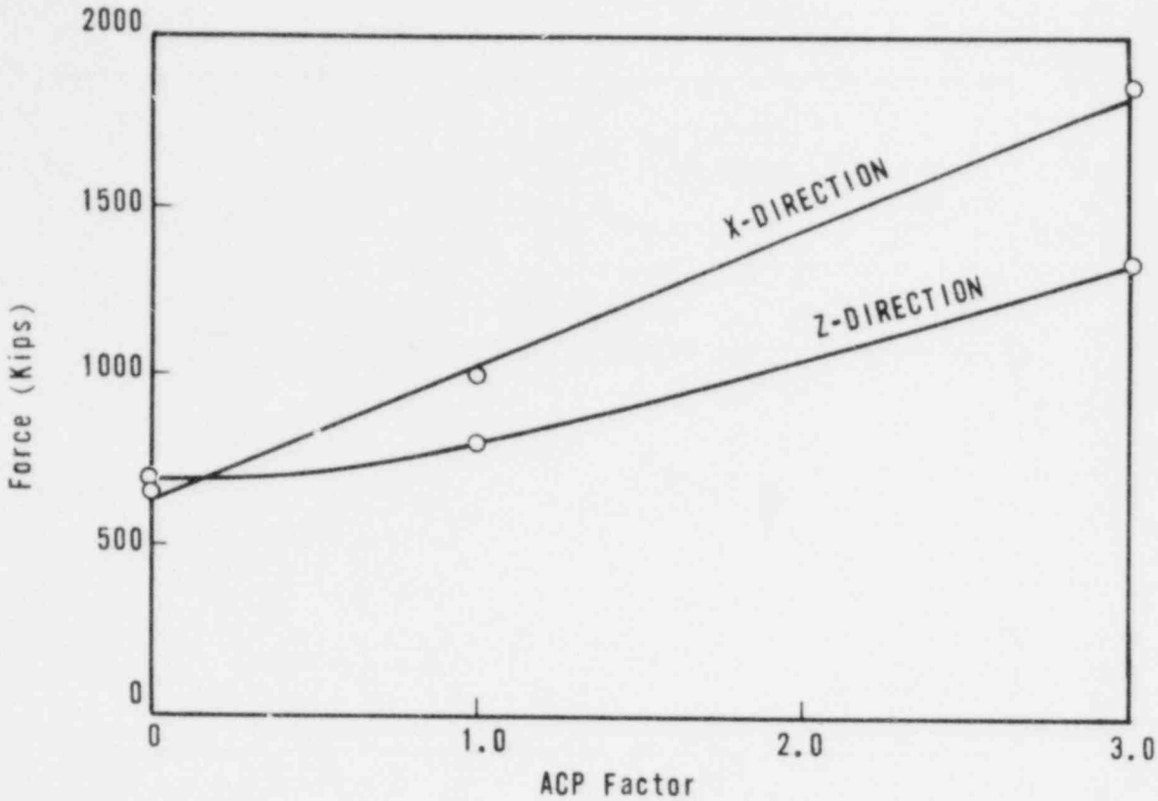

Figure 11.1-24. OTSG Upper Horizontal Support, Skirt-Supported Plant

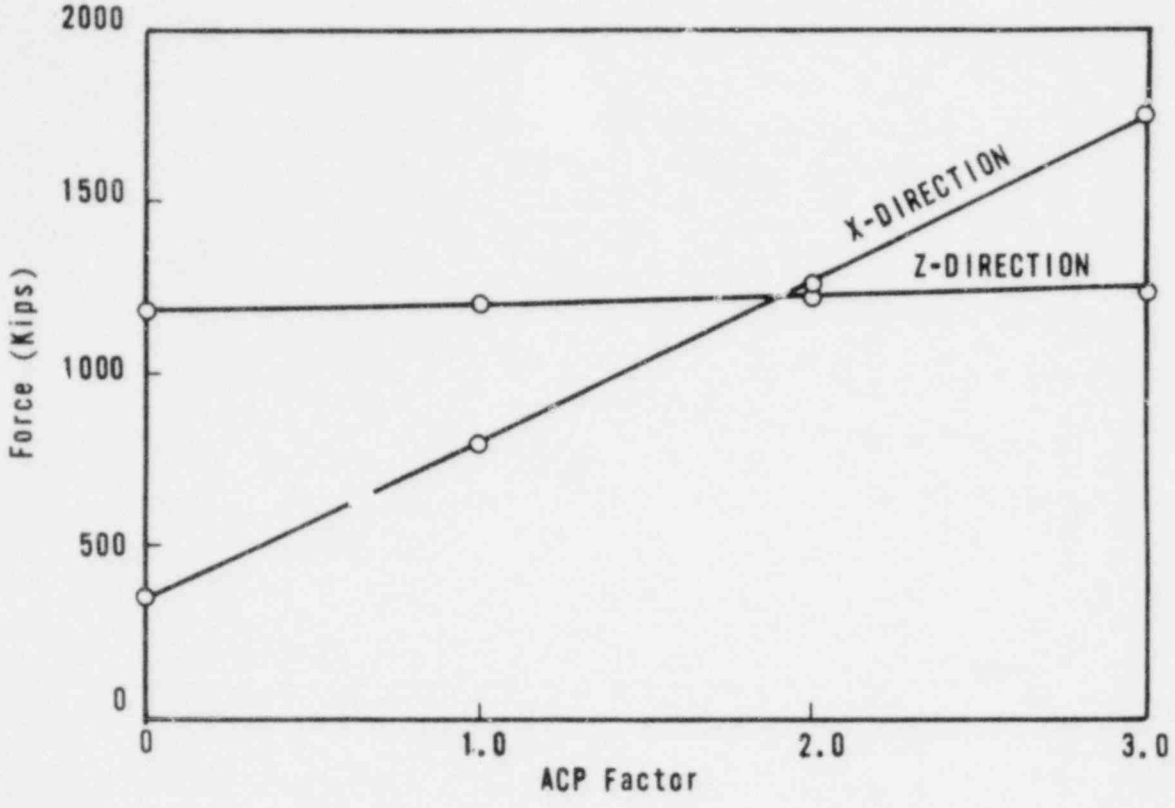

Figure 11.1-25. Skirt-Supported Plant, Elevation View (Supported Pump)

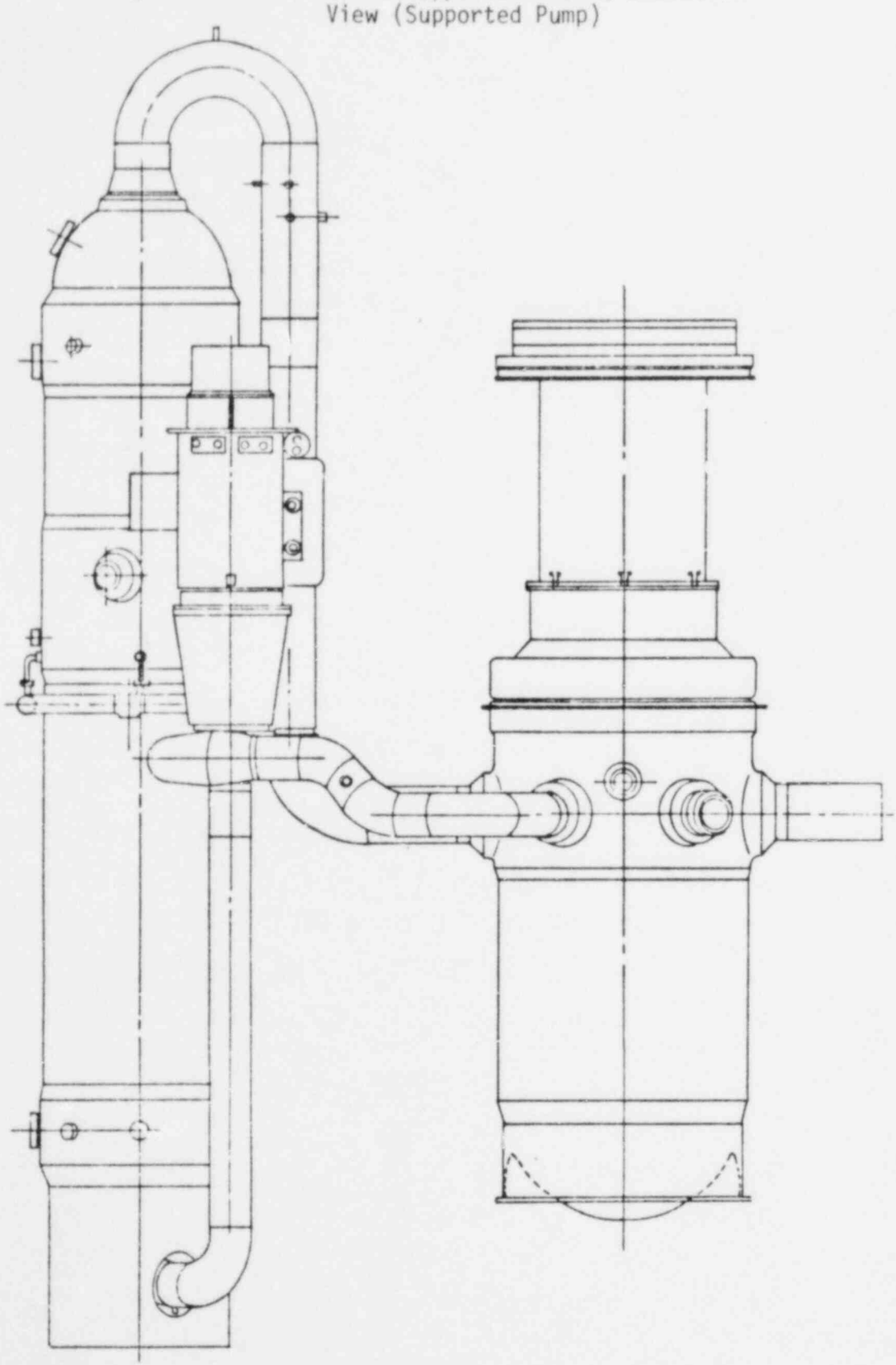

Figure 11.1-26. Skirt-Supported Plant, Plan View (Supported Pump)

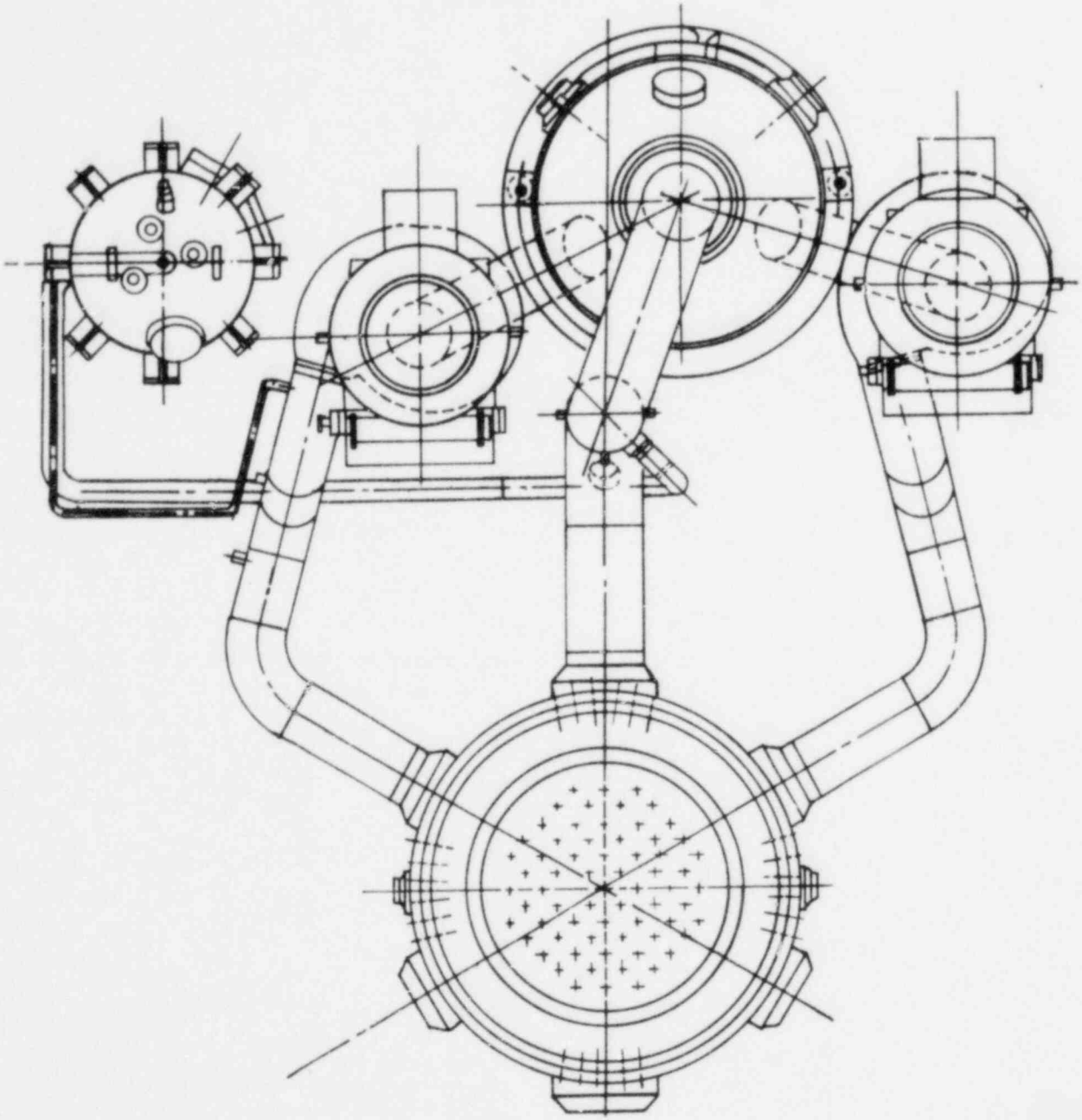

Figure 11.1-27. Skirt-Supported Plant, Elevation View (Unsupported Pump)

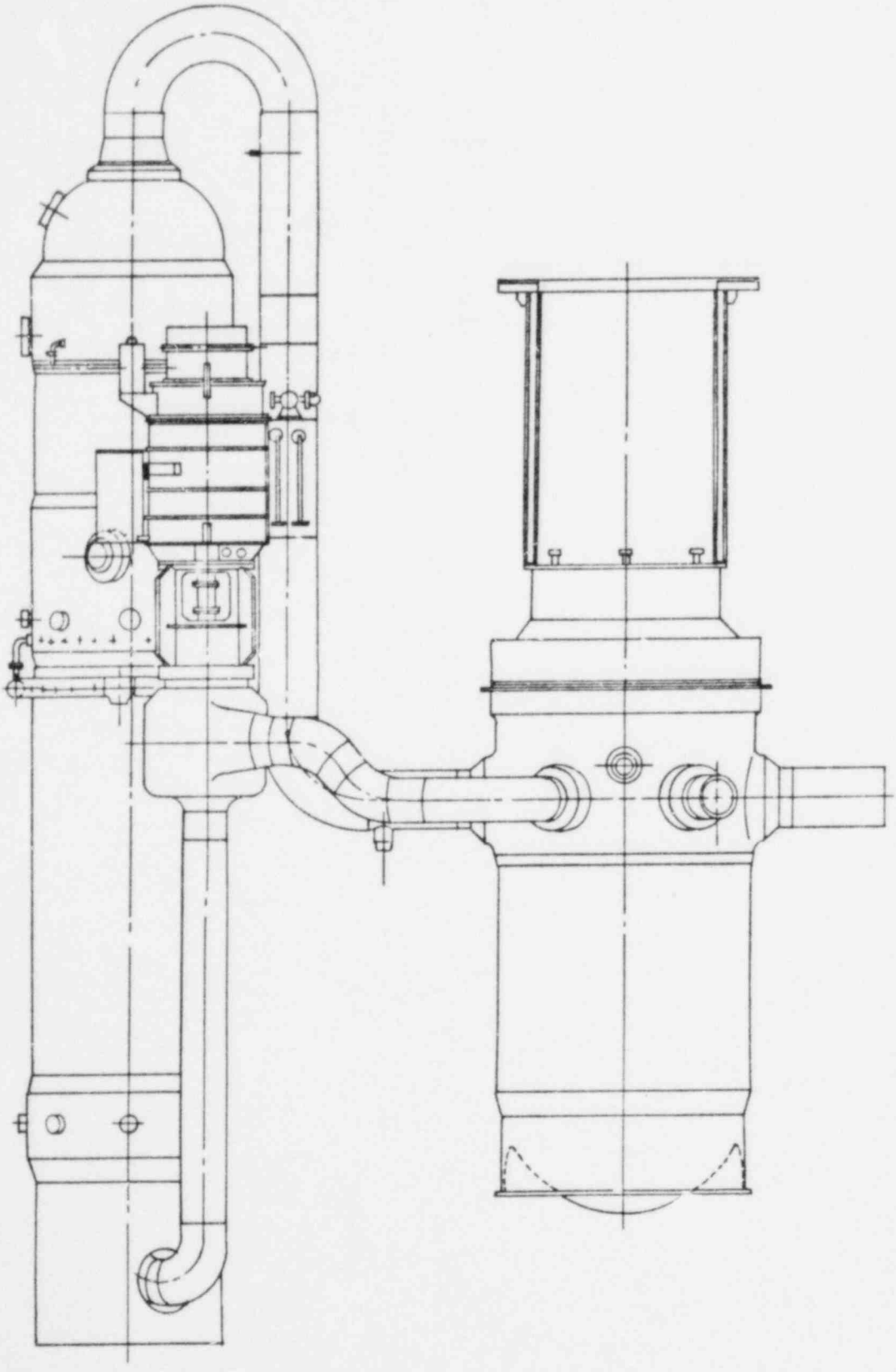

Figure 11.1-28. Skirt-Supported Plant, Plan View (Unsupported Pump)

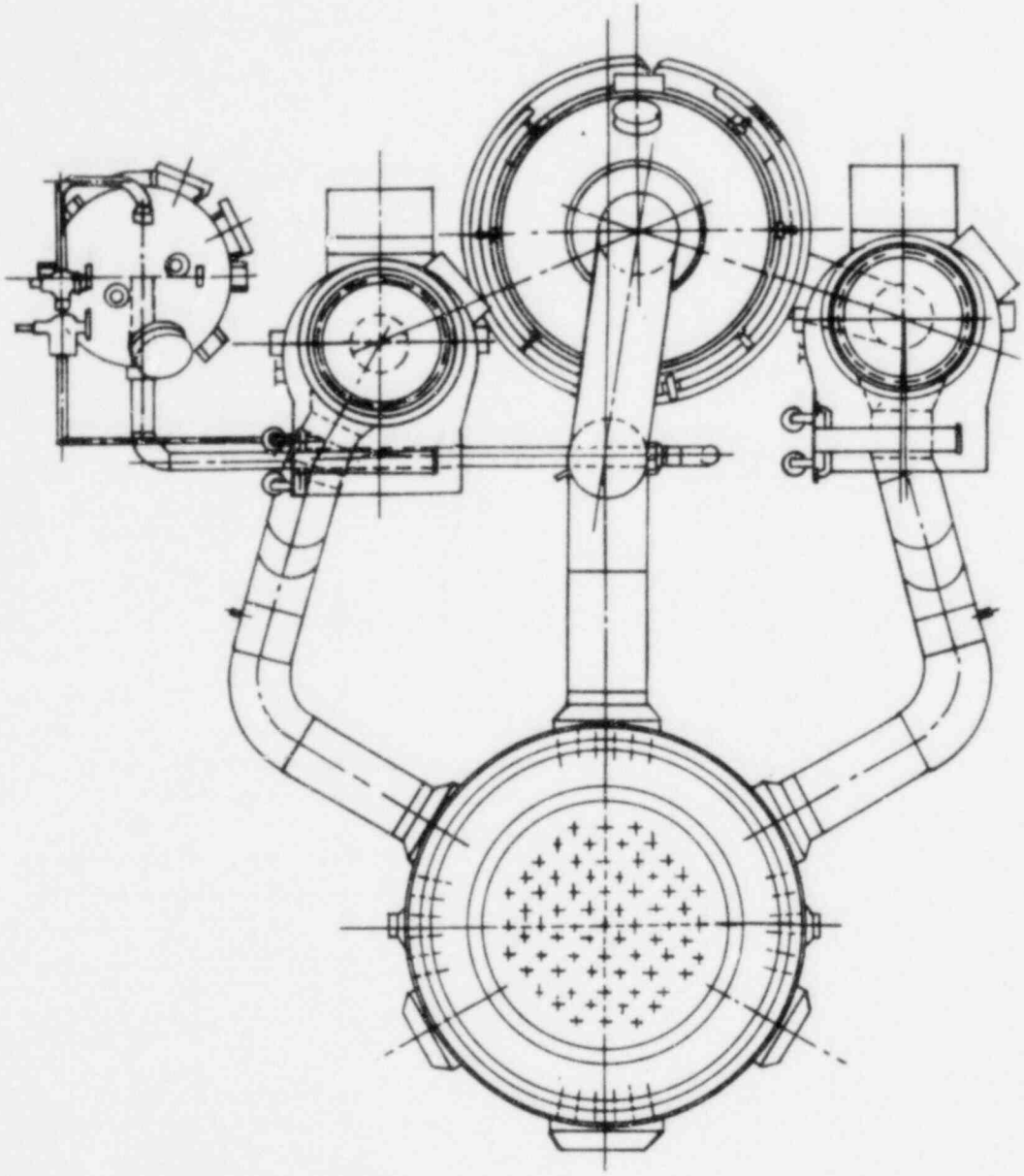

Figure 11.1-29. Nozzle-Supported Plant, Elevation View

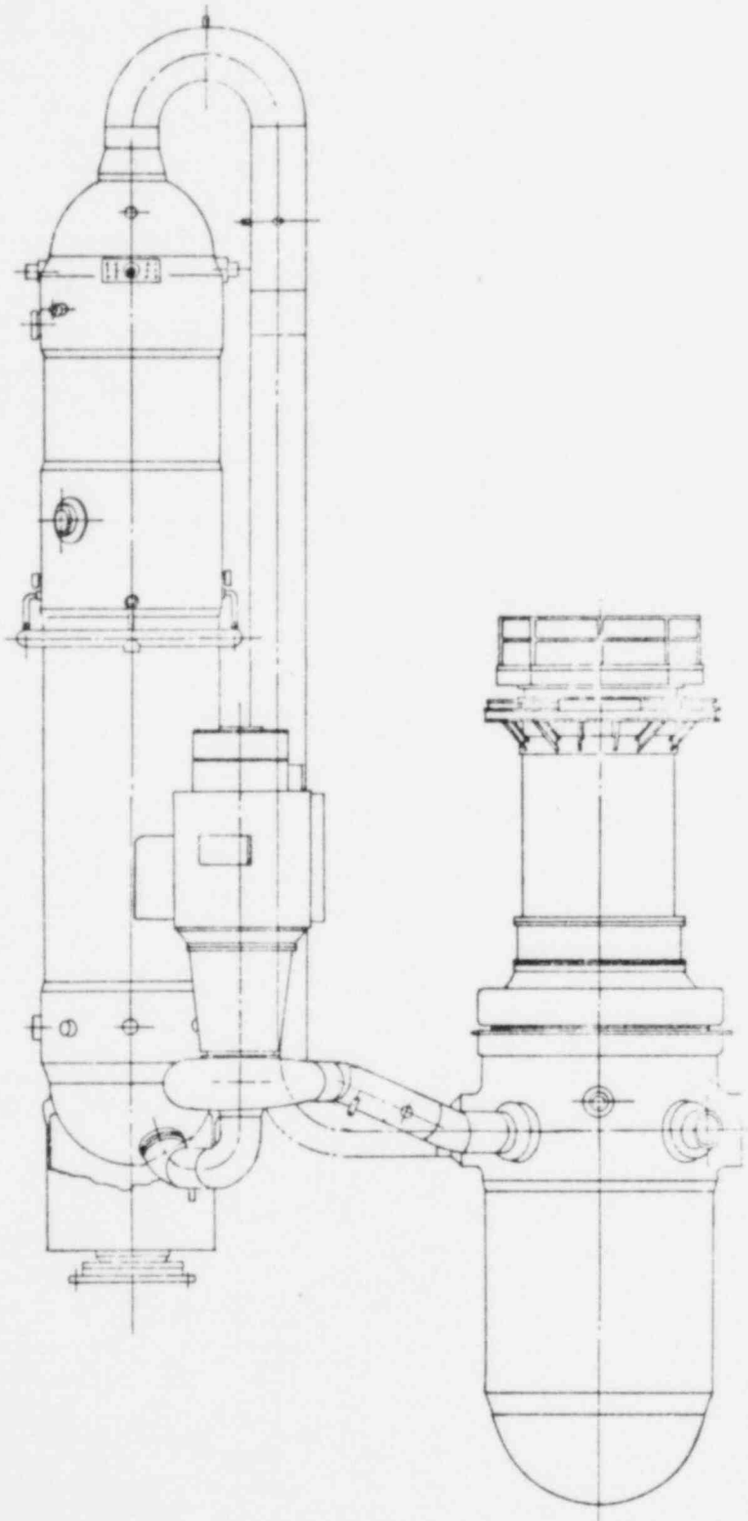

Figure 11.1-30. Nozzle-Supported Plant, Plan View

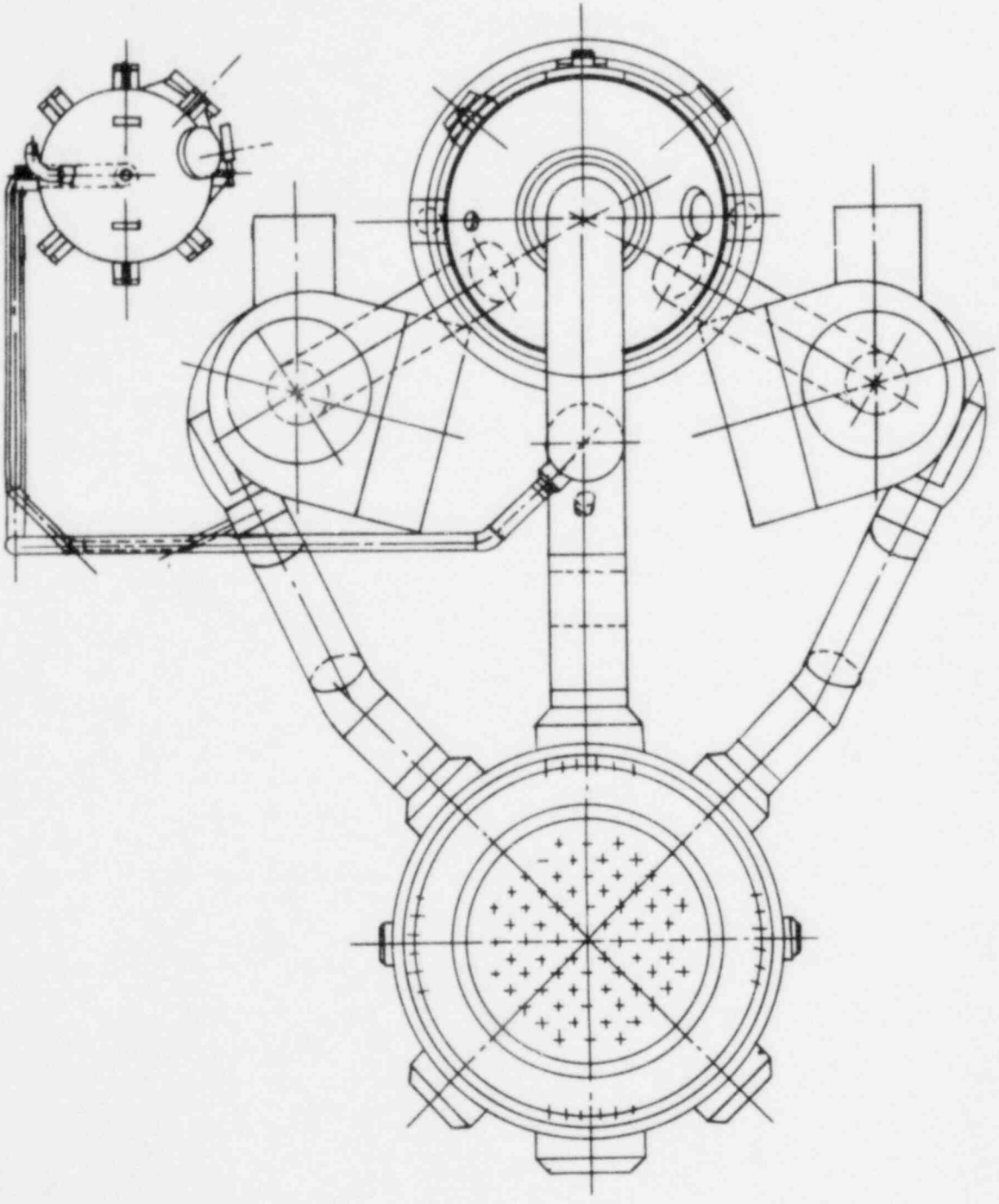

Figure 11.1-31. Steam Generator Base – Skirt-Supported Plant (Supported Pump)

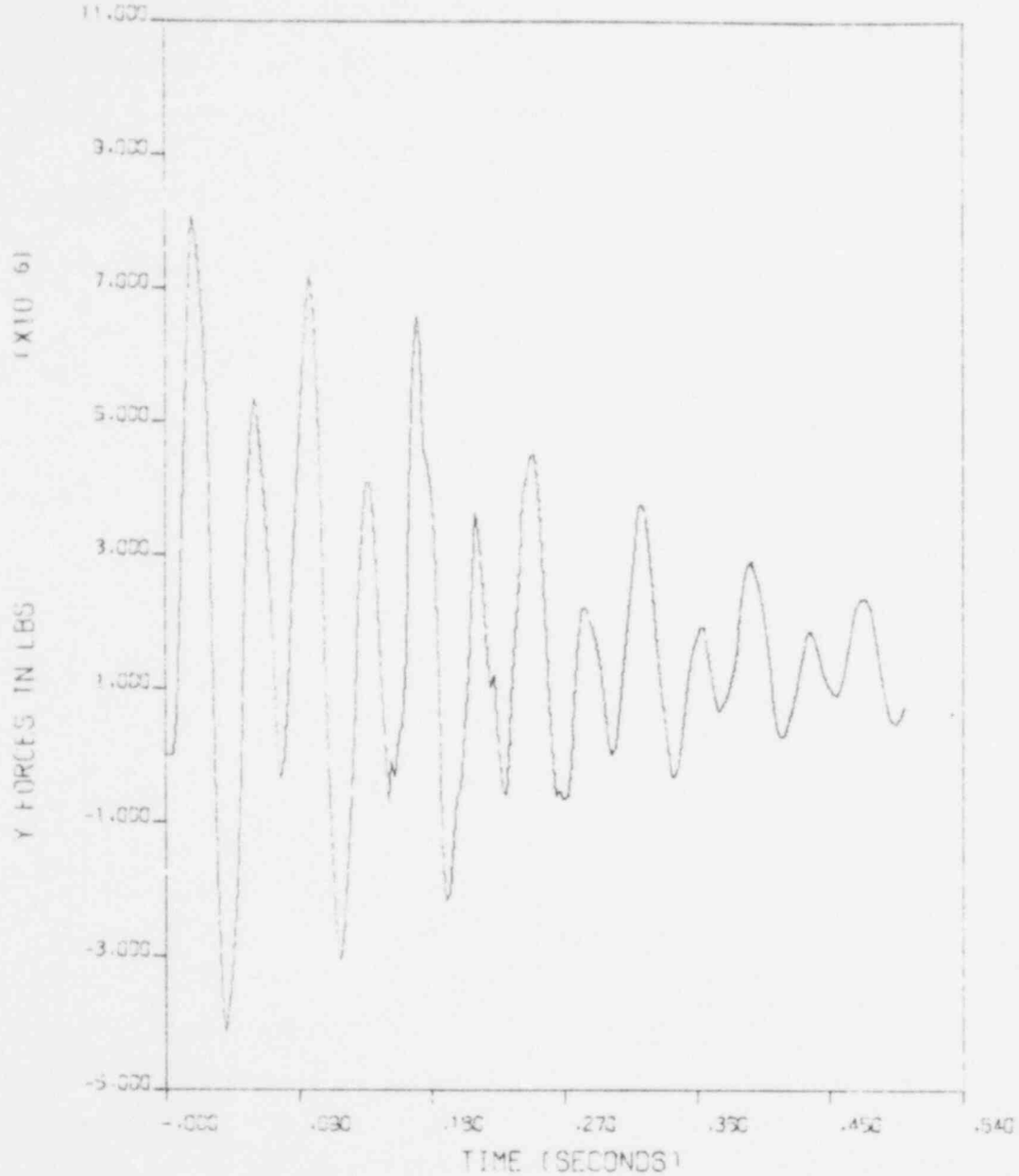

Figure 11.1-32. Steam Generator Base – Skirt-Supported Plant (Unsupported Pump)

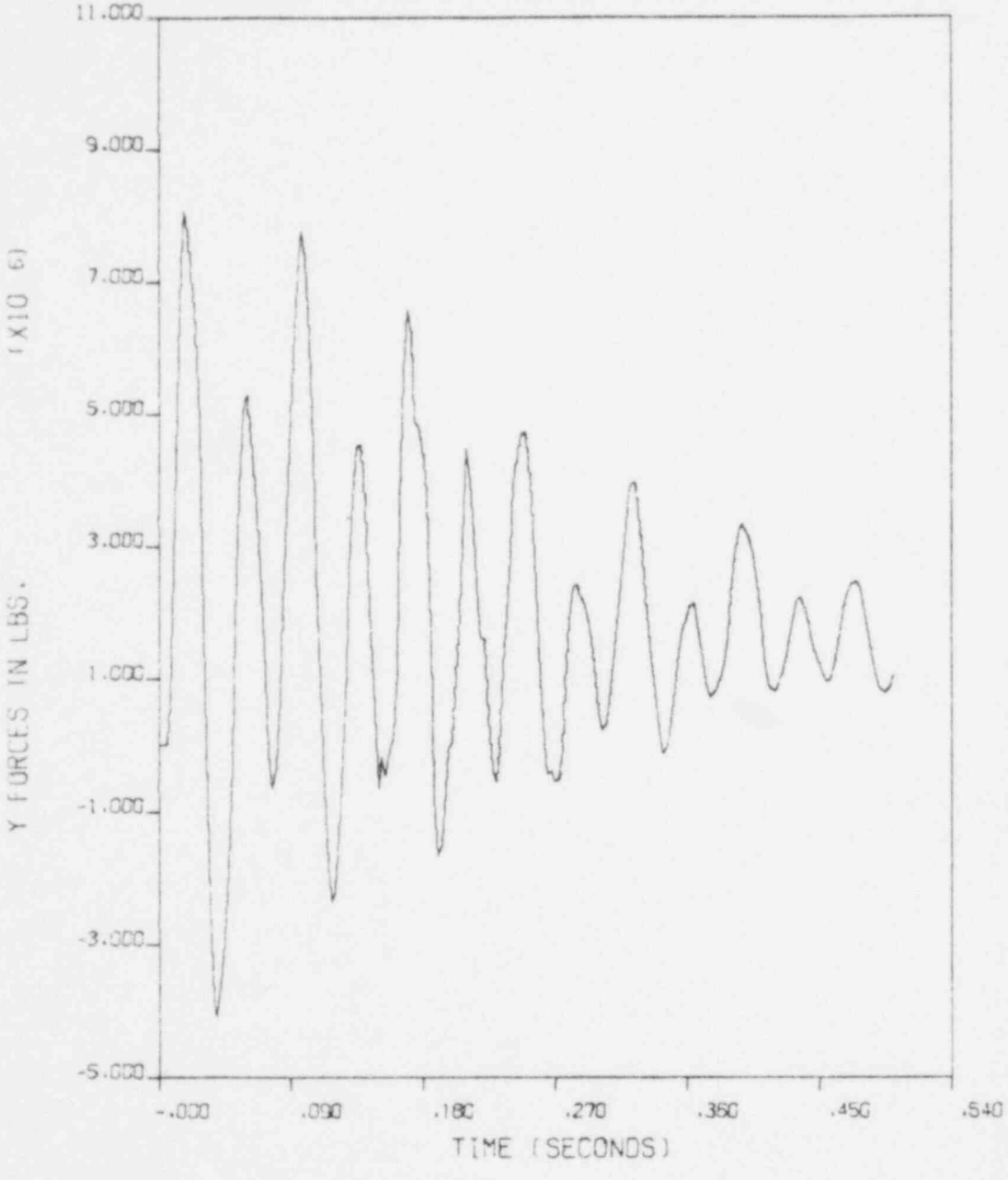

Figure 11.1-33. Steam Generator Base — Nozzle-Supported Plant

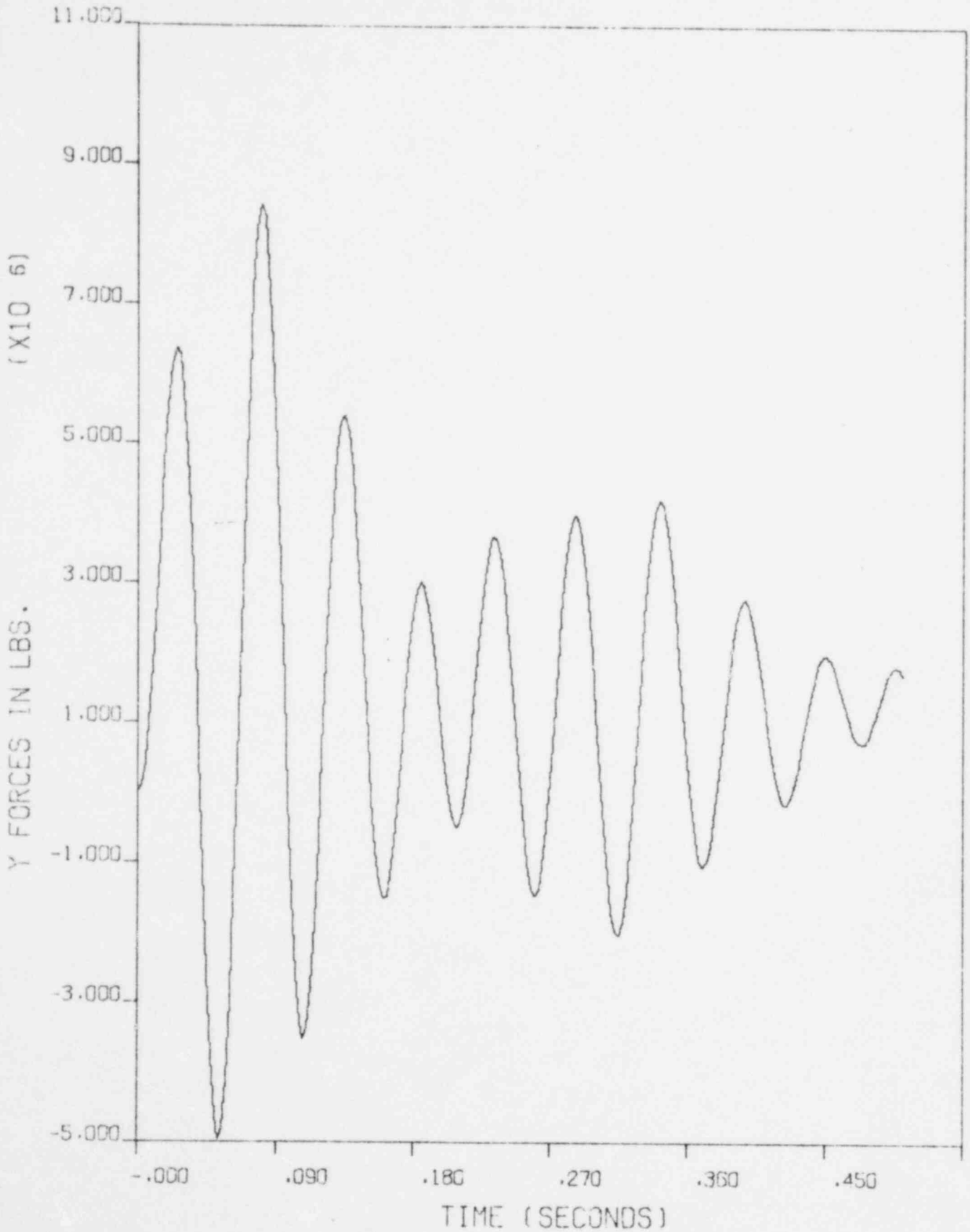

11.2. Evaluation of OTSG Upper Support Trunnions and Lower Supports

A comparative evaluation was performed to determine the acceptability of the steam generator supports for loads induced by pipe breaks in the steam generator compartment. This evaluation employed available detailed support analyses for LOCA loads. Both the upper restraint trunnions and lower support assembly have been evaluated.

11.2.1. Upper Restraint Trunnions

An analysis of the upper restraint trunnion of each Owners Group plant, based on design LOCA loads, was the basis for the evaluation of the LOCA loads described in section 11.1. These previous analyses were based on the same LOCA load components, i.e., F_X, F_Y, etc., given in section 11.1, but with different load magnitudes. Therefore, the loads of the base analyses can be used to evaluate the new LOCA loads.

11.2.1.1. Skirt-Supported RV Plants

The LOCA loads of section 11.1 are lower than the base design LOCA loads for the Oconee units. Therefore, the Oconee units are acceptable. Assuming that the geometry and material of the upper supports of the other units are similar to those of the Oconee units, all skirt-supported RV plants should be acceptable for the LOCA loads.

11.2.1.2. Nozzle-Supported RV Plants

The LOCA loads of section 11.1 for Davis-Besse 1 were compared to the design basis LOCA loads, which were higher than the new loads. Therefore, the upper support trunnions of the DB-1 plant are acceptable for the loads of section 11.1.

11.2.2. Lower Support Assembly

The asymmetric LOCA loads for the lower support skirt assembly were compared to the comparable loads in the stress report for the OTSG support skirt. Calculations were made where necessary to quantify significant differences.

11.2.2.1. Skirt-Supported RV Plants

The applied LOCA and deadweight loadings were resolved into a resultant horizontal force (F_R), a vertical force (F_Y), a resultant overturning moment (M_R),

and a torsional moment (M_Y) for direct comparison with the values analyzed in the previously completed stress report:

Applied LOCA loads + deadweight	F_R, kips	F_Y, kips	M_R, ft-kips	M_Y, ft-kips
Lower support skirt at base	6112	8205	42,751	2210

The previously completed stress report for Rancho Seco was used as a basis for evaluating the structural integrity of the OTSG support skirt. The comparable Rancho Seco design loads are shown below.

Design loads, Rancho Seco stress report	F_R, kips	F_Y, kips	M_R, ft-kips	M_Y, ft-kips
Lower support skirt at base	8439	1845	90,833	0

A review of the calculations in the Rancho Seco stress report shows that the majority of each significant stress was generated by F_R or M_R. These F_R and M_R values in the existing Rancho Seco analysis were much higher than the applied values. Therefore, the applied loads would result in lower stresses than those previously evaluated.

It was recognized that the applied values of F_Y and M_Y were somewhat higher than the Rancho Seco values. However, these are minor contributors to the total significant stresses (i.e., F_Y provides a flange-bearing contribution of 0.8 ksi and M_Y a shear contribution of 0.6 ksi, both of which are insignificant).

It is concluded that the OTSG support skirts for all plants are acceptable by comparison with the previously analyzed loadings for Rancho Seco.

11.2.2.2. Nozzle-Supported RV Plant

Applied LOCA loads + deadweight	F_X, kips	F_Y, kips	F_Z, kips	M_X, ft-kips	M_Y, ft-kips	M_Z, ft-kips
Sliding base	0	10,083* 3,347#	0	0	0	0

- - - - -

*Downward load on base.
#Upward load on base.

Design loads, stress report	F_X, kips	F_Y, kips	F_Z, kips	M_X, ft-kips	M_Y, ft-kips	M_Z, ft-kips
Sliding base	0	6653* 3347#	20.2	0	0	0

A comparison of the loads above for the OTSG lower support assembly shows that the applied load plus deadweight in the downward direction is significantly higher than the design loads in the stress report. Based on a comparison of the loads and a review of the stress report calculations, all areas of the lower support skirt assembly were shown to be acceptable except the fillet welds that join the support gussets to the top and bottom support discs of the center support. This is the primary area affected by the higher load. Consequently, a more detailed stress analysis was performed to demonstrate the structural adequacy of this weld.

11.2.3 Method of Evaluation

The lower support system for the OTSG with the sliding support base (required for the nozzle-supported RV plant) has a "wagonwheel"-like structure that is bolted to the sliding support. The structural configuration of this support is shown in Figures 11.2-1 through 11.2-3. The bottom section of the support skirt assembly contains the wagonwheel structure that provides the necessary structural stiffness and a load path for transmitting the loads between the OTSG and the sliding support base. The applied vertical loads are transmitted to the sliding support via the cylindrical skirt and the wagonwheel components (i.e., 12 support gussets, the center support, the top and bottom support discs, and the attaching fillet welds).

A finite element model representing one of the 12 support gussets was developed to determine more precisely the distribution of the reaction forces in the fillet weld that resulted from the maximum applied LOCA and deadweight loads. The more precisely defined reaction forces were used to determine the stresses in the fillet welds more accurately, particularly the 1-inch weld in question.

- - - - -

*Downward load on base.

#Upward load on base.

This planar model consisting of rectangular elements is shown in Figure 11.2-4. The built-in restraint along the three edges represents the boundary conditions of the support gusset provided by the fillet weld attachment to the center support and the top and bottom support discs. The maximum vertical applied loads were assumed to be evenly divided among the 12 support gussets. The support gusset is restricted from end rotations where it is welded to the cylindrical support skirt. Consequently, it was conservatively assumed that the model deformed as a quasi-guided cantilever.

11.2.4. Acceptance Criteria

All welds in the OTSG skirt support system are fillet welds. The acceptability of the 1-, 5/8-, and 1/2-inch fillet welds was based on the average shear stress in the throat region of the welds.

The allowable stresses for faulted conditions in Table NF-3712.1 of the ASME Code, Section III, Subsection NF*, were modified in order to obtain the allowable stress limits in a weld that connects two non-pressure-retaining members. For an elastic stress analysis of the component support, the stress limit is the greater of 1.5 times the S_m (stress intensity) or 1.2 times the S_y (yield stress) of the material (but greater than 0.7 of the ultimate stress, S_u). These criteria result in a stress limit of 48,600 psi for the critical 1-inch fillet welds.

As discussed in section 7.1.2.4, the ASME Code minimum values for ultimate and yield strengths can be increased by 5 and 10%, respectively, to obtain the maximum stress limit. The maximum stress limit using the 10% increase is 53,460 psi. However, as stated in section 7, the allowable shear stress in the fillet welds is 0.68 S_u, which is 49,980 psi with a 5% increase on ultimate. Therefore, the allowable stress limit is 49,980 psi.

11.2.5. Results of Evaluation

A maximum resultant shear stress of 57,900 psi was calculated for the combined maximum restraining forces parallel and transverse to the 1-inch weld; this exceeds the allowable limit by 16%. The overstressed region of the weld

- - - - -

*1971 Edition, Winter 1973 Addenda.

is confined to about 20% of the length of the horizontal weld at the point furthest from the center support. The remaining 80% of the horizontal weld, as well as the vertical weld, are loaded so that the shear stress is below the allowable stress limit.

For the worst case of gross plastic yielding, the three welded sides of the support gusset (see Figure 11.2-4) would be restrained by the bearing surfaces of the adjacent components, i.e., the top and bottom support discs and the center support. Consequently, the vertical downward displacement of the support gussets would be limited so the lower support skirt assembly would maintain its functional requirement – supporting the once-through steam generator.

Figure 11.2-1. OTSG Support Skirt Assembly, Elevation View

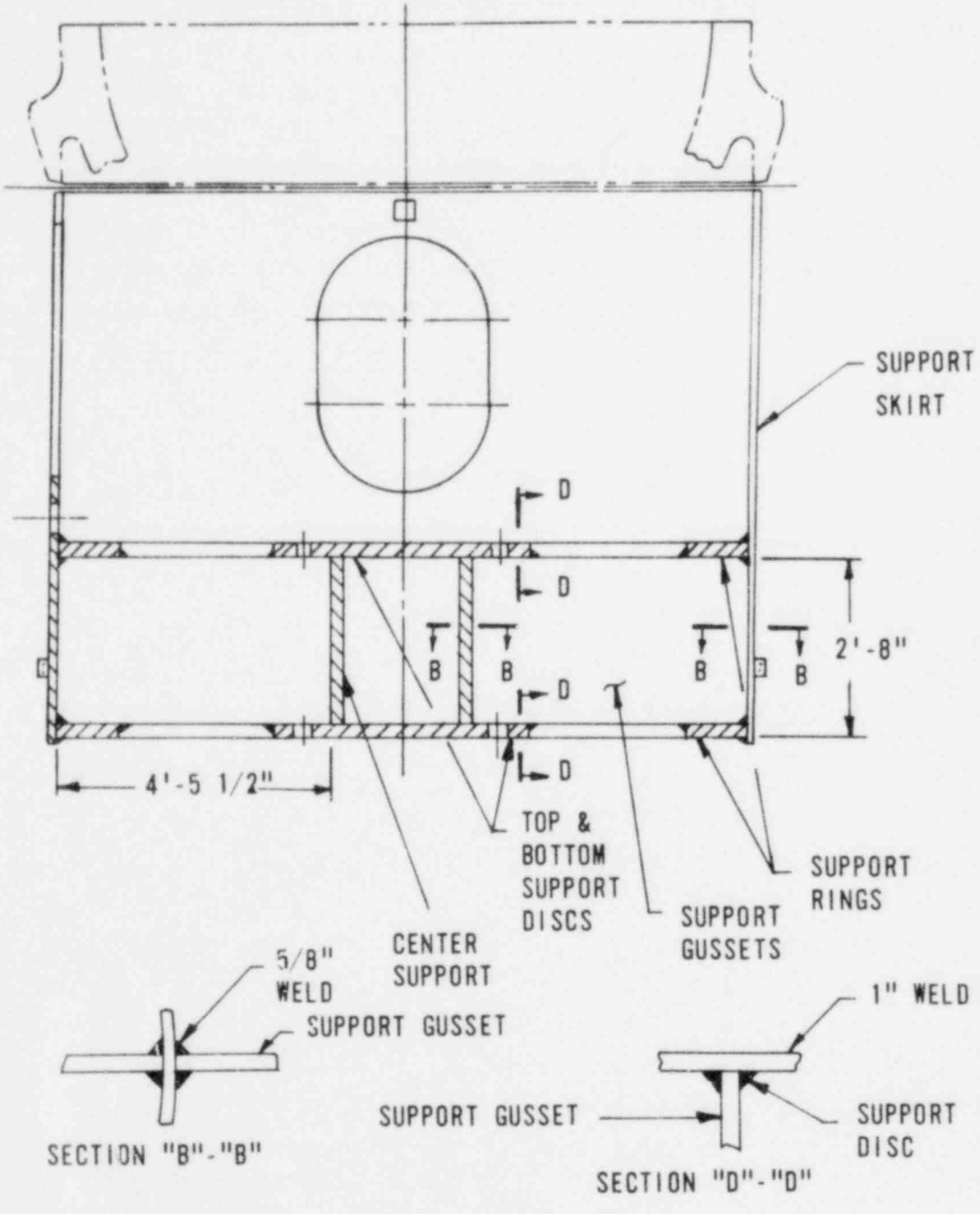

Figure 11.2-2. OTSG Support Skirt Assembly, Plan View

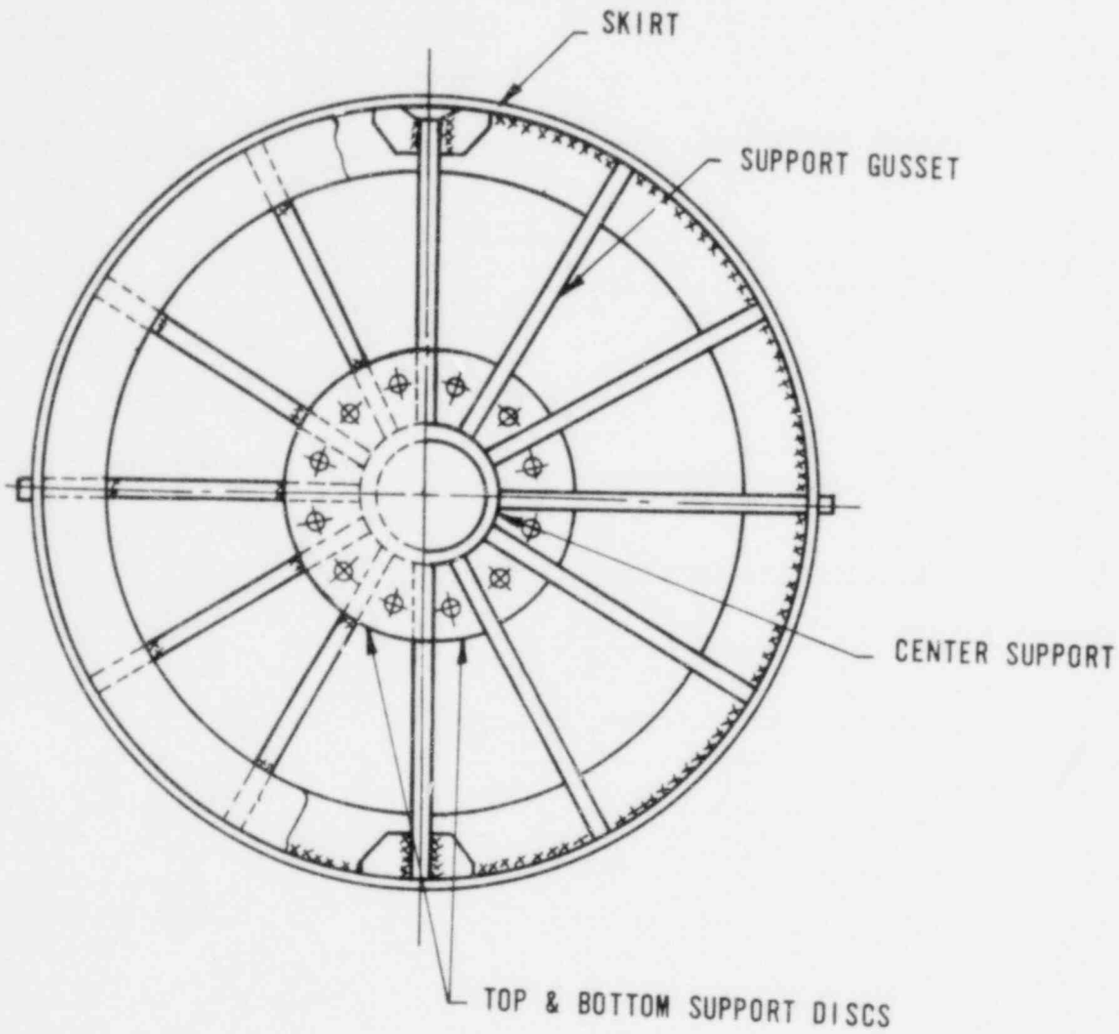

Figure 11.2-3. Lower Section of OTSG and Its Support System

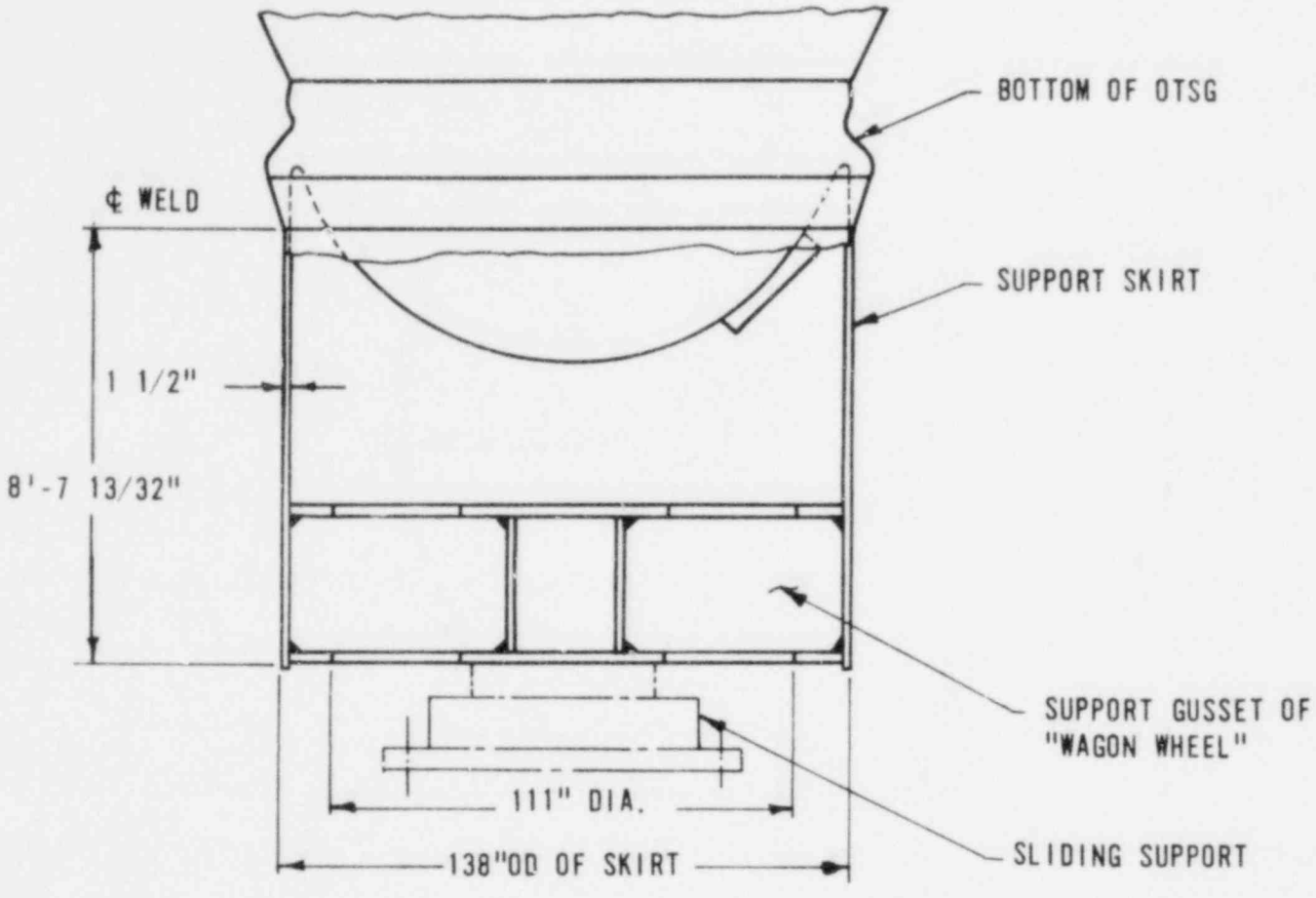

Figure 11.2-4. Planar Model of Support Gusset

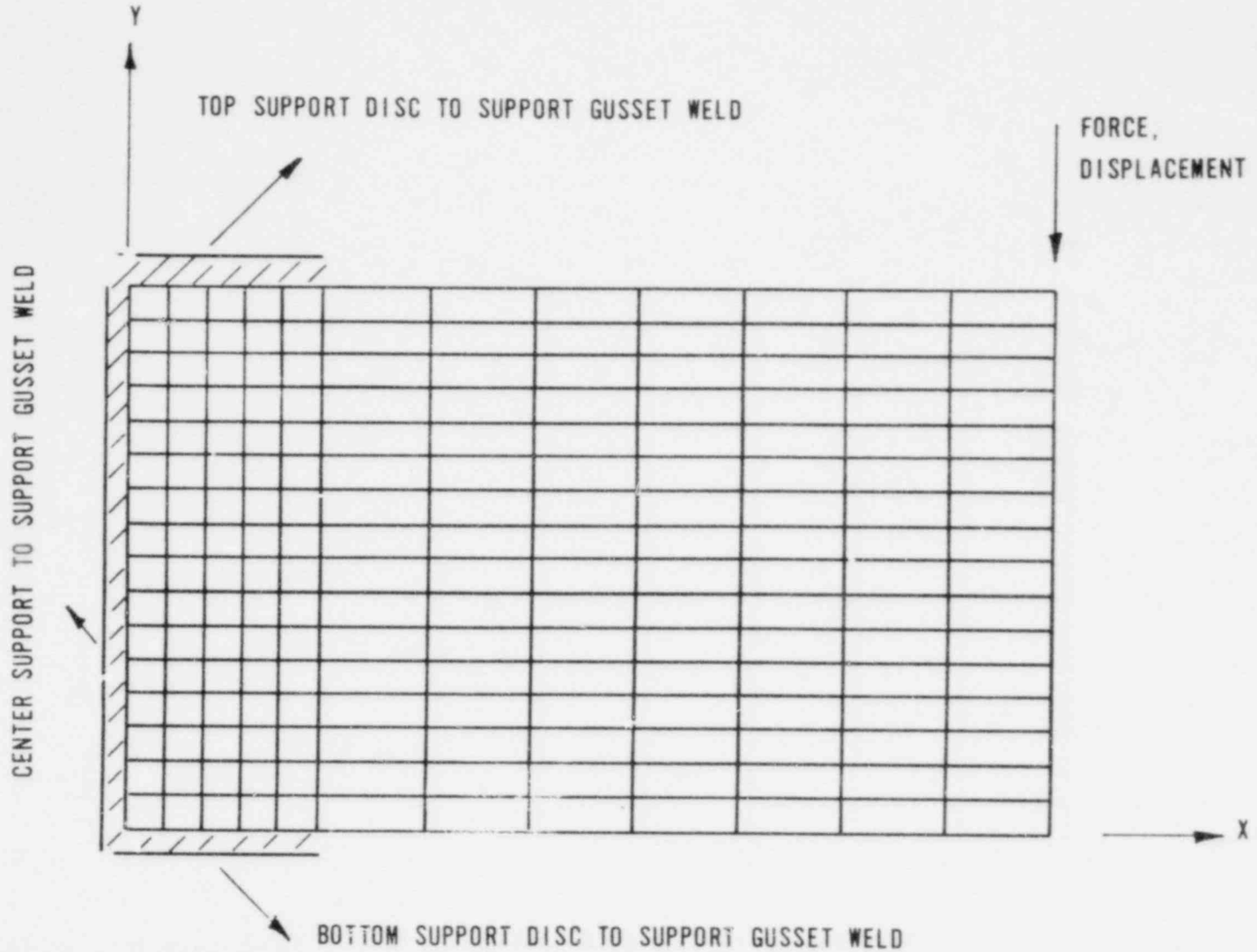

11.3. Unbroken Piping Loadings

11.3.1. Piping Load Development

The methods described in section 11.1 were also used to determine the loads for the unbroken primary piping. The identical model and input data base were used to calculate the piping loads, steam generator load, and loads in the other parts of the system.

11.3.2. Piping Loads

The absolute peak value of the time history for each component of force at each joint was stored on magnetic tape for use in the stress evaluation. This peak value was used irrespective of the fact that the peaks may not occur at the same time. Tables 11.3-1 through 11.3-3 provide typical peak piping moments at selected points in the unbroken piping. Each table is identified by LOCA case and by plant type.

Table 11.3-1. Skirt-Supported (Supported Pump) Plant, Maximum Values for LOCA LCL-5 Loads on Components

JOINT NAME OR NOZZLE					MOMENTS (FT-KIPS) MX	MY	MZ
RV CONNECTION	BAR	28	JOINT	200	5312.04	829.73	307.17
HORIZONTAL RUN	BAR	29	JOINT	186	3118.08	582.57	307.17
HORIZONTAL RUN	BAR	30	JOINT	179	1002.96	355.81	307.17
HORIZONTAL RUN	BAR	30	JOINT	162	1178.78	141.99	196.44
LOWER ELBOW	BAR	31	JOINT	144	1635.73	114.50	201.45
DECAY HEAT CONNECTION	BAR	32	JOINT	128	1452.95	114.50	223.01
SURGE LINE CONNECTION	BAR	33	JOINT	117	1326.94	114.23	492.59
VERTICAL RUN	BAR	34	JOINT	102	1351.34	114.23	661.83
VERTICAL RUN	BAR	35	JOINT	92	1428.19	114.23	722.77
VERTICAL RUN	BAR	36	JOINT	77	1471.12	114.23	657.20
VERTICAL RUN	BAR	37	JOINT	61	1499.41	114.23	625.03
VERTICAL RUN	BAR	38	JOINT	49	1475.41	114.23	602.56
VERTICAL RUN	BAR	39	JOINT	39	1429.17	114.23	487.29
VERTICAL RUN	BAR	40	JOINT	30	1224.79	114.23	464.46
MID POINT OF U-BEND	BAR	41	JOINT	24	2816.72	246.78	1000.66
U-BEND	BAR	42	JOINT	32	2535.40	670.87	879.86
OTSG CONNECTION	BAR	43	JOINT	15	2770.61	670.87	1031.16
P1A1-RV CONNECTION	BAR	75	JOINT	149	572.06	1113.40	659.14
P1A1-UPPER COLD LEG	BAR	76	JOINT	130	514.00	822.06	247.54
P1A1-UPPER COLD LEG	BAR	77	JOINT	111	386.56	694.75	144.75
P1A1-UPPER COLD LEG	BAR	78	JOINT	93	266.73	1129.36	164.54
P1A1-UPPER COLD LEG	BAR	79	JOINT	83	319.75	943.30	143.31
P1A1-UPPER COLD LEG	BAR	80	JOINT	54	790.34	981.75	334.36
P1A1 UPPER COLD LEG	BAR	81	JOINT	56	772.09	952.45	375.63
P1A1-UPPER COLD LEG	BAR	81	JOINT	37	587.35	903.19	333.76
P1A1-PUMP CONNECTION(U)	BAR	82	JOINT	47	766.33	815.41	371.88
P1A1-PUMP CONNECTION(L)	BAR	91	JOINT	46	968.20	212.46	474.78
P1A1 LOWER COLD LEG	BAR	92	JOINT	45	779.91	212.46	393.98
P1A1 LOWER COLD LEG	BAR	93	JOINT	29	534.45	212.46	503.02
P1A1 LOWER COLD LEG	BAR	94	JOINT	22	634.05	212.46	546.26
P1A1 LOWER COLD LEG	BAR	95	JOINT	6	470.32	212.46	454.70
P1A1 LOWER COLD LEG	BAR	96	JOINT	11	291.80	212.46	475.70
P1A1 LOWER COLD LEG	BAR	97	JOINT	8	616.16	266.43	836.73
P1A1 LOWER COLD LEG	BAR	98	JOINT	14	515.21	418.75	555.55
P1A1 LOWER COLD LEG	BAR	99	JOINT	19	519.67	688.39	1353.37
P1A1-OTSG CONNECTION	BAR	100	JOINT	21	477.84	771.15	1833.73

Table 11.3-2. Skirt-Supported (Unsupported Pump) Plant, Maximum Values for LOCA LCL-5 Loads on Components

JOINT NAME OR NOZZLE					MOMENTS (FT-KIPS) MX	MY	MZ
RV CONNECTION	BAR	28	JOINT	200	5460.22	520.71	625.42
HORIZONTAL RUN	BAR	29	JOINT	186	3194.06	360.60	625.42
HORIZONTAL RUN	BAR	30	JOINT	179	1467.60	231.56	625.42
HORIZONTAL RUN	BAR	30	JOINT	162	1431.67	144.25	580.58
LOWER ELBOW	BAR	31	JOINT	144	1636.90	158.29	502.66
DECAY HEAT CONNECTION	BAR	32	JOINT	128	1458.59	158.29	480.62
SURGE LINE CONNECTION	BAR	33	JOINT	117	1399.21	166.93	540.27
VERTICAL RUN	BAR	34	JOINT	102	1421.70	166.93	575.97
VERTICAL RUN	BAR	35	JOINT	92	1806.46	166.93	519.62
VERTICAL RUN	BAR	36	JOINT	77	1861.43	166.93	403.52
VERTICAL RUN	BAR	37	JOINT	61	1888.40	166.93	350.15
VERTICAL RUN	BAR	38	JOINT	49	1849.88	166.93	318.80
VERTICAL RUN	BAR	39	JOINT	39	1680.86	166.93	229.07
VERTICAL RUN	BAR	40	JOINT	30	1260.37	166.93	203.75
MID POINT OF U-BEND	BAR	41	JOINT	24	3237.07	136.04	756.92
U-BEND	BAR	42	JOINT	32	2694.14	427.50	445.00
OTSG CONNECTION	BAR	43	JOINT	15	3006.90	427.50	604.30
P1A1-RV CONNECTION	BAR	75	JOINT	149	796.15	1312.30	805.45
P1A1-UPPER COLD LEG	BAR	76	JOINT	130	587.14	761.07	440.11
P1A1-UPPER COLD LEG	BAR	77	JOINT	111	427.18	561.61	171.95
P1A1-UPPER COLD LEG	BAR	78	JOINT	93	291.51	1470.63	193.24
P1A1-UPPER COLD LEG	BAR	79	JOINT	83	371.79	1396.67	169.94
P1A1-UPPER COLD LEG	BAR	80	JOINT	64	774.48	1280.93	307.06
P1A1 UPPER COLD LEG	BAR	81	JOINT	56	885.59	1167.42	333.43
P1A1-UPPER COLD LEG	BAR	81	JOINT	37	756.76	1035.19	267.23
P1A1-PUMP CONNECTION(U)	BAR	82	JOINT	47	828.13	1037.18	269.45
P1A1-PUMP CONNECTION(L)	BAR	91	JOINT	46	637.90	351.34	559.01
P1A1 LOWER COLD LEG	BAR	92	JOINT	45	656.04	351.34	443.23
P1A1 LOWER COLD LEG	BAR	93	JOINT	29	661.01	351.34	363.33
P1A1 LOWER COLD LEG	BAR	94	JOINT	22	561.94	351.34	645.56
P1A1 LOWER COLD LEG	BAR	95	JOINT	6	436.95	351.34	842.37
P1A1 LOWER COLD LEG	BAR	96	JOINT	11	442.41	351.34	907.72
P1A1 LOWER COLD LEG	BAR	97	JOINT	8	587.84	315.26	898.94
P1A1 LOWER COLD LEG	BAR	98	JOINT	14	535.10	376.55	875.52
P1A1 LOWER COLD LEG	BAR	99	JOINT	19	520.49	575.76	1416.16
P1A1-OTSG CONNECTION	BAR	100	JOINT	21	471.70	644.98	1409.85

Table 11.3-3. Nozzle-Supported Plant, Maximum Values for LOCA LCL-5 Loads on Components

JOINT NAME OR NOZZLE					MOMENTS (FT-KIPS) MX	MY	MZ
RV CONNECTION HTL	BAR	14	JOINT	26	1191.97	626.65	386.30
RV CONNECTION HTL	BAR	14	JOINT	33	2208.21	836.13	386.30
OTSG CONNECTION HTL	BAR	31	JOINT	218	1137.22	806.45	468.61
OTSG CONNECTION HTL	BAR	31	JOINT	226	1489.82	836.49	601.04
P1A1-RV CONNECTION	BAR	58	JOINT	2	1124.82	632.20	272.82
P1A1-RV CONNECTION	BAR	58	JOINT	1	2095.01	1295.62	391.95
P1A1-PUMP CONNECTION(U)	BAR	64	JOINT	14	1100.17	1416.30	824.97
P1A1-PUMP CONNECTION(U)	BAR	64	JOINT	21	1656.51	1537.27	1101.14
P1A1-PUMP CONNECTION(L)	BAR	66	JOINT	44	1233.04	947.10	2637.68
P1A1-PUMP CONNECTION(L)	BAR	66	JOINT	54	1325.95	850.95	1682.47
P1A1-OTSG CONNECTION	BAR	71	JOINT	99	1538.94	1113.47	3502.67
P1A1-OTSG CONNECTION	BAR	71	JOINT	110	2169.33	1371.14	4405.54

11.4. Evaluation of Unbroken Primary Piping

For each of the primary piping LOCA loadings described in section 11.3, a simplified pipe stress analysis was performed in accordance with the rules of reference 6. A simplified analysis was performed first, considering pressure, deadweight, and LOCA moment loadings. Only the primary stresses (equation 9) were calculated and compared to an allowable stress of 3 S_m. If any joints in the piping system exceeded the allowable, a more detailed analysis was performed in accordance with reference 6 rules.

The maximum primary stress intensities calculated by this detailed method were compared to an allowable of 1.5 S_m^* where S_m^* is the lesser of either 2.4 S_m or 0.7 S_u, as discussed in reference 1.

As seen in Table 11.4-1, it was evident that the primary unbroken piping stresses for the skirt-supported plants satisfied the allowable limits. It was also evident (from Table 11.4-2) that the unbroken primary piping for the nozzle-supported plant exceeded allowable stress criteria at elbow joint number 3, which is located near a wagonwheel pipe restraint. The piping stresses at the remaining joints were within the acceptance limits.

Additional modeling refinements and possibly nonlinear analyses will be required to alleviate the localized high stressed condition at joint 3 for the nozzle-supported plant.

Table 11.4-1. Unbroken Primary Piping Stresses for Skirt-Supported Plants

Joint No.	Loading case No.	Max stress intensity, ksi	Allowable stress, ksi
149	2	55.56	73.5
111	2	66.13	70.1
93	2	47.38	
83	2	47.92	
64	2	26.30	
56	2	26.06	
37	2	25.44	
11	2	41.72	
8	2	45.01	
14	2	50.95	
14	4	32.05	
19	1	36.48	
19	2	51.12	
19	4	50.93	
19	8	39.29	
20	4	43.82	
20	8	39.58	70.1

Each of the joints above exceeded simplified equation 9 allowables. A detailed analysis was then performed, with the results above.

Case	LOCA[a]	Description
1	LCL-1	Skirt-supported (supported pump) model
2	UCL-7	Skirt-supported (supported pump) model
4	HTL-6	Skirt-supported (supported pump) model
8	HTL-6	Skirt-supported

[a] As described in section 11.3.

Table 11.4-2. Unbroken Primary Piping Stresses for Nozzle-Supported Plants

Joint No.	Loading case No.	Max stress intensity, ksi	Allowable stress, ksi
3	1	110.45	70.1
3	2	36.74	
3	3	117.94	
3	4	33.35	
44	3	38.09	
87	1	31.49	
87	3	34.59	
87	4	28.92	
99	1	33.16	
99	3	36.70	
99	4	33.43	
110	1	45.97	
110	3	52.88	
110	4	46.34	
185	4	35.34	
171	4	40.52	70.1

Each of the joints above exceeded the simplified stress analysis, equation 9, allowables. A detailed analysis was then performed, with the results above.

Case	LOCA[a]	Description
1	LCL-1	Nozzle-supported model
2	UCL-7	Nozzle-supported model
3	LCL-5	Nozzle-supported model
4	HTL-6	Nozzle-supported model

[a] As described in section 11.3.

12. ADDITIONAL EVALUATIONS AND ANALYSIS VERIFICATION

Additional evaluations were performed to validate certain assumptions used in this analysis and to confirm the final results. These additional evaluations are discussed in detail in this section.

12.1. Evaluation Service Support Structure Platform-Cavity Wall Connection

In some plants the platform at the top of the service support structure (SSS), is fastened to the cavity wall. Cable trays or walkways bolted to both the cavity wall and the SSS platform provide this connection, which is rigid enough to cause significant loadings in the SSS during the postulated pipe rupture. Oversized bolt holes provide some gap space, but in some instances it is not sufficient to prevent interference with the motion of the SSS platform. The SSS platform configurations evaluated in these analyses are (1) free – no connection, (2) gapped – a gapped connection, or (3) tight – a connection with no gap. The possibility that the total gap could be on the side opposite the initial motion of the structure required an evaluation of the effects of the tight connection.

The initial analysis assumed a free connection. The realization that Oconee, TMI-1, Crystal River 3, and Davis-Besse 1 could have connections with limited gaps (as shown in Table 12.1-1) necessitated a study of the effect of these connections.

The STALUM computer code was used to run three cases of SSS platform connections – free, gapped, and tight. All runs were made using the TMI-1, Crystal River 3 hot leg break. Running the nonlinear gapped case using the linear STALUM code required an iterative technique using an assumed input force time history to represent the force of the cavity wall on the SSS platform. The assumed time history is a function of the gap, the platform spring rate, and an assumed input displacement time history. After completing the computer run the output displacement time history was compared to the assumed input displacement time history, and a modified input displacement time history was then assumed for the next iteration.

Table 12.1-2 shows the RV skirt loads and SSS flange loads for the three cases evaluated. Note that although tight and gapped connections do alleviate RV skirt loads somewhat relative to the free case, the SSS flange loads increased beyond the allowable load of 16,400 ft-kips. It was also noted that at a gapped connection, the gap in the Z direction may be on either side or partly on each side. Therefore, it is necessary that both tight and gapped case loads be acceptable. Hence, it was determined that only a free connection would provide acceptable loads for the SSS flange.

12.1.1. Conclusions and Recommendations

For those plants (Oconee, TMI-1, Crystal River 3, and Davis-Besse 1) with connections between the SSS platform and the cavity wall, loads on the SSS flange can be reduced to acceptable values (see Table 12.1-2) by providing clearances in the connection. The required clearances in the horizontal directions are 2.0 inches for TMI-1 and Crystal River 3; 1.5 inches for Oconee; and 1.0 inches for Davis-Besse 1. These clearances may possibly be provided by (1) reducing bolt sizes to either make the connection less rigid or to provide the increased freedom needed, (2) increasing the size of bolt holes to increase gap, (3) showing the walkway/cable tray structure incapable of carrying significant load. Verifying the freedom needed would provide acceptable SSS flange loads via any of the three methods or any other acceptable method and would validate the Phase II analytical assumptions. Some plants had free connections; the minimum gaps required to maintain these connections are: TMI-2, 3 inches; ANO-1, 1.25 inches; and Rancho Seco, 1.75 inches.

Table 12.1-1. SSS Platform – Cavity Wall Gaps

	Freedom of movement gap, in.		
Contract	X	Y	Z
Oconee	0.5	Free	0.375
TMI-1	0.625	Free	0.625
CR-3	0.375	Fixed	0.625
DB-1	0.5	Free	0.5
Rancho Seco	Free	Free	Free
ANO-1	Free	Free	Free
TMI-2	Free	Free	Free

Table 12.1-2. Loads as a Function of SSS Platform-Cavity Wall Connection — CR-3, TMI-1 Hot Leg Break

Component	Load case	Forces, kips			Moments, ft-kips[a]		
		F_X	F_Y	F_Z	M_X	M_Y	M_Z
SSS flange	Free	99	196	725	11,009	23	1,481
	Tight	84	196	1,823	31,926	23	1,648
	Gapped	104	196	1,685	27,746	23	1,563
RV skirt	Free	514	6,358	9,618	249,063	1,470	11,724
	Tight	769	6,335	9,391	166,123	1,147	13,005
	Gapped	525	6,408	10,433	230,419	1,089	13,621

[a]Allowable moment: SSS flange 16,400 ft-kips, RV skirt 189,000 ft-kips.

12.2. Evaluation of Pipe Rupture Restraint Modifications

This section tabulates the resultant loads for hot leg restraint modifications for the TMI-1 and CR-3 plants to limit the hot leg break opening area. Two different modifications were analyzed for CR-3: loadings resulting from shimming the existing restraint 1 (Figure 12.2-1) to a 1.0-inch cold gap and a 2.0-inch gapped restraint in the penetration (Figure 12.2-2) while retaining the as-built restraint gaps for restraint 1. The hot leg restraint for CR-3 is identical for both the A and B coolant loops, so only A is described here.

The only modification that would provide acceptable break areas and restraint loadings for TMI-1 was a gapped restraint in the cavity penetration with the as-built gaps retained in the existing restraint (Figure 12.2-3). This was done for both the A and B steam generator loops since each coolant loop has a specific restraint configuration (Figures 12.2-3 and 12.2-4).

The gap of the restraint was chosen so that no break opening area (BOA) exceeds a ratio of 0.844. This BOA would mean that loadings applied to the reactor vessel due to the hot leg break (maximum 0.844 BOA) would be no larger than those generated by the 2.0A cold leg break.

Tables 12.2-1 through 12.2-4 provide peak loads for the affected U-bars on the existing restraints, loads on the analyzed restraint in the penetration area, and the peak resultant BOA. These restraint modifications and resultant loadings supplement the results in section 9.8 for the as-built restraint configurations. The hot leg BOAs for both plants (TMI-1 and CR-3) would be reduced by these modifications so that the results for the RV support and embedment would be acceptable. The restraint loads for CR-3 would remain within acceptable limits for either modification since the resultant loads would be lower than those used previously for restraint qualification. The restraint loads for TMI-1 would be reduced by this modification so that they will be within the acceptable limits reported in section 10.8.

Table 12.2-1. Crystal River 3 — Shimmed R1 to 1-Inch Cold Gap[a]

Restraint 1	Peak load, lb	Time, s	Status[b]
U-bar1	753,117	0.0306	T
2	741,617	0.0305	T
3	730,440	0.0304	T
4	695,353	0.0295	T
5	542,114	0.0292	T
6	55,434	0.0288	T
7	43,005	0.0283	T
8	30,896	0.0278	T
Total peak	3,517,350	0.0293	T

BOA/peak ratio = 0.6273 at 0.0310 second.

[a] See Figure 12.2-1.

[b] Status indicates whether the U-bar is in tension (T) or compression (C).

Table 12.2-2. Crystal River 3 – 2-Inch Gapped Restraint in Penetration, As-Built Restraint Gaps (R1)[a]

Restraint 1	Peak load, lb	Time, s	Status[b]
U-bar 1	755,220	0.0429	T
2	745,360	0.0431	T
3	735,540	0.0433	T
4	703,960	0.0444	T
5	694,840	0.0452	T
6	619,030	0.0473	T
7	57,690	0.0479	T
8	46,549	0.0485	T
Total peak	4,205,300	0.0434	T
Penetration Restraint			
	F_N = 1,785,200	0.0428	C
	F_S = 749,340	0.0425	--

BOA/peak ratio = 0.8184 at 0.0425 second.

[a] See Figure 12.2-2.

[b] Status indicates whether the U-bar is in tension (T) or compression (C).

Table 12.2-3. TMI-1 — Gapped Restraint in Penetration, 2-Inch As-Built Gaps for Restraint 1, Loop A[a]

Restraint 1	Peak load, lb	Time, s	Status[b]
U-bar 1	2,209,700	0.0253	T
2	2,199,800	0.0232	T
3	1,509,100	0.0216	T
4	729,500	0.0212	T
5	233,630	0.0210	T
6	48,249	0.0209	T
7	44,546	0.0209	T
Total peak	6,889,749	0.0211	T
Penetration restraint			
	F_N = 3,840,000	0.0241	C
	F_S = 1,881,600	0.0241	--

BOA/peak ratio = 0.70642 at 0.0245 second.

[a] See Figure 12.2-3.

[b] Status indicates whether the U-bars are in tension (T) or compression (C).

Table 12.2-4. TMI-1 — Gapped Restraint in Penetration, 2-Inch As-Built Gaps for Restraint 1, Loop B[a]

Restraint 1	Peak load, lb	Time, s	Status[b]
U-bar 1	2,250,140	0.0270	T
2	2,206,550	0.0268	T
3	1,806,240	0.0264	T
4	46,462	0.0560	T
5	31,747	0.0560	T
	414	0.0120	C
6	17,298	0.0556	T
	13,298	0.0182	C
7	3,022	0.0554	T
	29,513	0.0181	C
Total peak	6,351,235	0.0264	T
Penetration Restraint			
	F_N = 3,303,800	0.0245	C
	F_S = 1,618,900	0.0245	--

BOA/peak ratio = 0.76455 at 0.0258 second.

[a] See Figure 12.2-4.

[b] Status indicates whether the U-bars are in tension (T) or compression (C).

Figure 12.2-1. Hot Leg Model for CR-3 Shim Study-Shim Restraint

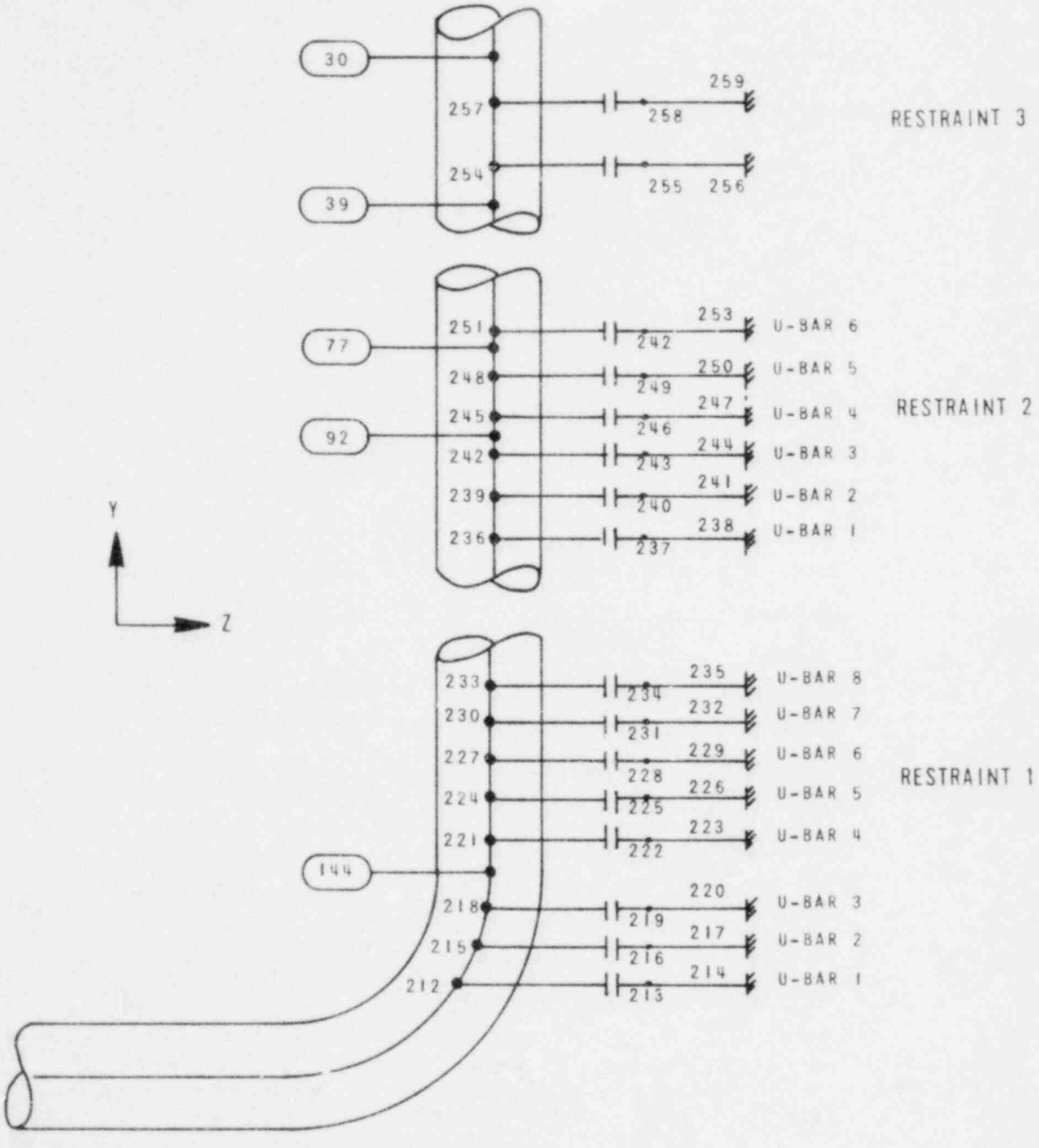

Figure 12.2-2. Hot Leg Model for CR-3 Shim Study With Restraint in Penetration Wall

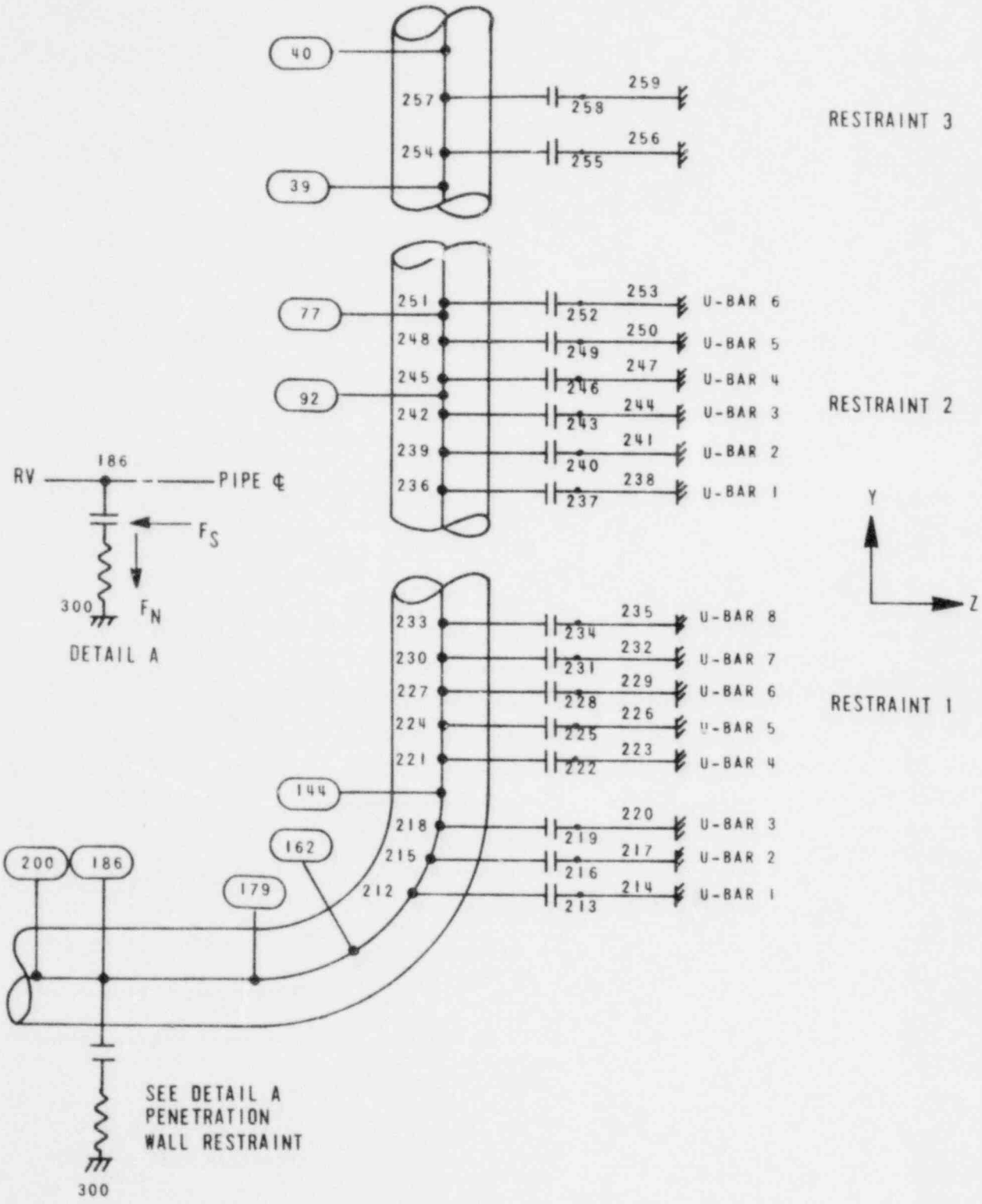

Figure 12.2-3. TMI-1 Hot Leg Loop "A" – Mathematical Model

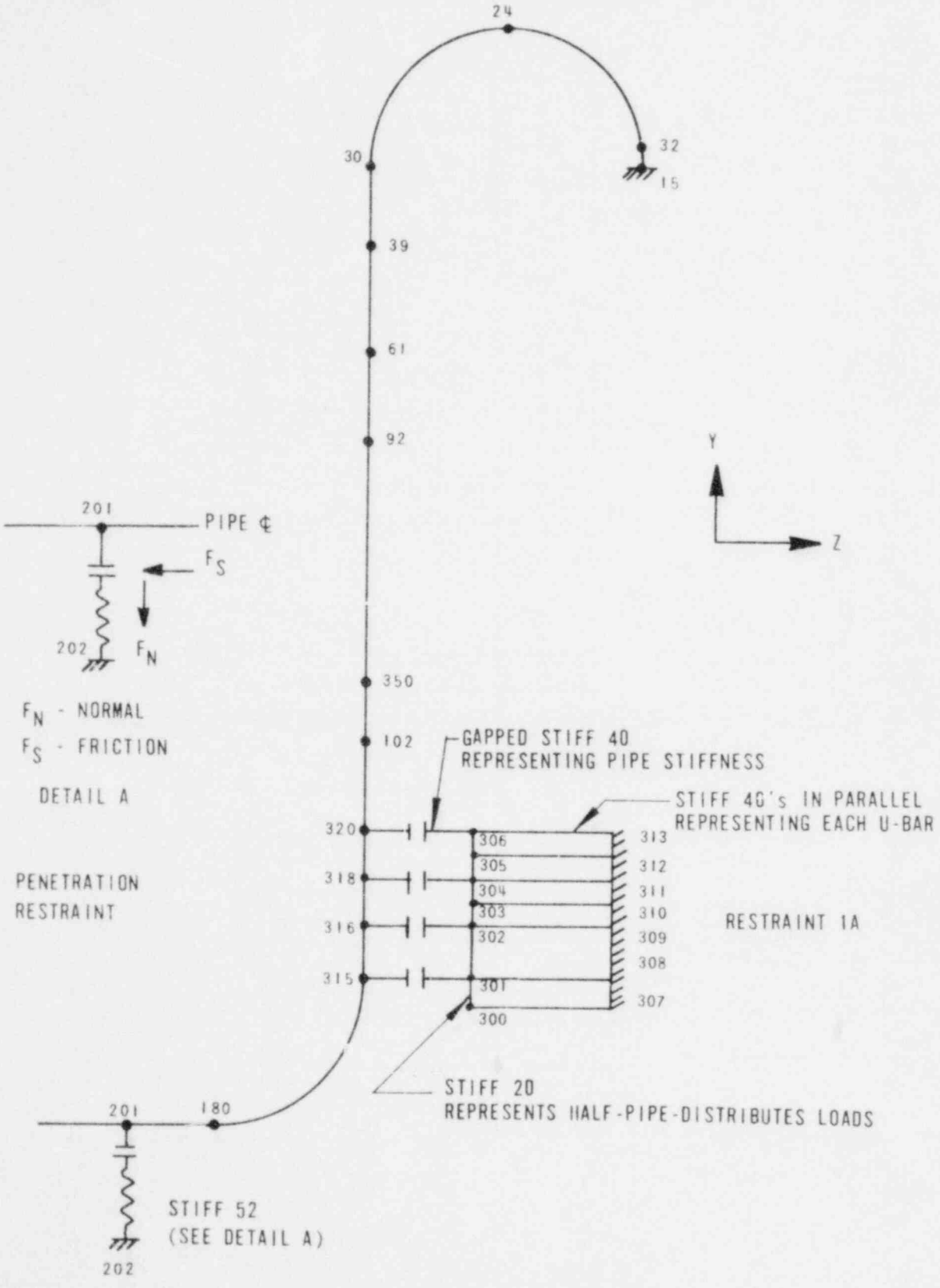

Figure 12.2-4. TMI-1 Hot Leg Loop "B" – Mathematical Model

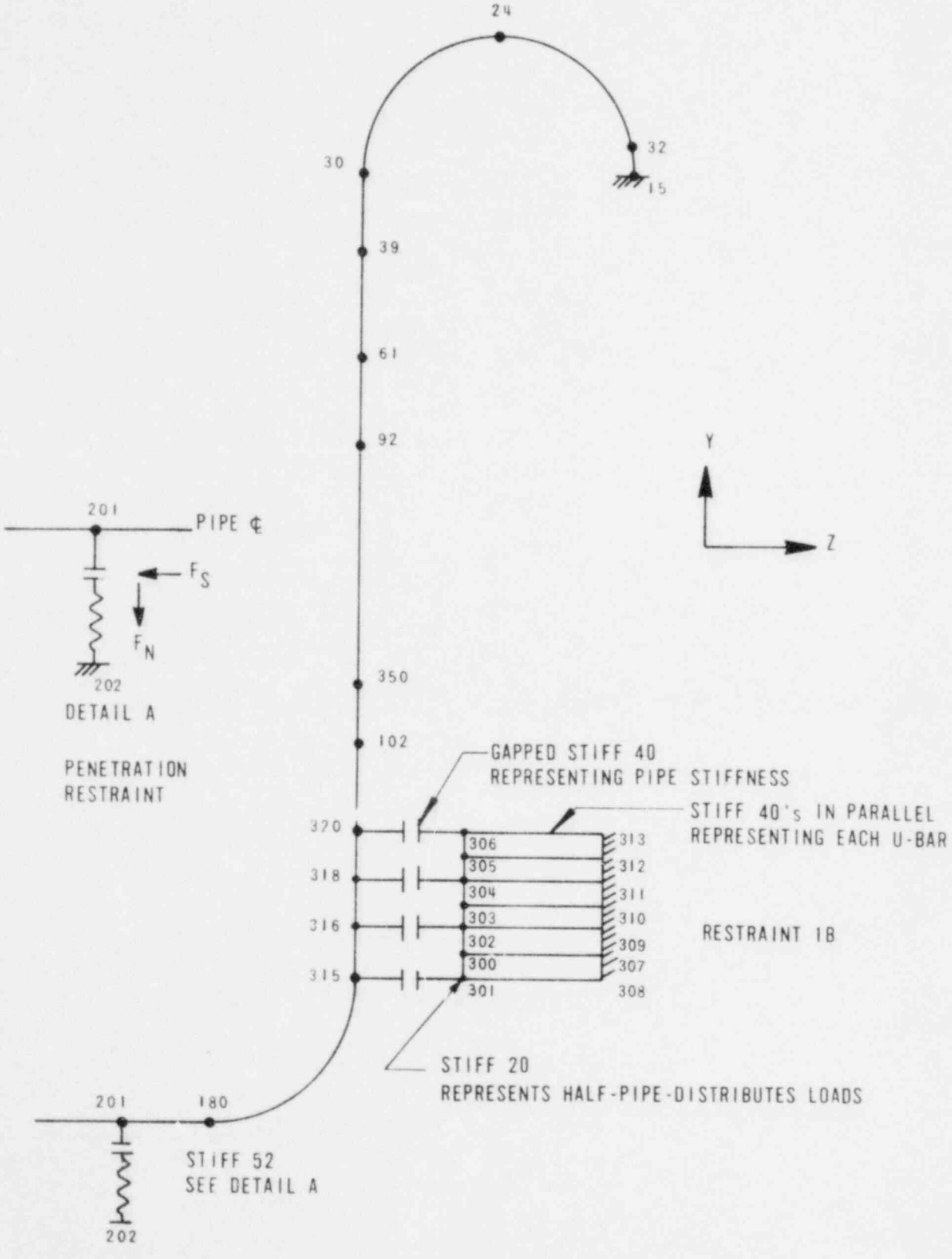

12.3. Asymmetric Loading Contribution of Cavity Pressures in Refueling Canal – Davis-Besse 1

The Davis-Besse 1 plant had neither neutron shield plugs nor a comparable restriction at the RV flange as did the remaining plants. Thus, a review was performed to evaluate the significance of cavity pressures in the refueling canal and the resultant component loadings.

12.3.1. Estimation of Loadings

The RV cavity for DB-1 was modeled to calculate the detailed pressures within it. The detailed portion of this model extended from the base of the RV cavity up to the base of the SSS cavity (the fuel transfer canal). The SSS cavity was not modeled in detail because its walls are much further removed from the structures than those of the RV cavity, resulting in much larger volumes. The large volumes in the SSS cavity produce much smaller pressures and thus smaller asymmetric pressures on the SSS.

In order to ensure that all loads on the RV and SSS have been considered, conservative calculations were used to predict the loads in the SSS cavity. These calculations employed the detailed RV cavity results, i.e., mass energy versus time, flow rates, and pressures/asymmetric pressures in the volumes directly below the SSS. The large volumes of the SSS cavity were also used for these calculations. The resulting asymmetric peak load in the SSS cavity was estimated to be 15% of the peak RV cavity asymmetric load. This increase was included in the evaluation of the RV supports, i.e., the wagonwheel restraints in the RV cavity penetrations.

12.3.2. Effect of Increased Loading

12.3.2.1. LOCA Ring Restraint

Consideration of the effect of the pressure load in the DB-1 SSS cavity (discussed in section 12.3.1) leads to an increase in the peak horizontal load on the LOCA ring restraints. Other DB-1 RV support loadings are unchanged.

The resultant peak horizontal load on a LOCA ring is approximately 15% greater than that considered in sections 6.2 and 10.2, where the qualification of these restraints is reviewed. Thus, further analysis of a cold leg LOCA ring was performed to verify their adequacy for this increased loading. Since the original analyses (section 10.2) showed this ring to be much more severely

loaded than that for a hot leg, conclusions as to its adequacy may be generically applied to all the LOCA rings.

Considerable conservatism was inherent in the original analyses, particularly with regard to the application of frictional loading. In the re-analysis of the cold leg LOCA ring, the methodology described in section 6.2 was refined to include a more accurate representation of the frictional loading. It was assumed that bounding friction coefficients of zero or 0.42 could act. For the former, frictionless case, the applied LOCA ring load was that derived from the RV isolated structural model analysis, appropriately increased for the flange load effect. For the latter case, a frictional load equal to 42% of this normal load was included, with these loads being adjusted so that the net resisting force opposing the blowdown thrust was preserved.

The results of the requalification showed that the acceptance criteria are met. Thus, the LOCA ring has the capacity to safely resist the increased loading.

The effect of the LOCA ring reactions on the cavity wall response was not re-evaluated. However, inspection of the results of the original analysis (section 10.10) show that the increased loading will not be critical.

12.3.2.2. Core Flood Lines

Consideration of the effect of the pressure load in the DB-1 SSS cavity also leads to an increase in the estimated core flood line nozzle displacements. The peak displacement of the nozzle is approximately 15% greater than that considered in sections 6.9 and 10.9. The DB-1 core flood lines were re-analyzed using this increased displacement; the methodology paralleled that described in section 6.9.

The re-analysis demonstrated that consideration of the increased loading does not alter the conclusions drawn in section 10.9 as to the adequacy of the Davis-Besse 1 core flood lines.

12.4. RV Stability Evaluation

Two studies were performed using nonlinear analyses – one each for the Oconee plants and Crystal River 3. The selection was based on the skirt and embedments; high ratios to allowables for the Oconee cold leg guillotine and for the CR-3 hot leg guillotine. The basis for these analyses was to demonstrate reactor vessel stability and to furnish displacements for ensuring core flood line integrity while using no restraint at the top of the SSS to represent the cable tray or walkway structures to limit motion.

A simplified model was constructed to perform a dynamic nonlinear analysis representing the skirt as a nonlinear beam and the embedment as a nonlinear spring. This model represents the reactor vessel, control rod drives, service support structure and vessel support skirt. A linear analysis was performed using the simplified model to verify the modeling process and the definition of applied loadings. The stress-strain curve for the skirt material shown in Figure 12.4-1 was used, incorporating the guidelines of section 7.1. The beam element modeling of the skirt has eight points that monitor nonlinearity around the circumference. The spring rate representation shown in Figures 12.4-2 and 12.4-3 are the plant-unique data for Oconee and Crystal River 3 embedments, respectively. The time history plots from this analysis (Figures 12.4-4 through 12.4-9) indicate that the RV is stable and will return to position with very little permanent deformation.

The peak displacements imposed on the core flood lines from RV motion are tabulated below in inches (Δ) and radians (θ).

	ΔX	ΔY	ΔZ	θ_X	θ_Y	θ_Z
Crystal River 3 Hot Leg Break						
Linear	0.039	0.025	0.871	0.00260	0.00003	0.00014
Nonlinear	0.006	0.007	1.053	0.00158	0.00000	0.00002
Oconee Cold Leg Break						
Linear	0.657	0.019	0.326	0.00094	0.00003	0.00190
Nonlinear	0.717	0.005	0.363	0.00084	0.00000	0.00154

The peak moments at the base of the RV are compared below for the linear and nonlinear analyses for the breaks analyzed in this stability study.

	Resultant moment, 10^3 ft-kips
Oconee Cold Leg	
Linear	208.0
Nonlinear	196.4
Crystal River 3 Hot Leg	
Linear	249.4
Nonlinear	197.7

Conclusions

The results of the nonlinear analysis verify that the hot leg break (without shim modifications) for CR-3 and the cold leg break for Oconee result in a stable reactor vessel with limited displacements. These results also show that the reactor vessel supports and embedments for these plants are capable of carrying the existing loadings even though they are over the acceptance limits using the linear analysis. Finally, the increased displacements resulting from the analysis above do not jeopardize the integrity of the attached core flood line.

Figure 12.4-1. RV Skirt Material Property Law

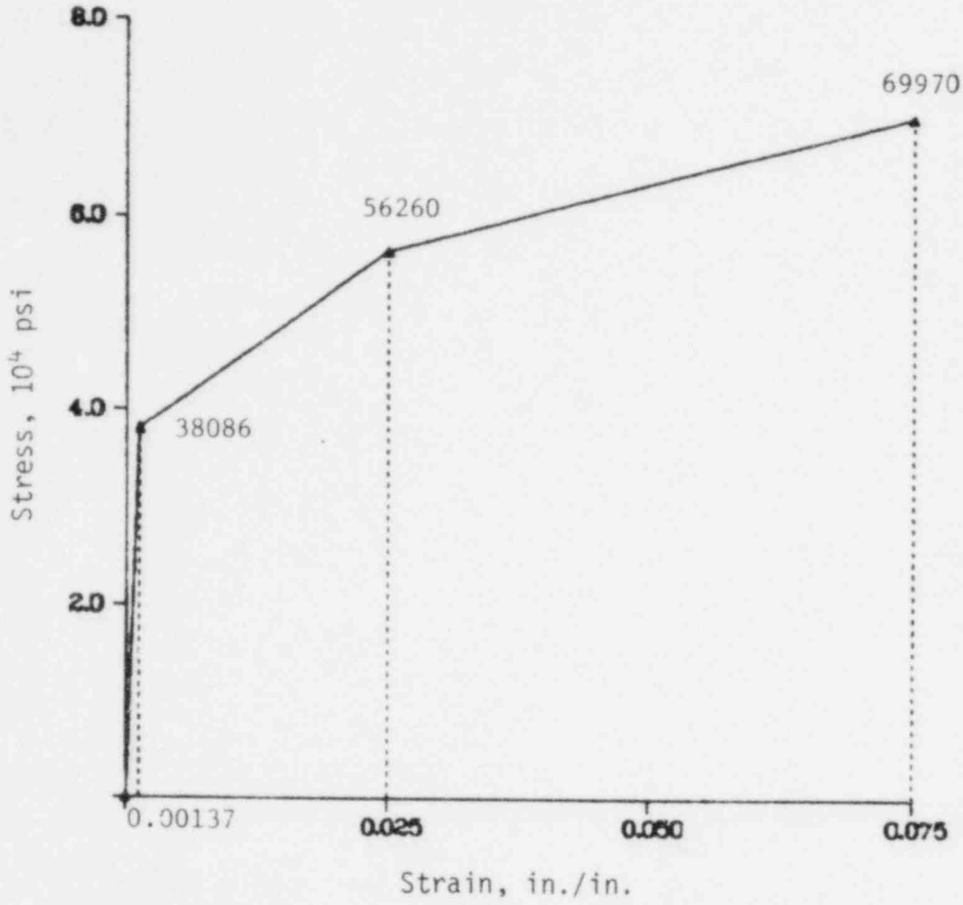

Figure 12.4-2. Embedment Spring Rates for Oconee 1, 2, and 3

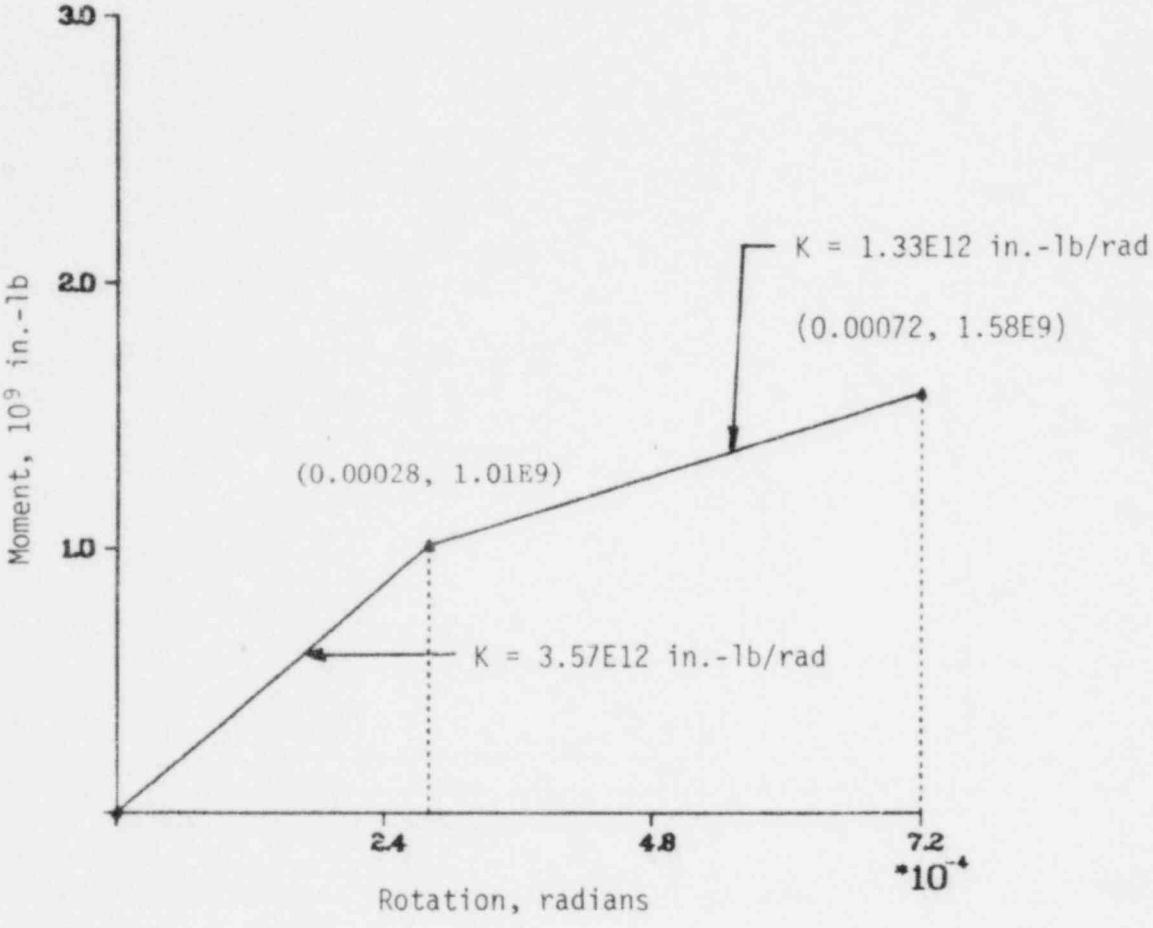

Figure 12.4-3. Embedment Spring Rates for Crystal River 3

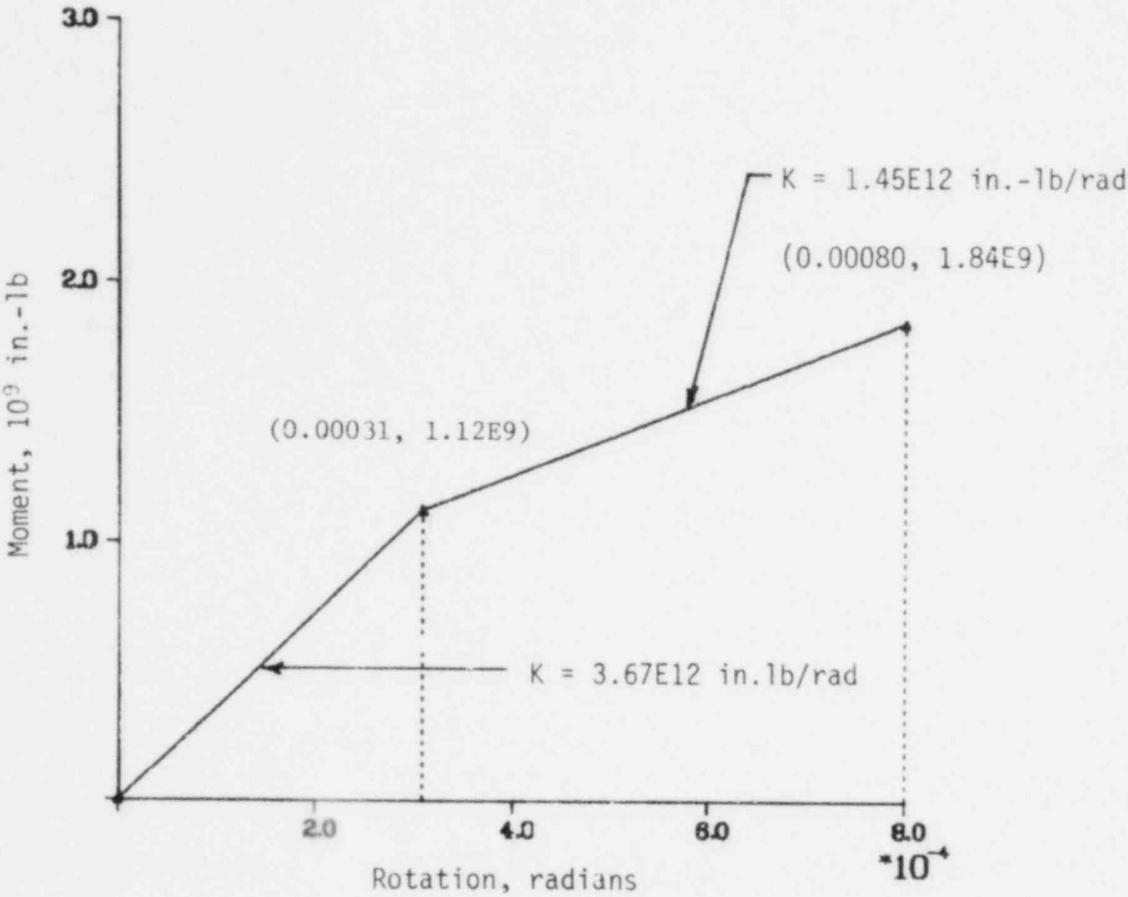

Figure 12.4-4. RV Displacement (X Dir) at Core Flood Nozzle — Oconee Cold Leg Break

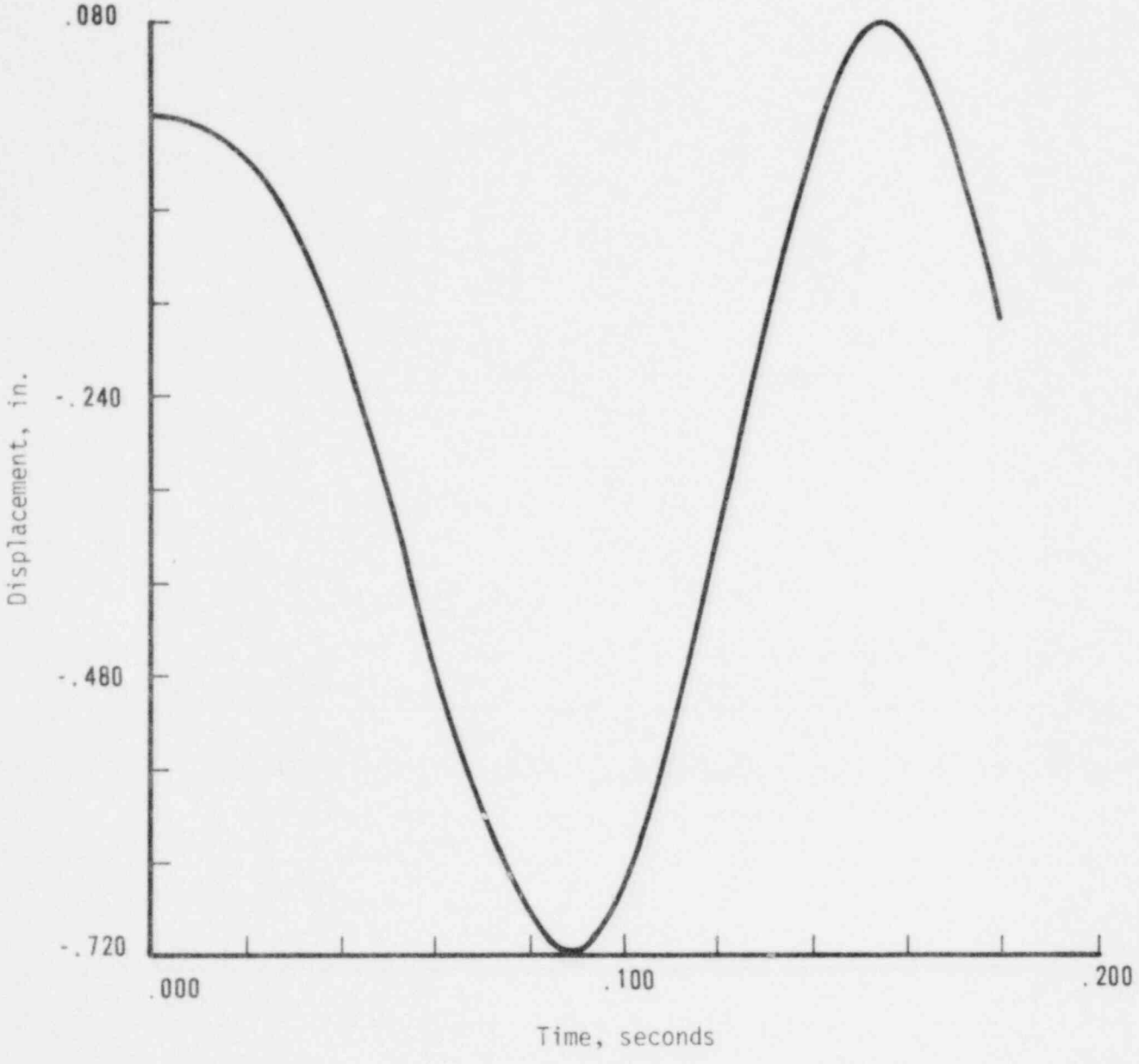

Figure 12.4-5. RV Displacement (Z Dir) at Core Flood Nozzle – Oconee Cold Leg Break

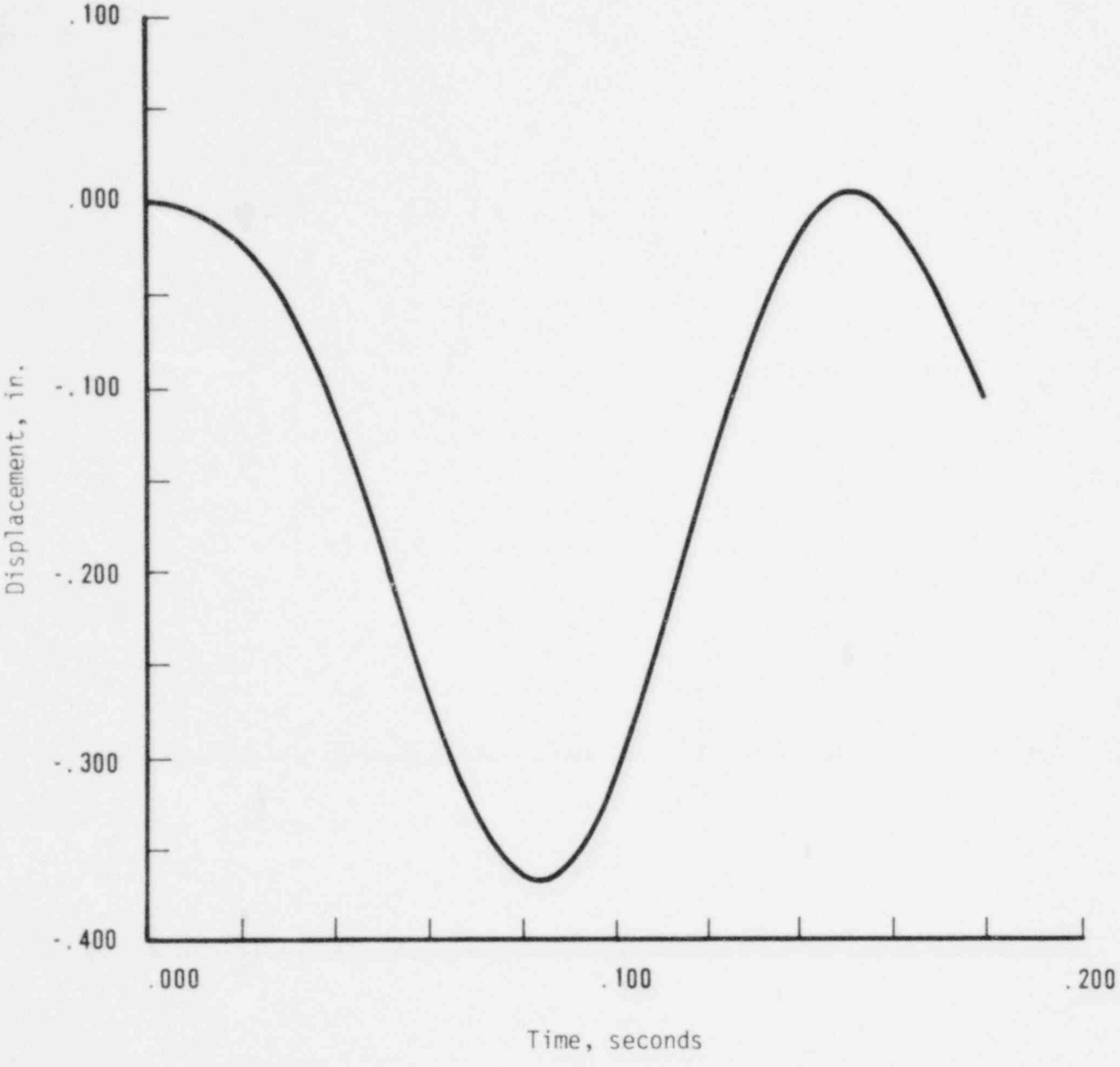

Figure 12.4-6. X Moment at Base of RV Skirt – Oconee Cold Leg Break

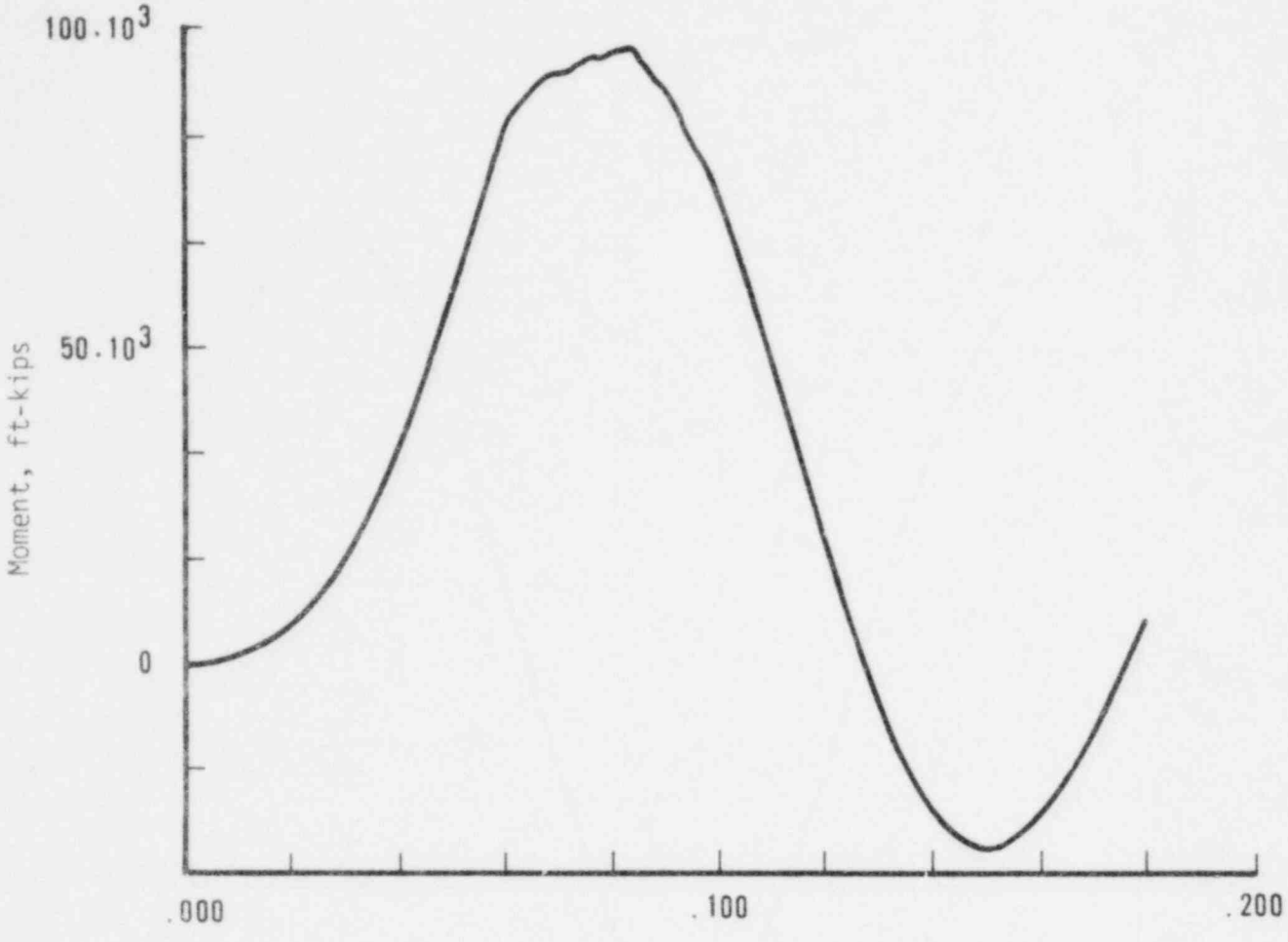

Figure 12.4-7. Z Moment at Base of RV Skirt – Oconee Cold Leg Break

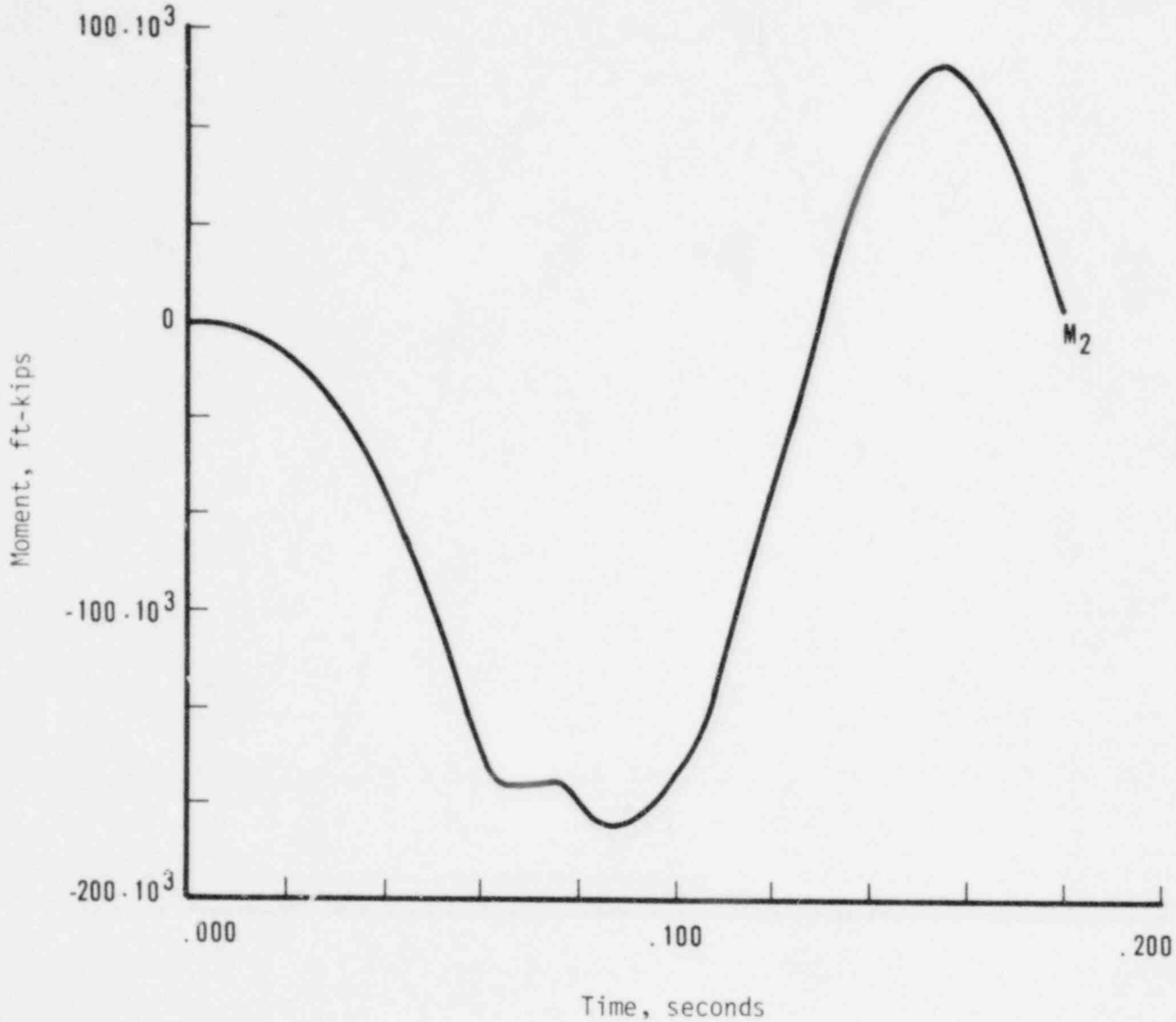

Figure 12.4-8. X Moment at Base of RV Skirt — Crystal River 3 Hot Leg Break

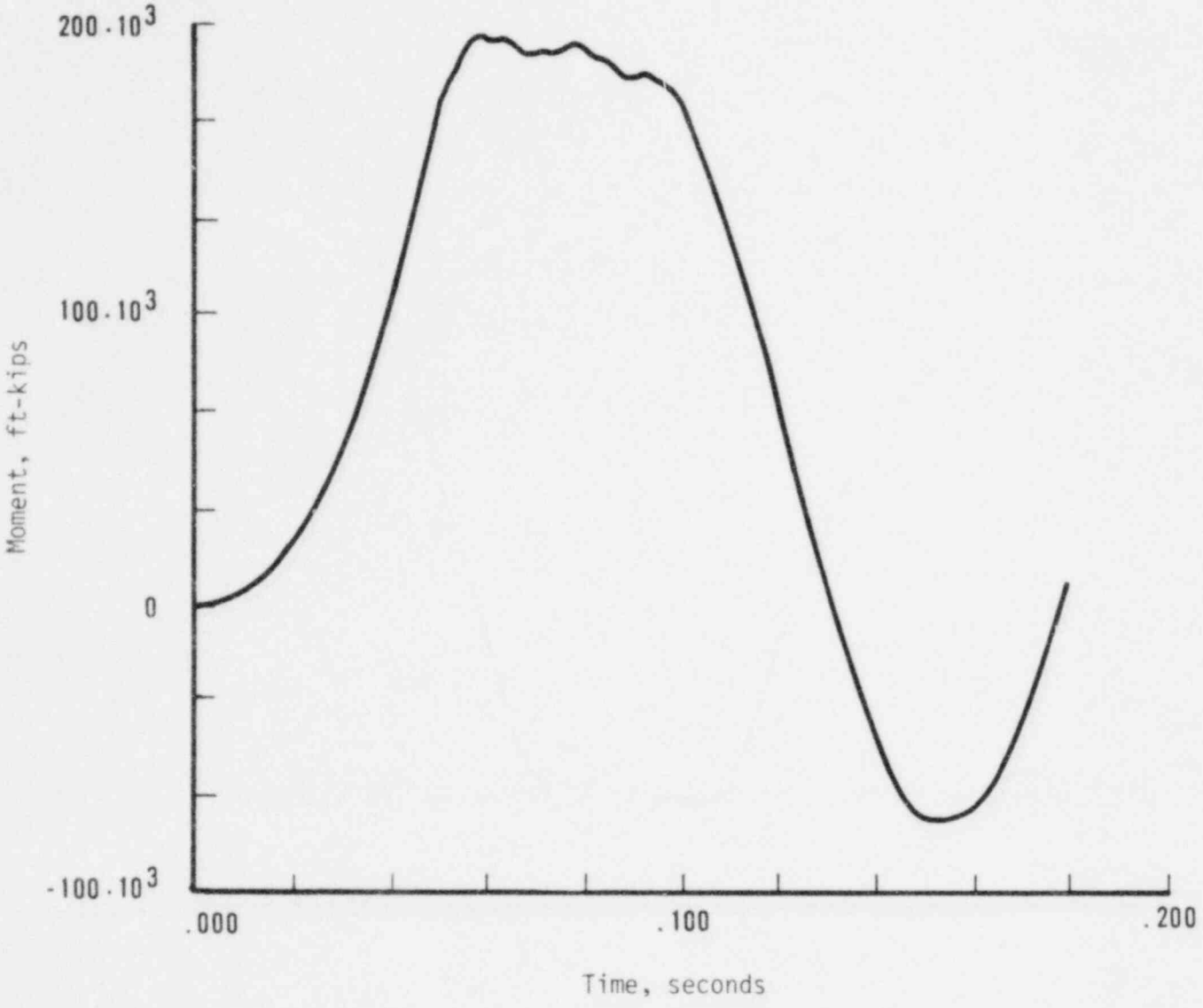

Figure 12.4-9. Crystal River 3 Hot Leg Break Displacement (Z Dir)

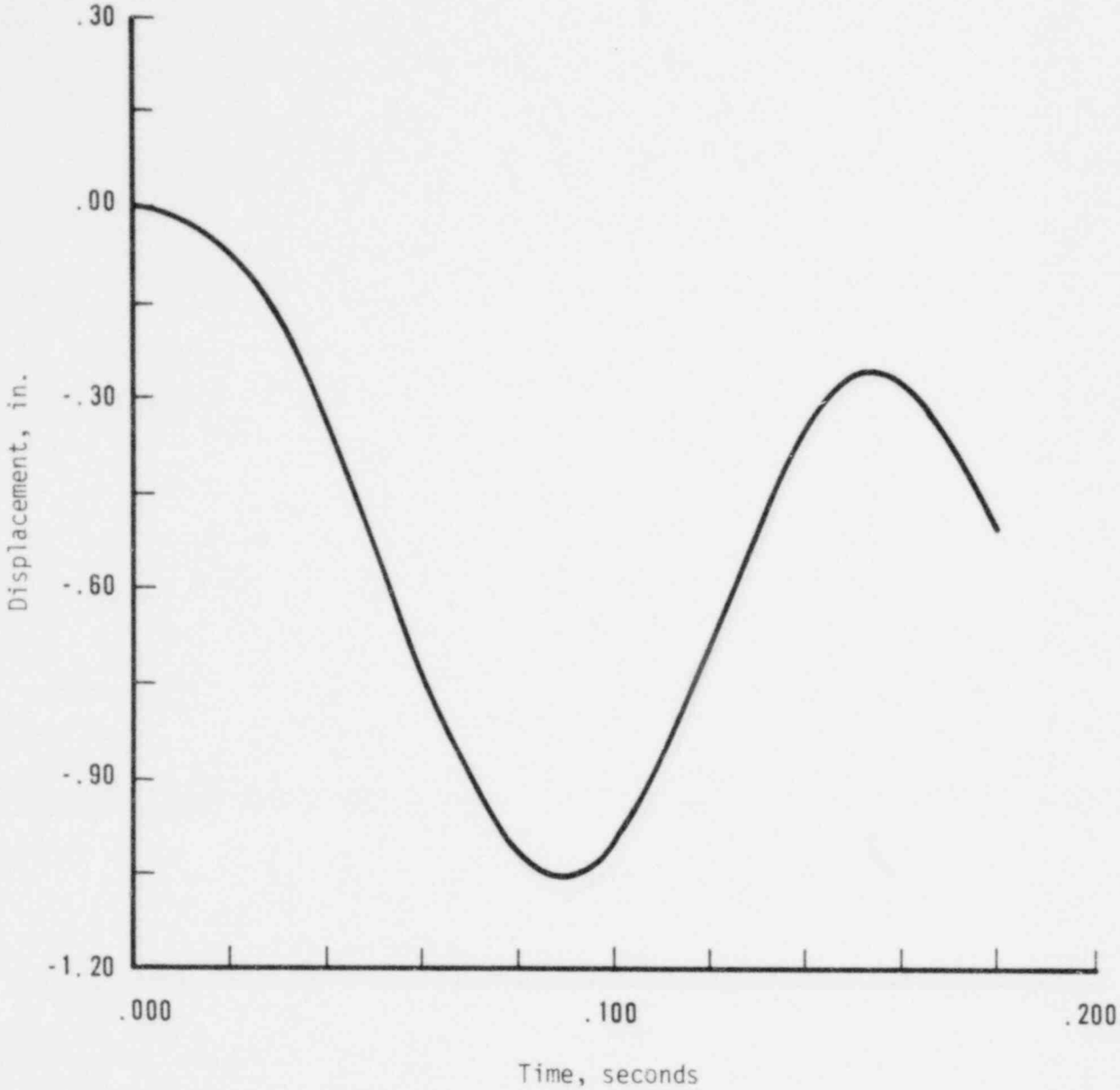

13. REFERENCES

13.1. Reference List A

The references listed below are referred to in sections 5.3, 6.2, 6.8, 6.9, 6.10, 7.1.1, 7.2, 7.3.2, 9.10, 10.2, 10.8, 10.9, and 10.10 and in Appendixes G. H, I, K, and N. References for the remaining sections and appendixes of the report are listed in Reference List B, section 13.2.

[1] Code Requirements for Nuclear Safety-Related Concrete Structures, ACI 349-76.

[2] B&W 177-FA Owners Group: Assumptions, Methodology, and Acceptance Criteria for Asymmetric LOCA Loads Evaluation — Phase 2, BAW-1538, Rev. 1, Babcock & Wilcox, April 1979.

[3] A. H. Mattock and M. Hawkins, "Shear Transfer in Reinforced Concrete — Recent Research," PCI Journal, March-April 1972, pp 55-75.

[4] Manual of Steel Construction, 7th Ed., American Institute of Steel Construction (1969).

[5] Recommended Practice for Evaluation of Compression Test Results of Field Concrete, ACI 214-65.

[6] Hardened Concrete: Physical and Mechanical Aspects, ACI Monograph No. 6.

[7] Code of Practice for the Structural Use of Concrete, British Standards Institution (1971).

[8] R. Park and T. Paulay, Reinforced Concrete Structures, New York: John Wiley & Sons (1975).

[9] EDS-SNAP — User's Manual, 1980 Version, EDS Nuclear, Inc., January 1980.

[10] K. J. Bathe and A. Cimento, "Some Practical Procedures for the Solution of Nonlinear Finite Element Equations," Journal of Computer Methods in Applied Mechanics and Engineering (publication pending).

[11] The ASME Boiler and Pressure Vessel Code, July 1, 1977, Edition.

[12] J. M. Biggs, Introduction to Structural Dynamics, New York: McGraw-Hill Book Co. (1974).

[13] PWHIP – User's Manual, 1977 Version, EDS Nuclear, Inc., October 20, 1977.

[14] "Determination of Break Locations and Dynamic Effects Associated With the Postulated Rupture of Piping," Section 3.6.2, Standard Review Plan, U. S. Nuclear Regulatory Commission.

[15] J. G. McGregor, "The Design of Reinforced Concrete Beams for Shear," Shear in Reinforced Concrete, Vol. 2, Publication SP-42 (1974), pp. 503-538.

[16] [17] [18] Not used.

[19] Y. Aoyagi, et al., "Behavior of Reinforced Concrete Containment Models Under Thermal Gradient and Internal Pressure," Trans. 5th Intl Conference on Structural Mechanics in Reactor Technology, Berlin (1979).

[20] K. J. Bathe and S. Ramaswamy, "On Three-Dimensional Nonlinear Analysis of Concrete Structures," Nuclear Engineering & Design, Vol. 52 (1979), pp 385-409.

[21] K. J. Bathe, Static and Dynamic Geometric and Material Nonlinear Analysis Using ADINA, Report 82448-2.

[22] K. J. Bathe, ADINA – A Finite Element Program for Acoustic Dynanic Incremental Nonlinear Analysis, 82448-1, Acoustics and Vibration Laboratory, M.I.T., September 1975 (revised May 1977).

[23] F. E. Richart, A. Brandtzaeg, and R. L. Brown, A Study of the Failure of Concrete Under Combined Compressive Stresses, Bulletin No. 185, University of Illinois Experimental Station (1928).

[24] A. Scanlon, Time-Dependent Deflections of Reinforced Concrete Slabs and Shells, Ph.D. Dissertation, University of Alberta, Edmonton (1971).

[25] C. S. Lin, Nonlinear Analysis of Reinforced Concrete Slabs and Shells, Ph.D. Dissertation, University of California, Berkeley (1973).

[26] S. Berg. P. G. Bergan, and I. Holand, "Nonlinear Finite Element Analysis of Reinforced Concrete Plates," Trans. of 2nd Intl Conference on Structural Mechanics in Reactor Technology, Berlin (1973).

[27] A. W. Beeby, A Study of Cracking in Members Subjected to Pure Tension, 42-468, Cement and Concrete Association, London, October 1974.

[28] J. Houde and M. S. Mirza, "A Finite Element Analysis of Shear Strength of Reinforced Concrete Beams," Shear in Reinforced Concrete, ACI SP-42 (1972).

[29] A. C. Scordelis, D. Ngo, and H. A Franklin, "Finite Element Study of Reinforced Concrete Beams With Diagonal Shear Cracks," Shear in Reinforced Concrete, ACI SP-42 (1972).

[30] J. W. Fisher and J. H. A. Struik, Guide to Design Criteria for Bolted and Riveted Joints, New York: John Wiley & Sons (1974).

[31] Final Safety Analysis Report – Three Mile Island Unit 1, Section 5.2.5.4.1.

[32] M. H. Khan and B. Saugy, "Evaluation of the Influence of Some Characteristics on Nonlinear Behavior of a Prestressed Concrete Reactor Vessel," Concrete for Nuclear Reactors, ACI SP-34 (1970).

[33] P. Launay and H. Gachon, "Strain and Ultimate Strength of Concrete Under Triaxial Stress," Concrete for Nuclear Reactors, ACI SP-34 (1970).

[34] V. Hansson and K. Schimmelpfennig, "Concrete Strength in Multiaxial Stress States," Concrete for Nuclear Reactors, ACI SP-34 (1970).

[35] J. H. Argyris, et al., "Recent Developments in the Finite Element Analysis of Prestressed Concrete Reactor Vessels," Nuclear Engineering & Design, No. 28 (1974), pp 42-75.

[36] G. Valente, "Nonlinear Analysis of Prestressed Concrete Reactor Pressure Vessels by Finite Elements," Trans. 4th Intl Conference on Structural Mechanics in Reactor Technology, San Francisco (1977).

[37] T. V. Galambos and M. K. Ravindra, "Properties of Steel for Use in LRFD," Journal of Structural Division, ASCE, September 1978.

[38] Final Report on Bar Tests for the Committee of Concrete Reinforcing Bar Producers, AISI by Wiff, Janney, Elstner & Associates, April 1970.

[39] Comparative Tests of Physical Properties of No. 18 Reinforcing Bars, AISI, by Wiff, Janney, Elstner & Associates, January 1971.

[40] Regulatory Guide 1.60, Revision 1, U. S. Nuclear Regulatory Commission, December 1973.

[41] Nonlinear Structural Dynamic Analysis Procedures for Category 1 Structures, NUREG/CR-0948, URS/John A. Blume & Associates, July 1979.

[42] N. M. Newmark, "A Response Spectrum Approach for Inelastic Seismic Design of Nuclear Reactor Facilities," Trans. of 3rd Intl Conference on Structural Mechanics in Reactor Technology, London (1975).

[43] A. Neville, Properties of Concrete, Pitman & Sons (1963).

[44] Building Code Requirements for Reinforced Concrete, ACI 318-77.

[45] Babcock & Wilcox to EDS Nuclear, Letter, "Asymmetric Loads Analysis," April 7, 1980.

[46] B. Bresler and V. V. Bertero, Olive View Medical Center Material Studies — Phase I, EERC 73-19, Earthquake Engineering Research Center, University of California, Berkeley, December 1973.

[47] Y. Aoyagi, O. Isobata, and N. Tanaka, "Design Method of Shell Wall End of Reinforced Concrete Containment Vessel (RCCV) Against Radial Shear," Trans. of 5th Intl Conference on Structural Mechanics in Reactor Technology, Belin (1979).

[48] T. Uchida, et al., "Behavior of Reinforced Concrete Containment Models Under the Combined Action of Internal and Lateral Force," Trans. of 5th Intl Conference on Structural Mechanics in Reactor Technology, Berlin (1979).

[49] Catalog PH-74, ITT Grinell Corporation (1974).

[50] Davis-Besse Verification Study of Pipe Whip Restraints on the Reactor Coolant System, Docket No. 50-346, Rev. 1, March 7, 1980.

13.2. Reference List B

[1] The ASME Boiler and Pressure Vessel Code, Section III, "Nuclear Power Plant Components," 1977 Edition.

[2] V. S. Reddy, FESAP – 3-D Finite Element Thermo-Elastic Stress Analysis Program, Nuclear Equipment Engineering, November 1975.

[3] R. J. Parekh and R. S. Horner, STARS – Structural Analysis of a Reactor System, NPGD-TM-176, Babcock & Wilcox, April 1972.

[4] Reactor Coolant System Structural Loading Analysis, BAW-10131, Babcock & Wilcox, November 1976.

[5] Reactor Coolant System Hydrodynamic Loadings During a Loss-of-Coolant Accident, BAW-10132P-A, Babcock & Wilcox, May 1979.

[6] USAS B32.7, 1969 Edition.

[7] Final Safety Analysis Report – Midland Units 1 and 2, Section 3.6.3.1.

[8] LOCA Pipe Break Criteria for the Design of B&W Nuclear Steam Systems, BAW-10127, Babcock & Wilcox, December 1976.

[9] G. J. de [illegible] and J. A. Swanson, ANSYS – Engineering Analysis System, Users Manual, Swanson Analysis Systems, Houston, Pennsylvania (1978).

[10] M. J. Yan, G. A. Krevolin, STALUM – Static and Lumped-Mass Dynamic, Finite Bar Segment Structure Analysis Program, NPGD-TM-376, Rev. J, Babcock & Wilcox, November 1979.

[11] B&W 177-FA Owners Group – Effects of Hydrodynamic Mass Coupling on the Transient Response of Reactor Internals to Asymmetric LOCA Load, BAW-1517, Rev. 1, Babcock & Wilcox, July 1979.

[12] C. G. Tinkler to R. P. Denise, Letter, "Summary of Meeting With B&W on CRAFT2 Code," September 10, 1979.

[13] B&W's ECCS Evalaution Model, BAW-10104, Rev. 3, Babcock & Wilcox, August 1977.

[14] J. H. Taylor (B&W) to R. L. Baer (NRC), Letter, June 8, 1977.

APPENDIX A

Description of Reactor Cavity Modeling Arrangement

A typical 177-FA lowered-loop reactor vessel concrete cavity is shown in Figure A-1. The volumes between the reacto vessel and the concrete represent the physical space that must be modeled for the subcompartment pressure calculation. Figure A-2 is a reactor vessel with attached piping which leads to Figures A-3 through A-8. Figure A-9 provides the representation of the annular space below the nozzles and the penetration volumes, Figure A-10 is a more detailed description of this modeling arrangement, and Figure A-11 presents the modeling for the core flood penetration.

Figures A-1 through A-11 were produced by a three-dimensional geometric modeling system using a Tektronix CRT terminal. The representation of levels and volumetric nodes is for visual representation and understanding only. In several volumes additional line segments are used to represent the curved or irregular surfaces. The analytical model noding philosophy is presented in section 4.3.

Figure A-1. Sectional View of Concrete in Reactor Vessel Subcompartment

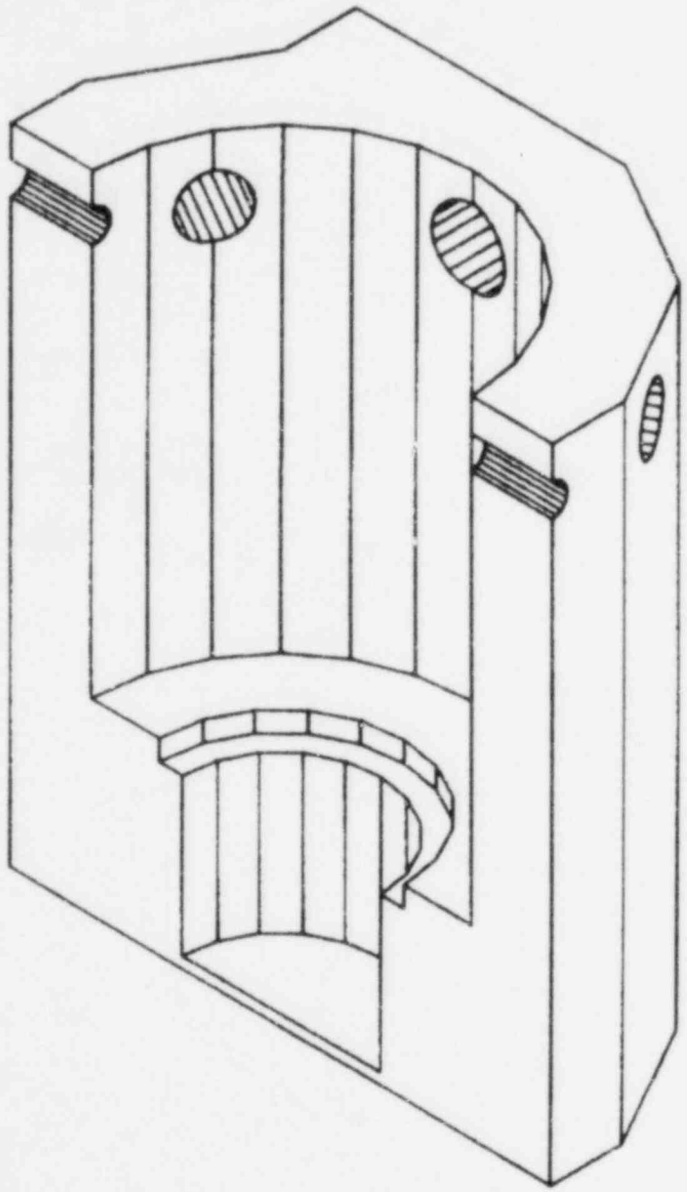

Figure A-2. Three-Dimensional View of Reactor Vessel Without Skirt or Nozzle Support

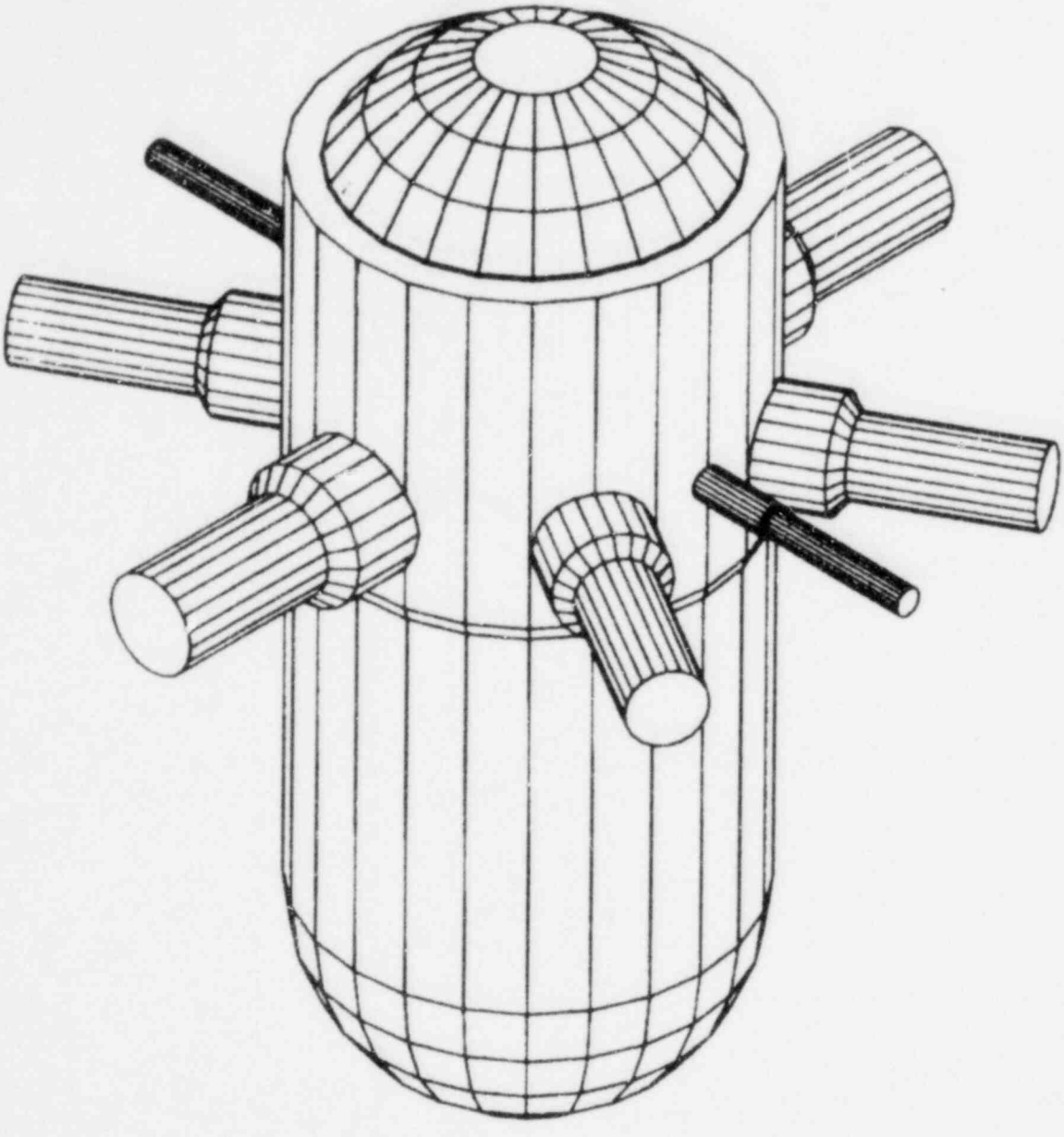

Figure A-3. Volumetric Nodes Above Nozzles in Reactor Vessel Cavity

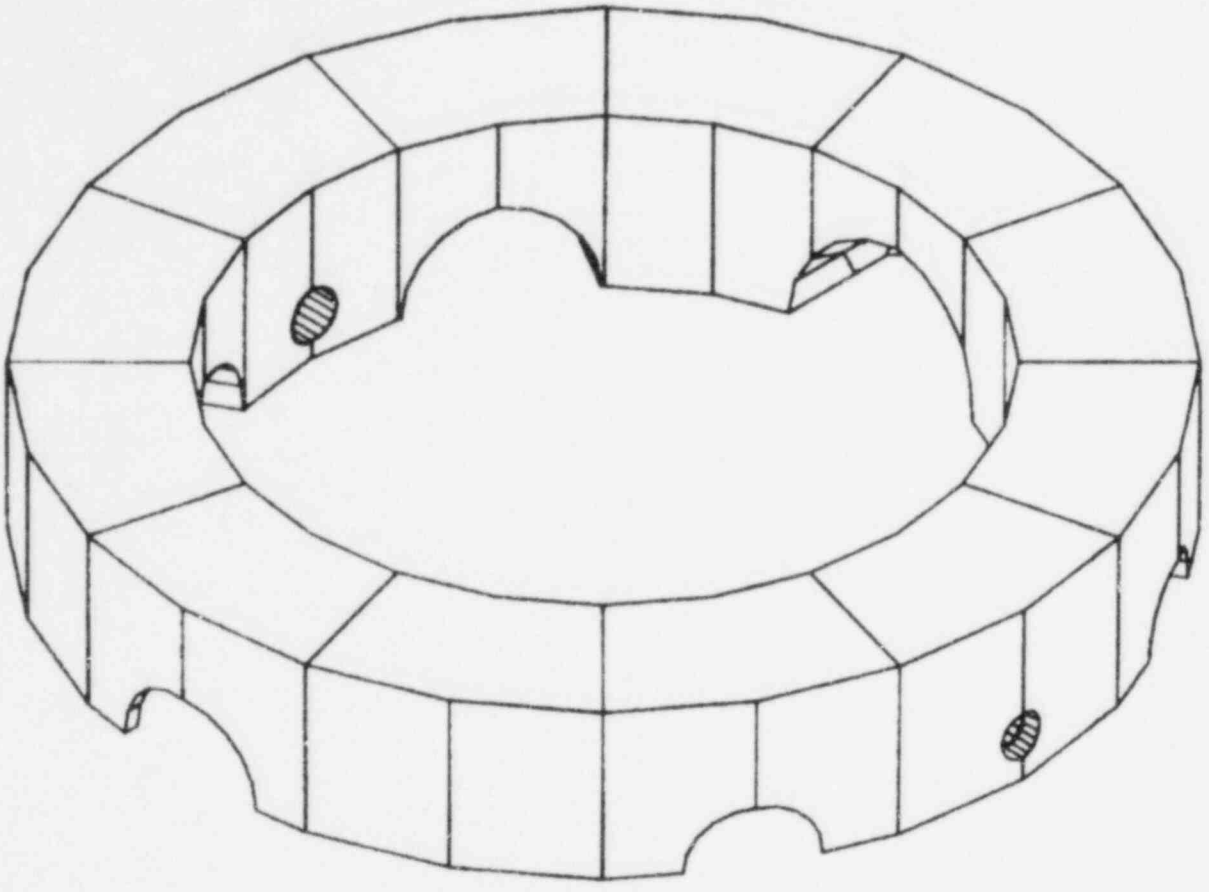

Figure A-4. Volumetric Nodes Below Nozzles in Reactor Vessel Cavity

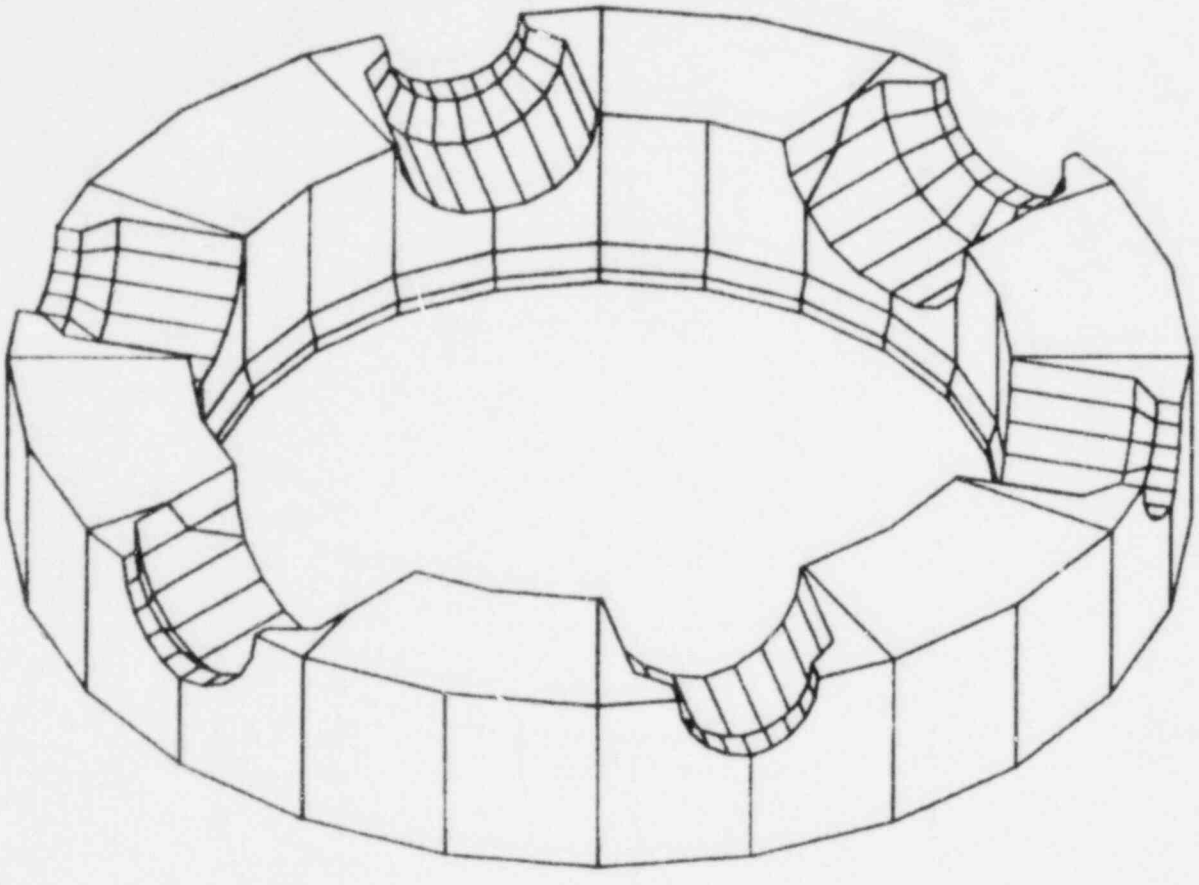

Figure A-5. Annular Nodes Below Nozzles, Level 3

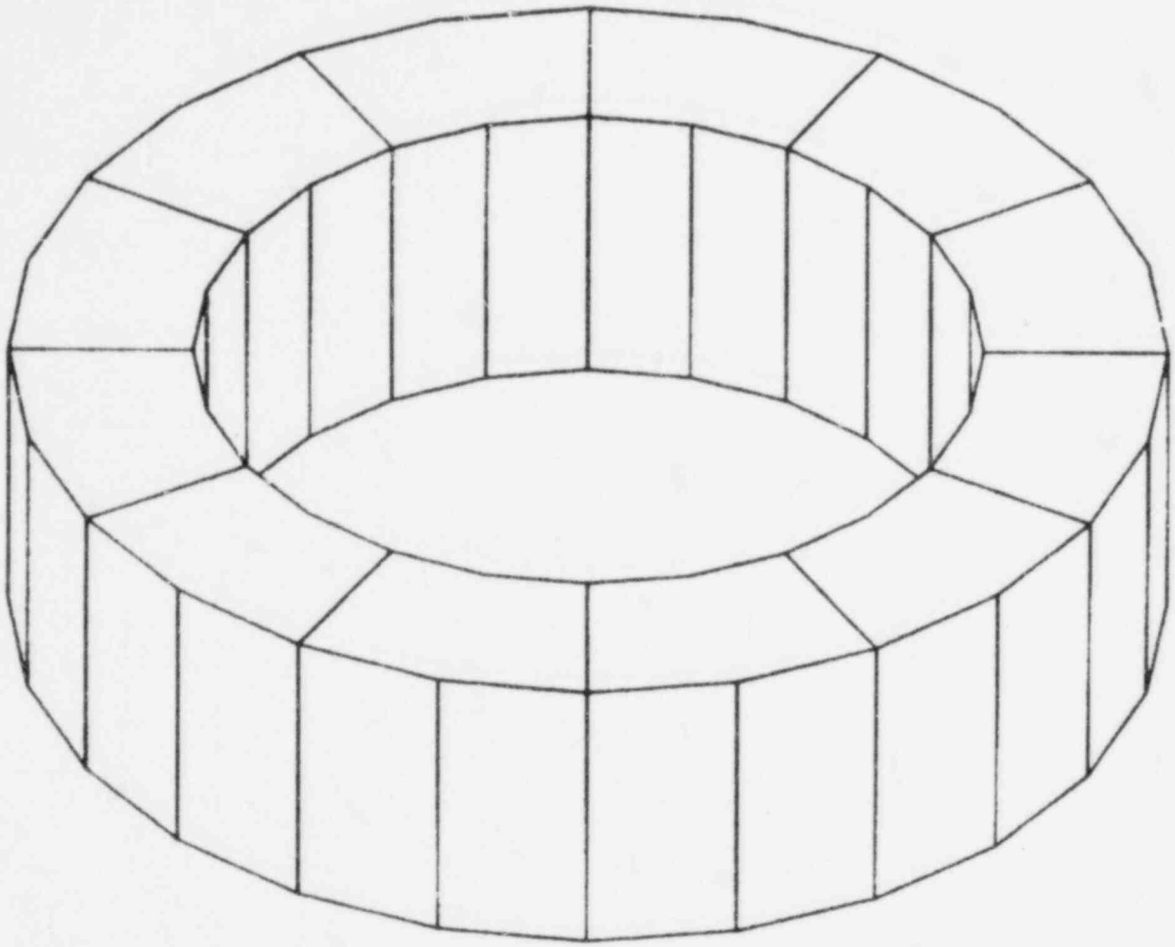

Figure A-6. Annular Nodes Below Nozzles, Level 2

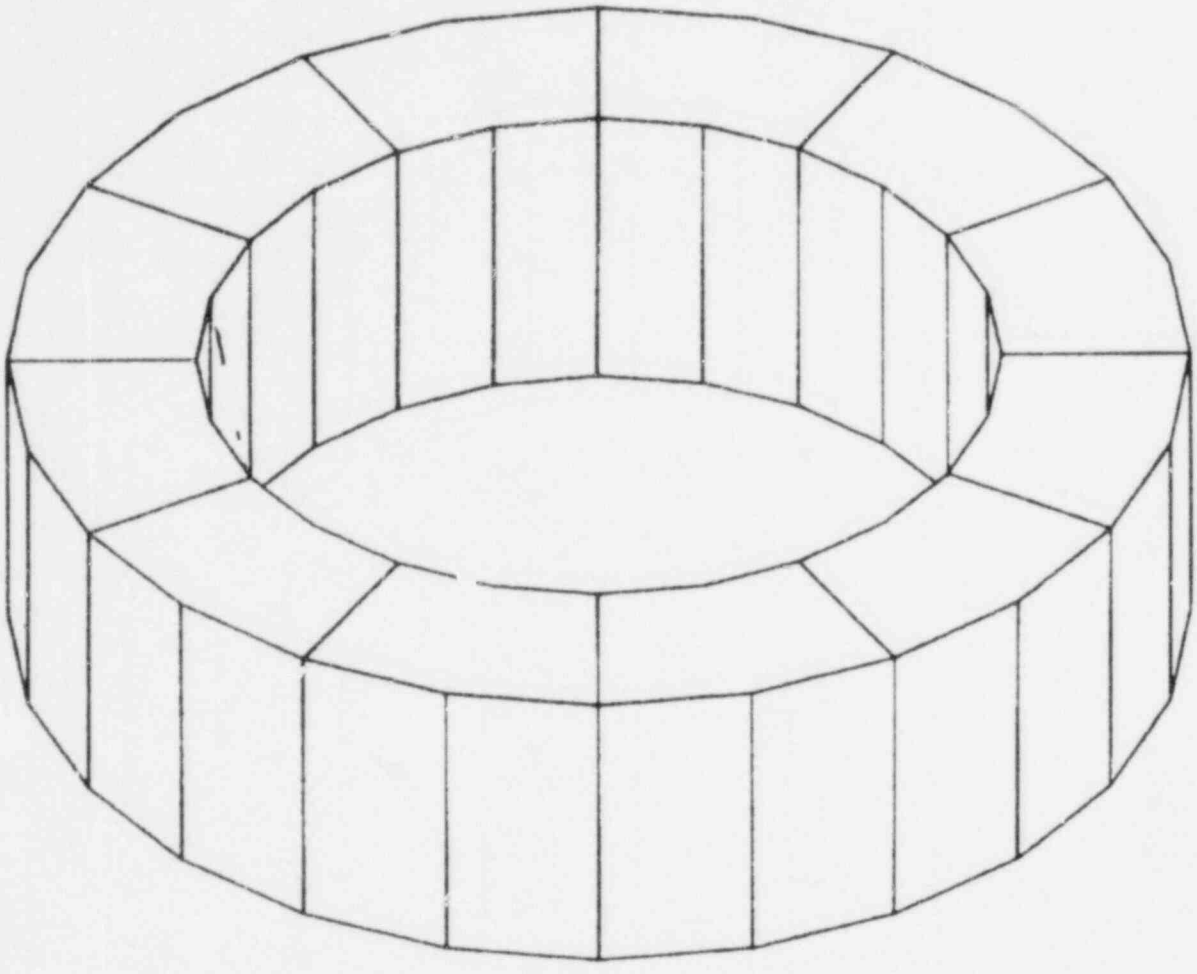

Figure A-7. Annular Nodes Below Nozzles, Level 1

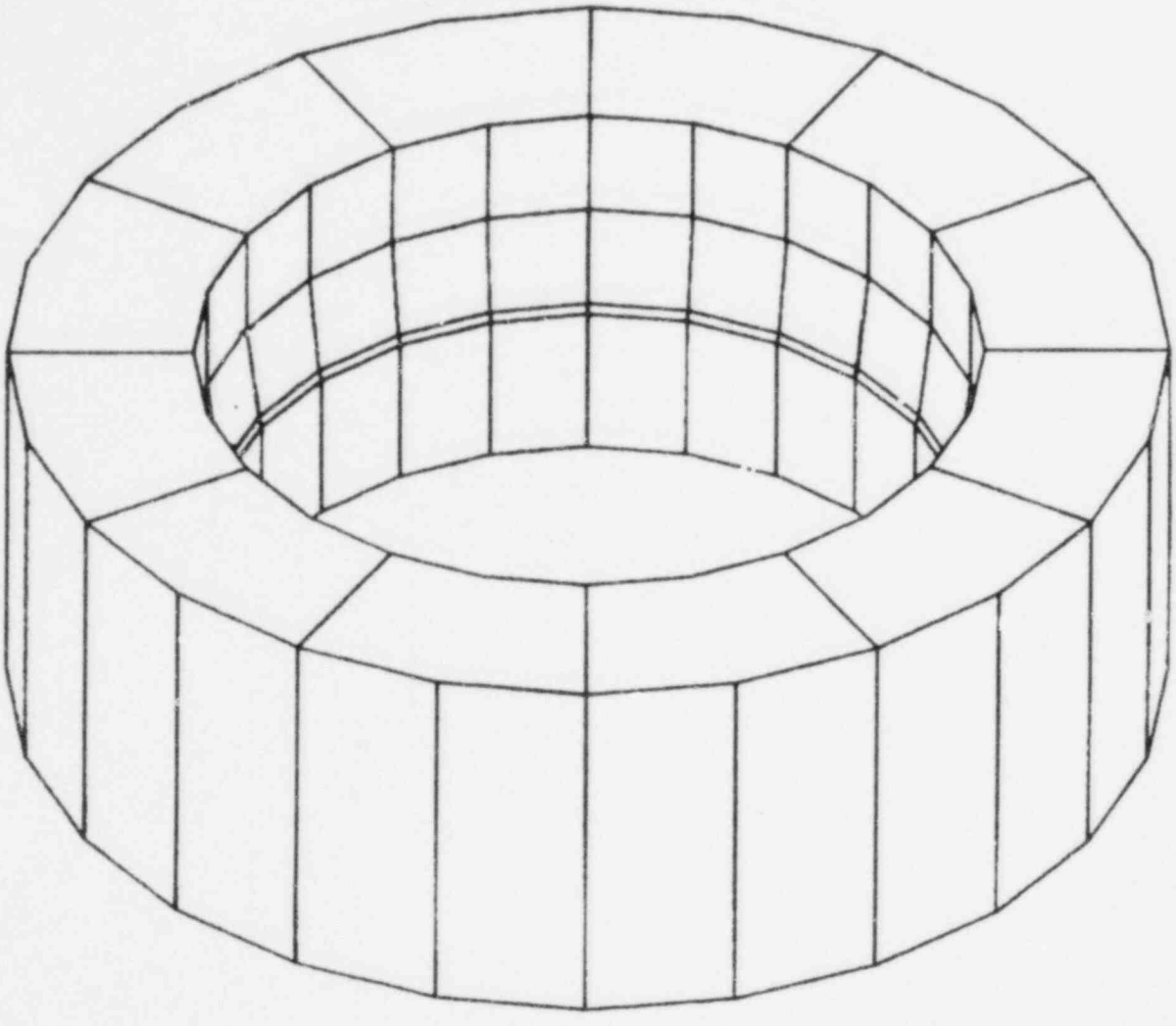

Figure A-8. Volumetric Nodes Below Reactor Vessel

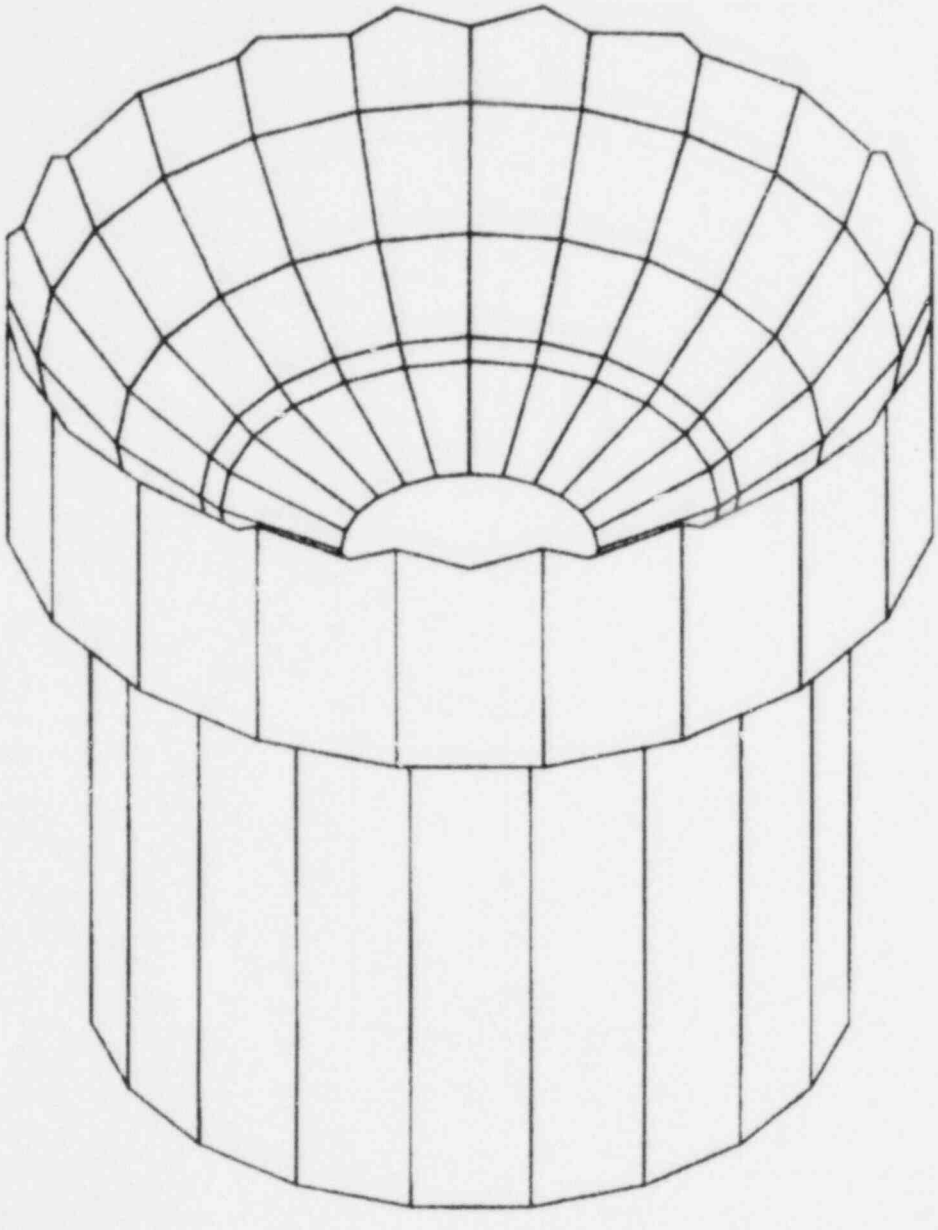

Figure A-9. Detailed Noding of Volumet.ic Nodes and Penetrations

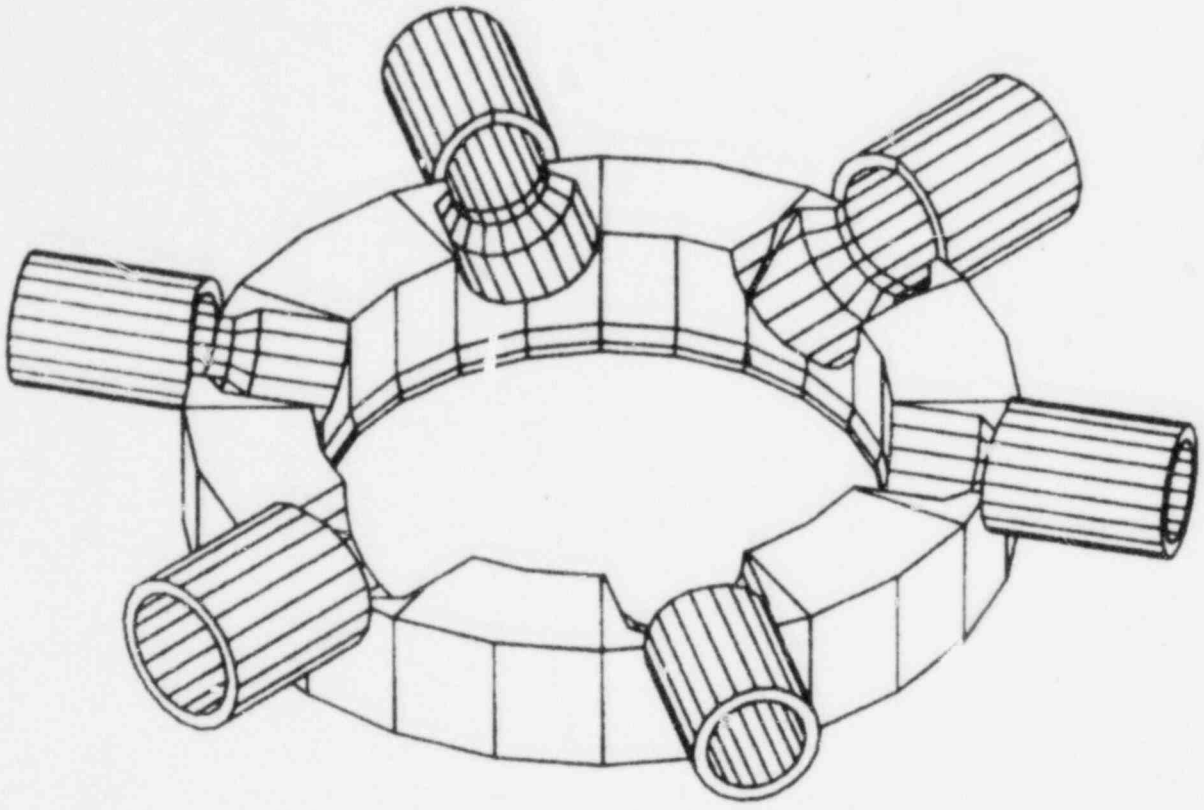

Figure A-10. Specific Modeling of Subcompartment Node and Penetration

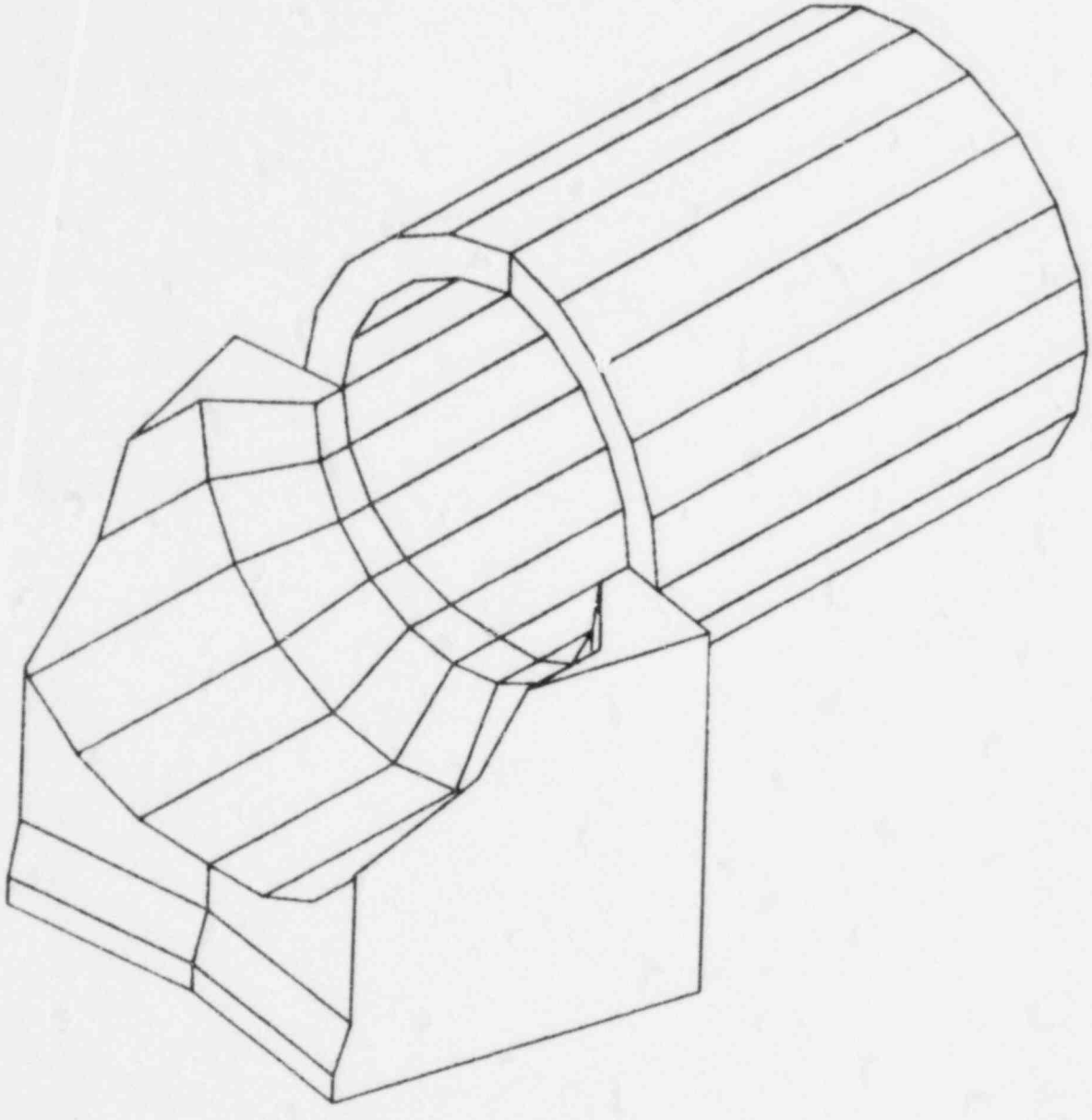

Figure A-11. Model of Core Flood Penetration

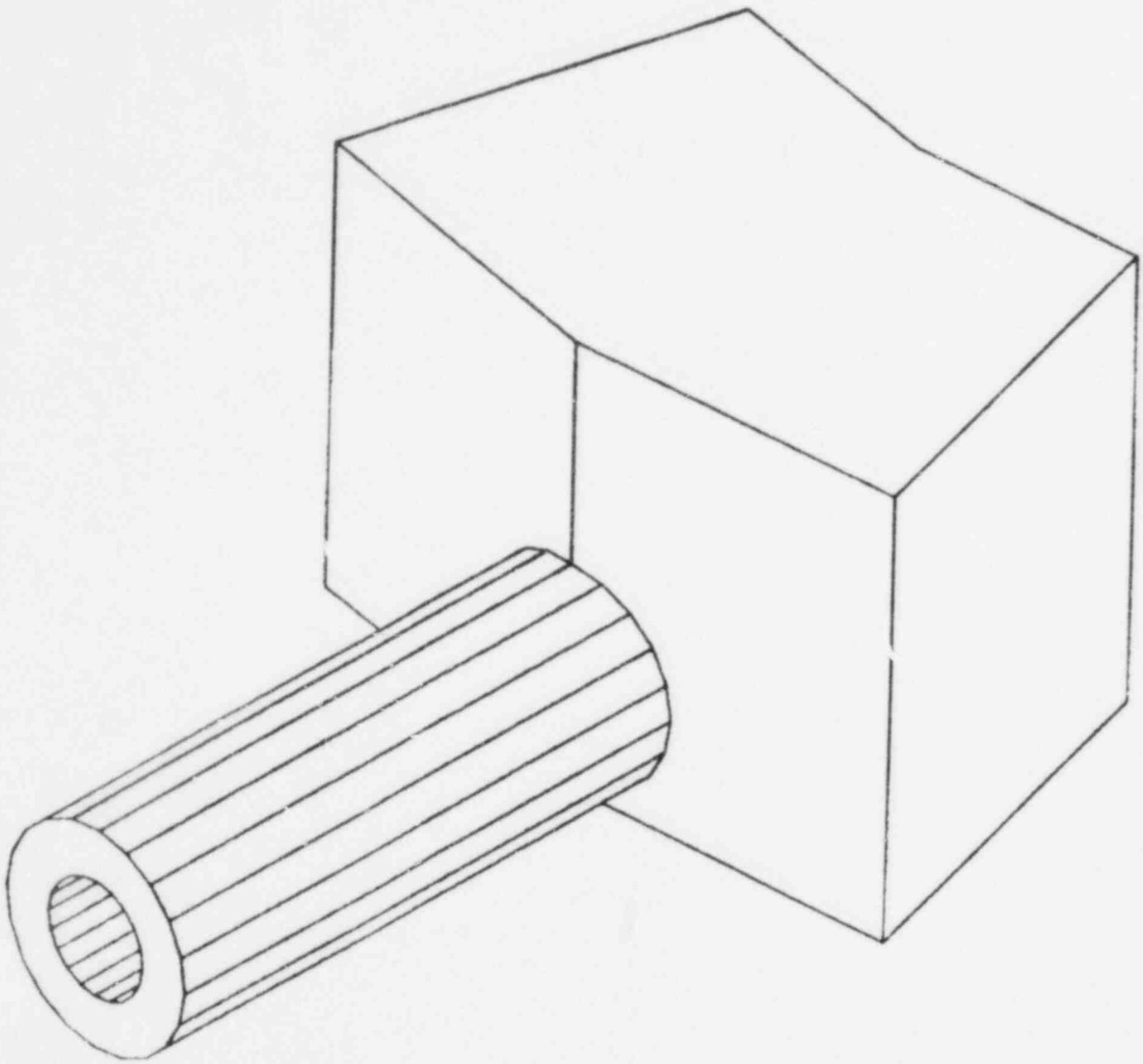

APPENDIX B
Pipe Whip Analytical Model Description

1. Introduction

This appendix briefly describes the unique plant pipe whip analytical models that were used in determining the break opening area time histories. The following models were used in determining the effects of pipe breaks on the equipment within the reactor vessel subcompartment:

Oconee 1, 2, and 3	Hot leg model Cold leg model
TMI-1	Hot leg model
TMI-2	Hot leg model
ANO-1 and Crystal River 3	Hot leg model
Rancho Seco	Hot leg model
Davis-Besse 1	Hot leg model Cold leg model

2. Oconee Hot Leg Model

The Oconee hot leg model is illustrated in Figure B-1. Restraint 2 was modeled by a number of ANSYS STIF40 elements to include both compressive and bilinear tensile spring rates.

Restraint 1 has sliding possiblities at either the hot leg or the steam generator. However, calculations established that the sliding would not occur at the steam generator. Consequently, the modeling was achieved with STIF52 elements for the elements adjoining the hot leg, with gaps to represent the clearance between the restraint and the steam generator. These elements were then connected to the steam generator by STIF40 elements. Both transverse and axial spring rates were modeled by modifying the coefficients of friction.

3. Oconee Cold Leg Model

The Oconee cold leg model is illustrated in Figure B-9. ANSYS STIF40 elements were used to represent the various effects of such restraints as the primary shield wall, turnbuckle and snubbers.

4. TMI-1 Hot Leg Model

The model of the hot leg piping consisted of ANSYS elements STIF20 and STIF60. Pipe whip restraints at the appropriate locations were modeled using STIF40 elements, as illustrated in Figure B-2.

The restraint U-bar (restraint 1) was modeled as seven independent gapped springs at the elevations listed in Table B-1. Nonlinearities of the U-bar were modeled by using three STIF40s in parallel for each U-bar. U-bar restraint 2 was modeled in a similar fashion. The collar restraint was modeled so that it would be active in either tension or compression. Results showed that only U-bar restraint 1 was impacted; neither the U-bar restraint 2 nor the collar restraint was active during the transient.

5. TMI-2 Hot Leg Model

The hot leg piping model consists of the ANSYS elements STIF20 and STIF60. Pipe whip restraints at the appropriate locations were modeled using STIF40 elements, as illustrated in Figure B-3.

Test runs were made to attempt to distribute the load throughout the restraint by modeling the restraint load distribution plate. U-bar compressive strength was restricted. Calculational results showed that the clips failed in less than a millisecond, and thus the distribution effect was negligible. The restraint was then modeled as seven independent gapped springs at the elevations listed in Table B-2. Nonlinearities of the U-bar were modeled by using three STIF40s in parallel for each U-bar.

Results showed that only U-bar restraint 1 was impacted; neither U-bar restraint 2 nor the penetration wall was active during the transient.

6. ANO-1 and Crystal River 3 Hot Leg Model

Pipe whip analyses for breaks in ANO-1 and Crystal River 3 hot legs have been performed using the models illustrated in Figures B-4 and B-5. The manner in which the restraints were modeled is described here.

6.1. ANO-1

Gaps, masses, and stiffnesses were modeled; the nonlinearity of the restraint was simulated by a number of ANSYS STIF40 elements in parallel.

6.2. Crystal River 3

The hot leg model for Crystal River was identical to that for ANO-1 except for the restraints. For restraints 1 and 2, all the U-bars were modeled separately; for restraint 3, the upper three and lower two U-bars were each modeled by one equivalent U-bar. The stiffness and mass were distributed accordingly. At other locations, properties of the entire restraints were scaled

equally for each U-bar. The nonlinearity was modeled by a number of ANSYS STIF40 elements for each U-bar. The load distribution plate between the U-bars was not modeled for the following reasons:

1. Close spacing of U-bars dictates that when the lower bars are impacted, the load distribution within them will not be significantly affected.
2. Although a stable solution can be reached, modeling the plate would require an extremely small time step, making the run time prohibitively long.

7. Rancho Seco Hot Leg Model

The Rancho Seco hot leg model is illustrated in Figure B-6. All restraints were modeled by a number of STIF40 elements to represent the multilinear stiffnesses of the restraints.

8. Davis-Besse 1 Hot Leg Model

The Davis-Besse 1 hot leg model is illustrated in Figure B-7. The hot leg LOCA ring was modeled with an ANSYS STIF52 element in series with several STIF40s in parallel. The elbow strap and horizontal LOCA rings were modeled using STIF40s in parallel. Spring rate nonlinearities are accounted for by using the STIF40 systems, and appropriate joints are rotated to satisfy ANSYS input requirements.

Table B-3 lists the hot leg model restraints, element types used, and transient status. Table B-4 provides coordinates for the centerline of all hot leg restraints.

9. Davis-Besse 1 Cold Leg Model

The Davis-Besse 1 cold leg model is illustrated in Figure B-8. The cold leg LOCA ring and the cold leg discharge restraint were modeled with a STIF52 in series with several STIF40s in parallel. STIF52 is a friction element to absorb energy and restrict the break opening area.

Wire rope restraints were modeled to be active only in tension using STIF40s. Wire ropes were located for restraining the pump in both the horizontal and vertical directions. The lower cold leg also had wire rope restraints modeled similarly.

Table B-5 lists the cold leg model restraints, element types used, and transient status. Table B-6 provides coordinates for the nodes along the centerline of all restraints.

Nonlinearities on the restraints were simulated with a number of ANSYS STIF40 elements in parallel.

Some of the model joints were rotated to apply the correct force component results on the restraint. For example, wire ropes only take tensile force along the axis of the rope.

Table B-1. TMI-1 Hot Leg Model — U-Bar Elevations for Hot Leg Restraints

U-bar No.	Joint No.	Elevation above RV nozzle belt, in.
1	300	43.50
2	301	55.5
3	302	79.5
4	303	91.5
5	304	103.5
6	305	115.5
7	306	127.5

Table B-2. TMI-2 Hot Leg Model — U-Bar Elevations for Hot Leg Restraints

U-bar No.	Joint No.	Elevation above RV nozzle belt, in.
1	300	43.5
2	301	59.0
3	302	74.5
4	303	90.0
5	304	105.5
6	305	121.0
7	306	136.5

Table B-3. Davis-Besse 1 Hot Leg Model — Pipe Whip Elements

Bars J1	Bars J2	Element	Restraint	Status[a]
601	605	STIF40	Hot leg LOCA ring	A (RV)
605	606	STIF52	Hot leg LOCA ring	A (RV)
606	607	STIF52	Hot leg LOCA ring	I
607	608	STIF40	Hot leg LOCA ring	I
611	614	STIF40	Hot leg LOCA ring	I
614	615	STIF52	Hot leg LOCA ring	I
615	616	STIF52	Hot leg LOCA ring	I
616	617	STIF40	Hot leg LOCA ring	I
56	620	STIF40	Hot leg elbow strap	A (RV, el)
622	621	STIF40	(Jt 622, 620 coupled)	A (RV, el)
628	629	STIF40	Hot leg horiz. ring 1	A (RV, el)
629	630	STIF40	Hot leg horiz. ring 1	A (RV, el)
638	641	STIF40	Hot leg horiz. ring 2	I
641	642	STIF52	Hot leg horiz. ring 2	I
642	643	STIF52	Hot leg horiz. ring 2	I
643	644	STIF40	Hot leg horiz. ring 2	I

[a] A: active, I: inactive, RV: active for RV break, el: active for elbow break.

Table B-4. Davis-Besse 1 Hot Leg Model Coordinates[a]

Joint	X	Y	Z
606	0.0	0.0	180.0
615	0.0	0.0	180.0
56	0.0	17.5736	246.4264
628	0.0	88.0	264.0
642	0.0	794.0625	264.0

[a] 0.0, 0.0, 0.0 represents the center of the reactor vessel at the nozzle elevation.

Table B-5. Davis-Besse 1 Cold Leg Model — Pipe Whip Elements

Bars J1	Bars J2	Element	Restraint	Status[a]
651	652	STIF40	Cold leg LOCA ring	A (RV)
652	653	STIF52	Cold leg LOCA ring	A (RV)
653	654	STIF52	Cold leg LOCA ring	I
654	655	STIF40	Cold leg LOCA ring	I
658	657	STIF40	Cold leg LOCA ring	A (RV)
657	656	STIF52	Cold leg LOCA ring	A (RV)
669	668	STIF40	Cold leg discharge restraint	I
668	665	STIF52	Cold leg discharge restraint	I
665	666	STIF52	Cold leg discharge restraint	A (el)
666	667	STIF40	Cold leg discharge restraint	A (el)
662	661	STIF40	Cold leg discharge restraint	I
661	670	STIF52	Cold leg discharge restraint	I
670	663	STIF52	Cold leg discharge restraint	I
663	664	STIF40	Cold leg discharge restraint	I
733	732	STIF40	Coolant pump restr, el. 576'-9"	A (el, RV)
730	731	STIF40	Coolant pump restr, el. 576'-9"	I
753	732	STIF40	Coolant pump restr, el. 583'-4"	A (el, RV)
750	751	STIF40	Coolant pump restr, el. 583'-4"	I
810	811	STIF40	Cold leg suction wire	I
813	812	STIF40	Rope restraint	I
771	772	STIF40	Coolant pump	I
774	775	STIF40	Vertical restraint	I

(a) A: active, I: inactive, RV: active for RV break, el: active for elbow break.

Table B-6. Davis-Besse 1 Cold Leg Model Coordinates[a]

Joint	X	Y	Z
653	-108.1873	0.0	108.1873
656	-108.1873	0.0	108.1873
670	-152.0002	24.8501	177.0794
665	-152.0002	24.8501	177.0794
813	-107.8202	-27.0	321.75
810	-107.8202	-27.0	321.75
733	-158.0496	69.00	292.7500
730	-158.0496	69.00	292.7500
753	-158.0496	148.0	292.7500
750	-158.0496	148.0	292.7500
773	-158.0496	57.0	292.75
770	-158.0496	57.0	292.75

[a] 0.0, 0.0, 0.0 represents the center of the reactor vessel at the nozzle elevation.

Figure B-1. Oconee Hot Leg Mathematical Model

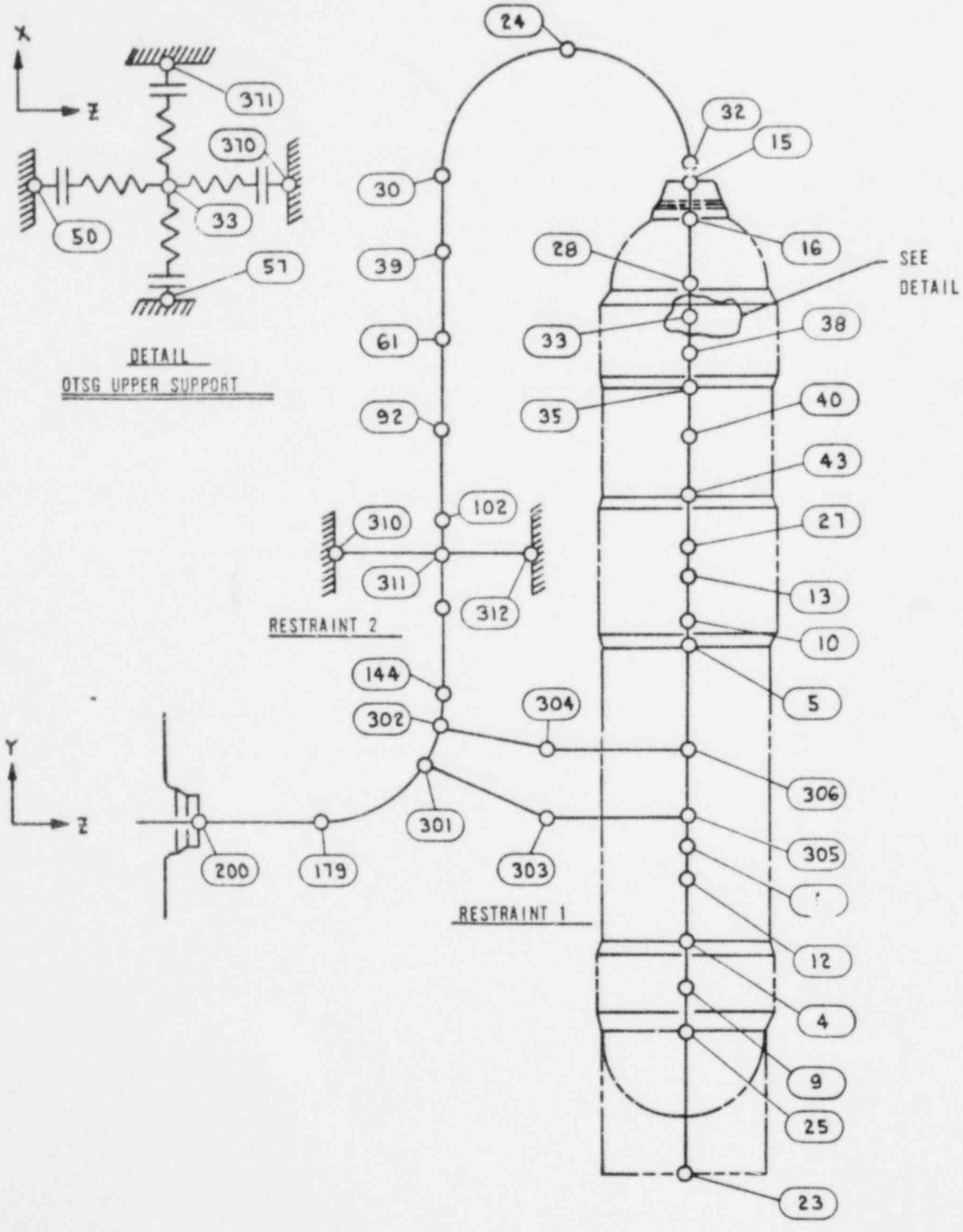

Figure B-2. TMI-1 Hot Leg Mathematical Model

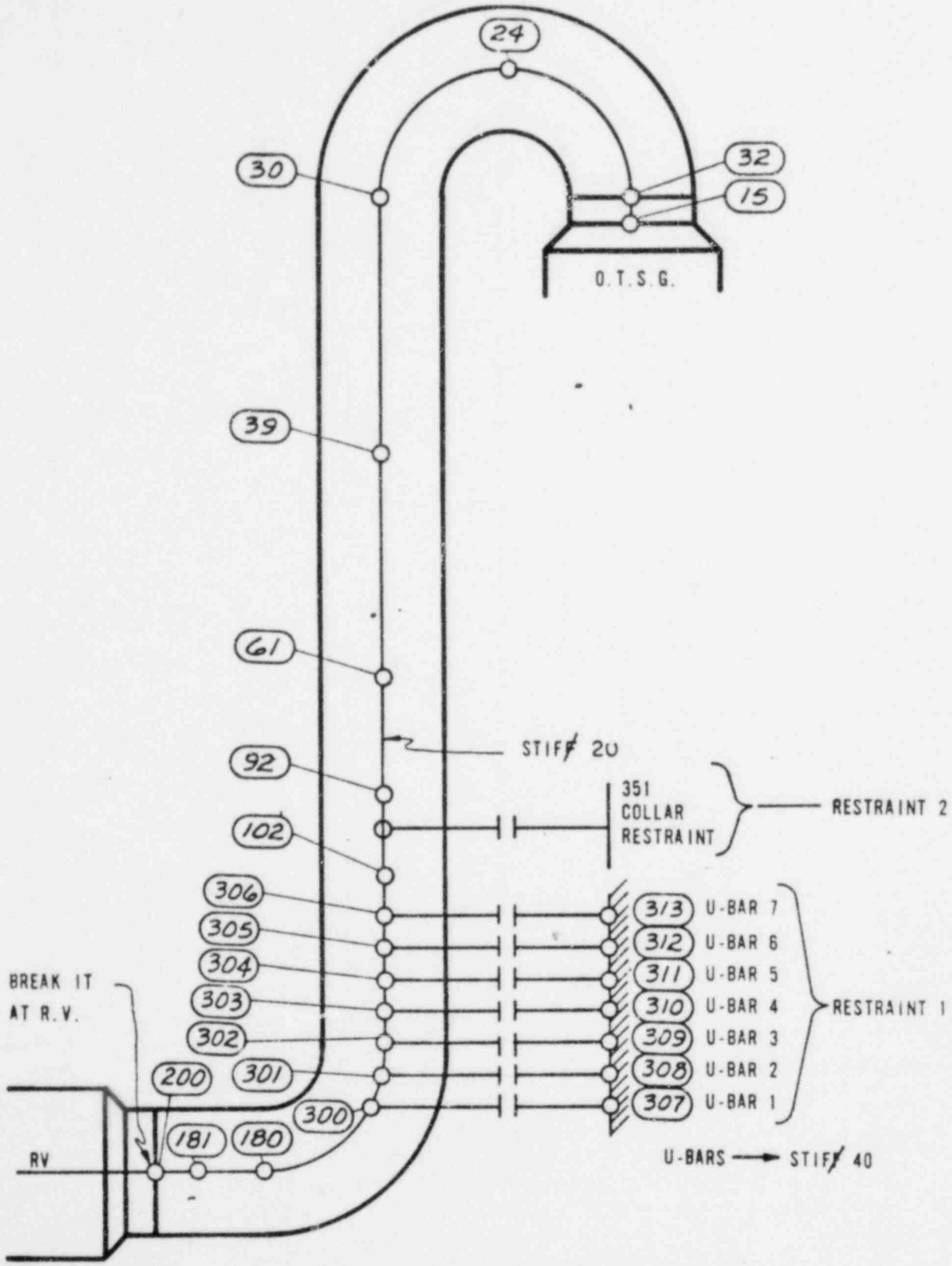

Figure B-3. TMI-2 Hot Leg Mathematical Model

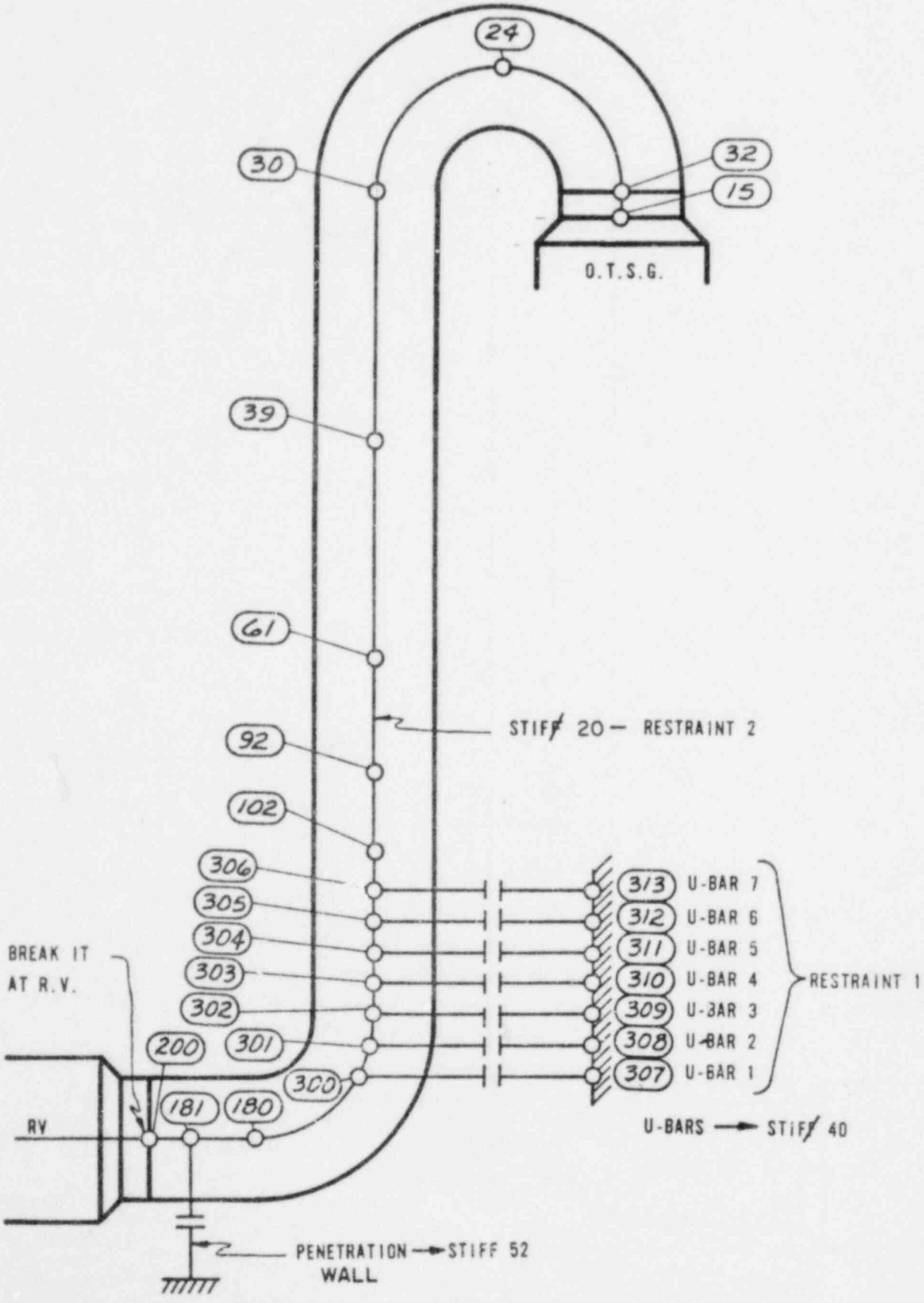

Figure B-4. Hot Leg Model for ANO-1

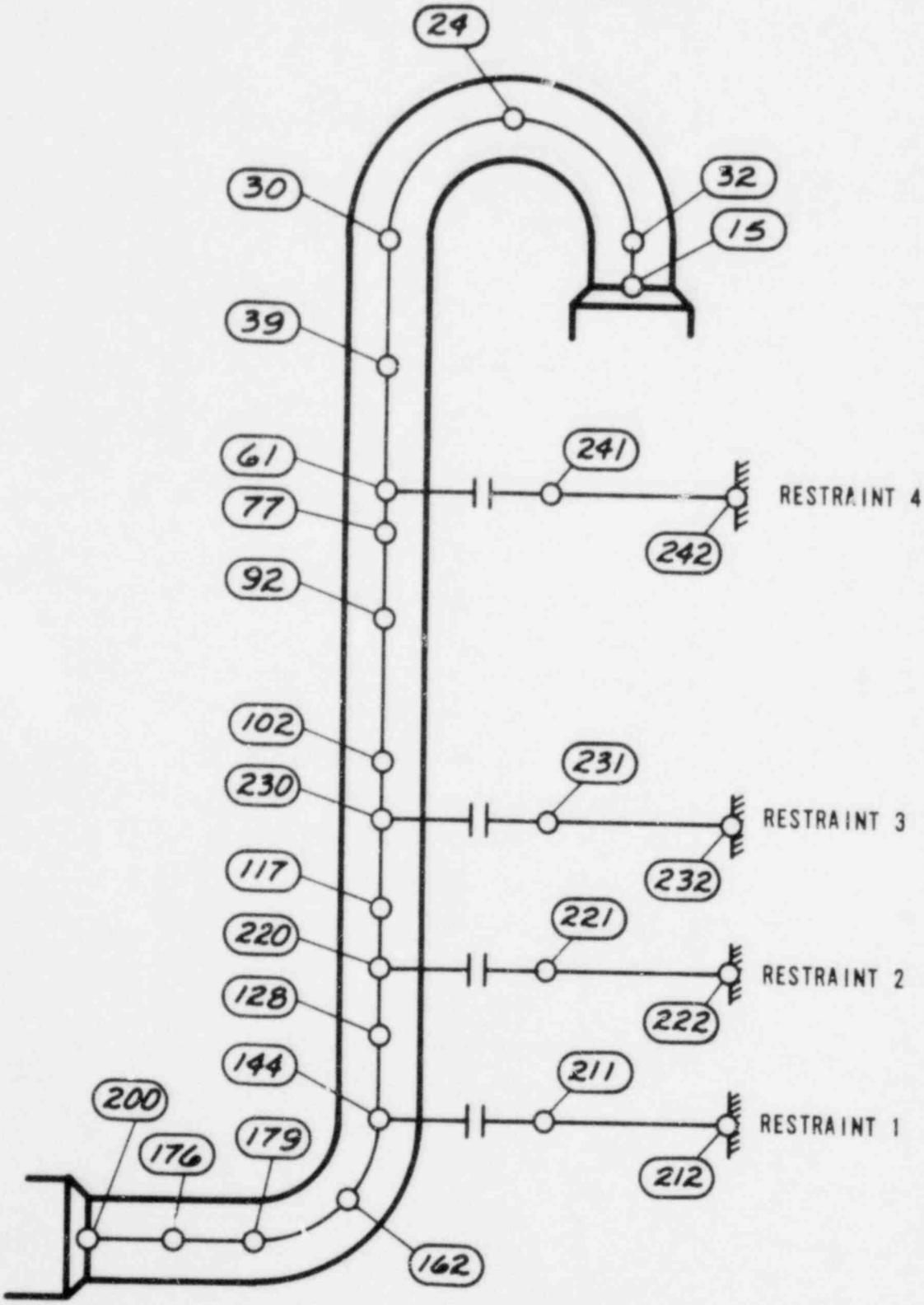

Figure B-5. Hot Leg Model for CR-3

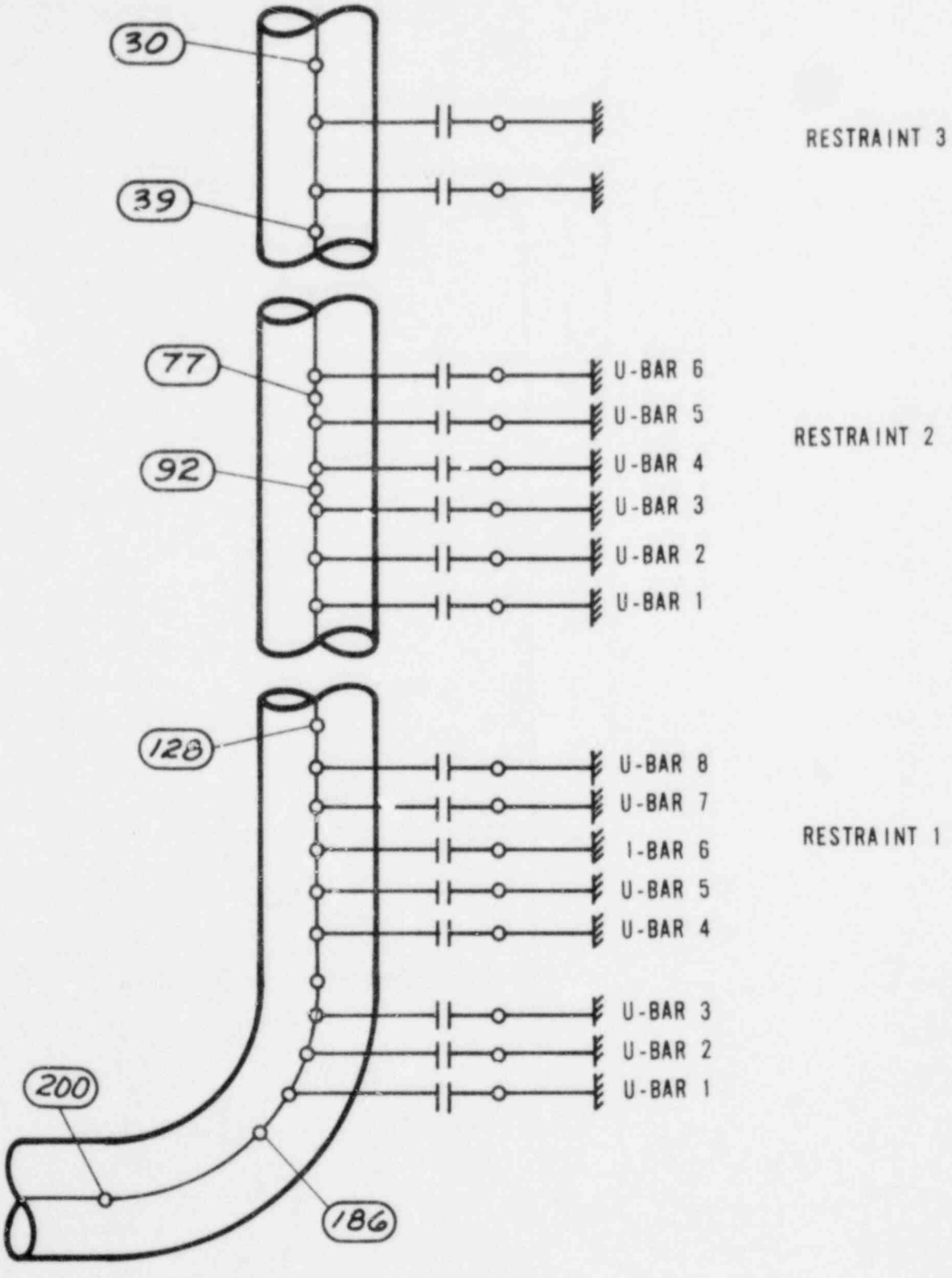

Figure B-6. Hot Leg Model for Rancho Seco

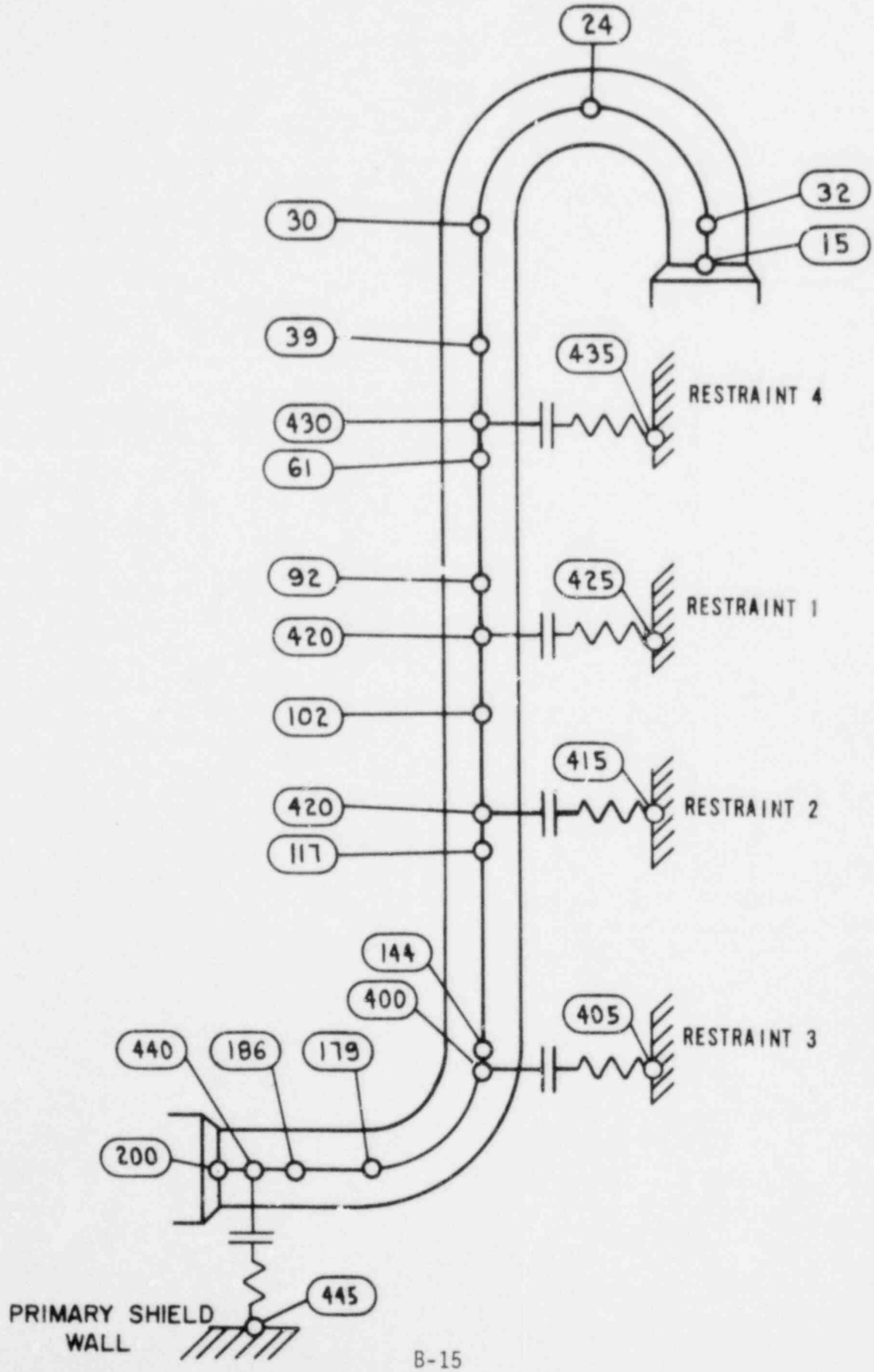

Figure B-7. Davis-Besse 1 Hot Leg Model

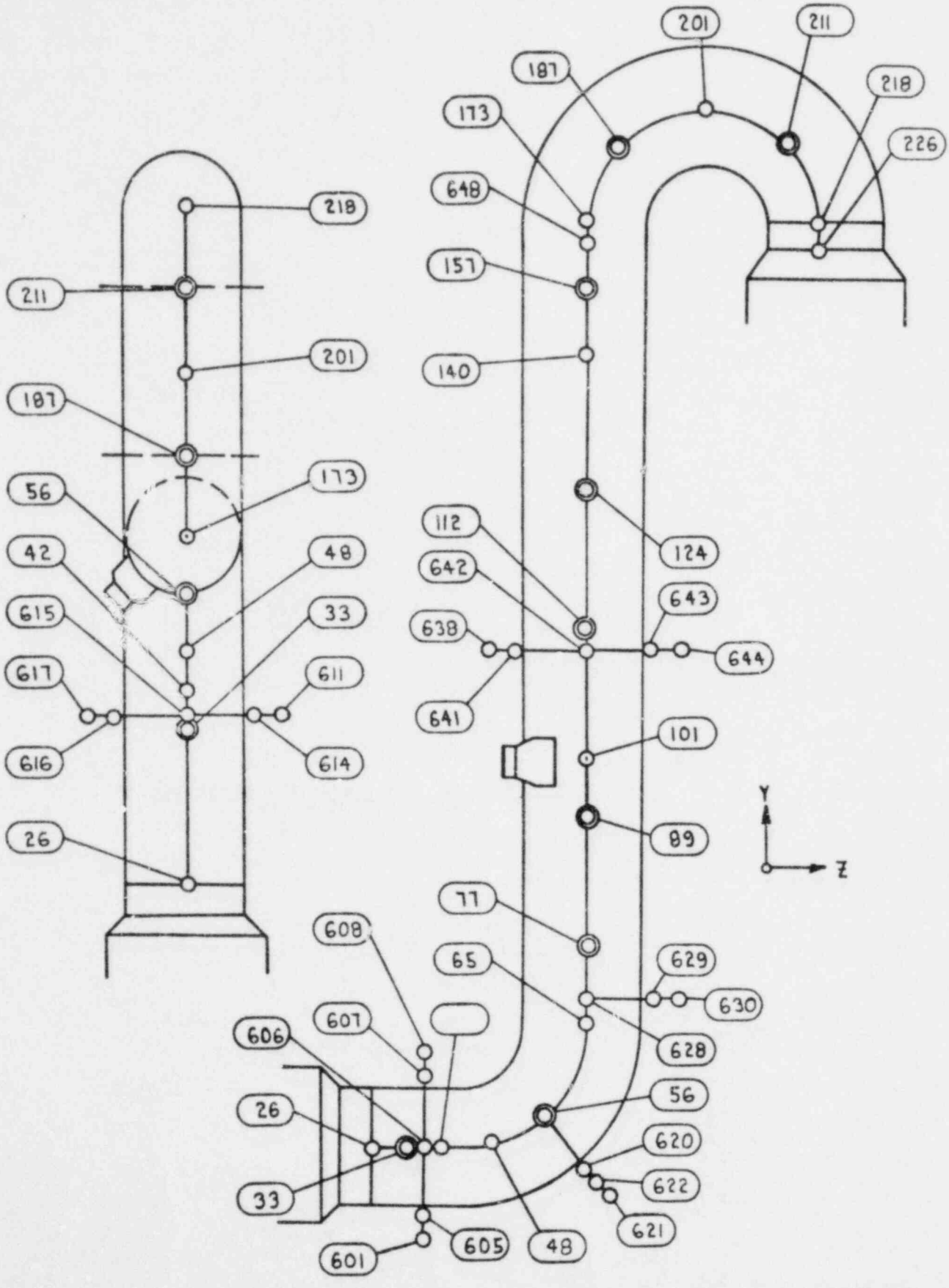

Figure B-8. Davis-Besse 1 Cold Leg Model

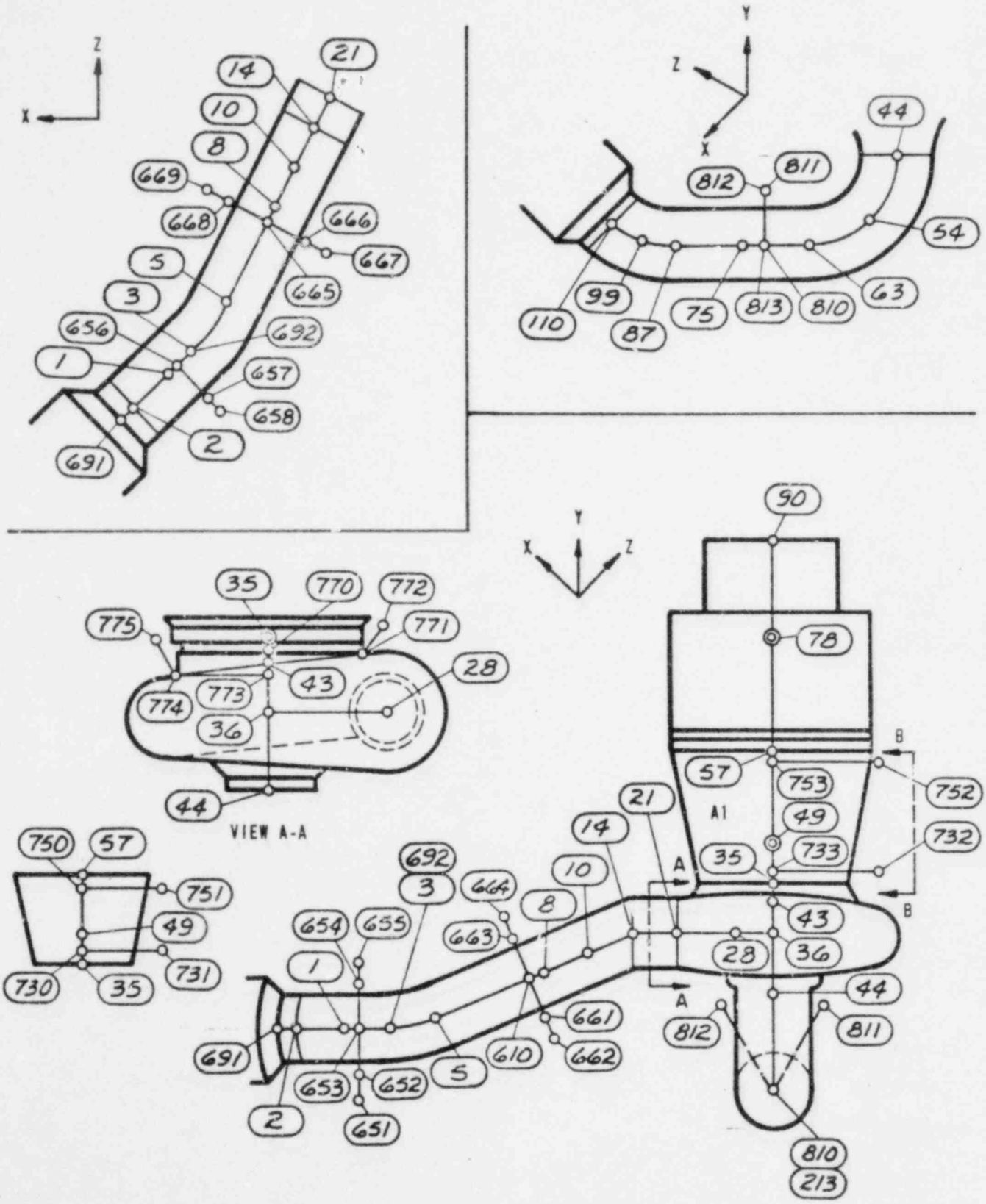

Figure B-9. Oconee Cold Leg Mathematical Model

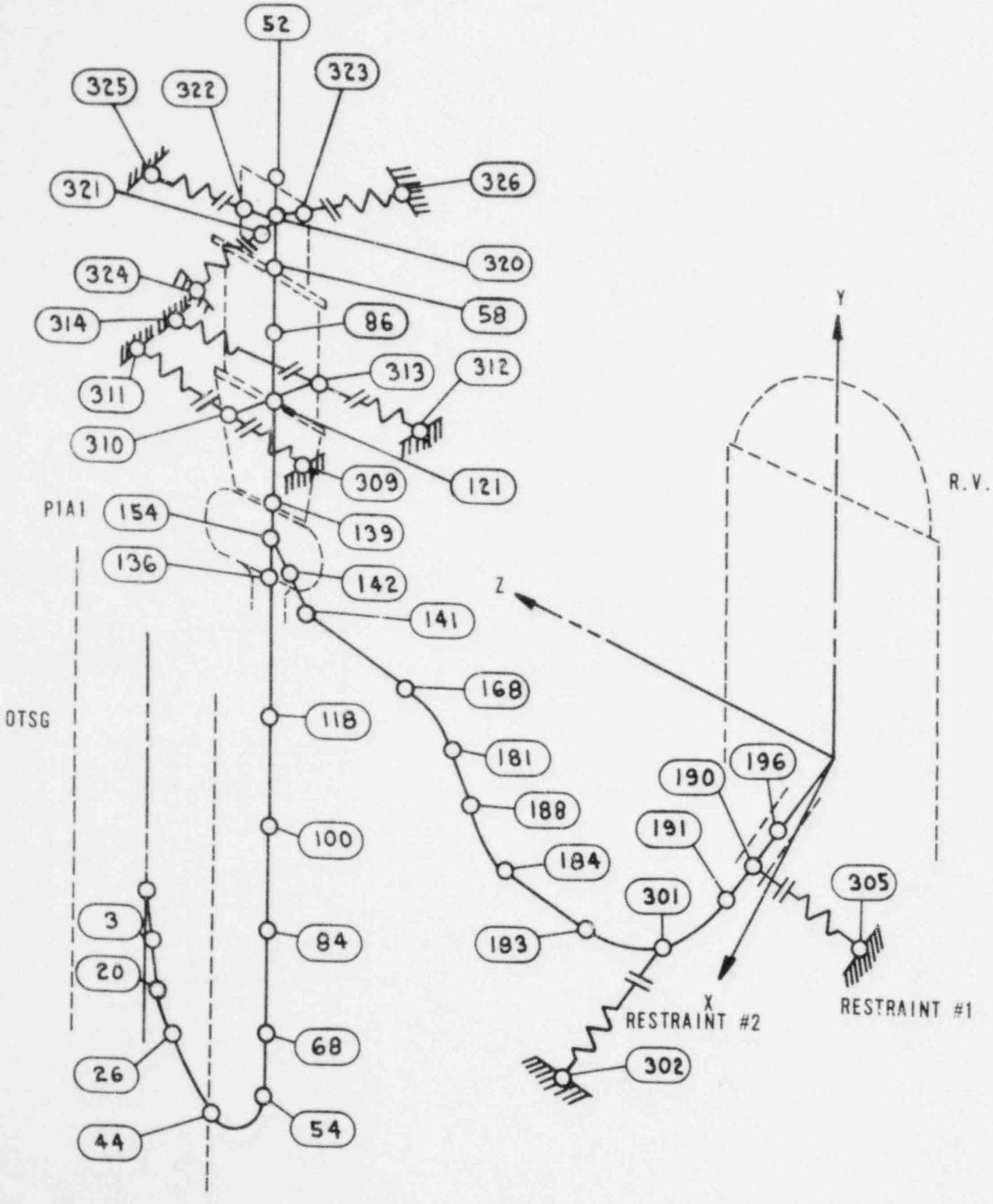

APPENDIX C
Reactor Internals Pressure Models

1. Introduction

For analysis of the internals on both skirt- and nozzle-supported plants, the transient differential pressure on the reactor vessel internals was calculated with the CRAFT2 computer code for a spectrum of pipe breaks.

2. Generic 177-FA Skirt-Supported Plants

The reactor vessel and the reactor coolant piping are hydrodynamically equivalent for all of the 177-FA skirt-supported plants. Therefore, a generic CRAFT2 model was developed to calculate the RV internals LOCA pressure differentials.

The noding diagrams for the steady-state CRAFT2 model are shown in Figures C-1 through C-7. As shown in these figures, the model incorporates a 12-node circumferential representation in the downcomer and a two-level model in the upper plenum; 10 control volumes in the upper level to accommodate the 10 holes in the plenum cylinder, and a quadrant model in the lower level. The eight vent valves were simulated using the dynamic vent valve model described in reference 5. A generic set of fluid conditions was established to serve as a conservative representation of the fluid conditions present in the 177-FA lowered-loop plants. These conditions are as follows:

Reference core power, MWt	2560
T_{inlet}, F	554.0
T_{outlet}, F	604
System mass flow, lbm/h	132×10^6

3. Specific 177-FA Nozzle-Supported Plant

This analysis was performed specifically for Davis-Besse 1. The noding diagrams of the steady-state CRAFT2 model are shown in Figures C-8 through C-11. It can be seen from these figures that the model incorporates quadrant representations of both the downcomer annulus and the upper plenum annulus regions. The four vent valves were simulated using the dynamic vent valve model described in reference 5. The following initial fluid conditions were used in this analysis:

Core power, MWt	2772
T_{inlet}, F	555
T_{outlet}, F	608
System mass flow rate, lbm/h	131×10^6

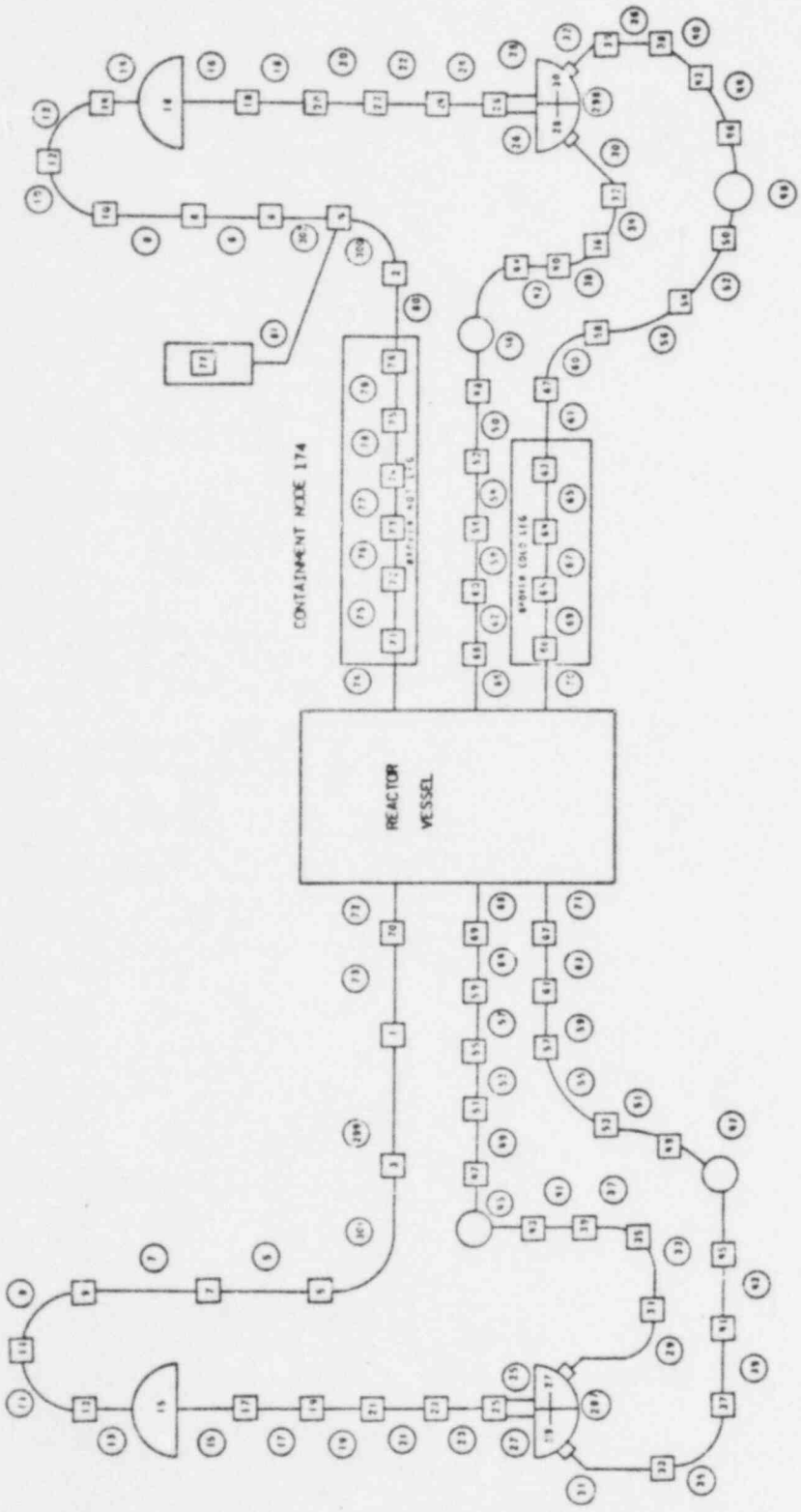

Figure C-1. CRAFT2 Noding Model — 177-FA Skirt-Supported Plant Reactor Coolant Piping and Steam Generator Noding

Figure C-2. CRAFT2 Noding Model — 177-FA Skirt-Supported Plant — Elevation View of Reactor Vessel Control Volumes

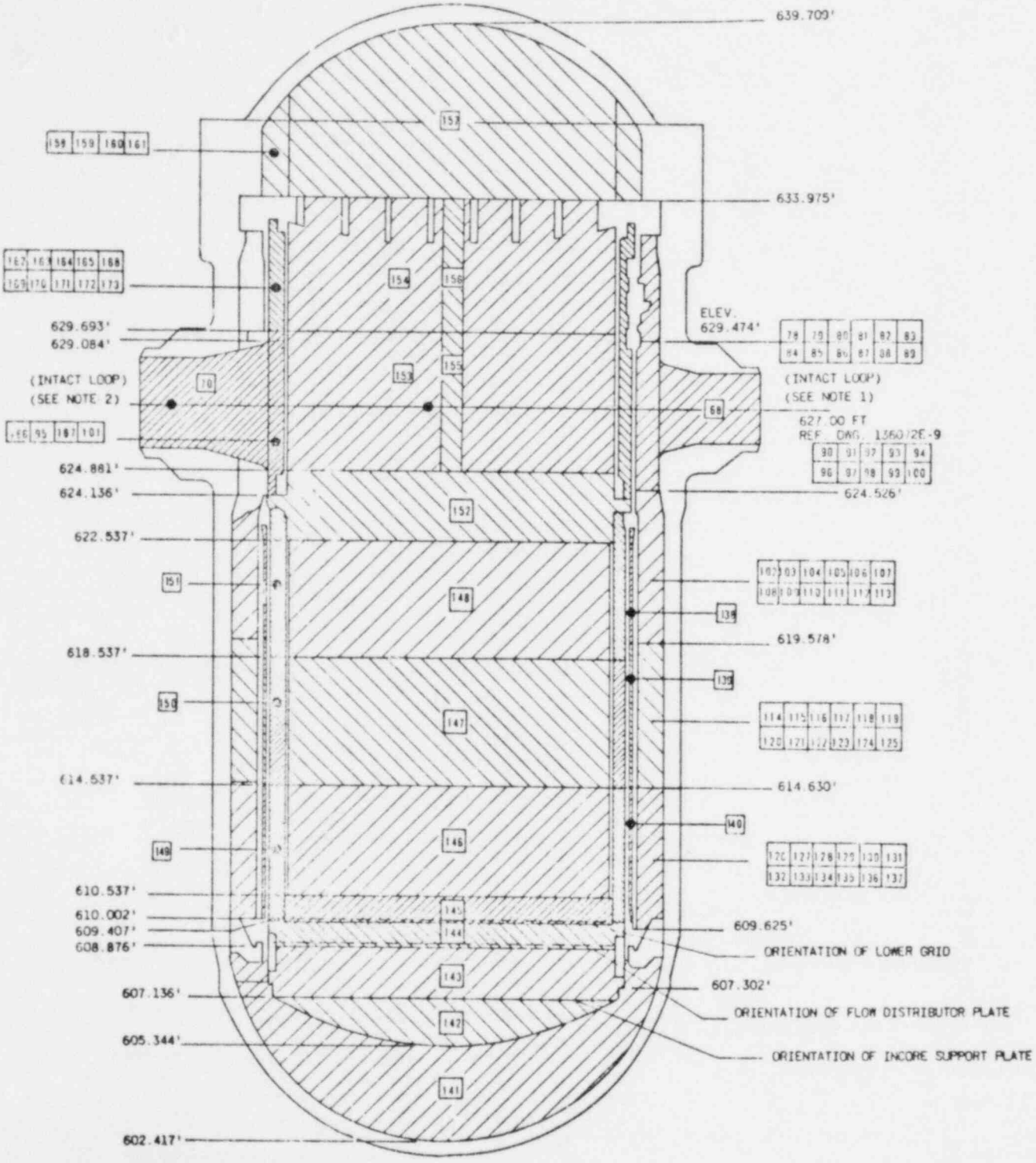

BROKEN LOOP NODING

NOTES: 1. THE RV INLET NOZZLE AT THE BREAK IS DIVIDED INTO FOUR NODES. REFER TO DRAWING OF PIPING NODING.

2. ONE OF THE RV OUTLET NOZZLES IS DIVIDED INTO SIX NODES TO CONSIDER HOT LEG BREAK AT RV.

Figure C-3. CRAFT2 Noding Model — 177-FA Skirt-Supported Plant — 58-Control Volume Downcomer

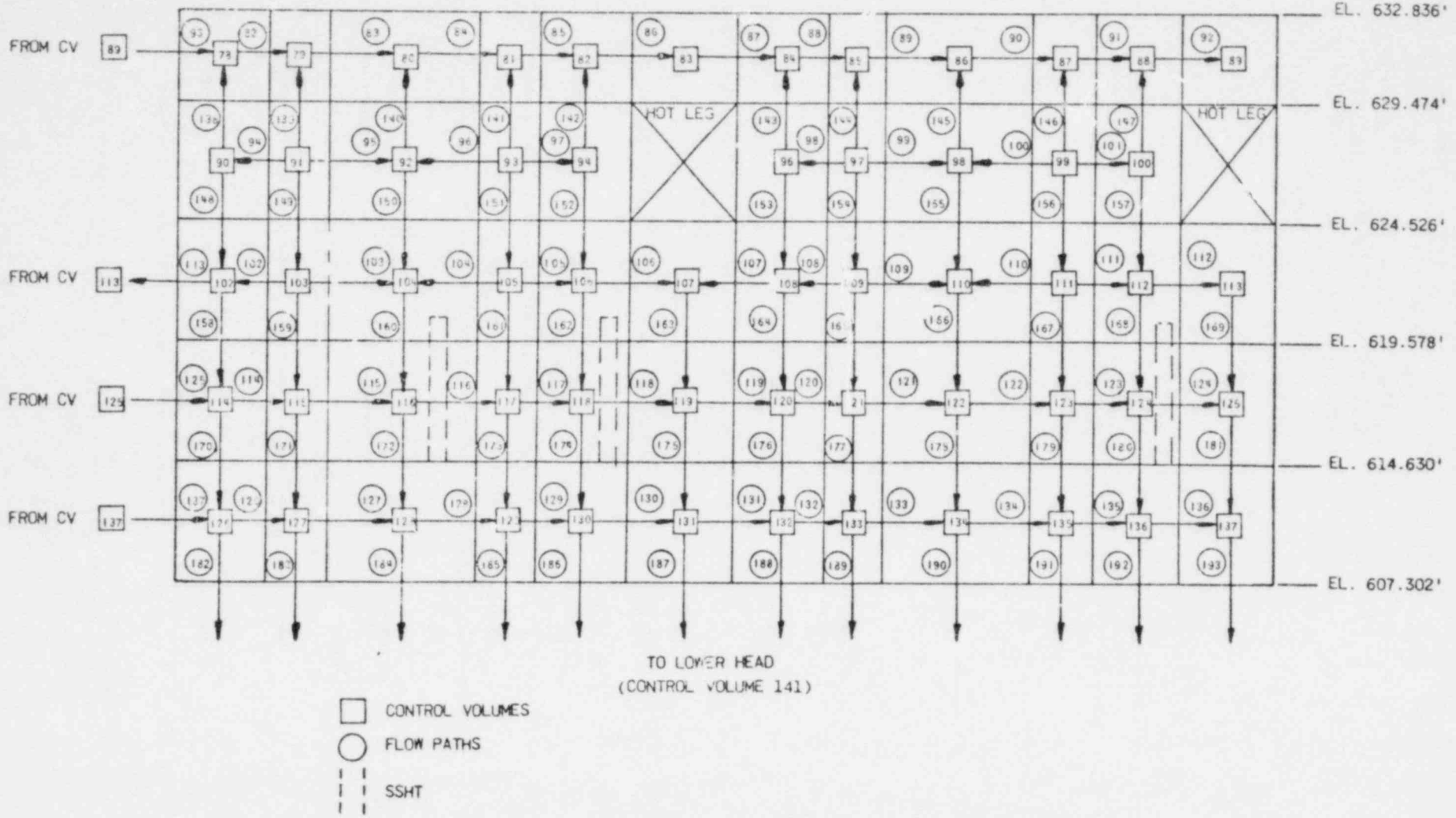

Figure C-4. CRAFT2 Noding Model — 177-FA Skirt-Supported Plant — Core and Lower Internals Region

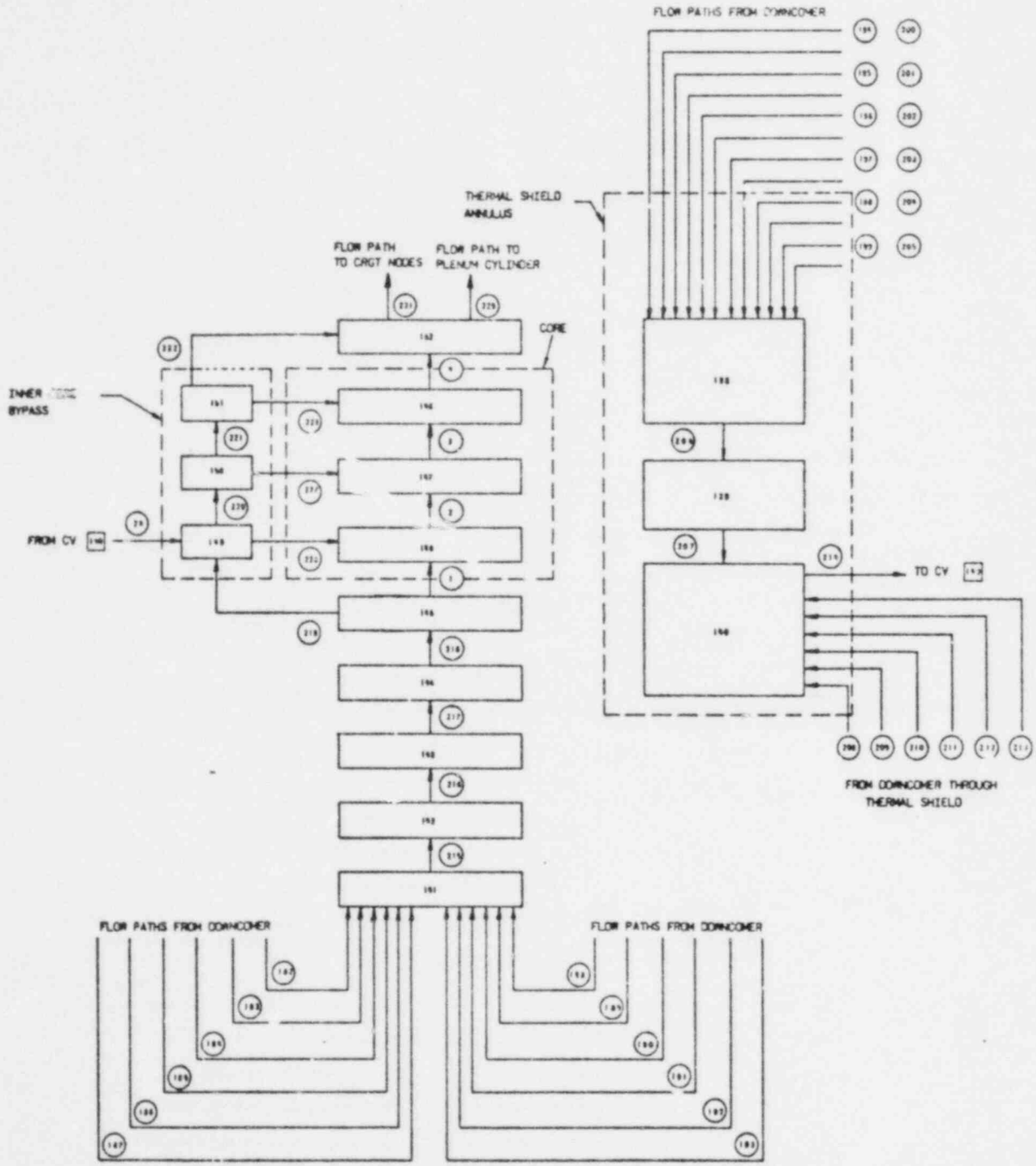

Figure C-5. CRAFT2 Noding Model — 177-FA Skirt-Supported Plant — Upper Plenum Axial Flow Path Region

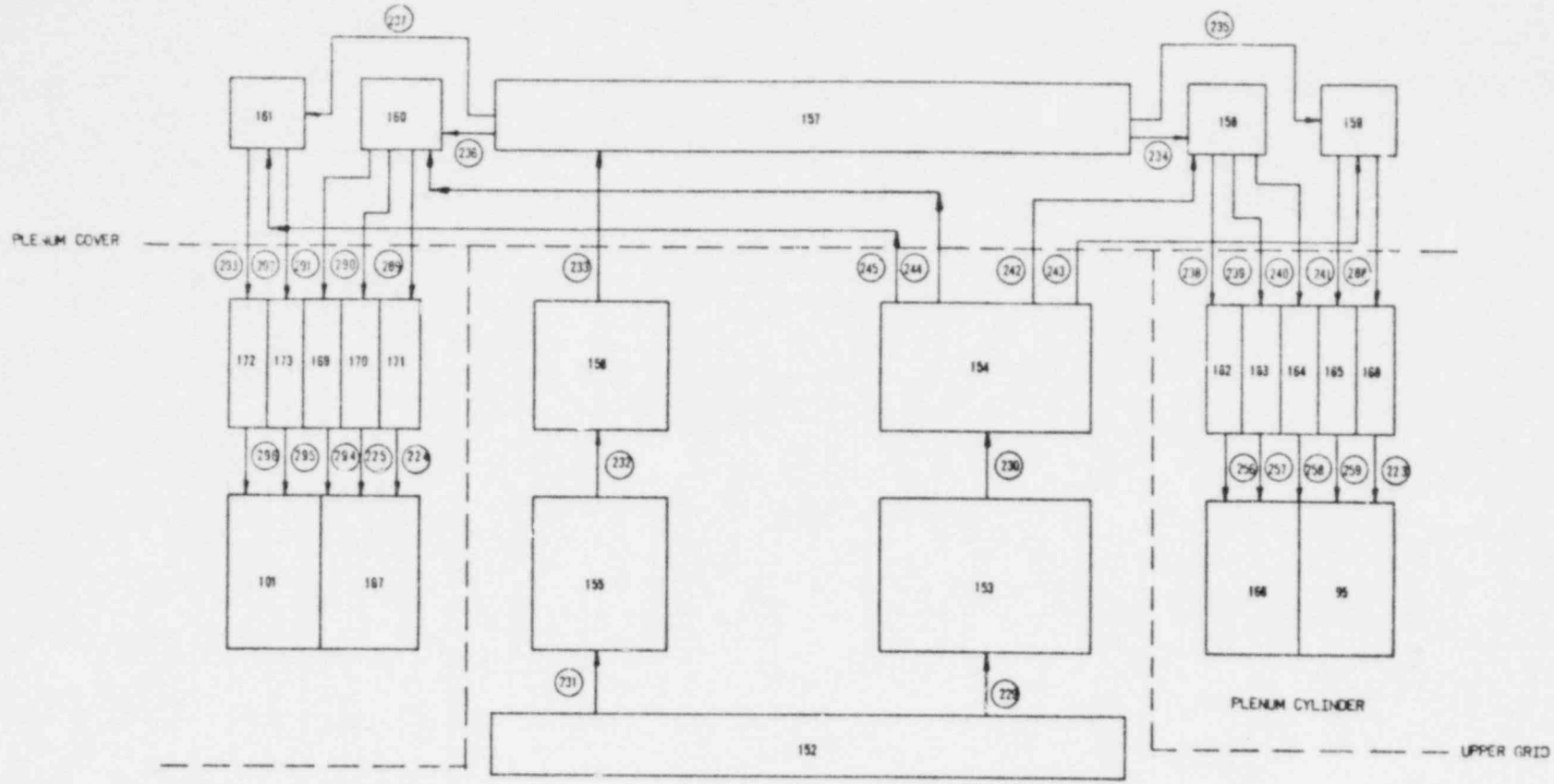

Figure C-6. CRAFT2 Noding Model — 177-FA
Skirt-Supported Plant —
Lower Plenum Region

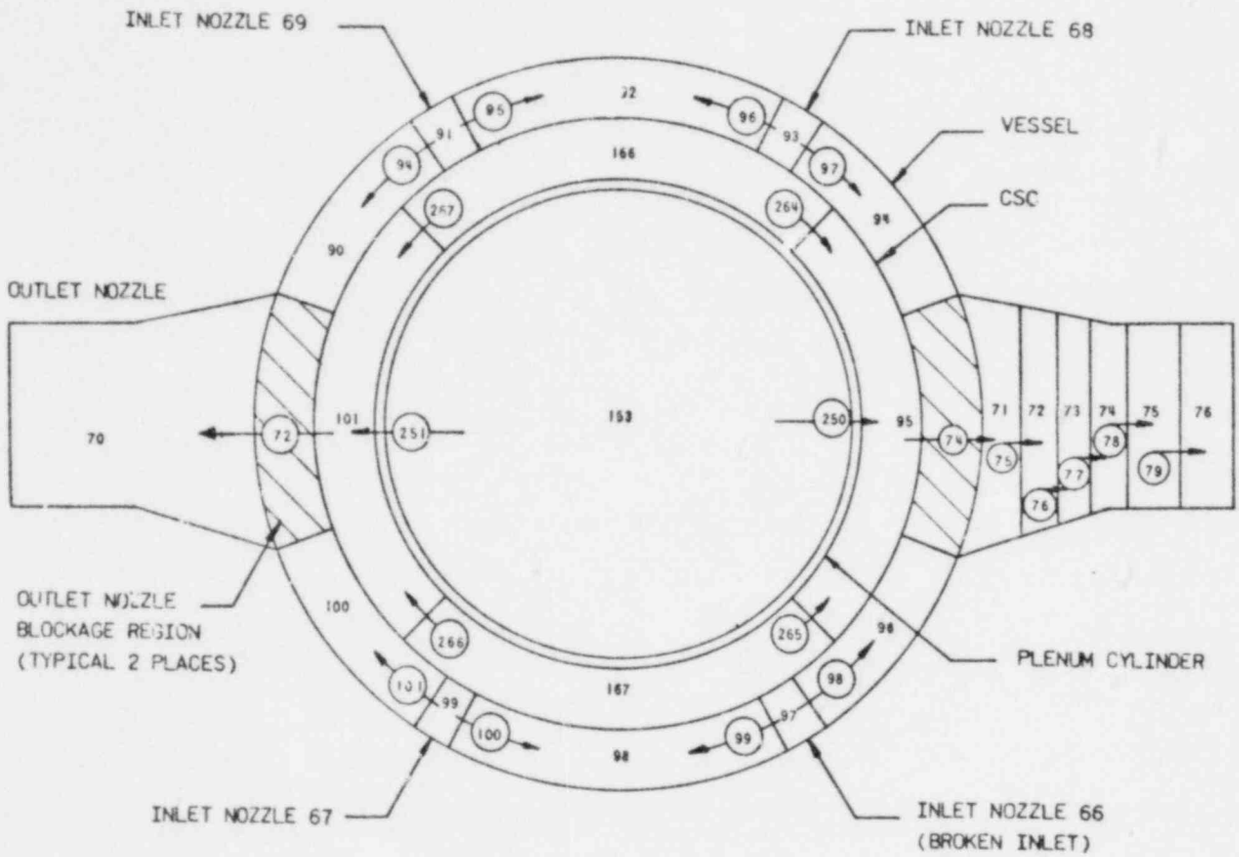

NOTES:

1. NODES 166,167,95 & 101 OUTLET ANNULUS INCLUDED ∡ 90°.
2. NODES 91,93,97 & 99 DOWNCOMER ANNULUS INCLUDED ∡ 7.39°.
3. NODES 90,94,96 & 100 DOWNCOMER ANNULUS INCLUDED ∡ 35.01°.
4. NODES 92 & 98 DOWNCOMER ANNULUS INCLUDED ∡ 52.47°.
5. BLOCKAGE REGIONS IN DOWNCOMER INCLUDED ∡ 42.31°.
6. NODE 153 O.D. IS 130 IN.

Figure C-7. CRAFT2 Noding Model — 177-FA Skirt-Supported Plant — Upper Plenum Region

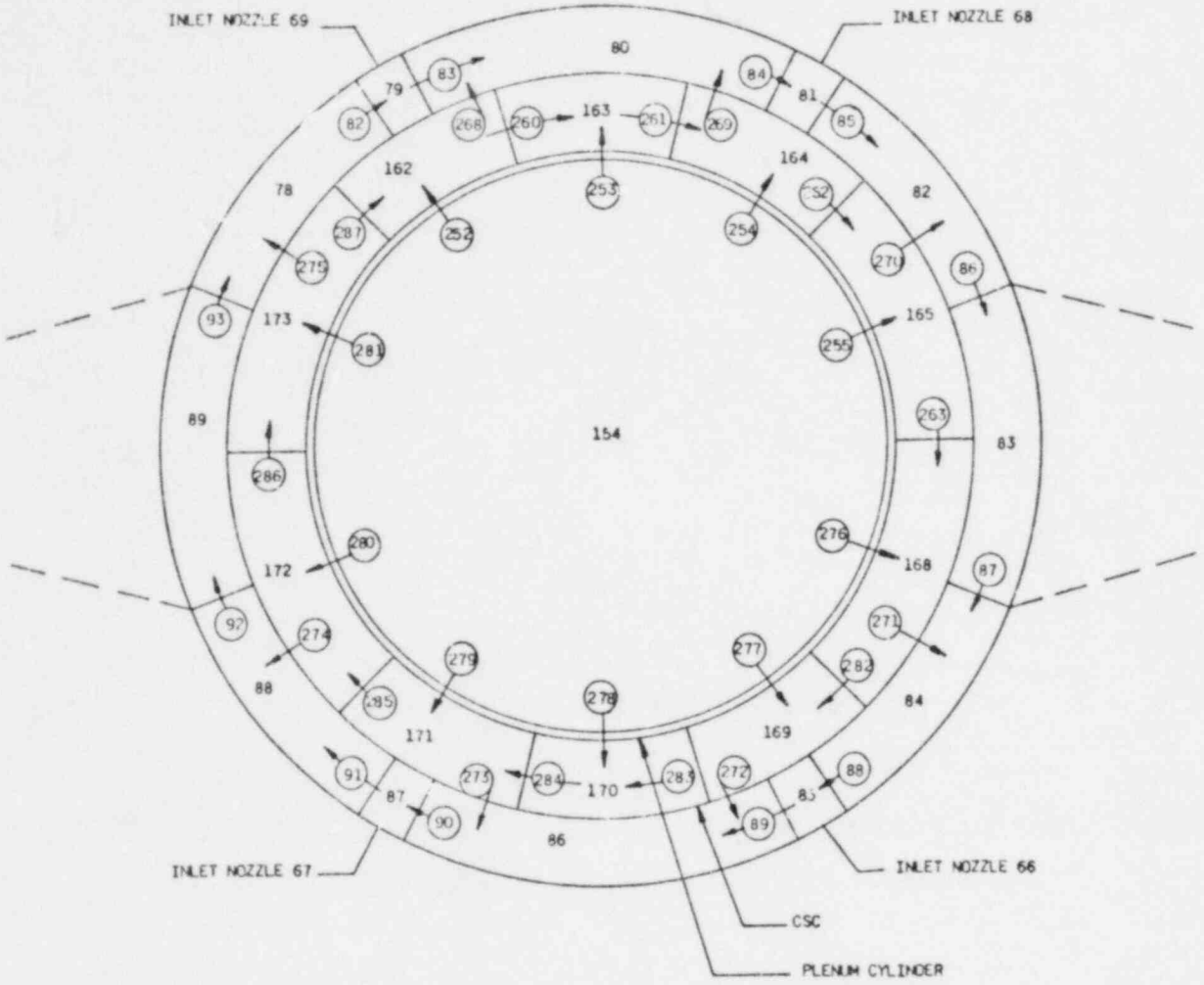

SECTION Y-Y UPPER PLENUM REGION

NOTES:

1. NODES 79,81,85 & 87 DOWNCOMER ANNULUS INCLUDED 7.39°.
2. NODES 78,82,84 & 88 DOWNCOMER ANNULUS INCLUDED 35.01°.
3. NODES 80 & 86 DOWNCOMER ANNULUS INCLUDED 52.47°.
4. NODES 83 & 89 DOWNCOMER ANNULUS INCLUDED 42.31°.
5. NODES 162,163,164,169,170 & 171 OUTLET ANNULUS INCLUDED 30°.
6. NODES 165,168,172 & 173 OUTLET ANNULUS INCLUDED 45°.
7. NODE 154 O.D. IS 130 IN.
8. VENT VALVES PATHS ARE 268 THROUGH 275.

Figure C-8. CRAFT2 Noding Model — 177-FA Nozzle-Supported Plant — 20-Control Volume Downcomer

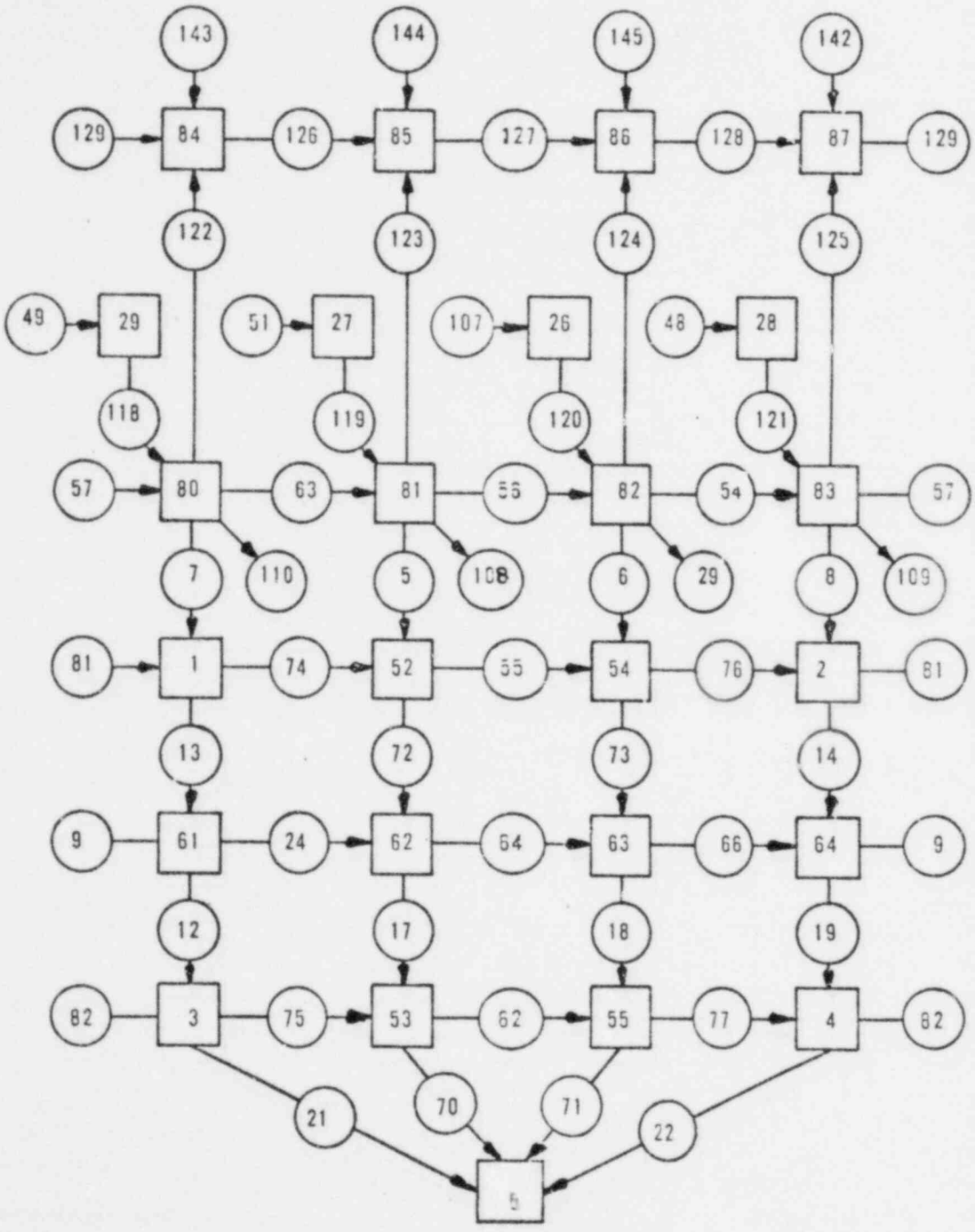

Figure C-9. CRAFT2 Noding Model — 177-FA Nozzle-Supported Plant — Elevation View of Reactor Vessel Control Volume

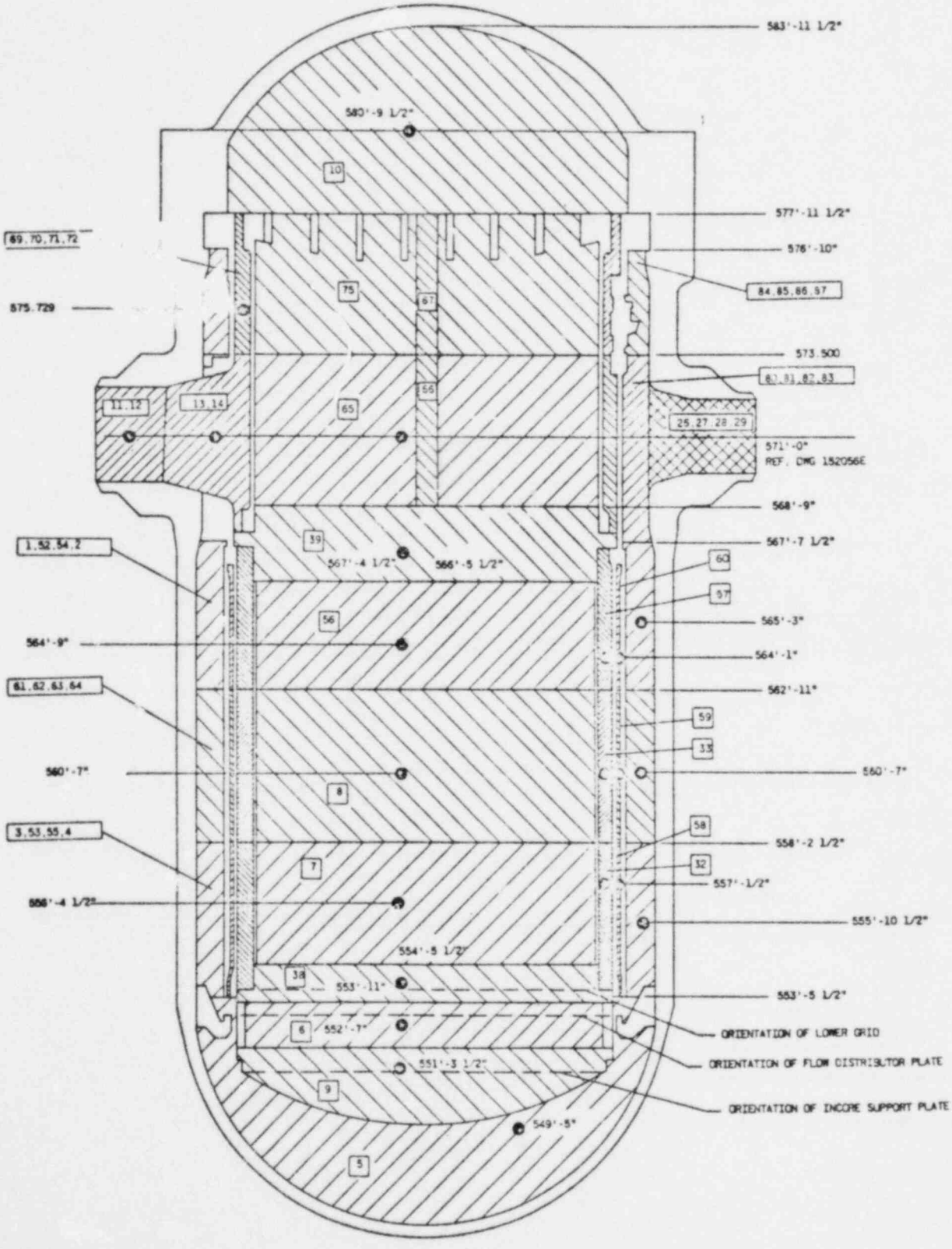

Figure C-10. CRAFT2 Noding Model – 177-FA Nozzle Supported Plant – Core and Lower Internals

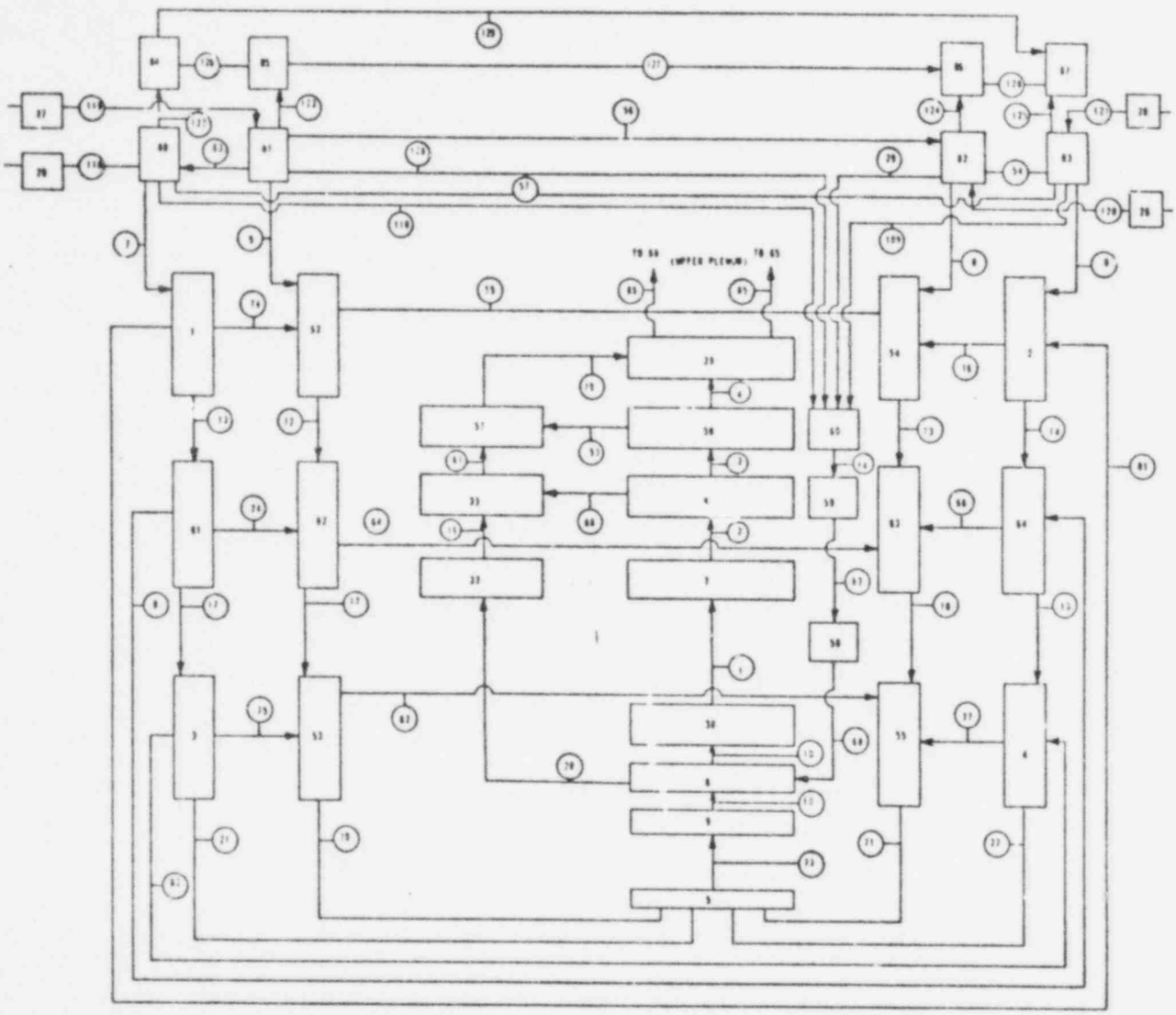

Figure C-11. CRAFT2 Noding Model — 177-FA Nozzle-Supported Plant — Upper Plenum Region

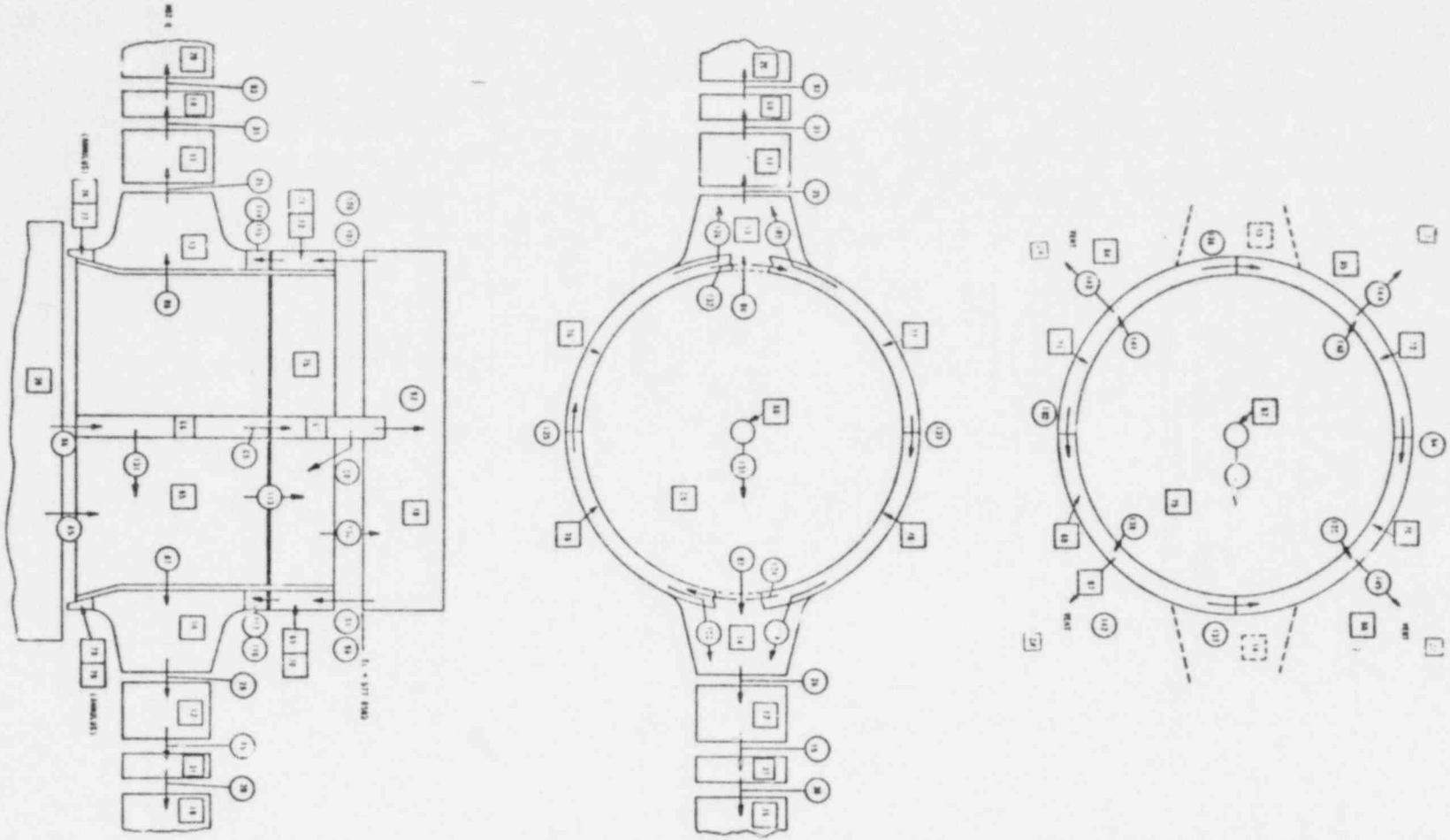

APPENDIX D

Reactor Vessel Isolated Structural Model — Description and Method of Analysis

1. Introduction

This appendix discusses the concept of a reactor vessel (RV) isolated model as it relates to the complete NSS, general dynamic analysis techniques, mathematical model representation of hardware, and the method of analysis for LOCA.

2. Reactor Vessel Isolated Model — Definition

A single basic RV isolated model has been constructed to cover all the 177-FA Owners Group plants. Modifications have been made to represent either skirt-supported or nozzle-supported plants.

Figure D-1 is an overview of the RV, RV internals, service support structure (SSS), and control rod drive mechanisms (CRDMs). The RV and its internal components, along with the SS and the CRDMs, are a natural portion of the nuclear steam generating system for structural isolation. The interaction of these components is significant. The movements of the RV influence the movements of its internal components, the SSS, and the CRDMs. All other components, e.g., pumps and steam generators, have a negligible effect on the RV and its internal components as well as the SSS and the CRDMs. For this reason the system has been substructured for LOCAs near the RV as shown in Figure D-2.

3. General Dynamic Analysis Techniques

3.1. Code Identification

The two basic computer programs in the analysis and the four data reduction codes used for the Phase II analysis are described below.

3.1.1. Structural Analysis Codes

1. HYDROE — A computer code used in calculating the hydrodynamic mass coupling of concentric cylinders.
2. STALUM — A computer program for analyzing three-dimensional, finite segment systems consisting of uniform or nonuniform bar/piping segments, closed-loop arrangements, and supporting elements. STALUM performs both static and dynamic structural analyses undergoing small linear, elastic deformations. The static analysis is based on the matrix displacement method. The static loadings are static mechanical forces, thermal, and/or support displacement loadings. The dynamic analysis is based on lumped-mass and normal-mode extraction techniques. The dynamic input loadings can be response spectra or force-time history.

The essential input to the program consists of the physical properties of the system, the boundary conditions, and/or the loading information; the essential output consists of the resultant joint displacements, rotations, forces, moments at both ends of each segment, and stresses at various locations in each segment.

3.1.2. Data Reduction Codes

1. FTRAN – A computer code used for Fourier analysis of forcing functions to determine the frequency content of the forcing function.
2. S1235 – A post-processor program used to tabulate forces, moments, displacements, and rotations in a specification format.
3. INTFCE – A program used to convert pressure-loading data to force-loading data acceptable for use by the structural analysis codes.
4. LOPL – A post-processor program used to provide time history tabulations and plots of spring forces and resulting loads and displacements.

3.2. Computer Input

In reviewing the overall analytical procedure, a flow chart has been developed and is presented in Figure D-3. Each program contributes a portion to the overall development of the equation of motion for the entire modeled structure. The paragraphs that follow serve to describe the relationship of each computer run to the development of the structural representation. A complete input description can be found in reference 10. General input requirements are presented here.

3.3. HYDROE Input

A dynamic coupling effect exists between cylinders immersed in a fluid. The HYDROE code represents this coupling in the form of a mass matrix generated by utilizing the height of the concentric cylinders, the distance between the two cylinders, and various parameters describing the fluid between the two cylinders. Off-diagonal mass matrix terms are generated and are carried throughout the analysis starting with the calculation of mode shapes and frequencies.

3.4. STALUM Input

In the next step in the analysis, the basic model geometry must be defined as well as all boundary conditions. The following is a listing of the input

requirements for the GEOM portion of STALUM, from which the flexibility and stiffness coefficients are derived:

1. Coordinates
2. Element connectivity
3. Section properties
4. Material properties
5. Desired degrees of freedom
6. Boundary conditions

Upon receiving this input, the program generates the reduced flexibility matrix for the entire structure and stores the information for subsequent programs. The initial STALUM run lays the foundation for successive computer runs; each utilizes information from the previous run and ultimately yields the complete equations of motion for the entire structure.

After the flexibility coefficients have been created, the LUMP portion of STALUM is used to calculate the frequencies and mode shapes for the structure. The input is as follows:

1. Mass matrix (includes off-diagonal masses for hydraulic effects)
2. Specified degrees of freedom
3. Flexibility matrix

From these data, LUMP calculates the undamped frequencies and mode shapes corresponding to the chosen degrees of freedom. The limitations are the total number of degrees of freedom and off-diagonal mass terms. One frequency and mode shape is obtained per degree of freedom.

3.5. Frequencies for Each Structure

In the event of a complete piping severence (a guillotine break), the frequencies and mode shapes for the structure must represent the structural discontinuity for a break in either the hot or the cold leg piping. A complete definition of LOCA analysis is offered in part 5 of this appendix. The number of frequency and mode shape calculations is dependent on the number of structural representations required to represent the postulated LOCA cases. The LOCA cases must include frequencies that participate significantly in the dynamic response.

3.6. Calculation of Resultant Loads

Upon completion of the frequency and mode shape calculations, the inertial response of the system is calculated. Inertial loads result from the dynamic input to the system on a time-dependent basis. Recall that the equation of motion is as follows:

$$[M]\{X\} + [C]\{X\} + [K]\{X\} = \{F(t)\}. \qquad \text{(D-1)}$$

In the event of a break in the primary piping, a pressure wave will propagate throughout the system and develop reaction loads on each component. The loads that excite the system under such an event are imposed on the system through the equation of motion in the vector $\{F(t)\}$, which varies with time. Once the mass, flexibility, and stiffness matrices for the structure have been calculated (by using STALUM), the solution to the equation can be expressed as

$$\{X\} = \sum_{i=1}^{n} \{\phi_i\} \cdot y_i \qquad \text{(D-2)}$$

where

n = number of dynamic degrees of freedom,

$\{X\}$ = resultant displacement,

$\{\phi_i\}$ = ith mode shape,

y_i = ith modal response.

The ith mode shape is calculated from equation D-3:

$$\left(\{\phi_i\}^T[M]\{\phi_i\}\right) \cdot \omega^2 = \{\phi_i\}^T[K]\{\phi_i\}. \qquad \text{(D-3)}$$

The modal response y_i for the ith mode is calculated from equation D-4:

$$\ddot{y}_i + \frac{\{\phi_i\}^T[C]\{\phi_i\}}{\{\phi_i\}^T[M]\{\phi_i\}} \dot{y}_i + \omega_i^2 y_i = \frac{\{\phi_i\}^T\{F(t)\}}{\{\phi_i\}^T[M]\{\phi_i\}} . \qquad \text{(D-4)}$$

In summary, the calculation of model displacements X can be described by the following procedure:

1. Using HYDROE, calculate a mass matrix reflecting coupling between cylinders surrounded by pressurized fluid.

2. Using STALUM, calculate the natural frequencies ω_i with their corresponding mode shapes ϕ_{ij} using equation D-1.

3. Calculate the modal response y_i through the use of equation D-4 by performing direct step-by-step integration.

4. Obtain {X}, the system displacements, by letting $\{X\} = \sum_{i=1}^{n} \{\phi_i\} y_i$.

After the calculation of the system displacements, the forces and moments can be calculated for the entire model. These calculations are performed statically on a time-for-time basis for a LOCA analysis.

1. Having obtained the mass joint displacements for the LOCA event under consideration, equivalent inertial forces can be found through the relationship [F] = [K]{X}.

2. The forces are then applied to the mass joints to obtain the system response (i.e., joint displacements and the elemental, free body forces and moments).

4. Mathematical Model Representation of Hardware

Figure D-4 illustrates the reactor vessel and its internal components, and Figures D-5 through D-10 present the Owners Group RV isolated math model. A general overview of the internal components is shown and appropriately labeled. Although the components are diagrammed as if they are displaced from the reactor vessel centerline, the RV and its internal components are actually a series of concentric cylinders. The fuel assemblies are located within the core barrel, which in turn is located within the thermal shield. Together these components are housed within the reactor vessel shell along its centerline in a coaxial orientation. The elements shown in Figure D-5 of the math model correlating to Figure D-4 are shown displaced for ease of visibility.

4.1. Reactor Vessel Shell

The RV comprises a cylindrical shell, a spherically dished bottom head, and a ring flange to which a removable, dome-shaped reactor closure head is bolted. Elements 73 through 90, shown in Figure D-5, represent the RV shell and closure head. Structural joints have been placed so that abrupt changes in cross-sectional area can be defined. Mass properties have been placed at appropriate

structural joints to ensure that at least the primary frequencies and mode shapes are represented by the RV model.

The upper and lower dome-shaped heads of the RV are treated in a special way in order to obtain the stiffness values for an equivalent beam. A separate finite element model, consisting of shell elements of each head, is made and subjected to loading. The directions of loading coincide with the known directions of force loading for which the head stiffnesses are required. The head is modeled using axisymmetric curved shell elements capable of non-axisymmetric loadings and is considered to be anchored at its base. It is loaded with an axial force F_y and a bending moment M. The resultant displacement y and rotation Θ at the free end are calculated using an appropriate shell program. The resultant stiffness F_y/y and M/Θ are used to calculate the equivalent beam cross-sectional area and its moments of inertia.

The elements making up the RV shell are beam elements whose radii and thicknesses are obtained through equipment drawings. The RV shell is approximately an order of magnitude stiffer than the internal structures, service support structure, and other components represented in the isolated model.

4.2. General Internal Arrangement

The RV internal components are arranged in three groups: the core support assembly, the plenum assembly, and the reactor core itself, as illustrated in Figure D-1. The major subassemblies of the core support assembly are the core support cylinder, the lower grid assembly, the flow distributor assembly, the core barrel assembly, and the thermal shield. The plenum assembly comprises the plenum cover, the plenum cylinder, the control rod guide tubes, and the upper grid. The reactor core comprises the 177 fuel assemblies. A detailed description of each component is provided in subsequent sections.

4.3. Core Support Cylinder

Housed within the reactor vessel and supported by the RV flange, the core support cylinder (CSC) is positioned within the RV shell coaxial with the vessel centerline. The important function of the CSC is to direct the flow of coolant downward, where the flow will eventually (after passing the thermal shield) be drawn inside the cylinder and over the fuel elements. Elements 131-138 (shown in Figure D-5 of the isolated model drawings) represent the CSC. The determination of element stiffness terms has been the result of

extensive efforts using elaborate finite element models which develop equivalent beam elements to represent shell structures.

4.4. Lower Grid Assembly

The lower grid assembly (LGA) represents the main floor system in the core support assembly. It consists of a top rib section, shell forging, lower grid forging, lower grid pad, lower grid distribution plate, and a series of support posts. The lower grid shell forging, which is basically a cylindrical shell, is welded to the lower grid forging. Support posts are also welded to the lower grid forging. The lower grid top rib section, which supports the reactor core, is bolted to the shell forging and to the support posts. A thin, perforated flow distributor plate is welded to the shell forging and the support posts at their midheight. This plate distributes the primary coolant entering the reactor core uniformly. The flow distributor assembly is bolted to the lower grid shell forging. The mass of the lower grid assembly is modeled at joint 16 of Figure D-5. Element 120, which is modeled as very stiff (at least 10 times as stiff as any of the surrounding elements), feeds the movement of the lower grid (LG) to the lower flanges of the core barrel assembly (CBA). In practice, the element is made stiff enough to prevent appreciable bending and roation, so that virtually no energy is lost in the assembly movements. Thus, energy is transmitted directly to the lower flanges of the CBA in a conservative manner.

4.5. Flow Distributor Assembly

The flow distributor assembly (FDA) consists of a flow distributor head, an incore guide support plate, and incore instrument guide tubes. The flow distributor head is a perforated spherical cap. The incore guide support plate is a perforated circular plate welded inside the flow distributor head. The incore instrument guide tubes are welded to both the head and the plate, extending to a height slightly below the fuel assemblies and attached to a spider assembly which is welded to the top rib section. Element 119, which is constructed as a very stiff element as previously described, connectes the flow distributor assembly to the lower grid assembly as shown in Figure D-5.

4.6. Core Barrel Assembly

The core barrel assembly (CBA) is a stiffened structure that shields the RV and provides for more uniform coolant flow as the coolant passes around and

through the fuel assemblies. The CBA comprises a uniform cylinder – a core barrel, horizontal former plates at eight elevations over the entire height of the shell, and vertical baffle plates that surround the core. The entire CBA is bolted to the lower grid assembly through a flange welded to the lower end of the core barrel. The idealized beam is derived by the same process as the core support cylinder and is incorporated in the isolated model by elements 140-146 of Figure D-5. Like the CSA representation, the centerline movements of the CBA are exhibited in the idealized beam derived using finite element models.

4.7. Thermal Shield

The thermal shield is a cylindrical shell surrounding the core barrel assembly. It serves as both a neutron shield to the reactor vessel and a neutron reflector for the core. It is bolted to the lower grid assembly at the bottom and clamped to the core barrel at the top to restrain horizontal motion and allow differential thermal expansion. The thermal shield structural properties were derived from a finite element model and modeled as a centerline, idealized beam as described previously. The thermal shield is represented by elements 121-130 in Figure D-5.

4.8. Plenum Assembly

The plenum assembly (PA) supports the upper regions of the fuel assemblies, guides the control rods, and enhances proper coolant flow characteristics through the upper portion of the CSA. It consists of the plenum cover, the plenum cylinder, the control rod guide tubes (also known as column weldments), and the upper grid.

The plenum cover is a perforated circular plate which is clamped in place, together with the plenum cylinder, between the RV flange and the RV closure head. The plenum cover is modeled as a rigid body.

The plenum cylinder is a cylindrical shell containing numerous large- and small-diameter holes to ensure proper flow characteristics. Its structural properties are derived from a finite element model and are represented in Figure D-5 as the centerline idealized beam elements 110-113.

At the lower end of the plenum cylinder, the upper grid assembly is bolted to the plenum cylinder to provide additional support for the upper portions of the fuel elements. The upper grid assembly comprises a grid forging and a

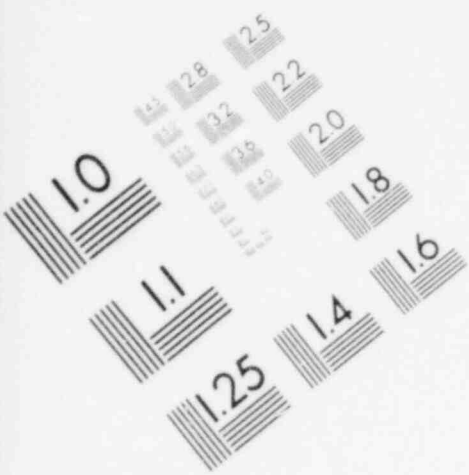

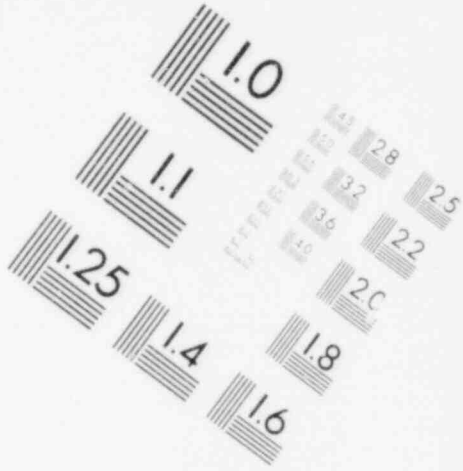

IMAGE EVALUATION TEST TARGET (MT-3)

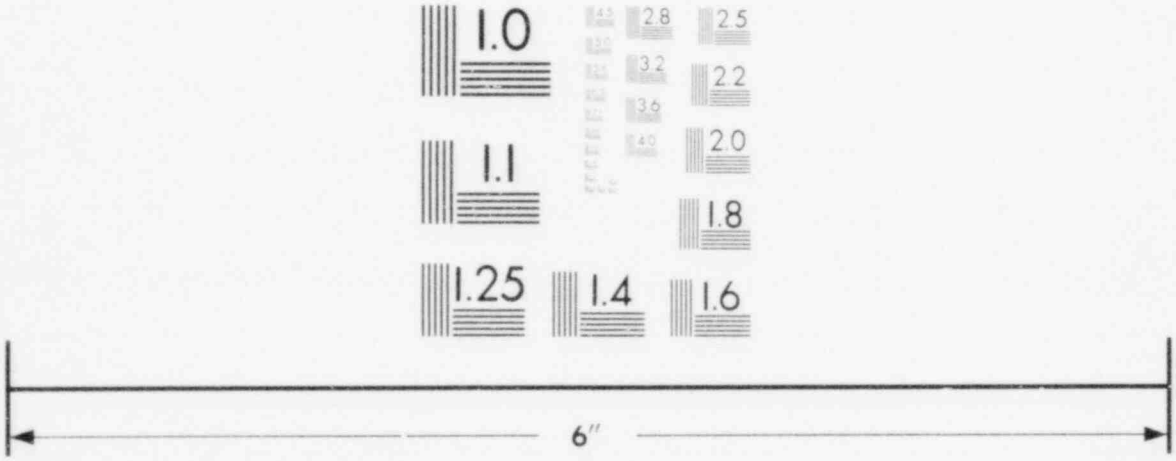

MICROCOPY RESOLUTION TEST CHART

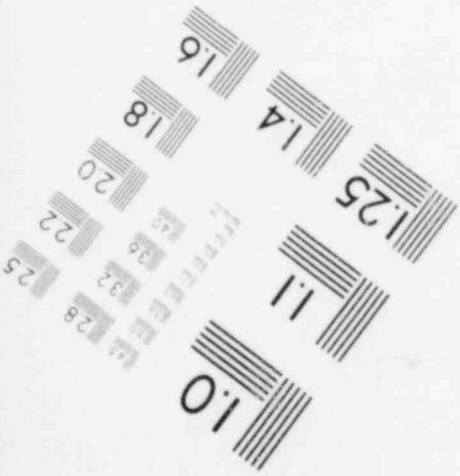

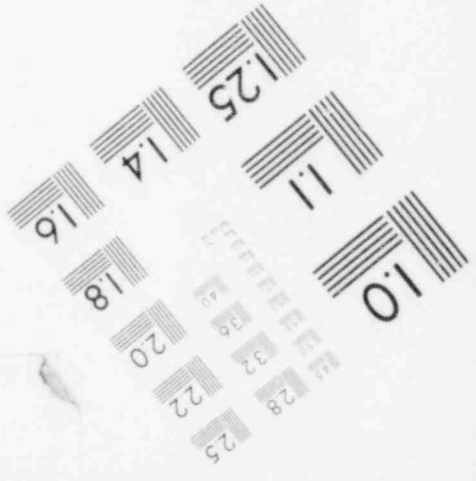

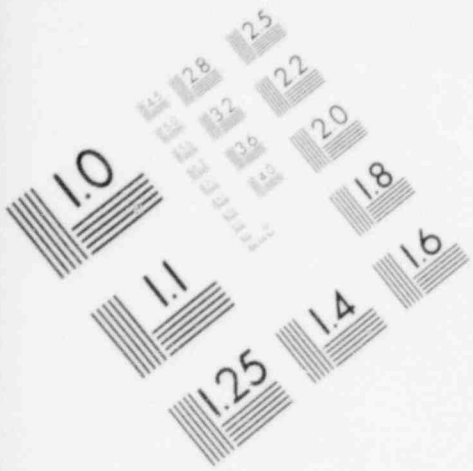

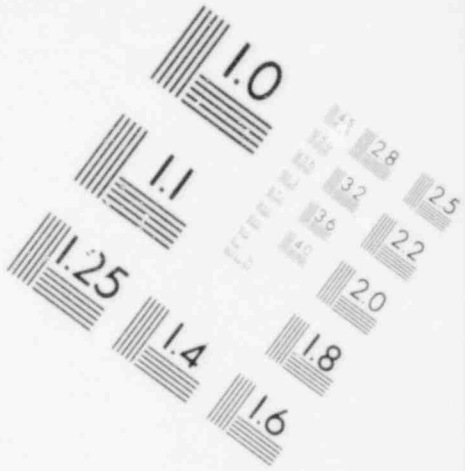

IMAGE EVALUATION
TEST TARGET (MT-3)

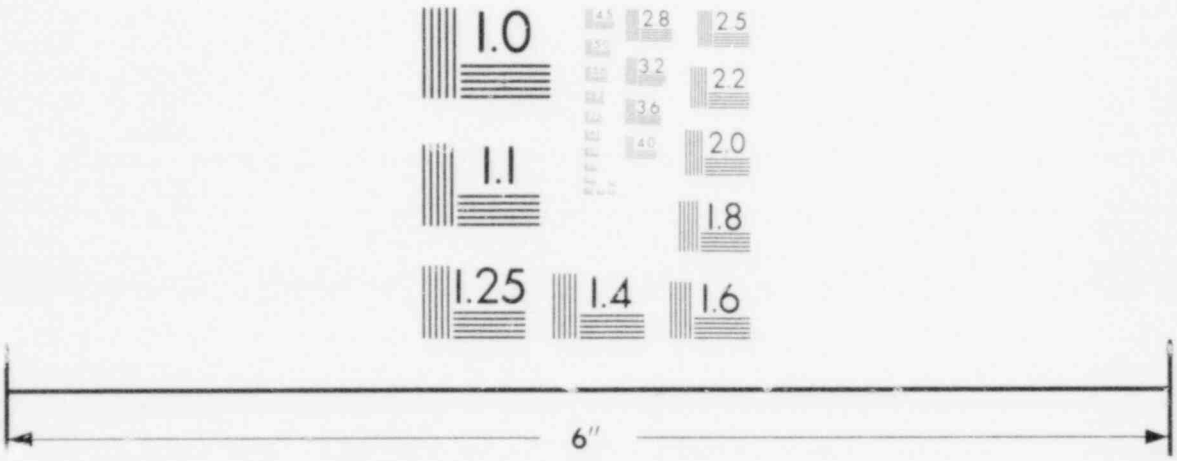

MICROCOPY RESOLUTION TEST CHART

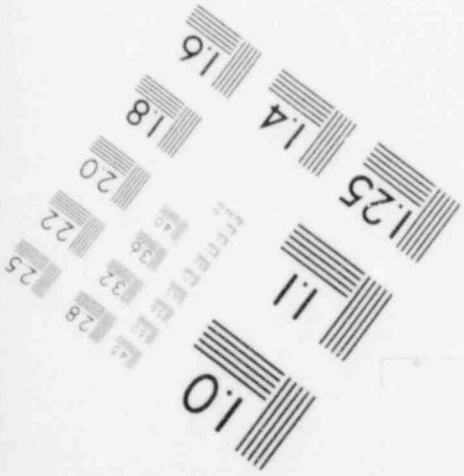

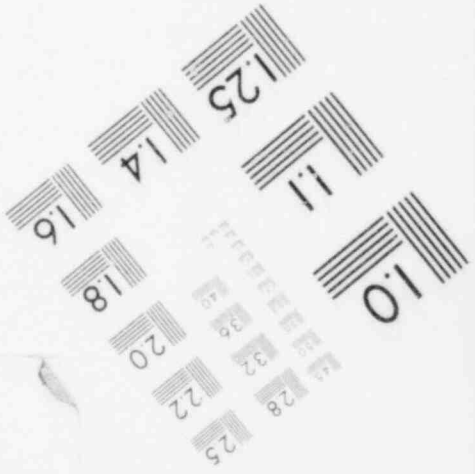

rib section which are also bolted together. The upper grid assembly is modeled as a rigid body.

The control rod guide tubes are bolted to the upper grid rib section and mechanically expanded into the plenum cover. Selected tubes house assemblies that guide the control rods into the reactor core. Structural properties for the tubes are derived using finite element models.

4.9. Fuel Assemblies

The fuel assembly (FA) is composed of fuel pins separated by intermediate spacers along the length of the pins. A FA is capped on each end with an end fitting. The upper end fitting is equipped with a holddown mechanism consisting of springs which interact with the upper grid. The actual physical properties of the fuel assembly are combined with test data to provide a model that has the fundamental frequencies of the FA. The properties of the FA model are multiplied by 177 to provide a representative centerline beam element model of all the FAs. The model, along with appropriate mass moments of inertia applied to the upper and lower grids, represents the FA structural interaction with the remainder of the reactor internals. The actual FA loading and stress analysis is done using a nonlinear analysis with the time history of displacements of the upper and lower grids generated in the RV isolated model analysis. The FAs are represented by elements 104-108 in Figure D-5.

4.10. CRDM and Service Support Structure

The control rod drive mechanism is based on the roller nut principle. An external motor stator surrounds the motor tube, which is primarily a pressure housing, and position indication switches are arranged externally along its length. The drive mechanism is a totally sealed unit in which the roller nut assemblies are driven magnetically by the stator coil through the motor tube pressure housing wall.

The leadscrew is a non-rotating component which raises and lowers the control rod element to its required elevation. The screw is driven by separating anti-friction roller nut assemblies which are rotated magnetically by a motor stator outside the pressure boundary. Current impressed on the stator causes the two segment arms containing the roller nut assemblies to close and engage the leadscrew. For rapid insertion in the event of a LOCA, the segment arms separate to release the screw, which moves into the core by gravity.

In modeling the CRDMs, each unit is considered as a long tube with its lower end joining a flange on the RV closure head. The upper end is supported by a clamp connecting to a framework that extends from the service support structure. The CRDMs are located within the cylindrical shell of the service support structure. Both ,s structure and the CRDMs have concentrated masses distributed along their lengths. The lumped masses include the additional weights of the drive motors, the electrical cables connected to the drives, and electric fans. The fans and cables rest partially or totally on the service support structure; consequently, the additional mass is lumped to the beam element model of that component.

The stiffness and mass properties of all CRDMs are combined into one single beam. Special boundary conditions exist for the upper support point of the CRDs at the service structure. Movement of the CRDMs in the vertical (Y) direction is not restrained by the clamp; however, horizontal movements (in the X and Z directions) are restrained.

The models just described are sufficient to include the influence of the SSS and the CRDMs on the RV and its supports. Figure D-5 illustrates these components as they are included in the RV isolated model. Elements 92-98 represent the SSS and 148-154 represent the CRDMs. The SSS rests on a skirt flange welded to the RV closure head.

4.11. RV Supports

The RV is supported by steel and reinforced concrete structures beneath the four inlet nozzle pads or from a steel skirt welded to the lower vessel head (as shown in Figure D-11). The pads are rectangular reinforcements on the underside of the nozzles. For LOCA analysis for Davis-Besse the RV pads are neglected and the wagonwheel support in the shield wall then becomes the RV support, along with the five unbroken pipes. Appropriate reinforced concrete spring rates at the wagonwheel have been considered.

4.12. Reactor Coolant Piping

Because of the capabilities of the computer programs used, the modeling of the reactor coolant (RC) piping has been greatly simplified. By defining the outer radius and thickness of the piping used, as given in equipment drawings, the actual stiffness of the piping is calculated within the computer code. Each pipe element is located in the model by reference to the joints at each

of its ends, which are located by their Cartesian coordinates. Elbows in the piping system are modeled by declaring the required elements curved and refering these elements to a joint lying at the center of curvature. For calculation of flexibility, cladding is neglected in the input of pipe cross sections; however, when the pipe weight is calculated to lump masses at the mass joints, the weights of cladding, insulation, and fluid contents are considered. Figures D-6 through D-10 illustrate the modeling of the RC piping. Each piping run starts at the RV nozzle and terminates at the steam generator inlet nozzle for the two hot legs and at the pump outlet nozzle for the four cold legs. At these six locations (four pump outlet and two steam generator outlet nozzles), 6-by-6 matrices are imposed as skew boundary conditions.

5. Method of Analysis for LOCA

The structural design criteria for nuclear power plants include consideration of a postulated primary pipe rupture that results in RC fluid discharge into the containment building. Design requirements have been established to protect against such postulated loss-of-coolant accidents (LOCAs) so that structures, systems, and components important to safety are protected against dynamic effects, including the effects of missiles, pipe whipping, and discharging fluids. LOCA means those postulated accidents, i.e., pipe breaks, that result in the loss of reactor coolant at a rate greater than the capability of the RC makeup system to replace the coolant. Breaks equivalent in size to the double-ended rupture of the largest pipe in the RC system must be considered. The treatment of LOCA as a structural event has evolved from static analysis with dynamic amplification factors to very complex time-history analysis, which accounts for the forcing functions acting simultaneously on a mathematical model of the RC system. A complex analysis is required because the loads calculated by simplified analyses often contain conservatisms that prohibit an economical design and in other cases oversimplification has caused important effects to be overlooked.

5.1. Analytical Considerations

The analysis for the pipe rupture response is performed using the time history methods described in part 5.4 of this appendix. The model of the RV is the primary concern for the breaks at the RV outlet or nozzles. An evaluation is

also important relative to the applied forcing functions. The analyst must consider the following parameters:

1. Total time of interest for the event.
2. Relative magnitude of forcing functions (some may be negligible compared to others).
3. Transient nature or frequency content of the forcing functions.
4. Detailed location for application of all forces.

The analysis must also consider nozzle forces, thrust forces, reactor vessel cavity pressure forces, and reactor vessel internal forces, which are discussed in more detail later in this section. Figure D-11 summarizes the various types of forces acting on the vessel and its associated components. Several analytical techniques are available to solve transient time-history problems; however, it is important that the chosen techniques accurately accommodate high-frequency structual modes and monitor the numerical stability of the solution.

Forcing functions are represented in a piece-wise linear manner, and accurate representations are required to ensure that the frequency content of the functions has been described correctly. The data points describing the forcing functions are the result of digital simulation of the transient event and thus have already considered the number of points or time steps required to define the functions. Thus, all points may be considered or, by examination, the linear portion of any curve may be represented by a reduced number of points. This provides a fast, accurate solution technique. The mathematical solution of the problem also involves the calculation of forces acting on each of the mass points in the system at each of the specified time intervals. The technique described above is commonly called the modal superposition method where forces are used to calculate internal, free-body forces and moments and joint displacements on a time step basis using the matrix method of structural analysis. The model must be detailed enough to that the eigenvalue solution includes the highest natural frequency of the structure that could be excited by the frequency characteristics of the applied forcing functions. The modal superposition method then sums over all modes to include the effect of the forcing functions on all structural modes.

5.2. Applied Forcing Functions on RV and Internals

The dynamic forces produced by a pipe rupture impose a discontinuity on the pressure boundary in two forms. First, the structural break has the effect of applying a load to each broken pipe which is equal to the load carried by the pipe prior to the break. Then the decompression or blowdown is initiated. The blowdown is characterized by large pressure gradients in the fluid induced by rarefaction (expansion) waves originating at the break location. As the blowdown progresses, pressure fluctuations are produced throughout the RV by a complex interaction of expansion and compression waves. The rapidly varying pressures inside the RV produce differential pressure loadings on the CSA. For breaks inside the reactor cavity, the mass and energy released to the containment building produce a local pressure buildup in the reactor cavity near the break, which results in asymmetric loadings on the RV shell.

Four steps are involved in developing the loadings for evaluation purposes. The first three steps are dynamic analysis steps which are performed in a straightforward manner. The fourth step would not be required if it were not for the variations in plant-specific data and the number of events that are to be analyzed. The principal analyses used in calculating the LOCA loadings and the development of the load data base are as follows:

1. Thermal-hydraulic pressure analysis.
2. Core bounce analysis.
3. System dynamic response analysis.
4. Development of plant-specific response loadings.

5.2.1. Thermal-Hydraulic Pressure Analysis

The methods described in section 4.4 and in Figures C-1 through C-11 produce the time-dependent pressure propagation throughout the internal pressure boundary. For the reactor vessel, the horizontal pressure gradient results in horizontal forces on the RV, the CSC, and the plenum cylinder. The vertical gradient results in vertical forces on the RV and internals.

The integration of the pressure-time history defines the time history forces which are applied at the discrete mass joints of the model in this appendix.

5.2.2. Core Bounce Analysis

The vertical response of the core and FAs results in a time varying force due to the structural representation and the differential pressures. Core bounce is the terminology given to this response. The nonlinear structural response to holddown springs and vertical gaps is calculated in a decoupled analysis. The FA core is simulated with a planar model consisting of beam elements, nonlinear axial springs, and lumped masses. Figure D-12 provides a description of the core bounce model. The ANSYS code is used to calculate the vertical reactions of the core, which are then used as applied force time histories on the reactor vessel in the steam dynamic analysis. The results of the core bounce analysis are also used to supply vertical loadings on the internals, which are added to the system dynamic response analysis.

5.2.3. System Dynamic Response Analysis

The model presented in this appendix represents the RV, internals, SSS, attached primary piping, and the vessel support. A linear elastic approach was used to develop the response of these structures. Representation of the fluid structure interaction between the CSC and the RV was obtained using the methods discussed in reference 11.

The loadings presented in the body of this report, section 8, were applied to the structure in a comprehensive time-phased mode; the event and the subsequently applied loads were evaluated in detail to determine the response. Thus, no superposition of worst-case response due to one portion of the event onto another worst-case response is included in the final results. This effort obtains the dynamic response, sometimes called dynamic amplification, to the event rather than to subsets of the event.

5.2.4. Development of Plant-Specific Response Loadings

The development of plant-specific response loadings from the time history analysis results is discussed in the body of the report, section 9.

5.3. Additional LOCA Loadings on Reactor Vessel

Analyses performed to determine the total LOCA loadings on the reactor vessel include, in addition to those discussed in section 9.2, cavity pressure and thrust.

5.3.1. Cavity Pressure Analysis

For LOCA breaks occurring inside the reactor vessel cavity, the effects of asymmetric pressures within the cavity are analyzed. The differential pressures within the cavity are determined using the CRAFT code. Pressures are derived for each specific break case. The output of the cavity pressure analysis consists of pressure-time histories acting at specified nodes over defined regions of the reactor vessel shell. The INTFCE computer code is used to integrate the pressures time-for-time, resulting in force-time histories. A detailed discussion of the plant-specific data is presented in the body of the report, section 8.

5.3.2. Thrust Analysis

The "thrust" force produced by the unbalanced pressure loading caused by losing the structural continuity (i.e., pipe severence) of the system is calculated by removing the area of the broken pipe from the pressure integration used to calculate forces on the internals and the RV and is approximately equal to the fluid pressure times the flow area of the broken pipe.

5.4. Combining Applied Forcing Functions for System Dynamic Response Analysis (5.2.3)

A linear dynamic analysis of the reactor vessel isolated model is performed to determine the response to a LOCA. Forces due to internal pressure differentials, core bounce, cavity pressure differentials, and thrust are included in the analysis. Horizontal forces due to integrated differential pressures are applied to the core support assembly, but the horizontal response of the CSA results from both the system motion and the applied forces. The vertical forces applicable to the CSA are applied to the CSA/reactor vessel interface, and no vertical forces are directly applied to the CSA components. The vertical CSA response determined in the dynamic analysis is entirely due to the CSA support motion at the RV ledge.

A preprocessing program is used to combine all load functions at each time point. The creation of one loading table preserves all unique peaks in the loading curves and their frequency characteristics. Preservation of the frequency content is of major importance due to possible resonance of the RV and related components. The time step increment used for combining all loads is based on the most detailed of the load functions. The least defined time

histories are interpolated and tabulated for each time step required to define the most detailed function. Thus, almost all loadings are structurally analyzed in a finer time history than in their original form, which ensures complete definition of the driving forces.

The primary results of the dynamic analysis are the time-varying displacements, accelerations, and internal forces. A flow chart of the analysis is given in Figure D-13.

Figure D-1. Reactor Internals and Service Support Structure

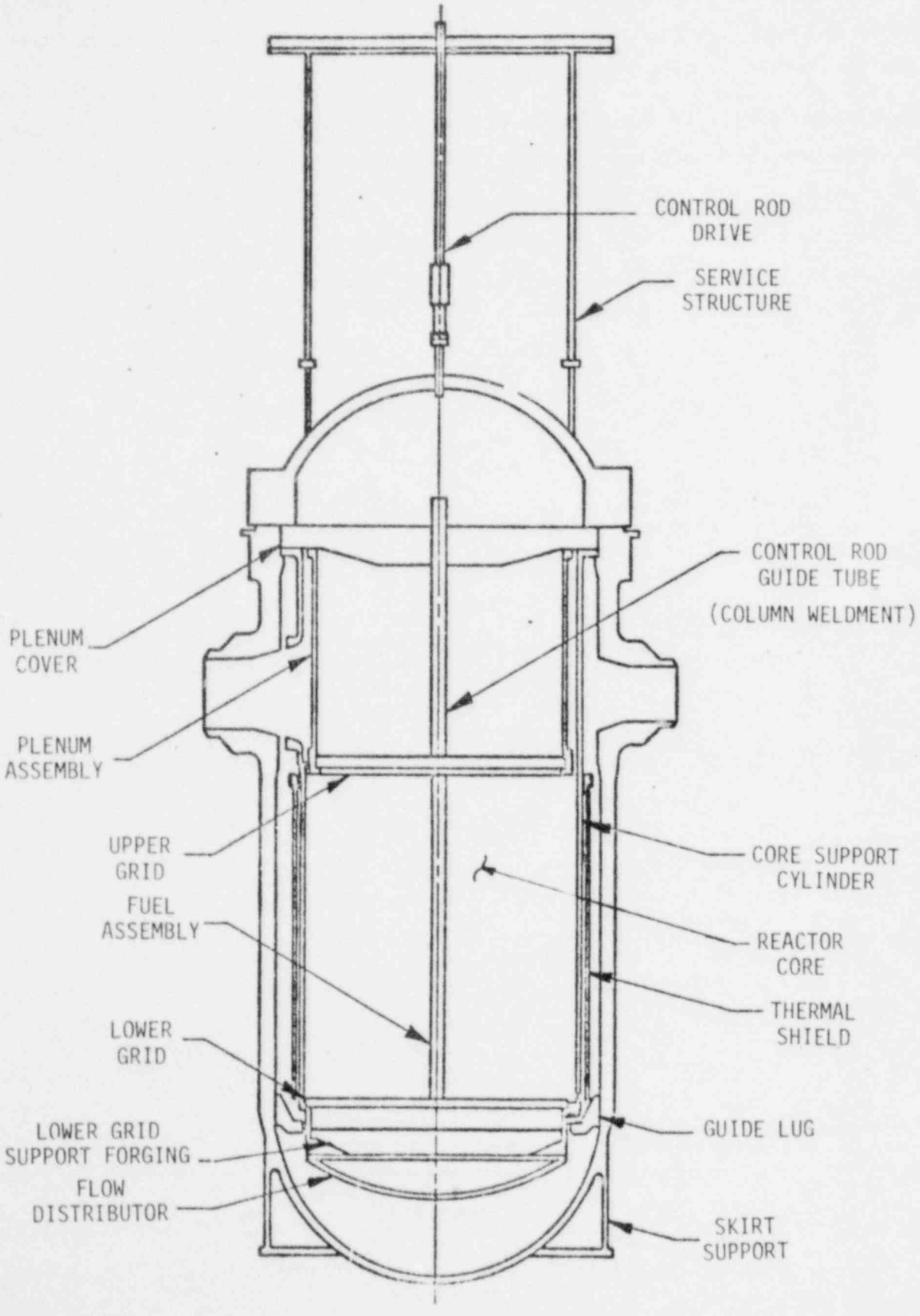

Figure D-2. Reactor Coolant System Boundaries

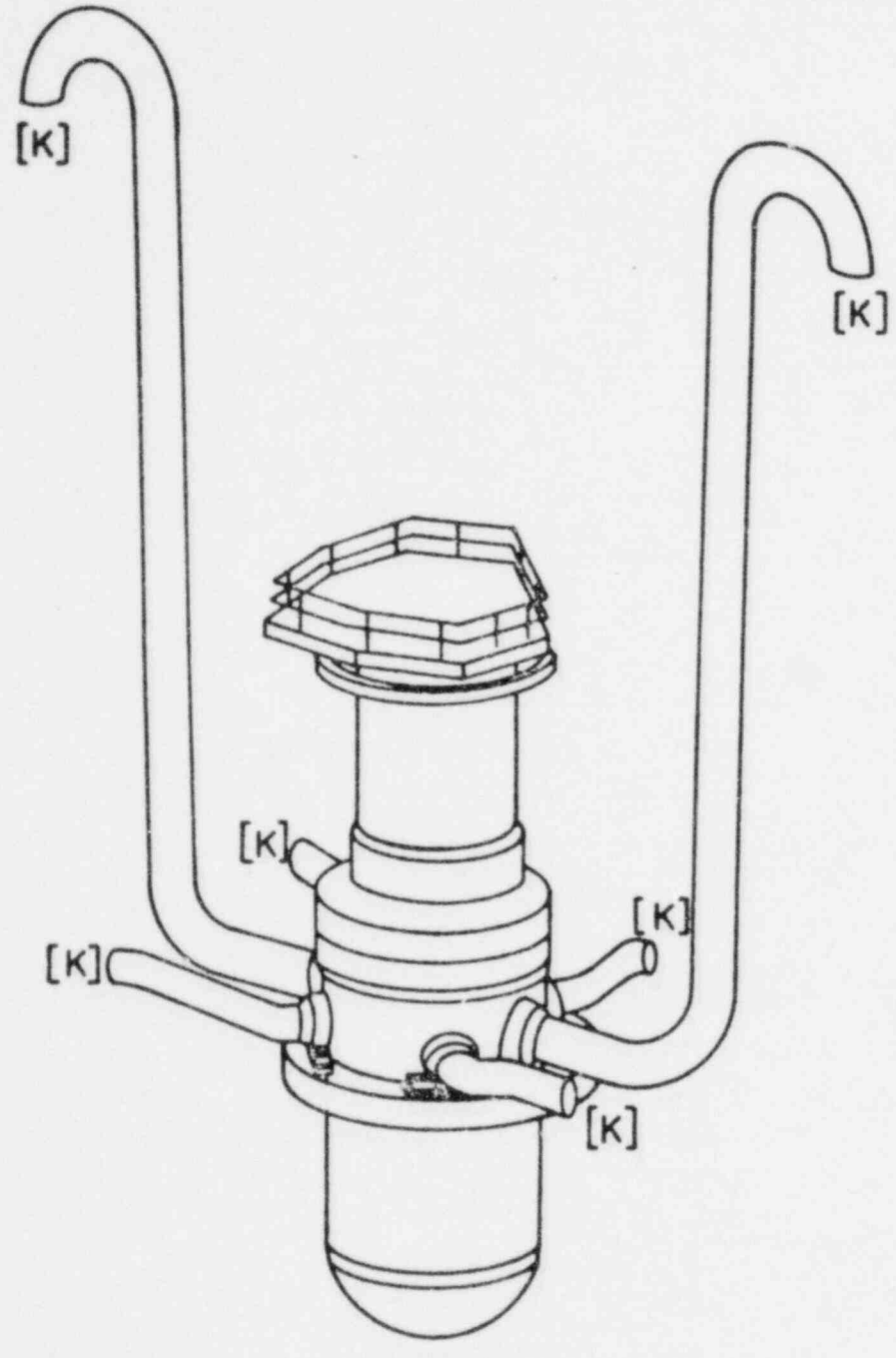

[K] = Stiffness matrix

Figure D-3. Utilization of Computer Programs

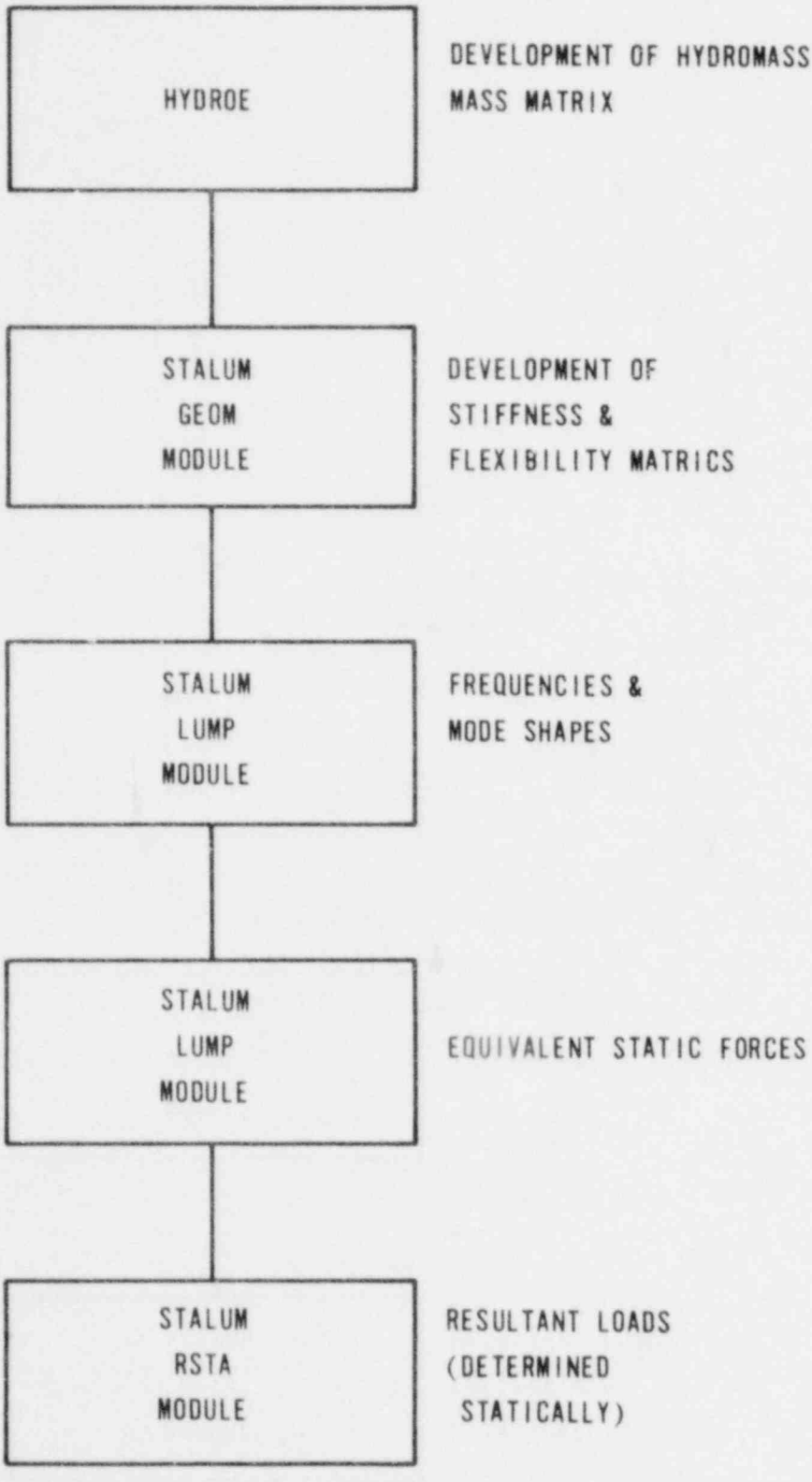

Figure D-4. Reactor Vessel — Cutaway View Showing Internals

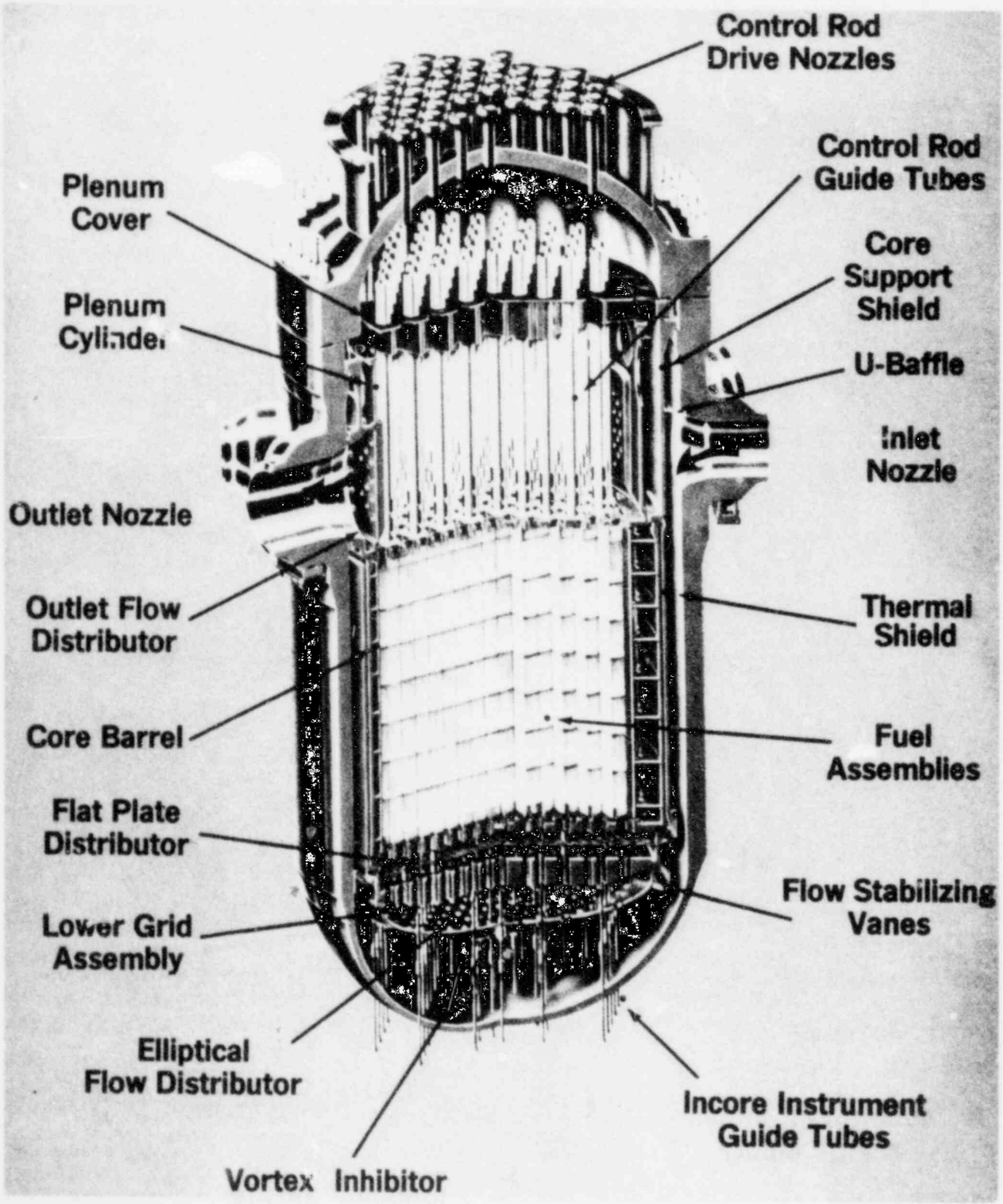

Figure D-5. RV Isolated Model, Reactor Internals and SSS

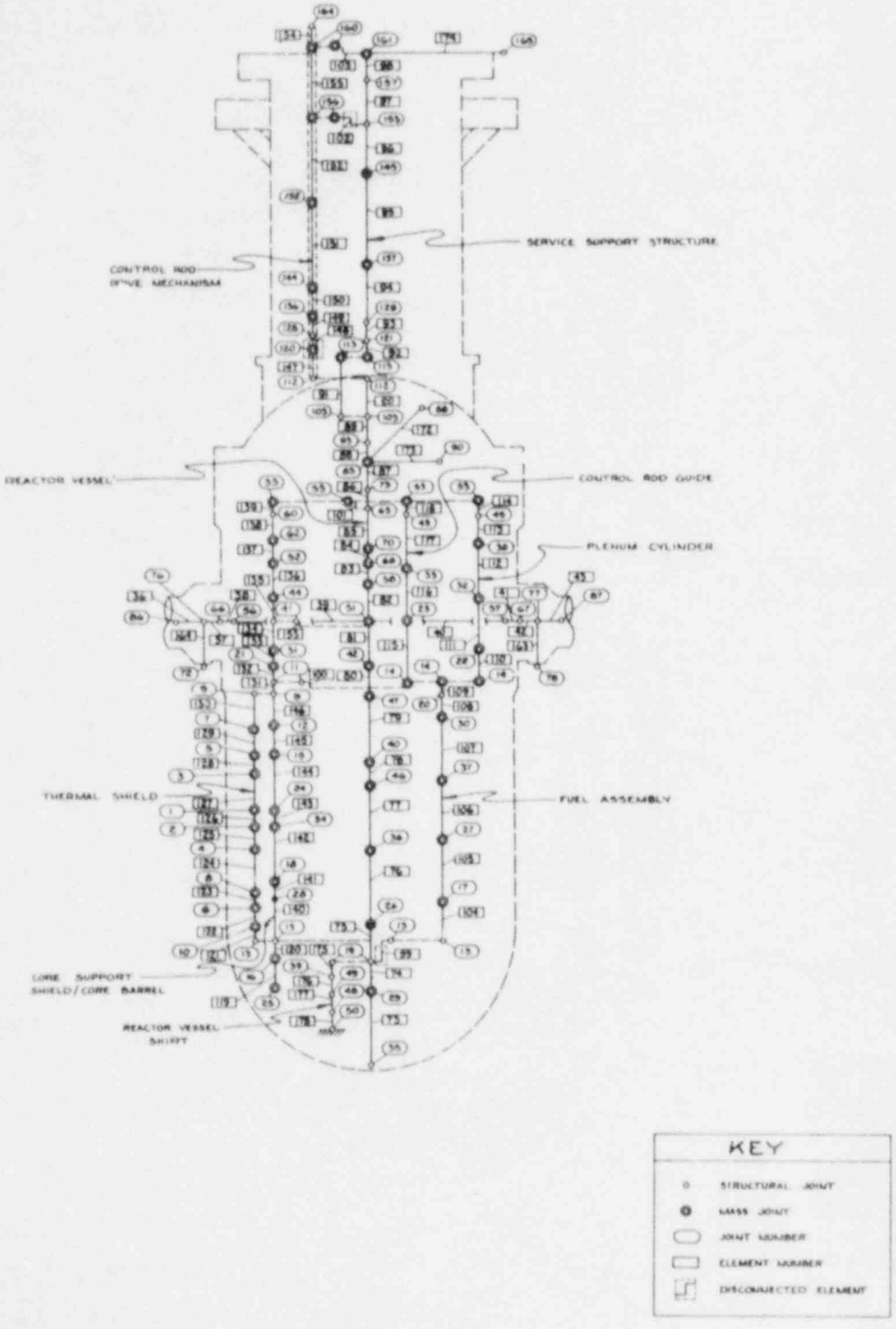

Figure D-6. RV Isolated Model, Skirt-Supported Plant, Plan View

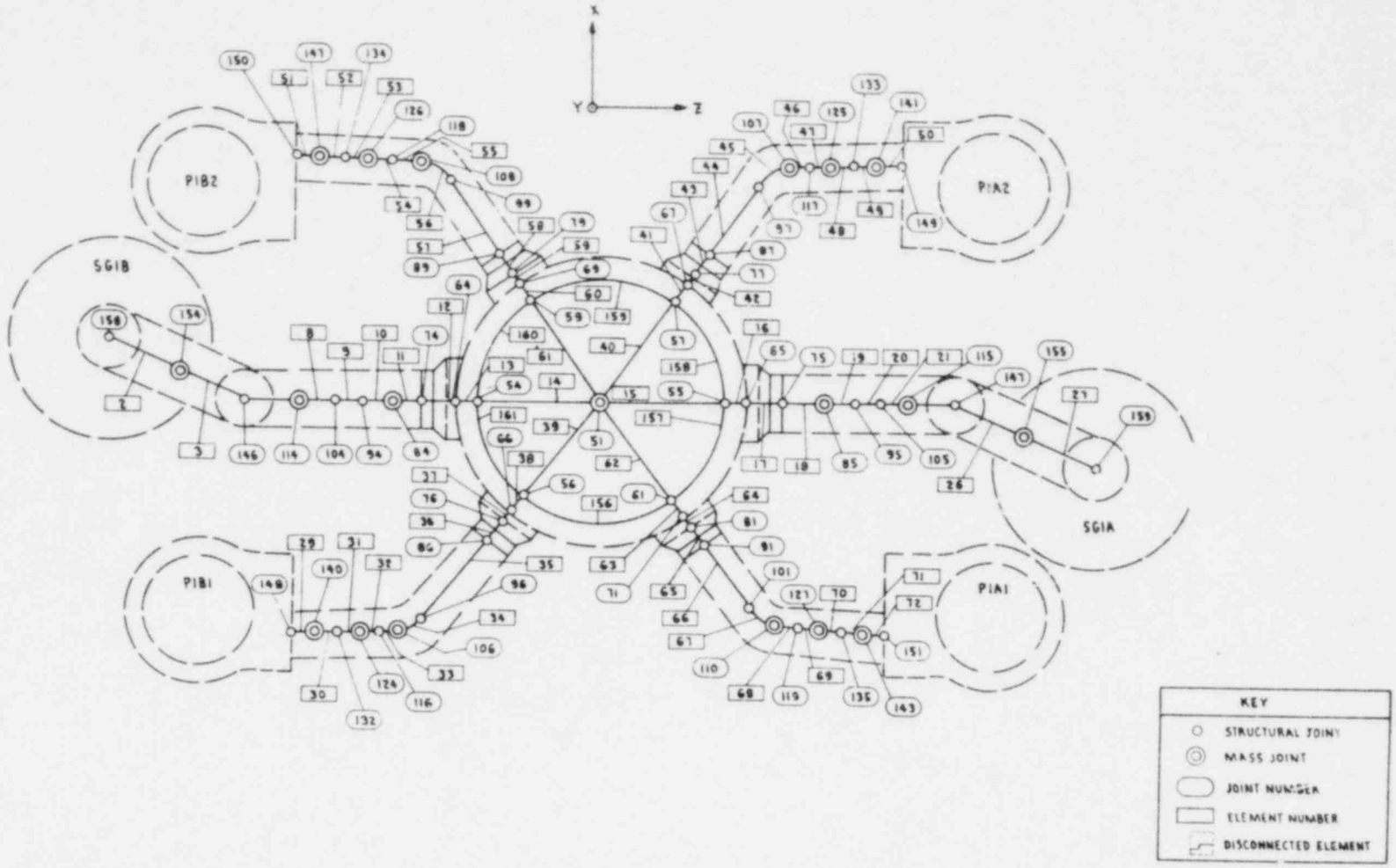

Figure D-7. RV Isolated Model, Nozzle-Supported Plant, Plan View

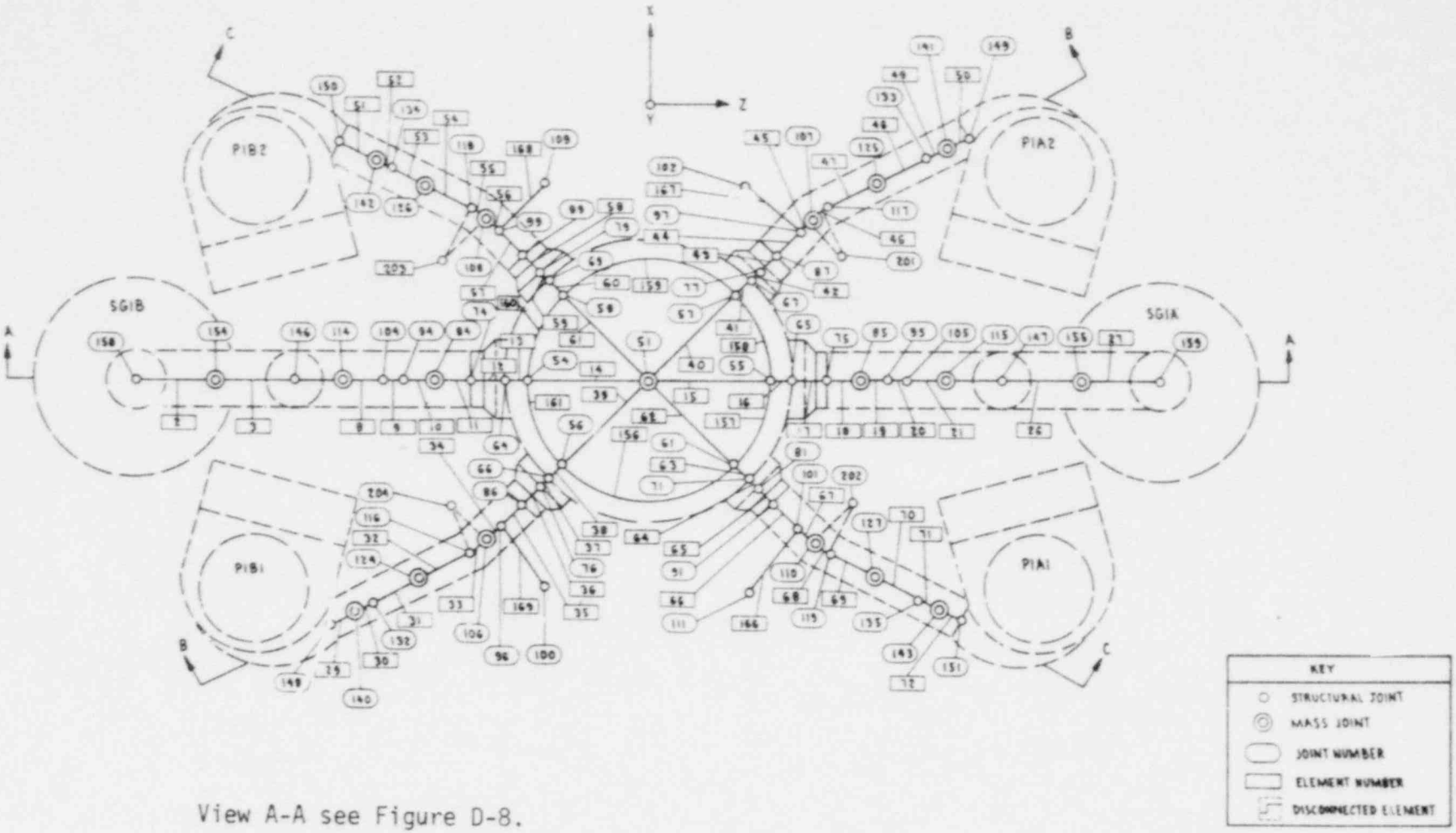

View A-A see Figure D-8.

View B-B see Figure D-9.

View C-C see Figure D-10.

Figure D-8. RV Isolated Model, Elevation
View A-A, Hot Leg

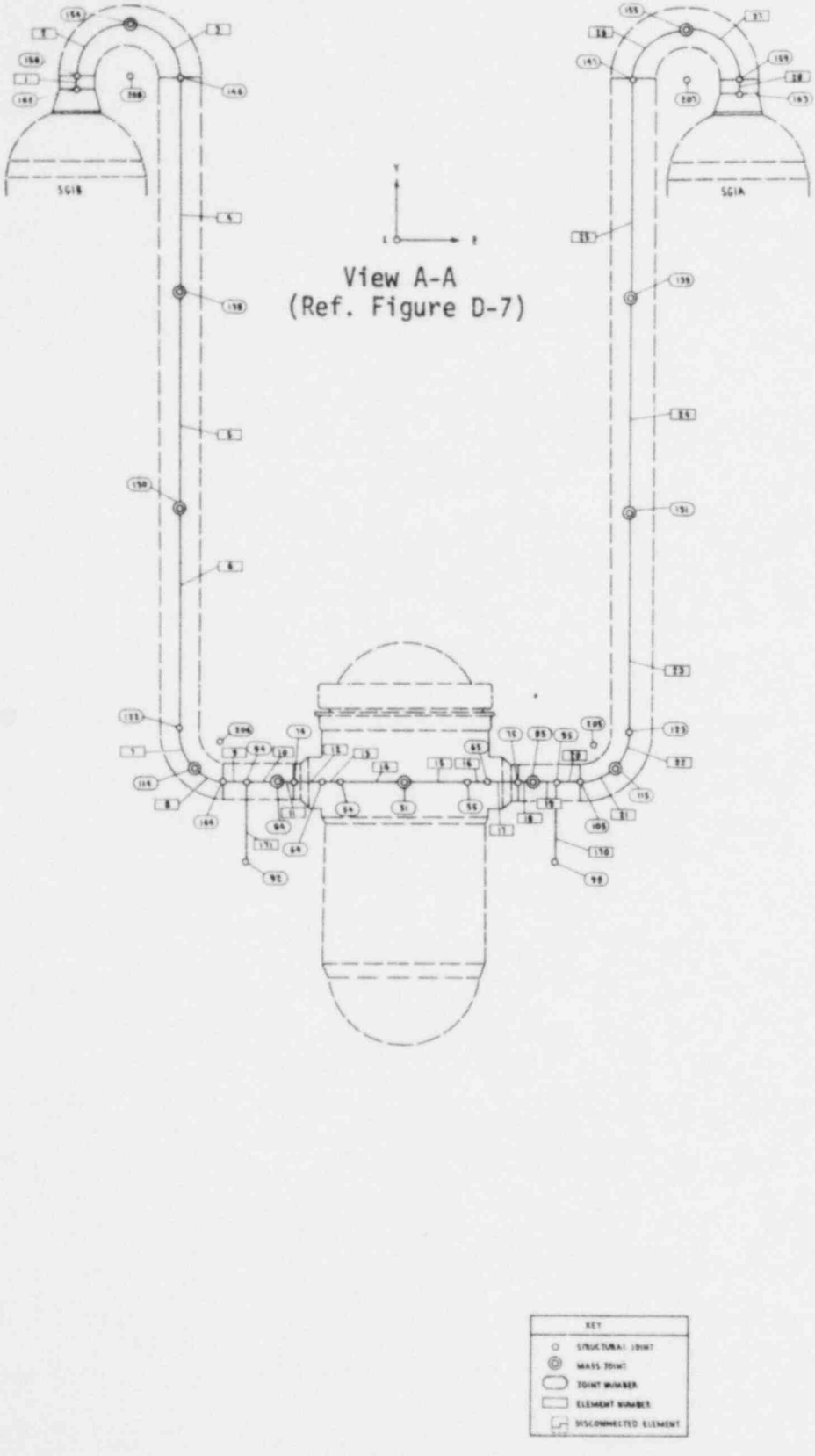

Figure D-9. RV Isolated Model, Elevation View B-B, Cold Leg

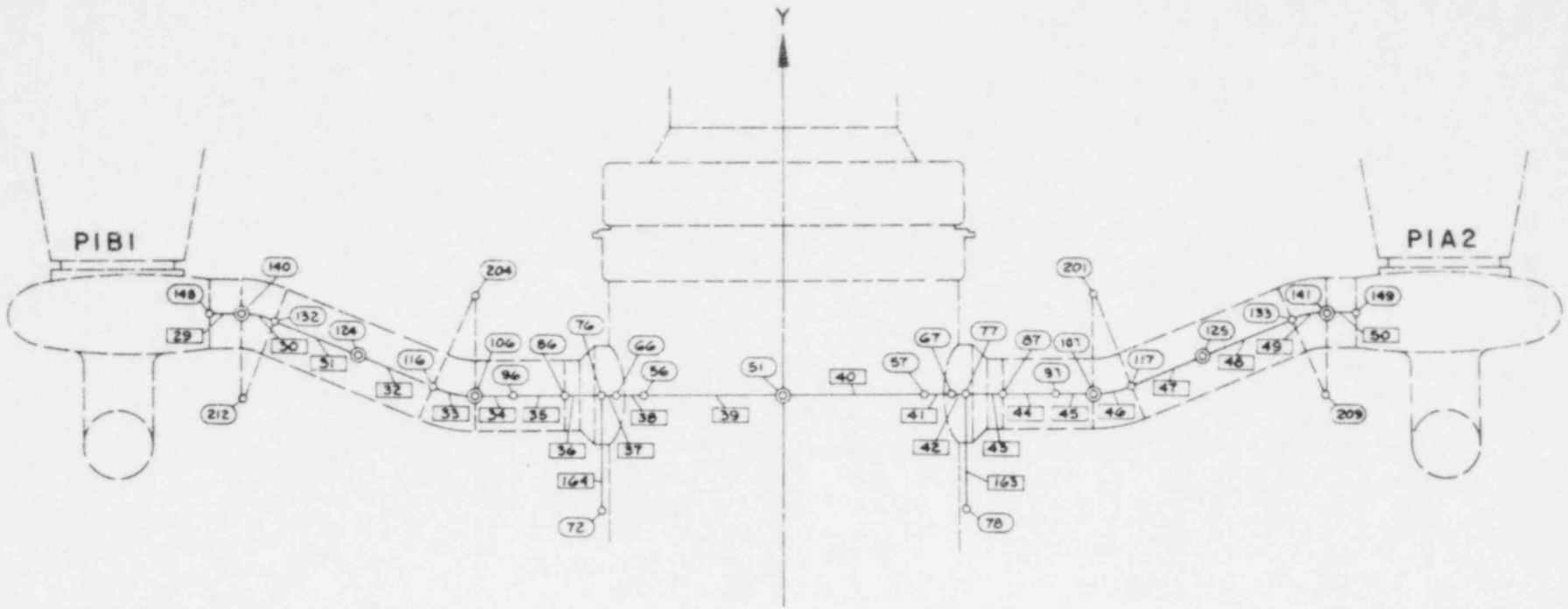

VIEW B-B

(REF. FIGURE D-7)

KEY

- STRUCTURAL JOINT
- MASS JOINT
- JOINT NUMBER
- ELEMENT NUMBER
- DISCONNECTED ELEMENT

Figure D-10. RV Isolated Model, Elevation View C-C, Cold Leg

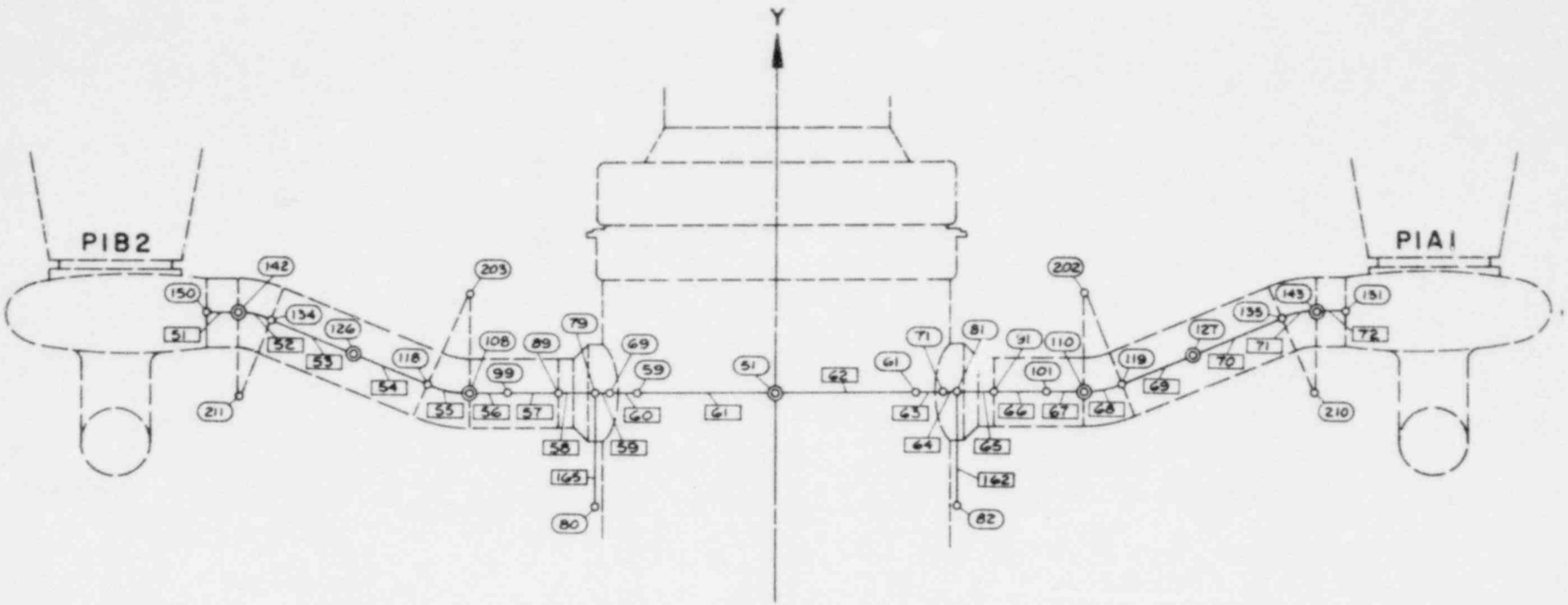

VIEW C-C

(REF. FIGURE D-7)

KEY

- STRUCTURAL JOINT
- MASS JOINT
- JOINT NUMBER
- ELEMENT NUMBER
- DISCONNECTED ELEMENT

Figure D-11. Reactor Vessel Loading Functions

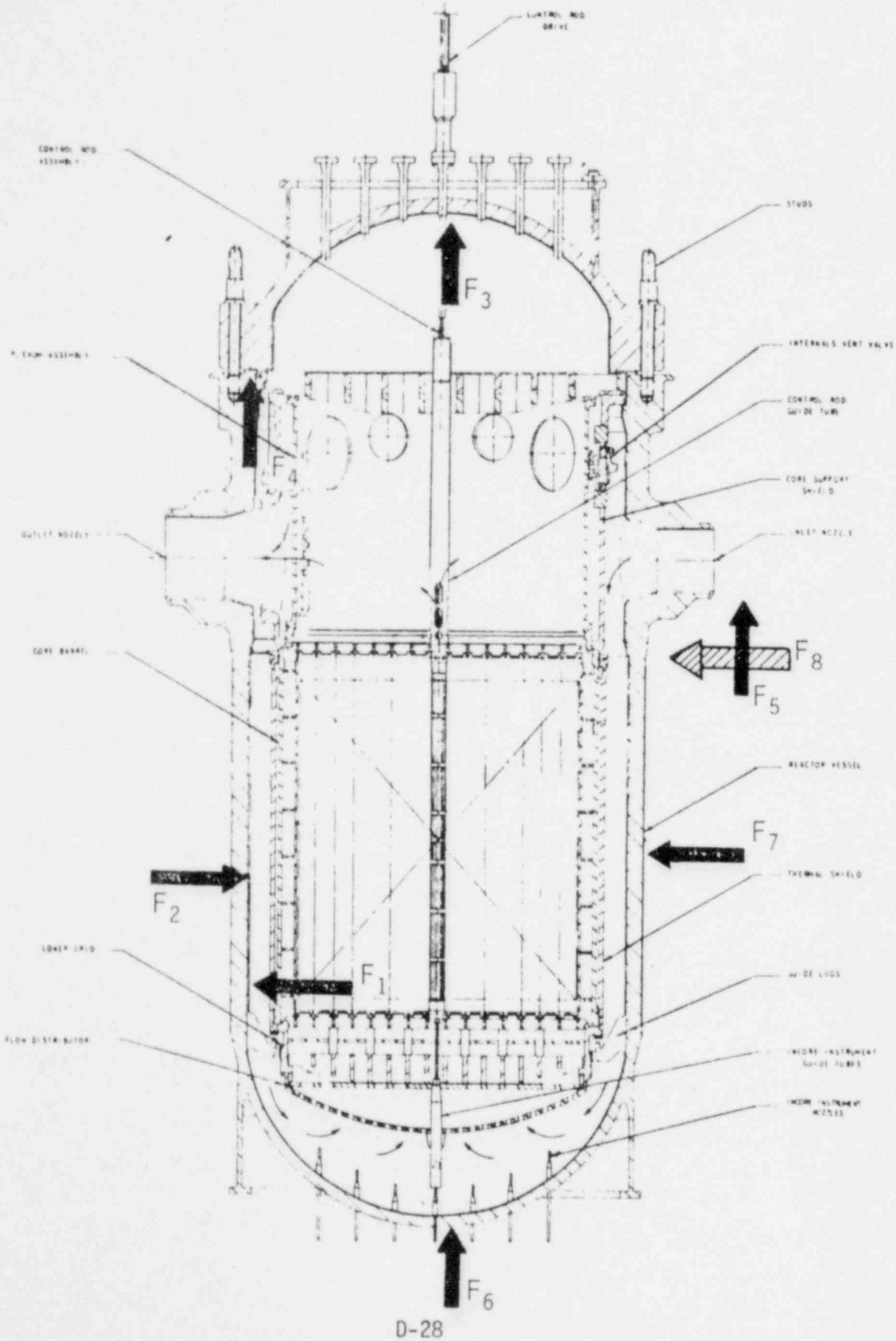

Figure D-12. Owners Group Core Bounce Analysis — ANSYS Model

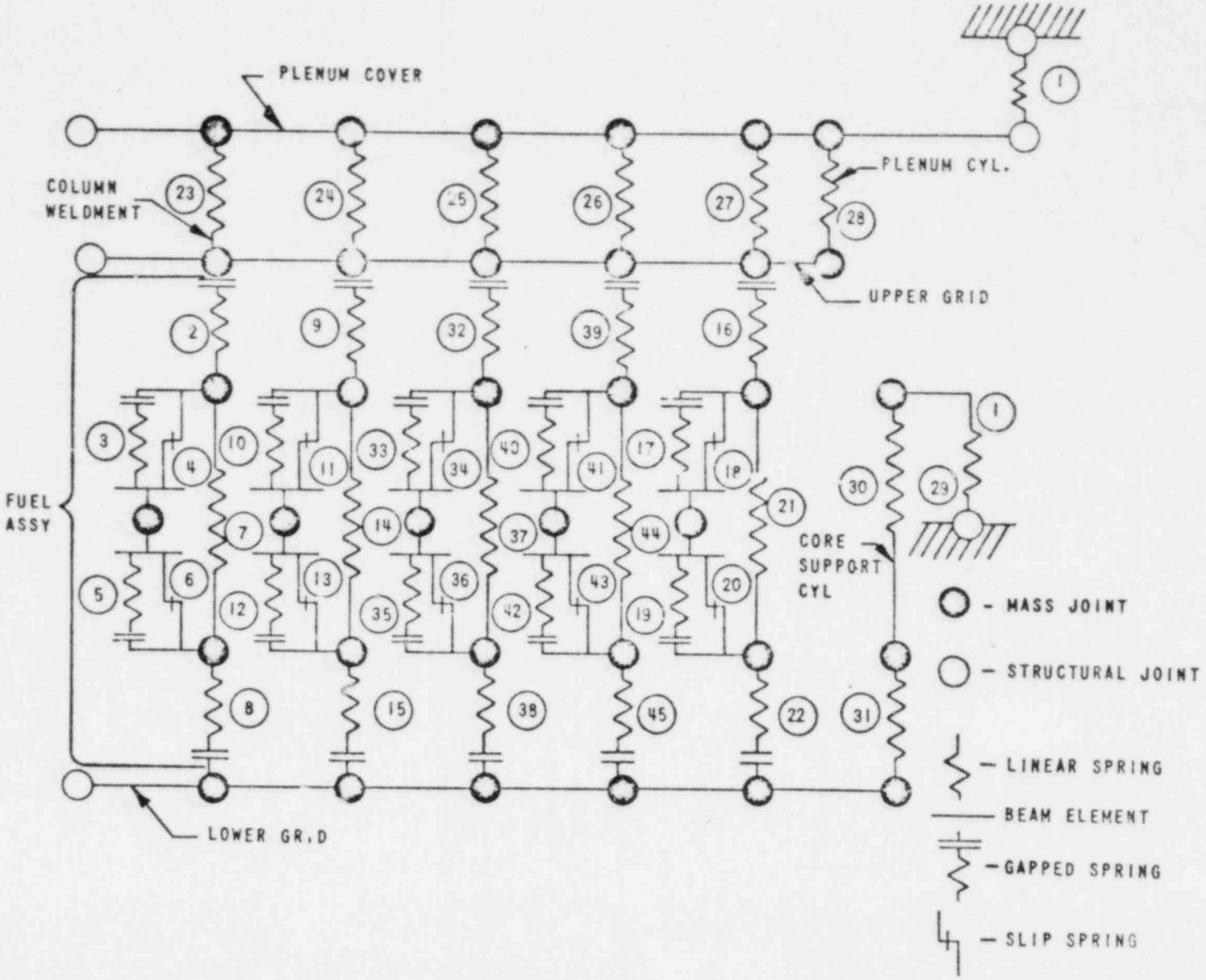

Figure D-13. Flow Chart for Generation of Applied Forcing Functions on Reactor Vessel and Internals

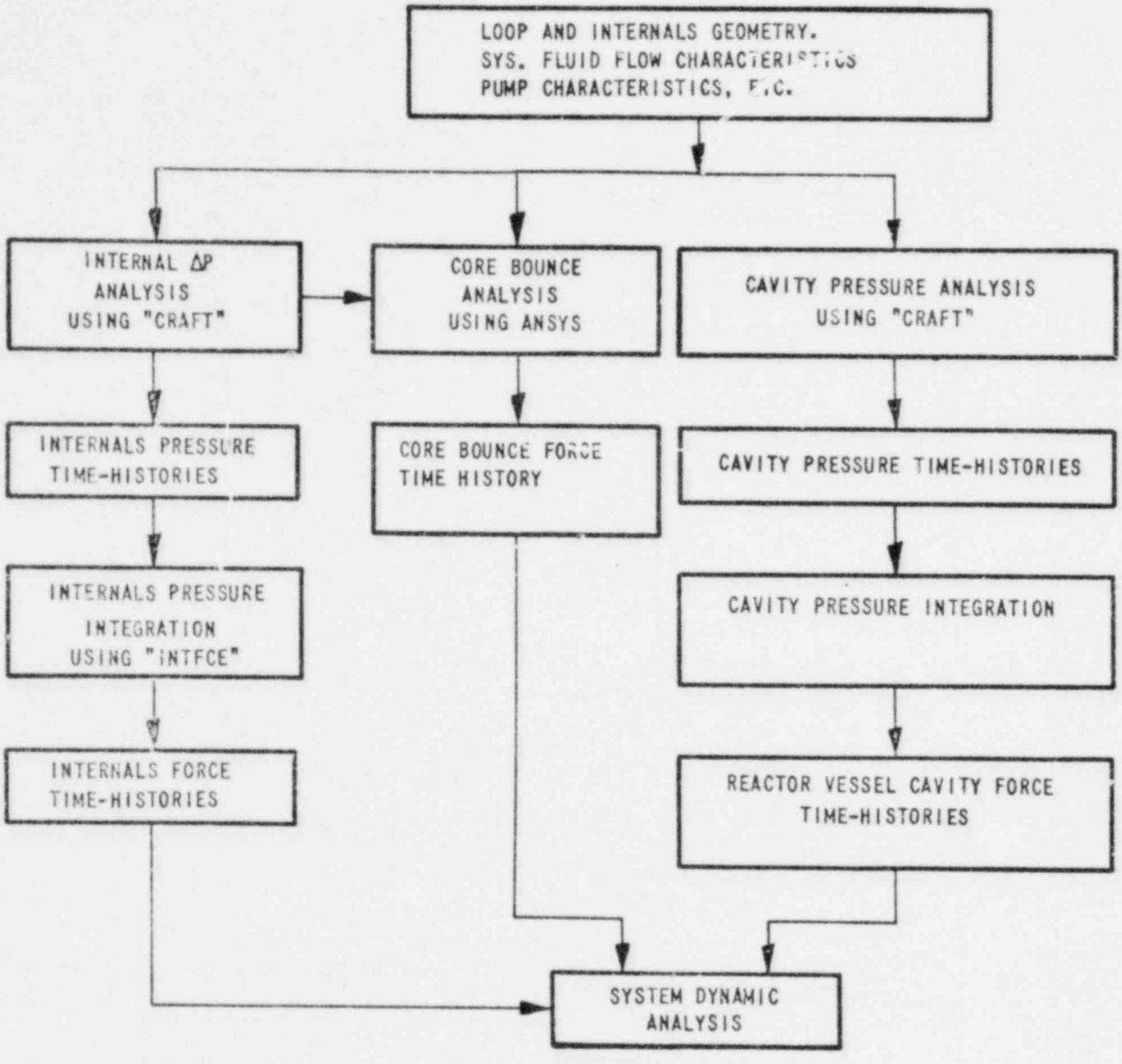

APPENDIX E

Reactor Vessel Support Skirt – Detailed Structural Model Description

1. Introduction

The supporting structure for the reactor vessel is the skirt shown in Figure E-1. The attached piping provides minimal stiffness effects on the reactor vessel; therefore, the skirt must sustain the dynamic loads and provide structural stability to the reactor vessel. All evaluations performed for asymmetric cavity pressure loadings indicate that the capability of the skirt and embedments must be evaluated in detail.

The model presented in Appendix D represents the skirt with a beam element and the embedment as linear elastic springs. The beam representation has been derived by correlation with the shell representation in Figure E-2.

The shell model provides a tool for defining the linear and nonlinear response of the structure. Localized yielding is allowed in supports while performing linear dynamic analysis, and careful interpretation of the resultant displacements is required. Movement of the reactor vessel due to deformation of the skirt translates into a horizontal displacement of the piping nozzles. The structural stability and definition of linear dynamic analysis is provided by evaluating the model in Figure E-2.

2. Model Description

The model shown in Figure E-2 comprises the skirt and its flange, spring elements representing the nonlinear characteristics of the anchor bolts and concrete, the portion of the reactor vessel adjacent to the skirt, and centerline beam elements representing the remainder of the reactor vessel. As indicated in the figure, only half of the structure has been modeled. Appropriate boundary conditions have been specified to simulate the complete skirt.

The skirt is modeled with plastic shell bending elements for which actual temperatures and corresponding nonlinear material properties have been specified. The supporting structures beneath the flange (bolts, concrete sole plate and shear keys) have been modeled using nonlinear axial springs arranged to respond to both compression and tension loads in vertical, tangential, and radial directions. Thus, the interaction of the bolts through the flange is accommodated properly.

External loads acting on the structure consist of bending moments, horizontal shears, and vertical forces which are applied at the centerline. In addition, reactor cavity pressures are specified (as applicable) to the shell elements representing the skirt.

3. Results

Based on load deflection relationships, the linear spring rates shown in Figures E-3 and E-4 have been developed for use in an independent linear beam model of the same structure. In addition to the force/deflection relationships, the ultimate load-carrying capacity of the skirt and its appurtenances were investigated. Results are shown on the dotted lines in Figures E-3 and E-4. The failure loads were shown to be at or slightly above the code allowables.

Figure E-1. Reactor Vessel Skirt Support

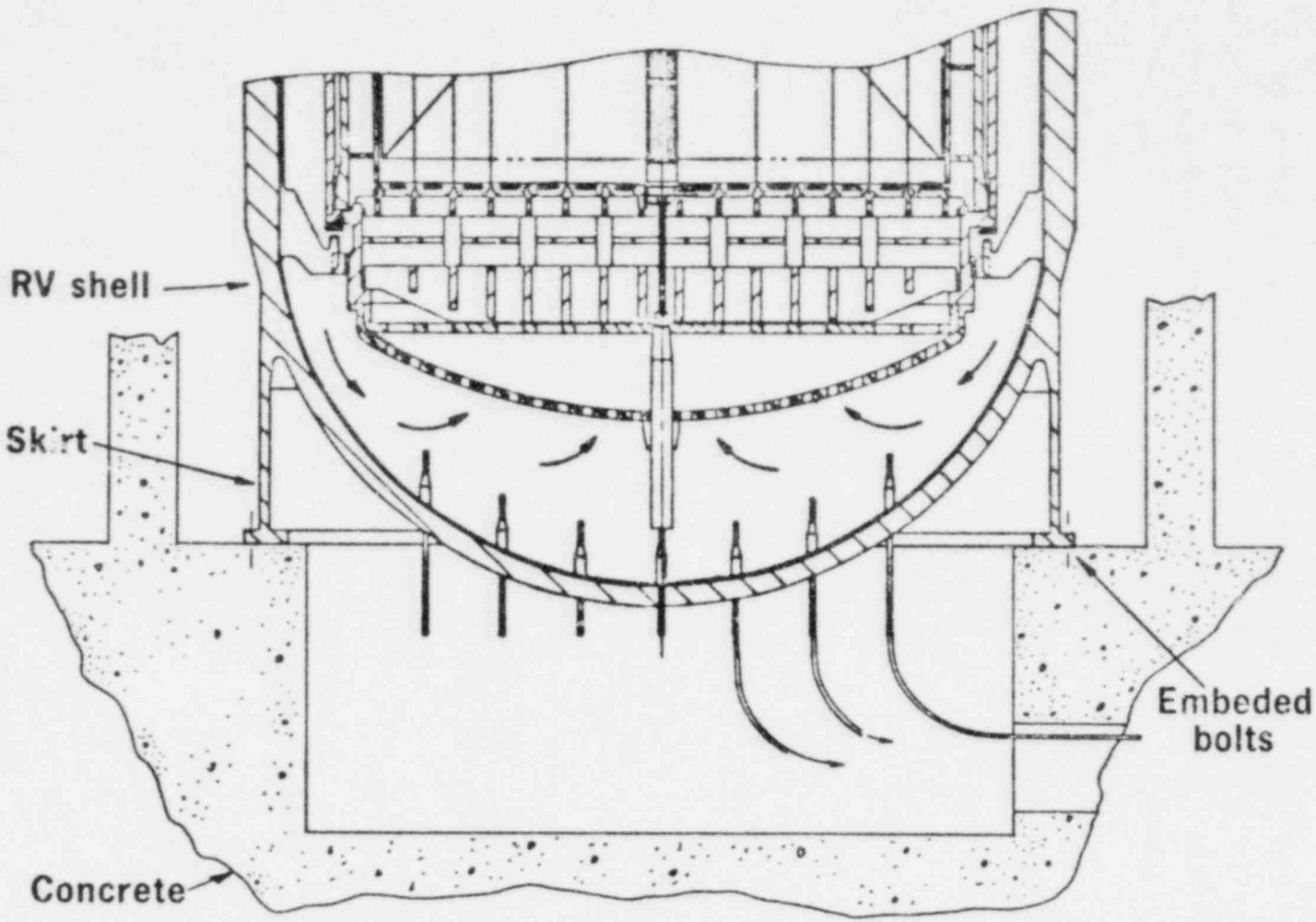

Figure E-2. Reactor Vessel Skirt, Mesh Generation

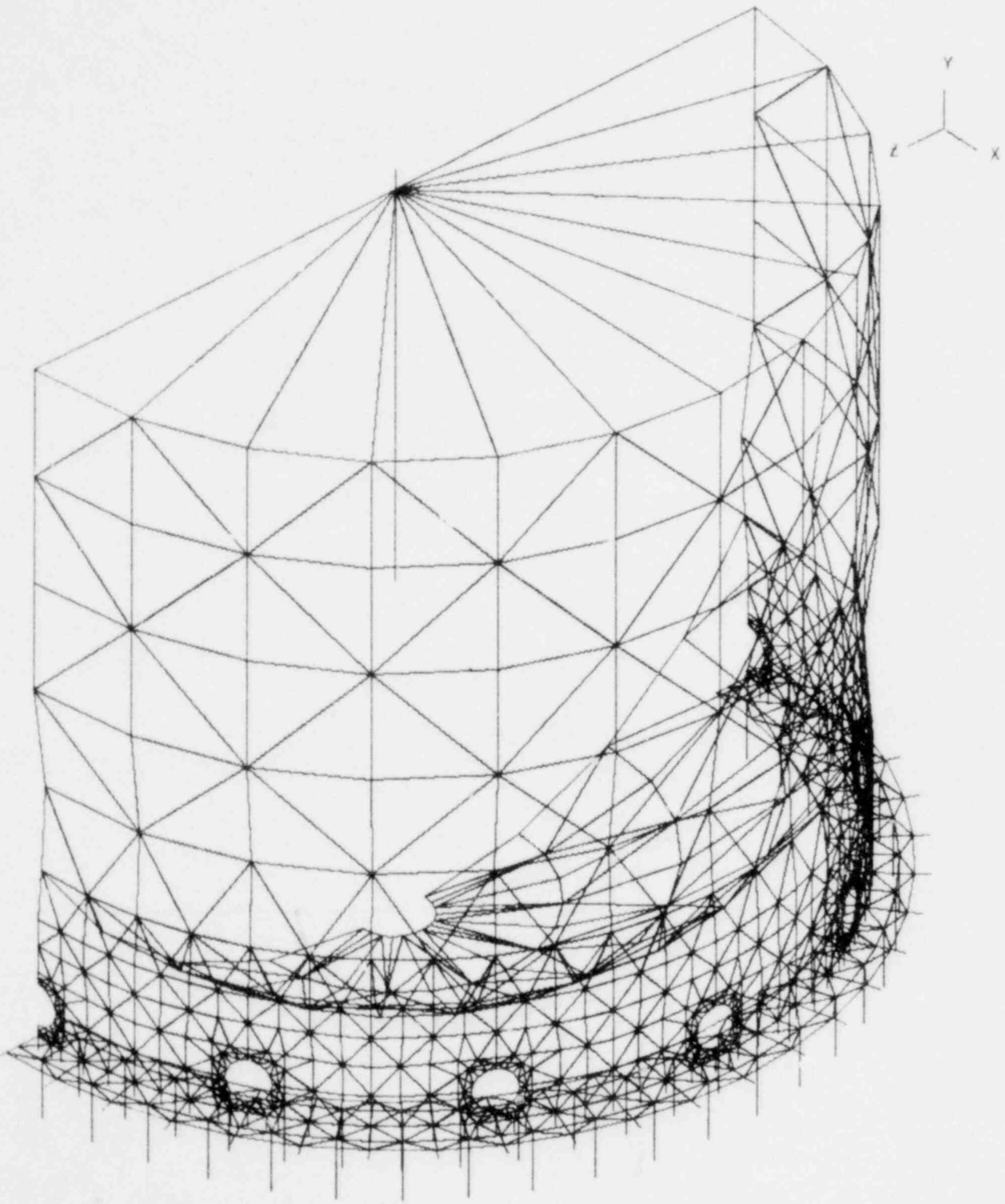

Figure E-3. Reactor Vessel Skirt Force/Deflection Relationship

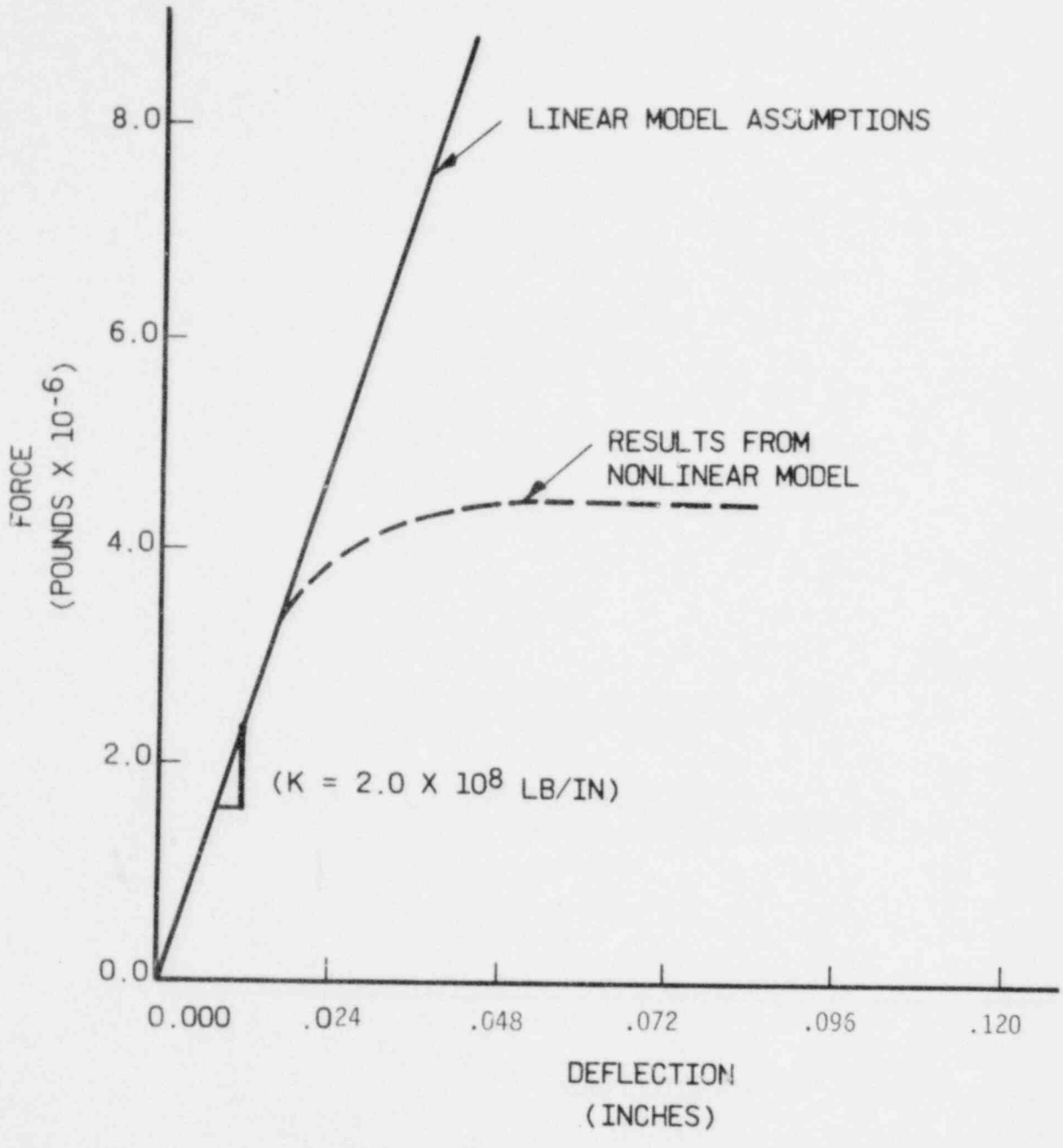

Figure E-4. Reactor Vessel Skirt Moment/Rotation Relationship

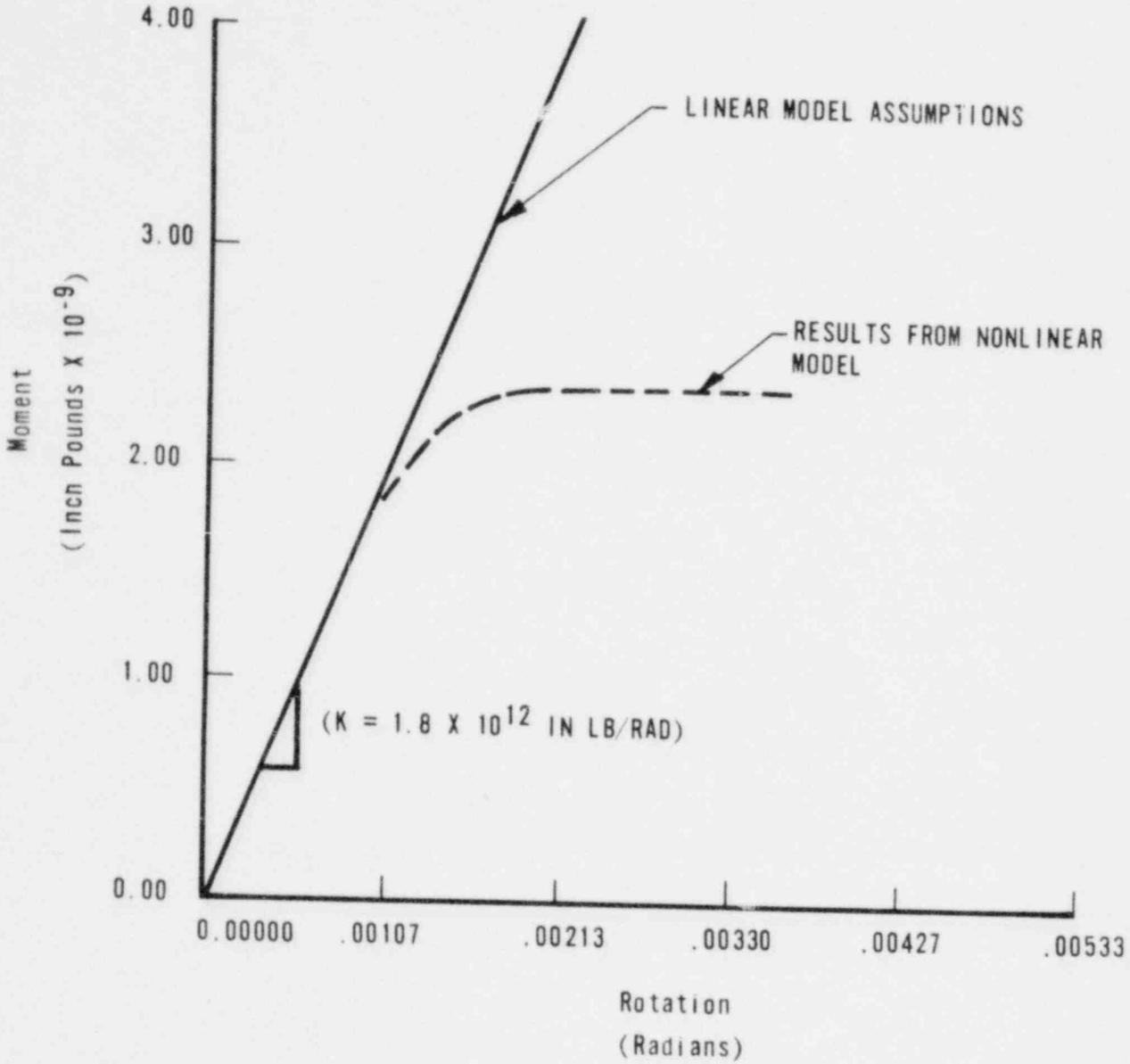

APPENDIX F

Reactor Coolant System Loop Model Description

This appendix provides illustrations of the mathematical models that were used to calculate the loads in the reactor coolant piping loop and its supports due to postulated pipe breaks within the steam generator compartment.

Figures F-1 through F-6 show the skirt-supported plant model with pump supports; the skirt-supported plant model without pump supports is essentially the same and is not illustrated. Figures F-7 through F-14 illustrate the nozzle-supported plant model.

Figure F-1. Mathematical Model of Reactor Coolant Piping Assembly, Elevation View E-E

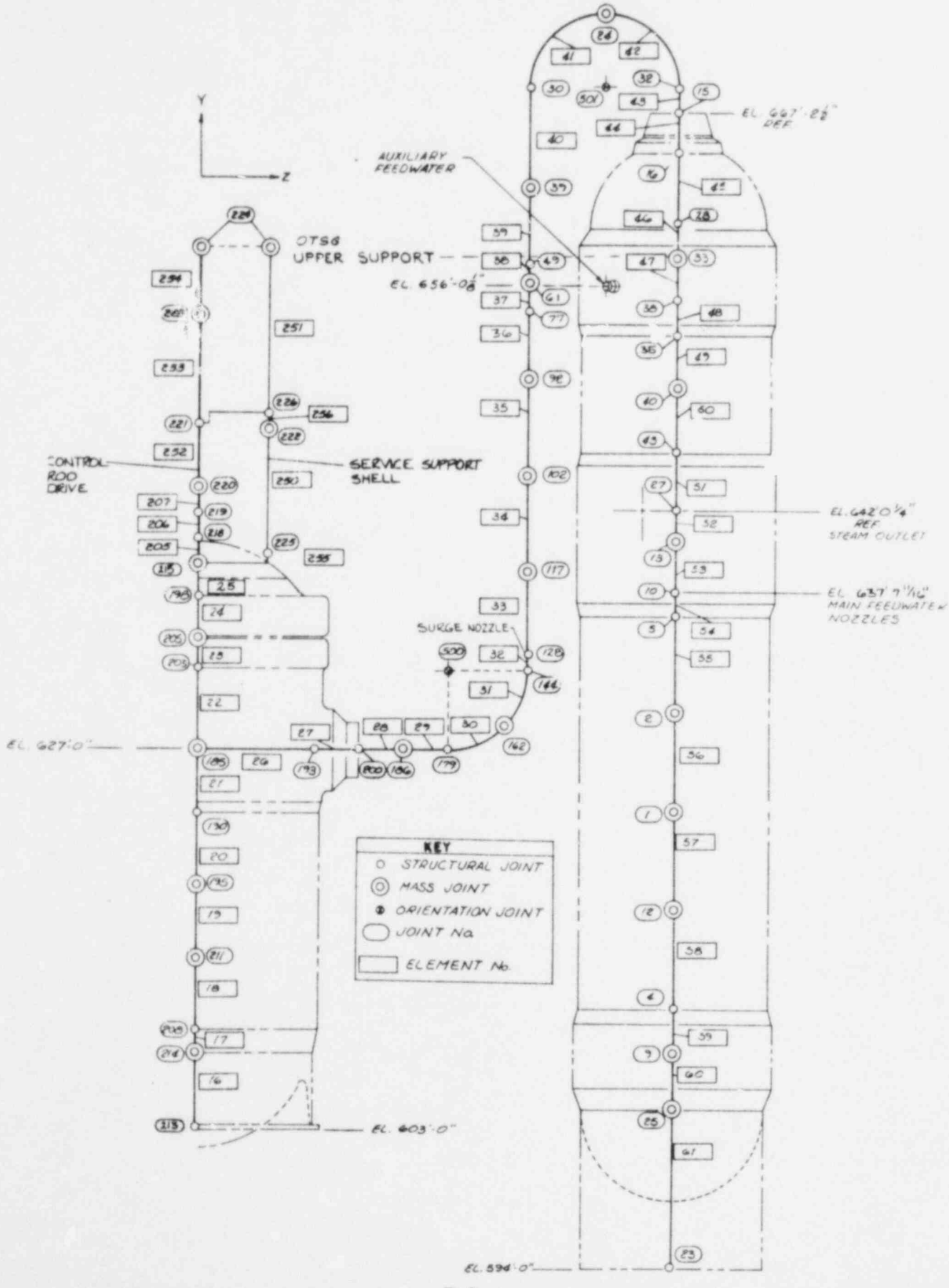

Figure F-2. Mathematical Model of Reactor Coolant Piping Assembly, Plan View – Skirt-Supported Plant

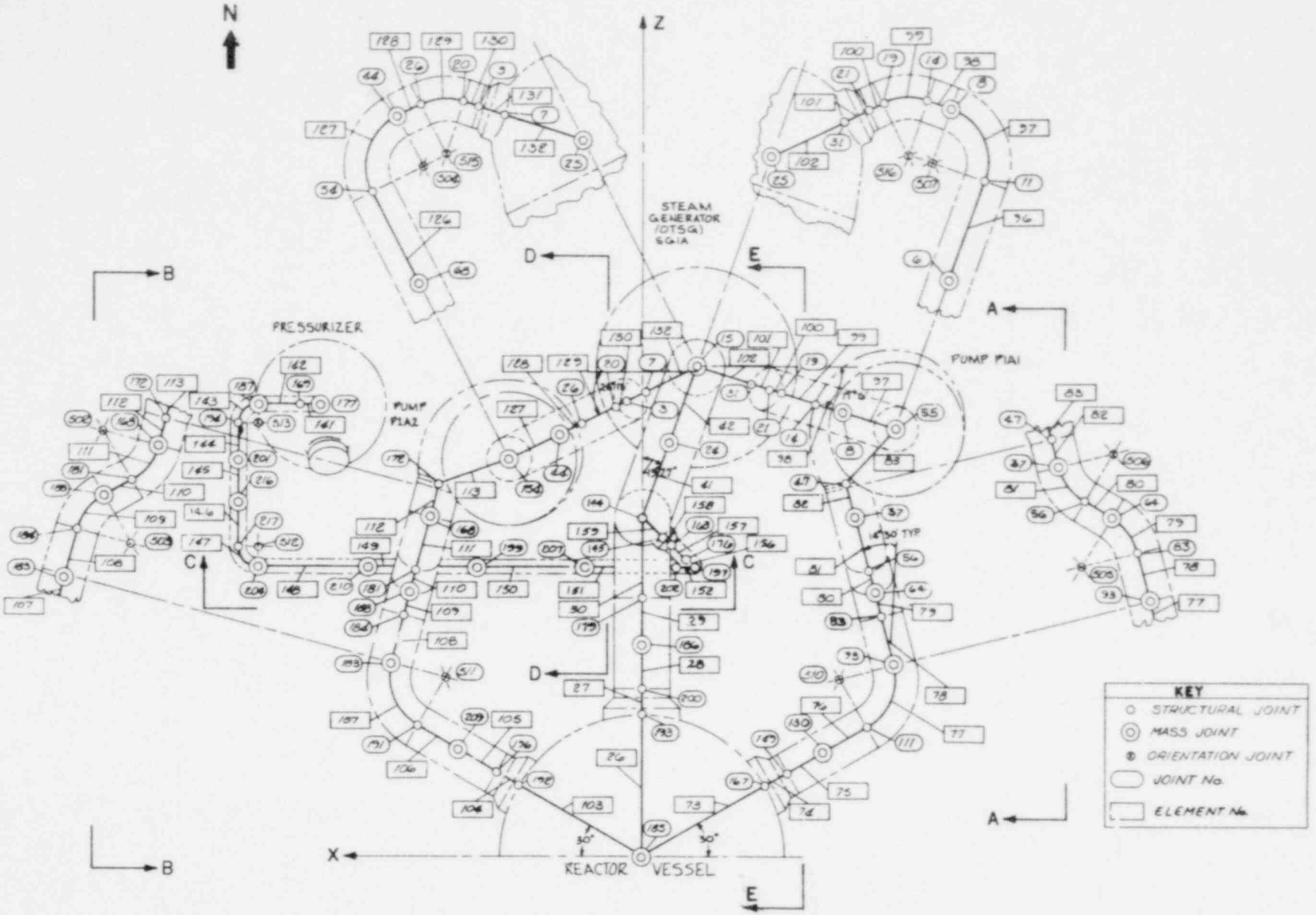

Figure F-3. Mathematical Model of Reactor Coolant Piping Assembly, Elevation View A-A, B-B — Skirt-Supported Plant

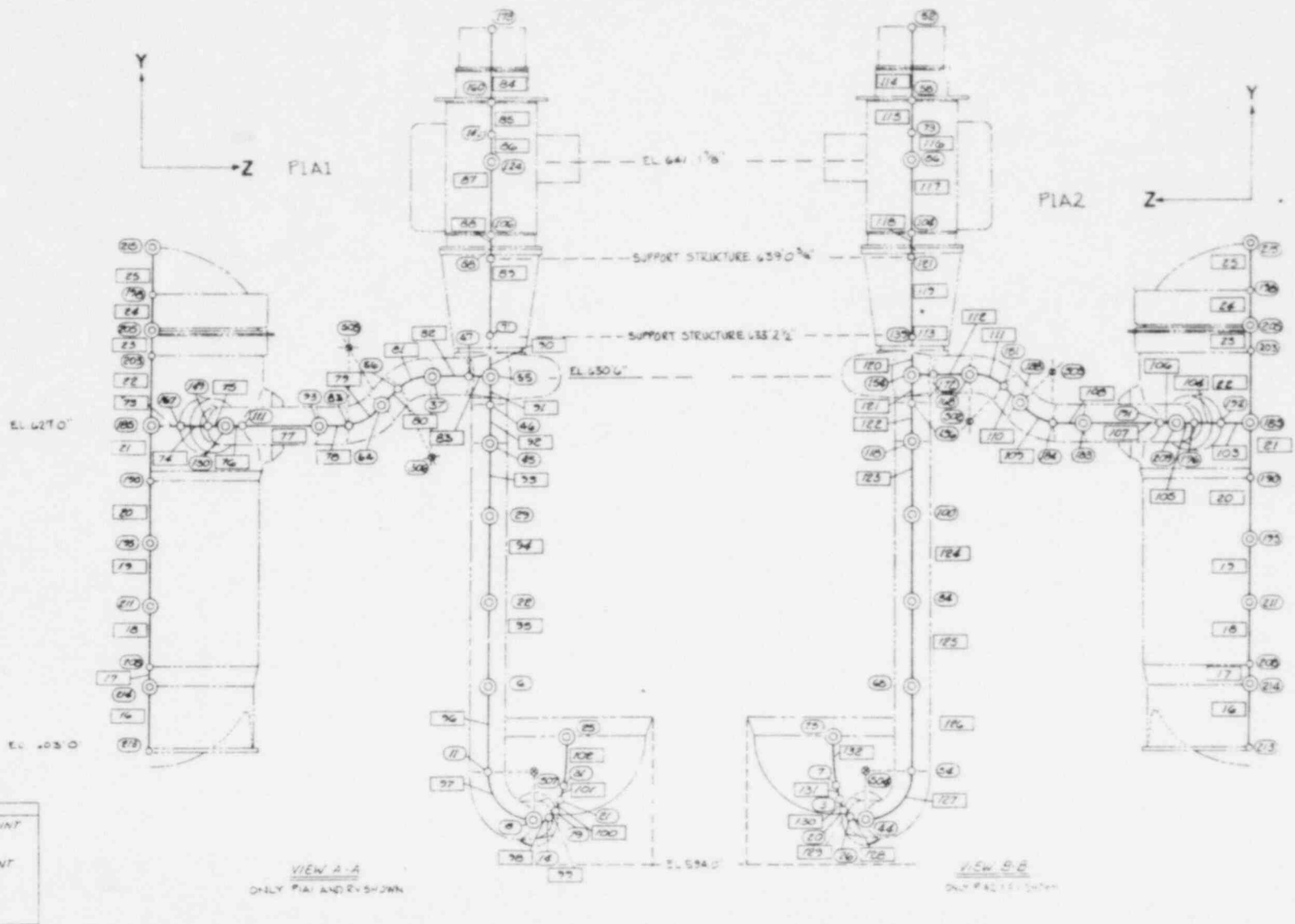

Figure F-4. Mathematical Model of Lower Level Support Restraint — Skirt-Supported Plant

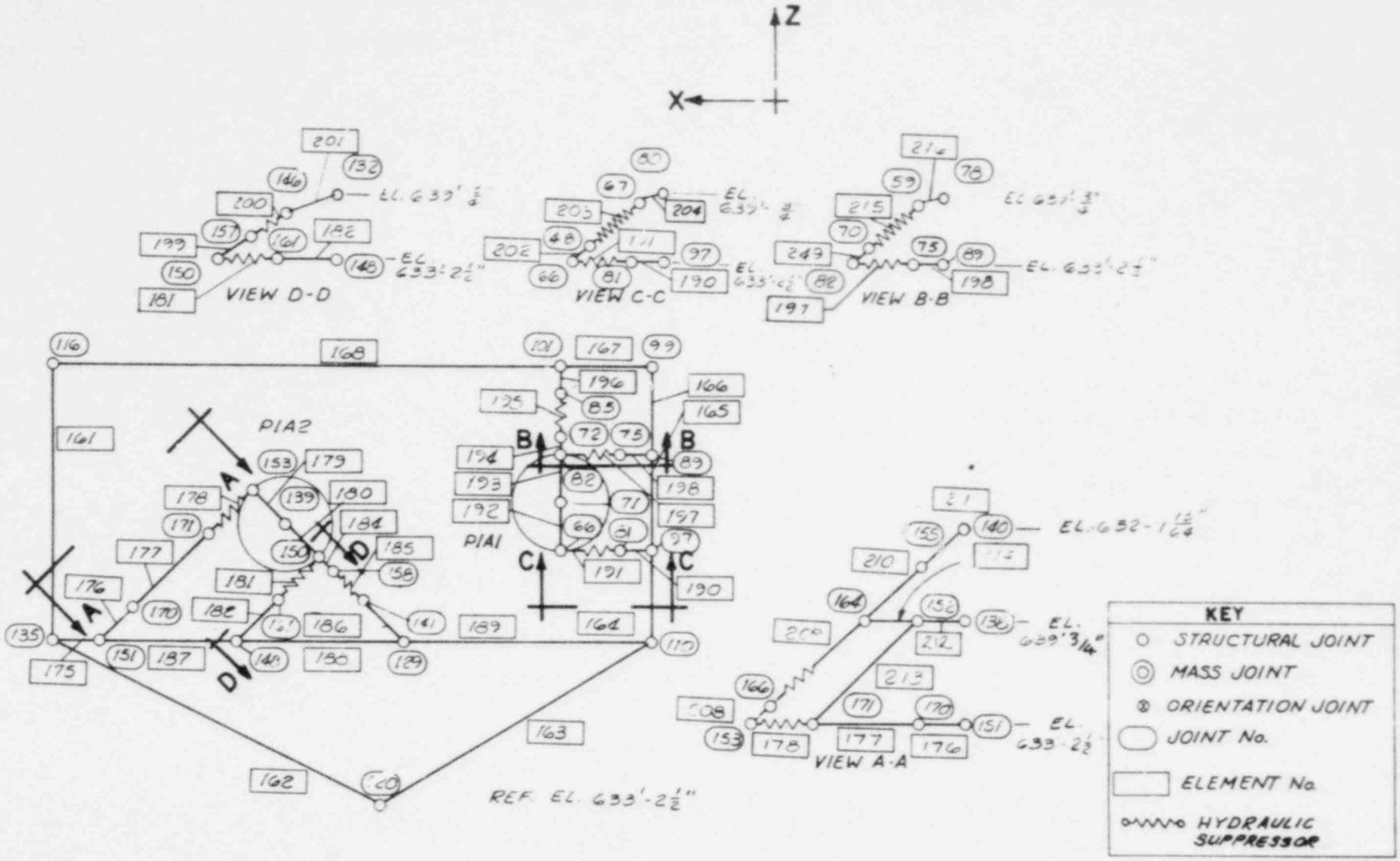

Figure F-5. Mathematical Model of Steam Generator Supports — Skirt-Supported Plant

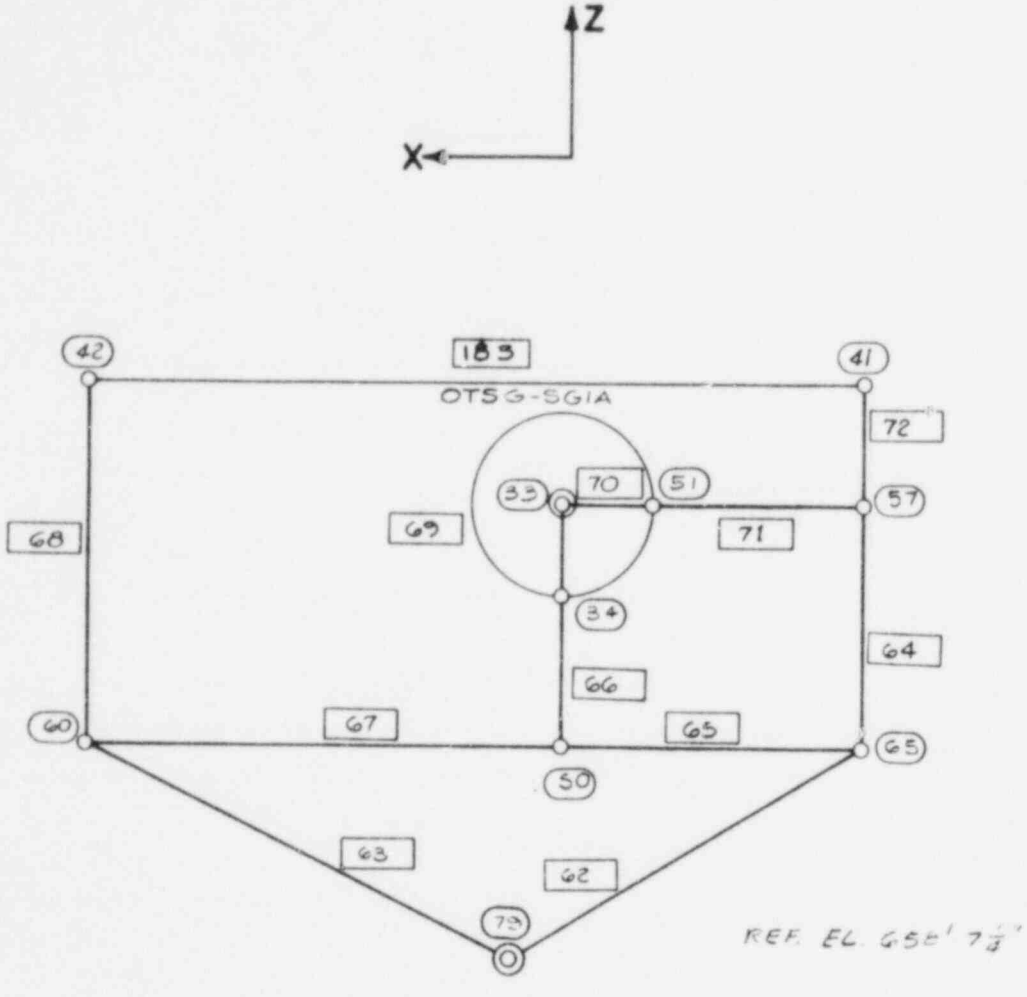

Figure F-6. Mathematical Model of Centerline Support Wall, Skirt-Supported Plant

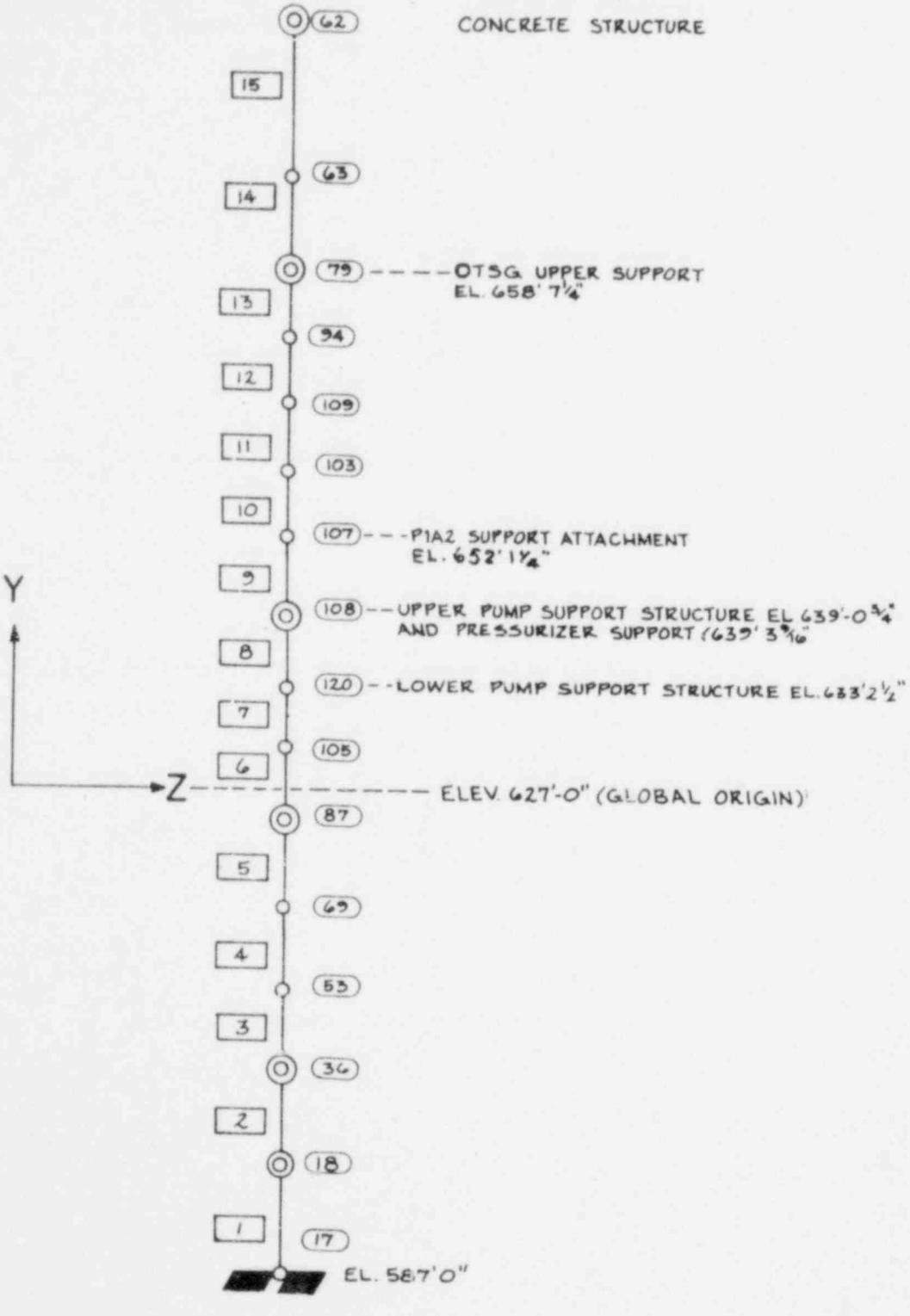

Figure F-7. Mathematical Model of Reactor Coolant Piping, Elevation View No. 1 — Nozzle-Supported Plant

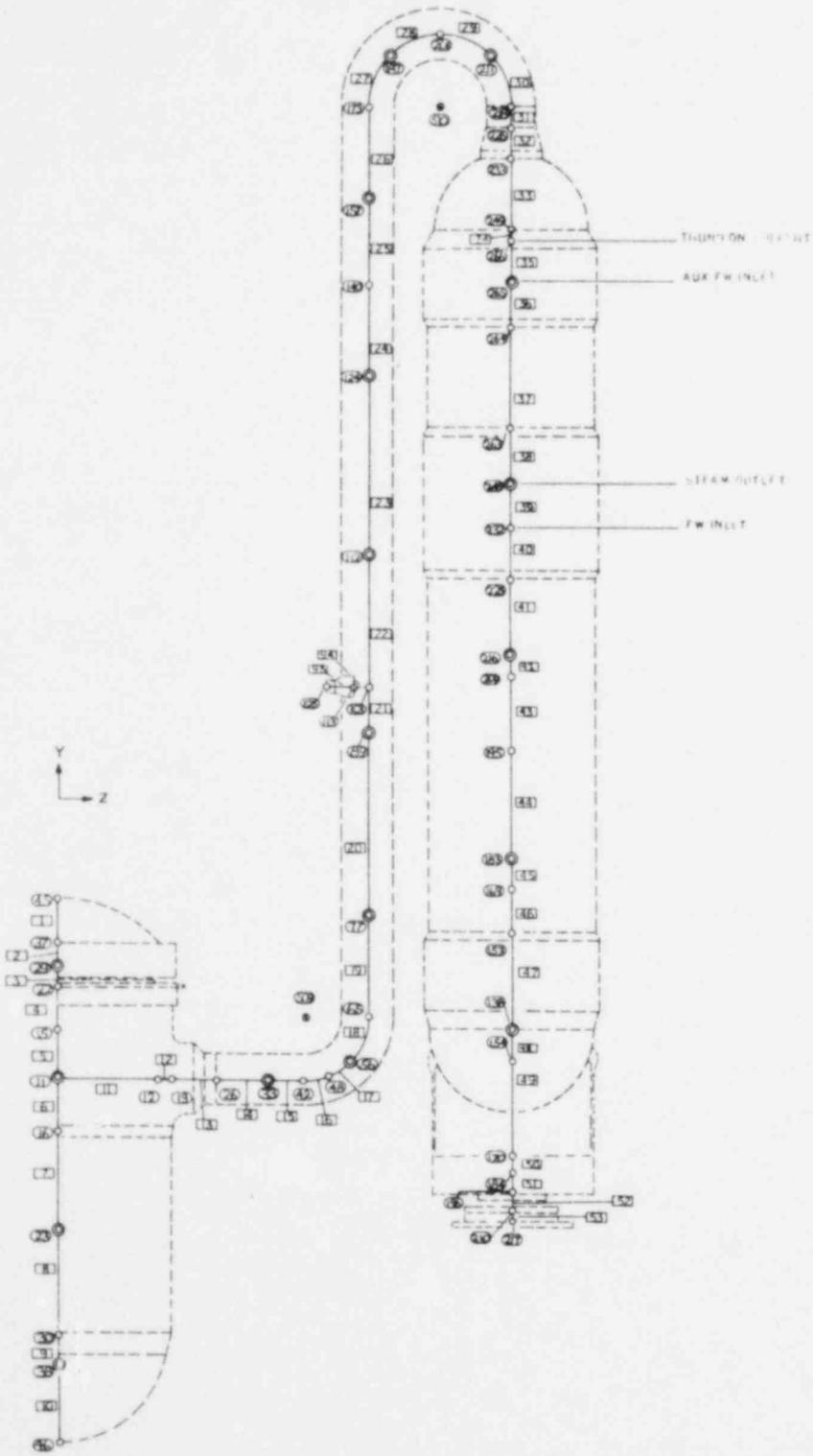

Figure F-8. Mathematical Model of Reactor Coolant
[illegible]ng, Plan View – Nozzle-
pported Plant

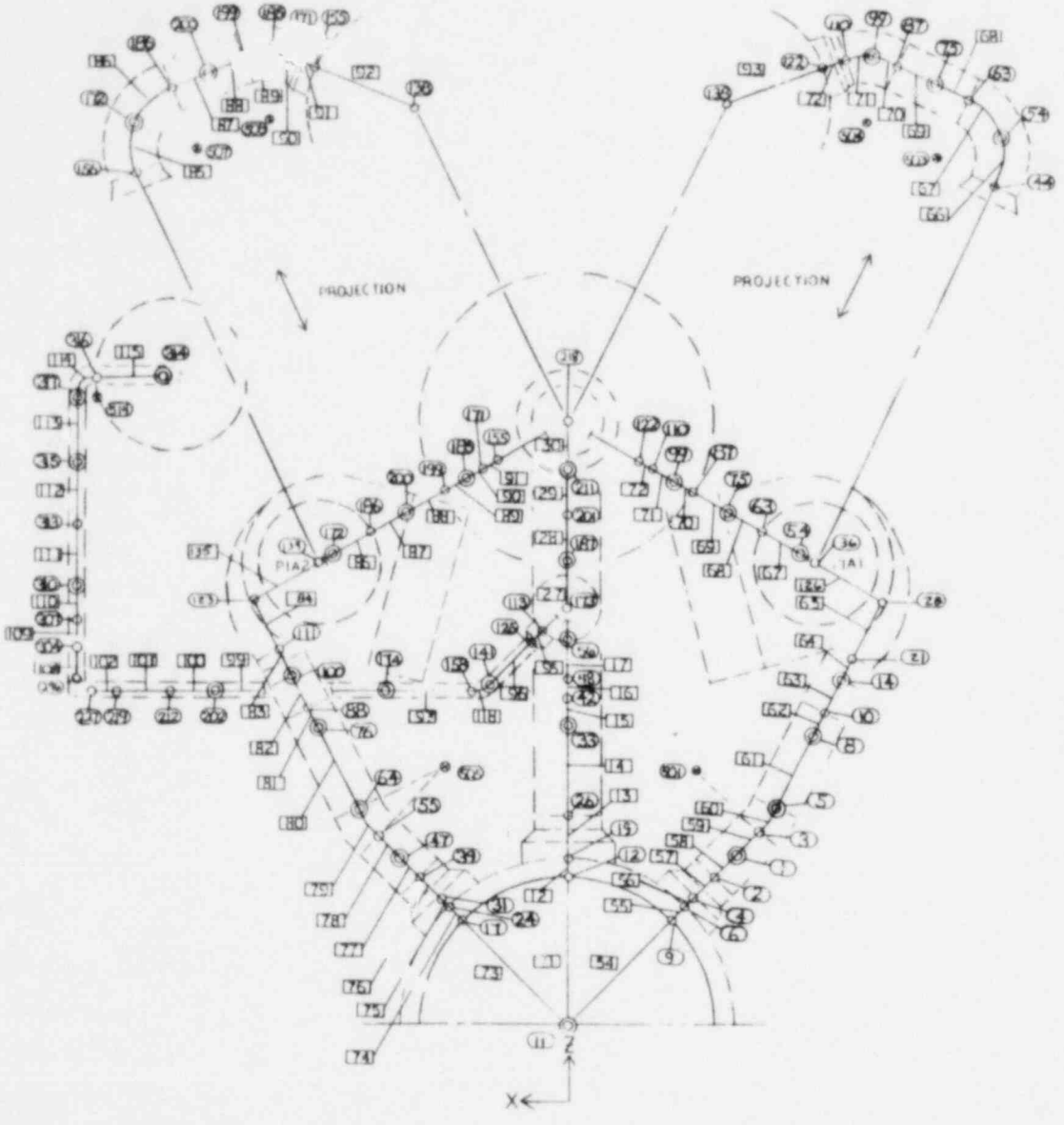

Figure F-9. Mathematical Model of Reactor Coolant Piping, Elevation View No. 2 — Nozzle-Supported Plant

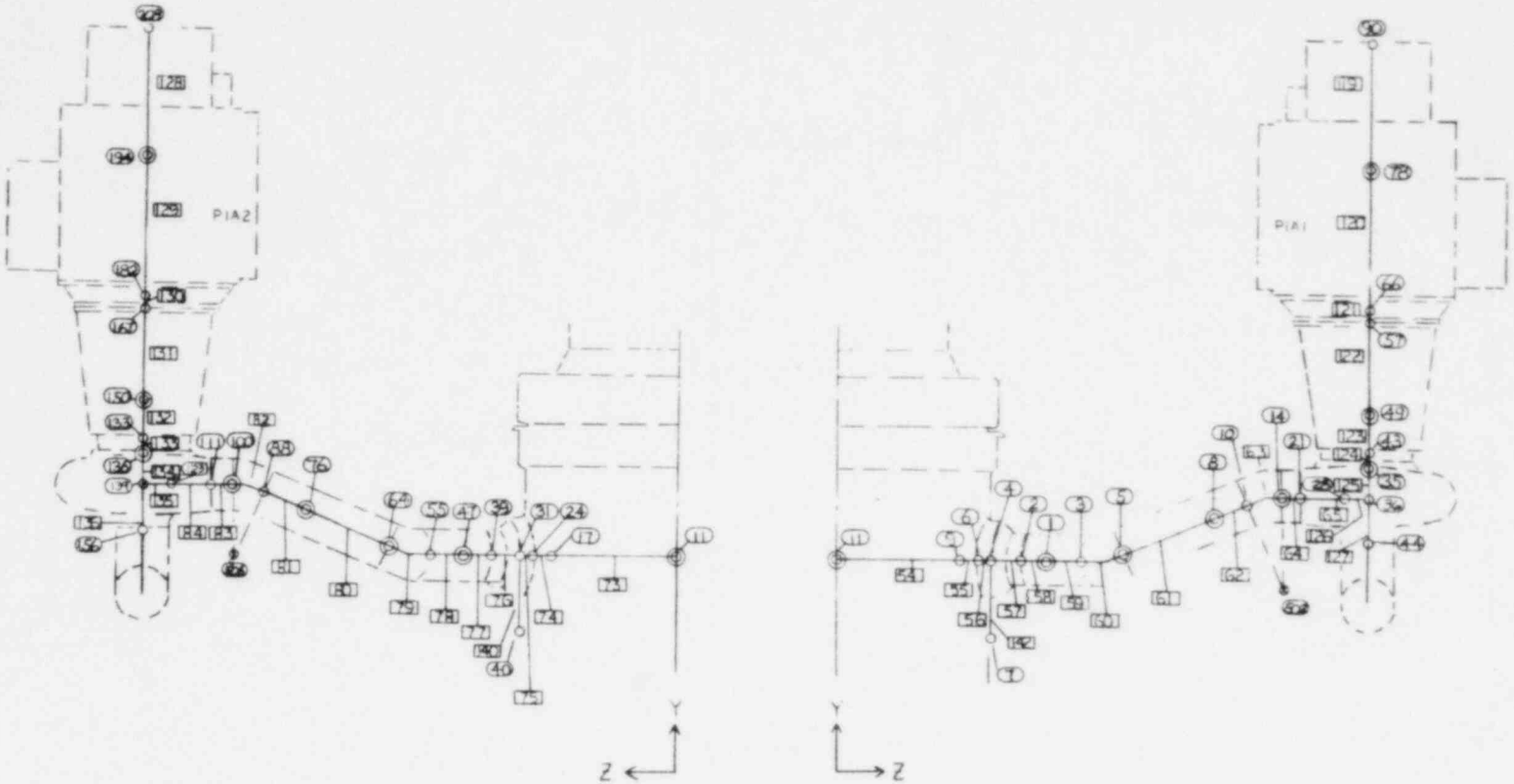

Figure F-10. Upper Pump Support, Plan View — Nozzle-Supported Plant

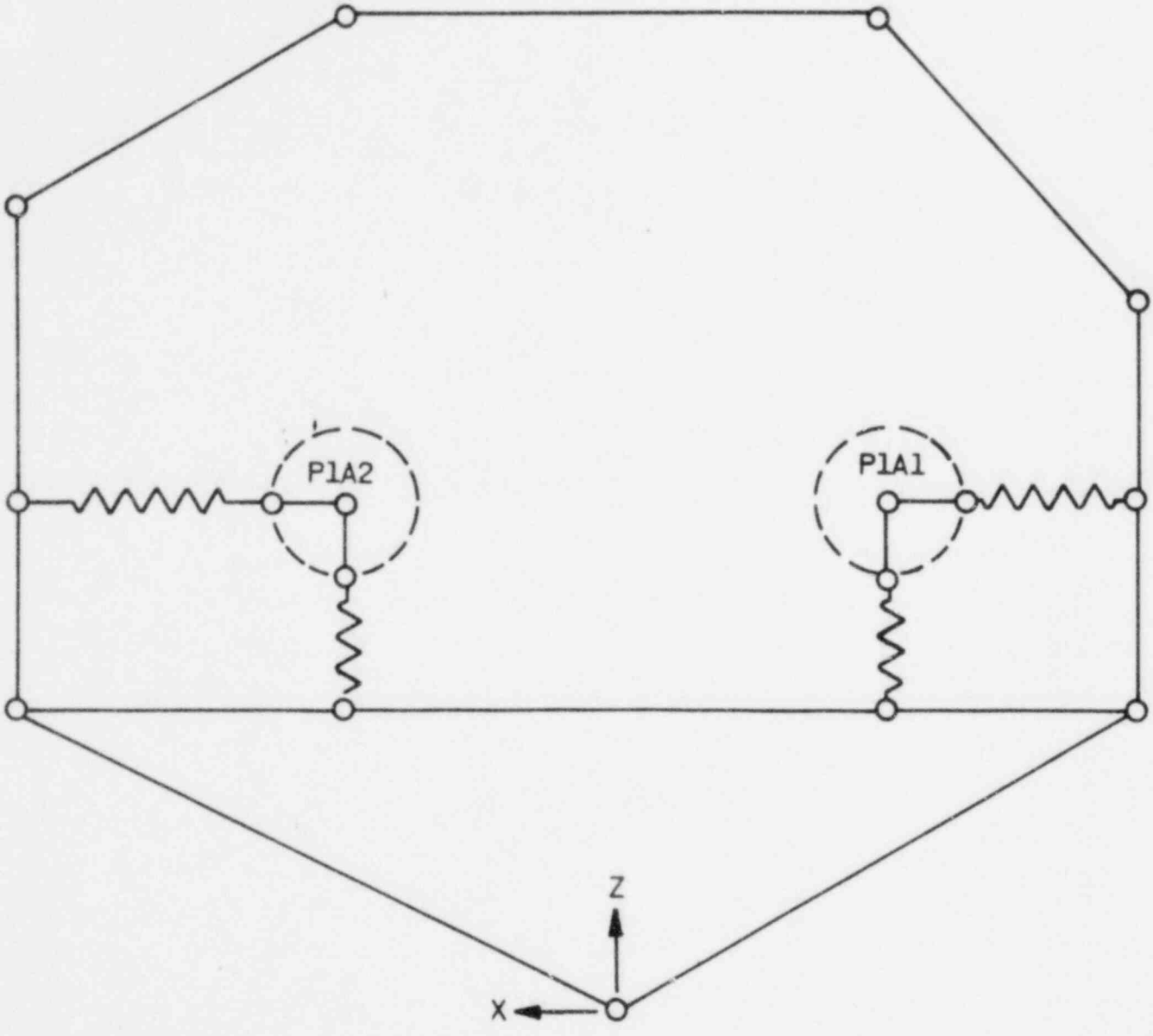

Figure F-11. Mathematical Model of Steam Generator Upper Support, Plan View — Nozzle-Supported Plant

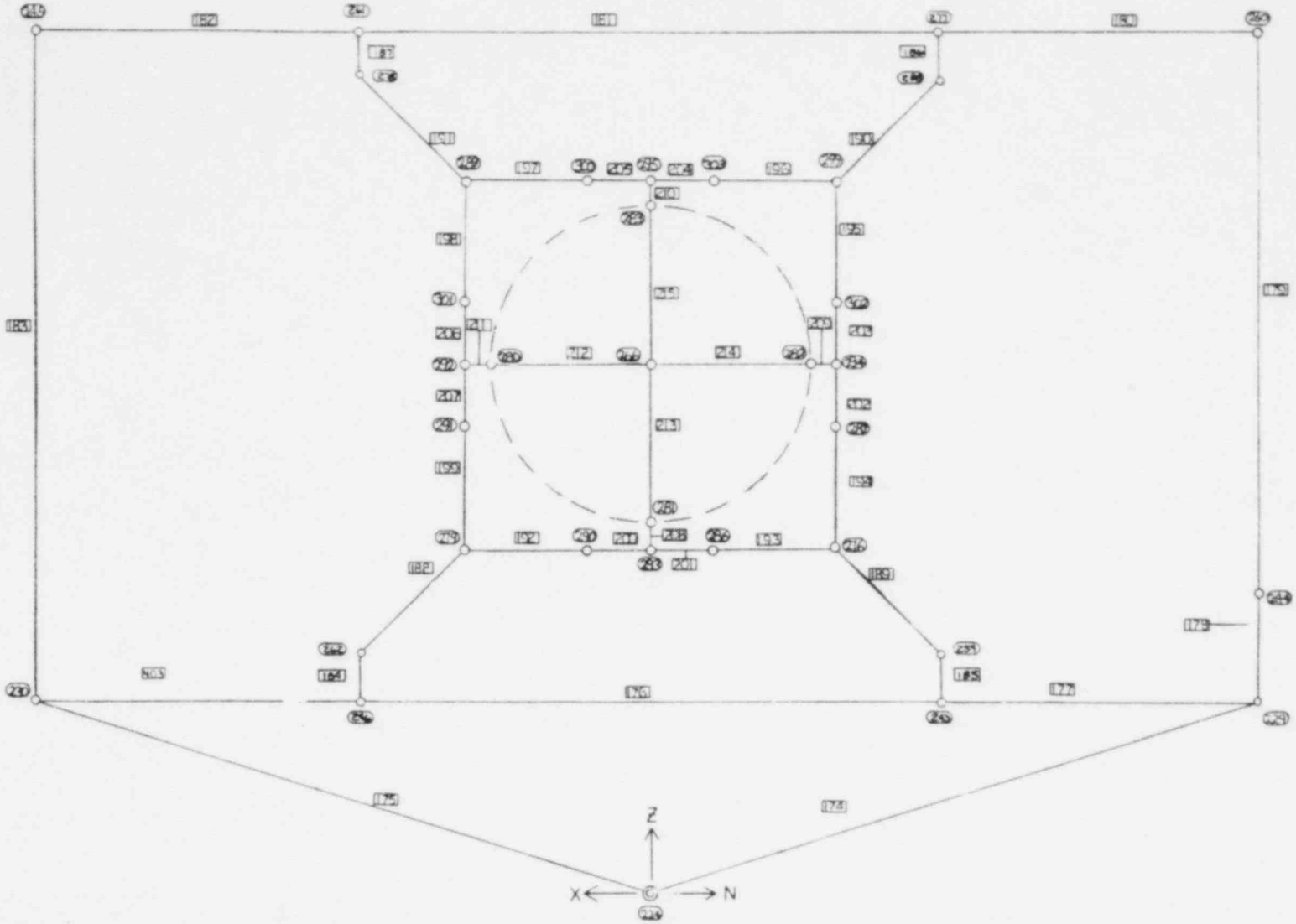

Figure F-12. Mathematical Model of Steam Generator Lower Support, Plan View — Nozzle-Supported Plant

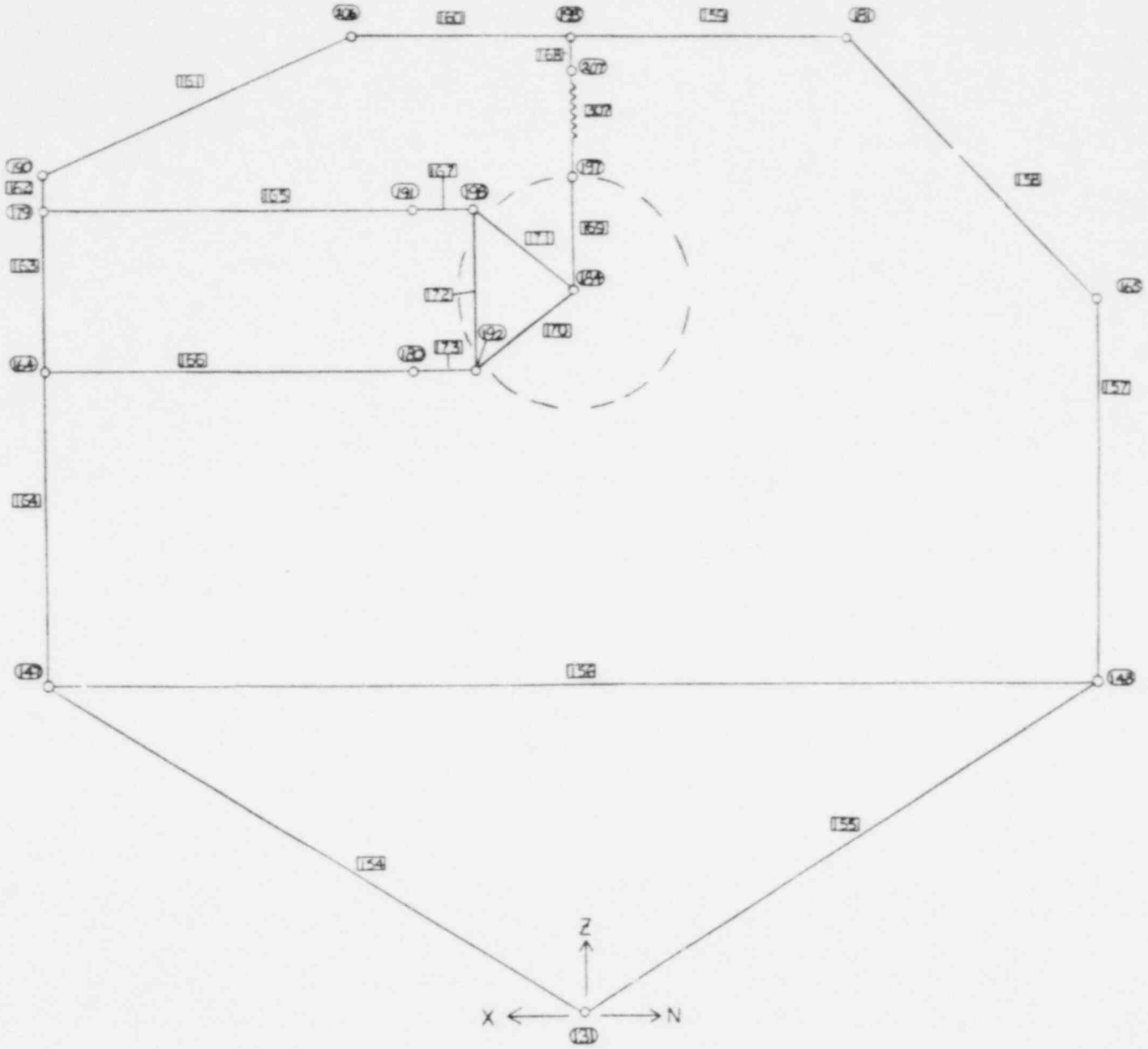

Figure F-13. Mathematical Model of RV Support Pad, Nozzle-Supported Plant

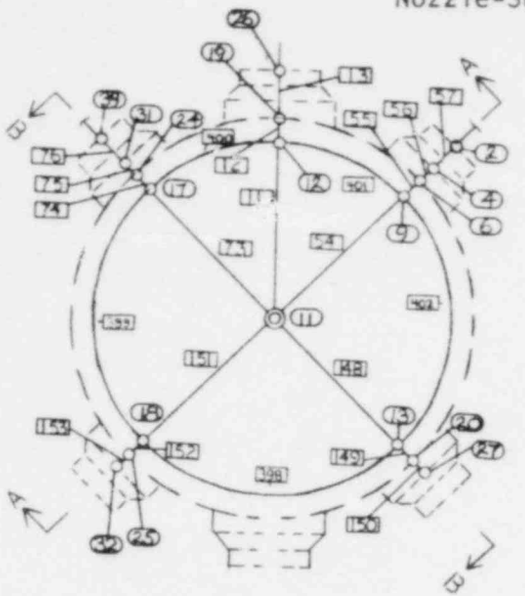

PLAN VIEW

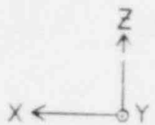

(FOR PLAN VIEW ONLY)

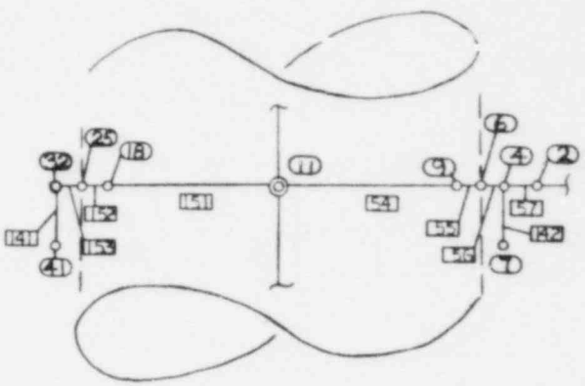

VIEW AA

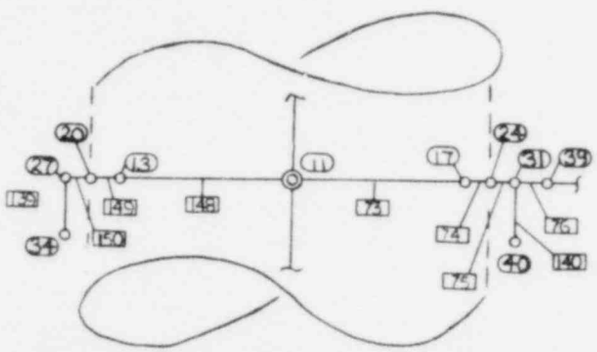

VIEW BB

Figure F-14. Mathematical Model of Internal Wall, Nozzle-Supported Plant

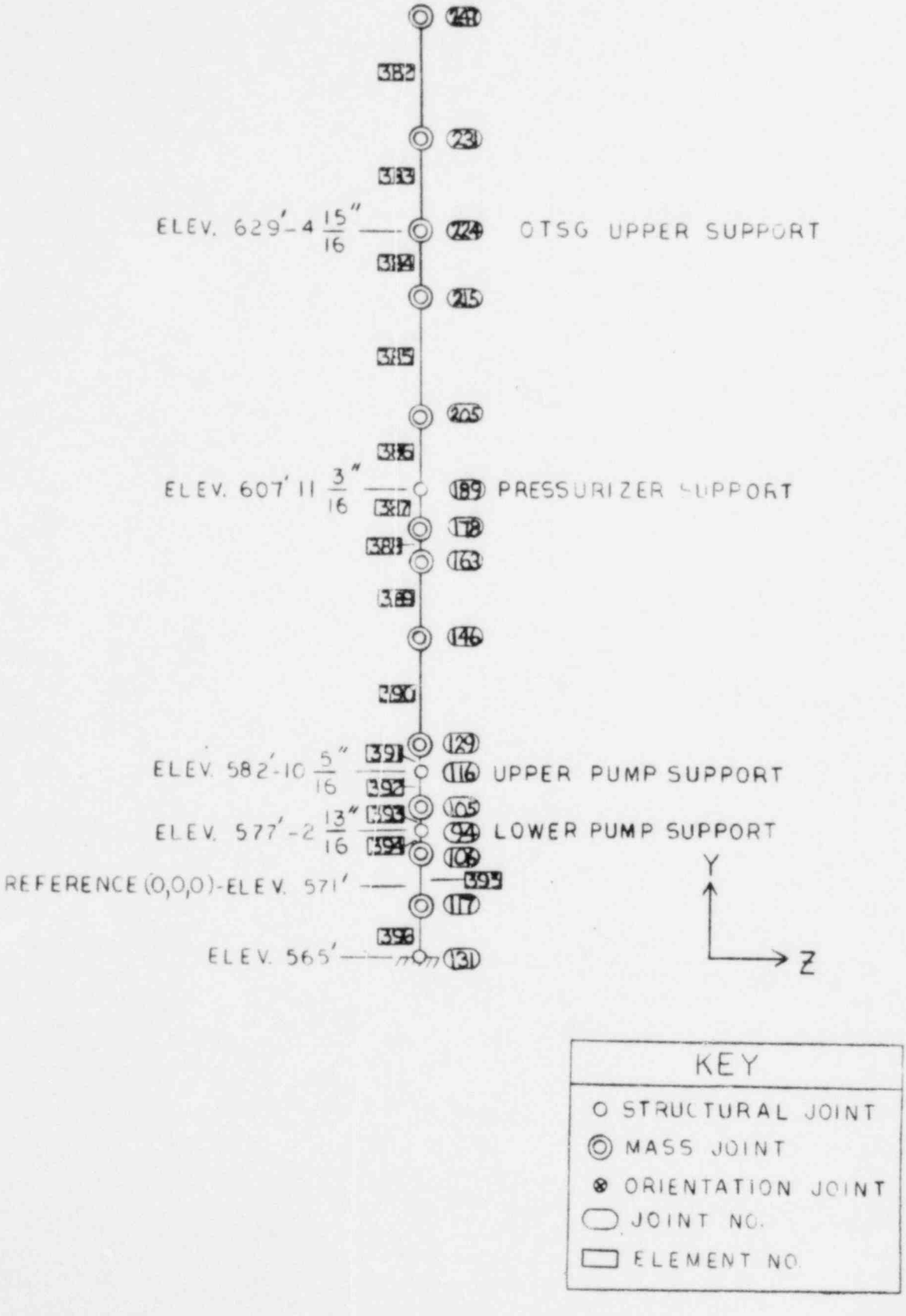

APPENDIX G

Pipe Whip Restraint Model Description

1. Introduction

Analyses of the response of all pipe whip restraints to the LOCA loading were performed to verify their structural integrity. Models of each restraint were developed and are described in this appendix. These models were used to determine the restraint properties for inclusion in the pipe whip analyses and to determine the adequacy of the restraints to withstand resulting loads.

Restraints which are not impacted during any of the postulated LOCA are not included in this appendix.

2. Oconee Pipe Whip Restraint Models

2.1. Oconee Hot Leg Bumper Restraint

A model was developed of the bumper restraint located on the lower elbow of the hot leg. The model was used to develop stiffness characteristics of the restraint for inclusion in the pipe whip analysis, and for its qualification to the resultant load.

The restraint consists of an assembly of linked plates, each of which lies in a plane normal to that of the elbow, as shown on Figure G-1. As the broken pipe whips away from the reactor vessel after the postulated LOCA, it forces the bumper restraint to bear against the steam generator. The restraint, which remains elastic, transmits both normal and transverse forces from the pipe onto the steam generator.

The bumper restraint was modeled in the pipe whip analysis by a combination of ANSYS STIF52 three-dimensional gap elements. To determine the properties of these elements, the restraint was divided into four sections. Each section consisted of three plates normal and three plates transverse to the hot leg elbow. Stiffnesses were developed for each section by determining the effective height and width of its constituent plates, and summing their effect. The properties of the ANSYS elements, two of which were used to represent each section, were defined to reproduce the restraint's actual compressive and shear stiffnesses. The ANSYS elements are shown on Figure G-2.

To account for the restraint's inertial properties, the mass of the restraint and the gap between it and the steam generator were determined. Both were included in the ANSYS model.

The resulting properties are summarized in Table G-1. The defined gap is the cold gap. Values for friction were based upon a nominal friction coefficient of 0.40 and were adjusted so as to give the correct sliding behavior between the restraint, the steam generator, and hot leg pipe surfaces.

This adjustment ensured that the restraint slipped under a lateral load equal to 40 percent of the applied axial load. An illustration of the methodology used to perform the adjustment is shown below:

Consider the two parallel ANSYS STIF52 elements, 1 and 2, in Table G-1. Defining:

P_i = axial load in element i
k_i = axial and shear stiffness of element i
u_i = coefficient of friction for element i
K_a = axial stiffness of combined elements
K_s = shear stiffness of combined elements

Then the following properties were input:

$$k_1 = K_a - K_s$$
$$k_2 = K_s$$
$$u_1 = 0.$$
$$u_2 = (0.40)\ \frac{K_a}{K_s}$$

and the force at which the restraint slides is

$$F = 0.40\ (P_1 + P_2)$$

Note that, by setting u_1 equal to zero, the lateral shear stiffness of the combined elements was uncoupled from the axial stiffness k_1.

2.2. Oconee Hot Leg Collar Restraint

The restraint is shown on Figure G-3. A curved channel section forms a collar around the pipe, and is attached to a hollow box section. The box section is, in turn, welded to embedment plates in the fuel canal wall.

The restraint constrains the pipe in directions both normal and parallel to the pipe axis. In tension, it constrains the pipe through forces induced in both the channel and the box section. In compression, the box section alone acts as a strut. Hence, the restraint can act as a compression or a tension member, with the axial spring rates shown on Figure G-4. As some non-axial movement of the pipe can occur during a hot leg LOCA, a transverse spring rate was also developed and is shown on Figure G-5.

2.3. Oconee Cold Leg Shield Restraint

The Oconee cold leg shield restraint is shown on Figure G-6. This restraint consists of an assembly of plates of varying shapes welded to an embedment system composed of wide flange sections.

The model was developed for use in the ANSYS pipe whip analysis. Elements 1 and 2 represent the axial and transverse stiffness of two sections of the restraint. These two elements have no gap.

Element 3, an ANSYS STIF52 element, represents the cold gap between the cold leg and the restraint, and has a coefficient of friction of 0.40 which accounts for energy absorption that may occur due to sliding of the cold leg along the restraint.

Table G-2 summarizes the axial and transverse stiffnesses, the coefficient of friction, the mass, and the gap for each element.

3. Three Mile Island 1 Hot Leg Restraint Model

The Three Mile Island 1 hot leg restraint consists of seven closely spaced U-bars. The U-bars are linked by a one inch thick, semi-circular plate. Pipe whip loads are transferred to the embedment in the fuel canal wall through a

clevis, clevis pin, and bracket assembly. The restraint is shown in Figure G-7.

The U-bars are made of A-490 high strength steel. The proportional limit for A-490 steel was established on the assumption that the strain at yield is twice the strain at the proportional limit. The clevis and clevis pin are also made from A-490 steel. The bracket plates are made from A-36 steel.

The gap used in the ANSYS analysis of this restraint is the cold gap. As the inside diameter of the restraint does not exactly match the outside diameter of the hot leg, some displacement of the hot leg pipe is required in order to "tighten" the restraint on the pipe. This displacement was determined to be 1.06 inches, and analysis showed that a load of 349 kips was required (total on all seven bars) to close this distance. Thus, the resulting load-deflection curve of this restraint shown in Figure G-8 is composed of three main portions: first, the restraint is soft, as the U-bars are not yet tightened onto the hot leg; next, the restraint stiffens up to its yield point; and, finally, the restraint exhibits generalized yielding.

Incorporated into this load-deflection curve is the local yielding of the A-36 bracket plate when subjected to loading by the clevis pin. The model of the bracket plate is shown in Figure G-9. The computer program EDS-SNAP was used to perform the nonlinear anaysis of this plate. Two-dimensional eight-node plane stress elements with elastic-plastic (von Mises yield criteria, isotropic hardening) properties were used to represent the bracket plate. Rigid beams were introduced to retain the shape of the pin hole where the A-490 pin pushes against the A-36 bracket. One- half of the bracket plate was modeled, and appropriate boundary conditions were used on the line of symmetry. The load-deflection characteristics of the bracket plate are shown in Figure G-10.

4. Three Mile Island 2 Hot Leg Pipe Whip Restraint Model

The Three Mile Island 2 hot leg restraint consists of seven closely spaced U-bars. The U-bars are linked by a one-inch-thick, semi-circular plate. Pipe whip loads are transferred from each U-bar to the embedment in the fuel canal wall through a clevis, clevis pin, and bracket assembly. This restraint is

shown in Figure G-11. The spring rate, dynamic mass, and effective gap for the restraint are given in Figure G-12. The effective gap was calculated from the initial clearance between the pipe and the U-bars, together with the amount of extension the U-bars must undergo before they are completely effective in tension. The spring rate calculation was based on the assumption that tension is the principal load carrying mechanism in the U-bars after the gap closes.

Figure G-13 shows the pipe whip model developed to analyze the inelastic response of this restraint to the actual load applied by the LOCA. A nonlinear analysis was performed using the computer program PWHIP to demonstrate the load distribution capacity of the rigid plate which connects the U-bars.

The U-bars were modeled using special U-bar type, gapped elements. Inelastic elements were used to model the rigid plate. Elastic, very flexible, dummy elements were introduced at each U-bar/plate interface to obtain a nonsingular stiffness matrix prior to the closing of the gap between the pipe and the restraint.

Load histories for each individual U-bar (from the ANSYS pipe whip analysis, Section 5.2.1) were applied to the model as a series of varying point loads.

5. Crystal River Hot Leg Pipe Whip Restraint Model

The Crystal River hot leg restraint consists of eight U-bars. The U-bars are connected by a one-inch-thick plate. This plate is semi-circular over the upper half of the restraint, reducing to a smaller segment over the lower half of the restraint. The load transfer mechanism is from the U-bar to the concrete embedment through the clevis, pin, and bracket plate components. This restraint is shown in Figure G-14. The effective gap, dynamic mass, and spring rate curve for the restraint are given in Figure G-15. The computation of the spring rate employed assumptions similar to those described for Three Mile Island 1, and the resulting curve is composed of three main sections: the curve is soft until the U-bars are tightened onto the hot leg; then the curve stiffens; and finally, the curve softens to reflect yielding of the U-bars.

6. ANO-1 Hot Leg Pipe Whip Restraint Model

The ANO-1 hot leg restraint is shown in Figure G-16. The restraint consists of a 3-inch by 10-inch steel strap which encircles the pipe and is welded to embedment plates in the fuel canal wall.

A spring rate was developed for this restraint accounting both for material nonlinearities and for the friction that develops when the pipe bears against the restraint. The friction reduces elongation of the strap where it is in contact with the broken hot leg pipe. The spring rate is shown in Figure G-17.

7. Rancho Seco Hot Leg Pipe Whip Restraint Models

A finite element model was developed for the upper and lower Rancho Seco hot leg pipe whip restraints. One model was used, as the restraints are essentially identical.

The restraints consist of curved steel straps. Each strap is a 10-inch-square box section composed of 2.25-inch-thick plates. The restraints encircle the hot leg pipe and are welded to embedment plates in the fuel canal wall. The restraints are shown in Figures G-18 and G-19.

The model (Figure G-20) was developed for use with the computer program EDS-SNAP. Two-node, two-dimensional, nonlinear beam elements were used to model the restraint strap. A fixed boundary condition was assumed at the wall to ensure that tension, shear, and moment loads could be applied to the embedment system.

A series of point loads were applied around the strap perimeter to model the force distribution developed between the pipe and the restraint. Loading at each point reflected the increasing contact area which develops as the strap yields.

Spring rates were developed for each restraint using this model. These are shown in Figures G-21 and G-22.

Table G-1. Oconee Hot Leg Bumper Restraint Spring Rate Data

Element[a]	Stiffness, Kips/inch	Coefficient of friction	Gap, inches
1	437,500	0	0
2	41,000	4.67	0
3	283,800	0	0
4	24,400	5.05	0
5	608,000	0	4.0
6	67,500	4.00	4.0
7	608,000	0	4.0
8	67,500	4.00	4.0

Node	Mass, Kip-sec^2/ft
1	0.081
2	0.081
3	0.081
4	0.081
5	0.081
6	0.081

(a) For element and node numbers, see Figure G-2.

Table G-2. Oconee Cold Leg Shield Restraint Spring Rate Data

Element (a)	Stiffness, Kips/inch	Coefficient of friction	Gap, inches
1	190,000 (axial) 54,600 (in strong direction) 4,900 (in weak direction)	0.0	0.0
2	120,000 (all directions)	0.0	0.0
3	assumed rigid	0.40	5.0

Node	Mass, Kip-sec^2/ft
1	-
2	0.0308
3	0.0171
4	0.0089

(a) For element and node numbers, see Figure G-6.

Figure G-1. Oconee Hot Leg Bumper Restraint

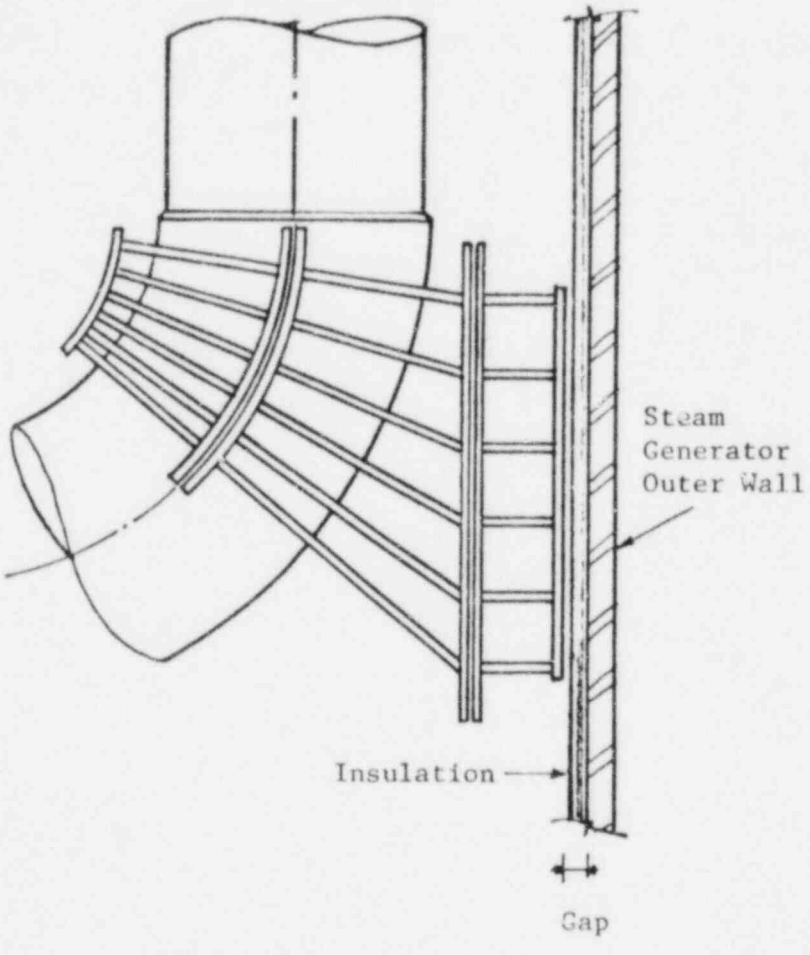

Figure G-2. Oconee Hot Leg Bumper Restraint ANSYS Model

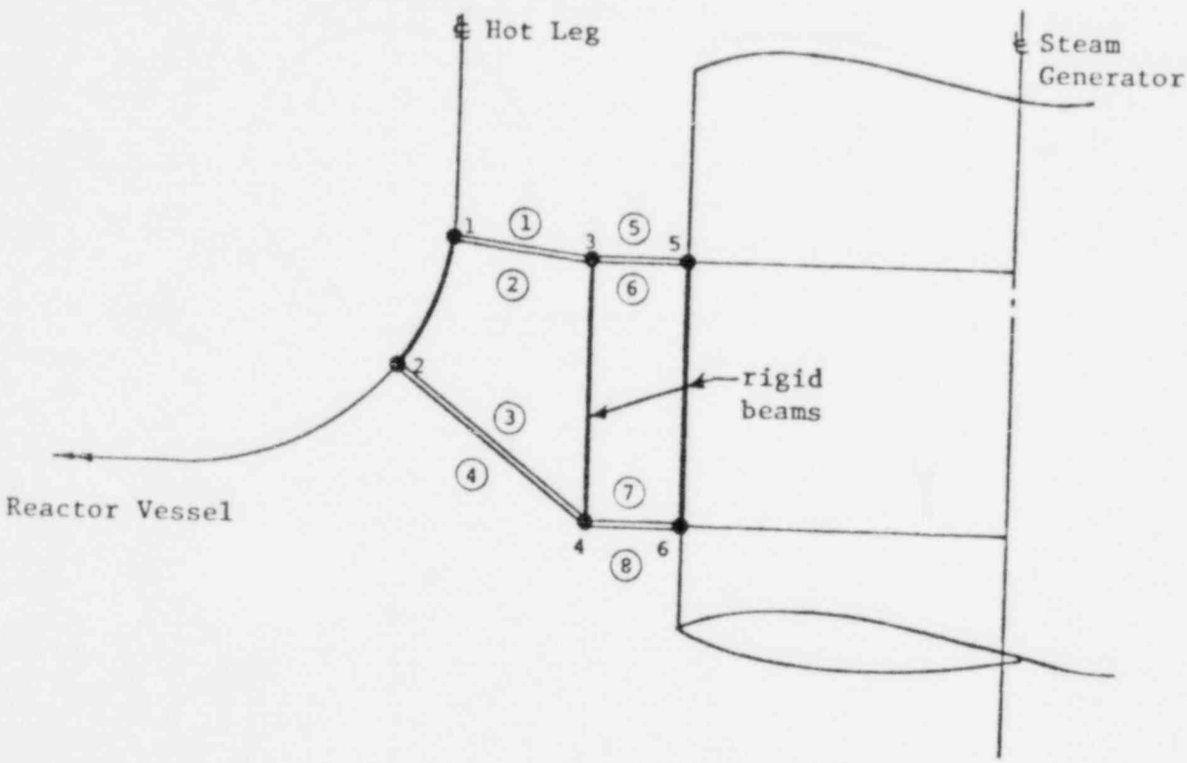

Figure G-3. Oconee Hot Leg Collar Restraint

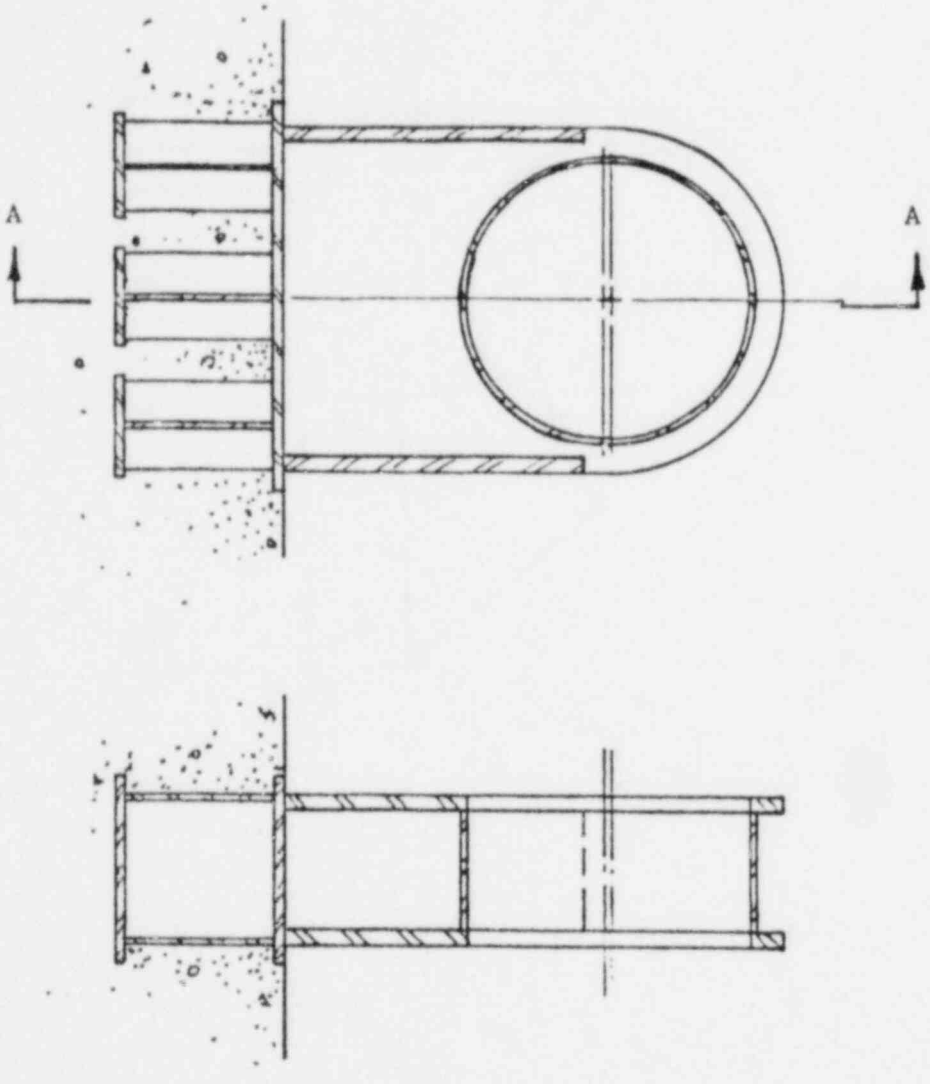

Section A-A

Figure G-4. Oconee Hot Leg Collar Restraint Axial Spring Rate

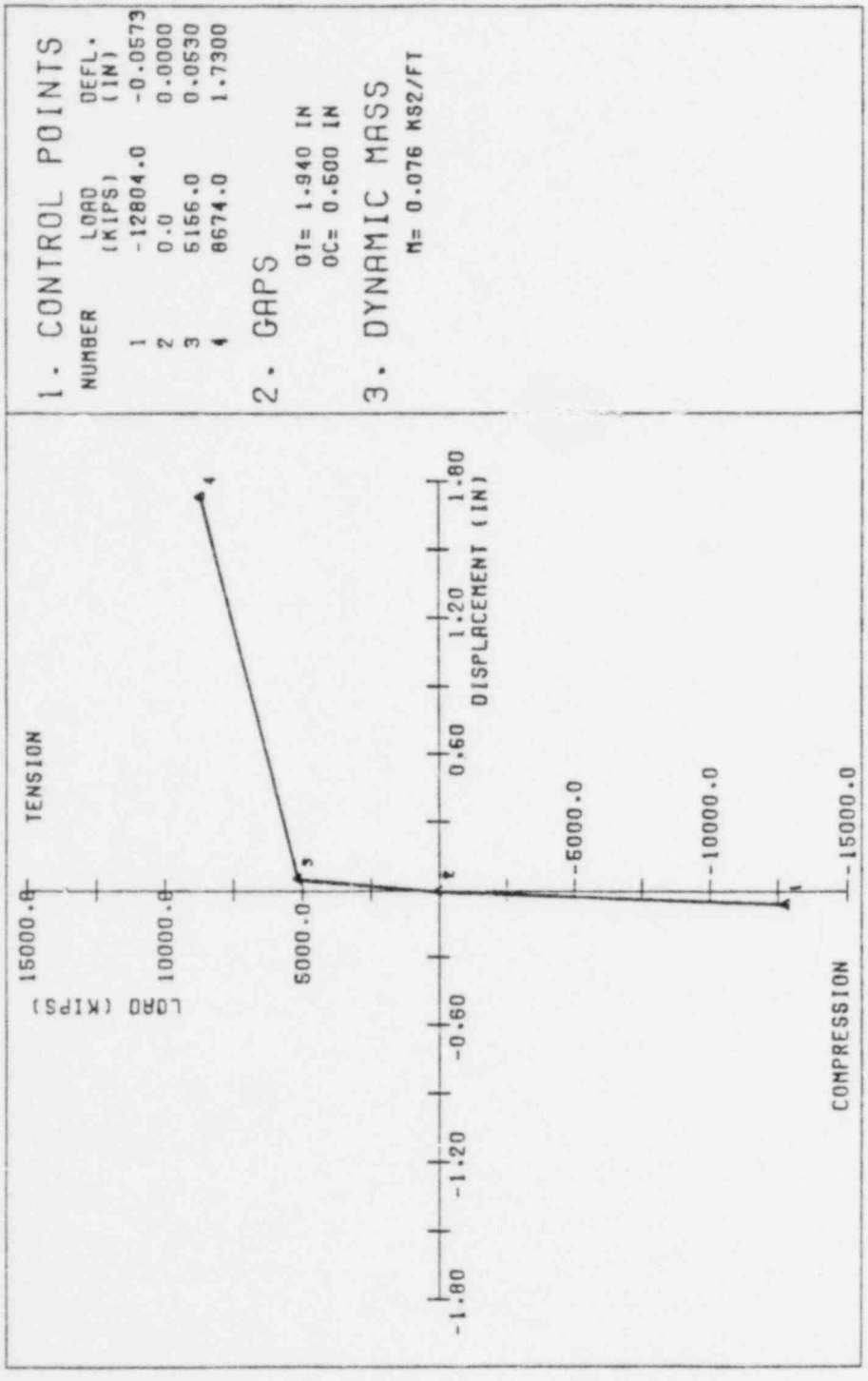

Figure G-5. Oconee Hot Leg Collar Restraint Transverse Spring Rate

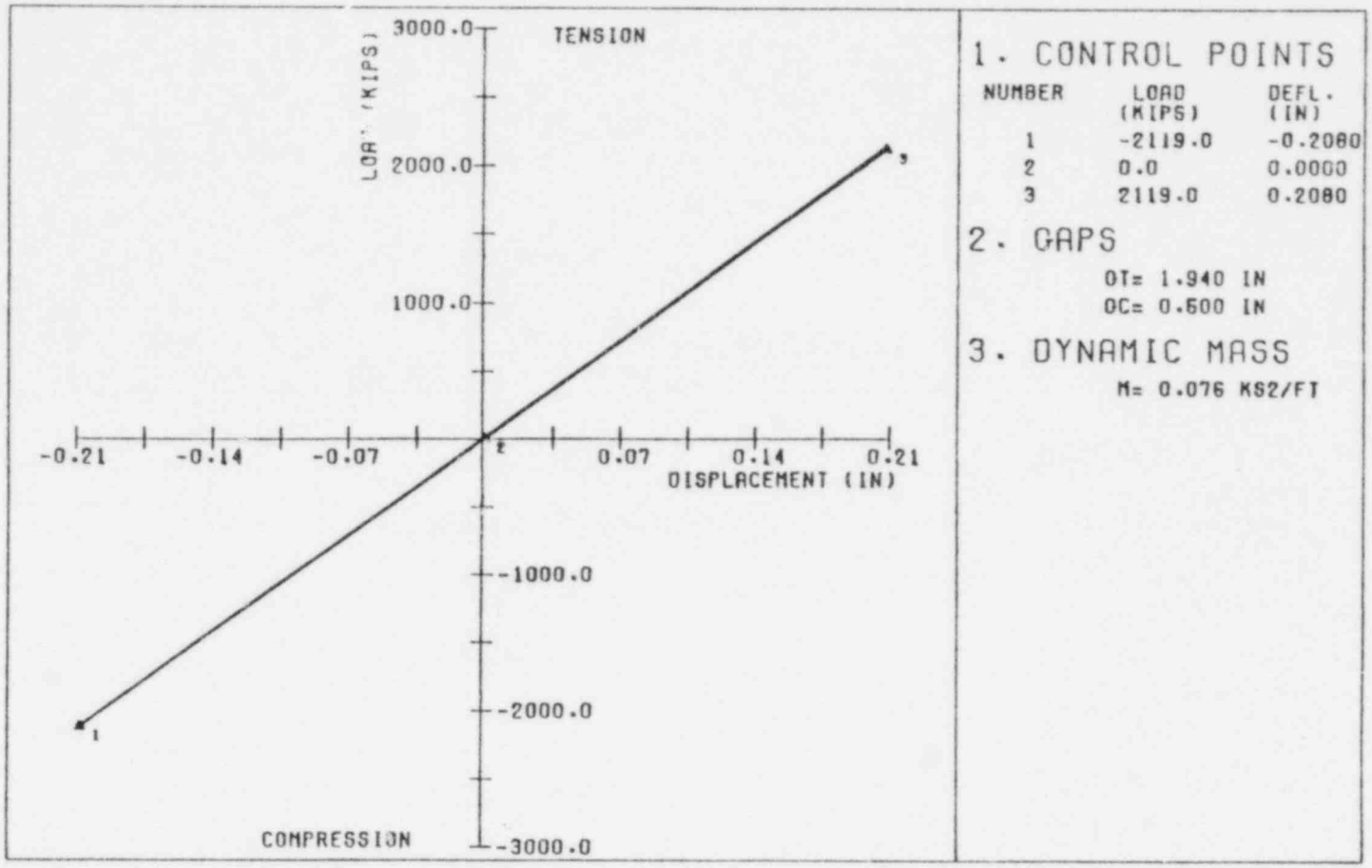

Figure G-6. Oconee Cold Leg Shield Restraint and ANSYS Pipe Whip Model

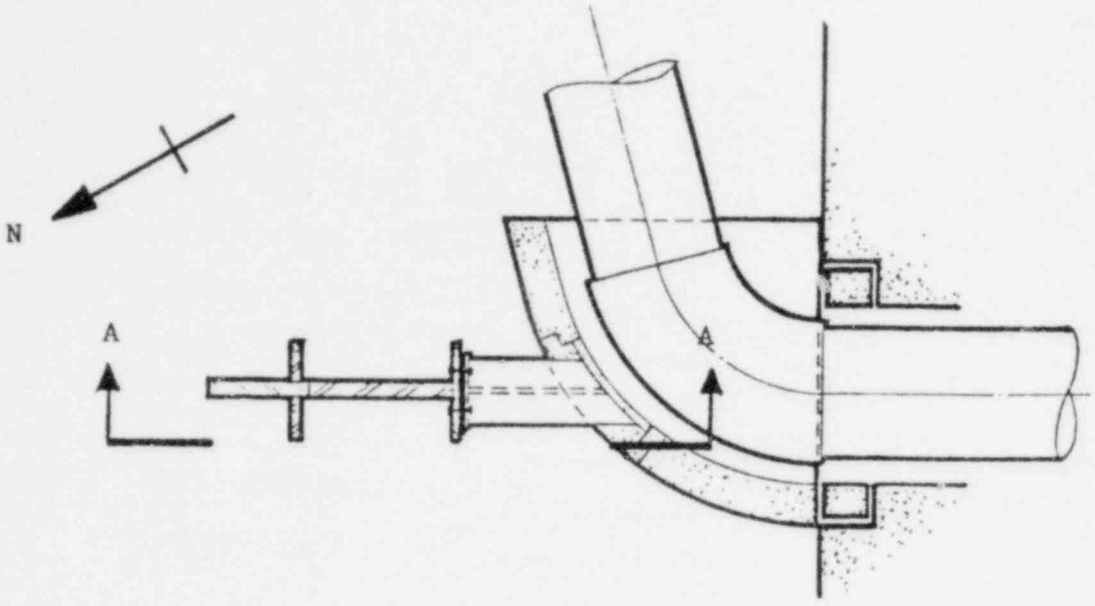

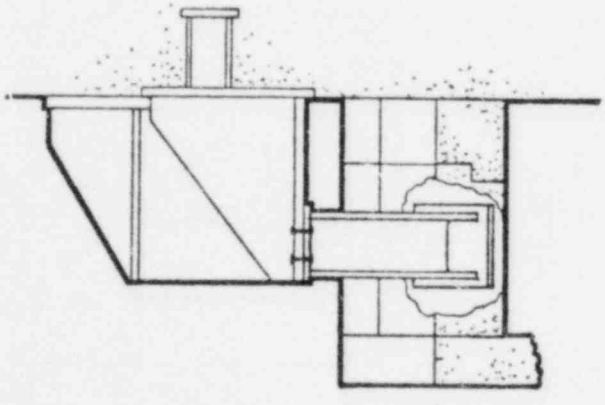

Section A-A

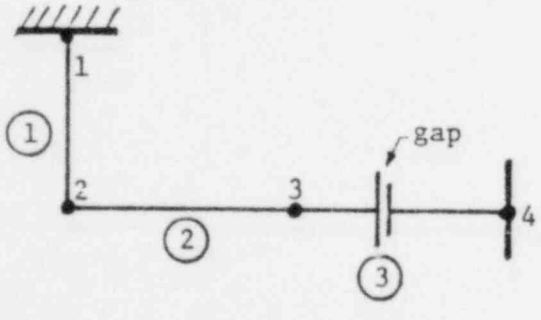

ANSYS Pipe Whip Model

Figure G-7. Three Mile Island 1 Hot Leg Restraint

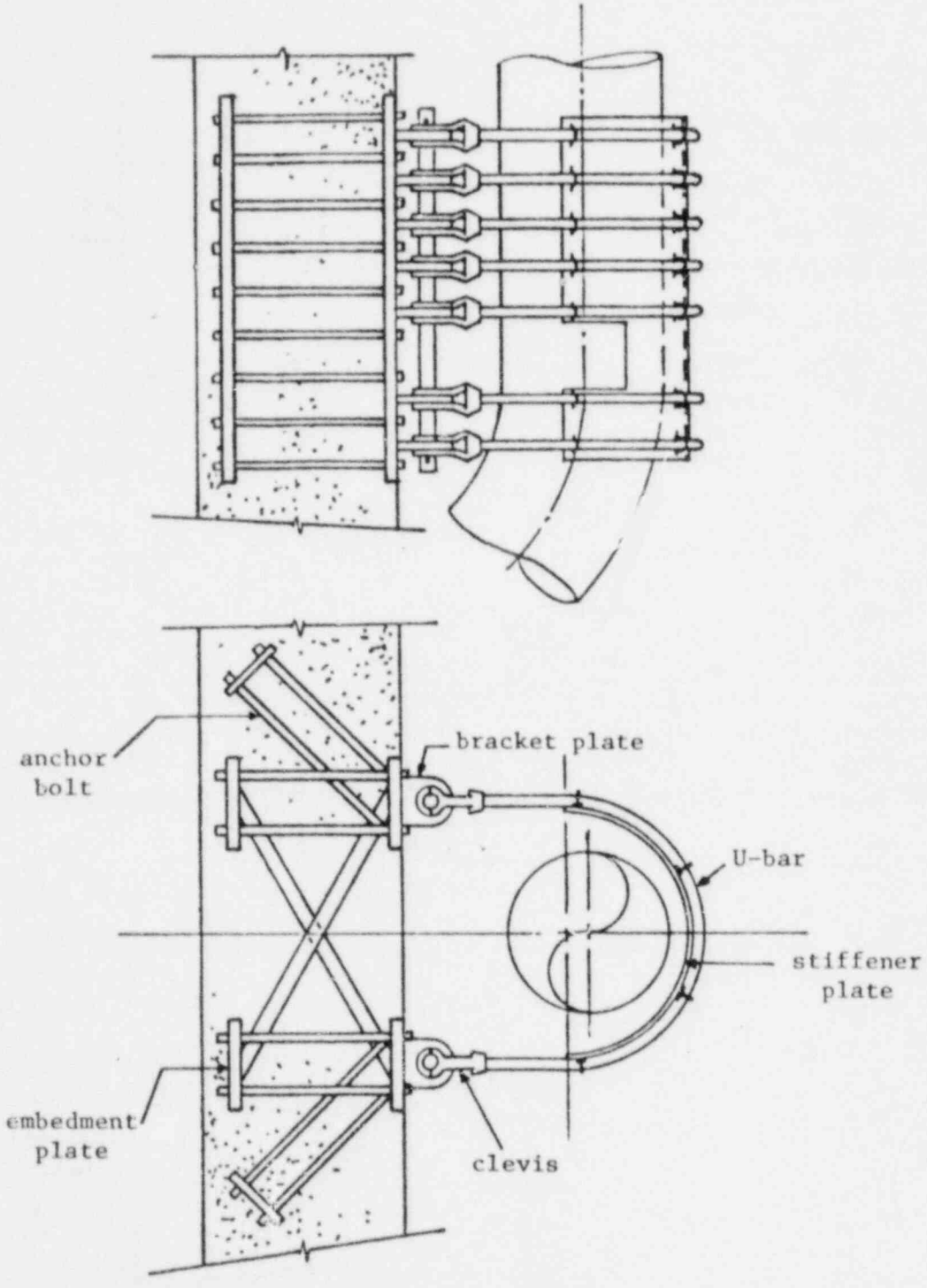

Figure G-8. Three Mile Island 1 Hot Leg Restraint Spring Rate

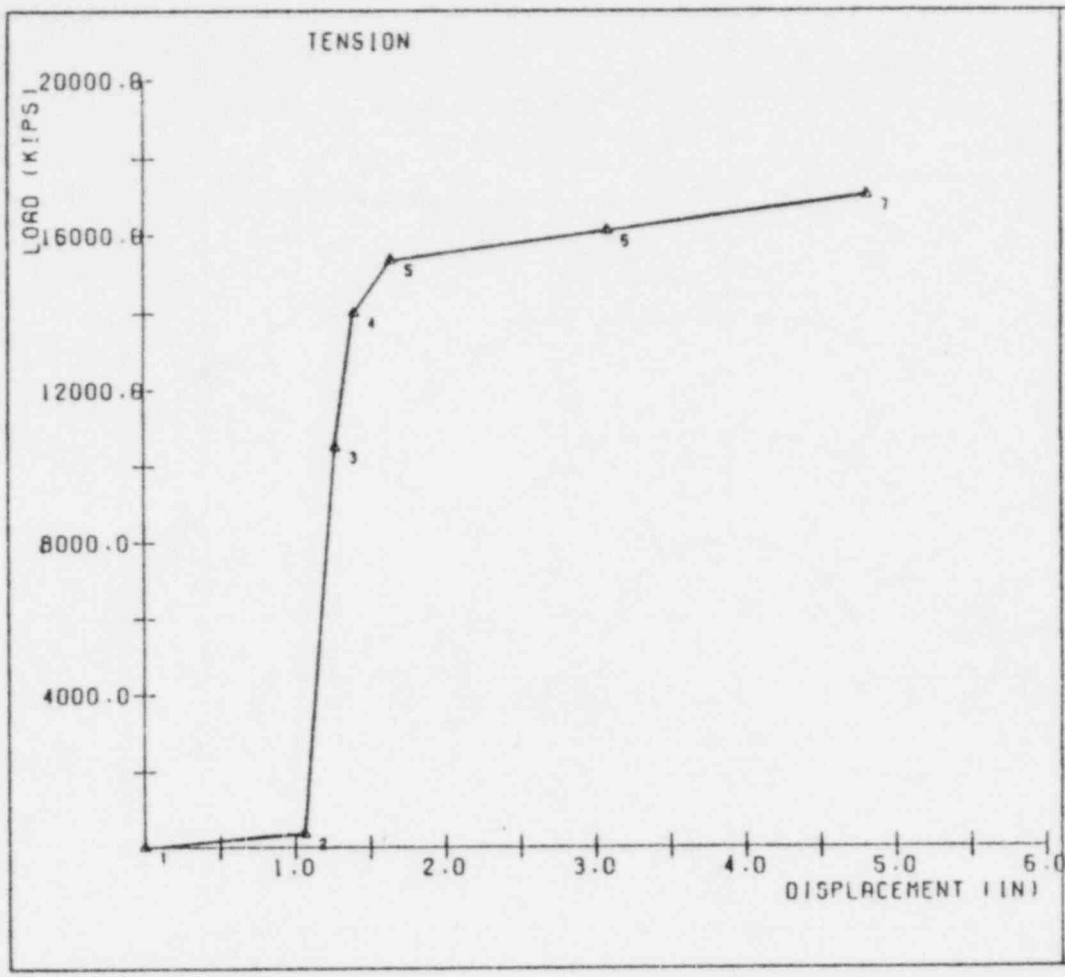

1. CONTROL POINTS

NUMBER	LOAD (kips)	DEFL. (in)
1	0.0	0.0000
2	349.0	1.0600
3	10500.0	1.2680
4	14000.0	1.3920
5	15357.0	1.6370
6	16100.0	3.0760
7	17000.0	4.8050

2. GAPS

For East Side Restraint, Gap for Lowest U-bar is 2.63 in., all other gaps are 2.56 in.

For West Side Restraint, all gaps are 2.66 in.

3. DYNAMIC MASS

M = 0.082 KS2/FT.

Figure G-9. Three Mile Island 1 Bracket Plate Model

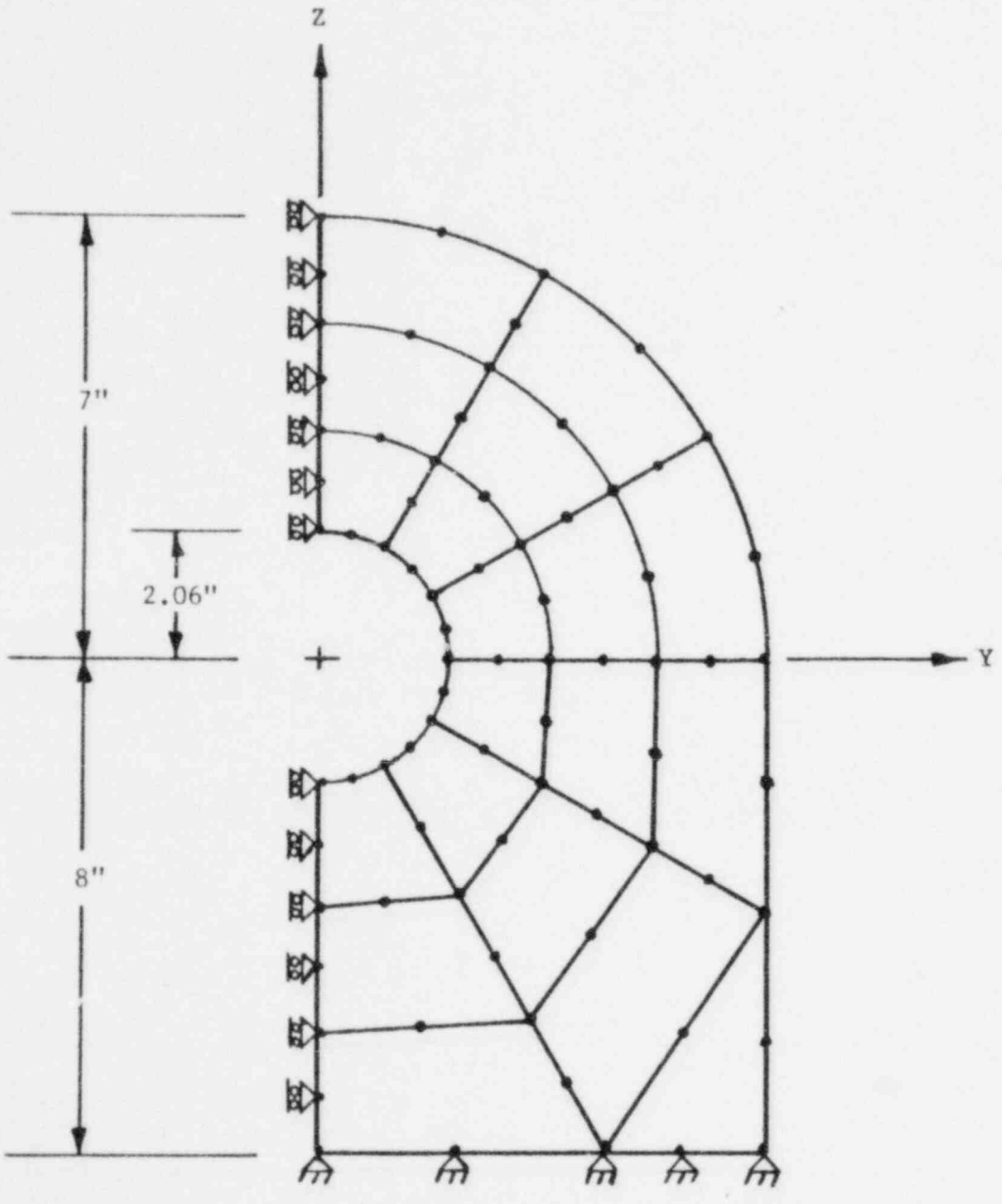

Figure G-10. Three Mile Island 1 Bracket Plate Load-Deflection Curve (per Bracket)

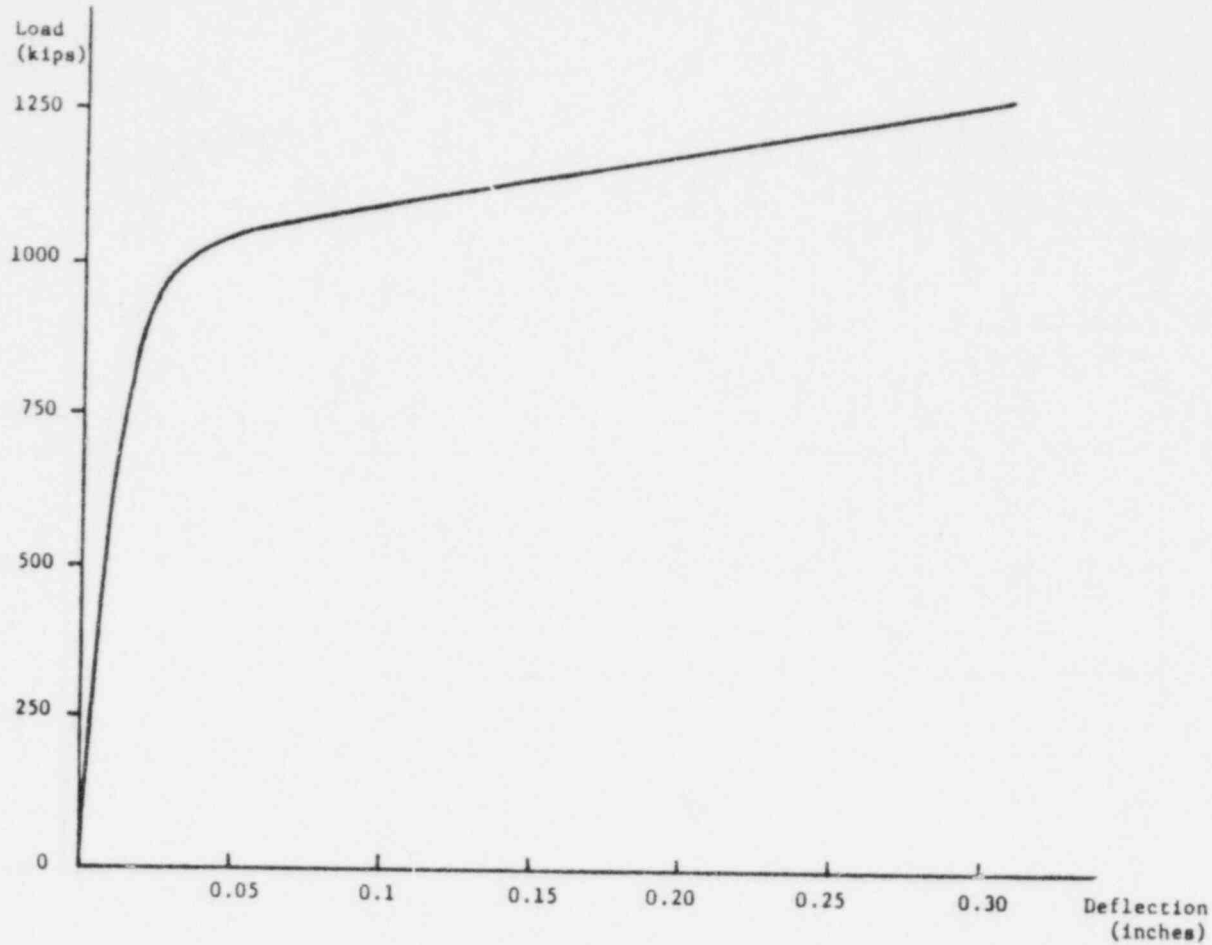

Figure G-11. Three Mile Island 2 Hot Leg Restraint

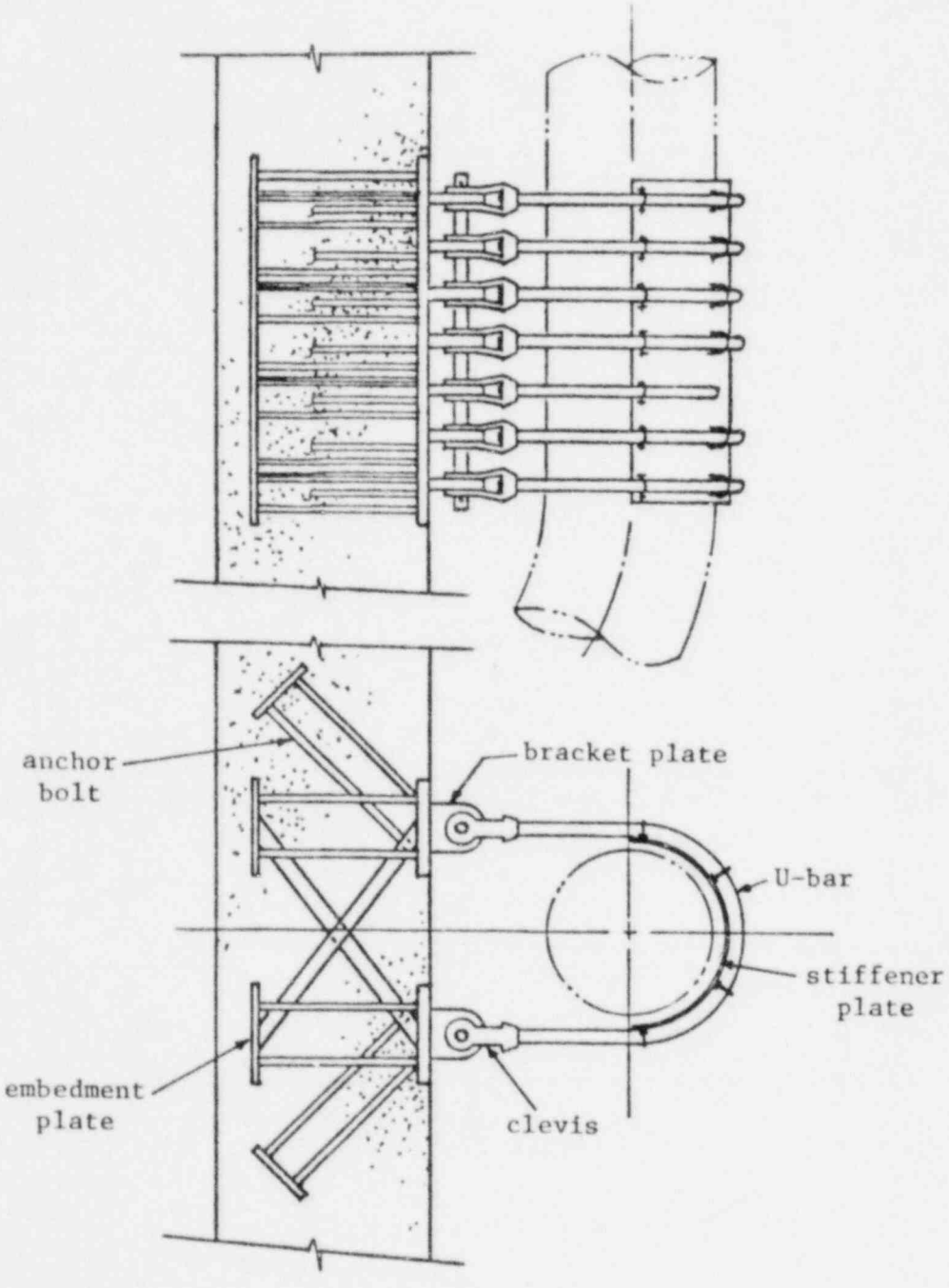

Figure G-12. Three Mile Island 2 Hot Leg Restraint Spring Rate

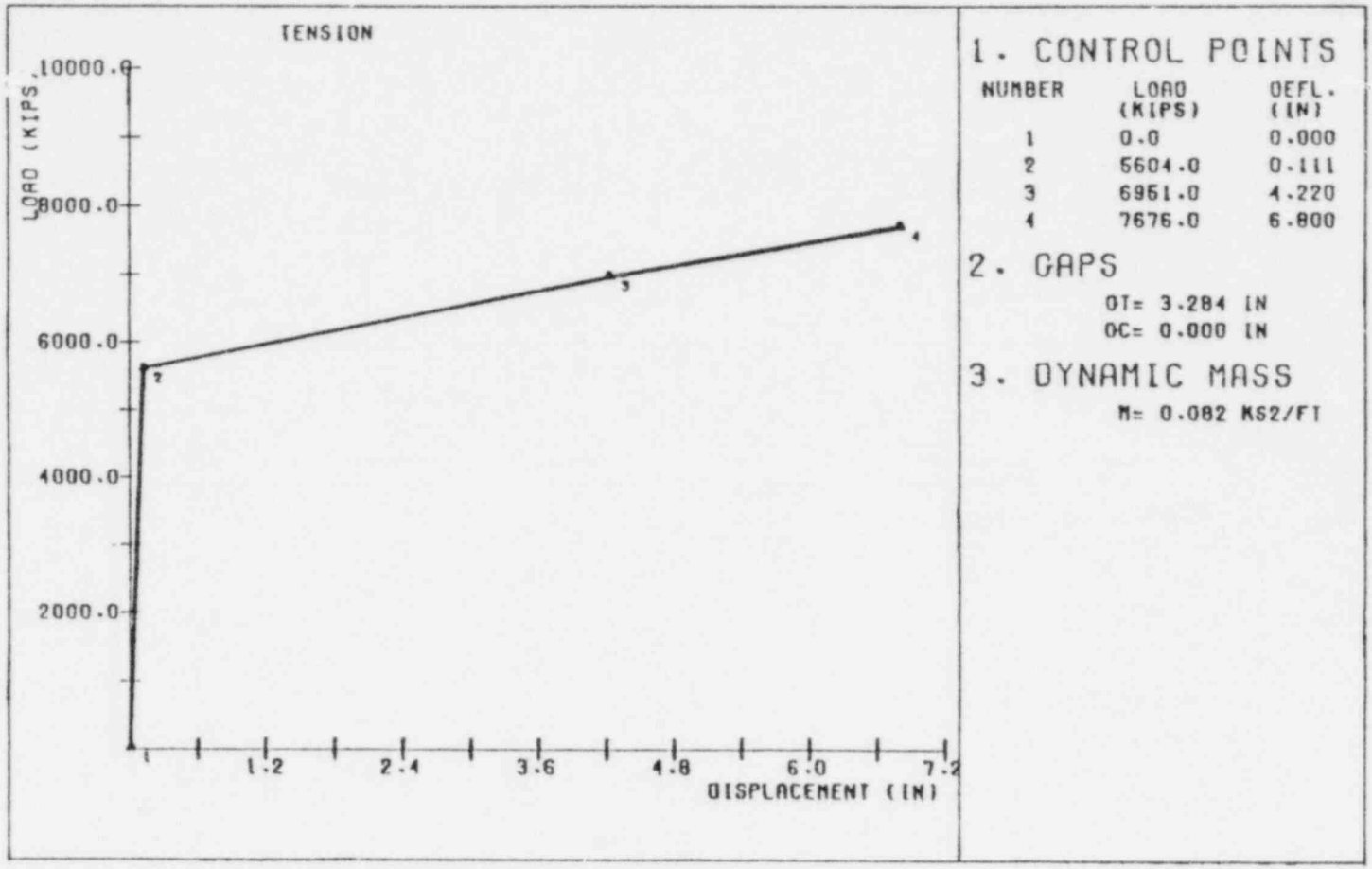

Figure G-13. Three Mile Island 2 PWHIP Model

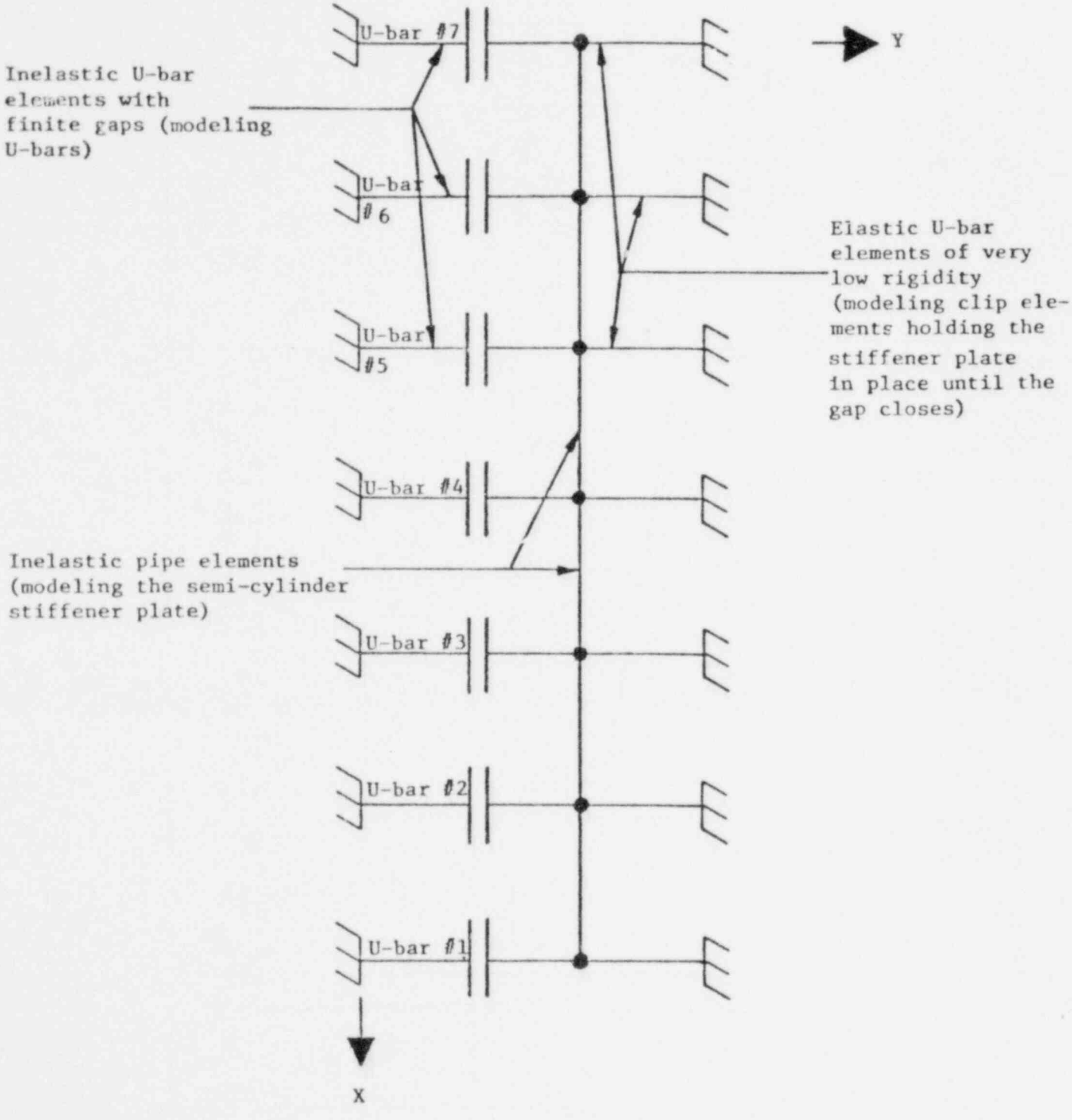

Figure G-14. Crystal River Hot Leg Pipe Whip Restraint

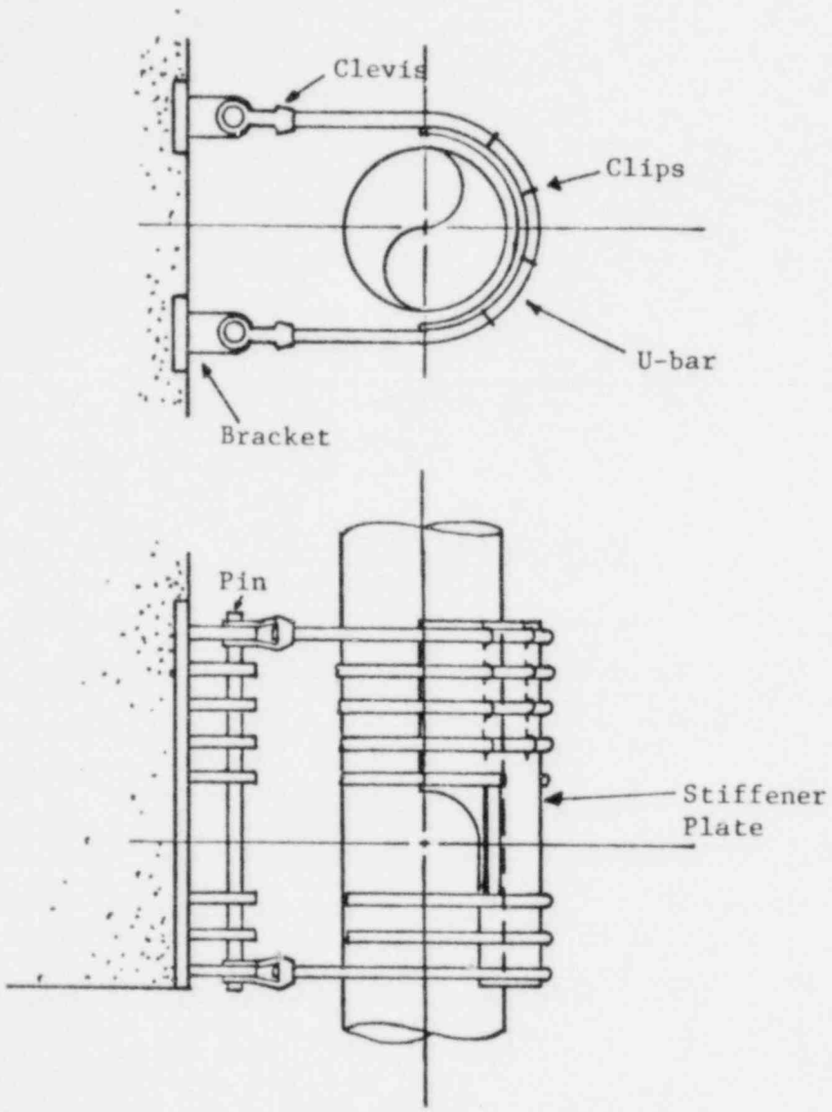

Figure G-15. Crystal River Hot Leg Restraint Spring Rate

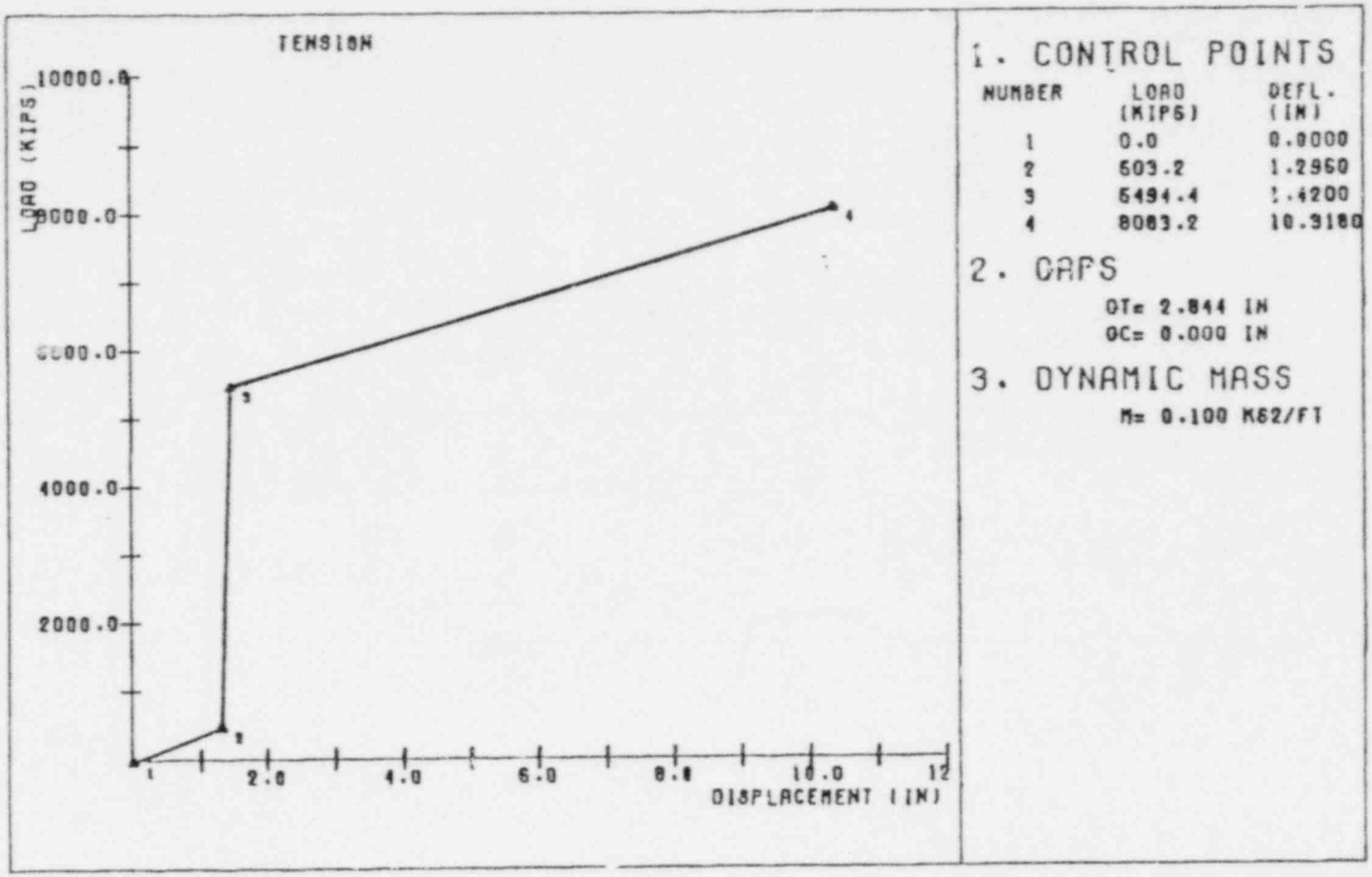

Figure G-16. ANO-1 Hot Leg Pipe Whip Restraint

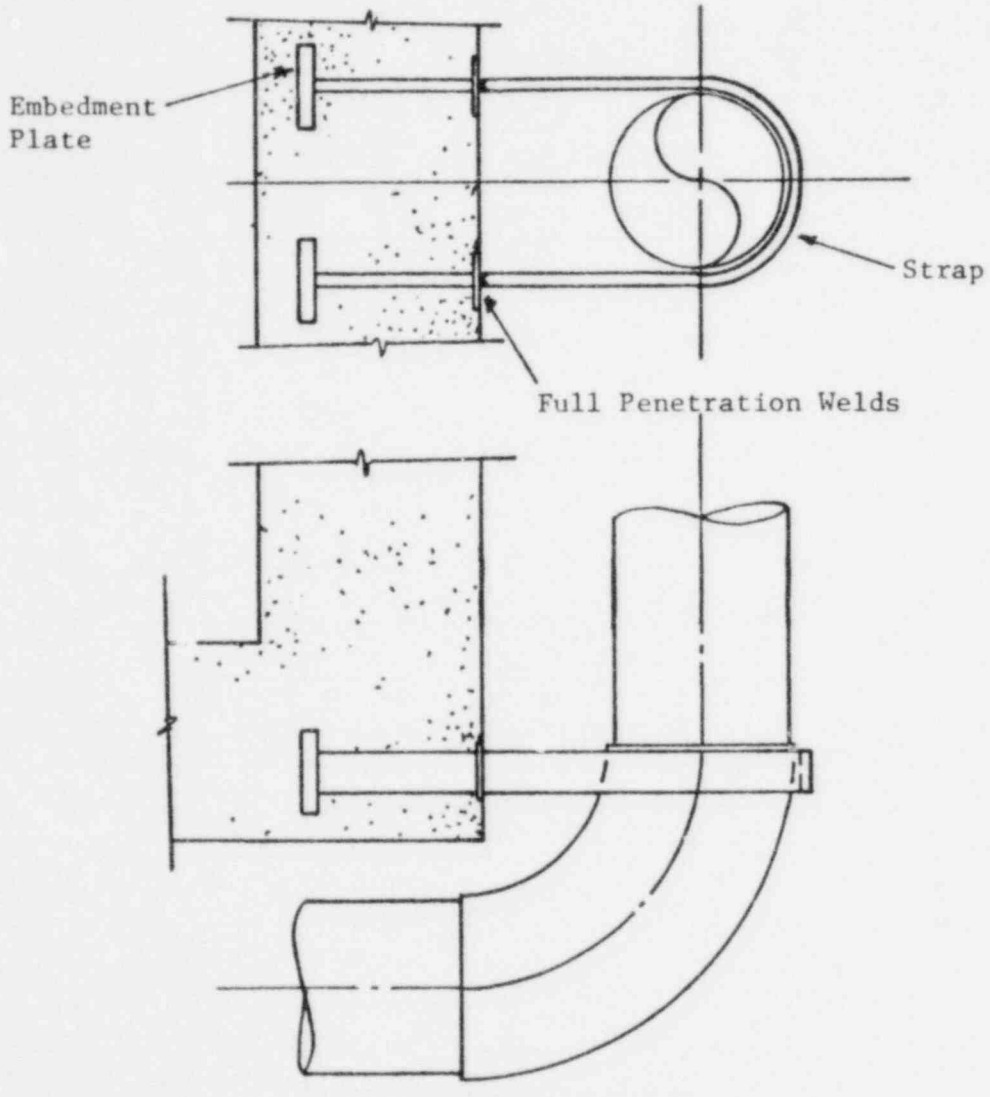

Figure G-17. ANO-1 Hot Leg Restraint Spring Rate

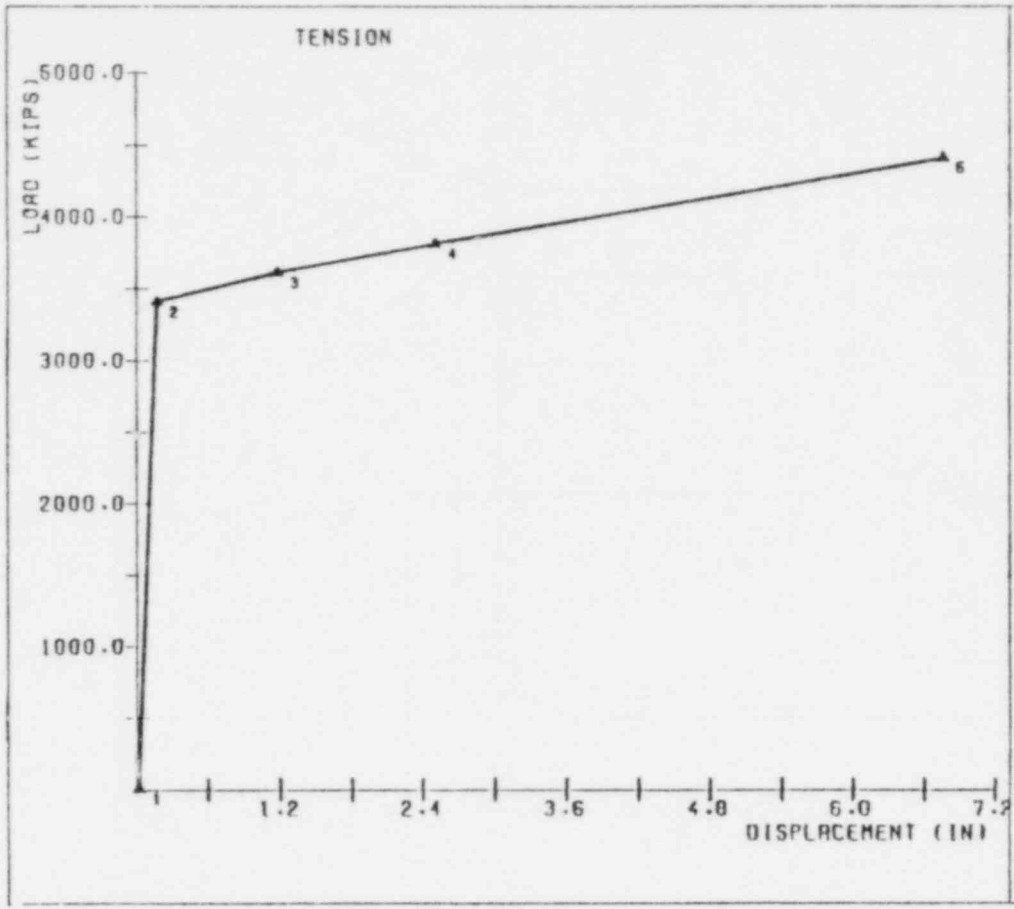

1. CONTROL POINTS

NUMBER	LOAD (KIPS)	DEFL. (IN)
1	0.0	0.0000
2	3400.0	0.1625
3	3600.0	1.1478
4	3300.0	2.4740
5	4400.0	6.7420

2. GAPS

OT= 1.780 IN
OC= 0.000 IN

3. DYNAMIC MASS

M= 0.030 KS2/FT

Figure G-18. Rancho Seco Upper Hot Leg Restraint

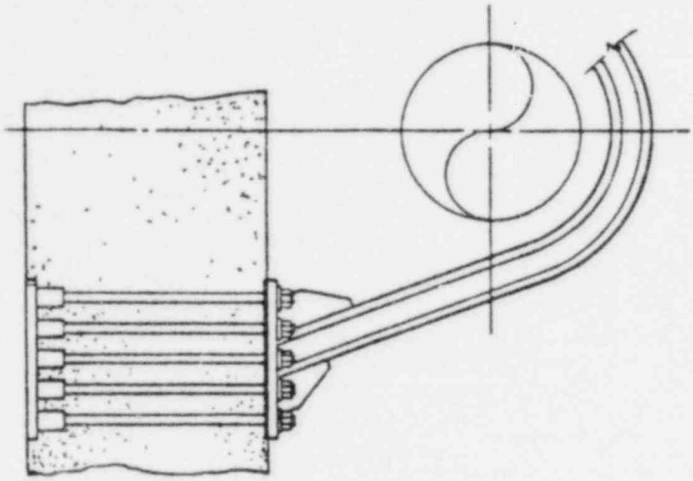

Figure G-19. Rancho Seco Lower Hot Leg Restraint

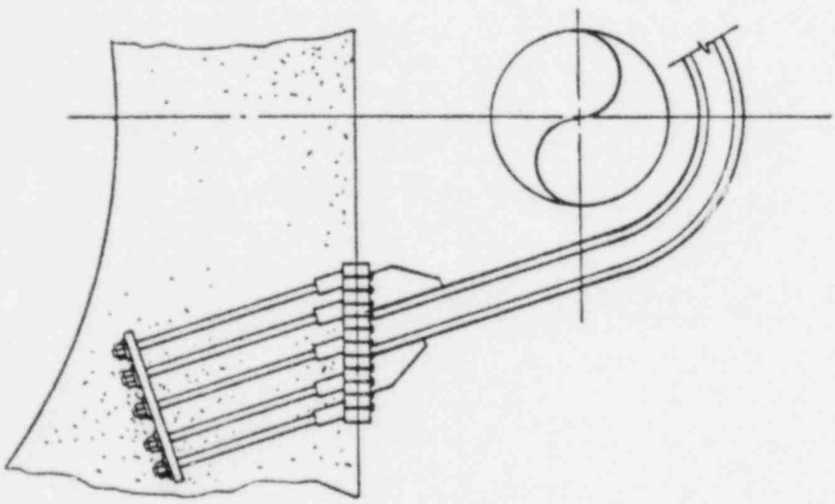

Figure G-20. Rancho Seco EDS-SNAP Model

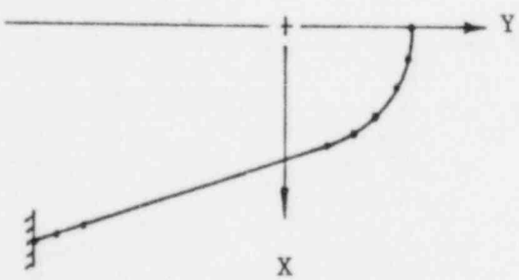

Figure G-21. Rancho Seco Upper Hot Leg Restraint Spring Rate

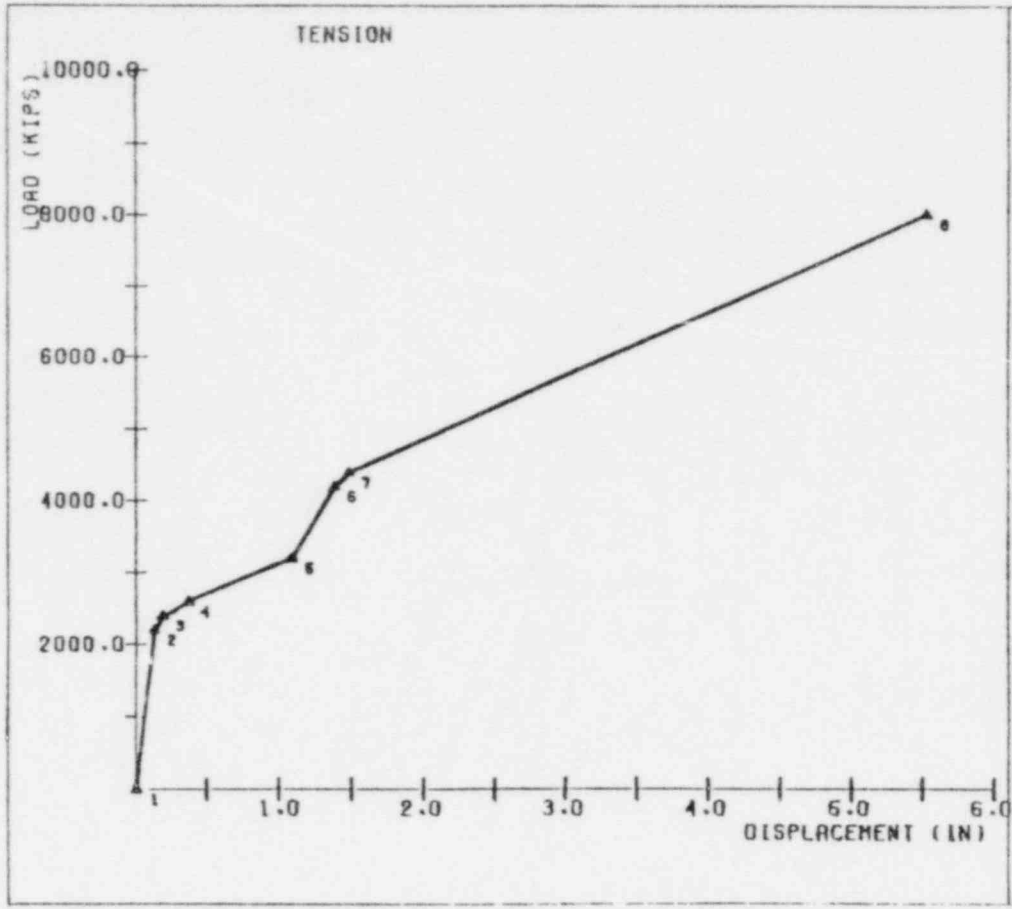

1. CONTROL POINTS

NUMBER	LOAD (KIPS)	DEFL. (IN)
1	0.0	0.0000
2	2200.0	0.1224
3	2400.0	0.1753
4	2600.0	0.3525
5	3200.0	1.0686
6	4200.0	1.3644
7	4400.0	1.4633
8	8000.0	5.5375

2. GAPS

OI= 2.000 IN
OC= 0.000 IN

3. DYNAMIC MASS

M= 0.078 KS2/FT

Figure G-22. Rancho Seco Lower Hot Leg Restraint Spring Rate

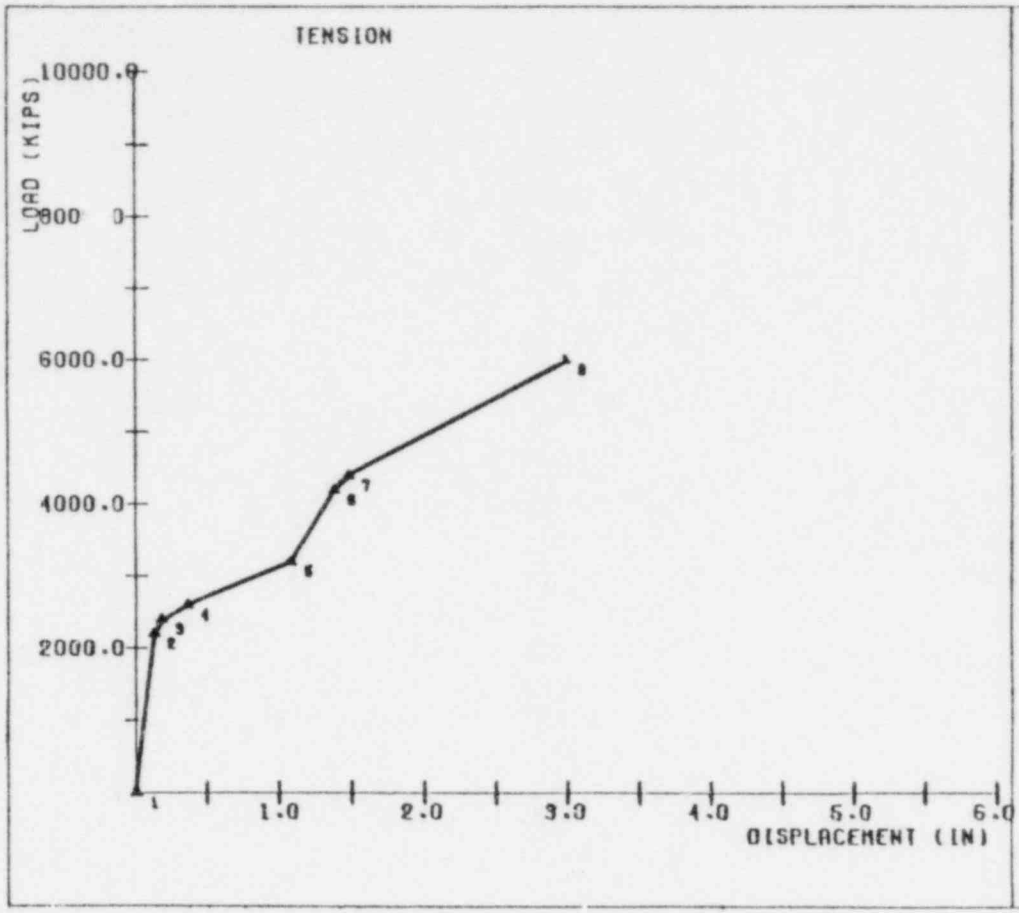

1. CONTROL POINTS

NUMBER	LOAD (KIPS)	DEFL. (IN)
1	0.0	0.0000
2	2200.0	0.1224
3	2400.0	0.1763
4	2600.0	0.3525
5	3200.0	1.0686
6	4200.0	1.3644
7	4400.0	1.4633
8	6000.0	2.9775

2. GAPS

GT= 2.686 IN
GC= 0.000 IN

3. DYNAMIC MASS

M= 0.077 KS2/FT

APPENDIX H

Core Flood Lines Model Description

1. Introduction

The core flood lines form part of the emergency core cooling system. Their function is to maintain a core coolable geometry in the event of a LOCA. Core flooding is automatically actuated when, as a result of the accident, the reactor pressure falls below a threshold value. At this point, borated water is released through two check valves on the flooding line, and flow is induced through a nozzle that penetrates the vessel above the core zone. The nozzle also serves as the return point for the flow from the decay heat removal system.

2. Model Description

Detailed mathematical models of the core flood lines were developed for analysis on the EDS Nuclear computer program SUPERPIPE. As-built dimensions were used. Isometric drawings of the modeled core flood lines are presented in Figures H-1 through H-9. Each model includes the main core flood line between the reactor pressure vessel nozzle and the core flood tank, two check valves, and a remotely controlled stop valve. The branch line, which is part of the decay heat removal system and connects the main core flood line to a containment penetration, was also included in the model. The reactor vessel nozzle, the core flood tank nozzle, and the containment penetration were modeled as anchors.

Key assumptions include:

1. The piping is analyzed as ASME Class 1 over its entire length;
2. Welds are modeled "as-welded";
3. Maximum operating pressure and temperature are used;
4. Snubbers are active for the LOCA event;
5. Transition joints are assumed at all valves, terminal ends and branch connections.

The pipe was modeled by straight and curved beam elements with six degrees of freedom at each node, using a lumped-mass formulation. The flexibility factors were computed by SUPERPIPE, based on the ASME Boiler and Pressure Vessel Code, Section III, Subsection NB-3687, for Class 1 piping.

The support types include spring hangers, mechanical and hydraulic snubbers, and frame-type rigid supports. Where insufficient data was available, frame-type supports were conservatively assumed to be rigid.

Figure H-1. Oconee Loop A Core Flood Line Math Model

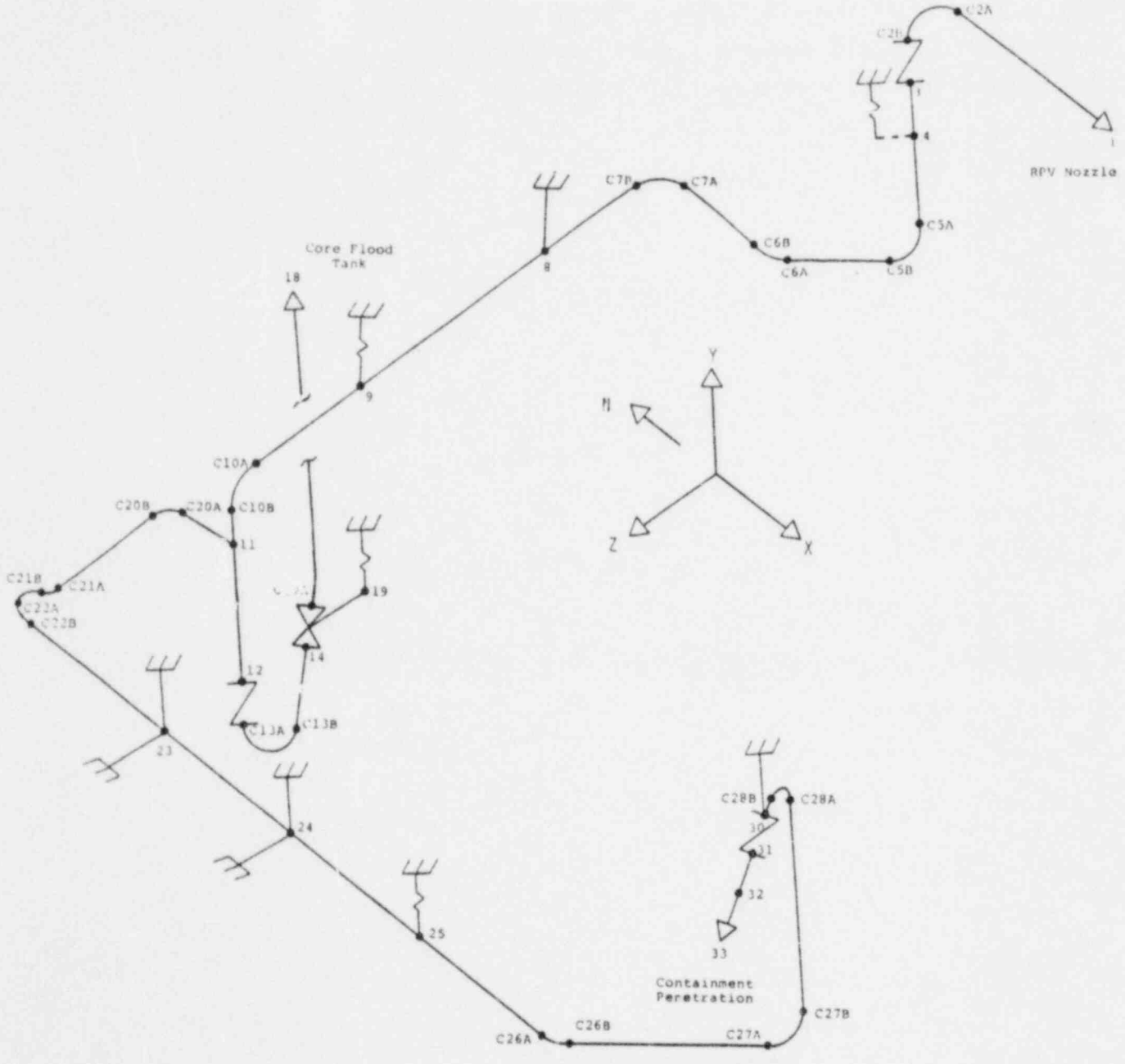

Figure H-2. Oconee Loop B Core Flood Line Math Model

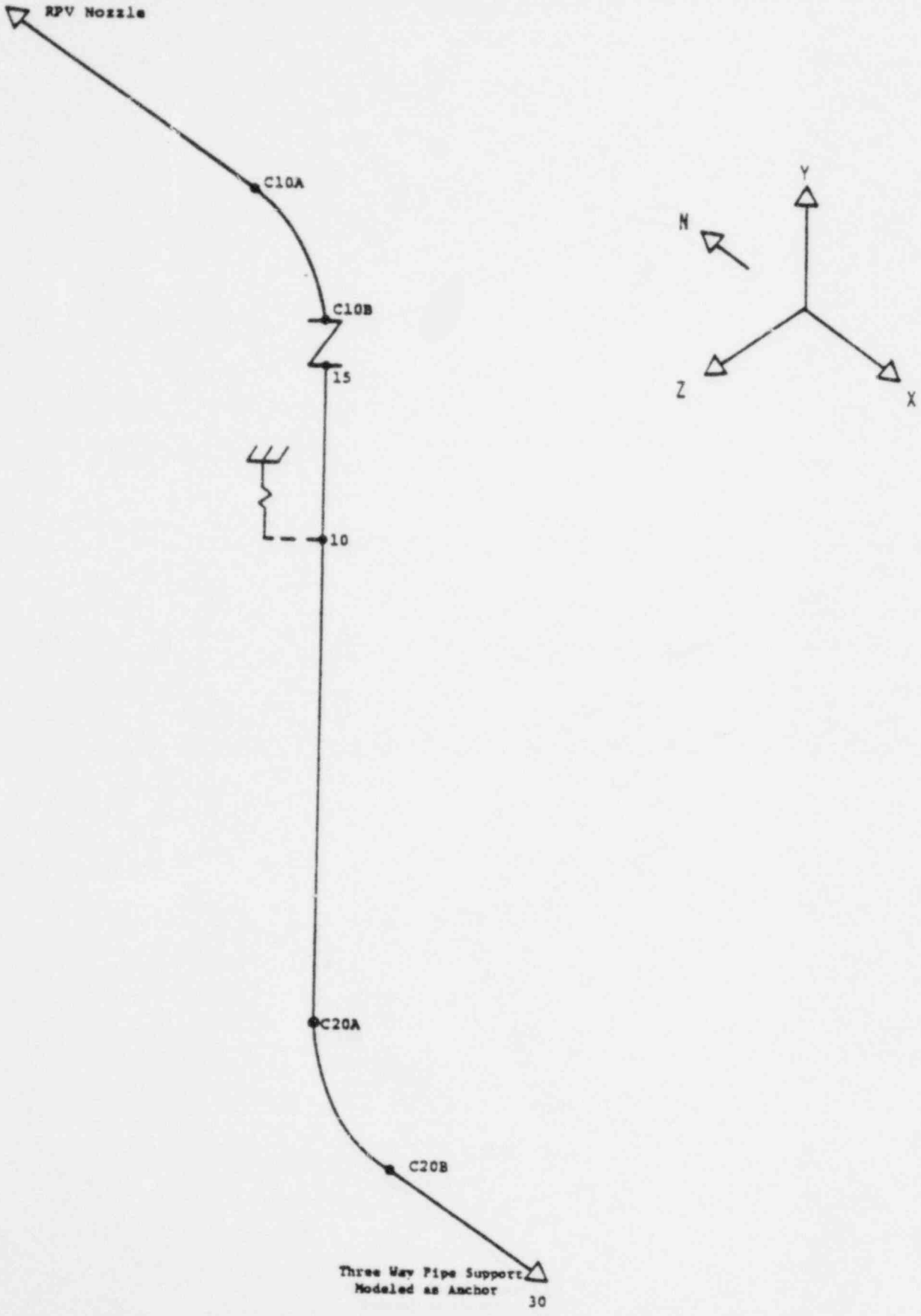

Figure H-3. TMI-1 Loop A Core Flood Line Math Model

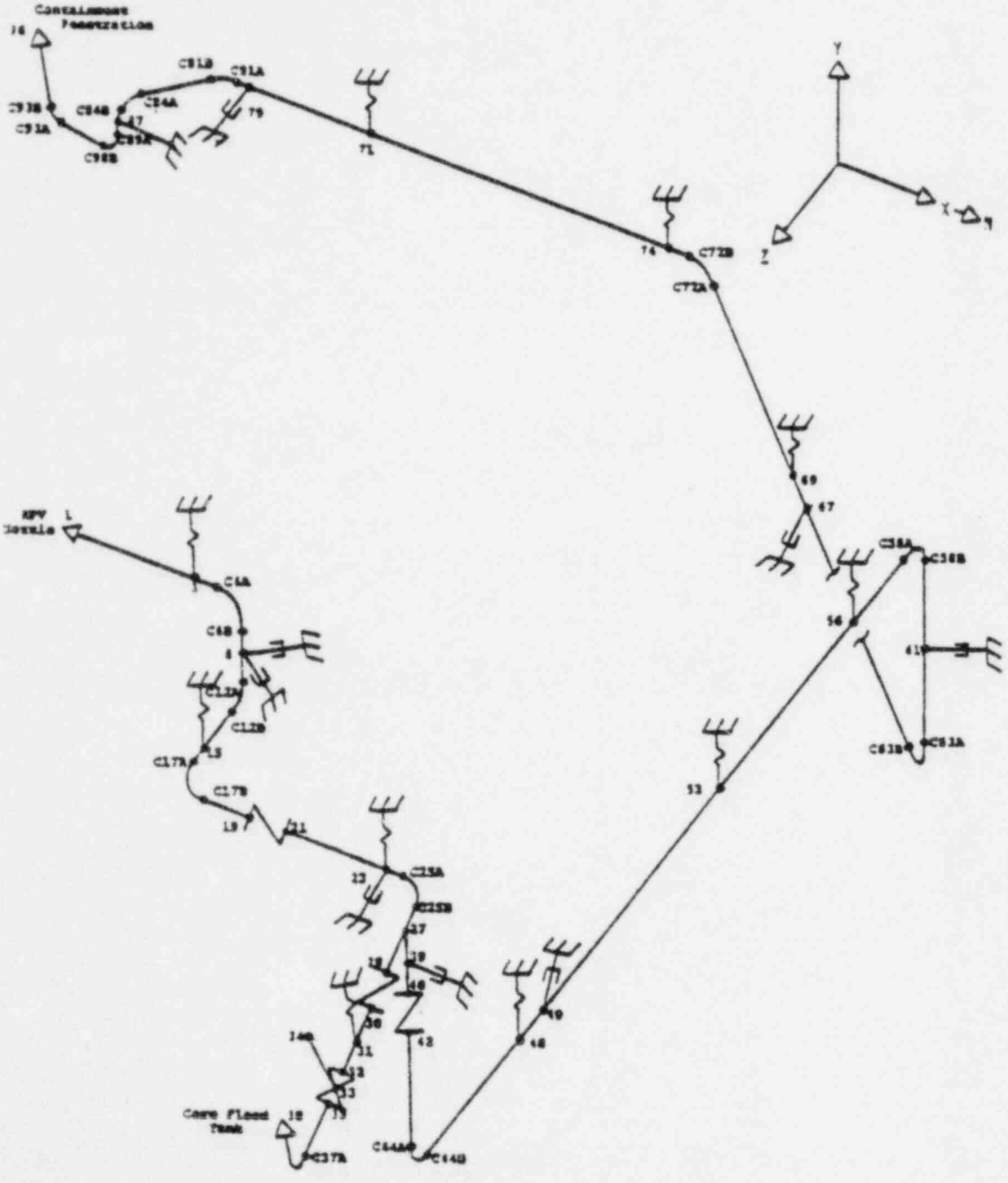

Figure H-4. TMI-1 Loop B Core Flood Line Math Model

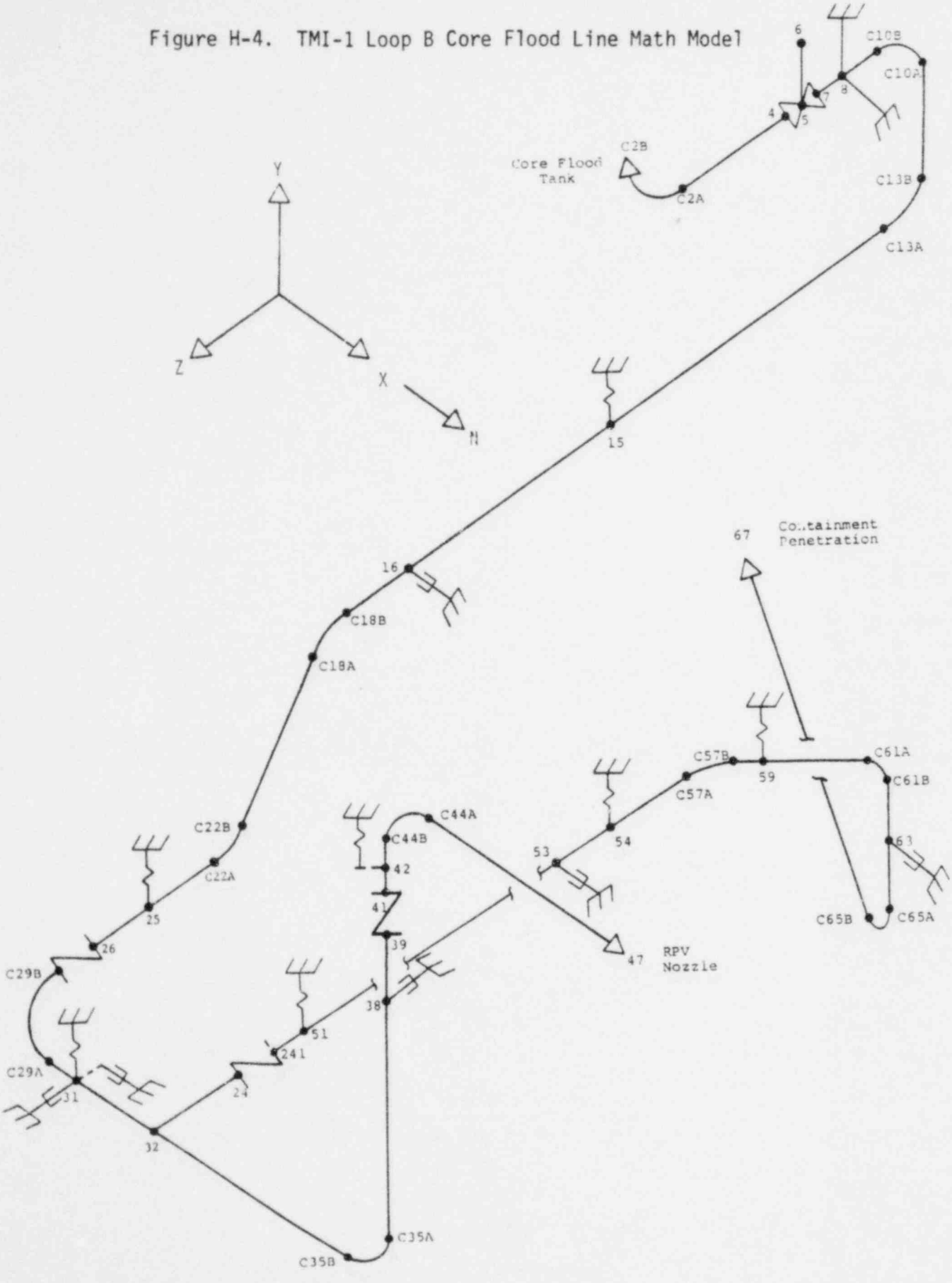

Figure H-5. Crystal River Loop A Core Flood Line Math Model

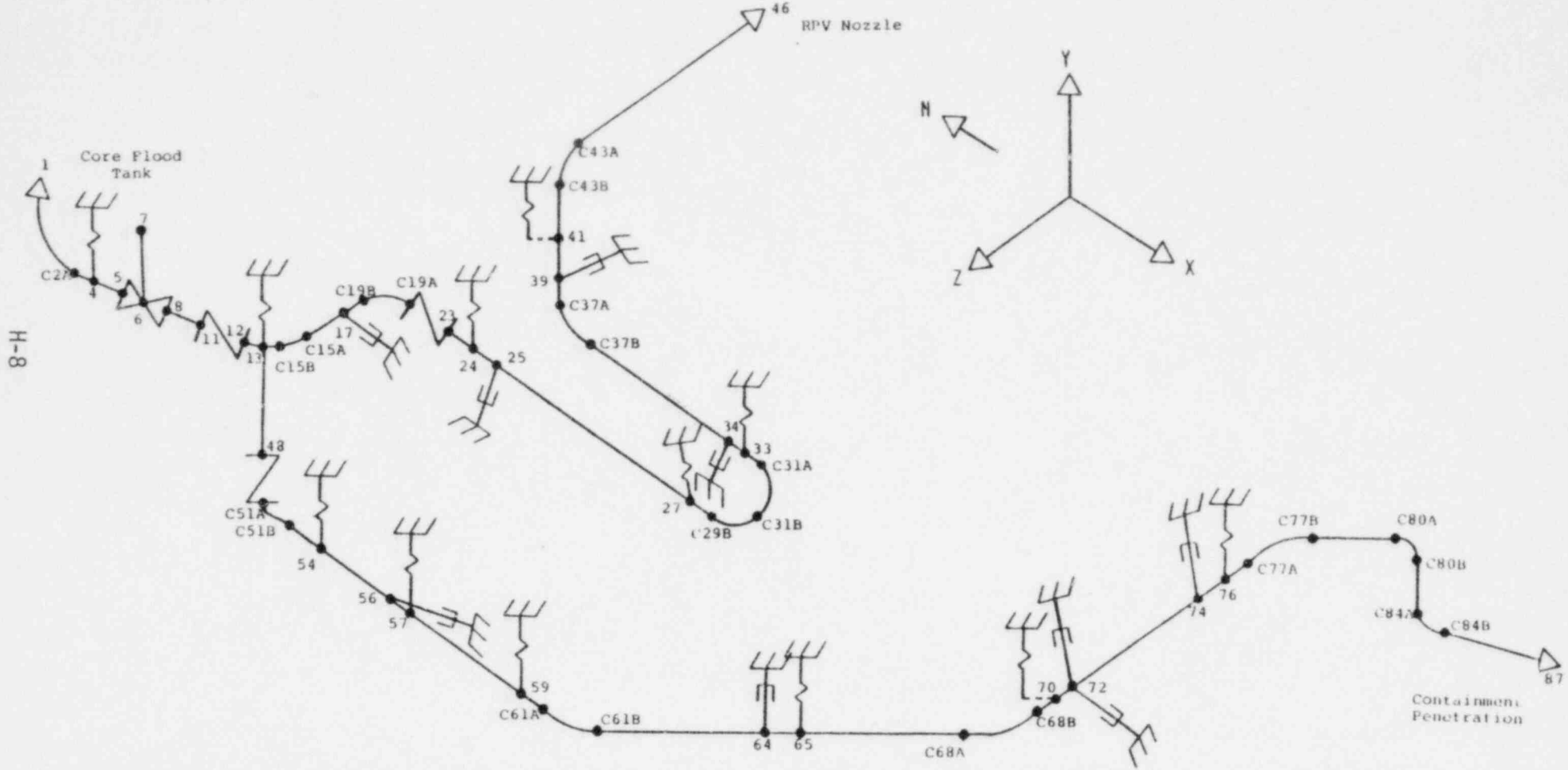

Figure H-6. Crystal River Loop B Core Flood Line Math Model

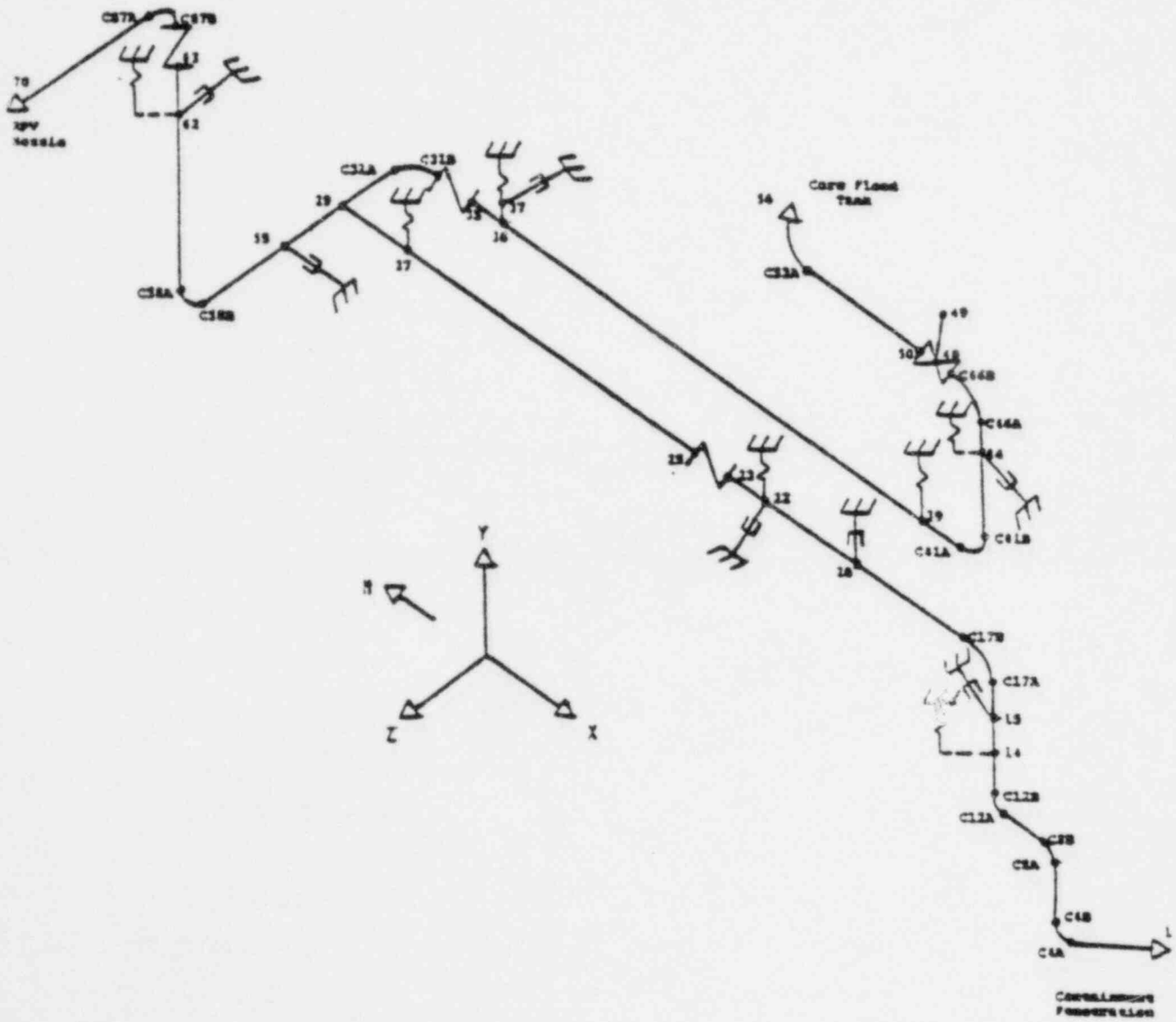

Figure H-7. ANO-1 Loop A Core Flood Line Math Model

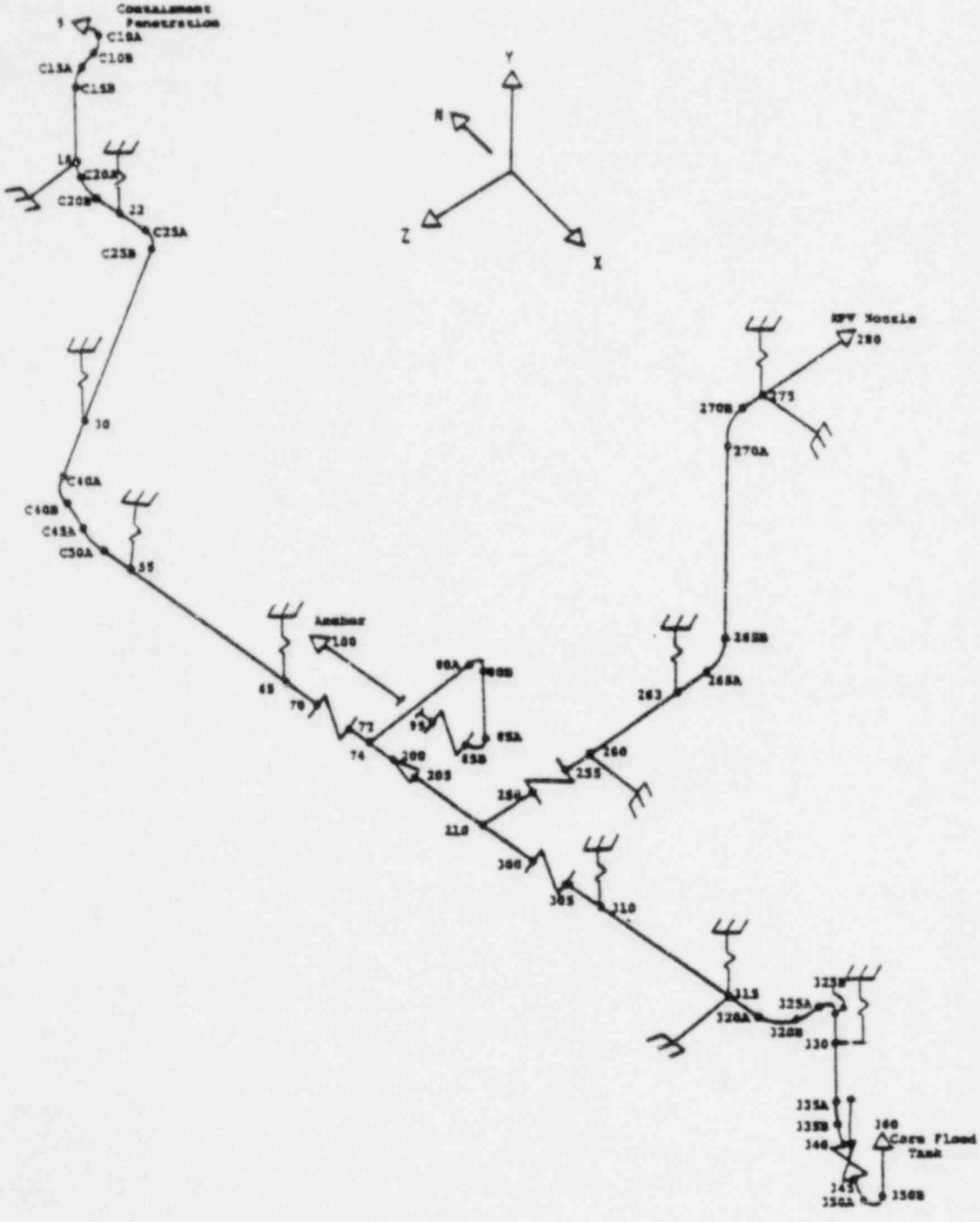

Figure H-8. Rancho Seco Loop B Core Flood Line Math Model

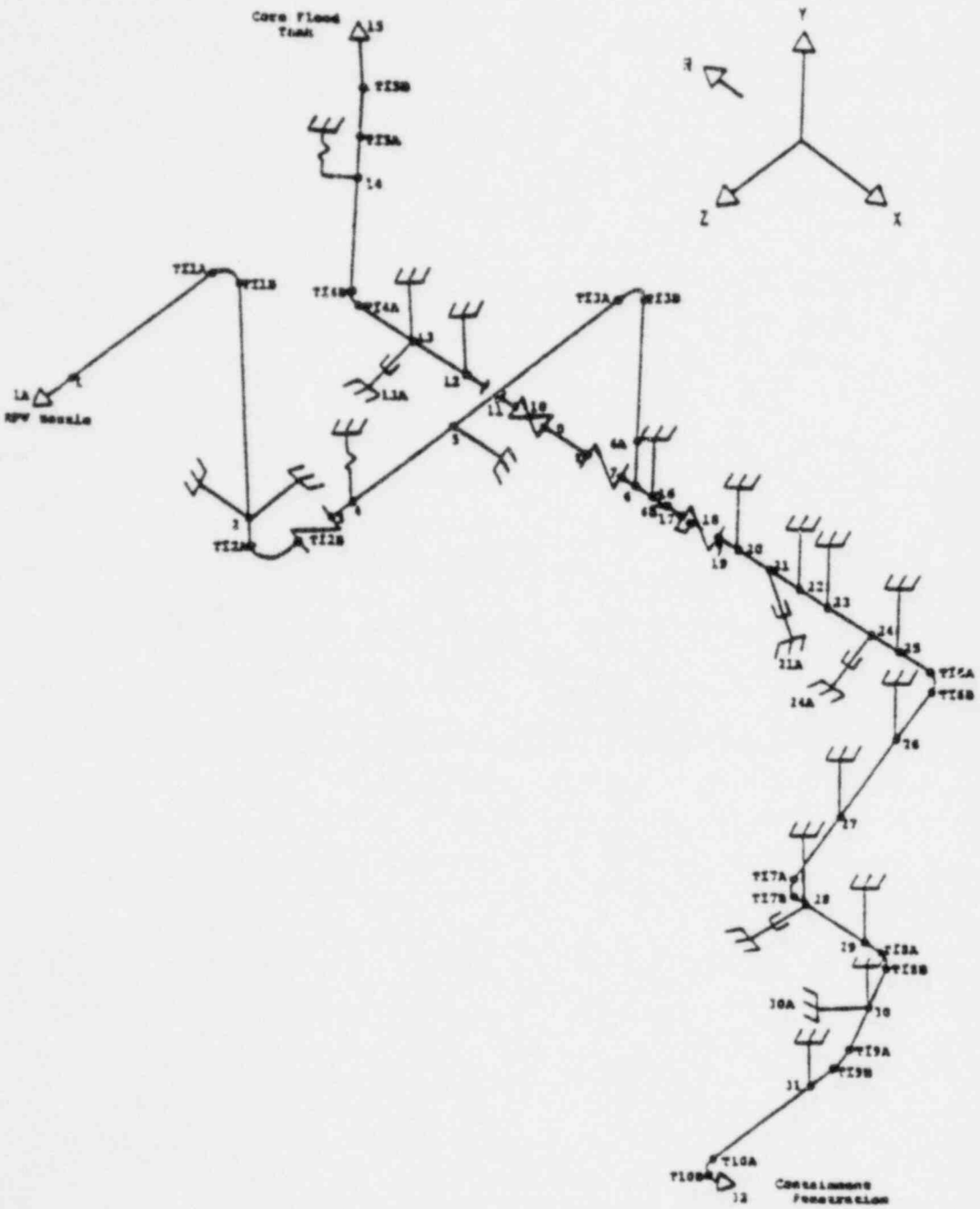

Figure H-9. Davis-Besse Loop A Core Flood Line Math Model

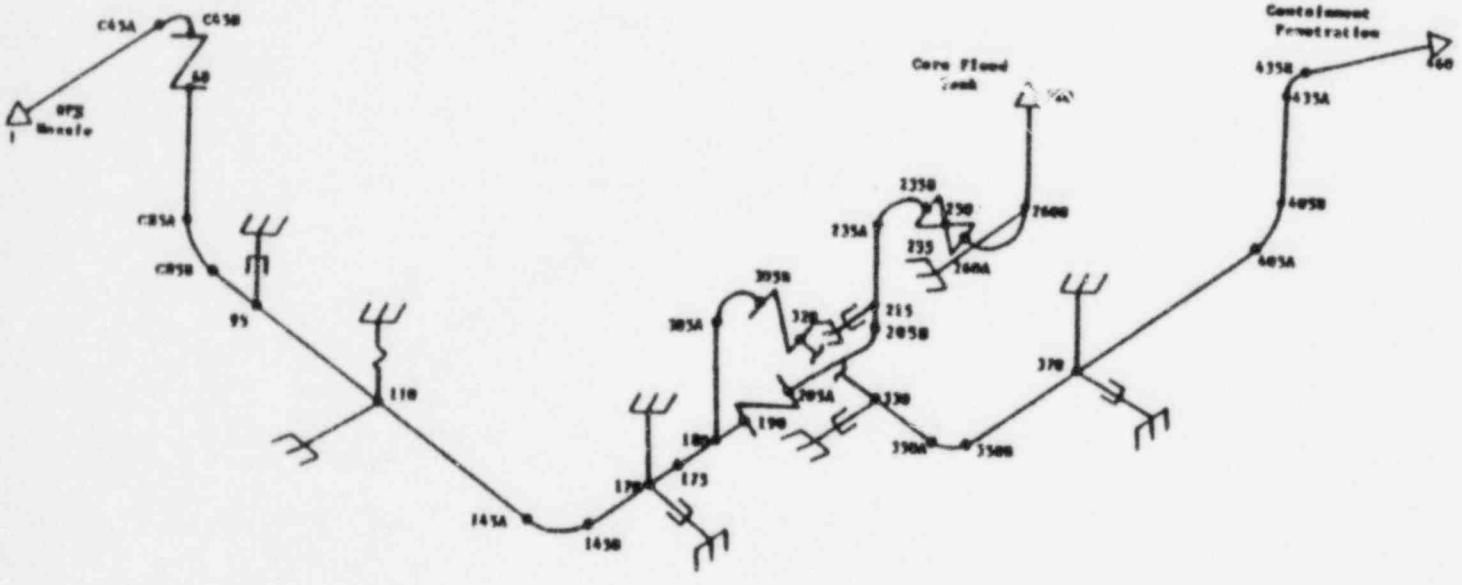

APPENDIX I

Cavity Wall Model Description

1. Introduction

Analyses of the response of the reactor vessel cavity walls were performed for a spectrum of pipe breaks. Due to variations in the cavity wall configurations, six separate linear models were developed. Similarities in configuration allowed linear analysis of the Three Mile Island 1 cavity wall to be performed on the Crystal River cavity wall model. In addition, a nonlinear finite element model of the Three Mile Island 1 cavity wall was developed.

Each model is described in detail in this appendix. Geometric and stiffness characteristics of each cavity wall are identified, and their modeling explained. Sensitivity studies, which were performed on a plant-specific basis but are of generic application, are discussed.

2. Generic Considerations

Each cavity wall is approximately symmetrical about its hot leg penetrations. Thus, most were modeled as 180-degree sectors. Table I-1 summarizes the key features of each cavity wall model. A typical cavity wall and surrounding structure is shown in Figure I-1.

The models were developed for analysis with the computer program EDS-SNAP, using three-dimensional, 20-node, isoparametric solid elements to represent the concrete structure. With the exception of ANO-1, the models included the fuel canal walls and the fuel canal floors. The core flood line shield walls were included in the Oconee, Three Mile Island 2, and Davis-Besse models. In general, fixed boundaries were assumed at the secondary shield walls and at the top of the pedestal. In locations where secondary shield walls were not considered rigid, equivalent boundary spring elements were used.

Each linear model has at least 720 degrees of freedom. The Davis-Besse and Crystal River models both have more than 2200 degrees of freedom. The nonlinear Three Mile Island 1 model has 372 degrees of freedom.

The hot and cold leg penetrations through the walls were included in the models, with their circular shape approximated by polygonal openings. The

modeling of openings matched the corresponding finite element mesh refinement, which was selected to reflect the complexity of the cavity wall geometry. Diamonds were used for Crystal River 3, Oconee, and Rancho Seco, while hexagons were used for Three Mile Island 2. A more refined mesh, using octagons, was used for Davis-Besse. Explicit curved elements were used to model the ANO-1 hot leg penetrations. Minor penetrations, insulation, and liner plates were not modeled, as their effect on global wall behavior is insignificant. Element faces on the insides of the cavity walls were curved to match the inside diameter of each wall.

The pressure developed in the cavity due to the postulated LOCA (Section 8.1) was applied to the inner surface of each cavity wall and its penetrations. Since the nodalization schemes for the CRAFT2 and EDS-SNAP models were not identical, a mapping procedure was employed which averaged the pressure loadings over the CRAFT2 "volumes" and the EDS-SNAP "surfaces". For those areas where the CRAFT2 and EDS-SNAP model surfaces did not correlate exactly, CRAFT2 volume pressure data were extended to match EDS-SNAP surfaces. Hence, equal or slightly greater loads were applied to the EDS-SNAP models from the previously generated CRAFT2 data. For Oconee, pressures were applied to the top of the fuel canal floor to account for blowout of the shield plug devices. For Three Mile Island 2 and Davis-Besse, pressures were also applied to the top of the fuel canal floor, as no shield plug devices exist at or below this elevation.

For the hot leg load analyses, the cavity walls were analysed as being symmetric with respect to both geometry and loading. For the cold leg load analyses, the loads are not symmetric about the hot leg centerline. Where other than 360-degree models were used, the cold leg pressure loads were divided into symmetric and antisymmetric components, and two analyses were performed. The results from the two analyses were combined to determine the stress distribution on the cavity wall.

Isotropic analyses were performed for all of the linear models except those for Three Mile Island 2 and ANO-1. The elastic modulus for concrete was calculated as

$$E_c = 57{,}000\ (f'_c)^{1/2}$$

Poisson's ratio was assumed to be 0.20.

For the ANO-1 and Three Mile Island 2 cavity walls, it was determined that isotropic analyses gave overly conservative hoop stresses. For these plants, quasi-nonlinear analyses were performed to incorporate the stress redistribution which occurs within the cavity walls when the concrete cracks in hoop tension. These were performed by using an orthotropic material law for concrete, such that the hoop stiffness was reduced to 10 to 15 percent of that for uncracked concrete. This reduction was determined by calculating the stiffness of the cavity wall in the hoop direction due to the hoop steel reinforcing alone, assuming the concrete to be completely cracked.

These orthotropic analyses showed that hoop forces decreased, while bending moments and shears at the cavity wall boundaries increased. As discussed in Section 6.10, hoop forces are considered to be the primary load resisting mechanism of the cavity walls. Since the isotropic analyses predicted higher hoop forces than the orthotropic analyses, qualification of the cavity walls using isotropic material laws is conservative.

To assess the significance of dynamic behavior of the cavity walls, studies were performed which compared the response of representative cavity walls to both dynamic and static loadings. The ANO-1 and Rancho Seco models were selected, since they represent lower and upper bounds to cavity wall stiffness. For these two models, dynamic analyses were performed for the first 0.20 seconds of the blowdown loading for a 2.0A hot leg break. Results from these analyses were compared with those from static analyses for the same load history. The study demonstrated that very little or no dynamic amplification occured, due to the high first mode frequency (30 Hz and greater) of the cavity walls. A conservative, enveloping dynamic load factor of 1.15 was applied to the stresses obtained from static analyses for the peak asymmetric load for other plants. In addition, dynamic analyses showed that the critical loading typically occurred after the asymmetric phase of the LOCA, when essentially steady-state pressures had developed. No dynamic load factor was applied to static analyses of the steady-state response.

3. Description of Models

3.1. Oconee Cavity Wall Model

The Oconee cavity wall has a circular inner face and a polygonal outer face. The inner radius is 11.5 feet and the minimum thickness 5 feet. The top of the cavity wall is monolithically attached to the four-foot-thick fuel canal slab and the fuel canal walls. The six major penetrations through the cavity wall (two hot legs and four cold legs) were incorporated into the model. In addition, a recess of three feet in height, width, and depth is located directly beneath the hot leg penetration, locally reducing the wall thickness to approximately two feet. It was conservatively assumed that the actual hot leg break occurred adjacent to this penetration.

A 180-degree model was developed of the cavity wall with the axis of symmetry through the hot leg penetrations. The model is shown in Figure I-2. Conservative approximations as to the cavity wall thickness were made in regions where the shape is irregular. The circular penetrations were modeled as diamonds, with the corner nodes reflecting the radius of the penetration. These diamonds tapered to match the varying diameter of the penetration through the thickness of the wall. Fixed boundary conditions were assumed at the base of the wall and at the interface of the fuel canal slab with the secondary shield wall. The stiffness of the core flood line shield walls was simulated by boundary spring elements of conservatively low stiffness. For the hot leg break analysis, symmetrical boundary conditions were applied along the plane of geometric symmetry. For the cold leg analysis, symmetric and antisymmetric analyses were performed, and the results combined to obtain final stresses.

Isotropic material laws were used for all elements in the model. The modulus of elasticity, however, was reduced by a factor of four for the fuel canal slab elements (hot leg break analysis only) to conservatively reduce the added strength that the fuel canal slab lends to the cavity wall. Thus, the model predicts conservatively high hoop stresses in the cavity wall, since the stiffness of the fuel canal slab is underestimated relative to the circumferential stiffness of the cavity wall.

3.2. Three Mile Island 1 Nonlinear Model

As an elastic analysis showed that significant yielding of the reinforcement would occur, a nonlinear model of the Three Mile Island 1 cavity wall was developed. Results using this model for the hot leg break pressurization were used for qualification purposes.

The model (shown in Figure I-3) includes the cavity wall, the pedestal, and that portion of the base mat beneath the pedestal but above the liner plate. Conservatively, the 60-inch cavity wall was modeled as being 46 inches thick to account for the 10-inch recesses and spalling of 4 inches of concrete cover.

The concrete and reinforcing steel were modeled explicitly. Eight-node axisymmetric concrete elements represent the concrete, while the hoop and vertical reinforcing steel was included as one-node ring and three-node truss elements respectively. The computer program EDS-SNAP was used for analysis.

For the concrete elements, three-by-three Gaussian integration was employed throughout. Sensitivity analyses were performed with one, two, and four elements through the cavity wall thickness. These showed that even one element through the thickness gave reasonably accurate results. However, for the final model used for qualification, two elements were employed. In the pedestal region, more elements were used to account for the size of the pedestal and to accurately model the placement of reinforcing steel.

In the nozzle belt region, the large hot leg and cold leg penetrations reduce the stiffness and strength of the cavity wall in the hoop direction. To account for this effect in the axisymmetric model, the concrete properties at this section were reduced in the ratio of the net volume (with the volume of the penetrations excluded) to the gross volume. A similar procedure was used to determine the properties of the hoop reinforcing steel in this region.

Elastic analyses of the cavity wall indicated that the critical stresses occur principally under the steady-state load condition, as discussed in Section 6.10.4.2. The applied pressure loads represent the maximum steady-state

pressures and varied from 52 psi at the pedestal region to 282 psi over the lower part of the cavity wall.

In defining boundary conditions, there was assumed to be no shear resistance between the liner plate and the concrete. At the top of the cavity wall, equivalent boundary springs were used to model the stiffness of the combined fuel canal floor and fuel canal wall system. Analyses using the fuel canal finite element model, which is described in Section 3.2.1 of this appendix, defined these support stiffnesses.

Although tensile cracking of the concrete matrix is the most important feature controlling the concrete's response in the cavity wall to the applied LOCA loading, a complete description of possible concrete material nonlinearities was incorporated. This includes tensile cracking, multi-axial nonlinear stress-strain behavior, and compressive crushing.

The nonlinear analyses entailed the computation of principal stresses at each integration point for each time step. These were then compared to the defined failure envelope. If the tensile strength was exceeded, it was assumed that a crack developed perpendicular to the principal stress direction. The normal and shear stiffnesses across the crack were then reduced and the corresponding normal stress released. This implies that no consideration was given to the gradual release of stress because of the tension stiffening effects. In the Three Mile Island 1 analysis, the normal and shear stiffnesses were reduced by ratios of 0.01 and 0.5 respectively after tension cracks formed at an integration point. A more detailed discussion of the concrete material model is included in Section 2.4 of Appendix K.

Strengths for the concrete were taken as the ninety-day compressive and tensile strengths, which are 6650 psi in compression and 460 psi in tension (see Section 6.2.1.4).

All steel was modeled as an elasto-plastic, strain-hardening material. The specification for the steel is ASTM A615 grade 40. An average yield stress of 45 ksi, from test results[31], was used. An ultimate stress of 73.5 ksi,

which is the minimum ASTM value increased by 5 percent to account for production overstrength, was assumed. The ultimate uniform strain was taken as 7.5 percent based on tests which determined the minimum elongation of grade 40 reinforcing bars.[46]

To solve the nonlinear problem, an incremental solution strategy was adopted. The pressure load was applied in increments of 2.5 percent to ensure that only slight cracking would occur in any one load step. Sensitivity studies varying the load step size were performed to ensure convergence and accuracy of the solution. By using three-by-three integration and two layers of elements, a total of six integration point layers exist through the wall thickness. This prevents "cracking" at multiple integration points in any one load step, thus precluding an unrealistic decrease in element stiffness.

3.2.1. Three Mile Island 1 Fuel Canal Model

Sensitivity analyses showed that the lower the resistance provided by the fuel canal floor/wall system, the more intense the response of the cavity wall. Due to the geometry of this floor/wall system (see Figure I-1), the resistance offered to the cavity wall will vary with azimuth direction. For instance, this system is softer with respect to outward radial displacements directly above the hot leg penetration than it is directly above the core flood line penetraton.

To calculate the lower bound resistance of the floor/wall system, a finite element model was developed (Figure I-4). The boundary conditions chosen assumed two lines of symmetry resulting in an equivalent 360^{o} model. A unit pressure was applied to the inner face of the model. Cracking in the concrete was accounted for by using the effective moment of inertia of the cracked section. As expected, the outward radial displacement above the hot leg penetration was the greatest. This displacement was then used to calculate the equivalent radial stiffness per radian of the floor/wall system. This was then incorporated into the axisymmetric model as boundary springs (shown schematically in Figure I-3).

3.3. Three Mile Island 2 Cavity Wall Model

The Three Mile Island 2 cavity wall is a five-foot-thick, 31-foot-high cylinder of 11.5-foot inner radius (Figure I-5). The top of the wall is connected to the fuel canal floor, which extends to the secondary shield walls. A two-foot-thick core flood line wall is connected to the side of the cavity wall, while two 45-foot-high fuel canal walls extend above it. The inside face of the cavity wall includes four one-foot-deep recesses. Each extends around 22 degrees of the wall face.

The model represents one-half of the cavity wall. It includes the cavity wall and the fuel canal floor and walls explicitly, while the core flood line walls are represented by boundary springs of conservatively low stiffness. The Three Mile Island 2 model also includes boundary elements which account for the flexibility of the secondary shield wall system. Hot and cold leg penetrations were modeled as hexagons, but the relatively small core flood line penetrations were not included.

An orthotropic material law was defined for all the cavity wall elements to determine the load distribution resulting from the concrete cracking under hoop stresses.

3.4. Crystal River Cavity Wall Model

For the Crystal River plant, the cavity wall is cylindrical, with an inside radius of 11.5 feet and a wall thickness of 5 feet. Vertical recesses decrease the wall thickness to 4.17 feet at four locations. The cavity wall is attached to the fuel canal slab and to the fuel canal walls.

A single elastic 360-degree model (shown in Figures I-6 and I-7) was developed to represent the cavity wall. Modeling the full circumference of the wall allowed both cold leg and hot leg analyses to be performed with a single model. Twenty-node, three-dimensional elements were used to model the cavity wall, the fuel canal floor, and the fuel canal walls. Fixed boundaries were assumed at the base of the cavity wall, at the interface between the fuel canal slab and the secondary shield walls, and at the sides of the fuel canal

walls. The four cold leg, two hot leg, and two core flood line penetrations were modeled as diamonds.

An isotropic material law was used for all elements of the model. This results in the prediction of conservatively high hoop stresses.

Due to similarities in geometery, the Crystal River model was also used to perform linear analyses on the Three Mile Island 1 cavity wall. These analyses predicted significant yielding due to pressurization by the hot leg nozzle break. For this break case, the nonlinear cracked concrete model described in Section 3.2 was used for qualification of Three Mile Island 1.

3.5. ANO-1 Cavity Wall Model

The ANO-1 cavity wall, like Oconee, has a circular inner face and a polygonal outer face. It has an inner radius of 11.5 feet, a minimum wall thickness of 5 feet, and is approximately 26 feet high. Unlike the other cavity walls, it is free of surrounding structure, and a layer of resilient material isolates it structurally from the fuel canal slab.

A 180-degree finite element model was developed, using three-dimensional, 20-node, solid elements. The model is shown in Figure I-8. As hoop stresses exceed those required to crack the concrete, linear elastic orthotropic material laws were adopted.

3.6. Rancho Seco Cavity Wall Model

The Rancho Seco cavity wall model is a 180-degree representation of the 5 foot-thick cavity wall, and includes the fuel canal floor and fuel canal walls. The model is shown in Figure I-9. An isotropic material law was used for all elements of the model. Rancho Seco is the only plant in which the fuel canal walls extend below the level of the fuel canal floor. Thus, this cavity wall is the stiffest of the skirt-supported plant cavity walls. As discussed in Section 6.10, its first mode frequency is approximately 50 Hz.

3.7. Davis-Besse Cavity Wall Model

The Davis-Besse cavity wall has a circular inner face of radius 11.5 feet. The outer face is polygonal with a minimum wall thickness of 5 feet. This minimum thickness occurs at the level of the hot and cold leg penetrations. Below the support beams, the wall thickens. The top of the cavity wall is monolithically attached to the 4-foot-thick fuel canal slab, which, in turn, is connected to the fuel canal walls. The model is shown in Figure I-10.

The Davis-Besse model has the most detailed mesh refinement of all the cavity wall models. The model represents a 90-degree segment of the cavity wall and includes the hot leg, cold leg, and core flood line penetrations. The model also includes the access tunnel and the sump cavity. Thus, the most vulnerable section of the wall was modeled. Conservatively, the secondary-fill concrete was disregarded.

Symmetrical boundary conditions were placed along the appropriate model edges, and the model was fixed at the cavity wall/pedestal interface. One-dimensional truss elements were used at the edge of the fuel canal floor to model the secondary walls.

Isotropic elements were used throughout resulting in conservative values for hoop stresses.

The hot and cold leg penetrations were modeled as octagons whose corner nodes reflect the radii of the penetrations. The diameters of the hot leg penetrations vary through the wall thickness; this was modeled as a linear taper. The core flood line penetration was modeled as a diamond.

Rectangular holes were included in the model to reflect the lack of hoop steel continuity where the support beam is embedded in the wall. The sump cavity was also modeled as a rectangular hole, extending the full height of the cavity wall.

Table I-1. Cavity Wall Model Features

Plant	Portion Modeled	Core Flood Line Shield Walls	Fuel Canal Floor	Fuel Canal Wall	Cavity Wall Recesses	Hot Leg Penetration	Cold Leg Penetration	Core Flood Line Penetration	Isotropic Analysis	Orthotropic Analysis
Oconee	180°	Yes	Yes	Yes	Yes[1]	Yes	Yes	No	Yes	No
TMI-1	Linear 360°	No	Yes	Yes	Yes[2]	Yes	Yes	Yes	Yes	No
	Nonlinear Axisymmetric	No	Note 3	Note 3	Note 3	Note 3	Note 3	Note 3	Cracked Concrete	
TMI-2	180°	Yes	Yes	Yes	Yes[2]	Yes	Yes	No	No	Yes
Crystal River	360°	No	Yes	Yes	Yes[2]	Yes	Yes	Yes	Yes	No
ANO-1	180°	No	No[4]	No[4]	No	Yes	Yes	No	Yes	Yes
Rancho Seco	180°	No	Yes	Yes[5]	No	Yes	Yes	No	Yes	No
Davis-Besse	90°	Yes	Yes	Yes	No	Yes	Yes	Yes	Yes	No

Notes:
1. One 3' deep recess immediately beneath the broken pipe hot leg penetration.
2. Approximately 1' deep recess at four locations around the cavity wall.
3. Lower bound values for stiffness were adopted for fuel canal floor and walls, and for hot, cold, and core flood line penetrations.
4. ANO-1 cavity wall not continuous with fuel canal walls/floors.
5. Fuel canal walls extend from pedestal upwards.

Figure I-1. Generic Cavity Wall

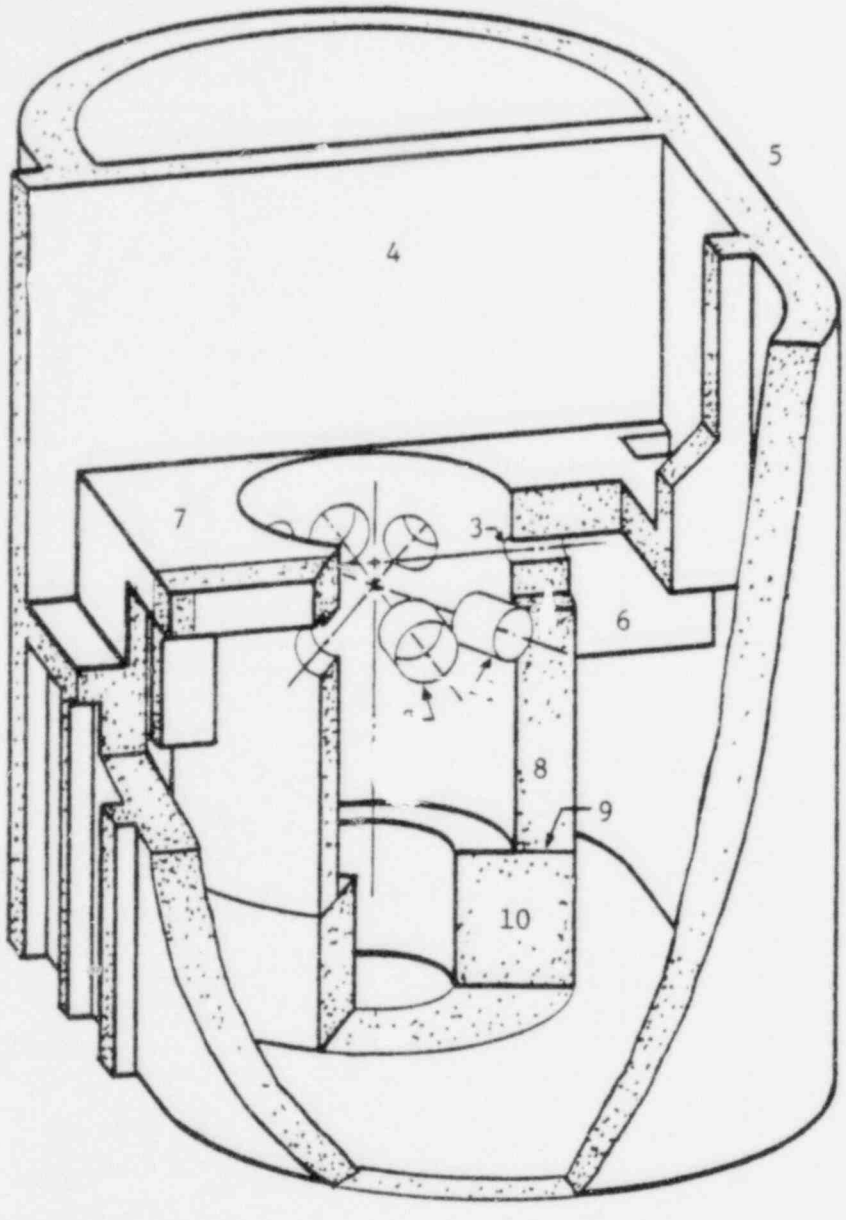

1 - Cold Leg Penetration
2 - Hot Leg Penetration
3 - Core Flood Line Penetration
4 - Fuel Canal Wall
5 - Secondary Shield Walls
6 - Core Flood Line Shield Wall
7 - Fuel Canal Floor
8 - Cavity Wall
9 - Pedestal - Cavity Wall Interface
10 - Pedestal

Figure I-2. Oconee Cavity Wall Model

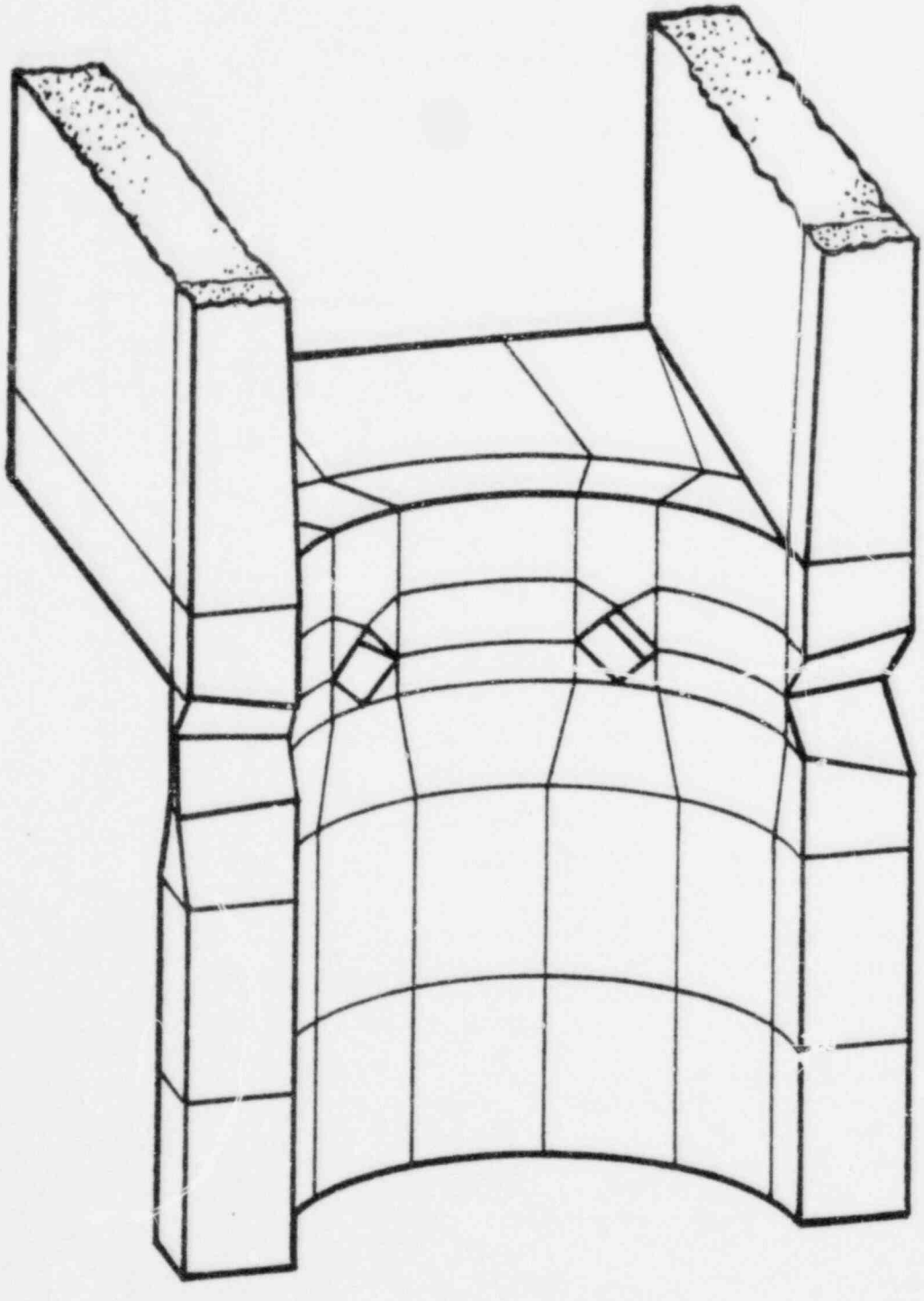

Figure I-3. Three Mile Island 1 Axisymmetric Cavity Wall Nonlinear Analysis Model

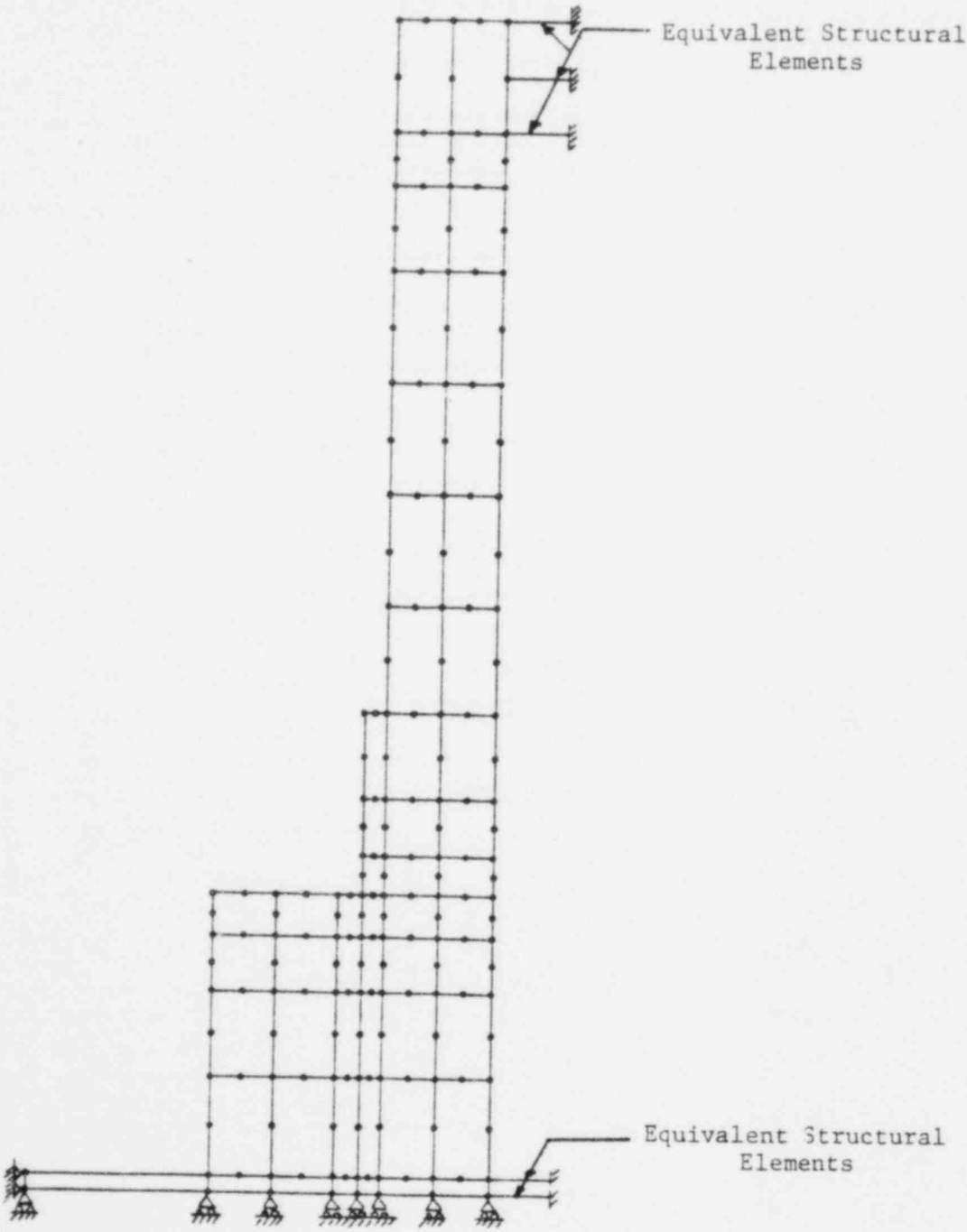

Figure I-4. Three Mile Island 1 Fuel Canal Slab Model

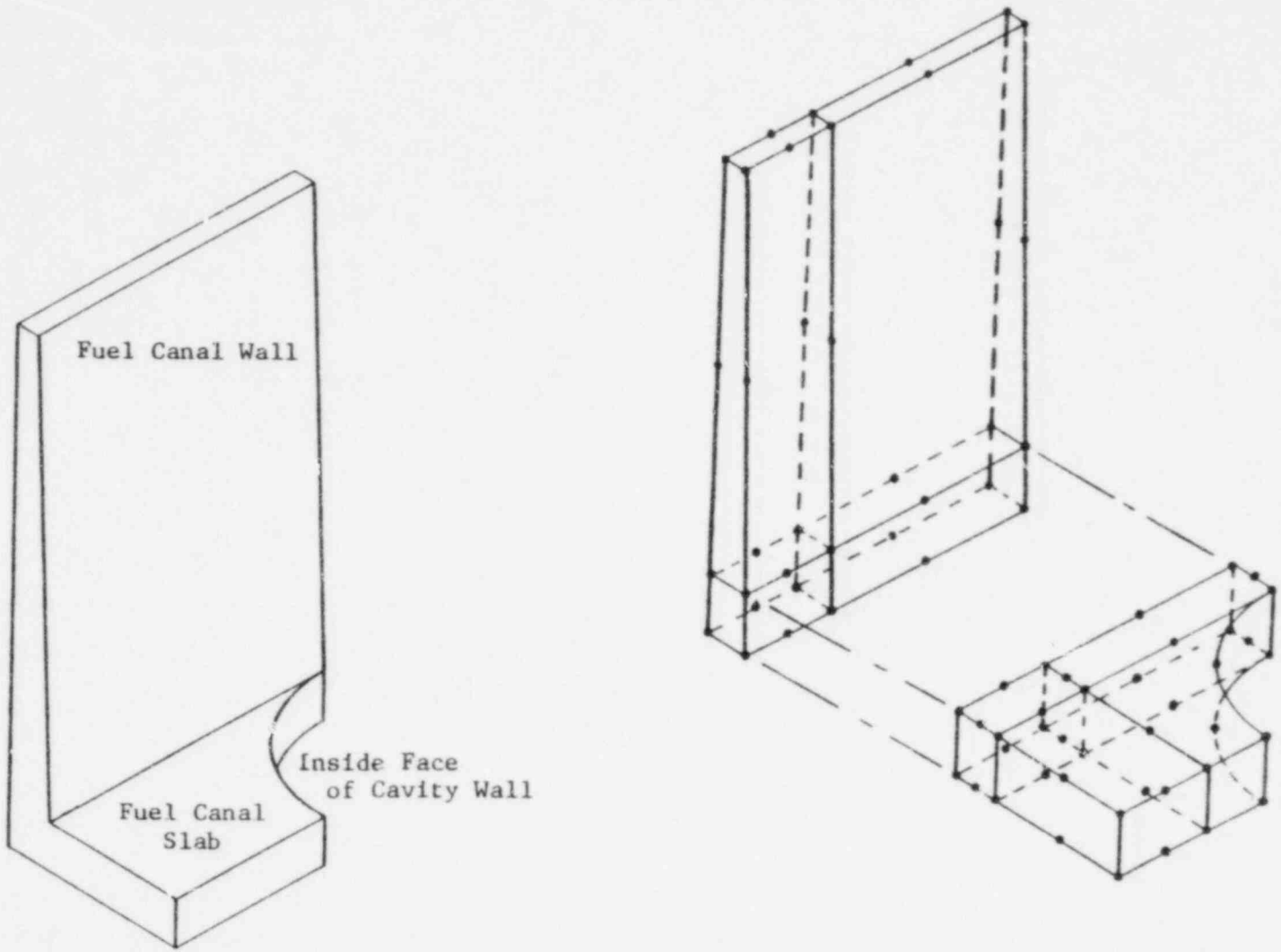

Figure I-5. Three Mile Island 2 Cavity Wall Model

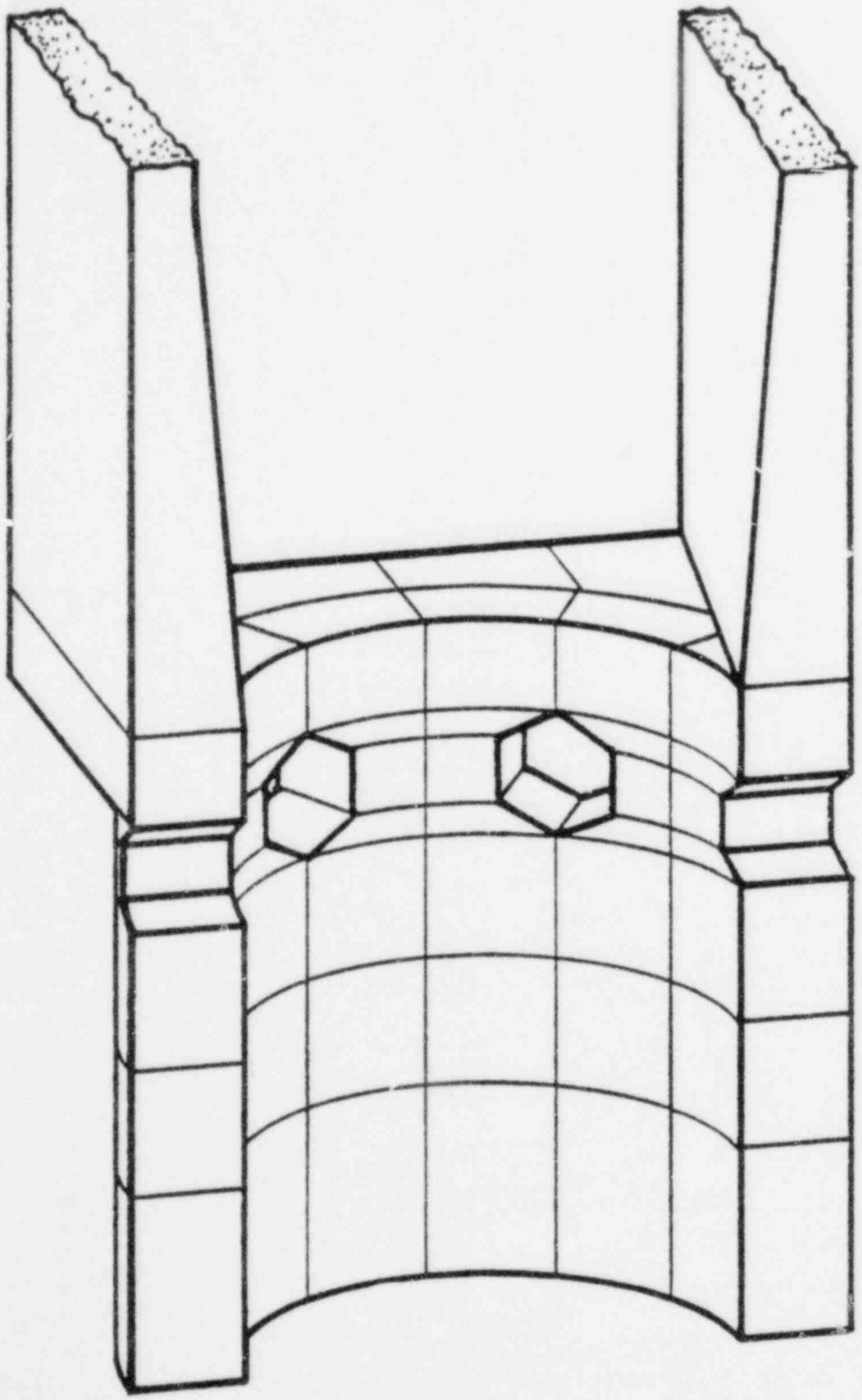

Figure I-6. Crystal River 3 360° Cavity Wall Model

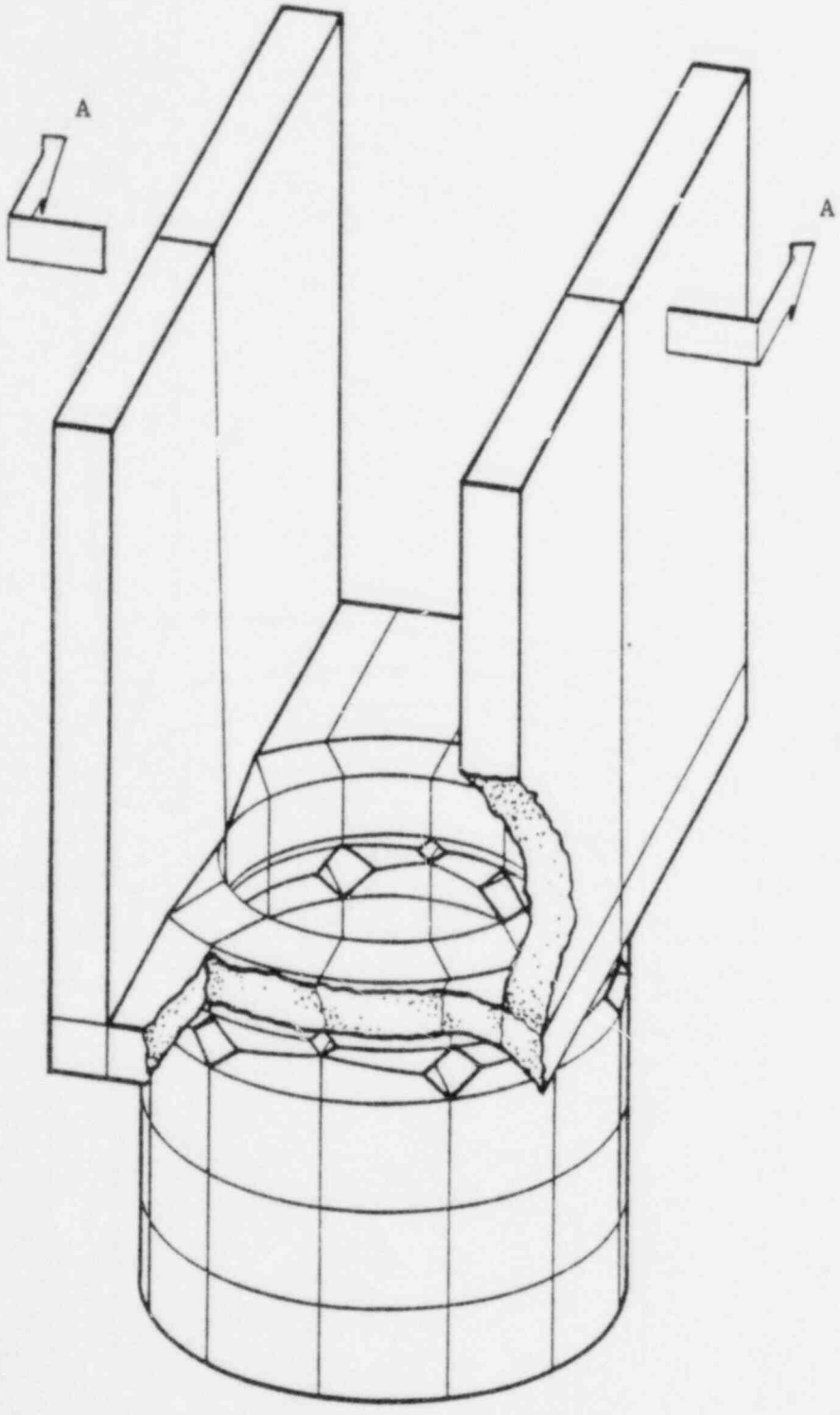

Figure I-7. Crystal River 3 Cavity Wall Model, Section A-A

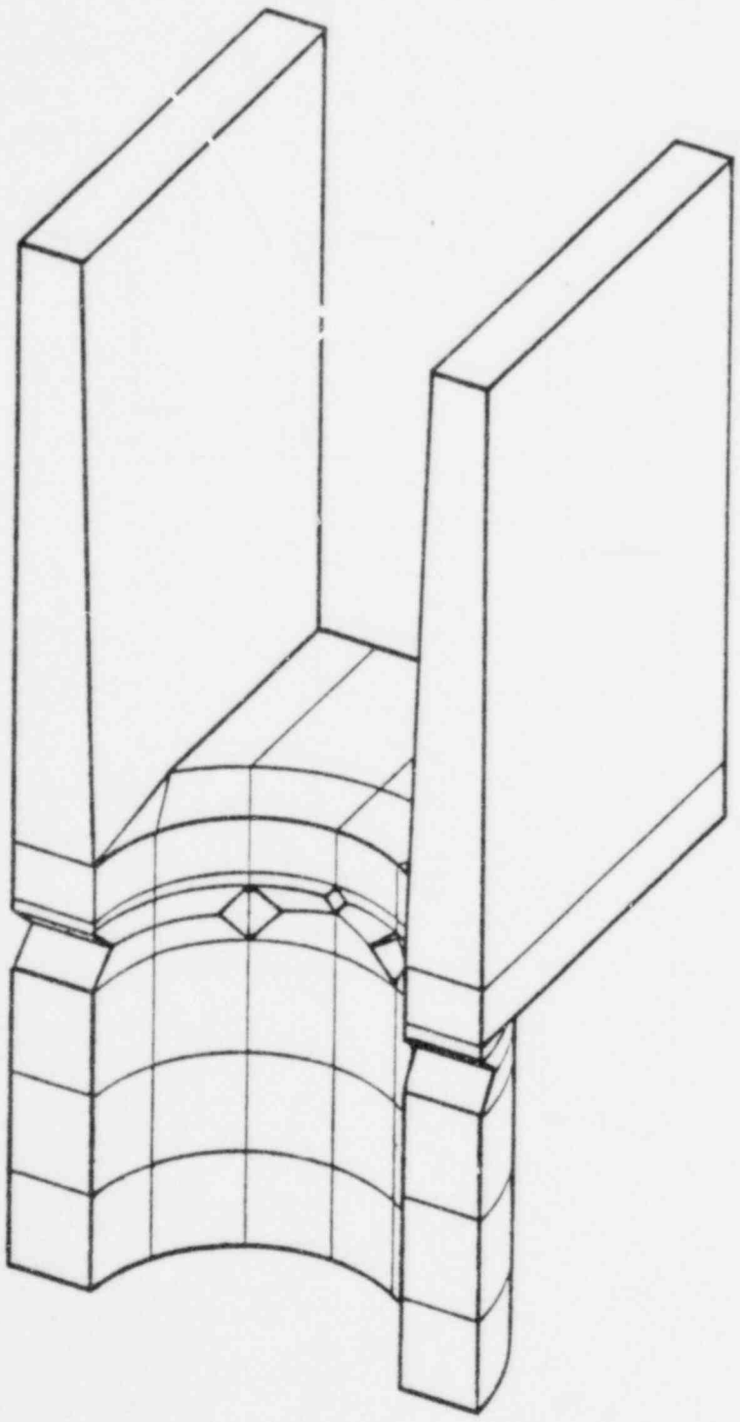

Figure I-8. ANO-1 Cavity Wall Model

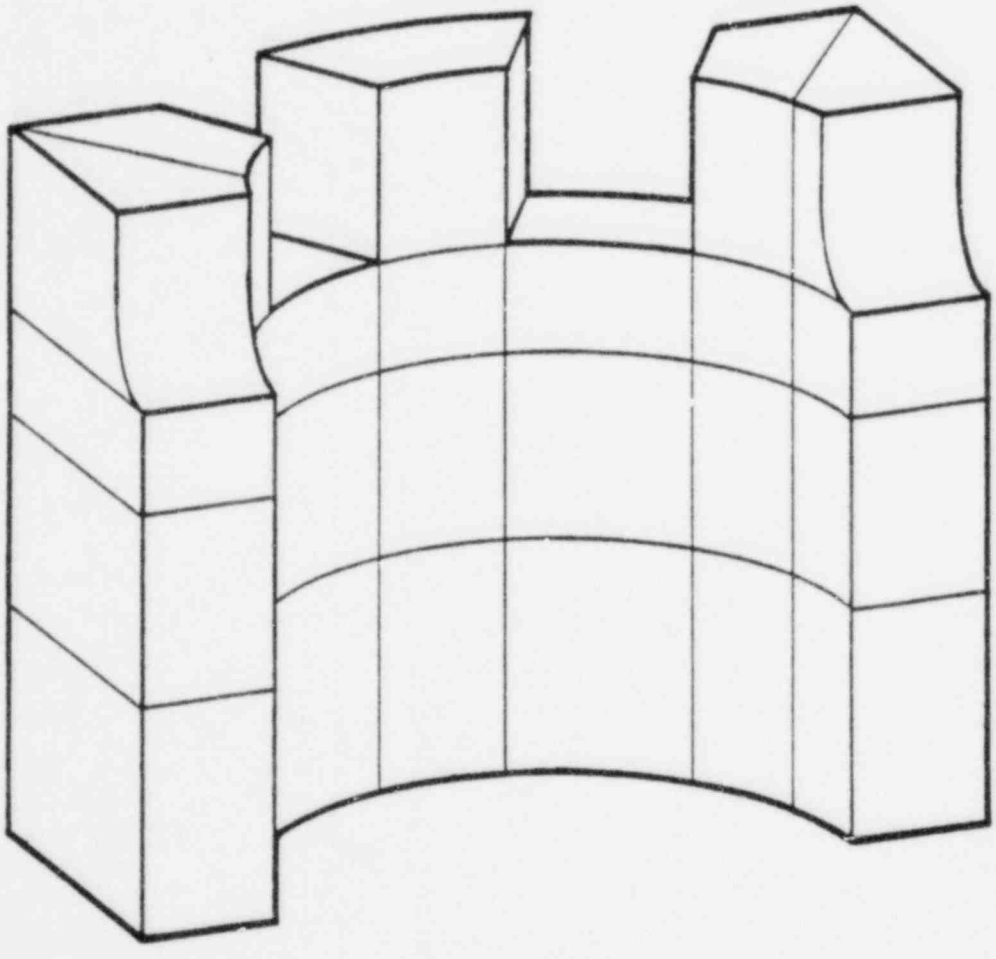

Figure I-9. Rancho Seco Cavity Wall Model

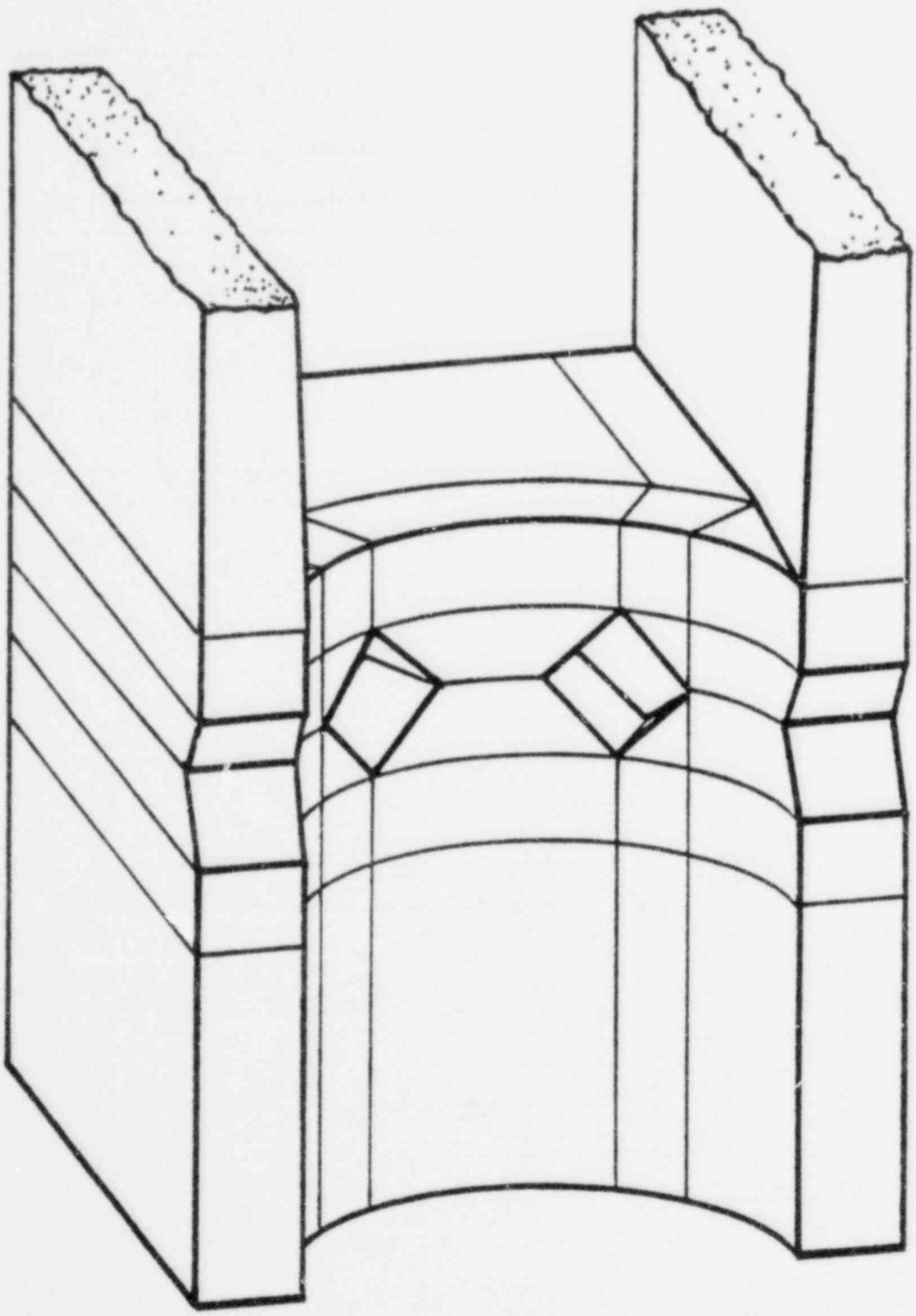

Figure I-10. Davis Besse Cavity Wall Model

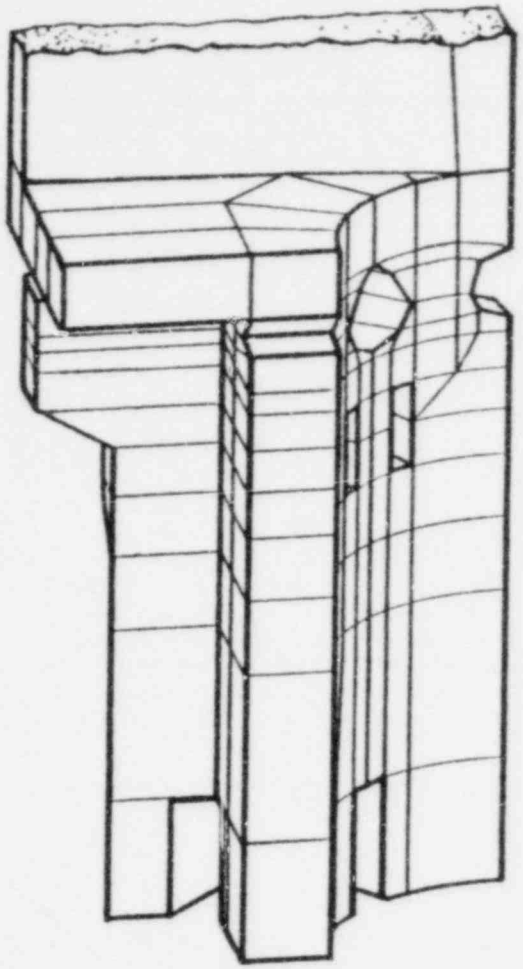

Partial Inside View of Wall

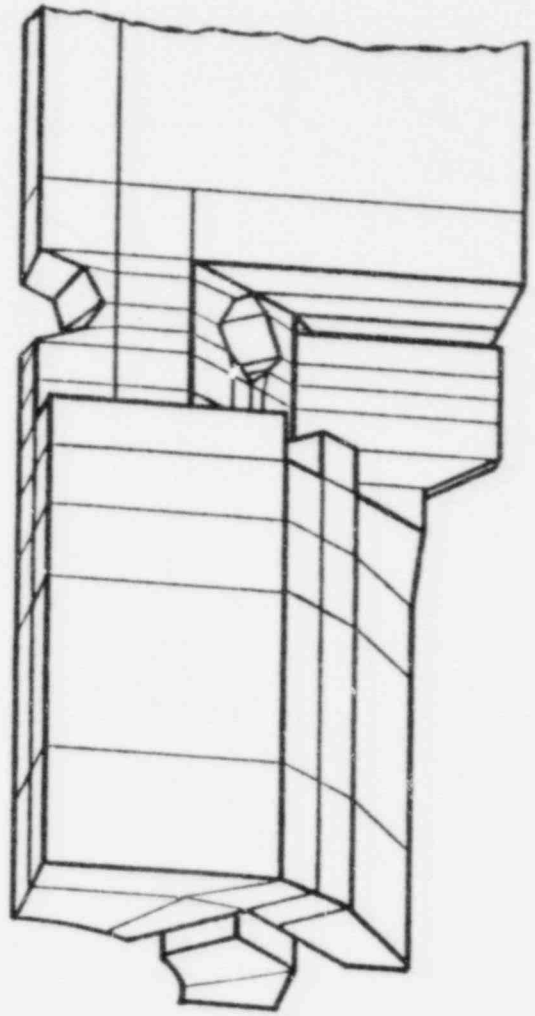

Outside View of Wall

APPENDIX J
Core Model Description

The detailed response of the fuel assemblies was determined using the core model shown in Figure J-1. The core model contains five co-planar fuel assemblies for a 177 FA plant. A parametric study was performed to determine the effect of the numbers of fuel assemblies in a core model verse the highest load on the spacer grids. The five fuel assembly model have the highest impact load and was selected on that basis. The mass of each fuel assembly was distributed at the spacer grid locations and at midpoint between the grid span. The fuel assembly contains eight grids – two of which (at the ends) can be considered as integral parts of the end supports; hence, they were not modeled. The fuel assembly model was used in the core model with rotational springs in conjunction with beam elements. The mass values were determined by the structural mass distribution and effective water mass. The values for the rotational springs were determined based on experimentally determined frequencies and mode shape of the fuel assembly.

Gapped springs were incorporated between adjacent fuel assemblies and between outer fuel assembly and the core baffle. These gapped springs were positioned at each spacer grid location. The gapped spring incorporated spacer grid dynamic properties, such as its impact stiffness and damping derived from test results. The spring gaps were based on the cold fuel assembly design spacing and were adjusted to operating temperature conditions. The spacer grid dynamic properties obtained from test results were also adjusted to reflect reactor operating temperature effects. The fuel assembly damping value used was established from the displacement tests on the fuel assembly in water at reactor operating conditions. The displacement time histories of the upper and lower grid plates were used as input excitation to the core model. It was assumed that the core baffle plates were rigidly attached to and have the same motion as the lower grid plates. The core model was analyzed using the STARS code[3] (which is discussed in Appendix N).

Figure J-1. Core Model

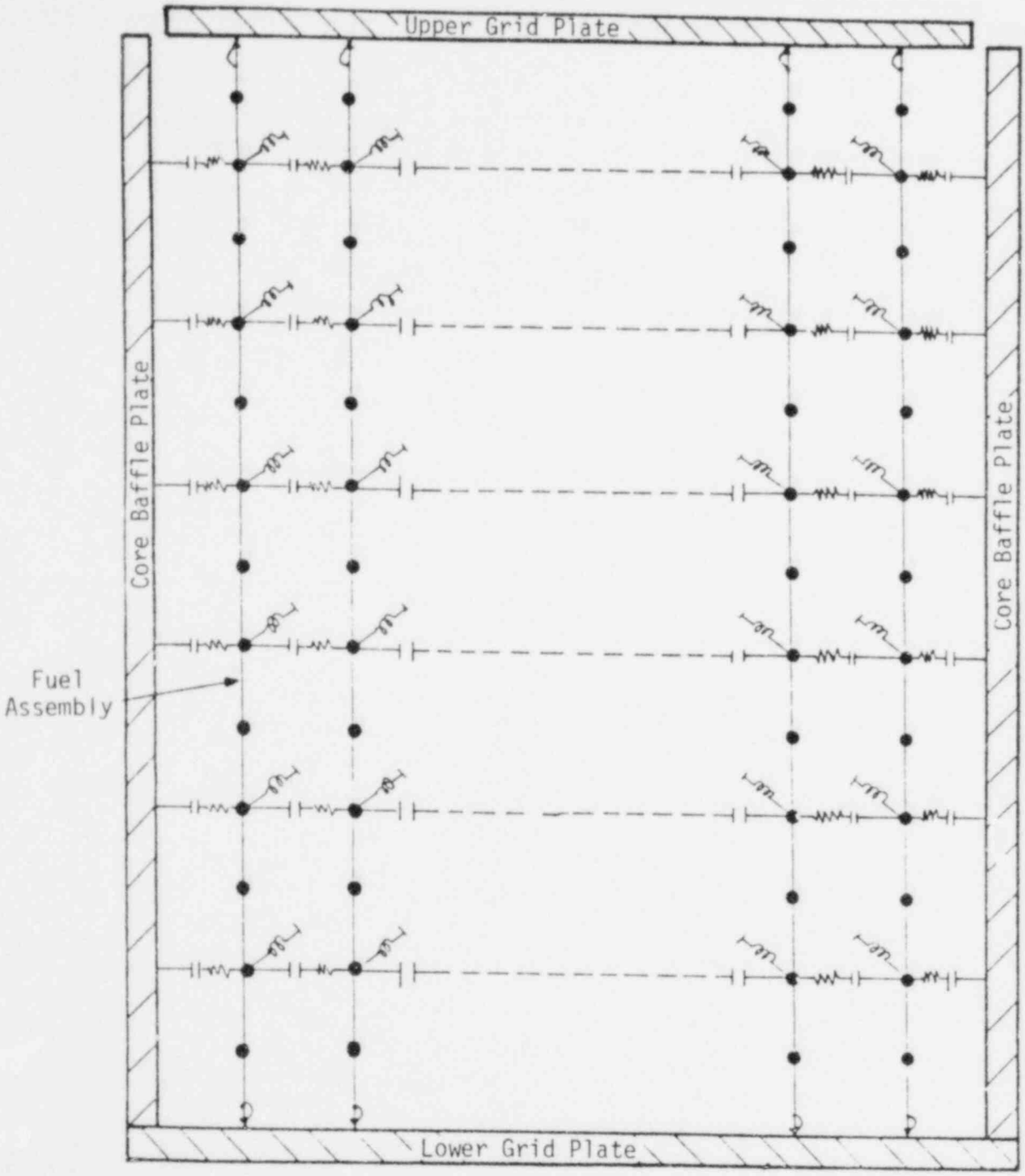

APPENDIX K
Reactor Vessel Support Embedment Model Description

1. Description of Reactor Vessel Support Systems

1.1. Skirt-Supported Plants

ANO-1, Oconee, Crystal River 3, Three Mile Island 1 and 2, and Rancho Seco are all skirt-supported plants. In a skirt-supported plant, the reactor vessel is supported on a short, wide, cylindrical steel skirt. This is, in turn, bolted down to a concrete pedestal which is fixed to the basemat and forms the base for the cavity wall.

This structural configuration is shown schematically in Figure K-1. The concrete pedestal is basically a thick-walled cylinder, to which the reactor vessel support skirt is fixed by 96 prestressed anchor bolts. These anchor bolts are attached deep in the pedestal to anchor plates, but are otherwise debonded from the surrounding concrete medium. Stiff steel plates are used to transfer loads from the skirt into the concrete, as shown in Figure K-2.

The asymmetric LOCA loading produces a large overturning moment and a lateral force on the skirt. These forces are resisted by the concrete pedestal, being transferred through the interface between the skirt and the pedestal. The LOCA also produces a torsional moment and an uplift force, both of which are relatively small.

Four finite element models were developed to determine the reaction of the embedments to LOCA loading. They are:

1. A generic embedment model, which is a detailed three-dimensional model of the skirt/pedestal interface and the pedestal concrete;

2. An axisymmetric model, which includes the cavity wall and the basemat, and was used for sensitivity studies;

3. A nonlinear embedment model, which was developed from the generic embedment model and allowed the inelastic behavior of the pedestal concrete to be taken into account; and

4. An embedment substructure model, which is a detailed two-dimensional model of the pedestal. It was used to determine the local nonlinear response of the concrete for input to the nonlinear embedment model.

1.2. Nozzle-Supported Plant

Davis-Besse is a nozzle-supported plant. The reactor vessel is supported by four pairs of support beams, one pair to each cold leg nozzle. The support beams are embedded in the cavity wall at elevation 565 feet, the level at which the wall thickens immediately below the adjacent penetrations. Figure K-3 shows a section through a typical support beam.

These support beams have considerable strength against vertical loading. Thus, they resist the dead-weight of the vessel together with the global vertical load and overturning moment induced by the asymmetric LOCA loading.

The support beams have less strength against horizontal loading, and, in certain instances, the lateral load induced by the LOCA is assumed to be completely resisted by the steel LOCA rings. These rings enclose each hot and cold leg in its respective penetration through the cavity wall. A cold leg LOCA ring is shown in Figure K-4. There is a small gap of about one eighth of an inch between the pipe and the LOCA rings.

For a postulated hot leg rupture, all four cold leg LOCA rings share in resisting the lateral load, and thus restrain the reactor vessel. For a cold leg rupture, two of the three remaining cold leg LOCA rings carry the load, together with the two hot leg LOCA rings.

2. Models for Skirt-Supported Plants

2.1. Generic Embedment Model

2.1.1. Introduction

The generic embedment model is a detailed finite element model of the combined reactor vessel anchor bolt/concrete pedestal system. The model, which is

shown in Figures K-5 and K-6, was developed to determine spring rates for this structural system and to calculate stress distributions for the qualification of the embedment to the applied LOCA loading. The spring rates were subsequently used to represent the embedment in the reactor vessel isolated structural models (Appendix D).

The LOCA loading consists of two principal components: a global moment and a lateral load, both of which arise from the asymmetric nature of the LOCA event. When the applied moment reaches a certain value, the uplift force on one side of the skirt exceeds the prestress holding it to the pedestal, and "lift-off" occurs. For analytical purposes, this phenomenon is nonlinear, since the stiffness characteristics of the structural system change.

Taking advantage of symmetry, the generic embedment model represents a 180-degree sector of the pedestal. It was developed and analyzed using the computer program EDS-SNAP[9], which is described in Appendix N. The full model has 1248 degrees-of-freedom and a maximum half bandwidth of 258, and includes 242 linear and nonlinear elements. The nonlinearity associated with lift-off was included. Solution of the nonlinear problem was achieved by equilibrium iteration, using either modified Newton iteration or the BFGS matrix update method.[10]

The model consists of four distinct components: the vessel support skirt, the anchor bolts and associated steel hardware, the pedestal concrete, and the basemat concrete beneath the pedestal.

The vessel support skirt was included in the model in order to reproduce accurately the load transfer mechanism at its interface with the concrete pedestal. The skirt is flexible with respect to deformations in the horizontal plane at its interface with the pedestal, but relatively rigid with respect to deformations normal to this plane. With the skirt included in the embedment model, any uncertainty as to the distribution of lateral load transfer into the pedestal was eliminated. Curvilinear, three-dimensional, thin-shell elements were used to represent the skirt, each element being defined by ten nodes. The rigidity imposed at the top of the skirt by the thick reactor vessel wall was modeled with the assumption that this section remained plane

and circular. Note that this model was not used for explicit stress analysis of the skirt, more detailed models being described in Appendix E.

The steel anchor bolts span between the bottom of the skirt and the pedestal concrete. There are 48 pairs of anchor bolts, each pair consisting of one anchor bolt at radius 83.75 inches from the reactor vessel centerline and one at 93.75 inches. Sets of two pairs were modeled as a single nonlinear truss element at a radius of 88.75 inches. To distribute the loads from these anchor bolt trusses into the pedestal concrete, linear elastic beams, representing the sole plates and the anchor plates, were included in the model.

The vertical transfer of load between the vessel support skirt and the top of the pedestal concrete was effected by connecting nonlinear truss elements between the two. These trusses are rigid in compression, but have zero stiffness in tension, and thus accurately reproduce the lift-off phenomenon. This modeling is illustrated in Figure K-6.

Transfer of the horizontal load from the vessel support skirt into the pedestal concrete was modeled in a similar manner. Radial horizontal truss elements, shown in Figure K-6, were included to model the load transferred by direct bearing through the vertical bearing plate. As with the vertical trusses discussed above, these radial trusses are only capable of carrying load in compression. Some load is also transferred through the underside of the sole plate. For those plants with shear anchors, this load transfer was modeled by specifying displacement continuity between the sole plate and its underlying concrete. For plants without shear anchors, leaving only friction to act, no displacement continuity was specified. In each case, these assumptions (of zero slippage and full slippage respectively) were subsequently checked and their adequacy verified.

The pedestal concrete was modeled by 42 isoparametric, curvilinear, three-dimensional solid elements, each of which is defined by 20 nodes and has 27 integration and stress output points. These elements are linear elastic. The influence of cracking in the concrete and the presence of openings in the pedestal were not explicity considered in the model; however, they were considered in the sensitivity studies which are reviewed in Section 2.5 of this appendix.

The basemat concrete was not modeled explicitly, but rather by an equivalent grillage of three-dimensional beam elements. The properties of these elements were calculated assuming the bottom of the basemat to be fixed; the validity of this assumption was verified by sensitivity analyses.

An initial state of stress exists in the embedment due to the prestressing of the anchor bolts. Using EDS-SNAP, this stress was incorporated into the analysis by defining an initial strain for the nonlinear trusses representing the anchor bolts. This initial strain produces out-of-balance forces in the model which are equilibriated in the solution.

For each skirt-supported plant, the design prestress force in each bolt is known, as is the dead-weight of the reactor vessel at the time of prestressing. The initial strain was input so that this condition would be duplicated. The model then allows for the relaxation of prestress when the full operating weight of the vessel is applied.

The generic embedment model can be used for all the skirt-supported plants: ANO-1, Oconee, Three Mile Island 1 and 2, Crystal River 3, and Rancho Seco. This is possible because the dimensions and properties of the embedment system vary little from plant to plant. Essential features of each plant are summarized in Table K-1.

Where dimensions such as the anchor bolt diameter or length, or the pedestal depth vary, the generic model was altered to suit. However, its basic configuration was preserved. Similarly, appropriate adjustments were made to material moduli and initial conditions.

2.2. Axisymmetric Embedment Model

An axisymmetric model of the pedestal/embedment support system was developed to determine the structural behavior of the support system when it is subjected to loadings applied through the reactor vessel support skirt. The model was used to identify those structural elements and material properties which could have a significant influence on the stress state in the pedestal, or on the embedment spring rates. Sensitivity analyses of the axisymmetric embedment

model thus served to confirm the validity of the more detailed, but less encompassing, generic embedment model.

The gross structural configuration of each of the skirt-supported plants is strongly axisymmetric, particularly in the vicinity of the embedments. Though certain structural elements, such as the secondary shield walls, are not truly axisymmetric, the asymmetry is not so marked as to induce significant error in the axisymmetric analyses.

The model (Figure K-7) includes the basemat and pedestal, a significant portion of the cavity wall, the resistance of the soil underlying the basemat, and the vessel support anchor bolts. The secondary shield walls, containment wall, and lesser structural elements were not included. Subsequent analyses confirmed that little distortion of the interfaces between these elements and the modeled structure occurs under the LOCA loading, thus verifying the adequacy of the model.

The model was analyzed using the finite element computer program ANSYS. Two types of ANSYS element were used, both of which are axisymmetric elements capable of handling harmonic, nonaxisymmetric loading functions. The first of these, the axisymmetric quadrilateral element, was used to model the concrete. The second, the axisymmetric conical shell element, reproduced the soil and anchor bolt stiffnesses. All elements were linear elastic.

To model the anchor bolts, the total area of the 96 discrete anchor bolts was calculated. The bolts were then replaced by a thin cylinder of equivalent area. As lift-off was not considered, the tops of the anchor bolts were coincident with the concrete surface. The reactor vessel support skirt was not modeled, but its effect was included by constraining the concrete surface at the interface between the skirt and pedestal to remain plane, while allowing it to distort within that plane. The soil stiffness on the underside of the basemat was modeled by conical shell elements as a series of discrete, uncoupled springs. A uniform soil stiffness per unit area of basement was assumed. This stiffness was determined by reference to theoretical solutions for rigid body displacements of a circular plate on an elastic, semi-infinite halfspace.

Two applied loading cases were considered, an applied moment at the reactor vessel support skirt/pedestal interface and an applied lateral load. These nonaxisymmetric loadings were represented by Fourier series. In both cases, the finite soil stiffness produced small rigid body displacements of the structure in addition to elastic deformations. As these rigid body motions are not of direct interest, their contribution to displacements at the interface between the pedestal and the reactor vessel support skirt was not included in the final analyses.

2.3. Nonlinear Embedment Model

The nonlinear embedment model determines the reaction of the pedestal to an applied moment, taking into account the nonlinear material behavior of the reinforced concrete. The model was developed from the generic embedment model to account for the redistribution of load due to nonlinear concrete response in the highly stressed compression zone. Both static and dynamic analyses were performed.

The model represents each 15-degree sector of the embedment with three nonlinear elastic truss elements and two lumped masses. One element models the concrete stiffness, one the anchor bolt stiffness, and the third, a rigid, compression-only element, was included for modeling purposes. One mass models the effective mass of a 15-degree sector prior to lift-off and the other the effective mass after lift-off. The model is shown in Figure K-8. As with the generic embedment model, this model considers a 180-degree sector and is analyzed using the computer program EDS-SNAP.

In order to represent the embedment in this way, it was necessary to adjust the stiffnesses of the individual sector trusses to reproduce the response determined by analyses of the generic embedment model. Assuming elastic concrete response, static analyses of the nonlinear embedment model correlated well with those of the generic embedment model both before and after lift-off.

The nonlinear truss elements representing the anchor bolts were given a bilinear stress-strain relationship in tension, appropriate to the bolt length, thickness, and material type. They were given zero stiffness in

compression. Definition of the anchor bolts as being fixed at the lower end, rather than coupled to the concrete, was possible because the flexibility of the bolts after lift-off is an order of magnitude greater than that of the concrete to which they are anchored.

The nonlinear truss elements representing the concrete were given multi-linear stress-strain relationships in compression. They have zero stiffness in tension, as lift-off prevents transmission of tension to the concrete.

A third group of nonlinear truss elements, rigid in compression but with zero tensile stiffness, was used to model the change in effective mass which occurs after lift-off. Before lift-off, when these elements are in compression, the masses are constrained to move as one. After lift-off, only the uppermost masses are mobilized.

The magnitude of the effective mass was determined from analyses of the axisymmetric model. The effective rotational mass of the complete embedment (and surrounding structure) was first calculated for conditions before lift-off, assuming that the dynamic deflected shape approximates the static deflected shape. The total mass assigned to each sector reproduces this global rotational mass. After lift-off in any sector, its effective mass decreases significantly. This post lift-off mass was assumed equal to the pre-lift-off mass decreased in the ratio of the post- to pre-lift-off stiffnesses of an individual sector.

Constraint equations were used to impose planar response on the free nodes, as the skirt flange does not undergo significant warping out of the horizontal plane. Prestress was incorporated into the model by defining an initial strain in the nonlinear anchor bolt trusses. The dead-weight of the reactor vessel was included in the loading. Thus, as in the generic embedment model, the correct initial conditions were reproduced.

2.4. Embedment Substructure Model

The embedment substructure model was developed to perform detailed nonlinear analyses of the reinforced concrete in the compression zone of the pedestal.

Analyses of this model defined the stiffness properties of the nonlinear concrete truss included in the nonlinear embedment model. In turn, the loads derived from analyses of the nonlinear embedment model were applied to the embedment substructure model. Results of the latter analyses were used for qualification purposes.

The model, which is shown in Figure K-9, represents a typical section through the pedestal. Plane strain behavior was assumed. The concrete and embedded steel, together with the effective reinforcement, were modeled explicitly. Linear and nonlinear two-dimensional elements represent the concrete, and beam and truss elements the embedded steel and reinforcement. The computer program EDS-SNAP was used for analysis.

Both the loading applied through the reactor vessel support skirt and the reactions imposed by the cavity wall were considered. The skirt loading consists of a vertical load, due to the reactor vessel weight and the applied LOCA moment, and a lateral thrust induced by the asymmetric LOCA load. The former is applied at the reactor vessel support skirt centerline, with distribution of the concentrated load to the pedestal concrete being effected by the beams modeling the relatively stiff sole plate and skirt flange. The method of application of the lateral load varied from plant to plant: friction between sole plate and concrete, radial thrust through the vertical bearing plate, and mechanical load application through shear anchors can all be modeled. The cavity wall reactions were represented by concentrated forces applied to the three nodes at the cavity wall interface.

Relatively high stresses occur under the compression flange of the reactor vessel support skirt. The inherently nonlinear behavior of concrete under high compressive stress, coupled with tension cracking, induces nonlinear response. Thus, twenty-nine EDS-SNAP nonlinear concrete elements were used in this region. The concrete element incorporates a nonlinear stress-strain relationship to allow for weakening of the material under increasing compressive stress, a failure envelope defining cracking in tension and crushing in compression, and the ability to model the post-cracking and post-crushing behavior of the material. A full description of the element can be found in References 20, 21, and 22.

The multi-axial stress-strain behavior of the element is developed from a defined uni-axial stress-strain law. A factor is incorporated to allow for the increase in the strain corresponding to maximum stress under multi-axial conditions. This maximum stress is defined by the failure envelope. The uni-axial stress-strain law proposed by Bathe and Ramaswamy[20] was adopted, with a strain corresponding to maximum uni-axial stress of 0.002. The strain corresponding to maximum stress under multi-axial conditions was then defined to increase 2.5 times faster than the failure stress. This value is consistent with the results of Richart, Brandtzaeg, and Brown[23] for the levels of confining stress present in the pedestal.

When the material is in tension or low compression, it is regarded as isotropic, and an equivalent multi-axial Young's modulus is adopted. Under high compressive stresses, an orthotropic material law is used, with the directions of orthotropy being defined by the principal stress directions. For the embedment substructure model, the orthotropic law was adopted when the maximum principal compressive stress was greater than one half the compressive failure strength under the current multi-axial stress state.

To identify material failure, the principal stresses are calculated at each integration point at each time step and compared to the defined failure envelope.

If the tensile strength is exceeded, a crack is 'formed' perpendicular to the relevant principal stress direction. In reality, this crack is localized. In the concrete element, however, a finite volume of concrete is assigned cracked concrete properties. The phenomenon of tension stiffening (see References 24, 25, 26, and 27) means that, analytically, a finite, residual tensile stress and stiffness should be applied in the region of the crack. The residual stress was conservatively set to zero in this model, as substantiated values are not currently available. In contrast to normal stress, considerable shear stress is transmitted across a crack due to aggregate interlock and reinforcement dowel action[8,28]. However, the shear stiffness in this plane is reduced[28,29]. In this model, a conservative value of 0.6 was used.

If the compressive strength is exceeded, crushing is defined to occur.

Away from the highly stressed zone, the concrete was modeled by linear elastic two-dimensional plate elements, with an elastic modulus equal to the dynamic secant modulus of the material. Beneath these elements, at the inter ace of the pedestal with the basemat, a fixed boundary was defined.

The reinforcement and anchor bolts were modeled by nonlinear trusses, of yield stress equal to the minimum required (appropriately increased for overstrength and strain rate). Allowance for the development length of reinforcement was made. An initial strain was introduced to the anchor bolt elements to account for prestress.

To solve the nonlinear problem, an incremental solution strategy was adopted. Stiffness reformation was performed at each load step, with iteration being carried out after the first load step to redistribute the out-of-balance load induced by the anchor bolt prestrain. Sensitivity studies were performed to confirm the adequacy of this solution strategy. These studies included comparison between analyses of varying load step, and between analyses with and without iteration being performed at each load step.

2.5. Sensitivity Studies

Sensitivity studies were performed to verify that the generic embedment model accurately reflects the force and stress distribution in the pedestal under the LOCA loading. These studies included comparison of stresses determined from the axisymmetric embedment model with those determined from the generic embedment model, as well as comparison of stresses obtained with variations in assumed properties and boundary conditions for the axisymmetric model.

The influence of two particular parameters was studied: the boundary conditions used in the generic model, and the presence of tension cracking or openings in the pedestal itself.

The boundary conditions investigated included the omission of the cavity wall from the generic model and the assumption that the underside of the basemat is

fixed. A series of axisymmetric analyses was performed to check the validity of these boundary conditions, using the axisymmetric embedment model described earlier:

1. Analysis of the full axisymmetric model, with an average soil stiffness;
2. Analysis of the axisymmetric model with half the above soil stiffness;
3. Analysis of the axisymmetric model without the cavity wall; and
4. Analysis of the axisymmetric model with the basemat fixed.

Contours of the three principal stresses within the pedestal were plotted and compared for each analysis. The values of the maximum shear stress on a vertical and a horizontal line through the highly loaded region of the pedestal were also compared. Both comparisons showed little variation between the four axisymmetric analyses. As a further check, the maximum shear stresses from an equivalent analysis of the generic embedment model were plotted against those of the axisymmetric analyses. The correlation was good.

Although these analyses were performed specifically for the Oconee plant, they can be applied generically, as the variation between plants is small.

Similarly, although the analyses were performed for loading prior to lift-off, the analyses are equally applicable after lift-off, when the deformations become more localized due to the relative flexibility of the anchor bolts.

Thus, the validity of the assumed boundary conditions for the generic embedment model was confirmed.

To determine the effect of tension cracking or of openings within the pedestal, the results of analyses of two generic embedment model configurations were compared. The first represented the full generic model. In the second, the stiffness of the two concrete elements immediately beneath the anchor plates was reduced on the tension side (Figure K-10). This latter model reproduced the probable effect of tension cracking or the presence of the partially open in-core instrumentation hatch. The redistribution of stress was found to be comparatively small. Again, the analyses were performed for the Oconee plant for loading prior to lift-off, but the conclusions are generic.

3. Models for Nozzle-Supported Plant

3.1. LOCA Ring Restraint Models

Both three- and two-dimensional models were developed for each LOCA ring. The three-dimensional models were used for final qualification analyses, while analyses of the two-dimensional models identified the correct load distributions to be applied to the LOCA ring. The models are described in the following sections.

3.1.1. Three-Dimensional Models

Three-dimensional, nonlinear finite element models of both the hot leg and the cold leg LOCA rings were developed. The models include the LOCA ring and the surrounding concrete medium. As neither is truly symmetrical, the full 360 degrees of each LOCA ring was modeled. The cold leg model is shown in Figure K-11; the hot leg model is similar. Analyses were performed using the computer program EDS-SNAP.

Both three-dimensional models consider explicitly the inner and outer plates of the LOCA rings, together with the webs which span between them. However, neither the pipe wall nor its interaction with the LOCA ring was modeled. Instead, the two-dimensional models were developed. These models, which are described in the next section, allowed the correct load distribution to the inner plates of the LOCA rings to be applied to the three-dimensional models.

Shell elements were used to model the inner and outer plates, while plane stress plate elements were used for the webs. An elastic-plastic material law was specified for the web elements for the cold leg model, which is the more highly loaded. An elastic material law was adopted for these elements in the hot leg model.

The surrounding concrete was represented by truss elements. For movement of the LOCA rings in their axial direction, as would be induced by friction loading, both the local deformation of the concrete and the global deflection of the cavity wall were considered. Conservatively, no yielding or slippage was permitted. For movement of the LOCA rings in the plane of the wall, only compressive contact stresses were allowed between the LOCA ring and the concrete.

Although Nelson studs impart a finite tensile strength to this interface, this strength will be small. To disregard it is conservative, and leads to the calculation of more severe loads on the LOCA rings.

The applied loading included both the normal and axial components. The calculation of the distribution of the normal component is described in the following section. Conservatively, the axial, or friction, component at each load point was assumed to be 42 percent of the normal load at that point.

3.1.2. Two-Dimensional Models

The two-dimensional models of each LOCA ring include the pipe wall to incorporate its interaction with the LOCA ring. However, they cannot analyze the LOCA ring response to axial, or friction loads, and thus were only used to calculate the distribution of loading to the LOCA ring.

As in the three-dimensional models, the full 360 degrees of the restraints and surrounding concrete was modeled.

The pipe wall was represented by linear elastic beam elements. Since the gap between the restraint and the pipe under operating conditions is small, it was not included in the model. However, sensitivity studies were conducted to ascertain whether local yielding of the pipe would significantly change the load distribution to the LOCA ring. These studies showed that the correct load distribution was obtained.

Nonlinear, elastic-plastic beam elements were used to model each component of the LOCA rings, while linear elastic plane strain elements were used for the surrounding concrete.

The interface between the pipe wall and the inner plate of the restraint, and the interface between the LOCA ring and the concrete, were assigned zero tensile strength. Nonlinear truss elements were used to transfer compressive loads across each interface.

For analysis, the applied load was distributed around the pipe wall in accordance with the theoretical shear distribution for a circular section.

3.2. Support Beam Model

A detailed finite element model of one support beam, its anchor bolts, one half of a support pad, and the surrounding concrete was developed. Analyses of this model for LOCA loading yielded accurate stress distributions in the steel beam, in the anchor bolts, and in the concrete immediately adjacent to the beam. For determination of the global stress distribution in the Davis-Besse cavity wall, due to both pressure loading and the forces transmitted through the support beams, see Section 6.10.

The support beam model (shown in Figure K-12) was analyzed using EDS-SNAP. Three-dimensional, plane stress, linear elastic plate elements were used to represent the steel beam. Each flange, web, and stiffener plate was explicitly modeled with the finite element mesh shown in Figure K-13. As the short, deep beam is principally loaded in shear, and local bending is of secondary magnitude, constant normal stress through the thickness of each element was assumed. Eight anchor bolts secure the beam to the concrete. These bolts, which are debonded over their length, were modeled by four truss elements, the lower ends of which were fixed.

Isoparametric, three-dimensional solid elements were used to model the concrete. The concrete mesh was extended to the line of symmetry between the support beams on one side, and sufficiently far in other directions to ensure that the correct local stress distribution was obtained.

The support beam pad transmits loads from the reactor vessel nozzle to the support beams. Elastic beams were used to model this pad.

The LOCA loading on the support beam will induce separation of the interface between steel and concrete where significant tension forces develop, since the bond strength between steel and concrete is typically low, and is often exceeded by normal thermal and shrinkage stresses. In the support beam model, the interface was assumed to have zero tensile strength. This is a conservative assumption, as it will result in higher local forces in both the beam and its surrounding concrete. Nonlinear, elastic truss elements were used to connect the beam to the concrete, and were given zero tensile

stiffness. A special condition was modeled at the inner face of the cavity wall where the beam enters the concrete. Flastic analysis indicated that very high contact stresses will develop here, stresses which would cause local crushing of a small zone of concrete. To allow for this, a nonlinear truss with a bilinear compression stress-strain curve was used at this location. This ensured that conservative, upper-bound stresses were determined for the support beam.

4. Support Stiffnesses

4.1. Embedment Stiffnesses for Skirt-Supported Plants

4.1.1. General

The stiffness of each reactor vessel support embedment was evaluated for inclusion in the reactor vessel isolated structural models (Appendix D). This stiffness was defined at the interface between the reactor vessel support skirt and the concrete pedestal, and accounted for the flexibility of the prestressed anchor bolts and the embedment.

When a global moment and a lateral force are applied to this interface, it both rotates and translates in the direction of the applied forces. This movement has three components:

1. Movement due to straining in the local embedment region of the pedestal;
2. Movement due to structural flexure in the thick basemat; and
3. Movement due to rigid body rotation and translation of the plant on its elastic soil foundation.

The first two, the non-rigid body components, produce relative deformations between the reactor vessel and its surrounding structure. The rigid body motion does not.

Studies were performed to determine the relative importance of the first two components (see Section 4.1.2 of this appendix). In summary, the deformations at the interface due to basemat flexure were found to be of equal importance to local embedment deformation prior to lift-off, but of secondary

importance after lift-off. This is due to the large relative flexibility of the steel anchor bolts. Before lift-off, the reactor vessel support skirt is in contact with the pedestal concrete around the full perimeter of the interface, and the flexible bolts are effectively linked in parallel with this interface. After lift-off, the contact between skirt and concrete is partially lost, and the bolts are effectively linked in series across the interface, which greatly increases the contribution of local straining to the overall deflection at the interface.

Embedment stiffness values were explicitly calculated for three skirt-supported plants using the generic embedment model. The plants considered were Oconee, Crystal River, and Rancho Seco. The axisymmetric model was used to study further the response of the Oconee plant to pre-lift-off loading. A parametric study was performed to derive stiffness values for the remaining three skirt-supported plants, ANO-1 and Three Mile Island 1 and 2. Sensitivity studies were made on both the generic embedment model and the axisymmetric model to verify the accuracy of the derived embedment stiffnesses.

All material was assumed to remain linear elastic for these analyses, though the influence of gross tension cracking in the concrete pedestal was studied to determine its effect on the stiffnesses. The elastic stiffness of the concrete was calculated from the following code formula (Reference 1, Section 8.3):

$$E_c = 33\, w^{1.5}\, (f'_c)^{1/2}$$

where E_c = modulus of elasticity, lb/in^2
w = weight of concrete, lb/ft^3
f'_c = specified compressive strength, lb/in^2

Poisson's ratio for concrete was assumed to be 0.2.

All stiffness values were defined as global spring constants, and included three terms. The first two of these terms were on-diagonal stiffness terms for a unit rotation and a unit translation at the interface respectively, while the third was the associated off-diagonal term. Inertial terms were not

included, as they are small in comparison to those associated with reactor vessel movement.

Studies using the generic embedment model established that an applied lateral load neither induces significant load in the anchor bolts nor, correspondingly, affects the contact stresses between skirt flange and concrete. Thus, the phenomenon of lift-off is independent of the magnitude of the applied lateral load. This allowed the moment-rotation stiffness to be considered independently of the lateral load. Further, the translation induced by the applied lateral load was shown to be insensitive to the manner in which it was distributed around the interface, allowing the lateral load-translation stiffness to be considered independently of lift-off and, hence, applied moment.

The stiffnesses to an applied lateral force were considered first. Analyses of the three specific plants using the generic embedment model, which assumes the basemat to be fixed on the underside, were performed. Based on these three analyses, the effects of pedestal geometry and concrete strength were evaluated, and equivalent stiffness values derived for the remaining three plants. The effect of basemat flexure was then determined, using an axisymmetric model analysis of the Oconee plant. An adjustment was made to include its influence on the lateral load-translation stiffnesses for all plants. As lift-off does not affect the lateral load-translation stiffness and the material behaviour is linear elastic, the resulting stiffnesses are constant. They are summarized in Figure K-14.

With respect to the stiffness of the embedments to an applied moment, two phases of response can be identified; pre-lift-off and post-lift-off. For the pre-lift-off phase, the analyses paralleled those described for an applied lateral load, with the exception that the anchor bolt properties were included in the parametric study. After lift-off, the influence of basemat flexure quickly diminishes, and the embedment response can be accurately assessed by generic embedment model analyses. Again, explicit analyses were performed for three plants, and parametric studies used to derive relationships for the remaining three. The full pre- and post-lift-off moment-rotation stiffnesses for each skirt-supported plant are given in Figure K-15.

The off-diagonal term, which defines the rotation induced by lateral load and the translation induced by moment, was derived from the above analyses. It is independent of lift-off.

Sensitivity studies were performed to verify the adequacy of the various spring rates. All sensitivity studies were performed for pre-lift-off conditions; however, the conclusions are equally applicable to the post-lift-off condition. The influence of the following parameters was investigated:

1. Soil stiffness;
2. Cavity wall stiffness; and
3. Tension cracking beneath the anchor plates.

The first two parameters were studied by varying the axisymmetric model for Oconee. Analyses were performed in which the average soil stiffness was reduced by one-half, and in which the cavity wall was assumed to have no stiffness. The resulting effect on the stiffnesses was small. The effect of tension cracking was determined by an analysis of the generic embedment model's response to an applied moment when certain elements were assumed to have zero stiffness (see Figure K-10). The effect on the global moment-rotation stiffness was small.

4.2. Support Stiffnesses for Nozzle-Supported Plant

4.2.1. General

The Davis-Besse reactor vessel is supported by four pairs of support beams, with further lateral restraint being provided by the LOCA rings on each hot and cold leg. The stiffness of each of these supports and restraints was evaluated for inclusion in the Davis-Besse reactor vessel isolated model structural analysis.

4.2.2. LOCA Ring Stiffness

The stiffness of each LOCA ring restraint was determined using the two-dimensional models described in Section 3.1.2. of this appendix. The

stiffnesses were calculated for movements normal to the pipe axis only. As the restraint imposed by friction was not considered in the reactor vessel isolated structural model, no stiffnesses were calculated for movements parallel to the pipe axis.

The nonlinearities induced by both material yield and separation at the interface between the LOCA ring and the concrete were considered. Figure K-16 shows the resulting spring rate for a horizontal displacement of a cold leg pipe against its LOCA ring.

4.2.3. Support Beam Stiffness

The stiffness of each individual support beam to applied LOCA loads was determined for inclusion in the reactor vessel isolated structural model.

To calculate the support beam stiffness to a vertical load, the support beam model was used. As no material yield occurs in the loading imposed by the LOCA, an elastic material analysis was performed. However, the effect of local concrete crushing under the beam where it enters the cavity wall, and of separation under tensile stresses at the interfaces between steel and concrete were considered. The resulting spring rate is shown in Figure K-17.

A similar model was used to develop a spring rate for a horizontal load on the support beam. The spring rate is shown on Figure K-18.

Table K-1. Embedment Properties for Skirt-Supported Plants

	ANO 1	Oconee	Crystal River 3	Three Mile Island 1	Three Mile Island 2	Rancho Seco
1. Pedestal Geometry						
a) Depth to basemat	126	126	132	132	132	126 in.
b) Inner radius	72	72	72	72	72	72 in.
c) Outer radius	198	198	198	198	198	198 in.
2. Anchor Bolts						
a) Total number	96	96	96	96	96	96
b) Diameter, inches	2.5	2	2.5	2.5	2.5	2.5
c) Approx. length, inches	66	70	92	92	92	109
d) Prestress, Kips/bolt	226	157	174	232	232	147
3. Concrete Design Strength, lb/in^2	5500	5000	5000	5000	5000	5000
4. Basemat Thickness, inches	108	102	150	108	138	96

Figure K-1. Embedment Layout for Skirt-Supported Plants

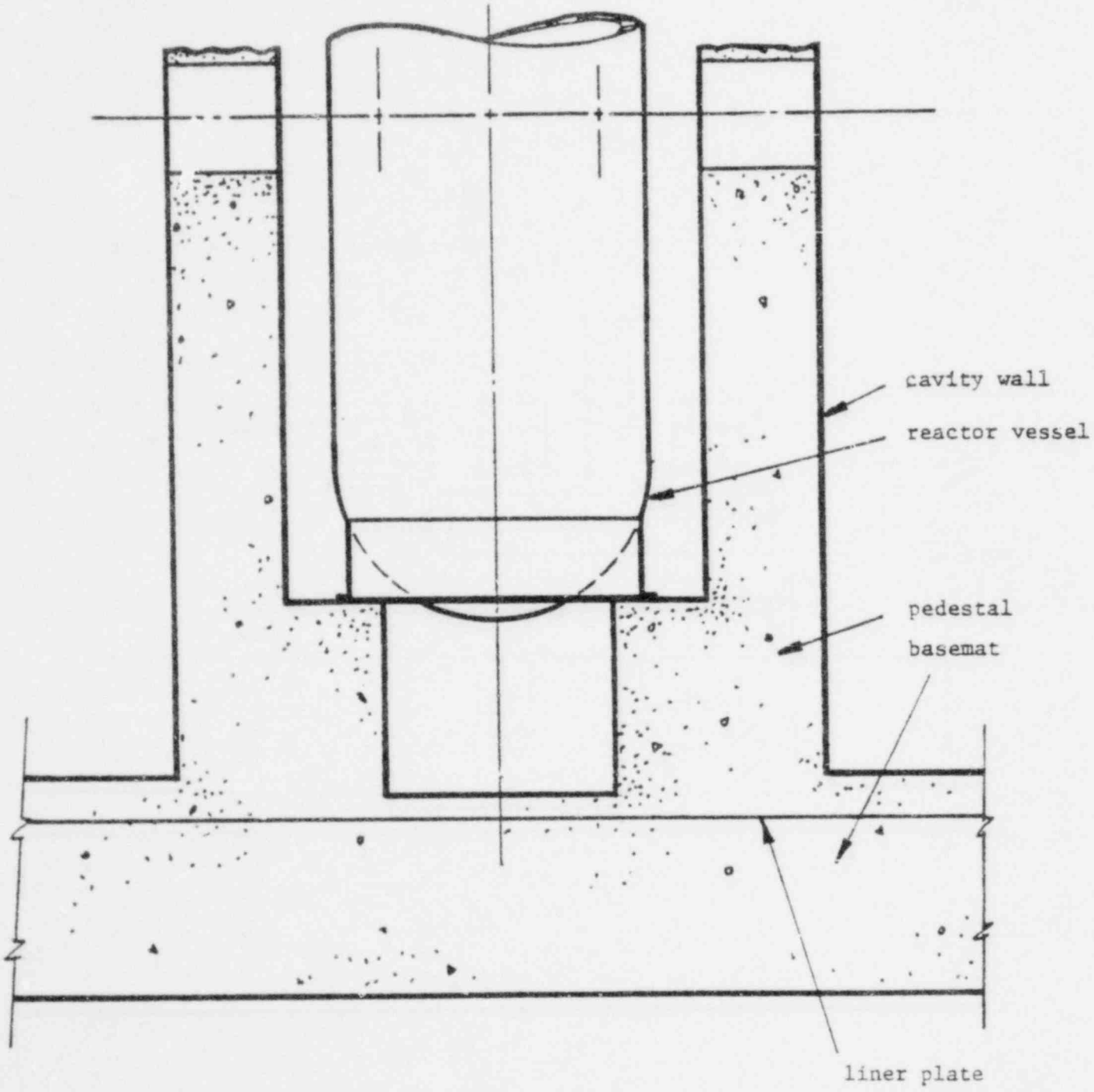

Figure K-2. Embedment Detail for Oconee

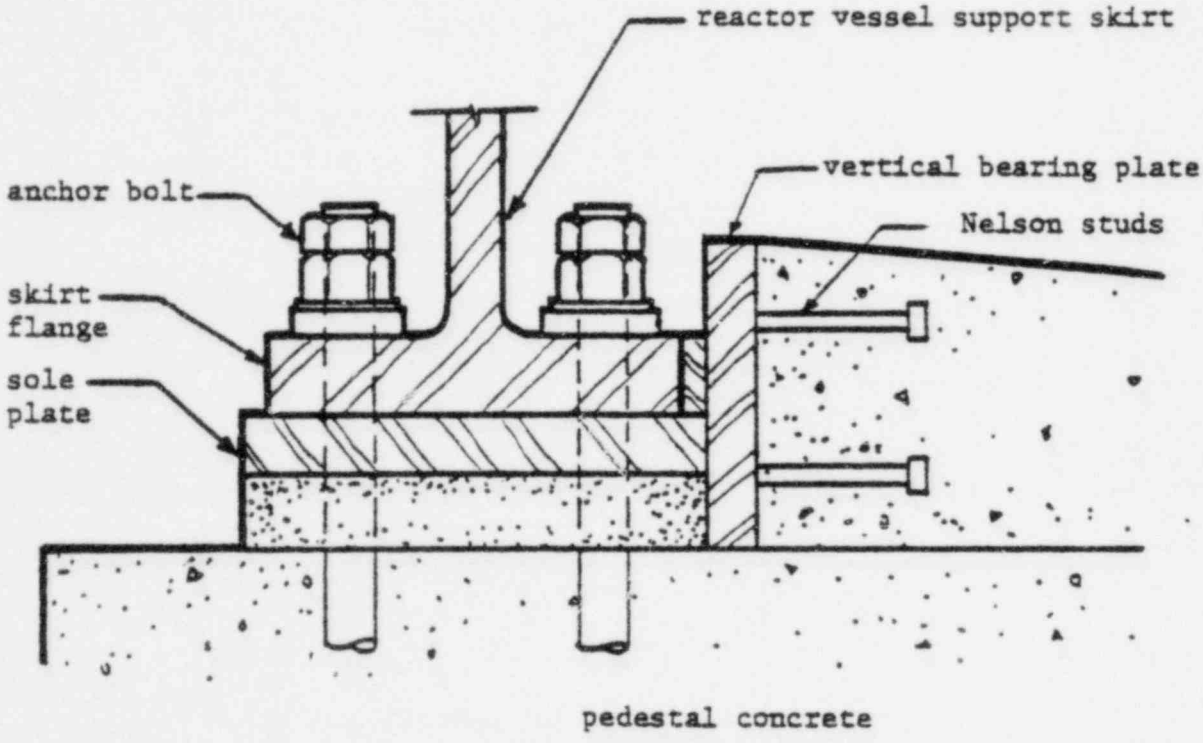

Figure K-3. Vertical Section Through Davis Besse Support Beam

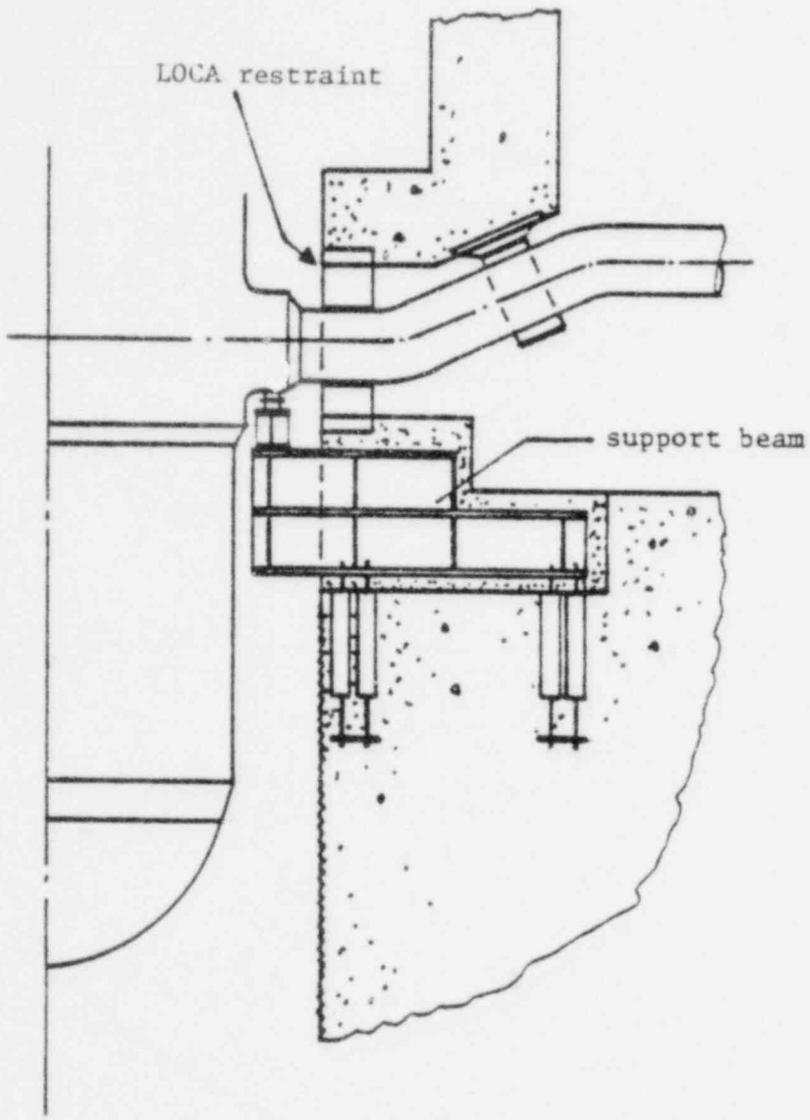

Figure K-4. Davis Besse Cold Leg LOCA Restraint

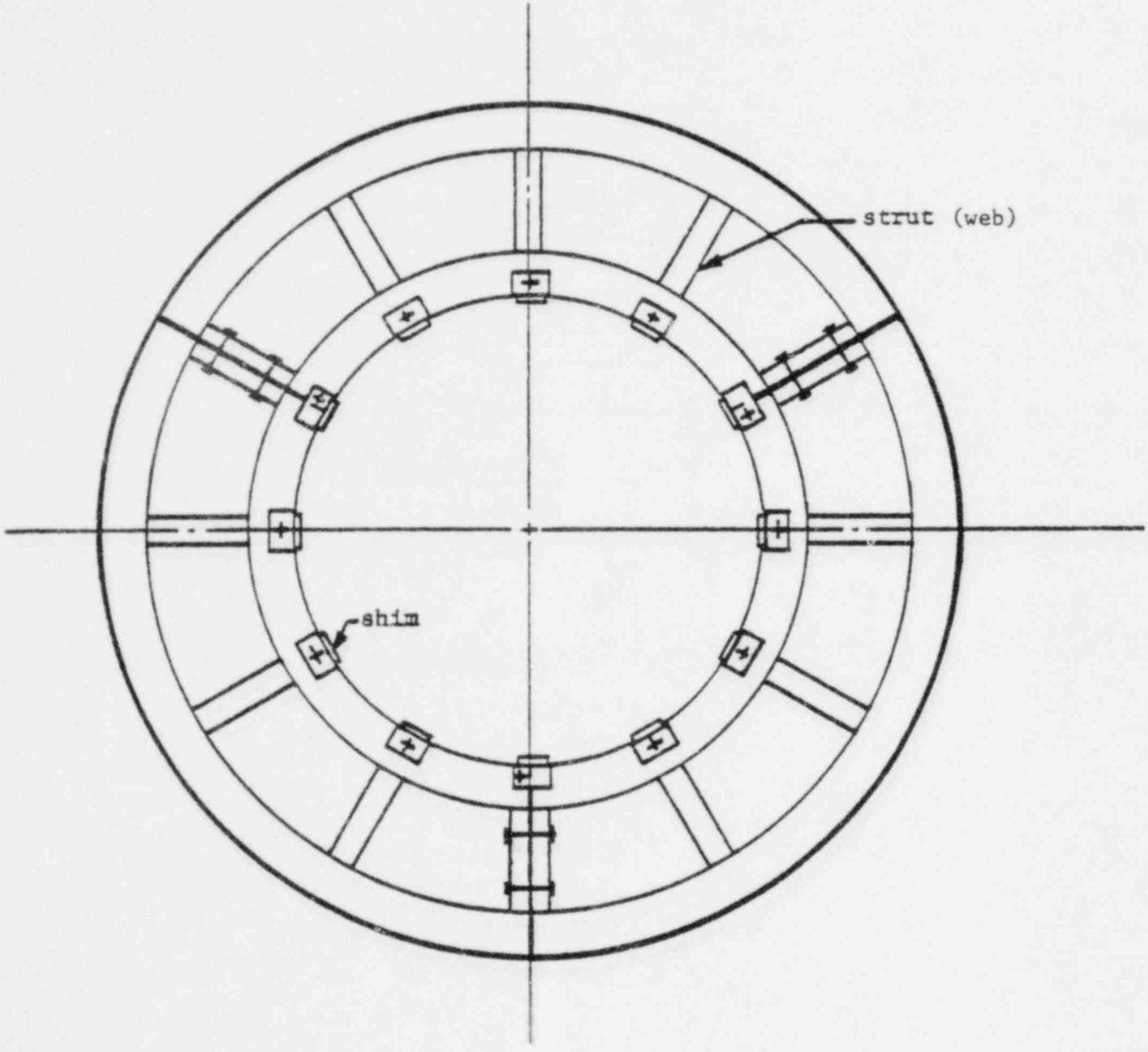

Figure K-5. Generic Embedment Model

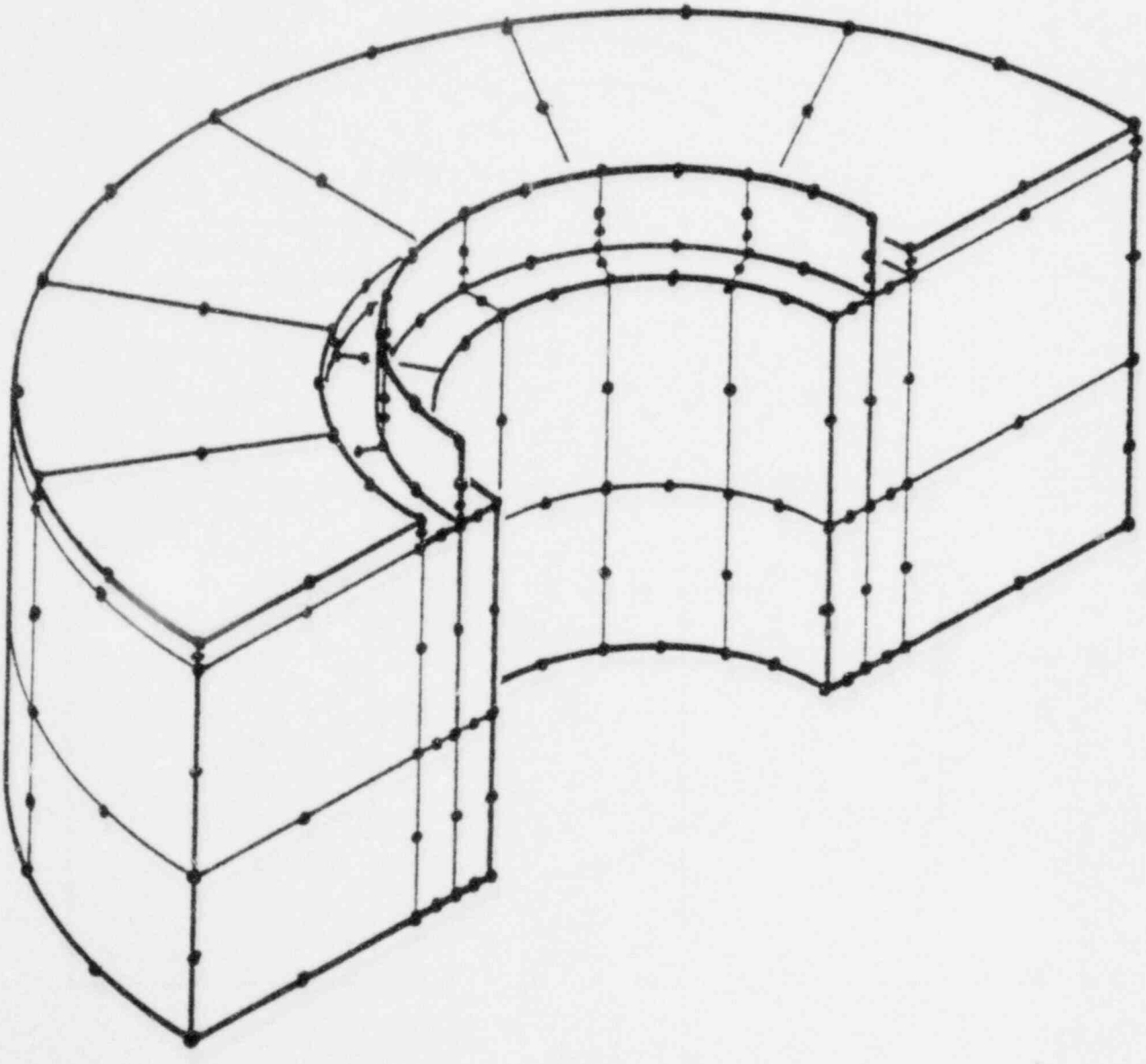

Figure K-6. Generic Embedment Model Sections

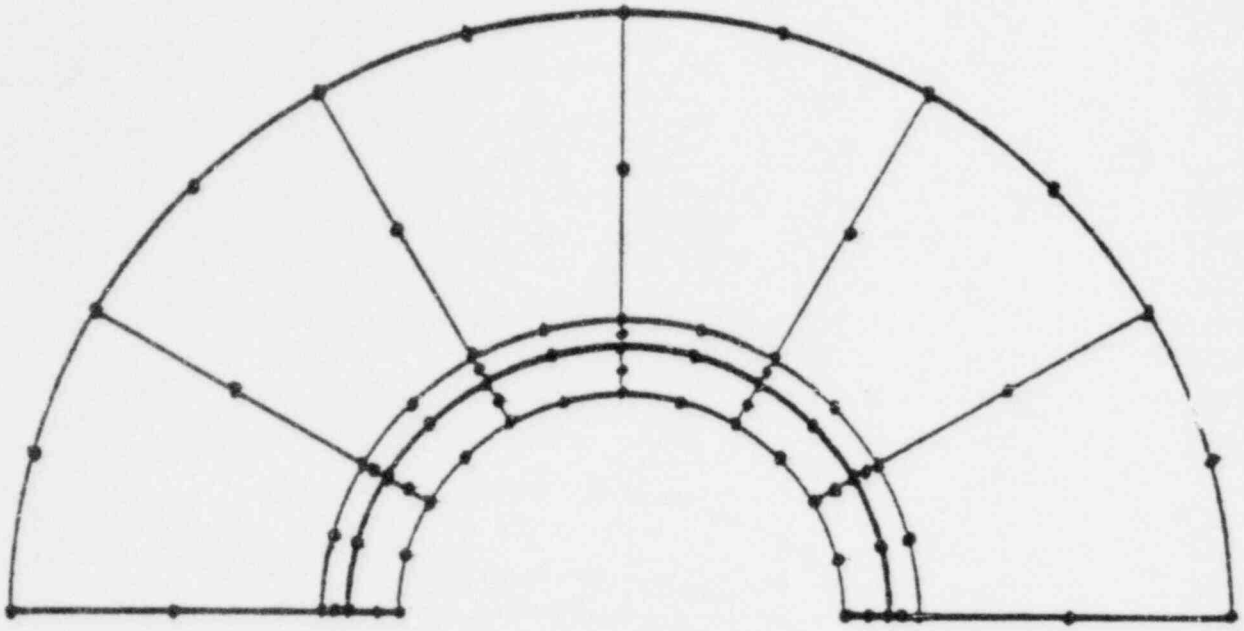

Plan

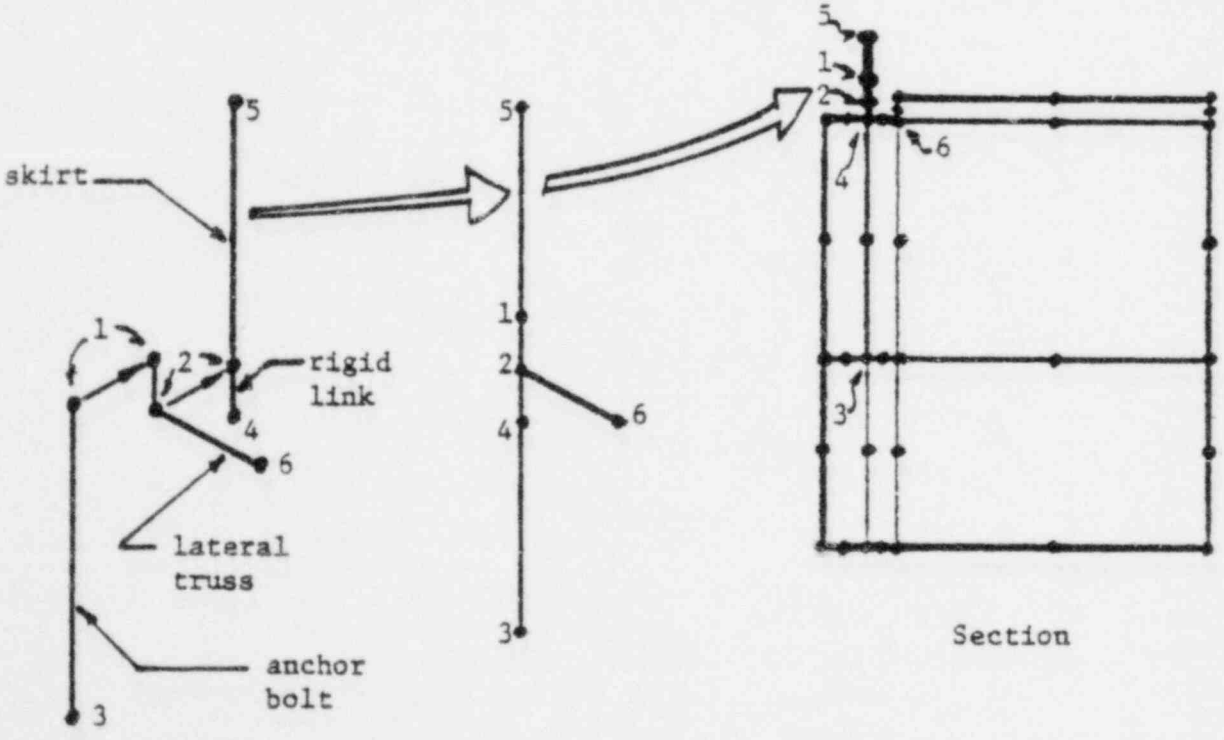

Interface Detail

Section

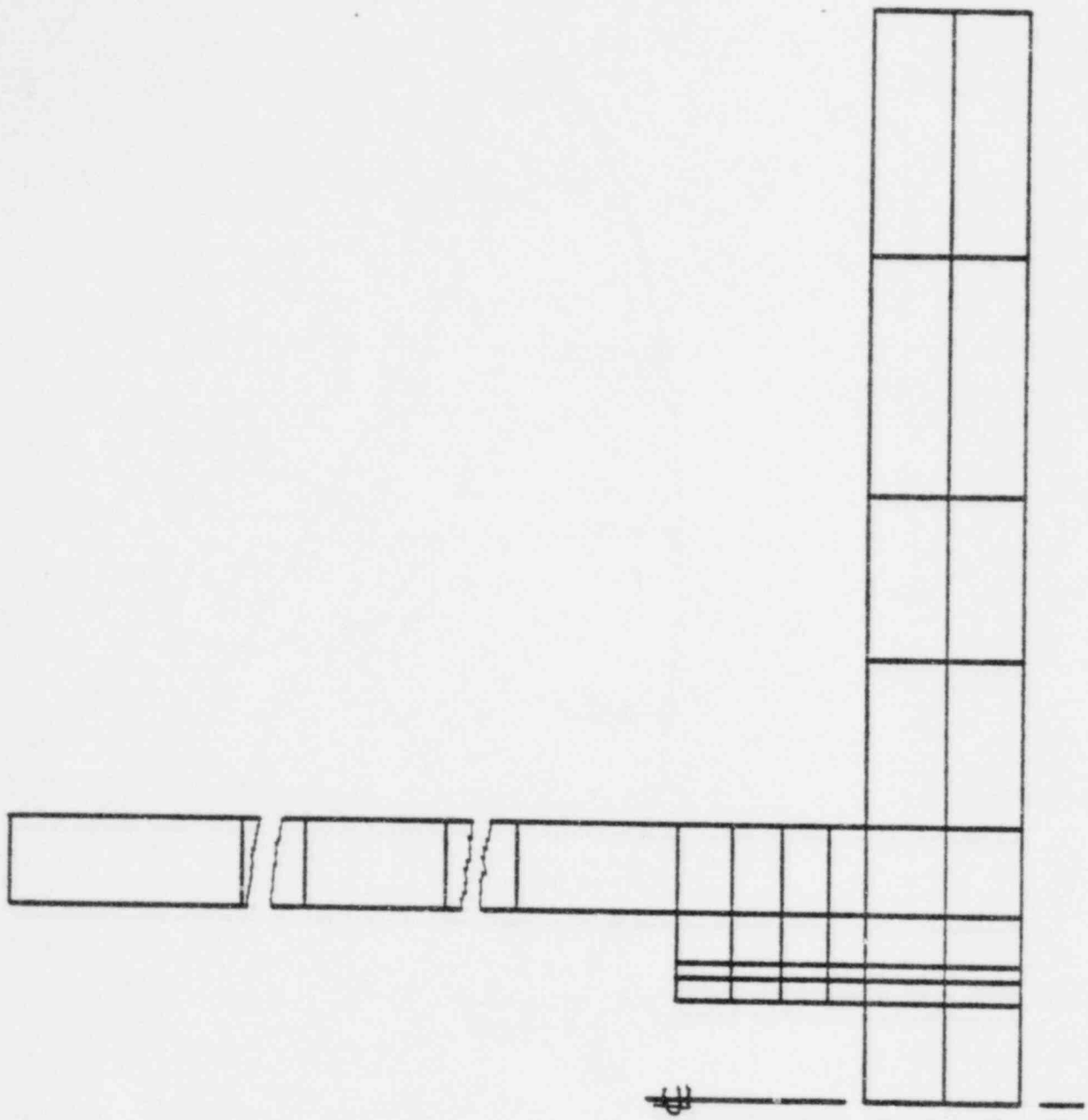

Figure K-7. Axisymmetric Model of Embedment

Figure K-8. Nonlinear Embedment Model

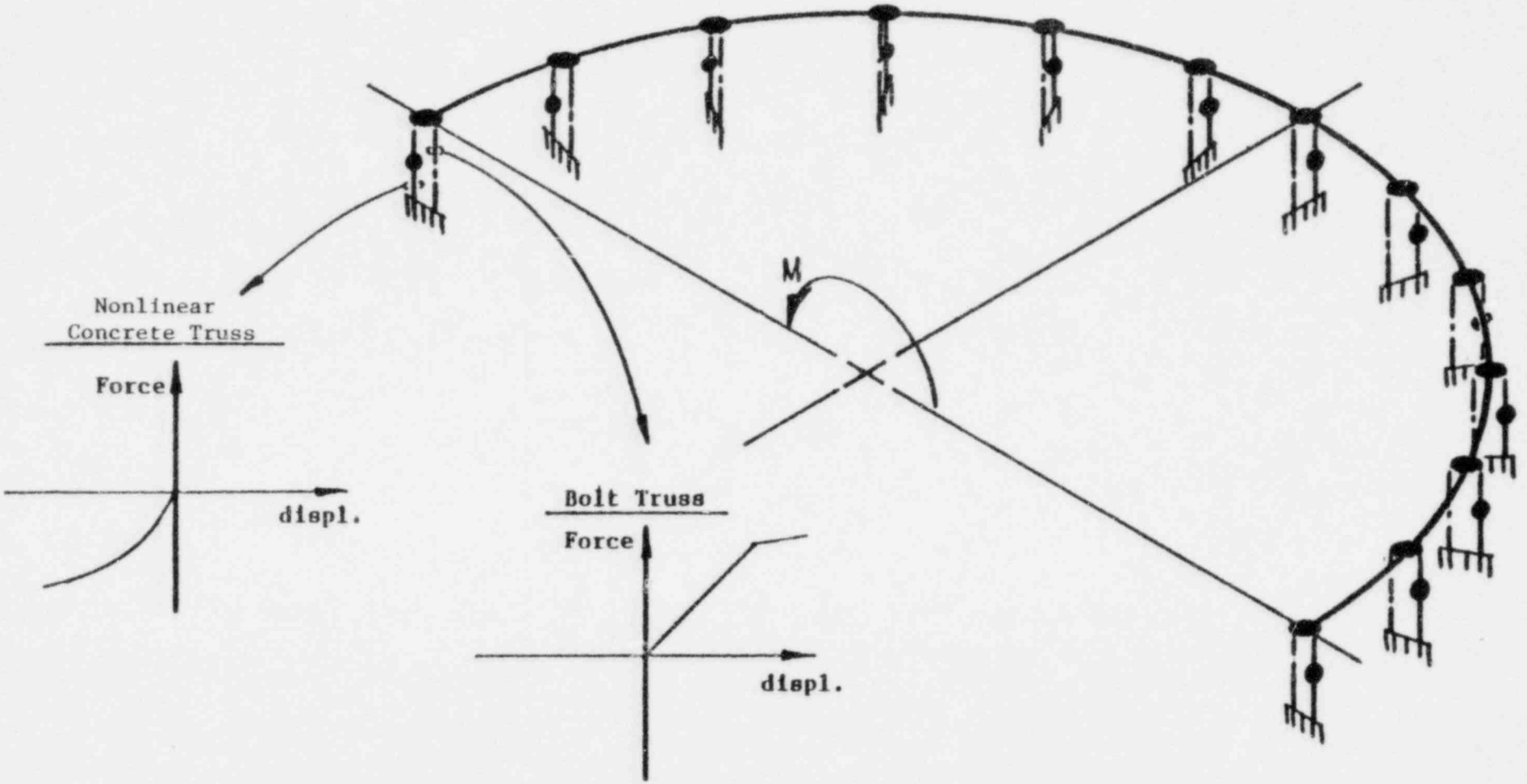

Figure K-9. Embedment Substructure Model

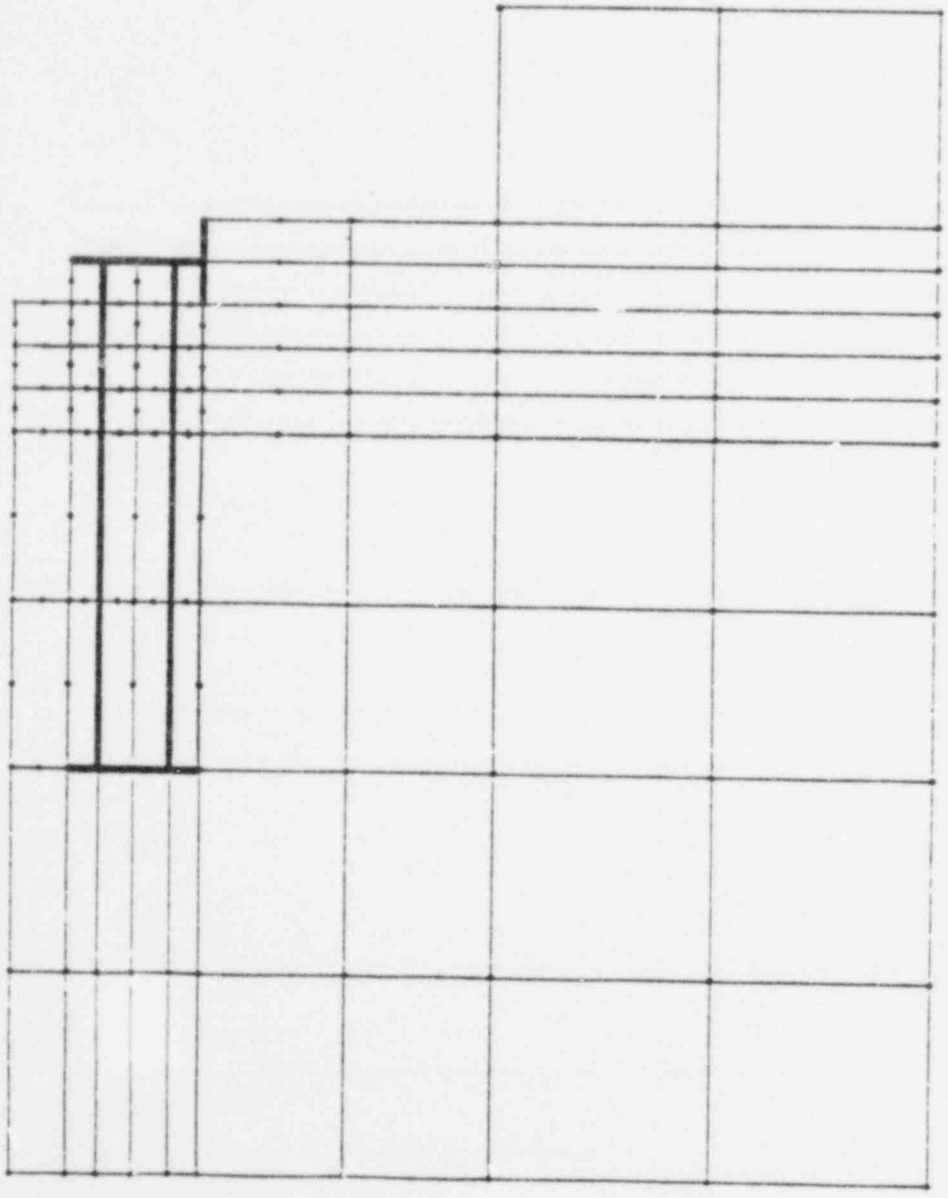

Figure K-10. Assumed Region of Tension Cracking in Generic Embedment Model

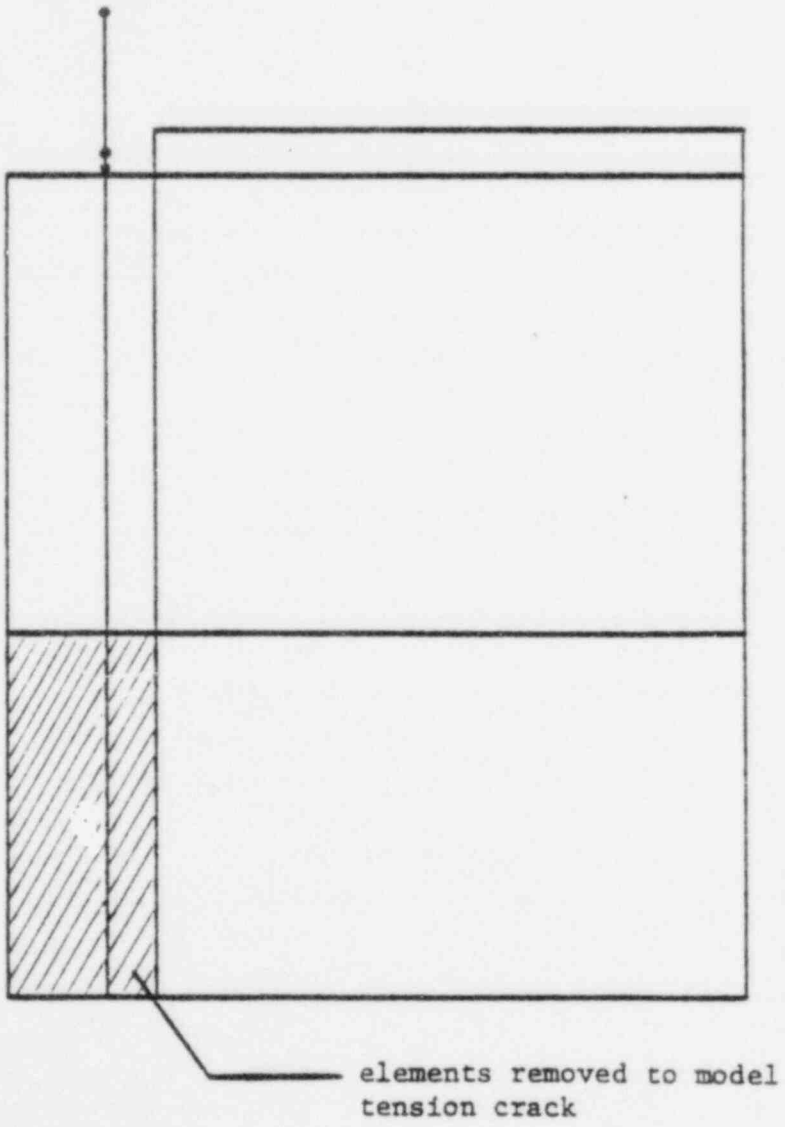

Figure K-11. Davis-Besse LOCA Restraint Model

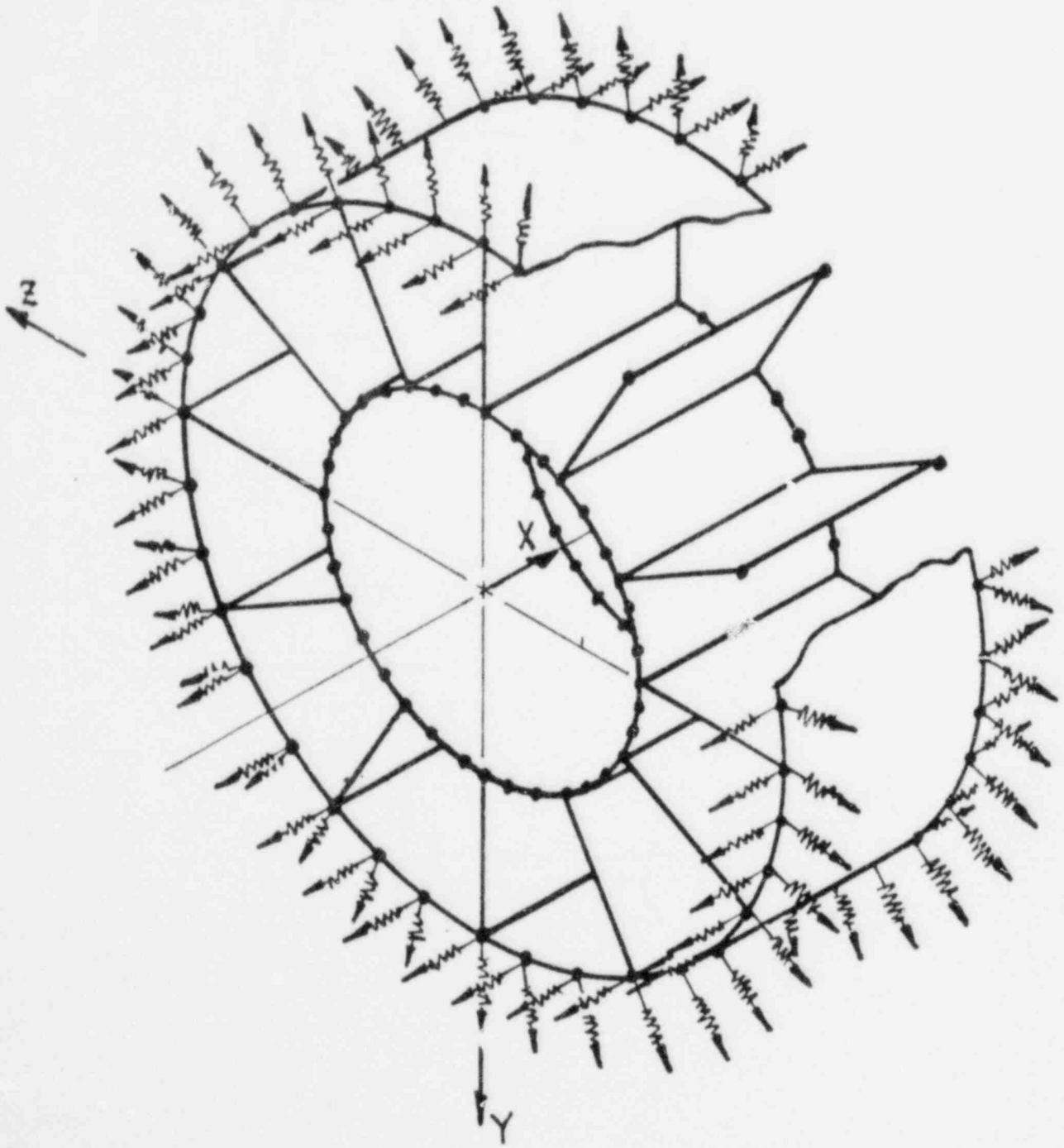

Figure K-12. General View of Support Beam Model

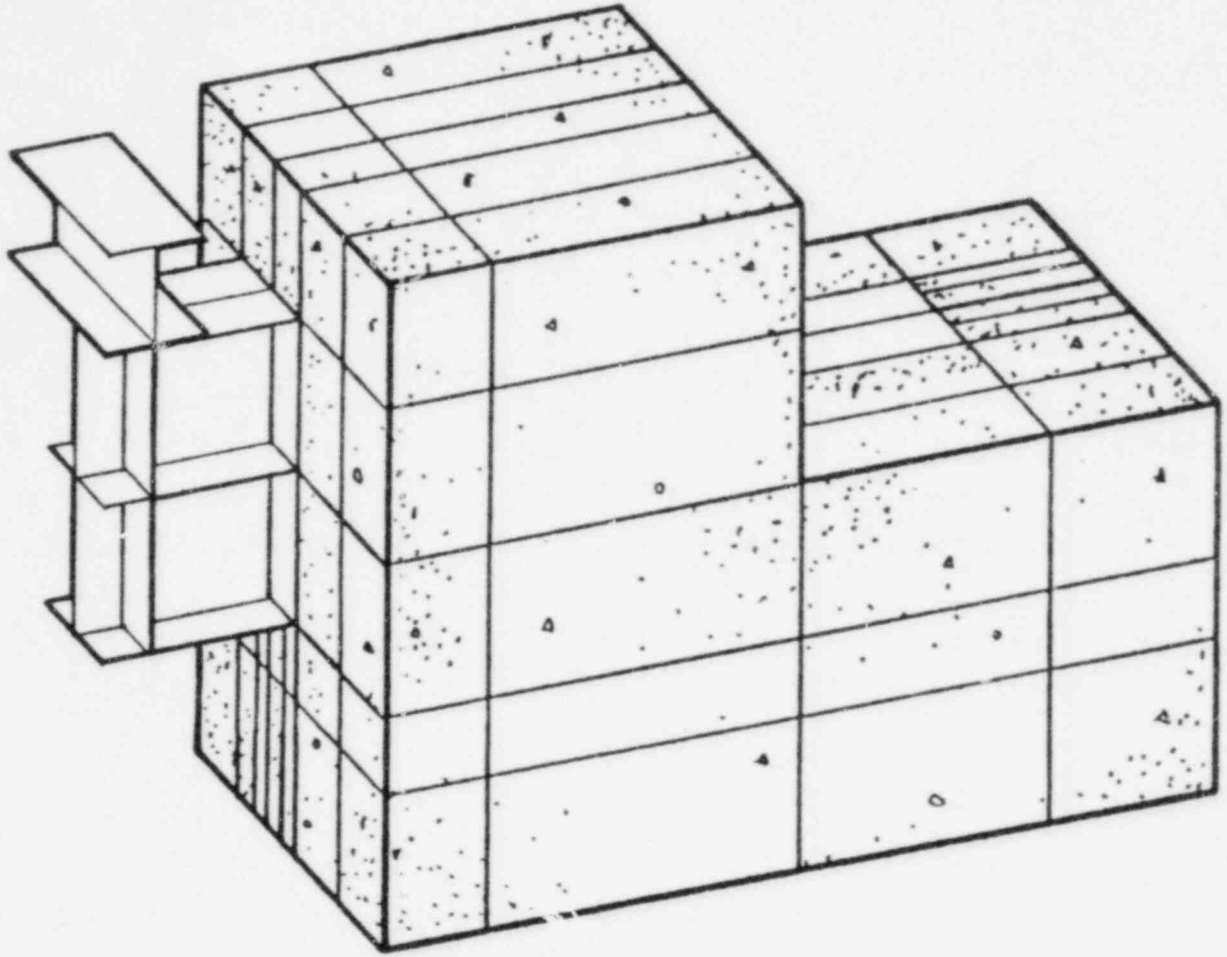

Figure K-13. Davis-Besse Support Beam Model

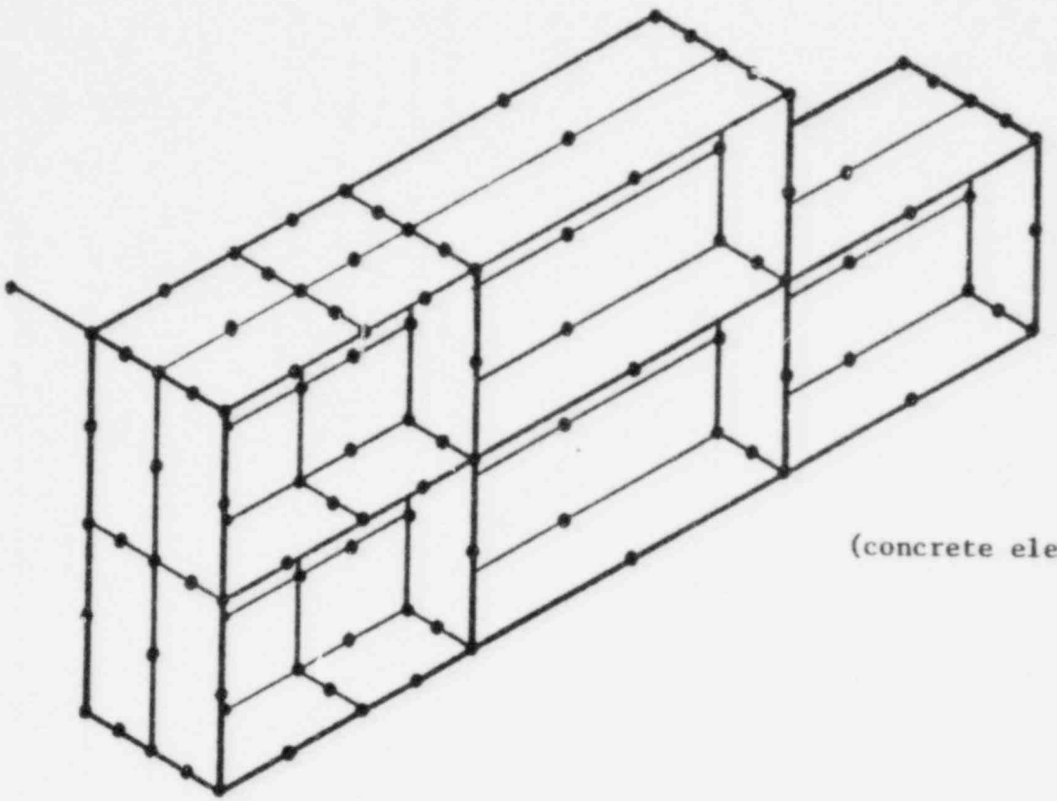

(concrete elements not shown)

Figure K-14. Elastic Spring Rates for Skirt-Supported Plants: Lateral Force Translation

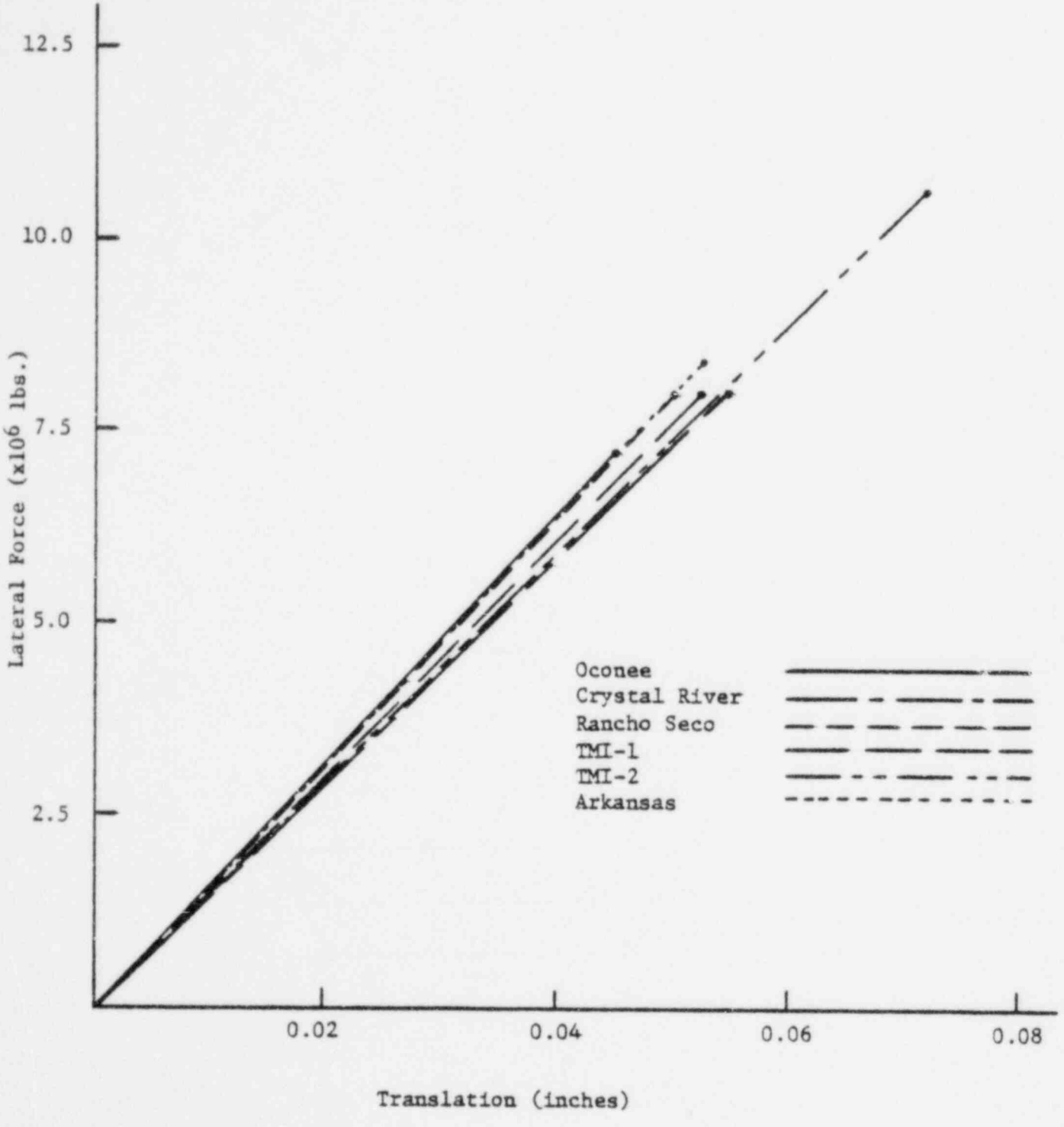

Figure K-15. Elastic Spring Rates for Skirt Supported Plants: Moment-Rotation

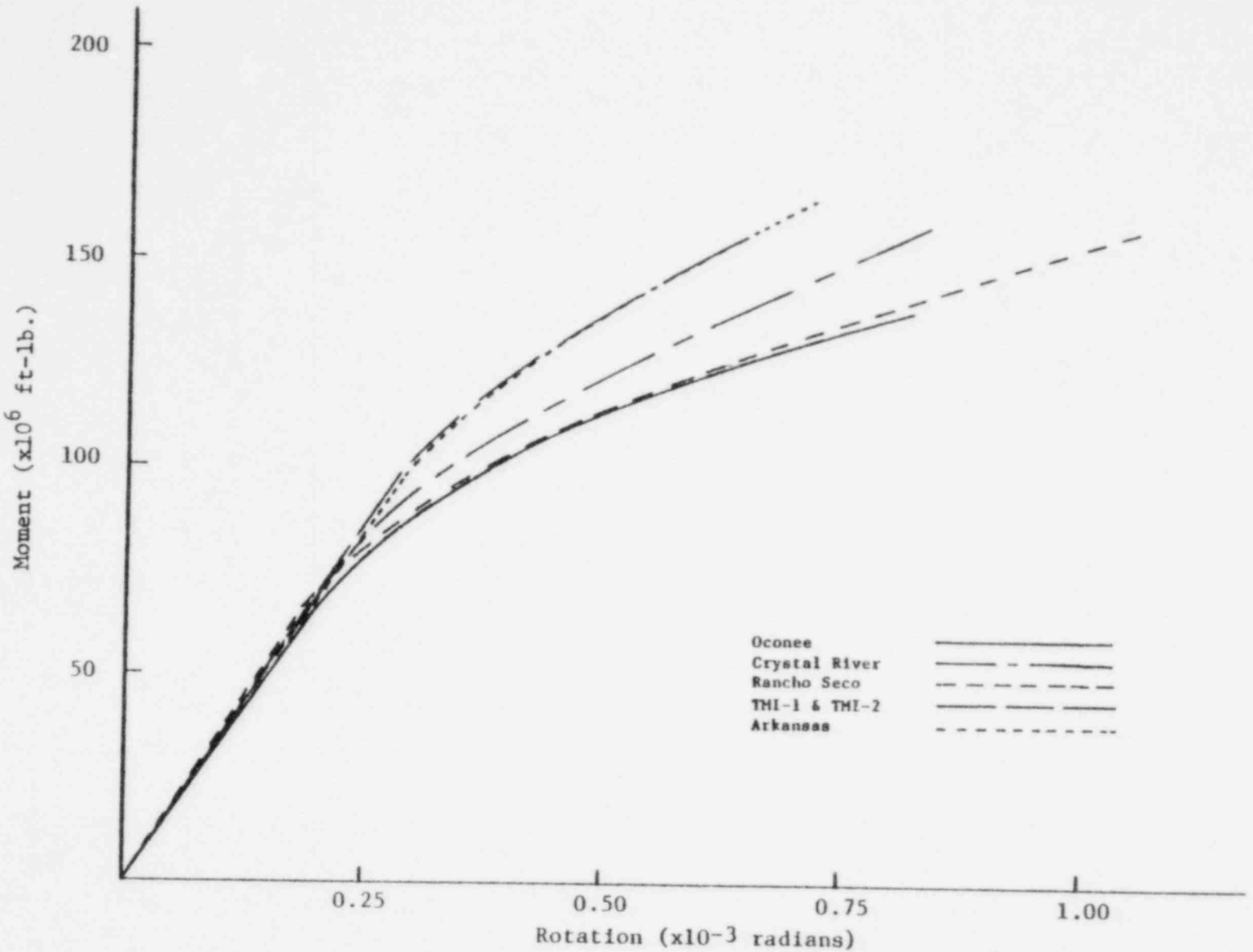

Figure K-16. Spring Rate for Davis-Besse Cold Leg LOCA Ring: Load Deflection

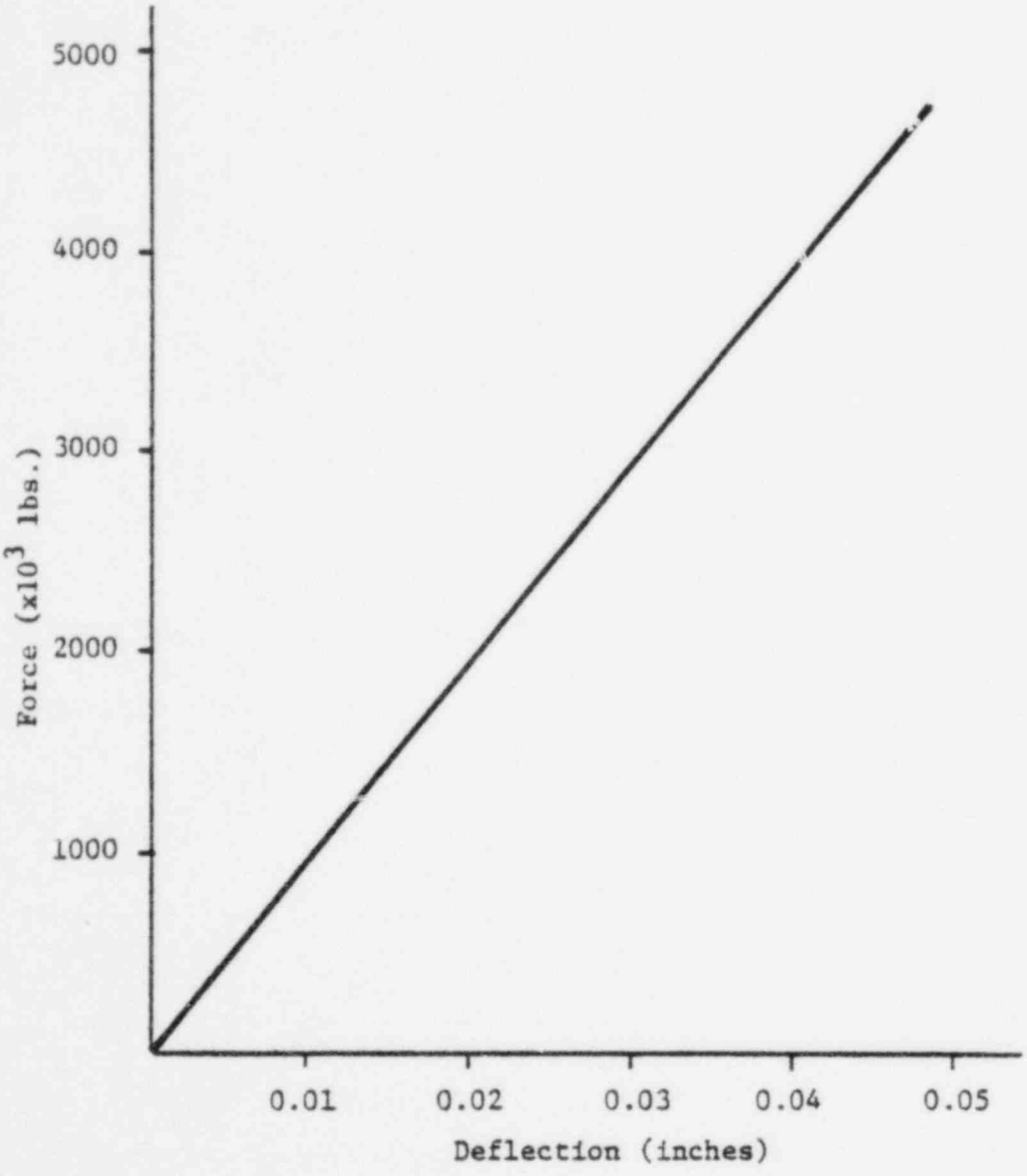

Figure K-17. Vertical Spring Rate for Davis-Besse Support Beam: Load Deflection

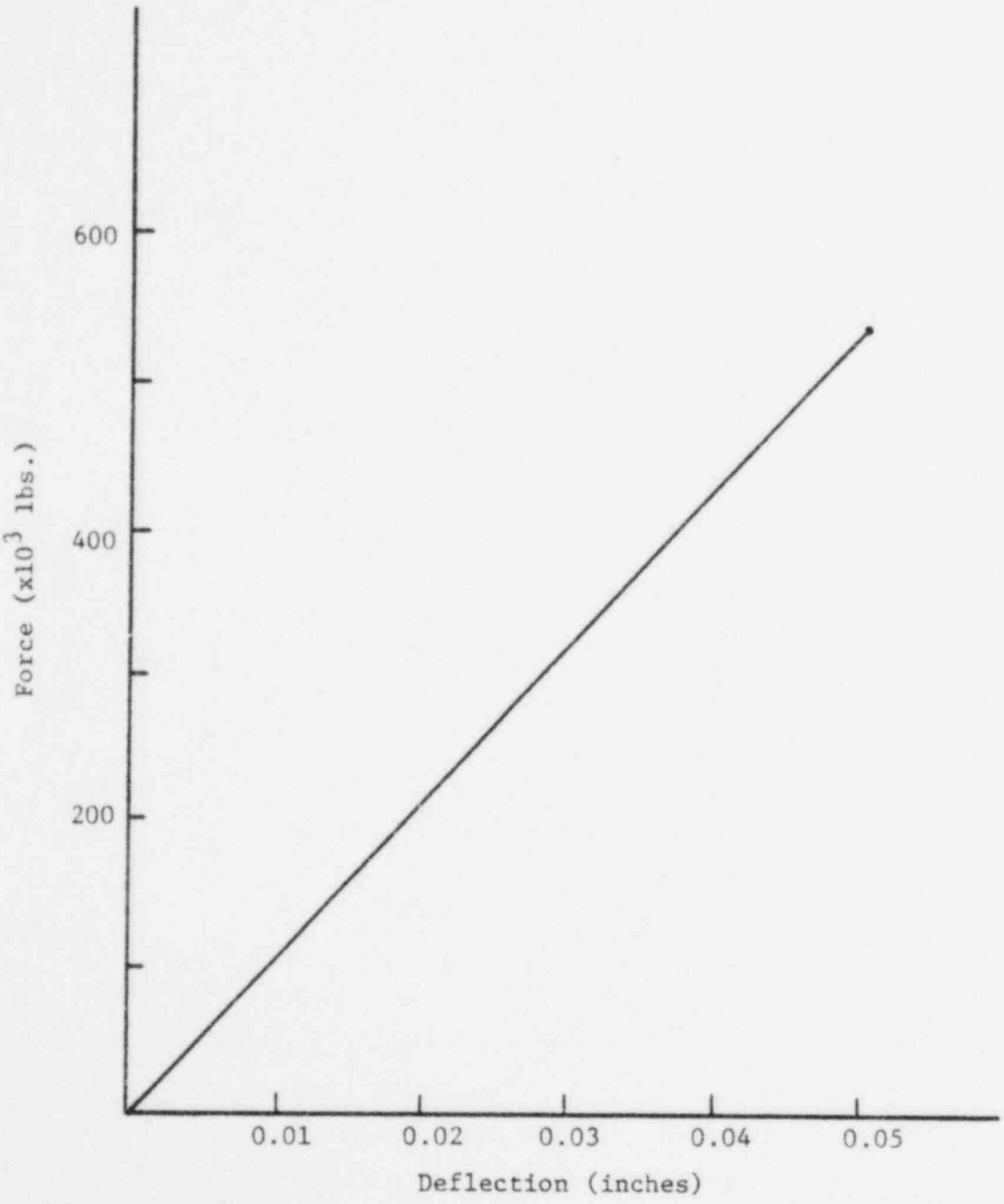

Figure K-18. Horizontal Spring Rate for Davis-Besse Support Beam: Load Deflection

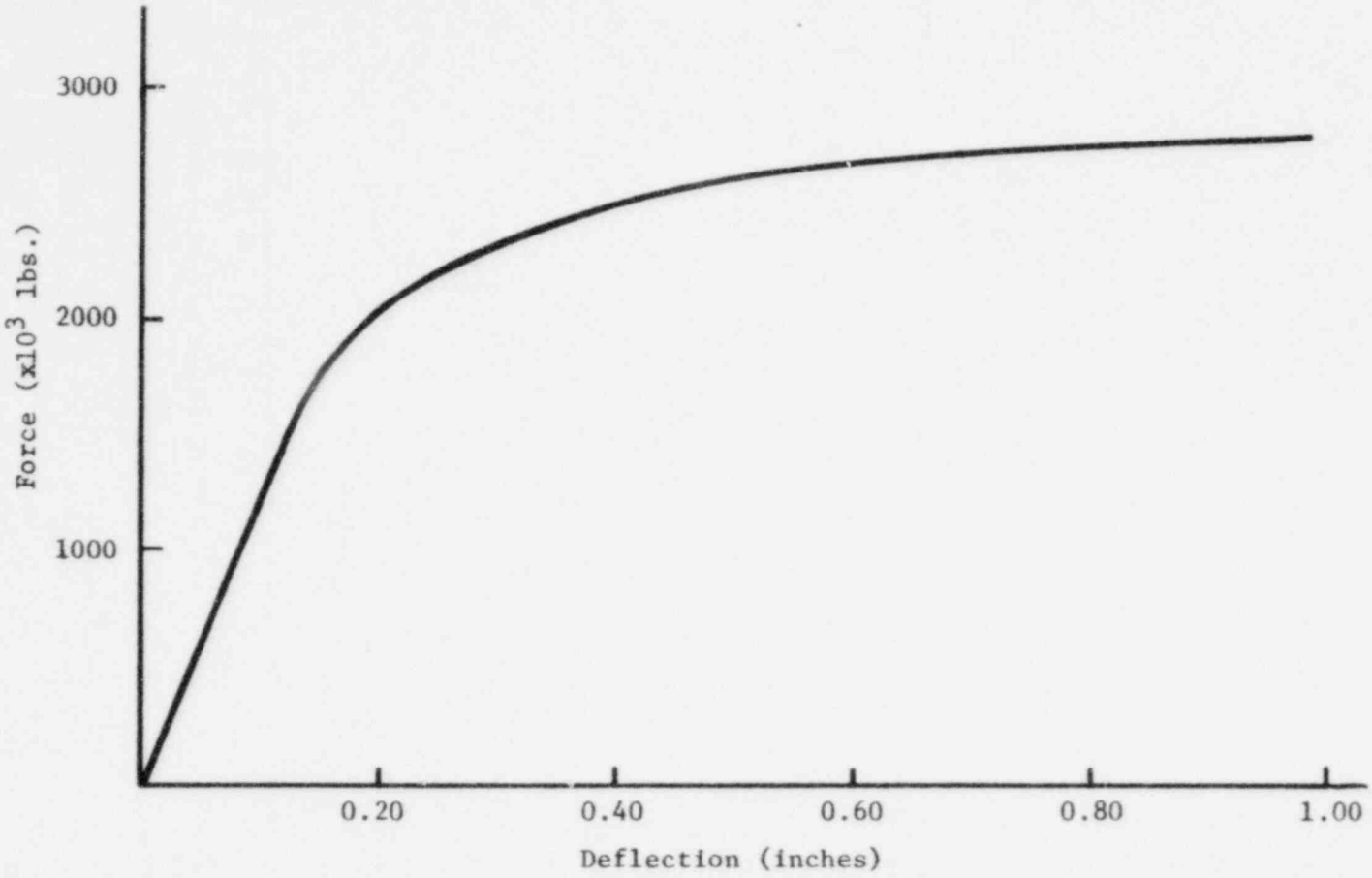

APPENDIX L

Finite Element Structural Model of Reactor Vessel Service Structure

An initial evaluation of the service structure assuming a very conservative load distribution resulted in the identification of several overstressed areas. In order to address the obvious redundancy of the service structure and to achieve a realistic load distribution, a finite-element analysis was conducted. It was determined that the model should concentrate on the overstressed areas — the gussets and their attachments — and provide only forces at these locations. This allowed for the construction of a somewhat simplified model. The NASTRAN computer code was selected for the analysis.

Since the service structure, shown in Figures L-1 and L-2, is redundant and asymmetric, it was necessary to model the complete configuration of plates, channels, and gussets on top of the shell. This would provide an accurate load path and geometric representation of the structure. The critical areas are located above the shell that attaches the service structure to the reactor vessel. The load must be transferred to the shell and then to the reactor vessel. Since the shell is not overstressed for the full LOCA loads, it need not be included in the model. Therefore, the top of the shell was assumed to be ground.

MPC and SPC equations were used to connect and restrain the motions at the structural interfaces. MPC (multipoint constraint) equations tie together in a mathematical relationship the rotations and translations of two points. They were used to tie bolted connections together. SPC (single-point constraints) were used to identify points that have no rotation or translation, such as channels welded to the shell.

Quadrilateral plate elements (QUAD-4) were used to model the perforated seismic tie plates. The plates contact each other physically and are captured on the perimeter by a backing angle. Each plate is modeled separately and properly attached to the corners by MPC equations. The plate thickness used in the model was an equivalent thickness that accounts for holes in the plate.

Simple beam elements (CBAR) were used to model the channels. The channels were attached via MPC equations to the seismic tie plates and attaching channels and fixed via SPC equations to the shell.

Linear scalar spring elements (CELAS-2) were used to model the stiffness of the gussets. Since the gussets vary in size and shape, the stiffness was

calculated for each one by determining an equivalent rectangular plate and treating it as a uniformly loaded cantilevered beam. The CELAS-2 elements, representing the gussets, attach the channels to the shell.

The model was loaded by applying the resultant force of the control rod drives equally to the four corners of each of the 69 seismic tie plates. The model generated a distributed load and provided forces at the gusset locations.

Figures L-3 and L-4 provide undeformed and deformed planar views of the service structure model. The deformed shape due to the CRDM loads is intuitively obvious and demonstrates that the applied loads and boundary conditions are properly specified.

Figure L-1. Side View of Service Structure

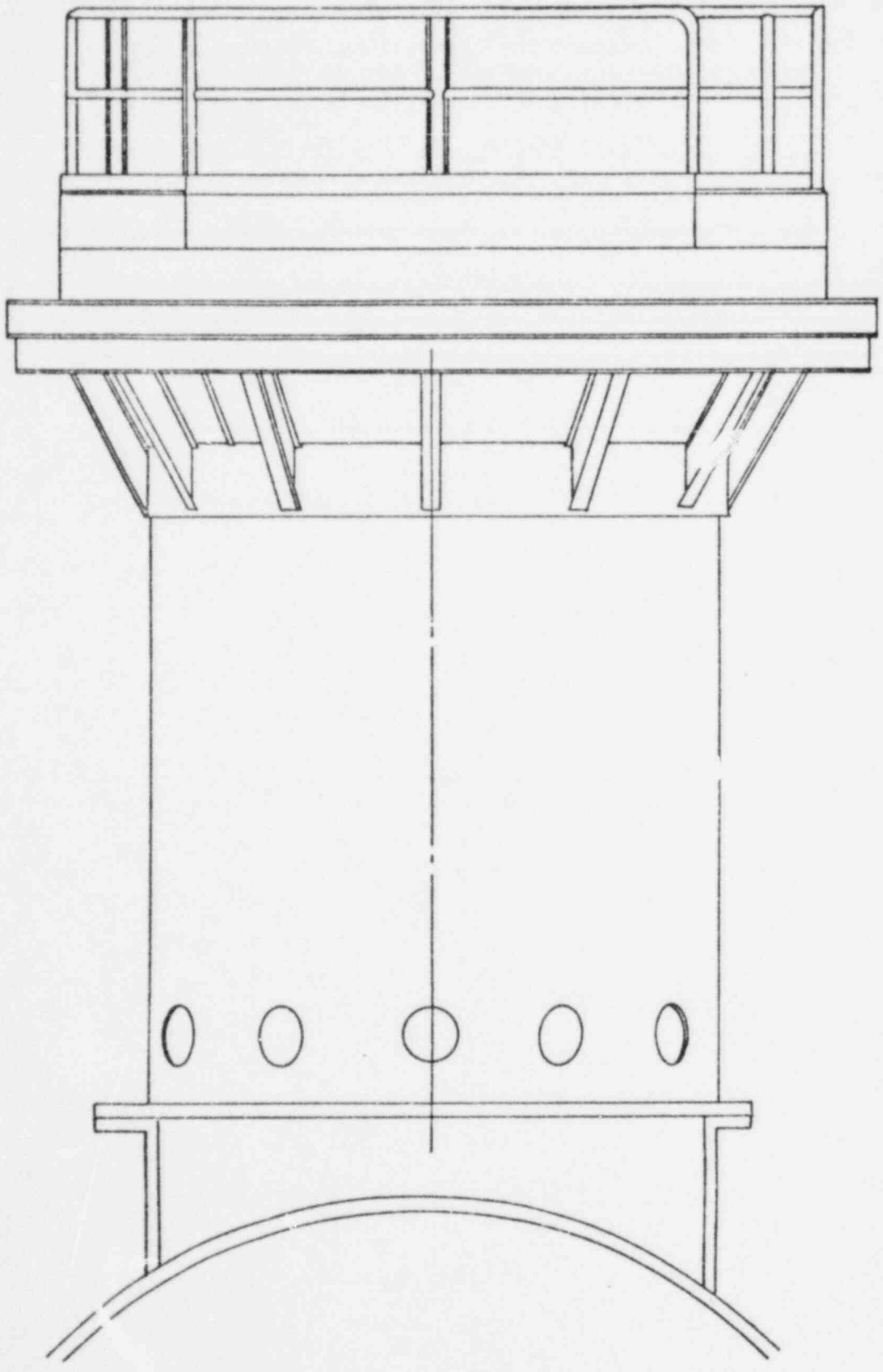

Figure L-2. Plan View of Service Structure

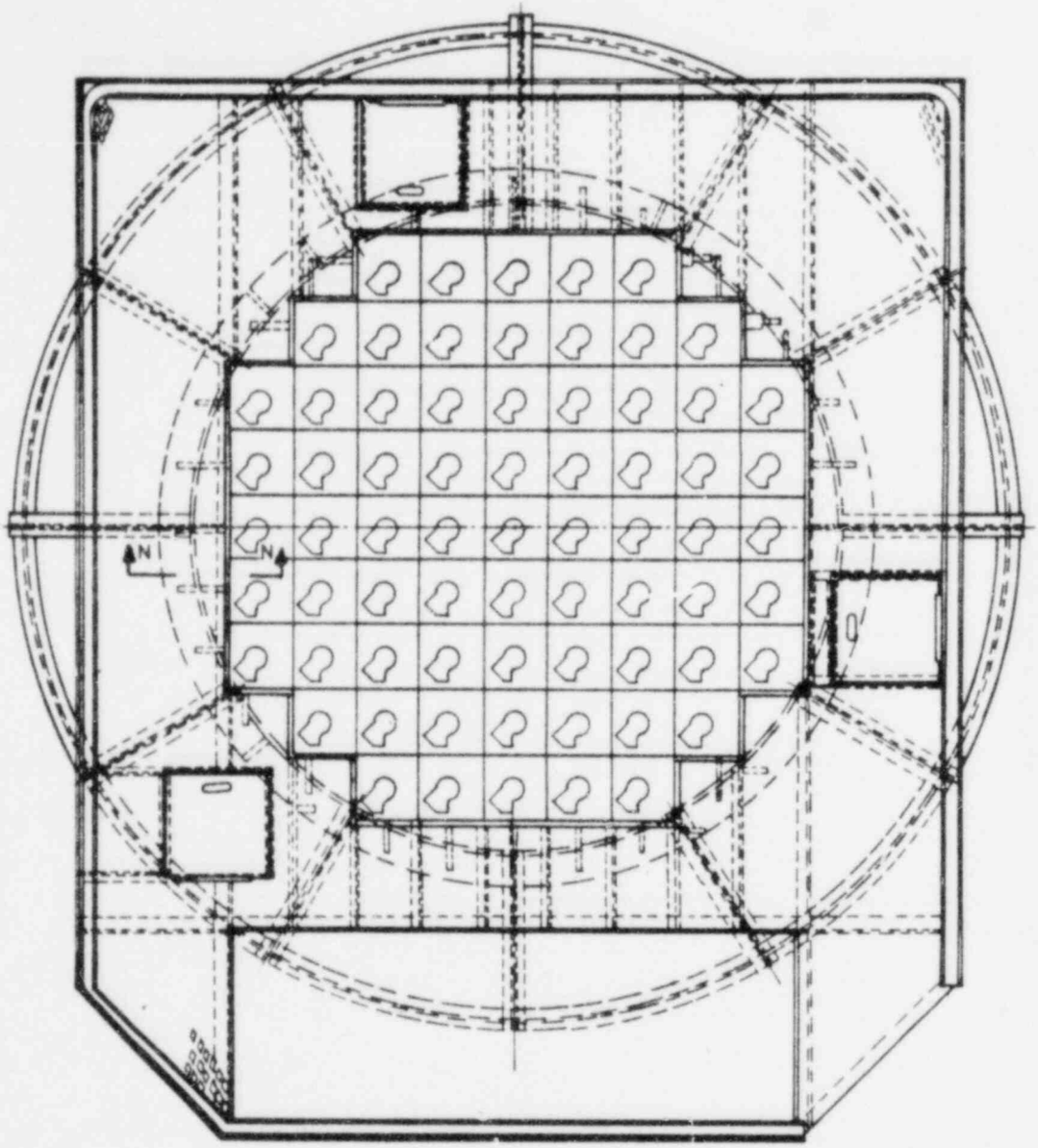

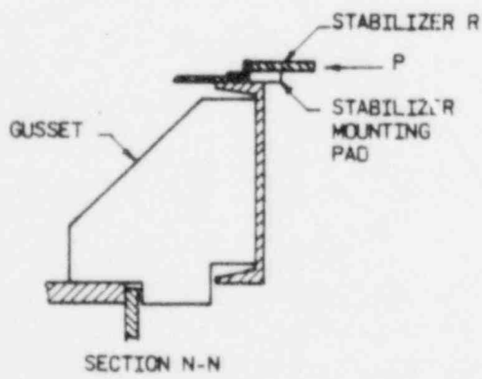

Figure L-3. Undeformed Plot of Service Structure Model

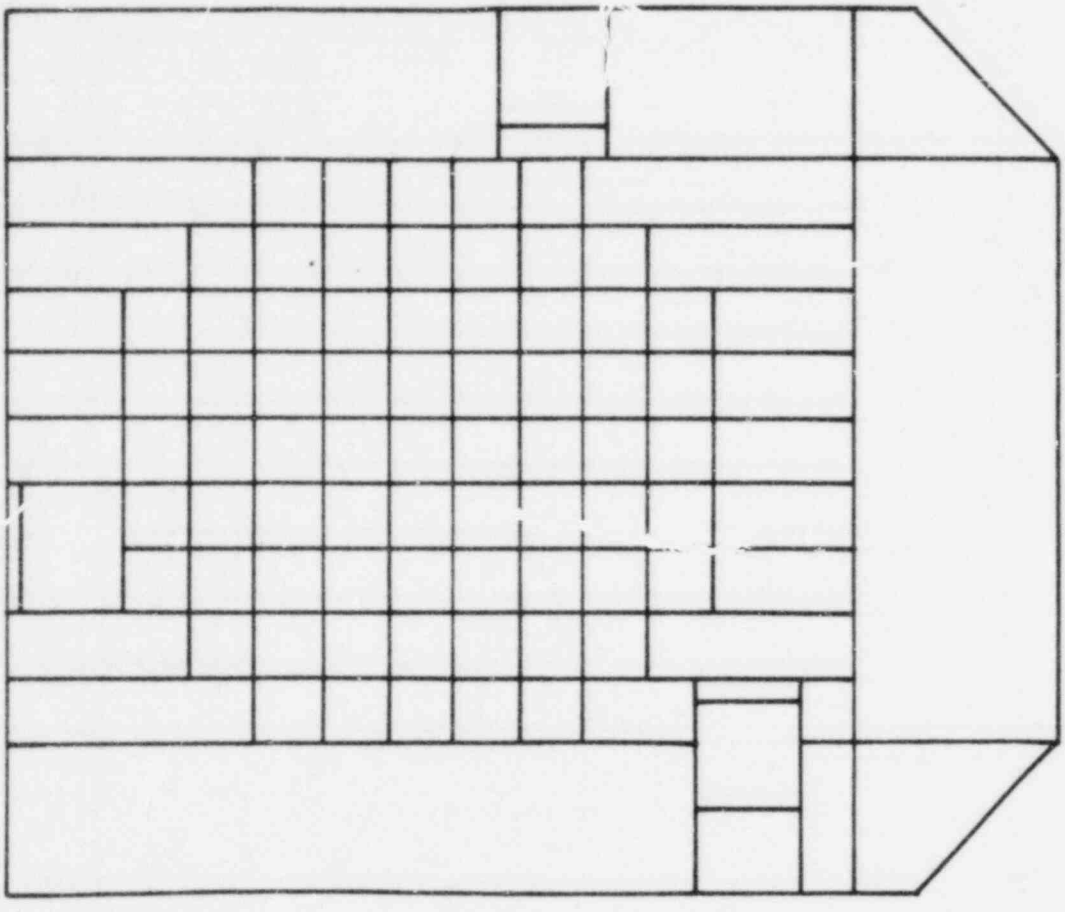

Figure L-4. Deformed Plot of Service Structure Model

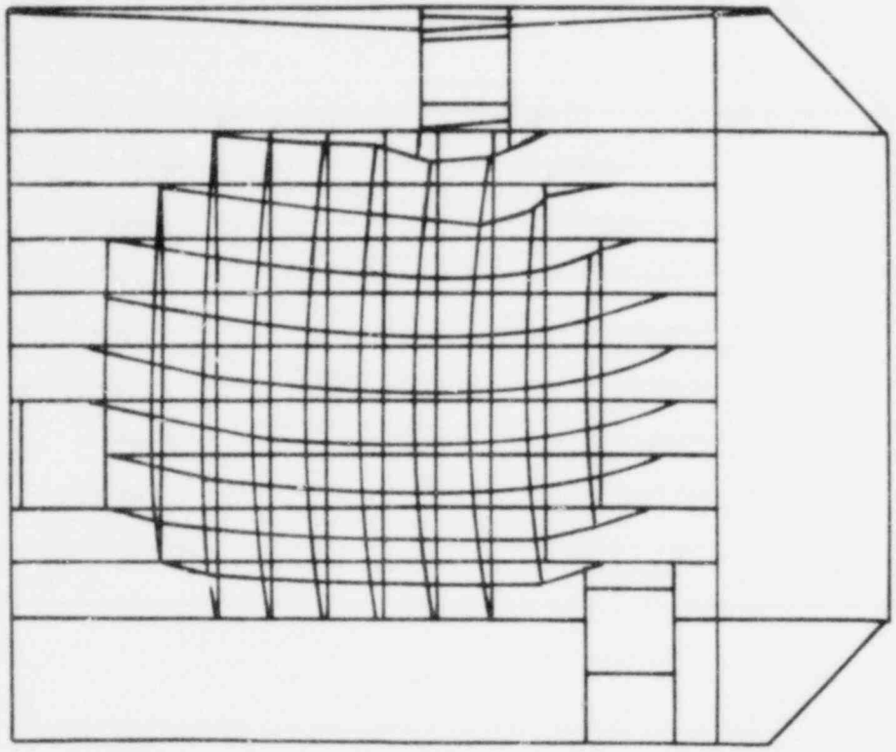

APPENDIX M

Dynamic Model Description for Control Rod Drive Mechanism (CRDM)

The dynamic model was developed to investigate the response of the CRDM to LOCA excitation. The ANSYS Code was used to construct the numerical model used in the analysis.

The model basically consists of concentric elastic pipe elements interfaced with gap elements. At those locations where the gaps are very small, direct coupling is used. Figure M-1 shows a typical region of the drive and how the components are coupled in the model. At appropriate axial locations, sets of four gap elements are placed circumferentially between concentric components. Thus, when two components come together at any point around their circumference, interactive forces are set up tending to push the pieces apart. While the exact gap widths are modeled accurately along the horizontal coordinate directions, any movement at some angle to these coordinates will produce an effective gap larger than specified. This is a conservative approximation as it will lead to somewhat more bending than is actually experienced.

Figure M-2 shows the complete dynamic model as it was used in the type A CRDM analysis. The model for the type C CRDM is similar. Each of the major components of the model (the leadscrew, the support tube and thermal barrier, the roller assembly and segment arms, the torque tube, and the motor tube) is formed from elastic elements whose length, radius and thickness are determined by the geometry of the corresponding drive section. Table M-1 defines those ANSYS elements used in the analysis along with their properties and uses.

Table M-1. Type of Elements Used in ANSYS Model

ANSYS STIF No.	Element Description	Use
9	Three-dimensional pipe — this element has tension compression, torsion, and, bending capabilities. It is defined by two nodes (one at each end of the pipe section), wall thickness and pipe radius, and has six degrees of freedom per node (three translational and three rotational).	This pipe element is used to model the concentric components of the CRDM, e.g. the motor tube, and leadscrew.
17	Point mass — this has a defined mass but no geometry specifications. It has three translational degrees of freedom.	The point mass was used to model certain components (such as the position indicator) which do not contribute any significant structural rigidity.
40	One-dimensional dynamic element — this has a combination of spring and damper in parallel coupled to a gap in series (only the gap was utilized in the analysis).	The dynamic (gap) element was used to model the effects of the interacting concentric components (e.g., the torque tube hitting the motor tube).
50	Super element — this is a user-constructed element and is composed of appropriate assemblies of standard ANSYS elements. In effect, the stiffness and mass matrices for complex system components can be created and stored on tape prior to the analysis.	Super elements were created for: (1) the leadscrew, (2) the support tube to the thermal barrier, (3) the roller assembly and segment arms, (4) the torque tube, and (5) the motor tube.

Figure M-1. Development of Gapped-Element Model

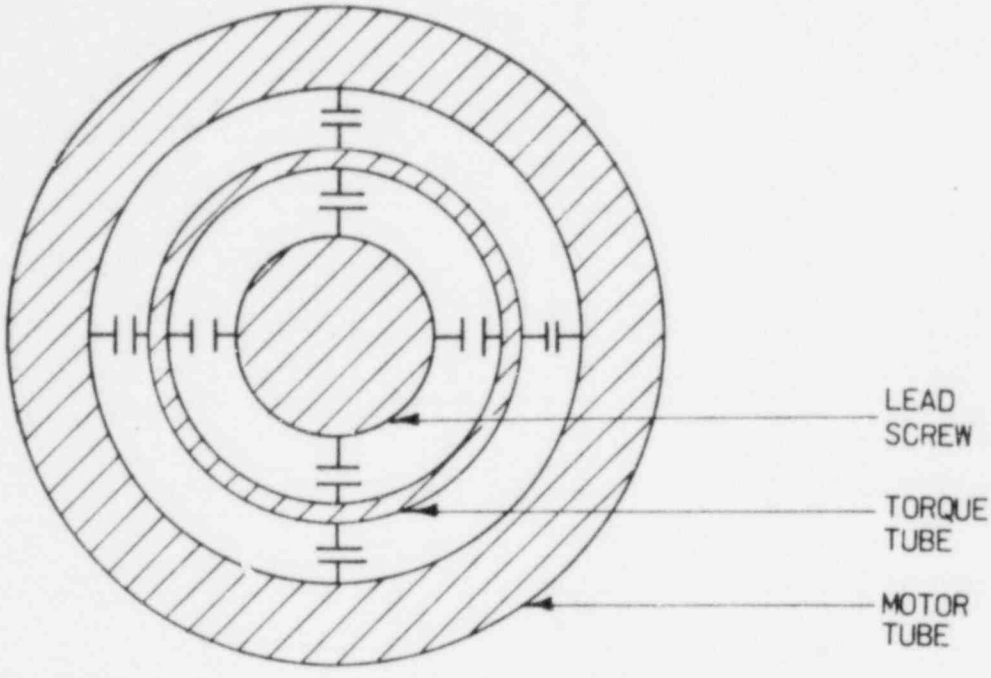

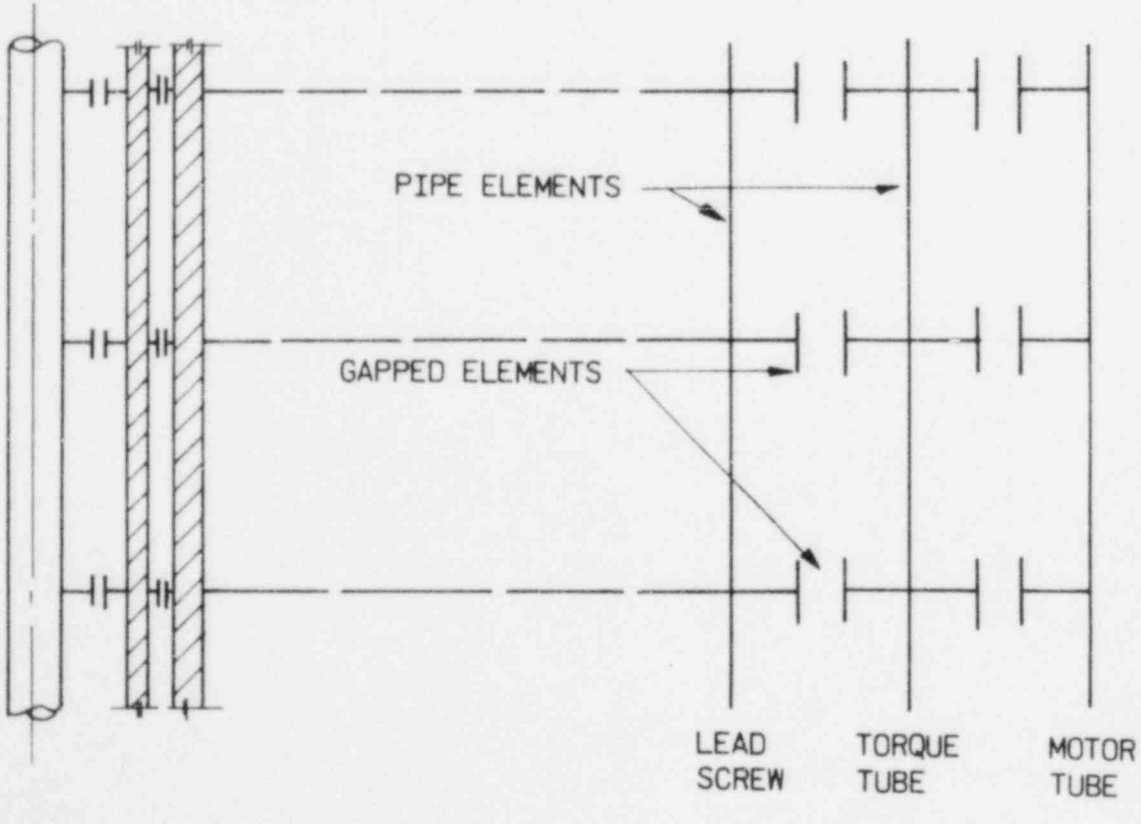

Figure M-2. ANSYS Dynamic Model of Type A Drive

NODE	DESCRIPTION
1-25	LEADSCREW
51-55	LEADSCREW SUPPORT TUBE
55-59	THERMAL BARRIER
59-62	SPACER, THRUST BEARING
75-79	ROTOR ASSEMBLY
101-109	TORQUE TUBE
178-179	FICTITIOUS ELEMENT
179-181	FICTITIOUS ELEMENT
181-301	NOZZLE
301-337	MOTOR TUBE

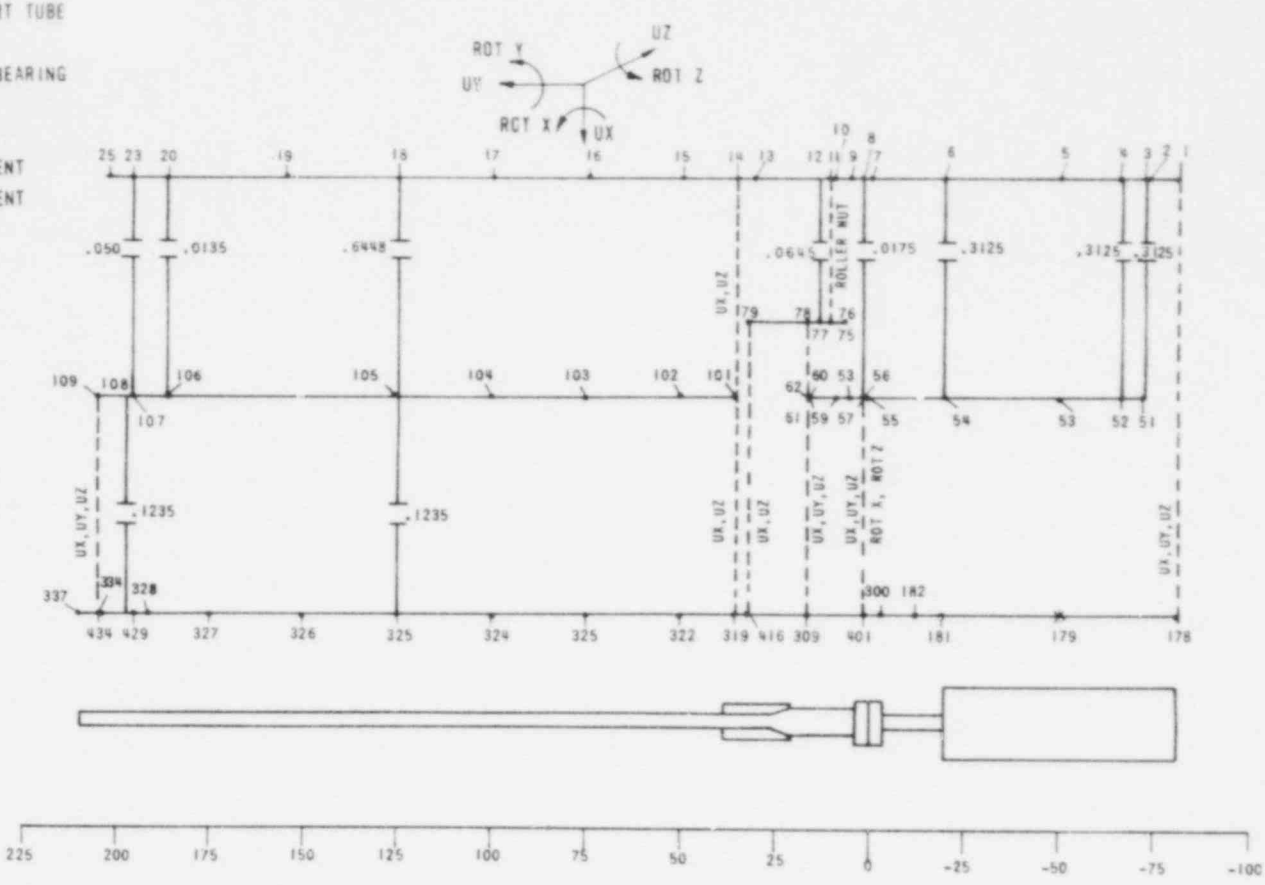

LEGEND

GAP ELEMENT
(RADIAL GAP SHOWN

COUPLING IN DIRECTIONS SHOWN EXCEPT WHERE ALL SIX D.O.F. ARE COUPLED

NOTE ⁽¹⁾ - POINTS WHERE LOCA DISPLACEMENT TIME HISTORY IS APPLIED

APPENDIX N
Computer Codes

STARS

The STARS computer code calculates the dynamic response of a discrete-mass planar model idealized by an assemblage of one-dimensional finite elements, i.e., elastic beam members with shear and bending stiffness and nonlinear inelastic spring elements, which may be gapped. The code monitors and accumulates the permanent deformations in the nonlinear springs and accounts for impacting. Ten types of spring elements are provided in the STARS code element library, in addition to the elastic beam elements. STARS is flexible with respect to the geometry, since the structural system is synthesized from compatibility requirements defined by the user.

The dynamic equations of motion of the discrete-mass system are formed and the coupled response is obtained in steps corresponding to specific instants of time. At a given time, the motions are held fixed so that the internal forces can be calculated. Based on the response motion and internal forces at earlier times, the responses at the time in question are predicted. With the predicted values of the motion, the internal forces are recalculated. Using these forces, a new response motion can then be determined. Therefore, at each time step, the relationship between the response motion and the internal forces is satisfied. This process is continued step-by-step throughout the time interval of interest. This numerical method used for this step-by-step solution involves two types of integration formulas. The fourth-order Adams-Bashforth "2/3" predictor-corrector method, which is a stable solution method, is used for the majority of the solution. However, this method is not self-starting, and the fourth-order Runge-Kutta method is used to start the solution process.

In addition to the step-by-step solution of the nonlinear equations of motion, the STARS code provides for the solution of the natural frequencies and mode shapes of the elastic system. The frequencies and modes are obtained by solving the eigenvalue problem using the sweeping technique. This technique uses a power method (i.e., an iterative) and the orthogonality relationships among the normal codes.

CRAFT2

CRAFT2 is a one-dimensional thermal-hydraulic code. It was developed to study the transient behavior of NSS system undergoing a LOCA. It solves the

conservation equation for mass and energy, the continuity equation, and equation of state for water. Fluid properties are obtained from equations that are surface fits to the ASME steam tables. CRAFT2 permits the user to select the nodal representation that results in the best finite differencing of the fluid system to be analyzed. The program uses the conservation equations for each node and momentum equation for each flow path between nodes. Various options as well as user input parameters enable the program to model the core, pumps, vessel, and connecting piping in any configuration and operating mode desired.

ANSYS

The ANSYS general purpose program solves a wide variety of engineering problems more efficiently than most special purpose programs. ANSYS includes capabilities for transient heat transfer analyses including conduction, convection, and radiation; structural analyses including static elastic, plastic, and creep, dynamic, and dynamic plastic analyses, and large deflection and stability analyses; and one-dimensional fluid flow analyses. The output from the transient heat transfer analysis is in the form required for thermal analysis at selected time points in the transient with the same analytical model.

HYDROE

HYDROE computes the hydrodynamic mass matrix for a system of coaxial cylindrical shells coupled by narrow fluid gaps. It is a continuum code based on eigenfunction expansion of the structural mode shapes in terms of the acoustic modes in the annulus.

STALUM

STALUM is a structural analysis code and is discussed in Appendix D.

FTRAN

FTRAN is a data reduction code and is discussed in Appendix D.

S1235

S1235 is a data reduction code and is discussed in Appendix D.

INTFCE

INTFCE is a data reduction code and is discussed in Appendix D.

LOPL

LOPL is a data reduction code and is discussed in Appendix D.

EDS-SNAP

EDS-SNAP is a general purpose program for linear and nonlinear static and dynamic finite element analysis. The finite element system response is calculated using an incremental solution of the equations of equilibrium. In dynamic analysis, implicit time integration (the Newmark or Wilson methods) or explicit time integration (central difference method) can be employed. The incremental solution scheme used corresponds to either an accelerated modified Newton iteration or the BFGS matrix update method.

PWHIP

PWHIP is a finite element analysis program developed to perform nonlinear dynamic time history analysis of three-dimensional structural systems subjected to arbitrary, dynamic, time varying forces. Both inelastic material nonlinearities and geometric gap nonlinearities may be explicitly incorporated.

SUPERPIPE

SUPERPIPE general purpose piping program performs comprehensive structural analyses of linear elastic piping systems for dead weight, thermal expansion, internal pressurization, seismic spectra, arbitrary force time histories, and other loading conditions. Analyses are performed to ASME requirements for Class 1, 2 and 3 systems.